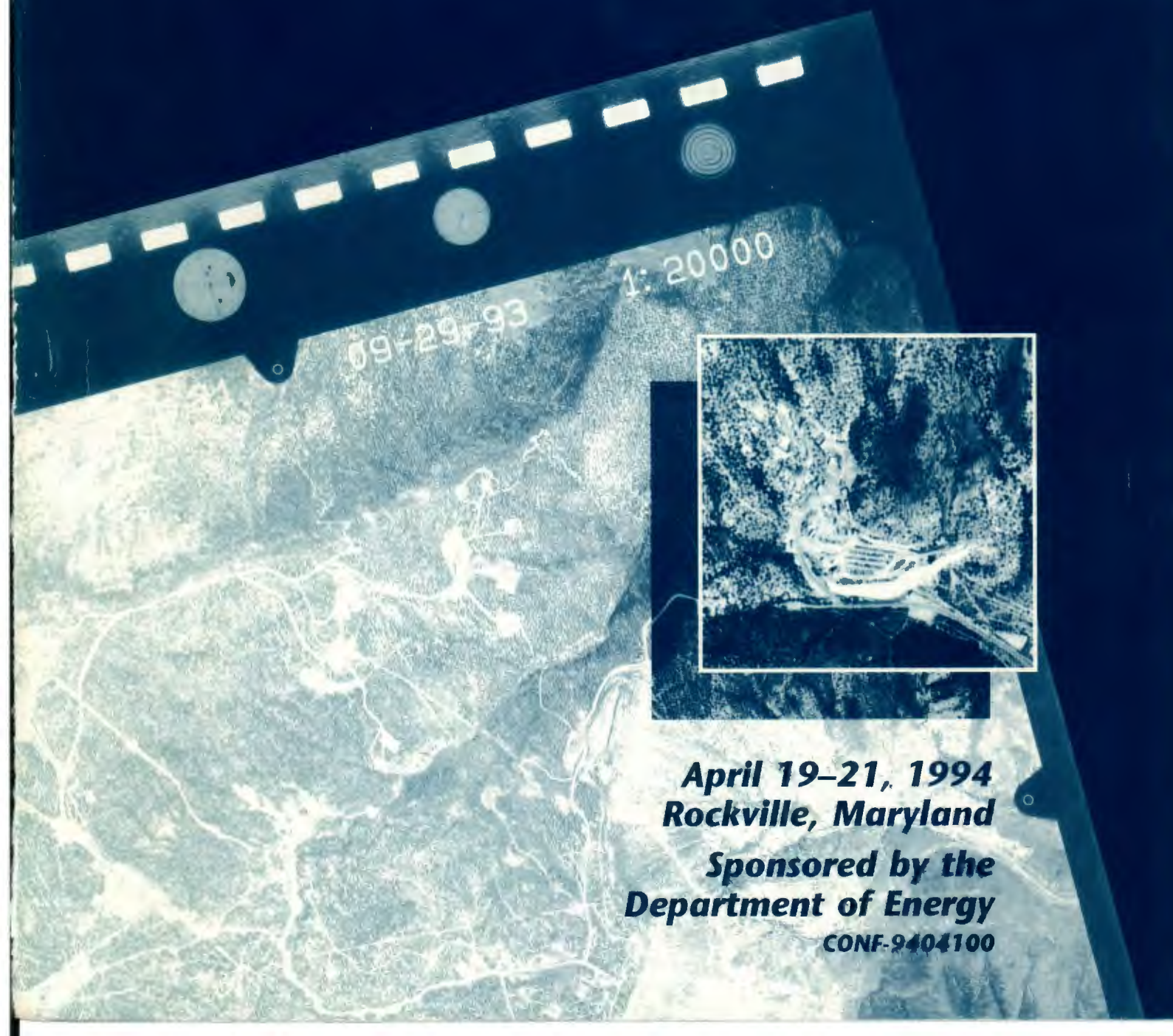


PROCEEDINGS

Symposium on the
NON-PROLIFERATION EXPERIMENT:
RESULTS and IMPLICATIONS FOR TEST BAN TREATIES



**April 19–21, 1994
Rockville, Maryland**

*Sponsored by the
Department of Energy*

CONF-9404100

DISCLAIMER

This document was prepared as an account of work sponsored by an agency of the United States Government. Neither the United States Government nor the University of California nor any of their employees, makes any warranty, express or implied, or assumes any legal liability or responsibility for the accuracy, completeness, or usefulness of any information, apparatus, product, or process disclosed, or represents that its use would not infringe privately owned rights. Reference herein to any specific commercial products, process, or service by trade name, trademark, manufacturer, or otherwise, does not necessarily constitute or imply its endorsement, recommendation, or favoring by the United States Government or the University of California. The views and opinions of authors expressed herein do not necessarily state or reflect those of the United States Government or the University of California, and shall not be used for advertising or product endorsement purposes.

**Proceedings of the Symposium on
The Non-Proliferation Experiment (NPE):
Results and Implications
for Test Ban Treaties**

April 19–21, 1994

Holiday Inn Crowne Plaza
Rockville, Maryland

Technical Editor: Marvin D. Denny
Production Editor: Susan P. Stull

Sponsored by
U.S. Department of Energy
Office of Nonproliferation and National Security
Office of Research and Development

Coordinated by
Lawrence Livermore National Laboratory
Treaty Verification Program

Acknowledgments

We would like to thank the Department of Energy (DOE) for sponsoring this event and the work that went into it. We also wish thank the people from the DOE National Laboratories; DOE Field Office, Nevada; EG&G; Raytheon Services; State Department; U.S. Geological Survey; Defense Nuclear Agency; Arms Control and Disarmament Agency; and DYNO NOBEL, Inc. We wish to thank all those from other groups that participated in the experiment and contributed to these proceedings. The groups include the Atomic Weapons Establishment, United Kingdom; Center for Atomic Energy, France; the Bureau of Energy, Mines, and Research, Ottawa, Canada; University of California, Berkeley; University of Nevada, Reno; University of Washington, Seattle; University of Texas, El Paso; University of Arizona; Duke University; and SAIC.

Special thanks go to Dr. John G. Keliher of the DOE Office of Intelligence and National Security, and to Mr. Max Koontz, Mr. Michael O'Connell, and Ms. Leslie Casey of the Office of Research and Development for their support throughout the long preparation period.

Contents

1. Introduction	
Introduction and Highlights Marvin D. Denny, Lawrence Livermore National Laboratory, Livermore, CA	1-1
2. Background	
The Non-Proliferation Experiment Willard J. Hannon, Lawrence Livermore National Laboratory, Livermore, CA	2-1
U.S. Comprehensive Test Ban Monitoring Goals Larry Turnbull, Arms Control Information Systems	2-12
Blasting Activity of the Mining Industry in the United States Paul G. Richards, Lamont-Doherty Earth Observatory, Palisades, NY, and Columbia University	2-16
A Review of Blasting Activity in the Former Soviet Union William Leith, U.S. Geological Survey, Reston, VA; and Leonid Bruk, BRUK Hydrogeological Consulting, Inc., Rockville, MD	2-36
Some Remarks on Rockbursts and Nuclear Proliferation A. McGarr, U.S. Geological Survey, Menlo Park, CA	2-45
3. Test Preparations	
Logistics and Preparations for the NPE Paul J. Thompson and John W. Miller, Lawrence Livermore National Laboratory, Livermore, CA	3-1
Lessons Learned from the Non-Proliferation Experiment Charles McWilliam and Steven Curtis, U.S. Department of Energy, Nevada Operations Office, Las Vegas, NV	3-12
4. EOS and Code Simulations	
Background on the Commercial Explosive Chosen for the Non-Proliferation Experiment Mark E. Mammelle, Dyno Nobel, Inc.	4-1
Performance Calculations on the ANFO Explosive RX-HD P. C. Souers, D. B. Larson, and C. M. Tarver, Lawrence Livermore National Laboratory, Livermore, CA	4-9
Explosive Performance of the Non-Proliferation Experiment Thomas O. McKown, Los Alamos National Laboratory, Los Alamos, NM	4-38
Modeling the NPE Randy Bos, Los Alamos National Laboratory, Los Alamos, NM	4-49
Preshot Predictions for the Near-Source Region in the Non-Proliferation Experiment Dan F. Patch, J. Eddie Welch, and James Zerkle, SAIC, San Diego, CA	4-57
The Influence of Material Models on Chemical or Nuclear-Explosion Source Functions L. A. Glenn and P. Goldstein, Lawrence Livermore National Laboratory, Livermore, CA	4-68
5. Rainier Mesa Structure	
Geology, Geophysics, and Physical Properties of the U12n.25 Non-Proliferation Experiment Site M. J. Baldwin, R. P. Bradford, S. P. Hopkins, D. R. Townsend, Raytheon Services Nevada, Mercury, NV; and B. L. Harris-West, Defense Nuclear Agency, Mercury, NV	5-1
High Resolution Seismic Imaging of Rainier Mesa Using Surface Reflection and Surface to Tunnel Tomography E. L. Majer, L. R. Johnson, E. K. Karageorgi, and J. E. Peterson, Lawrence Berkeley Laboratory, Berkeley, CA	5-15

6. Ground Motion Measurements

Comments on Some Results Derived from the NPE Indra N. Gupta, Multimax, Inc. Landover, MD	6-1
Seismic Source Parameters Lane R. Johnson, Lawrence Berkeley Laboratory and University of California, Berkeley, CA	6-3
Axisymmetric Magnetic Gauges B. L. Wright, K. R. Alrick, and J. N. Fritz, Los Alamos National Laboratory, Los Alamos, NM	6-19
Induced Shock Propagation on the Non-Proliferation Experiment Thomas O. McKown, Los Alamos National Laboratory, Los Alamos, NM	6-25
Cavity Pressure/Residual Stress Measurements from the Non-Proliferation Experiment Raymond A. Heinle and Billy C. Hudson, Lawrence Livermore National Laboratory, Livermore, CA; and Melton A. Hatch, Jr., EG&G Energy Measurements	6-36
NPE—Close-In Stress and Motion Measurements Carl W. Smith, Sandia National Laboratories, Albuquerque, NM	6-54
Free-Field Seismic Ground Motion on Non-Proliferation Experiment H. Douglas Garbin, Sandia National Laboratories, Albuquerque, NM	6-71
Free-Field Ground Motions for the Nonproliferation Experiment: Preliminary Comparisons with Nearby Nuclear Events Kenneth H. Olsen and Anthony L. Peratt, Los Alamos National Laboratory, Los Alamos, NM	6-83
Comparison of Chemical and Nuclear-Explosion Source Spectra from Close-In, Local, and Regional Seismic Data Peter Goldstein and Steve Jarpe, Lawrence Livermore National Laboratory, Livermore, CA	6-98
Recording Experiment on Rainier Mesa in Conjunction with a Reflection Survey Lane R. Johnson, Lawrence Berkeley Laboratory, Berkeley, CA	6-107
Near-Source Surface Seismic Measurements for the NPE, NPE Calibration, Hunter's Trophy, and Mineral Quarry Robert E. Reinke and J. Al Leverette, Defense Nuclear Agency, Kirtland AFB, NM; and Brian W. Stump, D. Craig Pearson, and C. L. Edwards, Los Alamos National Laboratory, Los Alamos, NM	6-121
Stochastic Source Comparisons Between Nuclear and Chemical Explosions Detonated at Rainier Mesa, Nevada Test Site Brian W. Stump and D. Craig Pearson, Los Alamos National Laboratory, Los Alamos, NM; and Robert E. Reinke, Defense Nuclear Agency, Kirtland AFB, NM	6-136
Relative Source Comparison of the NPE to Underground Nuclear Explosions at Local Distances Albert T. Smith, Lawrence Livermore National Laboratory, Livermore, CA	6-150
Modeling the NPE with Finite Sources and Empirical Green's Functions Lawrence Hutchings, Paul Kasameyer, Peter Goldstein, and Steve Jarpe, Lawrence Livermore National Laboratory, Livermore, CA	6-156
Yield of the Non-Proliferation Experiment from the Leo Brady Seismic Net H. Douglas Garbin, Sandia National Laboratories, Albuquerque, NM	6-169
Lawrence Livermore National Laboratory Seismic Yield Determination for the NPE Robert Rohrer, Lawrence Livermore National Laboratory, Livermore, CA	6-179
Investigations of the Low Frequency Seismic Waves Recorded at Near-Regional Distances from the Non-Proliferation Experiment Howard J. Patton, Lawrence Livermore National Laboratory, Livermore, CA	6-183

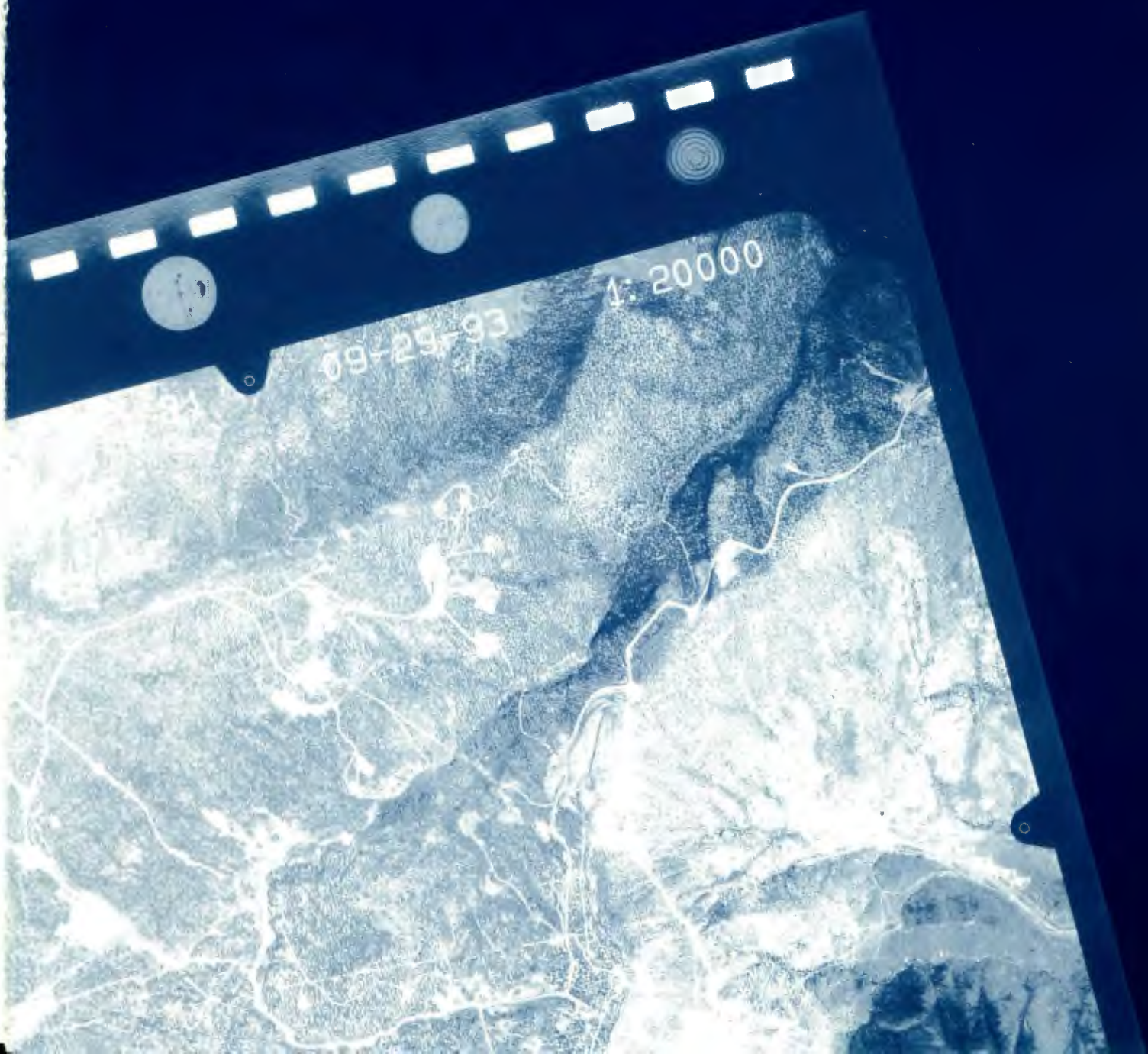
Regional Seismic Observations of the Non-Proliferation Experiment at the Livermore NTS Network	6-193
William R. Walter, Kevin Mayeda, and Howard J. Patton, Lawrence Livermore National Laboratory, Livermore, CA	
Lg Coda Moment Rate Spectra and Discrimination Using Lg Coda Envelopes	6-202
Kevin M. Mayeda and William R. Walter, Lawrence Livermore National Laboratory, Livermore, CA	
Dynamic Bayesian Filtering for Real-Time Seismic Analyses	6-213
David K. Blough, Alan C. Rohay, Kevin K. Anderson, and Wesley L. Nicholson, Pacific Northwest Laboratory, Richland, WA	
The Non-Proliferation Experiment Recorded at the Pinedale Seismic Research Facility	6-225
Dorthe B. Carr, Sandia National Laboratories, Albuquerque, NM	
Preliminary Results on the NPE Experiment	6-241
Y. Cansi, R. Crusem, J. P. Massot, J. L. Plantet, and B. Massinon, CEA/LDG, France	
Distance Effects on Regional Discriminants Along a Seismic Profile in Northwest Nevada; NPE and Nuclear Results	6-254
David A. McCormack, AWE Blacknest, U.K.; Keith F. Priestley, University of Cambridge, U.K.; and Howard J. Patton, Lawrence Livermore National Laboratory, Livermore, CA	
Separation of Source and Propagation Effects at Regional Distances	6-272
Peter Goldstein, Steve Jarpe, Kevin Mayeda, and William Walter, Lawrence Livermore National Laboratory, Livermore, CA	
Southern Sierra Nevada Continental Dynamics Project: 1993 Field Observations of the NPE	6-277
G. Randy Keller, University of Texas, El Paso, TX; Peter E. Malin, Duke University, Durham, NC; and Stanley D. Ruppert, Lawrence Livermore National Laboratory, Livermore, CA	
The NTS Ground Motion Data Base	6-285
Frederick N. App, Los Alamos National Laboratory, Los Alamos, NM	
7. Nonseismic Technologies	
Atmospheric Methods for Nuclear Test Monitoring	7-1
David J. Simons, Los Alamos National Laboratory, Los Alamos, NM	
Ionospheric Measurements for the Non-Proliferation Experiment	7-8
T. Joseph Fitzgerald, Los Alamos National Laboratory, Los Alamos, NM	
Infrasonic Measurements of the Non-Proliferation Experiment	7-24
Rodney W. Whitaker, Susan Noel, and Wayne Meadows, Los Alamos National Laboratory, Los Alamos, NM	
Hydroacoustic Observation of the NPE	7-26
D. Harris, T. Hauk, and E. Breitfeller, Lawrence Livermore National Laboratory, Livermore, CA; and G. D'Spain, Marine Physical Laboratory, University of California, San Diego, CA	
8. On-Site Inspection Technologies	
An Overview of the On-Site Inspection Measurements from the Non-Proliferation Experiment	8-1
John J. Zucca, Lawrence Livermore National Laboratory, Livermore, CA	
Post-Test Geologic Observations Made at the Non-Proliferation Experiment Site, N-Tunnel, Nevada Test Site	8-7
D. R. Townsend, R. P. Bradford, S. P. Hopkins, and M. J. Baldwin, Raytheon Services Nevada, Mercury, NV; and B. L. Ristvet, Defense Nuclear Agency, Kirtland AFB, NM	
EMP from a Chemical Explosion Originating in a Tunnel	8-14
Bob Kelly, Los Alamos National Laboratory, Los Alamos, NM	

Low-Frequency Electromagnetic Measurements at the NPE and Hunter's Trophy: A Comparison	8-21
Jerry J. Sweeney, Lawrence Livermore National Laboratory, Livermore, CA	
Comparison of the Non-Proliferation Experiment Aftershocks with Other Nevada Test Site Events	8-34
Steve Jarpe, Peter Goldstein, and J. J. Zucca, Lawrence Livermore National Laboratory, Livermore, CA	
Spontaneous Potential and Telluric Measurements on Rainier Mesa Related to the NPE	8-41
Jerry J. Sweeney, Lawrence Livermore National Laboratory, Livermore, CA	
The Non-Proliferation Experiment and Gas Sampling as an On-site Inspection Activity: A Progress Report	8-51
Charles R. Carrigan, Lawrence Livermore National Laboratory, Livermore, CA	
Low-Altitude Overhead Imagery Acquisition Pre- and Post-NPE	8-63
William L. Pickles, Lawrence Livermore National Laboratory, Livermore, CA; Janet E. Shines, David L. Hawley, Michael D. Pelan, and Stanley B. Brewster, Jr., EG&G RSL	
EMP at the Non-Proliferation Experiment	8-71
John Bell, AWE, Aldermaston, U.K.	

9. Panel Discussion

Panel Discussion	9-1
Participants: W. J. Hannon, P. W. Basham, L. Johnson, W. Leith, A. McGarr, P. G. Richards, D. J. Simons, T. C. Wallace, and J. J. Zucca	

INTRODUCTION



Introduction and Highlights

Marvin D. Denny
Lawrence Livermore National Laboratory

Every year tremendous amounts of chemical explosives are used world-wide in mining, quarrying, and civil engineering projects. In the United States alone, for example, industrial explosions of 50 tons or more number in the thousands (Richards *et al.*, 1992). Such industrial projects create a challenge for policy makers molding a test ban, since they could provide the necessary cover for a clandestine nuclear test.

To address a critical verification issue for the current Non-Proliferation Treaty (NPT) and for a possible future Comprehensive Test Ban Treaty (CTBT), the Department of Energy sought to measure certain differences between an underground nuclear test and a chemical test in the same geology, so that other explosions could be identified. This was done in a field experiment code-named the Non-Proliferation Experiment (NPE).

The NPE was a comprehensive experiment involving two chemical explosions. The first explosion, set off primarily for calibration purposes, was 300 lb of C4, a very efficient military compound. The second was 2,846,000 lb, or 1.29 million kg, of a commercial blasting agent based on a mixture of ammonium nitrate and fuel oil (ANFO). This is a relatively inefficient explosive, so more than a kiloton of it was required to produce an energy release of approximately 1.07 kt (1 kiloton = 4.186×10^{12} joules). Both explosions took place at the Nevada Test Site (NTS) in a Rainier Mesa tunnel, 390 m underground at the exactly the same location, 37.20193° N and 116.20986° E. The small explosion was detonated on October 30, 1992, at approximately 06:00 a.m. Pacific Standard Time. For the second explosion, a cylindrical chamber, approximately 15.2 m in diameter by 5.5 m high, was subsequently excavated such that its center was co-located with the center of the small explosion. Finally, the ANFO was placed in this chamber and detonated on September 22, 1993, at 00:01:00.080 a.m. Pacific Daylight Time.

This comprehensive experiment was designed to determine the signatures of chemical explosions for a broad range of phenomena for comparison with those of previous nuclear tests. If significant differences can be measured, then these measures can be used to discriminate between the two types of explosions. In addition, when these differences are understood, large chemical explosions can be used to seismically calibrate regions to discriminate earthquakes from explosions. Toward this end, on-site and off-site measurements of transient phenomena were made, and on-site measurements of residual effects are in progress.

Although seismic data have been collected on both chemical and nuclear explosions over the last several years, the differences between the two sources have been difficult to assess due to path differences, variations in the geologic emplacement conditions, and the amount of energy released.

These difficulties were minimized in the NPE because it was detonated in the same geology and within 500 m of several prior nuclear explosions of comparable energy. Thus, regional seismic signals between the NPE and nearby nuclear explosions can be compared directly.

Many types of measurements were made, most on the second explosion only. The NPE was extensively instrumented at ranges starting within the blasting agent itself and extending to regional and teleseismic distances. Within the blasting agent, several time-of-arrival cables and two particle-velocity gages were emplaced to determine the actual energy release. Approximately 50 accelerometers and stress gauges were deployed underground to track the shock wave's evolution to an elastic wave. On the mesa's surface, more than 60 stations recorded the shock wave to determine the extent of spall and to locate aftershocks. The permanent networks within and around NTS and approximately 400 portable stations in the western United States tracked the regional seismic wave evolution. Local seismic measurements of the 300-lb explosion were recorded on the test site to provide empirical Green's functions for later use in analyzing the kiloton explosion. Other phenomena recorded were the electromagnetic pulse, hydroacoustic signals, electrical resistivity on the mesa above the cavity, thermal emissivity, and other surface changes (the last two inferred from multispectral imagery acquired by fly-over before and after the explosion).

Data Availability

The experimental measurements were carried out by a broad range of U. S. government agencies and laboratories, universities, private companies, and foreign participants. All the experimentalists enjoyed a very high success rate. Over 90% of the deployed systems produced useful data. All parties who collected data agreed to exchange raw data, which is now available through the Incorporated Research Institutions for Seismology (IRIS).

Symposium Highlights

Here we present highlights from some of the sections of the *Proceedings* and attempt to integrate some seismic results that appear individually in more detail in the section on "Ground Motion Measurements."

Background

Dr. Turnbull pointed out that the United States has stated during the CTBT negotiations that an effective verification regime "could be capable of identifying and attributing with high confidence evasively conducted nuclear explosions of less than a few kiloton yield in broad areas of the globe."

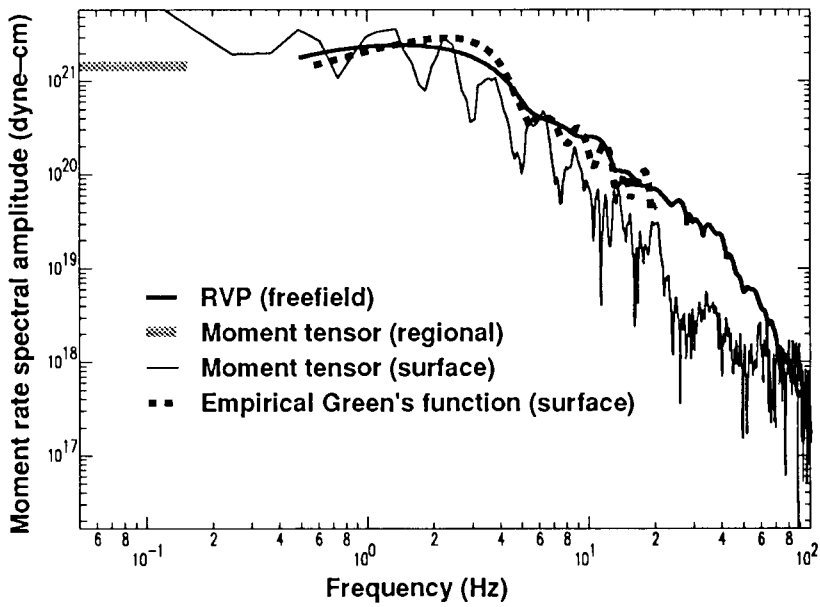


Figure 1. Multiple analyses of the NPE at different distances yield consistent spectral shape and isotropic moment results.

Test Preparations

The particular blend of ANFO chosen was extremely safe to handle as seen in a video presented by Gordon Coleman of IRECO. It could not be ignited when spilled onto the ground even with a torch.

EOS and Code Simulations

Finite-element calculations show that the outgoing wave quickly became spherical. CORTEX measurements show that the ANFO burned completely. The yield was calculated on the basis of the amount and chemical composition of the ANFO.

Ground Motion Measurements

Perhaps the most striking result was that the source function for the chemical explosion was identical to that of a nuclear one of about twice the yield. One might have intuitively expected that, for the same seismic moment, the corner frequency of the chemical explosion would be lower since the burn time is so much longer. But this is definitely not the case. The same conclusion was reached by all investigators, including those who studied the free-field data as well as those who studied local and regional data. The big difference, of course, is in the coupling of energy into the ground. The chemical explosion is most efficient in this respect. The equivalent nuclear yield was estimated to be in the range of 1.5 to 2.5 kt.

Estimates of the spectral shape and of the isotropic moment are in good agreement as shown in Figure 1. Spectral estimates from free-field and two kinds surface measurements are in good agreement with respect to shape up to about 10 Hz. Similarly, moment estimates from free-field and surface measurements show trends consistent with the regional measurements at long periods even though the surface and free-field measurements do not overlap in frequency with the regional measurement. The free-field estimates are contaminated at long periods by reflections arriving late in the signal, and the surface moment tensor inversion is contaminated at long periods by noise. So the short-period results from the free-field and surface measures seem to be quite consistent with the longer period regional estimate.

The Pn arrivals were found to be good replications of the source function while Lg and Pg are not. The NPE result is not an isolated case, since earlier work on the Bristol experiment had produced similar results using the same empirical Green's function approach of firing a small chemical charge very close to the nuclear one. This is evidence that the Pn arrivals are not head waves as initially believed; instead, they are really turning rays because such a ray is simply proportional to the source function while a head wave is proportional to the integral of the source function.

Ratios of Lg and Pg spectra to the source function were each found to be similar in shape to low-pass filters. In addition, the explosion spectra of Lg coda were found to have a peak that earthquake Lg coda spectra don't have. This information gave rise to considerable speculation that the cause is Rg-to-S phase conversion due to near source scattering.

The corner frequency for an earlier, partially decoupled shot was also obtained from the empirical Green's function provided by the 300-lb shot. It was found that the decoupled shot had the same corner frequency as a near-by tamped shot whose scaled isotropic moment was 20 times greater. An intuitive way to look at these results is that a decoupled shot has a larger source volume than does a tamped one of the same moment.

Nonseismic Technologies

Both near-infrasound and off-shore hydroacoustic techniques were successful in detecting the NPE, but the ionosound technique failed to detect a signal probably because of the poor night-time atmospheric conditions for transmission.

On-Site Inspection (OSI) Technologies

In some ways, the NPE was a good test for an OSI since there was no collapse crater due to the fact that the explosion was overburied. Of all the OSI experiments carried out, only the aftershock and EMP measurements have produced tangible results so far. The gas tracer and multispectral imagery are ongoing research efforts, and the jury is still out. The magnetotelluric sounding and electrical self-potential experiments are complete, but neither produced encouraging results. The aftershock

sequence was similar to that of nuclear explosions, with two significant conclusions: (1) explosion aftershocks have a lower corner frequency than earthquake aftershocks of the same magnitude, and (2) the recurrence rate for explosions tends to be lower than that for earthquakes. The most promising OSI technique is the extra-low-frequency electromagnetic pulse. The differences in frequency content are striking, but more data on chemical shots is needed for confirmation. These are very easy measurements to make but must be made close to the event, that is, within a few kilometers. So EMP measurement could be a confidence-building measure employed on very large, pre-announced chemical explosions.

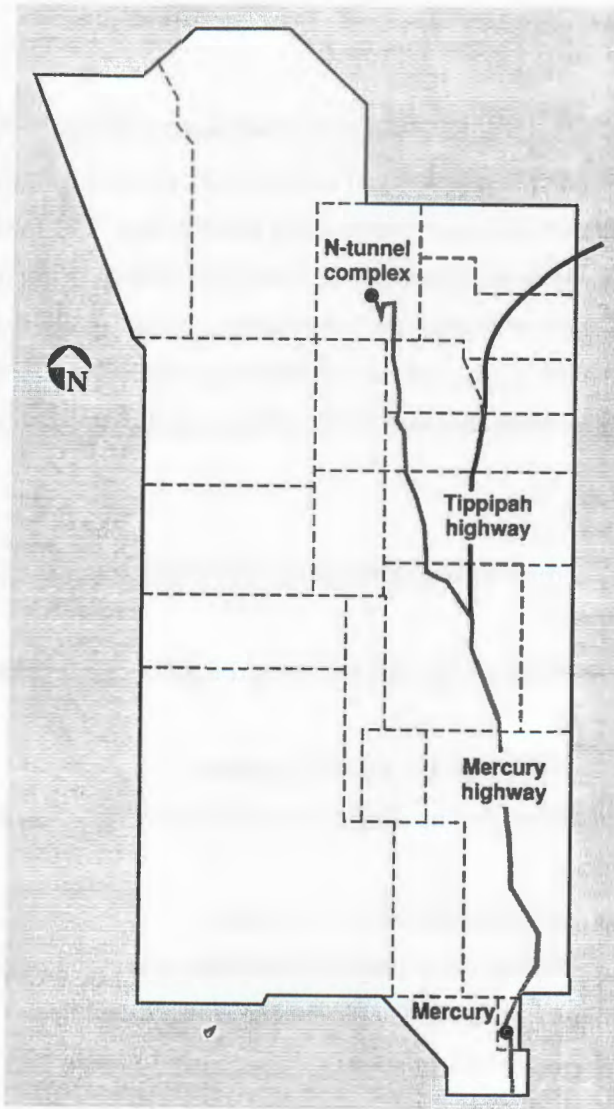
In summary, the NPE provided a broad variety of insights into the physics of the CTBT monitoring problem. Some of the results to date are

- A chemical explosion couples more energy into the ground than does a nuclear explosion of the same total energy.
- P_n is proportional to the source function, but P_g and L_g are not.
- Scattering or secondary sources may be the cause of poor P/S discrimination at low frequencies.
- A peak in the L_g transfer function identifies shallow events.
- Decoupled events in tuff have lower corner frequencies than do uncoupled events in salt.
- Two OSI diagnostics— aftershock rates and EMP—appear promising.

Reference

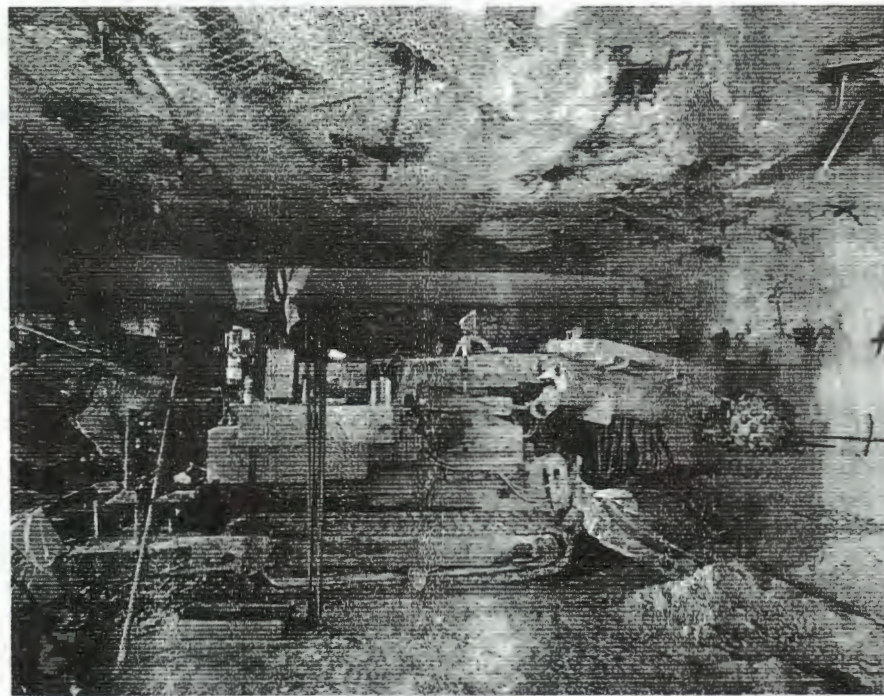
Richards, P.G, D.A. Anderson, and D.W. Simpson (1992), "A survey of blasting activity in the United States," *Bull. Seis. Soc. Amer.*, **82**, 1416.

■ Figure 1. A map of the Nevada Test Site, showing the route to and location of the N-Tunnel complex, where the Non-Proliferation Experiment took place.



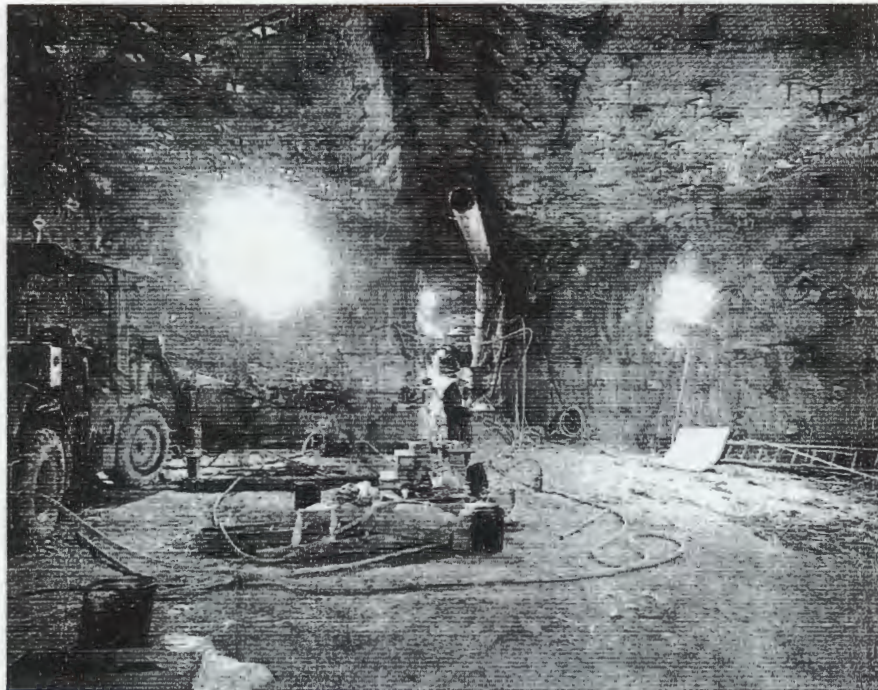


■ *Figure 2. Aerial view of the N-Tunnel entrance and associated staging area.*

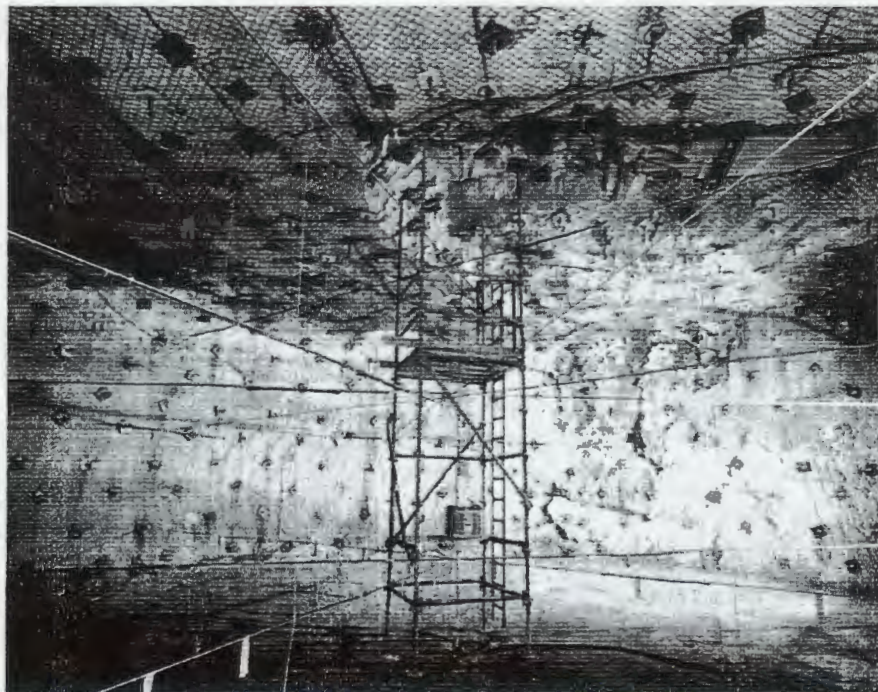


■ *Figure 3. The Alpine miner apparatus that drills the original shafts into the bedrock of the tunnel.*

■ Figure 4. A view from the back wall of the chamber looking toward the access drift. Mining of the chamber is nearing completion in this photo. The overhead pipe is for ventilation.

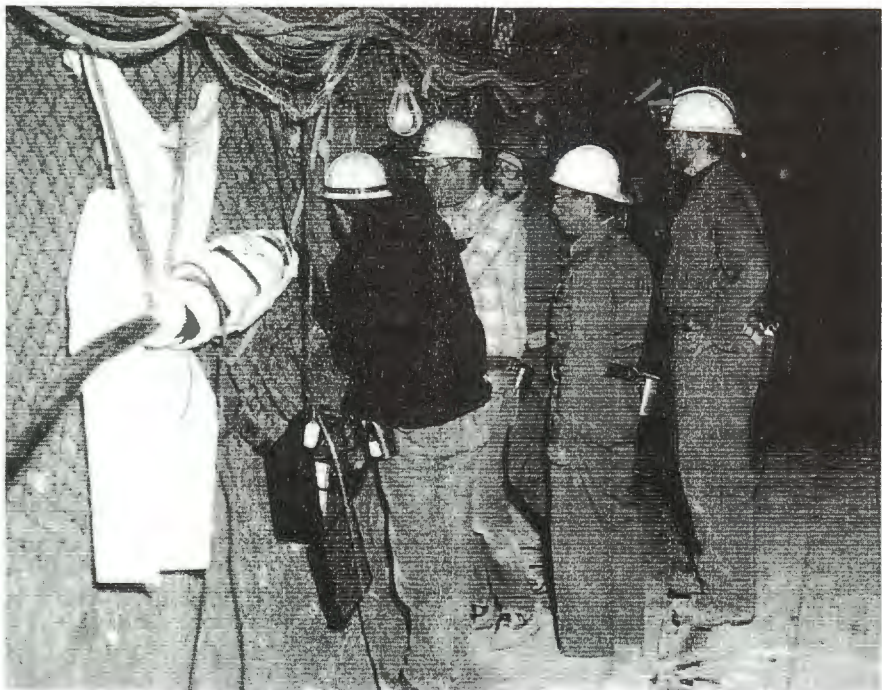


■ Figure 5. Chamber mining is complete. Auger pipes in the notch in the ceiling await the ANFO/emulsion mix. CORTEX time-of-arrival cables crisscross the room at three levels. The points at which they cross approximately define the axis of the cylindrical chamber. The scaffolding in the center of the room is for the installation of the detonator charges along the axis and was removed prior to installation of the ANFO/emulsion mixture.





■ Figure 6. Scientists from Los Alamos prepare particle-velocity gages for installation in the rock near the chamber wall.

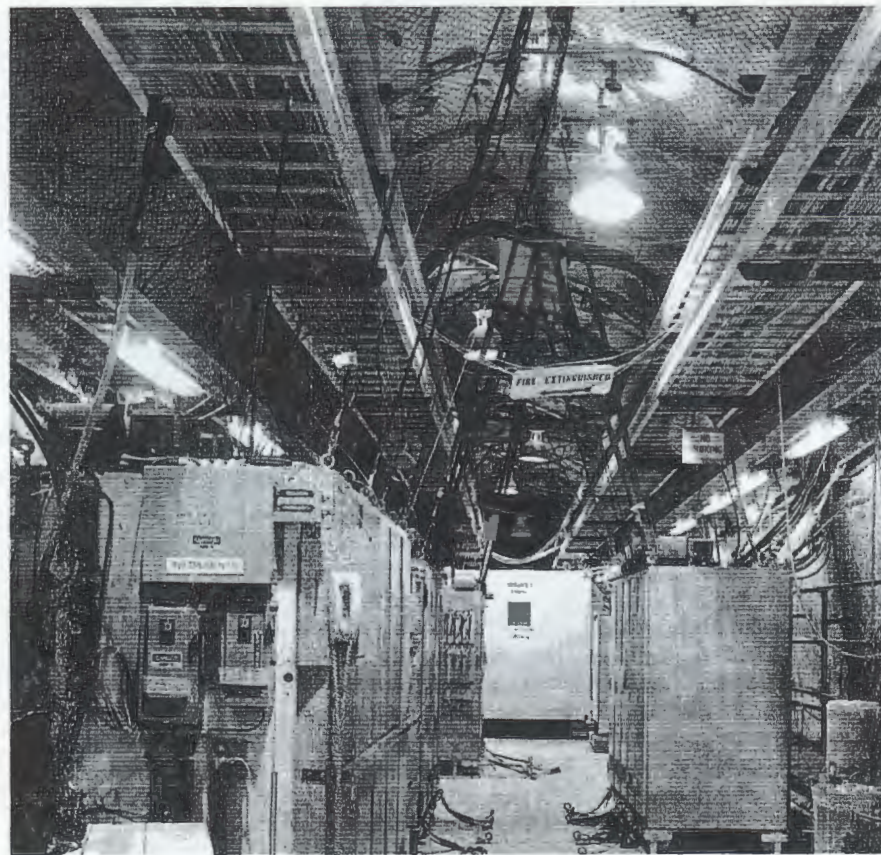


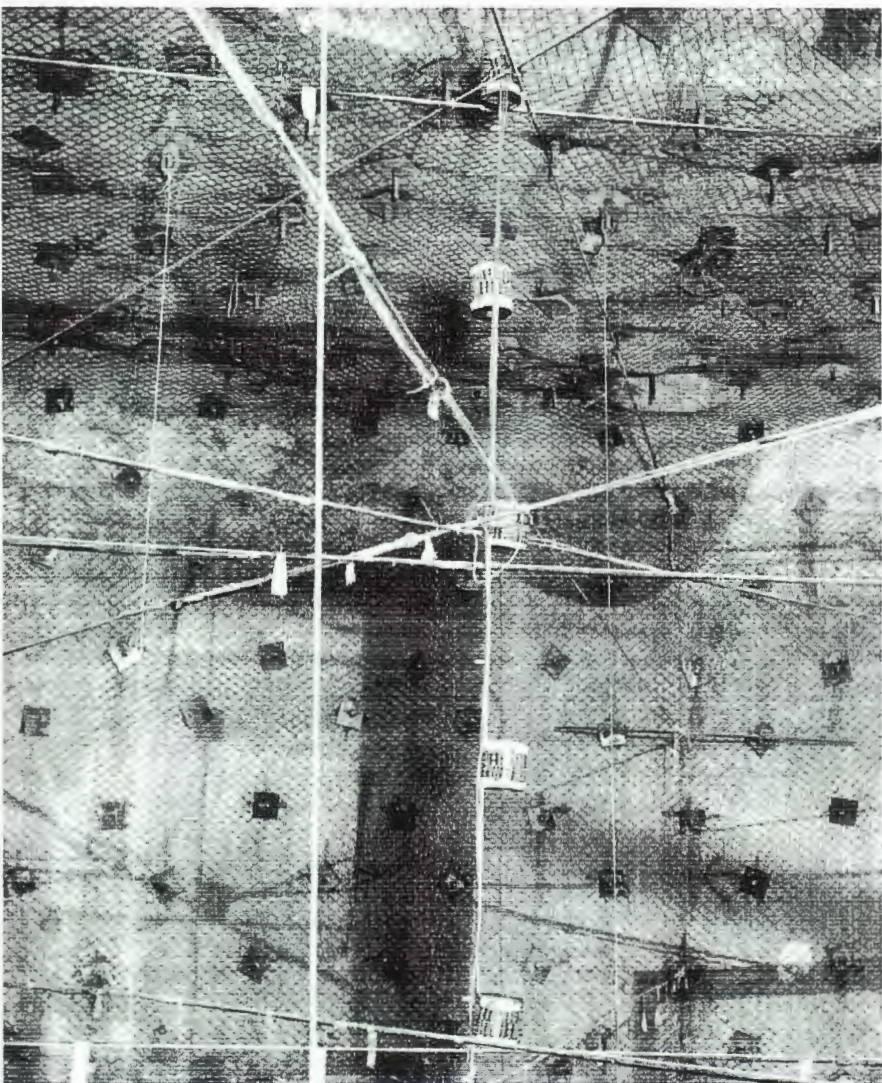
■ Figure 7. Tom McKown (second from left) leads a team of scientists from Los Alamos installing close-in instrumentation that will be used to measure time of arrival and ground motion associated with the planned explosion.

■ *Figure 8. Looking toward the portal of N-Tunnel in an alcove near the explosion chamber. Two LANL particle-velocity gage installations are visible on the right wall. On the ceiling and upper walls are the cables that led to the recording equipment in another alcove.*

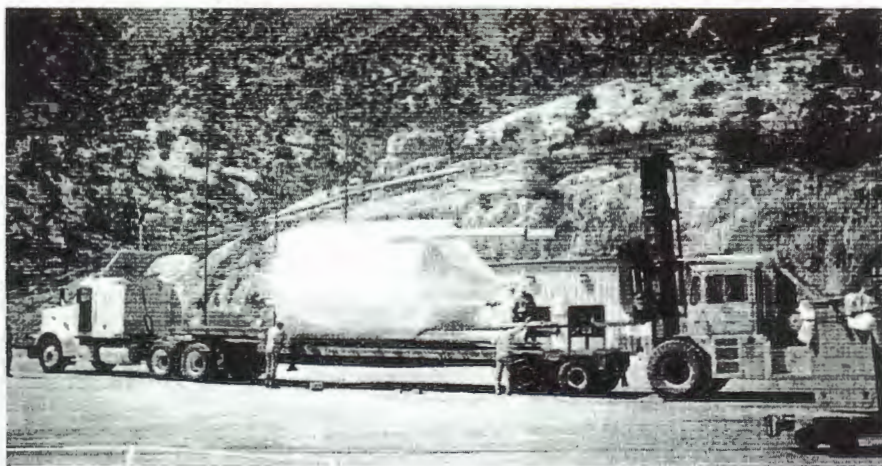


■ *Figure 9. The instrumentation alcove where all of the LANL and Sandia subsurface ground motion data were recorded.*



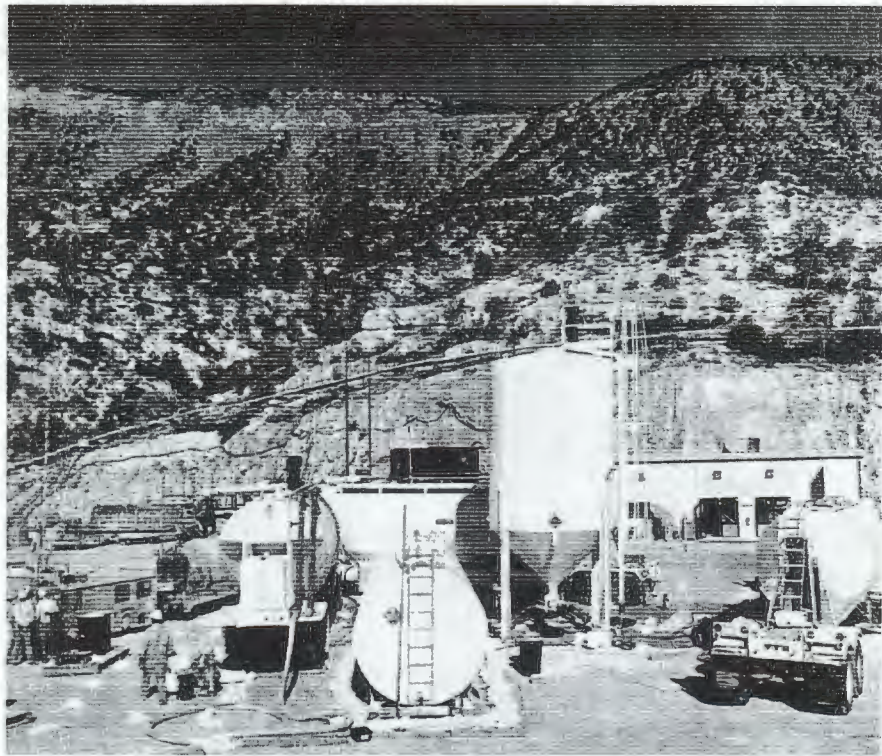


■ *Figure 10. Five equally spaced, high-energy booster charges, emplaced along the axis of the chamber, were used to detonate the blasting agent.*

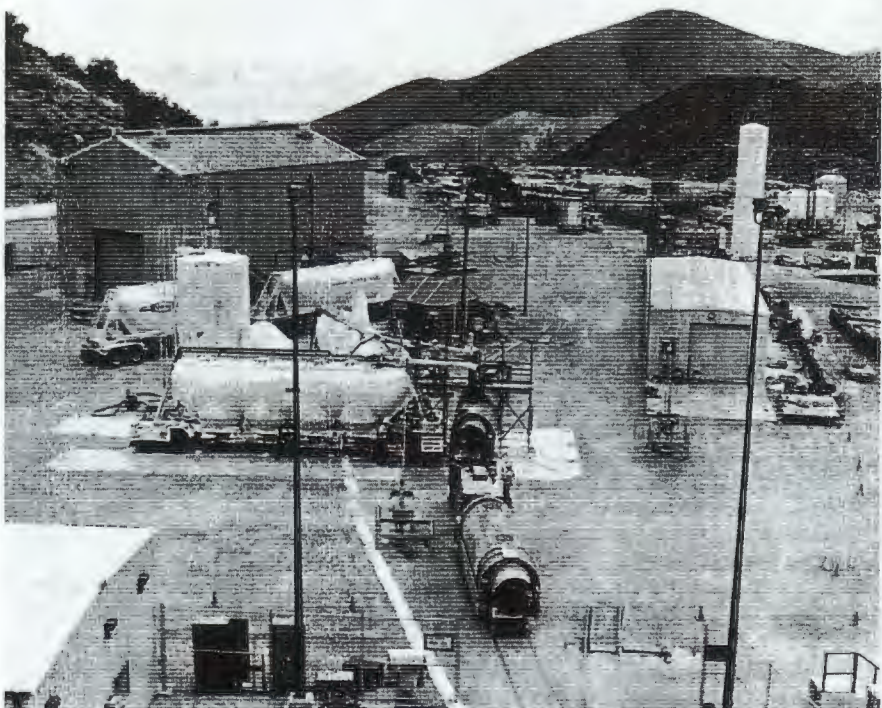


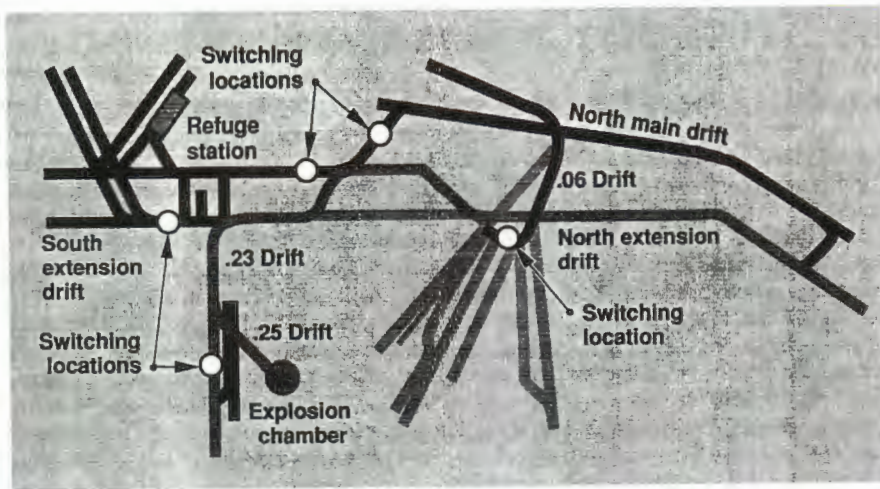
■ *Figure 11. One of the explosive storage tanks for the ANFO/emulsion mix arriving at the N-Tunnel processing area.*

■ *Figure 12. The explosive blending area with its various tanks and trailers used for storage and mixing the 50/50 blend of ANFO and emulsion.*

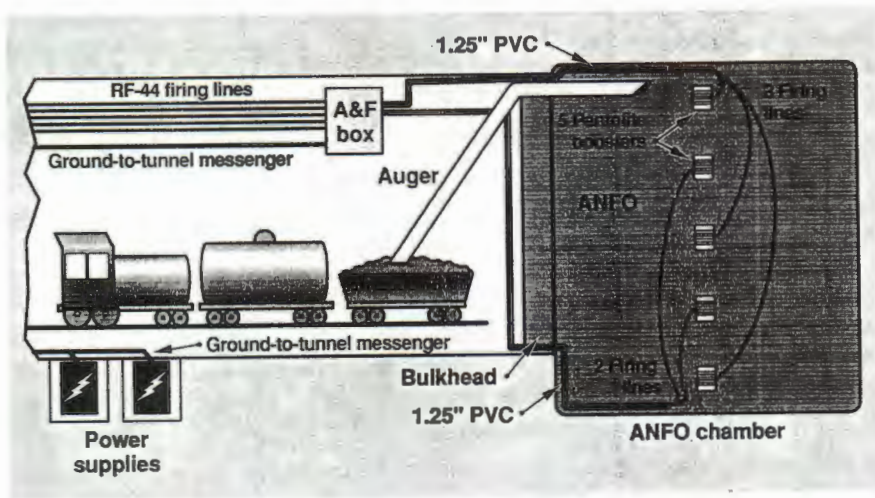


■ *Figure 13. The outdoor blending area in Area 12 N-Tunnel. An agitator car is being loaded with the explosive blend for transport underground to the explosion chamber.*



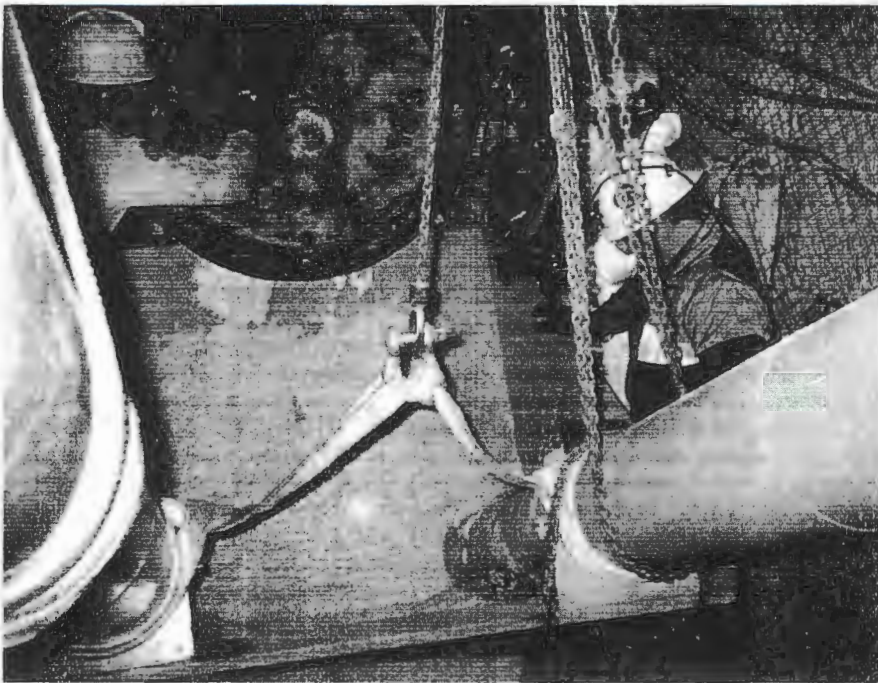


■ Figure 14. N-Tunnel complex including the north extension drift, .23 access drift, .25 access drift, and the explosion chamber.

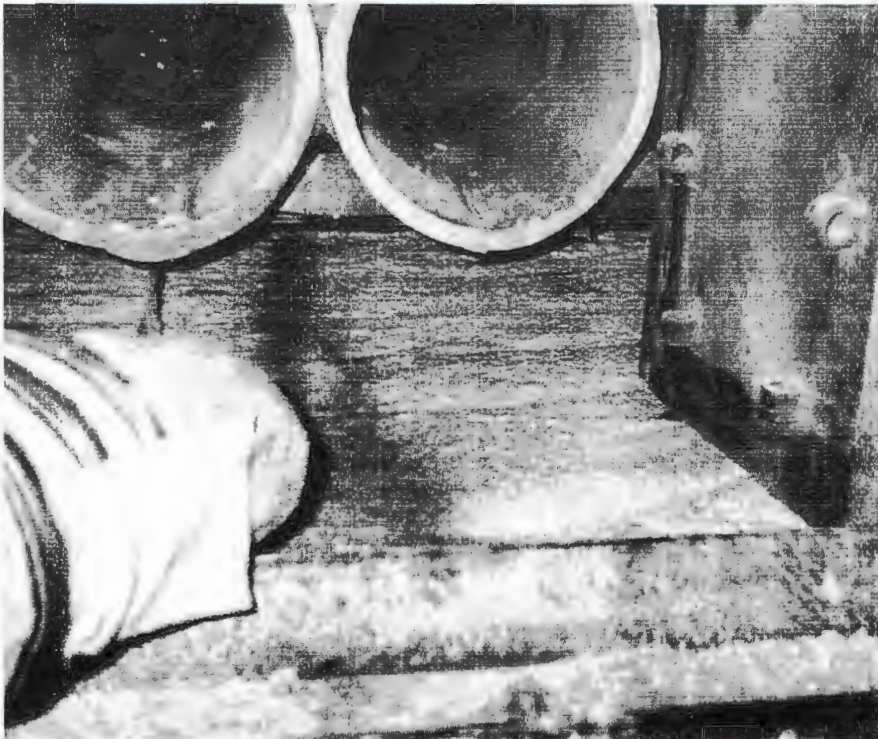


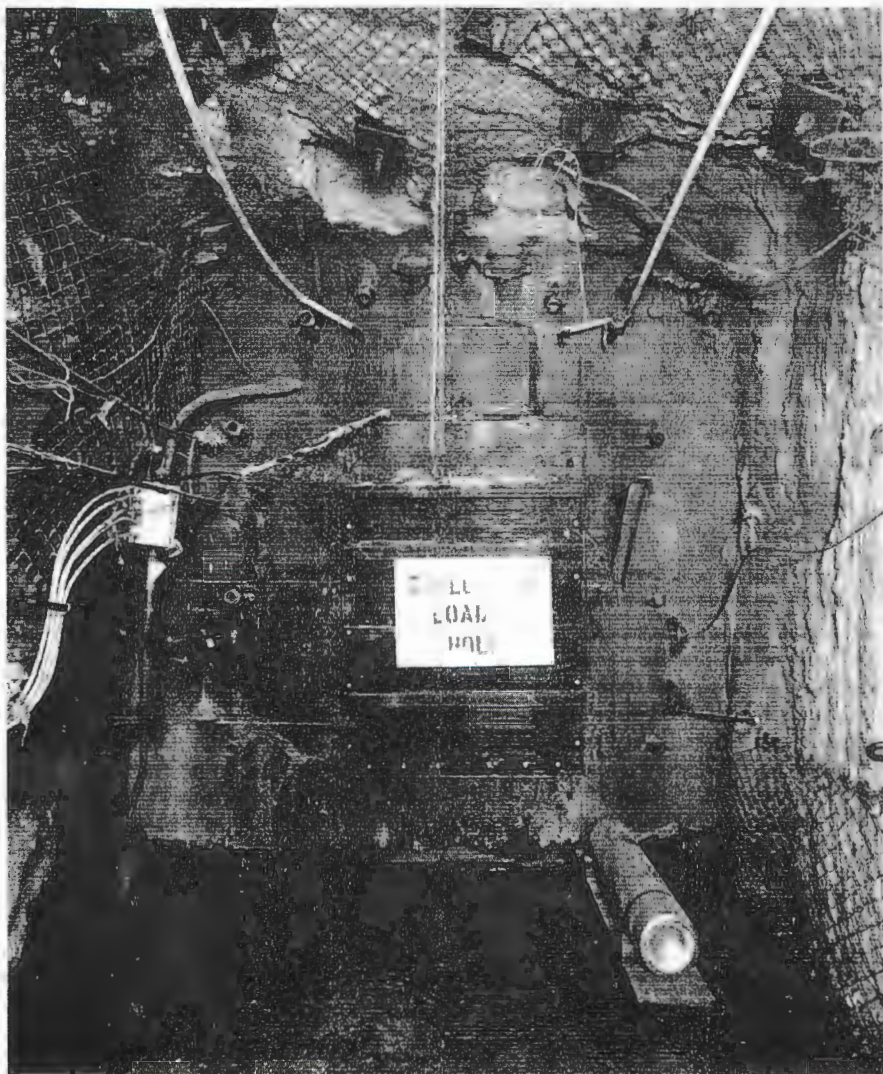
■ Figure 15. Schematic of the ANFO/emulsion blend chamber and placement area.

■ Figure 16. The agitator car unloading the explosive blend. The two auger tubes transported the blend into the chamber.



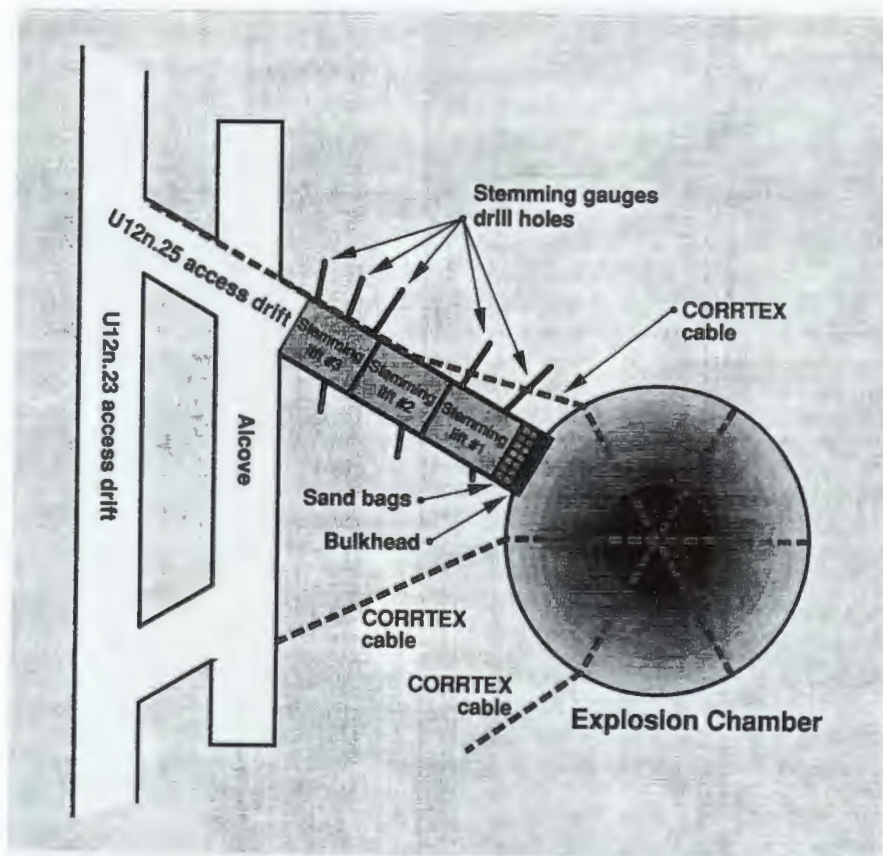
■ Figure 17. A view through the top of the bulkhead into the filled chamber. The two large tubes at the top of the photo held the augers that filled the chamber with explosive blend. Notches in the ceiling held the tubes so the explosive could truly fill up the chamber.



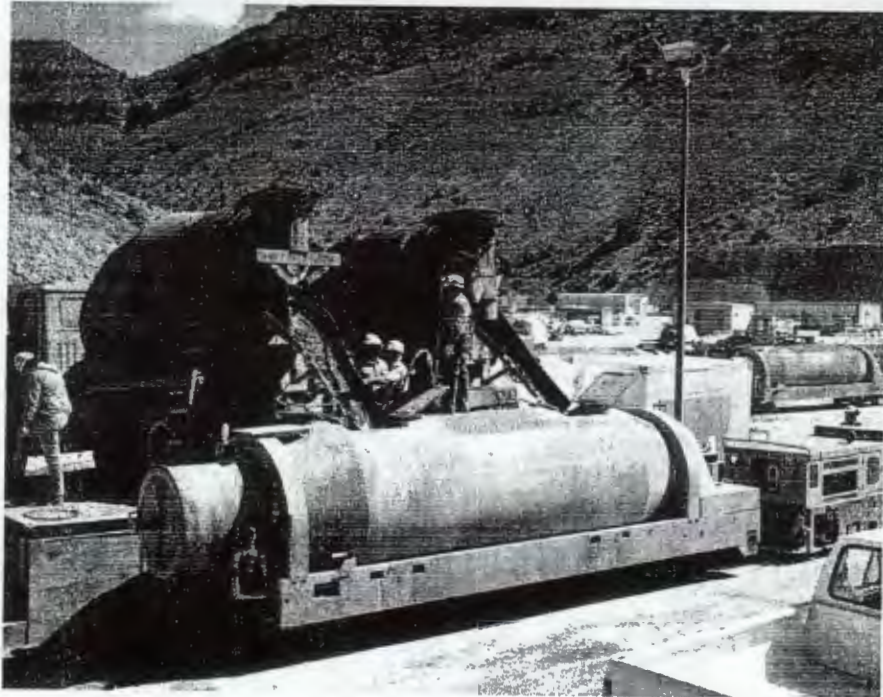


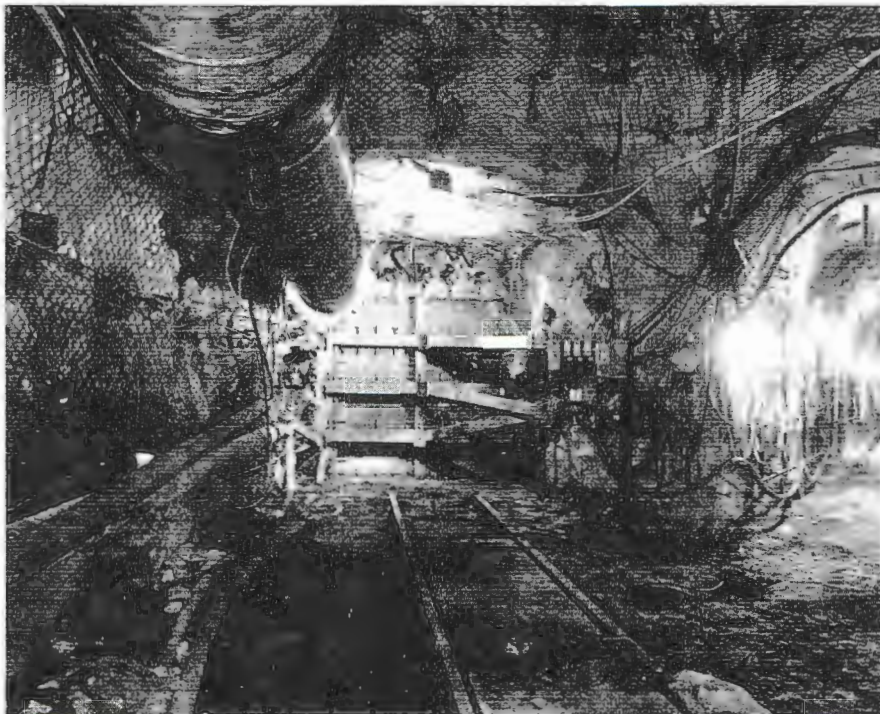
■ Figure 18. The bulkhead from inside the access drift. The cylinder on the floor contains a tracer gas (sulfur hexafluoride), which will be used in conjunction with a barometric pumping experiment to measure migration of gas through the overburden rock to the earth surface.

■ Figure 19. Schematic of the .25 drift stemming lifts, the bulkhead, and sandbags when the experiment components were in place.



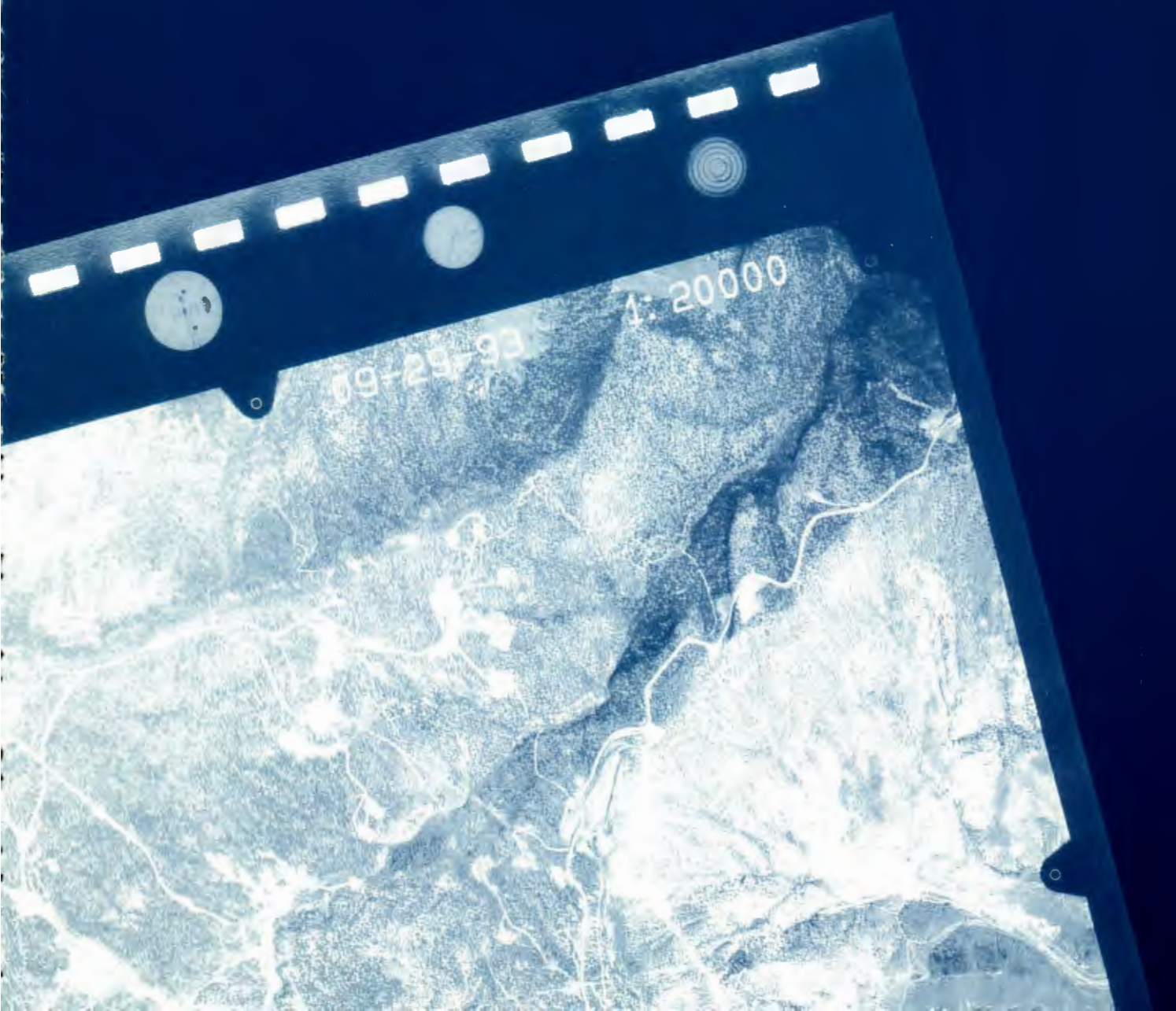
■ Figure 20. An agitator car is loaded with grout for stemming the access drift to the chamber.





■ *Figure 21. The access drift after the grouting was completed. The alcove at the right had experiments emplaced along its near wall.*

BACKGROUND



The Non-Proliferation Experiment

Willard J. Hannon
Lawrence Livermore National Laboratory, Livermore, California

Abstract

On September 22, 1993, the Department of Energy detonated more than 1.2 million kg of blasting agent in a tunnel in Rainier Mesa at the Nevada Test Site. The resulting explosion generated seismic, electromagnetic, and air pressure signals that were recorded on instruments deployed at distances ranging from a few meters to hundreds and, in some cases, thousands of kilometers. More than 12 organizations made measurements before, during, and after the explosions. The explosion and its associated experiments are known as the Non-Proliferation Experiment (NPE).

Analyses of the measurements made during the NPE and comparisons with similar measurements made on previous nearby nuclear explosions and on a co-located smaller explosion detonated at the same site are providing basic phenomenological insights into what is potentially one of the most challenging problems for verifying compliance with a Comprehensive Test Ban Treaty (CTBT) — distinguishing between nuclear explosions and some of the many conventional explosions that occur each year. The NPE is also providing information on the use of chemical explosions to develop empirical discriminants in regions where no nuclear explosions have been recorded.

In another verification application, several NPE projects are examining the utility of on-site, pre-shot, shot-time, and post-shot measurements of gas seepage, seismic activity, and other observables as a means of identifying the source of signals that appear like nuclear explosions at regional distances. Two related activities are being considered. First, challenge on-site inspections, conducted after an event has occurred, may be able to use the characteristics of phenomena that persist after the explosion to detect and identify the source of the signals that appeared ambiguous or explosion-like to remote sensors. Second, cooperative, on-site measurements made at the time of a pre-announced conventional explosion may provide assurance that a nuclear explosion did not occur as part of or in place of the pre-announced explosion.

The NPE had scientific goals in addition to its primary verification goals. Several universities deployed seismic stations throughout the western United States in order to study the structure and properties of the crust and upper mantle of the Earth in these regions.

This paper describes the motivation for the experiment, the execution of the explosions, the measurements that were made, and some preliminary results.

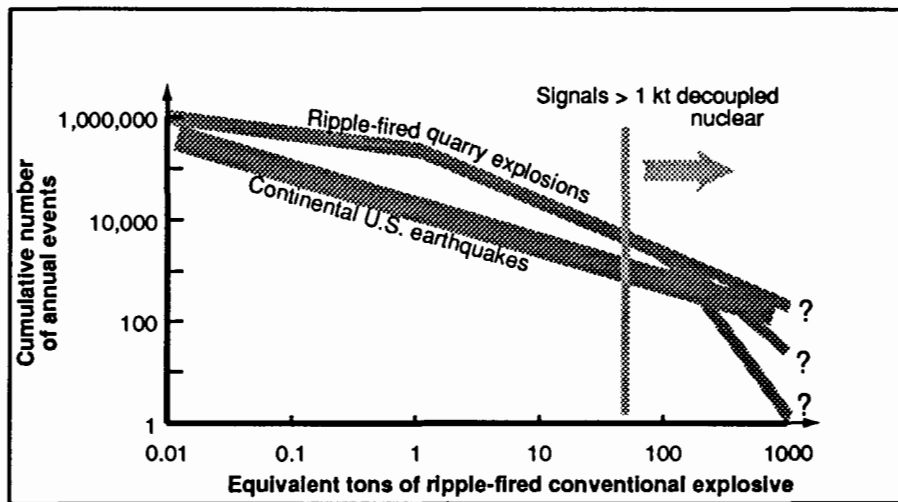


Figure 1. A comparison of U.S. ripple-fired quarry explosions and earthquakes, showing signals over about 80 equivalent tons are difficult to distinguish.

Introduction

Every year mining and quarrying operations, scientific experiments, and other industrial efforts detonate many conventional explosions (Figure 1).

In the United States most of these explosions are composed of discrete charges whose individual detonations are distributed in space and time in such a way that most of the energy breaks up rock. The seismic signal that is generated by the total detonation is often much smaller than the signal from a single nuclear explosion with the same total energy. In addition, the signals from many of these distributed conventional explosions exhibit an interference pattern that is not found in the signals from nuclear explosions. To the extent possible, the CTBT monitoring community will use these operationally induced characteristics in the efforts to distinguish between conventional and nuclear explosions.

Some U.S. explosions do not have these detonation patterns, and other countries are known to use considerably different blasting practices. Explosions that do not exhibit these patterns may be very difficult to distinguish from nuclear explosions. The potentially large number of ambiguous events could undermine confidence in compliance with the provisions of the Treaty. Furthermore, the signals from some of the larger explosions could mask the signals from a nuclear explosion whose signals were muffled by detonation in a large cavity.

The NPE's Goals

Given these potential threats to the stability of a CTBT, in late 1992 the Lawrence Livermore National Laboratory proposed that the Department of Energy (DOE) fund the detonation of a large conventional explosion as part of an effort that came to be known as the Non-Proliferation Experiment (NPE). The DOE agreed, and the NPE became part of an ongoing DOE research and development effort to study

CTBT monitoring issues and had several specific goals directly related to CTBT monitoring. The goals were to

- Record the seismic, electromagnetic, and infrasound signals generated by a large, spatially compact, instantaneously detonated, conventional explosion at distances ranging from a few meters to thousands of kilometers, and compare those signals with the signals from comparable, nearby, nuclear explosions in order to evaluate potential discriminants. The comparison would also provide the basis for using large conventional explosions to calibrate regions in which nuclear explosions have not been recorded at regional distances.
- Examine the evolution of the signals as a function of distance in order to determine which properties are related to the source region and which are introduced along the paths from the source to the receivers.
- To the extent possible, determine the mechanisms by which the signals are generated and identify the extent to which their properties could be controlled by the party carrying out the detonation in order to aid in evasion. Compare the signals from the NPE with those from nearby nuclear explosions in order to determine the two sources' relative efficiency in generating seismic waves.
- Determine the extent to which on-site, shot-time measurements on large, announced, conventional explosions could be used to provide confidence that a nuclear event has not been substituted for the announced explosion or masked by it.
- Determine the extent to which on-site, post-shot measurements of phenomena such as aftershocks and gas seepage could be used to identify the nature of the event that initiated these phenomena.

In addition to addressing the goals related to CTBT monitoring, a number of measurements made during the experiment would provide information about the seismic velocities and attenuation in the crust and upper mantle of the Earth in the western United States.

The following discussion and the papers included in these proceedings show that most measurement attempts were successful. Preliminary analyses of the data indicate that the experiment will achieve many of its goals.

Measurements from the NPE

On September 22, 1993, at 12:01 a.m. Pacific Daylight Time, Livermore, as part of a cooperative, multi-organization effort, oversaw the detonation of more than 1.29 million kg of a blasting agent composed of a mixture of ammonium nitrate and fuel oil (ANFO) in Rainier Mesa in the north central part of the Nevada Test Site, Figure 2(a). The blasting agent was located in a chamber that was excavated in an extension of N tunnel. (see Figure 2(b)). Previously, more than 18 nuclear explosions had occurred within 1500 m of the NPE explosion site, and many measurements were made on them. Many of the old

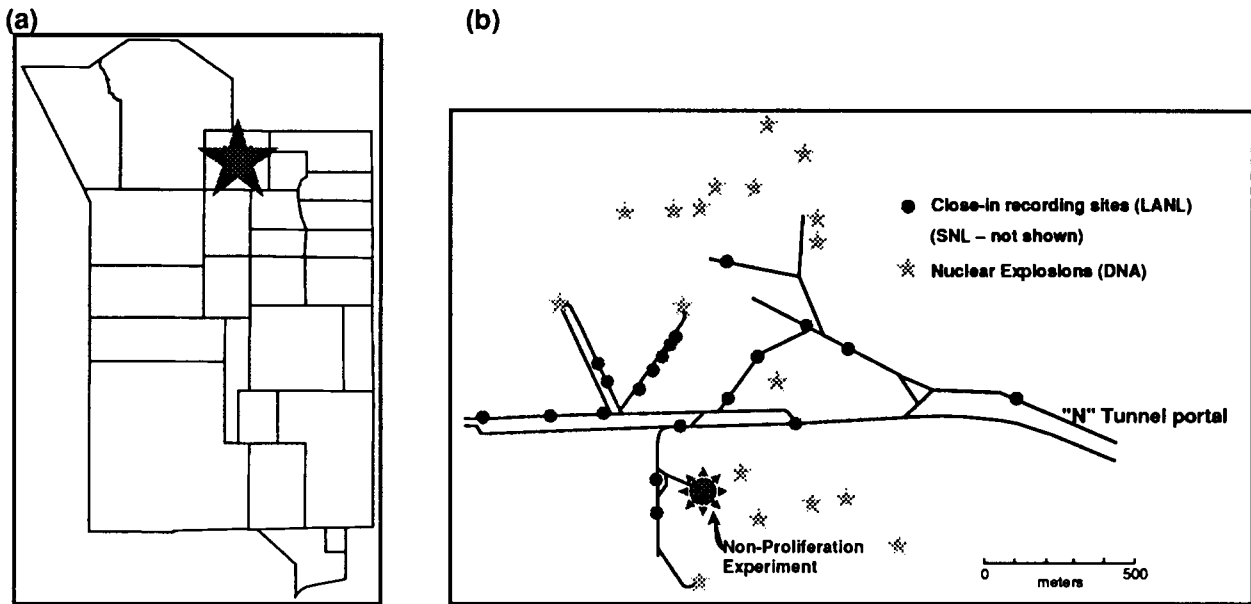


Figure 2. (a) Star shows location of the NPE at N Tunnel at the Nevada Test Site. **(b)** Some sites of explosions and measurements in N Tunnel.

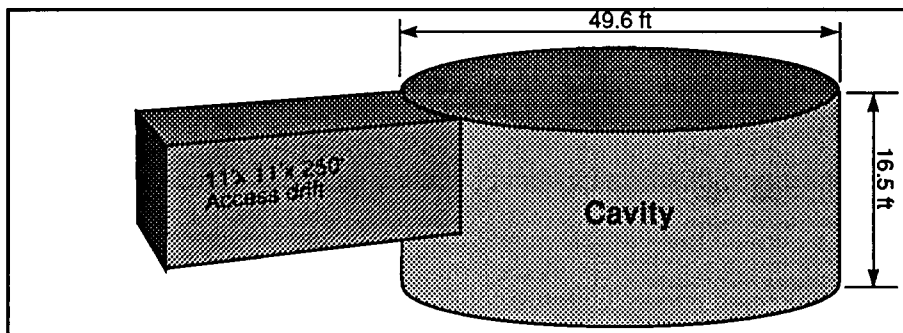


Figure 3. A schematic of the cylindrical cavity and access drift for the NPE.

measurement sites and even some of the instrumentation were still accessible. New sites and new instruments were also used.

The blasting agent filled the cylindrical chamber, which was 15.2 m in diameter and 5.5 m high (Figure 3). Electric currents applied to five detonators emplaced along the central axis of the chamber initiated the explosion (Figure 4). Hydrodynamic measurements made within the blasting agent determined the time of arrival of the detonation front and provided evidence that all of the blasting agent had detonated. Given that all of the blasting agent detonated, project scientists used the energy density of the blasting agent and the amount that had been emplaced (both provided by the supplier, DYNO-NOBEL, Inc.) to calculate that the explosion released an energy of 4.48 terajoules (1.07 kilotons).



Figure 4. A photo of the inside of the NPE explosion chamber and the electric currents to the detonators.

Many organizations made a variety of measurements before, during, and after the detonation (Table 1). The measurements address many monitoring and scientific issues.

- Electrical and seismic sounding measurements were made before and after the NPE explosion. These measurements will assist in determining the nature and extent of the permanent deformation that occurs in the neighborhood. These measurements may provide insight into the processes by which the remotely detected signals are generated.
- Hydrodynamic measurements were made within the blasting agent and in the surrounding rock at the time of detonation in order to verify that all of the blasting agent detonated and, if possible, to obtain an independent estimate of the energy generated in the source region.
- Electromagnetic pulse (EMP) measurements were made at the time of the explosion in order to determine the electromagnetic radiation that occurs due to the explosion processes and the interaction of the explosive energy with the surrounding rock. A comparison of these measurements with those recorded on some nuclear explosions indicates that on-site EMP measurements may provide a means of distinguishing the detonation of an announced conventional explosion from situations in which a nuclear explosion is detonated in place of or is masked by the announced explosion.
- Ground motion was measured underground close to the source (free-field measurements) in order to determine the source properties uncontaminated by either significant path effects or by interaction of the shock waves with the surface of the ground in the vicinity of the explosion. These measurements, when combined with the regional seismic measurements, show that some of the potentially useful regional seismic waves have time histories that are representative of the source region. Other time-history effects appear to have been affected by factors outside the immediate source region or are the result of poorly understood generation mechanisms.
- Ground motion was recorded on the surface of the Earth at local distances ranging from a few kilometers to a few tens of kilometers in order to understand the effects of the free surface and other near-source inhomogeneities on the properties of seismic waves. These local measurements, together with the

free-field and regional seismic waves, will also provide insights into the generation of regional seismic waves and the extent to which the properties of the signals can be altered by choices of emplacement conditions that could be made by a potential evader.

- Regional and teleseismic waves were recorded at distances ranging from several hundred to several thousand kilometers in order to study the properties of the signals that would actually be used for monitoring. (Signals measured at these distances will form the basis for detection, location, and identification in actual monitoring operations.) Comparison of the regional signals from the NPE with the signals from nearly collocated nuclear explosions is providing considerable insight into the mechanisms by which the two sources excite seismic waves and in the similarities and differences between the signals from the two source types. The results of the comparison have direct implications to discrimination between the two types of explosive sources. They also show that NPE-like conventional explosions could calibrate seismic discriminants between explosions and earthquakes in regions where no regional seismic records from nuclear explosions are available. Finally, the analyses of these signals are contributing to an improved understanding of the seismic wave velocities and attenuation in the western United States and ultimately to an understanding of the geologic structure and tectonics there.
- Hydroacoustic signals were recorded a few hundred kilometers off the coast of California in order to demonstrate the utility of such measurements for complementing land-based seismic measurements for events that occur on land near a coast. The successful recording of these waves during the NPE demonstrates their utility for detecting small events. Further work will need to be done to address their value for location and discrimination.
- Multispectral imagery was acquired from low-altitude overflights before and after the detonation in order to determine whether small, deeply buried explosions create observable effects on the optical and thermal properties of the ground or vegetation. If repeatable, identifiable effects are found, they may aid in reconnaissance efforts that may be part of post-event OSIs. They could also be used to monitor the sites of announced conventional explosions in order to ensure that nuclear explosions were not detonated in place of or in addition to the announced conventional explosion.
- Infrasound measurements were made using arrays of microbarographs and microphones in order to detect low-frequency pressure waves generated in the atmosphere by the motion of the source above the explosion. Although the greatest utility of such measurements may be in monitoring explosions in the atmosphere over broad ocean areas, detection of such waves from the NPE and analysis of their spectral characteristics again demonstrate a potential contribution to the detection, location, and identification of underground sources.
- Ionosonde measurements were made by reflecting radar waves off of the ionosphere. Variations in the reflection detect motions of the ionosphere caused by the upward propagation of the pressure wave generated in the atmosphere by the motion of the ground immediately above the explosion. If they had been successful, the measurements would have provided another demonstration of the ability of this

method to detect explosions at specific sites. Methods such as this would be useful for monitoring a site at which there is reason to believe that an explosion might occur. Unfortunately, the ionization diminishes at night in the region which the reflections occur. The principal investigators for this technology did not expect to see significant recordings from the NPE because it occurred at night, and they did not.

Preliminary Results

Although analyzing all of the data (which are expected to be a significant resource for future work) will take several years, some significant preliminary results are available already. In particular, some initial results have significant implications for CTBT verification.

The following discussion describes some measurements in more detail. Figure 5 shows the seismic waveforms from the NPE and four nearby nuclear explosions. All signals were recorded on a broad-band seismic station located at Kanab, Utah. The waveforms in Figure 5 were scaled to give the same amplitude for the first arrival. Two features are immediately obvious.

- First, the overall records are very similar. In large measure, this observation reflects the fact that the nuclear explosions are close to the NPE (within a kilometer), the depths are similar, and paths by which the energy travels from the sources to the recording station are virtually identical. These similarities cause the waves to arrive at the station at about the same time and with about the same relative amplitude for each explosion. Recordings at other stations exhibit similar characteristics.
- Second, the similarity of the first arrivals, labeled P_n , suggests that the source functions of all of the explosions are very similar. This is not surprising, given that the explosions are all primarily sources of compressional waves, and, to first order, they emit energy isotropically. The NPE confirmed this fact at a variety of distances, and the conclusion is reinforced by the data shown in Figure 6. These data show the

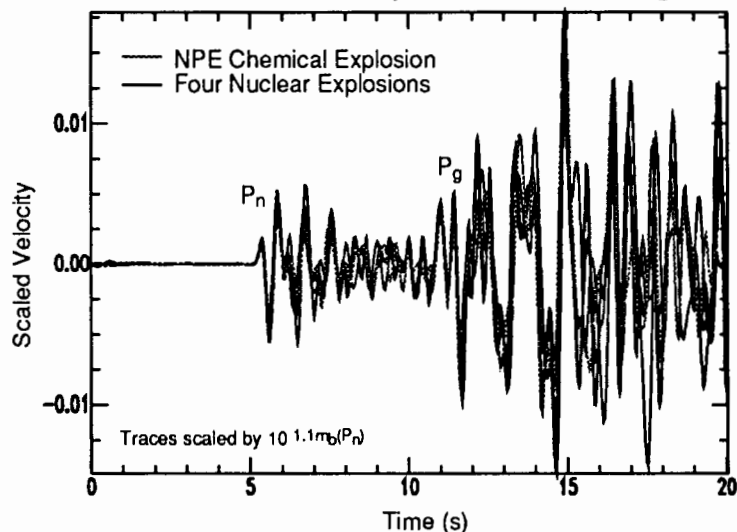


Figure 5. The NPE and four nearby nuclear tests recorded at Kanab, Utah.

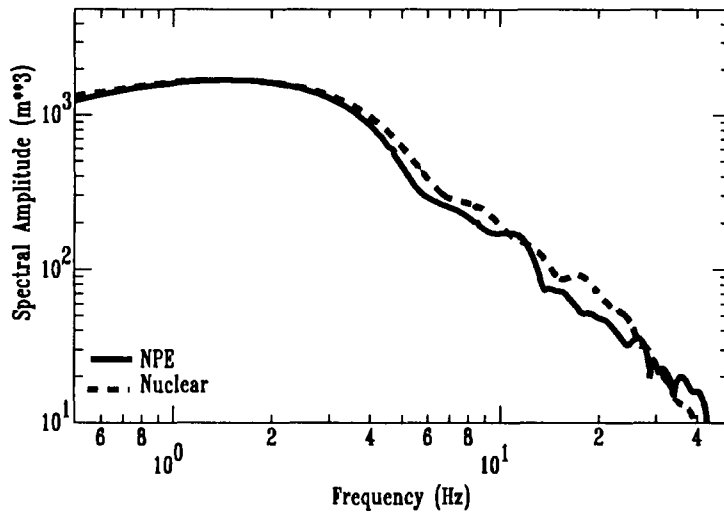


Figure 6. Freefield spectra from the NPE and other nuclear nearby nuclear experiments.

similarity of the spectral content of one of the nuclear explosions and the NPE explosion as measured in the freefield in the frequency range from 0.5 Hz to several tens of Hertz.

nuclear explosion in a large cavity can reduce the amplitude of the seismic signals by a factor of 70, with roughly a factor of 2 uncertainty. Thus, nuclear explosions with a 1-kiloton yield, if detonated in an appropriate cavity, could produce seismic signals similar in size and appearance to spatially compact, instantaneously detonated, conventional explosions with yields as low as 15 tons.) Some relief from the challenge posed by this scenario may be possible if the signals from decoupled nuclear explosions differ from those of fully coupled explosions, as has been suggested by some recent studies.

- Large chemical explosions could be used to calibrate discriminants that would distinguish between earthquakes and nuclear explosions. This calibration method could be used in regions where no previous discrimination work had been done or to calibrate a specific site, either before or after events of concern occur.

Inferences about the relative sizes of the signals from nuclear and conventional explosions are implicit in the above discussion. Several lines of evidence suggest that NPE-like explosions are a factor of 1.5 to 2.5 times more efficient in generating seismic waves than comparably sized nuclear explosions. For example,

- Comparison of the yields and scaling laws for the events shown in Figure 5 gives results in this range.
- The energy released by the nuclear explosion whose unscaled spectrum appears in Figure 6 is about twice the yield of the NPE explosion.

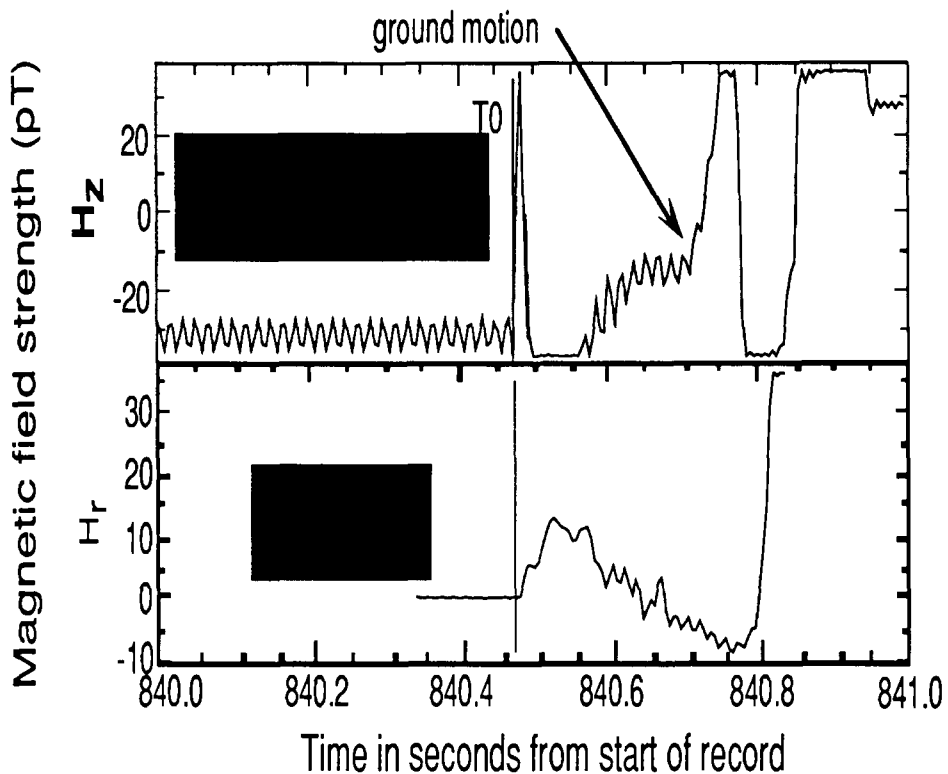


Figure 7. Magnetic fields from the NPE and a nearby nuclear explosion are compared

- Theoretical studies (not shown) support this conclusion.

The preceding results from the NPE reinforce concerns about the verification challenges posed by low-yield, NPE-like, conventional explosions that are detonated either alone or as elements of a larger explosion. These concerns are mostly applicable in areas where large cavities can be constructed, because kiloton-sized nuclear explosions must be muffled (decoupled by detonation in a cavity) in order to produce seismic signals that are small enough to be confused with the signals from most conventional explosions.

Another early result from the NPE is shown in Figure 7. This figure compares the magnetic fields measured within a kilometer of the emplacement points of the NPE explosion and Hunter's Trophy, one of the nearby nuclear explosions. The signals are aligned on the firing times (T_0). The first parts of the signals near T_0 from each event are significantly different. The initial signal from the nuclear explosion is a sharp spike, while the initial signal from the NPE explosion has an emergent character and the signal is slightly delayed. At present, there is no widely accepted explanation for these differences. The latter parts of the signals from both sources show similar behavior associated with the motion of the antenna caused by the arrival of the ground motion.

If these results are supported by additional measurements on conventional explosions and by a review of the limited data available from underground nuclear explosions, these differences could

provide the basis for a confidence building measure that could be implemented for large, announced conventional explosions. The absence of an instantaneous spike in the electromagnetic field measured on-site at shot time for an announced conventional explosion might be used as evidence that a nuclear explosion had not been detonated in place of or masked by the announced explosion. This confidence building measure could be deployed in situations in which remote observations might not differentiate between compliance and significant noncompliance.

In addition to these two results, the NPE has also produced significant insights into the nature of the regional seismic waves generated by explosions and discrimination between earthquakes and explosions. These results are discussed in some detail in other papers in these proceedings.

Summary

The Lawrence Livermore National Laboratory conducted the Non-Proliferation Experiment for the DOE in order to study phenomenology underlying discrimination between conventional explosions and nuclear explosions. The resulting information also will be useful for challenge inspections initiated in response to events that appear similar to nuclear explosions when observed remotely. In turn, this information will apply to confidence building activities that might be carried out on large, announced, conventional explosions in order to determine whether a nuclear explosion was substituted for or masked by the announced explosion.

The experiment included several major elements as well as a host of minor ones. The major elements included

- Detonation of 1.29 million kg of ammonium nitrate and fuel oil that released 4.48 terajoules of energy (1.0 kt nuclear equivalent) in N tunnel in Rainier Mesa at the Nevada Test Site provided the energy source for most of the experiments.
- Hydrodynamic measurements made in and nearby the explosion confirmed that all of the blasting agent detonated and gave a basis for estimating the energy release.
- Ground motion measurements made at distances ranging from a few meters to thousands of kilometers when combined with similar information from nearby nuclear explosions are providing insight into seismic wave generation and propagation phenomena that affect the performance of regional discriminants. The results to date indicate that conventional explosions detonated in configurations similar to the NPE generate seismic waves that are

- 1.5 to 2.5 times larger in amplitude than the seismic waves generated by nuclear explosions with the same energy release.
- Very similar in frequency content to nuclear explosions with the same energy release.

Together these results suggest that discrimination between spatially compact, instantaneously detonated conventional explosions and nuclear explosions will be very difficult to impossible using remote measurements. Conversely, the similarity of the regional seismic signals from NPE-like

conventional explosions and nuclear explosions may allow the use of conventional explosions to empirically calibrate the discrimination process for regions or locations in which no nuclear explosion has been recorded or detonated.

In practice, at least two additional factors must be considered First, many conventional explosions are not detonated under conditions like those of the NPE. For example, most U.S. industrial explosions are distributed in space and time. The spatial and temporal patterns introduce systematic variations in the signals that show promise as a discriminant. However, other countries do not appear to follow these practices to the same extent that the U.S. does, and the generality of the discriminant is uncertain. Second, kiloton-sized nuclear detonations that are well-coupled into the surrounding earth generate signals that would be detected with good signal-to-noise ratios in most regions of Earth. Such signals from a conventional industrial explosion would be unusual. If the nuclear explosion is detonated in a cavity, the signals would be much smaller and would not stand out to the same degree. Both factors are the focus of ongoing research.

Preliminary analyses of the NPE measurements are also producing useful information about OSI monitoring methods. One example is the differences in electromagnetic fields generated by conventional and nuclear explosions. The delayed, somewhat emergent, magnetic field signal observed from the NPE contrasts with the almost immediate spike observed on a nearby nuclear explosion. The generality of these observations should be explored further, but the difference offers some promise that electromagnetic measurements made in the neighborhood of large, announced conventional explosions provide confidence that a nuclear explosion was not substituted for or masked by the announced explosion.

Much NPE data remain to be analyzed. Multiple seismic measurements made at a variety of distances, hydroacoustic, infrasound, and other measurements all remain to be examined in detail. We expect the yield to be additional insight in the basic phenomenology for detection, location, discrimination, and on-site inspection. In addition, deployment of temporary seismic instruments will provide descriptions of the evolution of regional seismic waves from source to receiver and insight into the structure of the crust and upper mantle of the western United States. The NPE data will be a resource for many monitoring and scientific research efforts in the coming years.

References

- Richards, P. G., D. A. Anderson, and D. W. Simpson, "A Survey of Blasting Activity in the United States," *Bulletin of the Seismological Society of America* 82, 1416, 1992.
- Arms Control and Nonproliferation Technologies*, Department of Energy, DOE/AN/ACNT-94A, p. 62, 1994.
- Arms Control and Nonproliferation Technologies*, Department of Energy, DOE/AN/ACNT-94A, pg. 40, 1994.

US Comprehensive Test Ban Monitoring Goals

Larry Turnbull

Arms Control Information Systems

The purpose of this paper is to provide a Comprehensive Test Ban monitoring framework for the technical discussions about the DOE Non-Proliferation Experiment. The results of this experiment—even if they mostly identify what is not technically possible—will, in the long run, aid in the development of a monitoring regime for distinguishing between a single large chemical explosion and a decoupled nuclear explosion, or in detecting and identifying a decoupled nuclear explosion masked by a ripple-fired chemical explosion.

Ideally the U.S. monitoring goal for a Comprehensive Test Ban is to detect, identify, locate, and attribute a nuclear explosion of any yield conducted in any environment. In a practical sense, though, as most of you know, that goal is not technically possible. Balancing what should be technically achievable over the next several years against one of the primary policy goals of the United States—that of a CTB as a means to retard and even prevent the proliferation of nuclear weapons—the United States has stated during the CTB negotiations that an effective verification regime "could be capable of identifying and attributing with high confidence evasively conducted nuclear explosions of less than a few kilotons yield in broad areas of the globe."

In further elaboration of this goal, the United States has stated the following:

--The primary objectives of a CTBT verification regime should be to verify the absence of nuclear explosions in all testing environments, and to facilitate the resolution of ambiguous events.

-- The verification system should be able to detect and identify nuclear explosions, even when evasively conducted and attribute them with high confidence to specific states, on a timely basis.

--The system should be able to provide credible evidence to treaty parties to serve as the basis for collective or individual action.

--It should be able to minimize the occurrence of false alarms.

-- It should be able to confirm any declarations and notifications made by parties under the provisions of a Comprehensive Test Ban Treaty.

Translating these policy statements into what could be termed the technical challenge for monitoring the underground environment, I would like to highlight the following points:

"...a few kilotons evasively tested": The evasion scenario of most concern for the underground environment is the muffling of a nuclear explosion in a large cavity, with a potential reduction in coupled energy of a factor of 70 or greater at the seismic frequencies which will most probably be transmitted through complex geologies. In seismic terminology, a few kilotons decoupled translates into

a range of body wave magnitudes from 2.5 to 3.0, depending on the local geology and the regional seismic attenuation.

In judging whether this evasion scenario is credible, both the feasibility of constructing a large cavity and of containing the debris from the nuclear explosion must be examined. From the worldwide mining and petroleum literature, it is clear that the construction of large cavities in both hard rock and salt is feasible, with costs that would be relatively small compared to effort to produce the material for a nuclear device. It is also clear from the open literature and symposiums on containment that containing both particulate and gaseous debris is quite feasible in salt, and more difficult—though not impossible—in hard rock. Therefore, we judge that the cavity decoupling evasion scenario to be credible and should be factored into any underground CTB monitoring goal.

“...the system should be able to detect and identify nuclear explosions, even when evasively conducted and attribute them with high confidence...” In a CTB monitoring regime, we will be monitoring for low-probability/high consequence events—in other words, events which have a low probability of occurring, but if they do occur and are properly identified, they will have a high consequence in terms of their political impact. For those events, the policy community will desire a very high standard of evidence. And this evidence will need to be described in as much a factual, non-subjective manner as possible. For example, if an event is thought to be shallow, the technical specialists will be asked to determine the high confidence statistical uncertainty on its depth estimate? If an event produces measurable bodywave and surface wave data at either teleseismic or regional distances, are the ratio of phases more like an earthquake or an explosion, and what is the confidence in this assessment? If it is assessed to be “explosion-like,” does it exhibit any spectral tendencies which would indicate a ripple fired chemical explosion? And what is the statistical confidence in your assessment?

“...the regime should be able to confirm any declarations and notifications made by parties under the provisions of the treaty...”: It seems apparent that, unless the technical community is able to develop robust seismic discriminants between nuclear and chemical explosions, that cooperative measures—which include declarations, notifications, and on-site inspections—will be required to reduce the monitoring uncertainty brought about by the large number of chemical explosions. It is in the on-site inspection aspect of the problem, where through some technical means the inspecting party is able to confirm that a nuclear explosion did not take place, that this conference can make its most valuable contribution. If, among the vast amount of sensor data collected during the experiment, there is either one measurement or a suite of measurements that could be used during an on- site inspection which will demonstrate with high confidence that a nuclear explosion did not take place, then I think the Non-Proliferation Experiment will have made a major contribution to the building of a robust CTB verification regime.

In order to further elaborate on the technical analysis that would be required for an "event of interest," I thought I would use as an example an event I have discussed several times before, the Soviet Peaceful Nuclear Explosion conducted in the Ukraine in 1979.

Example of Monitoring Problem That Could Be Encountered Under a CTB

The Peaceful Nuclear Explosion of 16 September 1979 (from 27 June 1992 Izvestiya article).

- * Located in the Ukrainian Donetsk Oblast, Yunkom coal mine, beneath the town of Yunokommunarovsk.
- * Purpose was to eliminate or reduce presence of methane gas in the mine by creating fissures and fractures.
- * Device was detonated next to the mine after 8000 residents were evacuated as part of a "civil defense drill." They returned after one-half day, and the miners went to work the next day.
- * Detonated at noon on 16 September 1979; one-third kiloton; one kilometer deep.

An informal analysis of this event was conducted between seismologists in the U.S. and those in Norway. This analysis provided a good example of some of the problems that we are faced with in the monitoring community and that we have had to deal with for other ambiguous events. Some of the interesting points were:

- * This event was not listed in any of the published seismic event catalogs.
- * When the event occurred in 1979, a detection occurred at the large seismic array in Norway, and the computer program which automatically analyzed the data produced an event 7 seconds before the time and about 500 kilometers from the town location published in the Russian newspaper in 1992 with a seismic magnitude equivalent to about a hundred tons yield (3.3). The review by the Norwegian analyst at the time--and they are very competent--did not consider the computer solution of sufficient quality to include in the monthly bulletin. The area initially located has a history of underground rock bursts from mining.
- * When the seismic location for the event was adjusted to the location announced in 1992, the estimated origin time was very close to the announced time. The Norwegian scientists were then left with the conclusion that the event detected by them was the Soviet PNE.

Application of an Event of this Type to a CTB Monitoring Regime

- * Let us assume that this event, with a body wave magnitude of 3.3 (equivalent to about 5 to 10 kilotons decoupled), was detected at 4 to 6 seismic stations, was located within an area of 50

square kilometers, and by a regional discriminant was tentatively identified as "explosion-like" with a confidence level of 75 percent.

- * Some of the questions that would immediately be asked of the seismic community are:
 - What is the chemical explosion history of the region in question? What is the rock-burst history of the region? Are the explosions or rock bursts seldom or frequently seismically recorded? Is the event seismic magnitude anomalously high for this region?
 - Does the seismic spectra exhibit any similar characteristics to previously recorded explosion-like events? Of ripple fired chemical explosions? What is the confidence in this assessment?
 - Is the data and analysis sufficiently strong to warrant a request for a challenge on-site inspection? Or, should we think about a possible treaty mechanism for requesting an international on-site presence when the next chemical explosion of this magnitude is to be conducted in the same region?
 - Assuming that a request for pre-notification of another chemical explosion in the same region is accepted by the host country, what on-site technical means would help provide high confidence event identification?

I hope these brief comments provide a context for the importance of the DOE Non-Proliferation Experiment in a future CTB monitoring regime. I look forward to your presentations over the next three days.

Blasting Activity of the Mining Industry in the United States

Paul G. Richards

Lamont-Doherty Earth Observatory, Palisades, NY 10964, and
Department of Geological Sciences, Columbia University

ABSTRACT

About 2 megatons of chemical explosives are used annually in the U.S., principally in mining for coal and metal ores. Most of this explosive is used in surface mines rather than underground mines. On a typical work day there are about 30 explosions greater than 50 tons, including one shot greater than 200 tons. A few times a year, shots greater than a kiloton are carried out. Shots greater than 100 tons are thought of as large by the blasting industry and occur only at a limited number of mining operations. Shots in underground mines are typically much smaller, because of safety considerations.

Almost all chemical explosions above 1 ton in the U.S. are ripple-fired and almost all above 10 tons are also shallow. Almost all are intended to break rock or to remove overburden, and are therefore very inefficient, relative to contained single shots, in generating seismic signals at regional or teleseismic distances. These attributes make explosions used in industry quite different from the Non-Proliferation Experiment.

There is very little correlation between the total amount of explosive used in a ripple-fired blast, and the seismic magnitude. Statistics on blasting magnitudes are of interest in the context of estimating the number of signals that must be analysed at the data center of a global explosion monitoring network. There is a blast reported with regional (or duration) magnitude 3.5 or above, in the U.S., a few tens of times a year; but it would appear that the teleseismic magnitude (m_b) of such events are significantly lower than 3.5. Only about 10 to 30 chemical explosions per year in the U.S. are detected teleseismically with $m_b > 3$.

Methods of routinely discriminating most chemical explosions from other seismic sources use spectra of regional phases at frequencies up to about 30 Hz, which is significantly higher than frequencies needed for recording teleseismic signals. The best discriminants appear to be the high-frequency spectral ratio of waves with P-wave energy (e.g. Pn or Pg) to waves with S-wave energy (Sn or Lg); and the use of spectrograms, which can be particularly useful in identifying ripple-firing.

INTRODUCTION AND BACKGROUND

In the context of developing the verification regime for a Comprehensive Test Ban Treaty (CTBT), a detailed discussion of chemical explosions can quickly develop into an evaluation of intricate

evasion scenarios. But it is important first to recall the history of how requirements for CTBT monitoring have evolved. Only with such a background, which shows that monitoring standards have changed greatly since CTBTs were first discussed, can potential problems associated with blasting practices of the mining industry be placed in perspective.

The Limited Test Ban Treaty (LTBT) of 1963 was preceded by about five years of intense efforts to negotiate a CTBT, and by intense efforts over the same period to consider how the occurrence of underground nuclear explosions might be detected and identified. The U.S. requirements for seismic monitoring in the last stage of negotiations in 1963, in support of a trilateral CTBT between the U.S., the U.S.S.R., and the U.K., were essentially to have a detection capability down to about magnitude 4 for the Soviet Union; and identification capability for enough of the events in this region above magnitude 4.75, so that for the remaining unidentified events (above magnitude 4.75) a program of on-site inspection (OSI) could be relied upon (U.S. Congress, 1963).

At the time, magnitude 4.75 was thought to represent about 19 kilotons (Rainier coupling). Those negotiations failed, ostensibly over the number of OSIs that would be allowed. The inability in 1963 to demonstrate convincingly that identification capability was attainable above magnitude 4.75 contributed strongly to the decision not to ban underground testing in what then became the LTBT (the "atmospheric test ban treaty"), and hence to the underground test programs of the last three decades.

At that time, chemical explosions were deemed far too small to be of interest, since, except for accidents or very unusual construction shots, they did not (and still do not) occur with signals even approaching magnitude 4.75.

It has been apparent since the early 1970s that seismic data are in fact adequate to achieve identification down to well below magnitude 4.75 for Eurasia, and probably for the rest of the world, without the need for OSIs. And identification is even better with respect to a 19 kiloton reference, since for most of the U.S.S.R. the expert community began to realize in the late 1970s that magnitude 4.75 corresponds to only 2 - 3 kilotons. However, now that CTBT negotiations are again very real, the standards for effective verification have become much more stringent than was the case 30 years ago. For example, the networks of seismometers now under serious discussion for the international verification regime are expected to have detection thresholds down to around magnitude 3 - 3.5 for Eurasia; and thousands of additional seismic stations distributed around the world can potentially be drawn upon to achieve even better capabilities in some regions.

It will clearly be desirable to develop routine discrimination procedures that can identify events down into the magnitude range 3 - 3.5, thus reducing the number of detected but unidentified events to a level that is deemed manageable, even at magnitudes way below what was thought relevant in the 1960s. Signals of such low magnitude, if caused by underground nuclear explosions, could arise only from shots with yield on the order of 40 - 100 tons if tamped in hard rock; or conceptually from yields of a few kilotons if the shot were carried out as a major effort in decoupling.

The U.S. conducted a small decoupled nuclear shot on December 3, 1966, with a yield of 380 tons, that probably had a magnitude (it was never measured) of about 2. The U.S.S.R. conducted a partially decoupled nuclear shot of about 10 kilotons on March 29, 1976, in West Kazakhstan, that had a magnitude of about 4, with signals picked up at several stations in Scandinavia and elsewhere in Eurasia as well as at an array in Canada. Neither shot was clandestine.

It is only in the modern context of greatly improved detection capability and concern with evasion scenarios such as those traditionally associated with decoupling, that seismic signals associated with blasting activity are potentially problematic. Note also that mining is an activity often associated with uses of sophisticated drilling and earth-moving equipment, and therefore conceptually provides perhaps the most plausible environment for evasion of CTBT constraints, at least for underground testing. For example, conceptually a small fully-decoupled underground nuclear explosion might be carried out in a mine at the same time as a large routine chemical blast at the same general location. Or the nuclear shot might be carried out alone, and reported to inquirers as a chemical explosion.

In the U.S., there are on the order of a few chemical explosions a month reported as being above local magnitude 3.5; however, these shots typically have lower magnitudes on a teleseismic magnitude scale (which is the more relevant scale for characterizing the seismic signals from a nuclear explosion). There are perhaps hundreds of shots in the U.S. each week above local magnitude 2.5. Presumably, chemical explosions with similar seismic magnitudes occur in other countries with vigorous mining activity. For many regions where a seismic network exists that can detect all events down to magnitude 2, it is common to find that signals are picked up from far more chemical explosions than earthquakes.

Not recognized by these statistics is the fact that every few years in this century, a substantial accidental chemical explosion has occurred - usually at the Earth's surface but occasionally underground (White, 1994). For example, an underground accidental explosion of Swiss Army munitions occurred in November 1992 that had seismic magnitude about 4 and was widely recorded. In the U.S., the discovery of what today is the most commonly used blasting agent (ANFO, described further below) was made when two Liberty ships carrying thousands of tons of ammonium nitrate (intended for use as a fertilizer) blew up in a Texas harbor in 1947. Also in the U.S. there have been major accidental explosions in facilities that store natural gas, and in a factory manufacturing rocket fuel. There are many examples of accidentally exploded ammunition dumps.

The next section of this paper reviews the numbers of industrial explosions in the U.S. at different total charge size. A description is then given, of some examples of the major types of blasts, pointing out that almost all chemical explosions in the U.S. are "ripple-fired" - a practice that results in great reduction of magnitude with respect to that expected if all the charge were fired at once. A very brief review is given of methods for discriminating between earthquakes, industrial blasts, and single-fired explosions such as a small underground nuclear explosion; and an informal survey of the

numbers of blasts at different magnitude is reported, for different seismographic networks in the U.S.

The Non-Proliferation Explosion (NPE) conducted at the Nevada Test Site on September 22, 1993, was large (1 kiloton), deep and contained, and single-fired. While these properties make the NPE similar, in seismic excitation, to a small underground nuclear explosion, they also make the NPE unique among chemical explosions and certainly non-representative of industrial blasting. Explosions with the characteristics of the NPE serve no commercial purpose.

STATISTICS ON CHEMICAL EXPLOSIONS IN THE UNITED STATES

Information about blasting activity in the mining industry in the U.S. is available from various sources, but rarely from individual mines directly. Thus:

- the U.S. Bureau of Mines (USBM) publishes annual information on chemical explosives manufactured and used in the U.S., with breakdowns by state, by chemical explosive type, and by different industries;
- the Mine Safety and Health Administration (MSHA) maintains lists of active and inactive underground surface mines;
- manufacturers of chemical explosives are knowledgeable on which mines consume significant amounts of explosives, and blasting consultants maintain files on perhaps 30% of mining blasts.

From these sources, Richards et al (1992) showed that about 2.2 million metric tons of chemical explosives are used annually in the U.S., principally in mining for coal and metal ores (see Figure 1). Of this total, about 70% is used in the mining of coal, 8% in mining for metal ores, 10% in quarrying and nonmetal mining, and 7% for construction. There are now about 4000 active surface mines in the U.S. Shots greater than 100 tons are thought of as large by the blasting industry and occur only at a limited number of U.S. mines. Shots in underground mines are typically much smaller, because of safety considerations.

Subsequently, additional sources of information were developed. For example:

- the International Society of Explosives Engineers (ISEE) has about 3000 members in about 80 countries, holds annual meetings with about 1000 participants, and publishes proceedings volumes giving case histories of particular mining/construction operations; and
- several states require permits for any blasting above a certain size (for example, Kentucky, which manufactures more than twice as much explosive as any other state, requires a permit for blasting above 40,000 pounds - about 20 tons).

A goal of the Richards et al (1992) study was to estimate the rate at which the numbers of chemical explosions increase with decreasing shot size. The procedure for making the estimate, was first to document the distribution of shot sizes for a set of more than 20,000 shots monitored at more than 500 locations in the U.S. during 1987 by a group of consultants to the blasting industry. For this set of shots, with total explosive yield amounting to 135 kilotons, detailed information as to time, place and

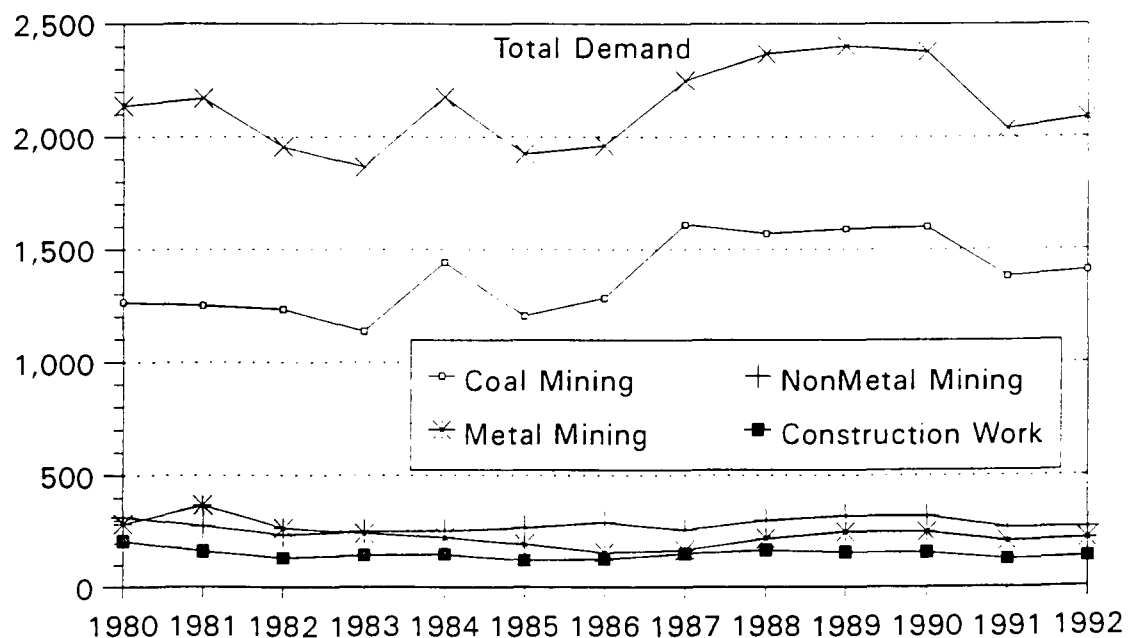
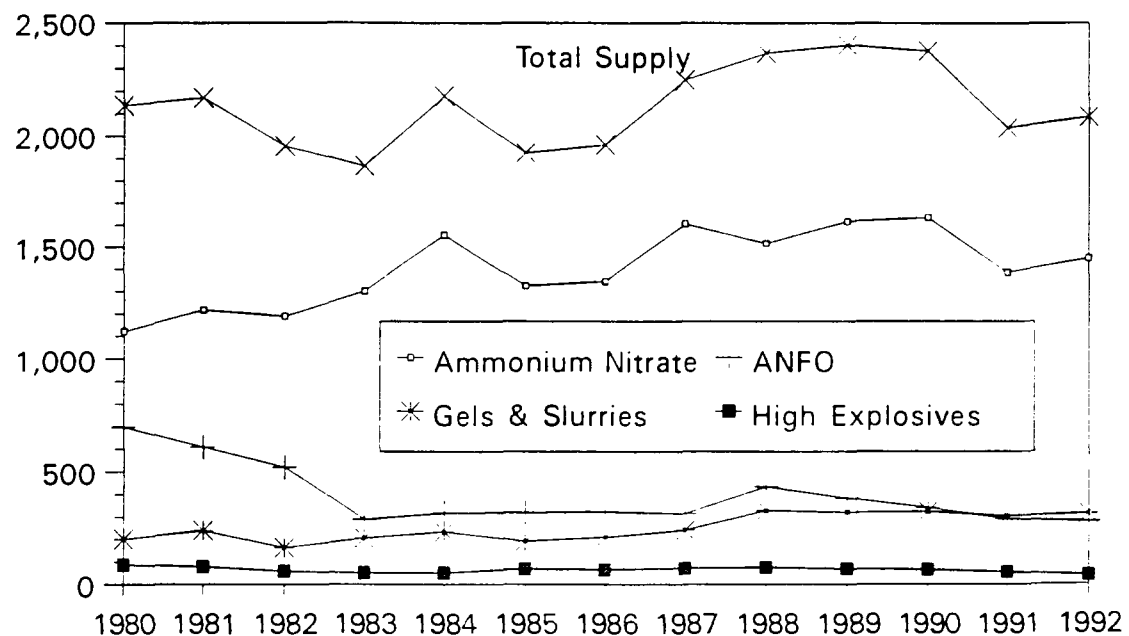


Figure 1. Supply and demand for U.S. industrial explosions (U.S. Bureau of Mines, 1993). A "short ton" is 2000 pounds.

purpose was made available. It was then possible to extrapolate upwards, using constraints on total amounts of explosive and total number of mines provided by the USBM and MSHA, to obtain an overview of blasting activity for the whole United States. On a typical work day in the U.S., there are about 30 explosions greater than 50 tons, including one greater than 200 tons. Shots bigger than a kiloton may occur a few times a year, for example at surface coal mines in Wyoming.

The blasting agent most commonly used for industrial explosions is known as ANFO (an acronym for ammonium nitrate and fuel oil), which delivers about 90% of the energy per unit mass obtainable with TNT. The bulk of U.S. consumption of industrial explosives (about 65%) is unprocessed ammonium nitrate, which is mixed with fuel oil by other manufacturers, often on-site at mines. ANFO produced centrally in final form, at plants for transport to sites where the explosive is used, constitutes about 15% of U.S. industrial explosives; and about another 15% is made up from ANFO-like products such as water gels, slurries and emulsions - which in some cases are usable in the presence of water, and/or have high values for the velocity at which the explosion front moves through the product (i.e. faster than for ANFO). High explosives - which have different detonation characteristics - amount to about 3%; and "permissible" explosives (for example, for use in underground mines) amount to less than 1%.

Very roughly, one kilogram of explosive is used to break one cubic meter of rock. From knowledge of the amount of coal and metal ores produced around the world, it is then possible to estimate approximate amounts of explosives used in different countries (Richards and Kim, 1992; Leith, this volume).

Richards et al (1992) pointed out that almost all U.S. industrial explosions are now "ripple-fired," meaning that tens or hundreds of holes are drilled in rock and separately filled with an individual charge, each having its own detonator system. The detonators are then fired in a sequence of predetermined delay times, in order to fragment the rock in a controlled fashion. I next describe some uses of chemical explosions, beginning with a blasting practice that predates ripple-firing, but which is important today in the context of CTBT verification and discussion of the NPE.

USES OF CHEMICAL EXPLOSIONS IN U.S. INDUSTRY

Of particular interest in the context of CTBT monitoring, are any explosions in which large amounts of explosive are fired all at once in a contained environment. A few decades ago, it was common practice in certain mines and quarries in the U.S. to drive a tunnel into a rock face, to fill the tunnel with chemical explosive, and to fire the whole charge at once. This practice is called *coyote blasting* in the U.S. (The name arose, because sometimes it was possible for blasters to find an existing tunnel, such as a coyote might be using.) The idea was to lift the body of rock upwards and sideways above the tunnel, so that the rock was fragmented as it fell back down (see Figure 2). This practice is known to produce strong seismic signals since the explosion is substantially contained, but coyote blasting is a notoriously dangerous practice because of the possibilities for miscalculation: too much charge and the

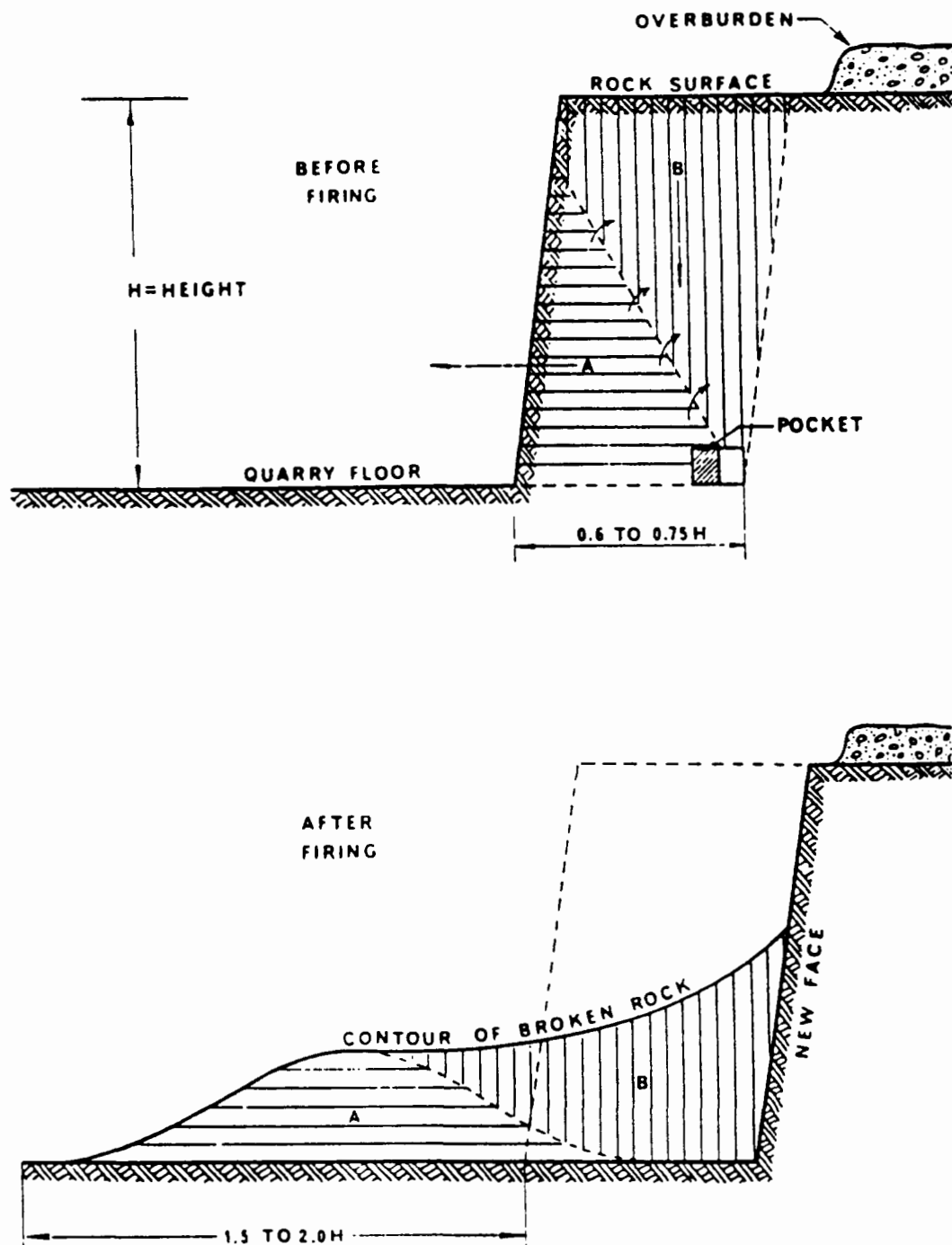


Figure 2. Mechanics of a coyote blast, in which shearing forces develop above the tunnel or pocket in which the charge is fired all at once (or in a small number of delays).

explosion will blow fragments far and wide; too little and the rock does not fragment as desired.

The following are my notes of a January 1994 interview with an expert old-time blaster, who executed many coyote blasts in the 1950s and 1960s:

"The Corona quarry in Southern California shot coyote blasts up to a million pounds in the 1950s... The Mapleton quarry, Pennsylvania, shot coyote blasts around 25-30,000 pounds until recently... The key is, to break the rock up small enough so it's easy to move. You could get a lot of rock for little money - but [coyote blasting] is a lawyer's delight today. The only place I know where it is still carried out regularly, is blasting in basalt in Oregon and Washington - maybe several thousand pounds at a time - to break rock used for logging roads."

(Seismic data from the network operated by the University of Washington confirms that some of the seismicity observed in logging areas appears to be due to blasting.)

The occasional coyote blast - apparently now an unusual event - is sometimes reported at annual meetings of the International Society of Explosives Engineers - such as a blast in the Maiden Rock Silica Quarry, near Butte, Montana in January 1992 (193,000 pounds in four separate charges, producing 300,000 tons of well-broken rock). This was highly-fractured silica rock, which macroscopically is both weak and brittle, for which there is no need to induce additional fractures by use of separate holes and ripple-firing.

The practical reason it has become possible in the U.S. to avoid the dangers of coyote blasting, is that drilling technology has improved so much. For the typical large chemical explosions now carried out for commercial purposes, ripple-firing with a sequence of preplanned delays is used exclusively. This conclusion is reached after interviews with numerous blasters, blast vibration consultants, and powder company executives.

The word "delay" is used in the blasting profession in several different ways. Sometimes it refers to the time between separate charges ("a delay of 200 ms."); sometimes to the time period in which a particular amount of charge is used ("2,000 pounds per delay"); and sometimes it is used to refer to the separate charge sizes directly ("a 100,000 pound shot with 2,000 pound delays").

The technology of blasting has become more and more sophisticated in recent years, with increasing reliance on accurate timing to achieve maximum desired fragmentation in a controlled blast. The mining industry now refers to high-tech ripple-firing as "millisecond delay initiation," however I follow common practice in referring to all blasting with use of delays as "ripple-firing."

The common purpose underlying almost all industrial blasting is to break or move rock. Often the goal is to break the rock into fragments of prespecified size. Before describing the typical layout of a ripple-fired blast, it is helpful to note how strongly the degree of fragmentation of rock can vary, for a single blast of given size within the rock, according as the distance of the blast from the nearest free surface is varied. This variability is shown in Figure 3. The distance to the free surface is referred to as the "burden." (The Figure will be familiar in principle to those who study the surface effects of

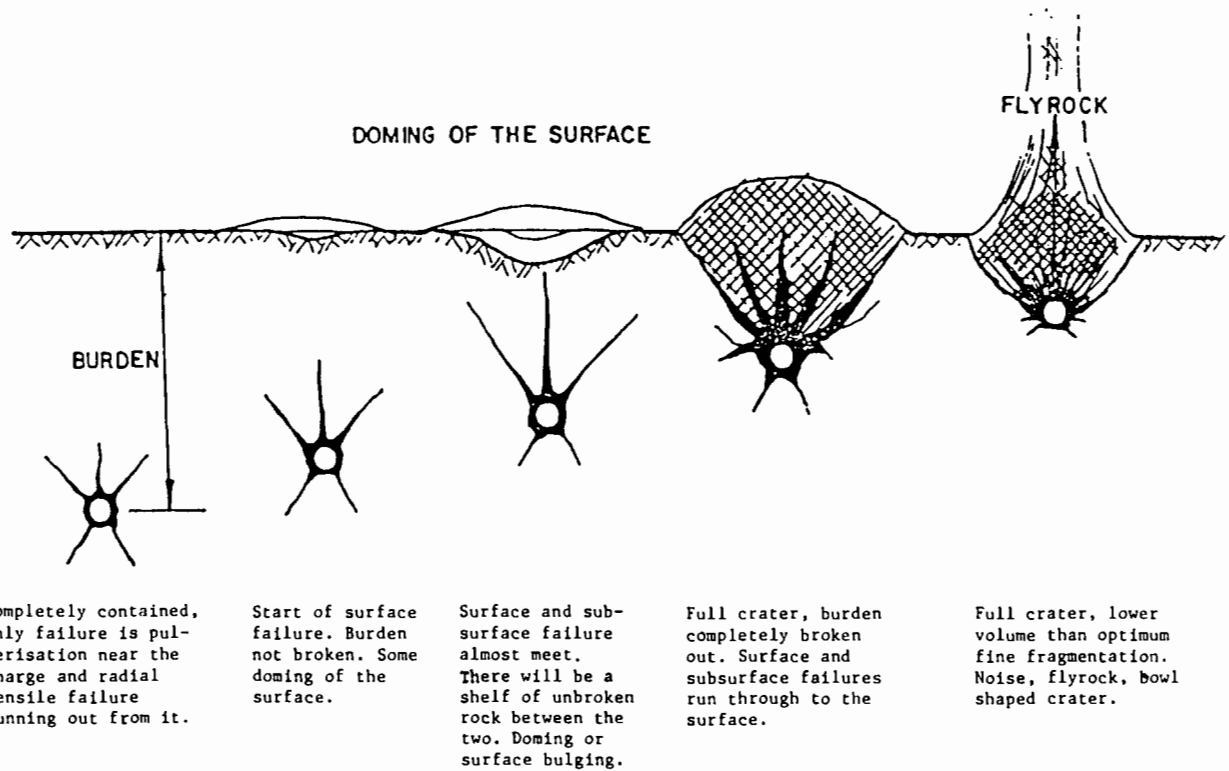


Figure 3. The effects of an exploding charge set off at different distances away from a free surface. This is a 2-D section through a 3-D structure in which the charge may be in a cylindrical hole that is nearly vertical, with the nearby free face being nearly vertical.

underground nuclear explosions, with the "burden" in this case being depth. A deep explosion may not form a chimney or subsidence crater and may have only a small cavity; and at the other extreme a throw-out crater is formed.) In mining and quarrying, the free surface is commonly nearly vertical, and the blast is based on a cylindrical charge that is nearly vertical.

Figure 4 shows the layout and associated terminology of a typical ripple-fired blast used not only to break but to move rock. Three rows of holes are shown in this case. When the holes in the row nearest the free face are fired, the rock "bulks" (the situation second from the right in Figure 3). That is, the rock begins to move away from the second row - which in turn is fired to move the rock between rows one and two, and so on for as many rows as the shot contains. Occasionally, whole rows may be fired simultaneously, but this can result in strong local ground vibrations, so it is much more common to have delays along each row, as well as delays between rows. A skilled blaster can in this way "throw" or "cast" the rock a considerable distance horizontally. In surface coal mining, such "cast blasting" is used to remove rock strata above the coal, exposing the coal itself to a dragline or other processor for removal ("strip mining"). Charges are usually fired from the bottom up in each hole, creating a rubble zone that inhibits efficient seismic wave generation. Often, such charges occur in loose, dry materials -

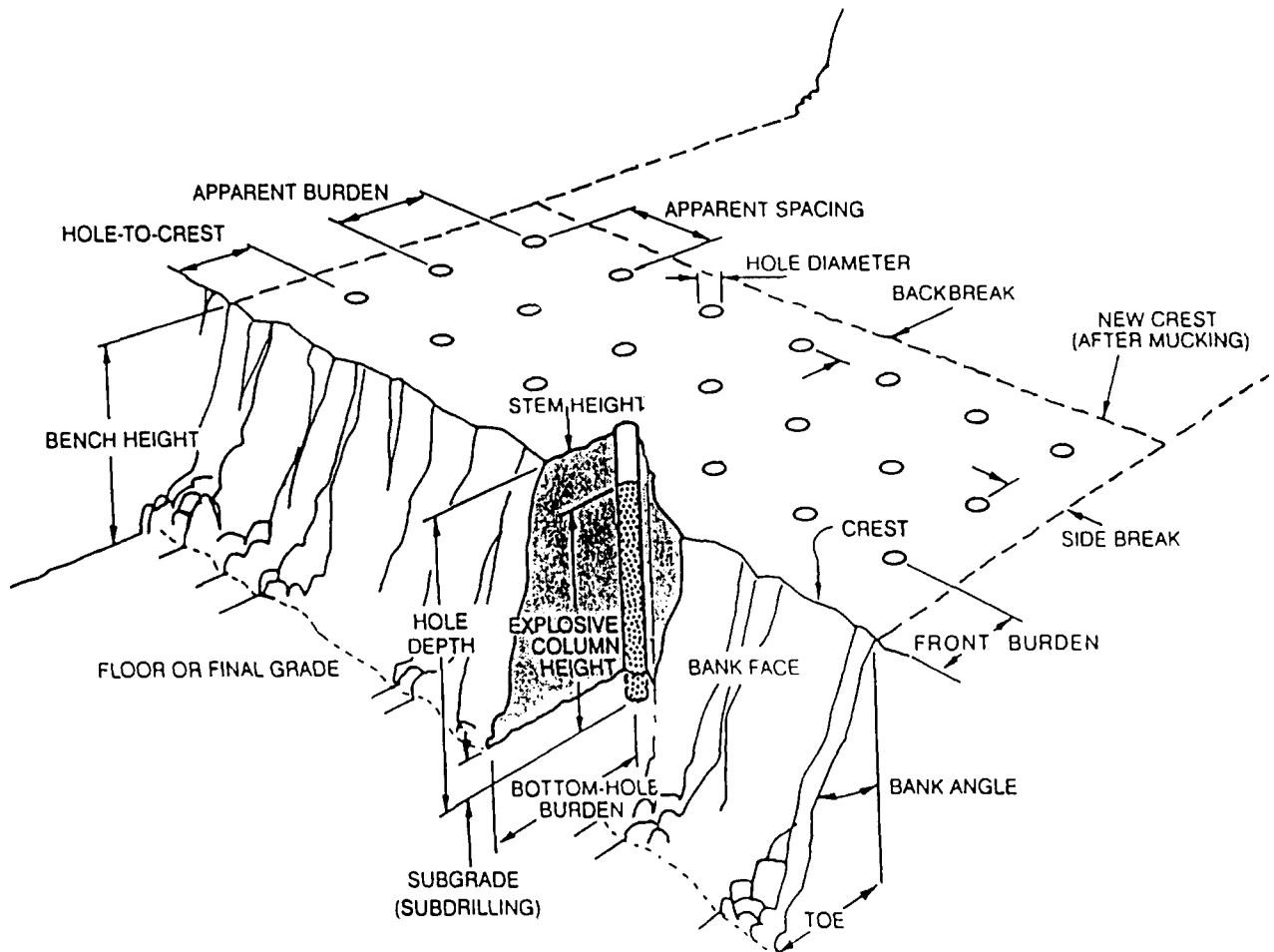


Figure 4. The layout and terminology of a ripple-fired shot. Large shots of this type use several tens or even hundreds of separate holes, each using typically on the order of a ton of blasting agent per hole.

which again inhibits good coupling into seismic waves. In an open pit mine (for example, for gold or copper ores), it is the ore body itself that is drilled and blasted to obtain fragments suitable for processing.

The amount of ground vibration is found in practice to be related to the maximum size of charge fired in any hole, rather than to the total charge size (Devine and Duvall, 1963; Nicholls et al, 1971). It appears that the seismic magnitude is also determined by the amount of charge set off in one component blast, which for a large industrial explosion will be on the order of 1% of the total. Since magnitude scales are logarithmic, the magnitude reduction due to ripple-firing in this case would be about 2 full units. Thus, blasts of over a kiloton in Wyoming surface coal mines are observed to have magnitude around 2 (whereas they would be expected to have magnitude around 4 for a contained kiloton fired all at once).

In the context of CTBT monitoring it is therefore of interest to study not only coyote blasting, but also any examples of explosions that use "large delays" (i.e. large amounts of explosive per component

in a ripple-fired shot). One such blasting practice occurs in the Athabasca Oil Sand deposits of Alberta - where the use of up to about 10 tons per hole was reported in 1993 (19th annual ISEE conference). In this case, the procedure at the Suncor, Inc. operation is to drill with augers in the tar sand to depths of around 110 feet (the thickness of the deposit). Hole diameters were increased from 18" to 22" to 30" in the early 1990s, but still it was not possible to meet production quotas. So, in about 1992, the operation went to 48" diameter holes about 100 feet apart, on a research basis, and thus developed the confidence to use such holes for production blasting. For example, a typical shot on September 17, 1992, with 14 holes each around 20,000 pounds, had a total charge size around 150 tons. Success with this technique has led to consideration of using 96" diameter holes - which presumably could have four times the charge size, per hole. However, one may speculate that tar sand (having very low Q?) is not a material that will result in efficient coupling into seismic waves.

Another type of blasting with effectively instantaneous detonations is presplit blasting, in which a single line of holes are lightly charged and all are fired together. The purpose of presplitting is to propagate a crack between holes to establish a fracture plane in the rock mass - for example, around the perimeter of a future excavation site, so that the finished face of the rock, left after the excavation has been completed, is smooth and undamaged. Since the intent is not to fragment the rock, presplit blasts do not use large amounts of explosive.

Explosions used in underground mining are typically much smaller than shots used in surface mining, in order to avoid danger to people and damage to underground equipment and structures. Again, as in surface mining, explosives underground are used to achieve prespecified sizes of rock fragments for later processing, and this is done by use of many charges set off in a series of delays. A common practice for underground mining is called vertical crater retreat (VCR) blasting, in which holes are first drilled vertically between two drifts. The holes are loaded and fired from the bottom so that the ore is dropped down, for later removal via the lower drift. Rock fragments that are too large for transport in underground tunnels represent major inefficiencies in a commercial operation, and much effort goes into planning the pattern of delays needed to achieve the most desirable fragmentation. At the largest underground mine in the U.S., the Homestake Mine in South Dakota, a medium-to-large VCR blast uses 2.5 to 4 tons of explosive, shot with delays. A large VCR blast uses 5 to 6 tons, and the largest VCR shot at Homestake was 60 tons. Underground coal mining is subject to many restrictions in the U.S. because of the dangers of underground fire, and most blasts in this environment are a small fraction of a ton.

Blasting practices in the U.S. in surface mining for coal underwent significant changes following 1986, when the Surface Mining Act prompted a series of regulations (30 CFR, paragraphs 816.61 to 816.67). These changes included rules governing how much explosive may be shot in any 8 ms period. As a result, the "maximum pounds per delay period" is now *defined* in U.S. industry to be the amount of explosives designed to be detonated within an 8 ms interval. The weights of two explosive charges will be counted together for regulatory purposes if their nominal firing times are within 8 ms. Regulations in the U.S. are often written in terms of limits on the amount of ground vibration allowed. One of the key

documents establishing safe blasting criteria for ground vibrations is Appendix B of Siskind et al (1980). Blasting is also highly regulated in West European countries. Even where there is little or no regulation, blasting in practice is carried out with ever-increasing attention to the smooth working of operations around the blast site. For example, in an open pit copper mine where millions of dollars of equipment must be used efficiently for a successful commercial operation, it is undesirable to stop operations for any length of time and pull equipment back from the vicinity of a blast site. The blasting industry in the U.S. (and presumably elsewhere) is still undergoing changes in professional practice, adopting more sophisticated techniques to minimize ground vibrations and maximize the intended function of the blast - which, again, is almost always to break rock safely and reliably into fragments of a chosen size. The outcome of these changing techniques in the U.S. has been a reduction, over a period of several years, in the magnitude of seismic motion associated with blasting activity.

In summary of this section, almost all aspects of industrial blasting in the U.S. emphasize practices that are different from that associated with execution of a deep, large (over 100 tons), single-fired chemical explosion, such as the NPE. The latter type of underground explosion is the least efficient way to break rock, and the most efficient way to make a telesismic signal.

BRIEF COMMENTS ON BLAST IDENTIFICATION, AND MAGNITUDE DISTRIBUTION

This section sketches (and/or gives references for) some of the methods for discriminating ripple-fired industrial explosions and single-fired explosions; and gives preliminary rough estimates of the number of regionally detected chemical explosions in the U.S. reported as above magnitude 3.

Just as the problems of discriminating between earthquakes and underground nuclear explosions were eventually solved in practice by programs of basic research to understand earthquake phenomena, so now it appears necessary (to the extent that there is a desire to interpret signals well below magnitude 4), to understand seismic signals from blasting activity, and the way in which signals from industrial blasting can be distinguished from signals of a small underground nuclear explosion.

For earthquakes and explosions with magnitude less than 4, telesismic records will often lack adequate bandwidth and/or signal-to-noise ratio, so that standard telesismic discriminants are ineffective. In such cases, where a source may be detected at a data center by a continuously reporting seismic station and located on the basis of telesismic data, the source may not be identified unless data is sought and acquired from a station that records regional seismic signals even at high frequency (at least up to 20 Hz, and preferably up to 40 Hz).

The question of how to identify explosions using regional data is now a central issue in seismic monitoring for a CTBT. However, it should be noted that operators of regional seismic networks - there are on the order of a hundred of such networks around the world - have to face on a daily basis the somewhat related problem of discriminating between small earthquakes and chemical explosions (albeit without the potentially serious consequences, associated with CTBT monitoring, of failing to identify a few of the explosions). Regional network operators are mostly interested in earthquakes, so

they often want to exclude explosion signals from further analysis. (They are concerned to avoid counting explosions as earthquakes, since this may result in false earthquake statistics and flawed interpretation of regional tectonics.) They typically use simple methods to make the identification - methods which may include an interpretation of the location, and/or recognition of signals that have a characteristic appearance and that occur at characteristic times of day.

In practice, many station operators will say that the appearance of seismic signals from typical blasts is commonly found to be so different from earthquake signals that (in cases of good signal-to-noise ratio) chemical explosions are routinely identified in practice even without making measurements on the signal. For example, Wü ster (1993) reported the following principal differences between seismograms of earthquakes and blasts occurring in the same epicentral region at a distance of about 180 km from a seismic station in Germany:

- the amplitude of P -wave impulses, compared to S , is much lower than for earthquakes;
- the frequency content of S -waves is higher for earthquakes; and
- the excitation of surface waves (Rg) is much stronger for explosions.

Similar rules have been developed empirically for many regions within the U.S., and are routinely applied by many station operators.

When such analysis "by eye" is unreliable and/or unacceptable, there appears to be no dominant method of data processing that can be used objectively for event identification in different regions. Rather, several different methods have been proposed, some being more effective, in certain regions, than others. Richards and Kim (1992) describe four different levels of ever more sophisticated processing that can be used for identifying chemical explosions using regional seismic data. One particularly successful method for identifying ripple-fired shots is based on spectrograms (i.e., amplitude spectra computed for a moving time window, thus enabling a display of the frequency content of the signal, and how it changes with time). The spectrogram of a ripple-fired shot typically shows a banded structure (Hedlin et al, 1989), indicating frequencies at which constructive and destructive interferences persist through times at which different seismic phases arrive, and through their cudas. Kim et al (1993) describe a practical method of discriminating between earthquakes and explosions, based upon linear combinations of spectral ratios between waves with P -wave energy (e.g. Pn or Pg) and waves with S -wave energy (Sn or Lg). In some respects this method is an extension, to higher frequencies, of the classical discriminant based on the relative amplitudes of P -waves and surface waves (m_b : M_s). The linear combination is chosen, to maximize the difference between signals from the two types of source. And Kim et al (1994) describe spectral methods, including the use of spectrograms, that explore the question of what data quality is needed, for successful practical discrimination of earthquakes, ripple-fired explosions, and single-fired explosions.

One important practical issue for design of a monitoring network, is that the time interval for digital sampling must be about 4 times shorter than the time between component ripples in a ripple-fired blast, in order to see in spectra the effects of constructive and destructive interference between ripples. In many regions, sampling rates must also be high (up to around 100 sps) to get the best discriminant using *P*-to-*Lg* spectral ratios for frequencies up to about 40 or 50 Hz..

Although the basis for any of the successful methods of discriminating chemical explosions is access to regional seismograms with adequate sampling rate and adequate signal-to-noise ratio, it is still of interest to know how well teleseismic stations can be used to study chemical explosions. For example, teleseismic data may be used for detection and location, triggering requests for additional data at regional distances, from sources that cannot be discriminated teleseismically. We then ask: how many chemical explosions are detected at m_b values that will be of concern under a CTBT? In view of the summary of U.S. blasting activity given in an earlier section ("On a typical work day in the U.S., there are about 30 explosions greater than 50 tons, including one greater than 200 tons..."), and the usual relationship between magnitude and explosion yield (for example, $m_b = \text{intercept} + 0.8 * \log (\text{yield in kt})$) where the intercept is around 4 to 4.3 for different regions and shot point coupling), it might at first be thought that around 30 explosions a day have magnitude 3 or greater. However, it appears that far fewer chemical explosions in the U.S. have $m_b > 3$. To reach this important conclusion, regional network operators were asked for information on the numbers of apparently large chemical explosions detected per year. A few tens of such events were then obtained, and a search was conducted for teleseismic detections on sensitive stations. Because this effort resulted in basic information about capabilities of various networks that does not appear to be readily available, the remainder of this section gives further details.

Thus, in March 1994 I sent an inquiry to operators of several U.S. regional networks, asking for any information they could give, on the seismic magnitude of the largest chemical explosions detected by their networks; and, in particular, how many shots per year they recorded at around magnitude 3 and above. Paraphrased responses from 9 networks, plus the USGS National Earthquake Information Service, were as follows:

From Rick Williams and Jeff Munsey (U. of Tennessee, Knoxville), summarizing the results obtained with the Tennessee Valley Authority network in East Tennessee: "the TVA network records perhaps 10-20 nontectonic events per year in the high magnitude 2 or low 3 range. The largest of these may be pillar bursts and collapse events rather than blasts."

From Shelton Alexander (Pennsylvania State University): "there is a relatively simple way to screen the recordings of past events for magnitude 3 and larger events in the northeastern United States by using the duration magnitude relationship for this region, which is:

$$\text{magnitude} = 2.21 \log D - 1.70$$

where D is the event duration in seconds. This magnitude scale gives results similar to the Lg magnitude. One only has to count the number of events where $\log D$ is greater than $4.7/2.21$ or 2.13 which translates to a duration greater than about 133 sec. I do not believe there would be many/week, almost certainly not more than one/day within 250 km of State College, Pennsylvania. The simple method outlined above for counting the number of events above magnitude 3 should work for other geographic areas as well, but the empirical constants may be different, as they are for example in the southeastern US."

From Arch Johnston (Memphis State University): "we record about 15-30 blasts per year that equal or exceed duration magnitude 3 with our southern Appalachian network. This is from either strip mines in western Kentucky, or quarries in the Appalachians and Cumberland Plateau or strip mines/quarries in Alabama. The main uncertainty is how applicable a duration magnitude scale is to blasts, when it was developed for and calibrated to earthquakes. We record several blasts per working day in the magnitude 2.5-3.0 range, yielding about 600-900 per year."

From Steve Malone (University of Washington): "Of our catalog from 1970 to the present (1994) with about 58,000 events we have located 5,431 as known or suspected blasts. Of these only 50 have a 'coda-duration' magnitude > 2.9 . However, we have one quarry in southwest Washington that shoots shots about 3-4 times a week of duration magnitude 2.7-3.3 and we do not locate or catalog most of these. We know these shots are indeed ripple fired and have up to 20-30 Klb/shot. They are simply recognized as 'Centralia Blasts' and usually discarded. Of the 5,431 located blasts in our catalog only 132 are from this site so we know that during the past 20 years there are approximately an additional 4000 blasts in the duration magnitude range 2.7-3.3. We also know that our coda-duration magnitudes are an overestimate of the local magnitude of these Centralia blasts by about 0.2 - 0.4 units. For other blasts we are not so sure though an overestimate of magnitude is likely. For most other blast sites we do try to locate all detected events and compute a coda magnitude for them. Here are some statistics for these other sites.

Mag range	Number of events
>3.5	1 (probably a mistake)
3.2-3.5	13
3.0-3.2	20
2.8-<3.0	35
2.6-<2.8	78
2.4-<2.6	150.

We also know from some statistical comparisons of time of day and day of week that we have probably identified only about 85% of the blasts that are occurring in our area, of the events we locate."

From Brian Mitchell (St. Louis University): "75 blasts were located for the period 1983–1988, and 13 had magnitude in the range 3 – 3.4 (i.e., about 2 per year at magnitude 3 or above.)"

From Jim Mori (USGS, Pasadena, California): "13,300 events are listed as quarry blasts in the S. California catalog from 1983 to the present. There were 405 events with magnitude 2.5 or greater in the list. Only nine events were magnitude 3 or greater, but this number is not reliable. Our network magnitudes are based on coda decay (i.e. duration) for the smaller events. I guess that if the quarry blast is only recorded on a few close stations, the coda magnitude would be an overestimate compared to earthquakes. This is because the shallow quarry blasts tend to have long ringing codas."

From David Oppenheimer (USGS, Menlo Park, California): "for the northern/central California region, from January 69 thru March 94 there are 11,475 events tagged as quarry explosions.

# of events >	3.0 =	17
	2.5 =	353
	2.0 =	3034.

Of the events above magnitude 3, there should be some qualification. Some may have been earthquakes, several were right at magnitude 3 in the Salinas Valley and the Sierra Nevada, others occurred near Mono Lake near the edge of our network where calibration may be a problem, and one event was the detonation of the Dumbarton Bridge in the S.F. Bay (magnitude 3.8) in 1985. Therefore there are almost no routine quarry blasts above magnitude 3 in northern and central California."

From Terry Wallace (University of Arizona): "we typically record 15 mine blasts a day from 8 mines in Arizona, New Mexico and Sonora. The largest blasts are approximately 3.0 (about 10 a year), and there are probably 30 events 2.5 or larger. These are local magnitudes. All the large explosions are associated with open pit copper mining operations. Typical shots have 64 to 128 holes."

From Martin Chapman (Virginia Polytechnic Institute): "I estimate that in one year, our network in western Virginia records approximately 900 explosions with L_g magnitudes greater than 2.75, and about 300 explosions with magnitudes greater than 3.0. The largest explosions recorded are approximately magnitude 3.6, and we see only about 1 of these per month, on average. These explosions are recorded at distances from 75 to 280 km, and are due to surface coal mining operations in West Virginia, Kentucky and Ohio." [This response is interesting, as indicating about ten times more events above magnitude 3, than any other regional network in the U.S.]

The U.S. Geological Survey (which currently publishes on average about 50 earthquake locations per day around the world) detects numerous explosions per day in the U.S. For example, blast data that could be obtained from the U.S. National Network and Telemetered Network stations, for Thursday and Friday (UTC), April 7 and 8, 1994, resulted in the following 16 blast locations:

Date/Time (UTC)	Lat	Long	Mag	Location
-----------------	-----	------	-----	----------

07 Apr 04:05:30.5 39.46 N 111.27 W 1.7 MD west of Price, Utah

06:49:01.8 39.31 N 114.84 W 2.9 MD Ely, Nevada

07:23:54.9 39.66 N 111.24 W 1.7 MD west of Price, Utah

16:03:35.3 39.45 N 111.21 W 1.7 MD west of Price, Utah

16:13:54.3 31.44 N 108.71 W 2.5 ML east of Douglas, Arizona

18:53:45.6 41.89 N 110.76 W ~2.0 ML Kemmerer, Wyoming

19:07:58.5 38.09 N 80.80 W 2.9 LG northeast of Beckley, WV

19:21:15.1 41.79 N 109.27 W 3.5 ML north of Rock Springs, Wyoming

22:47:01.1 46.80 N 122.82 W 3.0 MD Centralia, Washington

08 Apr 17:06:04.2 40.52 N 112.17 W 2.2 MD Bingham Canyon (Tooele), Utah

18:20:37.8 37.17 N 81.99 W 1.9 LG southwestern West Virginia

20:09:33.9 40.56 N 112.17 W 1.9 MD Bingham Canyon, Utah

21:33:38.3 36.41 N 110.25 W 2.3 ML Black Mesa (Kayenta), Arizona

21:48:37.3 46.82 N 122.84 W 2.3 MD Centralia, Washington

22:38:30.6 40.23 N 112.20 W 2.2 MD Bingham Canyon area, Utah

23:49:30.5 38.97 N 111.38 W 1.9 MD southwest of Price, Utah.

And for the same two-day period, the USGS National Earthquake Information Service also detected (but did not locate) many additional events, believed to be explosions, such as those recorded on the following selected stations:

Station	Code	Additional Events Detected
---------	------	----------------------------

Blacksburg, VA BLA 65 events

Black Hills, SD RSSD 44 events

French Village, MO FVM 30 events

Newport, WA NEW 7 events.

Most, if not all, of these events are estimated to be less than magnitude 2.5 (USGS information: personal communication, April 1994, John Filson).

Given the above descriptions of regional seismicity associated with chemical explosions, what can be done to estimate the number of events that will have teleseismic detections?

A very preliminary search for *P*-wave detections at teleseismic distances, on sensitive North American stations such as Yellowknife, Canada, was carried out for a few tens of mining blasts reported

by regional U.S. networks as having local, regional or duration magnitude above 3 and up to 3.6 (personal communication, Bob Blandford). Only a few of the events were detected in this search, even though sensitive stations do have teleseismic detection capability down to m_b 3 and routinely down to m_b 3.5 (Ringdal, 1990). This preliminary result is yet another indication that ripple-fired mining blasts, reported as having regional magnitude in the range 3 - 3.5, in fact have smaller teleseismic magnitudes - perhaps on the order of half a unit smaller, on average.

To summarize this discussion of magnitudes, it appears that only on the order of 10 to 30 U.S. chemical explosions per year are detected teleseismically, with $m_b > 3$. This estimate is surprisingly small, considering that around 10,000 chemical explosions of 50 tons and above occur per year.

Further work is needed to confirm this preliminary result, to obtain further details about those unusual chemical explosions which are detected teleseismically, to evaluate potential bias in different magnitude scales as applied to chemical explosions, and to obtain similar results for countries other than the U.S. that have significant usage of chemical explosions.

DISCUSSION AND CONCLUSIONS

Although each mine is different in its use of chemical explosives, and although much of the information presented in this paper is anecdotal and hard to document, yet it has still been possible to obtain useful statistics on U.S. industrial blasting. This paper reviewed statistics obtained earlier (Richards et al, 1992) on the amounts of chemical explosive used in different states in explosions of different sizes; and presented preliminary statistics on the seismic magnitudes of U.S. blasting.

Almost all chemical explosions above 1 ton in the U.S. are ripple-fired. Almost all are conducted at shallow depths. Almost all are intended to break rock or to remove overburden and are very inefficient in generating seismic signals at regional or teleseismic distances. None of these attributes pertain to the chemical explosion carried out in the Non-Proliferation Experiment (which was detected teleseismically with m_b around 4.1). The fact that seismic signals from the NPE were so similar to the signals of a small underground nuclear explosion, is simply a reflection of the fact that the NPE was designed to mimic such a nuclear explosion (in being single-fired, deep and contained, and of comparable size). The NPE seismic signals are not representative of seismic signals from industrial blasting, for which effective discrimination may be possible.

The concern over chemical explosions, in the context of verification of a CTBT, has arisen only in the last few years, as seismic network detection capabilities have improved to the point where signals from industrial blasting are commonly acquired.

It is a testament to the excellent detection capability of modern seismic networks, that on the order of hundreds of blasting events around the world may be detected on regional stations on a typical work day. In order not to waste time and effort examining irrelevant signals, it will be necessary to make choices (for example, of the magnitude range), to limit which signals of interest should be

analyzed, in the context of CTBT verification. In this context, it is important that for the United States, which uses about two megatons of chemical explosives a year, it appears that only about 10 to 30 chemical explosions per year are detected teleseismically with $m_b > 3$.

ACKNOWLEDGEMENTS

I am indebted to the co-authors of papers I have written on blasting - Doug Anderson, Won-Young Kim, and David Simpson - for much of the material presented here; to John Filson, Bill Leith and Bruce Presgrave of the USGS for information on NEIS activities; to operators of regional seismic networks for information on magnitude and frequency of blast signals; to many members of the International Society of Explosives Engineers for supplying information on blasting practice; and to Fran Rensvold and Bob Blandford for technical information and for many suggestions on presentation of results. My studies of blasting and discrimination have been supported by ARPA and the Air Force Phillips Laboratory over several years, and most recently by grant F49620-92-J-0497 from the Air Force Office of Scientific Research. This is Lamont-Doherty Earth Observatory Contribution No. 5219.

REFERENCES

- Devine, J.F., and W.I. Duvall, Effect of charge weight on vibration levels for millisecond delayed quarry blasts, *Earthquake Notes*, **34**, #2, 17-24, 1963.
- Hedlin, M.A., J.B. Minster, and J.A. Orcutt, The time-frequency characteristics of quarry blasts and calibration explosions recorded in Kazakhstan, USSR, *Geophysical Journal International*, **99**, 109-121, 1989.
- Kim, Won-Young, D.W. Simpson, and P.G. Richards, Discrimination of earthquakes and explosions in the Eastern United States using regional high-frequency data, *Geophysical Research Letters*, **20**, 1507-1510, July 1993.
- Kim, Won-Young, D.W. Simpson, and P.G. Richards, High-frequency Spectra of Regional Phases from Earthquakes and Chemical Explosions, accepted Dec 1993 for publication in the *Bulletin of the Seismological Society of America*, 1994.
- Nicholls, H.R., C.F. Johnson, and W.I. Duvall, Blasting vibrations and their effects on structures, *Bureau of Mines Bulletin* 656, 105p, U.S. Dept. of the Interior, Washington, 1971.
- Richards, Paul G., and Won-Young Kim, The Problem of Chemical Explosions and some Solutions, *Proceedings of a DOE/LLNL Symposium on Technologies for Monitoring Nuclear Tests Related to Weapons Proliferation*, pp 19-36, Las Vegas, May 6-7, 1992.
- Richards, Paul G., D.G. Anderson, and D.W. Simpson, A Survey of Blasting Activity in the United States, *Bulletin of the Seismological Society of America*, **82**, 1416-1433, June 1992.
- Ringdal, F., Teleseismic event detection using the NORESS array, with special reference to low-yield Semipalatinsk explosions, *Bulletin of the Seismological Society of America*, **80**, 2127-2142, special issue, December 1990.
- Siskind, D.E., M.S. Stagg, J.W. Kopp, and C.H. Dowding, Structure Response and Damage Produced by Ground Vibration From Surface Mine Blasting, Report of Investigations 8507, Bureau of Mines, U.S. Dept. of Interior, 1980.
- U.S. Bureau of Mines, Apparent Consumption of Industrial Explosives and Blasting Agents, in the United States, 1992, *Mineral Industry Surveys*, Washington, D.C., 1993.

- U.S. Congress, Hearings before the Joint Committee on Atomic Energy, March 5, 6, 7, 8, 11, 12, 1963.
- White, Jay, Exploding Myths: the Halifax Harbour explosion in historical context, *Proceedings of a Conference on the 75th Anniversary of the Halifax Harbour explosion*, St. Mary's University, Halifax, Nova Scotia, in press, 1994.
- Wü ster, Jan, Discrimination of chemical explosions and earthquakes in Central Europe - a case study, *Bulletin of the Seismological Society of America*, 83, August 1993.

A Review of Blasting Activity in the Former Soviet Union

*William Leith
U. S. Geological Survey
Reston, VA 22092*

*Leonid Bruk
BRUK Hydrogeological Consulting, Inc.
Rockville, MD 20852*

Abstract. Monitoring a comprehensive nuclear test ban by seismic means will require identification of seismic sources at lower magnitudes, where industrial explosions (primarily mining blasts) may comprise a significant fraction of the total number of events recorded and may, for some countries, dominate the seismicity. The USGS has recently obtained preliminary data on blasting activities in the former Soviet Union (FSU), one of the few countries in which the use of explosives exceeded that of the United States. A review of the Soviet data suggests that there are both similarities and differences in blasting practices between the U.S. and the FSU. These data are important because they provide some insight into variations from U.S. practice and because they can be used directly to estimate the assets needed to effectively monitor that country. Key findings include: 1) in 1988, approximately 2.6 million metric tons of high explosives were detonated in the FSU; this compares with 2.1 million metric tons in the U.S. in the same year; 2) about 80% of the explosives were used in mining, 10% in construction and 10% for other uses; 3) 84% of the explosives were consumed by only six Ministries of the FSU, and 66% were consumed in the three main mining industries: MinCherMet, MinTsvetMet and MinUgleProm; 4) in 1988 alone, the FSU conducted over 100 explosions in excess of 1 kt total charge (compare with one blast over 1 kt in the U.S. in 1987), and none of these were in the coal mining industry; 5) most very large blasts occurred on the surface, and in only a small number of mines; most underground blasts were less than 100 tons.

Introduction

Monitoring a comprehensive nuclear test ban by seismic means may require identification of seismic sources at magnitude levels where industrial explosions (primarily, mining blasts) may comprise a significant fraction of the total number of events recorded, and may for some countries dominate the seismicity. Thus, data on blasting practice have both political significance for the negotiation of treaties involving seismic monitoring of nuclear tests, and operational applications in terms of establishing monitoring and inspection needs on a mine-by-mine basis.

While it is generally accepted that mining explosions contribute to seismicity at lower seismic magnitudes (less than about magnitude 3.5), the rate of mining seismicity is unknown for most countries outside the U.S. This results in a large uncertainty when estimating the task of discriminating nuclear explosions from chemical explosions and earthquakes by seismic means, under a comprehensive nuclear test ban. This uncertainty directly affects estimates of seismic network enhancements required to achieve treaty verification requirements at magnitudes less than about 3.5.

This paper presents a general review of blasting activities in the former Soviet Union (FSU). The data illustrate that there are both similarities and differences in blasting between the U.S and the FSU (see Richards and others, 1992). Thus, the Soviet data are important both in that they provide some insight into variations from the U.S. and because they can be used directly to estimate the assets needed to effectively monitor the seismicity of Russia and the newly independent states.

The goal of this paper is to review and synthesize the existing information on blasting in the former Soviet Union, including the variety of explosive users and applications, and the quantity and frequency of blasts in mining and other areas of industry. Sources of information for this report include both published works (which are cited) and several unpublished, archival materials provided by Russian colleagues. Most of the Soviet publications available in the U.S. are devoted to the research of blasting theory, blast modelling, the fragmentation of rock by blasting, seismic discrimination of blasts from earthquakes, and various problems of a methodological character, while the desired statistical information on actual blasting practice is extremely limited. Personal knowledge and communications with Russian colleagues indicate that historical data on individual blasts, even in non-military applications, were considered proprietary to the State, and were not publishable.

History of Large Blasts

The former Soviet Union probably conducted most of the largest chemical explosions ever detonated. This includes many blasts in excess of 1 kiloton total charge, and Soviet advisors assisted the Chinese in their detonation of the world's largest known blast --a total charge of 15.7 kilotons-- detonated at the Bayinchan copper mine in 1973 (Geiman, 1978). The following examples provide a chronology of the some of the largest known blasts.

- In 1966, at the "Medvezhi Ruchey" (Bear Creek) mine of the Norilsk Mining-Metallurgy Combine, 7 million tons of ore were excavated with a total charge of 1.5 kilotons. Through at least 1988, such massive blasts were widely used at large mining enterprises, including those of Leninogorsk, Ziryanovsk, Krivoy Rog, Dzhezkazgan, Sarbai, Achisai, Norilsk, Vysokogorsk, and Apatity.

- At 11 am on 21 October 1966, at Lake Medeo in the mountains above Alma Ata, Kazakhstan, the Soviets detonated a charge of 5293 tons to create a rock-fall dam with a height of 63 m. The dam was designed to protect the town of Alma Ata from seasonal debris flows, and in 1973, it was successful in containing a flow of some 3 million m³ of mud-rock material. The explosion consisted of two charges, 1689 tons and 3604 tons, emplaced in tunnels and detonated with a 3.56 second delay. The second, larger blast had a body-wave magnitude of 5.1 (Moscow) and a surface wave magnitude of 3.7 (Moscow). On April 14 of the following year, 3942 tons of explosive were detonated in three charges, in an explosion to increase the height of the dam from 63 to 93 m, moving some 1 million tons of rock.
- In 1970, about 2000 tons of explosives, distributed in 10 charges, were detonated simultaneously to produce a rock avalanche, creating the Baypazan dam, on the Vakhsh River in Tadzhikistan.
- On June 11, 1989, 2100 tons of ANFO were detonated in three rows of charges on the Uch Terek River, in Kirghizia. This blast, which has a magnitude of 4.5 (m_b ISC), was a test explosion for a blast series designed to create the Kumbarata rock-fall dam. It was preceded by an experimental blast of 700 tons, detonated on the Burlikiya river in 1975. The Soviets had planned three even larger blasts as part of the Kumbarata dam construction effort; the largest proposed blast was to be 250 kt of chemical explosives, to be detonated in 14 charge rows.

While most of these giant explosions were for construction purposes, blasting was extensively used in the large-scale development of mineral resources. During the 1960's, for example, it is estimated that 40 million tons of mineral resources were extracted in the USSR by the blasting of more than 1 billion tons of rock (Geiman, 1978). In the mines of the Kuznetsk coal belt alone, more than 60 million charges were detonated each year -- an average of 170 thousand charges per day. By the late 1980's, close to 2 billion m³ of hard rock were excavated by blasts at mining enterprises (Beisebaev and others, 1973). The introduction of massive blasts at mines is said to have led to a 4-10 fold increase in productivity at all mining centers, and to have sharply decreased the net cost of mining per ton. The practice of mining ore in hard rock, established in the mines of the Leninogorsk Combine, where the largest underground blasts were conducted, became frequently used at many enterprises in the USSR. For blasting agents, the Soviets used a variety of chemical explosives, powerful electrical discharges, and gas/liquid explosive blends. In terms of chemical explosives, there are nearly 100 varieties, consisting of mixtures of chemicals and other various compounds, manufactured as granules, powders or liquid suspensions.

Consumers of Explosives

Table 1 lists the ministries of the FSU using explosives in 1988. The range of fields in which blasts were used includes: mining, construction (civil, hydrotechnical, road, and others), reclamation, metal processing (forging,

welding, reinforcement, etc.), the creation of underground storage, geophysical and geological exploration, fishing, enhancement of production at oil, gas, and water wells, fire control (in forests, oil fields and elsewhere), agriculture, the production of synthetic diamonds, stomatology, vulcanization, and in various applications of microexplosives. Occasionally, blasts were used absolutely unexpected fields, such as for the harvesting of crops for such fruits as oranges, apples, and pears (Geiman, 1978).

Table 1. Organizations of the FSU using explosives in 1988.

Mining Industries

Ministry of Non-Ferrous Metallurgy (*MinSvetMet*)

Ministry of Ferrous Metallurgy (*MinCherMet*)

Ministry of the Coal Industry (*MinUgleProm*)

Ministry of Fertilizers (*MinUdobreni*)

Construction, Transportation, and Energy Industries

Ministry of the Construction Materials Industry (*MinPromStroiMaterialov*)

Ministry of Transportation Construction (*MinTransStroi*)

Ministry of Special Assemblies and Constructions (*MinMontazhSpetsStroi*)

Ministry of Communications (*Ministerstvo Putei Soobsheniya - MPS*)

Ministry of Energy (*MinEnergo*)

Specialized blasting organizations of the Republics (examples)

Kazakh Blasting Enterprise (*Kazakhvzrivprom*)

Urals Asbestos (*UralAsbest*)

Reclamation Blasting Enterprise (*MelioVzrivProm*)

Vinnitsa Blasting Enterprise (*VinnitsaVzrivProm*)

Moldavian Blasting Enterprise (*MoldVzrivProm*)

In 1988, the last year for which statistical records are available, approximately 2.6 million metric tons (Mmt) of high explosive were detonated in the FSU (compare with 2.1 Mmt in the U.S. in the same year; see U.S. Bureau of Mines, *Minerals Yearbook*, 1988) This was a decrease from previous years, and further decreases have occurred in subsequent years (unpublished information suggests that blasting in 1993 was at about half of its former activity). Some 84% of the manufactured explosives were consumed by only six Ministries of the FSU, and 66% were consumed in the three main mining industries: *MinCherMet*, *MinSvetMet* and *MinUgleProm* (see Table 2).

Table 2. Consumption of manufactured explosives in the FSU, by Ministry, for 1988.

<u>Ministry</u>	<u>Commodities Mined</u>	<u>Explosive Use (%)</u>
<i>MinCherMet</i>	ferrous metals	26%
<i>MinUgleProm</i>	coal	23%
<i>MinSvetMet</i>	non-ferrous metals	17%
<i>MinMontazhSpetsStroi</i>	specialized constr.	7%
<i>MinPromStroiMaterialov</i>	construction mater.	6%
<i>MinUdobrenni</i>	fertilizer	5%
Others (see Table 1)	various	16%

The major consumers of explosives in the FSU fall into two general groups (see Table 2): Mining Enrichment Combines (*gorno-obogatitelni kombinat, or GOK*) and other specialized blasting organizations. Mining Enrichment Centers (e.g., the GOKs of *MinSvetMet* and *MinCherMet*), are located on identified ore deposits (examples are the Lebedinsk Stolinsk and Mikhailovski GOKs, located on the large iron ore deposit of the Kursk Magnetic Anomaly, 8 large GOK's in the Krivoy Rog iron-ore belts, the Dzezkazganski GOK in Kazakhstan, and others). In contrast, many other specialized organizations conduct blasting at a large number of facilities or sites, scattered throughout the country. For example, "*TransVzrivProm*" of the *Ministry of Transportation Construction* conducted, in the Kaluzhskoi region alone, blasting on seven building material quarries. "*SoyuzVzrivProm*" also worked quarries in this area. The same pattern is observed in the Viborgsky region of Leningrad, where "*TransVzrivProm*" worked at four large quarries, while "*SoyuzVzrivProm*" worked the neighboring quarries.

In addition to factory-prepared explosives, the mining enterprises also produced and consumed almost all locally prepared explosives (e.g., ANFO (*igdanit*) and hydrated gels and slurries). The remaining 16% of explosives of factory-prepared explosives were used by such branches as *MinTranStroi*, *MPS*, *MinEnergo* and others. In the majority of cases, these organizations conducted open-pit mining work, primarily in construction material quarries, of which there were over 300 in the USSR. Organizations outside of the mining industry that conducted underground blasts were primarily *MinTransStroi* (transportation construction), *Glavtunnelmetrostroi* (metro tunnel construction), and other organizations of *GidroSpetsStroi* (special hydro-construction).

While detailed data on explosive use are not available on a year-by-year basis, an indicator of the number of blasts is the relative outlay of explosives. Data for 1965-1984 (Table 3; after Mosinets, 1986) show that, in spite of the significant advances in this time period in both the theory and practice of blasting, the specific outlay of explosives for this period nevertheless increased.

Table 3. Growth of explosive use in the period 1965-1984.

<u>mine category</u>	<u>percent increase, 1965-1984</u>
nonferrous metal mines	36%
ferrous metal mines	150-200%
chemical resource mines	50%

Large Blasts in the Mining Industry

As described above, 80% or more of explosives produced in the former Soviet Union were used in the mining industry. Table 4 shows the nomenclature for blast size used in the FSU.

Table 4. Blast-size classification in Russia and the former Soviet Union.

<u>category</u>	<u>size range</u>	<u>typical application</u>
strong	more than 300 tons	ferrous metal mining
large	100-300 tons	non-ferrous metal mining
medium	10-100 tons	quarrying
small	less than 10 tons	underground construction

Strong blasts have occurred in a number of mining regions, shown in Figure 1. Limited statistical data for strong blasts in the FSU in 1988 are given in Table 5. During this year, blasting in the USSR was characterized by, 1) a relative decrease in the amount of use of explosives in nearly every organization conducting blasting, 2) a large number of specialized ministries conducting blasting (see Table 1), and 3) a large number of locations where blasts occurred. Most of the explosions listed in Table 5 were in surface (open-pit) mines, with the notable exception of the diamond mining activities at Aykhal in Siberia. Most underground blasts in 1988 were less than 100 tons. About 80% of blasts occur in the afternoon, from 2pm to 6pm.

Blasting in Other Industries

The various construction industries are second to the mining industry in consumption of explosives and number of blasts. Most large construction blasts are spatially and temporally localized; that is, blasts designed to move tens of thousands of cubic meters of rock and/or soil at one site for a single application. Such blasts were



Figure 1. Locations of mines in the former Soviet Union for which blasting data are given in Table 5.

Table 5. Summary of data on the frequency of large mining blasts in the former Soviet Union in 1988, by mining region (see location in Figure 1). The largest single and group explosions are associated with the surface mining operations in the major mining districts. Generally, the surface blasts are 2 to 100 times larger than underground blasts, with some exceptions. "N/A" = data not available.

<u>Mining Region</u>	largest group <u>explosion size (tons)</u>	approximate <u>no. per yr</u>	<u>commodity (note)</u>
Norilsk	up to 1500	rare	Cu, Ni
Kursk (KMA-M, L)	950-1200	50	Fe
Udachnaya	over 1000	50	Diamond
Krivoy Rog	over 1000	N/A	Fe
Tymiauz	less than 1000	N/A	Mo
Dzhezkazgan	500-600	50	Cu
Apatity	over 400	0-10	Apatite
Kursk (KMA-S)	200-250	50	Fe
Aykhal	N/A	25-30	Diamond

shown by the Soviets to successfully raise dams (as at Medeo, Kazakhstan and Baypazan, Tadzhikistan, as described above) and construct canals, in addition to their more routine application in establishing road routes in rugged terrain. With the help of blasting, hundreds of kilometers of irrigation and navigable canals were created: Volgo-Donski, Severo-Tashkentski, Bayautski, Khazarbaksi, Sari-Kurganski, Kara-Kumski named for Lenin, Volgo-Uralski, Pallasovski-magistralni, Glavni Murgabski, Glavni Kunya-Urgenski, Sumgarski and others. In canal construction, more than 80% of the work was done by blasting. The large size of many of these construction explosions was required because of the large losses of energy associated with excavation blasts.

Blasts have also found wide application in construction in frozen soils (seasonal or permafrost), where it is the only efficient method of large-scale surface construction. As a rule, about half of construction for the creation of canals, reservoirs, and other purposes is conducted in the winter months. For example, data for the Tyumen' region indicate that, in the winter of 1975, 1.6 million m³ of soils were excavated (of which more than 0.5 million m³ were frozen), with 2.239 million tons of explosives (Postonov and others, 1979).

Conclusions and Comparison with Blasting Practice in the U.S.

Blasting in the FSU in 1988 was characterized by a large expenditure of explosives (more than 2.6 million metric tons), a large number of blasting sites throughout the country, and a large number and great variety of organizations conducting blasting work. The primary users of explosives are the enterprises of the mining combines, which account for over 80% of all explosives expended. At the major mining GOK's, the total charge per blast can exceed 1000 tons, with dozens of strong blasts (over 300 tons) occurring per mine per year. At construction material quarries, total charges are ordinarily in the range of 10-20 tons and rarely exceed 50 tons, and blasts occur almost daily. Historically, the largest-yield blasts in the USSR were for construction activities, such as to build dams and canals. Blasting activity has decreased in the past decade, and unpublished data suggest that it was at about half its maximum in 1993.

Comparing the Soviet data for 1988 with U.S. data from the U.S. Bureau of Mines for the same year, and with a review of U.S. blasting practice for 1987 (Richards and others, 1992), the following points can be made:

- The FSU used about 20% more explosives than the U.S. For the FSU, this was a decrease from previous years, while for the U.S., it was an increase.
- The FSU conducted a much larger number of very large (over 1 kiloton) explosions than the U.S. --well over 100 per year.
- While about 70% of the explosives produced in the U.S. are used in coal mining, and many large mining blasts (over 50 tons) are associated with coal mining, only about 25% of explosives were used in coal mining in the FSU, and none of the largest blasts (over about 300 tons) are in coal mining regions.

References

- Beisebaev, V.N., Schneider, M.F., Ten N.A., Veselov, A.Ya. "Massive explosions in underground mines," Nauka, Alma-Ata, 1973.
- Geiman, L.M. "Blasting," Nauka, Moscow, 1978.
- Mosinets, B.G. "Modern condition and development of technology and methods for producing blasts in the quarries of the USSR," Vzrivnoe Delo n. 89/46, Nedra, Moscow, 1986.
- Postonov, V.V., Boiko I.F., Mezin, O.I. "Experience of conducting blasting in frozen soils." Use of Energy of Explosions in Ground Work, Vzrivnoe Delo, Nedra, Moscow, 1979.
- Richards, P.G., Anderson, D.A., Simpson, D.W., 1992, "A survey of blasting activity in the United States," Bull. Seismological Soc. Am., v. 82, p. 1416-1433.
- U. S. Bureau of Mines, Minerals Yearbook 1988, v. 1, U.S. Government Printing Office, Washington, 1991.

Some Remarks on Rockbursts and Nuclear Proliferation

A. McGarr
U.S. Geological Survey
345 Middlefield Road, Mail Stop 977
Menlo Park, California 94025

For three years starting in early 1986, the U.S. Geological Survey, with support from the Air Force Technical Applications Center (AFTAC), operated a seven-station seismic network (Figure~1) in and around the Witwatersrand goldfields, South Africa. Four of the stations (ERM, WDL, HBF, and PSM) used GEOS digital event recorders and were sited within four of the most seismically active mining districts. The remaining three stations (SWZ, SEK, and BFT) recorded continuously three components of short period ground motion, as well as the long period vertical, and were located several hundred kilometers outside the Witwatersrand basin. Part of the purpose of the network (Figure~1) was to record regional waveforms (\eg \$P_g\$, \$L_g\$) for comparison with ground motion recorded locally at epicentral distances of several kilometers. During three special experiments, each of several weeks duration, GEOS recorders were installed underground near the WDL and HBF stations, at depths similar to those of mining-induced seismicity, generally between 2000 and 3500~m.

During normal network operation, our South African colleagues airfreighted the local and regional station data tapes to Menlo Park, California every two weeks, or so, and these data would be entered into our computer system for processing and analysis. In addition, we received mine tremor hypocentral location data, determined from mine-operated networks, as well as the data bulletins of the South African Geological Survey, which operates a national seismic network.

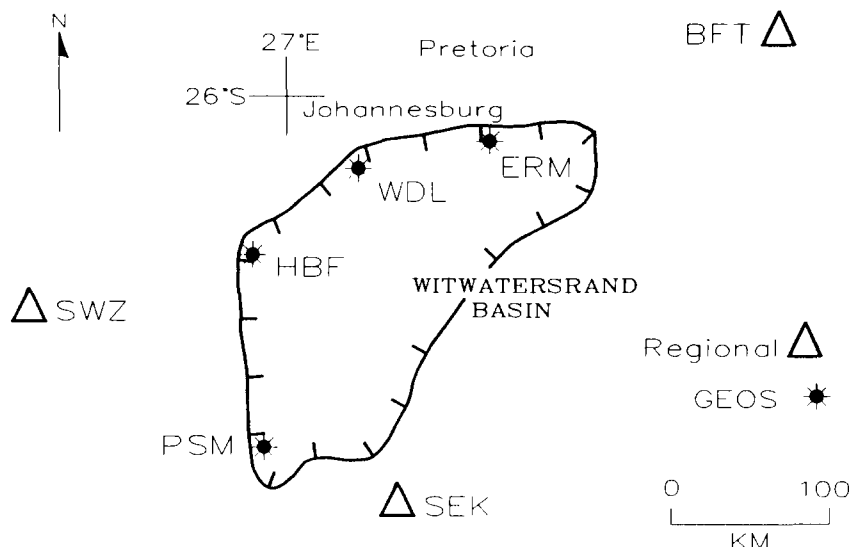


Figure 1. U.S. Geological Survey seismic network adapted from Figure~1 of McGarr et al., 1989.

In the presentation I describe three problems related to nonproliferation verification that challenged us to varying degrees. Possibly, these situations illustrate a few of the issues that might actually arise in the course of monitoring test ban treaties. As we shall see, in spite of the diversity of these three situations, there appears to be a common thread running through them involving an unanticipated aspect of the seismic source mechanism.

Mysterious Event

Our normal network operation routine was interrupted early in October 1987 by a special request from AFTAC to obtain the data for September 30th as quickly as possible. Several days later the tape from regional station BFT (Figure~1) arrived via air freight and the newspaper article (Figure~2) came several days later via FAX. The newspaper article, essentially a fourth-hand report from the *Johannesburg Star*, indicated the reason behind the special request. Even before reading this intriguing report, however, the mystery had already evaporated due to the seismograms (Figure~3) recorded at regional station BFT (Figure~1).

On September 30th, the largest event in South Africa produced the seismograms shown in Figure~3a. As soon as these records were played back it was clear that this event originated in the Klerksdorp mining district where GEOS station HBF is located. From the regional seismograms, even at only a single

'Massive blast detected on border' SA exploded nuclear bomb — Ziana report

The Star's
Africa News Service

HARARE — Zimbabwe's national news agency, Ziana, filed a story on Tuesday quoting the Press Trust of India agency as saying that South Africa was believed to have detonated a nuclear bomb near its border with Mozambique on September 30.

The report said a seismic array station at Gauribadanur in the southern Indian state of Karnataka recorded the event last Wednesday.

The Press Trust of India quoted sources at the Bhabha Research Centre who said the explosion had the characteristics of a nuclear explosion.

It said the explosion was traced to the border between Mozambique and

South Africa.

A spokesman for South Africa's Atomic Energy Corporation said the corporation did not com-

ment "on such highly speculative reports".

The Indian news agency said the strength of the explosion was estimated at 25 kilotons and the Gauribadanur Station could detect the location of a nuclear blast to an accuracy of 90 km.

The report said the station was awaiting confirmation from stations in Australia and the US.

HIROSHIMA

It said the blast generated signals with the double hump typical of nuclear explosions.

"The signals recorded compared very favourably with events of a similar nature recorded by stations in the USSR, the US and from French stations in the South Pacific, according to sources," said the PTI report.

● The Hiroshima atomic bomb was the equivalent of 12.5 kilotons, about half that of the reported blast.

Figure 2. Article from *The Star*, Johannesburg, October 8, 1987.

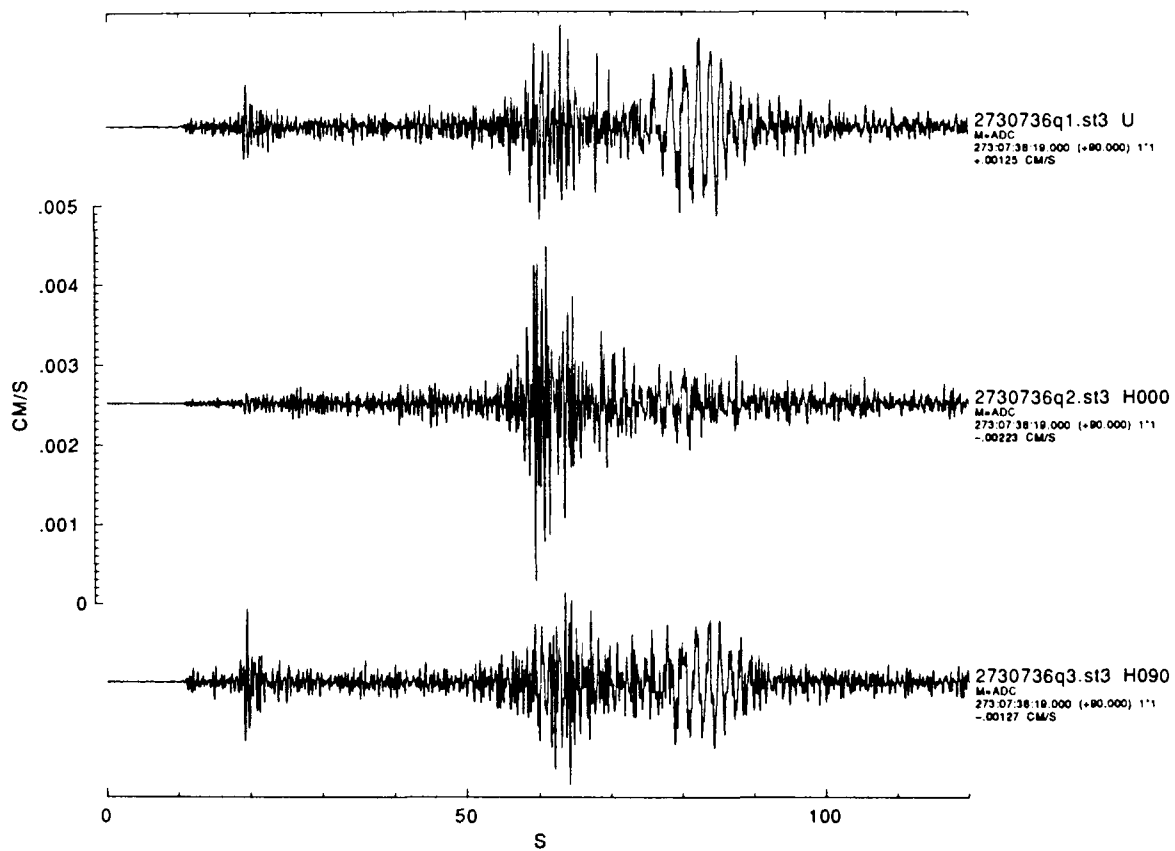


Figure 3a. M 4.4 event of September 30, 1987, recorded at regional station BFT (Figure~1). The phases \$P_n\$, \$P_g\$, \$L_g\$, and \$R_g\$ are all quite clear. The north component of ground motion is approximately transverse to the direction of propagation for a source near station HBF.

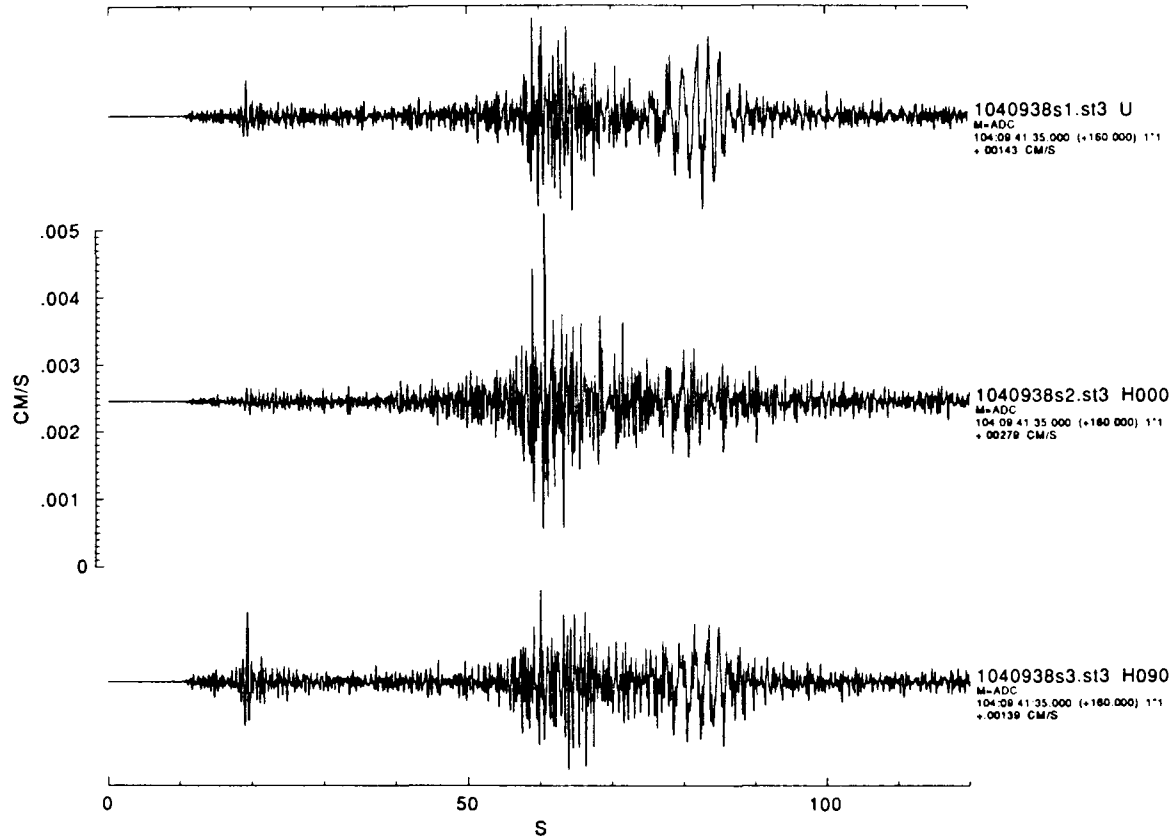


Figure 3b. M 4.4 event of April 14, 1987, recorded at station BFT.

station, it is easy to determine which mining district includes the epicenter. In the case of the September 30th event, we were able to narrow the location much further to the Five Shaft area of the Vaal Reefs mine even though local station HBF was out of service that day. Because the September 30 seismograms (Figure~3a) are highly similar both in amplitude and shape to those of a well studied event that occurred earlier in 1987 on April 14 (Figure~3b) it was clear that these two events were nearly co-located and of equal magnitude (4.4); this was confirmed later by underground damage reports from the Vaal Reefs mine.

Although the essential question of a clandestine nuclear test was readily resolved by means of the regional seismograms (Figure~3), there are several attendant problems that persist. First, the Vaal Reefs gold mine is roughly 600~km from the border with Mozambique. Station BFT (Figure~1), in fact, is located approximately at the midpoint of a line between the reported location (Figure~2) and the actual location, almost beneath HBF (Figure~1). Second, I have no idea why the newspaper article referred to "signals with the double hump typical of nuclear explosions." Possibly the newspaper reporters confused the seismic data with some other type of information. Third, the estimated yield of 25 kilotons corresponds to a magnitude m_b , based on P wave amplitudes, of 5.2 (Figure~1 of Evernden et al., 1986). Even though the large discrepancy between m_b 5.2 and M ~4.4 may also be attributable to inaccurate reporting, it is possible, perhaps even likely, that this difference reflects an aspect of the source mechanism that enhances m_b relative to M , measured primarily from S wave phases, a point to which I return.

Explosions and Earthquakes

Even though we established the USGS network (Figure~1) to investigate issues related to discriminating earthquakes from underground explosions, I did not expect to do such discrimination myself. Nonetheless, while I routinely scanned the April, 1986, seismograms recorded at local station HBF, a small event designated 1021030 caught my eye because of the unusual appearance of the P wave pulse (Figure~4). In contrast to nearly all tremors recorded at small epicentral distance (Figure~5) the P wave pulse of event 1021030 showed quite an impulsive upward initial motion (Figure~4); moreover, it was nearly impossible to reconcile both the P and S wave initial polarities with a double-couple source of any orientation.

A short time later I telephoned my colleagues in South Africa to explain my suspicion that event 1021030 was an explosion of low magnitude (M ~0.7). They soon discovered that a 150~kg tamped explosion had been detonated in a shaft pillar at a depth of about 2~km, 1~km north of station HBF, for purposes of calibrating the mine seismic network.

Our analysis of event 1021030, although interesting from the viewpoint of discriminating explosions from tremors, was frustrating in terms of understanding the seismic source mechanics of small explosions because the frequency bandwidth at surface station HBF was limited to 50~Hz at the high end; in con-

EVENT 1021030

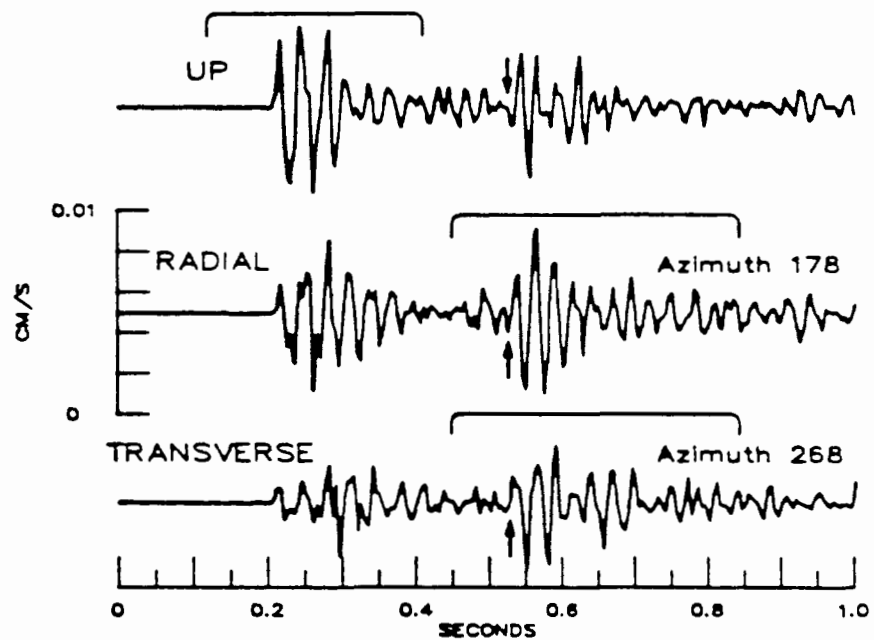


Figure 4. Vertical, radial and transverse components of ground velocity recorded at station HBF (Figure~1). Adapted from Figure~5 of McGarr et al., 1990.

EVENT 0991319

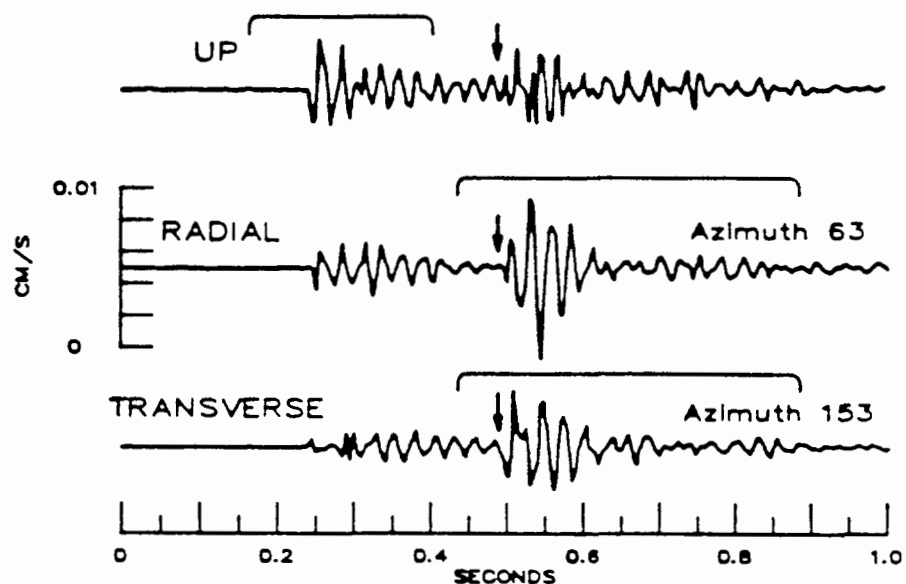


Figure 5. Ground velocity for nearby tremor recorded at station HBF. Adapted from Figure 6 of McGarr et al. , 1990.

trast, the spectral corner frequency of a 150~kg tamped explosion is expected to exceed 100~Hz. This frustration was alleviated by Steve Spottiswoode and Joanne Churcher, at the Chamber of Mines of South Africa, who provided data for two 50~kg explosions, as well as tremors of comparably small magnitude, recorded using a small, very broad-band underground array. The \$P\$-wave corner frequencies of these events were quite close to those predicted by scaling downward from nuclear explosion data (e.g., Evernden et al., 1986). Moreover, as seen in Figure~6, the low-frequency spectral plateaus for all three of these small chemical explosions are consistent with that of the 5-kton Salmon test in terms of the usual cube-root scaling.

Implosive Moment Tensor Components

As just mentioned, the \$P\$ waves of nearly all tremors recorded at surface stations (Figure~5) show initial downward motion. Although this general observation had been interpreted by some researchers as evidence of an implosive component in the source mechanism of mining-induced tremors, I had, until several years ago, concluded that slip across normal faults was the mechanism for the majority of tremors; underground observations of this normal faulting were the principal basis for this conclusion. At the same time, though, I had the nagging suspicion that this double-couple mechanism was not entirely compatible with such a remarkable preponderance of downward (dilatation) first motions.

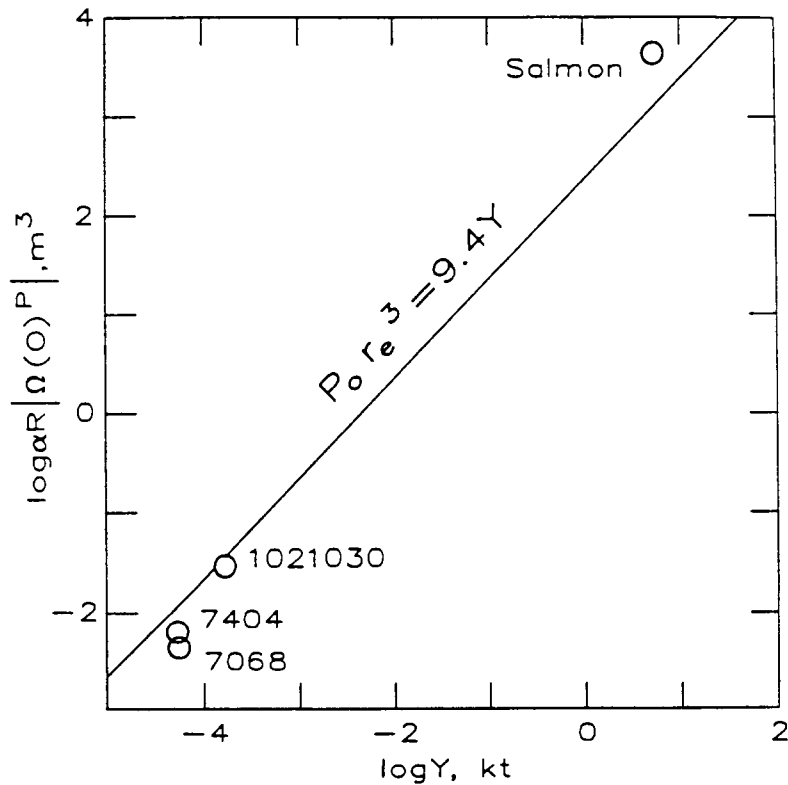


Figure 6. $\alpha R |\Omega(0)^P|$ as a function of explosive yield for small tamped chemical explosions in gold mines and the Salmon Test. α is the \$P\$-wave speed, R is hypocentral distance, and $|\Omega(0)^P|$ is the low frequency asymptote of the \$P\$-wave spectrum of displacement amplitude. r_e represents the elastic radius at the source and P_0 is the amplitude of the pressure pulse at hypocentral distance r_e (Evernden et al., 1986). From Figure 11 of McGarr et al., 1990.

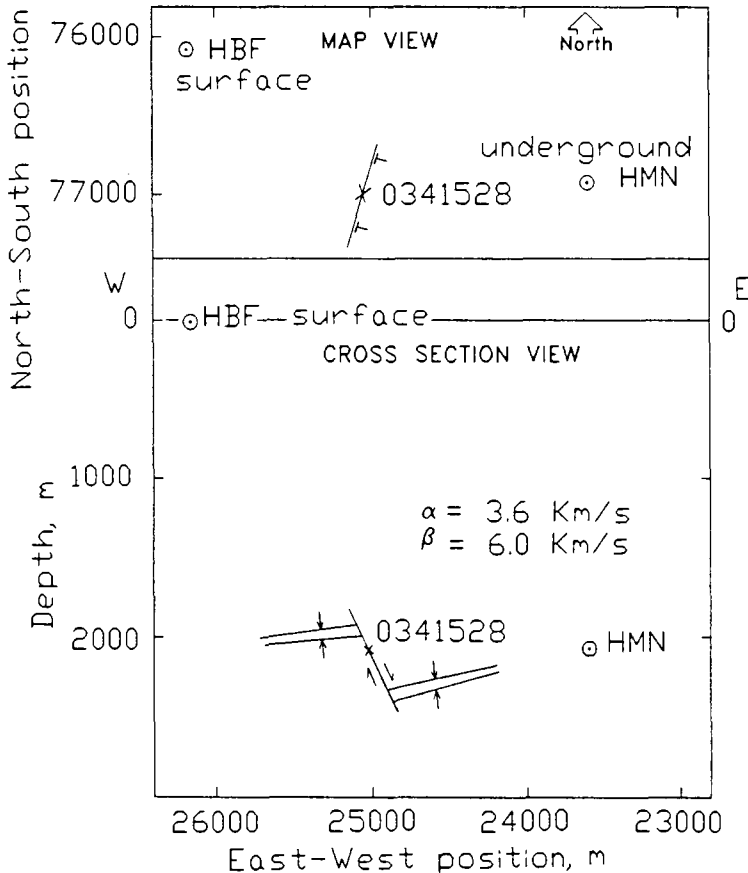


Figure 7. (Upper) Map view of event 0341528 epicenter and stations HMF and HBF (Figure~1). (Lower) East-west cross section view. A north-northeastward striking normal fault has offset the mine stope (exaggerated as seen here). Event 0341528 apparently involved both fault slip and coseismic closure of the nearby stope. (From Figure 2 of McGarr, 1992.)

Our understanding of the tremor mechanism changed substantially during the course of analyzing data from the special experiments, each of several weeks duration, involving underground recording with the broadband GEOS units beneath stations, WDL and HBF (Figure~1). Event 0341528, recorded in early February 1988, was located at a depth of about 2~km, 1.4~km due west of temporary underground station HMN, and a comparable distance southeast of surface station HBF (Figure~7). Acceleration measured at both sites was integrated twice to obtain exceedingly clear ground-displacement records (Figure~8) from which a complete moment tensor could be determined.

To my surprise, the resulting moment tensor for this M~2.4 event has a trace that is significantly negative. From the negative trace, the coseismic volume reduction of event 0341528 was calculated to be $88 \sim m^3$. Then, after the moment tensor is decomposed into implosive and deviatoric components, the contribution due to normal faulting was found to be $\Sigma AD = 117 \sim m^3$, where the summation is over fault planes of area A and average slip D ; for this event a north-striking normal fault accounted for most of the slip.

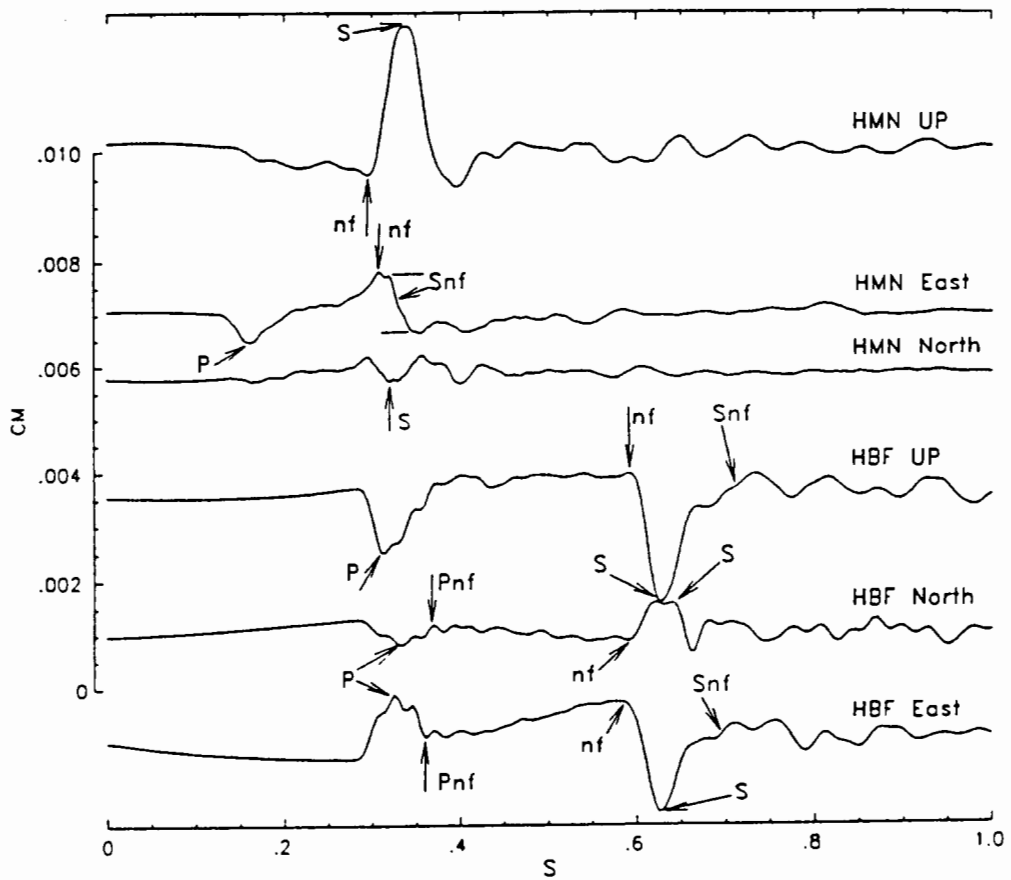


Figure 8. Ground displacement for event 0341528 recorded at underground site HMN and surface station HBF. In addition to the far-field \$P\$ and \$SS\$ waves, the phases indicated by the arrows include the static \$P\$ and \$SS\$ offsets, \$P_{nf}\$ and \$S_{nf}\$, as well as the near-field ground motion \$n_f\$, that builds in amplitude between the \$P\$ and \$SS\$ arrivals. The moment tensor was determined from measurements at the 19 points shown by the arrows. (From Figure 1 of McGarr, 1992.)

The cross section in the lower part of Figure~7 illustrates our interpretation of the moment tensor result. Located at a pre-existing geological fault that had offset the subhorizontal gold-bearing reef, by roughly 30~m, event 0341528 apparently involved several centimeters of additional fault slip plus closure of the adjacent stopes from which gold had been produced.

Moment tensor analysis of 16 events, including 0341528, yields two distinct categories. Event 0341528 typifies the majority of events (11 of 16) for which the coseismic volume decrease is comparable to, but somewhat smaller than, the deviatoric component \$\Sigma AD\$. The other category consists of deviatoric failure only, with no significant volume change (5 of 16). Interestingly, for the implosive-deviatoric events the \$P\$ waves are expected to have all dilational initial motions, consistent with the observation, mentioned before (Figure~5).

Needless to say, discrimination techniques that are based on \$P\$ to \$SS\$ phase ratios (e.g., \$P_g / L_g\$) may be poorly suited to discriminate mine tremors from explosive sources because the implosive

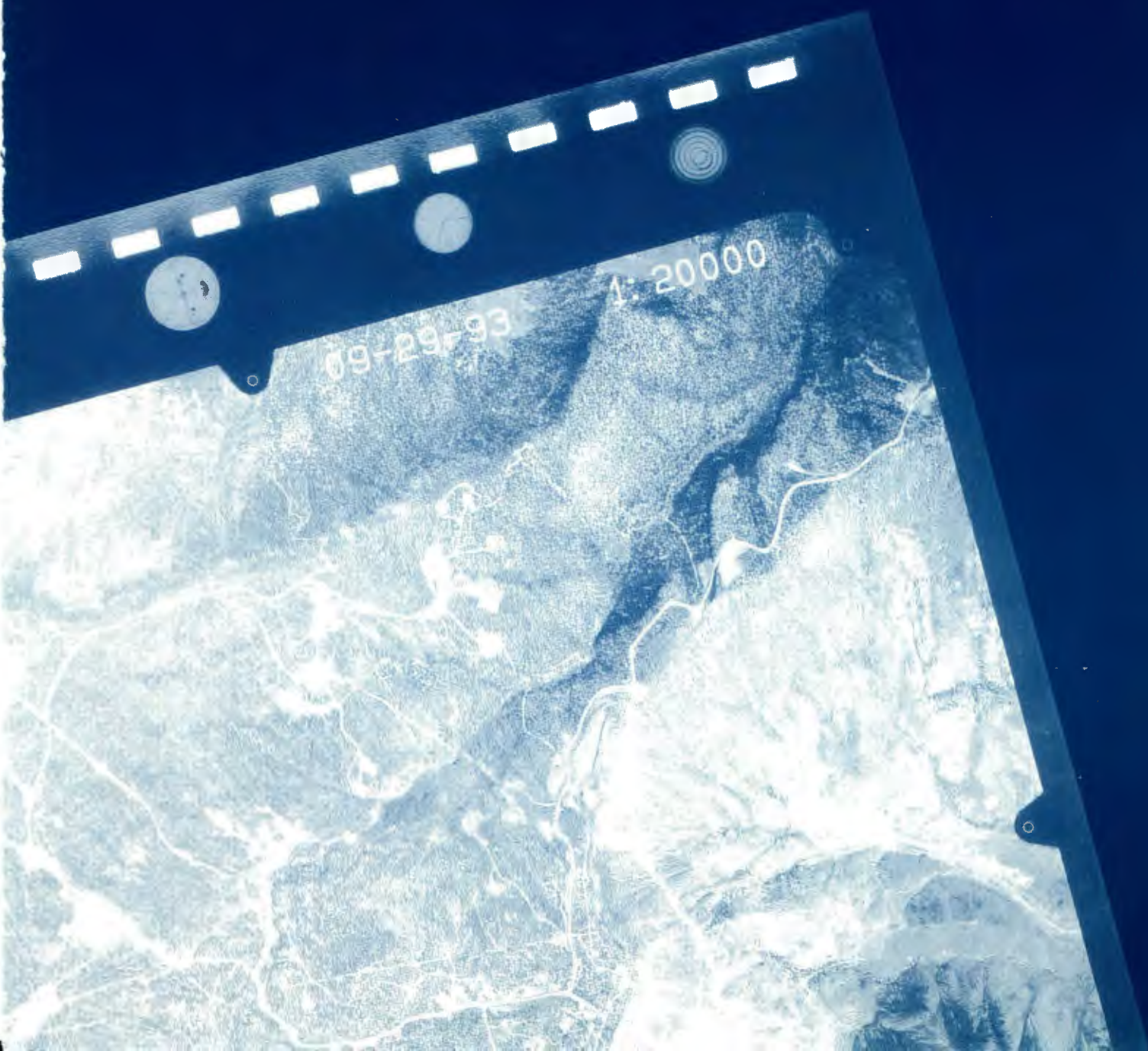
component in the moment tensor enhances the \$P\$ wave in the far field, but not the \$S\$ wave. In the case of the event of September 30, 1987 (Figure~4), misidentified as a clandestine nuclear test, this effect may have augmented \$m_b\$ thus making this event seem more like an explosion than an earthquake. To the contrary, if polarity information is used, as was the case for the event 1021030 (Figure~4), then the implosive-deviatoric mechanisms render the majority of tremors more distinct from explosions than would be the case if the mechanisms of all tremors were purely deviatoric (faulting).

References

- Evernden, J. F., C. B. Archambeau, and E. Cranswick, An evaluation of seismic decoupling and underground nuclear test monitoring using high-frequency seismic data, *Rev. Geophys. Letters*, **24**, 143–215, 1986.
- McGarr, A., An implosive component in the seismic moment tensor of a mining-induced tremor, *J. Geophys. Res.* **19**, 1579–1582, 1992.
- McGarr, A., J. Bicknell, E. Semenza, and R. W. E. Green, Analysis of exceptionally large tremors in two gold mining districts of South Africa, *Pure Appl. Geophys.* **129**, 295–307, 1989.
- McGarr, A., J. Bicknell, J. Churcher, and S. M. Spottiswoode, Comparison of ground motion from tremors and explosions in deep gold mines, *J. Geophys. Res.* **95**, 21, 777–21,792, 1990.

3

TEST PREPARATIONS



Logistics and Preparations for the NPE

Paul J. Thompson and John W. Miller
Lawrence Livermore National Laboratory
Nuclear Test Operations Department

EXPERIMENT & SITE DESCRIPTION

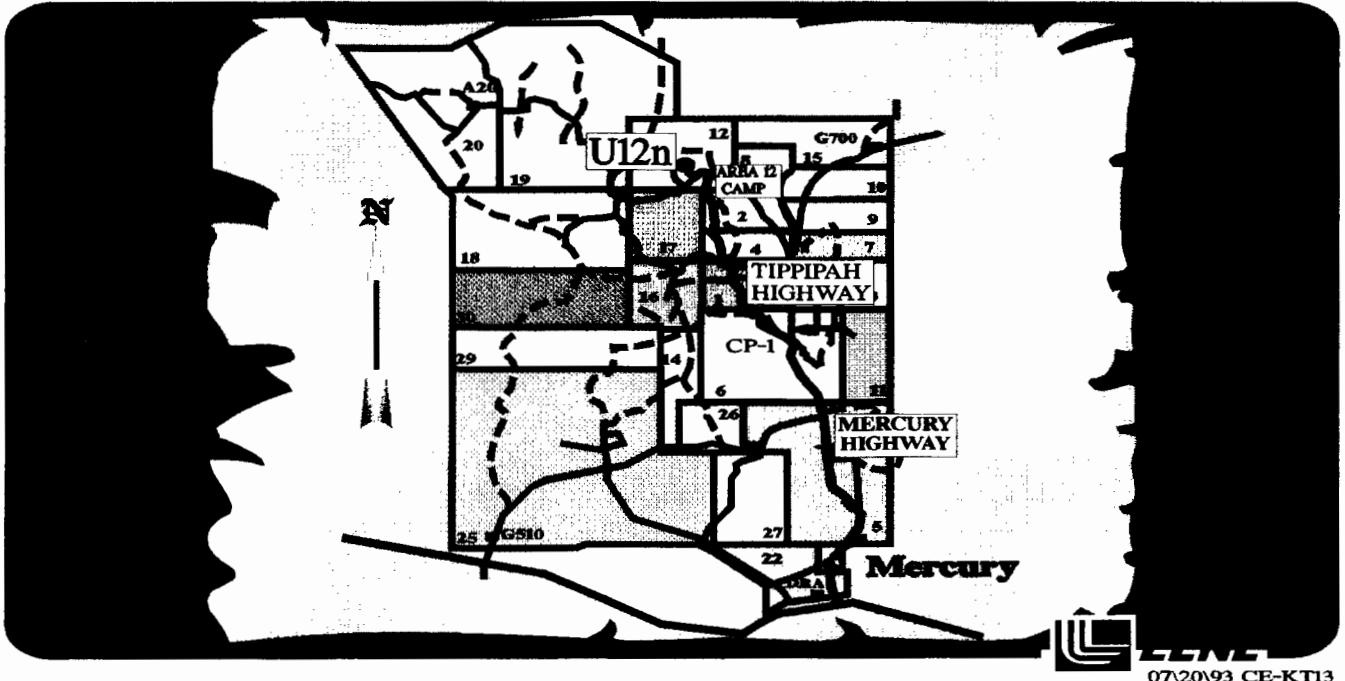
The purpose of this experiment was to simulate a one kiloton nuclear explosion using chemical explosives and try to differentiate the seismic signatures generated from that of previous nuclear detonations. In order to duplicate the geology of nuclear detonations as closely as possible, this experiment was carried out in the "N" Tunnel complex at the Nevada Test Site (NTS). The location of U12n tunnel is shown on the following sketch (CE-KT13). This location was particularly appropriate since data is available from previous nearby nuclear events for comparison with data to be collected from the Chemical Kiloton (CKT) Experiment. Since no further nuclear events are planned in "N" Tunnel, we operated on a non-interference basis with test program activities.

In order to generate the 1 kiloton equivalent energy release, a total of 2.9 million pounds of blasting agent was detonated using five 5 pound Pentolite booster charges, each initiated by a high energy Exploding Bridge Wire (EBW) detonator. The blasting agent consisted of a 50/50 emulsion ANFO mixture; the emulsion being an ammonium nitrate water mixture, and ANFO being an ammonium nitrate fuel oil mixture.

The explosive was emplaced at the end of a newly mined drift, designated U12n.25, which was 11' x 11' in cross-section and 250' in length. This drift branched off an existing drift in "N" Tunnel, U12n.23. A cavity approximately 49.5 feet in diameter and 16.5 feet high was mined at the end of U12n.25 and instrumented with arrays of Continuous Reflectometry for Radius Versus Time (CORTEX) cables, thermocouples, and pressure measuring instrumentation for both scientific and safety monitoring purposes.

Additional instrumentation, external to the cavity, was installed in several tunnel locations, as well as locations external to the tunnel, and on Ranier Mesa above the point of detonation. Data from these instruments and the instruments themselves, as possible, were retrieved after the detonation. More distant measurements were made at various permanently installed seismic stations across the country, as well as at some international locations. In particular, an attempt was made to coordinate this detonation with the National Science Foundation fielding of a seismic array emplaced by Duke University in the southern Sierra-Nevada mountain range (Nevada & California) during mid-September of 1993.

By its general nature, this location lent itself to easy control of unauthorized access (entry into the tunnel is easily controlled), as well as minimization of environmental impacts (the detonation took place underground, with complete containment and with no cavity collapse to the surface). Also, because of the previously detonated nuclear events, the site was suited for the scientific goals being pursued.



SEQUENCE OF OPERATIONS OVERVIEW

The following is sequence of operations, equipment setup, and equipment layout for the portal area and the emplacement area in the U12n.25 access drift.

Mine the drift and construct a 16-1/2' x 49-1/2' chamber for the explosive mixture.

PORTAL AREA

On receiving an operations permit from DOE the ALPHA explosive mixing and emplacement equipment were brought on site and setup. This consisted of mixing trailers, emulsion silo, diesel tank, diesel to hydraulic motors, electric motors, and a standby mix truck. The mixing equipment was setup at U12n portal area in front of "N" extension drift as shown on the following sketch (CE-KT7), "ANFO Blending Area Storage and Staging", mixing and load area.

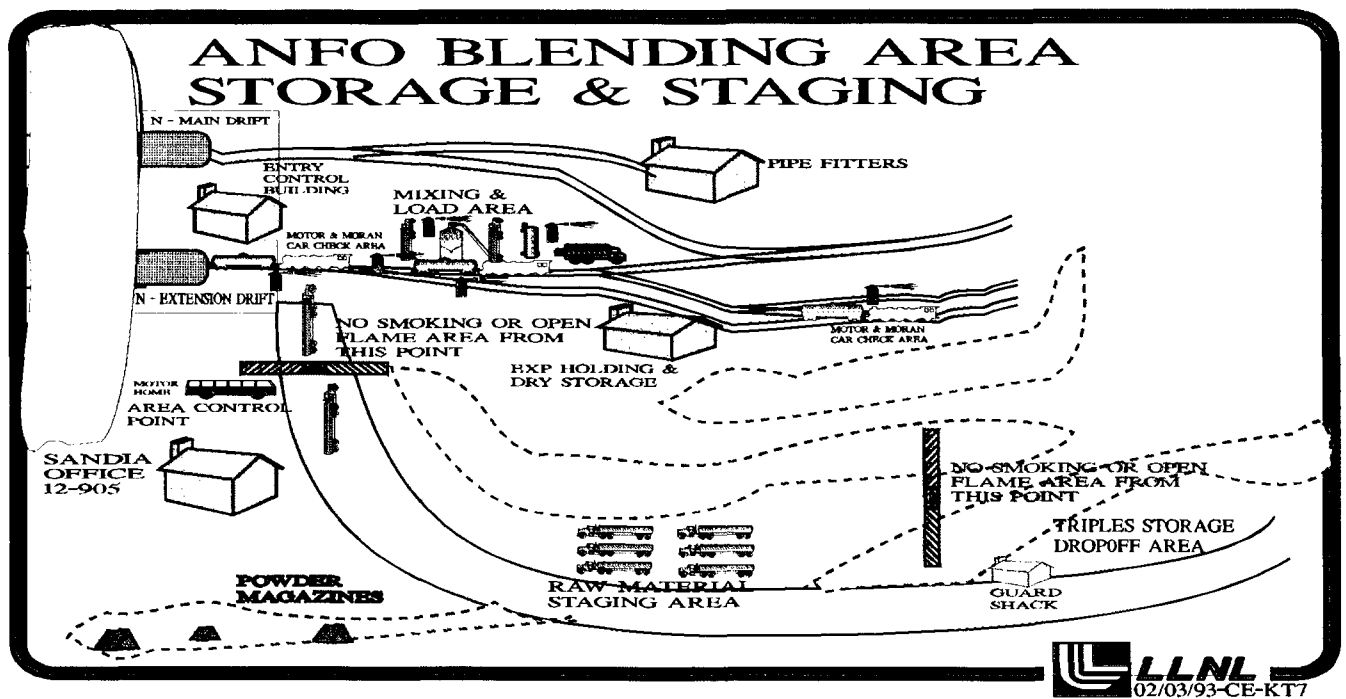
The mixing and load area had fire extinguishers placed around the area for easy access. Fire extinguishers were placed in the motor and agitator car check areas. There was a fire truck at the area control point. The motors had fire extinguishers and or fire suppression systems installed on them.

The triples storage drop-off area was for the Emulsion (blasting agent). The raw material staging area was for the AN Prills. The diesel tank was filled twice during the mixing operation. The Emulsion and AN Prills were delivered to the mixing area as needed.

The area control point was the primary control point for the portal area. An LLNL-N C&DE motor home was placed at the entrance to the portal area, an LLNL operations representative controlled all personnel entering the portal area. From the area control point on NO SMOKING OR OPEN FLAMES were permitted. LLNL operations representative initiated WSI Form 56 for all spark producing articles. All personnel entering the area were required to sign the Form 56 certifying that no spark or flame producing items were carried into the portal area.

Access control, due to the nature of this project, namely, the handling of explosives, was one of the most effective methods of mitigating hazards. Only persons essential to performing the required tasks were allowed access to the mixing area and the emplacement location in U12n.25 from the time explosives arrived on site until the clean-up was complete.

The motor and agitator (moran) car were checked by approved procedure at the back of the portal area, then moved to the mixing and load area, filled, and moved to the entrance of "N" extension drift where the motor and agitator car were checked by procedure. The underground emplacement area LLNL-C&DE controller was contacted to confirm that the loaded agitator car could be transported to the emplacement area. The agitator car was pushed by the motor to the emplacement area.

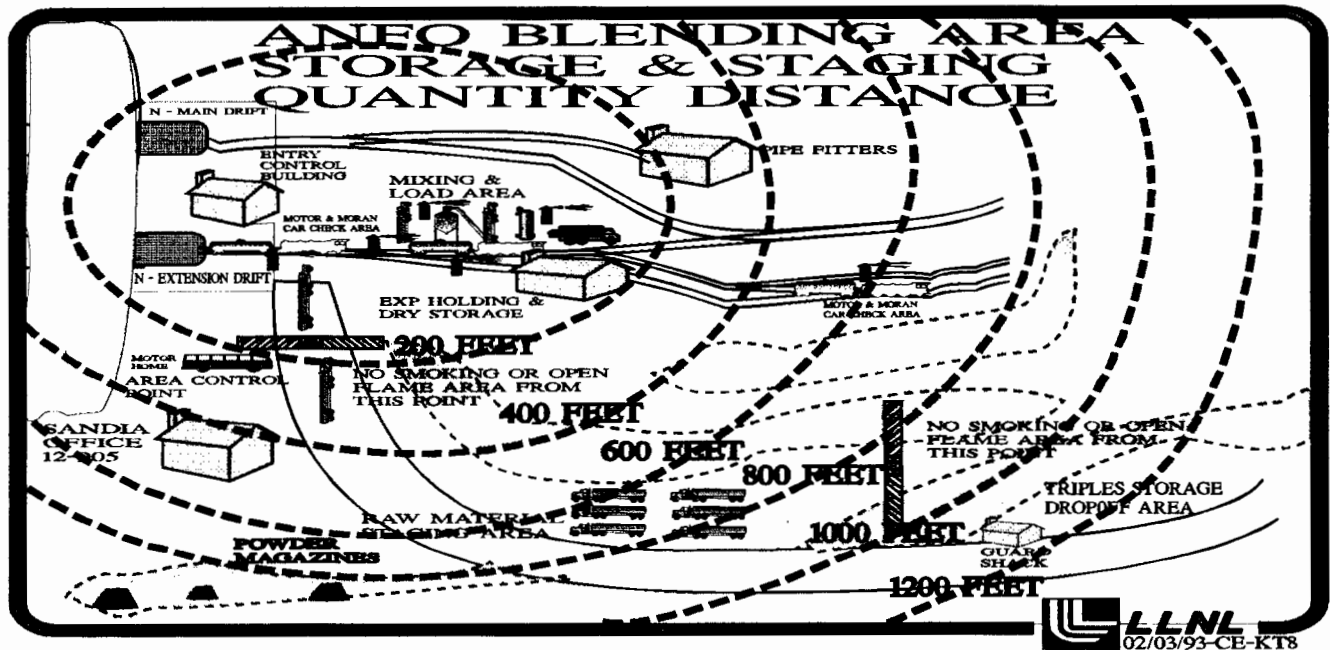


QUANTITY DISTANCE

The distance between the mix area and the storage areas were as shown on the following sketch (CE-KT8). Separations between the various areas were well over the required distances, in addition there are natural earth barriers which was additional safety barriers.

Quantity-distance requirements for explosive operations and storage was required to determine the safe separation distances for inhabited buildings, public highways, and the separation of storage magazines.

To determine the quantity-distance requirements for the mixing and temporary storage operations at the portal, the maximum quantity of explosives that was involved in the operation were used to determine the appropriate quantity distances. These calculations result in a separation requirement of 315 feet. As can be seen from the sketch below there is closer to 600 feet separation.

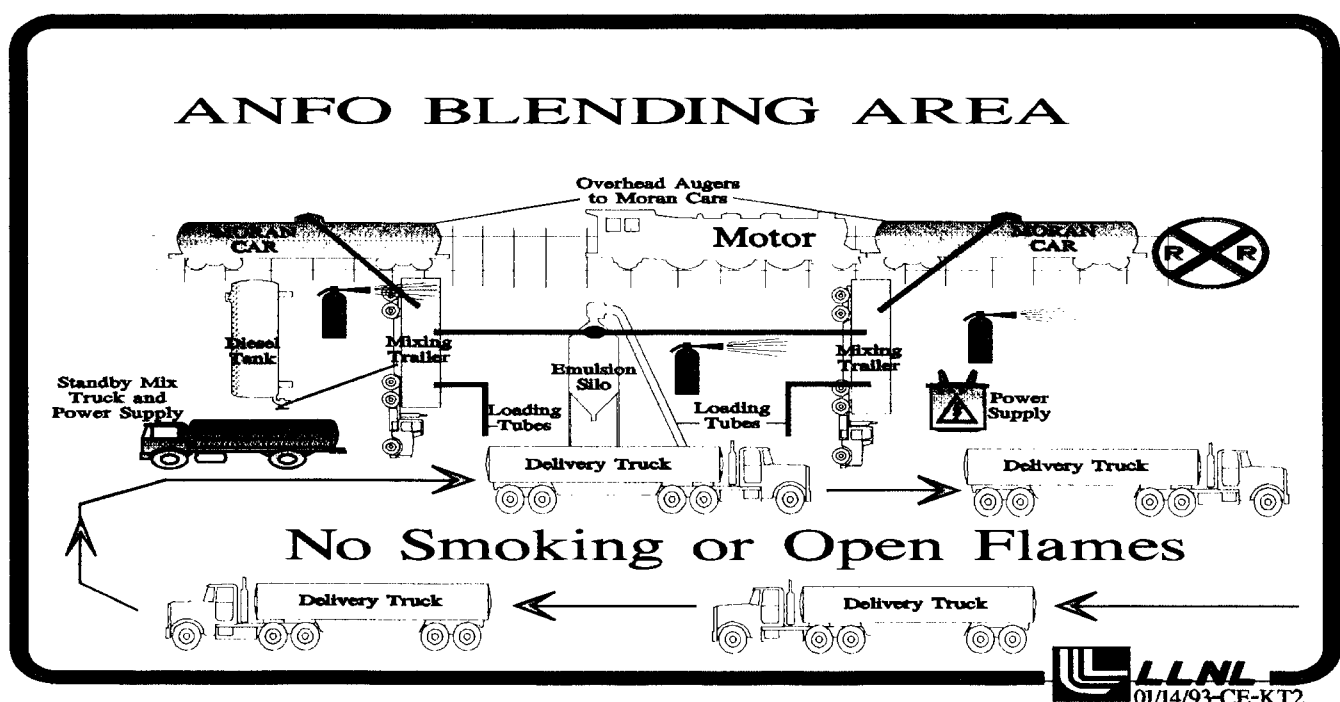


PORTRAL MIX OPERATION SETUP

The mix and load area is shown on (CE-KT2) "ANFO Blending Area" below. Mixing of the ANFO/Emulsion and loading of that product in the agitator cars took place in this area. Re-supply of raw materials also took place in this area. The mix and load area was approximately 150 feet from the portal opening.

The ALPHA explosive mixing and emplacement equipment were brought on site and setup in this area. This consisted of mixing trailers, emulsion silo, diesel tank, diesel to hydraulic motors, electric motors, and a standby mix truck. There were two redundant systems, only one system at a time was used to mix and auger the ANFO/Emulsion to the agitator car, the other system was a backup system. The standby mix truck and power supply was a third backup system.

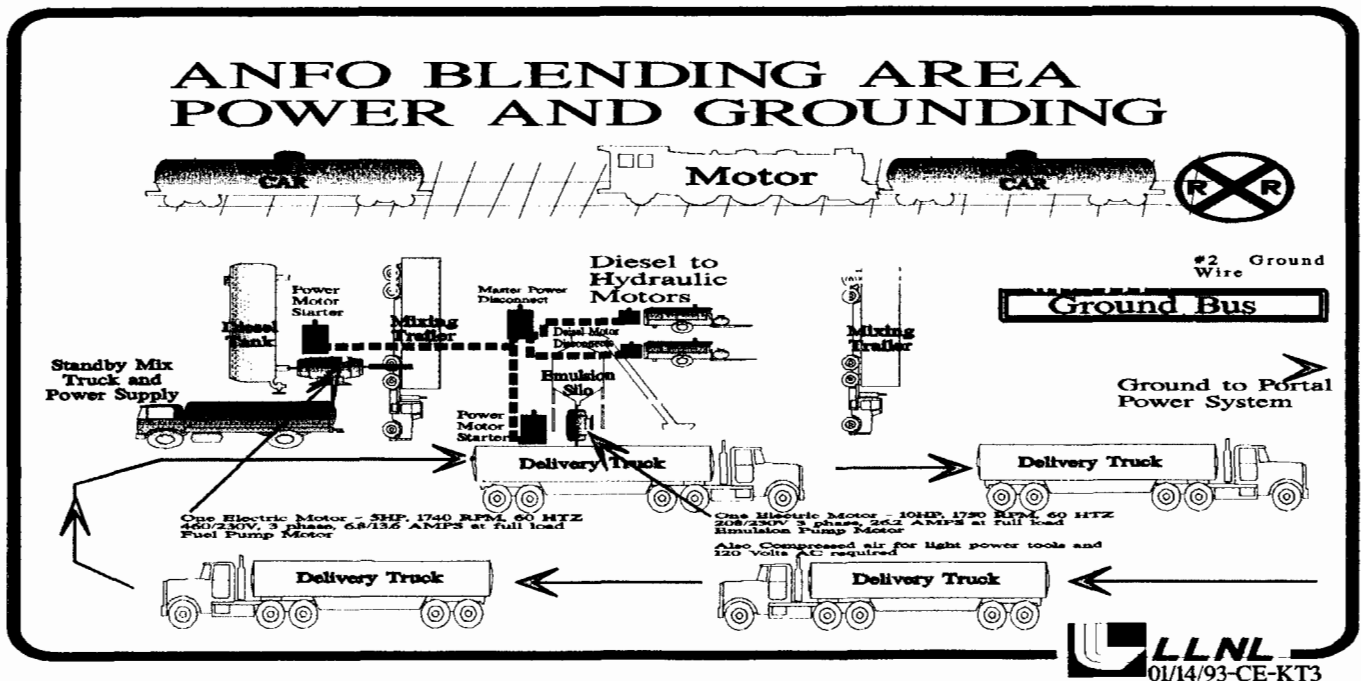
No smoking or open flames were allowed in the portal area from the start of the raw material delivery until the leftover ANFO/Emulsion was shipped from the portal area. The mixing and load area had fire extinguishers placed in the area for easy access.



PORAL MIX AREA POWER AND GROUNDING

In the portal mix area the power requirements consisted of the Diesel fuel pump motor, Emulsion pump motor, and two Diesel to Hydraulic motors; refer to the following sketch (CE-KT3) ANFO blending area power and grounding. The portal power system supplied power to the Diesel Fuel Pump Motor and the Emulsion Pump Motor. The Diesel fuel pump motor and the Emulsion motor had starter contactors installed to control their power. The two Diesel to Hydraulic motors had relays installed to control their operation. A master power disconnect switch was installed to control all power in the mix area.

Grounding consisted of an equal potential central ground bus single point grounded to the portal area grounding system. The rail tracks, mixing trailers, diesel tank, delivery trucks, electric motors, and the two diesel to hydraulic motors were individually grounded to the central ground bus. All of the grounded equipment was current monitored daily and logged, all fault current was corrected before the mixing operation started.

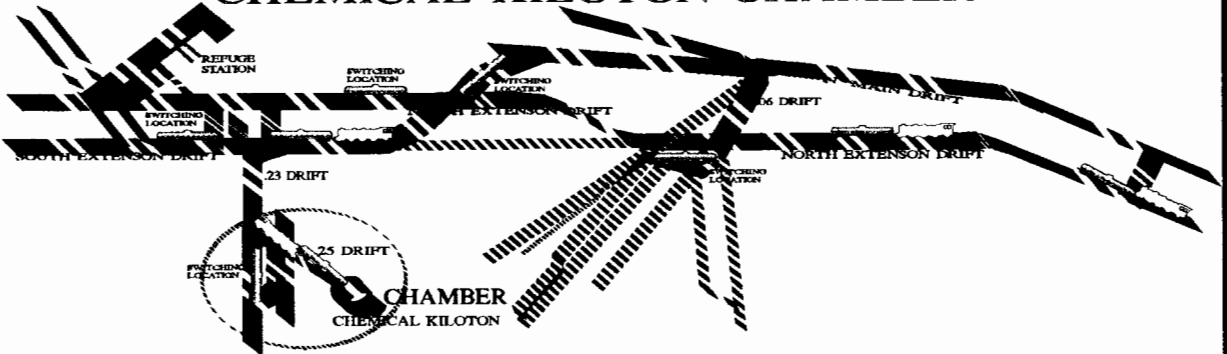


TUNNEL TRANSPORT

The ANFO loaded agitator car was pushed by the motor via the North extension drift, to the .23 access drift, then to the .25 access drift, to the chamber; refer to the following sketch (CE-KT10) "N Tunnel Complex, North Extension Drift, .23 Access Drift, .25 Access Drift, Chemical Kiloton Chamber".

The loaded agitator car always had the right away. Switch out locations for the empty agitator cars are shown on the following sketch. The motormen transported the loaded agitator car at a maximum speed of 10 miles per hour. The refuge station is also shown on the following sketch.

**"N" TUNNEL COMPLEX, NORTH EXTENSION DRIFT,
.23 ACCESS DRIFT, .25 ACCESS DRIFT,
CHEMICAL KILOTON CHAMBER**

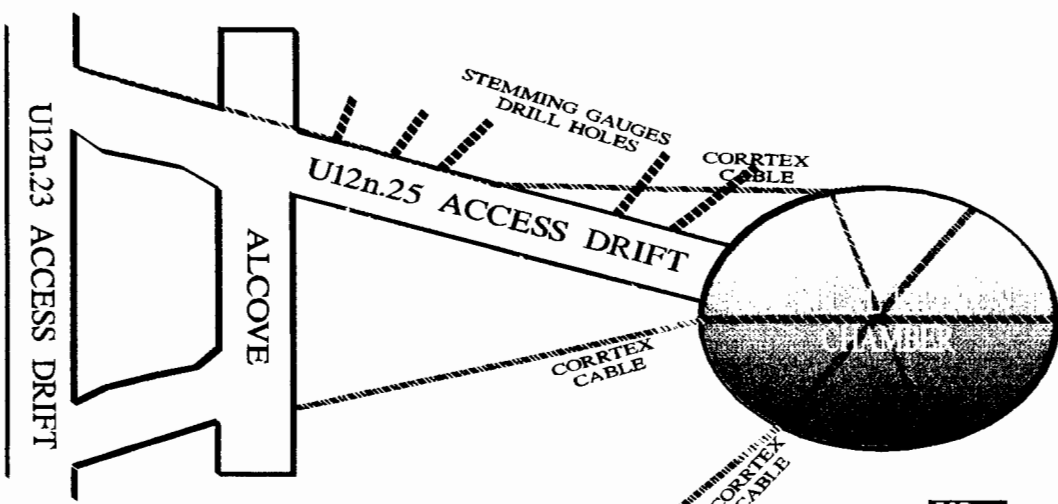


LLNL
07/15/93-CE-KT10

U12n.25 ACCESS DRIFT AND CHAMBER INSTRUMENTATION

The U12n.25 access drift had stemming gauges, (Axially Symmetric Magnetic and ground motion) through out, refer to the following sketch (CE-KT11) ".25 Drift and Chamber Instrumentation CORTEX and Stemming Gauges. The chamber had 12 CORTEX cables for yield verification. At the back of the chamber a tracer bottle of Helium-3 was installed in order to test "Sniffing Techniques" for explosive by-product gases.

**.25 DRIFT AND CHAMBER INSTRUMENTATION
CORTEX AND STEMMING GAUGES**



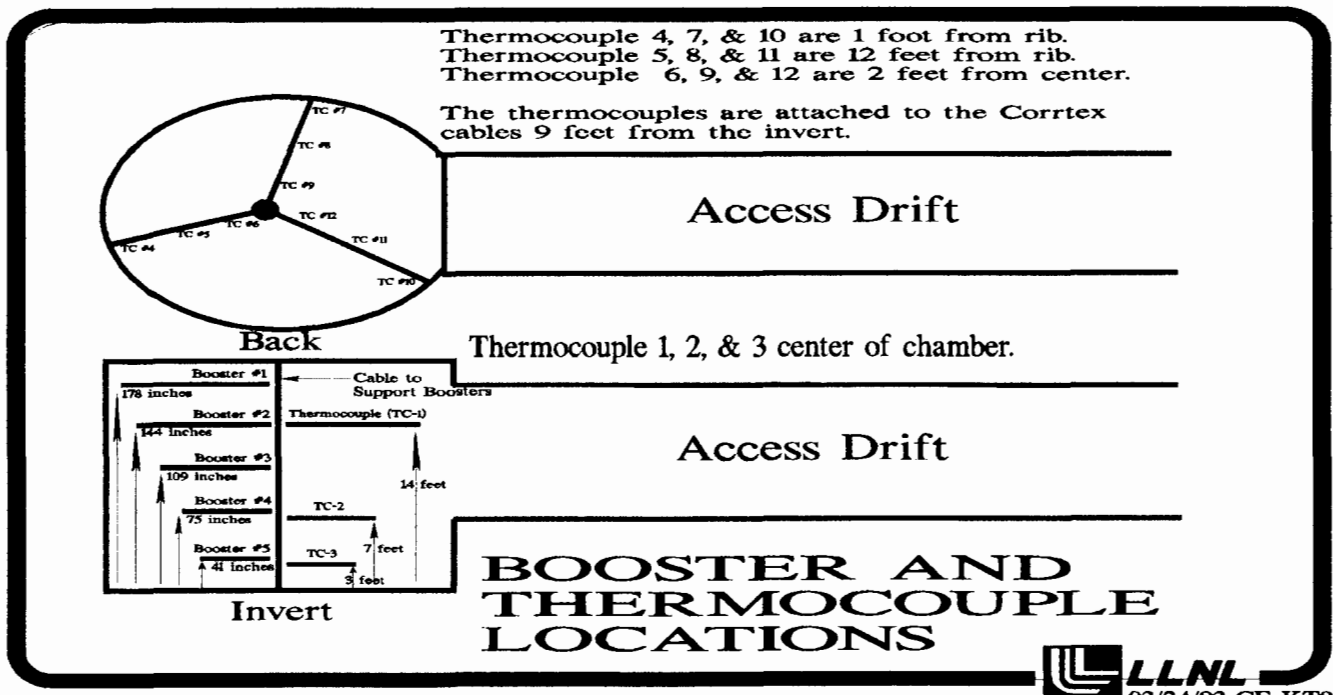
LLNL
07/15/93-CE-KT11

CHAMBER THERMOCOUPLES

The chamber was instrumented with an array of twelve thermocouples that were embedded in the ANFO charge, refer to the following sketch (CE-KT9) "Chamber Booster and Thermocouples Locations". The thermocouples were used to monitor the temperature and temperature distribution in the ANFO charge during the time from loading of the ANFO in the chamber until firing the charge.

The thermocouples were installed on the CORTEX support cables. Thermocouples 4, 7, & 10 were 1 foot from rib; 5, 8, & 11 were 12 feet from rib; 6, 9, & 12 were 2 feet from center; and 1, 2, & 3 were in the center of the chamber.

The thermocouples were monitored from the LLNL Device Systems alcove and from the Control room (Control Point #9 in area 6).



UNDERGROUND EMPLACEMENT PHASE ONE (GRAVITY FLOW)

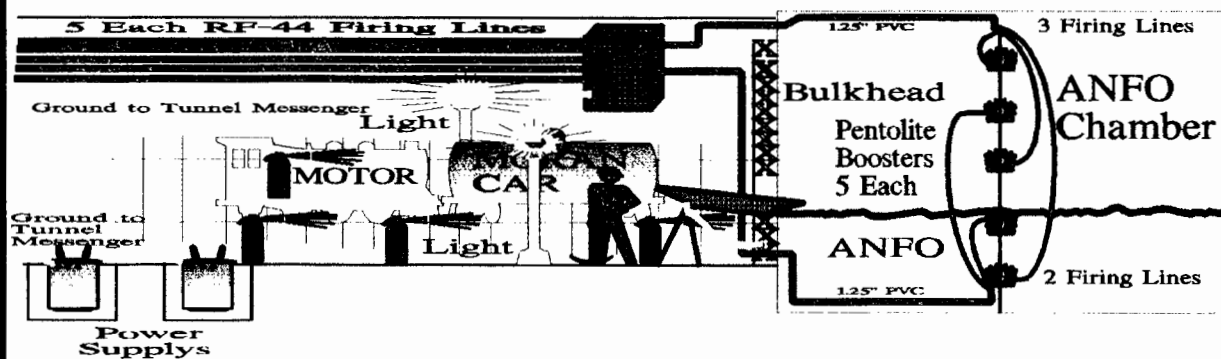
Five booster charges were placed in the center of the chamber. One booster would fire the ANFO charge, the other four boosters were backup. The top, center, and bottom boosters were used to fire the ANFO charge, these three boosters were wired across the top of the chamber. The other two boosters were wired across the bottom of the chamber and was used as a backup.

Phase One of emplacement consisted of positioning agitator cars close to the chamber bulkhead such that when the ANFO/emulsion product was offloaded it flowed onto a dump chute which directed the product into the chamber. Refer to the following sketch, (CE-KT6) "ANFO Blend Chamber and Placement Area".

The emplacement area had fire extinguishers placed in the area for easy access. As previously stated the motors have fire extinguishers installed on them and some have fire suppression systems installed. The fire extinguishers were more than adequate, the fire suppression systems were additional support. A charged water hose was also available in the emplacement area.

Lights were installed in the emplacement area for additional worker safety.

ANFO BLEND CHAMBER AND PLACEMENT AREA



LLNL
02/01/93-CE-KT6

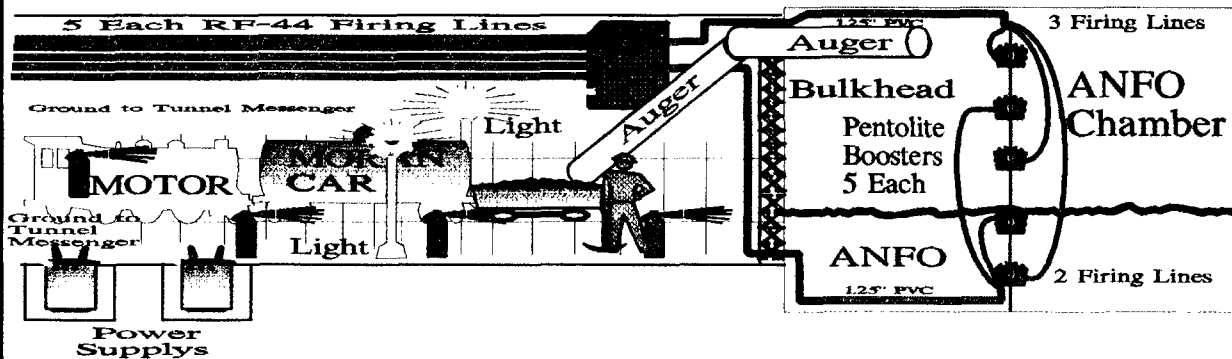
UNDERGROUND EMPLACEMENT PHASE TWO - (AUGER EMPLACEMENT)

Phase TWO emplacement was by augering the ANFO/emulsion product into the chamber. The dump chute was removed and the opening in the bulkhead was sealed. The ANFO hopper, vertical, and horizontal augers were installed. Refer to the following sketch (CE-KT4) "ANFO Blend Chamber and Placement Area.

The agitator car was placed so that the ANFO blend would flow out of the car into the hopper and then was augured into the chamber.

There were two vertical and horizontal auger systems, one was used and the other was a backup.

ANFO BLEND CHAMBER AND PLACEMENT AREA



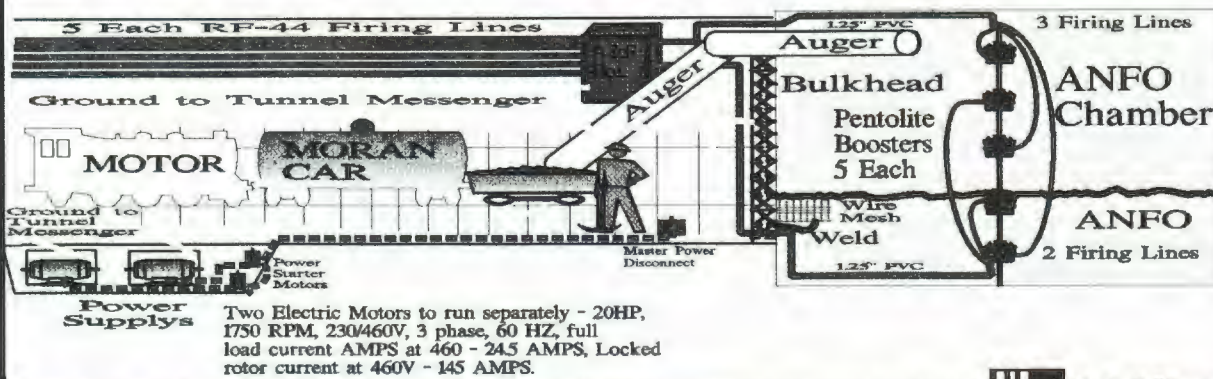
LLNL
01/14/93-CE-KT4

EMPLACEMENT AREA POWER AND GROUNDING

The two electric motors to hydraulic power packs had power starter contactors that controlled the power to the electrical motors. A master power disconnect switch was located by the augering system operator for emergencies.

The grounding system was equal potentiated; the wire mesh in the chamber was welded to the bulkhead, the tracks were bonded to the bulkhead, the tunnel messenger was bonded to the bulkhead, the hopper and auger system was grounded to the tracks, and the agitator car was on the tracks.

BLEND EMPLACEMENT AREA POWER AND GROUNDING



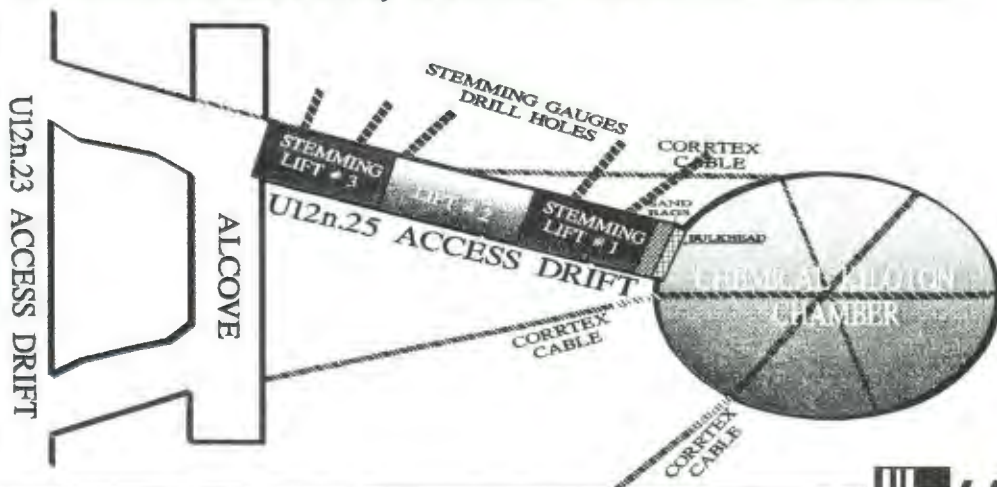
LLNL
01/14/93-CE-KT5

U12n.25 DRIFT STEMMING LIFTS 1, 2, AND 3

After the ANFO had been placed in the chamber the bulkhead was sealed and a five feet thick sand bag wall was placed directly adjacent to the bulkhead as a thermal barrier.

The stemming was done in three lifts, refer to the following sketch, (CE-KT12) .25 drift stemming lifts 1, 2, and 3.

.25 DRIFT STEMMING LIFTS #1, #2, #3, BULKHEAD, AND SAND BAGS



LLNL
07/15/93-CE-KT12

LESSONS LEARNED FROM THE NON-PROLIFERATION EXPERIMENT

Charles McWilliam and Steven Curtis

**United States Department of Energy
Nevada Operations Office
Arms Control and Nonproliferation Division**

Abstract

The Department of Energy sponsored Non-Proliferation Experiment (formerly known as the Chemical Kiloton) involved the detonation of blasting agent approximately equivalent to one kiloton of energy release on the Nevada Test Site in an effort to determine if (and if so, which) discriminators exist between conventional and nuclear detonations of similar yield. Coordination among hundreds of scientists from at least fifteen different organizations were required to design the experiments necessary to collect and interpret data from this unique and complex event. Stakeholders and members of the Group of Scientific Experts of the Conference on Disarmament observed the progress of the experiment first hand. The experiment was a success in that a vast majority of the expected data was collected and shared quickly and efficiently throughout the international scientific community. The management of the project was discussed among the major co-sponsoring organizations and the significant "lessons learned" are presented.

Introduction

The Nevada Test Site (NTS) serves as the principal field test facility for the DOE National Laboratories as well as other users. In many ways, the Nevada Test Site could be considered a research scientist's dream. Advanced facilities and personnel with decades of experience in supporting the most complicated and unique experiments are available for the cost of user fees. It would be hard to imagine being able to create a facility from scratch today which is so remote from the general population, so accessible to the scientific community, yet has the on-site capability to provide everything from food and accommodations to 500+ ton cranes.

The involvement of the Nevada Operations Office was mainly to ensure the experiment was conducted safely and in an environmentally sound manner. The Arms Control and Nonproliferation Division's job was to coordinate all Nevada Test Site services necessary to ensure the experiment was conducted as efficiently as possible within safety and environmental guidelines.

The Non-Proliferation Experiment essentially represented the transition of the Nevada Test Site from exclusive nuclear testing support priority to multipurpose experimental "marketing". This is a new word in the Nevada Test Site vocabulary. Recent changes in national political goals have mandated that this transition be a rapid one. The test site must now be "user-friendly" to a wide variety of "stakeholders" and "customers". The "paradigm" must be revised to accommodate this occurrence or the Nevada Test Site may revert to the Mercury Ghost Town.

An event like the Non-Proliferation Experiment requires an inordinate amount of coordination and control because of the large number of different organizations and experimenters participating on a daily basis. These issues are complicated by the existence of numerous safety and environmental regulations and the restricted budgets being mandated these days.

Despite all these complications, the Non-Proliferation Experiment was concluded with much fanfare, back-patting, and terabits of important data collected and disseminated in record time.

The great success can be mostly attributed to the inherent Nevada Test Site attitude of "CAN-DO" which seems to permeate every individual associated with this event. The major lesson learned is that no experimental goal is too difficult that it cannot be accomplished at the Nevada Test Site. The caliber of people who have inhabited this research and development oasis for over 40 years (some continuously) simply will allow no other outcome than success to exist.

Text of Presentation

In keeping with its research-oriented mission, the DOE Nevada Operations Office has historically conducted a post event review of every test or exercise conducted at the NTS to gain information useful for conducting future events. To this end, an after action review of the Non-Proliferation Experiment processes was conducted among all the major participants in the Non-Proliferation Experiment. All suggestions were incorporated into a final "lessons learned" report. Although many specific suggestions were made, they all fit into three major categories: Project Management, Customer Care, and Cost Estimating and Control. These were mostly simple coordination and administrative issues as opposed to mission threatening problems. The resolution of these should ensure the next mission conducted at the Nevada Test Site will not seem so much like an ordeal to some customers.

PROJECT MANAGEMENT

1. An individual DOE/NV project manager should be assigned to coordinate each Nevada Test Site activity. Customers deserve "one stop shopping" and DOE must vest responsibility in one person for accountability and efficiency reasons.
2. Principal control of Nevada Test Site activities should be retained at DOE/NV with major policy and budget support from DOE/HQ.
3. Sufficient advanced notice should be given to DOE/NV to ensure the approval process can be completed and necessary support activities can be coordinated in a timely fashion.
4. All organizations' points of contact must be involved in all planning exercises and meetings.
5. Department of Energy requirements for safety and environmental approvals must be documented and provided as early as possible, in easy to understand terms, to the affected users.
6. Checklists and procedures should be written and used for as many aspects of the project as practicable.

CUSTOMER CARE

1. DOE must provide orientation and written instructions for customers who expect to conduct activities at the NTS. These should be detailed enough so there is no doubt what the customer must do to implement their project. They must be simple and as transparent to the customer as possible so project overhead is kept at a minimum.
2. The project manager should make DOE/NV safety and environmental expertise available to the customer for complex projects. On the Non-Proliferation Experiment, a lot of time was required to develop acceptable safety and, to a lesser degree, environmental approval documents.
3. Memoranda of Agreement detailing duties in relation to the project should be developed between all participants before project inception.

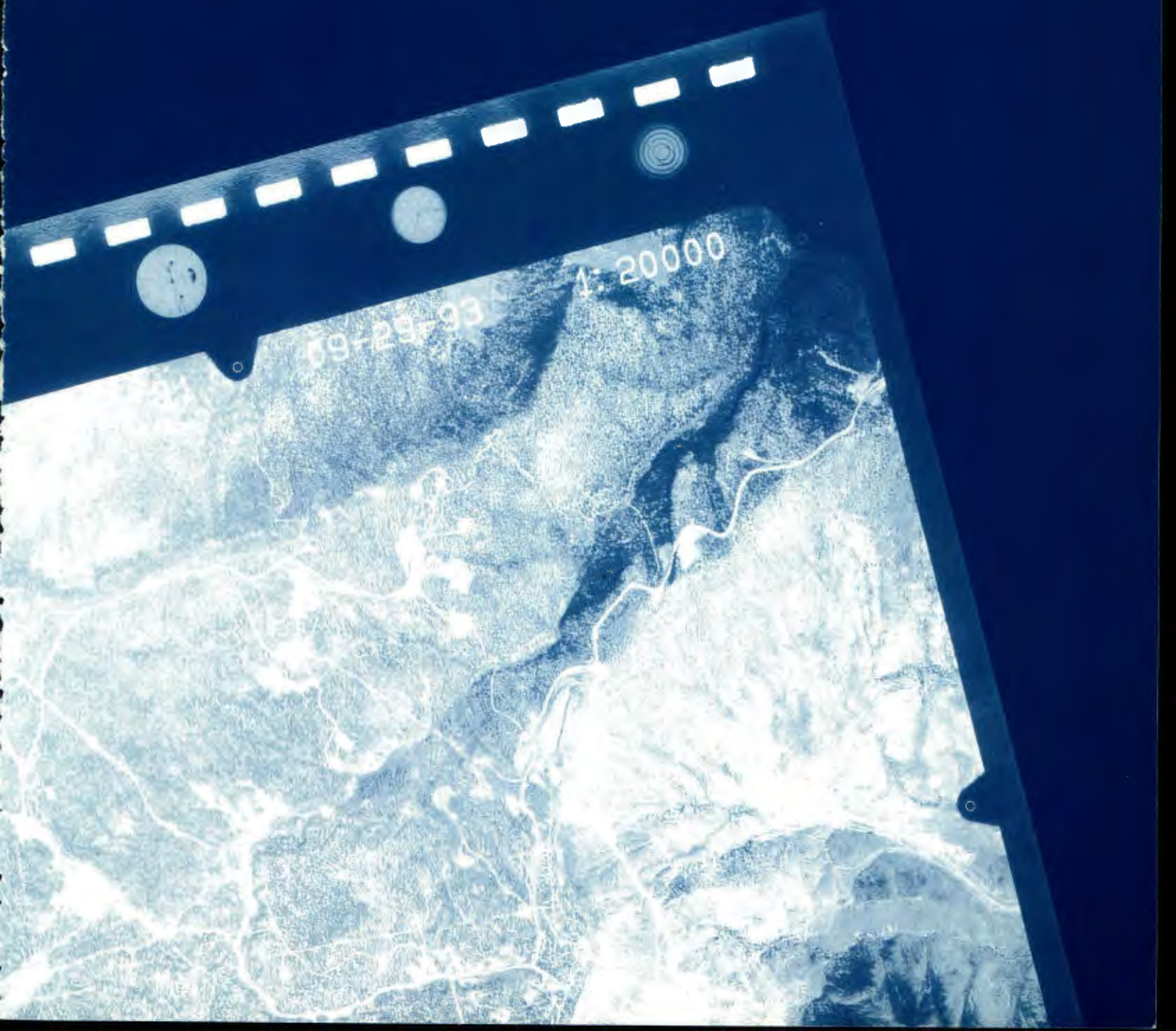
COST ESTIMATION AND CONTROL

1. Include budget preparation guidance for Nevada Test Site users similar to that for the project approval process. Particular attention should be given to disseminating precise figures for the NTS allocation cost.
2. Document all budget estimates and include the assumptions upon which they are based.
3. Assure that adequate levels of contingency funds are available and establish guidelines for their use and accountability.

Conclusion

The goal of the Nevada Test Site is to allow a wide range of scientific research and development to be conducted with a minimum of overhead requirements. Changing world conditions have refocused the primary purpose of the NTS, but the goal remains the same: Safe and efficient operation of a premier experimental platform for a variety of research and development projects.

EOS AND CODE SIMULATIONS



BACKGROUND ON THE COMMERCIAL EXPLOSIVE CHOSEN FOR THE NON-PROLIFERATION EXPERIMENT

**MARK E. MAMMELE
DYNO NOBEL INC**

ABSTRACT

The requirements of the Chemical Kiloton Experiment as outlined in the original explosives bid package provided DYNO NOBEL/Alpha-Ireco Inc. with a unique challenge. The size of the chamber, the total volume of explosives required, the chemical energy equivalent of one kiloton, the time-frame of loading the chamber, transportation, safety, were all necessary considerations in choosing this particular explosive. The rationale for choosing this particular emulsion/ANFO blend of blasting agent explosive will be presented. DYNO NOBEL INC in-house theoretical predictions as to the explosive performance potential of this blasting agent will be compared to some of the actual data acquired upon detonation. The results of this type of experiment may provide new insight as to the efficiency of the energy release of typical commercial explosives.

Introduction

In the fourth quarter of 1992, Alpha-Ireco Incorporated was invited to participate in the bid process for the explosives product to be utilized in the non-proliferation experiment. Alpha-Ireco is a 50/50 joint venture distributor and licensed manufacturer of DYNO NOBEL INC (formerly IRECO Incorporated) explosives manufacturing company with corporate headquarters located in Salt Lake City, Utah.

DYNO NOBEL INC is a subsidiary of DYNO, an international company with corporate headquarters in Oslo, Norway. DYNO NOBEL INC is a leading manufacturer of a full range of commercial explosives and initiation systems sold and used in North America in all types of commercial applications. These applications include mining (surface and underground), quarry, construction, demolition, seismic exploration, etc.

Alpha-Ireco - DYNO NOBEL Partnership Participation

The non-proliferation experiment explosives requirements were bid through Alpha-Ireco Inc. The size, volume and time frame required for loading the chamber required two separate emulsion product manufacturing sites be utilized. One located in Lincoln, CA, one located in Lehi, UT. The emulsion product manufactured at both locations utilized the same formulation developed by DYNO NOBEL Research and Development Group for use in many commercial blasting applications. The same raw ingredients were used at both manufacturing locations to insure that consistent high quality emulsion product would arrive at the test site.

The transportation coordination, on-site blending equipment, emulsion manufacturing at Lincoln, CA, manpower, safety, ANFO procurement, were the responsibility of Alpha-Ireco.

The technical aspects, such as, proper formulation, quality control parameters, SOP of manufacturing, emulsion manufacturing at Lehi, UT, safety, laboratory testing, raw ingredient recommendations were the responsibility of DYNO NOBEL INC.

Explosive Requirements for Non-Proliferation Experiment

The explosive requirements necessary for the success of the non-proliferation experiment were interesting in that they included not only energy requirements, but also volume, physical characteristics, timely manufacturing, transportation restraints, quality control parameters, detonation characteristics, safety, and environmental concerns.

All of these characteristics and/or requirements are met daily within the commercial blasting community but not typically on the time and volume scale required for the non-proliferation experiment.

The two most important requirements from a commercial manufactures point of view were:

- 1) Ability of explosive chosen to completely fill the excavated chamber with no personnel access inside the chamber once loading begins.
- 2) Energy equivalent of one kiloton of explosive energy defined as:

$$1\text{kt} = (1.0 \times 10^{12} \text{ calories}).$$

The term "Emulsion" from this point forward refers to an emulsion matrix of the "water in oil" type. The discontinuous phase consisting of a super saturated nitrate salt solution. The continuous phase consisting of a liquid carbonatious fuel and emulsifier combination.

The initial information we received indicated that the cylindrical chamber would be 15.1 meters in diameter and 5.0 meters high. The "chosen" explosive was to be a 30% emulsion/70% Anfo blend.

When this information was relayed to DYNO NOBEL via Alpha-Ireco, immediately a "red flag" went up within the technical and R&D group at DYNO NOBEL. The red flag was simply this. Any 30% emulsion, 70% Anfo blend of explosive product would not be able to meet the criteria of completely filling the excavated chamber without human or mechanical assistance due to inherent physical characteristics of a 30/70 emulsion/Anfo blend. Therefore, Alpha-Ireco/DYNO NOBEL suggested that a 50% emulsion, 50% Anfo blend be the explosive product of choice.

A 50/50 emulsion/anfo blend was recommended and eventually chosen because of its viscosity, and fluidity characteristics. One critical term used was "self leveling", in that the product must be "self leveling" once placed into the chamber. To achieve this self leveling characteristic, a very specific emulsion formulation was chosen. This emulsion formulation required specifications that would insure the final product (50/50 Emulsion/Anfo) blend would be itself "self leveling".

Bulk emulsion formulations can have a rather wide range of fluidity or viscosity characteristics as well as a wide density range, see chart below:

TYPICAL BULK EMULSION RANGES

	<u>Viscosity</u>	<u>Density</u>
Low	7,000 Centipoise	1.05 g/cc
High	40,000 Centipoise	1.42 g/cc

The viscosity range for typical bulk emulsions used in the explosives industry would produce the physical character of fluidity of approximately 50 wt. motor oil at 7,000 centipoise to a self supporting mayonnaise type fluidity in the 40,000 centipoise range.

The viscosity range chosen for the emulsion phase of this project was 7,500 to 9,000 centipoise with the average viscosity of the emulsion product being 8,400 centipoise hence, very fluid.

When this emulsion phase is blended with 50% by weight of Anfo, the final product viscosity is approximately 18-25,000 cps. Within this range, the final explosive blend product is still very flowable and self leveling but would be fairly difficult to pump. This explosive blend was then augured into the moran cars and either dumped directly into the test cavity or augured once more into the top of the cavity.

The fluidity of this final 50/50 emulsion/anfo blend was sufficient to completely fill the cavity with very minimal product slope (angle of repose). It was evident at the start of the chamber filling process that the blend would be self leveling.

A typical 30% emulsion 70% Anfo blend will maintain a rather steep angle of repose of 30 to 45 degrees because of its lack of fluidity and the physical nature of the Anfo particles surrounded by the emulsion matrix.

Energy Release

The requirement of one kiloton of energy in terms of 1.0×10^{12} calories was another very important criteria to be met.

This necessitated the review of our emulsion formulation in terms of density and energy output as well as the density and energy output of the final product, the 50/50 emulsion/anfo blend.

Our first thought was to blend an unsensitized emulsion oxidizer with 50% Anfo to achieve maximum density and energy per unit volume. We were unable to obtain a commitment as to a firm length of time in which the explosive blend would be required to "sleep" within the chamber after loading but prior to detonation. Because we were not totally sure of the "sleep time" required prior to detonation, we chose to use an emulsion formulation classified as a blasting agent. We increased the sensitivity of this emulsion to detonation by the addition of voids or "hot spots" via density reducing agents such as microballoons. This in effect lowered the density of the emulsion and 50/50 blend and also increased the sensitivity of the emulsion and 50/50 blend. This final blended product would allow for the possibility of unexpected, extended "sleep time" of the explosive product within the chamber.

The emulsion formulation chosen to best meet all the needs of the experiment was a commercially used bulk emulsion blasting agent having the DYNO NOBEL trade name designation of RXHD. This bulk emulsion blasting agent has been used successfully for many years by many of our end use customers. Alpha-Ireco and DYNO NOBEL had the utmost confidence in the performance of this explosive formulation due to our past history of successful performance in the field with this formulation.

To calculate the theoretical energy release of an explosive formulation, DYNO NOBEL INC uses a computer code developed in-house by the name of "PRODET". This "PRODET" code was used to help theorize the total energy release in terms of calories for the product used in this experiment, with a goal of 1kt (1.0×10^{12} calories).

The RXHD emulsion formulation is a trade secret, proprietary formulation. The 50/50 emulsion/anfo blend can be generically represented by the following non-proprietary formulation:

	<u>Weight Percent</u>	<u>Formula</u>
Ammonium Nitrate	78.65	$\text{H}_4\text{N}_2\text{O}_3$
Calcium Nitrate	5.52	$\text{N}_2\text{O}_6\text{Ca}$
Water	9.45	H_2O
Fuel	6.38	C_7H_{12}

Our in-house Prodet code on the specific 50/50 explosive product blend used for the experiment calculates an expected energy release output of 765 calories per gram of product.

The total weight of explosive product loaded into the chamber was 2,855,140 pounds. Using the theoretical energy calculation of 765 calories per gram, we theorize that the total mass of explosives within the chamber had the energy equivalent of:

991,618,673,400 calories

This equates to 99.2% of the target 1×10^{12} calories, one kiloton of energy.

Velocity of Detonation

Another indication of energy output is a measurement of the velocity of detonation of any particular explosive formulation.

This measurement is routinely performed at our manufacturing plants as a very good quality control indicator and as a verification of performance when investigating newly proposed explosive test formulations.

The 50/50 blend product used for this experiment has a measured velocity of detonation in the range

of 4.800 kilometers per second for a 6-inch diameter test charge. The RXHD emulsion only has a measured velocity of detonation of 6.00 kilometers per second in a 6-inch diameter charge.

Our Prodet calculations concerning the prediction of ideal velocity of detonation and detonation pressure for the 50/50 blend detonated inside the chamber are as follows:

<u>Density (g/cc)</u>	<u>Velocity (km/sec)</u>	<u>Pressure (kbar)</u>
1.250	6.265	135.92
1.280	6.358	142.52
1.300	6.420	147.01
1.320	6.482	151.56
1.340	6.544	156.19
1.350	6.575	158.53
1.360	6.606	160.89
1.380	6.668	165.66

One important variable in predicting ideal velocity of detonation rates is the density of the particular explosive. During the chamber loading procedure, product density readings were taken periodically throughout the entire process. The target density of the 50/50 product blend was $1.34\text{g/cc} \pm 0.02\text{g/cc}$. There were 539 density QC samples taken and checked. The average density of the 539 samples proved to be 1.3376g/cc and all density samples were within the $\pm 0.02\text{g/cc}$ range.

There have been some questions raised concerning possible density gradients within the chamber after the product was loaded. This is a possibility. Since there were no in situ density monitoring devices within the chamber, it is impossible to determine, if in fact there was a density gradient, what that gradient may have been. It would be more likely to have a larger gradient, due to entrapped air, in the upper portion of the chamber, as compared to the lower portion because of the different mechanical loading methods employed.

Conclusions

Alpha-Ireco and DYNO NOBEL INC are pleased with the results of having participated in the non-proliferation experiment. We were not in a position to acquire data regarding the detonation of the explosive within the chamber. A few of us within the Alpha-Ireco and DYNO NOBEL organizations have had the opportunity to speak with a number of the experimenters concerning their measurements. From the conversations we have had, it is interesting that items such as explosive yield as measured by seismic stations, and velocity of detonation measurements within the explosive chamber, seem to indicate a yield of at least one kiloton of explosive energy, and possibly even more than originally expected. We hope that information shared among the experimenters may give ourselves, as commercial explosives manufacturers, a better insight as to possible means of improving the efficiency of our explosive products.

1	1.330	41	1.347	81	1.331	121	1.351	161	1.338	201	1.336
2	1.330	42	1.348	82	1.337	122	1.355	162	1.340	202	1.317
3	1.330	43	1.348	83	1.335	123	1.339	163	1.348	203	1.329
4	1.320	44	1.344	84	1.344	124	1.345	164	1.351	204	1.319
5	1.333	45	1.341	85	1.339	125	1.337	165	1.345	205	1.311
6	1.337	46	1.341	86	1.339	126	1.335	166	1.343	206	1.310
7	1.339	47	1.347	87	1.335	127	1.347	167	1.347	207	1.314
8	1.335	48	1.347	88	1.337	128	1.345	168	1.343	208	1.318
9	1.335	49	1.334	89	1.341	129	1.355	169	1.336	209	1.315
10	1.330	50	1.330	90	1.337	130	1.342	170	1.337	210	1.324
11	1.360	51	1.333	91	1.345	131	1.342	171	1.335	211	1.323
12	1.344	52	1.333	92	1.346	132	1.344	172	1.333	212	1.337
13	1.346	53	1.347	93	1.348	133	1.350	173	1.343	213	1.331
14	1.344	54	1.346	94	1.352	134	1.344	174	1.337	214	1.335
15	1.343	55	1.337	95	1.355	135	1.355	175	1.339	215	1.335
16	1.340	56	1.344	96	1.342	136	1.356	176	1.343	216	1.346
17	1.343	57	1.336	97	1.336	137	1.360	177	1.345	217	1.339
18	1.338	58	1.334	98	1.346	138	1.355	178	1.352	218	1.349
19	1.341	59	1.352	99	1.330	139	1.356	179	1.347	219	1.347
20	1.345	60	1.326	100	1.349	140	1.358	180	1.323	220	1.351
21	1.335	61	1.348	101	1.340	141	1.344	181	1.331	221	1.340
22	1.349	62	1.343	102	1.344	142	1.349	182	1.326	222	1.344
23	1.343	63	1.353	103	1.342	143	1.354	183	1.320	223	1.348
24	1.339	64	1.328	104	1.354	144	1.358	184	1.333	224	1.345
25	1.335	65	1.334	105	1.346	145	1.333	185	1.331	225	1.341
26	1.337	66	1.327	106	1.342	146	1.346	186	1.337	226	1.346
27	1.327	67	1.328	107	1.342	147	1.357	187	1.339	227	1.341
28	1.336	68	1.342	108	1.345	148	1.359	188	1.332	228	1.347
29	1.345	69	1.334	109	1.346	149	1.335	189	1.331	229	1.348
30	1.342	70	1.331	110	1.352	150	1.337	190	1.337	230	1.343
31	1.344	71	1.334	111	1.341	151	1.346	191	1.328	231	1.343
32	1.343	72	1.333	112	1.343	152	1.331	192	1.330	232	1.350
33	1.344	73	1.333	113	1.344	153	1.350	193	1.335	233	1.343
34	1.344	74	1.345	114	1.340	154	1.349	194	1.333	234	1.322
35	1.348	75	1.331	115	1.345	155	1.332	195	1.339	235	1.326
36	1.350	76	1.339	116	1.344	156	1.333	196	1.328	236	1.326
37	1.345	77	1.332	117	1.346	157	1.344	197	1.336	237	1.331
38	1.349	78	1.329	118	1.350	158	1.346	198	1.311	238	1.325
39	1.346	79	1.340	119	1.343	159	1.338	199	1.323	239	1.330
40	1.351	80	1.334	120	1.348	160	1.337	200	1.335	240	1.347

241	1.348	281	1.332	321	1.315	361	1.343	401	1.342	441	1.341
242	1.345	282	1.333	322	1.327	362	1.326	402	1.332	442	1.337
243	1.341	283	1.336	323	1.322	363	1.328	403	1.340	443	1.340
244	1.339	284	1.336	324	1.326	364	1.336	404	1.331	444	1.343
245	1.341	285	1.334	325	1.327	365	1.338	405	1.336	445	1.335
246	1.339	286	1.340	326	1.324	366	1.347	406	1.337	446	1.339
247	1.338	287	1.342	327	1.340	367	1.346	407	1.337	447	1.330
248	1.337	288	1.324	328	1.336	368	1.338	408	1.340	448	1.346
249	1.345	289	1.340	329	1.350	369	1.339	409	1.327	449	1.341
250	1.343	290	1.348	330	1.333	370	1.341	410	1.327	450	1.388
251	1.344	291	1.345	331	1.329	371	1.338	411	1.321	451	1.335
252	1.345	292	1.345	332	1.341	372	1.341	412	1.325	452	1.344
253	1.345	293	1.343	333	1.339	373	1.341	413	1.326	453	1.344
254	1.347	294	1.343	334	1.325	374	1.345	414	1.324	454	1.339
255	1.342	295	1.343	335	1.322	375	1.347	415	1.338	455	1.333
256	1.344	296	1.342	336	1.336	376	1.337	416	1.337	456	1.336
257	1.340	297	1.332	337	1.323	377	1.345	417	1.345	457	1.329
258	1.348	298	1.343	338	1.336	378	1.342	418	1.337	458	1.330
259	1.337	299	1.341	339	1.340	379	1.342	419	1.341	459	1.325
260	1.331	300	1.341	340	1.345	380	1.333	420	1.340	460	1.328
261	1.341	301	1.338	341	1.340	381	1.341	421	1.327	461	1.327
262	1.345	302	1.329	342	1.329	382	1.325	422	1.331	462	1.324
263	1.346	303	1.329	343	1.343	383	1.337	423	1.339	463	1.332
264	1.338	304	1.341	344	1.336	384	1.340	424	1.339	464	1.327
265	1.333	305	1.345	345	1.331	385	1.332	425	1.328	465	1.320
266	1.339	306	1.350	346	1.329	386	1.326	426	1.334	466	1.323
267	1.347	307	1.352	347	1.331	387	1.324	427	1.340	467	1.328
268	1.344	308	1.348	348	1.332	388	1.326	428	1.337	468	1.328
269	1.332	309	1.347	349	1.333	389	1.336	429	1.336	469	1.328
270	1.341	310	1.351	350	1.330	390	1.338	430	1.340	470	1.328
271	1.335	311	1.347	351	1.326	391	1.332	431	1.325	471	1.326
272	1.336	312	1.333	352	1.332	392	1.332	432	1.334	472	1.331
273	1.332	313	1.332	353	1.329	393	1.330	433	1.334	473	1.320
274	1.332	314	1.339	354	1.330	394	1.335	434	1.334	474	1.331
275	1.341	315	1.343	355	1.321	395	1.331	435	1.338	475	1.323
276	1.350	316	1.333	356	1.346	396	1.338	436	1.338	476	1.329
277	1.337	317	1.339	357	1.351	397	1.335	437	1.337	477	1.329
278	1.334	318	1.316	358	1.330	398	1.319	438	1.338	478	1.340
279	1.337	319	1.325	359	1.324	399	1.335	439	1.336	479	1.334
280	1.339	320	1.314	360	1.334	400	1.341	440	1.339	480	1.335

481	1.333	521	1.337
482	1.334	522	1.341
483	1.329	523	1.326
484	1.328	524	1.329
485	1.326	525	1.328
486	1.328	526	1.329
487	1.333	527	1.323
488	1.337	528	1.325
489	1.328	529	1.326
490	1.332	530	1.326
491	1.332	531	1.334
492	1.332	532	1.345
493	1.341	533	1.341
494	1.329	534	1.328
495	1.336	535	1.336
496	1.335	536	1.338
497	1.335	537	1.341
498	1.333	538	1.342
499	1.335	539	1.343

Performance Calculations on the ANFO Explosive RX-HD

P. C. Souers, D. B. Larson, and C. M. Tarver

1. Introduction

Recently, on September 22, 1993, a very large conventional ammonium nitrate-fuel oil (ANFO) shot was fired at the Nevada Test Site as the Non-Proliferation Experiment.¹ The explosive, called RX-HD, was an ANFO emulsion blend made by DynoNobel (Ireco). It contained these major components:²

	weight %	TMD (g/cc)	Mol. Wt. (g/mol)	ΔH_f (kJ/mol)	mol fraction
Ammonium Nitrate	78.65	1.72	80.04	-365.1	0.611
Fuel oil(C ₇ H ₁₂)	6.38	0.83	96.17	+293	0.041
Calcium Nitrate	5.52	2.50	164.09	-937.2	0.021
Water	9.45	1.00	18.02	-285.8	0.326

(1)

Also present were about 0.08% plastic microballoons used to create hot spots. The fuel oil was Diesel Fuel #2, which is a mixture close to the composition C₇H₁₂. The pure compound with the same composition, 1-heptyne, has a density of 0.73 g/cc and a less energetic heat of formation of +103 kJ/mol.³ Hence, the Diesel Fuel listed in Eq. 1 contains heavier compounds in solution with a lighter solvent, and it is much more energetic than 1-heptyne. The water does not burn and is dead weight. In the table above, TMD is the theoretical material density; also given are the molecular weight and the heat of formation.

RX-HD is a viscous liquid explosive, made up of a mixture of ANFO pellets in a liquid ANFO emulsion. The purpose of the emulsion is to fill in the spaces between the pellets. The pellets, called prill, are 2 to 3 millimeter bee-bees of ammonium nitrate, into which the fuel oil has been absorbed, like water in a sponge. The emulsion is made by dissolving ammonium nitrate and calcium nitrate in water at 65 to 75°C. This solution is then mixed with fuel oil at 60°C in a high-speed blender. The aqueous oxidizer droplets are 0.1 to 10 µm in size and are suspended in the fuel oil. The fuel oil ultimately spreads itself out to the 6% amount in both the slurry and the prill. However, it is not known whether the fuel actually reaches to the center of the ammonium nitrate pellets.²

The RX-HD was poured and augered from tank trucks into an underground cavity in a water-saturated tuffaceous rock 390 feet below the surface of the ground. The cavity was in the shape of a hockey puck lying on a flat side. The effective dimensions of the chamber were: radius 7.738 m, height 5.22 m and volume 981.8 m³. From the mass of the explosive and the chamber volume, an overall explosive density of 1.32 g/cc was calculated. This compares with the 1.34 g/cc determined from density

measurements on 532 samples of the blend. The theoretical maximum density of the RX-HD is 1.54 g/cc, so that the differences are caused by the presence of air pockets.² The explosive was thought to be well-stirred, so that radial density differences would not exist.

A total of 2.846 million pounds of RX-HD was fired. This poundage corresponds to a yield of 1.1 ± 0.05 kilotons.

The explosion was initiated by five Pentolite (50 wt% PETN and 50 wt% TNT) boosters, which were placed on the vertical axis at heights from the bottom of 1.04, 1.91, 2.77, 3.66 and 4.52 m. The three boosters at 1.04, 2.77 and 4.52 m were fired to start the experiment. The boosters at 1.91 and 3.66 m were not fired at the start but detonated when the shock wave hit them. The 5-pound detonators were chosen to substantially overdrive the RX-HD. A TC-234 Exploding Bridgewire Detonator set off 250 mg of PETN, which led to a 3.51 g PBX 9407 pre-booster and then into the Pentolite main booster.^{1,4} The Pentolite was 50 wt% TNT and 50 wt% PETN at a density of 1.60 g/cc. The detonation velocity specification of the Pentolite was reported as being 7.77 to 8.23 mm/ μ s. The detonation pressure specification was reported as 25 GPa. This is 9 GPa over the estimated C-J pressure of the RX-HD.

We will just briefly mention the experimental arrangement. CORTEX lines were installed to measure detonation velocities. The cables were laid in star patterns at each of the three levels at which detonators were fired. The star patterns were in the horizontal plane at each detonator. Velocities were measured outward from the detonator so that the time behavior could be seen. The cables were^{1,}

Lower Level (1.04 m)	K1, K4 and K10	
Mid Level (2.77 m)	K2, K5, K7, K8, K9 and K11	
Upper Level (4.52 m)	K3, K6 and K12.	(2)

In addition, two Lexan ASM particle velocity gauges were placed inside the explosive. These gauges did not provide a particle velocity measurement but did provide the transit time through the plastic. This, along with the detonation velocity, allowed a calculation of the pressure in the explosive. These gauges were positioned about a foot from the inside wall of the side of the hockey puck, so that the result should represent the explosive fully initiated.

2. Hand-Calculating the Yield

The total energy of detonation, E_o , is easy to estimate by a hand calculation. The mol fractions of the i th reactants are given by

$$y_i = \left[\frac{(\text{wt\%})_i}{M_i} \right] \left[\sum_{i=1}^4 \left\{ \frac{(\text{wt\%})_i}{M_i} \right\} \right]^{-1}, \quad (3)$$

where wt % is the weight % and M is the molecular weight, both from Eq. 1. The average molecular weight of the RX-HD, considering the fuel oil to be C₇H₁₂, is

$$M(\text{react}) = \sum_{i=1}^4 y_i M_i = 62.23 \text{ g/mol}, \quad (4)$$

where M_i is the molecular weight of the ith constituent and we sum over all four constituents. The overall reactant heat of formation is

$$\Delta H_f(\text{react}) = \sum_{i=1}^3 y_i \Delta H_{fi}(\text{react}) = -230.79 \text{ kJ/cc}, \quad (5)$$

where the summation is only to 3. The original water in the RX-HD is left out, because it is already burned and is dead-weight.

The one mol of the four-mixed reactants creates gaseous products plus a solid. We assume that 1) all hydrogen goes to water, 2) all carbon goes to CO₂ and 3) the calcium becomes calcium oxide. The products and their heats of formation are listed here, with water in the gaseous condition:³

Products	Product		
	mols calc	Product mols	ΔH _f (kJ/cc)
H ₂ O(AN)	(4/2)*0.611	1.223	-238
CO ₂ (FO)	7*0.041	0.289	-392
H ₂ O(FO)	(12/2)*0.041	0.248	-238
CaO	1*0.021	0.021	-635

(6)

The second column lists the calculations needed to get the mols/mol of original explosive formed, z_i, which is listed in column 3. For example, the first water comes from the 4 H atoms in the ammonium nitrate (AN), with (4/2)(0.611) = 1.223 mols/mol. The fuel oil (FO) and calcium nitrate are also listed, but the initial water is not. The product heat of formation is given by

$$\Delta H_f(\text{prod}) = \sum_{i=1}^4 z_i \Delta H_{fi}(\text{prod}) = -476.87 \text{ kJ/cc}. \quad (7)$$

All four products from Eq. 6 (which excludes the initial water) are summed. In the calculation, all the nitrogen in the RX-HD is assumed to go to N₂, which has a zero heat of formation.

The difference between the heats of formation is

$$\frac{\rho_0 [H_f(\text{prod}) - H_f(\text{react})]}{M(\text{react})} = -5.22 \text{ kJ / cc.} \quad (8)$$

This assumes that water is a gas at the standard temperature of 298 K.

We may estimate the amount of energy left in the hot products at 1 atmosphere after the expansion is over. From the CHEQ code (to be described below), we obtain a calculated ending temperature of 324 K. The energy between this temperature and 298 K, to which Eq. 8 is referenced, is not available for mechanical work.

From the TIGER product library, the gaseous heat capacity, C_p , is given by this equation⁵

$$C_p = (C_1 + C_2\Theta + C_3\Theta^2 + C_4\Theta^3 + C_5/\Theta + C_6/\Theta^2 + C_7/\Theta^3)R \quad (9)$$

where $\Theta = T/1000$, with T being the absolute temperature and R, the gas constant, is 1.9871 calories/mol·K. With the heat capacity being in units of calories/mol·K, the coefficients C_1 to C_7 are, respectively, for water, nitrogen and carbon dioxide: 6.85015, 0.360374, -0.0497482, 0.002491629, -2.992808, 0.96209152 and -0.0961517; 5.211, -0.1393, 0.01627, -0.000514, -1.572, 0.4740, and -0.04544; 8.815, -0.2968, 0.04112, -0.001437, -2.464, 0.4737 and -0.03511. The mols of products are 1.80 for water, 0.61 nitrogen and 0.29 carbon dioxide, which gives 0.03, 0.01 and 0.01 kJ/cc. The heat locked up in the small amount of calcium oxide may be ignored. The total heat is then 0.27 kJ/cc. The true total detonation energy, E_o , is

$$E_o = 5.22 - 0.05 = 5.17 \text{ kJ/cc} \quad (10)$$

If we use the average density of 1.32 g/cc, we have a hand-calculated, preliminary maximum theoretical yield of

$$\frac{(2.846 \times 10^6 \text{ lbs})(454 \text{ g / lb})(5.17 \text{ kJ / cc})}{(1.32 \text{ g / cc})(4.186 \times 10^9 \text{ kJ / kt})} = 1.21 \text{ kilotons} \quad (11)$$

3. The Yield from Thermochemical Codes

We also ran RX-HD with the thermochemical code TIGER and its LLNL in-house successor, CHEETAH. We will digress to discuss how these codes work. They take as input the compositions, amounts in weight % or mols, heats of formation and molar volumes at the theoretical (maximum) density of each of the reactants. They have a library of products with heat capacities for the gases and

densities and compressibilities for liquids and solids. They assume the validity of C-J Theory, ie. that the reactants turn instantly into products at a detonation point in thermodynamic equilibrium. TIGER is an old code from the 1970's; CHEETAH has been recently written by Larry Fried of our laboratory, and this is its first appearance in action.

The codes first calculate an explosion point, created by turning the solid explosive into gas at 1 atm. The Rankine-Hugoniot energy conservation equation is used, along with thermodynamic relations and thermochemical data to trace the Hugoniot curve to smaller volumes and higher pressures. At the same time, a sample Rayleigh Line is determined, with a slope of $\rho_0 D^2$, where D is the detonation velocity. The code iterates many times until the two curves become tangent to one another at the C-J point, where detonation begins.

Next, the codes allow the mixture of products to expand at constant entropy, thereby creating the Principal Adiabat. All P, v, E, and T parameters can be output at any relative volume. The products are usually frozen to a final equilibrium at 1800 K to agree with calorimetric data on small samples.⁶⁸ This usually comes at a volume of about 1. These codes have trouble with relative volumes greater than about 100, but they can be extended with a last jump down to 1 atm and 298 K. The version of TIGER and CHEETAH used here is BKWR, which uses a imperfect-gas compressibility function.

TIGER has always calculated the total detonation energy with the last jump to 298 K and 1 atmosphere. CHEETAH calculates this point but also calculates the detonation energy at the first adiabat volume that reaches either 1 atmosphere or 298 K. This adiabat energy is the true mechanical energy of detonation, E_o , wanted for the yield. Unfortunately, the model being used in the code is BKWR, a 20-year-old version originally designed to optimize detonation velocity and C-J pressure. The low value of the constant Θ causes the C-J temperature to be low by 1000 K. Also, the detonation energies on the adiabat are too large and the adiabat plunges too quickly, reaching 298 K at only a relative volume of 20 for RX-HD. The same problem is found with version JCZ3, because both models were only normalized at the C-J point. A new renormalized version BKWC in being created, which will include adiabat energies derived from the cylinder test.

We are probably best served by inserting our hand-calculated value of the thermal energy. For RX-HD with no freeze, we find from CHEETAH

Total Energy of Detonation	-4.79 kJ/cc	
Thermal Energy Adjustment	<u>0.05</u>	
Mechanical Energy of Detonation, E_o	-4.72 kJ/cc	(12)

Assuming that hot, 1 atm gas exists at the end of the detonation, the yield is

$$E_o(\text{CHEETAH}) = -4.72 \text{ kJ/cc} = 1.11 \text{ kilotons.} \quad (13)$$

The result with an 1800 K freeze of products applied is -4.66 kJ/cc, lower by only 0.06 kJ/cc.

We next ran the same problem in CHEQ. This is also a thermochemical code, it includes all the known physics of detonation.⁷ It was created by F. Ree, with assistance from M. van Thiel, and has been recast into a Windows format by A. Nichols. It takes overnight to run as opposed to a few minutes for TIGER or CHEETAH. Instead of using a compressibility function like BKW, it uses intermolecular potentials, so that JCZ3 was its ancestor. Unlike TIGER or CHEETAH, it has the ability to calculate multiple phases of carbon or nitrogen-water. Because calcium does not exist in the CHEQ library, an equal amount of phosphorus was burned to PH₃. The correction for E_o for this difference amounts to -0.09 kJ/cc. With this correction, we obtain for the equilibrium calculation:

$$E_o(\text{CHEQ}) = -4.54 \text{ kJ/cc} = 1.07 \text{ kilotons.} \quad (14)$$

We recall that the final, 1 atmosphere- 324 K point from CHEQ was used to adjust the CHEETAH output, so that all the calculations are connected.

One difference between the full-CO₂ hand calculation and the codes is in the products, which do not burn all the way to CO₂. We have:

	Hand	BKWR	CHEQ
H ₂ O	1.8	1.71	1.74
N ₂	0.61	0.61	0.63
CO ₂	0.29	0.25	0.28
NH ₃	0	0.037	0
H ₂	0	0.025	0
CO	0	0.013	0
CaO	0.021	0.021	*

(15)

We now consider all the other things a thermochemical code can calculate. At 1.32 g/cc, we obtain these properties:

	CHEETAH	
	BKWR	CHEQ
P _q (GPa)	16.1	18.8
D (mm/μs)	7.08	7.29
T _q (K)	2180	3627
T(1 atm, K)	298	324

(16)

The low C-J temperature is to be expected in BKWR, where the normalization of the constants artificially produces this effect. We accept the temperatures in CHEQ as being more probable.

However, more can be learned by comparing calculations using the same code. Thus, we ran the equilibrium RX-HD in CHEETAH BKWR with different densities, with the following results.

Density (g/cc)	Code		Adjusted		
	Velocity (mm/μs)	Det	Det	Det	Det Energy, E _o (kJ/cc) kilotons
		Velocity	Pressure		
1.20	6.61	6.42	13.1	-4.35	1.12
1.25	6.80	6.62	14.3	-4.54	1.12
1.30	7.00	6.82	15.6	-4.72	1.12
1.32	7.08	6.90	16.1	-4.79	1.12
1.34	7.16	6.98	16.6	-4.86	1.12
1.39	7.36	7.17	18.1	-5.04	1.12
1.44	7.56	7.38	19.6	-5.22	1.12

(17)

E_o is the total energy of detonation, with water in the gaseous state at 298 K. The yield is the same as defined by Eq. 11, because the total number of pounds of explosive is unchanged. Eq. 17 states that the energy density increases linearly with the density, which can affect local behavior in the explosive but not the total.

The results of CHEETAH BKWR were used to derive a JWL for RX-HD. The 3-point process of deriving a JWL has been described.⁷⁸ Detonation energies were calculated at relative volumes of 2.2, 4.1 and 6.5. These energies need to be corrected downwards by about 10% using PETN at 1.763 g/cc as the standard. These energies are then compared with the standard PETN JWL. We find that RX-HD has 54.0, 55.0 and 55.0% of the detonation energy of PETN at the three volumes. It must be said that basing a JWL on TIGER or CHEETAH calculations only is not a good idea. This is because the adiabats from the codes often have a different shape from those experimentally obtained in cylinder tests. However, for RX-HD at this time, we have no choice.

The regular JWL was then determined. In this EOS, the pressure on the Principal Adiabat, P_s, is given by

$$P_s = A \exp(-R_1 v) + B \exp(-R_2 v) + C / v^{(1+\omega)}, \quad (18)$$

where v is the relative volume and the rest are constants. These three JWL's, calculated from TIGER, illustrate the perils of the JWL business.

	1	2	3
A(Mbars)	13.862	4.824512	4.071301
B(Mbars)	0.136746	0.141036	0.056251
C(Mbars)	0.007476	0.014716	0.006417
R ₁	6.47	5.075	4.679
R ₂	1.50	2.00	1.05
ω	0.45	0.55	0.45
E _o (kJ/cc)	-4.45	-4.80	-4.7
P _q (GPa)	14.0	16.0	16
D(mm/ s)	7.0	7.0	6.9
ρ _o (g/cc)	1.32	1.32	1.32

(19)

JWL #1 was the first try. It used a preliminary 7.0 mm/ s detonation velocity that had come back from the NTS test. The energy was an estimate from an early TIGER run. The result was a JWL with a unusually large A-term. Lew Glenn, in his early analysis of the far field NTS data, thought this JWL worked best.⁹ However, Glenn wanted a JWL with a more normal A-term as befits ANFO, so #2 was born. This was used for most calculations and ultimately was found acceptable by Lew Glenn. JWL #3 was constructed for this report using all the best input values obtained to date. Its value of $\gamma + 1$ is 3.928. We recall that the negative E_o values are rendered positive in the input to a hydrocode. While it is not necessary for the JWL E_o to equal the calorimetrically-determined value, it appears to be close for many homogeneous explosives.^{7,8} This means that the JWL equation handles total energy in a manner that is close to being correct.

4. The Density Gradient Issue

The measurements program on the Non-Proliferation experiment has provided some curious results. The first data of interest is the steady state detonation velocity, as seen by the CORTEX cables. These are the rounded-off 90%-confidence values listed by McKown.¹

Level	Cable	mm/ s
low	K1	7.12 ± 0.05
	K4	7.16 ± 0.01
mid	K2	6.86 ± 0.01
	K5	6.87 ± 0.00
	K7	6.76 ± 0.01
	K8	6.72 ± 0.01
	K9	6.73 ± 0.01
	K11	6.80 ± 0.01
upper	K3	6.42 ± 0.01
	K6	6.43 ± 0.01
	K12	6.49 ± 0.01

(20)

It is easy to see that the detonation velocities are reported as different at each of the three levels. It was noted that the explosive emulsion settled downwards in the cavity after being pumped in, so that the presence of a gravitationally-created density gradient was suspected. We return to Eq. 15 to the calculated detonation velocities as a function of density and lower them all by 0.29 mm/ s. This brings the detonation velocity at 1.32 g/cc down to 6.79 mm/ s. We have the fit

$$\rho_0 = -0.385 + 0.251D. \quad (21)$$

We then calculate

Level	Det Velocity	Density
Top	6.45	1.23 g/cc
Middle	6.79	1.32 g/cc
Bottom	7.14	1.41 g/cc

(22)

We get an estimated density gradient of ± 0.09 g/cc.

5. Reappraising the Detonation Velocities

The density gradient calculated above appears to be too large. The material is a viscous liquid into which small air pockets are trapped. We, therefore, return to further consider the CORTEX cable data, which is listed as having been corrected and referenced to the the cable end. We differentiate the data and then smooth across sets of five points from K4, K5, K6, K9 and K11. The five best sets of original data are listed in Table 1 and Fig. 1 and show the best examples from each of the three levels. These results are

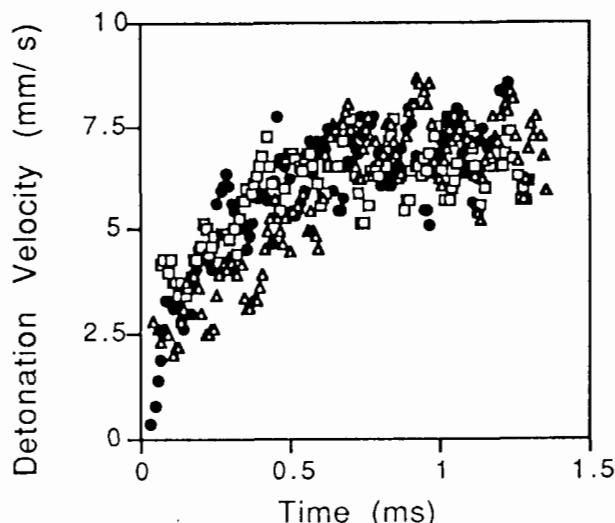


Fig. 1. Detonation velocity as a function of time for three levels in the RX-HD. Almost no difference is seen. The samples are:xxK4 (low) (Δ); K9 (middle) (\bullet); and K6 (\square).

derived by differentiating the as-received length data and then smoothing once using a 5-point moving average. We find that there is no difference among the different levels at long times within the extensive scatter of the data. At short times, the lower level K4 data does lie below the others. Unfortunately, the other two low level lines at K1 and K10 did not provide data.

Lower	K2	7.1 ± 0.8
Middle	K5	7.0 ± 0.8
	K7	7.0 ± 0.4
	K8	7.0 ± 0.8
	K9	6.8 ± 0.8
	K11	6.9 ± 0.4
	K3	6.6 ± 0.9
Upper	K6	6.5 ± 0.6
	K12	6.6 ± 1.0

(23)

We note that a bias toward a density gradient appears in the average detonation velocity values, but the spread of the error is large enough that the differences are not significant. The measured steady state value in the center would be

$$D = 6.9 \pm 0.7 \text{ mm/ s.} \quad (24)$$

This error is so large that we hesitate to assign different values to the different levels.

Nevertheless, we return to the density gradient question. Using Eq. 17, we reset the detonation velocities by -0.18 mm/ s , so that we have 6.9 mm/ s at 1.32 g/cc . These modified values are the adjusted values in Eq. 17. The fit is

$$\rho_o = -0.412 + 0.251D. \quad (25)$$

The RX-HD manufacturer states that the voids in the explosive are air pockets, which are trapped and compressed by the weight of the material above. We describe the theoretically dense explosive by the equation $\rho_t = m / V_t$, where ρ_t , the density, is 1.54 g/cc , the volume, V_t , equals 1.00 and the mass, m , is a constant at 1.54 g . Then, the density in the experiment is

$$\rho_o = \frac{m}{V_t + \Delta V}, \quad (26)$$

where $\&v$ is the void space. For ρ_0 of 1.32 g/cc, $\&v$ is 0.167 cc. The pressure, above that of the air, caused by half the stack of explosive of height 2.62 m is

$$P_h = \rho_0 gh, \quad (27)$$

where g is the acceleration due to gravity of 9.80 m/s². From Eq. 27, we obtain 0.034 MPa, so that the total pressure is 0.101, 0.135 and 0.169 MPa at the top, center and bottom. Then from the Perfect Gas Law

$$\frac{V(\text{bottom})}{V(\text{center})} = \frac{P(\text{center})}{P(\text{bottom})} = 0.80. \quad (28)$$

Then, $\&V$ becomes $0.8(0.167) = 0.134$ cc at the bottom. We next use Eqs. 25 and 26 to obtain these densities and detonation velocities.

Level	Density	Det Velocity
Top	1.274 g/cc	6.72 mm/s
Middle	1.32 g/cc	6.90 mm/s
Bottom	1.358 g/cc	7.05 mm/s

(29)

This reduces the density gradient to more reasonable values than those obtained in the first calculation using the highly smoothed CORTEX data.

6. Distance to Detonation

The distance to detonation data is the most interesting result to come from this experiment. In Fig. 2, we take the best data from K9 in the middle section and plot detonation velocity vs. run distance. The fit to this data is

$$D \sim 6.9[1 - \exp(-r)], \quad (30)$$

where r is the variable radius and the 1/e-distance constant is 1.0 meter. We do not expect Eq. 30 to really start at zero but it does start at a small value. We use four exponential distance constants to define the distance to detonation, x_r . This gives

$$x_r(1.32 \text{ g/cc ANFO}) \sim 4 \text{ meters.} \quad (31)$$

In other words, we find that it takes 4 meters for the ANFO emulsion blend detonation to come to steady state.

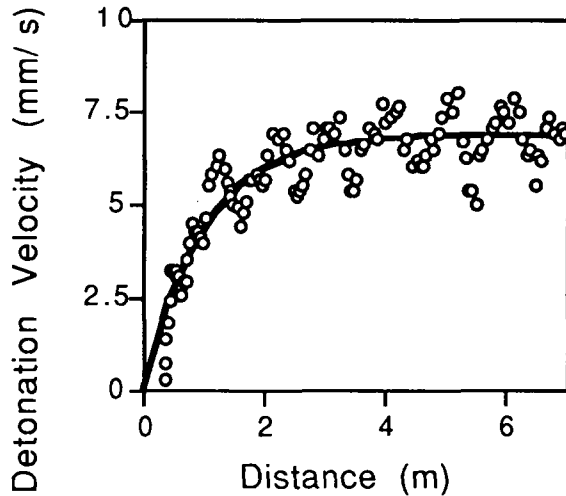


Fig. 2. Detonation velocity vs. distance for K9.
The line is the fit.

Suppose we now set the fraction of explosive burned immediately, F , proportional to D in Eq. 30. We then integrate outward from the center to the edge, assuming cylindrical symmetry and no wall interactions at top and bottom. We integrate

$$F(\text{total}) = \int_0^R [1 - \exp(-r)] r dr, \quad (32)$$

where R is the outer radius of 7.7 m. Cylindrical symmetry dictates that the smallest volumes are the most non-ideal. We end up with

$$F(\text{total}) \sim 0.967. \quad (33)$$

This suggests that most of the energy comes out quickly despite the slow initiation. The rest has probably all come out before the shock wave hits the cavity wall. Thus, it is not clear that the non-ideal behavior of the explosive should influence the far-field seismic results.

We digress to consider an anomaly in Fig. 2:xx the appearance of oscillations with a period of about 125 s. We took the raw data of the three best middle-level cables (K5, K9, and K11), smoothed the distance twice with a 5-channel polynomial, differentiated and smoothed the velocity twice. The results are shown overlaid in Fig. 3. We see apparent oscillations of ± 0.2 to ± 0.3 mm/s amplitude, which would correspond to density differences of about ± 0.08 g/cc. These oscillations, however, are an artifact of the interpolator in the CORTEX lines and do not represent any physical phenomenon in the explosive.⁴

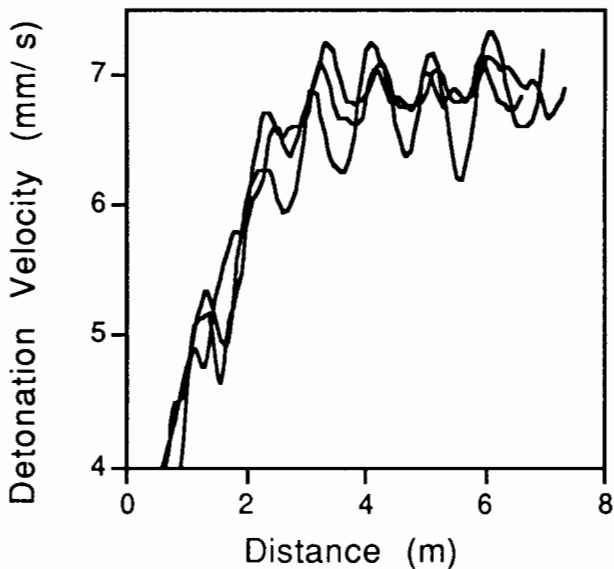


Fig. 3. The search for oscillations in the detonation velocities of the three best cables shows a possible positive result after careful smoothing. The cables are K5, K9 and K11.

7. The Cylinder Shots

It was desirable to determine the equation of state (EOS) of the ANFO emulsion blend using a cylinder shot to better define the JWL parameters. At that time, the 8-inch results were unknown. However, the following results were available.²

unconfined 5-inch diameter	4.4 ± 0.5 mm/s	
12 oz. Pentolite booster		
unconfined 6 3/4-inch diameter	3.98, 5.25, 5.42 mm/s	(34)

These velocities were well below the TIGER value of 7 mm/s, and it was not clear how to interpret them. It was felt by two old-timers that the confinement of the cylinder test would be sufficient to move the detonation velocity, even at a 4-inch diameter, close to steady state.

A full 4-inch diameter, full-wall copper cylinder shot was fired. The full shot uses a precision copper tube and a particular point on the surface is carefully monitored in order to obtain wall velocities that can be changed into the EOS. For the wall measurement to be useful, the detonation velocity must be known accurately. The cylinder was 100 mm long with pin rings 37.5 and 49 mm up from the bottom end. Another pin ring sat 2.5 mm below the top of the cylinder.

Detonation velocity results were obtained from the bottom two pin rings. The results were:

Distance (mm)	Det Velocity (mm/ s)	(35)
37.5	3.64	
49	3.16	

It appeared that the reaction started to initiate and then fizzled out.

The decision was then made to schedule an 8-inch diameter steel cylinder test. This shot consisted of a non-precision tube with pins along the tube in order to obtain the detonation velocity as a function of distance; this test, however, is not able to deliver an EOS. Six pin rings were placed along the 1200 mm length of the tube. The detonation velocities, as measured in each section between pin rings, are given by these values.

Distance (mm)	Det Velocity (mm/ s)	
298	2.92	
475	2.71	
653	2.53	
831	3.25	
1011	3.63	
1204	4.34	

(36)

These results show that the reaction starts slowly, dips, recovers and is moving more strongly at the end. It appears that the detonation is building but would need more cylinder length to reach steady state. These results suggest that it would be futile to attempt a full-blown 8-inch copper EOS test.

8. Description of the Ignition & Growth Model

The Ignition & Growth (Reactive Flow) model in the DYNA2D hydrodynamic code was next brought into action. Using the 4-inch cylinder fizzle, the Dyno Nobel unconfined cylinder data and the NTS shot itself, we proposed to provide a definitive answer to the question of whether steady state could be achieved in an 8-inch diameter cylinder, the upper size limit for explosion at Site 300.

Ignition & Growth (I&G) is an advanced EOS model.⁷ It is not used in production codes, where program burn (lighting time) dominates. I&G is the only available LLNL code that can model the slow turn-on of an explosive that is initiating its way toward full detonation. Two JWL EOS's are used: one for the unreacted explosive and the other for the reaction products (this latter EOS is the only one used in most codes). A set of reaction rate equations move the sample from being unreacted to full reaction.

Someone well-schooled in this code then estimates all the parameters until they produce behavior similar to what is measured. While not scientifically rigorous, the results are closer to the actual behavior than can be had with any other approach.

The EOS parameters used in this study are listed in Table 2. These constitute a result in themselves and may be used in further modeling of RX-HD. The two detonator and booster materials, Detasheet and Pentolite, are listed with the regular, non-temperature dependent JWL's.

Again, we emphasize that Table 2 is an equation-of-state, which gives a more accurate description of the non-ideal RX-HD than does a regular JWL.

The JWL's for RX-HD are temperature-dependent. The equation is

$$P_s = R_1 \exp(-R_5 v) + R_2 \exp(-R_6 v) + R_3 T/v, \quad (37)$$

where T is temperature. There is one for the shocked, unreacted explosive and a second for the reaction products.

The fraction reaction, F , proceeds with two terms

$$\frac{dF}{dt} = F/t|_1 + F/t|_2 \quad (38)$$

The first term is

$$\frac{\partial F}{\partial t}|_1 = F_q (1 - F)^{F_r} \left[\frac{1}{v_e} - 1 - C_{crit} \right]^\eta, \quad (39)$$

This term ignites some of the solid explosive as it is compressed by a shock or compression wave creating heated areas (hot spots) as the voids in the material collapse. Generally the amount of explosive ignited by a strong shock wave is of the order of the original void volume, which was 16.7%.

The second term is

$$\frac{\partial F}{\partial t}|_2 = G_1 (1 - F)^{s_1} F^{a_1} P_s^m, \quad (40)$$

This represents the growth of reaction from the hot spots into the remaining solid. During shock initiation, this term models the relatively slow spreading of reaction in ammonium nitrate in a deflagration-type process of inward or outward grain burning with pressure exponents close to one ($m = 1$ in Eq. 40). The burning of the fuel oil, which acts as the match to light the ammonium nitrate, is included in this term. A third term, which is available in the code, is not used in this case.

9. Results of the I&G Model

Unconfined cylinders that mock up the industrial tests were first run to set up the model. A 16 mm length of Pentolite was placed at the bottom of the cylinder. The Pentolite and RX-HD were then modeled with 1 zone/mm. The LLNL cylinder test were assumed to be initiated with Detasheet, a PETN mixture. The Steinberg-Guinan copper material model plus the Gruneison EOS were used. Fig. 4 shows the results on 4-inch diameter cylinders, 400 mm long, both unconfined and with the copper jacket. The Y-axis variable is F_{init} , the fraction burned immediately as the shock wave passes that point. Three values of F_{igmax} , the limit set to the first term, are used. The value of 0.16 was selected to cause the detonation to start to fail at 40 cm distance down the cylinder. We see that the total fraction reacted is not large- it peaks at about 0.18 as the greatest amount burned near the front end by the time the detonation wave has reached the rear end.

With F_{igmax} set at 0.16, Fig. 5 shows the detonation velocities for three-sized cylinders. The curves are bumpy, because the distances and times are taken from graphs and differentiated to get the velocities. (Unfortunately, I&G does not output detonation velocities directly). In any case, the detonation velocities decline to about 4 mm/s by the end of the cylinder, in agreement with the cylinder data available at the time the code was being run.

The second input that went into defining the I&G parameters was the Non-Proliferation Experiment data itself. A knowledge that several meters was needed to reach steady state went into the selection.

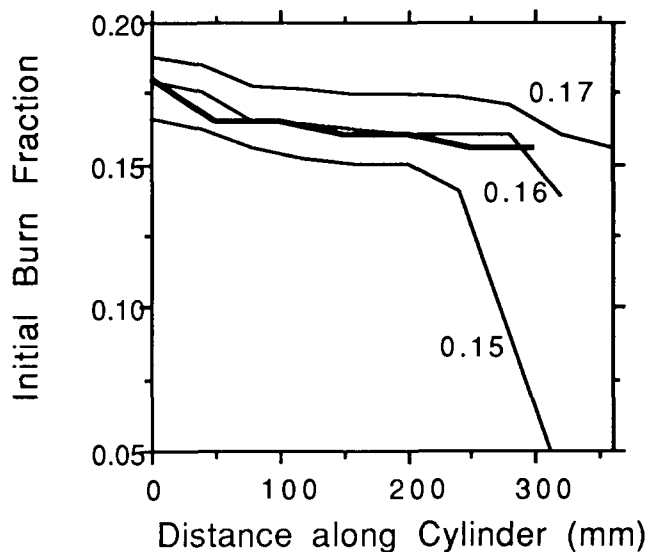


Fig. 4. Initial burn fraction, F_{init} , for 4-inch diameter cylinders modeled by Ignition & Growth. The light lines are unconfined; the heavy line is the confined copper cylinder. The numbers are the values of F_{igmax} used in the code. The reaction just sustains itself at 0.16.

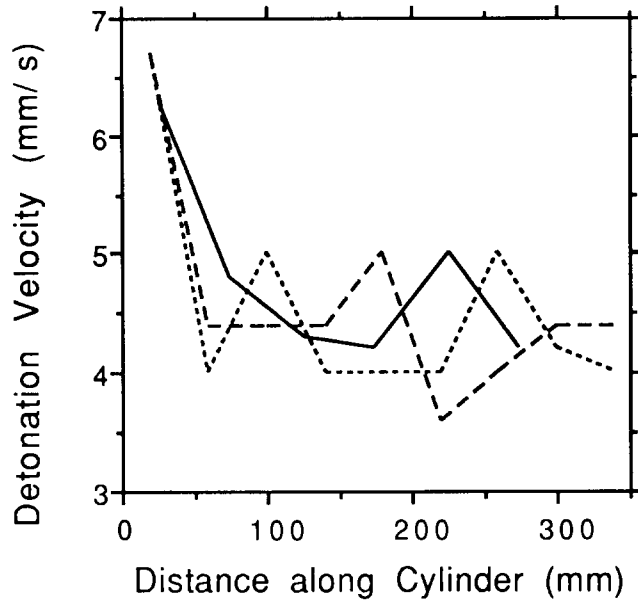


Fig. 5. Calculated detonation velocity for cylinders:xx4-inch diameter, confined (full line); 5-inch unconfined (pointed line); and 6-inch unconfined (dashed line). All fall to about 4 mm/s at the end of the cylinder.

Fig. 6 shows these results at three different times for the experimental cavity as viewed from the side. Fig. 6a at 200 s shows the explosion moving out from the three detonators. The two undetonated Pentolite boosters have not been reached. Fig. 6b shows the results at 400 s. The two in-between boosters have detonated and are perturbing the wavefront, which is beginning to stabilize. At 600 s in Fig. 6c, the wavefront is straight. Plotted in these figures is the fraction reacted, which has reached perhaps 99% in the center in the last picture. At this time, the wavefront has moved out 2.5 m. The shock wave will be moving at full power with a burn fraction of 1.00 by the time it hits the sides of the cavity.

Fig. 7 shows the pressure contours at 600 s. The barely visible edge is at a detonation pressure of 14.5 GPa. The particle velocity gauges in the RX-HD gave a measurement of 20 GPa in apparent disagreement. However, the I&G model first pre-compresses the RX-HD to the spike pressure of the undetonated material. Then the material drops down the Rayleigh Line to the detonation pressure, where the explosive follows the Principal Adiabat. If the size is infinite and all explosive is burned at the detonation point, the measured pressure would be close to the C-J point predicted by thermochemical codes. In this case, the I&G model shows a spike pressure of 20 GPa, in agreement with the measured value from the particle velocity gauges.

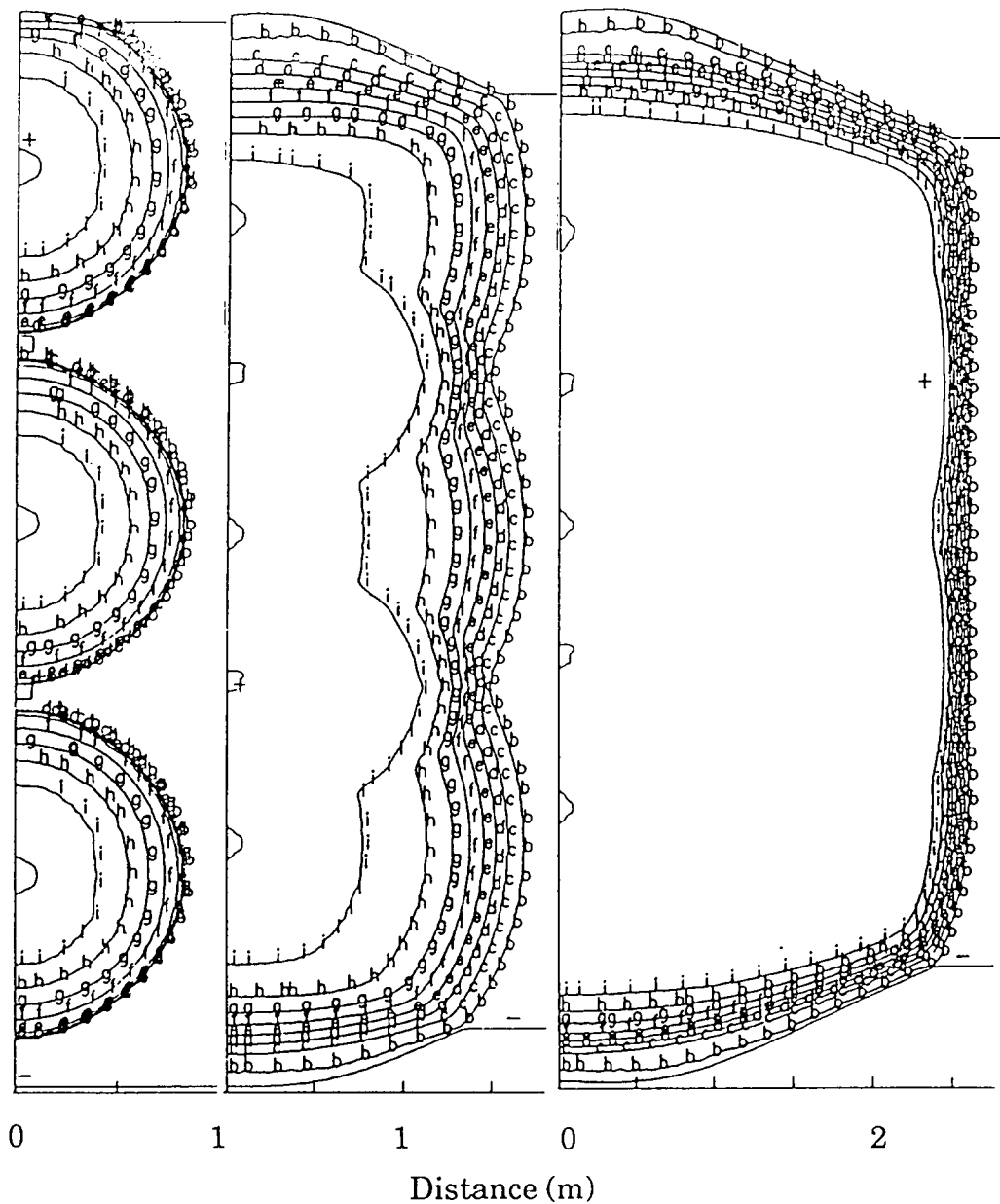


Fig. 6. Burn fraction of RX-HD at 200, 400 and 600 μ s in the Non Proliferation Experiment as modeled by I&G. The cavity is seen in a side view. The detonation started at the far left and is proceeding to the right, with the edge of the explosive out of sight at 4 meters. The Y-axis is the height of the explosive and the scale is slightly different in the three pictures. The burn fraction contours are, from a to i:xx6a (left) 0.00, 0.08, 0.12, 0.16, 0.20, 0.24, 0.28, 0.32 and 0.36; 6b (center) and 6c (right) 0.00, 0.20, 0.30, 0.40, 0.50, 0.60, 0.70, 0.80 and 0.90. The areas inside the 0.90 burn fractions quickly approach 1.00.

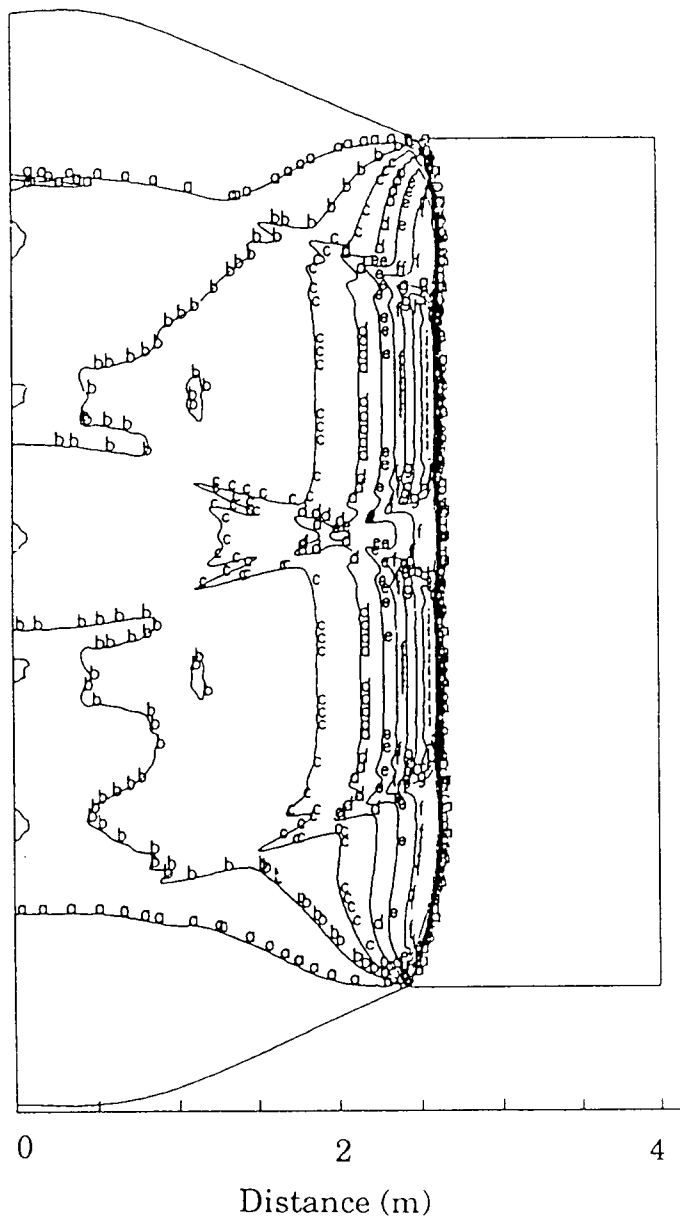


Fig. 7. Pressure contours at $600 \mu\text{s}$ in the I&G model of the RX-HD Non Proliferation Experiment. The cavity is seen in a side view. The detonation started at the far left and is proceeding to the right, with the edge of the explosive out of sight at 4 meters. The Y-axis is the height of the explosive. The contours from a to i are 1.5, 3.2, 4.8, 6.4, 8.0, 9.6, 11.2, 12.9 and 14.5 GPa. The last pressure is close to the expected detonation pressure.

All of the available input data went into selecting the I&G parameters, which were used to model the unknown 8-inch steel cylinder. The results are shown in Fig. 8. Both curves confirm that 8-inches is too small to reach steady state. I&G predicts that only 38% of the RX-HD detonates. The code was halted once it became evident that infinite diameter behavior would not be reached. The I&G model was run

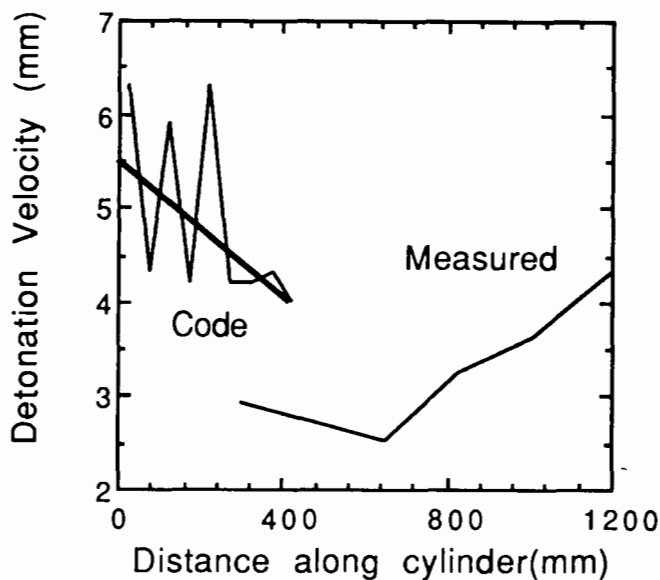


Fig. 8. Calculations and measurement of the 8-inch cylinder. The heavy line averages through the calculated values. This confirms the failure to reach steady state in a cylinder of this size. Better I&G constants would be needed to match the data.

before the actual shot was fired, and the differences arise from the imperfect knowledge of the I&G constants. The model, however, shows I&G at its best. It accepted input from large and small experiments and then interpolated in between, giving a valid answer to a specific question.

Finally, we attempt to measure the "reaction zone" width in the model. Strictly speaking, this is the distance from the spike to the detonation point in the explosive. This width is almost impossible to define for a small burn fraction and it becomes obvious only at the longer times when the detonation front becomes well-defined with almost complete burning at the back end. The results are shown in Fig. 9. In the early part, the reaction zone is the distance traveled, because the fraction burned is increasing constantly. Farther out, the detonation front begins to coalesce and the bulk of the contours fall into an ever shorter distance. We may guess that, at steady state, in an infinite-diameter geometry, the reaction zone is about 0.10 m. With the distance to steady state of about 4 m, this gives a ratio of about 40 for these two numbers.

10. Why the RX-HD was not Overdriven

We next consider the initiation of RX-HD by analogy with LX-17, a much-studied explosive at LLNL (92.5 wt% TATB; 7.5% kel-F, where TATB is triaminotrinitrobenzene). We find these approximate pressure relations.

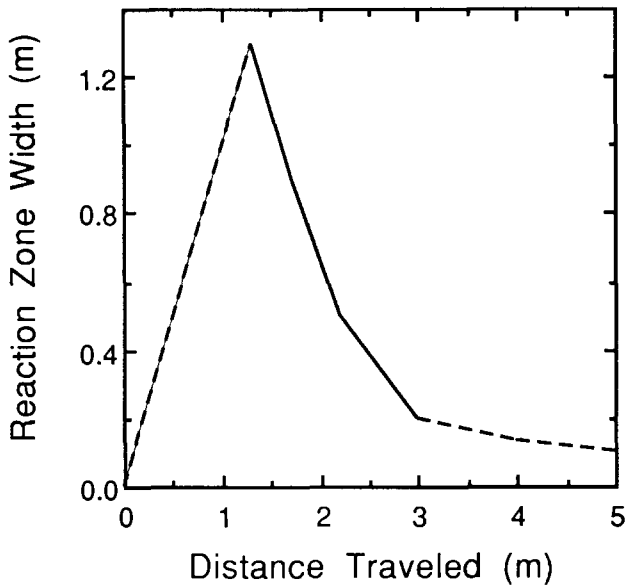


Fig. 9. Approximate reaction zone width in RX-HD as modeled by I&G. The full line is from the model; the dashed lines are our extrapolations.

	Booster Pressure (GPa)	C-J Pressure (GPa)	Ratio	Result	
LX-17	36	26	1.4	Overdriven	
RX-HD	25	15	1.7	Initiating	(41)

The pressure ratios look comparable. The LX-17 is overdriven as expected and dips back down to steady state. But the RX-HD is initiating, even though we hit it with a pressure well above the detonation pressure. This is clearly seen in Figs. 1 and 2, where the detonation velocity starts from a very low initial value, despite the big pressure start. There is a definite difference between these two explosives. We next consider the following comparable distances and times:

	Detonation Distance (mm)	Reaction Zone (mm)	Reaction Zone (s)	
LX-17	20	2	0.25	
RX-HD	4000	100	15	(42)

Based upon these comparisons, we suggest that we are undergoing thin-pulse initiation. We suggest that thick-pulse detonation occurs when

booster pulse length ~ steady state reaction zone length, and (43)

that once achieved, the result of thick-pulse detonation is to create

distance to steady state detonation ~ 10*steady state reaction zone length. (44)

A pulse time of 0.25 s needed for detonating LX-17 is easy to get, even with an electric gun. In a gas gun with a heavy sabot, a 3 s plateau pressure can be sustained. However, the 15 s needed for RX-HD is too long to be obtained by any easy process.

To summarize, we are in a regime with the RX-HD where we are not hitting it long enough at high pressure to take it near quick or overdriven detonation. Furthermore, theory does not appear to exist to predict the thin-pulse case.¹⁰

We also note that the LLNL cylinder shots were carried out with Detasheet EL-506C (63 wt% PETN, 8 wt% nitrocellulose and 29 wt% acetyl-tributylcitrate) boosters which have detonation pressures of about 18 to 20 GPa, lower than that of Pentolite. This would have further reduced the extent of progress to detonation in the cylinder test.

11. Considerations for the Future

The amount known about the non-ideality of RX-HD was near-zero before this shot. The NTS shot itself was the Equation-of-State experiment. This was one of the few infinite-diameter ANFO shots, and the measured steady state detonation velocity was used as a check of the performance of the CHEETAH code.⁷ We were lucky that the run to detonation of 4 meters was less than the radius of 7.7 meters, a fact not considered before the shot. No thought was given as to the pulse time of the booster. In retrospect, the cylinder shots were a hopeless attempt at getting an infinite-diameter result.

Twice before, huge ANFO shots were fired, giving comparable "infinite-size" data. The detonation velocities of these two shots are shown in Fig. 10. In 1976, 109 tons of 0.82 g/cc ANFO was fired in the Dice Throw event conducted by LLNL and LANL.¹¹ The explosive sat above ground in an igloo shape about 7 meters high and 5.6 meters in diameter. Cylinders of 51 to 292 mm diameter were tested and gave about the same detonation velocities. A smaller wall velocity was seen in the smaller cylinders. The ANFO was represented with JWL's but was not modeled using I&G. Rate sticks 400 mm long were used to measure the detonation velocities and these velocities appeared to be constant within error. The sticks began about half way out along the radius,¹² so the measured distance to steady state was 1.4 meters or less. Better data was obtained from the cylinder test, so that

x_r (0.8 g/cc ANFO) \approx 0.5 meters. (45)

The data points are the crosses in Fig. 10. The pressure ratio was larger here than for RX-HD. Besides the Pentolite boosters, octol ($P_j \sim 34$ GPa) was used to create a line initiation source along the vertical axis. According to TIGER BKWR, the C-J pressure of 0.8 g/cc ANFO is about 6.3 GPa, so the booster/explosive pressure ratio was about 5. The low density resulted in a low detonation pressure, and the powerful booster was then able to vastly overdrive it.

The second shot was the Middle Key 4 event at White Sands conducted by the Defense Nuclear Agency in September, 1993.¹³ The explosive charge was 20 tons (20569 kg) sitting above ground and detonated with pentolite boosters. The explosive sat in a bag with a radius of about 1.5 meters. It was a mixture of 40 wt% RDX and 60 wt% creamed ANFO, ie. essentially the emulsion part of RX-HD, made by Dyno Nobel. The density was nominally 1.47 g/cc.¹⁴ Without any prill and laced with RDX, the explosive would be expected to reach steady state quickly. The data shown in Fig. 10 was taken from two rate sticks in the explosive. One showed no change in detonation velocity; the other showed an overdriven state with a settling-down distance of 1/3 meter. The distance to steady state is

$$x_f (1.5 \text{ g/cc QM-100R}) \leq 1/3 \text{ meter with overdriving.} \quad (46)$$

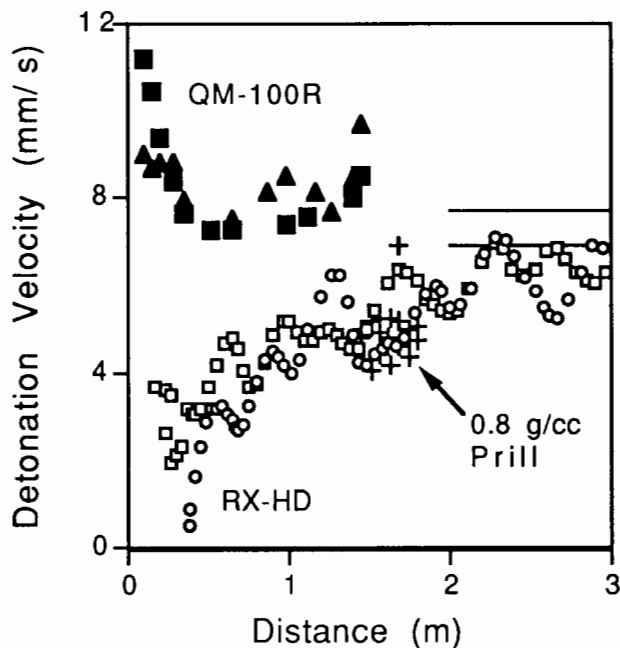


Fig. 10. Comparison of steady state distances for three large ANFO shots. Two RX-HD cables (○, □) overlap with the limited steady state data for 0.8 g/cc ANFO (+). The RX-HD data is never at steady state. The QM-100R data (■) reaches steady state in 1/3 meter or less. The horizontal lines are the steady state values.

Based on these results, we make these recommendations.

- 1) The extreme non-ideality of RX-HD may not matter. All of it will burn, but some burning may occur at late times, compared with the passage of the shock front. If this matters, then we suggest the use of a HMX-based booster for maximum pressure. We also suggest a center-filled line detonation, which is modeled before the actual test using the Ignition & Growth model to maximize the pulse length.
- 2) Should small 20 to 50 ton shots be planned in the future, the use of QM-100R should be considered. It will be closer to ideal and JWL cylinder tests have been conducted at LLNL.
- 3) More effort should be given to measurements within the explosive. This should include detonation velocity as a function of distance from the detonator to the edge plus the inclusion of particle velocity gauges and stress-time history gauges along this same track.

References

1. T. O. McKown, Explosive Performance on the Non-Proliferation Experiment, Los Alamos National Laboratory preprint, private communication, January 11, 1994.
2. Don Cranney, Dyno Nobel, Inc., private communication, 1994.
3. Handbook of Chemistry and Physics, 62nd ed., R. E. Weast, ed. (Boca Raton, FL, CRC Press, 1981), pp. C-323, D-34 to D-35, D-68.
4. J. D. Johnston, Los Alamos National Laboratory, private communications, 1993-1994.
5. M. Cowperthwaite and W. H. Zwisler, TIGER Computer Program Documentation, Stanford Research Institute, Menlo Park, CA, SRI Publication No. Z106, January, 1973.
6. D. L. Ornellas, Calorimetric Determinations of the Heat and Products of Detonation for Explosives:xxOctober 1961 to April 1982, LLNL Report UCRL-52821(1982).
7. P. C. Souers and L. C. Haselman, Jr., Detonation Equation of State at LLNL, 1993, UCRL-ID-116113, to be published 1994.
8. P. C. Souers and J. W. Kury, Propellants, Explosives and Pyrotechnics 18, 175 (1994).
9. Lew Glenn, LLNL, private communication, 1993.
10. B. D. Trott and R. G. Jung, "Effect of Pulse Duration on the Impact Sensitivity of Solid Explosives," Proceedings Fifth Symposium (International) on Detonation, Pasadena, CA, August 18-21, 1970, p. 191.
11. F. Helm, M. Finger, B. Hayes, E. Lee, H. Cheung and J. Walton, High Explosive Characterization for the Dice Throw Event, UCRL Report UCRL-52042 (1976).
12. Ron Boat, Los Alamos National Laboratory, private communication, 1994.
13. G. Goodfellow and N. Baum, Middle Key 4 TOAs, Data report for Field Command Defense Nuclear Agency, Contract No. DNA001-93-C-0147(December, 1993), kindly given us with a verbal description by Joe Renick, Logicon RDA, Albuquerque, NM.
14. R. H. Hales, Final Report for the QM-100R Program, Ireco, Inc., West Jordan, Utah. Submitted to New Mexico Engineering Research Institute, Albuquerque, NM.

Table 1. Raw CORTEX data for the five best positions. The data has been corrected to zero-time at the detonators.

K4- Lower		K5- Middle		K9- Middle		K11-Middle		K6-Upper	
Time (ms)	Cable Length (m)								
0.0191	0.0042	0.0451	0.0335	0.0099	0.3606	0.0391	0.0049	0.0427	0.0362
0.0291	0.0504	0.0551	0.0547	0.0199	0.3683	0.0491	0.0618	0.0527	0.0787
0.0391	0.0890	0.0651	0.0972	0.0299	0.3683	0.0591	0.0618	0.0627	0.1211
0.0491	0.1044	0.0751	0.1184	0.0399	0.3760	0.0691	0.0902	0.0727	0.1565
0.0591	0.1198	0.0851	0.1467	0.0499	0.3760	0.0791	0.1115	0.0827	0.2060
0.0691	0.1429	0.0951	0.1750	0.0599	0.3760	0.0891	0.1400	0.0927	0.2414
0.0791	0.1815	0.1051	0.3022	0.0699	0.4069	0.0991	0.1542	0.1027	0.2910
0.0891	0.2046	0.1151	0.2244	0.0799	0.4377	0.1091	0.1968	0.1127	0.3193
0.0991	0.2354	0.1251	0.2527	0.0899	0.4686	0.1191	0.2110	0.1227	0.3688
0.1091	0.2509	0.1351	0.2810	0.0999	0.4994	0.1291	0.2395	0.1327	0.3900
0.1191	0.2663	0.1451	0.3234	0.1099	0.5380	0.1391	0.2679	0.1427	0.4254
0.1291	0.2817	0.1551	0.3517	0.1199	0.5689	0.1491	0.2963	0.1527	0.4608
0.1391	0.3125	0.1651	0.3800	0.1299	0.5920	0.1591	0.3603	0.1627	0.5033
0.1491	0.3434	0.1751	0.4083	0.1399	0.6306	0.1691	0.3959	0.1727	0.5386
0.1591	0.3896	0.1851	0.4366	0.1499	0.6537	0.1791	0.4385	0.1827	0.5670
0.1691	0.4205	0.1951	0.4790	0.1599	0.6769	0.1891	0.4883	0.1927	0.6165
0.1791	0.4667	0.2051	0.5214	0.1699	0.7000	0.1991	0.5167	0.2027	0.6731
0.1891	0.5053	0.2151	0.5780	0.1799	0.7386	0.2091	0.5451	0.2127	0.7156
0.1991	0.5361	0.2251	0.6275	0.1899	0.7772	0.2191	0.5807	0.2227	0.7651
0.2091	0.5669	0.2351	0.6770	0.1999	0.8312	0.2291	0.6162	0.2327	0.8217
0.2191	0.5978	0.2451	0.7053	0.2099	0.8775	0.2391	0.6731	0.2427	0.8642
0.2291	0.6132	0.2551	0.7406	0.2199	0.9238	0.2491	0.7015	0.2527	0.8925
0.2391	0.6286	0.2651	0.7689	0.2299	0.9546	0.2591	0.7655	0.2627	0.9420
0.2491	0.6594	0.2751	0.8184	0.2399	0.9932	0.2691	0.8224	0.2727	1.0057
0.2591	0.6980	0.2851	0.8750	0.2499	1.0395	0.2791	0.8650	0.2827	1.0297
0.2691	0.7288	0.2951	0.9386	0.2599	1.0780	0.2891	0.9006	0.2927	1.1075
0.2791	0.7828	0.3051	0.9810	0.2699	1.1552	0.2991	0.9432	0.3027	1.1358
0.2891	0.8213	0.3151	1.0305	0.2799	1.2323	0.3091	0.9788	0.3127	1.1853
0.2991	0.8676	0.3251	1.0729	0.2899	1.2863	0.3191	1.0356	0.3227	1.2420
0.3091	0.8984	0.3351	1.1154	0.2999	1.3403	0.3291	1.0925	0.3327	1.2773

Part 2	K4		K5		K9		K11		K6	
	Time (ms)	Length (m)								
0.3191	0.9447	0.3451	1.1719	0.3099	1.3943	0.3391	1.1351	0.3427	1.3269	
0.3291	0.9909	0.3551	1.2285	0.3199	1.4002	0.3491	1.2062	0.3527	1.3976	
0.3391	1.0218	0.3651	1.2709	0.3299	1.4619	0.3591	1.2489	0.3627	1.4684	
0.3491	0.1053	0.3751	1.3133	0.3399	1.5082	0.3691	1.3200	0.3727	1.5250	
0.3591	1.0911	0.3851	1.3558	0.3499	1.5544	0.3791	1.3768	0.3827	1.5760	
0.3691	1.1143	0.3951	1.4063	0.3599	1.6007	0.3891	1.4266	0.3927	1.6170	
0.3791	1.1528	0.4051	1.4558	0.3699	1.6470	0.3991	1.4692	0.4027	1.7019	
0.3891	1.1836	0.4151	1.4982	0.3799	1.6856	0.4091	1.5190	0.4127	1.7798	
0.3991	1.2222	0.4251	1.5830	0.3899	1.7473	0.4191	1.5591	0.4227	1.8505	
0.4091	1.2530	0.4351	1.6467	0.3999	1.8090	0.4291	1.6018	0.4327	1.9142	
0.4191	1.2916	0.4451	1.7103	0.4099	1.8862	0.4391	1.6586	0.4427	1.9779	
0.4291	1.3455	0.4551	1.7669	0.4199	1.9325	0.4491	1.7084	0.4527	2.0275	
0.4391	1.4072	0.4651	1.8164	0.4299	1.9780	0.4591	1.7582	0.4627	2.0841	
0.4491	1.4689	0.4751	1.8729	0.4399	2.0328	0.4691	1.8079	0.4727	2.1336	
0.4591	1.5151	0.4851	1.9295	0.4499	2.0868	0.4791	1.8648	0.4827	2.1761	
0.4691	1.5768	0.4951	1.9861	0.4599	2.1716	0.4891	1.9359	0.4927	2.2468	
0.4791	1.6076	0.5051	2.0285	0.4699	2.2488	0.4991	2.0070	0.5027	2.3247	
0.4891	1.6539	0.5151	2.0851	0.4799	2.3259	0.5091	2.0780	0.5127	2.4167	
0.4991	1.7001	0.5251	2.1558	0.4899	2.3722	0.5191	2.1491	0.5227	2.4733	
0.5091	1.7772	0.5351	2.2548	0.4999	2.4339	0.5291	2.1989	0.5327	2.5158	
0.5391	1.8432	0.5451	2.3184	0.5099	2.4956	0.5391	2.2558	0.5427	2.5794	
0.5491	1.9203	0.5551	2.3608	0.5199	2.5573	0.5491	2.3268	0.5527	2.6502	
0.5591	1.9743	0.5651	2.4103	0.5299	2.5959	0.5591	2.4192	0.5627	2.7351	
0.5691	2.0360	0.5751	2.4881	0.5399	2.6345	0.5691	2.4761	0.5727	2.8059	
0.5791	2.0668	0.5851	2.5729	0.5499	2.7039	0.5791	2.5472	0.5827	2.8554	
0.5891	2.1130	0.5951	2.6366	0.5599	2.7734	0.5891	2.6112	0.5927	2.9191	
0.5991	2.1670	0.6051	2.6931	0.5699	2.8505	0.5991	2.6609	0.6027	2.9757	
0.6091	2.2133	0.6151	2.7497	0.5799	2.9199	0.6091	2.7391	0.6127	3.0394	
0.6191	2.2595	0.6251	2.8204	0.5899	2.9894	0.6191	2.7747	0.6227	3.0819	
0.6291	2.3520	0.6351	2.8770	0.5999	3.0202	0.6291	2.8458	0.6327	3.1456	
0.6391	2.4522	0.6451	2.9335	0.6099	3.1128	0.6391	2.9239	0.6427	3.2093	
0.6491	2.5293	0.6551	2.9901	0.6199	3.2054	0.6491	3.0164	0.6527	3.3013	
0.6591	2.5756	0.6651	3.0891	0.6299	3.2748	0.6591	3.0803	0.6627	3.3650	
0.6691	2.6373	0.6751	3.1810	0.6399	3.3365	0.6691	3.1230	0.6727	3.4074	
0.6791	2.7221	0.6851	3.2376	0.6499	3.3905	0.6791	3.1940	0.6827	3.4711	

Part 3	K4		K5		K9		K11		K6	
	Time (ms)	Length (m)								
0.6891	2.8300	0.6951	3.2942	0.6599	3.4368	0.6891	3.2794	0.6927	3.5702	
0.6991	2.9071	0.7051	3.3790	0.6699	3.4985	0.6991	3.3647	0.7027	3.6551	
0.7091	2.9687	0.7151	3.4780	0.6799	3.5448	0.7091	3.4215	0.7127	3.7330	
0.7191	3.0381	0.7251	3.5346	0.6899	3.6065	0.7191	3.5211	0.7227	3.7896	
0.7291	3.0921	0.7351	3.5911	0.6999	3.6760	0.7291	3.5282	0.7327	3.8391	
0.7391	3.1538	0.7451	3.6406	0.7099	3.7608	0.7391	3.6277	0.7427	3.8816	
0.7491	3.2154	0.7551	3.7113	0.7199	3.8303	0.7491	3.6845	0.7527	3.9453	
0.7591	3.2771	0.7651	3.7962	0.7299	3.8997	0.7591	3.7130	0.7627	3.9877	
0.7691	3.3850	0.7751	3.8386	0.7399	3.9537	0.7691	3.7841	0.7727	4.0443	
0.7791	3.4621	0.7851	3.9093	0.7499	4.0154	0.7791	3.8907	0.7827	4.1151	
0.7891	3.5392	0.7951	3.9942	0.7599	4.1466	0.7891	3.9689	0.7927	4.2000	
0.7991	3.5700	0.8051	4.0790	0.7699	4.1929	0.7991	4.0115	0.8027	4.2566	
0.8091	3.6317	0.8151	4.1497	0.7799	4.2700	0.8091	4.0897	0.8127	4.3062	
0.8191	3.7165	0.8251	4.1921	0.7899	4.3317	0.8191	4.1466	0.8227	4.3557	
0.8291	3.8013	0.8351	4.2628	0.7999	4.4011	0.8291	4.2390	0.8327	4.4477	
0.8391	3.8784	0.8451	4.3548	0.8099	4.4706	0.8391	4.3172	0.8427	4.5255	
0.8491	3.9478	0.8551	4.4325	0.8199	4.5323	0.8491	4.3670	0.8527	4.6105	
0.8591	4.0094	0.8651	4.4820	0.8299	4.5709	0.8591	4.4309	0.8627	4.6671	
0.8691	4.0711	0.8751	4.5457	0.8399	4.6403	0.8691	4.4949	0.8727	4.7378	
0.8791	4.1405	0.8851	4.6164	0.8499	4.7020	0.8791	4.5660	0.8827	4.7874	
0.8891	4.1868	0.8951	4.6871	0.8599	4.7715	0.8891	4.6229	0.8927	4.8369	
0.8991	4.2638	0.9051	4.7437	0.8699	4.8486	0.8991	4.7011	0.9027	4.8794	
0.9091	4.3718	0.9151	4.8002	0.8799	4.9103	0.9091	4.7793	0.9127	4.9501	
0.9191	4.4643	0.9251	4.8709	0.8899	4.9643	0.9191	4.8574	0.9227	5.0209	
0.9291	4.5414	0.9351	4.9699	0.8999	5.0492	0.9290	4.9072	0.9327	5.1058	
0.9391	4.5876	0.9451	5.0406	0.9099	5.1418	0.9390	4.9570	0.9427	5.1624	
0.9491	4.6955	0.9551	5.0830	0.9199	5.2420	0.9490	5.0423	0.9527	5.2049	
0.9591	4.7958	0.9651	5.1467	0.9299	5.2883	0.9590	5.1205	0.9627	5.2615	
0.9691	4.8806	0.9751	5.2527	0.9399	5.3655	0.9690	5.1987	0.9727	5.3535	
0.9791	4.9422	0.9851	5.3164	0.9498	5.3867	0.9790	5.2697	0.9827	5.4243	
0.9891	5.0116	0.9951	5.3800	0.9598	5.4561	0.9890	5.3408	0.9927	5.5021	
0.9991	5.0733	1.0051	5.4366	0.9698	5.5101	0.9990	5.3764	1.0027	5.5658	
1.0091	5.1272	1.0151	5.5073	0.9798	5.5564	1.0090	5.4617	1.0127	5.6366	
1.0191	5.1889	1.0251	5.5780	0.9898	5.6182	1.0190	5.4830	1.0227	5.6790	
1.0291	5.2429	1.0351	5.6346	0.9998	5.7030	1.0290	5.6038	1.0327	5.7427	

Part 4	K4		K5		K9		K11		K6	
	Time (ms)	Length (m)								
1.0391	5.3431	1.0451	5.6911	1.0098	5.7802	1.0390	5.6607	1.0427	5.7852	
1.0491	5.4202	1.0551	5.7760	1.0198	5.8496	1.0490	5.7531	1.0527	5.8489	
1.0591	5.4973	1.0651	5.8608	1.0298	5.9113	1.0590	5.8100	1.0627	5.9338	
1.0691	5.5435	1.0751	5.9315	1.0398	5.9807	1.0690	5.8668	1.0727	5.9861	
1.0791	5.6052	1.0851	5.9881	1.0498	6.0887	1.0790	5.9308	1.0827	6.0710	
1.0891	5.7131	1.0951	6.0447	1.0598	6.1582	1.0890	6.0232	1.0927	6.1488	
1.0991	5.8056	1.1051	6.1507	1.0698	6.2122	1.0990	6.1014	1.1027	6.2337	
1.1091	5.8827	1.1151	6.2214	1.0798	6.3048	1.1090	6.1583	1.1127	6.2904	
1.1191	5.9025	1.1251	6.2780	1.0898	6.3588	1.1190	6.2294	1.1227	6.3611	
1.1291	5.9564	1.1351	6.3487	1.0998	6.4282	1.1290	6.2791	1.1327	6.4177	
1.1391	6.0258	1.1451	6.4063	1.1098	6.4745	1.1390	6.3573	1.1427	6.4743	
1.1491	6.0721	1.1551	6.4629	1.1198	6.5362	1.1490	6.4142	1.1527	6.5027	
1.1591	6.1414	1.1651	6.5760	1.1298	6.5825	1.1590	6.4853	1.1627	6.5663	
1.1691	6.2108	1.1751	6.6467	1.1398	6.6751	1.1690	6.5538	1.1727	6.6583	
1.1791	6.2879	1.1851	6.6891	1.1498	6.7368	1.1790	6.6107	1.1827	6.7433	
1.1891	6.3650	1.1951	6.7457	1.1598	6.8294	1.1890	6.6960	1.1927	6.7929	
1.1991	6.4575	1.2051	6.8305	1.1698	6.9065	1.1990	6.7671	1.2027	6.8353	
1.2091	6.5038	1.2151	6.9083	1.1798	6.9296	1.2090	6.8524	1.2127	6.9060	
1.2191	6.5654	1.2251	6.9790	1.1898	7.0145	1.2190	6.9093	1.2227	6.9839	
1.2291	6.6734	1.2351	7.0356	1.1998	7.0916			1.2327	7.0688	
1.2391	6.7659	1.2451	7.0992	1.2098	7.1765			1.2427	7.1396	
1.2491	6.8507	1.2551	7.1699	1.2198	7.2459			1.2527	7.2032	
1.2591	6.9201	1.2651	7.2265	1.2298	7.3462			1.2627	7.2740	
1.2691	6.9740	1.2751	7.2831					1.2727	7.3165	
1.2791	7.0357	1.2851	7.3679					1.2827	7.3802	
1.2891	7.0974	1.2951	7.4386					1.2927	7.4226	
1.2991	7.1359	1.3051	7.5235					1.3027	7.5005	
1.3091	7.2284	1.3151	7.5800							
1.3191	7.3209	1.3251	7.6861							
1.3291	7.4134									
1.3391	7.4597									
1.3491	7.5213									
1.3591	7.5907									

Table 2. Equation of state parameters for the explosives in this study.

	DYNA2D Manual	Tar- ver's terms	RX-HD (ANFO)	PENT- OLITE	DETA- SHEET
Unreacted Explosive JWL	density (g/cc)	ρ_0	1.32	1.70	1.48
	R_{1e} (Mbars)	A	100		
	R_{2e} (Mbars)	B	-0.026959		
	R_{3e} (Mbar/K)		1.53E-05		
	R_{5e}	R_1	9.8		
	R_{6e}	R_2	0.98		
	ω_e	ω	0.5647		
	c_{ve}	C_v	2.717E-05		
	T_0 (K)	T_0	298		
	P_k (Mbars)		0.200		
Reacted Products JWL	D (mm/ μ s)	D	7.0	7.53	7.20
	R_{1p} (Mbars)	A	4.8245	5.4094	3.738
	R_{2p} (Mbars)	B	0.14104	0.093726	0.03647
	R_{3p} (Mbar/K)		5.5E-06	3.5E-06	3.0E-06
	R_{5p}	R_1	5.075	4.5	4.2
	R_{6p}	R_2	2.0	1.1	1.1
	ω_p	ω	0.55	0.35	0.30
	c_{vp}	C_v	1.0E-05	1.0E-05	1.0E-05
	Q_r (Mb.cc/cc)	E_0	0.048	0.081	0.07
	P_j (Mbars)		0.16	0.255	0.205
Initiation Term	F_q (μ s $^{-1}$)	I	25		
	F_r	b	0.667		
	C_{crit}	a			
	η	x	4		
Fast Growth Term	G_1 (μ s $^{-1}$ Mb-Z)	G_1	0.4		
	s_1	c	0.667		
	a_1	d	0.667		
	m	y	1		
Limits	$F_{max, ig}$	F_{igmax}	0.16		
	$F_{max, gr}$	F_{G1max}	1		

**EXPLOSIVE PERFORMANCE
ON THE
NON-PROLIFERATION EXPERIMENT***

by

**Thomas O. McKown
Los Alamos National Laboratory**

ABSTRACT

The Explosive Effects Physics Project at the Los Alamos National Laboratory planned and conducted experiments on the Non-Proliferation Experiment (NPE) as part of its effort to define source functions for seismic waves. Since all investigations were contingent on the performance of the emplaced chemical explosive, an array of diagnostic measurements was fielded in the emplaced explosive. The CORTEX (COntinuous Reflectometry for Radius vs Time EXperiment) system was used to investigate the explosive initiation and to determine the detonation velocities on three levels and in a number of radial directions. The CORTEX experiments fielded in the explosive chamber will be described, including a description of the explosive emplacement from the perspective of its impact on the CORTEX results. The data obtained are reviewed and the resulting detonation velocities are reported. A variation of detonation velocity with depth in the explosive and the apparent underdetonation and overdetonation of the explosive in different radial directions is reported.

INTRODUCTION

The Non-Proliferation Experiment (NPE) was planned and conducted by Lawrence Livermore National Laboratory (LLNL), to compare the seismically produced signals of a large conventional explosive to those of a nuclear test. Consequently the experiment was conducted on the Nevada Test Site (NTS) in the N-tunnel complex in geologic media similar to that of previous underground nuclear tests. The test consisted of approximately 2.9 million pounds of a 50-50 Ammonium Nitrate-Fuel Oil (ANFO) and emulsion blend^{**} in a 15.2 m diameter, 5.2 m high right cylinder (the explosive chamber). Detonation occurred simultaneously at three locations along the axis. This will be described in greater detail later.

The Los Alamos National Laboratory (Los Alamos) group P-15 participated in the NPE to characterize the explosive performance and to characterize the time-dependent shock-wave evolution in the region around the explosive chamber. To achieve these objectives, an existing array of 20 accelerometer packages, deployed on several previous N-tunnel events, was supplemented with an additional four NPE specific packages. Twelve Axially-Symmetric Magnetic (ASM) gauges for measuring particle velocity were fielded, ranging from approximately 7.2 m from the chamber axis (2.0 m outside the explosive chamber wall) to 64.0 m. Two ASM gauges were fielded within the explosive chamber, in the blasting agent. Combined with the detonation velocity of the blasting agent, the particle velocity measured with these two gauges will permit an in-situ determination of the equation-of-state of the actual blasting agent detonated. Twelve time-of-arrival

* This work supported by the United States Department of Energy.

** Technically, this blend is classed as a blasting agent, not an explosive. However, both terms will be used, particularly explosive because it is shorter and its use is easier in, for example, explosive chamber.

(CORRTEX) sensing elements were fielded in two regions of interest. Figures 1 and 2 show these sensing elements in four groups of three cables, fielded in the free-field and stemming regions, exterior to the explosive chamber (drill holes KH-1, KH-2 and KH-3 and the access drift). The instrumentation described above was fielded to characterize the shock-wave evolution in the region external to the explosive chamber.

Within the explosive chamber the twelve CORRTEX sensing elements, entering through drill holes or the access drift, were arrayed to directly determine the burn velocity of the blasting agent on three principal levels and in six directions radial to the axis of detonation. These measurements will help characterize the explosive performance. The remainder of this paper will address this subject. The statements earlier of the larger objectives and the near-field instrumentation fielded by LANL P-15 were provided to put these measurements into perspective. Those measurements and the experiment as a whole was driven by the explosive performance.

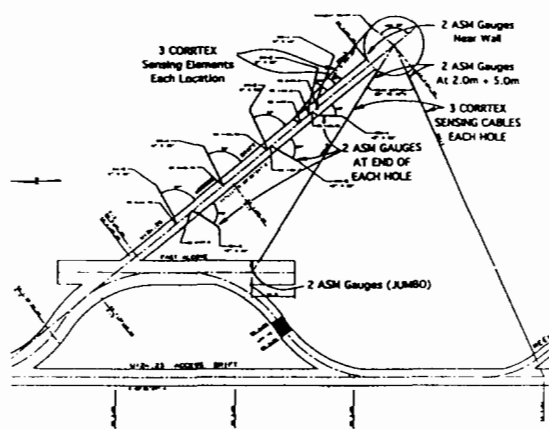


Figure 1. Engineering site plan for the non-proliferation experiment.

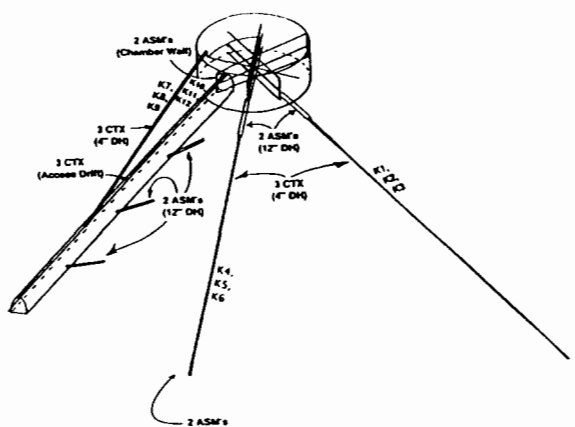


Figure 2. CORRTEX instrumentation on the non-proliferation experiment.

EXPLOSIVE CHAMBER CORRTEX INSTRUMENTATION

The objective in the CORRTEX sensing element placement in the explosive chamber was to provide direct measurement (reduction and analysis without complicated geometric corrections) of the detonation velocity in approximately one quadrant of the chamber on three levels and in the middle level, covering approximately 240 degrees of the chamber.

A site plan for the NPE is shown in Figure 1. This engineering drawing shows the planned positions of the drill holes and access drift with respect to the explosive chamber within the N-tunnel complex. Figure 2 is an attempt to show the planned type and number of CORRTEX instruments in some perspective, but not to scale, with emphasis on the array of cables within the explosive chamber. Figure 3 shows plan views, based on as-built survey information, of the lower, middle and upper levels, with the cable designations and direction on each cable indicating the direction of burn from the chamber axis toward the cable exit from the chamber. Figures 2 and 3 combine to show for example, that cables designated K-1* (lower level), K-2 (middle level) and K-3 (upper level) exit the chamber together through the KH-1 drill hole. The other cables similarly join in groups of three to exit.

In the explosive chamber, the sensing elements were installed, under tension, on Kevlar rope messengers stretched across the chamber. Sensing elements K-8 and K-9 were installed in the middle level on the same messengers as cables K-2 and K-5 respectively, but radial from the chamber axis in directions

* The cable designations K-n and Kn are synonymous and will be used interchangeable.

opposite to K-2 and K-5. All sensing elements with the exception of K-9 were installed "beyond" the axis of the chamber, resulting in a significant loss of cable on first crush. Figure 4 is a photograph of the explosive chamber taken just prior to the booster and detonator installation. The CORTEX sensing elements are again indicated with their letter designation at the exit end toward which the blasting agent will burn.

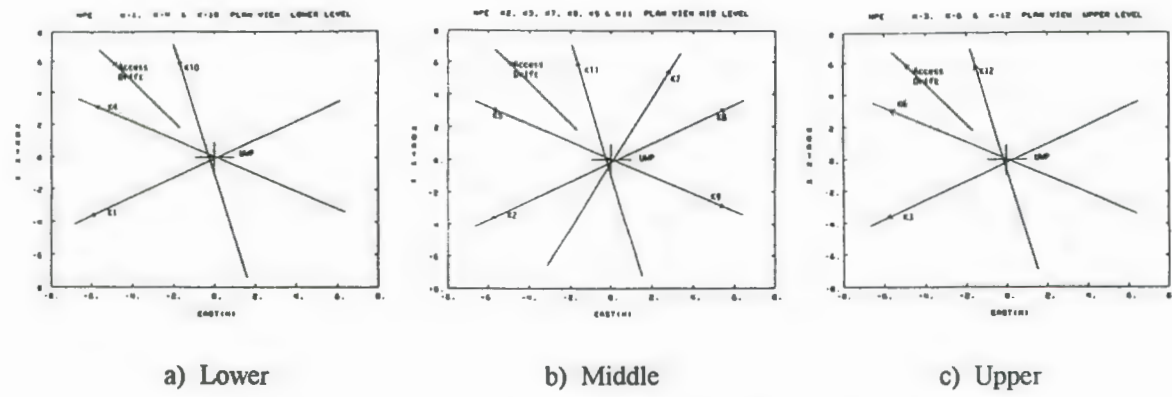


Figure 3. Plan views of the as-built CORTEX sensing elements.

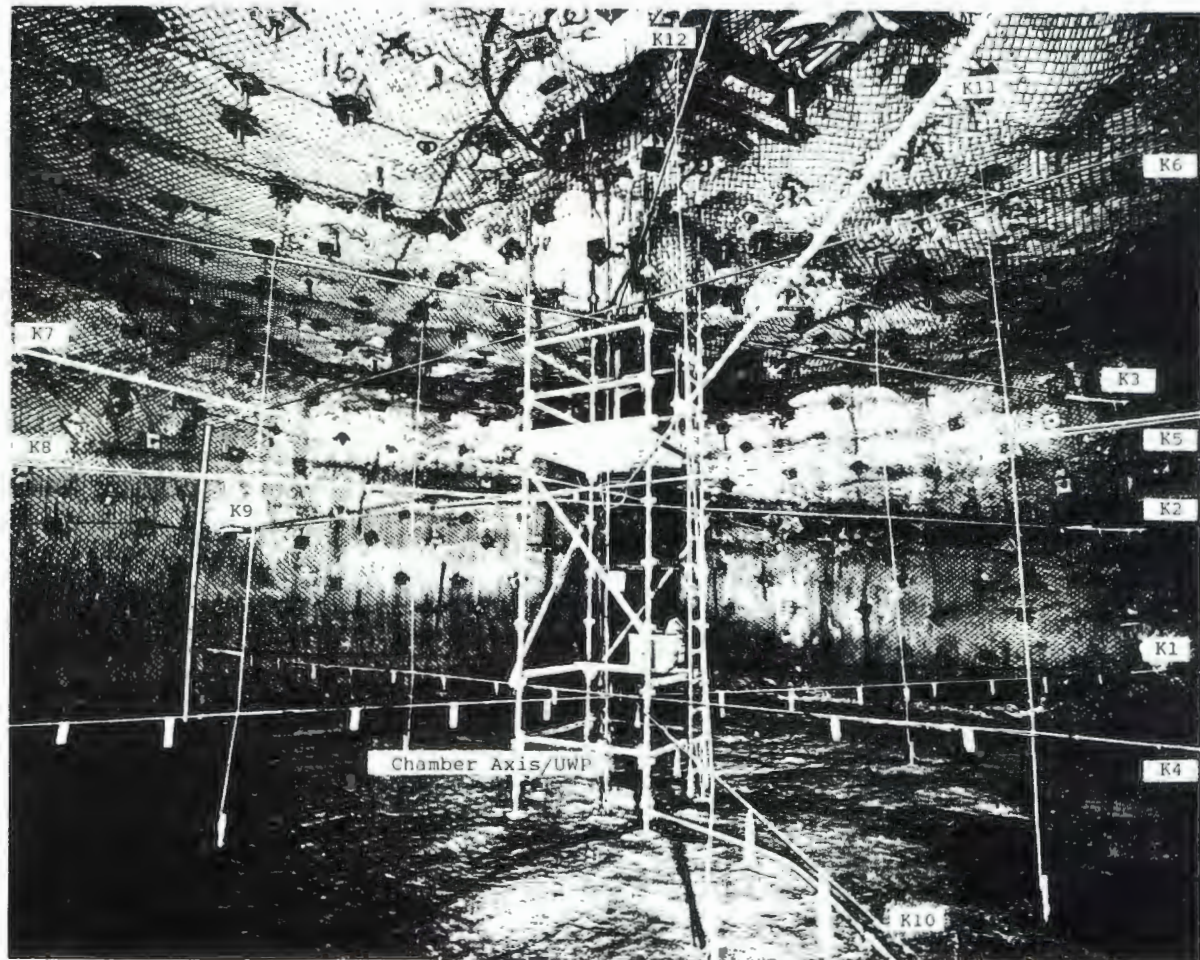


Figure 4. Photograph of the CORTEX sensing element installation in the explosive chamber.

The axis of the chamber was a taut steel aircraft cable anchored from back (ceiling) to invert (floor). Figure 4 identifies this installation. This location was referred to for survey purposes as the Users Working Point (UWP) and was not actually coincident with the planned WP. (The planned WP was 0.177 m west and 0.061 m south of UWP, a distance of 0.178 m.) Figure 5 is a representative, as-built diagram of an installed CORTEX cable. Of particular interest is the documented location of the chamber axis or center line for the cable and the last linear point or "wall" point on each cable, prior to exiting the explosive chamber. The documented position on each installed CORTEX sensing element of the UWP is made with a normal from the sensing element to the UWP. This becomes the axis reference position (RD) for that cable. In the example, RD is 12.695 m. The documented "wall" position is 24.768 m. Two locations at the explosive chamber extremities of the sensing element are denoted with numerals, specifically, #11 and #12. These were marked locations on the sensing element or installation messenger and denoted survey locations. Using the surveyed UWP at the elevation of each sensing element, the intersection of a normal from the line of each sensing element to the UWP (at that elevation) was computed. The documented position of RD and the position computed from the as-built survey data are in excellent agreement. The data will therefore be referenced to the position denoted RD on each sensing element.

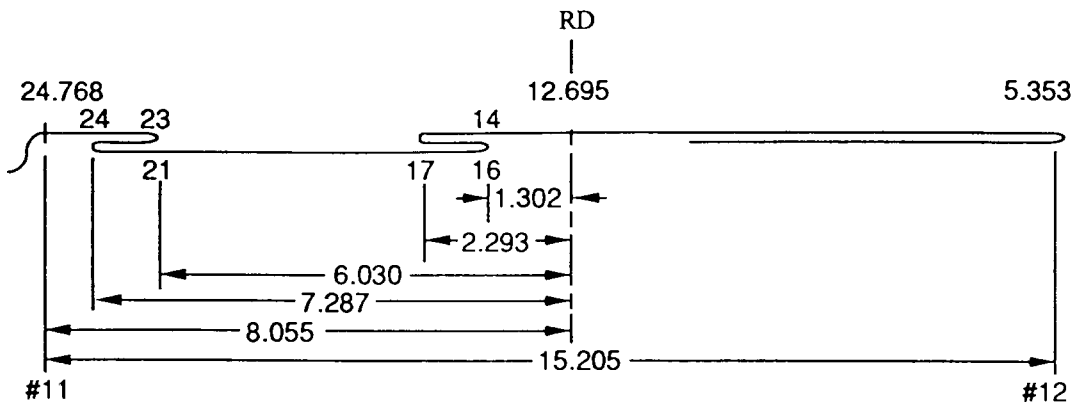


Figure 5. Representative as-built diagram of an installed CORTEX sensing element.

A final comment on the route by which K-10, K-11 and K-12 exited the explosive chamber down the access drift. These three sensing elements were dressed along the chamber wall vertically and then around to the left rib (side, facing toward WP) of the access drift. Before exiting, the three cables looped together back toward the chamber center about 0.60 m where they were anchored and then run straight along the access drift left rib. Because of this loop back toward UWP, K-10, K-11 and K-12 were crushed at this location prior to the shock arrival at the chamber wall. This will be reflected in the data and results presented later.

DETONATORS AND TIMING

The UWP described above established the axis of the explosive chamber for the CORTEX installation and reference. It is necessary to examine the detonator and booster installation to later discuss the initiation of the blasting agent, the onset of crush of the CORTEX cables and some conclusions drawn from the CORTEX data. The burn of the blasting agent was initiated with Exploding BridgeWire (EBW) detonators embedded in 5 inch diameter (about 5.5 inch with casing), 6 inch long cylinders of pentolite high explosive. Figure 6 is an approximate sketch of the detonator-booster combination. Of significance is the placement of the EBW centrally in the vertical direction but considerably off center in the

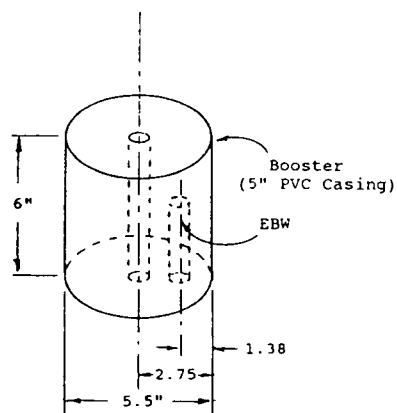


Figure 6. Detonator-booster diagram.

radial direction.

Figure 7 is a photograph of the boosters after installation. They were mounted on the UWP steel cable and for reference, are numbered one through five from the bottom to top. Detonators one, three and five were the primary detonation system with two and four to be used only on failure of the primary system. Boosters three and five were each installed in a "triangle" of CORTEX sensing elements. Due to a short detonator cable, booster one was installed adjacent to the K-4 sensing element but somewhat above K-1 and K-10. Figure 7 (and a close-up view of boosters one and two) were the only photos taken and no further documentation was made of the booster emplacement, and in particular the location of the detonators within the boosters. This is believed to have been significant to the blasting agent initiation as measured by the CORTEX cables.

Detonation timing is summarized in Figure 8. The firing signal was sent from the LLNL control room to the Capacitive Discharge Unit (CDU). From the CDU, simultaneous signals were sent to the EBW detonators and the red shack for distribution to experimenters. The time from EBW detonation to the pentolite booster breakout for a centrally detonated booster is 5.08 μ s. For a detonator located as shown in Figure 6, the configuration for the NPE, the minimum booster breakout time is estimated to be 2.54 μ s. The net time to reference CORTEX unit n to "minimum boost" is [3.701 + T(n)] - 9.362 μ s.

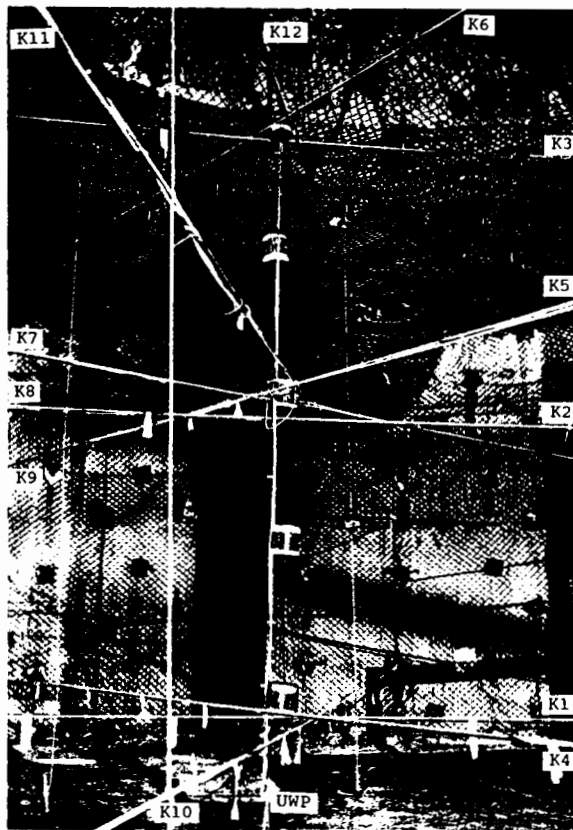


Figure 7. Photograph of the boosters in place in the explosive chamber.

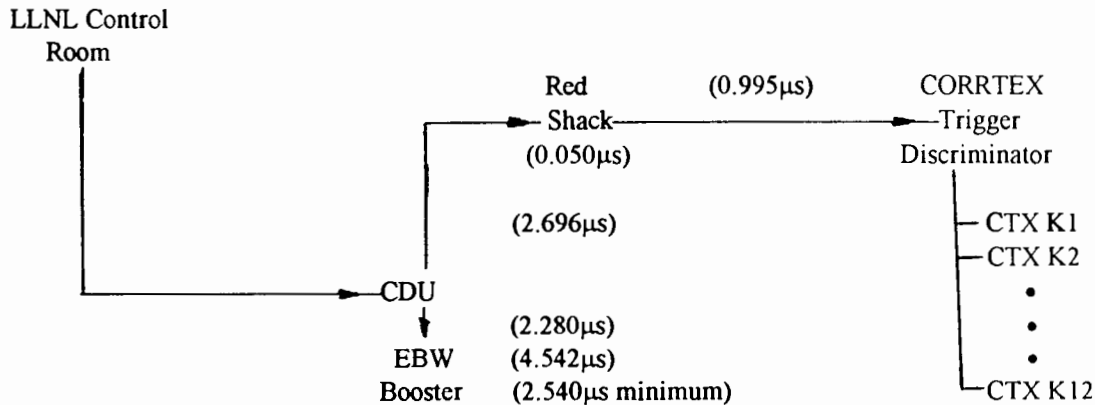


Figure 8. Diagram of the trigger signals with times.

EXPLOSIVE EMPLACEMENT

The explosive was emplaced with two methods. The access drift connected to the explosive chamber

between the installed K-4, 5 and 6 vertical location and the K-10, 11 and 12 vertical location, with the chamber invert about eight feet below the drift invert. A steel bulkhead with door formed the interface between the access drift and explosive chamber. Initially, the ANFO-emulsion blend was dumped from transport vehicles through the bulkhead door. This resulted in a mound of explosive between sensing elements K-4 on the right and K-10 on the left. This mound did not flow like water, forming multiple uniform layers of explosive, but rather a mass of viscous material, spreading across the chamber only under force of further material being dumped onto this pile.* This "lava flow" (author's description) of material across the chamber covered the lower level of sensing elements only.

The second method of explosive emplacement, which filled the chamber to the back and covered the middle and upper sensing element levels, was through an auger system located in the access drift just outside the chamber bulkhead. The explosive was augered to a point just short (5 to 8 feet short) of the chamber axis, between K-5 and 6 on the right and K-11 and 12 on the left, dropped into the chamber and allowed to spread "radially" in all directions. The operation continued until visually, the chamber was full to the back. The explosive remained in place for just over a week while stemming operations and final preparations took place.

CORRTEX RECORDING SYSTEM

The CORRTEX recording system for the NPE included twelve CORRTEX recorders, each connected to a single CORRTEX sensing element. The recording units and associated trigger, power, communication and monitor hardware were located underground in the slow alcove, approximately 1000 feet from the explosive chamber. The units were fielded in prepushing mode with a $10 \mu\text{s}$ pulse rate. Control and monitor of the units and data retrieval was from the Los Alamos Control Point (CP) monitor room. All recorders were triggered by the red shack supplied trigger described earlier, and therefore reference timing is to the described "minimum boost". Details of the recording parameters, beyond those mentioned, may be obtained from the author or from the raw CORRTEX data records. All twelve units functioned properly and all data were retrieved and transmitted to the CP within minutes of the detonation.

CORRTEX DATA

Excellent explosive chamber data were recorded from ten of the twelve installed sensing elements. The K-10 sensing element (lower level, RDX1-50) opened at about the 26.3 m location on the sensing cable during the first pour of the stemming operations. K-10 was installed along the left rib of the access drift, linear from a point about 0.60 m inside the explosive chamber. An open indicates that the cable "tore" rather than crushed and the 26.3 m location places this point about 0.7 m into the sandbag region beyond the explosive chamber-access drift bulkhead. There is, at present, no explanation of this loss since K-11 and K-12 were together with K-10 in this location and were not damaged.

The K-1 (lower level, FSJ1-50) data are questionable. While data were recorded, the 2.0 m signature loop installed at 14.0 m in the sensing element (a 16.0 to 14.0 loop) appears as a 1.22 m discrete jump in the unadjusted data. The second loop is slightly distorted and the data to about the final 2.0 m in the explosive chamber are not linear. The K-1 data beyond the chamber wall were excellent, which permitted the complete data set to be reduced and permitted some results to be computed and some conclusions to be made regarding the explosive chamber data. K-1, K-4 and K-10 were the three sensing elements installed on the lower level. Only the results from the exit end of the K-1 data could therefore support the excellent K-4 data.

In Table 1, organized by installation level, the time with respect to "minimum boost" and position along the cable of first crush is listed for each cable, as is the RD and the difference, first crush data - RD. A negative difference indicates that first crush was "beyond" RD.

* Timing, detonator, booster and explosive emplacement information was supplied by Ray Peabody, Sandia National Laboratory and event detonation/timing and firing engineer.

Table 1. Initial crush of explosive chamber sensing elements.

Level	Cable Label	Time (ms) Initial Crush	Location (m)** Initial Crush	RD	Difference
Low	K-1	0.239	12.520	12.695	-0.175*
	K-4	0.019	14.210	14.206	+0.004
	K-10	N/A	N/A	7.445	N/A
Mid	K-2	0.168	12.409	12.202	+0.207
	K-5	0.015	12.500	12.601	-0.101
	K-11	0.009	9.383	9.492	-0.109
	K-7	0.127	10.281	10.309	-0.028
	K-8	0.174	7.045	6.912	+0.133
	K-9	N/A	N/A	-0.371	N/A
Up	K-3	0.089	10.557	10.435	+0.122
	K-6	0.013	10.930	11.007	-0.077
	K-12	0.020	11.068	11.160	-0.092

* Possibly meaningless due to the questions with K-1.

** Position along the cable of first crush from cable end.

Table 2 presents a summary of information relative to the detonation front arrival at the chamber walls. For each location presented, the table contains the Nevada elevation in feet, the radial distance from UWP in meters and the best time or estimate of time available. Some locations required projection over a known distance at the determined burn velocity, because the data record was cutoff prior to arrival at the chamber wall. All data relative to the wall or exit location of the sensing elements were some inches inside the chamber walls and therefore the times presented in Table 2 have taken this into account. The uncertainties presented reflect the necessity to extrapolate times from some inner location to the chamber wall. Except for K-8 and K-9, all times generally fell between 1.3 ms and 1.4 ms.

Table 2. Times of detonation burn arrival at certain wall locations (Chamber Center at 6077.93 feet.)

Level	Location Designation	/	Elevation (feet)	/	Radial Distance (m)	/	Arrival Time (ms)
Low	K-1(?)	KH-1*	K-4(u)	KH-2	K-10(n/a)		
	6072.26/7.134 1.39 ± 0.01	6073.56/8.453 1.45 ± 0.01	6072.32/7.223 1.38 ± 0.01	6072.80/7.754 1.39 ± 0.01	6072.01/7.595 N/A		
Mid	K-2(o)	KH-3	K-5(u)	K-11(u)	K-7(o)**	K-8(u)**	K-9(u)**
	6078.01/7.442 1.34 ± 0.01	6078.02/7.246 1.33 ± 0.01	6078.07/7.423 1.31 ± 0.02	6078.18/7.296 1.30 ± 0.01	6077.87/7.867 1.27 ± 0.03	6078.25/7.589 1.23 ± 0.03	
Extra					6081.81/7.986 1.38 ± 0.01		
Up	K-3(o)	K-6(u)	K-12(u)		Access drift		
	6084.16/7.413 1.34 ± 0.01	6083.76/7.239 1.33 ± 0.01	6083.97/7.084 1.27 ± 0.03		6083.97/6.925 1.31 ± 0.02		

* KH-1 recessed into the chamber wall due to sloughing around the drill hole collar.

** K-7, K-8 and K-9 ran around the chamber circumference to KH-3.

RESULTS--DETONATION VELOCITIES

A parameter of explosive performance is its detonation velocity. The blasting agent used on the NPE, ANFO-emulsion blend, required initiation and the method used was described earlier. Initiation may result in an overdriven or underdriven detonation, an explosive burn accelerating or slowing to a constant velocity or steady-state detonation. On the NPE, the detonation required both time and distance from UWP to reach a constant velocity and the interval over which analysis was performed had to be selected for each data record. Table 3 presents a summary of the detonation velocities computed by a linear least squares fit to the data, over the intervals indicated.

The final column of Table 3 presents the results of computing the velocity, over the interval indicated, of the 90% confidence function.* This value, the author believes, better represents the measured velocity of detonation by each CORTEX sensing element. The computed standard deviation for each method of determining velocity is also presented in Table 3. Figure 9 shows a plot of a CORTEX data record from each level, along with the 90% confidence function determined for that data set.

Since the K-1 data beyond the explosive chamber were excellent, and consistent with the K-2 and K-3 data, the correct propagation factor for K-1 could be determined. Using the subsequently adjusted data, an analysis on only the 0.250 ms of data prior to exiting the explosive chamber yields a velocity of detonation of 7.119 m/ms, a value not inconsistent with the K-4 velocity of 7.162 m/ms.

Table 3. Computed detonation velocities from the CORTEX data.

Level	Cable Label	Interval (ms)	Linear Least Squares Velocity (m/ms)	
			All Data	90% Confidence
Mid	K-1	1.10 - 1.35	7.122 ± 0.049	7.119 ± 0.046
	K-4	0.57 - 1.35	7.164 ± 0.010	7.162 ± 0.010
	K-2	0.40 - 1.32	6.810 ± 0.018	6.857 ± 0.009
	K-5	0.50 - 1.33	6.885 ± 0.008	6.873 ± 0.004
	K-11	0.45 - 1.22	6.809 ± 0.009	6.802 ± 0.006
	K-7	0.40 - 1.31	6.772 ± 0.013	6.763 ± 0.006
Up	K-8	0.40 - 1.27	6.812 ± 0.015	6.723 ± 0.008
	K-9	0.50 - 1.23	6.731 ± 0.014	6.731 ± 0.012
	K-3	0.35 - 1.34	6.448 ± 0.010	6.424 ± 0.007
Low	K-6	0.33 - 1.30	6.442 ± 0.008	6.427 ± 0.006
	K-12	0.40 - 1.21	6.491 ± 0.011	6.491 ± 0.011

In the middle level, the K-2 and K-5 90% confidence velocities of 6.857 m/ms and 6.873 m/ms are slightly higher than the 6.802 m/ms and 6.763 m/ms for K-11 and K-7 which are in turn higher than the K-8 and K-9 velocities of 6.723 m/ms and 6.731 m/ms. The three upper level velocities are rather consistent with an average value of 6.447 m/ms. Of course the progression from a lower level velocity of about 7.14 m/ms, to

* If a least squares generated linear function F models the steady-state detonation and if the position X1 is a normally distributed random variable for the corresponding time T1, then a 90% confidence interval (Y1, Y2) about F(T1) can be determined, such that the assertion that the true position at time T1 will be contained between Y1 and Y2, will be correct 90% of the time. If X1 lies outside this confidence interval (Y1, Y2) for time T1, then the point (T1, X1) is rejected. Those points satisfying these conditions are then used to regenerate a least squares linear function and the process continues iteratively until no points are rejected. The resulting least squares generated linear function is defined to be the 90% confidence function.

a middle level velocity between 6.73 and 6.87 m/ms and to an upper level velocity of about 6.45 m/ms is obviously a gradation of velocity associated with depth in the explosive chamber.

Finally, some observations about explosive initiation. The plots presented in Figure 9 show that with K-4 for example, the initial burn velocity was low, accelerating to a constant velocity by about 0.570 ms and 2.0 m from RD, an indication of underinitiation. Although the times and distances vary, a similar situation exists for K-5, K-6, K-9, K-11 and K-12. The remaining four plots, K-2, K-3, K-7 and K-8 (excluding K-1) initially "hump", slowing slightly to a steady-state detonation velocity. Interestingly, K-2, K-3, K-7 and K-8 also show significantly longer times to first crush (Table 1).

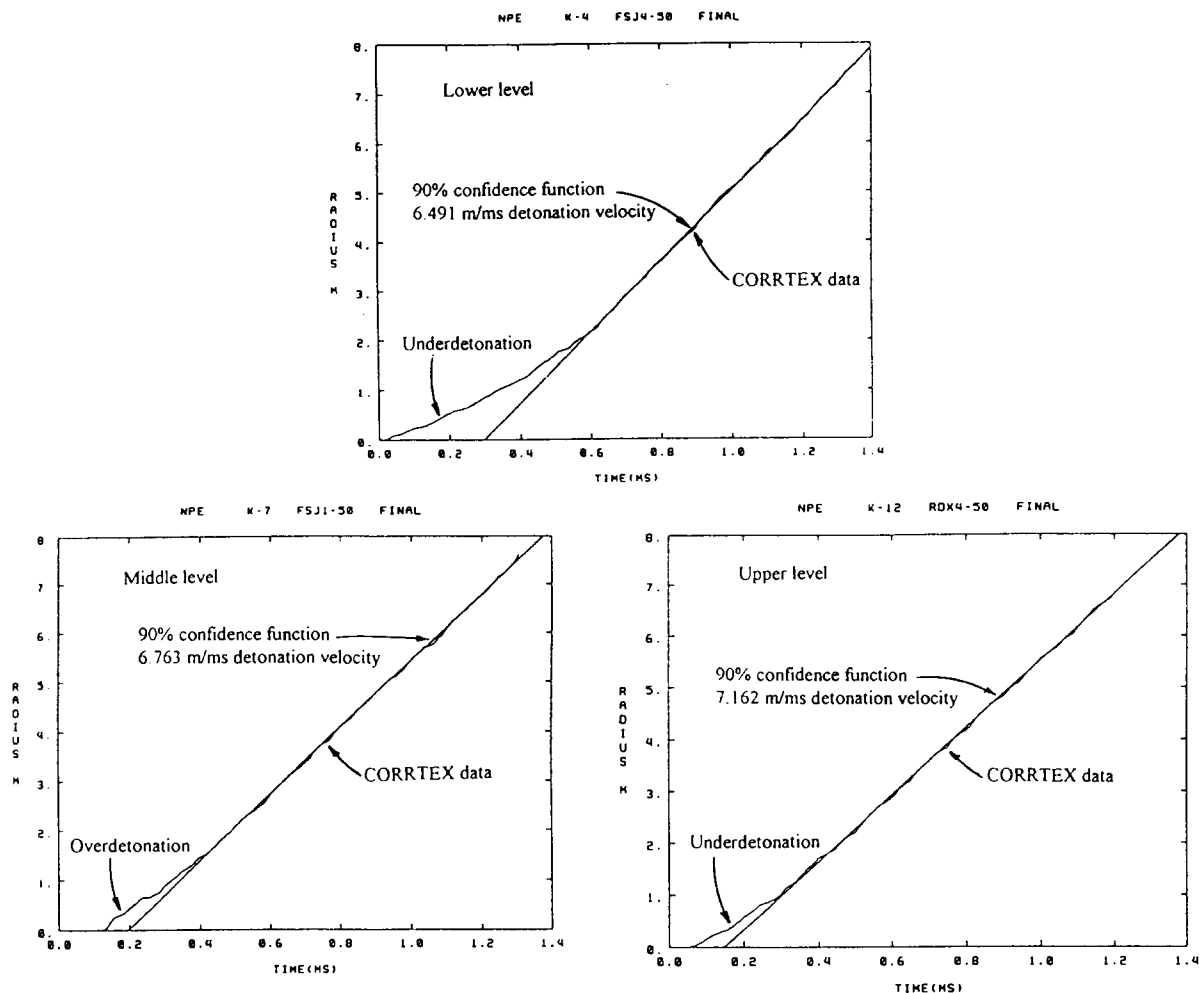


Figure 9 Plots of CORRTEX data on each of the explosive chamber levels with 90% confidence functions.

CONCLUSIONS

Initiation

The primary detonation system with boosters one, three and five (a three point axial detonation) initiated the explosive burn. The KH-2 drill hole cables K-4, K-5 and K-6 on the three installation levels, show first crush (Table 1) at 0.019 ms, 0.015 ms and 0.013 ms respectively. They were recorded on three separate commonly triggered CORRTEX recorders. An independent system cross-timing the receipt of triggers to each CORRTEX recorder and the detonation trigger further confirmed the system timing.

The data show both underdetonation and overdetonation. Plots for K-4, 5, 6, 9, 11 and 12 as illustrated in Figure 9, clearly show an accelerating explosive burn, reaching a constant velocity by about 0.400 ms (K-6 at 0.330 ms and K-4 at 0.570 ms are the extremes). The plots for K-2, 3, 7 and 8 show the rapid breakout, rolling over at about 0.400 ms to a constant velocity, indicative of overdetonation. As noted earlier, these four sensing elements, and only these four elements excluding K-1, also exhibit delayed first crush. The author suggests that perhaps this is one result of the non-centrally detonated boosters. Because there is no documentation of exact detonator position in each booster with respect to any CORTEX sensing element, it can only be suggested that detonation on the short (minimal breakout) side of the booster resulted in underdetonation while booster burn of about three-fourths the booster diameter slightly delayed the ANFO initiation, but did so at a "higher order".

Steady-State Burn

All records, including belatedly K-1, show a constant detonation velocity. The computed velocities shown in Table 3 and their standard deviations support this conclusion. Comparing data on the three levels also supports the conclusion of a gradation in velocity with depth in the emplaced explosive. This is consistent with an explosive density increasing with depth.

Does the data from the array in the middle level support a conclusion of asymmetric burn around the chamber? The middle level cables were arrayed around the chamber in the order listed in Table 3 where the 90% confidence velocities are decreasing from K-5 through K-8 and almost, K-9. Whether these differences are significant must be left to explosive experts. The author will suggest however that consideration be given to the method of emplacement which emplaced the explosive between K-5 and K-11 on the middle level and K-6 and K-12 on the upper level. The upper level results would argue against any general conclusions based on the middle level results alone. The general decrease in detonation velocities from the "near" side to the "far" side is interesting.

K-1 Revisited

A final consideration of K-1 is speculation based on the delayed first crush of K-1, the general shape of the K-1 plot to about 1.0 ms and the description of the explosive emplacement. K-1 was installed across the explosive chamber in such a manner that the mound of explosive being emplaced would push directly against the sensing element and its messenger. A scenario whereby the sensing element was pushed away from booster #1 and the UWP, down, up or any direction away, and the loops relaxed under the tension is consistent with the observed data. Approximately one-half to two-thirds of the way from the chamber axis to the wall, K-1 was anchored vertically with a nylon rope from back to K-3, K-2, K-1 and invert. This vertical anchor could have maintained the outer portion of K-1 in place, permitting the reasonably consistent data obtained over the final two meters of sensing element.

Concluding Remarks

The global objectives of the experiment were seismic and the shock induced into the chamber walls was the source of the signals observed. All evidence presented here indicate a complete and efficient explosive burn. It has been suggested that in order to model this experiment, density corrections on a centimeter scale with depth are necessary, to reflect the observed gradation of detonation velocity with depth. This seems excessive given the methods of explosive emplacement and the large uncertainties associated with detonator and booster emplacement which in turn affects absolute timing and absolute determination of the location of the axis of detonation. However, none of the uncertainties identified alters the computed velocities of detonation which are indicative of explosive performance. The explosive chamber is a far cry from the point-source modeling typically done for nuclear events and so it is hoped that the results presented here can be folded into subsequent modeling efforts and experiments. We have applied in some instances a microscope to data from an experiment whose objectives were macroscopic, but having at least made these measurements, we can with some assurance, proceed to move out from the explosive chamber.

ACKNOWLEDGMENTS

The work reported here required the cooperation of many organizations and the assistance of many individuals. They all deserve thanks, but particularly the hard working hands of Keith Alrick, Randy Bos and Brad Wright of LANL, our LLNL colleagues and the EG&G-NTS crew, who stuck in there for the long haul and kept the systems functioning over the long delays. Thanks also to J-6, EG&G-LAO, RSN, DNA, REECO and all the rest of the alphabet soup.

REFERENCES

1. B. G. Craig, J. N. Johnson, C. L. Mader and G. F. Lederman, "Characterization of Two Commercial Explosives," Los Alamos Scientific Laboratory report LA-7140 (May 1978).
2. R. G. Deupree, D. D. Eilers, T. O. McKown and W. H. Storey, "CORRTEX: A Compact and Versatile System for Time Domain Reflectometry," Twenty-seventh International Instrumentation Symposium, Instrumentation for a Blast Environment Session, Indianapolis, Indiana, April 27-30, 1980, Los Alamos Scientific Laboratory document LA-UR-80-3382.
3. T. O. McKown, "Explosive Performance on the Non-Proliferation Experiment," Los Alamos National Laboratory report LA-12748-MS, March 1994.
4. T. O. McKown, H. C. Goldwire, D. D. Eilers and F. J. Honey, "ANFO Detonation Velocity Measurements for G-7 Colony Mine Shots 79-2 and 79-3," Los Alamos Scientific Laboratory memorandum J-15-OU-79-102, (August 6, 1979).
5. L. Pirkl and M. Sullivan, H-RD-4 CORRTEX III Recorder, EG&G Energy Measurements, LAO-355, Volume I Operating Manual, December, 1990.
6. W. H. Storey, D. D. Eilers, T. O. McKown, et al., "CORRTEX II, Dual Microprocessor Controlled Instrument for Dynamic Shock Position Measurements," Conference on Instrumentation for Nuclear Weapons Effects, March 30 - April 1, 1980, Defense Nuclear Agency, Vol.II-Proceedings, pp 98-111.

MODELING THE NPE

Randy Bos

Los Alamos National Laboratory

Abstract

Calculations using the Sandia National Laboratory Eulerian hydrodynamic code **CTH** were performed to model the NPE. The calculations were primarily intended to confirm the adequacy of the tuff equation of state for near field calculations. Results compared with experimental data indicate good agreement in the range that the eos is considered to be valid (>1GPa). Results for the intermediate field are also given and show where the near field eos starts to be suspect.

Introduction

In an ongoing program to understand the equations of state that adequately describe the behavior of geologic media from the source region out to the seismic regime, the NPE provides an opportunity to compare an extended energy source in both time and space with a compact energy source. What appears to be especially appealing about the NPE is the high caliber of the data from many diverse experiments. For the NPE, a program has developed to model the experimental results in the near, intermediate, and far fields. The effort includes understanding the ANFO reaction, getting results from near to far fields with appropriate equations of state for tuff, and doing comparisons with nuclear events in the same type cavity and geologic material. This report deals with two aspects of this program, namely the HE reaction characterization and the near field results. Other aspects of the program are continuing.

Code Description

The Eulerian code **CTH** was used for the results presented in this paper. **CTH** was developed by Sandia National Laboratory (SNL) and is maintained by the **CTH** Code Development Team at SNL.

One of the attributes of **CTH** is its handling of HE equations of state (eos). Because of this and the Eulerian nature of the code, we decided to use **CTH** to run the HE burn part of the problem and compare specifically with near field experimental results. Given a good modeling of the HE burn, we could then turn to a direct comparison of the experimental near field observations with the model results using a SESAME eos for tuff (SESAME table 71243). If the results of that comparison were reasonable, we would feel comfortable

with other calculations out to the far field where coupling between 71243 and a far field eos would be necessary.

Problem Setup

A 2D calculation was set up with a chamber of radius 7.6 meters and height 5.2 meters. The chamber was partitioned into three layers of ANFO corresponding to the densities surmised from the CORTEX data obtained within the chamber (T.McKown). Table 1 gives the JWL parameters for the three layers.

The material surrounding the chamber was tuff described by SESAME table 71243 and by the elastic plastic parameters given in table 2 for a Von Mises type yield surface model. The elastic plastic parameters were obtained from the eos to be used for the far field calculations (J.Kamm). Although the CTH model chosen for handling the elastic-plastic properties of the tuff is simplistic, for the purposes of the calculation described above it was felt to be an adequate first order approximation.

TABLE 1

JWL (jwl units)	BOTTOM	MIDDLE	TOP
rho 0	1.3573	1.2859	1.2004
A	4.824512	4.824512	4.824512
B	.141036	.141036	.141036
C	.01537	.01413	.01270
R1	4.9355	5.20958	5.58064
R2	1.94504	2.05304	2.19927
omega	.55	.55	.55
D	.716	.68499	.64601
P	.16	.16	.16

TABLE 2

yield strength	300e06 Pa
poisson ratio	.274
yield at zero pressure	469.5e06 Pa
dy/dp	-.4137
csmn	2319.

HE SIMULATION

The experimental observations of the HE burn obtained by the CORTEX sensors (T.McKown) showed three items of relevance to modeling the burn. First, the burn did not stabilize until after a few meters from the initiators. Second, the burn velocities of the three CORTEX sensor levels (low, middle, and high) were graduated with the slowest burn at the top level and the fastest burn at the lowest level. Third, the burn front impacted the wall of the chamber first at the top level and last at the bottom level.

We decided that we could not model the under-initiation of the HE with the information available. Since at most this would comprise less than a eighth of the total burn mass, we felt it would be safe with respect to the total energy released to ignore this effect. The second observation implied some sort of material difference, probably density gradients , from top to bottom of the chamber. Assuming cylindrical symmetry of the ANFO, we decided to use three layers of ANFO having the densities calculated by backing out the observed burn velocities. Using the original JWL parameters supplied by P.Souers of LLNL, J.D. Johnson produced the JWL parameters listed in table 1.

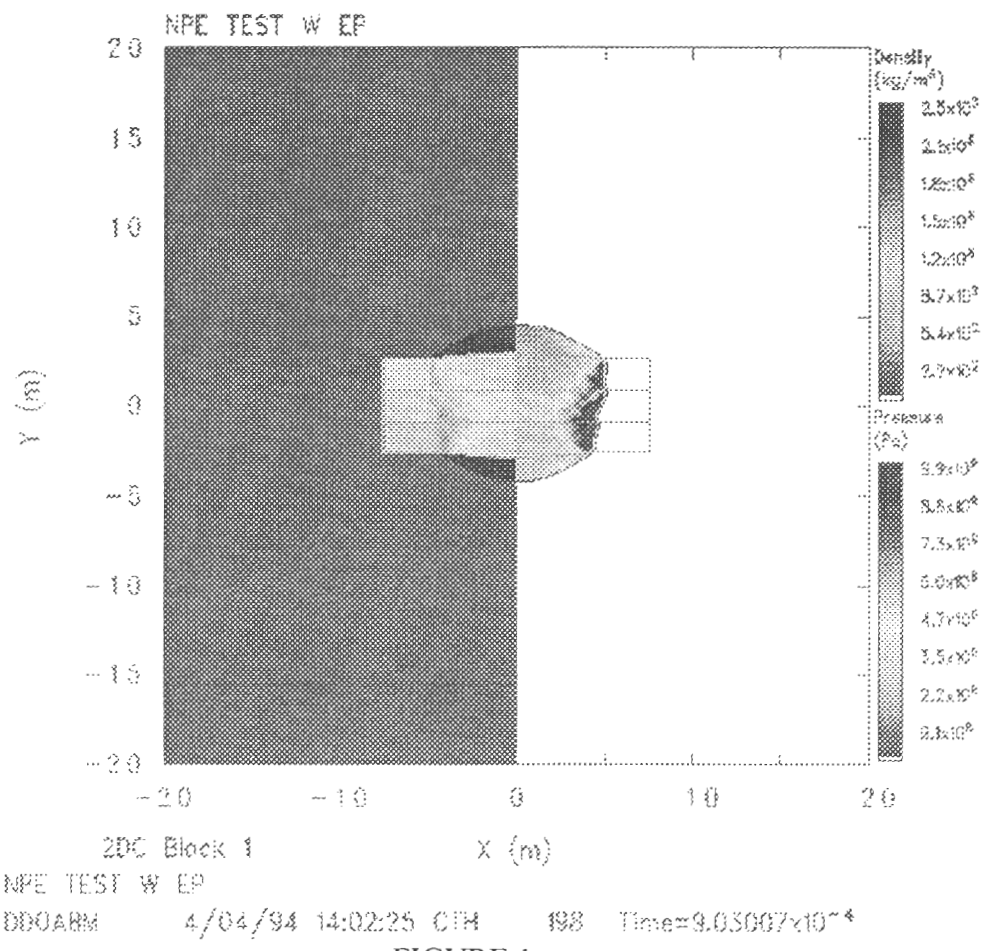


FIGURE 1

The last observation was the exact opposite of the previous observation. The part of the burn front impacting the wall of the chamber first was the top layer which had the slowest burn velocity. To model this, we had to do two things. First, the initiation of the burn in the lower two layers had to be delayed with respect to the upper layer. Second, the top initiator had to be moved upward in the model from its true position in the chamber. This was to keep the burn front from getting into the middle layer prior to the middle initiation and then having a burn front race ahead in the middle layer. As can be seen from Figure 1, this race condition still posed somewhat of a problem. Figure 2 shows the burn front just prior to impact on the chamber wall. Note that Figures 1 and 2 show density on the left half and pressure on the right half.

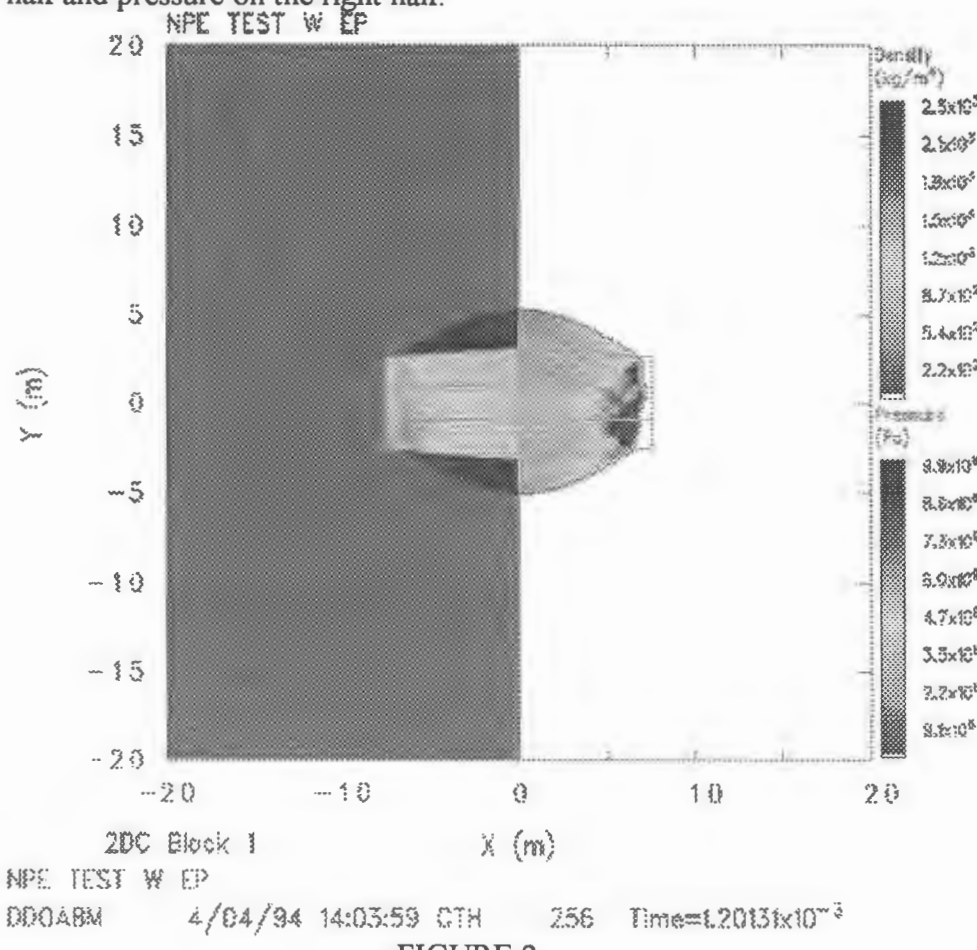


FIGURE 2

The result of this setup was that the burn front hit the wall at 1.25ms whereas the observations show an impact closer to 1.3 ms (T.McKown). It does hit the wall first at the top followed correctly by the other two layers. The CJ pressure reached was 13 GPa. The amount of energy produced was 1.05 kt. It is interesting to note that after the burn front hits the wall, some of the energy is reflected back toward the center of the chamber. After reaching the chamber center it rebounds and produces another shock about 6 ms after the first. Figure 3 shows the propagation of the second shock at the 13 meter location. This shock is much reduced in amplitude and spread out in time. As time progresses it falls further behind the main shock and continues to spread out in time but the amplitude falls

off much less rapidly than the initial shock wave. Since this observation is in the region for which the eos is probably not as good, these results will await confirmation from other simulations.

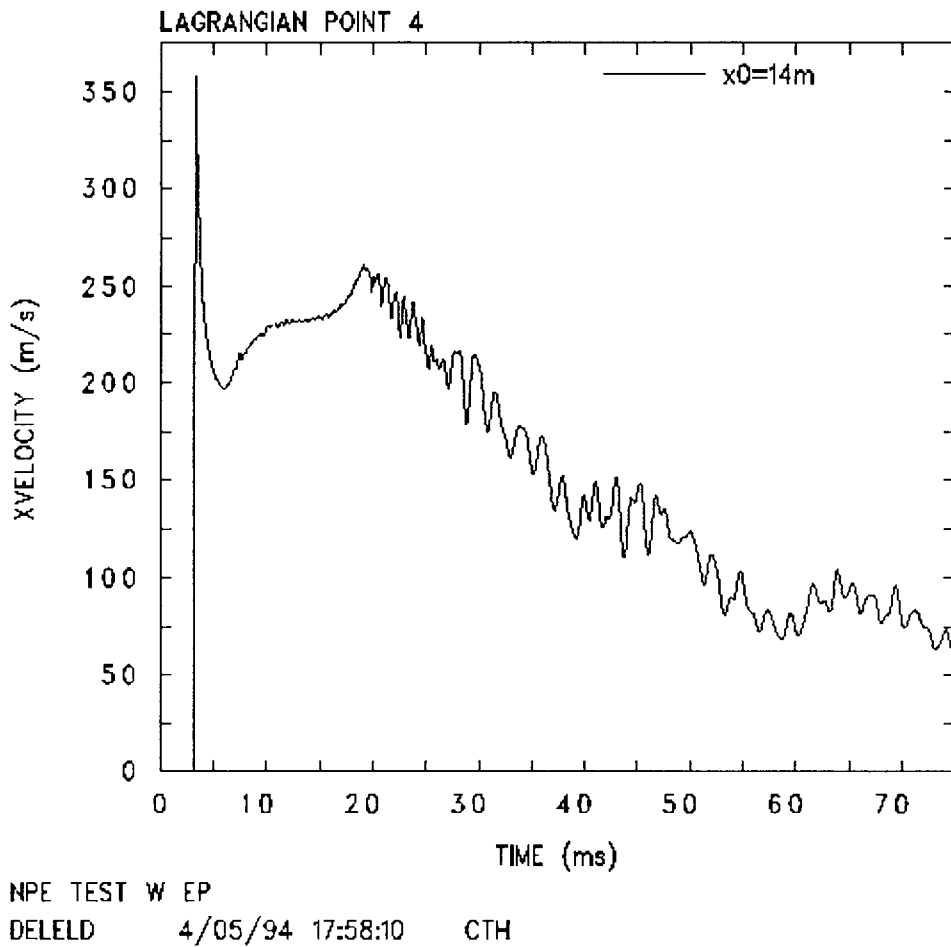


FIGURE 3

Near Field Comparisons

The SESAME table 71243 should be a good description of the tuff above 10 GPa and a fair description down to 1 GPa. This pressure range was found out to a radius of 20 meters from the center of the chamber. Figures 4-6 show a comparison of the observed shock front time of arrival (TOA), particle velocity, and pressure with model results. The pressure observations are from SNL (C. Smith), velocity observations from SNL (C. Smith) and LANL (B. Wright, et. al.), and TOA are from the previous two experiments and the CORTEX sensor data (T. McKown). All three Figures show that there is generally good agreement of the model with the experimental results in the near field. The TOA Figure (Figure 4) shows deviation even below 20 meters as expected if the eos is only approximately correct. It should be noted that the peak velocity measurements from the closest ASM gauges were obtained by backing out the observed velocities from Lexan,

then grout, and then into the tuff. The values shown here are the best comparison with the model and were obtained with a porous grout model (B.Wright, et. al.)

TIME OF ARRIVAL COMPARISONS INTERMEDIATE FIELD

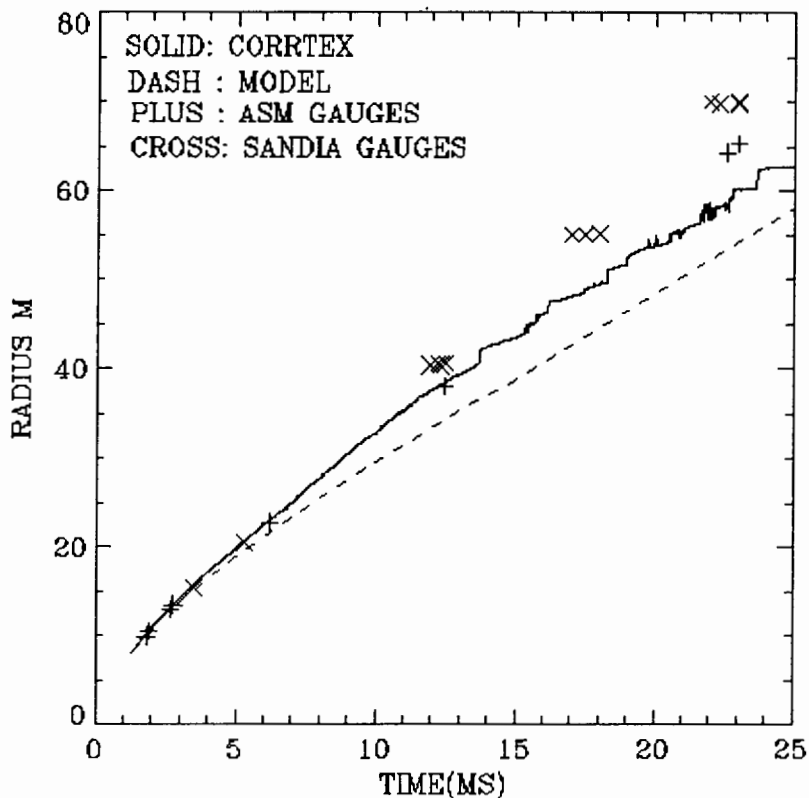


FIGURE 4

Intermediate Field Comparisons

Figures 4-6 from 20 meters out to 100 meters show a comparison in the intermediate field of the TOA, velocity, and pressure. As expected, the good agreement seen in the near field is lost in the far field. Again the TOA plot (Figure 4) shows the increasing deviation between the experimental observation and model results. Interestingly, the pressures actually agree well even out to the furthest gauge (Figure 6)

PEAK VELOCITY COMPARISONS INTERMEDIATE FIELD

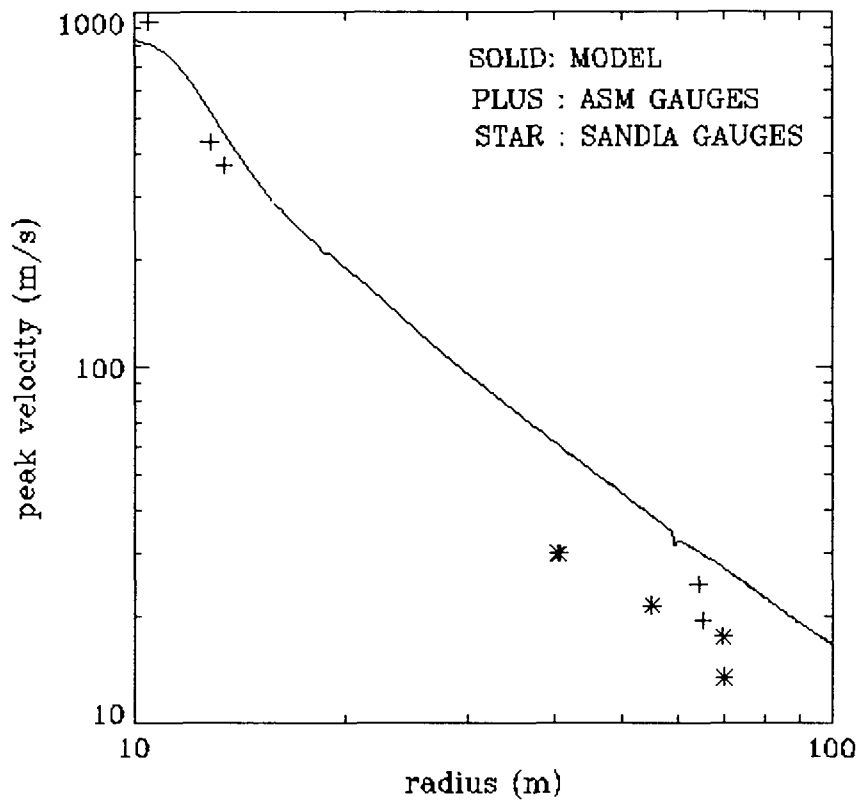


FIGURE 5

Conclusion

This model simulation shows that the HE can be modeled sufficiently well to agree with the near field experimental observations to the accuracy of the eos used. The simulation results also indicate SESAME table 71243 eos for tuff is good for representing the near field observations and good for use as a transition eos to the far field eos. Further work is continuing using the far field eos.

PEAK PRESSURE COMPARISONS INTERMEDIATE FIELD

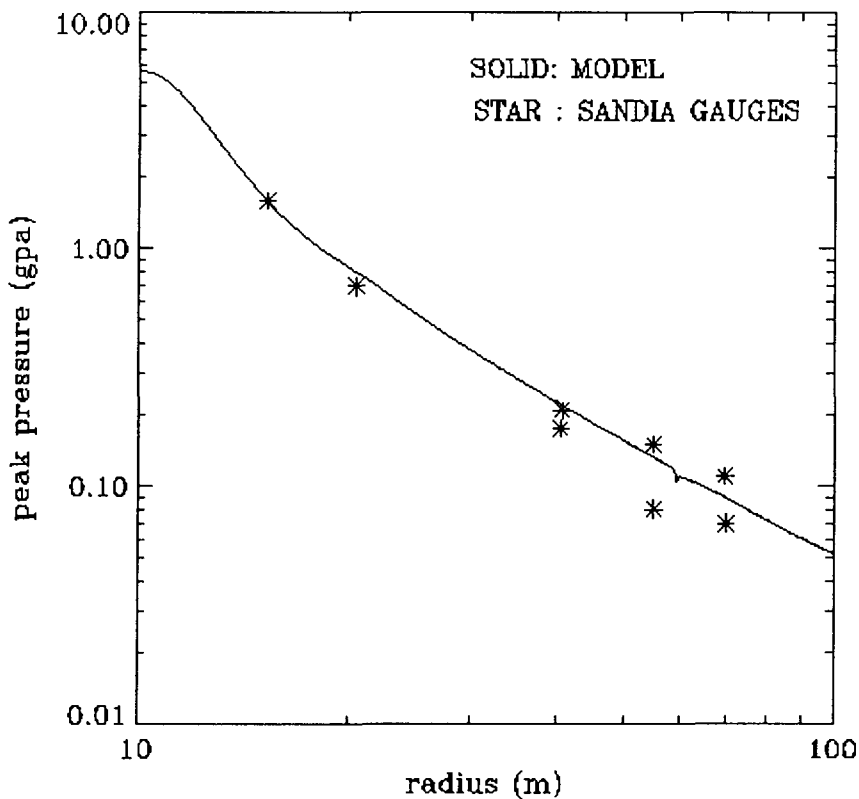


FIGURE 6

References

1. T. O. McKown, Explosive Performance on the NPE, these proceedings.
2. J. Kamm, EES-3 Los Alamos National Laboratory, private communication.
3. P.C.Souers and D.B.Larson, TIGER Calculations and the NPE Energy Yield, these proceedings.
4. J.D.Johnson, T-1 Los Alamos National Laboratory, private communication.
5. C.Smith, NPE Close-In Stress and Motion Measurements, these proceedings.
6. B.L.Wright, K.R.Alrick, and J.N.Fritz, Axisymmetric Magnetic Gauges, these proceedings.
7. T. O. McKown, Induced Shock Propagation from the NPE, these proceedings.

PRESHOT PREDICTIONS FOR THE NEAR-SOURCE REGION IN THE NON-PROLIFERATION EXPERIMENT

Dan F. Patch, J. Eddie Welch and James Zerkle
SAIC/Simulation Technology Operation,
10260 Campus Point Drive
San Diego, CA 92121

1. NUMERICAL STUDIES

This paper summarizes a number of one and two-dimensional, ground motion calculations made in support of the Non-Proliferation Experiment (NPE), a 1 KT high explosive shot fired on 22 September 1993 at the Nevada Test Site. These calculations were sponsored by the Defense Nuclear Agency's late-time containment program, and were completed well before the test was executed. They addressed a variety of test design, analysis and construction issues, and sought to identify any potential safety concerns.

The test site model used in these calculations was based in large part on earlier work performed at SAIC and by other Defense Nuclear Agency (DNA) contractors for the nearby underground nuclear test, code named MISTY ECHO. In particular, to obtain physical property and quasi-static material response data for the site, a number of core samples recovered near the MISTY ECHO working point (WP) were tested by TerraTek. We then used these data to develop a numerical response model for the site.

Our initial test design studies for the NPE test consisted of a series of one-dimensional calculations using our Lagrangian code, SIMONE. These calculations examined the sensitivity of stress and particle velocities to be measured near the charge to uncertainties in the equation of state (EOS) for the high explosive. This information was needed by Sandia National Laboratories (SNL) to properly set gauge ranges for their near-field instrumentation, and by DNA to estimate the level of damage that might be expected in nearby open tunnels. An additional 1-D calculation was run using a nuclear source in place of the HE charge. Results from this calculation were used to establish a preshot estimate for the HE/nuclear energy equivalence factor for the nearly saturated tuff medium found at the NPE site. Finally, we felt that these preshot calculations were needed to provide a qualitative measure of the current predictive capability of ground motion calculations for a familiar and well characterized medium.

Following the 1-D calculations, we completed a series of more detailed two-dimensional simulations in STAR, a well developed finite difference,

Lagrangian code. These calculations explicitly modeled the high explosive burn and the near-source, dynamic ground motion phases of the experiment. Both the one- and two-dimensional calculations included a hydrostatic overburden stress, but layering and gravitational gradient effects were not modeled. A central objective of the 2-D calculations was to define the extent and evolution of non-isotropic source effects associated with the non-spherical charge geometry and initiation. These effects were of concern for close-in stress measurements, and of potential interest in the far-field.

2. EQUATIONS OF STATE

2.1. Site Response Model

Over the years, a series of material response models have been developed for use in nuclear test containment calculations. These models were based on laboratory test data obtained using core samples recovered from the region of greatest interest in each test. Although this earlier work forms the overall basis for the material model used in our calculations, data and models from older nuclear tests were not directly employed in the NPE study. Rather, the NPE site model was based on material test data developed for the nearby MISTY ECHO nuclear test. This was necessary because the traditional set of geophysical and quasi-static laboratory material test data normally developed for a nuclear test was not available for the NPE event. Fortunately, MISTY ECHO was fielded in close proximity to NPE (~ 270 m) and in a very similar geologic setting. Therefore, physical properties and the mechanical response of the MISTY ECHO tuff should be representative of the NPE site response. The particular model developed for the NPE test was first used to study the potential for gauge inclusion artifacts in free-field stress measurements obtained by Sandia on the MISTY ECHO event. Table 1 summarizes some of the more important EOS parameters used in the numerical model.

It has long been known that shock attenuation near the charge (*i.e.*, inside the elastic radius) is strongly influenced by the porous crush response of the rock. Not only is the total air-filled porosity important, but the model must accurately capture the details of the crush behavior (*i.e.*, the shape of the crush curve) and the unloading response. Figure 1 illustrates the crush response used in our NPE studies. The pressure-volume (p-v) behavior shown in this figure was determined by averaging laboratory data that showed considerable variation from sample to sample ($V_a \approx 0.25\text{--}1.5\%$), as has typically been our experience in Area 12 tuffs at NTS.

The NPE calculations utilized a relatively simple elastic-plastic deviatoric response model that incorporated strength reduction for shock damaged material. Figure 2 illustrates the initial yield response for undamaged material, as determined by averaging measured stress difference curves obtained in uniaxial strain tests on MISTY ECHO tuff. The response of fully

damaged tuff that has been loaded to a peak pressure of more than 400 MPa is also shown in this figure. The strength of material loaded to intermediate pressures between 100 and 400 MPa is interpolated from these two curves as a linear function of the minimum specific volume reached by the sample during compression. This damage model formulation was developed using quasi-static laboratory test data on tuff, and has been employed in a number of earlier containment calculations. A radial return (non-associative) flow rule was used in this study to avoid the effects of dilation that an associative flow rule would have produced in material located near the charge.

Table 1. NPE tuff equation of state constants.

Variable	Physical Constant	Value
ρ_0 (gm/cm ³)	Ambient Density	1.946
K_0 (GPa)	Ambient Bulk Modulus	7.50
G_0 (GPa)	Shear Modulus	2.50
V_a (%)	Initial Air-Void Content	0.70
A (GPa)	Tillotson EOS Constant	7.50
B (GPa)	Tillotson EOS Constant	50.0
$a = b = e_s'$	Tillotson EOS Constants	0.0
α	Tillotson EOS Constant	5.0
β	Tillotson EOS Constant	5.0
e_s (erg/gm)	Tillotson EOS Constant	4.5×10^{11}
e_m (erg/gm)	Tillotson EOS Constant	1.0×10^{11}
a (MPa)	Virgin Failure Surface	22.33
b	Virgin Failure Surface	0.025
c (MPa)	Virgin Failure Surface	16.50
d (MPa ⁻¹)	Virgin Failure Surface	0.026
a' (MPa)	Damaged Failure Surface	22.33
b'	Damaged Failure Surface	0.025
c' (MPa)	Damaged Failure Surface	19.83
d' (MPa ⁻¹)	Damaged Failure Surface	0.006

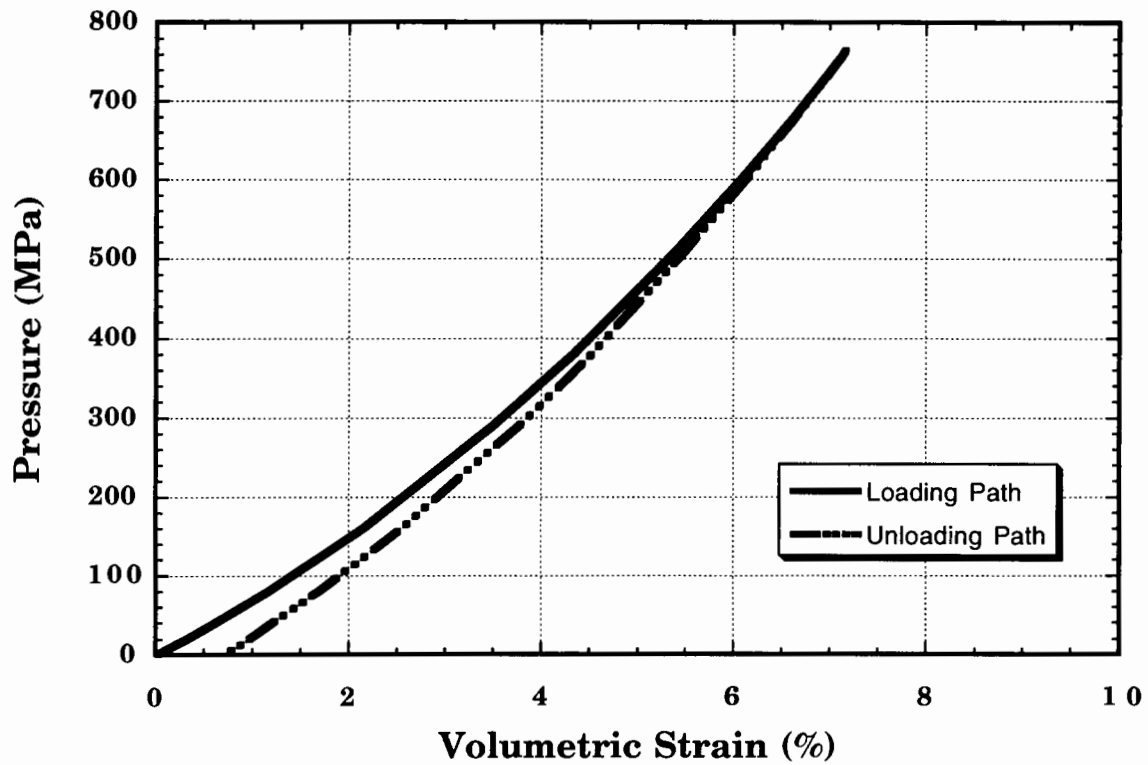


Figure 1. NPE tuff crush response.

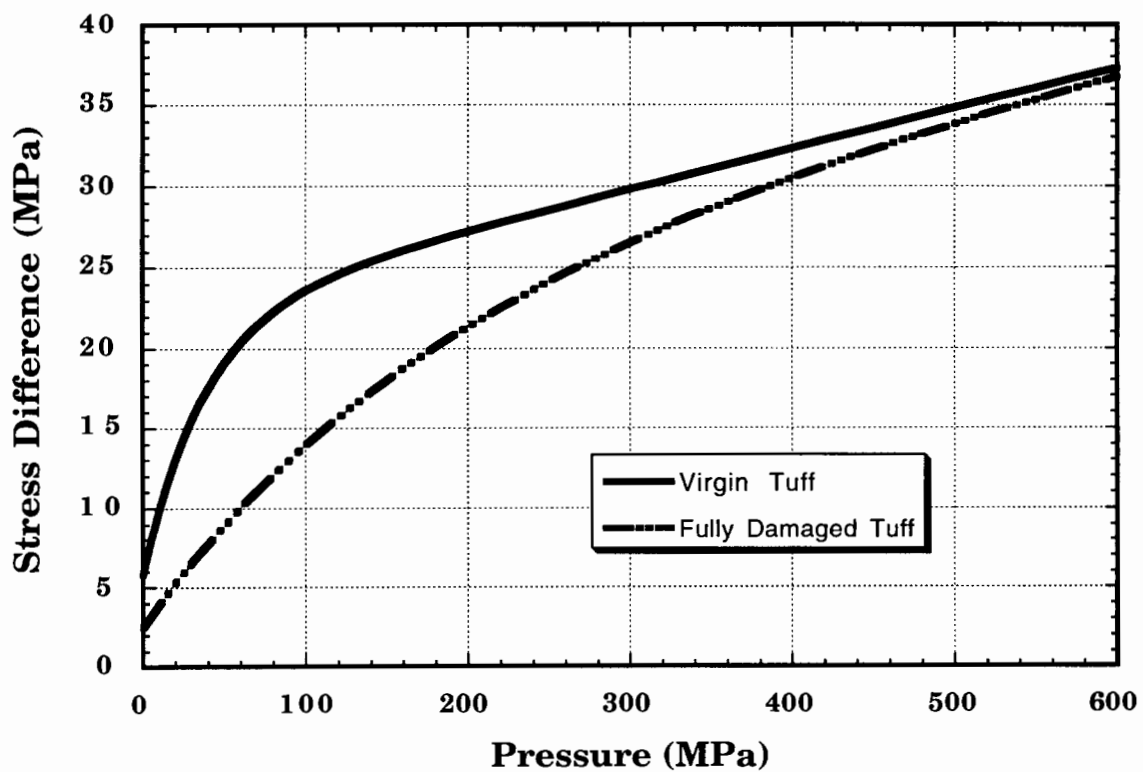


Figure 2. Yield surface for virgin and fully damaged NPE tuff.

2.2. NPE Charge Equations of State

Our one-dimensional studies were begun more than a year before the NPE test was executed. At this early date the charge composition was uncertain and therefore detailed high explosive EOS data were not available. Given the fundamental importance of the source characteristics to the prime objective of the experiment, we believed that it would be prudent to examine the sensitivity of the experiment to the explosive mixture formulation and to uncertainties in the high explosive equation of state. Results of these calculations are summarized in the following Section 3. In this section we outline the HE EOS models that were used in our NPE calculations.

Given the substantial mass of explosive required for the NPE test, it was clear that the chosen explosive should be inexpensive. As discussed by Olsen at LLNL, some type of ammonium nitrate-fuel oil (ANFO) mixture was the obvious choice, although technically ANFO is a blasting agent rather than a high explosive. Further consideration of the charge emplacement requirements suggested that a liquid ANFO product would be more desirable than a dry ANFO product. Initially, a 70% ANFO-30% emulsion mix was recommended. Unfortunately, in the absence of HE characterization data for the actual explosive mixture, the proprietary nature of the emulsion considerably increased the uncertainty regarding the exact detonation characteristics of the charge. Adding to this uncertainty were questions regarding the performance of such a massive charge.

All of our calculations used the familiar JWl formulation to model the equation of state for the explosive. Our initial HE model (Model 1) was based on Olsen's estimated performance for a balanced (5.5% fuel oil) ANFO explosive. In order to examine the sensitivity of the calculational results to the late-time cavity gas pressure, a second charge model (Model 2) was developed using a higher value for the JWl EOS parameter " ω " while maintaining the Model 1 values for C-J pressure, detonation velocity, density and energy release (see Table 2). A third EOS (Model 3) was developed for the 70-30 charge by using LLNL explosive test data obtained on a 75% ANFO-25% emulsion mixture adjusted to the energy density of the 70-30 mixture. Finally, relatively late in the design phase of the NPE test, the charge mixture was changed to an RX-HD blend, which was essentially a proprietary 50-50 ANFO-emulsion mixture. Data supplied by the manufacturer from chemical burn codes were used to develop the HE EOS for this mixture, designated Model 4 in Table 2.

3. ONE-DIMENSIONAL STUDIES

Peak stress versus range predictions from most of our one-dimensional studies for the NPE event are compared to the test data in Figure 3. Note that all of the studies (including the 2-D work discussed in Section 4) were completed well before the test.

Table 2. Equation of state parameters used for the various high explosive models used in the NPE calculations.

Variable	Physical Constant	Model 1 70–30	Model 2 $\omega = 0.3$	Model 3 75–25	Model 4 50–50
ρ_0 (gm/cm ³)	Ambient Density	1.280	1.280	1.280	1.340
e_0 (cal/gm)	Energy Release	872	872	872	770
u_{cj} (km/s)	Detonation Velocity	5.40	5.40	6.448	6.849
A (GPa)	JWL Constant	200.02	185.00	363.67	424.50
B (GPa)	JWL Constant	6.7575	6.5000	9.6535	9.6535
R ₁	JWL Constant	6.4026	6.4026	6.4026	6.4026
R ₂	JWL Constant	1.5872	1.3000	1.9840	1.9840
ω	JWL Constant	0.220	0.300	0.220	0.22
Γ_{cj}	C-J Gamma	2.950	2.950	2.950	3.307
P _{cj} (GPa) [†]	C-J Pressure	8.25	8.25	12.50	14.40

[†] Note: Calculated from JWL EOS.

Close to the source, the “Model 1 – Hot Gas” calculation is much lower than the “Model 1 – ANFO Estimate” calculation; crossing over at a range of ~18 meters and then overshooting the “ANFO Estimate” by roughly 10% before returning to essentially the full detonation result by a range of 100 meters. The two Model 1 calculations are identical, with the exception that the “Hot Gas” calculation was initiated as fully burned HE at normal density (*i.e.*, equivalent to a “single cell” deflagration), while the “ANFO estimate” study utilized a detailed detonation calculation through the 32 cell region in the HE portion of the grid. All other HE calculations in Figure 3 included a complete burn phase. The objective of this calculation was to investigate the level of error to be expected if the charge were simply modeled as a high pressure, HE gas. For reference, note that an error of 10% in peak stress translates to an equivalent energy error of approximately 30%.

Results shown in Figure 3 for Model 2 address the issue of the effect of the JWL constant “ ω ” which controls the late-time cavity pressure during the highly expanded phase of the explosive product. We had some concern that the value, $\omega = 0.22$, determined by LLNL for the 75–25 HE mixture might be too low based on typical values for other similar explosives. As discussed in Section 2, several other JWL parameters were adjusted slightly in Model 1 to give similar detonation characteristics for the Model 2 HE. As would be expected, peak radial stress for Model 2 slowly diverges with range, so that

by a range of ~100 meters this HE EOS gives a distinctly higher peak stress in comparison to the other HE models.

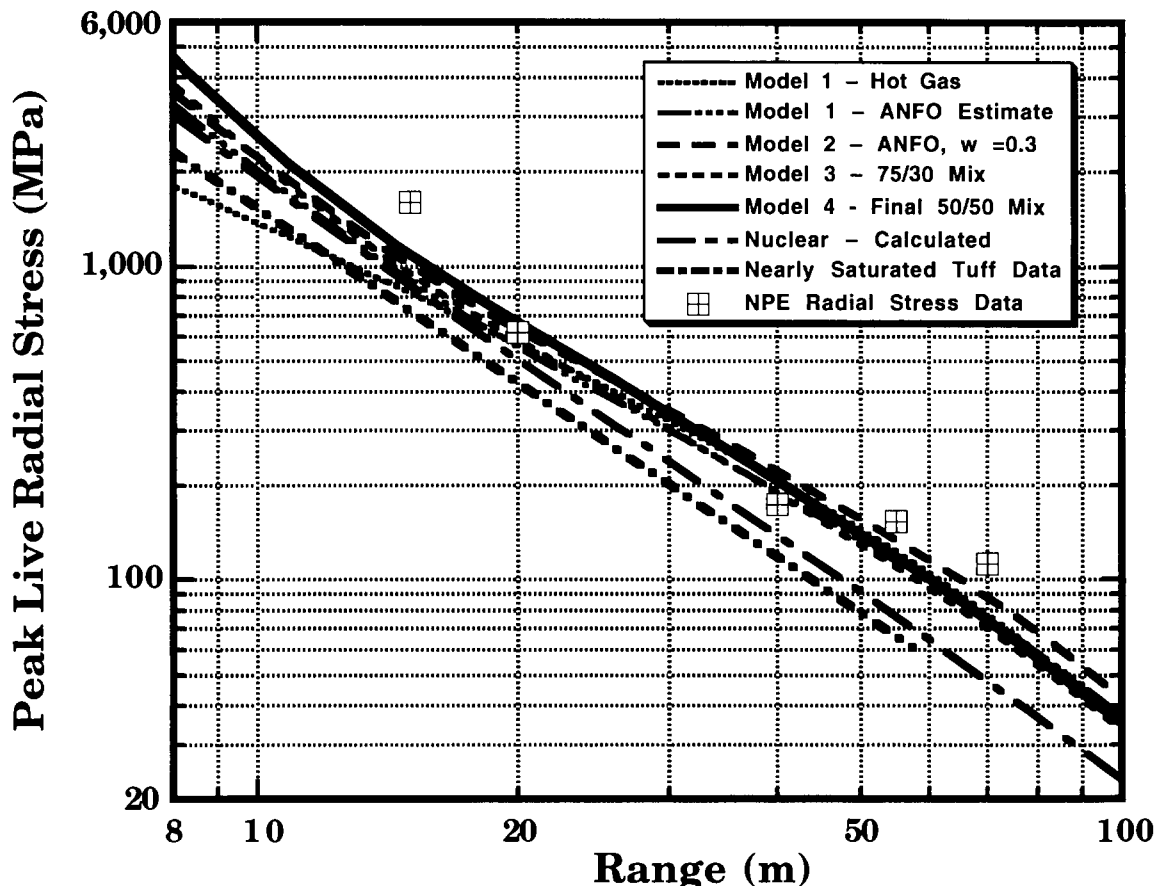


Figure 3. Peak radial stress for SAIC, 1-D NPE calculations using various JWL models for the explosive EOS. Also shown are an average response for DNA tests in wet tuff cube root scaled to 1 KT nuclear yield as determined by Robert Bass at Sandia, and an SAIC nuclear calculation (at 1 KT) using the NPE site model.

The calculated nuclear case is slightly above, but well within the scatter of the nuclear test database that was used to establish the “Nearly Saturated Tuff Data” curve in Figure 3. Since the ~0.70% air-void content measured at the NPE site is on the low edge of our experience in Area 12, results from the nuclear calculation are as expected, and we believe that they should be a good estimate of the performance of a 1 KT nuclear test at this site. If this is true, then the more effective nature of the NPE explosive in comparison to a nuclear source is evident from the results shown in Figure 3.

In summary, all of the high explosive models gave similar peak stress predictions at the more distant ranges, except for the high “ ω ” model (Model 2), with its higher late-time cavity gas pressure. Given the scatter in the data, all of our HE calculations are in essentially similar (good) agree-

ment with the NPE data. Neither our 1-D NPE calculations nor the NPE ground motion data are consistent with the lower level of peak stress expected for a 1 KT nuclear test at this site, based on both calculations and data. Our studies suggest that the NPE HE/nuclear equivalence factor was close to a factor of two (depending on the variable and range of interest).

4. TWO-DIMENSIONAL CALCULATIONS

4.1. Calculational Studies

Our initial 2-D calculation (code named EQR) used the Model 3 EOS discussed in Section 2 to characterize the charge. In this calculation the charge was initiated by igniting the row of cells on the centerline of the numerical mesh (10 cells, or 0.15% of the charge mass). The second calculation (EQY) utilized the same charge initiation, with the HE EOS changed to Model 4 (see Table 2). The final 2-D calculation (EQZ) changed the charge initiation from a line source to a center detonation scheme (a 3 by 3 block of cells), as sketched in Figure 4. Symmetry about the mid-plane of the charge allowed us model the charge in half-space using a total of 300 cells, with all 2-D calculations using the same mesh geometry. A slip surface was used at the charge boundary to allow HE gas flow along the inner surface of the cavity. The outer grid boundary remained beyond the shock front during the calculations. Our first calculation, EQR, was run to a residual stress time of 250 ms. To carry the calculation out to this late time the basically rectangular 2-D mesh was overlaid into an extended R- θ mesh geometry at 40 ms. The remaining 2-D studies were stopped at 10 ms since we were only interested in studying close-in charge dynamics in these calculations.

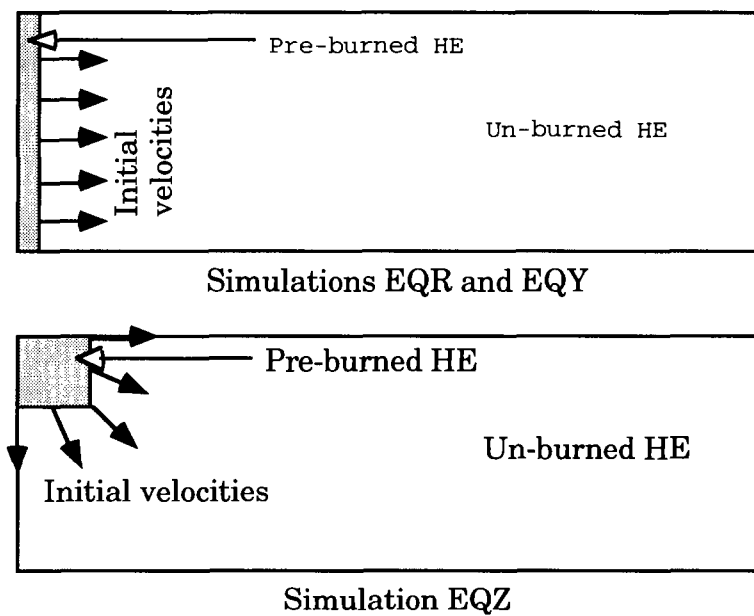


Figure 4. Schematic of pre-burn regions for 2-D calculations.

4.2. Influence of 2-D Charge Geometry

The line-initiated detonation produces relatively low initial pressures on the flat faces of the cavity as the detonation front burns radially outward, normal to their surfaces. As shown in Figure 5, by a time of 2 milliseconds, stagnation of the detonation shock against the outer charge boundary launches a strong, non-spherical shock into the surrounding tuff medium.

After reflecting from the outer boundary, the shock in the HE gas rapidly propagates back toward the center of the cavity (see Figure 6). Pressure from this shock acts on the top and bottom of the cavity to begin the process of converting the free-field shock structure into a more uniform, spherical configuration. Indeed, the planar geometry of the these faces produces a considerably stronger shock in the vertical directions at intermediate times, as illustrated in Figure 7. This effect noticeably enhances both the peak stress and impulse versus range curves for the ground shock traveling inside a range of roughly 70 meters. Note that the cavity still has an aspect ratio of about 1.3 to 1 at 10 milliseconds in Figure 7, but that it is rapidly growing toward its final nearly spherical geometry. At late-times the residual stress field and cavity shape in EQR are closely approximated by the Model 3, 1-D results.

Comparing the 2-D results to the 1-D results shows that peak stresses along the mid-plane of the charge (*i.e.*, the gauge horizon in the test) are significantly above the expected 1-D prediction only inside a range of about 20 meters. Closer proximity to the charge than would be the case for a spherical charge geometry is responsible for this enhanced close-in peak stress level. Calculated 2-D time histories at 15 and 20 meters are in excellent agreement with the SNL data. Beyond 20 meters, both the one- and two-dimensional code results are consistent with the SNL near-field stress and particle velocity data. At more distant ranges (beyond 70 m) calculations that explicitly model the geostructure of the site are needed, although the simple one-material site model used in this study still gives a credible approximation to the SNL velocity data at 200 meters.

4.3 Charge Initiation Effects

Calculated stress contours for the center detonated charge are shown in Figure 8 for comparison to the line-detonated case (see Figure 6). Differences in the shock systems produced by the two different charge initiation geometries are pronounced only at the earliest times. By a time of 5 milliseconds, differences in the shock profiles are very small. We conclude that the two initiation geometries are essentially equivalent for the purposes of the experiment, so that choosing between the two alternatives should be governed by safety and other operational considerations.

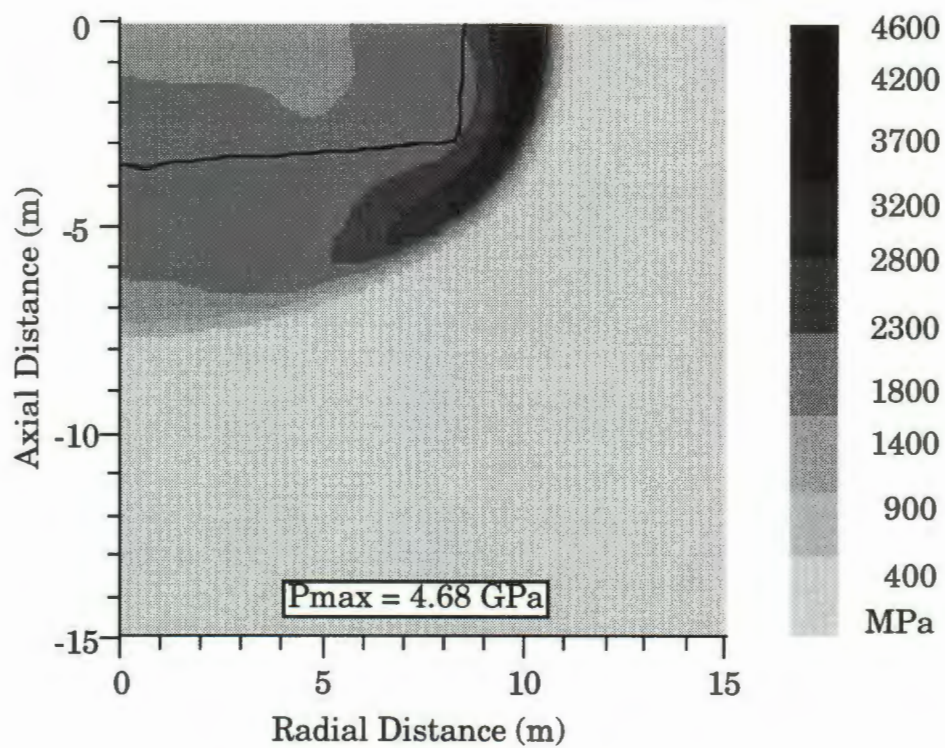


Figure 5. Pressure at 2.0 ms for calculation EQY.

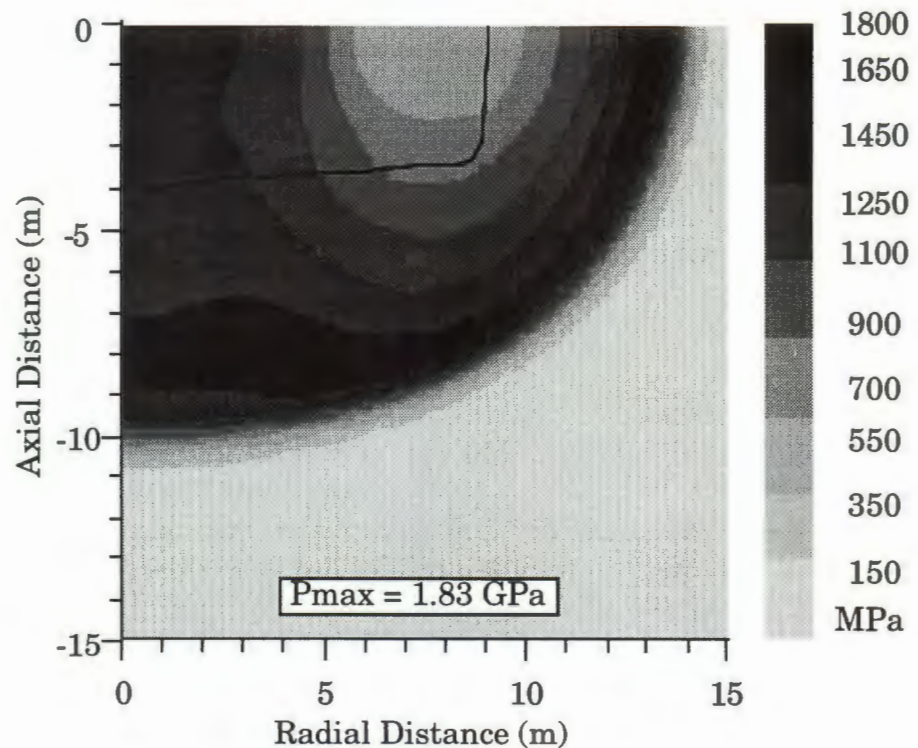


Figure 6. Pressure field at 3 ms for calculation EQY (line detonated).

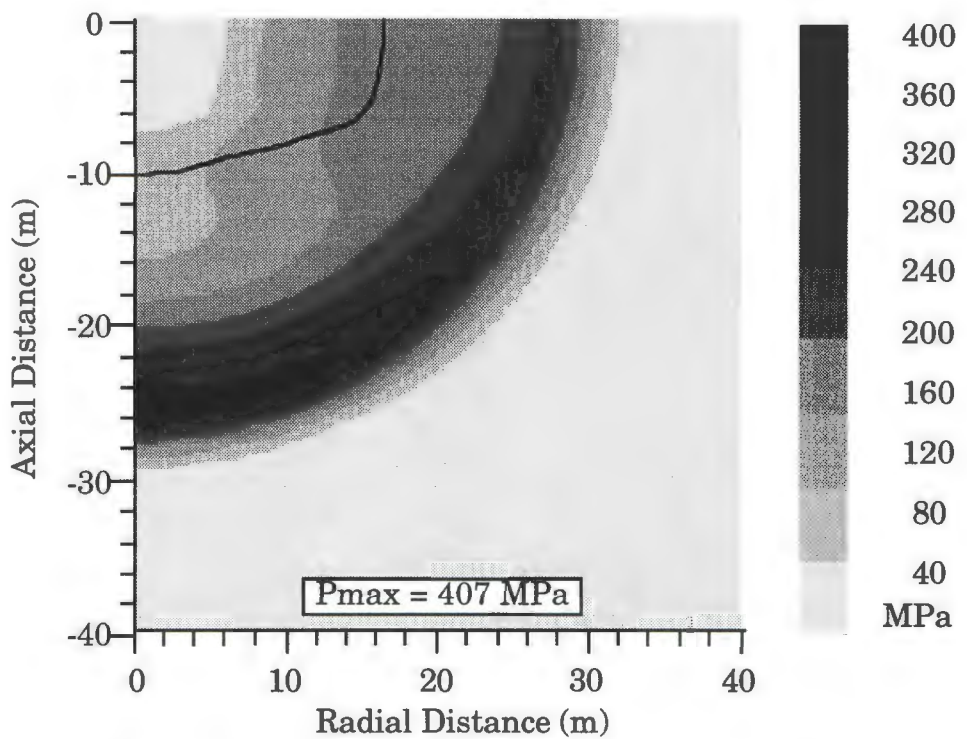


Figure 7. Pressure at 10.0 ms for calculation EQY.

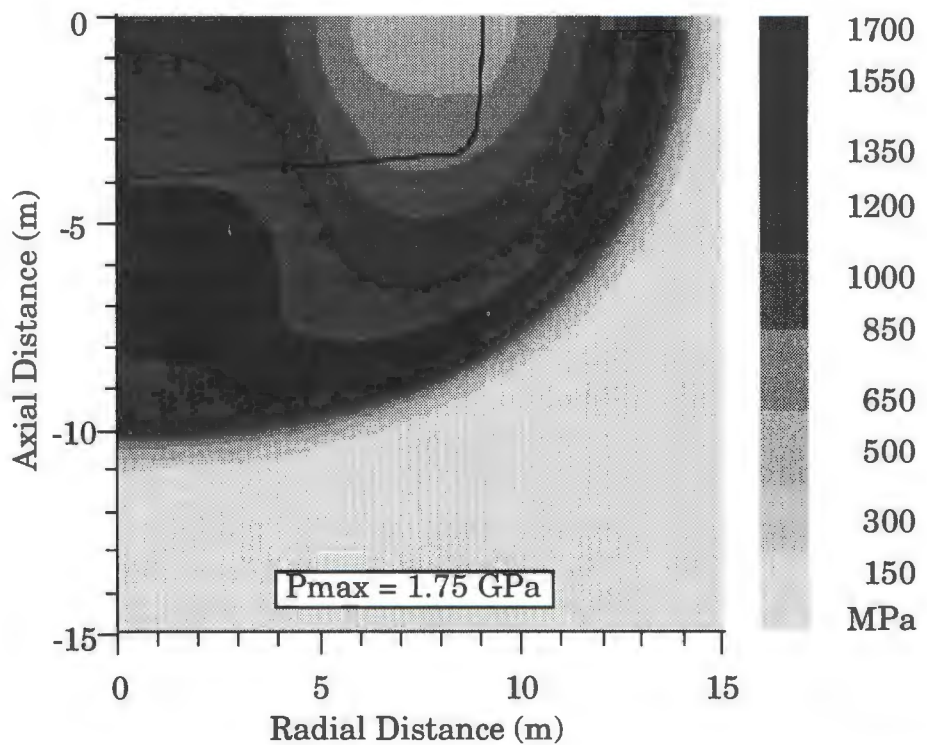


Figure 8. Pressure field at 3 ms for calculation EQZ (point detonation).

THE INFLUENCE OF MATERIAL MODELS ON CHEMICAL OR NUCLEAR-EXPLOSION SOURCE FUNCTIONS *

L. A. Glenn

P. Goldstein

University of California

Lawrence Livermore National Laboratory

prepared for submittal to:

*DOE Symposium on the Non-Proliferation Experiment Results
and Implication for Test Ban Treaties*

ABSTRACT

Physical models of explosion sources are needed to explain the variations in the performance of existing discriminants in different regions, and to help develop more robust methods for identifying underground explosions.

In this paper, we assess the sensitivity of explosion source functions to material properties by means of numerical simulations. Specifically, we have calculated the effect of varying the yield strength, overburden pressure, and gas porosity on the spectra of the reduced velocity potential for both nuclear and chemical explosions, and compared these with experimental results derived from free-field particle acceleration and regional seismic (LNN) data. The chemical-explosion calculations were intended to simulate the kiloton experiment recently conducted in Area 12 of the Nevada Test Site (NTS) that has been dubbed the Non-Proliferation Experiment (NPE).

We found that the asymptotic (long period) value of the reduced displacement potential, ϕ_∞ , for explosions with the ANFO blasting agent used in the NPE, was larger than that derived for a tamped nuclear explosion of the same yield by a factor of 1.9, in good agreement with the experimental results derived from free-field particle velocity measurements, and also with $m_b(P_n)$ data from the Livermore Nevada Network (LNN). Beyond the corner frequency, the spectra calculated for the chemical and nuclear explosions were indistinguishable, also in good agreement with experiment. It was found possible to match the spectral characteristics by varying both the yield strength and the gas porosity, but the strength required to obtain this match was considerably less than measured in laboratory experiments with small cores pulled from the vicinity of the emplacement. Previous experience, however, is that laboratory measurements on core-sized rock samples may not be representative of the extant rock mass from which the samples derive.

LNN DATA

Chemical and nuclear explosives are fundamentally different in at least two ways: 1) the energy density is initially much higher with nuclear explosives, and 2) the pressure (at the same energy density) is significantly higher with chemical explosives. Both of these properties are responsible for the higher predicted value of ϕ_∞ when concentrated chemical explosives are substituted for nuclear explosives of the same yield (Glenn, 1993; Glenn and Goldstein; 1994). Figure 1 shows the seismic amplitude as a function of scaled (initial emplacement) cavity radius, as derived from the LNN; note that the abscissa, $r_0 W^{-1/3}$, is the inverse cube root of the initial energy density and the ordinate is effectively the yield-scaled seismic amplitude. The points numbered 1-18 derive from nuclear explosions nearby the site of the NPE, where number 1 was the closest and number 18 the furthest from the NPE site, all within a radius of 2 km. It is observed that most of the nuclear explosions had $r_0 W^{-1/3} \approx 1 \text{ m}/\text{kt}^{1/3}$, whereas for the ANFO-emulsion blend employed in the NPE, $r_0 W^{-1/3}$ was $\approx 6 \text{ m}/\text{kt}^{1/3}$. It is also seen that the yield-scaled seismic amplitude measured in the NPE was roughly twice that of most of the nuclear explosions. Our simulations, discussed below, found a factor of 1.9 when the explosive employed was the ANFO-emulsion mix used for the NPE; with TNT, the factor was approximately 1.6, and in neither case was there any significant dependence on the properties of the surrounding rock. Different explosives produce slightly different results because the effective ratio of specific heats of the explosion products, γ_{eff} , varies with the chemical makeup of the explosive and the cavity pressure is directly proportional to the quantity $(\gamma_{eff} - 1)$.

FREE-FIELD DATA

Figure 2 plots the yield-scaled magnitude of the reduced velocity potential-spectrum, $|i\omega\hat{\phi}|/W$, as a function of yield-scaled frequency, $fW^{1/3}$, where $f = 2\pi\omega$. The heavy black curve is the lognormal average derived from LANL free-field particle acceleration measurements on the NPE and the heavy gray curve plots similar data from a nearby nuclear event; both sets of free-field measurements were provided by F. App of LANL. The dotted curves represent ± 1 standard deviation from the mean. For the nuclear event, 7 gages were employed to calculate $|i\omega\hat{\phi}|/W$. These were all located at ranges beyond $257 \text{ m}/\text{kt}^{1/3}$; data from gages closer to the explosion were available, but these were found to be within the inelastic region and were therefore excluded for purposes of seismic analysis. We note that the calculation of $\phi(t)$ from the particle acceleration records, $\dot{u}(t)$, required truncation of the records to exclude non-spherical motion in the coda; guidance for the location of the truncation point was provided by reference to the simulations, discussed below. For the NPE results shown in Figure 2, 12 gages were used, all beyond $284 \text{ m}/\text{kt}^{1/3}$.

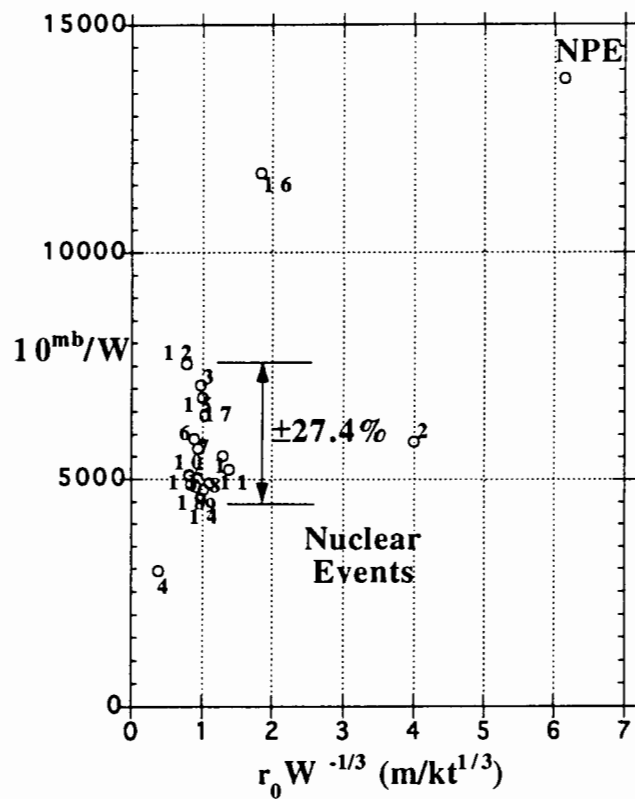


Fig. 1 Seismic amplitude as a function of initial emplacement radius.
Numbers refer to location of nuclear events relative to the NPE.

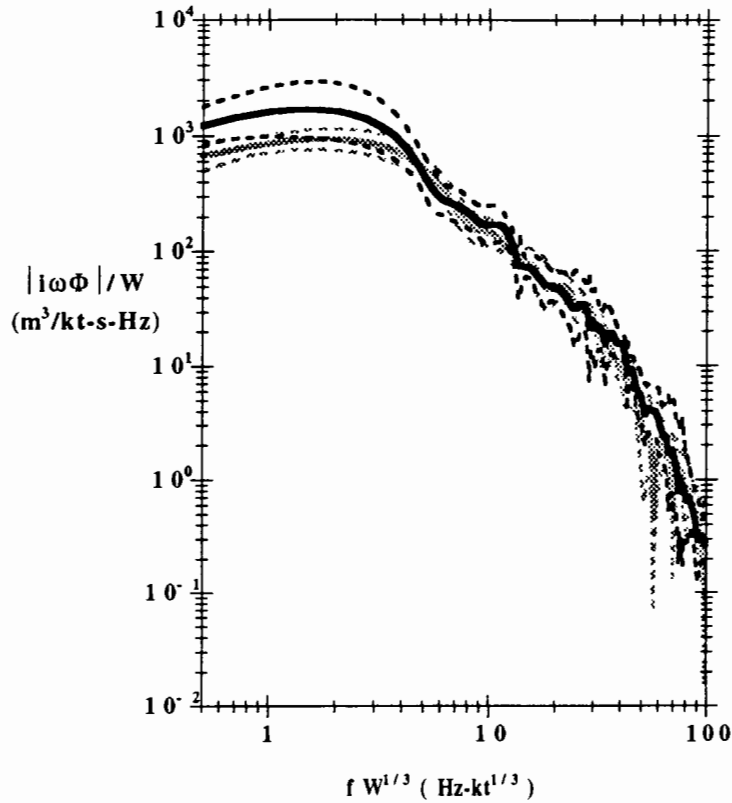


Fig. 2 Experimental free-field spectra. The solid curves are lognormal means,
black for the NPE and gray for a nearby nuclear event. Dashed curves
show ± 1 standard deviation.

At $fW^{1/3} = 1 \text{ Hz}\cdot\text{kt}^{1/3}$, the lognormal average value of $|i\omega\hat{\phi}|/W$ for the NPE was found to be $1583 \text{ m}^3/\text{kt}\cdot\text{s}\cdot\text{Hz}$, compared with $819 \text{ m}^3/\text{kt}\cdot\text{s}\cdot\text{Hz}$ for the nearby nuclear event; the amplitude ratio is 1.93. Figure 2 shows that beyond $4 \text{ Hz}\cdot\text{kt}^{1/3}$, however, the average amplitude spectra are virtually indistinguishable.

In what follows, we have attempted to reproduce these results via direct simulation. The computer code employed has been described elsewhere (Glenn, 1978; 1993). Our procedure was to compare calculations with the nuclear-explosion data and to vary the important elements of the material model for the surrounding rock until an adequate representation was achieved; then, without changing the rock properties, we substituted the ANFO-emulsion blasting agent for the nuclear-explosion source and compared the computed seismic response with the results of the NPE.

MATERIAL MODELS

The most important elements of the rock model are the strength and gas porosity. Our constitutive model for the nearly saturated tuff employed a tabular equation of state that was fitted to previously obtained shock Hugoniot and elastic-wave data. The shock-wave data are relatively insensitive to small-scale inhomogeneities so that it is generally possible to determine the high-pressure properties of the rock quite accurately. The elastic moduli are also known accurately via wave speed measurements. By contrast, it is difficult to obtain unambiguous strength or porosity data due mainly to the spatial inhomogeneities inherent at most sites.

In our model, the compressive strength of tuff depends on the pressure, temperature, and on a *damage* parameter that measures the degree of degradation due to tensile fracture. Specifically,

$$\sqrt{3J'_2} \leq Y = (1 - D)\bar{Y} + \beta D\bar{Y} \quad (1)$$

where $J'_2 \equiv \frac{1}{2}\sigma'_{ij}\sigma'_{ij}$, σ' is the deviatoric stress tensor, β is a constant, typically 0.25, and D is a scalar function of the volumetric component of the void strain tensor (Rubin and Attia, 1990). For this study, $D = \epsilon_{ii}^V/\epsilon_{max}^V$ and ϵ_{max}^V was taken as 5×10^{-3} . Also,

$$\bar{Y} = \left[Y_0 + \frac{p}{a + (\frac{p}{Y_u - Y_0})} \right] \max\{(1 - T/T_m)^b, 0\} \quad (2)$$

Y_0 is the unconfined compressive strength, Y_u is the ultimate compressive strength, T is temperature, and $T_m(p)$ is the melting point. Here, the cohesion parameter, a was taken as 1.35 and the parameter b was assumed equal to unity.

The equation of state is based on the well-known $p - \alpha$ concept developed by Carroll

and Holt (1972), i.e.,

$$p(\nu, e) = p_m(\nu/\alpha, e)/\alpha = p_m(\nu_m, e_m)/\alpha \quad (3)$$

and

$$\alpha = \alpha(p) \quad (4)$$

where $\nu = 1/\rho$ is the specific volume, and the subscript m refers to the matrix material in which the pores are embedded. The parameter α is related to the gas porosity, Ψ , and is defined by the relation

$$\alpha \equiv \nu/\nu_m = \rho_m/\rho = (1 - \Psi)^{-1} \quad (5)$$

At ambient pressure, $\alpha = \alpha^0$, the initial value, and at some high pressure, p_c , the pores will be completely crushed and $\alpha(p_c) = 1$. For $p > p_c$, the Grüneisen form, p_m , employed in equation (3) smoothly transitions into the tabular form $p_m(\rho, T)$.

Equations (3) and (4) apply to loading for $p < p_c$, but to unloading only when $p < p_{el}$; in this small, but important, range the pore volume behaves in strictly elastic fashion. In the range $p_{el} \leq p < p_c$, unloading occurs at constant gas porosity.

SIMULATIONS

Figure 3 exhibits calculations of the tamped nuclear explosion where the ultimate yield strength, Y_u , has been varied from 5 MPa to 205 MPa. The gas porosity, Ψ was set to 0 and the overburden pressure, p_{ovb} to 4 MPa; all other parameters were fixed as well. It is observed that the corner frequency decreases significantly with decreasing strength and that the curve derived from the free-field experiments is best matched with the lowest strength.

The nominal overburden pressure for the NPE was roughly 8 MPa. Figure 4 shows the effect of varying p_{ovb} while keeping all other parameters fixed; in this case we have $Y_u = 65$ MPa, more nearly the nominal value derived from laboratory analysis (Patch *et al.*, 1994), and $\Psi = 0$. It is seen in the figure that the corner frequency is little affected with $2 \leq p_{ovb} \leq 16$ MPa.

Although the simulation with $Y_u = 5$ MPa gives a good fit to the corner frequency, figure 3 shows that the low-frequency ($1 \text{ Hz-kt}^{1/3}$) amplitude is too high in this case, a situation that can be remedied by increasing the gas porosity; we note that the geological data for the N-tunnel region exhibits significant variations in the measured gas porosity, with the typical range being $0 < \Psi < 0.05$. Figure 5 displays the results of simulations with the gas porosity fixed at 1% ($\Psi = 0.01$) and the overburden pressure fixed at the nominal 8 MPa. Again, we find the calculation with $Y_u = 5$ MPa gives a good match to the experimental spectra, and this time the low-frequency amplitude is below that

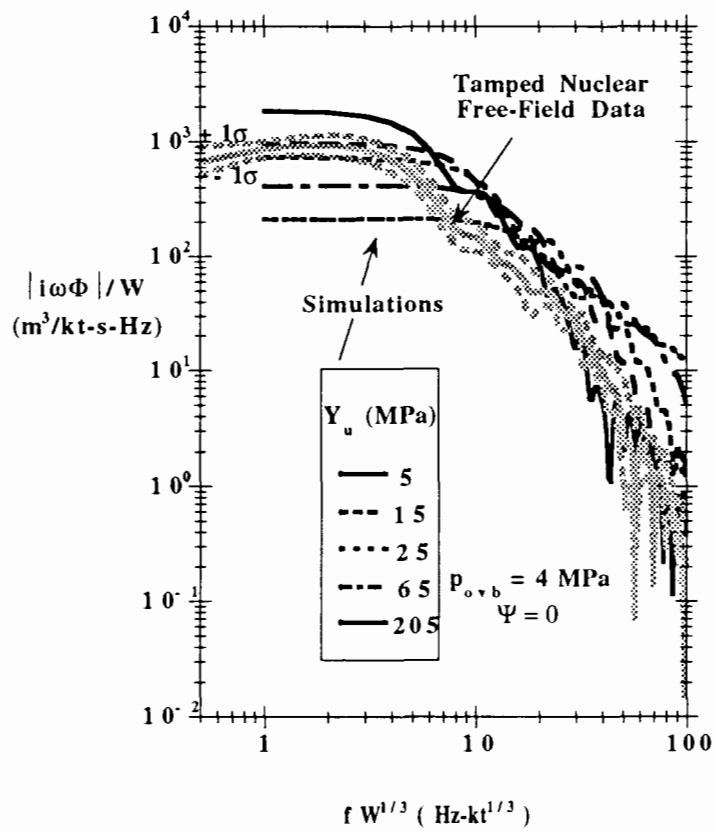


Fig. 3 Effect of varying the ultimate yield strength on seismic spectra.
The corner frequency in the experimental data is best matched by
the simulation with $Y_u = 5$ MPa

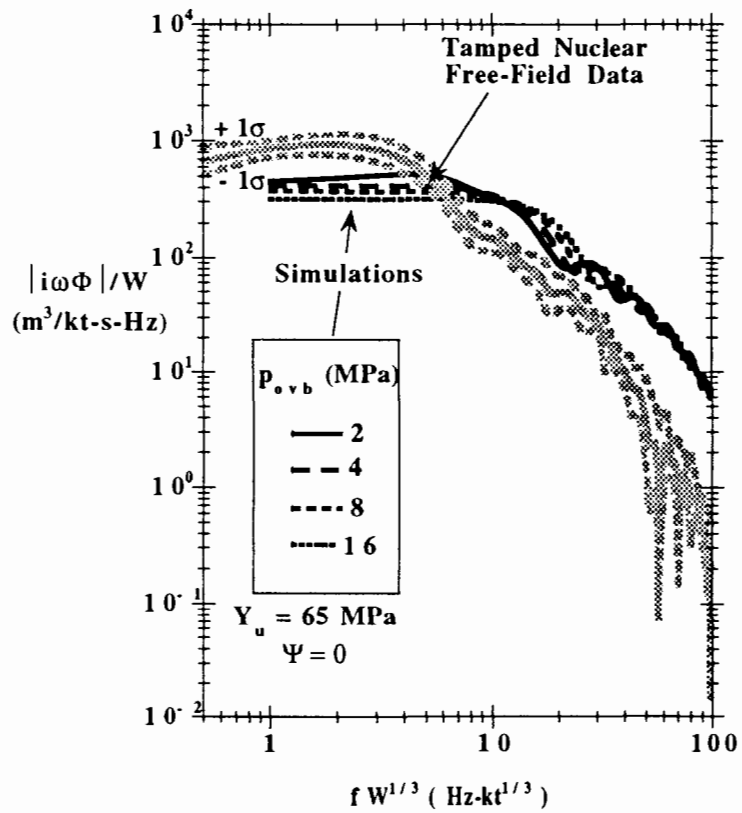


Fig. 4 Effect of varying the overburden pressure on seismic spectra.
The corner frequency is relatively unaffected by changes in p_{ovb} .

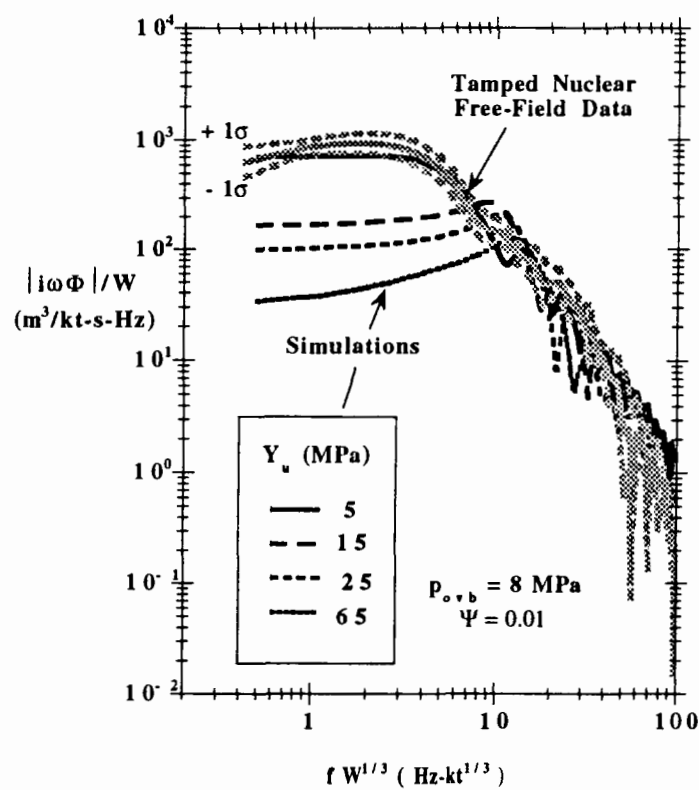


Fig. 5 Effect of varying the ultimate strength with $\Psi = .01$ & $p_{ovb} = 8$ MPa.
The corner frequency in the experimental data is best matched by the simulation with $Y_u = 5$ MPa.

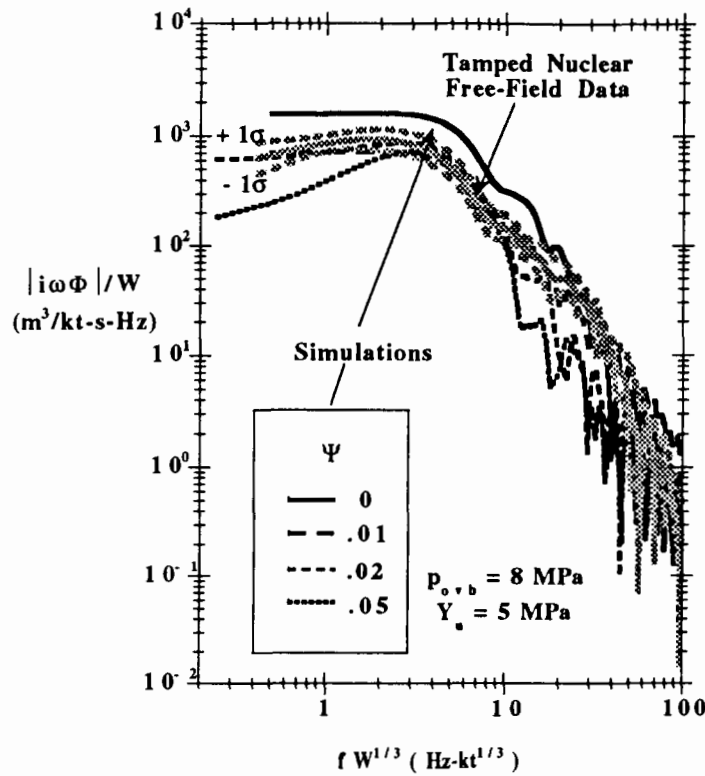


Fig. 6 Effect of varying the gas porosity with $Y_u = 5$ MPa & $p_{ovb} = 8$ MPa.
The corner frequency is nearly independent of Ψ & the best fit to the experimental data is obtained with $0 < \Psi < 0.01$.

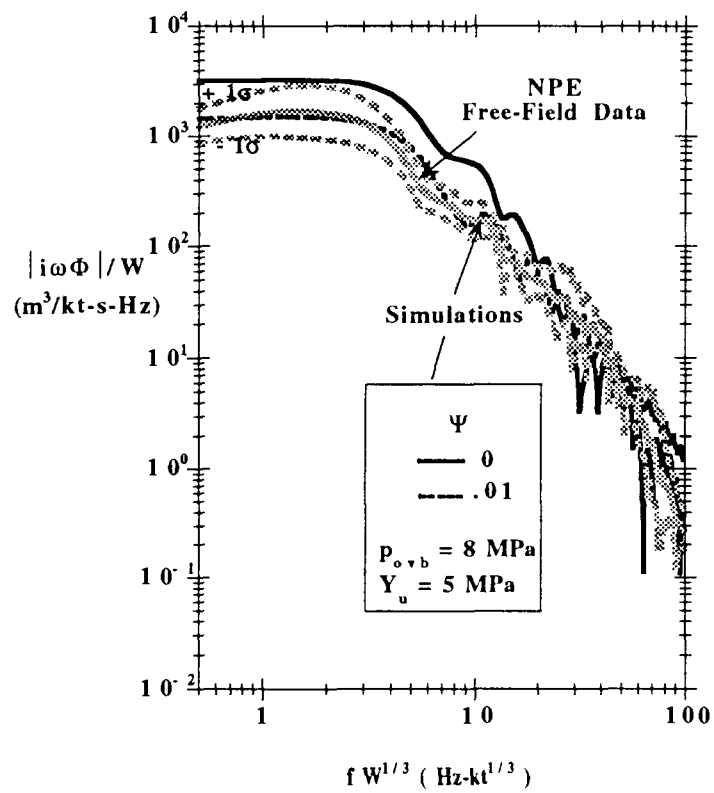


Fig. 7 Simulations of the NPE, with $0 < \Psi < 0.01$, $Y_u = 5$ MPa & $P_{ovb} = 8$ MPa. This parameter set is in good agreement with the experimental data for both the NPE and the nearby nuclear event (see Fig. 6).

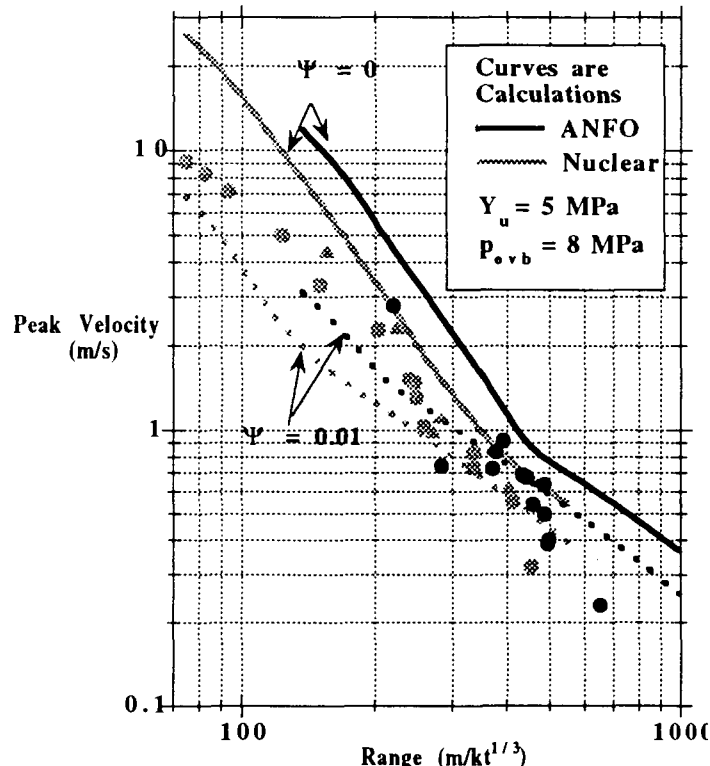


Fig. 8 Peak particle velocity as a function of range. Black dots are experimental data from the NPE and gray dots from nearby nuclear events.

derived from the free-field data. We note in passing that whenever $p_{ovb} > 2Y/3$, as is the case here, the region around the source excavation cannot be in a fully elastic state *prior to the explosion*. This, however, does not preclude mechanical equilibrium from being established, as was demonstrated, for example, by Wells (1969).

Figure 6 shows the effect of further increase in gas porosity. No significant effect on corner frequency is noted but, for example, with $\Psi = 0.05$ both the low- and high-frequency amplitudes are substantially below the experimental data. A quite good fit to the experiment is observed for $0 < \Psi < 0.01$. The simulations with $\Psi = 0.01$ and 0.02 are practically congruent below the corner frequency, although the $\Psi = 0.02$ simulation evidences a slight overshoot and falls significantly below the experimental data at frequencies above $10 \text{ Hz-kt}^{1/3}$.

Figure 7 exhibits simulations of the NPE, with the same parameters that provided the best fit to the nearby nuclear event, i.e., $Y_u = 5 \text{ MPa}$, $0 < \Psi < 0.01$, and $p_{ovb} = 8 \text{ MPa}$. These calculations differ from those in figure 6 only in that the ANFO-emulsion blasting agent was substituted for the nuclear device; a JWL equation-of-state was employed for the blasting agent, with the parameters derived from analysis via the TIGER code (Souers and Larson, 1994). Figure 7 shows that the simulations are in equally good agreement with the NPE; in this case the 1%-porosity calculation is closer to the experiment than in the nuclear case.

Finally, the comparison of the peak particle velocities derived via the simulations with those measured is shown in figure 8. Most of the experimental data fall in between the simulations with 0 and 1%-gas porosity. For the NPE, and beyond a range of $400\text{-}500 \text{ m/kt}^{1/3}$, the data fall somewhat below the 1%-calculation. A slightly higher gas porosity would certainly account for these data, and is by no means excluded based on the geological characteristics of the N-tunnel explosion site.

CONCLUDING REMARKS

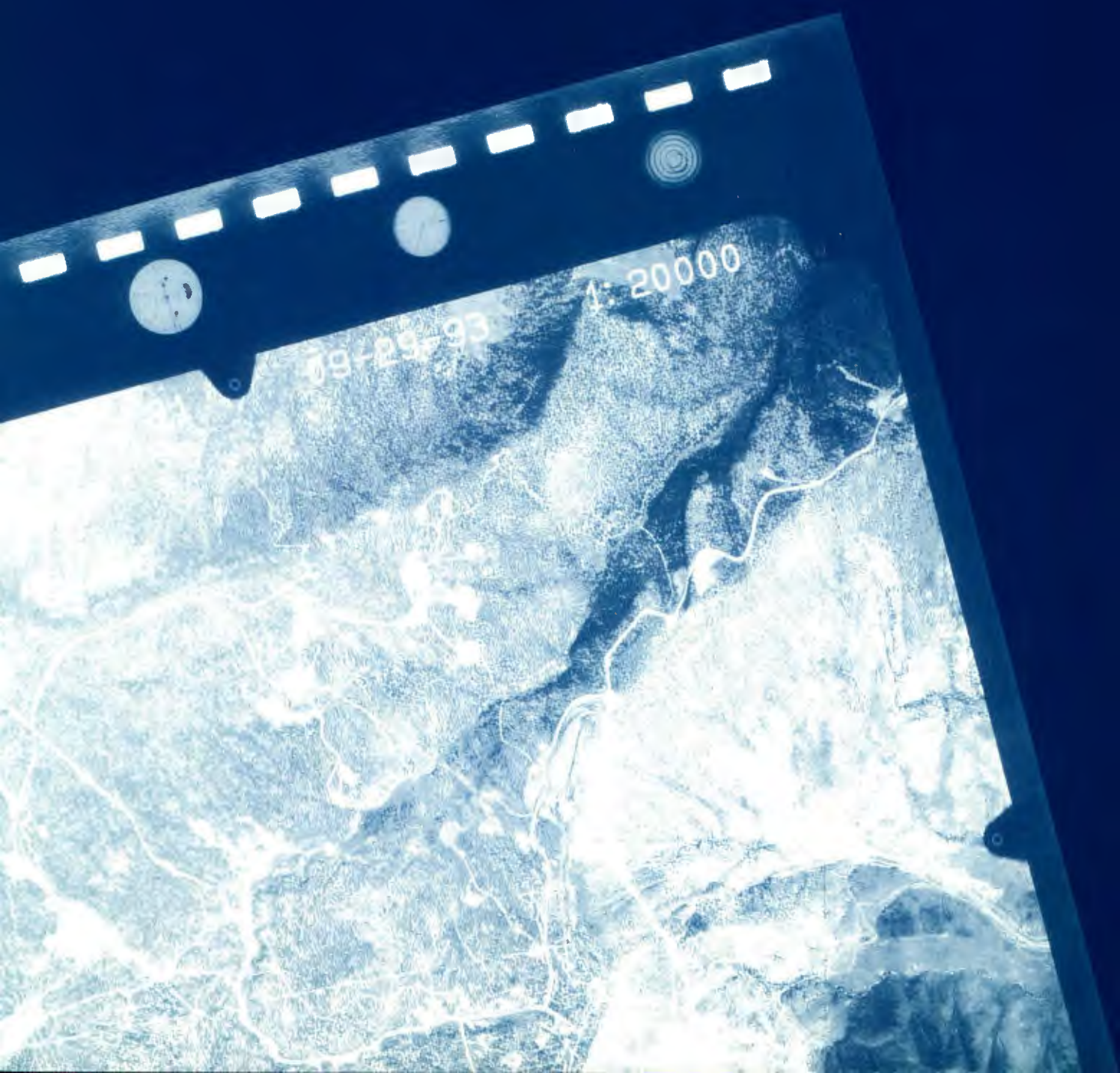
The most important elements in simulating the seismic response to underground explosions are the representation of material strength and gas porosity. Other factors such as the high-pressure equation-of-state, elastic moduli, and the overburden state contribute to the result, but strength and porosity are the main determinants of long-period amplitude and corner frequency is mainly set by the strength. We found that it was possible to get a reasonably good match to seismic spectra from both the NPE and a nearby nuclear event with the same material model. However, the strength that provided the match was roughly an order of magnitude less than that determined via laboratory analysis of core samples taken from the vicinity of the test site. This is not an unusual occurrence and derives from the fact that the rock media in which the testing takes place are generally quite inhomogeneous, so that laboratory measurements

on core-sized rock samples may not be representative of the extant rock mass from which the samples derive. We note that this is an inherent limitation in employing simulations to the monitoring function, i.e., simulation of explosions at unidentified (clandestine) locations implies an imperfect knowledge of the *in situ* material properties and emplacement geometry.

REFERENCES

- Carroll, M. M. and A. C. Holt. Suggested modification of the p- α model for porous materials, *J. Appl. Phys.*, **43**, No. 2, 759-761, 1972.
- Glenn, L. A. AFTON Revisited: An improved algorithm for numerical solution of initial value problems in continuum mechanics; part 1, the one-dimensional equations, Lawrence Livermore National Laboratory Report, Livermore CA, UCRL-52512, 1978.
- Glenn, L. A. Energy-density effects on seismic decoupling, *J. Geophys. Res.*, **98**, B2, 1933-1942, 1993.
- Glenn, L. A. and P. Goldstein. Seismic decoupling with chemical and nuclear explosions in salt, *J. Geophys. Res.*, in press; see also University of California, Lawrence Livermore National Laboratory Preprint UCRL-JC-114711, August 1993.
- Patch, D. F., Welch, J. E. and J. Zerkle. Preshot predictions for the Near-Source Region in the NPE, this symposium.
- Rubin, M. B. and A. V. Attia. A continuum tensile failure model with friction, University of California, Lawrence Livermore National Laboratory Report UCRL-ID-104759, August 21, 1990.
- Souers, P. C. and D. B. Larson. TIGER calculations and the NPE energy yield, this symposium.

RAINIER MESA STRUCTURE



GEOLOGY, GEOPHYSICS, AND PHYSICAL PROPERTIES OF THE U12n.25 NON-PROLIFERATION EXPERIMENT SITE

by

**M. J. Baldwin, R. P. Bradford, S. P. Hopkins, D. R. Townsend
Raytheon Services Nevada
P.O. Box 328, Mercury, NV 89023**

and

**B. L. Harris-West
Defense Nuclear Agency
P.O. Box 208, Mercury, NV 89023**

ABSTRACT

The Nuclear Non-Proliferation Experiment was conducted in the U12n.25 drift in N-Tunnel at the Nevada Test Site. The geologic characterization of the site was performed by Raytheon Services Nevada geologists in the standard manner used for all underground nuclear weapons-effects tests executed by the Defense Nuclear Agency.

The U12n.25 test bed was constructed in zeolitized ash-fall tuff of the Tunnel Beds Tuff, Subunit 4K, 389.0 m below the surface of Rainier Mesa. The structural geology of the site was simple, with the nearest fault plane projected to be 12 m below the mined cavity at closest approach, and an average bedding dip of seven degrees to the northwest. The cavity excavation revealed several small fractures, including one which produced minor amounts of free water during construction. The physical properties of the site were well within the range of experience for the zeolitized tuff of N-Tunnel and no geology-related problems were encountered during construction.

The zeolitized tuff of N-Tunnel has been the site of twenty nuclear tests conducted by the Defense Nuclear Agency. The similarities of geologic setting, site geometry, and physical properties allow many comparisons of Non-Proliferation Experiment results with the large nuclear-test data base.

INTRODUCTION

The geology of the Non-Proliferation Experiment (NPE) site in N-Tunnel at the Nevada Test Site (NTS) is well known as a result of geologic investigations carried out in support of the experiment and by the projection of preexisting data from extensive mining and drilling conducted by the Defense Nuclear Agency (DNA) during preparation of test beds for several nearby underground nuclear weapons effects tests. This report presents geologic data obtained at the U12n.25 site and summarizes geological, geophysical, and physical/mechanical data extrapolated from nearby sites. All the drifts and test locations in central N-Tunnel are shown on Figure 1.

South-central N-Tunnel
 was selected for the Non-Proliferation Experiment (in part) for its accessibility and the existence of adequate facilities such as alcoves and utilities, and because the well-characterized Tunnel beds tuff had been utilized for several nuclear tests with yields similar to that planned for the NPE. The U12n.25 cavity was located at a site that was expected to be free of faults and water, 232 m south of the N-Extension South drift and 85 m east of the U12n.23 Access drift. The NPE site is 198 m from the nearest expended nuclear working point (WP), but no visible evidence of shock conditioning was found in the Access drift or cavity. The center point of the cavity (referred to here as the WP or working point) is 1852.6 m above mean sea level, which is 389.0 m below the surface of Rainier Mesa.

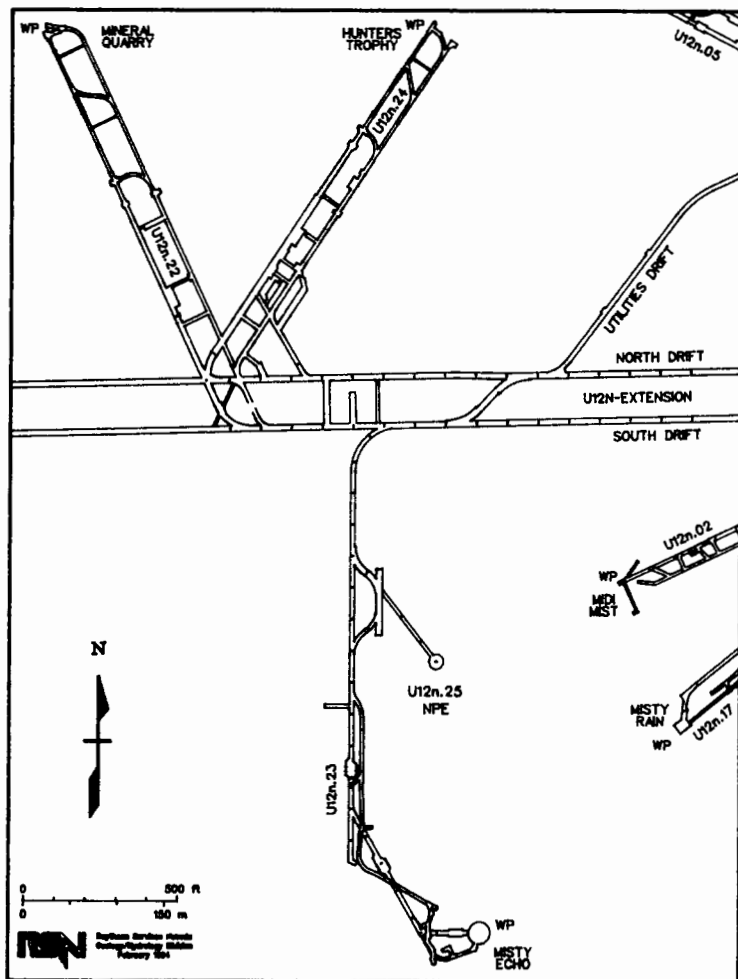


Figure 1

Reference map of central N-Tunnel, showing location of the U12n.25 NPE site.

DATA SOURCES

The geology of the U12n.25 Access drift and cavity, as well as that of most nearby nuclear test beds, was mapped in detail by Raytheon Services Nevada (RSN) geologists on a day-to-day basis during mining. Detailed geologic characteristics of much of this area were presented in the containment prospectuses prepared for the DNA tests MINERAL QUARRY, MISTY ECHO, and HUNTERS TROPHY.

Horizontal core hole U12n.23 UG-1 was drilled a total of 641.3 m south from the N-Extension South drift in 1987, prior to the mining of the MISTY ECHO chamber. The hole passes 21 m east of the U12n.25 WP and is the prime source of geotechnical data for the NPE site. RSN geologists logged the core and conducted resistivity and sonic-velocity surveys in the borehole, and physical properties were measured on 30 core samples. Core hole U12n.07 UG-3 was drilled due west from the U12n.07 Main drift in 1972 and passes 144 m south of the U12n.25 site; data from this hole were used to help develop the geologic interpretation of the area (Figure 2).

Two nearby vertical drill holes also provide data for three-dimensional interpretation of the geology of the U12n.25 site. Core hole UE12n#1 was drilled from the surface to a depth of 610.0 m in 1973 and is located approximately 260 m west of the U12n.25 cavity. The core was logged by the U. S. Geological Survey (later relogged by RSN to update the stratigraphy), and a suite of geophysical logs was obtained in the borehole. Core hole UE12n#14 (298 m south of the NPE WP) was drilled from the mesa surface to a depth of 529.6 m in 1987 to help characterize the U12n.23 MISTY ECHO site. RSN geologists logged the core, but no geophysical logs were obtained because the drill rods became stuck in the hole. Physical and mechanical properties were measured on a large suite of cores from this hole.

GEOLOGIC SETTING

Stratigraphy

The details of the geology of the U12n.25 area are shown on Figure 3. Stratigraphic symbols used on this and all other maps and cross sections are given in Table 1. Mapping units used in Area 12 tunnels were originally developed by the USGS on the basis of engineering properties, and have evolved over the years to incorporate our growing understanding of the stratigraphy of Rainier Mesa. Some aspects of the latest revision of NTS stratigraphy,^[1] still in progress, have been incorporated into Table 1, though most workers in Rainier Mesa still use the older system.

Nine mappable subunits (4AB through 4K, with 4K being the youngest) are commonly identified within Tunnel bed 4 in Area 12 tunnels. The U12n.25 cavity and Access drift were mined within the lower portion of Subunit 4K (Tt4K) which is described below.

Lithology

Most of the U12n.25 cavity was constructed within a 4-m-thick, zeolitized, calcalkaline ash-fall tuff. The tuff is fine- to medium-grained, consisting of 40-50% groundmass, 30-40% phenocrysts (mostly feldspar and quartz), 5-10% pumice less than 10 mm in size, and approximately 5% lithic fragments up to 5 mm in size. The upper part of the bed is slightly silicified, but the lower 0.9 m of the subunit is somewhat

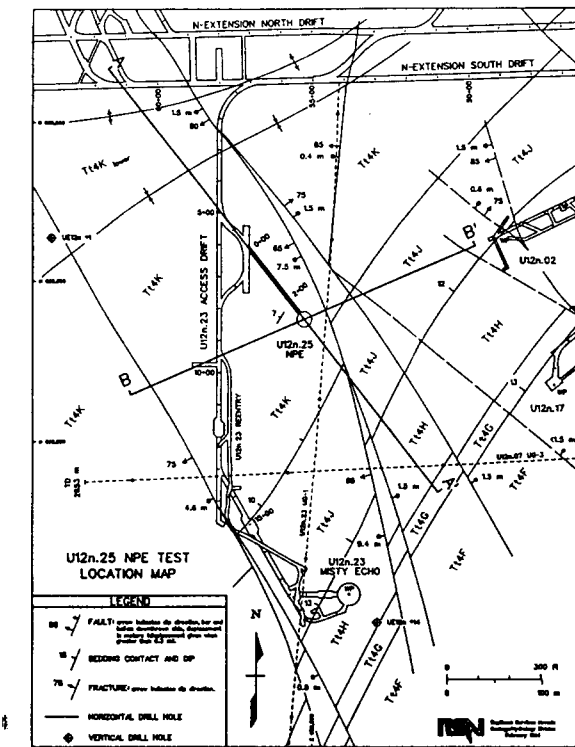


Figure 2 Geologic map of south-central N-Tunnel, showing locations of geologic cross sections.

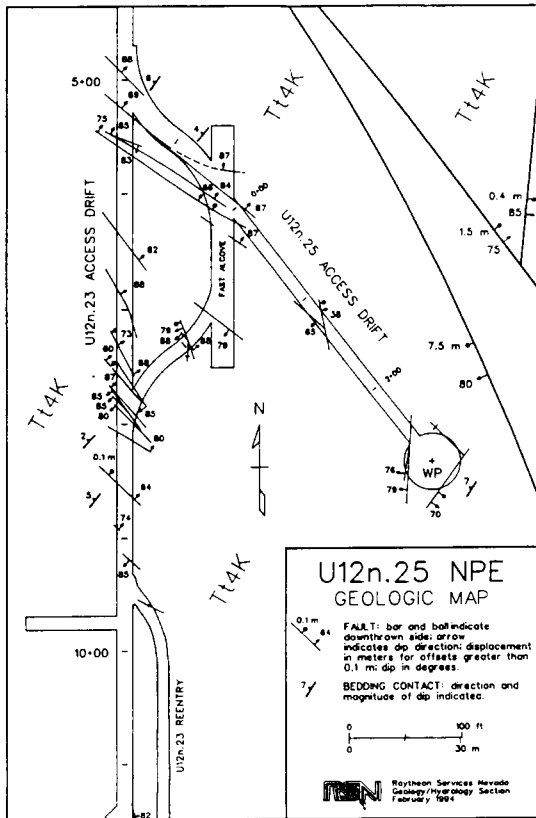


Figure 3 Detailed geologic map of the U12n.25 NPE site.

argillized. Directly below this bed is a 0.5-m-thick, coarse-grained, peralkaline ash-fall tuff which contains almost no phenocrysts and pumice fragments up to 25 mm in size. The U12n.25 Access drift was mined through alternating beds of fine- to medium-grained calcalkaline and coarse-grained peralkaline ash-fall tuff 0.2 to 0.8 m thick. In most of the calcalkaline beds the pumice fragments are selectively argillized.

Table 1 Stratigraphic section at the U12n.25 Working Point.

MAP SYMBOL	STRATIGRAPHIC UNIT	THICKNESS AT WP (m)	LITHOLOGIC DESCRIPTION
Tmr	Rainier Mesa Tuff Timber Mountain Group	131.4	Upper portion, densely to moderately welded ash-flow tuff; lower portion, nonwelded to partially welded, vitric ash-flow tuff.
Tp	Paintbrush Tuff *(includes Wahmonie Fm. and other pre-Rainier, post-Grouse Canyon formations)	182.3	Vitric, bedded ash-fall and reworked ash-fall tuff and tuffaceous sandstone.
Tbg	Grouse Canyon Tuff Belted Range Group	11.9	Densely welded ash-flow tuff.
Tt5 *(Tbgb)	Tunnel beds Unit 5 (bedded portion, Tbg)	26.5	Vitric, bedded ash-fall tuff.
Tt4 *(Tn4)	Tunnel beds Unit 4 (Tunnel Formation Tunnel 4 Member)	(above WP) 36.9 (below WP) 92.5	Zeolitized, bedded ash-fall and reworked ash-fall tuff.
Tt3 *(Tn3)	Tunnel beds Unit 3 (Tunnel Formation Tunnel 3 Member)	57.1	Zeolitized, bedded ash-fall and reworked ash-fall tuff.
Tbt *(Tub)	Tub Spring Member Belted Range Tuff (Tub Spring Tuff, Volcanics of Big Dome)	8.7	Zeolitized, bedded ash-fall tuff.
Tt2 *(Ton2)	Tunnel beds Unit 2 (Tunnel bed 2, Volcanics of Oak Spring Butte)	66.9	Zeolitized, bedded ash-fall and reworked ash-fall tuff.
Tyf *(Toy)	Tuff of Yucca Flat (Yucca Flat Tuff, Volcanics of Oak Spring Butte)	88.7	Zeolitized, nonwelded to partially welded ash-flow tuff.
Tot	Older Tuff Units	71.6	Zeolitized, bedded ash-fall and reworked ash-fall tuff, and nonwelded to partially welded ash-flow tuffs.
CpCw	Wood Canyon Fm. and Stirling Quartzite	-	Schist and quartzite.

* Equivalent units of the proposed Southwestern Nevada Volcanic Field. [1]

Structural Geology

Bedding strike at the U12n.25 cavity averages N30°E and the dip of bedding is approximately seven degrees to the northwest. Throughout N-Tunnel, the presence of a shallow, northeast/southwest-trending depositional syncline controls the strike of bedding. The NPE site is located on the southern flank of the syncline; bedding dips gradually become shallower toward the northwest and steepen to 13°-15° southeast of the WP.

The average strike of through-going faults in N-Tunnel is N10-30°W, though less continuous faults and fractures have been observed to strike almost any direction. No through-going faults were encountered during mining of the U12n.25 complex. A normal fault with an estimated displacement of 7.5 m is projected to be 12 m east of the NPE cavity. This fault is part of a system that splay into several planes, the nearest of which strikes N30°W and dips 65° to the west. The displacement of this fault increases (at tunnel level) to the south and lower in the stratigraphic section, but conversely was observed to decrease where it was mapped higher in the stratigraphic section, north of the NPE site (Figure 2). Another fault system parallels this fault, and is approximately 162 m west of the NPE WP at closest approach at tunnel level. This fault has 4.6 m of normal displacement, down to the west.

Several fractures and small displacement faults were mapped in the U12n.25 Access drift, the Fast alcove, and the U12n.23 Access drift (Figure 3). Most of these structures are subparallel to the major faults described above, and have fairly steep dips (65° to 89°). One shallow-dipping normal fault (dip of 38° east; less than 0.1 m offset) was mapped in the U12n.25 Access drift, approximately 47 m from the NPE WP. None of these faults/fractures produced water.

A fault with approximately 0.03 m of normal displacement was mapped on the southeast wall of the NPE cavity. This fault strikes N30°E and dips 70° east (away from the WP); it has a clayey gouge fill and vertical slickensides, but produced no water. Three fractures, subparallel to the strike of through-going faults, were also mapped within the NPE cavity, and are probably the result of stress relief that occurred during mining of the opening. The vertical plane seen on the northeast wall of the cavity was tight and dry, but a pair of planes dipping 76° and 79° west on the west wall of the cavity (extending through the cavity entrance into the U12n.25 Access drift) temporarily produced a small amount of water.

Geologic Cross Sections

Cross sections shown on Figures 4 and 5 were constructed to illustrate the three-dimensional relationships of the U12n.25 complex and geologic features. Cross section A-A' was constructed parallel to the U12n.25 Access drift through the NPE WP, approximately parallel to the strike of bedding in the area, so that the true thicknesses of the beds are shown (Table 1 lists the thicknesses of the major stratigraphic units

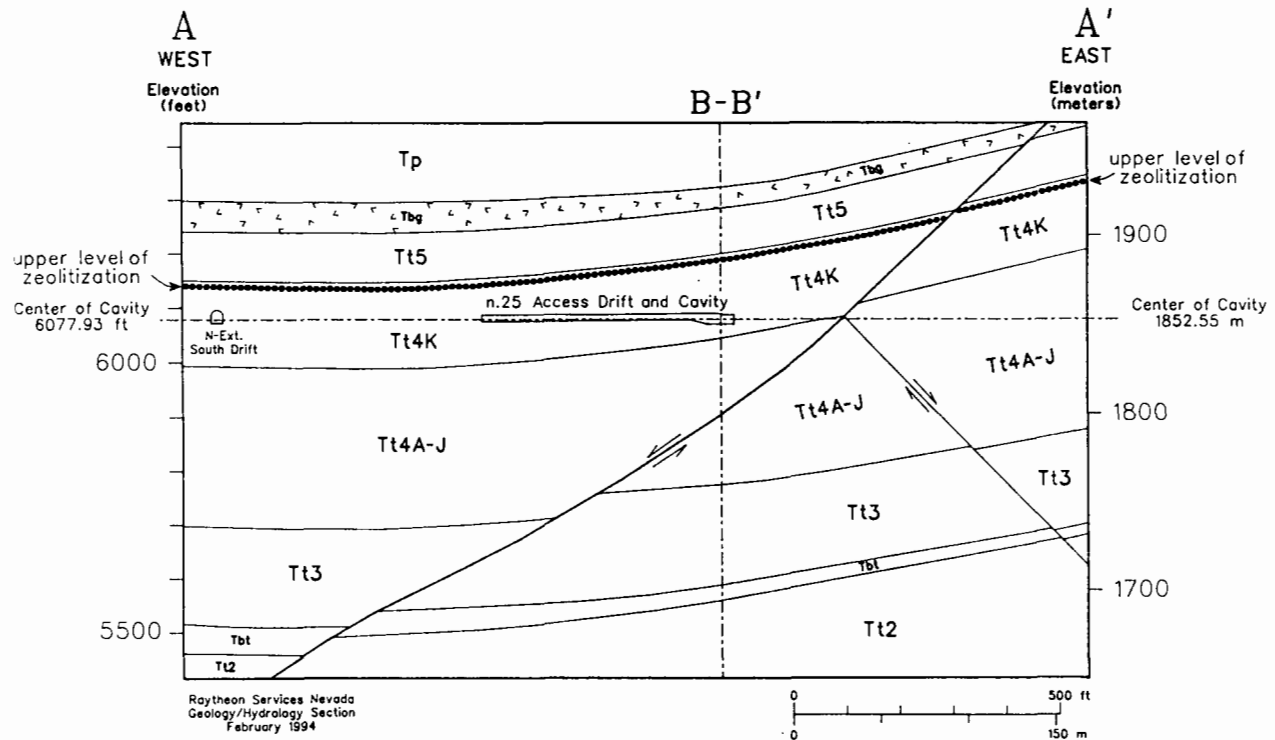


Figure 4 Cross section A-A', constructed through the NPE working point, parallel to the U12n.25 Access drift (see Figure 2 for cross section locations).

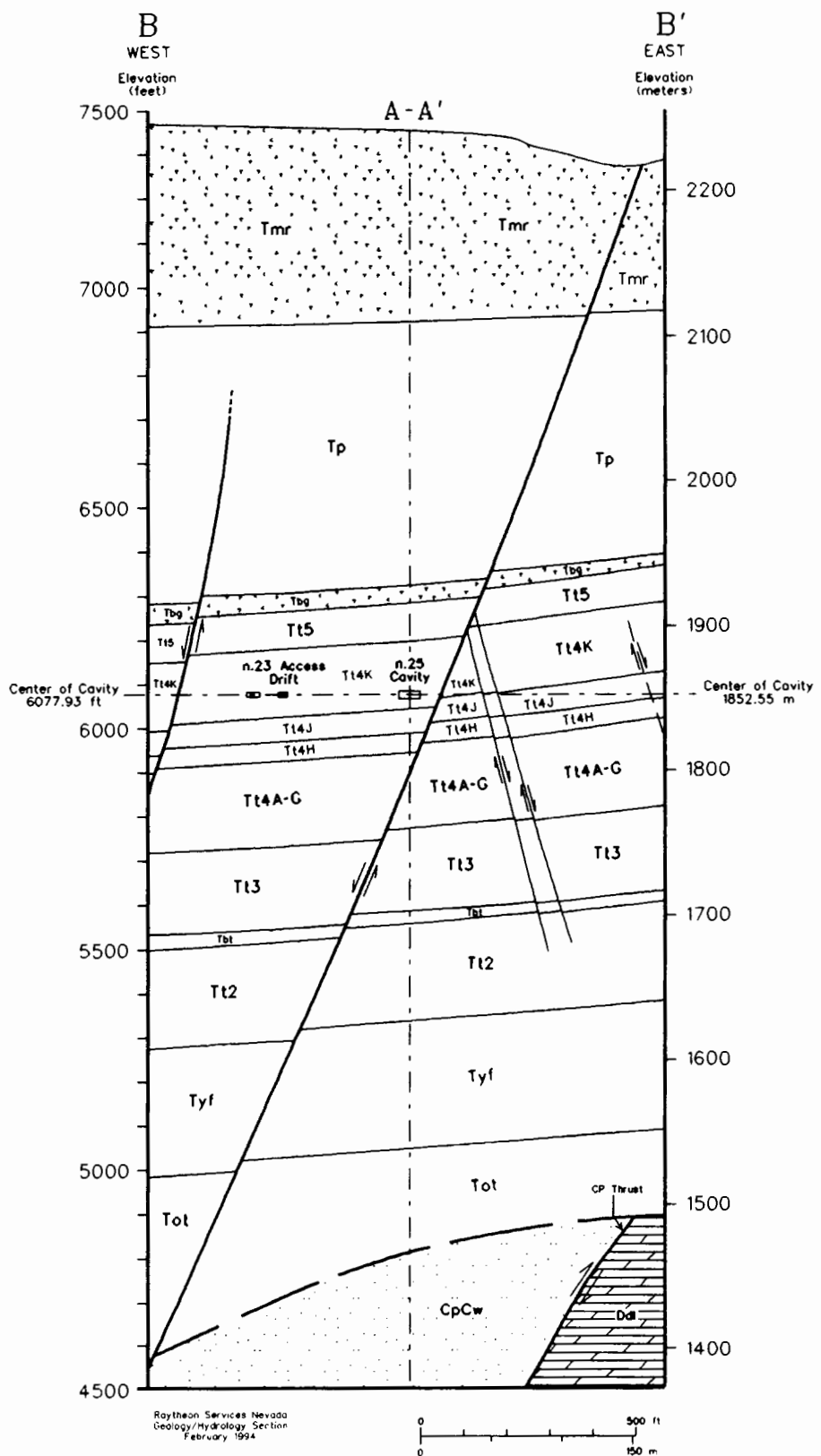


Figure 5 Cross section B-B', constructed through the NPE working point, orthogonal to cross section A-A'; extended to the mesa surface and to the pre-volcanic surface (see Figure 2 for cross section locations).

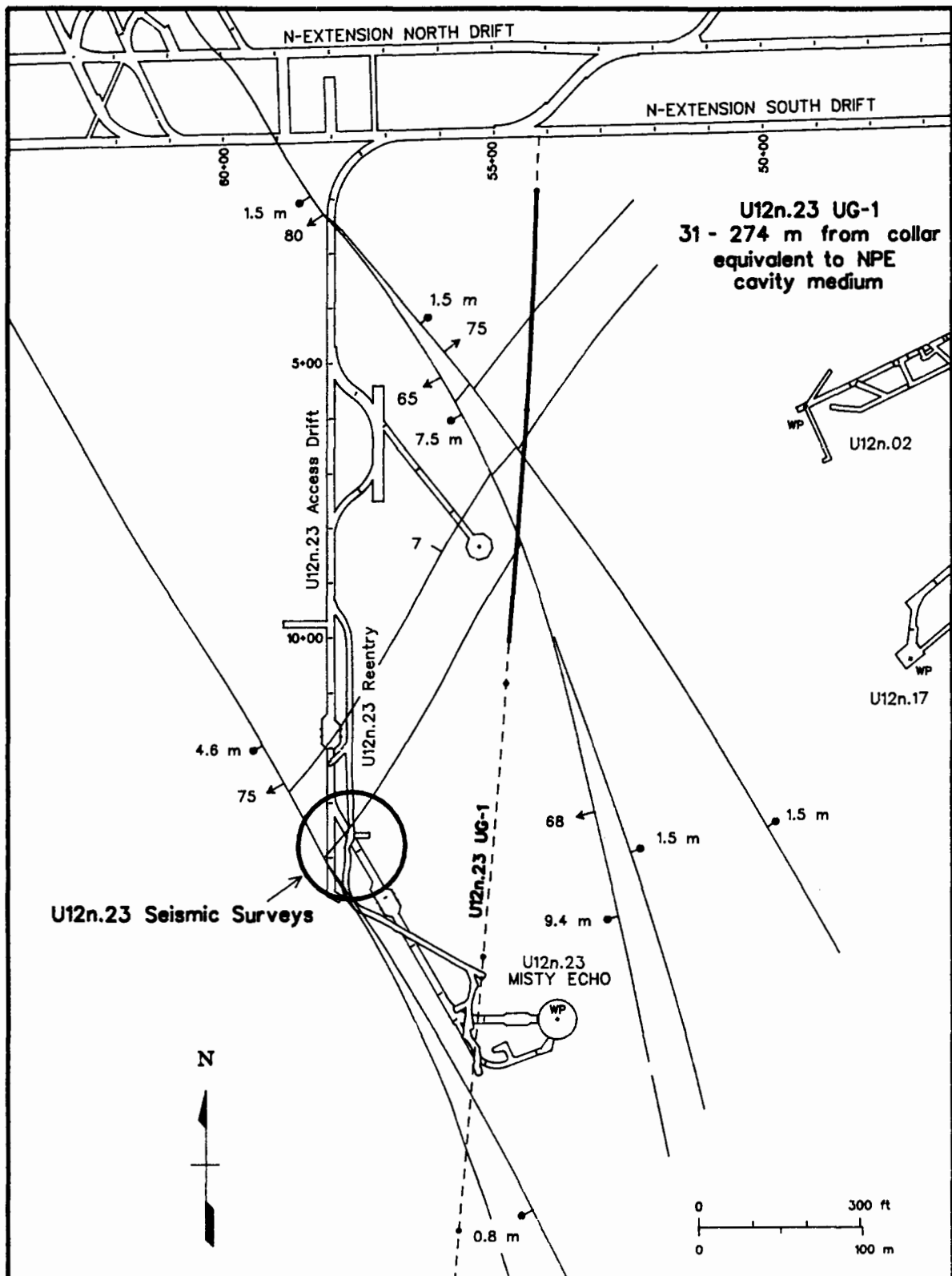


Figure 6 Simplified geologic map of the NPE site showing the stratigraphic location of the cavity and the sources of geophysical data.

and gives brief descriptions of each). The upper level of zeolitization, marked with a dashed line approximately 33 m above the WP, is the level above which the tuff is vitric to partially devitrified and less saturated than the underlying zeolitized tuff.

Cross section B-B' (Figure 5) was constructed through the WP at right angles to the structure in the area and thus illustrates the true position of the cavity relative to the faults. The closest fault to the NPE cavity is a 7.5-m-displacement normal fault that is believed to extend to the surface, and is projected to be approximately 21 m east of the WP (12 m from the edge of the cavity) at closest approach below the cavity. Section B-B' was extended vertically to illustrate geologic features from the mesa surface to the pre-volcanic surface.

In Situ Stress Data

Measurements of in situ stress have been made at several sites in N-Tunnel by both hydrofracture and 3-D overcore methods.^[2,3] Minimum stress directions, determined by both methods, range from N23°W to N74°W. At the closest test location to the NPE site (U12n.23 cavity, 266 m south) the minimum stress direction was found to be N23°W by the hydrofracture method, assuming that the minimum stress direction is at right angles to the strike of the created hydrofractures (N67°E). The average strike of natural faults and fractures in south-central N-Tunnel is N10-30°W, which seems to indicate that the in-situ stress orientation has changed since formation of most of the local faults and fractures. Minimum stress magnitudes measured during these investigations range from approximately 2.4 MPa to 6.6 MPa.

MATERIAL PROPERTIES

Physical properties, ultrasonic velocities, and mechanical properties were measured on 42 cores from vertical exploratory drill hole UE12n#14. These samples represent most of the volcanic units at N-Tunnel, so Table 2 has been included here as a source of physical data for the stratigraphic section above and below the U12n.25 site. Table 3 lists data obtained on 30 cores from drill hole U12n.23 UG-1. The complete data sets of material properties measurements on cores from both holes were presented in reports prepared for DNA by TerraTek Incorporated.^[4,5] The NPE WP is located stratigraphically between 10 and 20 m above the base of Tunnel beds Subunit 4K. This 10-m-thick region is shown on Figure 6 which is a simplified geologic map of the U12n.25 site that illustrates the locations of physical and geophysical measurements used in calculations of the average physical and geophysical properties for the NPE site.

Average physical properties of the U12n.25 medium were obtained by averaging values from nine samples from drill hole U12n.23 UG-1 that are stratigraphically equivalent to the U12n.25 site (Figure 6; drill-hole depths of 31.4-274.1 m).

DEPTH		1 DENSITY (Mg/m ³)			Water Content (% wet weight)	Porosity (%)	Saturation (%)	2 Calc. Air Voids (%)	3 Perm. Vol. Comp. (%)	1 ULTRASONIC VELOCITY		Unconf. Comp. Strength (MPa)	Strati-graphic Unit
Meters	Feet	Natural State	Dry Bulk	Grain						Long (km/s)	Shear (km/s)		
45.7	150.0	2.39	2.29	2.56	4.1	10.7	90.8	1.0	*	4.22	2.13	*	
80.8	265.2	2.32	2.23	2.47	3.9	9.6	94.4	0.5	*	4.73	2.76	*	
107.3	352.1	1.73	1.38	2.41	20.2	42.8	81.5	7.9	9.60	2.13	0.81+	6.0	Tmr
140.0	459.4	1.63	1.16	2.37	28.6	51.0	91.3	4.5	*	1.38	0.67+	*	
180.9	593.6	*	*	*	*	*	*	*	**	1.13+	0.46+	*	
249.0	817.0	1.83	1.42	2.42	22.3	41.2	99.0	0.4	4.78	1.33+	0.55+	2.0	Tp
274.4	900.4	1.69	1.20	2.44	28.5	50.6	95.0	2.5	4.76	1.87+	0.84+	2.0	
287.9	944.6	1.61	1.07	2.38	33.7	55.0	98.7	0.7	3.05	2.18	0.67+	*	
302.0	990.9	2.21	2.06	2.46	6.6	16.2	90.2	1.6	**	4.73	2.27	*	Tbg
303.6	996.2	2.17	2.02	2.51	7.2	19.8	79.2	4.1	**	4.32	1.67	*	
311.7	1022.5	1.58	1.09	2.33	31.1	53.3	92.3	4.1	4.30	1.21	0.47	*	
312.7	1025.9	1.58	1.08	2.32	31.8	53.5	93.8	3.3	**	1.08	0.43+	1.0	
320.5	1051.6	1.72	1.28	2.36	25.5	45.7	95.9	1.9	2.59	1.66	0.51	7.0	
324.2	1063.6	1.65	1.18	2.38	28.6	50.4	93.9	3.1	3.28	1.63	0.52	*	
326.5	1071.3	1.74	1.29	2.42	25.7	46.6	95.8	2.0	3.07	1.87	0.60	*	
327.1	1073.3	1.65	1.15	2.39	30.6	52.1	97.1	1.5	7.05	2.05	0.58+	5.0	
329.7	1081.8	1.68	1.17	2.42	30.7	51.7	99.9	0.04++	***	2.25	0.91	*	
331.4	1087.4	1.70	1.20	2.38	29.1	49.6	99.4	0.3	***	2.08	0.85	*	
334.9	1098.7	1.97	1.67	2.44	15.5	31.6	96.5	1.1	1.19	3.57	2.03	*	
336.3	1103.3	1.99	1.70	2.41	14.5	29.5	97.6	0.7	0.66	3.32	1.77	*	
337.7	1107.8	1.91	1.58	2.41	17.5	34.6	96.4	1.2	1.62	3.50	1.64	28.0	
339.3	1113.2	1.90	1.53	2.43	19.2	37.0	98.4	0.6	1.37	3.10	1.55	*	
343.0	1125.2	1.73	1.26	2.41	27.1	47.6	98.5	0.7	0.69	2.62	1.04	23.0	
357.5	1172.9	1.96	1.63	2.49	17.2	34.5	97.6	0.8	-0.32	2.79	1.28	18.0	
367.0	1204.2	1.96	1.62	2.46	17.3	34.4	98.7	0.5	**	2.93	1.45	25.0	
372.8	1223.1	1.93	1.58	2.48	18.5	36.4	98.3	0.6	1.82	2.56	1.13	14.0	
382.1	1253.7	1.93	1.55	2.50	19.4	38.0	98.5	0.6	0.11	2.76	1.28	11.0	Tt4J
390.0	1279.6	2.05	1.74	2.55	15.3	31.8	98.8	0.4	0.28	2.67	1.34	11.0	
397.2	1303.1	1.75	1.29	2.39	26.1	46.0	99.1	0.4	1.08	2.68	1.30	11.0	Tt4H
404.0	1325.3	1.91	1.57	2.42	18.2	35.3	98.5	0.5	0.50	2.91	1.43	24.0	
410.9	1348.0	1.79	1.34	2.46	25.3	45.5	99.5	0.2	0.52	2.41	1.21	*	Tt4G
418.9	1374.4	1.98	1.68	2.41	15.0	30.3	98.5	0.5	**	3.02	1.46	8.0	
425.0	1394.4	1.91	1.56	2.44	18.5	36.0	98.1	0.7	**	3.18	1.47	12.0	
434.9	1426.7	1.88	1.50	2.44	20.1	38.4	98.1	0.7	2.30	3.12	1.57	12.0	Tt4F
441.0	1446.8	1.77	1.32	2.43	25.1	45.6	97.1	1.3	2.17	3.38	1.46	12.0	
449.2	1473.7	1.93	1.60	2.40	17.1	33.2	99.7	0.1	0.00	2.81	1.33	18.0	Tt4E
460.0	1509.2	1.94	1.59	2.45	17.9	35.2	98.7	0.5	2.96	3.25	1.49	30.0	Tt4AB
462.2	1516.5	2.23	2.02	2.59	9.2	21.9	93.0	1.5	**	3.63	1.76	*	Tt3D
489.5	1605.9	1.93	1.56	2.46	18.8	36.4	99.3	0.2	**	2.61	1.24	22.0	Tt3BC
501.8	1646.4	2.24	2.01	2.62	10.1	23.2	97.8	0.5	**	4.03	2.23	9.0	Tt3A
508.7	1669.1	1.98	1.65	2.51	16.6	34.3	95.5	1.5	*	*	*	*	Tbt
520.0	1706.1	1.95	1.65	2.39	15.5	30.9	97.8	0.7	-0.08	2.95	1.42	*	Tt2

¹ TerraTek reported data to three-decimal-point accuracy. Values shown here have been rounded off.

² Calculated using densities at three-decimal-point accuracy.

³ Permanent volume compaction after unloading from 4kb (400 MPa).

* Test not performed

+ Velocity determined from weak signal

++ Value less than precision of measurement

** Sample sheared during test

*** Unable to complete test

TerraTek Report TR88-43

Table 2 Physical properties, ultrasonic velocities, and permanent volume compactions measured on natural-state cores from vertical exploratory hole UE12n#14.

Metres	DEPTH Feet	1 DENSITY (Mg/m ³)			Water Content (% wet weight)	Poros- ity (%)	Satur- ation (%)	2Calc. Air Voids (%)	3Perm. Vol. Comp. (%)	1ULTRASONIC VELOCITY		Unconf. Comp. Strength (MPa)	Strati- graphic Unit
		Natural State	Dry Bulk	Grain						Long (km/s)	Shear (km/s)		
31.4	102.9	2.04	1.74	2.52	14.7	31.1	96.5	1.1	0.18	2.85	1.23	13.0	
60.0	196.7	1.83	1.39	2.49	24.0	44.1	99.5	0.2	0.34	2.54	1.18	3.0	
92.0	301.8	2.00	1.67	2.52	16.4	33.7	97.7	0.8	0.53	2.99	1.27	11.0	
122.9	403.2	2.02	1.70	2.56	15.8	33.6	94.7	1.8	0.91	2.71	0.97	5.0	
154.4	506.6	1.89	1.49	2.50	21.0	40.4	98.1	0.8	*	*	*	*	
184.7	606.0	1.93	1.55	2.50	19.3	37.8	98.4	0.6	0.63	2.62	1.01	12.0	Tt4K
212.1	696.0	2.10	1.82	2.57	13.3	29.1	96.3	1.1	0.52	2.82	1.18	*	
242.5	795.7	2.04	1.76	2.49	13.8	29.4	95.4	1.3	0.63	2.81	1.08	14.0	
274.1	899.4	1.91	1.53	2.46	19.7	37.6	99.9	0.1	-0.09	2.47	0.99	7.0	
305.9	1003.5	1.95	1.57	2.52	19.3	37.8	99.3	0.3	1.16	2.65	1.06	7.0	
336.3	1103.5	1.98	1.69	2.41	14.6	29.9	97.0	0.9	-0.12	2.95	1.40	27.0	
365.9	1200.5	1.94	1.59	2.47	17.9	35.4	97.9	0.7	0.58	3.07	1.36	13.0	
382.0	1253.2	1.85	1.46	2.43	21.0	40.0	97.1	1.2	0.64	3.25	1.29	13.0	
397.3	1303.5	1.90	1.52	2.48	20.0	38.8	97.9	0.8	1.09	2.54	1.01	6.0	
412.0	1351.8	1.91	1.54	2.47	19.4	37.8	97.6	0.9	0.74	2.64	1.07	8.0	
426.6	1399.6	1.92	1.56	2.48	19.0	37.3	97.7	0.9	-0.17	2.69	1.03	12.0	Tt4J
443.1	1453.7	2.00	1.66	2.52	16.9	34.2	98.7	0.5	0.90	2.82	1.07	10.0	
457.1	1499.8	1.81	1.38	2.42	23.5	42.9	99.0	0.4	0.75	2.56	0.97	12.0	
471.5	1546.9	1.95	1.59	2.50	18.2	36.3	97.4	0.9	0.63	2.78	1.09	10.0	
488.3	1602.0	2.01	1.68	2.53	16.6	33.6	99.0	0.3	0.54	2.76	1.09	10.0	
502.9	1650.0	1.91	1.53	2.51	19.9	39.0	97.7	0.9	0.39	2.57	1.04	6.0	
518.8	1702.1	1.80	1.38	2.39	22.9	42.1	97.5	1.0	0.43	2.72	1.24	26.0	
536.1	1758.9	1.89	1.53	2.43	19.0	37.2	96.4	1.4	0.08	2.97	1.42	21.0	
548.8	1800.5	1.95	1.61	2.48	17.3	34.9	96.5	1.2	0.60	2.87	1.32	15.0	Tt4H
565.9	1856.6	1.91	1.56	2.41	18.4	35.5	98.9	0.4	0.58	2.96	1.29	15.0	
579.5	1901.1	2.01	1.72	2.44	14.2	29.3	97.7	0.7	0.70	3.11	1.55	38.0	
594.1	1949.3	1.87	1.51	2.38	19.2	36.5	98.4	0.6	0.05	2.88	1.31	*	
610.1	2001.5	1.88	1.51	2.41	19.7	37.5	98.4	0.6	0.33	3.07	1.19	15.0	Tt4G
625.9	2053.6	1.91	1.55	2.44	18.6	36.4	97.8	0.8	0.23	3.13	1.05	19.0	
637.1	2090.1	1.93	1.59	2.45	17.7	35.0	97.7	0.8	0.32	2.80	1.25	16.0	Tt4F

* Data unavailable.

¹ TerraTek reported data to three decimal point accuracy. Values shown here have been rounded off.

² Calculated using densities at three decimal point accuracy.

³ Permanent volume compaction after unloading from 4kb (400 MPa).

TerraTek Report TR88-24

Table 3 Physical properties, ultrasonic velocities, and permanent volume compactions measured on natural-state cores from horizontal exploratory hole U12n.23 UG-1.

Average physical properties of the portion of Tunnel beds Subunit 4K in which the NPE cavity was mined are listed in Table 4. The density values given here are similar, to slightly higher, than average values for other N-Tunnel sites, possibly because the U12n.25 site appears to have a slightly higher percentage of clay than other sites. This interpretation is based on resistivity measurements and core observations; no x-ray mineralogical data are available for this site.

Table 4. Average physical properties of lower Tunnel beds Subunit 4K at the U12n.25 site.

Density (Mg/m^3)			Water Content (% by Wet Weight)	Porosity (%)	Saturation (%)	Calc. Air Voids (%)	*Perm. Volume Comp. (%)	Ultrasonic Velocity (km/s)		Unconf. Comp. Strength (MPa)
Natural State	Dry Bulk	Grain						Long	Shear	
1.97	1.62	2.51	17.6	35.5	97.7	0.8	0.53	2.73	1.11	9.3

* After unloading from 4 kb (400 MPa) in a uniaxial test.

All physical, mechanical, and core velocity data were provided to DNA by TerraTek Inc. [4]

GEOPHYSICAL PROPERTIES

Resistivity and sonic velocity data applicable to the NPE site were obtained from drill hole U12n.23 UG-1 by RSN geologists, who also made seismic velocity measurements in the U12n.23 drift (Figure 6). No geophysical data are available from vertical hole UE12n#14.

In zeolitized tuff, resistivity data are used by DNA to help identify regions where a high clay content could cause construction difficulties. The presence of clay is suspected when values less than 20 ohm-m are measured.^[6] RSN geologists used a Bison earth resistivity system to conduct the electrical resistivity survey in U12n.23 UG-1. The electrodes were spaced 0.9 m apart and arranged in a Wenner array. Discrete measurements were made in the borehole every three meters.

An average resistivity of 43 ± 24 ohm-m was calculated using 63 data points (ranging from 13 to 109 ohm-m) from U12n.23 UG-1 in the interval 94.5-274.3 m, which is equivalent to the stratigraphic section of the NPE site (no data were obtained from the collar to 94.5 m). The low values in this interval probably reflect the presence of argillized pumice disseminated throughout some of the beds. One slightly more argillized bed logged in this interval correlates with a bed projected to be present above the NPE cavity.

An EG&G Mount Sopris two-receiver acoustic velocity tool (receivers located 0.3 m apart) was used to obtain in-hole sonic data. Measurements were made in U12n.23 UG-1 at discrete locations every three meters. An average sonic velocity of 2594 ± 291 m/s was calculated using 27 measurements (with a range of 2112 to 3368 m/s) between the depths of 176.5 and 274.0 m. No data were obtained between the collar and 176.5 m.

A seismic survey was conducted in 1988 in the U12n.23 Access drift using explosives and 14-Hz geophones placed 6.1 m apart on the invert. An average seismic velocity was calculated (from time-distance plots) from the small portion of the survey area that is stratigraphically equivalent to the NPE medium (approximately 183 m from the NPE site). An average compressional velocity of 2640 m/s and a shear velocity of 1235 m/s were measured.

SUMMARY

Standard practices for characterizing the geology of DNA tunnel test beds were employed at the U12n.25 site. Certain physical and geophysical data that were not obtained within the U12n.25 complex itself were extrapolated from nearby drifts and drill holes. The NPE cavity was excavated in zeolitized to slightly argillized tuff of Tunnel beds Subunit 4K, in an area nearly free of geologic structure. Only four very small, discontinuous fault/fracture planes were found in the cavity during mining. The physical, mechanical, and geophysical properties of the site are similar to those of twenty nuclear tests previously conducted in N-Tunnel. These similarities should thus allow comparisons of the chemical and nuclear explosion data.

REFERENCES

1. Ferguson, J.F., A.H. Cogbill, and R. G. Warren, in press. A geophysical-geological transect of the Silent Canyon Caldera complex, Pahute Mesa, Nevada: Appendix. Accepted for publication in *Journ. Geophys. Res.*, late 1994.
2. Ellis, W. L. and J. E. Magner, 1980. Compilation of results of three-dimensional stress determinations made in Rainier and Aqueduct Mesas, Nevada Test Site, Nevada. U.S. Geological Survey Open-File Report 80-1098, 27 pages.
3. Smith, C. W., 6 January 1983. MINI JADE Hydrofrac. Written communication to J. W. LaComb, DNA.
4. Lupo, J. and W. Klauber, 1987. Physical and mechanical characterization of cored tuff from U12n.23 UG-1. TerraTek Report TR 88-24, 116 pages.
5. Torres, G., W. Martin, W. Klauber, and J. Lupo, 1988. Material properties of cored tuff from vertical borehole UE12n#14. TerraTek Report TR 88-43, 163 pages.
6. Carroll, R. D., 1990. Electrical logging and electrical properties of rocks in Rainier Mesa area, Nevada Test Site, Nevada. U. S. Geological Survey Open-File Report 90-31, 90 pages.

High Resolution Seismic Imaging of Rainier Mesa Using Surface Reflection and Surface to Tunnel Tomography

E. L. Majer, L. R. Johnson, E. K. Karageorgi, and J. E. Peterson

Center for Computational Seismology, Lawrence Berkeley Laboratory
Berkeley, California 94720

Abstract

In August 1993, two high resolution seismic experiments were performed in N-Tunnel and on the surface of Rainier Mesa above it. The first involved a surface-to-tunnel imaging experiment with sources on the surface and receivers in tunnel U12n.23 about 88 meters west of the NPE. The data obtained in this part of the experiment were of limited quality because of overwhelming 60 Hz noise in the tunnel. However, it was possible to estimate that the apparent average velocity between the tunnel and the surface was approximately 2.0 km/sec, which does provide a constraint on the mean velocity of P waves between the depth of the NPE and the surface. In a separate experiment, a high resolution reflection experiment was performed in order to image the lithology in Rainier Mesa down to the depth of the NPE and possibly greater. Good quality, broad band, reflections were obtained from depths extending into the Paleozoic basement, well below the NPE. A preliminary interpretation of these data yields several reflectors which correlate well with the lithology derived from drill hole logs. A high velocity layer near the surface is underlain by a thick section of low velocity material, providing a nonuniform but low average velocity between the depth of the NPE and the surface.

Introduction

In the interpretation of seismic data to infer properties of an explosion source, it is necessary to account for wave propagation effects. In order to understand and remove these propagation effects, it is necessary to have available a model of the material properties in the region between source and receiver which the elastic waves have sampled. An open question concerning this matter is the detail and accuracy which must be present in the velocity model in order to produce reliable estimates in the estimated source properties. While it would appear that the reliability of the results would be directly related to the accuracy of the velocity and density models used in the interpretation, it may be that certain deficiencies in these models can be compensated by the type and amount of seismic data which is used in the inversion. The NPE provided an opportunity to test questions of this sort, as the experiment was announced well in advance and the site was available for ancillary experiments. Taking advantage of this opportunity, two companion experiments were performed, the first involving controlled source surveys in the vicinity of the NPE which were designed to produce high resolution information on the velocity structure, and the second involving the recording of waveform data from the NPE which could use this velocity structure in its interpretation. The results of the first of these experiments are

described in the present paper, and the results of the second can be found in Johnson (1994).

In August two controlled source, high resolution, seismic surveys were carried out at Rainier Mesa in the vicinity of the NPE. Both involved a surface profile along a north-south line about 660 meters long and located about 600 meters west of the epicenter of the NPE. The relation of this profile to the NPE is shown in Figure 1. During the first part of the experiment, controlled sources were placed along this profile and receivers were placed in the tunnel U12n.23 near the NPE, which is also shown on Figure 1. This part of the experiment was designed to provide the data for a surface-to-tunnel imaging study. During the second part of the experiment, the surface profile was the site of both sources and receivers in order to collect data for a conventional multi-fold reflection study.

Surface-to-Tunnel Experiment

In the tunnel U12n.23 extending south toward Misty Echo, 96 30-Hz geophones were placed at 3 meter increments along the wall of the tunnel and connected to a 96-channel high resolution Bison model 90-96 seismograph. After the geophones were deployed, a Bison EW-4 impact source was used at the surface of the mesa to provide an energy source for the surface-to-tunnel tomographic imaging experiment. The source was used at 15 meter increments along a line on the surface approximately parallel to the tunnel but offset about 600 meters to the west, as shown in Figure 1.

Due to overwhelming 60 Hz noise in the tunnel, the data acquired for the tomography experiment were of limited quality and a full image was not possible. However, it was possible to identify first arrivals on the seismograms for some of the surface sources. On the basis of these arrival times an apparent average velocity between the surface and the tunnel, calculated as the ratio of the slant distance to the travel time, was estimated to be 2.0 km/sec. Because the tunnel was only 88 meters west of the NPE, this result provides a constrain on the mean velocity for similar paths between the NPE and the surface profile.

Surface Reflection Experiment

The surface reflection experiment was similar to the surface-to-tunnel experiment in most respects, the same equipment being used, but the receivers were now placed on the surface along the same profile as the sources. The receivers were the same 30 Hz vertical component geophones with a 3 meter spacing. The same impact source was used with a 6 meter spacing in source points. The recording system had 48 channels with a 0.5 msec sampling rate and a total recording interval of 1 sec. The passband of the recording was flat between 64 and 500 Hz.

Conventional reflection survey techniques were used in processing the data. The processing procedure was designed primarily to estimate the one dimensional P velocity as a function of depth in Rainier Mesa. After trace editing and trace scaling, the data were filtered to pass the 5 to 75 Hz band. After application of shot and receiver geometries, the data were sorted to common depth point (CDP) gathers, with maximum fold 24 traces. During the velocity analysis, several trial stacked profiles were generated using velocities from 500 m/sec to 6000 m/sec at 500 m/sec steps. A velocity semblance calculation was performed in order to estimate the mean velocities that yielded the most coherent normal-move-out stacks. A velocity function was then estimated and used to compute the final stack. Spiking and predictive deconvolution were also applied, but these did not significantly improve the data quality. The results were migrated after the stack. Automatic gain control with a characteristic time of 100 msec was then applied to the final section.

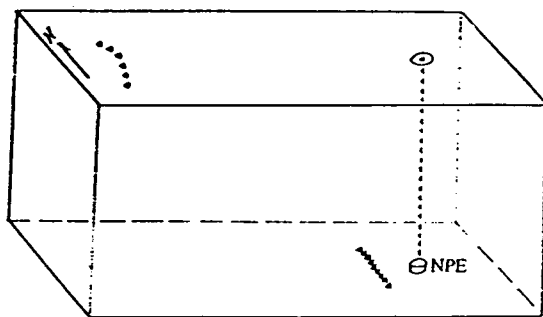
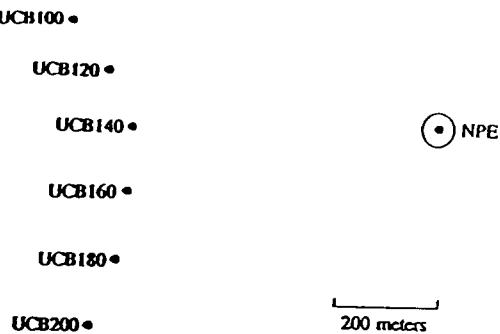


Figure 1. Relation of the surface profile to the location of the NPE. Also shown is the location of the tunnel U12n.23 which was a shot level and west of the shot point.

In Figure 2 the migrated section is shown as a function of travel time. This section shows numerous reflection events that extend throughout the recorded time interval of 1 sec. Some of these reflectors are quite strong, such as those arriving at two-way travel times of approximately 80, 200, and 600 msec. While there is definitely some lateral variations in the strength and continuity of these reflections over the length of the profile, the general picture is one of roughly horizontal layering. With the intention of obtaining a preliminary one-dimensional interpretation of the reflection data, the data were processed so as to enhance horizontal correlations in the reflectors. These results are shown in Figure 3. While this type of filtering has tended to smooth out any lateral variations in the reflectors, it has helped to identify the reflectors which have the most coherence over the length of the profile.

The reflection data of Figures 2 and 3 have been interpreted with the aid of the geological information contained in drill holes, as described in the paper by Baldwin et al. (1994). While the reflection data give accurate information on the two-way travel times of prominent reflectors, the information on interval velocities is much less accurate, and thus fixing the depth of the reflectors remains a problem. However, in most cases it was possible identify the reflector with a change in the lithology noted in the drill hole logs, and the combination of these two types of information was sufficient to fix the likely depth of the reflector. The preliminary one-dimensional velocity model for P waves that has emerged from this type of interpretation is shown in Figure 4.

The sections in Figures 2 and 3 show a strong reflector at a two-way travel time of about 80 msec, and the semblance and normal-move-out stacks indicate that this reflection is caused by a decrease in velocity. This is interpreted in Figure 4 as a decrease in velocity within the Rainier Mesa Tuff (Tmr) at a depth of about 80 meters. At a time of about 180 msec in Figure 3 there is another

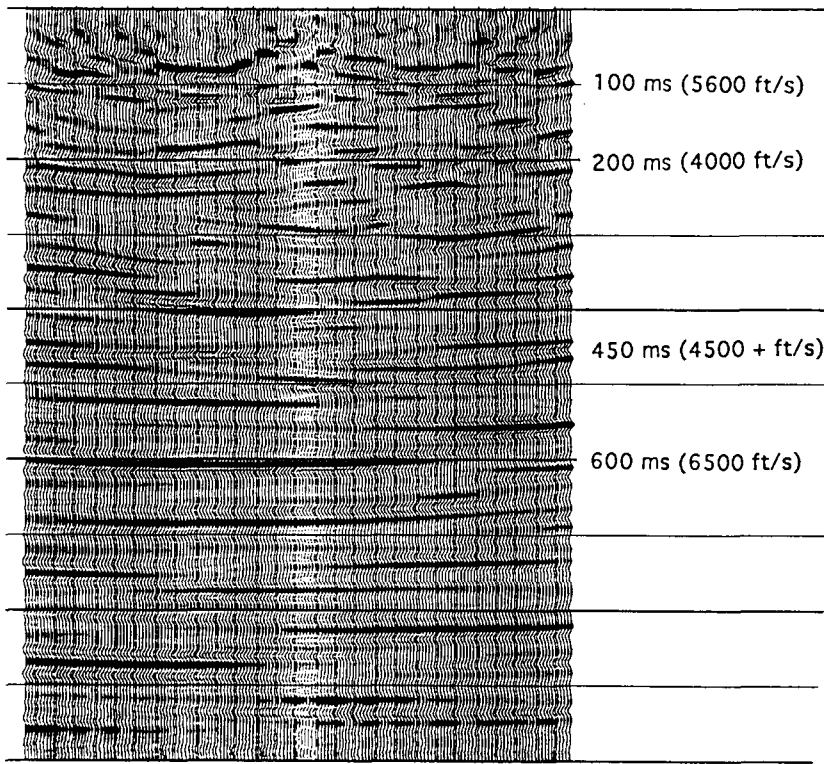


Figure 2. Migrated stacked section as a function of two-way travel time. The velocities on the left are those which were used in the stacking and migration process. The north end of the profile is on the left and the south end on the right.

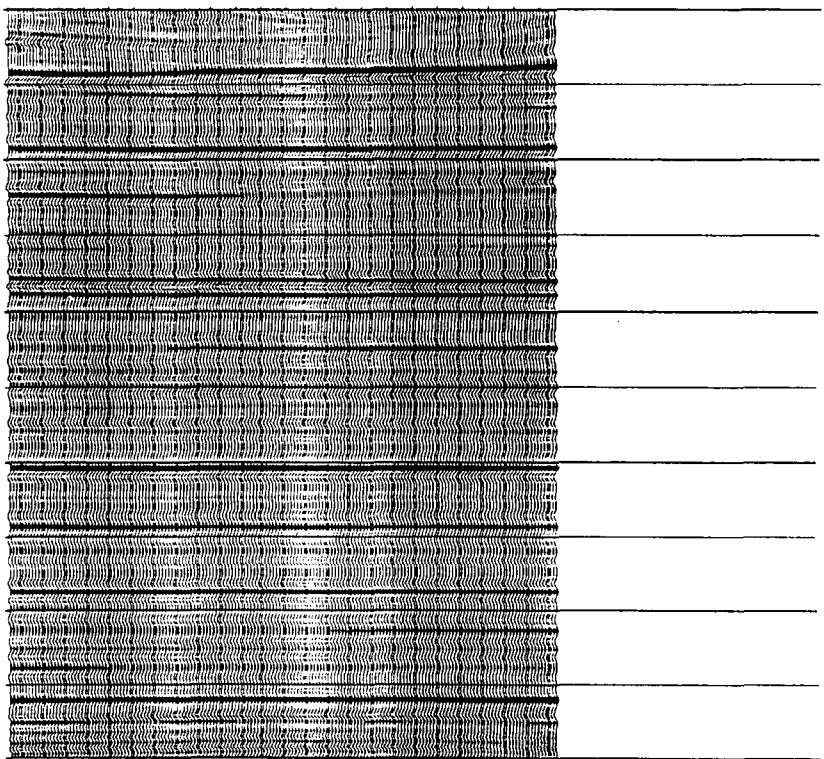


Figure 3. Similar to Figure 2 except that the data have been filtered to enhance lateral coherence.

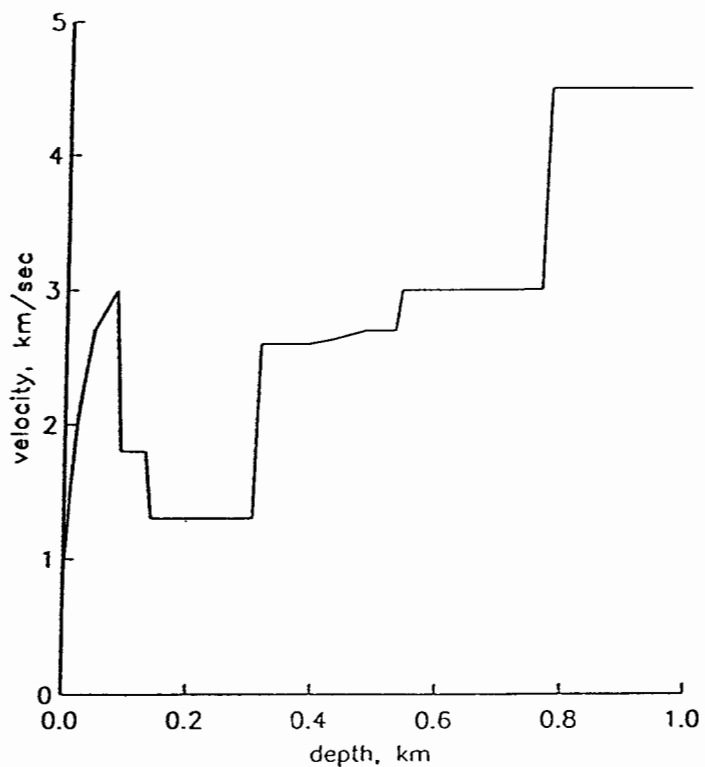


Figure 4. The preliminary one-dimensional velocity model for P waves which was derived on the basis of the reflection data.

reflector, but the velocity stacks are insufficient to indicate whether this represents an increase or decrease in velocity. In Figure 4 this is represented as a further decrease in velocity at a depth of about 130 meters, with the interpretation that this represents the transition from the ash flows of the Rainier Mesa Tuff (T_{mr}) to the ash falls of the Paintbrush Tuff (T_p). The velocity below this reflector appears to be quite slow, less than 1.5 km/sec. Although there is some evidence of reflectors at times of about 360 to 370 msec in Figure 3, the evidence in Figure 2 is somewhat uncertain. However, at a time of about 450 msec there is a better defined reflector which represents an increase in velocity to more moderate values of about 2.7 km/sec. This is interpreted as the boundary between the Paintbrush Tuff (T_p) and the Grouse Canyon Tuff (T_{bg}) at a depth of 315 meters. The next strong reflector is at a time of 610 msec and this is a further increase in velocity. It appears to be the boundary between the Tunnel Beds Tuff (T_{t3}) and the Belted Range Tuff (T_{bt}) at a depth of 530 meters. There appears to be another reflector at a time of 680 msec, but the interpretation of this event in terms of the geology is still not clear. At a time of 770 reflector there is a reflector which appears to represent the transition to the Paleozoic basement, the boundary between the Older Tuffs Units (T_{ot}) and the Wood Canyon Formation (C_{pcw}). At a time of 920 msec there is still another strong reflector, which appears to be a reflector from within the basement at a depth of approximately 1100 meters.

The forgoing interpretation of the reflection data, as represented in Figure 4, is a preliminary attempt to reconcile the travel times of prominent reflectors, the velocities suggested by the semblance and normal-move-out stacks, and the geological information contained in the drill holes. It is worth noting that the model which has emerged is generally consistent with the low apparent average velocity that was obtained in the surface-to-tunnel experiment, primarily because of the low velocity in the thick section of the Paintbrush Tuff unit. The resulting velocity model is noteworthy because of the

relatively high velocity layer near the surface which is underlain by a thick section of quite low velocities. The model suggests, however, that at the depth of the NPE (389 meters) the velocity has increased to a more moderate value of about 2.6 km/sec.

Discussion and Summary

This study illustrates the type of information which can be obtained with simple, efficient, controlled source, velocity surveys. These experiments were performed in a single day, and the processing up to this point has been fairly standard. While it remains to be shown just how useful these data will be in the interpretation of the NPE data, it has been demonstrated that rapid acquisition and interpretation of velocity data of this type could be easily incorporated into a verification scenario if it was deemed useful.

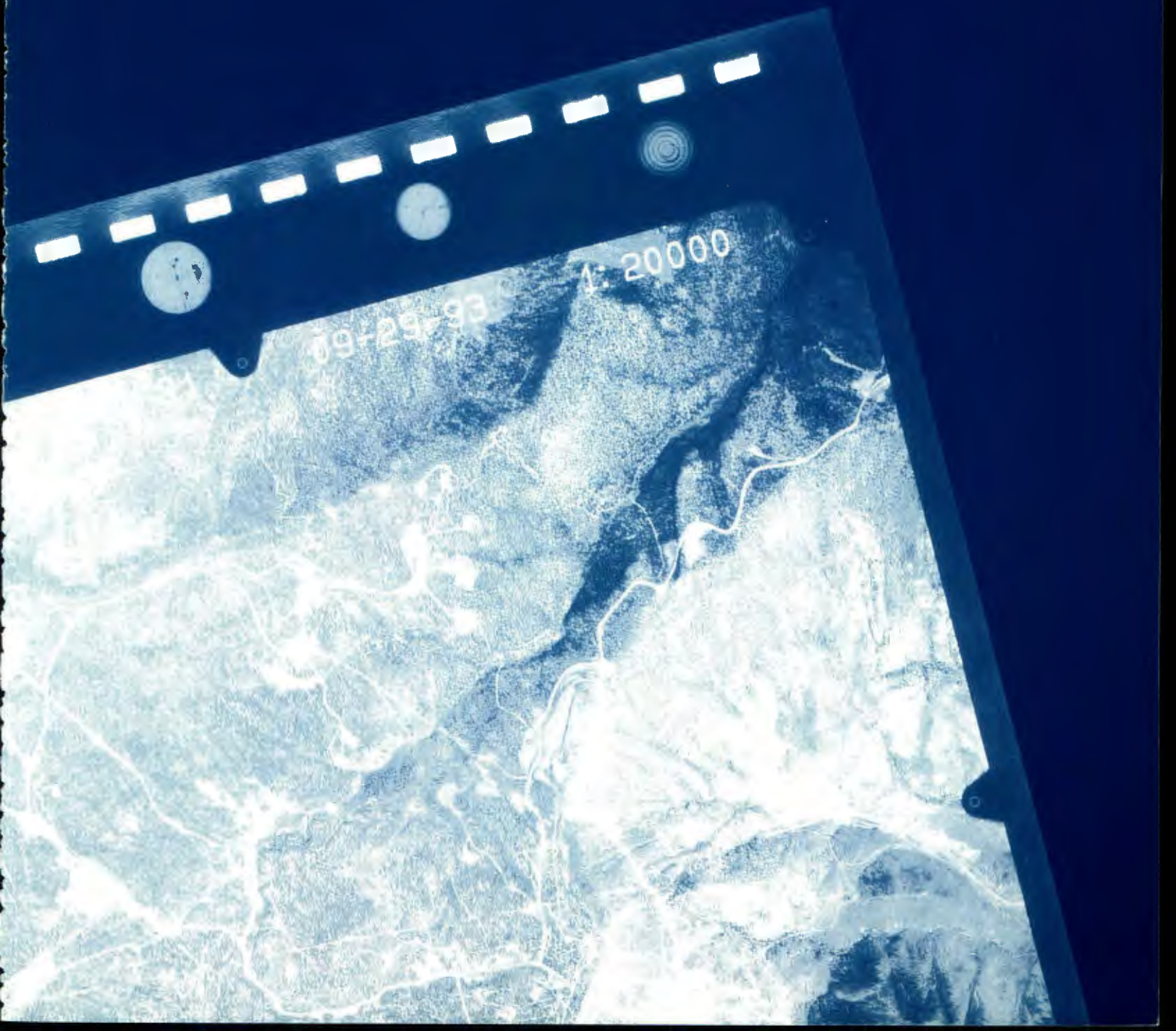
The surface-to-tunnel survey suffered from the large amount of 60 Hz electrical noise that existed in the tunnel, but, anticipating this type of problem in future experiments, there might be methods of mitigating this problem. Nevertheless, this part of the experiment did provide some useful information on the mean velocity of the upper 400 meters of Rainier Mesa, which turns out to be quite low.

The surface reflection survey employing an impact source produced good quality, broad band, reflections with good penetration. High resolution data were obtained down to depths that are well below that of the NPE. The length of the profile was rather short for this survey, but it was still possible to distinguish between high and low velocity segments of the section by using standard velocity stacking procedures. Such information can be critical in removing propagation effects from waveforms registered from explosions.

References

- Baldwin, M. J., R. P. Bradford, S. P. Hopkins, D. R. Townsend, and B. L. Harris-West, Geologic characteristics of the NPE site in the U12n.25 drift of N-tunnel, Nevada Test Site, in Proceedings of the Symposium on the Non-Proliferation Experiment Results and Implications, M. D. Denny et al. (eds), Lawrence Livermore National Laboratory, Livermore, CA, CONF-9404100, 1994.
- Johnson, L. R., Seismic source parameters, in Proceedings of the Symposium on the Non-Proliferation Experiment Results and Implications, M. D. Denny et al. (eds), Lawrence Livermore National Laboratory, Livermore, CA, CONF-9404100, 1994.

GROUND MOTION MEASUREMENTS



Comments on Some Results Derived from the NPE

Indra N. Gupta

Multimax, Inc., 1441 McCormick Drive, Landover, Maryland 20785

It seems to me that the Symposium on the Non-Proliferation Experiment was very useful in improving our understanding of the generation of both low and high frequency Lg and transverse motion from explosions. Patton's (1994) investigation of near-regional data from the NPE led him to conclude that near-source scattering of Rg, generated by the explosion (including its associated CLVD), is mainly responsible for the low-frequency Lg. His study was based on the analysis of long period data. By analyzing broadband data from the NPE and other NTS explosions recorded at the network of stations operated by the Lawrence Livermore National Laboratory, both Walter *et al.* (1994) and Mayeda (1994) found Rg-to-S scattering to have a dominant role in generation of the low-frequency Lg. These results appear to provide confirmation of the mechanism for the generation of low-frequency Lg by scattering of the explosion-generated Rg into S by near-source heterogeneities, proposed by Gupta *et al.* (1992). Furthermore, for higher frequencies, Walter *et al.* (1994) and Mayeda (1994) observed strong dependence of Lg on gas porosity of the shot medium. Since gas porosity strongly influences the shot medium velocity, these results are in agreement with the suggestion that the higher-frequency Lg originates from the pS phase and the shot-point velocity strongly influences the degree to which pS is trapped and contributes to Lg (Frankel, 1989; Gupta *et al.*, 1992). It appears therefore that the generation of both low- and high-frequency Lg can be explained by two distinct mechanisms proposed earlier by Gupta *et al.* (1992). Spall probably has a much smaller role in excitation of the low-frequency Lg than that proposed by several investigators including McLaughlin *et al.* (1990).

In order to explain the observed "growth" of the transverse component with distance for several explosions, Gupta and Blandford (1983) suggested that the transverse motion is mostly due to scattering along the propagation path. Explosion data mostly from the eastern United States showed the transverse motion in Lg to be initially small and increasing progressively with distance such that it finally appeared to be larger than the other two components because of the effect of the free surface. However, most data from the western United States show large transverse motion at both short and large distances and a lack of gradual increase with distance. In fact, McLaughlin *et al.* (1983) observed a strong low frequency SH pulse arriving directly from the NTS explosion, Colwick. Analysis of three-component data from the NPE by Stump *et al.* (1994) also showed large transverse motion at all distances. A possible mechanism for the generation of this low-frequency SH motion can be the scattering of explosion-generated Rg into S, with the S wave having significant SH component if the source region is strongly heterogeneous. More data will need to be examined to explore this possibility.

Lastly, if Rg-to-S scattering is dominant, at least for the NTS shots, Rg-to-P should also be expected to make an important contribution to waves immediately following direct P. This agrees with the earlier suggestion (Gupta *et al.*, 1991) that the large-amplitude, low-frequency arrivals, immediately following P in several teleseismic observations, are due to the near-source scattering of Rg into P. F-k analysis of teleseismic data from several Yucca Flat explosions, recorded at several stations, provided direct evidence for Rg to P scattered arrivals (Gupta *et al.*, 1990).

References:

Frankel, A. (1989). Effects of source depth and crustal structure on the spectra of regional phases determined from synthetic seismograms, DARPA/AFTAC Annual Seismic Research Review, 97-118, Patrick Air Force Base, Florida.

Gupta, I. N. and R. R. Blandford (1983). A mechanism for generation of short-period transverse motion from explosions, Bull. Seism. Soc. Am. 73, 571-591.

Gupta, I. N., C. S. Lynnes, T. W. McElfresh, and R. A. Wagner (1990). F-k analysis of NORESS array and single station data to identify sources of near-receiver and near-source scattering, Bull. Seism. Soc. Am. 80, 2227-2241.

Gupta, I. N., T. W. McElfresh, and R. A. Wagner (1991). Near-source scattering of Rayleigh to P in teleseismic arrivals from Pahute Mesa, NTS shots, in Explosion Source Phenomenology, Geophysical Monograph 65, Am. Geophys. Union, Washington, D.C., 151-159.

Gupta, I. N., W. W. Chan, and R. A. Wagner (1992). A comparison of regional phases from underground nuclear explosions at East Kazakh and Nevada test sites, Bull. Seism. Soc. Am. 82, 352-382.

Mayeda, K. M. (1994). Lg coda spectral ratios of the NPE, paper presented at the Symposium on the Non-proliferation Experiment, April 19 - 21, 1994.

McLaughlin, K. L., T. G. Barker, and S. M. Day (1990). Implications of explosion-generated spall models: regional seismic signals, GL-TR-90-0133, Geophysics Laboratory, Hanscom Air Force Base, Massachusetts.

McLaughlin, K. L., L. R. Johnson, and T. V. McEvilly (1983). Two-dimensional array measurements of near-source ground accelerations, Bull. Seism. Soc. Am. 73, 349-375.

Patton, H. J. (1994). Investigations of the Low-frequency seismic waves recorded at near-regional distances from the NPE, paper presented at the Symposium on the Non-proliferation Experiment, April 19 - 21, 1994.

Stump, B. W., D. C. Pearson, C. L. Edwards, and R. E. Reinke (1994). Analysis and interpretation of free-surface ground motions from the NPE, paper presented at the Symposium on the Non-proliferation Experiment, April 19 - 21, 1994.

Walter, W. R., H. J. Patton, and K. M. Mayeda (1994). Regional seismic observations of the NPE at the Livermore NTS network, paper presented at the Symposium on the Non-proliferation Experiment, April 19 - 21, 1994.

Seismic Source Parameters

Lane R. Johnson

Center for Computational Seismology, Lawrence Berkeley Laboratory
Department of Geology and Geophysics, University of California
Berkeley, California 94720

Abstract

The use of information contained on seismograms to infer the properties of an explosion source presents an interesting challenge because the seismic waves recorded on the seismograms represent only small, indirect, effects of the explosion. The essential physics of the problem includes the process by which these elastic waves are generated by the explosion and also the process involved in propagating the seismic waves from the source region to the sites where the seismic data are collected. Interpretation of the seismic data in terms of source properties requires that the effects of these generation and propagation processes be taken into account. The propagation process involves linear mechanics and a variety of standard seismological methods have been developed for handling this part of the problem. The generation process presents a more difficult problem, as it involves non-linear mechanics, but semi-empirical methods have been developed for handling this part of the problem which appear to yield reasonable results. These basic properties of the seismic method are illustrated with some of the results from the NPE.

Introduction

The study of seismic sources is based on the fact that any rapid change of conditions within the earth will generate elastic waves that then propagate outward from the source region to other parts of the earth. The motions caused as these elastic waves pass various locations are recorded as a function of time to form graphs called seismograms, and the analysis of these seismograms is a fundamental task of seismology. An extensive set of analysis techniques have been developed for determining the location of the source, properties of the source such as its magnitude and focal mechanism, and the velocity structure of the earth. These analysis techniques, which were originally developed for the study of earthquakes, are easily adapted to the study of underground explosions. In the case of an explosion the source properties which are of interest are its size (yield), physical dimensions, type of explosive, method of detonation, and the coupling efficiency.

The purpose of this presentation is to give a general outline of methods by which the study of seismograms can lead to estimates of various properties of an explosive source. While this is just one aspect of the more general problem of seismic verification, it is one of the more critical aspects because it attempts to make definitive inferences about the physical properties and processes of the explosion itself. Some of the basic steps of this process will be illustrated with data and results from the NPE.

Seismic Verification - Basic Problems

In considering the general problem of seismic verification, it is important to keep in mind two features of the problem which strongly influence the methods which must be employed. The first is the fact that seismic waves are not produced directly by the explosion, but are only an indirect consequence of the disturbance within the earth caused by the explosion. This means that a geophysical inverse problem must be solved in order to convert the information contained in seismic waves into estimates of the explosion properties. The second is the fact that the fraction of the explosive energy that is converted to seismic waves is actually quite small, generally only a few percent. This second feature increases the difficulty of the inverse problem which must be solved and tends to magnify the uncertainty of the results.

Seismic Verification - Basic Methods

The various methods that have been developed for estimating the properties of explosions on the basis of seismic data can be roughly grouped into three different approaches:

- direct comparisons
- magnitude-based methods
- solution of an inverse problem

The method of direct comparison depends upon having a calibration explosion of known properties located at the same point and recorded with the same instrumentation as the explosion under study. Then, a direct comparison between the seismograms from the calibration explosion and seismograms from the explosion of interest is possible, which can lead to estimates of the relative strength and dimensions of the two explosions. Such a calibration event was included in the NPE and presentations which discuss direct comparisons include Goldstein and Jarpe (1994), Hutchings (1994), Reinke et al. (1994), and Stump et al. (1994). An advantage of this approach is that it involves the fewest number of assumptions and thus has the potential to obtain the most accurate results. A disadvantage is that a very specific calibration event is required, and this may not be included in all verification scenarios.

The second approach is a group of related methods which are essentially extensions of the magnitude scales which were developed for measuring the size of earthquakes. Such methods were developed first and are still the most commonly used for the estimation of explosion properties. The basic idea is to assemble a comprehensive set of seismic observations that have been obtained from a group of seismic sources having known properties, and from this data set develop empirical relationships that relate measurements made on the seismic data to properties of the explosion source. The previous presentation by Garbin (1994a) provides a general overview of this approach and examples of its application can be found in many of the papers of this symposium, including Garbin (1994b), Mayeda (1994), Patton (1994), Rohrer (1994), Smith (1994), and Walter et al (1994). Advantages of this approach are that estimates of uncertainty are conveniently included and it lends itself to both discrimination and source parameter estimation problems. A disadvantage is that it requires an extensive calibration data set and misleading results can be obtained when it is applied to events that differ significantly from the calibration set.

The third approach includes the more formal methods which attempt to characterize the estimation procedure as the solution of a geophysical inverse problem. Actually, as described below, it is

necessary to consider two separate inverse problems. The first is the conversion of the observed seismograms to an estimate of the seismic source, while the second involves the conversion of the seismic source to an estimate of the explosion properties. The remainder of this presentation will concentrate on a description of this third approach, not because it is the best or most popular, but because it requires an explicit examination of most of the fundamental problems that are common to all methods of estimating explosion source properties.

Basic Physics of Elastic Wave Generation by Explosions

In the case of tamped underground explosions there are a number of different processes that are involved in the generation of elastic waves. These are illustrated schematically in Figure 1. The explosion is initially contained within a cavity of radius R_c which has been excavated from the surrounding rock. At the time of detonation a hot pressurized gas is created within the cavity which causes it to expand. Some of the surrounding rock may be vaporized and added to the cavity at this time also. The sudden expansion of the cavity generates a shock wave which propagates outward and causes major damage to the surrounding rock, first in a crushed zone and then in a fractured zone. The energy density of this shock wave decreases with distance from the explosion, partly due the fact that it is spreading in three dimensions and partly due to the fact that energy is being used to crush and fracture the rock. Thus the shock wave gradually decays into an inelastic wave, which is still strong enough to involve nonlinear motions and permanent deformation of the material. This nonlinear wave also decays with distance from the explosion and eventually a radius is reached where the motions are sufficiently reduced so that they can be satisfactorily described by the ordinary elastodynamic equations of linear elasticity. Beyond this distance, labeled R_s and called the elastic radius, the disturbance caused by the

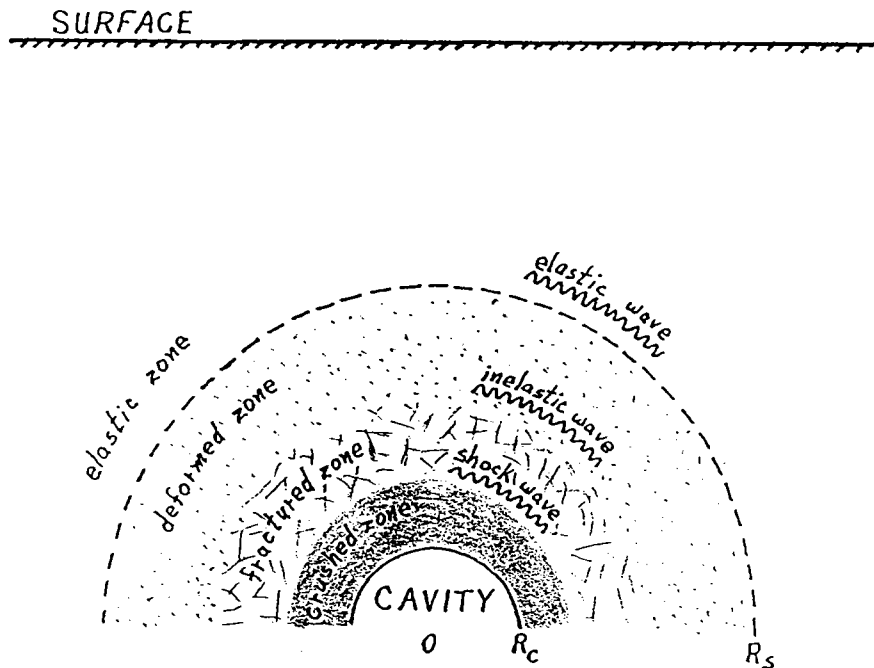


Figure 1. Diagram showing some of the different zones and processes that surround a buried explosion.

explosion propagates as elastic waves, and hence in this region all of the standard linear methods of seismology can be applied to explain how these waves propagate throughout the earth, including the reflection and refraction that takes place when variations in earth structure are encountered, the conversion between different types of elastic waves, and the generation of surface waves. It is the motions caused by these elastic waves that are generally recorded on seismograms.

This simple description of the explosion process is sufficient to illustrate the fundamental problems of using seismic waves to estimate properties of the source. The basic task is to take seismograms observed some distance from the explosion and extract from these records information about the properties of the source. However, the seismogram is a product of all of the processes that have taken place, including the explosion process that takes place within the radius R_c , the nonlinear processes that take place between the radius R_c and R_s , and the linear wave propagation processes that take place outside the radius R_s . Thus, if one wants to extract information about the source process, it is first necessary to remove the effects of the other processes that have taken place between the source and the location where the seismogram was recorded. In effect, removing the effects of these other generation and propagation processes is equivalent to moving the observation point back to the surface of the explosion cavity. This concept of transporting the information on the seismogram from the observation point back to the explosion source is conveniently divided into two steps. The first involves movement from the observation point to the elastic radius R_s , and this consists of removing the linear effects of ordinary elastic wave propagation. The result of this first step is an estimate of the motion that occurred at the radius R_s , and this will be referred to as the *seismic source*. The second step involves movement from the elastic radius R_s to the cavity radius R_c , and this requires that the strongly nonlinear effects of shock waves and inelastic waves be described and removed. The final result is an estimate of the motion that occurred at the cavity radius R_c , and this will be referred to as the *explosion source*.

The basic problem of using seismic waves to estimate the properties of an explosive source can now be stated. The observational data, the seismograms, contain the combined effects of the explosion process, the nonlinear processes that lead to the generation of the elastic waves, and the propagation processes that carry the elastic waves out to the locations where the data are recorded. In order to isolate the explosion process and thus determine the explosion properties, it is necessary to remove the effects of both the propagation process and the generation process.

Estimation of the Seismic Source

Consider the processes which take place as elastic waves propagate outward from the elastic radius R_s to the location where the seismogram is recorded. If the displacement at this elastic radius is known and if the properties of the surrounding material are sufficiently well known, then the propagation process can be modeled and it is possible to predict the time history that appears on the seismogram. This is known as a forward problem and is written schematically as

$$\text{seismogram} = \text{seismic source} \times \text{propagation process}$$

In practice, the solution of this problem consists of solving the differential equations that describe linear elastic wave propagation, and methods for obtaining such solutions are relatively well established. However, this is not actually the problem of interest in the present situation because it is the seismogram, being the observational data, which is known and it is the seismic source which is not known.

Thus what must actually be solved is the inverse problem

$$\text{seismic source} = \frac{\text{seismogram}}{\text{propagation process}}$$

The right-hand side of this expression represents the process of deconvolving the propagation process from the observed seismogram. Although the solution of this inverse problem is more complicated than the forward problem, fortunately it too has a well behaved solution with properties which have been extensively studied. Obtaining such a solution requires that the earth structure in the region outside the elastic radius be known and depends upon the fact that the propagation process involves ordinary linear mechanics. What results is a linear inverse problem. This means that, given sufficient observational data (generally a minimum of six different seismograms), it is possible to obtain a unique estimate for the seismic source. Of course, as in all inverse problems, this estimate will carry with it a certain amount of uncertainty, but there are methods of estimating this uncertainty also.

One of the consequences of considering the estimation of the seismic source as the solution of an inverse problem is that it forces one to examine the question of how the seismic source is to be represented. It turns out that a method used in many branches of physics, the method of multipole expansions, provides a convenient method of representation. The forces acting in the source region are expanded in terms of moments of various orders, as shown by Stump and Johnson (1977). The monopole term in this expansion is zero because the source exerts no net force on the earth. The first nonzero terms involve dipoles and these dominate higher order terms for localized sources such as an explosion. Thus it is usually sufficient to retain only the dipole terms in the force-moment expansion, and the complete set of these force couples is depicted in Figure 2. In seismology these dipole terms are known collectively as the *seismic moment tensor*. This is a symmetric second-order tensor and

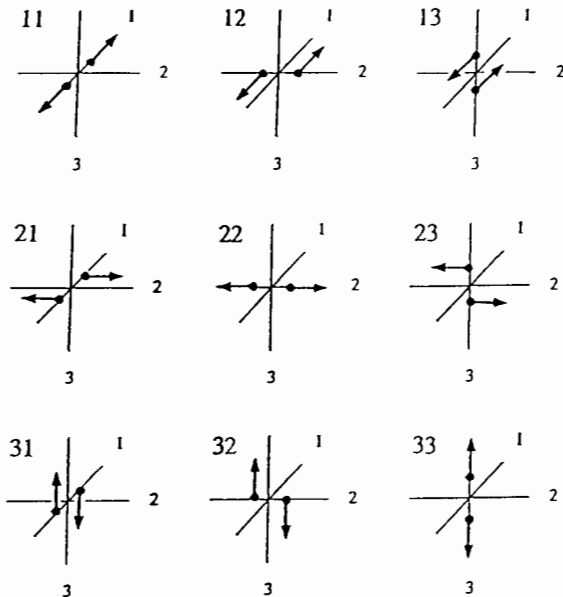


Figure 2. The orientation of the force couples that comprise the second-order seismic moment tensor. The usual orientation of the axes is 1 north, 2 east, and 3 down. Conservation of angular momentum for the earth requires symmetry relations for the shear couples of the form: $12 = 21$, $13 = 31$, and $23 = 32$.

consists of six independent terms, with three terms being extensional force couples and three being shear force couples. It serves as a convenient mathematical representation of the seismic source.

This process of estimating the seismic source can be illustrated with some of the data collected for the NPE (Johnson, 1994). Figure 3 shows the accelerations measured in the vertical direction at six different sites located on the surface of Rainier Mesa, with slant distances ranging between about 700 and 850 meters. Records such as these contain the combined effects of both the seismic source and the propagation process and comprise the basic data for the inverse problem. The propagation process is represented by calculating Green functions for elastic wave propagation in a model of the Rainier Mesa structure, in this case obtained from a reflection survey performed prior to the NPE (Majer, et al., 1994). Then the result of solving this first inverse problem, the seismic moment tensor estimate for the NPE, is shown in Figure 4. Note that the extensional force couples (11, 22, and 33 terms) dominate the shear force couples (21, 31, and 32 terms), which is exactly what is predicted for an explosion. In contrast, an earthquake would be dominated by the shear force couples, so this analysis has already established that the NPE was definitely an explosion. Also note that the 33 term is somewhat larger than the 11 and 22 terms, which indicates there was some asymmetry in the explosion, with the expansion in the vertical direction greater than in the horizontal directions. The seismic moment tensor of Figure 4 represents the solution to the first inverse problem, the elastic propagation effects having been removed so that an estimate of the motion at the elastic radius R_s is now available.

Estimation of the Explosion Source

The next step is to understand the relationship between the seismic source, which is a description of the elastic displacements at the radius R_s , and the explosion source, which is a description of what

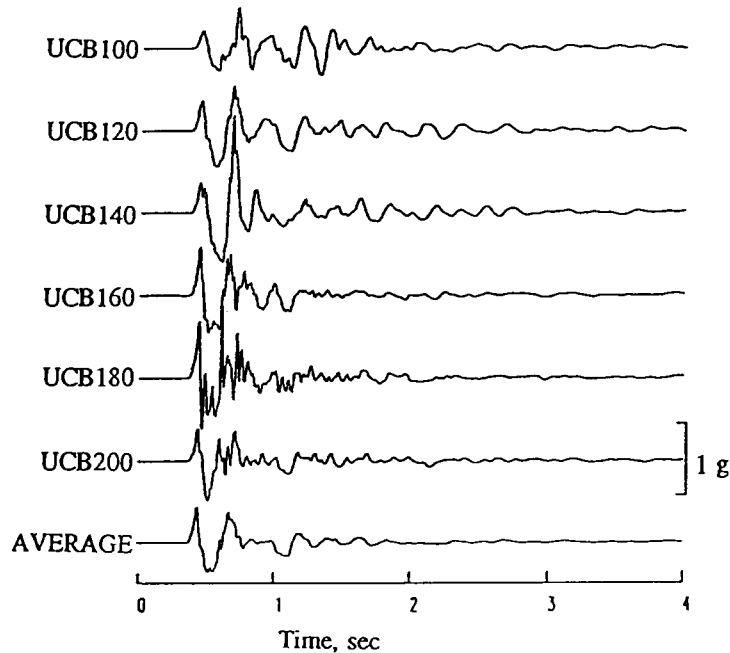


Figure 3. A sample of the seismograms that were recorded from the NPE. These seismograms show the vertical accelerations that were recorded on the surface of Rainier Mesa along a north-south line about 600 meters west of the epicenter.

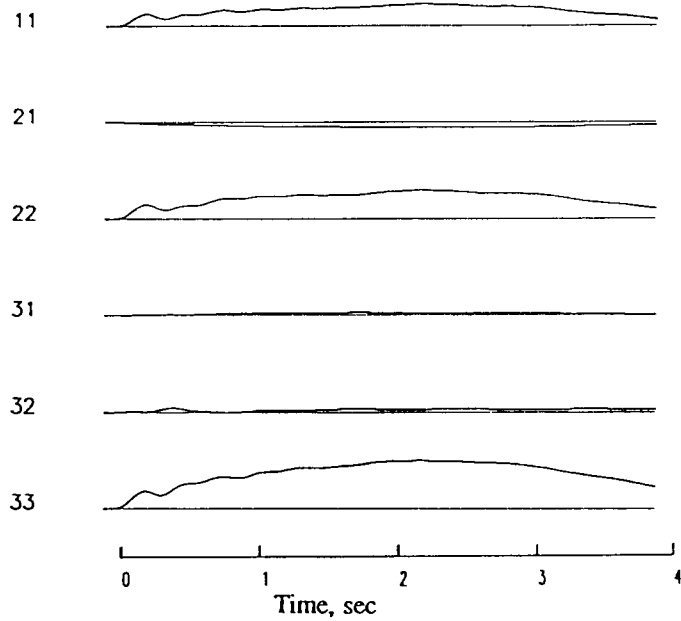


Figure 4. The six independent elements of the second-order seismic moment tensor that were estimated for the NPE.

happens at the radius R_c . First consider the forward problem in which it is assumed that the explosion source is known and that the physical processes that take place between R_c and R_s , here collectively called the generation process, are well enough understood so that it is possible to predict the seismic source.

$$\text{seismic source} = \text{explosion source} \times \text{generation process}$$

Solutions to this forward problem are possible, but the task is much more difficult than the forward problem involved in the estimation of the seismograms. This is because the generation processes for the most part are non-linear, involving the propagation of shock waves and non-linear elastic waves and permanent changes in the material properties, such as crushing, fracturing, and collapse of pore space. Considerable effort has gone into modeling these phenomena, resulting in the development of a series of fairly elaborate hydrodynamic computer codes. An important part of these calculations is the equation of state for the material in the vicinity of the explosion, and this type of information must often be obtained by extensive laboratory and field testing. The NPE provided an opportunity to check these types of calculations and the results are described in the papers by Bos (1994), Glenn and Goldstein (1994), Hill (1994), McKown (1994), Patch et al. (1994), and Souers and Larson (1994).

As before, the problem to be solved is actually an inverse problem, as it is assumed that an estimate of the seismic source has been obtained from the analysis of the seismograms and the objective is to convert this to an estimate of the explosion source. This inverse problem can be represented as

$$\text{explosion source} = \frac{\text{seismic source}}{\text{generation process}}$$

In order to solve this inverse problem it is necessary to estimate the effects of the generation process and remove these from the representation of the seismic source. Unfortunately, as discussed above, this

generation process involves some strongly non-linear mechanics and this makes it very difficult to construct a formal solution to the inverse problem. In fact, at the present time no direct methods of solving this particular inverse problem have been developed, and this represents one of the major obstacles in the study of explosion sources using seismic methods. Even if direct methods can be developed for solving this problem, because of the basic nonlinearity of the processes involved, the solution is likely to be highly non-unique and contain considerable uncertainty. Thus, the complexity and strong non-linear character of the forward problem in the immediate vicinity of an explosion source creates a situation where it is very difficult to obtain a satisfactory solution to the inverse problem that must be solved in order to obtain an estimate of the explosion source. Faced with this fundamental conundrum, some indirect methods of obtaining certain properties of the solution have been devised, and these will be described below. Fortunately, some of these indirect methods appear to be quite successful in circumventing the basic difficulties of the generation process.

One indirect method of solving this inverse problem is to solve the forward problem for a variety of different assumed explosion sources, and then select as the solution the one that produces a simulated seismic source which is the most similar to the observed seismic source. In principle, this could be formalized into a Monte Carlo procedure, although this is rarely done for this particular problem. It is important to keep in mind that the solutions obtained with this approach contain a fundamental non-uniqueness and uncertainty, and both of these properties are difficult to characterize in a quantitative manner. Contributing to this non-uniqueness and uncertainty is the fact that material properties in the source region play an important and complex role in determining how the explosion source at radius R_c is transformed into the seismic source at the radius R_s . Included in the relevant material properties for this region are:

- density, natural and compressed
- bulk elastic properties, modulus and strength
- shear elastic properties, modulus and strength
- porosity
- type of material in pores
- overburden pressure
- tectonic stress field

There is still not complete agreement about how these material properties should be incorporated into the forward calculations, and in many practical applications they may be poorly known. However, these types of parametric studies of the forward problem play an important role in providing guidelines and limits for more empirical studies.

There is another indirect approach to the inverse problem for the explosion source which does not produce an actual solution but does attempt to estimate certain properties of that solution. The basic idea is to parameterize both the explosion source and the seismic source and then try to find simple relationships that connect the parameters of these two sources. In general, these relationships are guided by the relevant theory but also have an empirical component, and, in view of the discussion above, one would expect them to be dependent upon the material properties of the source region. The following section describes one approach to the parameterization of the seismic and explosion sources, and this is followed by a discussion of some possible relationships between the parameters.

Spectral Models for Explosions

Given that a satisfactory solution to the inverse problem that converts the seismic source into the explosion source has not yet been developed, it is worth considering whether it might be possible to relate certain properties of the seismic source to the explosion source. A common approach of this type makes use of the fact that some of the pertinent properties of these sources are more easily identified in the frequency domain than in the time domain. For instance, if the explosion is assumed to be symmetric, then the seismic moment tensor can be reduced to a single time function, the *isotropic moment tensor*. This is simply the average of the three extensional force couples (the 11, 22, and 33 terms in Figure 4). Then taking the Fourier transform of the time derivative of the isotropic moment tensor and extracting the modulus of this quantity as a function of frequency, one arrives at amplitude spectrum of the moment rate tensor. Such a spectrum for the NPE (calculated from the results of Figure 4) is shown in Figure 5.

The spectrum shown in Figure 5 illustrates the basic features which are common to the spectra of most seismic sources. At low frequencies the spectrum approaches a constant level which is called the *low frequency level*. At high frequencies the spectrum decreases with increasing frequency at a more or less constant rate known as the *high-frequency decay rate*. The intersection between the low frequency level and the high frequency decay is the *corner frequency*. In the vicinity of the corner frequency there may be some peaking in the spectrum, which is known as the *spectral overshoot*. Simple theoretical models can be used to relate these spectral features of the seismic source to properties of the explosive source. The rough correspondence is as follows:

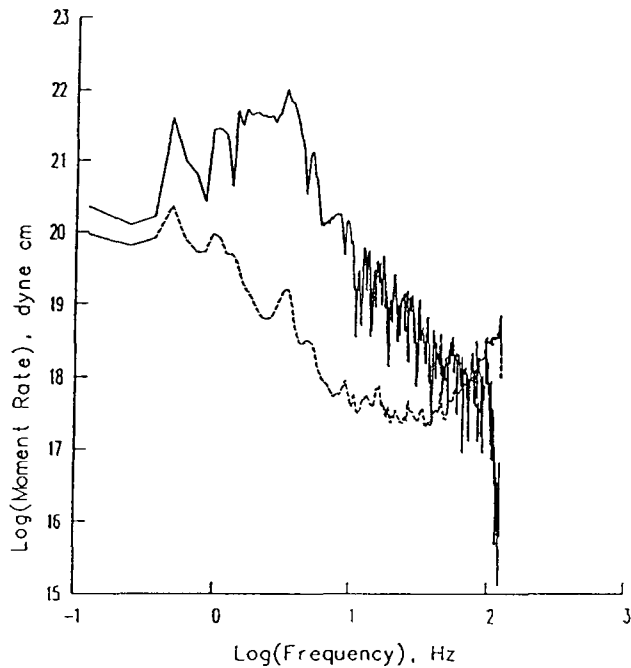


Figure 5. The modulus of the amplitude spectrum of the isotropic part of the seismic moment rate tensor which was calculated from the estimates contained in Figure 4. The dashed line is an estimate of the noise.

<i>spectral feature</i>	<i>explosion property</i>
low frequency level	yield
corner frequency	physical dimension
spectral overshoot	amount of oscillation
high-frequency decay rate	sharpness of initial pulse

Note that the low frequency level of the spectrum is also known as the *scalar seismic moment*, and is proportional to the constant part of the *reduced displacement potential*.

To proceed further with this approach of relating spectral features of the seismic source to explosion properties it is necessary to obtain quantitative estimates of the spectral features. This is commonly done by fitting parameterized models to the spectrum. A variety of such models have been proposed, some based on theoretical models of a simple explosion and some being purely mathematical, and the properties of these models are listed in Table 1 of Denny and Johnson (1991). Figure 6 shows what happens when one of these models is fit to the spectrum of the isotropic moment tensor estimated for the NPE. The estimates of the spectral features which were obtained with this fit are as follows:

<i>spectral feature</i>	<i>estimate</i>
low frequency level	$20 \cdot 10^{20}$ dyne cm
corner frequency	3.3 Hz
spectral overshoot (damping)	0.09
high-frequency decay rate	2.6

The next step is to relate these estimates of the spectral features to explosion properties such as yield or source dimension. Unfortunately, the simple theoretical models of an explosive source which

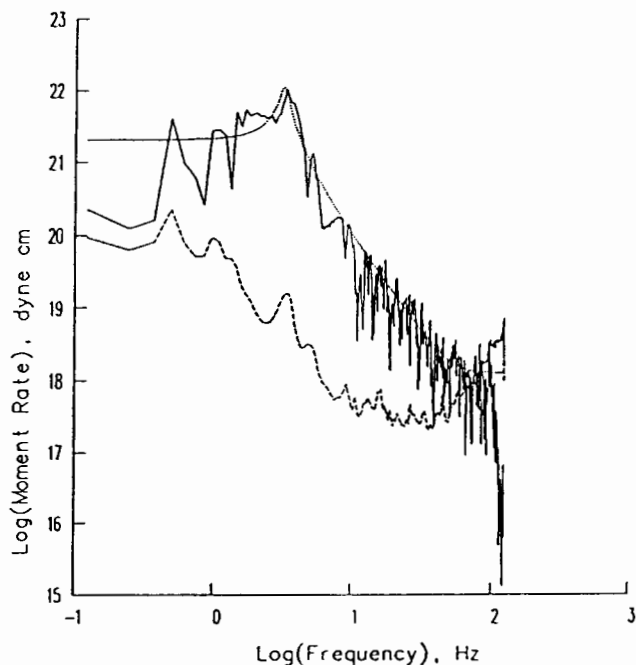


Figure 6. Similar to Figure 5 with the addition of the dotted line which is a spectral model which has been fit to the estimated modulus.

were used to model the spectrum are not adequate for this purpose, primarily because these models do not take into account the strong non-linear processes which take place in the interval between R_c and R_s . Although these models suggest a qualitative relationship between spectral features of the seismic source and properties of the explosion source, they do not allow a quantitative estimates of these explosion properties. It is thus necessary to appeal to more empirical approaches in order to make these quantitative conversions between seismic source and explosion source.

Scaling Relationships

A common method used to quantitatively relate spectral models of the seismic source to explosion properties consists of deriving a set of scaling relationships. The mathematical forms of these scaling relationships are guided by simple models of an explosive source and by results of the hydrodynamic code simulations, but the constants of the relationships are obtained by fitting these equations to empirical data. In setting up these scaling relationships it is important to identify and attempt to isolate the several independent factors that can affect the manner in which the seismic source is produced when an explosion is detonated. Some of the factors which must be considered are as follows:

- effects of explosion yield and dimension
- effects of depth of burial
- effects of material properties in the source region
- effects of type of explosive
- effects of tectonic strain release

Some of these effects enter directly into the scaling relationships, but others enter in an indirect manner. A good example of an indirect effect is that of depth. While the models of an explosion do not contain an explicit dependence upon depth, many of the parameters in the models such as confining pressure, elastic properties, density, and porosity are directly dependent upon depth, and thus, acting through these parameters, depth may have a significant indirect effect.

As an example of a scaling relationship, consider how the yield of an explosion is related to the low frequency level of the seismic source. Figure 7 is taken from Denny and Johnson (1991) and shows empirical data of this type for a variety of different types of explosions, ranging from small chemical explosions in the laboratory to large buried nuclear explosions. These explosions were also detonated in a variety of different media, ranging from alluvium to granite. Taking all of these factors into account, it is possible to estimate the following empirical relationship between explosion yield and low frequency level of the seismic source (Denny and Johnson, 1991).

$$W = 294 \cdot 10^{-12} \beta^{1.1544} P_o^{0.4385} 10^{0.0344GP} \frac{M_o}{4\pi\rho\alpha^2} \quad (1)$$

where

W is explosion yield in kilotons

M_o is low frequency spectral level in Newton meters

and the material properties involved are

α is P velocity

β is S velocity

ρ is density

P_o is overburden pressure

GP is gas porosity

A similar type of scaling relationship can be developed between the corner frequency of the seismic source and the cavity radius R_c . Using material properties appropriate for the NPE and the spectral fit shown in Figure 6, the following explosion properties of the NPE are obtained:

$$\text{yield } W = 1.4 \text{ kt}$$

$$\text{cavity radius } R_c = 15.5 \text{ meters}$$

The scaling relationship given above as Equation 1 illustrates why this type of approach has been more successful than one might initially suspect. Note that, while the material properties enter this equation in a fairly complicated manner, the basic relationship between the low frequency level of the spectrum of the seismic source and the yield of the explosion is linear. This implies that, while a variety of non-linear processes are involved in the generation of elastic waves by an explosion, it

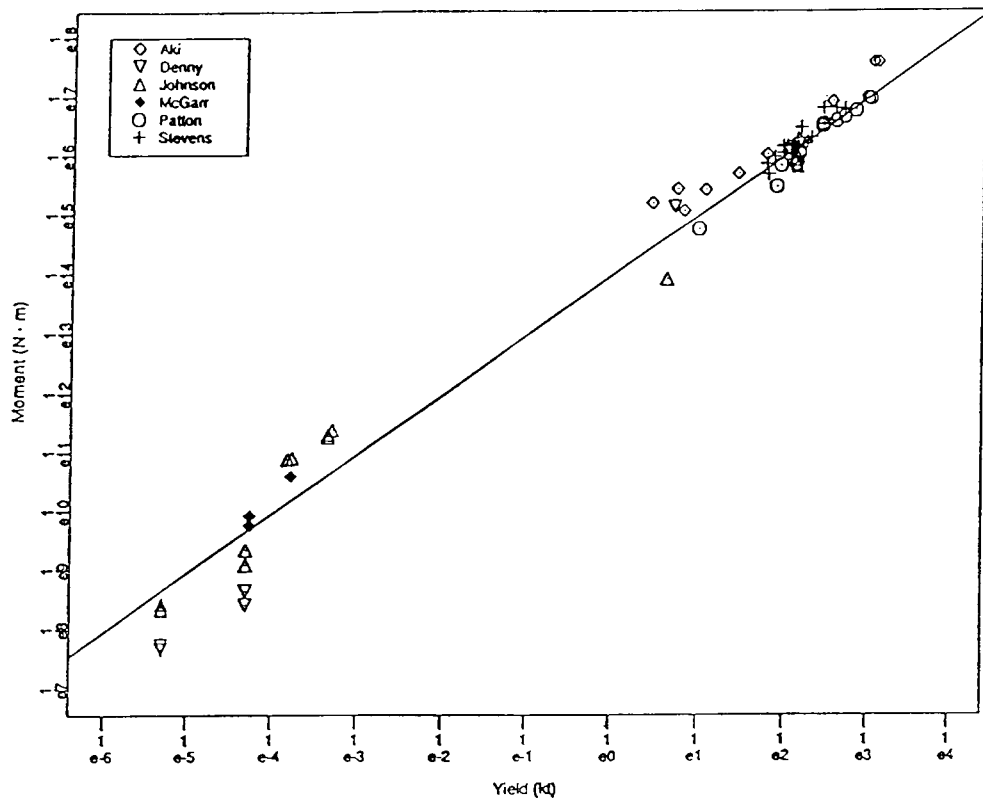


Figure 7. Figure taken from Denny and Johnson (1991) showing the relationship between seismic scalar moment and yield for explosions, with the data compiled from various published studies which used different types of data and different analysis methods to arrive at the estimated moments. These explosions were also detonated in a variety of source media, which accounts for some of the scatter in the data.

appears that these processes act in such a way that the fraction of energy which goes into low frequency seismic waves is independent of the size of the explosion. In essence, the explosion is acting as a self-similar event with respect to the generation of elastic waves. While this is basically an assumption of the method, it seems to be verified by the validity of the straight-line fit in Figure 7, which spans almost nine orders of magnitude in the explosion size. The existence of relationships such as this which express a fairly simple scaling between properties of an explosion source and the properties of the seismic source is a key element of all seismic methods and a crucial factor in their success. Of course, given the complexity of the generation processes that are involved and the empirical nature of the method, it is important that relationships such as this be continually checked against observational data in order to uncover any deficiencies.

Discussion and Summary

All methods which use seismic data to infer properties of a seismic source must deal with the same set of fundamental difficulties. The seismic waves are only an indirect effect of the explosion and represent only a small fraction of the energy which is released. Given this indirect nature of the problem, some interpretation procedure must be used to convert properties of the seismic waves to properties of the explosion source. This interpretation procedure must take account of the fact that several different processes are involved in converting the motion of the explosion cavity to the motion of the ground recorded by the seismograms. These processes are conveniently grouped into two classes, the nonlinear processes which lead to the generation of the elastic waves at the elastic radius R_s and the linear processes which are associated with the propagation of the seismic waves out through the rest of the earth. The seismograms are the combined effect of the explosion source plus these generation and propagation processes, and thus any attempt to infer properties of the explosion is successful only to the extent that the effects of these intervening processes can be removed. The treatment of the propagation processes is amenable to many of the standard methods of seismology, as it involves the linear mechanics of elastic wave propagation. The generation process is more difficult to handle, as it involves a number of strongly non-linear processes that depend upon a variety of material properties in the source region, and at the present time this part of the problem is treated with various empirical scaling relationships. Fortunately, the explosion source appears to have some self-similar properties which allow such scaling relationships to be used as a substitute for a complete treatment of the rather complicated generation process.

It is interesting to compare the different approaches to the seismic verification problem in terms of how the difficulties with the generation and propagation processes are addressed. The method of direct comparison takes advantage of the fact that the propagation processes are independent of the type of source and uses a calibration event to cancel out the propagation processes. This method also generally assumes the existence of simple scaling relationships between the explosion source and the seismic source. Because the material properties in the source region also cancel out in the comparison process, one is left with the particularly simple situation where the ratio of amplitudes on seismograms is equal to the ratio of explosion sizes. As mentioned earlier, this approach has the potential for the most accurate results, but does require the existence of a calibration event. The method of empirical Green functions belongs to this general class of methods.

The magnitude-based methods take the additional step of treating both the generation and propagation processes as empirical corrections. That is, the propagation process is characterized as a simple

distance correction that can be used to relate the seismograms to properties of the seismic source. As in the case of direct comparison, this method also assumes simple scaling relationships between the explosion source and the seismic source. In some cases the scaling relationship of the generation process is combined with the distance correction to provide a single relationship between measurements on the seismogram and properties of the explosion source. For example, relationships have been developed that relate the amplitude of a particular phase on seismograms to the yield of the explosion source. A limitation of this approach is that the distance corrections used to approximate the propagation process are known to be dependent upon the type of seismic phase which is being considered and the earth structure in the entire region between source and receiver. Thus the method must be calibrated for each different region of the earth. However, some imaginative techniques have been developed whereby a combination of different types of magnitudes may be less sensitive to the details of the calibration process than either of the magnitudes separately.

The approach of formulating the explosion estimation procedure as a formal inverse problem is useful in that it brings out the basic problems and assumptions that are common to all approaches. For instance, it is clear that two inverse problems must be solved, one involving removal of the propagation processes and the other involving removal of the generation processes. The first inverse problem is linear and well posed, and a variety of methods have been developed for the purpose of removing the propagation effects from the seismogram. All depend upon having available a model of the earth structure which was sampled by the propagating waves, but calibration explosions and calibration data sets are not explicitly required. Most of the waveform modeling methods of studying explosion sources belong to this general approach, although in many such cases the inverse problem is effectively solved by a series of trial and error solutions of the forward problem. The second inverse problem, that of removing the generation processes, can be clearly stated with this approach, but the complexity and non-linear nature of these processes prevent a direct solution of this problem at the present time. Thus, just as with the other two approaches described above, this part of the estimation process must be treated by relying on empirical scaling relationships.

It is clear from the above discussion that all seismic methods currently being employed to estimate the properties of explosion sources contain an implicit assumption that the non-linear zone surrounding an explosion can be bridged by empirical scaling relationships. This is a critical assumption, and the success of seismic methods as they are currently practiced is heavily dependent upon it. While there are arguments that provide a theoretical basis for the use of such scaling relationships (see for example Latter et al., 1959), the fact remains that they contain a strong empirical component. Consequently, it is important that the applicability of these relationships be continually checked against observational data. In particular, some of the assumptions implied by the use of these relationships may not be suitable for all applications. For instance, there is the question of whether the same scaling relationships can be used for both nuclear and chemical explosions, for both contained and partially contained explosions, and for both symmetric and unsymmetric explosions.

This discussion of the seismic method of estimating properties of explosion sources has attempted to outline the general foundations of the method and to highlight some of the areas where additional research is required. This last element is particularly appropriate in the case of the NPE, as this experiment was specifically designed to answer some of these remaining questions. All of the seismic methods outlined above were represented in the experiment, so the relative merits of the various

approaches can be checked in a quantitative manner. It should also be possible to compare the information contained in various types of data, as the experiment included the collection of seismic data in the free-field, local, and regional distance ranges. The choice of the explosion site allows a close comparison between nuclear and chemical explosions. The comparison of small and large explosions, both chemical and nuclear, in the same source environment permits a very useful check on empirical scaling relationships. Finally, the broad scope of the experiment should allow a useful comparison between seismic methods and other methods of quantifying the properties of explosion sources.

References

- Bos, R. J., Modeling the NPE, in Proceedings of the Symposium on the Non-Proliferation Experiment Results and Implications, M. D. Denny et al. (eds), Lawrence Livermore National Laboratory, Livermore, CA, CONF-9404100, 1994.
- Denny, M. D., and L. R. Johnson, The explosion seismic source function: models and scaling laws reviewed, in Explosion Source Phenomenology, Geophys. Monograph 65, American Geophysical Union, Washington, D.C., 1991.
- Garbin, H. D., Seismic performance, in Proceedings of the Symposium on the Non-Proliferation Experiment Results and Implications, M. D. Denny et al. (eds), Lawrence Livermore National Laboratory, Livermore, CA, CONF-9404100, 1994a.
- Garbin, H. D., NPE yield from Leo Brady Seismic Network, in Proceedings of the Symposium on the Non-Proliferation Experiment Results and Implications, M. D. Denny et al. (eds), Lawrence Livermore National Laboratory, Livermore, CA, CONF-9404100, 1994b.
- Glenn, L. A., and P. Goldstein, The influence of material models on chemical or nuclear explosion source-time functions, in Proceedings of the Symposium on the Non-Proliferation Experiment Results and Implications, M. D. Denny et al. (eds), Lawrence Livermore National Laboratory, Livermore, CA, CONF-9404100, 1994.
- Goldstein, P., and S. P. Jarpe, Comparison of chemical and nuclear explosion source-time functions from close-in, local, and regional seismic data, in Proceedings of the Symposium on the Non-Proliferation Experiment Results and Implications, M. D. Denny et al. (eds), Lawrence Livermore National Laboratory, Livermore, CA, CONF-9404100, 1994.
- Hill, R., EOS and simulations, in Proceedings of the Symposium on the Non-Proliferation Experiment Results and Implications, M. D. Denny et al. (eds), Lawrence Livermore National Laboratory, Livermore, CA, CONF-9404100, 1994.
- Hutchings, L. J., Modeling with finite sources and empirical Green's functions, in Proceedings of the Symposium on the Non-Proliferation Experiment Results and Implications, M. D. Denny et al. (eds), Lawrence Livermore National Laboratory, Livermore, CA, CONF-9404100, 1994.
- Johnson, L. R., Recording experiment on Rainier Mesa in conjunction with a reflection survey, in Proceedings of the Symposium on the Non-Proliferation Experiment Results and Implications, M. D. Denny et al. (eds), Lawrence Livermore National Laboratory, Livermore, CA, CONF-9404100, 1994.
- Latter, A. L., E. A. Matinelli, and E. Teller, Seismic scaling law for underground explosions, Phys. of Fluids, 2, 280-282, 1959.

- Majer, E. L., L. R. Johnson, E. K. Karageorgi, and J. E. Peterson, High-resolution seismic imaging of Rainier Mesa using surface reflection and surface-to-tunnel tomography, in Proceedings of the Symposium on the Non-Proliferation Experiment Results and Implications, M. D. Denny et al. (eds), Lawrence Livermore National Laboratory, Livermore, CA, CONF-9404100, 1994.
- Mayeda, K. M., Lg coda spectra ratios of the NPE, in Proceedings of the Symposium on the Non-Proliferation Experiment Results and Implications, M. D. Denny et al. (eds), Lawrence Livermore National Laboratory, Livermore, CA, CONF-9404100, 1994.
- McKown, T. O., Explosive performance on the NPE, in Proceedings of the Symposium on the Non-Proliferation Experiment Results and Implications, M. D. Denny et al. (eds), Lawrence Livermore National Laboratory, Livermore, CA, CONF-9404100, 1994.
- Patch, D. F., J. E. Welch, and J. Zerkle, Preshot predictions for the near-source region in the NPE, in Proceedings of the Symposium on the Non-Proliferation Experiment Results and Implications, M. D. Denny et al. (eds), Lawrence Livermore National Laboratory, Livermore, CA, CONF-9404100, 1994.
- Patton, H. J., Investigations of the low-frequency seismic waves recorded at near-regional distances for the NPE, in Proceedings of the Symposium on the Non-Proliferation Experiment Results and Implications, M. D. Denny et al. (eds), Lawrence Livermore National Laboratory, Livermore, CA, CONF-9404100, 1994.
- Reinke, R. E., A. Leverette, B. W. Stump, D. C. Pearson, and C. L. Edwards, Near-source seismic measurements for the NPE, in Proceedings of the Symposium on the Non-Proliferation Experiment Results and Implications, M. D. Denny et al. (eds), Lawrence Livermore National Laboratory, Livermore, CA, CONF-9404100, 1994.
- Rohrer, R., Seismic yield determination from the NPE, in Proceedings of the Symposium on the Non-Proliferation Experiment Results and Implications, M. D. Denny et al. (eds), Lawrence Livermore National Laboratory, Livermore, CA, CONF-9404100, 1994.
- Smith, A. T., Relative source comparison of the NPE to underground nuclear explosions at local distances, in Proceedings of the Symposium on the Non-Proliferation Experiment Results and Implications, M. D. Denny et al. (eds), Lawrence Livermore National Laboratory, Livermore, CA, CONF-9404100, 1994.
- Souers, P. C., and D. B. Larson, TIGER calculations and the NPE energy yield, in Proceedings of the Symposium on the Non-Proliferation Experiment Results and Implications, M. D. Denny et al. (eds), Lawrence Livermore National Laboratory, Livermore, CA, CONF-9404100, 1994.
- Stump, B. W., D. C. Pearson, and C. L. Edwards, Analysis and interpretation of free-field ground motions from the NPE, in Proceedings of the Symposium on the Non-Proliferation Experiment Results and Implications, M. D. Denny et al. (eds), Lawrence Livermore National Laboratory, Livermore, CA, CONF-9404100, 1994.
- Stump, B. W., and L. R. Johnson, The determination of source properties by the linear inversion of seismograms, Bull. Seismol. Soc. Am., 67, 1489-1502, 1977.
- Walter, W. R., H. J. Patton, and K. M. Mayeda, Regional seismic observations of the NPE at the Livermore NTS Network, in Proceedings of the Symposium on the Non-Proliferation Experiment Results and Implications, M. D. Denny et al. (eds), Lawrence Livermore National Laboratory, Livermore, CA, CONF-9404100, 1994.

AXISYMMETRIC MAGNETIC GAUGES*

B.L. Wright, K.R. Alrick, and J.N. Fritz

Los Alamos National Laboratory
Los Alamos, New Mexico 87545

Abstract

Axisymmetric magnetic (ASM) gauges are useful diagnostic tools in the study of the conversion of energy from underground explosions to distant seismic signals. Requiring no external power, they measure the strength (particle velocity) of the emerging shock wave under conditions that would destroy most instrumentation. Shock pins are included with each gauge to determine the angle of the shock front. For the Non-Proliferation Experiment, two ASM gauges were installed in the ANFO mixture to monitor the detonation wave and 10 were grouted into boreholes at various ranges in the surrounding rock (10 to 64 m from the center of explosion). These gauges were of a standard 3.8-inch-diameter design. In addition, two unique Jumbo ASM gauges (3-ft by 3-ft in cross section) were grouted to the wall of a drift at a range of 65 m. We discuss issues encountered in data analysis, present the results of our measurements, and compare these results with those of model simulations of the experiment.

The Axisymmetric Magnetic Gauge

Axisymmetric magnetic (ASM) gauges¹ were fielded at the NPE event to measure the shock-wave particle velocity out to a range of 65 m. The basic principle of operation of these gauges is shown in Fig. 1. When an incident shock wave encounters the conducting metal plate, the plate's free-surface motion compresses the flux of a permanent magnet, inducing a voltage, $V(t)$, in the pickup coil. Knowledge of the dipole strength of the magnet and the geometry of the assembly allows the free-surface velocity, $U_{fs}(t)$, to be deduced from the recorded waveform. This quantity in turn gives the particle velocity, $U_p(t)$, in the material in front of the plate. Shock-wave matching conditions based on equations of state are then used to deduce $U_p(t)$ in the native rock.

A cross section of the 3.8-inch-diameter ASM gauges used in NPE boreholes is shown in Fig. 2. This design was developed primarily for measurements of strong shocks at ~ 1 GPa and above. The conducting plate is a 0.25-mm-thick aluminum disk and the coil is wound with 6 turns. The outer body of the gauge is made of Lexan. Proper recording of the free-surface motion is limited by the time interval ($\sim 25 \mu\text{s}$) during which the coil and magnet positions remain unaffected by the presence of the shock. Thus the peak value of U_p will not be recorded if the shock-front rise time is greater than this interval.

Data from these gauges can be interpreted even if the direction of propagation of the shock is not parallel to the gauge axis, providing the angle of departure does not exceed $\sim 10^\circ$. As an essential aid to this interpretation, a set of 6 ferro-electric shock pins are located at 60° intervals around the periphery of the gauge. Discrete pulses from these pins are either combined with the ASM gauge signal or recorded separately. Built-in variations of the axial displacements of these pins and the use of different resistances in the individual pin circuits allow the incident shock angle to be determined from the timing and amplitude of the pin pulses.

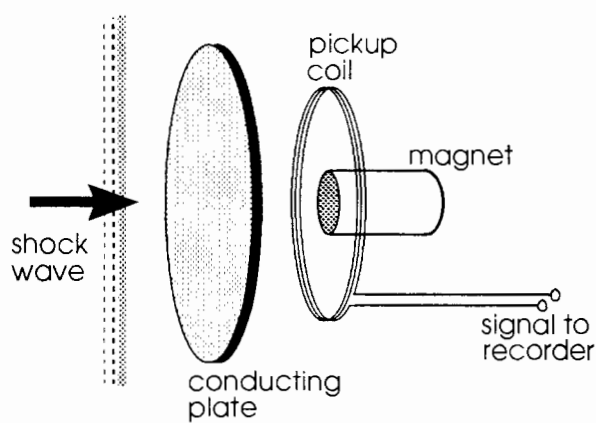


Fig. 1 The ASM principle.

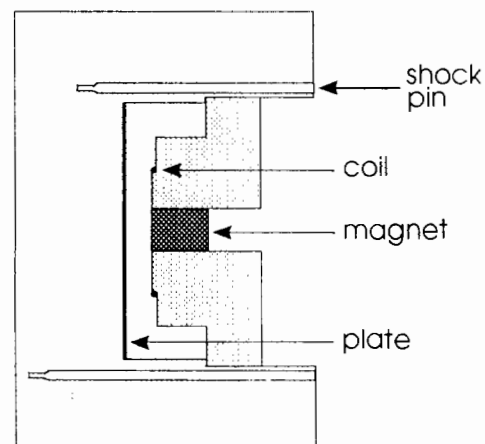


Fig. 2 ASM design.

*. This work supported by the US Department of Energy.

The Jumbo ASM Gauge

Weaker shocks with slower rise times cannot be recorded with the borehole design described above. To extend the range of ASM gauge measurements, a unique Jumbo ASM gauge² was designed for the NPE. For the Jumbo model, the travel distance of the plate was increased by a factor of 48 (from 0.25 to 12 inches). The plate itself was a 3-ft by 3-ft square piece of 1/4"-thick aluminum, the pickup coil had 25 turns with a diameter of 12 inches, and the magnet was a 2-inch cube of Nd₂BFe₁₂ with a dipole moment of 1.6×10^6 G-cm³. Fig. 3 shows the plastic core structure on which the magnet and coil were mounted. Also shown is the array of 8 shock pins used to determine the angle of arrival of the plate. The gauge is constructed by suspending the core in a 2' × 3' × 3' wooden box with the plate forming the front wall. The arrangement of 6 suspension strings shown in Fig. 4 allows accurate alignment. Release of string tension "levitates" the core during data acquisition.

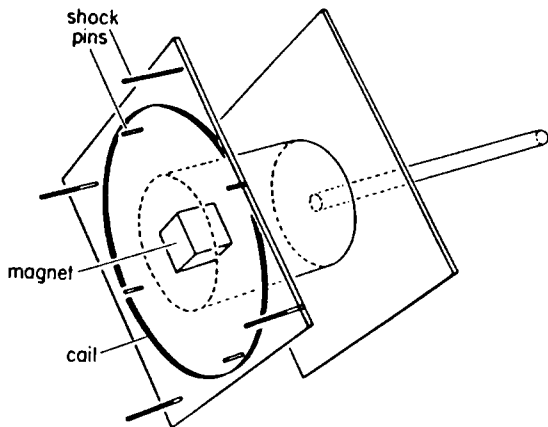


Fig. 3 Jumbo ASM core-structure assembly.

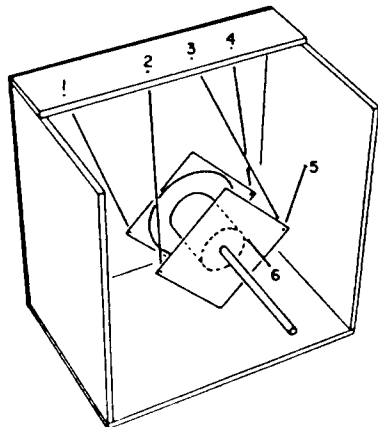
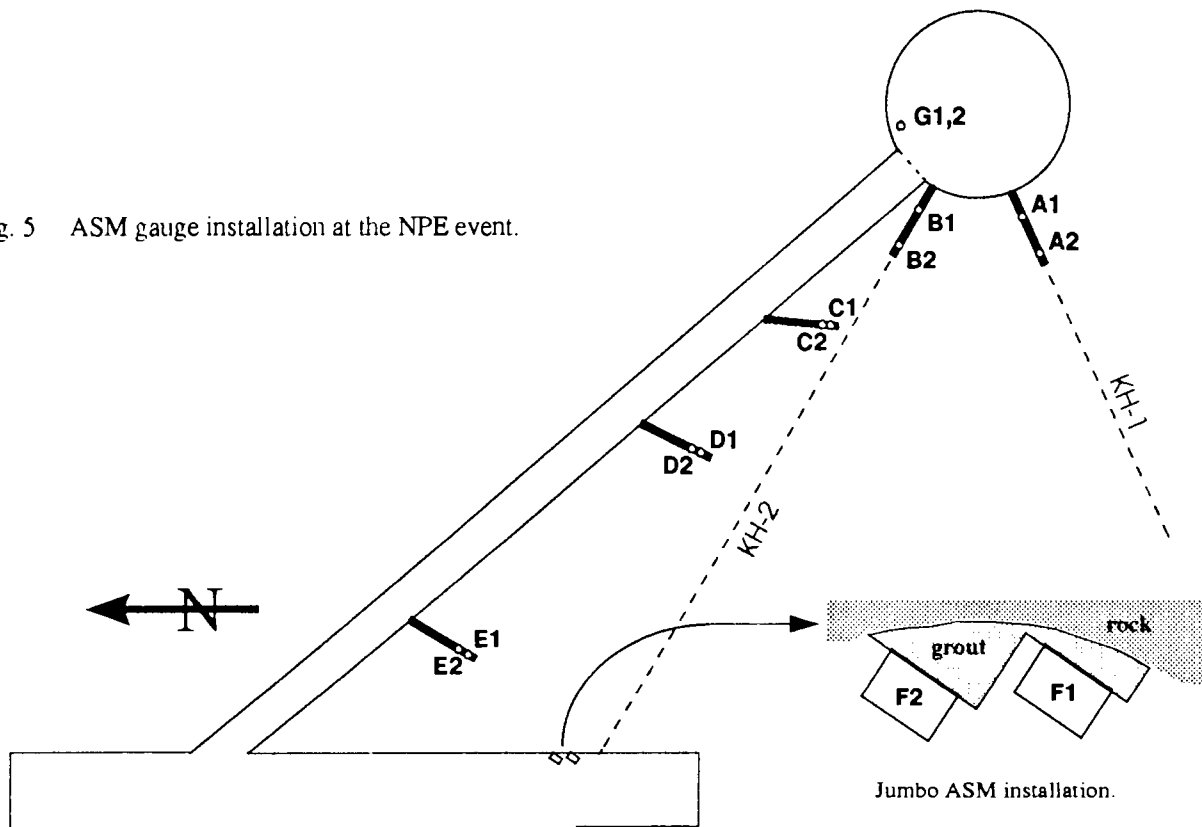


Fig. 4 Jumbo ASM gauge suspension.

Fig. 5 ASM gauge installation at the NPE event.



NPE Installation

The locations of 14 ASM gauges fielded at the NPE event are shown in Fig. 5. The 4"-diameter radial boreholes KH-1 and KH-2, used for CORTEX cables, were widened to 12" diameter over the first 20 feet and gauges A1, A2, B1 and B2 were installed at distances of 2.0 m and 5.0 m from the ANFO/rock interface. The elevations of these gauges varied between 1.1 m and 1.5 m below the planned elevation of the center of explosion (COE). Similarly, gauges C1, C2, D1, D2, E1, and E2 were located in pairs, with 0.6 m spacing, in 20'-long, 12"-diameter boreholes that angled forward from the access drift. The approximate ranges of these gauge pairs relative to the planned COE were 23 m, 38 m, and 64 m. Two Jumbo ASM gauges, F1 and F2, were grouted in step-wise fashion to the rock face of the alcove at a range of 65 m, near the exit of borehole KH-2, and well away from the access drift. These gauges were level with the COE. Finally, two of the smaller ASM gauges, G1 and G2 were mounted, one above the other, in the explosive chamber at a radius of 6.82 m and at elevations of 0.35 m and -0.04 m with respect to the COE.

Data and Analysis

The close-in gauges A1, A2, B1 and B2 all produced data of good quality. The combined coil voltage and shock-pin record of gauge B1 is shown in Fig. 6. For this gauge (as for the others), the 6 shock pins were set in an alternating pattern at two displacements, 2.0 and 20.2 mm, from the front surface of the gauge. Thus if the shock normal vector were parallel to the gauge axis, we would expect to see 2 bursts of 3 pulses each. The fact that the pulses were spread out indicates that the shock arrived at an angle with respect to the gauge. Indeed, plate motion had already begun by the time the last two pins were encountered. Analysis of the 6 recorded pulse times indicates that the shock normal in the Lexan formed an angle, θ , of 11.0° with the gauge axis. Because of the invariance of the pin structure with respect to 120° rotations, the azimuthal angle of the shock normal, about the gauge axis, remains ambiguous. This ambiguity is removed by an appeal to the pulse-height coding applied in the pin circuits. In particular, the fact that the first and third pin pulses from gauge B1 are stronger than the rest indicates that the shock arrived from a direction 8.0° above the axis and 7.6° to the right.

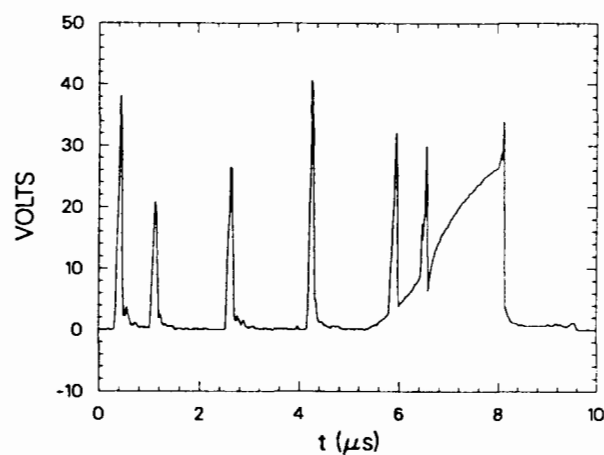


Fig. 6 Recorded waveform, gauge B1.

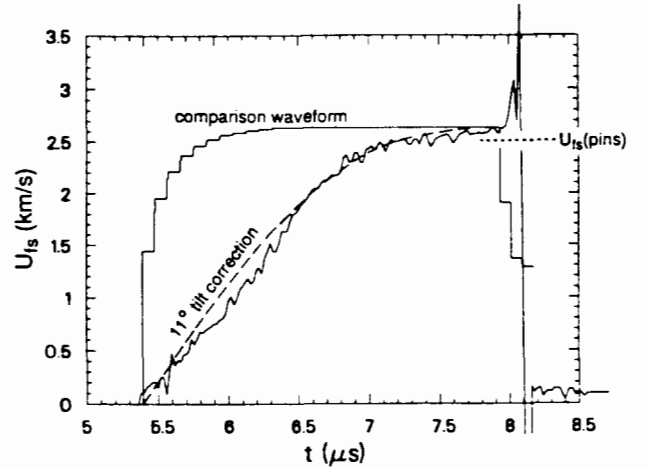


Fig. 7 Free-surface velocity vs. time, gauge B1.

In Fig. 7, the inferred free-surface velocity of the plate, $U_{fs}(t)$, is shown for gauge B1. A final value of 2.6 km/s is indicated, but the rise time is slowed because the shock struck the plate at an angle. The expected $U_{fs}(t)$ for a normally incident shock with a constant particle velocity in the Lexan of $U_p^L = 1.32$ km/s is also shown for comparison (U_{fs} is essentially twice U_p). Here the rise time is determined by the ring-up of the aluminum plate. The dashed curve indicates the comparison waveform after correction for the measured 11.0° angle of incidence.

Accepting U_p^L (ASM) = 1.3 km/s as a measurement of the particle velocity in the Lexan, a corresponding shock velocity, U_s^L (ASM) = 4.35 km/s, is indicated by the Lexan equation of state. For comparison, the shock velocity determined directly from the shock-pin data is U_s^L (pins) = 4.28 km/s. A similar comparison is made by computing the free-surface velocity, U_{fs} (pins) predicted by the pin data. This value (2.51 km/s) is indicated in Fig. 7.

The gauges C1 and C2 yielded uninterpretable ASM waveforms with no clear indication of shock-pin pulses. It was discovered later that, due to a trigonometric error, both gauges were misaligned with respect to the radial direction by about 20°. It is felt that useful data would have been obtained had the alignment been correct. However, the absence of pin signals cannot be explained by misalignment alone.

The gauges D1, D1, E1, and E2 showed no appreciable signal of either type. These gauges were installed in the low-pressure region in case a fast-rising shock front might still exist there. In the event, as shown also by stress gauges fielded by C. Smith of Sandia National Laboratory³, wave profiles with rise times exceeding a millisecond had developed before the D and E gauges were encountered.

In contrast, the Jumbo ASM gauges F1 and F2 were designed to deal with slow-rising wave profiles. The pickup coil voltage, $V(t)$, and the separately recorded shock pin signals are shown together in Fig. 8. The voltage waveform is qualitatively different from that of the conventional ASM gauges (Fig. 6) because the plate-to-coil separation is larger relative to the coil diameter. The gauge is therefore relatively less sensitive to plate motion at earlier times in the record. The measured free-surface velocities (twice $U_p(t)$ in the grout) are shown in Fig. 9 for both gauges. Also shown are the plate impact velocities measured with the pins. Both profiles show a small shoulder half way up the ~2 ms rise that is indicative of precursor development (see also ref. 3). Once peak velocity is attained, the aluminum plate becomes uncoupled from the ground motion and should move at constant speed; the apparent variations on the flatter portions of the waveforms are associated with data-reduction uncertainties. Because of its more favorable installation geometry (see Fig. 5), we feel that the waveform of gauge F1 is the more reliable of the two.

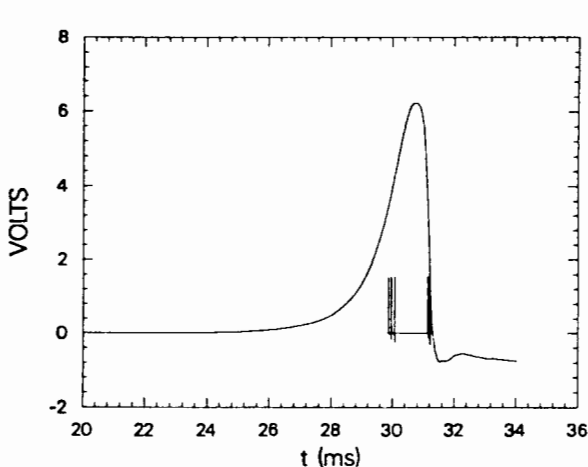


Fig. 8 Recorded waveform and pin signals, Jumbo ASM gauge F1.

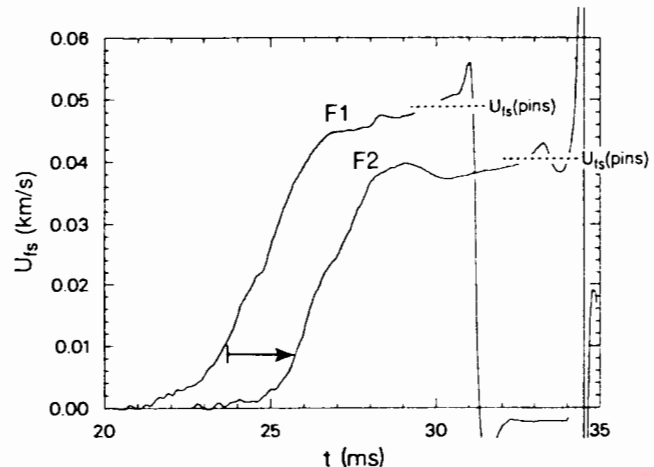


Fig. 9 Jumbo ASM free-surface velocity vs. time. The signal from F2 is displaced 2 ms.

In the Jumbo ASM gauges, the shock pins measured the arrival times and angles of the conducting plate, not of the shock in the medium. Of the 8 pins installed in the core structure (Fig. 3), 2 extended 63 mm in front of the structure, 2 extended 50 mm, and 4 were flush with its front surface. The data show that, within an uncertainty of a few millimeters due to warping, the plates of both F1 and F2, moved at essentially zero angle with respect to the gauge axes. With the very low U_p/U_s ratio observed at this range ($U_p/U_s \sim 0.017$), a small angle between the plate velocity vector and the surface normal is expected from elementary considerations [$\theta_{plate} \approx (2U_p/U_s)\theta_{inc}$]. Thus the pin data cannot be reliably used to infer the angle of the incident wave.

The gauges G1 and G2 mounted in the ANFO mixture generated waveforms that, though similar in form to that of Fig. 6, gave problems in interpretation. The voltage recorded for gauge G1 was twice what was expected. A straightforward analysis of $V(t)$ would yield (1) a plate velocity, U_{fs} , that was inconsistent with the duration time of the signal and (2) a value of U_p^L much larger than that implied by the very accurate pin measurement of U_s^L . If a multiplier of 1/2 is applied to $V(t)$ then agreement is obtained (see Table 1 below). However, pre-shot calibrations and post-shot investigations of the instrumentation do not support such a correction. The gauge G2 showed pin signals that echoed and appeared to be electronically differentiated, indicating a fault in the signal cable. The recorded $V(t)$, sent over the same line, included an anomalous early portion whose rise time was too short to have come from the ASM coil. When this apparently extraneous component is removed, gauge G2 gives consistent data.

Table 1: ASM Gauge Results

Gauge	U_p^L (ASM)	U_s^L (ASM)	U_s^L (pins)	θ	α	β
A1	1.15 km/s	4.10 km/s	3.95 km/s	11.2 °	7.0 °	6.3 °
A2	0.70	3.40	3.20	7.8	6.7	- 5.3
B1	1.30	4.35	4.30	11.0	4.4	-10.3
B2	0.75	3.50	3.30	10.7	1.9	-12.4
G1	[2.40]	[6.05]	6.00	5.1	4.7	- 0.1
G2	2.50	6.25	6.30	7.4	7.6	- 0.3

Results and Comparison with Modeling

Results for the 6 compact ASM gauges that gave analyzable data are given in Table 1. Here are shown the peak particle velocities in the Lexan, U_p^L (ASM), as determined from $V(t)$, along with the corresponding inferred shock-front velocities, U_s^L (ASM). These may be compared with the shock velocities U_s^L (pins) determined from the pin data. Measurement accuracies are of the order of $\pm 5\%$. It may be noted that the ratio U_s^L (ASM)/ U_s^L (pins) is of the order of 1.03 for A1 and B1, and 1.06 for A2 and B2. This observation is consistent with the known phenomenon of shock front steepening during transit of the Lexan--an effect that becomes more noticeable (as in the case of A2 and B2) as the shock weakens. Also shown in the table are the values, in brackets, that would be obtained from gauge G1 if the factor of 1/2 could be applied.

The angle, θ , that the shock normal in the Lexan formed with the gauge axis is given in the fifth column of the table. Because the gauges listed were all well aligned with respect to the COE, these values indicate local departures from radial propagation, both in the ANFO and in the nearby rock, that lie in the range of 5 to 10 degrees. To be more specific, the last two columns give the inferred direction of shock propagation with respect to the NPE cavity axis ($\pm 0.5^\circ$). The angle α represents vertical tilt: a positive value indicating a shock coming from a direction above the horizon of the gauge. The angle β represents horizontal deflection: a positive value indicating a shock appearing to come from the left of the cavity axis. Because of the 120° degeneracy described above, the angles α and β depend on a subjective reading of the pin pulse heights and are therefore less reliable than the angle θ . Nonetheless, some comparisons can be made. In the ANFO (G gauges) the shock front appears to have been pointing radially ($\beta = 0$) and downward ($\alpha > 0$). This result is consistent with time-of-arrival data for the two gauges (the upper gauge was hit first) that indicate a tilt in the ANFO of 8.7 degrees. In the nearby rock (A and B gauges), departures from azimuthal symmetry ($\beta \neq 0$) are evident as well. These may have been induced by irregularities in the geometry of the explosive chamber. For instance, the entrance of borehole KH-2 (containing B1 and B2) was 0.65 m closer to the COE than was the entrance of borehole KH-1 (containing A1 and A2).

Gauges G1 and G2 were installed to investigate the blast wave in the ANFO mixture. The shock-pin results from these gauges imply pressures in the lead part of the wave (19.3 and 20.7 GPa) that are higher than the expected CJ detonation pressure (16 to 18 GPa) inferred from the equation-of-state parameters of the mixture. The short time that the G gauges observed the lead portion of the blast wave ($\sim 2 \mu s$) may well be comparable to or less than the reaction time in the ANFO. We would therefore be measuring the von Neumann spike, the shocked state of the unreacted components, rather than the CJ state.

Table 2 shows the results of converting the gauge data to peak particle velocity in the rock, U_p^r . In the case of the Jumbo F gauges, the conversion was directly accomplished by using $U_p^r = 0.5 U_{fs}$. In the case of the A and B gauges, the conversion requires not only an analysis of shock strength in the Lexan (Table 1 above), but also consideration of the effects of the grout in the borehole. Because the boreholes KH-1 and KH-2 were only a few degrees from being aligned on the COE, it was assumed that the shock ran parallel to the borehole axis. In this case, the shock velocity, U_s^g , in the grout is driven to match U_s^r in the surrounding rock. The inferred state of the grout is then related to U_p^L in the Lexan, and ultimately to U_{fs} (ASM), with standard matching conditions. Lacking an equation of

Table 2: Particle Velocity in the Rock

Gauge	Range	Time of arrival	U_p' (measured)		U_p' (model)
			$\rho_{\text{grout}} = 2.01$	$\rho_{\text{grout}} = 1.95$	
B1	9.88 m	1.826 ms	1.26 km/s	1.13 km/s	0.83 km/s
A1	10.51	1.904	1.07	0.94	0.75
B2	12.83	2.662	0.58	0.43	0.49
A2	13.45	2.754	0.52	0.37	0.42
F1	64.33	21.0	0.0245 km/s		0.030
F2	65.35	21.0	0.0195		0.028

state for the grout used in the NPE boreholes, we used the EOS for MINI JADE grout in this analysis. Two cases have been considered: fully compacted grout (density = 2.01 gm/cm³) and grout with air-filled porosity (density = 1.95 gm/cm³). The EOS used for the rock was the same as that used in a model comparison⁴.

The results of the model calculation of U_p' are shown in the last column of Table 2. This calculation was done using the Sandia National Laboratory Eulerian code CTH. The ANFO reaction was modeled using a JWL formalism, and the rock equation of state (SESAME table 73124) was based on data obtained from events conducted in similar tuff. The range parameter listed in the table is the direct distance from the COE to each gauge. Recall, however, that the gauges A1, B1 were 2.0 m, and the gauges A2, B2 were 5.0 m from the ANFO/rock interface. This lack of correspondence between range and distance from the chamber wall creates some ambiguity when comparing the ASM measurements with the 2-D model results. Because, as seen in Table 2, U_p' (meas.) decreases uniformly with range, we have used the range in these comparisons. In particular, the equivalent gauge locations used in the model are vertically at the level of the midplane of the chamber and horizontally at a radius equal to the quoted range. The effects of uncertainties in range and grout characteristics are apparent in the listed values of U_p' (meas.). The model results agree reasonably well, considering the degree of variability allowed, though the measurements show consistently higher values of the ratios $U_p'(A1)/U_p'(A2)$ and $U_p'(B1)/U_p'(B2)$. In view of uncertainties encountered in extending the model to the low-pressure regime, its agreement with Jumbo ASM gauge F1 is quite good. [Recall that gauge F2 was less ideally coupled to the rock.]

Summary

Useful particle motion data were taken at the NPE event with ASM gauges in the explosive-filled chamber, in nearby radial boreholes, and at the relatively extreme range of 65 m. In the ANFO mixture (G gauges), difficulties in interpreting the coil waveform were reduced by a consideration of shock-pin data. These gauges indicated particle velocities at the front of the blast wave that are thought to represent the shocked state of the unreacted explosive. The shock-pin and time-of-arrival data indicate a shock front that is directed slightly downward at the G gauge locations. Similar downward propagation angles, as well as lateral deflections up to $\sim 10^\circ$ were recorded with shock pins in the A and B gauges located 2 and 5 m beyond the ANFO/rock interface. The A and B gauges gave reliable free-surface plate velocities that could be related to the particle velocity of the shock wave in the surrounding rock--subject to an analysis of the effect of the grout. The wall-mounted Jumbo ASM gauges (F gauges) performed well in recording the longer-rise-time motion encountered at greater distances. Collectively, the ASM data should be of value to the effort to define a proper computational model of the effects of the NPE explosion in the inelastic zone. Their utility has already been demonstrated in comparisons with a currently-used model.

References:

1. J.N. Fritz and J.A. Morgan, An Electromagnetic Technique for Measuring Material Velocity. *Rev. Scient. Instr.*, 44(2):215-221
2. B.L. Wright, K.R. Alrick, and J.N. Fritz, Measurement of Large Ground Motions with the ASM Gage. Joint AIRAPT/APS Conference on High Pressure Science and Technology, Colorado Springs, CO, June 28-July 2, 1993
3. C. Smith, NPE Close-In Stress and Motion Measurements, these proceedings
4. R.J. Bos. Modeling the NPE, these proceedings

INDUCED SHOCK PROPAGATION
ON THE
NON-PROLIFERATION EXPERIMENT*

by

Thomas O. McKown
Los Alamos National Laboratory

ABSTRACT

The Explosive Effects Physics Project at the Los Alamos National Laboratory planned and conducted experiments on the NPE as part of its effort to define source functions for seismic waves. Beyond the explosive chamber, the detonation induced shock propagated through the saturated tuff of the N-tunnel complex. The CORTEX (COntinuous Reflectometry for Radius vs Time EXperiment) system was used to investigate the shock propagation in two drill holes and the access drift. The CORTEX experiments fielded will be described. The data obtained are reviewed and an apparent asymmetry in the radiating shock discussed.

INTRODUCTION

The Non-Proliferation Experiment (NPE) was planned and conducted by Lawrence Livermore National Laboratory (LLNL). The global objectives of the test were to investigate whether signals are produced which may be used to seismically differentiate a large conventional explosion from a nuclear explosion and to calibrate the energy released to previous nuclear events. The experiment was conducted on the Nevada Test Site (NTS) in the N-tunnel complex, the site of numerous previous nuclear events. Therefore, the geologic media should be a constant in the analysis of seismic signals produced by the NPE detonation.

The test consisted of approximately 2.9 million pounds of a 50-50 blend of Ammonium Nitrate-Fuel Oil (ANFO) and emulsion in a 15.2 m diameter by 5.2 m high right cylinder (the explosive chamber). Detonation occurred simultaneously at three locations along the chamber axis. The defined axis of the explosive chamber was a taut steel aircraft cable anchored from back (ceiling) to invert (floor). This location was referred to for survey purposes as the Users Working Point (UWP) but was not actually coincident with the planned WP. (The planned WP was 0.177 m west and 0.061 m south of UWP, a distance of 0.178 m.) All references will be to the UWP. A complete description of the explosive emplacement, including the booster-detonator construction, their emplaced locations and the event timing is contained in the explosive performance report (2).

The Los Alamos National Laboratory (Los Alamos) group P-15 participated in the NPE to characterize the explosive performance and to characterize the time-dependent shock wave propagating through the saturated tuff surrounding the explosive chamber. This report addresses the second subject, the region beyond the explosive chamber. Some reference to the results reported in the explosive performance report may be necessary. The instrumentation in this region consisted of twelve CORTEX sensing elements for the time-

*This work supported by the United States Department of Energy.
Italic numbers in parentheses refer to items in the list of references.

dependent shock position or time-of-arrival (TOA) information and twelve Axially-Symmetric Magnetic (ASM) gauges for measuring the particle velocity. The particle velocity results will be the subject of a separate report and only the TOA information from the ASM gauges will be compared to the CORTEX data. Also, the results from the accelerometers arrayed throughout the N-tunnel complex will be presented in a separate report.

CORTEX INSTRUMENTATION(1,4,5)

The CORTEX sensing elements exited the explosive chamber in four groups of three cables each. It is unfortunate that the induced shock could only be monitored in these four directions and yet the redundancy strengthens the analysis of the explosive burn results where single cables were arrayed throughout the explosive chamber. Figure 1 is an engineering site plan for the NPE, showing drill holes KH-1, KH-2 and KH-3 and the access drift, through which the sensing elements exited the explosive chamber. The sensing element designations K1, K2, ..., and K12 appear beside their respective exit routes. The drill holes were four inch diameter holes except for the first (explosive chamber end) 20 feet of KH-1 and KH-2 which were reamed to 12 inches. The CORTEX sensing elements in the three drill holes were individually pulled taut with kellums and turnbuckles at each drill hole end. The installations in KH-1 and KH-2 were referenced to a plumb line off survey spads (called the drill hole collar reference) placed above each hole collar. The access drift sensing elements were installed on a Kevlar rope messenger along the left rib (side, facing toward WP), about 6 feet above the invert. Reference points on the access drift cables were surveyed in place.

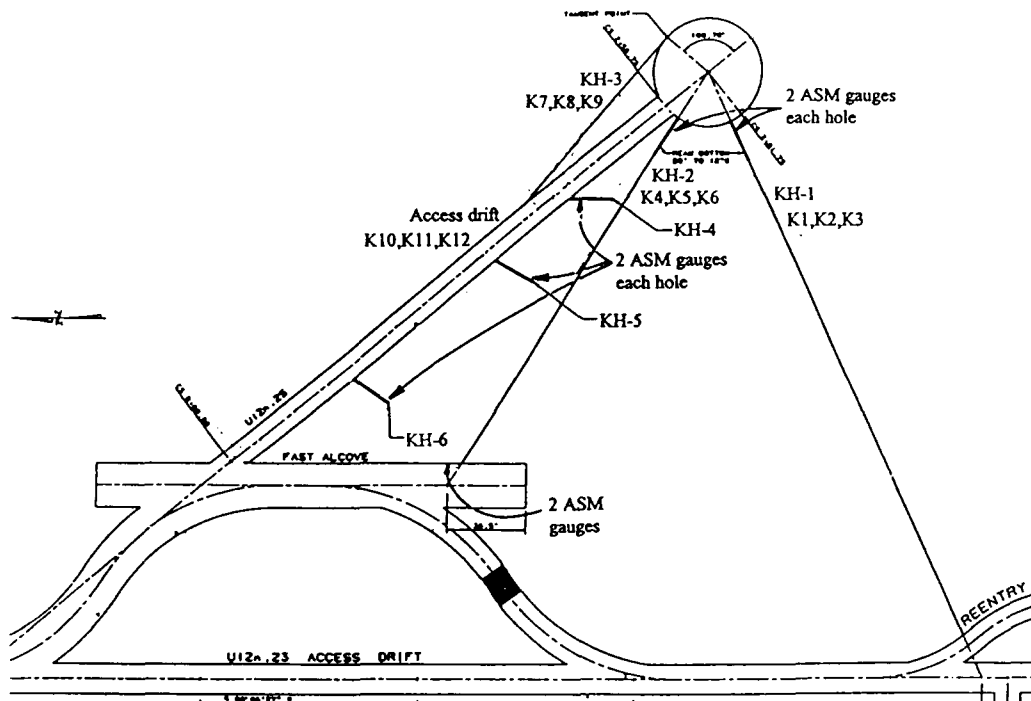


Figure 1. Engineering site plan for the non-proliferation experiment.

ASM gauges were installed at 2.0 m and 5.0 m from the drill hole collar reference in the 12 inch diameter portions of KH-1 and KH-2. Drill holes KH-4, KH-5 and KH-6 were each 12 inches in diameter and 20 feet long. Each contained two ASM gauges nominally at 19 feet and 17 feet from the drill hole collar references. A final pair of ASM gauges were installed adjacent to the portal end of drill hole KH-2. Locations for these twelve gauges are indicated in Figure 1 and their radial distances from the UWP are included in Table 1. The slant distance is to the planned elevation of the center of the explosive chamber but on the UWP. The horizontal distance is the distance at the gauge elevation to the UWP.

* The sensing element designations Kn and K-n are synonymous and will be used interchangeably.

Table 1. ASM gauge locations and times-of-arrival.

ASM Gauge/ Location	Slant Distance (m)	Horizontal Distance (m)	Time-of-Arrival (ms)*	
			ASM Gauge	CORTEX
A1/KH-1	10.51	10.44	1.910	1.900 - 1.910
A2/KH-1	13.45	13.40	2.762	2.750 - 2.760
B1/KH-2	9.88	9.77	1.832	1.820 - 1.830
B2/KH-2	12.83	12.76	2.669	2.660 - 2.670
C1/KH-4	22.59	22.59	6.040	6.160
C2/KH-4	22.94	22.93	6.190	6.210
D1/KH-5	38.01	38.01	—	12.430
D2/KH-5	38.15	38.15	—	12.510
E1/KH-6	64.00	64.00	—	24.7±0.1
E2/KH-6	64.11	64.11	—	24.8±0.1
F1/**	64.33**	64.33	22.600	24.9±0.2
F2/**	65.35**	65.35	23.000	25.5±0.3

* Timing with respect to the capacitive discharge unit.

** Located at portal end of KH-2, measurements made and coordinates supplied by Brad Wright, Los Alamos.

The six drill holes were stemmed with a rock matching (density matching) non-slumping grout. Because these holes were stemmed in place well before the explosive detonation, the grout is considered to have reached its maximum compressive strength of 3000 PSI. The working point ends of K10, K11 and K12, the access drift sensing elements, were anchored about 60 cm inside the explosive chamber. Their linear path down the access drift passed through a steel bulkhead at the access drift-explosive chamber interface, through five feet of sand bags filled with desert fines and through three stemming zones. Because the sensing elements were installed high in the access drift and the grout mixes used for stemming the first two zones of the access drift were high slumping and topped-off with a different mix (same mix as was poured in the third zone), it is uncertain exactly which stemming material surrounded these sensing elements. The density was however, near or slightly higher than the native rock. Since detonation occurred just several days after completing stemming, neither of the grout mixes used had reached their maximum compressive strengths. All this information to state that although the sensing elements installed outside the explosive chamber are described as "free field" measurements of the induced shock traveling through saturated tuff, the reality is that they were grouted in place, and in the access drift this comprised a significant portion of the medium surrounding the sensing elements installed there.

CORTEX DATA

The data presented and discussed in this report are, of course, an extension of that presented in reference 2. Because each CORTEX sensing element was installed with two geometric signatures (loops) in the explosive chamber and three in the "free field" region, the data reduction process could use the known locations of the loops, to determine the propagation velocity of pulses in each sensing element at the time of the detonation. This results in a more accurate computation of the shock location along the path of the installed sensing element. Standard CORTEX data reduction procedures were followed in producing final data sets for each sensing element. Table 2 summarizes some information relative to each sensing element. Included is the selected cable type and the time of first crush in the "free field" medium (the access drift cables are a projection because of their loop back into the explosive chamber). Different cable types are used because of differing physical characteristics (such 1/4 inch cables vs. 1/2 inch cables) and crush thresholds, the shock pressure at which the sensing element ceases to crush uniformly. The data will show which of the installed cable types have the lower crush thresholds.

Table 2. Sensing element locations, types and times of first crush in the "free field."

Designation	Location	Cable Type	First Crush (ms)
K1*	KH-1	FSJ1-50	1.444±0.005
K2*	KH-1	FSJ1-50	1.443±0.005
K3	KH-1	FSJ4-50	1.454±0.005
K4	KH-2	FSJ4-50	1.384±0.005
K5*	KH-2	FSJ1-50	1.389±0.005
K6*	KH-2	FSJ1-50	1.388±0.005
K7	KH-3	FSJ1-50	1.372±0.005
K8	KH-3	FSJ4-50	1.379±0.005
K9	KH-3	FSJ4-50	1.375±0.005
K10	Access drift	RDX1-50	N/A***
K11**	Access drift	FSJ1-50	1.304±0.015
K12**	Access drift	RDX4-50	1.305±0.015

* A 2.0 m loop was installed at the drill hole collar.

** The times given are projected from the survey point 7, located in the explosive chamber, the point to which the access drift sensing elements looped before exiting the explosive chamber.

*** K-10 was damaged during stemming at a point just outside the explosive chamber.

The data records will first be examined as recording the same induced shock along the individual installation paths, that is, K1, K2 and K3 in drill hole KH-1, etc. When comparing data between sensing elements installed together, their position reference will be their common point upon exiting the explosive chamber. In each installation path, the position on each sensing element at the drill hole collar reference was carefully fixed. For example, K1 and K2 each contained 2.0 meter loops, 28.0 to 26.0 meters, at the KH-1 drill hole collar reference. The 26.0 meter mark on K3 was made to coincide with this same position. Therefore, the position along the sensing element at the drill hole collar reference is very precisely known. The same situation held for KH-2 and KH-3. For K10, K11 and K12, the loop back into the explosive chamber was placed precisely at the 25.0 m mark on each sensing element. The second comparison will be between different exit paths, such as, KH-1 and KH-2, etc. In this case, the data position will be referenced to the UWP, that is, radial data from the UWP. Timing is to "minimum boost", the minimum time required for booster breakout(??).

The KH-1 Data

Figures 2 and 3 present and show two comparisons of the three data sets from KH-1. On the scale of Figure 2, the K1, K2 and K3 data are coincident to about 5.0 ms. The Figure 3 plots show the differences, K3 - K1 and K3 - K2 respectively, over the initial intervals. The mean difference is -0.025 m for K3 and K1 and -0.030 m for K3 and K2. This is excellent agreement between the three independent measurements of the induced shock location in the KH-1 direction, which represents ranges of 8.0 to 20.0 m from UWP. Clearly, the K3 sensing element, 1/2 inch FSJ4-50, has a lower crush threshold than either K1 or K2, both 1/4 inch FSJ1-50. Experience has shown that when data begin to stair-step, as the K3 record exhibits in Figure 2, that the shock location is the upper envelope of the data. This is indicated by the dashed curve.

The KH-2, KH-3 and Access Drift Data

The KH-2, KH-3 and access drift data will be presented and compared in less detail. Figures 4, 5 and 6 present the three records in each of these "free field" paths. The plot scales are the same as for Figure 2 so that the major differences in the induced shocks, as measured in the separate exit paths, is apparent. Geometric corrections and reference to a common point have not yet been made in these data sets. The difference information shown for KH-1 in Figure 3 is summarized for all sensing elements in Table 3. In each case, a lower crush threshold cable was selected as the standard against which the other two data records

were compared in each exit path. It is apparent from Figures 4, 5 and 6 , and the mean differences in Table 3, that there is excellent agreement between the data records within each of the four exit paths. Therefore, when comparing data between different "free field" paths, a single low crush threshold sensing element will be selected for each path.

Comparing the K3 plot in Figure 2 with the K4 plot in Figure 4, it is apparent that K4 ceased responding to the induced shock wave in the KH-2 direction much earlier than K3 in the KH-1 direction. This comparison is valid because K3 and K4 are identical cable types and the drill holes were close to radial from UWP.

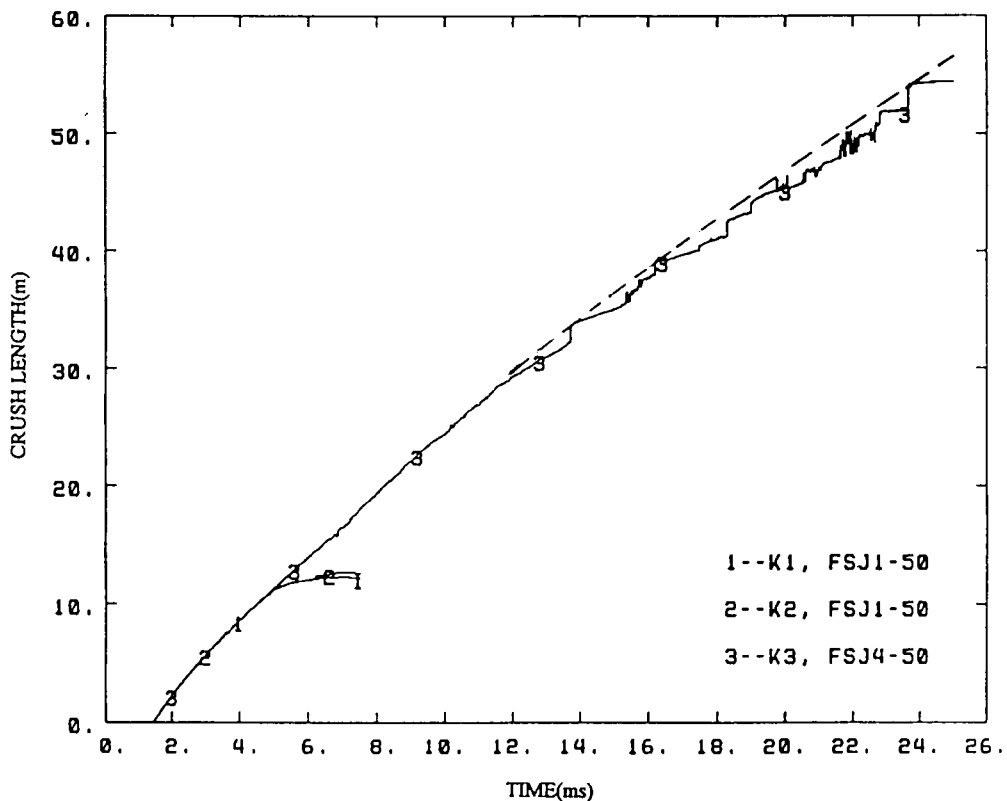


Figure 2. Drill hole KH-1 data.

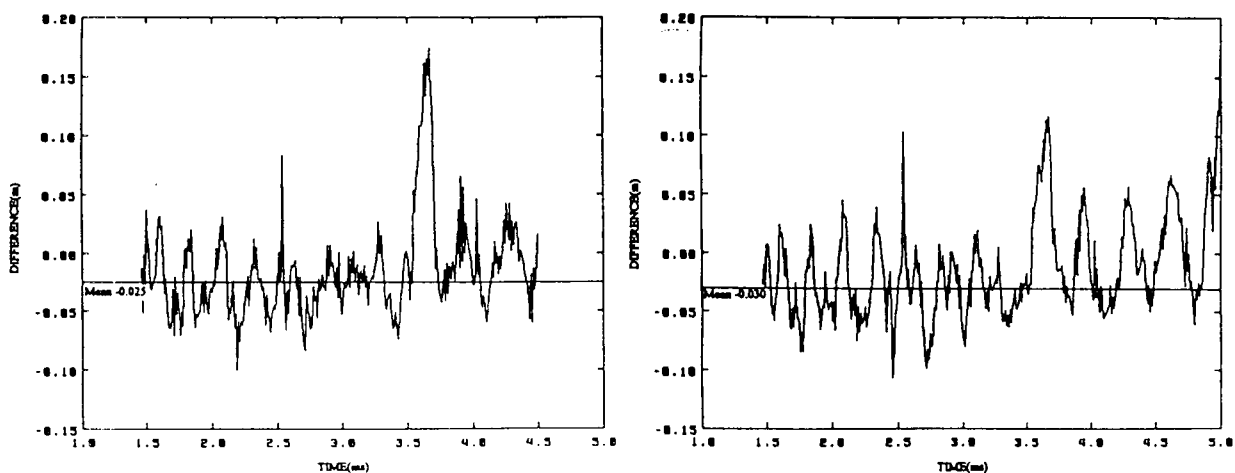


Figure 3. Difference plots of K3 - K1 and K3 - K2.

Table 3. Mean difference between data along each "free field" path

Standard	Mean Differences, Standard - Data			
	Data	Difference	Data	Difference
K3	K1	-0.030±0.019	K2	-0.025±0.019
K4	K5	-0.018±0.022	K6	-0.033±0.025
K9	K7	0.000±0.025	K8	-0.008±0.021
K10	K11	-0.028±0.023	K12	0.011±0.038

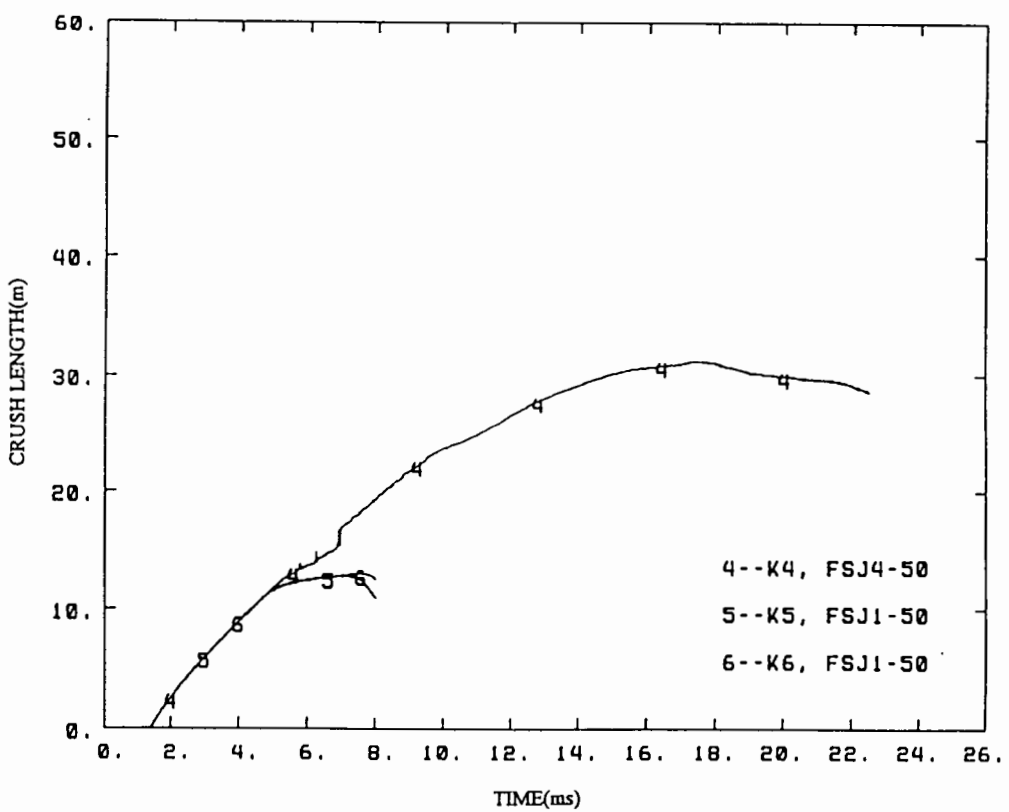


Figure 4. Drill hole KH-2 data.

The installation path for K7, K8 and K9 was through the KH-3 drill hole to the explosive chamber access drift. There, the KH-3 and access drift sensing elements joined, and as a bundle were routed linearly along the drift left rib. The transition of the sensing elements from KH-3 to the access drift is marked in the data record of Figure 5. Interestingly, at this point the KH-3 sensing element response to the induced shock improved considerably, possibly indicating a higher pressure in the grout filled access drift than in the KH-3 drill hole. As a final note, the KH-3 data can be compared to the access drift data along their common path. The 61.0 m mark on each of the KH-3 cables was installed coincident with the 57.0 m mark on the access drift cables, a difference of 4.0 m in cable length to this common point. Comparing the K9 data (KH-3) to the K10 data (access drift) over several intervals beyond the transition point yields a mean difference of 4.003 ± 0.110 m. Again, extremely consistent agreement between the independently reduced data.

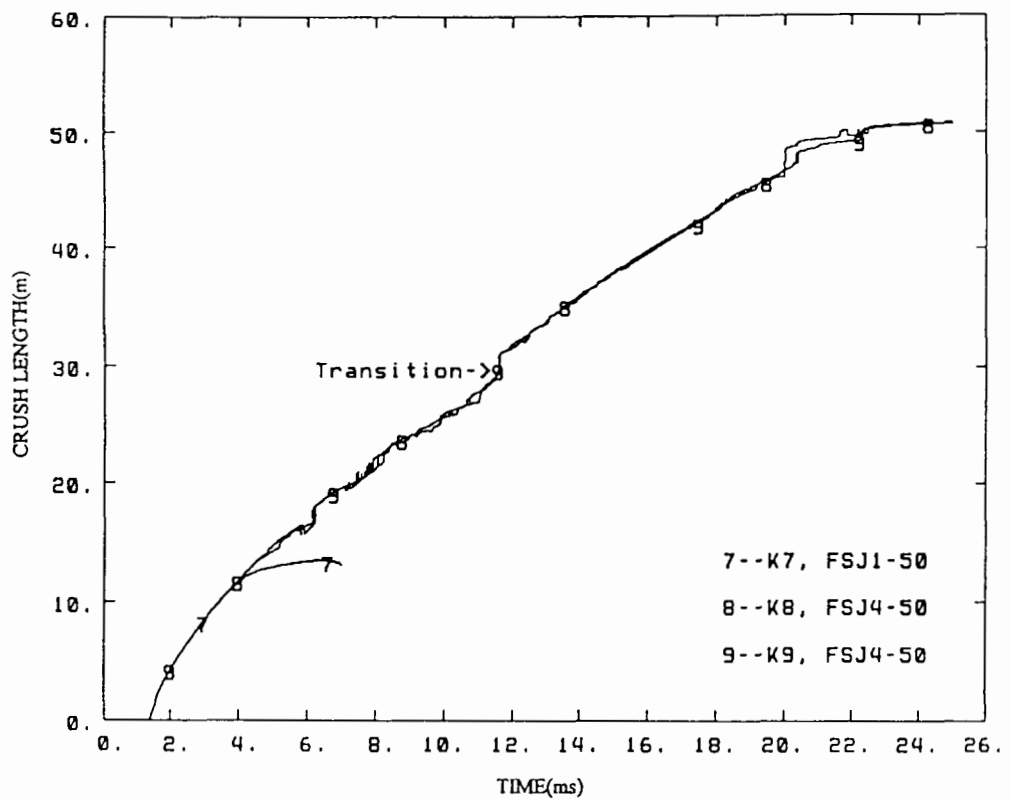


Figure 5. Drill hole KH-3 data.

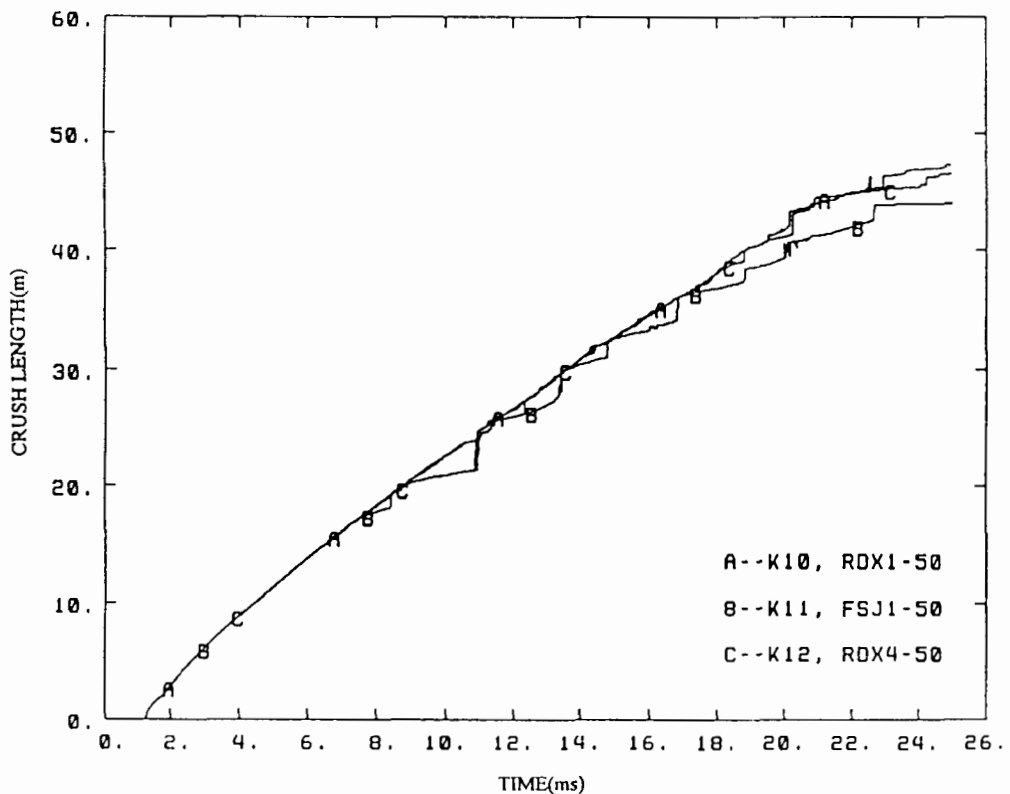


Figure 6. Access drift data.

Interpath Comparisons

Figures 2, 3, 4, 5 and 6, along with Table 3, made intrapath comparisons. The absolute consistency within each exit path permits selecting one record from each path to examine the induced radial shock wave along different paths. Figure 7 includes K3 from KH-1, K4 from KH-3 and K10 from the access drift. These records have been geometrically converted to time-dependent radial position with respect to UWP.

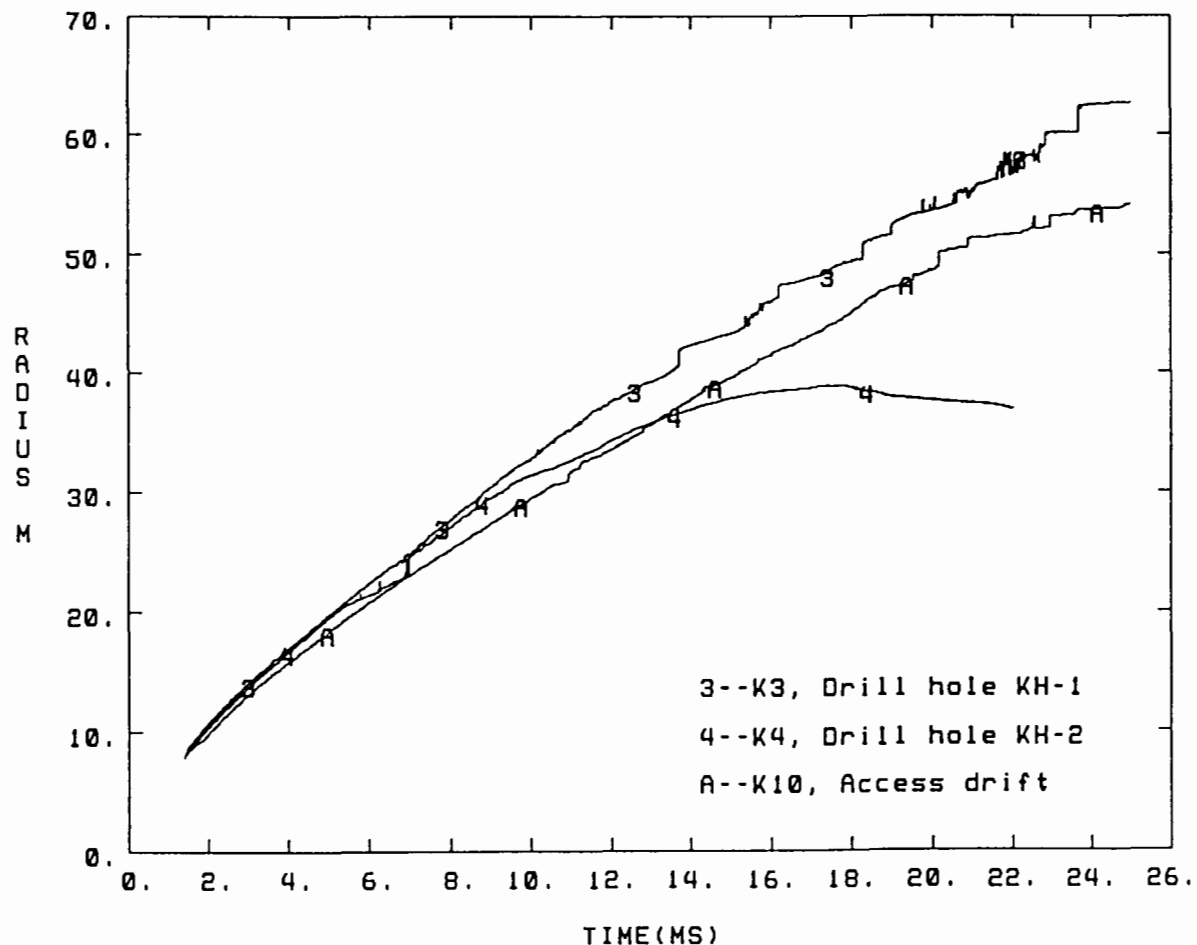


Figure 7. CORTEX measured shock induced into the saturated tuff, beyond the explosive chamber.

It was observed earlier that K4 ceased responding to the induced shock much earlier than did K3. Figure 7, based on a common reference, makes this difference clearer. Also K10 from the access drift, although lagging behind both K3 and K4 in early time, continues to respond well beyond the range of K4 but still behind K3. K10 is a cable type which typically has a lower crush threshold than the cable type of K3 and K4. Thus, its lagging behind K3 must be due to the shock induced into the grout of the access drift versus the grout filled hole KH-1. To further support this observation, it is again noted that K8 and K9, which are both FSJ4-50, the same as K3 and K4, from their transition from KH-3 to the access drift were in excellent agreement with K10 (4.003 m vs 4.0 m difference in cable length). Therefore, in just the three instrumented directions of KH-1, KH-2 and the access drift, there are measurable differences in the induced shock wave, both in terms of the apparent shock pressure and the time-dependent radial position.

Examining the data from a different perspective, however, may perhaps yield additional insight. Although it is difficult to observe on the scale of Figure 7, there are early time differences between the K3 and K4 data. Figure 8 is an enlargement of that data which makes it clearer that there is an apparent constant difference between K3 and K4 which persists to 4.0 or 5.0 ms, before K4 begins to fall off. The insert in

Figure 8 is a plot of the K3, K4 difference with the mean difference shown as 0.338 ± 0.021 m. Figure 9 is a replot of the time-dependent radial position of just K3 and K4, but with 0.338 m subtracted from the K3 data.

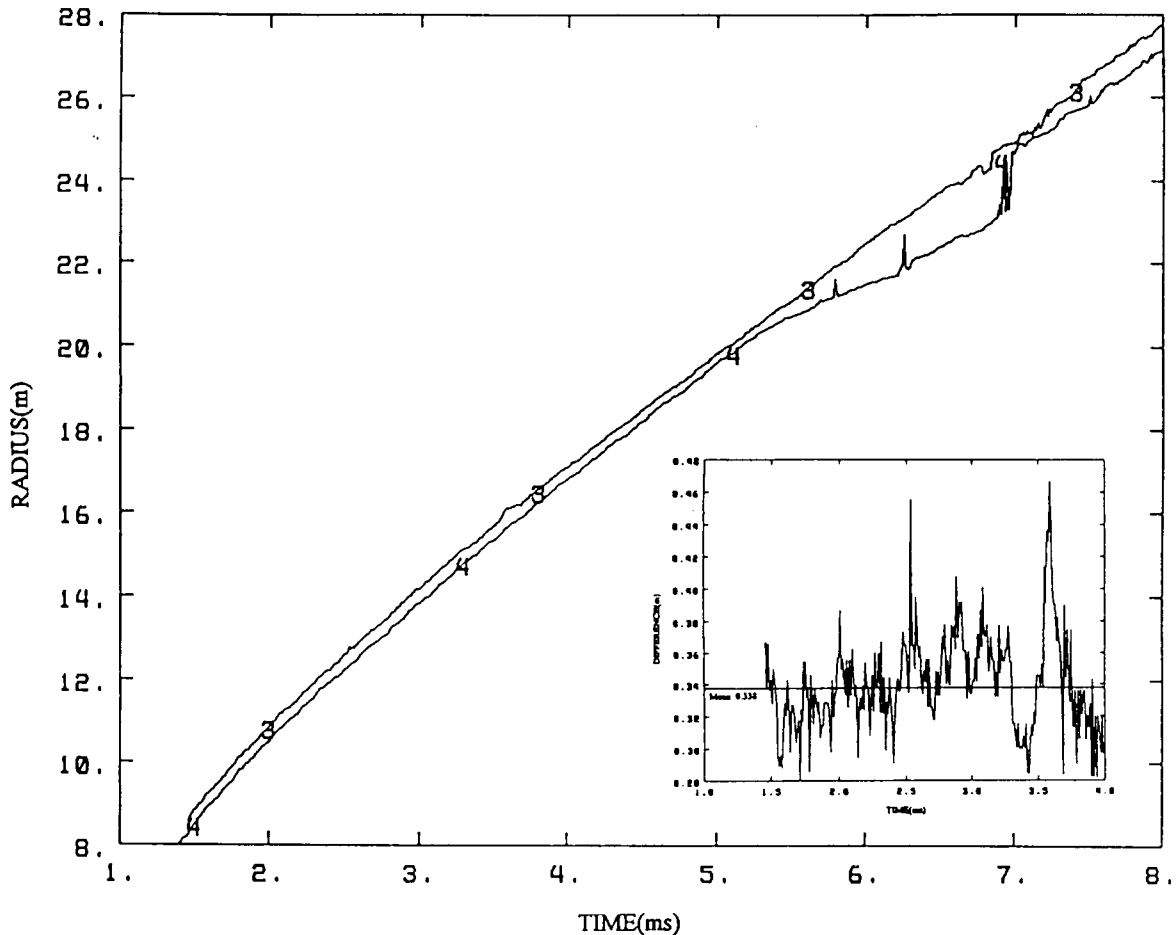


Figure 8. Enlarged view showing the difference between the KH-1 data and KH-2 data.

Can this apparent constant difference be explained? For a possible explanation, it is necessary to examine the explosive burn at the collars of drill holes KH-1 and KH-2. Based on survey, the distance from UWP (note: UWP is the best location of the center or axis of explosion available) to the KH-1 collar is 8.557 m while to the KH-2 collar it is 7.910 m. Both collars were about the same elevation, which was just slightly above the lower of the three levels instrumented with CORTEX in the explosive chamber. The time of explosive burn arrival at the collar of KH-2, as determined from the CORTEX data, is 1.389 ms. The first recorded point by K3 in KH-1 was radially 8.615 m at 1.459 ms. However, the induced shock as measured in KH-2 was 8.248 m radially from UWP at 1.459 ms, a difference radially of 0.367 m. This difference is derived from the fact that the detonating explosive was radiating from UWP toward the greater distant KH-1 collar, faster than the induced shock was traveling in the saturated tuff/grout at KH-2. Therefore, although the shock induced at the KH-1 collar occurred later, its greater radial distance placed the induced shock into the surrounding medium radially ahead of the induced shock at KH-2. Is it just coincidence that K3 is, on the average, 0.338 m ahead of K4? The 0.367 m radial difference at KH-1 and the K3 - K4 difference of 0.338 m are well within the experimental error budget at 8.0 m from UWP!

ASM Times-of-Arrival

Determining a comparable CORTEX time-of-arrival for the ASM gauges located in KH-1 and KH-2 is simple because the sensing elements were installed with the gauges, two each in KH-1 (A1 and A2) and

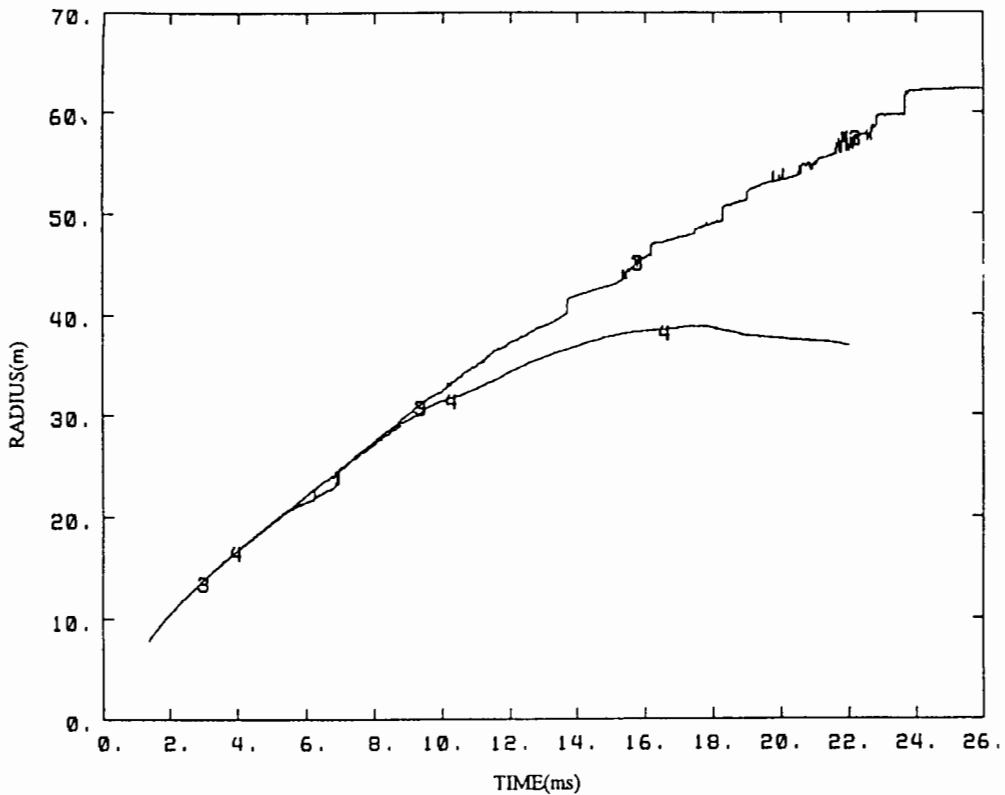


Figure 9. The KH-1 (K3) data shifted by -0.338 m and the KH-2 (K4) data.

KH-2 (B1 and B2). The gauge TOA and corresponding CORTEX times are given in Table 1. The ranges shown for the CORTEX times are due to there being data from three independent sensing elements. Similar values for the two gauges in each of KH-4 (C1 and C2), KH-5 (D1 and D2) and KH-6 (E1 and E2) are more difficult. The sensing elements installed in KH-2 were the closest records to these six ASM gauge locations. However, the induced shock, as monitored by the KH-2 sensing elements, fell below the crush threshold of all three installed cables before reaching the radial distances of all these gauges. The shift of the K3 data to coincide with the early time K4 data, as shown in Figure 9, permits an estimate to be made of the TOAs for these six gauges. These are the values presented in Table 1 and should perhaps be considered, no-earlier-than estimates. TOA values were obtained for C1 and C2 and they are consistent with the corresponding CORTEX times. The failure of any KH-2 sensing elements to respond to the induced shock beyond about 38 meters, may indicate why no discernible record was observed on the KH-5 and KH-6 ASM gauges. The F1 and F2 ASM gauges were actually beyond the range of any CORTEX data.

CONCLUSIONS

CORTEX could instrument only four exit paths from the explosive chamber. The data reported have been shown to be absolutely consistent within each exit path and in some cases between different paths (KH-3 and access drift). Some exit paths showed different responses. The sensing elements installed in KH-2 ceased responding to the radiating induced shock at about 38.0 m while the KH-1 and access drift sensing elements, located on either side of KH-2, continued to respond to beyond 60.0 and 50.0 m respectively. Assuming that the cable response, drill hole stemming and the incident angle of the radiating shock on the sensing elements are not significantly different in each exit path and the cable response is indicative of shock pressure, there are clearly differences in the radiating shock pressure.

The induced shock monitored in KH-1 uniformly preceded the shock in KH-2 and both differed from the shock down the access drift. The difference in the data from the KH-1 and KH-2 exit paths appears to be the result of a difference in the radial distances of the KH-1 and KH-2 drill hole collars from the detonation

axis. The explosive chamber was not a uniform construction, besides being a right cylinder which was "axially" detonated. What irregularities in the induced shock did this introduce? Within the range which CORTEX was able to monitor, there were differences in both the position of the radiating induced shock and in the apparent pressure of the shock wave.

Concluding remarks

This report has been concerned with sub-millisecond differences in time and tens of centimeter differences in radial position. While these differences are significant on the time and distance scales of this report, the transmission of signals over time and seismic distances perhaps tend to obscure the differences reported here. We have moved from the explosive chamber to the very near surrounding medium and found differences. The microscope applied to the data acquired within the explosive chamber has perhaps lost some of its resolution when examining the measured induced shock in the surrounding medium. But if CORTEX was able to measure these differences with just the very limited instrumentation of this experiment, what other differences exist and how much further out do these anomalies persist?

ACKNOWLEDGMENTS

The work reported here required the cooperation of many organizations and the assistance of many individuals. They all deserve thanks, but particularly the hard working hands of Keith Alrick, Randy Bos and Brad Wright of LANL, our LLNL colleagues and the EG&G-NTS crew, who stuck in there for the long haul and kept the systems functioning over the long delays. Thanks also to J-6, EG&G-LAO, RSN, DNA, REECO and all the rest of the alphabet soup.

REFERENCES

1. R. G. Deupree, D. D. Eilers, T. O. McKown and W. H. Storey, "CORTEX: A Compact and Versatile System for Time Domain Reflectometry," Twenty-seventh International Instrumentation Symposium, Instrumentation for a Blast Environment Session, Indianapolis, Indiana, April 27-30, 1980, Los Alamos Scientific Laboratory document LA-UR-80-3382.
2. T. O. McKown, "Explosive Performance on the Non-Proliferation Experiment," Los Alamos National Laboratory report LA-12748-MS, March 1994.
3. T. O. McKown, H. C. Goldwire, D. D. Eilers and F. J. Honey, "ANFO Detonation Velocity Measurements for G-7 Colony Mine Shots 79-2 and 79-3," Los Alamos Scientific Laboratory memorandum J-15-OU-79-102, (August 6, 1979).
4. L. Pirkle and M. Sullivan, H-RD-4 CORTEX III Recorder, EG&G Energy Measurements, LAO-355, Volume I Operating Manual, December, 1990.
5. W. H. Storey, D. D. Eilers, T. O. McKown, et al., "CORTEX II, Dual Microprocessor Controlled Instrument for Dynamic Shock Position Measurements," Conference on Instrumentation for Nuclear Weapons Effects, March 30 - April 1, 1980, Defense Nuclear Agency, Vol.II-Proceedings, pp 98-111.

Cavity Pressure/Residual Stress Measurements from the Non-Proliferation Experiment

Raymond A. Heinle and Billy C. Hudson

Lawrence Livermore National Laboratory

Melton A. Hatch, Jr.

EG&G Energy Measurements

Abstract

The Lawrence Livermore National Laboratory planned and conducted experiments on the Non-Proliferation Experiment to determine post-detonation gas pressure inside the explosive cavity and the residual rock stress in the region immediately outside the cavity. Before detonation there was significant concern that steam and detonation products would create very high temperatures and pressure in the blast cavity that would exist for weeks and months after firing. This could constitute a safety hazard to personnel re-entering the tunnel. Consequently the Lawrence Livermore National Laboratory was asked to field its Cavity Pressure/Residual stress monitor system on the Non-Proliferation Experiment. We obtained experimental data for the first 600 ms after the explosion and again several weeks after detonation upon tunnel re-entry. We recorded early-time cavity pressure of about 8.3 MPa. In addition we believe that the ends of our sensor hoses were subjected to an ambient driving pressure of about 0.5 MPa (absolute) that persisted until at least three weeks after zero time.

Introduction

Before the detonation of the Non-Proliferation Experiment, there was considerable concern that steam and explosive detonation products would create very high temperatures and pressure in the detonation cavity. It was thought that these could exist for weeks or months after detonation and could constitute a safety hazard to personnel upon re-entry into the tunnel. Figure 1 shows a plot of the expected pressure and temperature histories for the NPE cavity.¹

With no further information it was considered necessary to disallow access to the tunnel beyond the gas seal plug for 48 hours after detonation and that no one could go beyond the entrance to U12n.23 drift for at least two weeks after detonation. Consequently the Lawrence Livermore National Laboratory Containment Program was asked to field its Cavity Pressure/Residual Stress monitor system on the NPE. If the cavity pressure experiment worked, immediate readout of the pressure inside the cavity could be provided and thus faster re-entry might be allowed.

¹Cliff Olson, July 6, 1993, private communication to Bernie Roth, based on calculation by Bob Nilson and Kay Lie of S-Cubed.

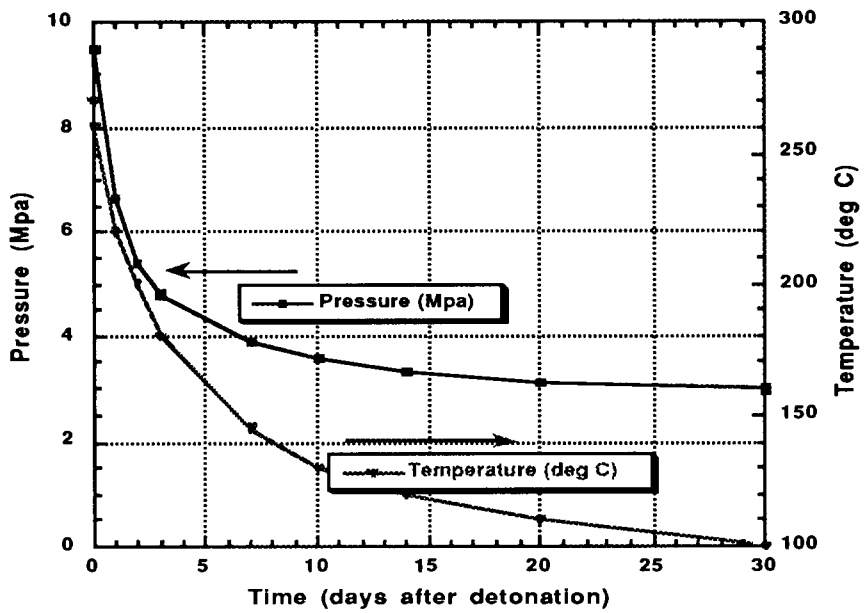


Figure 1. The NPE cavity pressure and temperature was expected to remain dangerously high for at least 30 days.

This system, which was first assembled for use in a vertical shaft, was re-configured and installed on the NPE in about three weeks. Figure 2 shows a schematic of the system that we installed.

The Cavity Pressure Experiment

In the cavity pressure experiment three 3.2-mm ID steel tubes extended to the edge of the explosive cavity where a rupture disk was located at the end of each tube. This was to ensure that the tubes would open in the event of improper explosive performance. Each of the tubes was filled with water and pressurized to about 10 MPa the day before the event. This pressurization was to prevent the tubes from closing under the high pressure that would occur inside the cavity and upon the passing of the hydrodynamic shock wave from the explosion. Figure 3 shows the three rupture diaphragms that were installed at the edge of the ANFO cavity.

The 3.2-mm ID steel tubes extended to just beyond the edge of the grouted section of the tunnel. At this point a transition was made to 6.4-mm-ID high-pressure rubber hose that extended to the cavity pressure and data acquisition module that was located 146 m from the center of the cavity. The length of the steel tubing and rubber hoses was about 150 m.

Inside of the pressure and data acquisition module were 0-10.3-MPa pressure transducers, one for each of the three sensor lines. In addition, channel 51A had a 0-52-MPa transducer to increase the dynamic range of the system. One additional transducer monitored the internal pressure of the package.

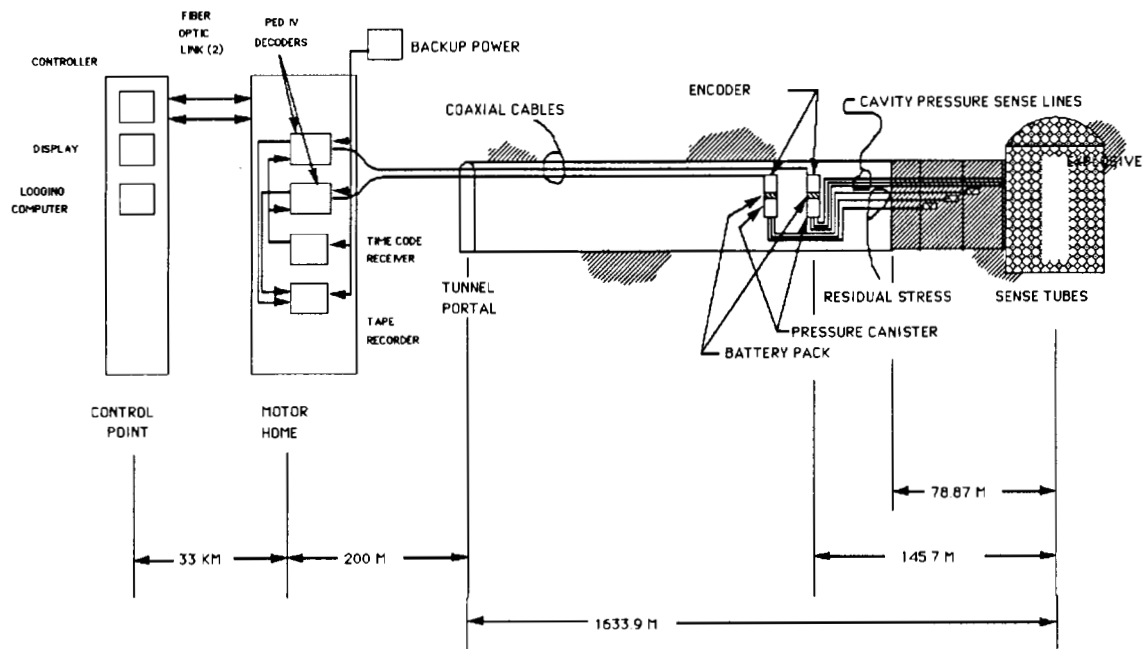


Figure 2. Cavity Pressure/Residual Stress Experiment on the NPE.



Figure 3. Rupture diaphragms at edge of ANFO cavity.

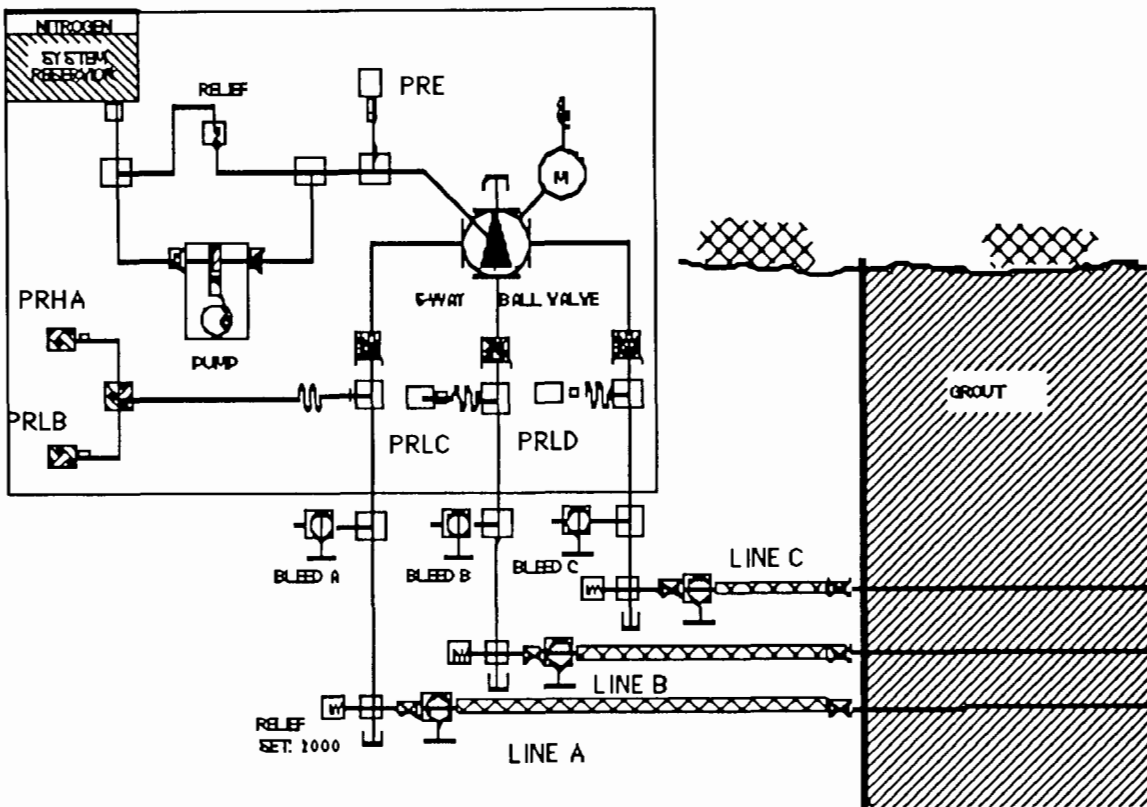


Figure 4. The cavity pressure experiment used four pressure sensors on three steel tubes leading into the NPE cavity.

The pressure was provided by a small battery-operated pump forcing the water from a small reservoir. Since there were three sensor lines and only one pump, a motor-operated ball valve was used to switch the pump from one line to another. A schematic diagram of the cavity pressure experiment is shown in Figure 4.

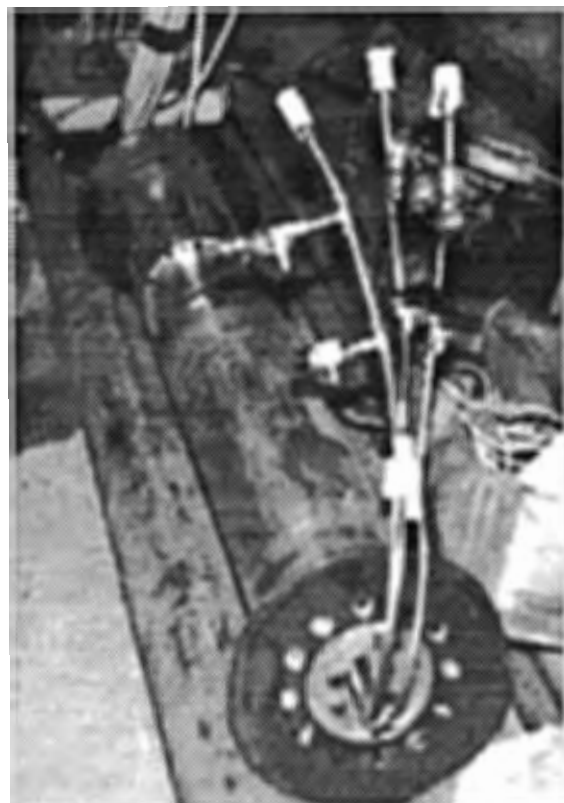
Table I shows a summary of each data channel and the status of each sensor. Note that the Cavity Pressure experiment has three lines of tubing leading to the explosive cavity. These three lines are labeled A,B,C on Figure 4. There are four transducers on these three lines, 51PRHA, 51PRLB, 51PRLC, and 51PRLD. Thus transducer D is actually on line C.

Figure 5 shows the cavity pressure package and the three steel tubes leading from the cavity. At this stage of assembly, the tubes on the package had not yet been connected to the long rubber hoses or the sensor tubes.

Unfortunately the system was designed for use in a vertical borehole and not a horizontal tunnel; one of the internal check valves was not designed to function in the horizontal position. Consequently the cavity pressure canister was mounted in the vertically. The cavity pressure canister was placed inside a steel "coffin" which was suspended using ropes in the vertical position. Figure 6 shows the canister placed inside its steel "coffin." The cavity pressure canister was mounted in polystyrene plastic foam to give it resistance to high frequency shocks.

Table I. Data channel summary.

Channel	Dist. from WP meters	Pk. Press. MPa	Status
Cavity Pressure			
51PRHA	7.6	15	Tube broke at 420 ms
51PRLB (A and B on same line)		Gage Saturated	
51PRLC	7.6	Gage Saturated	Comm. lost until re-entry
51PRLD	7.6		Tube broke before firing
51PRE	145.7	8	Internal pressure
Residual Stress			
52PRHA	28.58	12	Survived until shutdown
52PRHB	39.41	10	Tube broke at 600 ms
52PRHC	48.9	8	Tube broke at 600 ms
52PRD	162.5	8	Internal pressure

**Figure 5. Cavity pressure canister showing the three steel sensor tubes.**

After the pressure canister was fully prepared, the steel container was closed, and the entire assembly was raised into the vertical position. It was then secured by ropes. Figure 7 shows the cavity pressure experiment after it had been secured into place in the tunnel.

The Data Acquisition System

The signal from each transducer was fed into an analog to digital (A/D) converter and data multiplexer that was designed for use at the Nevada Test Site. The multiplexer (PED for Plug Emplacement Diagnostic) is commonly used for vertical-hole containment diagnostics at the Nevada Test Site and was mounted on the pressure canister for the cavity pressure experiment. The signals were digitized and multiplexed together before they were transmitted by a coaxial cable to a motor home parked outside the tunnel portal, about 1800 m from the working point. The digitization was at the maximum rate of 80 samples/s (12.5 ms/sample) but was slowed down to one sample every 5 minutes several hours after the event.

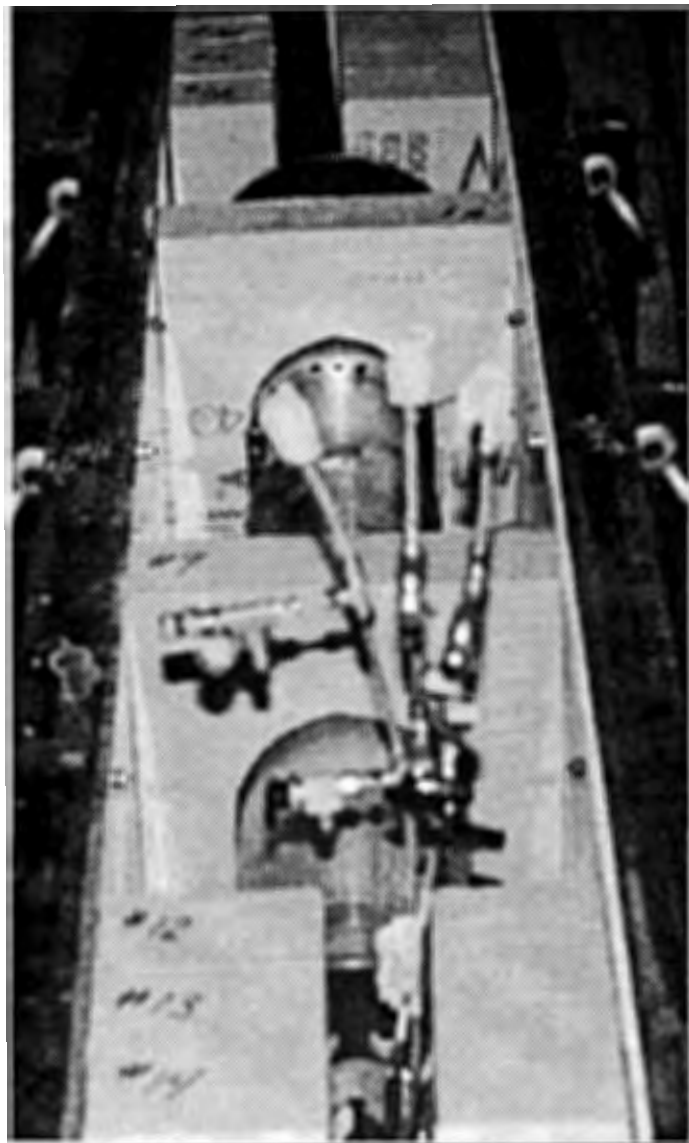


Figure 6. Cavity pressure canister inside its steel "coffin."

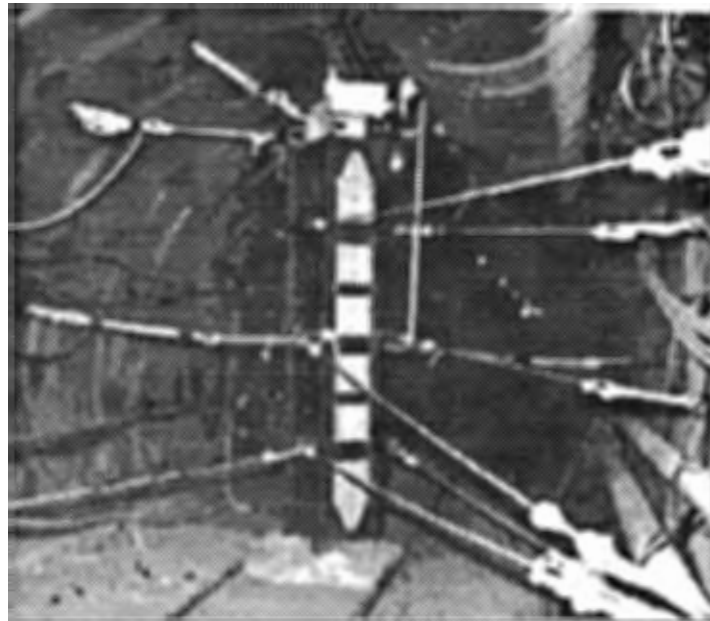


Figure 7. Steel "coffin" suspended in tunnel by ropes.

In the motor home the signals were de-multiplexed and recorded on the magneto-optical disk of a VAX computer. These data were also transmitted to a digital-to-analog converter and recorded onto a backup analog magnetic tape. The digital signals were also sent by a fiber optics link to another VAX computer that was located in the CP-9 Control Room, about 33 km from the working point. This computer had a real-time monitor that was used for data readout during the event. This computer also recorded the data onto an another optical disk for redundancy. The entire computer system that was used to ingest the data is called SMIDS for Special Measurements Integrated Data System. This system has been under development for the last few years.

Residual Stress System

Conventional containment theory predicts that there may be a compressive hoop stress field about the explosive cavity (filled with high pressure gas after a detonation). If this hoop stress field exceeds the cavity internal pressure, that pressure will be contained. Should the cavity pressure drop below the hoop stress, cavity rupture is possible. The purpose of the residual stress measurement was to determine the magnitude (in a semi-quantitative manner) of this residual stress field.

The residual stress measurement that we fielded on the NPE was almost identical to the cavity pressure system. This experiment, also designed and built for vertical holes was installed at the same time as the cavity pressure experiment. The only difference between these two was that the residual stress measurement used helical stainless steel tubes (305 m long) for the run into the grout. The tubes were terminated in 3-m lengths of high-pressure rubber hose. These three rubber hoses were placed inside the grouted main access drift at distances of 28.58 m (52PRHA), 39.41 m (52PRHB), and 48.9 m (52PRHC). These distances are from the center of the ANFO cavity to the center of the sensor tube. Rock stress was to

have squeezed the rubber sensor hoses, yielding a qualitative indication of the hoop stress in the containment cage about the cavity. Figure 8 shows a schematic of the residual stress experiment. Note that this is very similar to the cavity pressure system, except that the sensor tubes terminate with closed-off rubber hoses inside the grout instead of steel tubing. Also there were only three transducers for the three sensor tubes instead of the four that were on the cavity pressure experiment. Table I shows a summary of all of the cavity pressure and residual stress data channels which we fielded on the NPE.

The pressure canister and PED multiplexer was located in the main access drift about 163 m from the working point. From that location the data were transmitted over a coaxial cable to the motor home at the tunnel portal. The residual stress experiment used the same data acquisition system as the cavity pressure measurement.

Digital Accelerometers

To estimate the relative g-loading experienced by each of the pressure measurement stations, we installed shock transducers on the station 51 canister, on the right rib of the tunnel, and the railroad track on the tunnel invert (Table II). These sensors were Dallas Instruments Shock Rangers. These accelerometers gave rough limits on the acceleration. Readout was done by observing LEDs. If a given LED was lit, that meant that the acceleration was greater than the threshold value at which that LED was

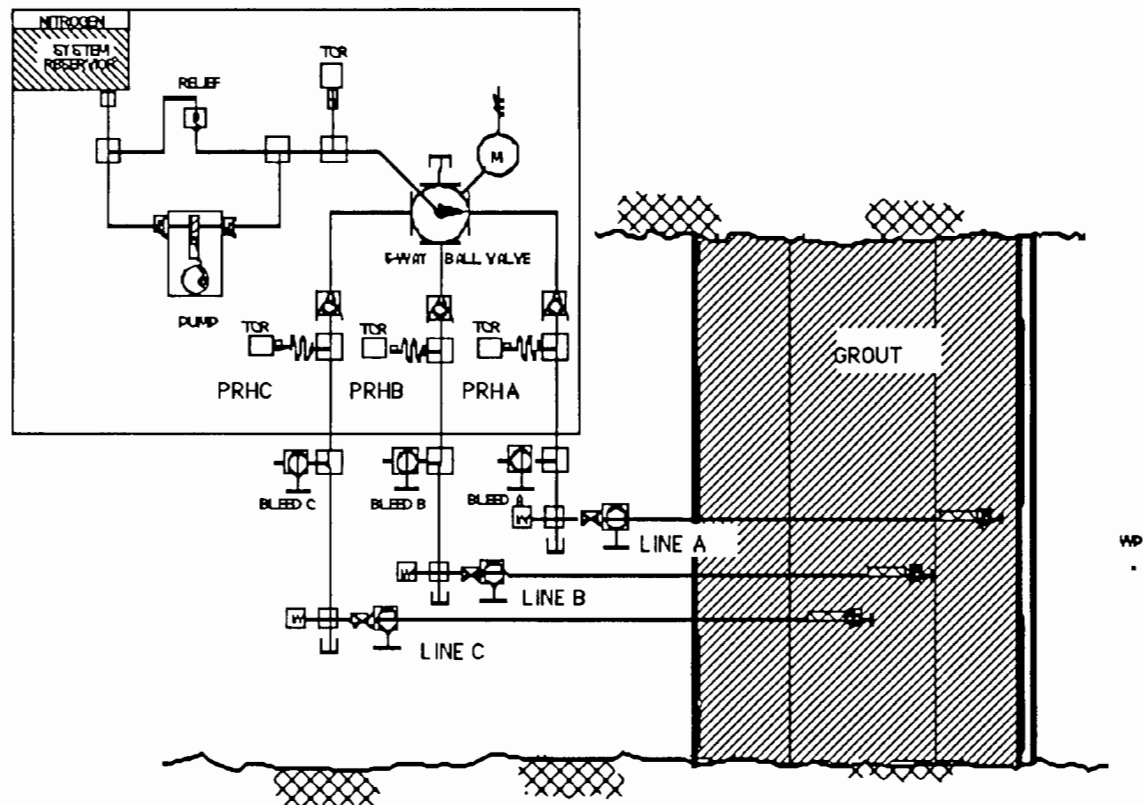


Figure 8. The residual stress experiment recording package was almost identical to the cavity pressure experiment.

Table II. Shock loading in the vicinity of the Station 51 multiplexers.

Name	Distance (m)	Range g
51 Radial	146	$a < 30$
51 Vertical	146	$30 < a < 60$
Drift Wall	146	$40 < a < 80$
RR Track Vertical	146	$a > 160$

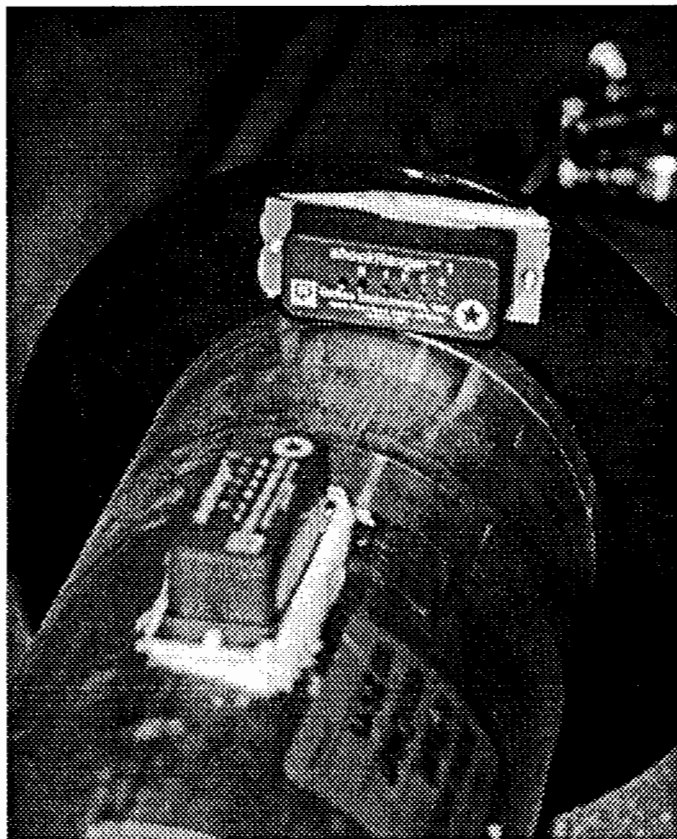


Figure 9. The digital accelerometers gave approximate limits of the g-loading received by the recording system.

calibrated. Figure 9 shows one of these accelerometers installed on the cavity pressure canister. Table II shows the results of these measurements. The "Drift Wall" and "RR Track Vertical" Shock Rangers were mounted on the tunnel rib and invert, which are free surfaces. Thus these gages are not good indicators of rock motion.

Experiment Timing

It is helpful to understand the timing of shock arrival at the various points of this experiment. The ANFO burns relatively quickly; within 1.4 ms of detonation initiation, the ANFO had burned out to the

edges of the cavity.² At station 51, 145.7 m from the cavity center, the first shock to arrive is the ground shock at about 61 ms, followed by the pulse through the water in the tube, followed by the air blast from the shock arrival at the grouted end of the tunnel. At station 52 the freefield ground shock arrives at 68 ms, followed by the water pulse at 204 ms (the pulse had much farther to go through the helical tubing) and then the air blast at 279 ms. These times are summarized in Table III.

Early-Time Results of the Cavity Pressure Experiment

Before zero time all sensors were operational except for channel 51PRLD (not shown on the data records) because the tube failed to hold high pressure. Immediately after grouting the first section of the access drift apparently something broke the integrity of the sensor tube.

For the first 420 ms all the rest of the sensors worked properly. At about 440 ms after zero time the tube connected to channels 51a and 51b was apparently severed by debris broken loose by the shock wave. Figure 10 shows four of the channels of station 51. The early-time data records shown here are from the analog tape backup records; software problems with the SMIDS system prevented the direct digital recording of the first 1-s of data. The dip at about 200 ms is a loss of frame synchronization and not a real phenomenon. At about 600 ms, falling debris broke the coaxial cable leading to the tunnel portal and all the signals from station 51 were lost. Channel 51c, the pump internal pressure, was perfectly flat except for the frame synchronization glitch at 200 ms until communication was lost at 600 ms.

At zero time, the pressure was 9.7 MP; then at 100 ms the pressure began dropping when the end of the high-pressure tube was severed and the liquid pressure equilibrated with the cavity pressure. At 100 ms the drop in pressure is consistent with a pressure wave traveling down the rubber hose at the speed of sound in water. (see Table III) The minimum, (about 8.3 MPa), is obliterated by the frame sync glitch at 200 ms. The pressure continued to rise to a peak of 15 MPa. The 15 MPa peak may be due to the shock wave from the air blast squeezing on the rubber hose connection the sensor tubes with the experiment. This peak is recorded on channel 51a; channel 51c was saturated until 400 ms when it recovered. The plateau from 450 to 550 ms (about 8.6 MPa) is probably representative of the peak cavity pressure. At about 440 ms channels 51a and 51b(line A) broke and the pressure dropped rapidly. Channel 51c continued on until 600 ms when communication was lost.

Previous experience³ has normally shown three stages to the cavity pressure profile from a nuclear explosion:

²Tomas O. McKown,"Explosive Performance on the Non-Proliferation Experiment", Non-Proliferations Symposium, Washington, D.C., April 1994.

³B. Hudson, R. Nilson, E. Peterson, and T. Stubbs, "Recent Nuclear Cavity Pressure Measurements," *Proc. 5th Symposium on Containment of Underground Nuclear Explosions* (Missior Research Corp. Santa Barbara, CA), September 19-21, 1989.

Table III. Expected shock arrival times at various points in tunnel.

Location	Distance (m)	Wet Tuff (ms)	Water (ms)	Air (ms)
Anfo Cavity	7.6			
End of Grout	79	33	53	
Station 51	145.7	61	97	229
Station 52	162.5	68		279
Station 52 (along helix)	305		204	
Sound speed (m/sec)		2400	1497	340

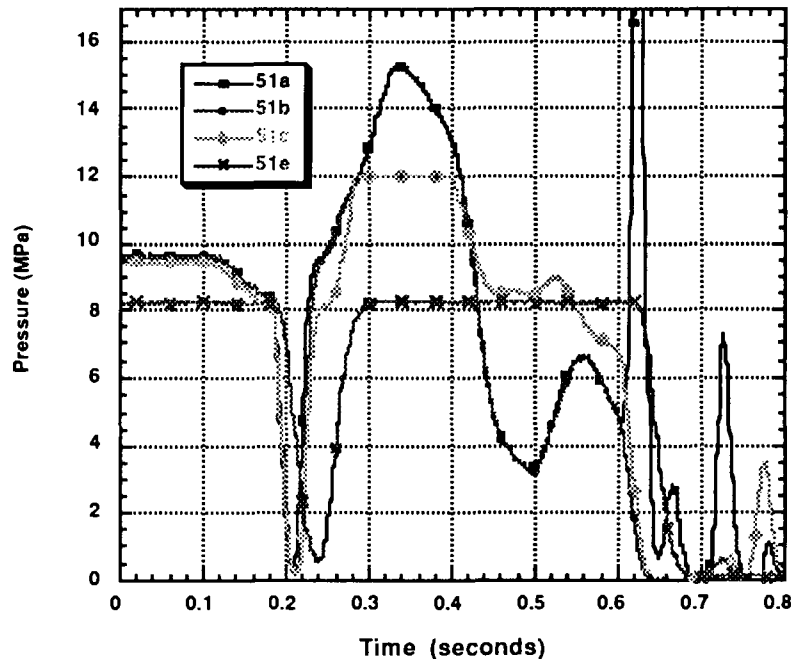


Figure 10. Early time history of the cavity pressure experiment, channels 51A,B,C,E.

Stage I - Initial pressure drops quickly because of hydrofracture into the ambient medium. This stage might last less than a minute for a nuclear explosion.

Stage II - The addition of mass combined with additional hydrofractures maintain a nearly constant pressure for a relatively long period, perhaps for as long as an hour.

Stage III - Heat conduction and Darcian flow out of the cavity causes a monotonic pressure decay until collapse.

Figure 1 does not show these three stages because the time scale is too long: only stage III is actually represented in the figure. The peak pressure reached in stage I would be mostly the result of expansion of

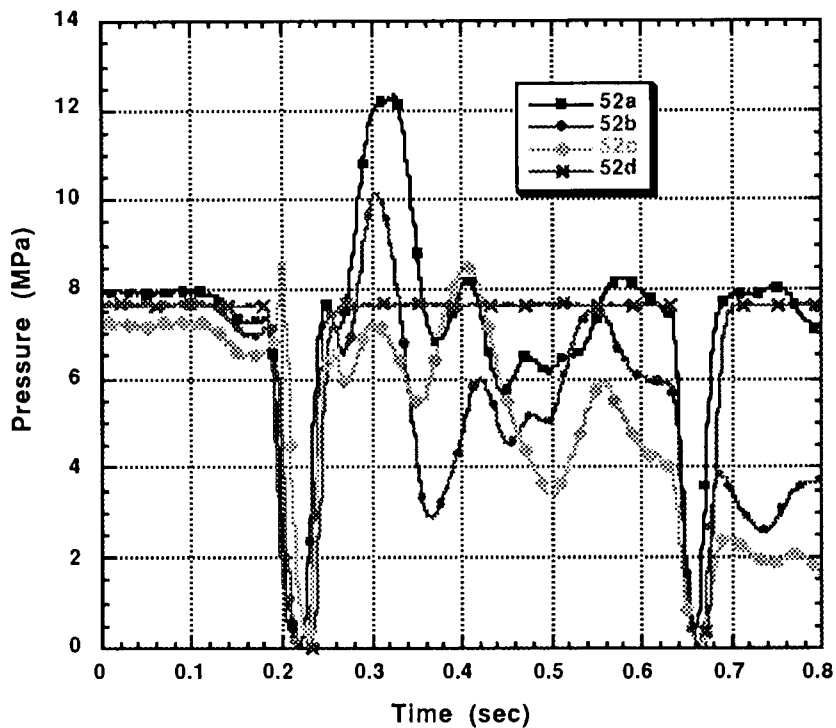


Figure 11. Early time history of the residual stress experiment, channel 52.

the explosive gasses. This is different than the nuclear case where large quantities of rock are vaporized⁴. Also stage II would be very much abbreviated for a chemical explosion such as the NPE because the only mass addition possible would be vaporization of the water trapped in the pores in the rock. In the NPE phase II was expected to last several minutes⁵. Hydrofracture pressure loss ceases to be important after the pressure drops below the rock overburden pressure (3.5-7 MPa). Knowing this we can probably identify the plateau from 350-550 ms with stage II in the cavity pressure profile although the data quits too early to establish a transition time into stage III.

Early-Time Results of the Residual Stress Experiment

Figure 11 shows the early time history of the residual stress measurement, station 52. For station 52 the communication was not lost and recording is continuous. The early-time data records shown here are also from the analog tape backup records. The dips at 200 and 660 ms are frame synchronization

⁴E. Peterson, K. Lie, N. Rimer, and R. Nilson, "Thermodynamic Evolution of Nuclear Cavities", *Proc. 6th Symposium on Containment of Underground Nuclear Explosions* (Lawlor Events Center, University of Nevada, Reno, Nevada) September 24-27, 1991.

⁵E. Peterson, Maxwell, S-Cubed Division, March 31, 1994, private communication.

dropouts. Channel 52d, the sensor monitoring the internal pressure of the residual stress experiment did not change except for the data frame dropouts.

The lines were pumped up to about 8.3 MPa before the event. At about 110 ms the pressure dropped to about 7.6 MPa, then peaked at three different pressures, depending on which channel. We do not understand the pressure drop at 110 ms, but it may be due to contraction of the helical tubing as it was moved by the hydrodynamic shock wave. Note that channel 52a recorded a peak pressure of 12.4 MPa, channel 52b recorded a peak pressure of 10.3 MPa and channel 52c recorded a peak pressure of 7.2 MPa, consistent with the progressively larger distances from the explosive cavity. As a function of distance, the magnitudes of these pressures drop only about half as fast we would expect for a point source explosion. (This is not unexpected considering the extended source we are dealing with). After about 550 ms channels 52b and 52c started to drop in pressure; apparently they had been severed by falling debris.

Re-Entry

When the tunnel was re-entered electrical communication was re-established with station 51 (the Cavity Pressure experiment). When the data were read out, channel 51c had not broken but was found to still have a pressure of 3.8 MPa when the cable was reconnected. However, when a mechanical gage was attached to the line to verify the pressure we were observing, the pressure immediately dropped to 3.3 MPa, indicating that we were observing the pressure of a small volume of liquid, not a large cavity. This line continued to hold pressure, but dropped exponentially until the final tests before shutdown.

Figure 12 shows the two sensors, channels 51C and 52A, that were showing nonzero values of pressure. Note that channel 51C does not appear until after tunnel re-entry at 15 days, when communication with the tunnel multiplexer was re-established. On day 21 channel 51c was bled to zero pressure and the line closed off. Overnight the pressure returned to 0.5 MPa.

Channel 52a continued to record pressure that appeared to be exponentially approaching about 0.5 MPa. During day 15, channel 52a was pumped up to over 0.7 MPa. The pressure dropped back down over the next few days to 0.5 MPa. Channel 52a was bled to zero pressure and then left overnight. The pressure returned to about 0.5 MPa overnight. The system was then shut down and the instrumentation was removed from the tunnel.

Figure 13 shows an enlargement of the time region from reentry until the final shutdown. Note how channels 51C and 52A are both approaching 0.48-0.52 MPa before the systems were bled down the day before shutdown. After they were bled down, both lines appeared to again be returning to 0.48-0.52 MPa. This behavior has been observed before on other tests. Were these two lines in communication with the cavity that had an ambient pressure of about 0.5 MPa? Because the communication with the cavity was almost certainly poor, we cannot establish that the 0.5 MPa pressure was from the cavity. The lines may have been crimped somewhere along their length into the cavity region. Alternatively if the two lines in

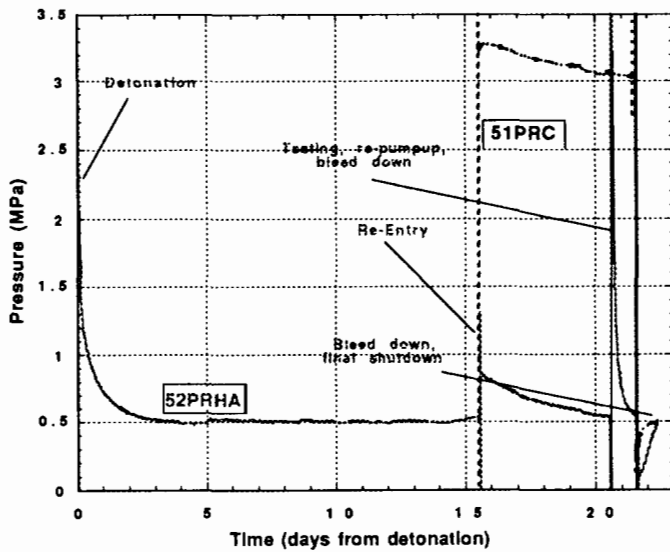


Figure 12. 51PRHA and 52PRC from detonation until experiment shutdown.

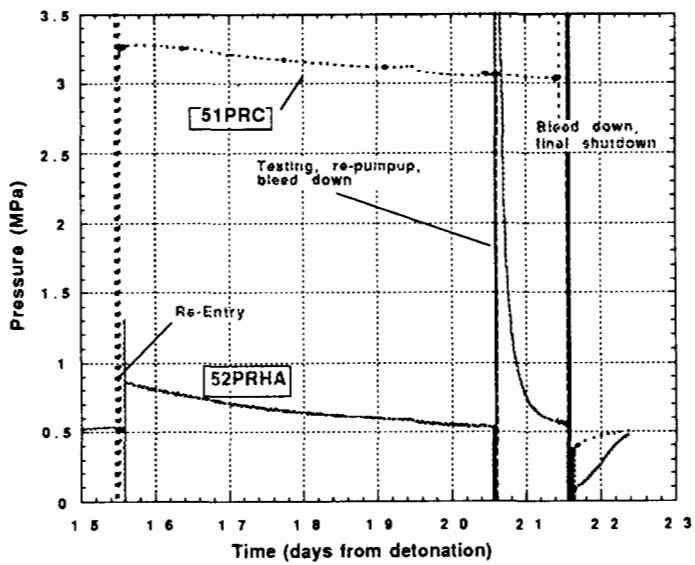


Figure 13. 51PRHA and 52PRC after re-entry until experiment shutdown.

question were broken somewhere in the grouted region, pore pressure in the grout might be responding to the residual hoop stress and be driving the sensor tube response. The 0.5 MPa might then be an indicator of residual stress.

Figure 14 shows the rubble at the end of the tunnel; The tunnel had collapsed to within 18 m of station 51 and no protection was afforded the hoses. The helical residual stress lines are visible on the left hand side of Figure 14.

Before the tunnel collapsed on the lines we believe that several of the tubes were severed outside the explosive cavity because the pressure one those lines dropped abruptly. This was most likely caused by debris being flung from the tunnel ribs or invert. Figure 15 shows a pre-event photograph of the point where the high-pressure lines exited the grout. Note the large pipe that lay near the cavity pressure lines. This pipe and other heavy objects could have easily been flung into the fragile cavity pressure and residual stress tubes. Flying debris could have been avoided by continuing the tunnel grouting out along



Figure 14. The pressure lines may have been pinched off by falling rock.



Figure 15 . Pre-event photograph of the end of the grouted area of tunnel showing pipes and other things that could have damaged pressure lines.

the tunnel further. This tamping would have held loose items in place. Alternatively, sandbagging the lines or burying them in the tunnel invert would have protected them.

The coaxial cable on station 51 was probably hit by the falling ductwork, shown in Figure 16. In some areas the ductwork was crushed; in other areas it exploded. Except for the ductwork, the cavity pressure and residual stress "coffins" were not visibly damaged, although the ropes had loosened up under stress. Figure 17 shows one of the "coffins" after the event.

Conclusion

Although the cavity pressure and residual stress experiments did not deliver all the data that we had expected, we accomplished many of the goals that we had set. We recorded a peak cavity pressure of about 8.3 MPa about 350 ms after the explosion. In addition, we believe that the ends of the sensor tubes were subjected to a driving pressure of about 0.5 MPa about 21 days after the blast, considerably lower than the 3.1 MPa that we would expect from the calculations leading up to Figure 1. We cannot be sure that the late time pressure we observed is indicative of cavity pressure, or whether it is due to residual stress related pore pressure in the rock and grout.

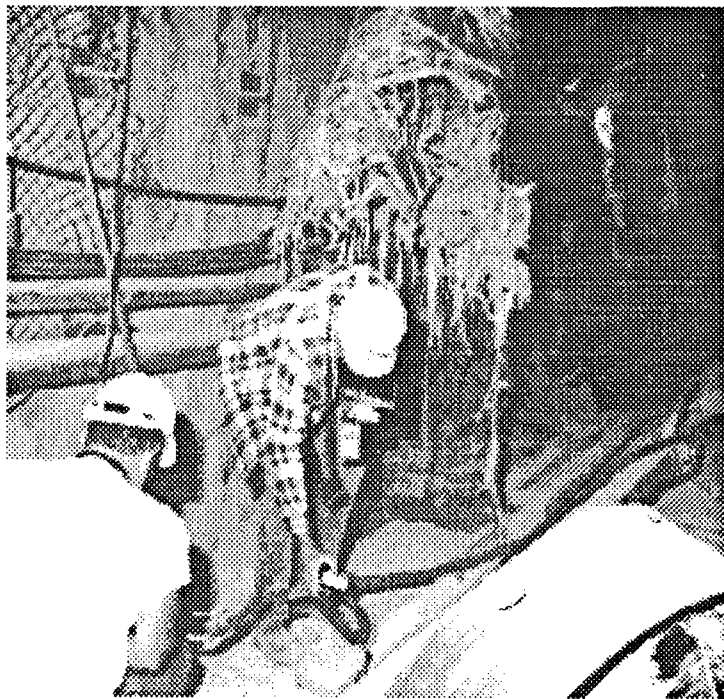


Figure 16. Damage to tunnel and ducting in vicinity of the experiments.

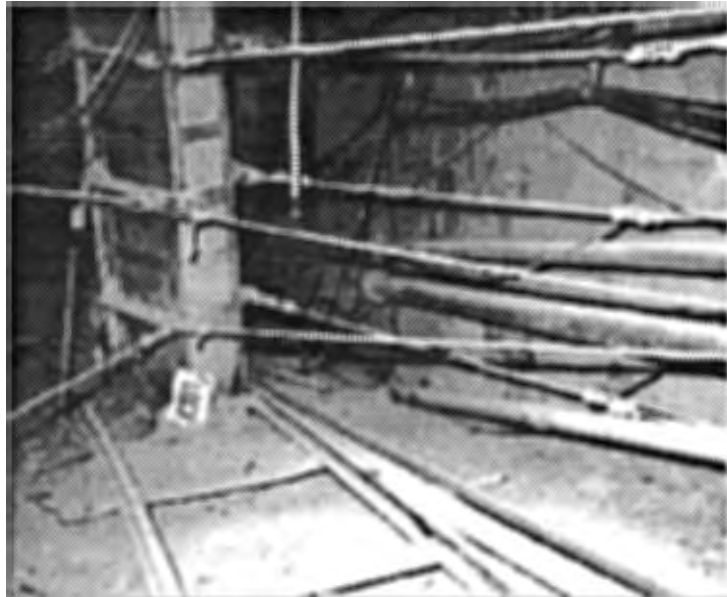


Figure 17. One of the coffins after the detonation.

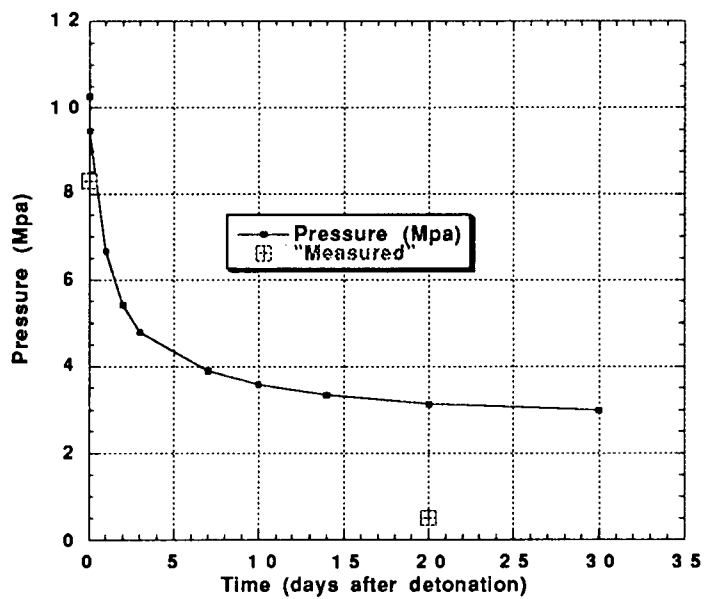


Figure 18. Pressure data points overlayed on the S-Cubed prediction.

Figure 18 shows the 8.3-MPa early-time pressure point and the late time 0.5-MPa pressure point overlayed on the S-Cubed prediction. Depending on the rock model used the 8.3-MPa value is well within the expected range. The 0.5-MPa value is low for cavity pressure but not unreasonable.

The data from the residual stress measurement is questionable because minor leaks, both into and out of the sensor tubes made data interpretation difficult. If we had been able to stem the tunnel out further

from the working point we could have been able to protect the tubing from being hit by flying debris, as well as protecting the plumbing from the collapsing tunnel walls. None of these changes would have been particularly difficult, but they were not possible in the three week's time that we had to plan and install our hardware in N-tunnel.

We gained much valuable experience in the fielding of the SMIDS system. The NPE was a very good test of the multiplexer system; the multiplexers survived very well under the shock loading they experienced. The NPE also gave a very good test to the SMIDS software. We anticipate various non-weapons-related applications for SMIDS in the near future.

References

B. Hudson, R. Nilson, E. Peterson, and T. Stubbs, "Recent Nuclear Cavity Pressure Measurements," *Proc. 5th Symposium on Containment of Underground Nuclear Explosions* (Missior Research Corp. Santa Barbara, CA), September 19-21, 1989.

Tomas O. McKown, "Explosive Performance on the Non-Proliferation Experiment", Non-Proliferations Symposium, Washington, D.C., April, 1994.

Cliff Olson, July 6, 1993, private communication to Bernie Roth, based on calculation by Bob Nilson and Kay Lie of S-Cubed.

E. Peterson, K. Lie, N. Rimer, and R. Nilson, "Thermodynamic Evolution of Nuclear Cavities", *Proc. 6th Symposium on Containment of Underground Nuclear Explosions*, (Lawlor Events Center, University of Nevada, Reno, Nevada) September 24-27, 1991.

E. Peterson, Maxwell, S-Cubed Division, March 31, 1994, private communication.

NPE - Close-In Stress and Motion Measurements

Carl W. Smith
Sandia National Laboratories

ABSTRACT

On the Non-Proliferation Experiment we measured stresses and accelerations in the nonlinear regime. Measurements were made in the host rock and in the grout stemming of the access drift. The thrust of the measurements was to provide data for a comparison with waveforms from nuclear events and with calculations of the process. Measured stress waveforms show greater amplitudes than yield-scaled waveforms from nearby nuclear events. Specifically, the five stress peaks suggest an equivalent nuclear yield of more than two kilotons. Material velocity data from NPE also show amplitudes greater than nuclear data. The risetimes of the NPE data are slower than risetimes of scaled nuclear data. The ratio of risetimes is about two; this difference may prove useful in discriminating between nuclear and chemical explosions. Non-radial accelerations show some departure from symmetric wave propagation. Tuff strengths - inferred from differences between radial and hoop stresses - show values that are about twice laboratory determined values.

INTRODUCTION

Between the scaled range of 10 to 100 m/kt^{1/3} an explosive-generated stress wave evolves from a shock wave (>10 kbar) to a large amplitude stress wave (~0.2 kbar). Through this region significant energy is dissipated in the compression and unloading cycle of the rock and in generating motion on faults and fractures. These losses strongly affect the amount of energy available for the seismic regime. Wave propagation measurements in this range lead to a phenomenological understanding of the dissipation process. With this knowledge calculational models may be improved. Measurements are again used to confirm calculational predictions.

At five locations between 15 and 70 meters from the center of the explosion we measured radial stress in the rock. At the farther three ranges we also measured hoop stress and acceleration. The acceleration waveshapes were integrated to yield particle velocity, that is, the physical motion of the material. In addition to radial acceleration, vertical and transverse components were measured at selected locations. These nonradial components show deviations from symmetric wave propagation. Finally, we fielded radial stress and acceleration instruments in the stemmed access drift to provide a comparison of grout stresses and motions with those in the host rock.

THE EXPERIMENT

Figure 1 shows a plan view of the explosive cavity, the 77 meter long access drift, and one N-tunnel drift. The gages were located in holes drilled in the left rib of the access drift and in the grout stemming that filled the access drift. Also indicated is the location of the cable junction box in the open drift at the end of stemming.

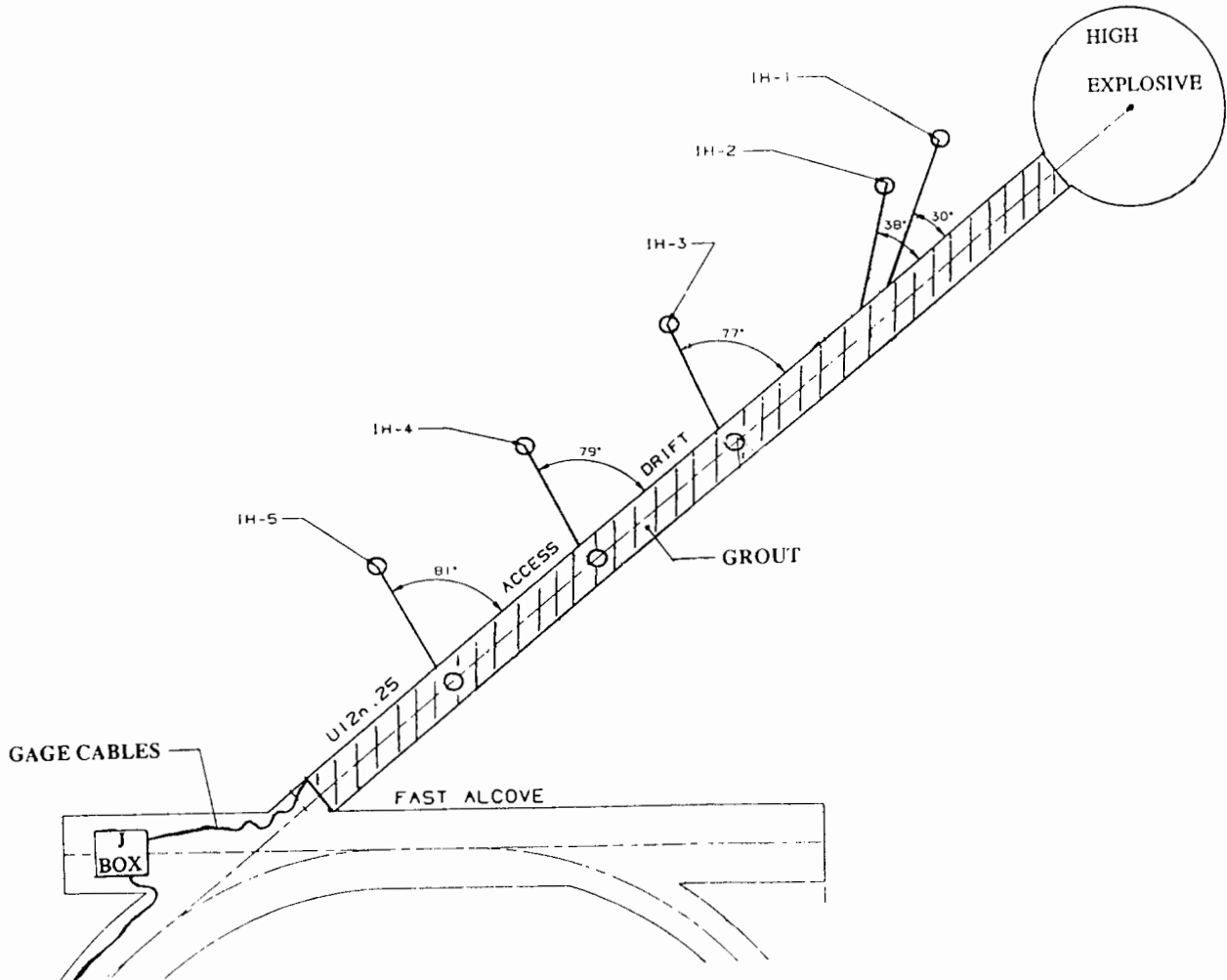


Figure 1. Plan View of the Experiment. O Marks SNL Gage Locations.

No measurements of material properties were made for this event. The tuff, however, had been judged by DNA geologists to be similar to that at two nearby nuclear events. Tables 1 and 2 show measured physical properties for those events. The measurements were obtained by DNA and are reported in classified documents on those events.

Table 1. Physical Properties for the U12n.23 and U12n.24 Events

Material	U12n.23	U12n.24
	Zeolitized Tuff	Zeolitized Tuff
Average Bulk Density (Mg/m ³)	1.91	2.01
Average Grain Density (Mg/m ³)	2.45	2.49
Average Water content (%) (by wet weight)	19.1	16.2
Porosity(%)	36.7	32.5
Saturation (%)	99.4	100.0
Gas Filled Voids (%) calculated	0.7	--
permanent compaction (after 4 kbar compression)	1.4	0.9
Average Compressional Speed (m/sec)	2860 (core ultrasonic)	2700 (tunnel seismic)

GAGE DETAILS

Ytterbium fluid coupled paddle gages (YBFC) were fielded to measure radial and hoop stresses. This gage package had been developed to measure residual stress on nuclear and high explosive events. For insertion in holes the radial and hoop stress gages were aligned 90 degrees to each other and attached to an aluminium fixture. Exiting these packages was "wire rope cable". This cable was made for us by a wire rope fabricator. Our standard RG22 electrical cable was substituted in place of a wire core during the process of fabricating a wire rope. Use of this hardened cable on a recent nuclear event notably lengthened cable survival times. The accelerometer packages contain Endevco piezoresistive accelerometers with ranges of 1000 to 6000 g. (g is the acceleration due to gravity, 9.8 m/s².) To measure the radial, transverse, and vertical components some packages were built with three orthogonal accelerometers. These packages are attached to the fiberglass stress gage packages.

An underground instrumentation container, located 283 meters from the explosion center, contained gage power supplies, signal conditioning, and digitizing equipment. Digitized data was sent via fiber optics to a recording facility located about four kilometers from the portal of N-tunnel.

The free field gage packages were located in holes, 15 centimeter in diameter. Hole lengths varied to provide a minimum of 6 meters between gage locations and the drift - see the earlier figure. Holes dipped a minimum of 5 degrees below horizontal. A cement-like grout was used to couple the gages to the rock host. It was pumped through tubing to the end of the hole, displacing water that had been placed in the hole. This technique is used to eliminate air bubbles around gages; air voids have a significant effect on the local stress and acceleration. A GSHSG-R91 grout was used for this installation. This is a Waterways Experiment Station developed grout whose bulk modulus is an approximate match to that of the host rock.

Gage packages were also installed in the access drift (U12n.25) to measure radial stress and acceleration. A paddle-like assembly of fiberglass board and epoxy contains the fluid filled cell (YBFC); accelerometer packages were attached to the paddles. Electrical leads for these gages also used the "hardened" cable described earlier.

The table below gives gage names, ranges from the center of the explosion, gage locations, and gage types.

Table 2. Gage Details

<u>Gage</u>	<u>Range (m)</u>	<u>Hole</u>	<u>Gage Types</u>
1YR	15.27	IH1	radial YBFC paddle
2YR	20.51	IH2	radial YBFC paddle
3YR	40.34	IH3	radial YBFC paddle
3YT	40.34	IH3	hoop YBFC paddle
3AR	40.34	IH3	radial accelerometer
3AT	40.34	IH3	transverse accelerometer
3AV	40.34	IH3	vertical accelerometer
3SYR	40.56	drift	radial YBFC paddle
3SAR	40.56	drift	radial accelerometer
4YR	55.06	IH4	radial YBFC paddle
4YT	55.06	IH4	hoop YBFC paddle
4AR	55.06	IH4	radial accelerometer
4SYR	55.01	drift	radial YBFC paddle
4SAR	55.01	drift	radial accelerometer
5YR	69.77	IH5	radial YBFC paddle
5YT	69.77	IH5	hoop YBFC paddle
5AR	69.77	IH5	radial accelerometer
5AT	69.77	IH5	transverse accelerometer
5AV	69.77	IH5	vertical accelerometer
5SYR	70.01	drift	radial YBFC
5SAR	70.01	drift	radial accelerometer

MEASUREMENTS

The table that follows again gives gage names and ranges; new information is the time of arrival of the first energy, i.e. the foot of the wave, the peak value, and notes. The latter include peak

squares fit to the five points and constrain the slope to be the nuclear value. The Y intercept is related to the yield. This procedure gives a yield and standard deviation of 3.2 ± 1.5 kT.)

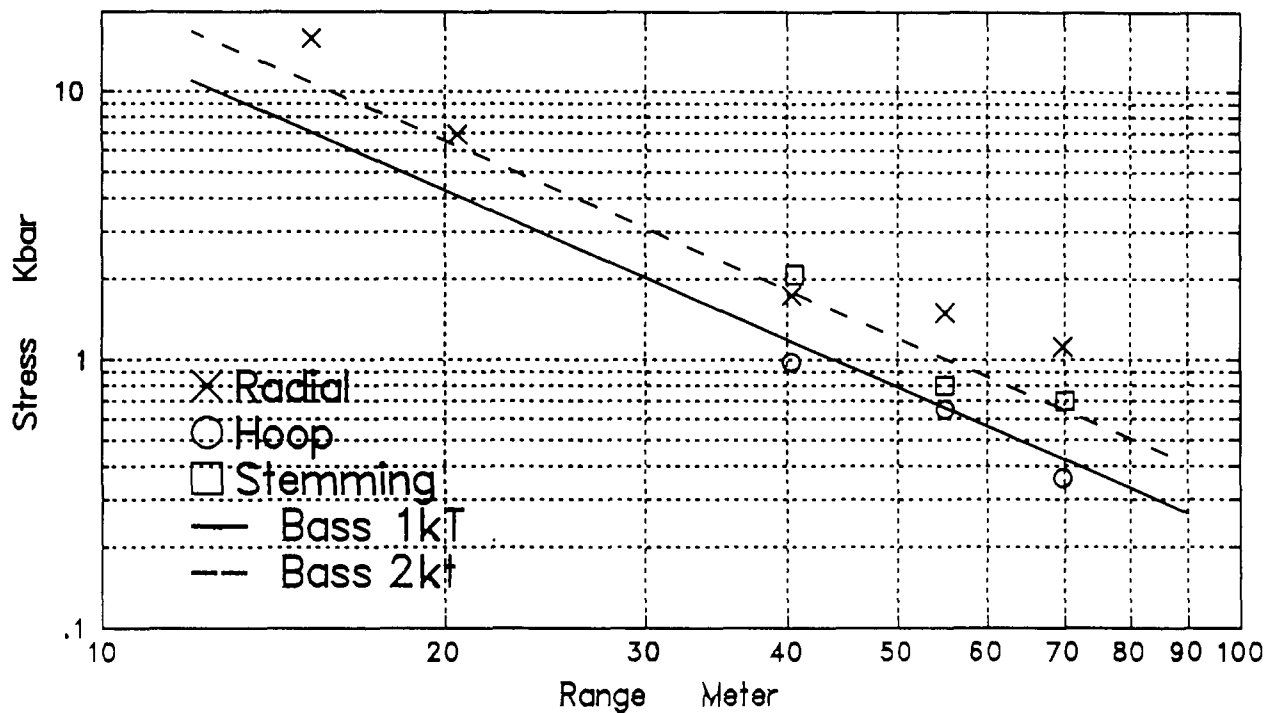


Figure 2. Measured Peak Radial, Hoop, and Stemming Stresses Versus Range and Predictions from the Nuclear Data Base.

Figure 3 shows peak acceleration versus range from measurements in the rock and stemming. The arrow on the 1000 g point is to indicate that this level is a lower bound; the gage broke during its risetime. The two points at 70 meters in the stemming are values from the double peaked wave-shape. Also plotted are two peaks from measurements at 191.4 and 200.7 meters; these measurements are described by Garbin in a separate Symposium paper. Again, the solid line is Bass' prediction from the nuclear database for one kiloton.

Figure 4 shows peak particle velocity data versus range; these were obtained from the integration of the acceleration waveforms. The arrow on the 40 meter point indicates a lower bound. Peak particle velocities also lie above the Bass' prediction for one kiloton, and the majority of them lie above the two kiloton prediction. We have included Garbin's data at 200 meters.

FREE FIELD STRESS

We turn now to the measured waveforms. Figure 5 shows radial stress waveforms from the 1YR and 2YR gages. At ranges of 15.27 and 20.51 meters the risetimes shown by these gages are rapid. Gage traces survive to a surprising 9 and 12 milliseconds. The nuclear database shows notably shorter recording times for gages subjected to these stress levels. We believe that the angle holes, shown in figure 1, and the wire rope cables contributed to the lifetimes. Prior to gage

particle velocity (PV) values.

Table 3. Time of Arrival Data and Peak Values

<u>Gage</u>	<u>Range(m)</u>	<u>TOA(msec)</u>	<u>Peak</u>	<u>Notes</u>
1YR	15.27	3.5	15.9 kbar	
2YR	20.51	5.3	6.9 kbar	
3YR	40.34	12.3	1.74 kbar	
3YT	40.34	13.5	0.98 kbar	
3AR	40.34	11.9	1640 g	PV > 30 m/sec
3AT	40.34	12.7	+170 g, -540 g	
3SYR	40.56	12.5	2.08 kbar	
3SAR	40.56	12.2	>1000 g	broke during risetime
4YR	55.06	18	1.55 kbar	
4YT	55.06	18	0.65 kbar	
4AR	55.06	17	550 g	PV = 21.4 m/sec
4SYR	55.01	17.5	0.8 kbar	
5YR	69.77	23	1.12 kbar	
5YT	69.77	23	0.36 kbar	
5AR	69.77	22.3	400 g	PV = 17.5 m/sec
5AT	69.77	22.6	+46 g, -40 g	
5AV	69.77	22.8	+175 g, -125 g	PV = 3.95 m/sec
5SYR	70.01	23	0.7 kbar	
5SAR	70.01	22	+195 g, +224 g	PV = 13.5 m/sec

A least squares fit was made to the time of arrival data from the stress gages in the rock. It gave the speed of the foot of the wave as 2774 m/sec. This value is within 3% of the data shown in Table 1 from the two nearby nuclear sites.

In the next series of figures we have plotted values from the above table. Figure 2 shows the measured peak stress versus gage range. Noted separately are the peak values of radial and hoop stress in the free field, i.e. drill holes, and the three radial peaks in the stemmed drift. The solid line is the prediction from the nuclear database for one kiloton; the dashed line is a similar prediction for two kilotons. Bass - reference 1 - collected and analyzed peak stress data from nuclear events in nearly saturated tuffs and developed a predictive relationship. The one sigma amplitude variation of the data from the log stress versus log range fit is given as $\pm 11.6\%$. With this small sigma we see that measured radial, free field stress peaks lie well above the one kiloton nuclear prediction; further, four of the five peaks lie above the two kiloton prediction. (One can calculate a least

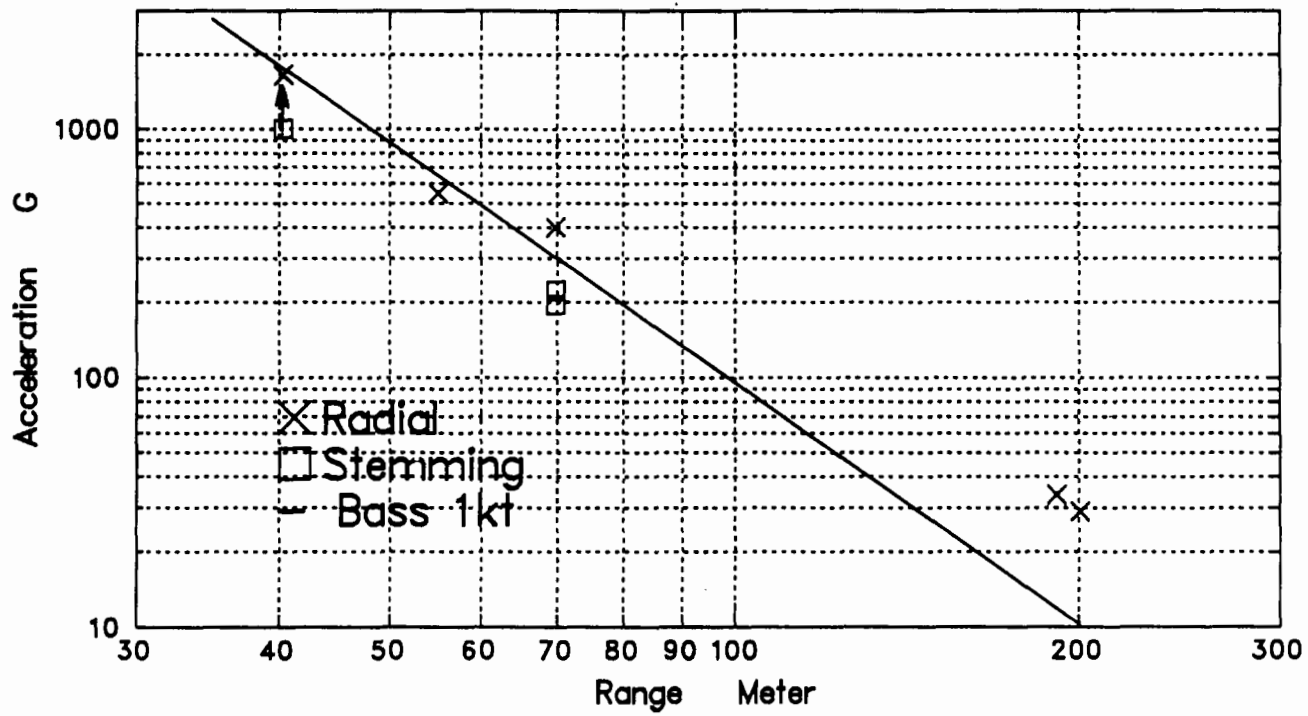


Figure 3. Measured Peak Radial Acceleration and One Kiloton Prediction from the Nuclear Data base. Arrow Indicates a Lower Bound.

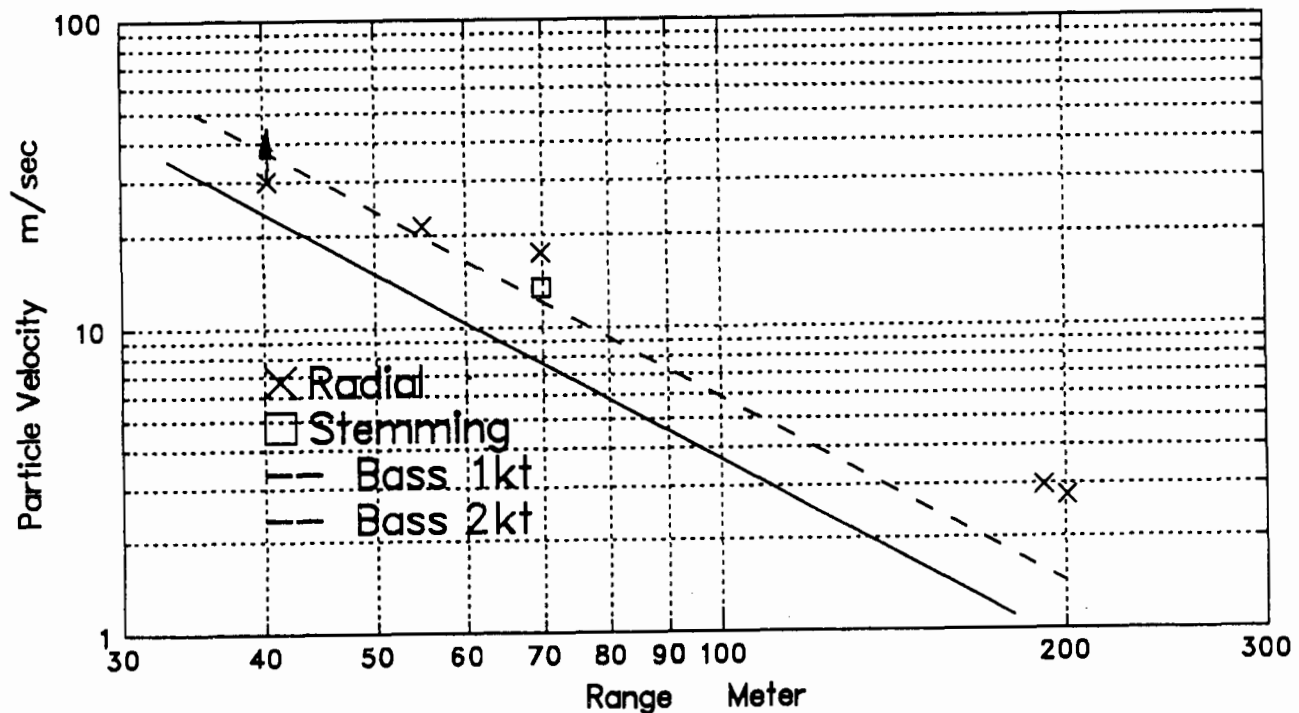


Figure 4. Peak Radial Particle Velocity and Predictions from the Nuclear Database. Arrow Indicates a Lower Bound.

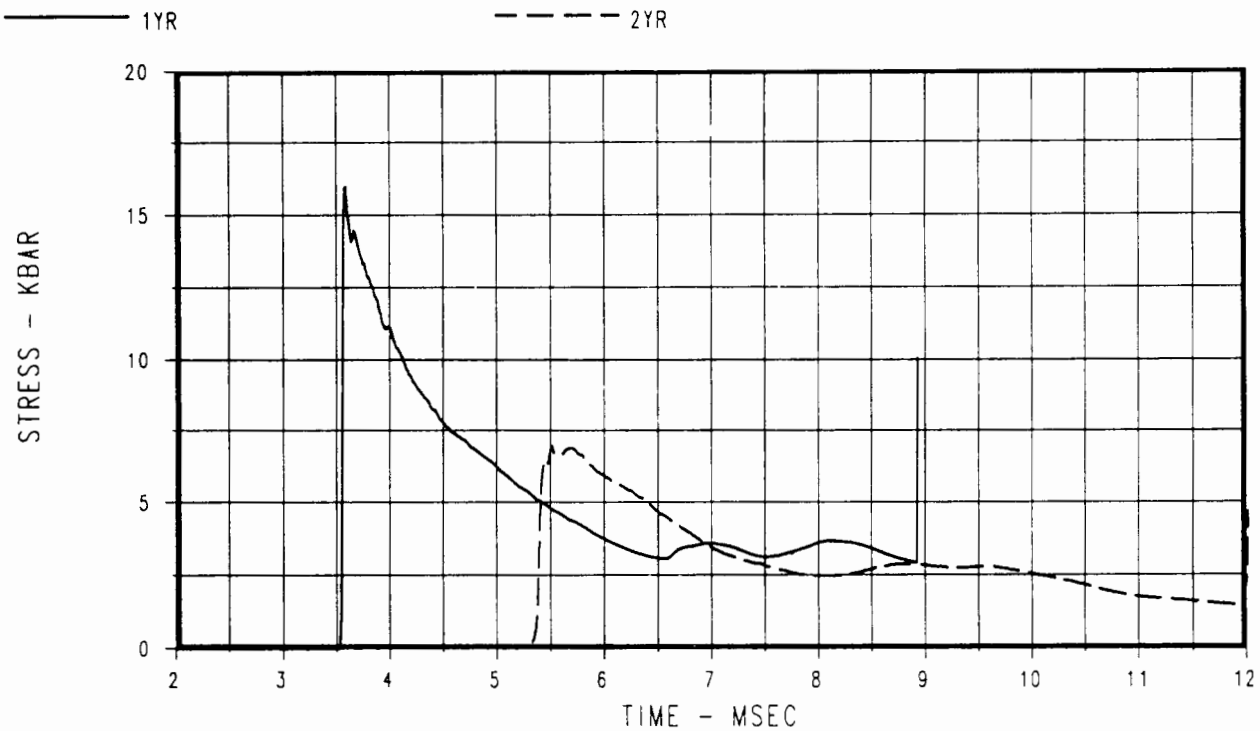


Figure 5. Radial Stress from Gages 1YR at 15.27 m and 2YR at 20.51 m.

breakage we see oscillations in the waveforms; these may be related to reverberations in the high explosive cavity. Figure 6 shows radial stress in the rock at the outer three ranges. With greater range one sees increasing risetimes. At the far range, 70 meters, the risetime is nine milliseconds. That figure times the wave speed (2774 m/sec) gives a distance from the foot to the peak of the

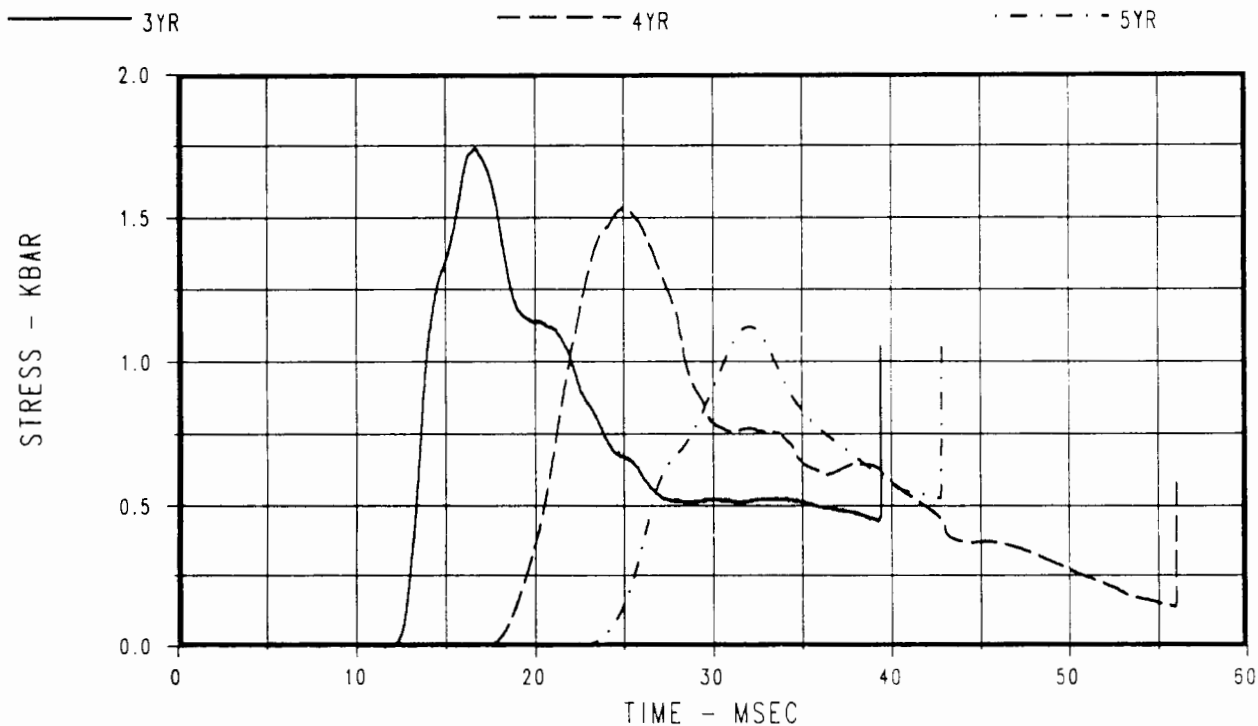


Figure 6. Radial Stress from Gages 3YR (40.34 m), 4YR (55.06 m), and 5YR (69.77 m).

wave of 25 meters. This is noted to convey the scale of the phenomena.

Figure 7 shows free field hoop stress measurements made at the locations of the outer three radial stress waveforms. Subtracting these waveforms from the radial components we obtain peak stress differences of 0.75, 0.9, and 0.75 kilobars. These differences are considered to be a measure of the rock strength, however, these in situ values are large compared to typically used values for N-tunnel. The latter are laboratory determined and range from 0.3 to 0.4 kilobars.

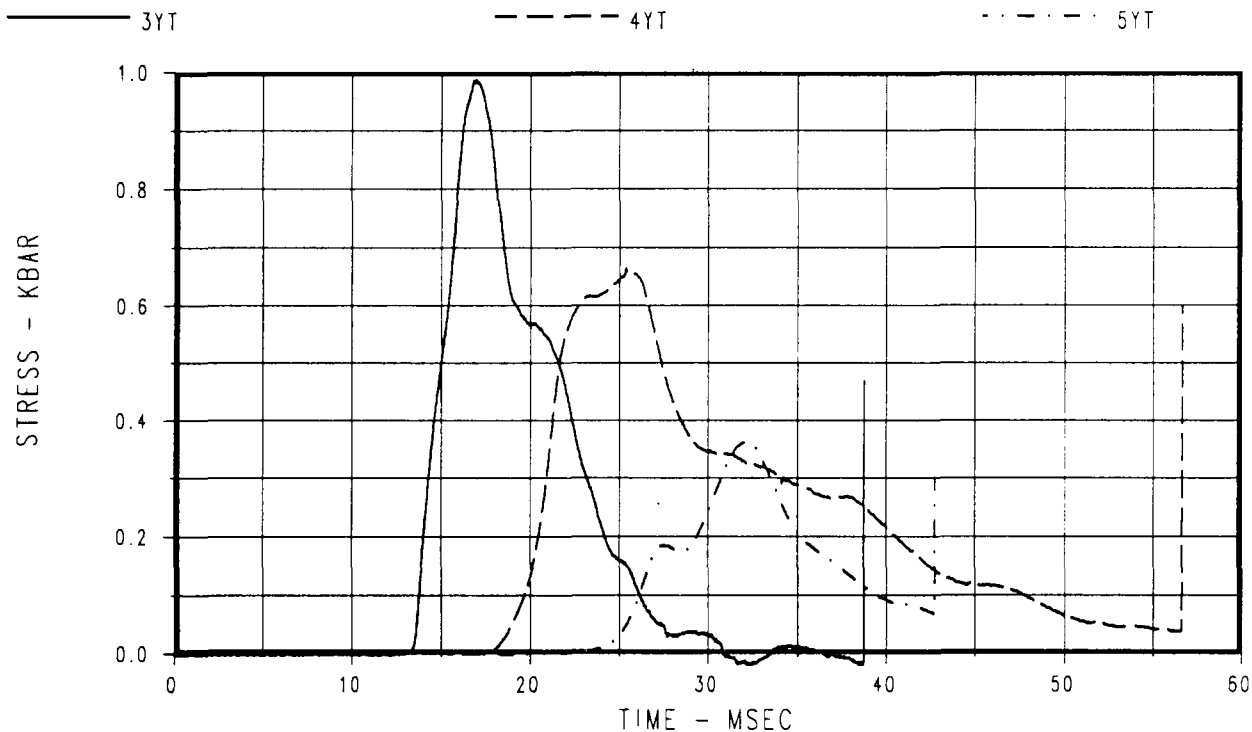


Figure 7. Hoop Stress from Gages 3YT (40.34 m), 4YT (55.06 m), and 5YT (69.77 m).

In the stemmed access drift we measured the three radial stress waveshapes shown in figure 8. The waveshape at the closest range shows a peak that is 20% higher than the measurement in the rock, but the outer two gages show peaks that are 53 and 63% of those in the rock. Waveshapes also differ. We conclude that the response of the rock is different from that of the stemming material. The unloading portion of the waveshape at the third range may have been affected by energy reflected off an open drift - the "fast alcove" - shown in figure 1. After reflection, the foot of the wave arrives back at the 5SYR gage at 28.2 milliseconds. (This is calculated by using the gage location and center of the explosion as foci of an ellipse; the smallest ellipse that is tangent to the "fast alcove" is related to the minimum time. One then measures the range from the explosion center to the tangent point and adds it to the distance from the tangent point to the gage location.) The wave is not a shock; thus it is later than 28.2 milliseconds when the main portion of the reflected wave can influence the outward propagating pulse. The reduction to near zero stress at 40 milliseconds may be the influence of the reflection.

Using the gage TOA values and the wave speed (2774 m/sec) we find that the foot of the stress

wave arrives at the end of stemming at 26 milliseconds. Shortly after, ground shock reaches the cable junction box - see the plan view - and generated motions that broke gage cables. (On the DNA nuclear events the stemmed drifts were of greater length; notably longer gage recording times were usually obtained than on this event.)

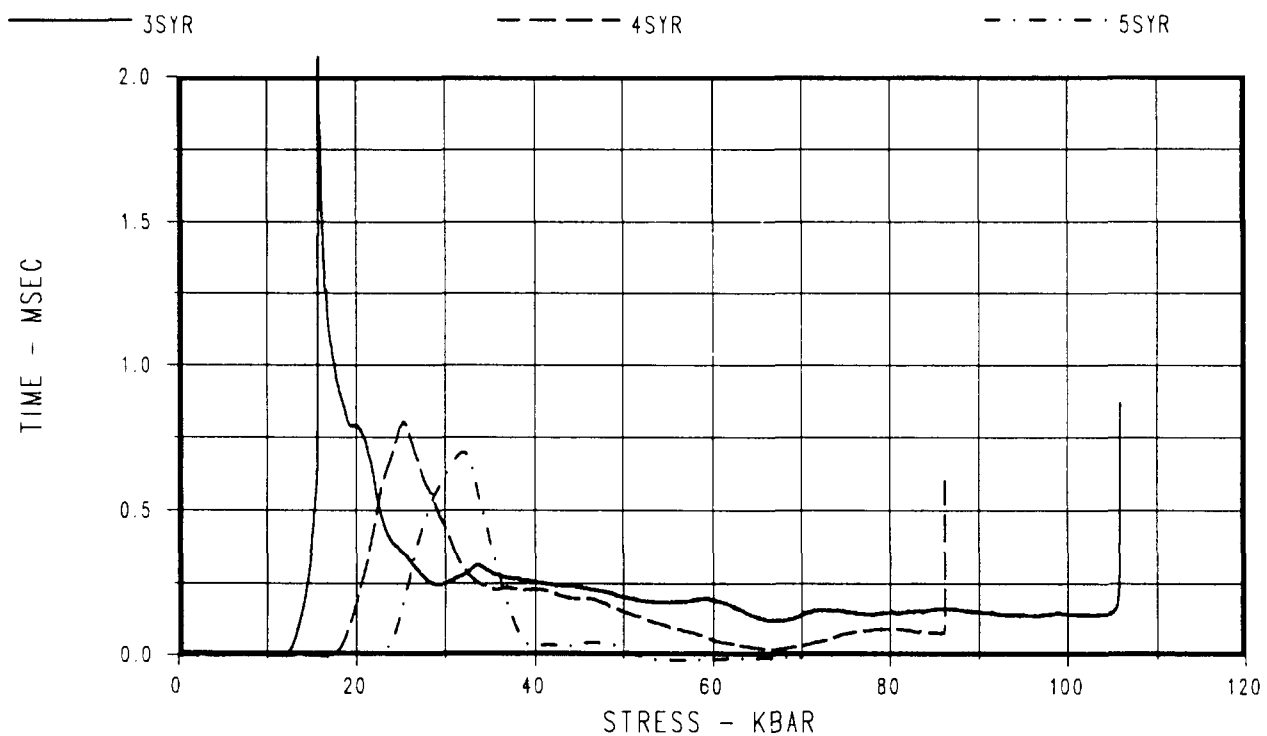


Figure 8. Radial Stress in the Stemmed Drift from gages: 3SYR (40.56 m), 4SYR (55.01 m), and 5SYR (70.01 m).

FREE FIELD ACCELERATION

Figure 9 shows three acceleration waveforms. The closest gage (3AR) broke before completing its positive phase. Thus, when integrated to obtain particle velocity, the trace does not reach a peak value. This incomplete trace is shown in figure 10; gage breakage occurred when the amplitude was 30 m/sec. The outer two accelerometers gave particle velocity traces, see figure 10, that last to later times, but not long enough to show a zero crossing, i.e. motion reversal. As mentioned earlier, this is related to the short stemmed drift. At the fifth range we also measured a non-radial component of acceleration. The vertical 5AV gage shows a positive, i.e. up, 175 g amplitude followed by a negative 125 g peak. The trace was lost at 47 milliseconds. Figure 11 shows the integration of this acceleration trace. After TOA we see a rise to a maximum upward velocity of 4 m/sec, followed by a slowing down to zero motion at 40 milliseconds, and then a slight negative motion. The vertical peak is about 23% of the radial peak motion shown in figure 10. These deviations from spherical symmetry were regularly observed on nuclear events and are believed to be related to geologic layering.

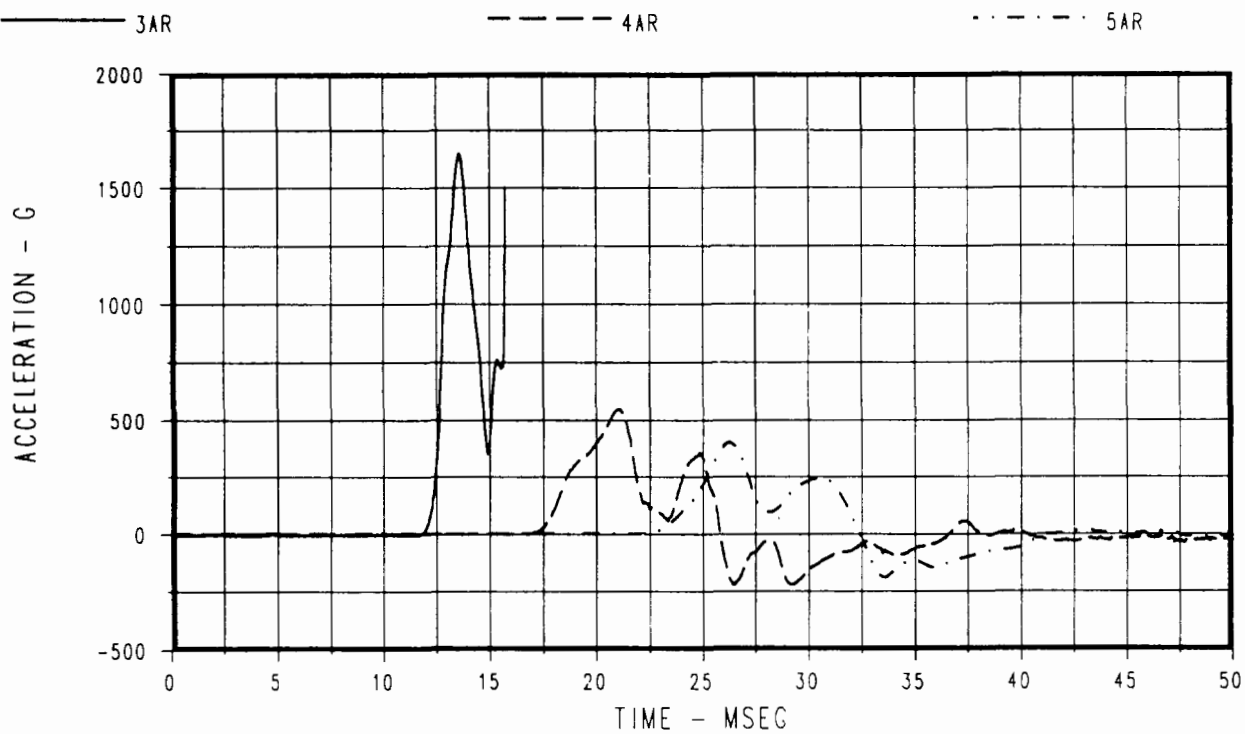


Figure 9. Acceleration Waveforms from Gages 3AR (40.34 m), 4AR (55.06 m), and 5AR (69.77 m).

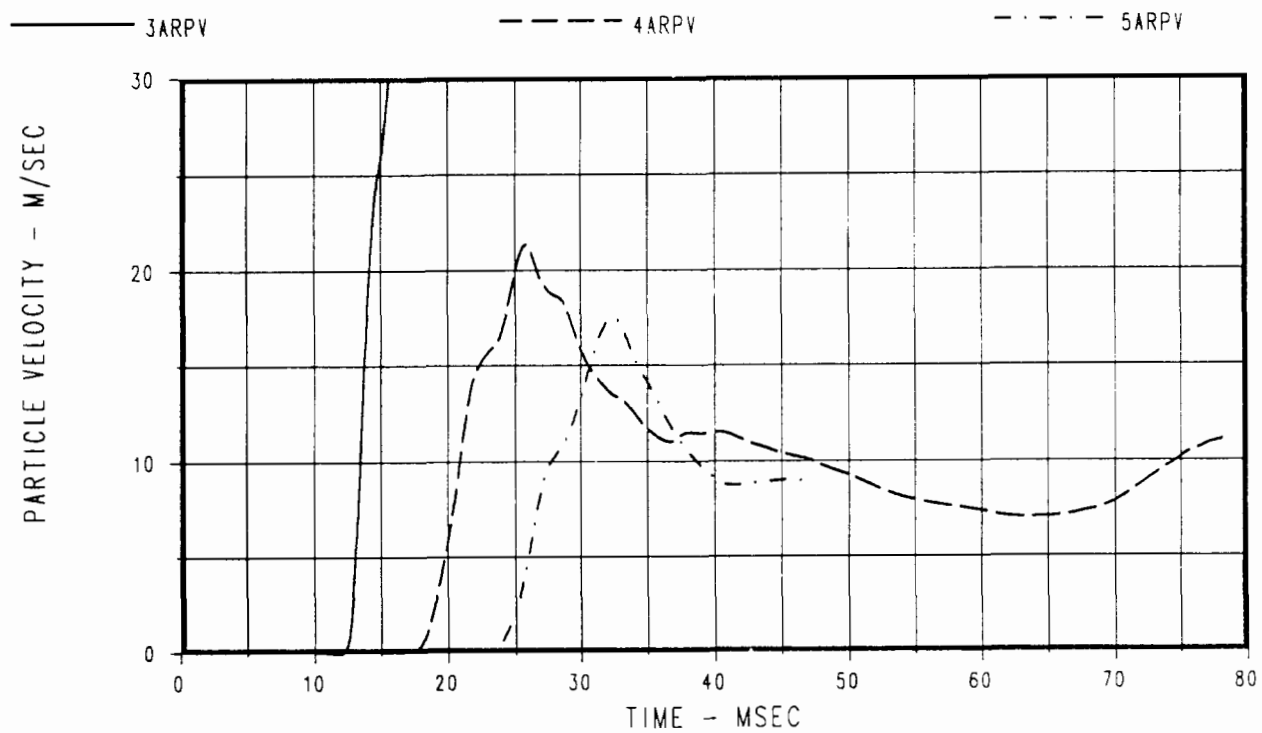


Figure 10. Particle Velocity Waveforms 3ARPV, 4ARPV, and 5ARPV Derived from Accelerometers 3AR, 4AR, and 5AR. 3ARPV Shows 30 m/sec when Gage 3AR Breaks.

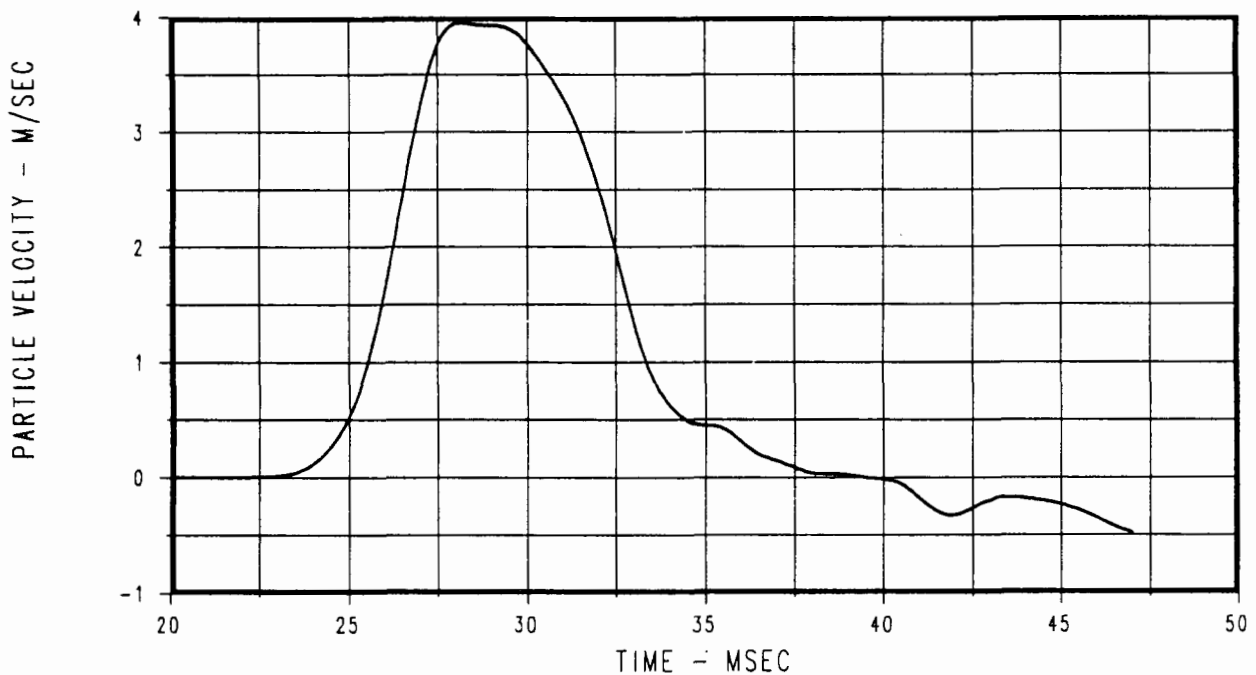


Figure 11. Vertical Motion Trace 5AVPV from the Integration of Gage 5AV (69.77 m).

COMPARISON

We now compare radial stress waveforms from the NPE event with those from nearby nuclear events. To scale the nuclear data to one kiloton we have used traditional yield scaling. For stress waveforms one scales the range to the gage and the time axis by multiplying both by the cube root of the ratio of the yields.

Figure 12 shows the 3YR and 4YR waveforms from NPE along with two measurements from nuclear event A. The scaled ranges for the nuclear data are 35.0 and 49.9 meters; the 3YR and 4YR ranges are 40.3 and 55.1 meters. Although both ranges for the NPE waveforms are greater than the scaled ranges for event A, we see 1.4 and 1.6 times greater amplitudes for the high explosive waveforms.

In figure 13 we again compare 3YR at 40.3 meters with a waveform from a second nuclear event. Again, the nuclear measurement was made at a closer scaled distance (33.5 meters) and shows a lower amplitude than the high explosive waveform. There was, however, a fault in front of the gage on the nuclear event; we suspect that movement on the fault truncated the peak and caused the double structure near the peak.

Figure 14 compares a five kilobar waveshape from a third nuclear event with 2YR from NPE. Here the ranges are the same - 20.5 meters. The difference in the time of arrivals is related to the different wavespeeds at the sites of the two events. Again we see that the NPE peak is about 1.4 times greater than the nuclear peak.

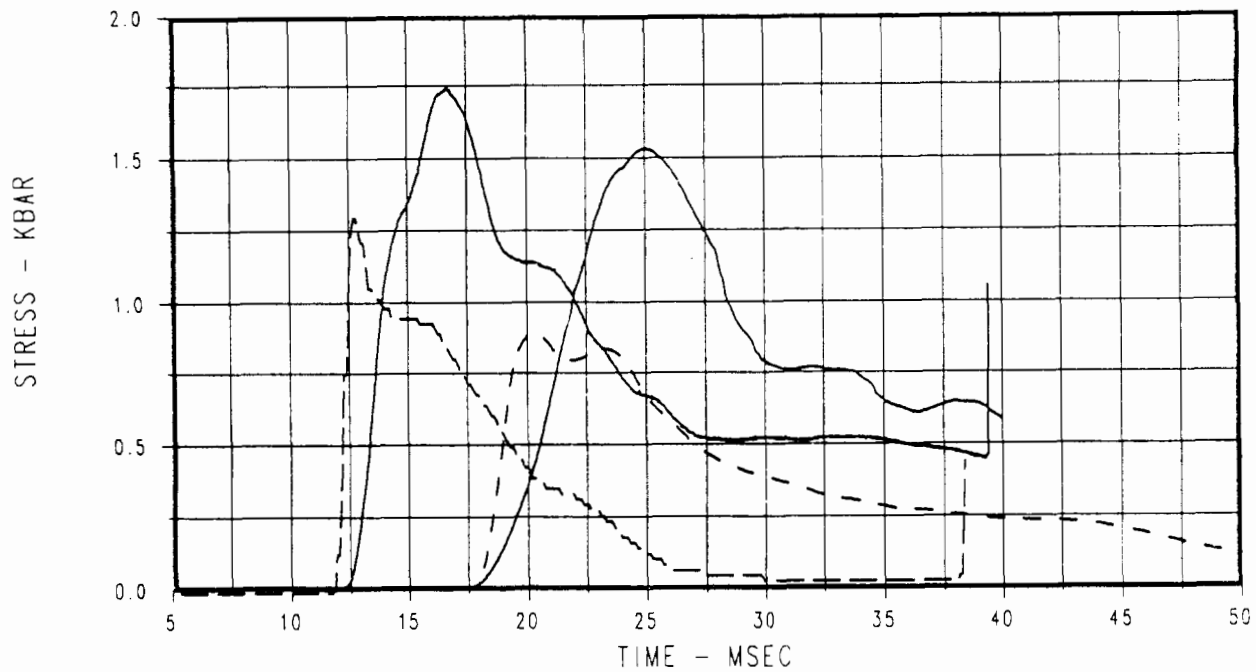


Figure 12. Comparison of Stress Waveforms: NPE - Solid Traces and Nuclear Event A - Dashed Traces.

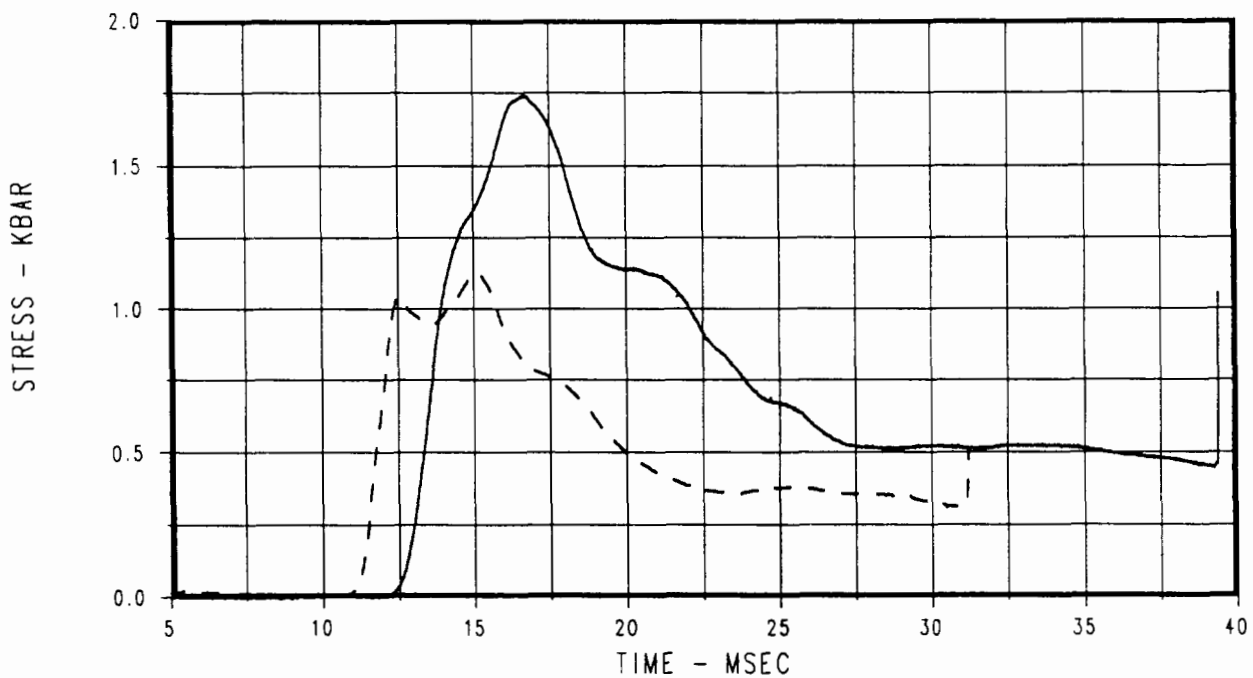


Figure 13. NPE Stress Waveform - Solid trace - and Nuclear Event B Waveform - Dash.

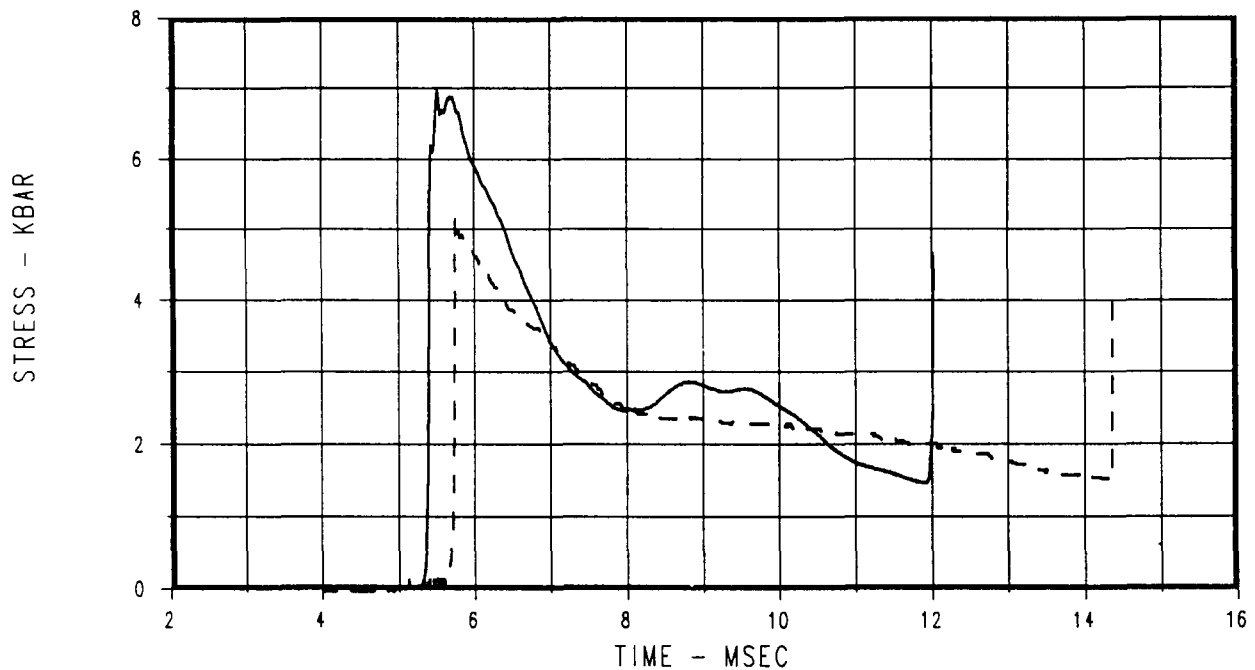


Figure 14. Comparison Stress Waveforms: NPE - Solid Trace, and Nuclear Event C - Dashed Trace.

At a greater scaled range on the third nuclear event there are two more radial stress records at comparable ranges to 3YR and 4YR. Figure 15 shows these two NPE waveforms at 40.3 and 55.1 meters and the two from the nuclear event at their scaled ranges of 37.4 and 53.3 meters. The 37.4 meter nuclear waveform shows a larger amplitude than the high explosive waveform, however, its range is shorter than the NPE waveform. Projecting the 3YR waveform back to 37.4 meters one obtains an amplitude of 2.0 kilobars which is 1.1 times the amplitude of the nuclear waveform. At the greater range one sees that the NPE amplitude for 4YR is 1.7 times the nuclear amplitude.

The risetimes shown in figures 13 and 14 look similar for the nuclear and high explosive events. In the other two comparison figures the risetimes appear faster for the nuclear events than for the NPE event. The range differences cloud the comparison. We have expanded the plots and measured the risetimes. Figure 16 shows the resulting risetime data versus range. We suspect that the variation in the nuclear risetimes is related to varying material properties of strength and air void content at the three nuclear sites. There is, however, a clear separation of the high explosive data from the average through the nuclear data. This factor of two difference may provide a basis for discriminating between chemical and nuclear explosions.

We now show a comparison - figure 17 - between the two NPE particle velocity waveforms, previously shown in figure 10, and four scaled motion waveforms from nuclear event A. The scaled ranges of the nuclear data bracket the high explosive data. (49.9 and 50 meters for the closest nuclear waveforms, 71.8 and 72 meters for the outer ones; and 55.1 and 69.8 meters for the NPE waveforms.) Like the stress comparison, the high explosive data are larger than the scaled nuclear data, and show an amplitude ratio of 1.2 and 1.8.

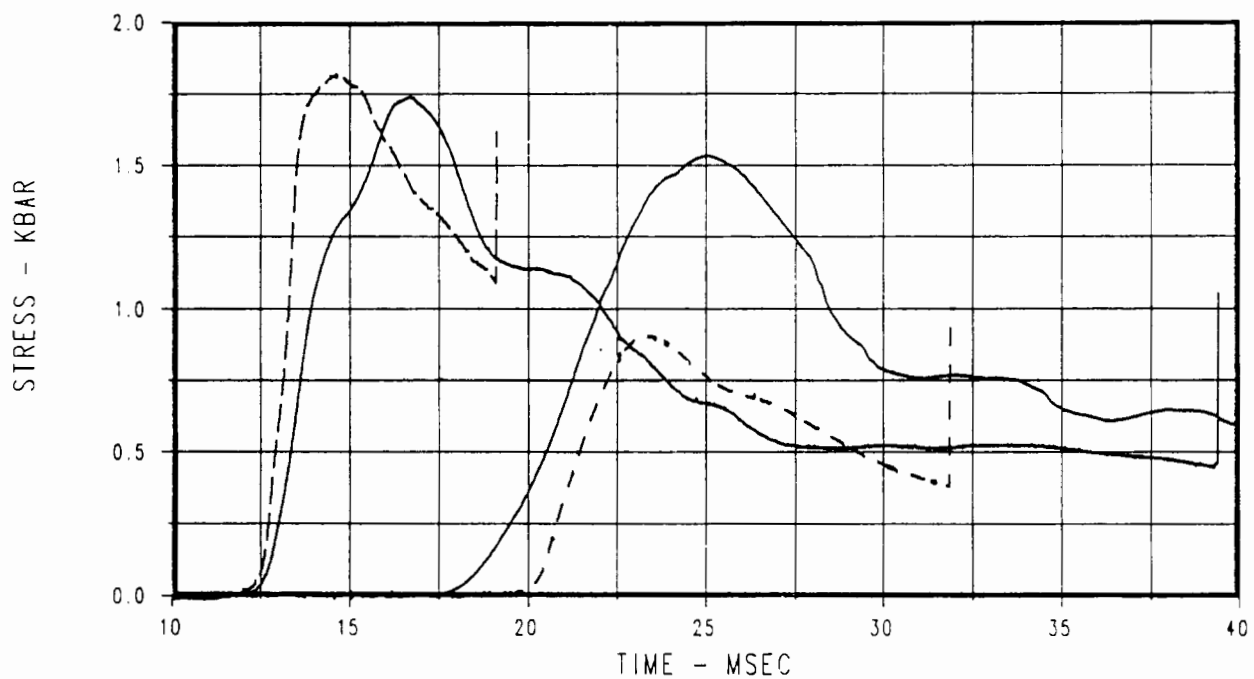


Figure 15. Comparison of Stress Waveforms: NPE - Solid Traces and Nuclear Event C - Dashed Traces.

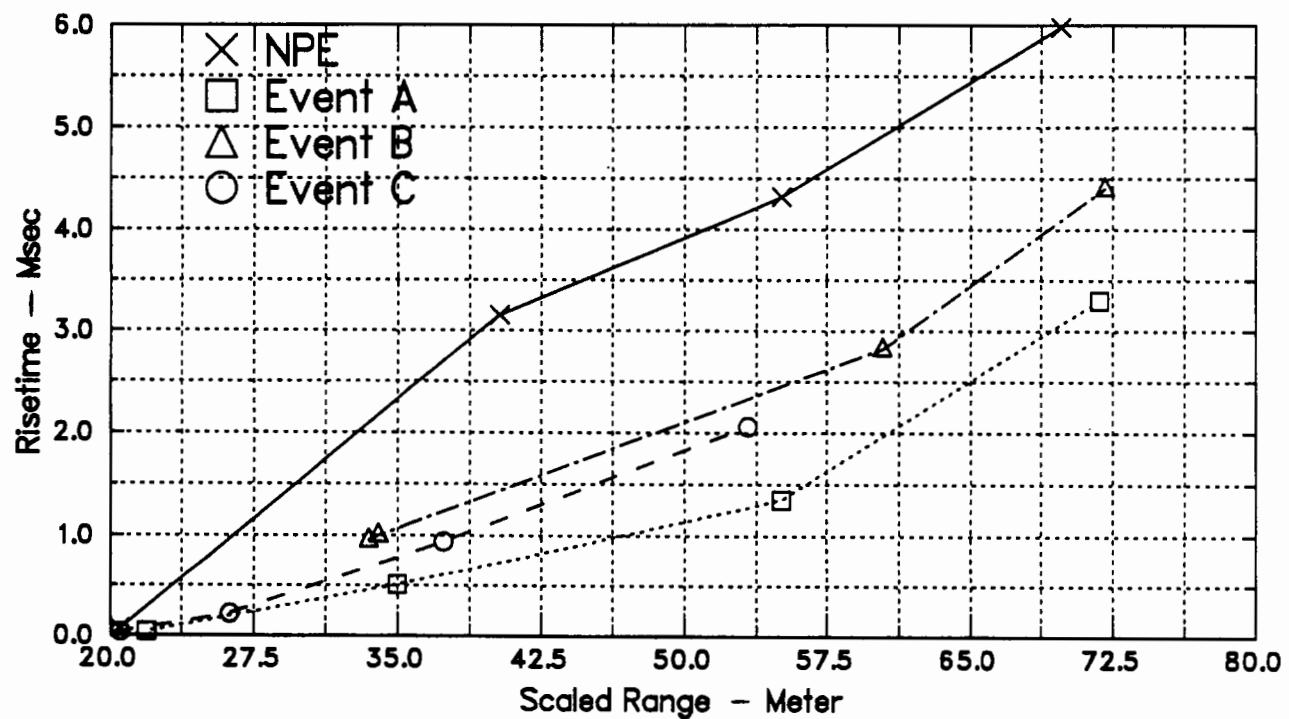


Figure 16. Risetime Versus Range for NPE Data and Scaled Nuclear Data.

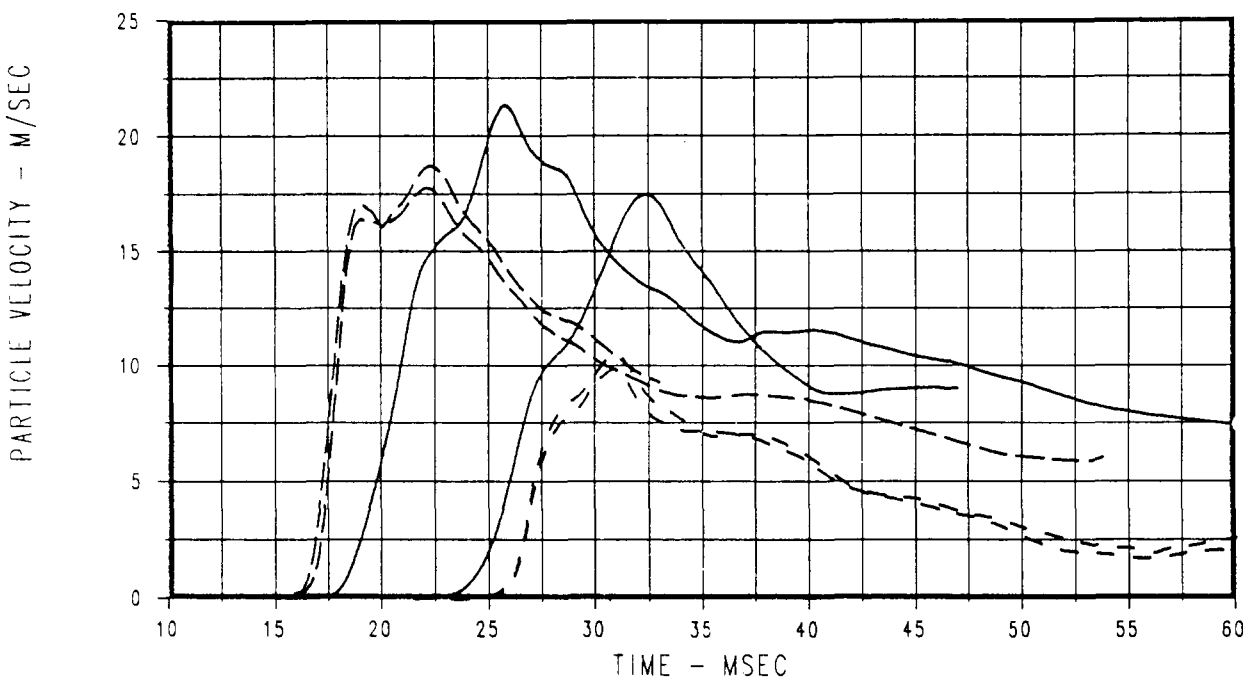


Figure 17. Comparison of Velocity Data: NPE - Solid Traces and Nuclear Event A - Dashed Traces

SUMMARY

We successfully measured a series of stress - time waveforms in the rock host and in the stemmed drift. Included were both radial and hoop stresses. Also measured were a series of acceleration - time waveforms. The main component was radial acceleration; a number of vertical and transverse components were also obtained. Integration of the accelerometer records produced motion data. These data will aid in verifying or modifying theoretical models and code calculations of the seismic source region.

Measured stress and motion waveforms show significantly more amplitude than yield-scaled waveforms from nearby nuclear events. Specifically, the five radial stress peaks suggest an equivalent nuclear yield of more than two kilotons. Risetimes from the NPE event are about twice as long as the average risetimes from nearby, scaled nuclear events. The risetime difference has potential to aid in the discrimination between the two types of events.

Tuff strength - inferred from the difference between radial and hoop stresses - show values that are about twice the typically used values which are obtained from laboratory measurements.

Acknowledgments The fine work of numerous people was needed to make these successful measurements. Gages were built by Ed Vieth and Cliff Kinabrew. Sonny Peppers fielded the gages and handled the interface with the recording people. Mike Burke and Jerry Chael guided the project and handled numerous tunnel details. We would also like to acknowledge the support of Preston Herrington and Larry Walker.

Reference: R.C. Bass, Free Field Stress, Acceleration, Velocity, and Displacement Data Available from Contained Detonations at The Nevada Test Site, Proceedings of the DOE/LLNL Symposium on Explosion-Source Phenomenology, Lake Tahoe, Ca. 14-16 March 1989.

This work was performed by Sandia National Laboratories under contract DE-AC04-76DP00789 with the US Department of Energy.

Free-Field Seismic Ground Motion on Non-Proliferation Experiment

**H. Douglas Garbin
Sandia National Laboratories
Department 9311**

Abstract

In addition to stress and acceleration measurements made in the inelastic regime, Sandia fielded two tri-axial accelerometer packages in the seismic free-field for the NON-PROLIFERATION EXPERIMENT (NPE). The gauges were located at ranges of 190 and 200 m from the center of the ANFO-laden cavity on the opposite sides of a vertical fault. This location allowed us to assess several different seismological aspects related to non-proliferation. The radial and vertical components of the two packages show similar motion. Comparisons are made with similar data from nuclear tests to estimate yield, calculate seismic energy release and to detect spectral differences between nuclear and non-nuclear explosions. The wave forms of NPE differ significantly from nuclear explosions. The first two peak amplitudes of NPE are comparable while the nuclear explosion initial peak is much larger than the second peak. The calculated seismic energies imply that the conventional explosions couple to the medium much better at low frequencies than do nuclear explosions and that nuclear explosions contain more high frequency energy than NPE. Radial and vertical accelerations were integrated for displacement and indicate there was movement across the fault.

Introduction:

Over the past three decades, there has been a great deal of research on discrimination between nuclear explosions and earthquakes. However very little has been done in studying differences between conventional and nuclear explosions. This is of great concern in treaty verification because of the large number of explosions worldwide that occur daily in normal industrial use. NPE is designed to confront at least two of these verification concerns. What is the nuclear yield equivalence of this conventional explosion (ANFO) and is it possible to discriminate between conventional and nuclear explosions? As part of a comprehensive plan to obtain a better understanding of the differences between these two explosion phenomena, Sandia National Laboratories (SNL) installed a number of instrument packages situated at ranges between 15 and 200 m from the center of an ANFO laden cylindrical cavity. This paper discusses only two of these locations in which two 3-component accelerometers were placed in the MISTY ECHO access drift. The ranges of the two sites were about 190 and 200 m from the cavity and outside of the inelastic regime of the explosion. The gauges were placed at these locations for two reasons. First we wished to study the source by recording the ground motion resulting from the explosion and compare it with similar data recorded on two other nearby nuclear events. We hoped that differences observed in the nuclear and conventional signals would be useful as fingerprints to discriminate between the two types of sources. If one follows the analogy of the comparison of an earthquake to a nuclear explosion, spatial extent and timing between the two phenomena imply that the earthquake would have relatively more energy in the lower frequencies. Although the spatial extent of NPE is comparable to a nuclear explosion, the energy density of NPE is much lower and is deposited into the media at a slower rate than in the nuclear case. With this in mind, I will examine the data collected on NPE and compare it with similar data from nuclear explosions.

To address the nuclear yield equivalence issue, two calculations of yield are made comparing results to nearby nuclear events. The first calculation estimates yield from the low frequency spectrum and the

second calculates the free-field energy coupled into the ground. A further purpose of these particular gauge locations is to see if the explosion initiated any fault motion. The accelerometers were placed on the opposite sides of a vertical fault and the radial and vertical components of acceleration are integrated for displacement in an effort to detect any relative motion across the fault due to the explosion. This has implications in the source characterization since significant fault motion would act as a secondary source super-imposed on the explosion and significant fault motion might cause discriminates to fail. Also, the integration of the radial acceleration is required in determining the Reduced Displacement Potential (RDP) which is important in characterizing the source. This integration helps to evaluate the quality of the data for this additional step.

Experiment Description:

Plan View In N-Tunnel

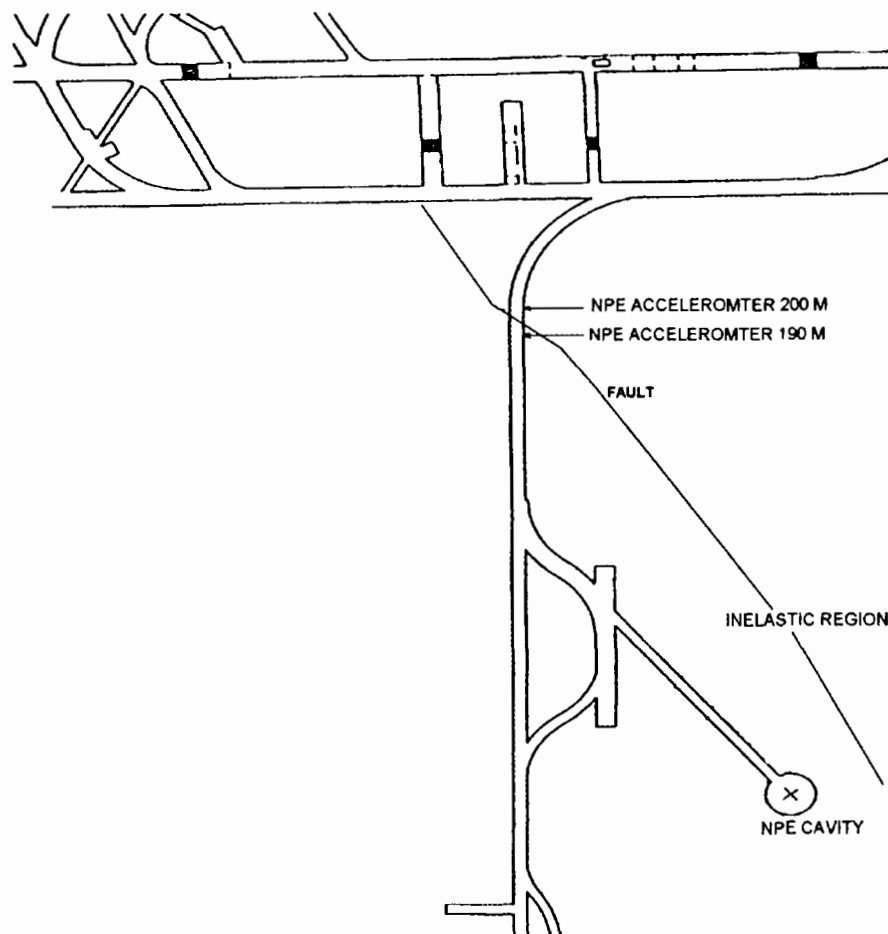


Figure 1

NON-PROLIFERATION EXPERIMENT

Fault Structure at Measurement Location

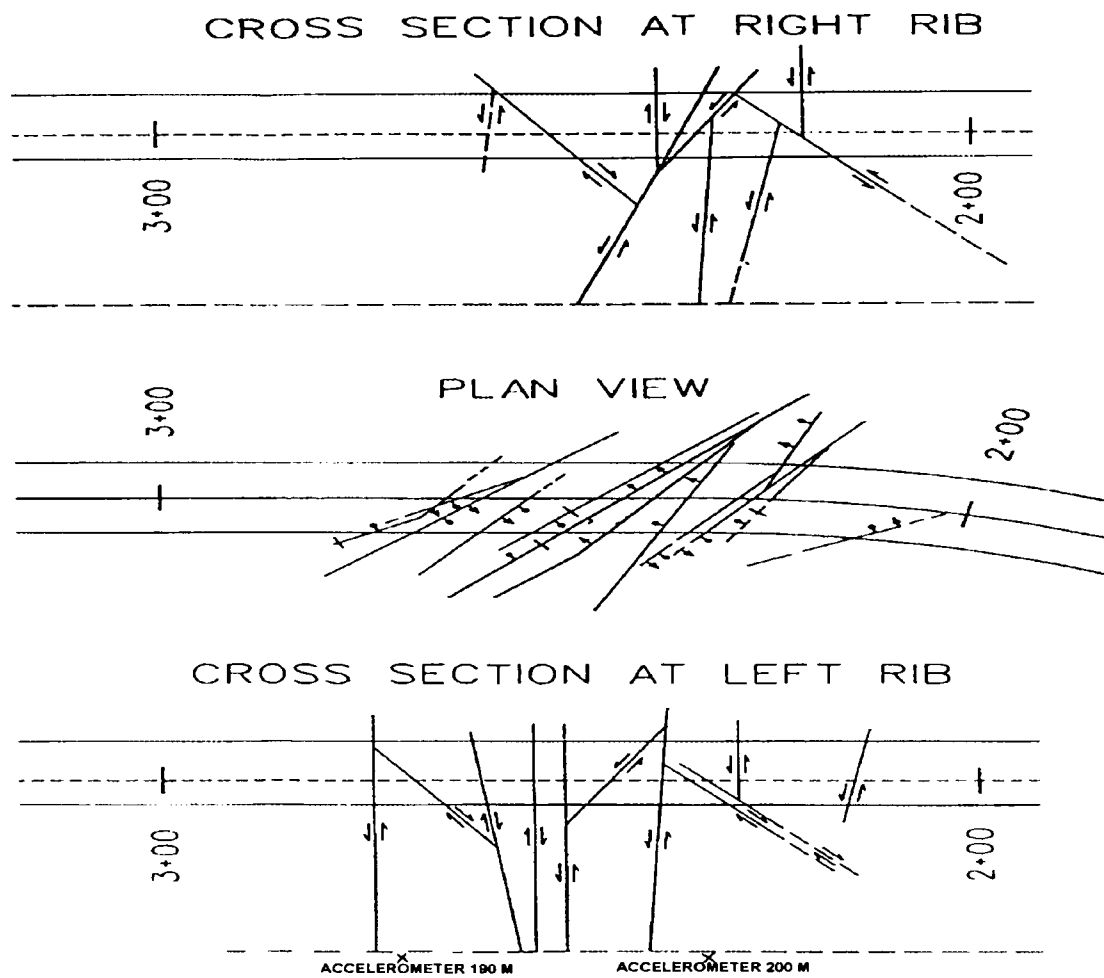


Figure 2

Figure 1 is an overhead view of the NPE cavity and tunnel configuration. Outlined in the figure is a fault which crosses the access drift where the accelerometers are located. The fault extends down to within 40 m of the cavity surface. The locations of the two accelerometers are indicated on the figure in the access drift at a range near 200 m. These packages were placed in two 6" boreholes that were drilled in the floor of the tunnel near the left side to a depth of 10 m. On both sides of the fault, the tri-axial accelerometers were aligned such that the radial component pointed toward the center of the cavity. This alignment sets

the radial and vertical components nearly parallel to the fault plane and the transverse component normal to it. The accelerometer package was clamped to a PVC pipe and lowered into the hole. Alignment was done manually before the hole was grouted. The boreholes were located in tuff at ranges of 190 and 200 m from the cavity and separated by 13m. Figure 2 shows a mapping of the local fault and the gauge locations. Cables from the gauges transmitted the signals to a nearby recording area.

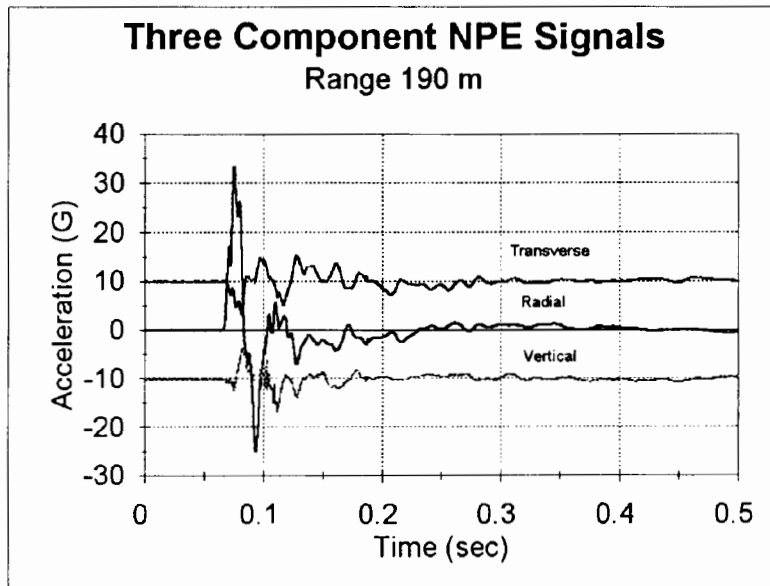


Figure 3

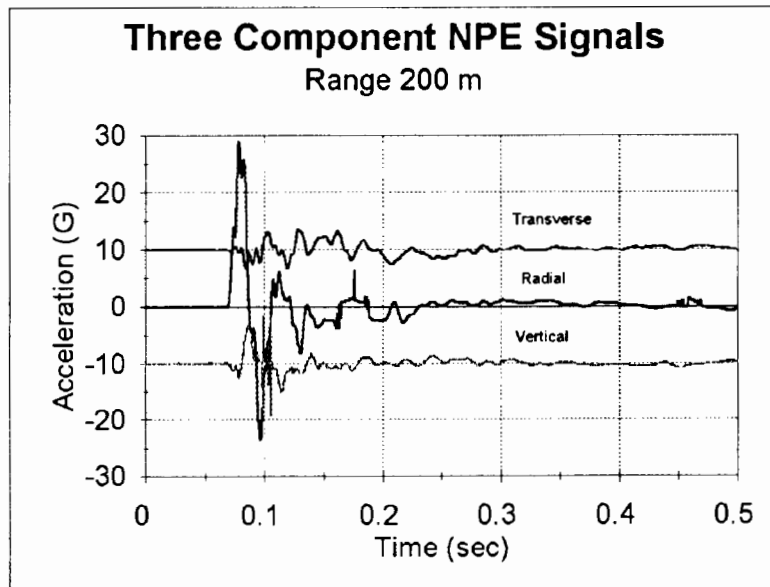


Figure 4

Results:

Figures 3 and 4 are plots of the 3-component accelerometers at 190 and 200 m respectively. These plots are abbreviations of the total time of 8 seconds that was recorded and the signals are offset to avoid cluttering the plots. The radial peaks are about 30 g and the vertical peaks are near 7 g. Figure 5 presents plots of the two radial signals and Figure 6 shows two vertical waveforms. Comparisons of the corresponding components of the two sites are in good agreement. Some of the differences that exist can be attributed to non seismic-glitches. Note that the radial gauge at 200 m has an anomalous behavior at 160 msec and both vertical gauges have some high frequency behavior near 100 msec. 160 msec is about the time the wave arrives at the recording alcove and the location of other electronic equipment. Whether this is the cause of the curious behavior is unknown. The radial signals are almost identical in the first 200 msec before there is some divergence. The vertical wave forms began to diverge near 110 msec. These differences have implications in the integration of the signals.

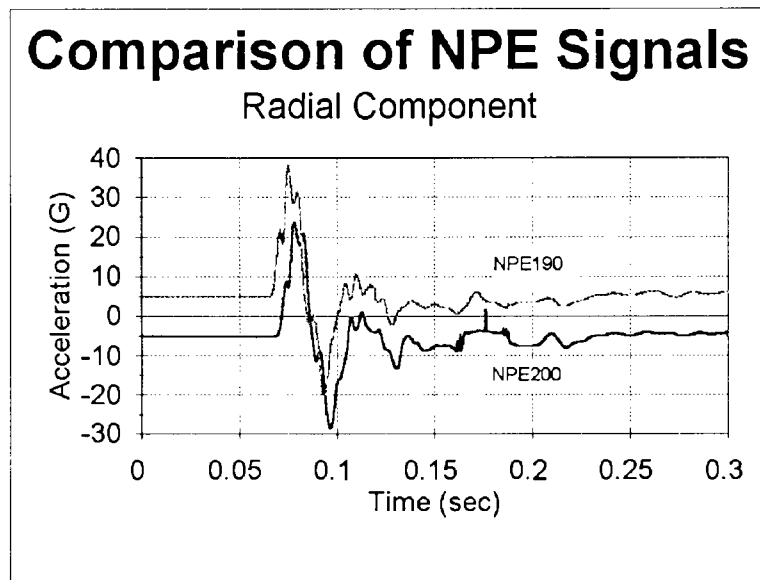


Figure 5

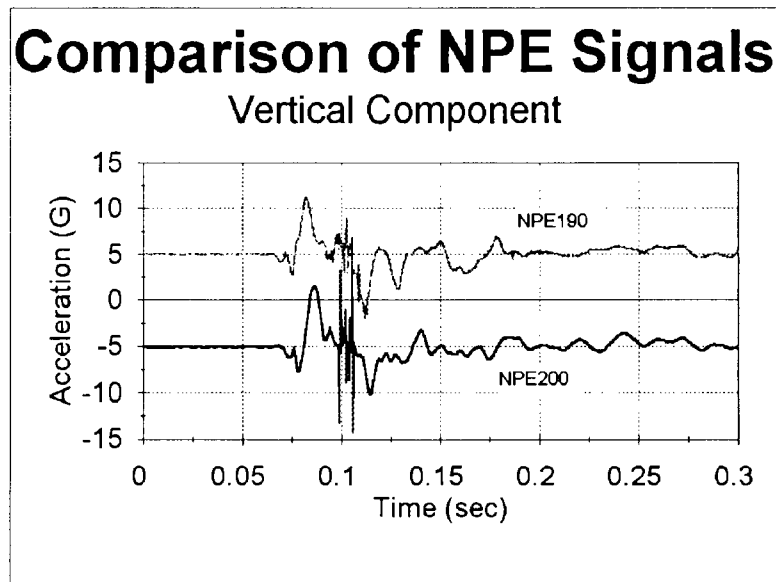


Figure 6

Analysis:

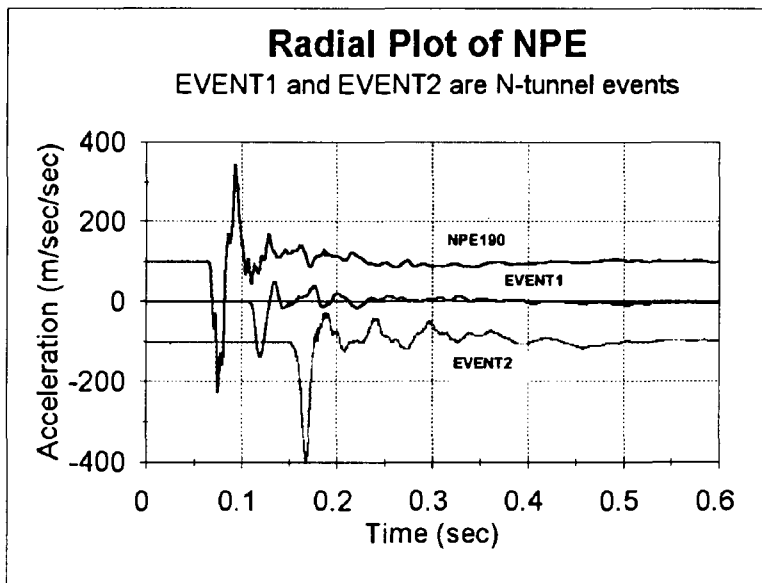


Figure 7

SNL has fielded gauges in the free-field on several nuclear events in N-tunnel near NPE . I have picked two with which to make comparisons. Figure 7 is a plot of the radial components of the three explosions. The complexity of the NPE event is noticeable in comparison with the two nuclear events. The initial peaks of the nuclear explosions are smooth with no interference in the rise times, whereas NPE has several little wavelets superimposed on the main signal. Whether this is due to propagation effects or the source is unknown . Note that the wave form of NPE is distinctly different than the nuclear events. The maximum and minimum peaks in the NPE waveform are comparable in amplitude whereas the first peak of the nuclear explosions are considerably larger than the second peak. If the ratio of the first peak to the second peak is calculated, the value for NPE is about 1.2 while the two nuclear events (EVENT1 and EVENT2) are 2.6 and 4.6. With only one large conventional explosion as a data point, it can not be said with any certainty that the above differences are local discriminants, but it does point us in directions for further studies.

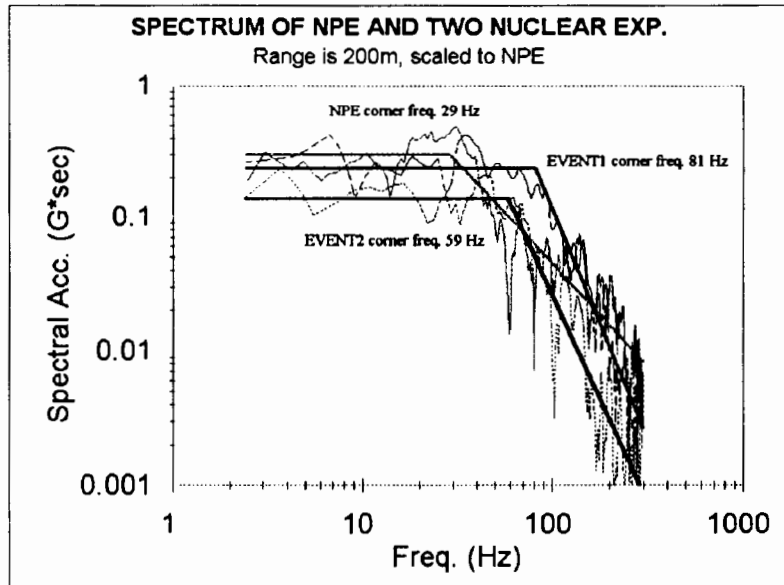


Figure 8

Figure 8 shows the acceleration spectral plots of NPE and two nearby nuclear tests that have been scaled to 1 kT. Superimposed on these plots are corner frequency curves found by fitting two straight lines, one to the low frequency dc segment of the spectrum and another to the high frequency spectral fall off. This figure reveals a number of things. First, NPE has a much lower corner frequency than the two nuclear events by at least a factor of two. More of NPE energy resides at lower frequencies since its DC offset is higher than either nuclear event. Also the high frequency roll-off is more gentle for NPE when compared to these two nuclear explosions. The high frequency slope for NPE is -1.5 compared to -3.4 and -3.0 for EVENT1 and EVENT2 respectively. The low frequency spectrum is higher on average for NPE which is consistent with the regional seismic yield estimates of 1.7 to 2 kT. The yield estimate using the low frequency spectrum of these events is 1.9 kT. The high value of corner frequencies for nuclear events is a possible discriminant with respect to conventional explosions. The question of whether these spectral differences can be detected at regional ranges is unanswered by this data. High frequencies attenuate signals very quickly and at regional ranges wipe out the data above 25 Hz for events originating from NTS^(1,2). NTS is known for its high attenuation and any results at regional ranges are a worse case since signals propagate much better in other areas of the world.

The yield equivalence estimated from the regional Leo Brady Seismic Net gave an yield of 1.7 kT² which is consistent with the spectral analysis shown above. As further confirmation of these results, I can also make an estimate of the energy coupling from these accelerometers by calculating the near-field seismic energy. Since there are only two gauges on essentially the same azimuth, this calculation is based on the assumption that the source is emitting energy equally in all directions. The time rate of energy transmitted across a surface is given in equation (1):

$$\frac{dE}{dt} = \int_{\Sigma} \tau_{rr} u_r dS \quad (1)$$

where E is the energy.

t is the time.

τ_{rr} is the radial stress

u_r is radial velocity.

Σ is the spherical surface of integration centered about a source with the gauge located on the surface.
 dS is the surface element.

Converting this to frequency space, it can be shown that³:

$$E_0 = \frac{2\rho}{\alpha} \int_{-\infty}^{\infty} |-\omega^2 \phi(\omega)|^2 d\omega \quad (2)$$

where:

ρ is the medium density.

ϕ is the Reduced Displacement Potential.

ω is the angular frequency.

α is the compressional velocity.

E_0 is the seismic energy radiated from the source.

Assuming ϕ can be represented by spherical waves, it can be shown:

$$E_0 = \frac{2\rho}{\alpha} \int_{-\infty}^{\infty} \frac{|a(\omega)|^2 r^4}{1 + (kr)^2} d\omega \quad (3)$$

where a is the Fourier acceleration.

r is the radial distance from source.

$k = \omega/\alpha$ is the wave number.

The above integral is numerically calculated for NPE and the two nuclear events discussed earlier. The integration is carried out over different frequency bands all beginning at 1 Hz. The results of these calculation are given in Table I in the form of the percentage of seismic energy release to the yield of the explosion.

TABLE I
 Percentage of Seismic Energy coupled into Ground

Freq. Band /Event	1-6 Hz	1-10 Hz	1-20 Hz	1-30 Hz	1-50 Hz
NPE	5.6%	7.3%	8.7%	9.7%	10.1%
EVENT 1	4.8%	5.5%	6.0%	6.2%	6.2%
EVENT 2	1.5%	1.9%	2.0%	2.1%	2.1%

Normally the percent of seismic energy produced in tuff is less than 3%⁴. This depends on the type of medium in which the source is located, porosity, and other local physical properties. EVENT 2 exhibits the usual energy ratio behavior, however EVENT 1 and NPE appear to be anomalous. Note that in each of the different frequency bands, NPE percentage is larger than either nuclear event and significantly larger than EVENT 2 by nearly a factor of 5 in the 1-50 Hz band. One explanation why this higher factor is not evident in the far-field is that the regional yield estimates are made at relatively low frequencies. The spectra between 1-10 Hz reflects the coupling that would be seen in the far-field since the high frequencies are attenuated. The table indicates that NPE's energy percent drops significantly more than

the nuclear tests as the frequency bands are reduced. NPE still has 5.6% coupling between 1-6 Hz which is relatively high compared to nuclear tests. Some caution must be exercised with results of these calculations. The source is assumed to be spherical and this is not true since the cavity on NPE is cylindrical. This requires the surface integration to have some angular dependence. In addition, there could be stress release or fault motion in the medium adding to the signal making the source even less symmetrical. The anomalous EVENT 1 was not used in the regional yield determination and a comparison with EVENT 2 implies a yield equivalence above 3 kT. If coupling is assumed to be an average of the two nuclear events, a yield of 1.8 kT is found.

As a final study, I examine the records for relative motion across the fault. As noted earlier, these gauges were located on opposite sides of a fault zone. In order to evaluate the motion of the fault, the radial and vertical components of acceleration at each site are doubly integrated for displacement. Integration of such signals is dangerous because of the various types noise in the signals and the possibility that the gauges tilted. Small offsets or linear trends embedded in the time series can result in large errors during integration. I attempt to remove these errors at various stages of the integration procedure described below. However, the problem in the removal of these offsets and trends in the analysis is that the method is very subjective and probably non-unique. Because the general behavior of the radial signal from an explosion is known, I begin with the radial integration first.

The procedure begins with removing any pre-signal dc offset in the acceleration by averaging the data prior to signal arrival and subtracting this off the entire signal. Integrating the resulting time series for velocity may show a linear trend due to an additional offset inside the acceleration signal caused either by a tilt in the gauge or electrical offset. I attempt to eliminate this by applying a straight line regression fit to the late time velocity and subtracting it off in a time window with the constraint that the velocity is near zero at late time. This time series is integrated again for displacement... If the displacement shows the standard form of a single positive peak with an overshoot that approaches an asymptotic permanent displacement, I feel the analysis is reasonable. If not, I restart the method doing either a new regression or picking a new window to apply the regression. This is done until a reasonable solution is reached. Of course I realize this analysis is subjective, but proceeding, figure 9 shows the displacements for the radial signals of NPE190 and NPE200. The plots indicate that both gauges initially move together for the first 200 to 300 msec. The NPE190 gauge flattens out at about 4 cm offset from the cavity. NPE200 continues back toward the cavity until it is about 2 cm nearer the cavity than when it started. The total offset between the two sides of the fault is 5 - 6 cm. The major distortion in the NPE200 signal at 0.16 seconds is removed. This is done by replacing the signal in a small window around 0.16 seconds with the corresponding data from NPE190.

RADIAL DISPLACEMENTS

Ranges of 190 and 200 m

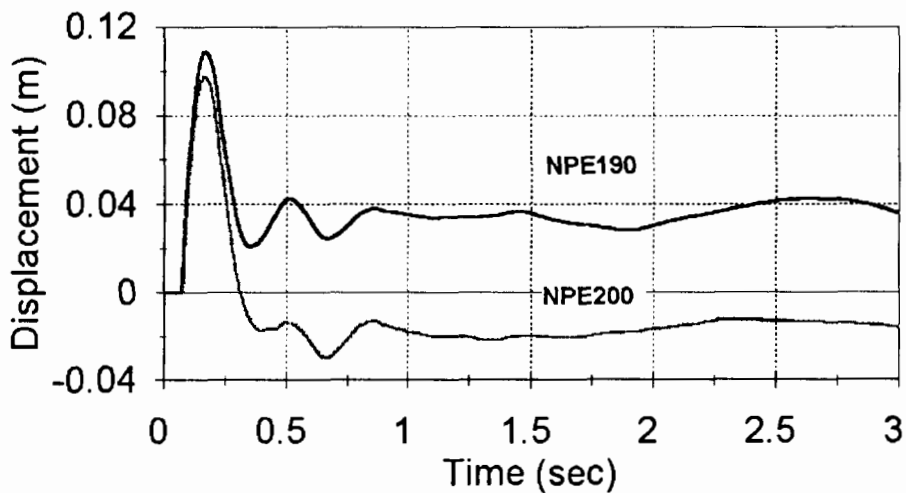


Figure 9
Displacements at 190 and 200 m

Applying this analysis to the vertical acceleration is more difficult since in the radial case I have a gross idea of what the radial signal looks like. However, applying the same methods, a displacement is calculated with some additional processing. Figure 6 exhibited some rather erratic behavior near 100 msec and if this raw signal is integrated, it leads to some unphysical results. To suppress these high frequency signals, I low pass filter the data with a corner frequency of 100 Hz prior to integration. The loss of the high frequency is unimportant since I am interested in the gross motion and not the fine details. The result is shown in figure 10. The two displacements are offset at late times but otherwise follow the same periodicity. Like the radial signals, the two gauges move with each other until 200-300 msec and then begin to separate. The integration is carried out for 3 sec and show a final separation of 2 cm with NPE200 displaced 5 cm higher and NPE190 3 cm higher.

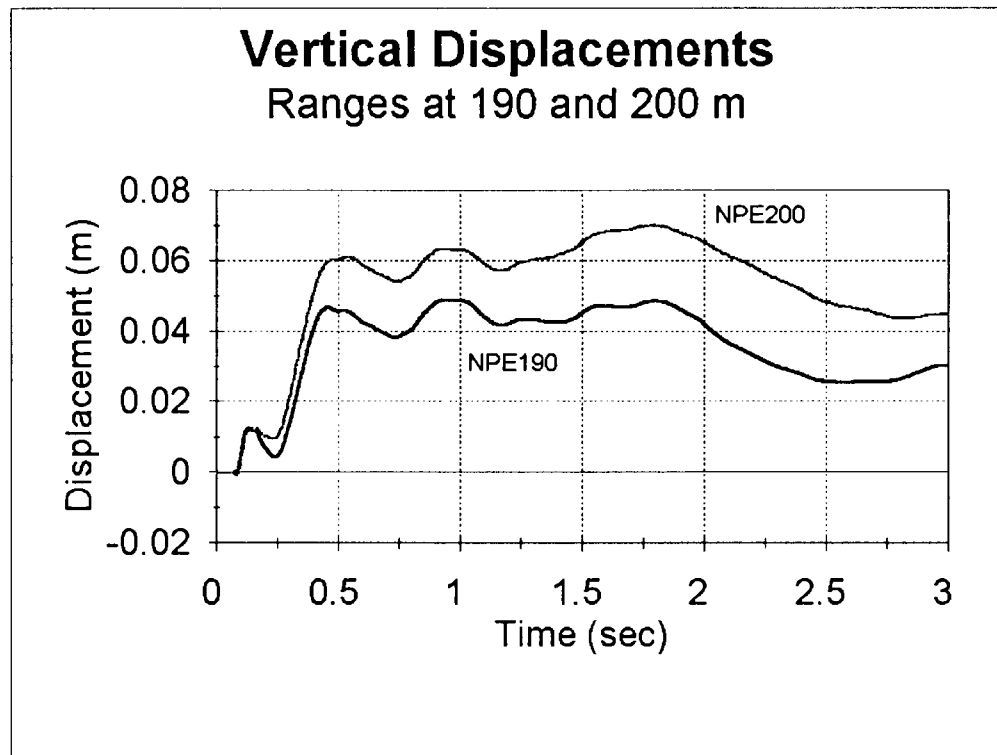


Figure 10

Conclusions:

As part of a free-field array on NPE, Sandia fielded two triaxial acceleration packages in the elastic region located 200 m from the cavity on opposite sides of a fault. The recorded signals are used to study explosion phenomenology and to compare with signals of nuclear sources. In addition, the radial and vertical gauges were examined for induced relative displacement across the fault. The two radial signals on NPE are very similar, but show more complexity in the time series when compared to nearby nuclear tests. In addition, the wave forms are distinctly different in that NPE's second peak is nearly equal to the first peak. The second peak of two nuclear explosions was much less than the first. The spectral plots exhibit corner frequencies of the nuclear explosions at least twice that of NPE. Also, NPE spectral high frequency decay is lower than the two nuclear tests. The seismic energy generated by NPE was a greater percentage of the total energy than either nuclear explosion. 10% of the NPE energy went into seismic ground motion while the two nuclear explosions coupled 6.2% and 2.1% into seismic energy. Attempts were made to integrate acceleration for displacement. The two sides of the fault do show relative offsets from their initial position. NPE190, the gauge on the side of the NPE cavity moved 4 cm radially and 2 cm vertically. NPE200, the opposite gauge moved -2 cm inward and 5 cm vertically.

Acknowledgments:

I wish to thank all the people associated with making the free-field experiment a success. The gauges were built by Cliff Kinabrew and Sonny Peppers fielded the gauges and interacted with the recording people. The recording was accomplished with Departments 9321, 9323 and 9324. Gary Miller, Mike Burke and Jerry Chael provided invaluable service at NTS handling numerous tunnel details and hardening the recording equipment from the ground shock. Al Chabai gave continued support throughout the project with valuable discussions. I would also like to acknowledge the support by Preston Herrington and Larry Walker.

References:

1. E. P. Chael, "Spectral Discrimination of NTS Explosions and Earthquakes in the Southwestern United States Using High-Frequency Regional Data", *Geophys. Res. Lett.*, 15, 625-628, 1988.
2. H. D. Garbin, "Yield of the Non-Proliferation Experiment From the Leo Brady Seismic Net", *Proceedings of the DOE Symposium on the NON-PROLIFERATION EXPERIMENT Results and Implications for test Ban Treaties*, Rockville, MD, 19-21 April 1994.
3. J. R. Murphy and Mueller, R. A., "Seismic Characteristics of Underground Nuclear Detonations Part II. Elastic Energy and Magnitude Determinations", *Bull. Seism. Soc. Am.*, 61, 1693-2704, 1971.
4. N. A. Haskell, "Analytic Approximation for the Elastic Radiation from a Contained Underground Explosion", *J. Geophy. Res.*, 72, 2583-2587, 1967.

This work was performed by Sandia National Laboratories under contract DE-AC04-76DP00789 with the US Department of Energy.

FREE-FIELD GROUND MOTIONS FOR THE NONPROLIFERATION EXPERIMENT: PRELIMINARY COMPARISONS WITH NEARBY NUCLEAR EVENTS

KENNETH H. OLSEN and ANTHONY L. PERATT

Explosion Effects Physics Project, Group P-15, Los Alamos National Laboratory, Los Alamos, NM 87545, kolsen@geophys.washington.edu; alp@aerie.lanl.gov.

Revised Abstract

Since 1987, in an effort to provide more extensive *close-in* (<10 km) data sets for modern regional and teleseismic source function studies, we have installed fixed arrays of tri-axial accelerometers in the free-field near the shot horizons for low-yield (≤ 20 kt) nuclear events in the N-tunnel complex beneath Rainier Mesa. For the Nonproliferation Experiment (NPE) we augmented the array to achieve 23 free-field stations. Our accelerometer arrays span distance intervals between the non-linear material failure region—where peak stresses are the same order as rock strengths (<200 bars and ranges typically ~ 50 – 150 m)—and distances (~ 1 km) where linear-elastic response is expected (stress <50 bars; accelerations <1 g). Goals are: (a) to examine robustness and stability of various free-field source function estimates—e.g., reduced displacement potentials (RDP) and spectra; (b) to compare close-in with regional estimates to test whether detailed close-in free-field and/or surface ground motion data can improve predictability of regional-teleseismic source functions; (c) to provide experimental data for checking two-dimensional numerical simulations. We report preliminary comparisons between experimental free-field data for NPE (1993) and three nearby nuclear events (MISTY ECHO, 1988; MINERAL QUARRY, 1990; HUNTERS TROPHY, 1992). All four working points are within 1 km of each other in the same wet tuff bed, thus reducing concerns about possible large differences in material properties between widely separated shots. Initial comparison of acceleration and velocity seismograms for the four events reveals: (1) There is a large departure from the spherical symmetry commonly assumed in analytic treatments of source theory; both vertical and tangential components are surprisingly large. (2) All shots show similar first-peak particle-velocity amplitude decay rates $\sim R^{-1.8}$ suggesting significant attenuation even in the supposedly purely elastic region. (3) Sharp (>20 Hz) arrivals are *not* observed at tunnel level from near-surface pP reflections or spall-closure sources—but broadened peaks are seen that suggest more diffuse reflected energy from the surface and from the Paleozoic limestone basement below tunnel level.

Introduction

Close-in free-field measurements of stress wave propagation in geologic media with well-documented material properties can play a unique role in establishing a fundamental physical basis for predicting equivalent elastic seismic source functions for most types of underground explosions in

arbitrary geological environments. Since 1987, as part of a coordinated experimental program to study the basic physics of the evolution of explosion waves from the hydrodynamic and highly non-linear material response regions very close to the source out to purely elastic motions at distances < 10 km, we installed fixed arrays of tri-axial accelerometers in the free-field at the shot horizons for low-yield (≤ 20 kt) nuclear events in N-tunnel complex beneath Rainier Mesa at NTS. We supplemented the arrays for additional free-field observations of the Non-Proliferation Experiment (NPE). Our main purpose has been to help bridge the "knowledge gap" between numerous essentially high-pressure equation of state (EOS) and shock physics studies very close to the explosion and the also numerous surface seismic measurements made at distances beyond a few km. Our measurements focus principally on the "nonlinear-to-linear transition zone" at distances between about 50 m and 1000 m, which should include the indistinct region loosely known as the "elastic radius." Goals are both (a) to provide experimental "ground-truth" data for detailed comparison with state-of-the-art two-dimensional numerical models, and (b) to provide detailed free-field data in the vicinity of the "elastic radius" against which seismic inversion and equivalent source function scaling techniques can be critically tested.

Table 1 is a summary of locations and seismic parameters for the four underground explosions at N-tunnel for which we have made free-field observations. In a previous paper (Olsen and Peratt, 1993), we made selected comparisons of *first peak (only) transient values* of acceleration, particle velocity, and displacement for the three nearby nuclear events (MISTY ECHO, 1988; MINERAL QUARRY, 1990; HUNTERS TROPHY, 1992) preceding the NPE. In this short contribution, we show preliminary free-field results from our NPE observations together with selected data from the MISTY ECHO nuclear event, but we will present waveform data in preference to only transient first-peak values. However, because the yields of the nuclear shots have not yet been declassified, we are unable at this time to present a satisfactory detailed quantitative comparison between the nuclear and "chemical" sources. Instead, we will stress general features of the waveform data for all four explosions that pertain chiefly to the basic physical processes occurring in the free-field, nonlinear-to-linear transition zone. More extensive analyses using spectral and reduced displacement (RDP) techniques are underway but will not be reported here.

Free-field waveform data

Figure 1 is a schematic cross section showing general features of underground free-field accelerometer array installation for our Rainier Mesa seismic source physics experiments. Figure 2 displays a plan view of part of the N-tunnel complex and shows the final 23-station configuration of the accelerometer array that was in place for the NPE. As discussed in the caption, the N-tunnel accelerometer array grew piecemeal with time as successive shots were planned and executed over the years in the N-tunnel complex; only seven stations were installed for the initial 1988 MISTY ECHO shot, for instance. In designing the underground arrays, we always tried to achieve as broad range-interval and azimuthal distributions with respect to each new source as was possible within the tunnel-access constraints of the time.

Table 1. Seismic Parameters of Four Underground Explosions in N-Tunnel, Rainier Mesa, Nevada Test Site.

Event Event Name, Hole ID	Location				Origin Time			Magnitudes				
	N Latitude	W Longitude	Surface Elevation m	DOB m	Date	Time, UT (DOE)	m_b (NEIC)	m_b (ISC)	$m_{bpn}^†$	$m_{blg}^‡$	M_L (BRK)	
MISTY ECHO U12N.23	37° 11' 56.54"	116° 12' 34.00"	2259	400	10 Dec. 1988	2030:00.055	5.0	5.0	4.81	5.16	5.0	
MINERAL QUARRY U12N.22	37° 12' 24.73"	116° 12' 51.33"	2243	400	25 July 1990	1500:00.057	4.7	4.8	4.53	4.94		
HUNTERS TROPHY U12N.24	37° 12' 24.93"	116° 12' 35.94"	2239	385	18 Sept. 1992	1700:00.008	4.4		4.18*	4.57*		
NPE = (NON-PROLIFERATION EXPERIMENT) U12N.25 (a.k.a., "CHEMICAL KILOTON")	37° 12' 06.95"	116° 12' 35.50"	2243	390	22 Sept. 1993	0701:00.080	4.1		4.16	4.59		

† For definition and discussion of the LLNL 4-broadband-station regional magnitude, m_{bpn} , see: Denny, M. D., S. R. Taylor, and E. S. Vergino, Investigation of m_b and M_S formulas for the Western United States and their impact on the M_S/m_b discriminant, *BSSA* 77, 987-995, 1987.

‡ For definition and discussion of the LLNL 4-broadband-station regional magnitude, m_{blg} , see: Patton, H. J., Application of Nuttli's method to estimate yield of Nevada Test Site explosions recorded on Lawrence Livermore National Laboratory's digital seismic system, *BSSA* 78, 1759-1772, 1988.

* These are 3-station values rather than 4-station averages.

Because most of our instrument packages operated by design in the distal portions of the crush and shear region where peak accelerations and stresses seldom exceeded ~500 g and ~1 kilobars respectively, most of these grouted, sealed instrument packages with associated cabling usually survived and could be reactivated for succeeding shots. However, this often meant that individual instrument sensitivities (i.e., Volts/g) and gauge linearity limits (both unchangeable after initial grouting-in) could not be optimized for following experiments. In practice, as the number of stations in the array grew, most new added instruments were high-g-limit units installed close to the newest working point in order to acquire as much new data in the nonlinear material (rock) response regime as possible.

For several reasons, the 7-station MISTY ECHO (ME) array achieved the highest performance of all of the 4 experiments in terms of gage sensitivity, fully optimized digital dynamic recording ranges, and lowest electrical and data processing noise levels. The MISTY ECHO data set thus usually displays the clearest examples of many of the general free-field waveform characteristics that we wish to point out in this contribution. We will first overview the NPE data and then display selected waveform plots from the ME data set in order to better understand the more important general characteristics of the free-field data sets from all our N-tunnel experiments.

(A word of caution in viewing the plots is in order: We display here mainly *velocity* and *displacement* waveforms which are derived by integration of the primary *acceleration* data. After integration, one



Surface Accelerometers and Seismometers

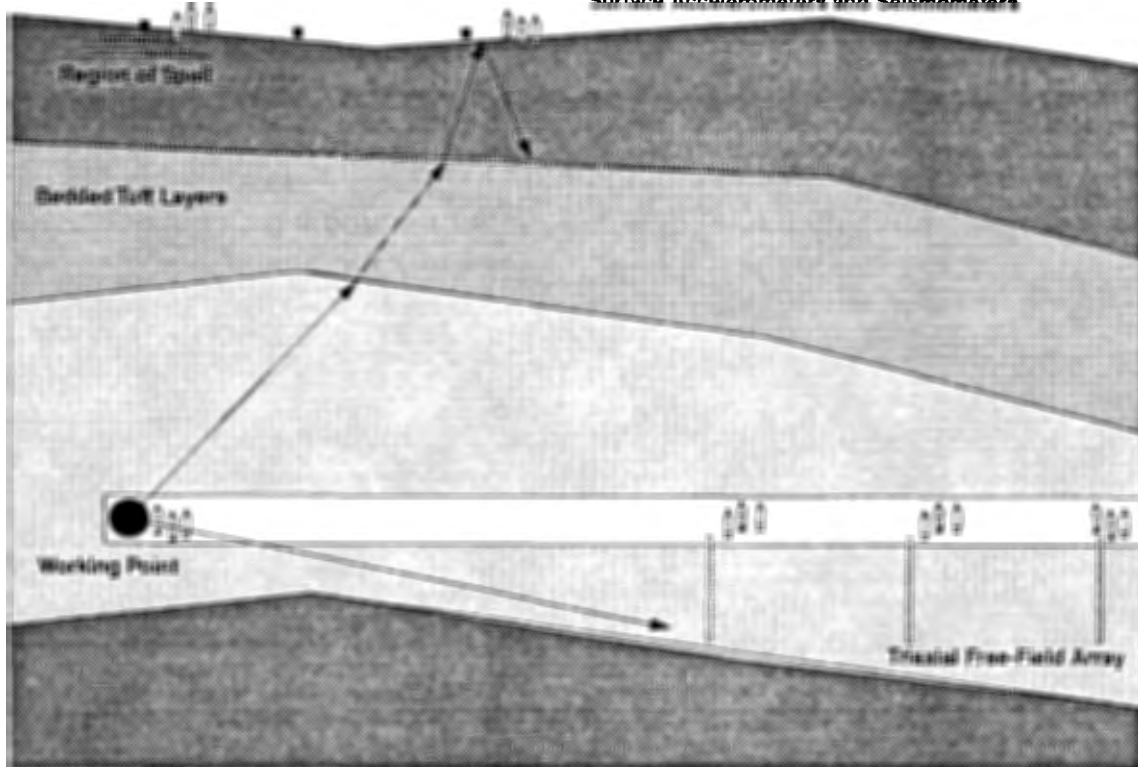
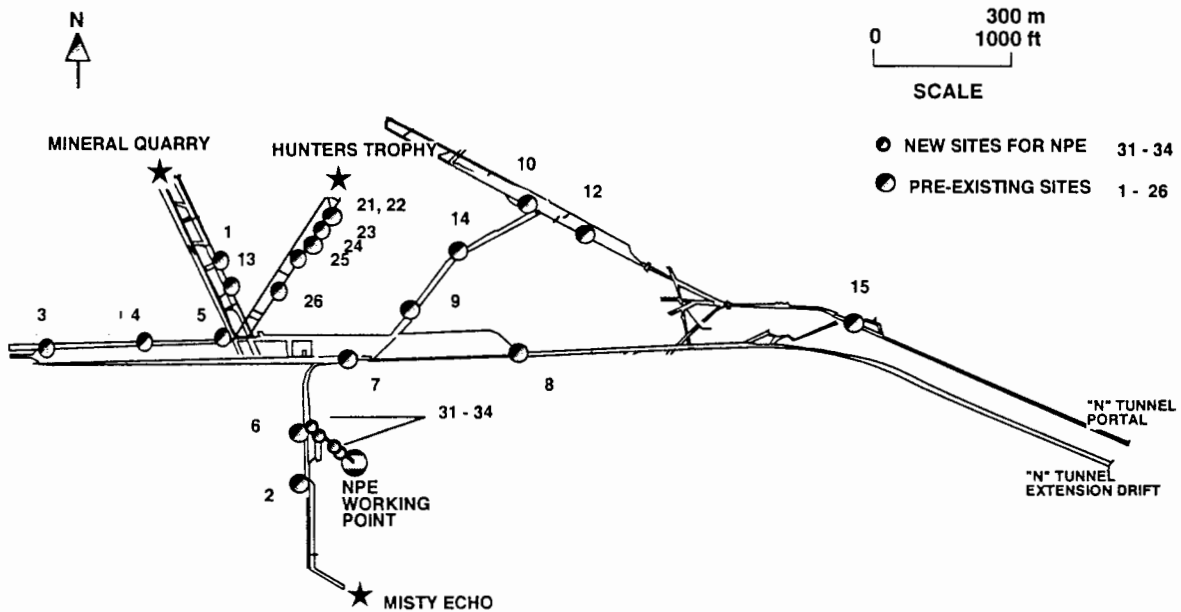


Fig. 1. Cartoon cross-section of Rainier Mesa, NTS, illustrating the general layout of triaxial free-field accelerometer units in relation to the close-in, high-stress gauges and the mesa-top surface measurements fielded by other experimenters. Oriented triaxial free-field accelerometer packages are typically grouted into boreholes at depths at least 2-tunnel-diameters (6 m) below the tunnel floor in order to eliminate small effects of tunnel-wall motions on the desired free-field accelerograms.

normally makes corrections (1) for long-term trends due to any electronic noise introduced by the data processing/recording system hardware and also (2) to remove 'ramps,' and trends resulting from the integration process. For example, integrated *velocity* values should return to the zero baseline at very long times (> 20 s in our case). However, our initial attempts to apply very simple filtering and correction processes to achieve this often severely modified 'intermediate' frequency ($\sim 1\text{-}2$ Hz) signals that were obviously geophysical in origin. For this initial overview, we have elected *not* to apply any long-term corrections. Thus, values for some integrated parameters, such as "permanent" particle displacements, steady-state values of the RDP, and "DC-levels" for spectra should be recognized as possibly somewhat uncertain and inaccurate at this time.)

Slant-range and gauge performance data for the NPE free-field array is summarized in Table 2. Unfortunately, due to a faulty grout mixture during installation of the four new high-g units (TM 31-34) closest to the NPE charge about 10 months prior to the shot, these gauges failed at very low stress levels and gave invalid acceleration readings shortly after initial shock arrival. Thus, much of the higher-stress-

"N" TUNNEL COMPLEX
NTS



Free-field accelerometer array for the Non-Proliferation Experiment

Fig. 2. Map of part of the N-tunnel complex (approximately 400 m beneath the mesa surface) showing locations for the 23-station free-field accelerometer array activated for the Non-proliferation experiment (NPE). Also shown are the working points (H) for three previous nearby nuclear events (MISTY ECHO [ME]; MINERAL QUARRY, [MQ]; and HUNTERS TROPHY [HT]) which were recorded by fewer-station predecessors of our free-field accelerometer network. [The first event, ME, had only a seven stations (#'s: 2, a pair near 4, 6, 7, 8, and 12). Stations 1, 3, 5, 9, 10, 14, and 15 were added for MQ; stations 21-26 were added for HT; and stations 31-34 were added for NPE.] Depending somewhat on source yield, stations generally closer than about 100-200 m from the WP undergo non-linear material failure (crush and shear), whereas beyond 200-300 m, rock responses are nearly elastic.

EOS portion of our experiment was lost, but most of the more distant existing stations yielded good data that extended well into the elastic zone.

Figures 3a, 3b, and 3c display the first two seconds of the NPE *particle velocity* records for the Radial, Tangential, and Vertical (Z) components respectively. *A priori*, one would expect to observe that the higher frequency energy is attenuated more rapidly with distance due especially to nonlinear crush and shear processes close-in. Indeed, this initial pulse broadening and selective attenuation of higher frequencies in the coda during about the first second of record can be seen—particularly on the radial and vertical components. (This effect is displayed even more clearly on the ME records of Fig. 6a and Fig. 6b).

While one can readily trace the evolution with distance of several high-frequency waveform features and phases on both the radial- and vertical-component stacks, transverse-components (Fig. 3b) appear to show very little coherence in this respect between successive seismograms in the stack. Indeed, there

Table 2 . Slant-ranges and gauge performance for NPE free-field array

U12N.25		
Sta ID	Slant range (m)	Comments
TM 31 (L1)	54.206	Shorted @ D-2 (Grout failure)
TM 32 (L2)	84.629	Grout failure(>50g)-shock rise only ($t < 50$ ms)
TM 6	93.987	Exceeded gauge linearity (>25g)
TM 33 (L3)	98.326	Grout failure(>50g)-shock rise only ($t < 50$ ms)
TM 2	100.321	Exceeded gauge linearity (>25g)
TM 34 (L4)	114.226	Grout failure(>50g)-shock rise only ($t < 50$ ms)
TM 7	228.435	Early data only-some axes failed $t \sim 1$ s
TM 5	384.151	
TM 9	392.315	
TM 26	406.446	
TM 8	438.789	
TM 25	450.748	
TM 13	459.779	
TM 4	472.709	Inoperative after previous shot
TM 24	475.036	
TM 14	503.870	
TM 23	504.299	
TM 1	512.146	
TM 22	514.983	Early data only-some axes failed $t \sim 200$ ms
TM 21	523.020	Inoperative after previous shot
TM 3	673.779	Inoperative after previous shot
TM 10	675.821	
TM 12	724.065	
TM 15	1099.229	

appears to be poor consistency even in the polarities of the initial pulses. We interpret this to mean that transverse energy arises here mainly from scattering and multi-pathing due to small, random inhomogeneities throughout the bedded tuffs of Rainier Mesa. We intend to evaluate such effects more thoroughly by future detailed studies of both acceleration and velocity spectra.

The NPE vertical component velocity waveform stack (Fig. 3c) displays many of the same high-frequency (~50 Hz) features and phases shown on the corresponding radial seismograms (Fig. 3a). There is a high coherence between the radial and vertical seismograms (high R-Z coherence also is seen on the primary accelerograms). The good coherence between radial and vertical components for N-tunnel free-field data is principally due to the fact that there is a particular bedded tuff layer immediately below

NPE Velocities - Radial

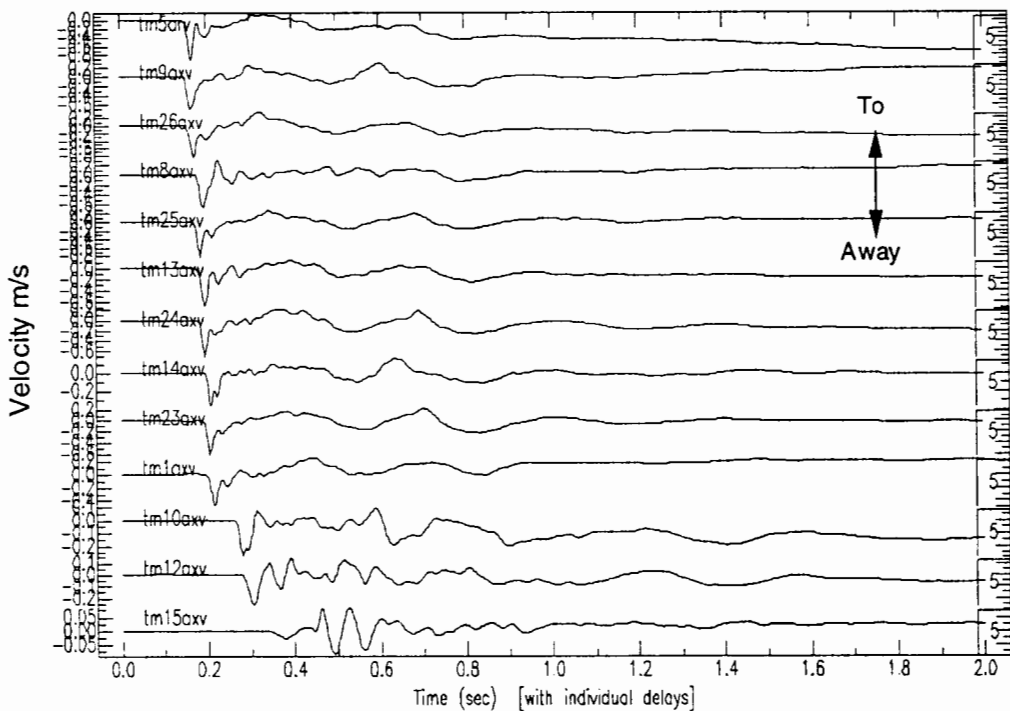


Fig. 3a. Stack of trace-normalized particle-velocity seismograms from the NPE arranged in order of distance (see Table 2) from the NPE working point. (a) Radial components. (b) Tangential components. (c) Vertical components. Only the first 2 seconds of the seismograms are shown. Note how the first transient pulse broadens and the dominant frequencies of the first 1 second of high-frequency (~50 Hz) coda decrease with range. Also, observe the approximately 2-Hz low-frequency, in-phase energy appearing mainly on vertical components (Fig. 3c). No corrections have been made for any offsets or long-period drifts arising from either the recording system or from integration of primary acceleration data.

tunnel level in this part of Rainier Mesa which has a strong positive velocity gradient (velocity increases downward). Thus, much initially down-going energy is refracted back upward by this strong positive gradient; significant vertically-traveling energy is evident on all our seismograms—even at the closest ranges ~50 m. Also of great interest are the “long-period” (~ 2 Hz) oscillations that are particularly evident on all the vertical velocity-seismograms. These oscillations can also be seen, but less obviously, on the radial component waveforms, but appear only intermittently and less clearly on transverse components. Similar long period oscillations—chiefly on the vertical components—appear on free-field seismograms for all four N-tunnel shots, both for the NPE ANFO charge and for all three nuclear sources. These long-period oscillations are most clearly seen on the MISTY ECHO vertical velocity records (Fig. 6b). We will comment more extensively on these oscillations when we discuss details of the ME records below.

NPE Velocities - Transverse

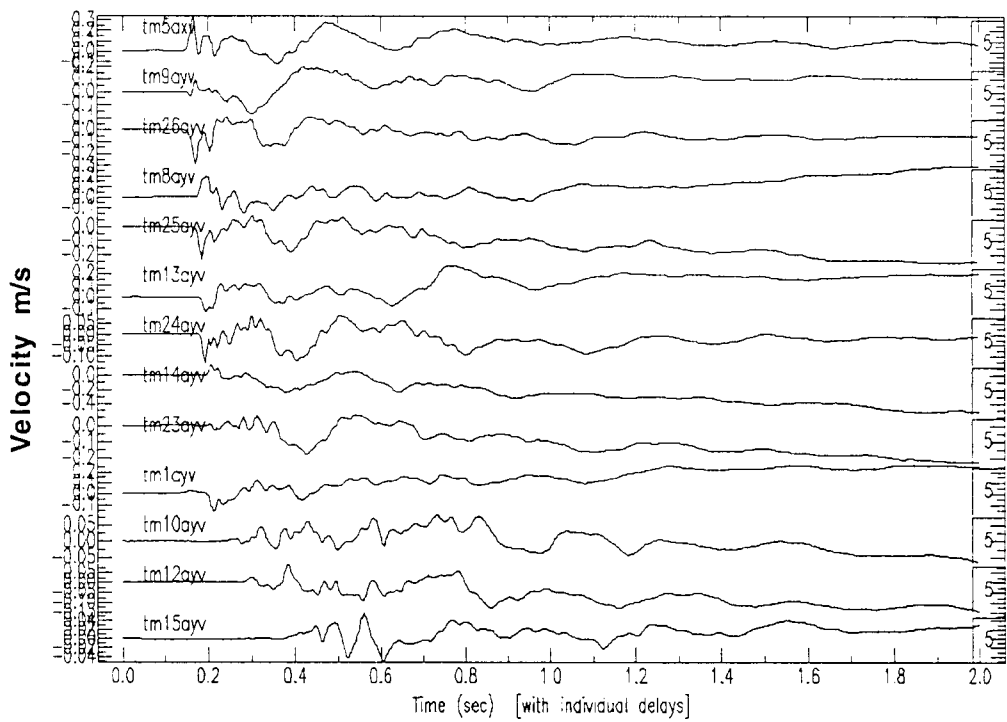


Fig. 3b. Tangential components. (See caption for Figure 3a)

NPE Velocities - Vertical (Z)

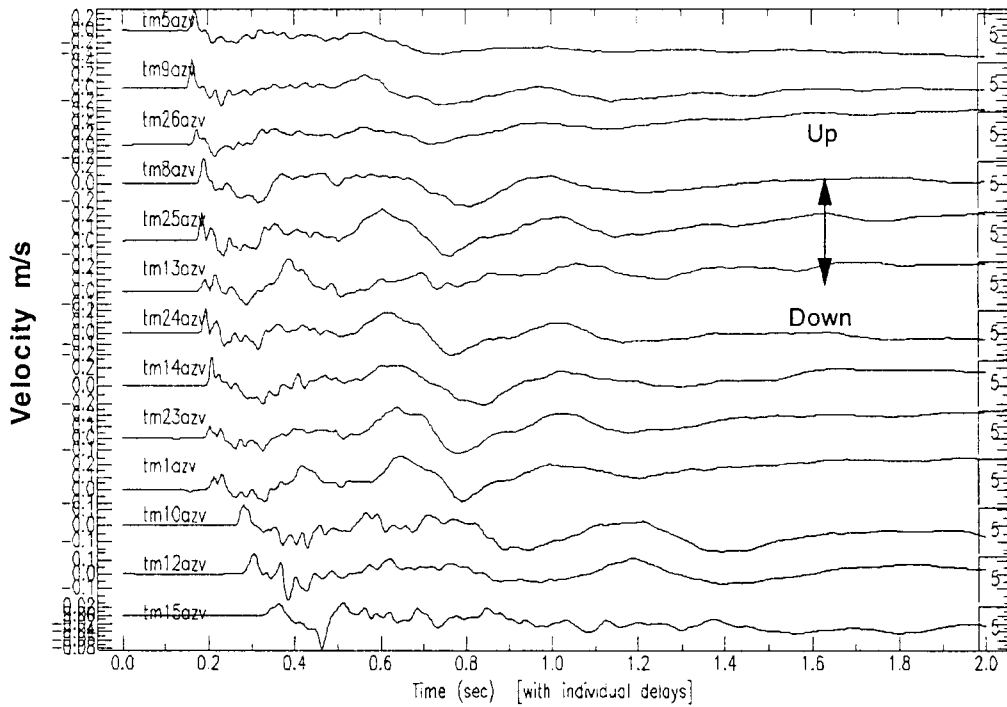


Fig. 3c. Vertical components. (See caption for Figure 3a)

NPE - Station TM-10 (676 m)

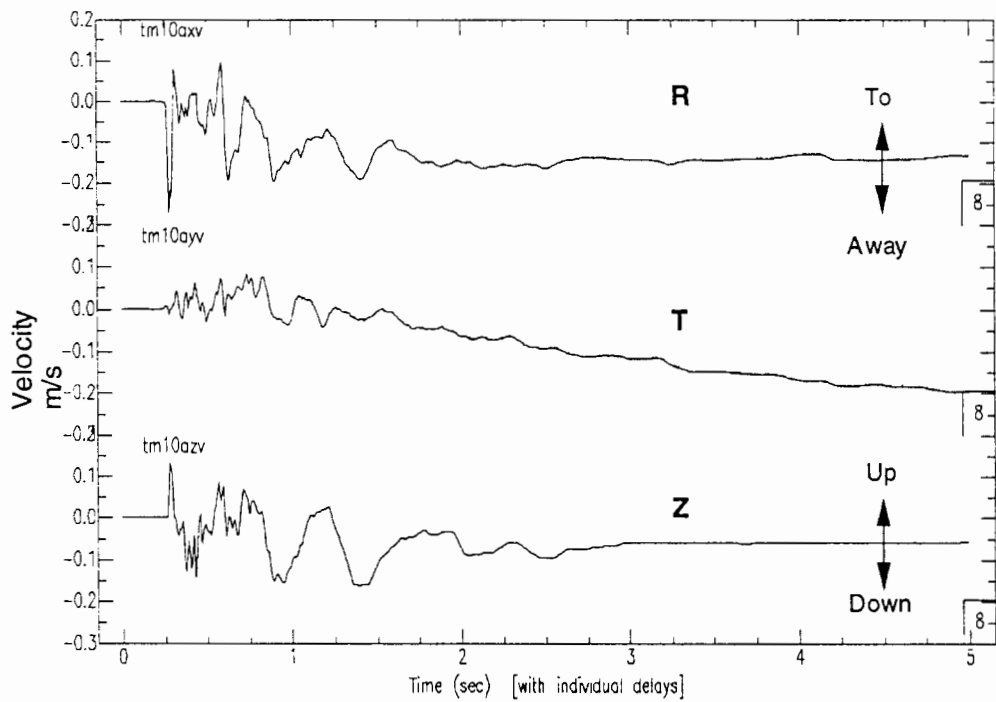


Fig. 4 Comparison of Radial (R), Transverse (T), and Vertical (Z) component velocity waveforms from free-field station TM-10 for the NPE. Station is at a range of 676 m from the charge center, well outside the "transition zone" in a region where the tuff response should be elastic. All components are plotted at the same amplitude scale. Note that for frequencies greater than ~10 Hz, there is an approximate 'equipartitioning' of energy among all components. "Long-period" (~2 Hz) energy is clearly seen on both Z and R components. (All uncorrected for offsets or long-period drifts.)

Figure 4 displays Radial, Transverse and vertical component velocity waveforms for a single triaxial NPE station (TM-10), all plotted at the same amplitude and time scales. One is immediately struck with how large are the rms-amplitudes (particularly for frequencies >10 Hz) of the vertical and transverse components as compared with corresponding radial component amplitudes. We clearly observe this near-equality of rms component-amplitudes on almost every station for all four shots (e.g., see also the ME station discussed in Fig. 7 below). Thus, there obviously is a very large departure from the spherical symmetry that commonly is assumed in analytic treatments of source theory. This suggests that one should carefully re-evaluate the practice of comparing only radial-component, close-in, free-field data with spherically-symmetric equivalent seismic source functions derived from inversion of distant seismic observations. We noted above that the relatively large amplitudes of vertical components has at least a partial explanation because of strong upward refraction from the strong velocity gradient just beneath tunnel level, but this cannot satisfactorily account for all the effect in the surprisingly large transverse

components. In discussing transverse waveforms in Figure 3b, we suggested that much of the non-radial, higher-frequency energy arises from scattering and multi-path propagation due to roughly meter-size inhomogeneities of the surrounding geological medium. Strong scattering and multi-pathing would lead to an effective equipartitioning of rms energy over propagation distances of a few tens- to hundreds-of-meters. In all our tunnel experiments, we do indeed observe (details not shown here) such an increase in equipartitioning versus propagation distance both with respect to rms amplitudes and for first-peak transient acceleration, velocity, and displacement pulses. In previous surface-array ground motion measurements on shots in the alluvium of Yucca Flats (Stump, et al., 1994), we have also seen strong evidence in displacement spectra for long-duration, complex wave trains and equipartitioning between components. In the Yucca Flats alluvium experiments, however, the distance-scale over which the equipartition process takes place appears to be about ten-times greater than that for tunnel tuffs (i.e., for alluvium, waveforms/spectra are ‘simple’ at ranges \sim 500 m but complex/‘equipartitioned’ at \sim 5 km, whereas for N-tunnel tuffs the corresponding distances are more like 50 m and 500 m, respectively).

The other noteworthy feature seen in Figure 4 (and already pointed out in comments on Fig. 3c above) is the “2-Hz long-period” oscillation which is particularly well developed on the vertical component at times after 0.5 s. In Figure 4, we observe that this “2-Hz” oscillation also is seen quite well on the radial component and is effectively in phase with the vertical oscillation. However, the case for a corresponding long-period oscillation on the transverse component is unconvincing. Again, we defer discussion of the long period oscillation until we examine some MISTY ECHO records below.

We now turn to an examination of selected MISTY ECHO waveforms. As noted above, the reason for discussing ME records here is that most general characteristics of all our free-field data sets are particularly well displayed due the more optimal recording conditions for the ME shot. Figure 5 shows the evolution with distance of the radial component *displacement* (doubly integrated acceleration) waveforms for ME. These nicely illustrate “overshoot” and “rebound” of transient free-field displacements and the eventual decay to a “permanent” displacement value. For instance, at the closest ME station (TM-2 at 341-m-range) the displacement of the tuff medium first expands to about 25 cm (overshoot), then rebounds back to 7 cm and then expands again to reach an apparent steady-state value of about 12 cm after 2 seconds. These motions mirror similar but larger motions of the explosion cavity wall. Although not shown here, vertical and transverse components of displacement show similar waveform characteristics, but again, these amplitudes are surprisingly large. (Comfortingly, “permanent” displacement values for both T- and Z-components in these uncorrected ME records return to within a few millimeters of zero.) We note that the full sequence of overshoot–rebound–steady-state takes place in a time scale of about 2 seconds. This implies that good free-field records of *at least* two-seconds-duration are required in order to derive reliable estimates for *long-period* RDP parameters for NTS tunnel shots. (We maintain that good records of at least 10-s duration are necessary to derive meaningful estimates of long-period spectral levels [for moment estimation].)

MISTY ECHO Displacements - Radial

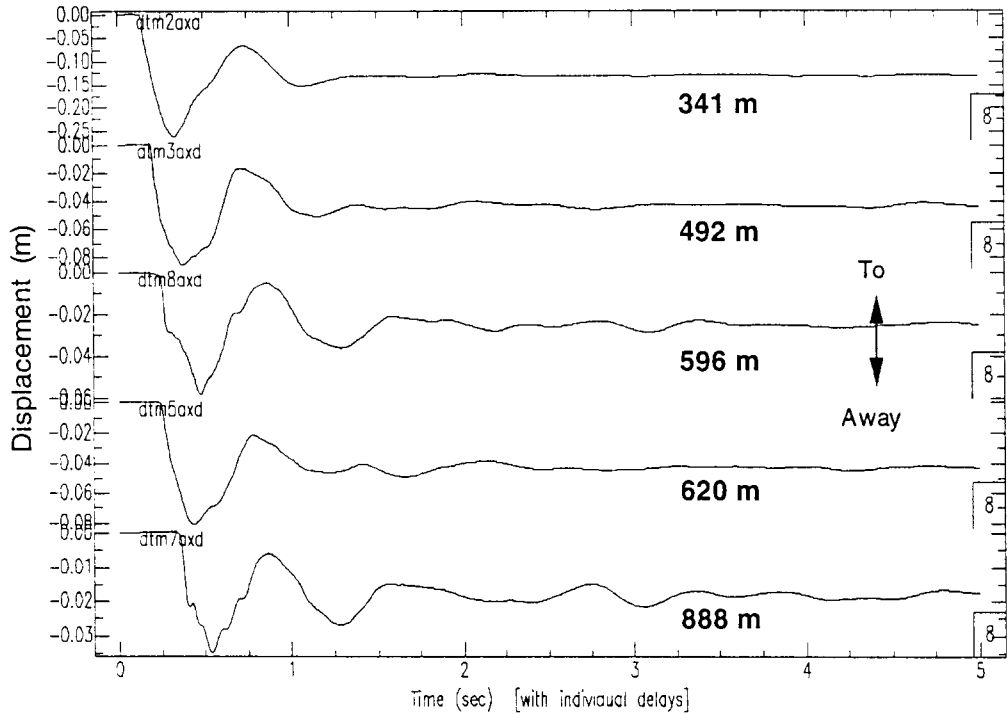


Fig. 5. Plot of Radial component, *Displacement* waveforms as function of range for the MISTY ECHO nuclear event, to illustrate "overshoot" and "rebound" of transient free-field displacements and the eventual decay to a "permanent" displacement value. Because of uncertainties due to possible as-yet-uncorrected long-term instrumental and integration drifts, some caution about the precision of 'permanent' displacement values is recommended. (Trace-normalization; no corrections for offsets or long-period drifts.)

We return to examining velocity waveforms in the remaining figures. Figures 6a and 6b display the evolution with distance of MISTY ECHO velocity waveforms for radial and vertical components, respectively. Due to the much lower long-term drifts in the ME data as compared to NPE, it is possible to display 5-second-duration records in Figures 6a and 6b rather than only 2 seconds as for NPE (Figs. 3a, 3b, and 3c). Comparing radial components for the two events (Fig. 6a and Fig. 3a), we again note the broadening of the initial pulse and the selective decay of higher (>20 Hz) frequencies in the pulse coda, probably mainly due to strong, close-in attenuation processes—including non-linear crush and shear particularly at ranges <200 m. Although we are unable to quantitatively demonstrate them here because of classification constraints, comparison of *initial peak values* of acceleration (directly related to peak forces on buried structures), velocity, and displacements for the three nuclear sources versus those from the NPE ANFO charge suggests the lower-energy-density NPE event is *about twice as effective as tamped nuclear sources* as in producing mechanical effects, such as peak shock forces on buried structures, etc. Such an approximately double equivalency factor for completely buried High-Explosive charges ("TNT") over

MISTY ECHO - Radial Velocity waveforms

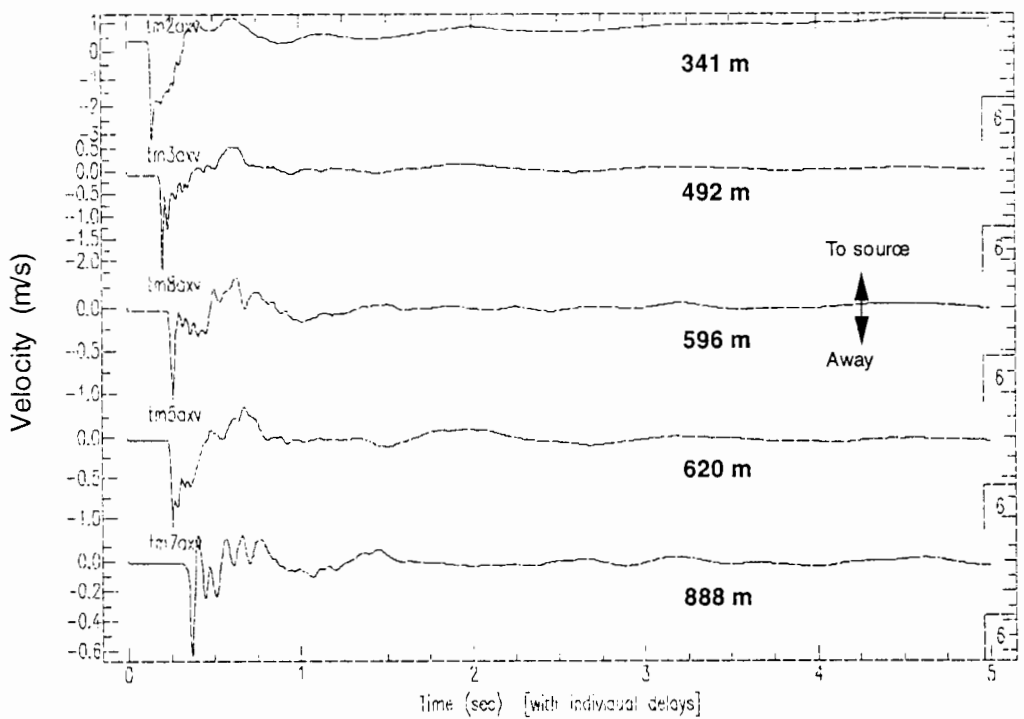


Fig. 6a. Evolution of the Radial-component, Velocity waveforms for the MISTY ECHO event. Compare with (2-second) NPE data shown in Figure 3a. Again, note loss of high frequencies in initial pulse coda for greater distances. (Trace-normalization; no corrections for offsets or long-period drifts.)

tamped nuclear sources has been well known for a number of years among nuclear effects modeling and explosion cratering specialists within the U.S. defense research community (e.g., Killian, et al. 1987). Although the approximate HE/nuclear equivalency factor quoted here refers strictly to the stronger high-frequency signals near the beginning of the free-field waveforms, our preliminary evidence suggests that a nearly equal factor also pertains to the lower-frequency energy characterizing radiated seismic energy from the two source types.

Figure 6b displays vertical velocity waveforms for ME which show even more clearly several features already noted for NPE (Fig. 3c). In addition, we call particular attention to the large, "long-period" (~ 1 Hz) oscillations, in-phase on all components, which dominate the vertical wave trains at times $>1.5\text{--}2$ seconds. We observe such 1-Hz vertical oscillations at later times on all four N-tunnel shots (NPE and 3 nuclear) for which we have made free-field measurements (the 2-second-duration NPR records of Fig. 3c are not quite long enough to display these clearly). This universality leads us to tentatively conclude that these 1-Hz vertical oscillations are more indicative of larger features of Rainier Mesa geological structure than they are of wave propagation effects close to the individual shot points. Consideration of

MISTY ECHO - Vertical (Z) Velocity waveforms

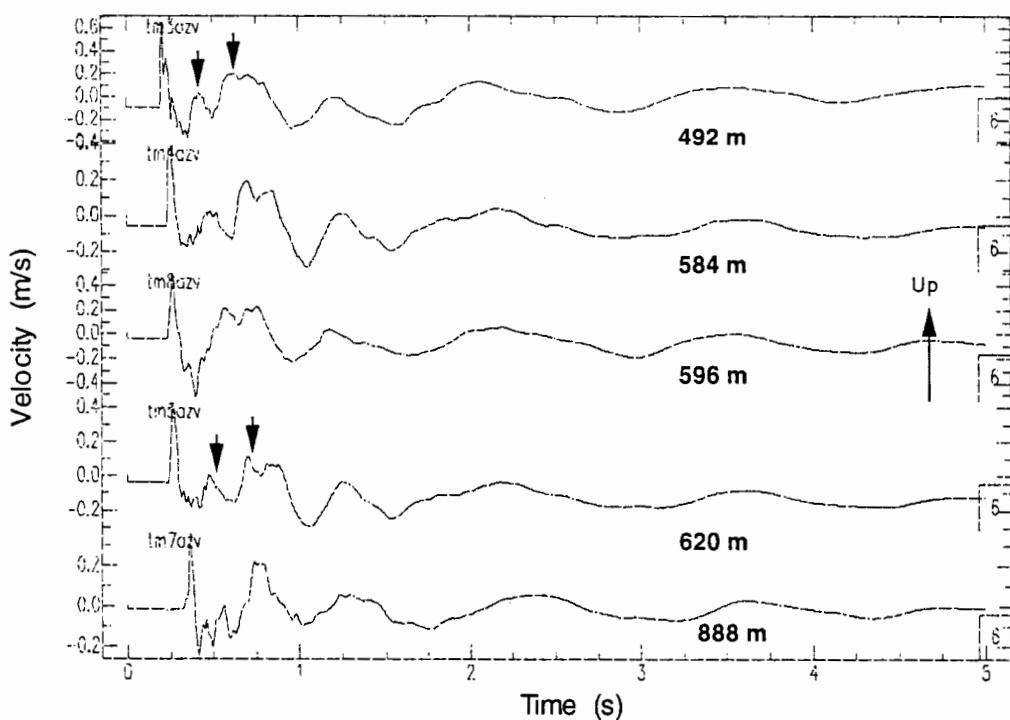


Fig. 6b. Evolution of the Vertical-component, Velocity waveforms for the MISTY ECHO event. Compare with (2-second-duration) NPE data shown in Figure 3c. Particularly note the two broadened upward peaks (arrows) at about 250 ms and 400-500 ms after the first, sharp, "shock" pulse on all seismograms. Pending detailed forward modeling, we suggest these are diffused reflections from the free-surface above (pP), and from the Paleozoic limestone basement about 200-400 m below these tunnel-level gauges. As for radial components, the loss of high frequencies in the initial pulse coda at greater distances is evident. Also noteworthy are the "long-period," in-phase oscillations which here show frequencies somewhat below 1 Hz for times greater than 2 seconds. (Trace-normalization; no corrections for offsets or long-period drifts.)

an additional separate line of evidence leads us to suggest an explanation for several features of the vertical free-field seismograms. One cannot readily discern on vertical seismograms any *sharp* pulse returning after near-total reflections (a pP reflection) from the Mesa-top free-surface. Actually, there should be *two* reflection pulses: one due to pP from the surface and another from the large velocity contrast between the mesa tuffs and the Paleozoic limestone basement about 200-400 m below the tunnel-level gauges (the reflection coefficient here should be fairly large because the P-velocity contrast probably exceeds 1 km/s). Examination of Figure 6b suggests the presence of two, *broadened* upward peaks at about 250 ms and 400-500 ms after the initial sharp, "shock" pulse on all seismograms. Pending detailed forward modeling, we suggest these are the diffused reflections from the free-surface above (pP), and from the Paleozoic limestone basement below. Thus, considerable mainly vertically-traveling, seismic energy is

MISTY ECHO Velocities - Station TM-3 (492 m)

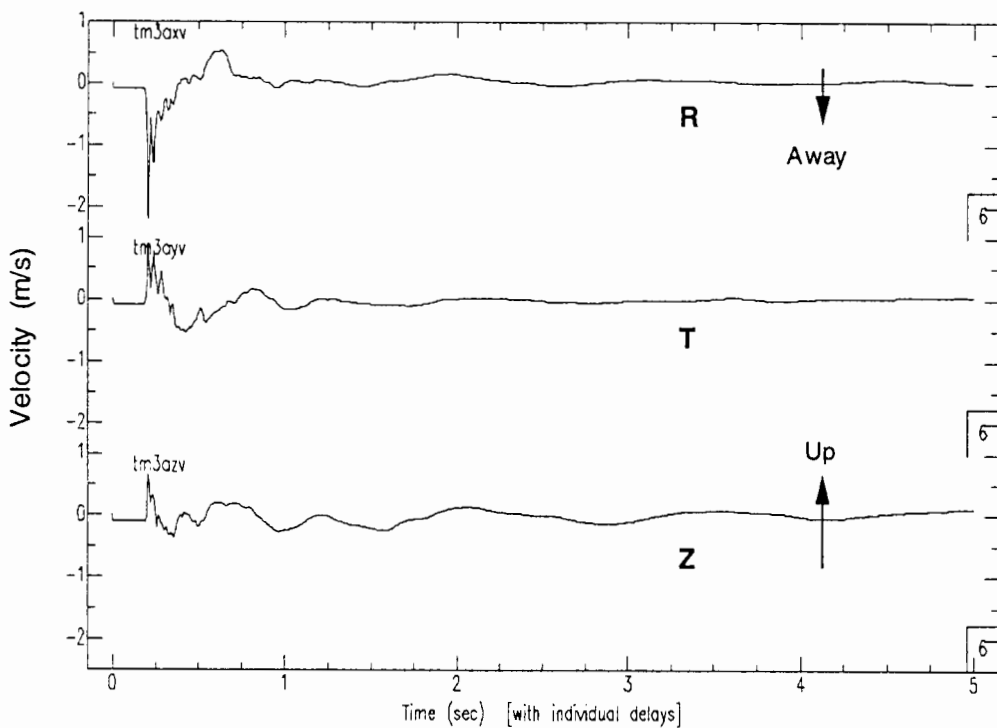


Fig. 7. Comparison of Radial (R), Transverse (T), and Vertical (Z) component, velocity waveforms from free-field station TM-3 for the MISTY ECHO nuclear shot. Station is at a range of 492 m, which—for the somewhat larger yield ME event—places it in the outer portion of the non-linear (“crush and shear”) transition zone. Compare with NPE data of Figure 4. Again, the approximate ‘equipartitioning’ of energy among components is noticeable even at this position somewhat inside the “elastic radius” for this shot.

reflected back and forth between these two strong largely-horizontal reflectors leading to “trapping” of energy and rather coherent, mostly vertical oscillations which probably cause Rainier Mesa to vibrate vertically essentially as a unit. This preliminary explanation needs to be tested by more detailed data analysis and by numerical modeling.

Finally, shown in Figure 7 are radial, transverse and vertical-component velocity waveforms for a single triaxial MISTY ECHO station (TM-3), all plotted at the same amplitude and time scales (compare with NPE in Fig. 4). In contrast to NPE signals of Figure 4, this ME station is located at a somewhat larger peak stress level (probably still within the nonlinear crush and shear failure zone) so the radial component dominates and “equipartitioning” between components has not proceeded as far. Nevertheless, there already is significant higher frequency energy (> 20 Hz) in both the vertical and transverse components.

Concluding remarks

The main important points from this initial overview of the NPE free-field experiments are:

- Both nuclear & NPE shots show an approximately bi-modal energy distribution with frequency:
 1. High frequencies (> 10-20 Hz) arise from the expanding/attenuating shock front.
 2. Low frequency (~1-2 Hz) of lower amplitudes at later times in seismogram (Significant as a large portion of total energy radiated as seismic waves to regional and teleseismic distances).
- Conversion to low frequencies appears very efficient on vertical component seismograms (large surface [pP] and basement reflections)
- For high-frequency, first-peak strong-motion accelerations & velocities, NPE is more efficient (roughly x 2) than tamped nuclear sources.

In surveying free-field ground motions from all four N-tunnel shots, we continue to be impressed by the large amount of close-in seismic energy residing in the vertical and transverse components and at the "non-spherical" complexity of close-in free-field ground motions even at the relatively close ranges explored by our N-tunnel experiments. This complexity suggests that considerable care needs to be observed in comparing and understanding the basic physics of seismic source function estimates as derived by close-in and by distant seismic techniques.

References

- Killian, B. G., J. R. Rocco, and E. J. Rinehart, *Comparisons of Nuclear-TNT Equivalencies and Effects Environments in Different Geological Media*, Defense Nuclear Agency, Washington, DC, DNA-TR-87-152, 1987.
- Olsen, K. H., and A. L. Peratt, Free-field ground motion measurements in the nonlinear-to-elastic transition region, in S. R. Taylor and J. R. Kamm (eds.), *Proceedings of the Numerical Modeling for Underground Nuclear Test Monitoring Symposium*, Los Alamos report LA-UR-93-3839, pp. 397-404, 1993.
- Stump, B. W., R. E. Reinke, K. H. Olsen, and L. R. Johnson, Isotropic and deviatoric characterization of the Coalora nuclear explosion in Yucca Flats, *Geophys. J. Int.* 116, 538-552, 1994.

Comparison of Chemical and Nuclear-Explosion Source Spectra from Close-in, Local, and Regional Seismic Data

Peter Goldstein and Steve Jarpe

Lawrence Livermore National Laboratory

Abstract

Verification of a Comprehensive Test Ban Treaty (CTBT) will require the ability to discriminate chemical and nuclear explosions as well as explosions and earthquakes. In this study, we determine whether there are differences in the seismic signals generated by concentrated chemical explosions and nuclear explosions and whether these differences might be useful for discrimination. We also examine the possibility that concentrated chemical explosions could be used to calibrate a region, for discrimination between earthquakes and explosions. We address these questions by comparing close-in, local, and regional estimates of the source spectrum of the Non-Proliferation Experiment (NPE), a concentrated, one kiloton chemical explosion in N-tunnel at Rainier Mesa on the Nevada Test Site, with those of nearby nuclear explosions. We also compare regional waveforms and spectra of these explosions.

We find that the low-frequency (~ 1 Hz) amplitude of the scaled source spectrum ($|\omega\phi(\omega)|/W$) of the NPE is approximately twice as large as those of nearby nuclear explosions. We also find that the scaled corner frequency of the NPE is lower than that of nearby nuclear explosions. However, when the data are scaled to the same peak spectral level, they are almost indistinguishable. The same cannot be said of source spectra of explosions in different media. For example, the source spectrum of an explosion in a medium with a high gas-filled porosity ($\sim 10\text{-}20\%$) was found to have much steeper high-frequency falloff than those in saturated media.

In a CTBT monitoring environment, where the yield and source region material properties of an explosion would not be known, it is unlikely that large concentrated chemical explosions and nuclear explosions could be discriminated. However, the similarity of source functions and regional waveforms of the NPE and nearby nuclear explosions suggests that chemical explosions may be useful for calibrating a region for discrimination. Efforts to perform such calibrations could be complicated by variations in material properties within the region of interest. Preliminary analysis suggests that below approximately 10 Hz, the shape of attenuation corrected, regional Pn spectra are similar to that of the explosion source spectrum and might be used to account for differences in material properties.

Introduction

Verification of a Comprehensive Test Ban Treaty (CTBT) will require the ability to discriminate chemical and nuclear explosions as well as explosions and earthquakes. The discrimination of concentrated chemical explosions from nuclear explosions may be very important for verification of a CTBT because of the large number of these types of blasts throughout the world (Leith, 1994). Although a number of studies suggest that ripple fired chemical explosions, which are detonated as a sequence of smaller explosions, can be identified as such from spectra of their seismic signals (e.g., Hedlin et al., 1990), the discrimination of concentrated chemical explosions from nuclear explosions is more difficult because of the similarity of their size and duration. Furthermore, Smith (1993) suggests that it might be possible to test a nuclear explosive evasively if a small decoupled nuclear explosion were detonated simultaneously and in close proximity to a ripple fired event.

In this study, we compare close-in, local, and regional waveforms and spectra of the Non-Proliferation Experiment (NPE), a concentrated, one kiloton chemical explosion in N-tunnel at Rainier Mesa on the Nevada Test Site, with those of nearby nuclear explosions with the aim of identifying similarities and differences in the seismic signals they produce. These similarities and differences help determine whether concentrated chemical explosions can be seismically discriminated from nuclear explosions and whether they can be used to calibrate regions for discrimination between explosions and earthquakes.

We find significant differences in the scaled spectra of the NPE and nearby nuclear explosions. However, these differences are shown to be insignificant from the standpoint of seismic discrimination. In contrast, we find that variations in material properties can cause large differences in source spectra. These results suggest that discrimination of concentrated chemical explosions and nuclear explosions will be very difficult. The similarity of waveforms and spectra of the NPE and nuclear explosions suggests that concentrated chemical explosions may be useful for calibration.

Can Concentrated Chemical Explosions Be Discriminated From Nuclear Explosions?

Fundamental differences between chemical and nuclear explosion sources include their initial energy density (the ratio of the available explosive energy or yield to the volume of explosive material) and the effective distribution of the energy they release in thermal and mechanical forms. Based on these differences, chemical explosions are expected to have a significantly larger asymptotic reduced displacement potential (ϕ_{∞}) than nuclear explosions of the same yield (Glenn, 1993; Glenn and Goldstein, 1993; Glenn and Goldstein, 1994). In this paper, we investigate whether such differences manifest themselves in a way that is useful

from the standpoint of seismic discrimination. In Figure 1, we compare yield-scaled amplitudes of the reduced velocity potential spectra ($|\omega\phi(\omega)|/W$) of the NPE and a nearby nuclear explosion as a function of yield-scaled frequency $fW^{1/3}$. Where, $\phi(\omega)$ is the Fourier transform of the reduced displacement potential $\phi(t)$, ω is the angular frequency, W is the yield of the explosion, and f is frequency. These spectra, which we refer to as source spectra, were obtained by averaging scaled, reduced-velocity potential spectra obtained from free-field accelerations at distances found from calculations and data to be beyond the inelastic region (approximately 257 m/kt^{1/3}), excluding non-spherical motions in the coda.

The results shown in Figure 1 show that the NPE's scaled, low-frequency (~1 Hz), source spectral amplitude is enhanced relative to that of nearby nuclear explosions by about a factor of two. Scaled, high-frequency spectral amplitudes are indistinguishable.

Finding or observing of source spectral differences is important because it helps improve our understanding of explosion source physics and phenomenology; however, the differences are probably not significant from the standpoint of seismic discrimination. From a discrimination standpoint, any differences in source spectra can only be considered useful if they can be identified from the data without prior knowledge of an event's source type or yield. Identifying such differences at regional distances also requires accurate corrections for path effects that do not scale. Assuming such path corrections have been made, the data can be scaled in any way

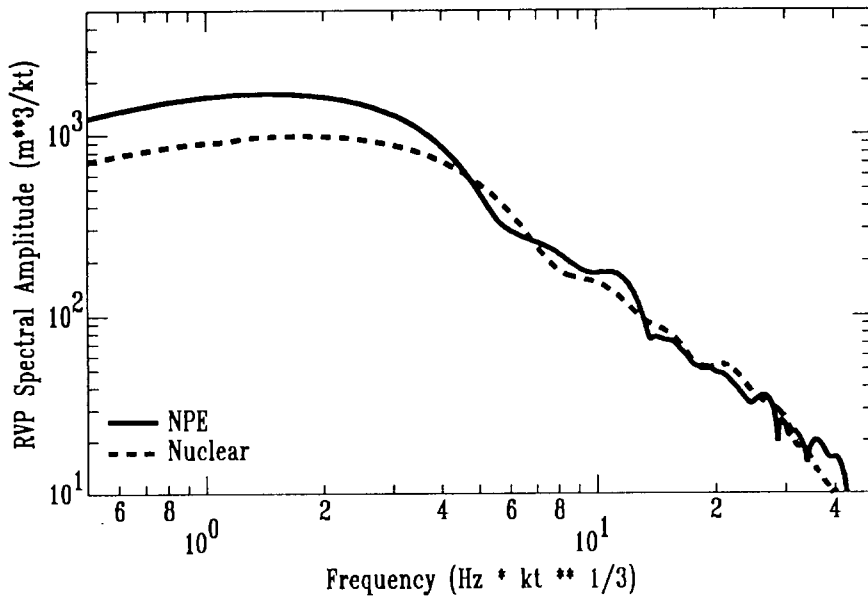


Figure 1. Comparison of yield-scaled NPE (solid line) and nuclear explosion (dashed line) source spectra. Note that the NPE's low-frequency (~1 Hz) source spectral amplitude is approximately twice that of nearby nuclear explosions, while its corner frequency is slightly smaller than that of the nearby nuclear explosions.

that allows comparison in the frequency band of interest. For example, in Figure 2 we compare source spectra of the NPE and nearby nuclear explosions after scaling them to the same peak spectral amplitude. In this example, frequencies are scaled by the cube-root of the constant required to convert the peak amplitudes of the nuclear data to that of the NPE data. Although most of the NPE's source spectral amplitudes fall below those of the nuclear data, these differences are insignificant from a regional monitoring standpoint given the uncertainties in the spectra and the fact that path corrections will undoubtedly add to these uncertainties.

Even if very accurate path corrections were available and the above differences were thought to be significant, it would probably be impossible to distinguish them from differences due to variations in material properties. Numerous studies provide evidence that source spectra depend on material properties (see Denny and Johnson, 1991, for a review). In Figure 3 we show source spectra of nuclear explosions in a variety of media. The differences between these spectra are much greater than those between the NPE and nearby nuclear explosions detonated in the same material. This indicates that source spectra are more sensitive to material properties such as gas-filled porosity (GFP) and strength than they are to the type of explosive used. For example, the explosion in dry alluvium (high GFP) has a much steeper rolloff than those in saturated tuff or salt. The explosion in salt, which has greater strength than the tuff or dry alluvium, has a much higher scaled corner frequency. These differences are also consistent with predictions of numerical models (Glenn and Goldstein, 1994).

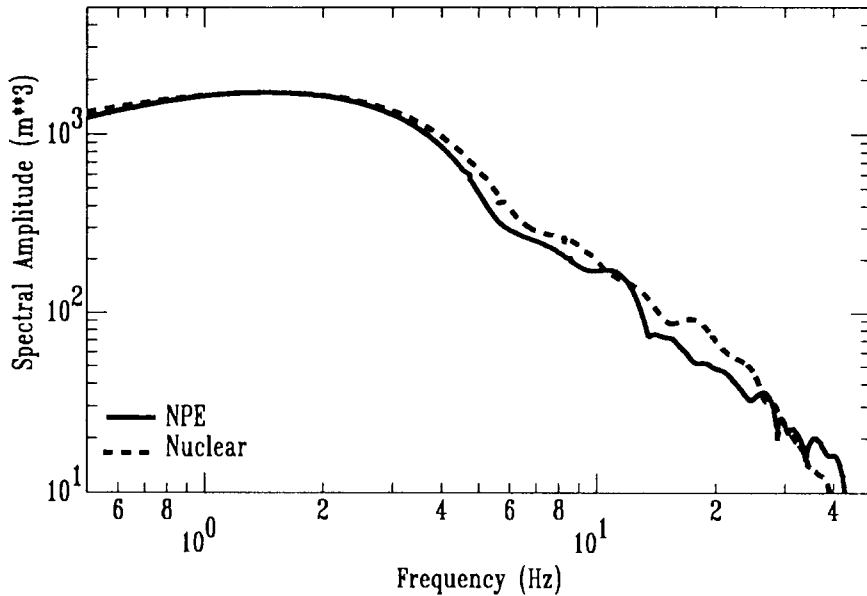


Figure 2. Comparison of NPE (solid line) and nuclear (dashed line) explosion source spectra. Peak spectral amplitudes have been scaled to that of the NPE. Frequencies are scaled by the cube root of the nuclear to NPE peak amplitude ratio. The overlap of these spectra and their uncertainties suggests that differences between nuclear and concentrated chemical explosion source functions are insignificant from the standpoint of seismic discrimination.

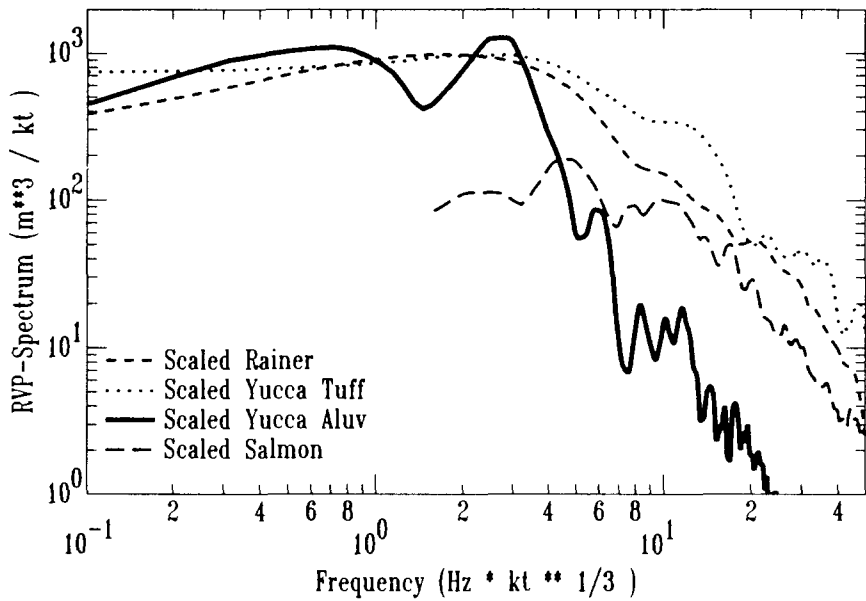


Figure 3. Comparison of nuclear explosion source functions in a variety of media. The dashed curve is for an explosion in tuff at Rainier Mesa. The dotted curve is for an explosion in tuff at Yucca Flats. The long dashed curve is for Salmon, an explosion in salt. The thick solid curve is for an explosion in dry (high gas-filled porosity) alluvium. The sensitivity of the shape of these source functions to material properties is important because it can affect the performance of regional discriminants.

The sensitivity of source spectra to material properties is significant because the performance of some discriminants is expected to depend on differences in spectral shape. For example, spectral ratio discriminants, which compare spectral amplitudes of an event in different frequency bands, will certainly be sensitive to differences in corner frequency and high-frequency spectral falloff. Given accurate numerical modeling capabilities, source differences might be corrected for using estimates of in-situ material properties. However, it may be difficult to obtain accurate estimates of material properties in regions where access is limited.

Can Chemical Explosions be used to Calibrate a Region for Discrimination?

In order to develop robust discriminants and apply them with confidence in a particular region we need accurate estimates of the signals that would be expected from nuclear explosions in that region. Based on the similarity of close-in source function estimates of the NPE and nearby nuclear explosions (Figure 2) and the excellent agreement between their regional waveforms (Figure 4), large concentrated chemical explosions are a potential tool for estimating such signals.

Issues that need to be addressed include (1) how can recordings of a calibration explosion be corrected for properties such as yield, material properties, depth, and source-receiver distance.

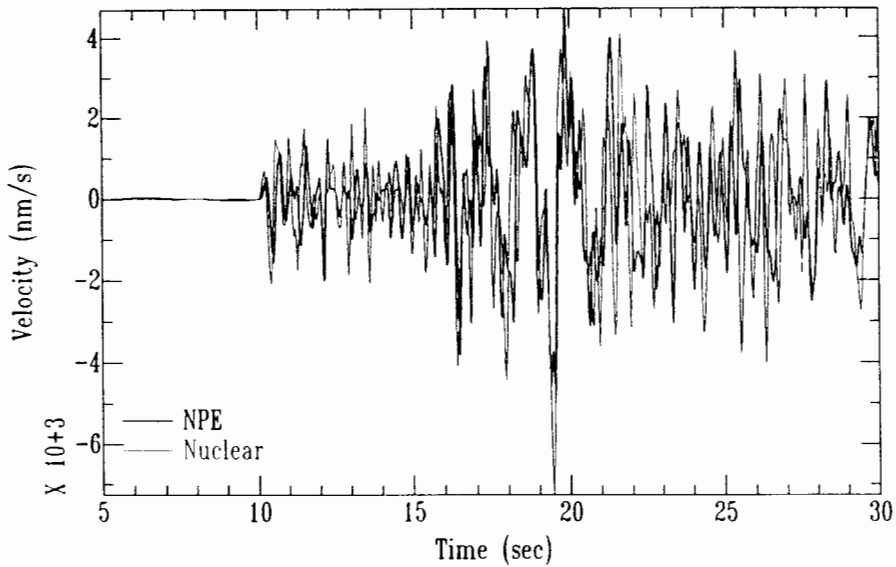


Figure 4. Comparison of regional waveforms of the NPE and a nearby nuclear explosion. Both the phase and amplitude of these waveforms are in good agreement.

And (2), what are the contributions of secondary sources, near source asymmetries, and source mechanism.

If the source function contribution is the same at close-in, local, and regional distances it is possible to circumvent some of these issues by removing source contributions from regional waveforms using the close-in or local estimates (see Goldstein et al., 1994). Based on excellent agreement between freefield, close-in surface, local and regional estimates of the source function of the NPE (Figure 5), close-in and local estimates of source functions of overburied explosions like the NPE can be used to correct regional waveforms for source effects or near source material properties.

Freefield estimates of the explosion source function were obtained from measurements of freefield accelerations as described above. Rainier Mesa surface, local, and regional estimates were obtained by deconvolving empirical Green's functions from recordings of the NPE. For the Rainier Mesa surface, and local data empirical Green's functions are recordings of a 300-pound explosion, which was detonated over a year before the NPE and was located at the center of the then-unmined NPE cavity. For the regional data, we used recordings of a smaller, nearby nuclear explosion. The primary constraint on our empirical Green's functions is that they have corner frequencies that are much higher than those of the NPE.

Source function estimates such as the ones discussed above may be difficult to obtain in a realistic monitoring situation. If they were available, they could be very useful for discrimination if significant systematic differences between source functions of earthquakes,

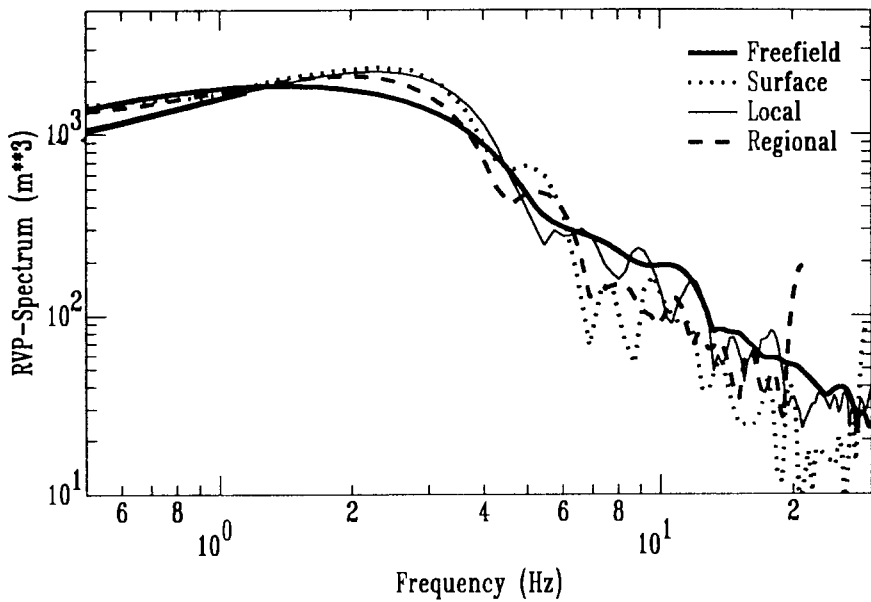


Figure 5. Comparison of freefield, surface, local, and regional estimates of the NPE source function. The NPE source function shows no significant dependence on distance or secondary sources.

concentrated explosions, and quarry blasts can be identified. Alternatively, the removal or correction for source differences could be very useful if discrimination techniques were most sensitive to differences due to path.

Based on the sensitivity to material properties demonstrated above, it will probably be difficult to predict source functions using numerical modeling without detailed knowledge of the material properties. Although such knowledge may be available for selected regions, an empirical estimate may be the only viable option in many areas. Based on analysis of a small number of explosions, we suggest that attenuation corrected, regional Pn spectra might provide such an empirical alternative. For example, we find good agreement between our estimate of the NPE's source function and its attenuation corrected, regional Pn spectrum below approximately 10 Hz (Figure 6). Additional measurements are needed to determine whether such spectra can be used for source corrections.

Conclusions

The above results help constrain how source functions contribute to the performance of discriminants and may be useful for designing more robust discriminants. These observations suggest that: (1) source functions of concentrated chemical explosions are very similar to those of nuclear explosions, (2) explosion source functions are most sensitive to material properties such

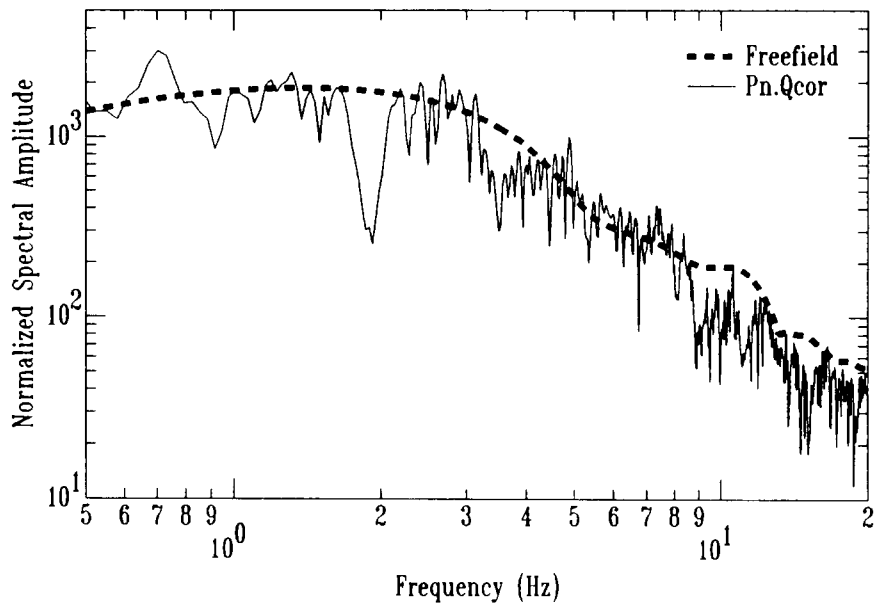


Figure 6. Comparison of the NPE's freefield source spectrum (thick dashed line) with its attenuation corrected, regional Pn spectrum (thin solid line). The spectra are in good agreement up to about 10 Hz.

as gas-filled porosity and strength, (3) explosion source functions of overburied explosions do not depend on distance, and (4) attenuation corrected, regional Pn spectra appear to be very similar to that of the explosion source function and may be useful for correcting for source differences.

Acknowledgments

We thank Fred App of Los Alamos National Laboratory for generously providing the freefield measurements of acceleration. This work has been performed under the auspices of the U.S. Department of Energy by Lawrence Livermore National Laboratory under Contract No. W-7405-Eng-48.

References

Denny, M. D., and L. R. Johnson (1991), "The Explosion Seismic Source Function: Models and Scaling Laws Reviewed," *Geophys. Monogr. Ser.*, vol. 65, edited by S. R. Taylor, H. J. Patton, and P. G. Richards, AGU, Washington, D. C., 1-24.

Glenn, L. A. (1993), "Energy density effects on seismic decoupling," *J. Geophys. Res.*, 98, B2, 1933-1942.

Glenn, L. A., and P. Goldstein (1993), "Seismic decoupling with chemical and nuclear explosions in salt," *J. Geophys. Res.*, in press; see also University of California, Lawrence Livermore National Laboratory Preprint UCRL-JC-114711.

Glenn, L. A., and P. Goldstein (1994), "The influence of material models on chemical and nuclear-explosion source functions," *Proceedings of the Symposium on the Non-Proliferation Experiment Results and Implications*, M. D. Denny et al., editors, Lawrence Livermore National Laboratory, Livermore, CA, CONF-9404100.

Goldstein, P., S. P. Jarpe, K. Mayeda, and W. R. Walter, "Separation of source and propagation effects at regional distances," *Proceedings of the Symposium on the Non-Proliferation Experiment Results and Implications*, M. D. Denny et al., editors, Lawrence Livermore National Laboratory, Livermore, CA, CONF-9404100.

Hedlin, M. A., J. B. Minster, and J. A. Orcutt (1990), "An automated means to discriminate between earthquakes and quarry blasts," *Bull. Seis. Soc. Am.*, 80, 2143-2160.

Leith W., "Large chemical explosions in the former Soviet Union and blasting estimates for countries of nuclear proliferation concern," *Proceedings of the Symposium on the Non-Proliferation Experiment Results and Implications*, M. D. Denny et al., editors, Lawrence Livermore National Laboratory, Livermore, CA, CONF-9404100, 1994.

Smith, A. T. (1993), "Discrimination of explosions from simultaneous mining blasts," *Bull. Seis. Soc. Am.*, 83, 160-179.

Recording Experiment on Rainier Mesa in Conjunction with a Reflection Survey

Lane R. Johnson

Center for Computational Seismology, Lawrence Berkeley Laboratory
Department of Geology and Geophysics, University of California
Berkeley, California 94720

Abstract

The chemical explosion of the NPE was recorded on the surface of Rainier Mesa along the same line which had previously been the site of a high resolution reflection survey. Six three-component accelerometer stations were distributed along the 550 meter line, which was offset about 600 meters from the epicenter of the explosion. The bandwidth of the acceleration data extends to 100 Hz. Even though the separations of the stations was only about 100 meters, the waveforms and the amplitudes exhibited considerable variability, especially for the transverse component of motion. The maximum accelerations ranged between 0.27 g and 1.46 g, with the maximums of the average traces being 0.57 g on the radial component, 0.28 on the transverse component, and 0.50 g on the vertical component. Using the results of the reflection survey to help constrain the velocity model, the acceleration data were inverted to obtain a preliminary estimate of the seismic moment tensor of the NPE. This result is a strong diagnostic for the NPE being an explosion, showing a somewhat asymmetric extensional source with very small shear components. When interpreted in terms of a spectral model and scaling relationships, the isotropic moment tensor indicates a yield of 1.4 kt, an elastic radius of 116 meters and a cavity radius of 15.5 meters. This interpretation includes a source time function which contains appreciable overshoot, and, if shown to be reliable, this feature of the explosion could have a significant effect upon the analyses of other types of seismic data.

Introduction

The waveforms recorded on seismograms represent the combined effects of the seismic source and wave propagation through the material intervening between the source and receiver sites. All verification methods that use seismic data must first deal with these wave propagation effects, as these essentially have to be removed in order to isolate the information on the seismogram which is useful in making inferences about properties of the seismic source. Success in the task of verifying explosion sources is directly related to the proficiency in removing these propagation effects.

One of the standard methods of studying seismic sources is known as *moment tensor inversion*. With this approach the seismogram is shown to be a convolution between the seismic source, described

as a second order *seismic moment tensor*, and a Green function which contains the propagation effects. The Green function can be obtained by solving the elastodynamic equations of motion in an earth model which is representative of the geological structure in the region where the source and receivers are located. This representation of the problem is linear so that standard inverse methods can be used to extract an estimate of the seismic source from the waveform data contained on the seismograms. With this approach all propagation effects are contained in the Green functions and so the reliability of the results is directly related to the accuracy of these functions, which is in turn related to the fidelity between the earth model and the actual earth structure. Thus it would appear that the availability of an accurate estimate of earth structure would be a critical requirement for the success of the moment tensor inversion method.

The NPE provided an excellent opportunity to check seismic methods of estimating explosion properties in general, including the method of moment tensor inversion. In order to check the dependence of this method on the model assumed for the earth structure, an attempt was made to obtain a fairly detailed estimate of the velocity structure in the vicinity of the experiment. Prior to the NPE a surface reflection profile was obtained along a north-south line on the surface of Rainier Mesa slightly to the west of the epicenter (Majer et al., 1994). The data from this profile were processed to obtain an estimate of the velocity and density structure of Rainier Mesa in the vicinity of the NPE. At the time of the NPE this surface reflection profile was reoccupied with seismographs. Thus the data recorded by these seismographs can be subjected to the moment tensor inversion method using the velocity model which had been obtained specifically for this region. This would appear to be an optimum situation for moment tensor inversion, and thus the results should allow a critical evaluation of the capabilities of this method. The primary objective of the present study is to apply the moment tensor inversion method to the data recorded from the NPE and evaluate the results.

Experiment Parameters

The shot information for the NPE which was used in this study is as follows:

origin time = 00h 01m 0.080s
latitude = 37.20193 degrees N
longitude = 116.20986 degrees W
elevation = 1852.6 meters
depth = 389 meters

The explosion was recorded at six sites distributed on the surface of the Rainier Mesa along the profile which had previously been occupied for the reflection study. The geometrical relationship between the recording sites and the NPE is shown in Figure 1. The six recording sites were located along a roughly north-south line about 550 meters in length and located about 600 meters west of the NPE epicenter. The slant distances to the recording sites from the NPE shot point ranged between 709 and 853 meters. Details of the recording locations are given in Table 1.

The seismographs were accelerometers (FBA-23 models) with nominal natural frequencies of either 50 or 100 Hz. Each station had three components oriented in north, east, and vertical directions. The data were digitally recorded at 24 bit resolution and a sampling interval of 0.004 sec. Timing was by an internal clock which was synchronized to satellite time.

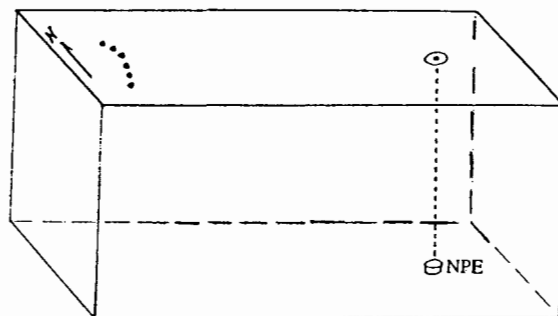
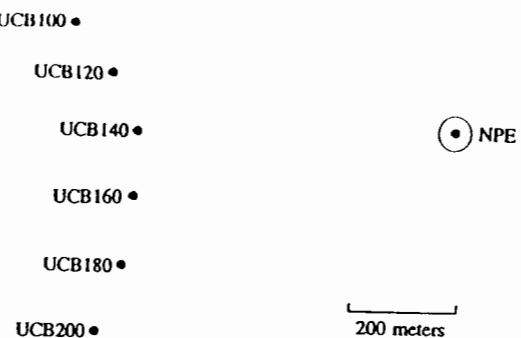


Figure 1. Geometry of the six recording sites and their relationship to the location of the NPE.

Table 1. Locations of Seismic Recording Stations

Station	Latitude deg N	longitude deg W	Elevation m	Range m	Azimuth deg
UCB100	37.20364	116.21800	2242	747	285
UCB120	37.20287	116.21716	2237	656	279
UCB140	37.20196	116.21661	2235	599	270
UCB160	37.20086	116.21667	2236	616	259
UCB180	37.19987	116.21689	2237	668	249
UCB200	37.19874	116.21746	2239	762	242

Waveform Data

All of the recording units operated successfully with 100% data recovery. For the purposes of display, the horizontal records were rotated into radial and transverse components using the azimuths listed in Table 1. The recorded data are shown in Figures 2, 3, and 4. First motions are always in the same direction on the vertical and radial components, up and away from the source, but have variable directions on the transverse components. The maximum accelerations at all stations are listed in Table 2. The maximum accelerations ranged between 0.27 g and 1.46 g with considerable variation between near-by stations. The maximum acceleration appears on either the vertical or radial component with the maximum on the transverse component always being the smallest, averaging about 55% the mean of the other two components.

The six recording stations of this experiment span a rather limited range in distance and azimuth from the NPE, and thus only a small fraction of the focal sphere has been sampled by the direct waves which arrive at these stations. In spite of this and the fact that the separation between adjacent stations was only about 100 meters, the waveforms and amplitudes exhibit considerable variability. While the polarity of first motions and general waveforms on the vertical and radial show a general similarity between stations, there are some later arriving pulses which have high frequencies, large amplitudes, and significant differences between the stations. The variability on the transverse components is quite pronounced. Few of the waveforms correlate between adjacent stations and even the polarity of first motions is not consistent across the profile.

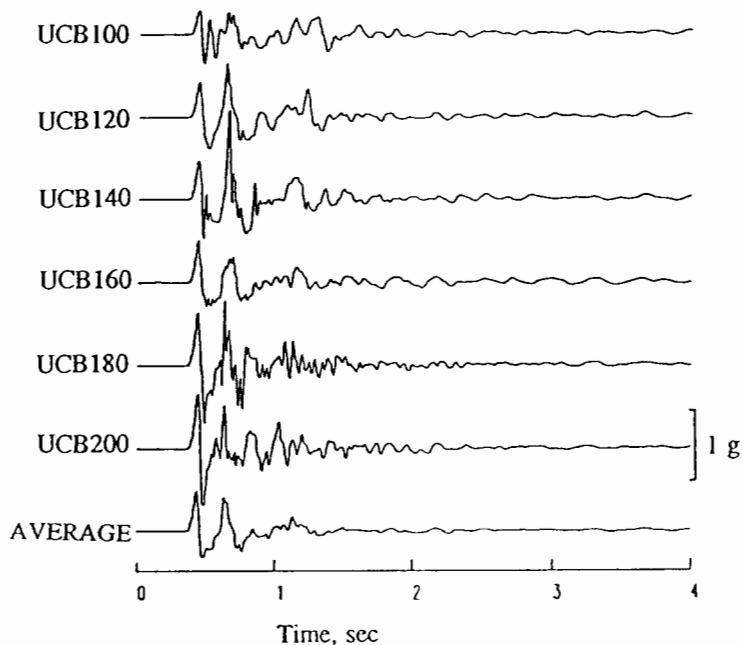


Figure 2. The radial accelerations recorded from the NPE with up motion on the seismograms indicating motion of the ground away from the source. Also shown at the bottom is the average of the six radial components. All seismograms are to the same scale, which is shown on the right where 1 g = 9.8 m/s.

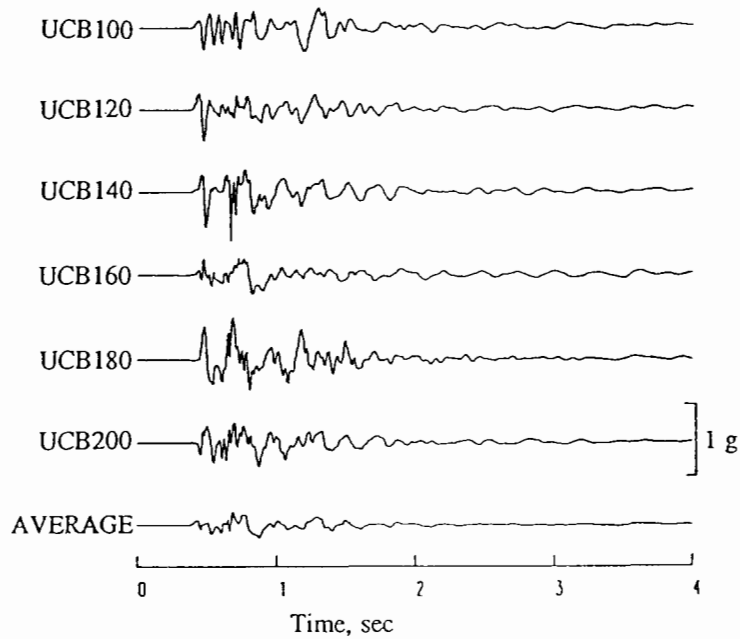


Figure 3. The transverse accelerations recorded from the NPE with up motion on the seismograms indicating motion of the ground clockwise around the source as viewed from above. Also shown at the bottom is the average of the six transverse components. All seismograms are to the same scale, which is shown on the right where $1\text{ g} = 9.8\text{ m/s}$.

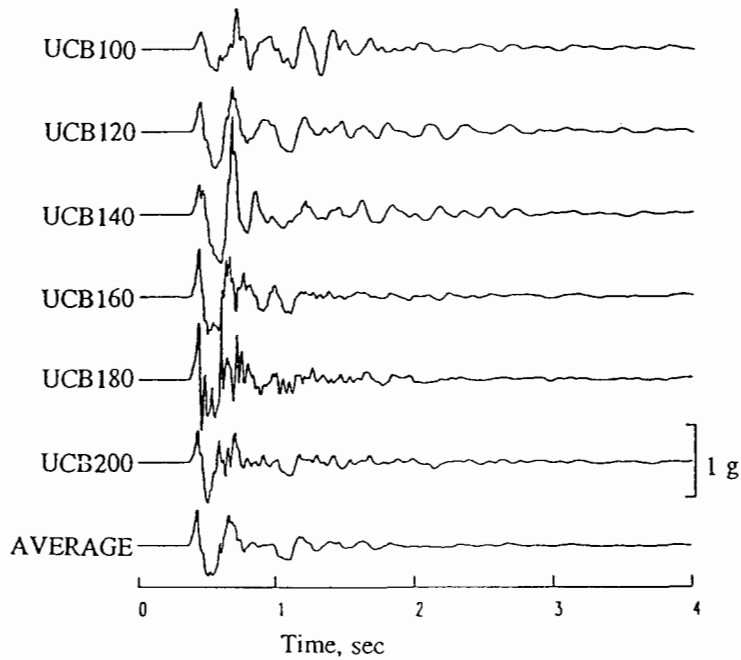


Figure 4. The vertical accelerations recorded from the NPE with up motion on the seismograms indicating upward motion of the ground. Also shown at the bottom is the average of the six vertical components. All seismograms are to the same scale, which is shown on the right where $1\text{ g} = 9.8\text{ m/s}$.

Table 2. Maximum Accelerations from Event NPE

Station	Azimuth deg	Range m	Distance m	max R cm/s**2	max T cm/s**2	max Z cm/s**2
UCB100	285	747	841	420	346	642
UCB120	279	656	759	790	463	661
UCB140	270	599	709	1310	706	1436
UCB160	259	616	724	615	266	714
UCB180	249	668	769	944	607	1053
UCB200	242	762	853	809	351	595

After time shifting to line up the first motions on the records, the seismograms at the six stations were averaged for each of the components separately to arrive at the traces shown in Figure 5. Note that the maximum accelerations on the average traces are less than the maximum accelerations on almost all of the stations (compare with Table 2), suggesting that the sharp peaks that are causing the maximum accelerations at the individual stations are not coherent between the stations. In general the average traces have the appearance of having less high frequency energy than the individual traces for the vertical and radial components, but not on the transverse component.

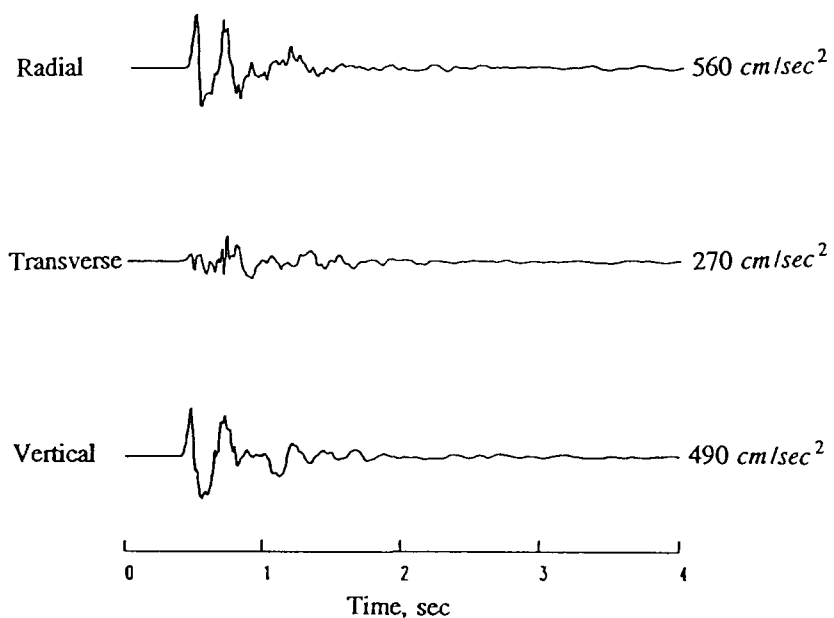


Figure 5. The average of the accelerations at the six stations for each component of motion. Time shifts to line up the first motions on the records were applied before the averages were calculated.

First Arrival Times

With the origin time of the NPE known and absolute timing at the recording stations, it was possible to measure the time of first arriving energy at each station and then calculate the travel time. These travel times are listed in Table 3 along with an apparent average velocity, which was obtained by dividing the slant distance by the travel time. These apparent velocities are rather slow, generally less than 2.0 km/sec. Also apparent in Table 3 is the fact that there is a systematic change in the apparent average velocity along the profile, with the north end generally being slower than the south end. This could be caused by either a lateral gradient in the average velocity of Rainier Mesa in the upper 400 meters or by a lateral change in delays in low velocity material in the upper few meters of Rainier Mesa.

Table 3. Travel Times from Event NPE

Station	Azimuth	Range deg	Distance m	Travel Time sec	Mean Vel. km/sec
UCB100	285	747	841	0.476	1.77
UCB120	279	656	759	0.432	1.76
UCB140	270	599	709	0.393	1.80
UCB160	259	616	724	0.363	1.99
UCB180	249	668	769	0.381	2.01
UCB200	242	762	853	0.402	2.12

Velocity Model

As mentioned in the introduction, an earlier part of this experiment had included a reflection survey on the surface of Rainier Mesa along the same profile where the recording stations were located. The velocity profile produced by the interpretation of these reflection data was thus available for the interpretation of the waveform data recorded from the NPE. The initial analysis of the data has used a one-dimensional model of the structure, with material properties varying only in the vertical direction. This model is shown in Figure 6. Only the P velocity of this model was derived from the reflection data, and considerable use of the geological information obtained from drill holes (Baldwin et al., 1994) was used in the interpretation. That is, where the reflection data provided evidence of an increase or decrease of P velocity in a particular depth range, the model depth was adjusted to be in general agreement with the changes in lithology suggest by the logging information from the drill holes. The P velocity model was also constrained to agree with the travel times of first arrivals given in Table 3, which is essentially an apparent average velocity of 2.0 km/sec between the NPE and the recording profile. The S velocity and density were then derived from the P velocity using ratios consistent with measurements of velocity and density obtained from the drill holes. The net result is a one-dimensional model which is generally consistent with the reflection data, the geological data, and the first arrival times from the NPE.

The general features of the velocity model include rather low velocities in the weathered layer at the surface but these increase rapidly in the caprock of the mesa, the Rainier Mesa Tuff. There appears

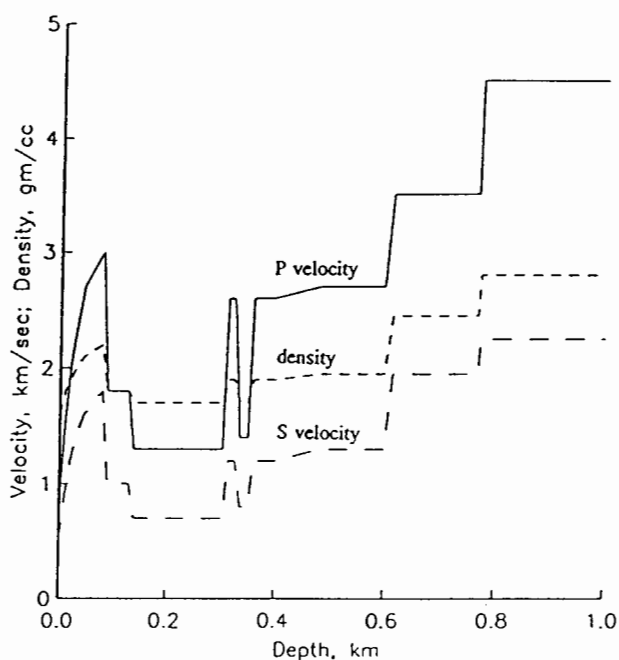


Figure 6. Velocity and density model for the upper part of Rainier Mesa in the vicinity of the NPE.

to be a decrease in velocity part way through this unit (depth of 80 meters) and a further decrease at its bottom. The underlying unit, the Paintbrush tuff, has very low velocities, but the velocities increase before reaching the depth of the NPE (389 meters) in the Tunnel Beds Units. Below the explosion depth there is a further increase in the velocity and then the Paleozoic basement is encountered at a depth of about 775 meters. In this model the material properties at the depth of the NPE are

$$P \text{ velocity} = 2.6 \text{ km/sec}$$

$$S \text{ velocity} = 1.2 \text{ km/sec}$$

$$\text{density} = 1.9 \text{ gm/cc}$$

Moment Tensor Solution

The waveform data recorded by this experiment were subjected to the standard moment tensor inversion method (Stump and Johnson, 1977). All three components from the six stations were used in the inversion, for a total of eighteen seismograms, and the first 8.1 sec of data were included from each seismogram. Estimates for the six independent elements of the force moment tensor are shown in the time domain in Figure 7. It is clear that the moment tensor is dominated by its diagonal elements, as one would expect for a simple explosion. There is a slight asymmetry in these diagonal elements, the 33 term being larger than the 11 and 22 components. This same effect has been observed for other explosions at NTS and suggests that the explosion expands more in the vertical direction than in the horizontal direction, but the exact cause of this effect is not understood.

The *isotropic moment tensor* (average of the three diagonal elements) was taken as the symmetric part of the seismic source and subjected to further analysis. The modulus of the time derivative of this isotropic moment tensor is shown in the frequency domain in Figure 8. Comparing this modulus to the

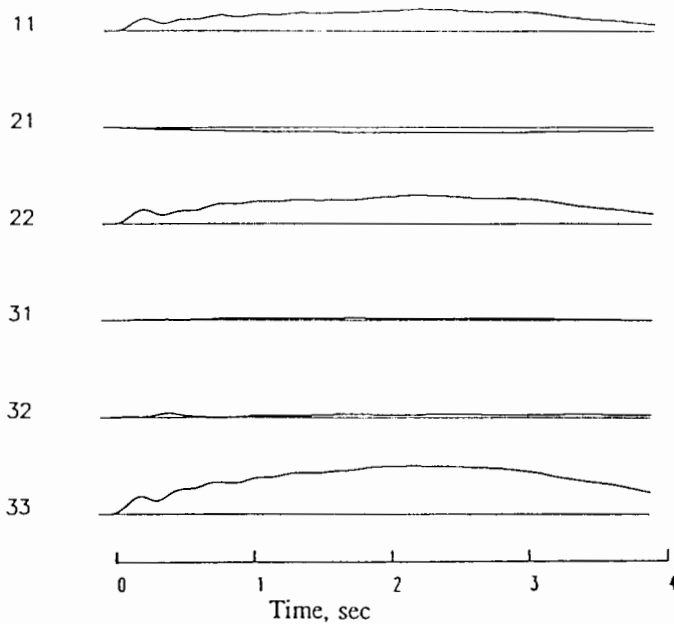


Figure 7. Estimates of the force moment tensor for the NPE. The directions are chosen so that 1 is north, 2 is east, and 3 is down. The maximum on the 33 component has a value of $160 \cdot 10^{20}$ dyne cm.

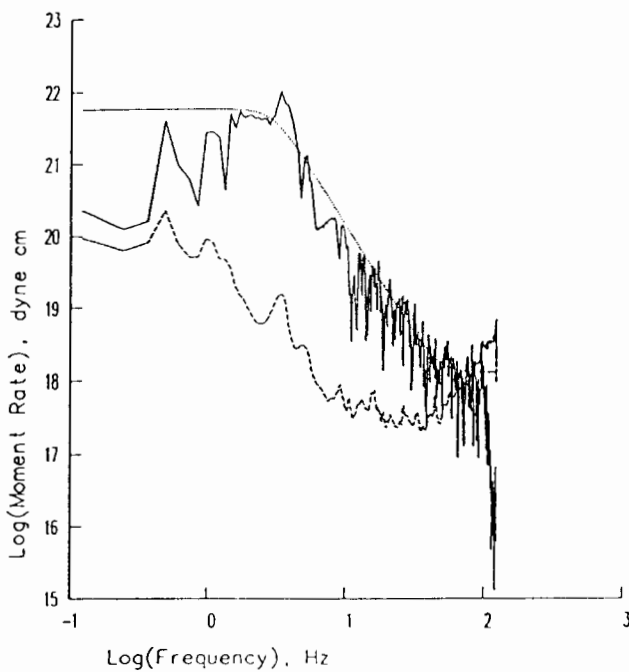


Figure 8. The modulus of the Fourier transform of the isotropic moment rate tensor (solid line). The dashed line is an estimate of the uncertainty in the estimate and the dotted line is a parametric model which was fit to the modulus.

estimated uncertainty, there appears to be a good signal-to-noise ratio in the range between about 0.4 and 60 Hz. Within this range there is a slight increase in the modulus with increasing frequency up to a corner frequency at about 3 Hz, although the data show considerable variation in this low frequency range. Beyond the corner frequency the modulus shows a steady decrease with increasing frequency until the noise floor is reached.

The interpretation of the spectrum of the isotropic moment tensor is facilitated by parameterizing it in terms of a spectral model. In the present study the spectral model was

$$|M(f)|^2 = \frac{P_1^2}{1 + 2(2P_4^2 - 1)(f/P_2)^{P_3} + (f/P_2)^{2P_3}} + P_5$$

where

- P_1 is the low frequency level, or scalar moment
- P_2 is the corner frequency
- P_3 is the high frequency decay rate
- P_4 is the damping parameter (1 for critical damping)
- P_5 is the variance of the signal independent white noise

This model was fit to the observed spectral modulus by a maximum likelihood procedure using an algorithm developed by Ihaka (1985). The dotted line in Figure 8 was obtained with this procedure with the damping constrained to have a critical value ($P_4 = 1.0$). Critical damping means that there is no peaking in the frequency domain and no overshoot in the time domain. With this type of model the estimated parameters are

- spectral parameters - without overshoot
- | | |
|----------------------|------------------------|
| scalar moment | $57 10^{13} N \cdot m$ |
| corner frequency | 2.9 Hz |
| damping | 1.0 |
| high-frequency decay | 3.0 |

It is clear in Figure 8 that the parametric fit without overshoot does not do a good job of representing the spectrum at frequencies less than the corner frequency. Thus another fit was performed in which the damping was unconstrained and this produced the results shown in Figure 9. The estimated parameters in this case are

- spectral parameters - with overshoot
- | | |
|----------------------|------------------------|
| scalar moment | $20 10^{13} N \cdot m$ |
| corner frequency | 3.3 Hz |
| damping | 0.09 |
| high-frequency decay | 2.6 |

This fit is considerably better at low frequencies, suggesting that a model with damping considerably less than critical is appropriate for the estimated isotropic moment tensor. Note that the two fits to the spectrum differ primarily in their values for the scalar moment, which is more than 2.5 times smaller for the case with overshoot.

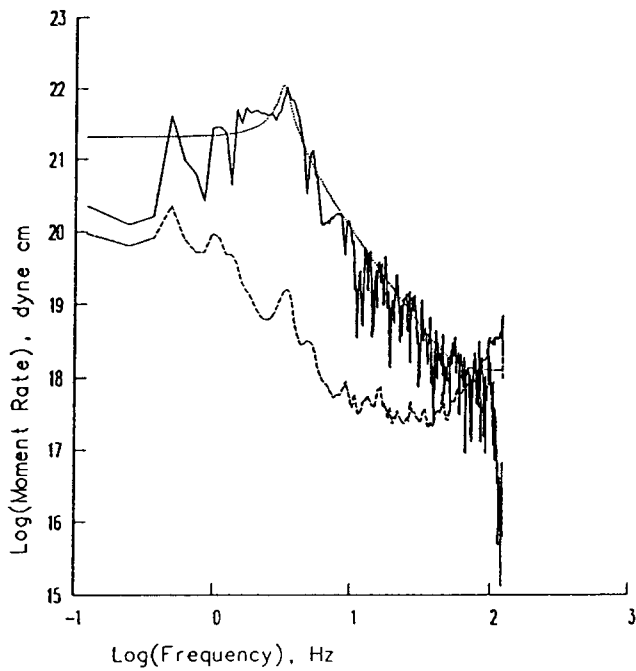


Figure 9. Similar to Figure 8 except that the parametric model fit to the modulus (dotted line) includes a damping parameter.

Scaling Relationships

The spectral parameters estimated for the isotropic moment tensor of the NPE were converted to source properties using the scaling relationships of Denny and Johnson (1991). The working point properties which were used in these calculations were as follows:

P velocity	$\alpha = 2.6 \text{ km/sec}$
S velocity	$\beta = 1.2 \text{ km/sec}$
density	$\rho = 1.9 \text{ gm/cc}$
pressure	$P_o = 7.2 \text{ MPa}$
gas porosity	$GP = 1\%$

Then the relationship between the yield W and scalar moment M_o is given by

$$W = 294 10^{-12} \beta^{1.1544} P_o^{0.4385} 10^{0.0344GP} \frac{M_o}{4\pi\rho\alpha^2}$$

Using the scalar moment estimated above for the case where overshoot is included, the estimated yield for the NPE is

$$W = 1.4 \text{ kt}$$

which is about 30% greater than the announced yield for this event. The scalar moment can also be converted to the static reduced displacement potential Ψ_∞ through the relation

$$\Psi_\infty = \frac{M_o}{4\pi\rho\alpha^2}$$

which yields in the present case

$$\Psi_{\infty} = 1240 \text{ m}^3$$

The relationship between the elastic radius R_s and the corner frequency f_c is given by

$$R_s = \frac{\beta}{\pi f_c}$$

Again using the parameters estimated for the case with overshoot, the result is

$$R_s = 116 \text{ m}$$

This can be converted to the cavity radius R_c using the scaling relationship

$$R_c = \frac{9443}{(\rho \beta^2)^{0.7245} P_o^{-0.2897}} R_s$$

which yields

$$R_c = 15.5 \text{ m}$$

Summarizing the results for the case where overshoot is allowed in the parametric model of the moment tensor, the estimates for the NPE are as follows:

scalar moment	$M_o = 20 \cdot 10^{13} \text{ N m}$
static RDP	$\Psi_{\infty} = 1240 \text{ m}^3$
yield	$W = 1.4 \text{ kt}$
elastic radius	$R_s = 116 \text{ m}$
cavity radius	$R_c = 15.5 \text{ m}$

If these calculations are repeated with the fit to the isotropic moment spectrum that does not have overshoot, the results are:

scalar moment	$M_o = 57 \cdot 10^{13} \text{ N m}$
static RDP	$\Psi_{\infty} = 3530 \text{ m}^3$
yield	$W = 4.1 \text{ kt}$
elastic radius	$R_s = 132 \text{ m}$
cavity radius	$R_c = 17.6 \text{ m}$

It is clear that inclusion or exclusion of overshoot in the spectral model can have a significant effect upon the estimated yield.

Discussion and Summary

The present study was only a preliminary interpretation of one of the seismic experiments which was performed in the local distance range. It was rather limited in the amount of seismic data which were used and the fraction of the focal sphere which was sampled. However, it did have the advantage of being coordinated with a companion study specifically designed to determine the velocity structure which is required in the interpretation of the waveform data. It was possible to make estimates of several properties of the NPE explosion, including its yield, its physical dimension, and the amount of overshoot in its time function. Of course, the validity of these estimates can only be determined by comparing them with the other results that were obtained for the NPE.

In this preliminary interpretation of the data, only a one-dimensional velocity model was used. The variation in travel times of first arrivals, however, indicates that there are some definite three-dimensional effects which should be investigated. It is not clear whether these are systematic variations that involve the upper few hundred meters of the mesa or just local effects that involve the upper few meters under each seismographic station. The fact that some of the high frequency acceleration pulses on the seismograms do not correlate well between adjacent stations suggests that some of these local effects are present. Further study is necessary in order to explore the sensitivity of the results to the details of the velocity model used in the inversion.

The interpretation of the spectrum of the moment tensor in terms of properties of the explosion source requires reliable estimates of frequencies below the corner frequency. In this case where the size of the explosion is actually quite small, the quality of these low frequency estimates is still rather marginal. The spectrum appears to be reliable above about 0.4 Hz, based on the signal-to-noise ratio, but there is considerable scatter in this range. Thus there is considerable uncertainty in extrapolating these values to zero frequency where the scalar seismic moment is defined, and this uncertainty translates directly into uncertainty in the estimated yield of the explosion.

The results of this study indicate that significant overshoot existed in the source time function of the NPE. This is suggested by the peaking in the spectrum of the isotropic moment tensor in the vicinity of the corner frequency and the fact that parameterized fits to the spectrum are better when overshoot is included. Further study to definitely establish the presence of this overshoot are warranted because it has several ramifications. If present, it implies that the spectral shape below the corner frequency is not flat, and thus various seismic methods that use different frequencies in this range to estimate the yield of the explosion will yield different results. In the present study it was found that including the effect of the overshoot changed the estimate of the yield of the NPE by almost a factor of 3.

The interpretation of the data collected in this experiment indicates a yield of 1.4 kt for the NPE, which is about 30% greater than the actual yield. It is important to understand the reason for this difference. First, it should be pointed out that most of the other seismic methods which have been applied to the NPE also overestimated the yield, so this discrepancy is not confined to the moment tensor inversion method. One possibility relates to the fact that the scaling relationships used to convert seismic measurements to yield are based primarily upon empirical data from nuclear explosions, and it is possible that different scaling relationships are required for chemical explosions. The study of Denny and Johnson (1991), which was used for the scaling relationships in the calculations of the present study, did include both chemical and nuclear explosions, but it contained very little data, either chemical or nuclear, on yield versus moment in the range around 1 kt. Thus this question of the difference between nuclear and chemical explosions still does not have a satisfactory answer.

The results presented in this preliminary study are incomplete in that uncertainties in the estimated values have not been given, a deficiency which will hopefully be corrected by further analysis. Part of this problem is straightforward, as formal uncertainty analysis has already been included in the fitting of spectral models and the use of the scaling relationships, so carrying such uncertainties through to the final estimates is possible. It should also be possible to place uncertainty bounds upon the material properties at the working point which were used in the calculations. However, there are other parts of the uncertainty issue which are more difficult to analyze. These involve

such matters as the uncertainty in the velocity model and various assumptions which were used in the inversion process. It appears that such effects will have to be investigated by repeating the analysis for a number of different sets of models and assumptions and in this way determine their effects upon the final estimates. While this is not a completely satisfactory approach from the viewpoint of a formal uncertainty analysis, it is better than ignoring such effects altogether.

Acknowledgements

The assistance of Don Lippert and Russell Sell in the field operations of this experiment is gratefully acknowledged.

References

- Baldwin, M. J., R. P. Bradford, S. P. Hopkins, D. R. Townsend, and B. L. Harris-West, Geologic characteristics of the NPE site in the U12n.25 drift of N-tunnel, Nevada Test Site, in Proceedings of the Symposium on the Non-Proliferation Experiment Results and Implications, M. D. Denny et al. (eds), Lawrence Livermore National Laboratory, Livermore, CA, CONF-9404100, 1994.
- Denny, M. D., and L. R. Johnson, The explosion seismic source function: models and scaling laws reviewed, in Explosion Source Phenomenology, Geophys. Monograph 65, American Geophysical Union, Washington, D.C., 1991.
- Ihaka, R., Ph.D. Dissertation, University of California, Berkeley, 1985.
- Johnson, L. R., Seismic source parameters, in Proceedings of the Symposium on the Non-Proliferation Experiment Results and Implications, M. D. Denny et al. (eds), Lawrence Livermore National Laboratory, Livermore, CA, CONF-9404100, 1994.
- Majer, E. L., L. R. Johnson, E. K. Karageorgi, and J. E. Peterson, High-resolution seismic imaging of Rainier Mesa using surface reflection and surface-to-tunnel tomography, in Proceedings of the Symposium on the Non-Proliferation Experiment Results and Implications, M. D. Denny et al. (eds), Lawrence Livermore National Laboratory, Livermore, CA, CONF-9404100, 1994.
- Stump, B. W., and L. R. Johnson, The determination of source properties by the linear inversion of seismograms, Bull. Seismol. Soc. Am., 67, 1489-1502, 1977.

Near-Source Surface Seismic Measurements for the NPE, NPE Calibration, Hunter's Trophy, and Mineral Quarry

**Robert E. Reinke and J. Al Leverette
Field Command Defense Nuclear Agency
1680 Texas St., SE
Kirtland AFB, NM 87117**

**Brian W. Stump, D. Craig Pearson, and C. L. Edwards
Geophysics Group, EES-3, MS-C335
Los Alamos National Laboratory
Los Alamos, NM 87545**

ABSTRACT

An extensive seismic network was deployed on the surface of Rainier Mesa for both the Non-Proliferation Experiment (NPE) Calibration shot as well as the full scale NPE event. This network was very similar to previous deployments for the nuclear events MISTY ECHO, MINERAL QUARRY, and HUNTERS TROPHY. For the full scale NPE event three-component accelerometers and seismometers were fielded at 32 sites across the mesa. A slightly smaller network with 28 stations was in operation for the 300 pound NPE calibration event. The mesa top array included both accelerometers and seismometers. The accelerometers were used to obtain data from the main NPE event while the seismometers with their higher sensitivity were used to record the 300 pound cal shot and several hundred after events from the NPE. Large spatial variations in ground motion are evident in both the full mesa data set as well as a small (80 m on a side) aperture, 9-element triangular array. This paper summarizes the data and discusses wave propagation effects. A companion paper (Stump et al.) presents a comparative source analysis.

INTRODUCTION

A cooperative DOD/DOE/ARPA experimental program was begun in 1988 to define the experimental elastic source function for nuclear explosions. As part of this integrated investigation, free-field (Olsen and Peratt, These proceedings) and free-surface observations were made on the nuclear explosions MISTY ECHO (ME, 10 Dec. 1988), MINERAL QUARRY (MQ, 25 July, 1990), and HUNTERS TROPHY (HT, 18 Sept., 1992) and the chemical explosions NON-PROLIFERATION EXPERIMENT (NPE, 22 Sept. 1993) and the NON-PROLIFERATION EXPERIMENT CALIBRATION (NPE CAL, 30 Oct. 1992) (Figure 1.). The same receiver sites were used for all events, thereby minimizing the influence of local receiver site effects upon the seismic source

study. The combination of free-field, free-surface, near-source network and free-surface small aperture array (8-80m) provides a unique opportunity for separation of propagation path effects from source processes. The data set includes observations from both nuclear and chemical sources. This coupled with the range of yields make the data set a unique resource for the characterization of source dominated processes which may be important in monitoring explosions in other environments.

This paper summarizes the data and presents some results of an effort to quantify stochastic wave propagation effects observed in the data set. The results of this characterization indicate that stochastic propagation effects are significant contributors to the observed waveforms, even at relatively low frequencies (< 10 Hz). The results of a stochastic source characterization are described in a companion paper (Stump, et al., These proceedings) describes a stochastic comparison of the various explosive sources in the frequency domain.

RAINIER MESA NETWORK DESIGN AND INSTRUMENTATION

The Rainier Mesa free-surface, seismic network is shown in Figure 1 together with locations of the surface GZs for the nuclear and chemical events. This network was in operation for the MINERAL QUARRY, HUNTERS TROPHY, NPE CALIBRATION and the NPE tests. A similar but less extensive array was in operation for MISTY ECHO. A small aperture, 9-element, nested triangle array was operated as part of the overall network (Figures 1 and 2). The network station locations were chosen in order to provide a uniform distribution of stations across the mesa while remaining on roads and existing previously disturbed areas to minimize environmental impact. The small aperture array was included as part of the network in order to study spatial variability in ground motion, scattering and effects of heterogeneity, and small scale receiver site effects.

Terra Technology 3-component, force-balance accelerometers (0-100 Hz response) were used as the sensors for all of the large events. Sprengnether S-6000, 3-component seismometers (2 Hz natural frequency) were used to measure the relatively low level after events following the large tests as well as signals from the small NPE CAL shot. A combination of 3-channel Terra Technology 12 bit recorders and 6-channel Refraction Technology 16 bit units was used to record signals from all of the events. The station locations were surveyed with hand held GPS receivers. Recorder timing was provided by WWVB time signals for the Terra Technology recorders and GOES satellite clocks for the Refraction Technology units.

RAINIER MESA FREE-SURFACE INSTRUMENTATION PLAN

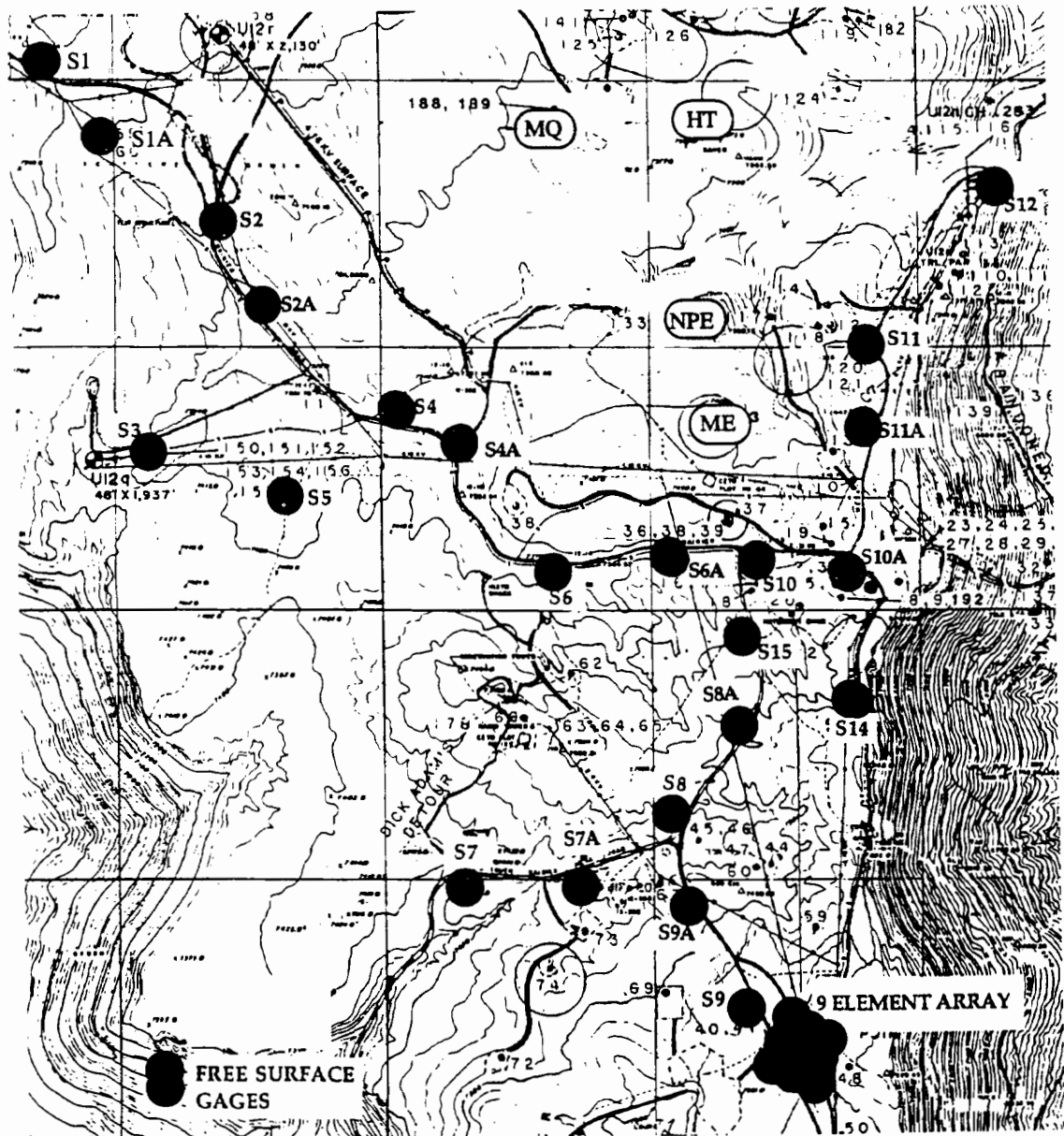


Figure 1. Rainier Mesa near-source free surface network for the experiments Misty Echo (ME), Mineral Quarry (MQ), Hunters Trophy (HT), Non-Proliferation Experiment (NPE) and NPE CAL (same location as the NPE).

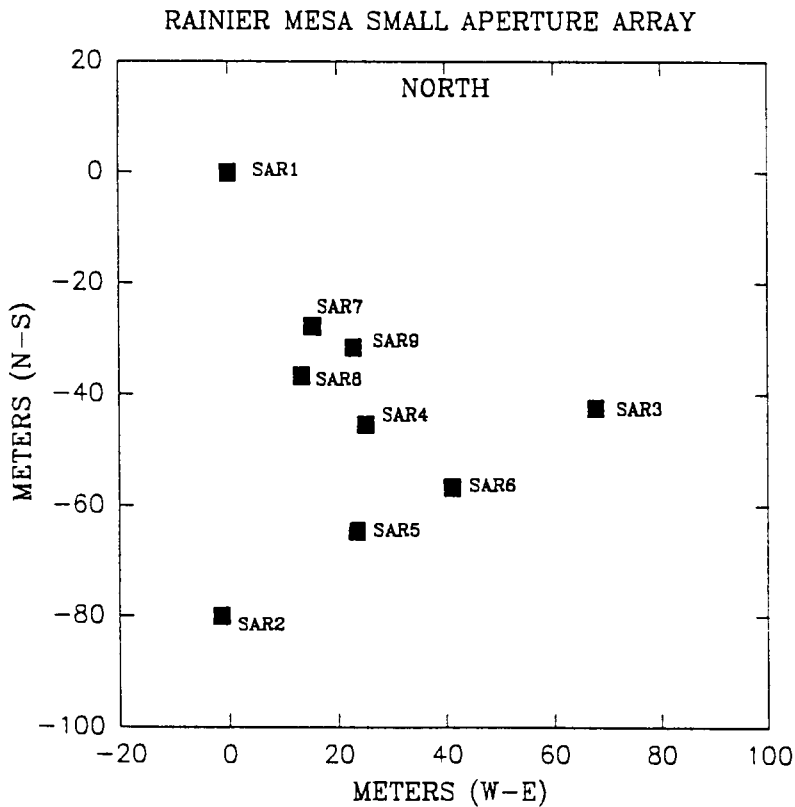


Figure 2. Layout of the small aperture array.

DATA SUMMARY

The following data sets have been recovered from the Rainier Mesa Seismic Network:

- MISTY ECHO - 32 channels acceleration
- MINERAL QUARRY - 99 channels acceleration
- HUNTERS TROPHY - 96 channels acceleration, 57 channels velocity
- NPE CALIBRATION - 81 channels velocity
- NPE - 93 channels acceleration, 60 channels velocity

A sample of the observed network seismograms for the HUNTERS TROPHY, NPE, and NPE CAL events is shown in Figures 3a and 3b. The variability in the waveforms illustrate the wide variation in site response observed across the mesa. The HUNTERS TROPHY peak amplitude vs range plot in Figure 4 serves to further illustrate this point. Almost an order of magnitude variation in peak amplitude across the mesa is present at the same range from the surface GZ. Figure 5 shows a comparison of the NPE CAL peak amplitudes vs range with the Perret and Bass (Perret and Bass, 1974) predictions for wet and dry tuff. The observed scatter in the data is of the same order as the separation between the wet and dry tuff predictions.

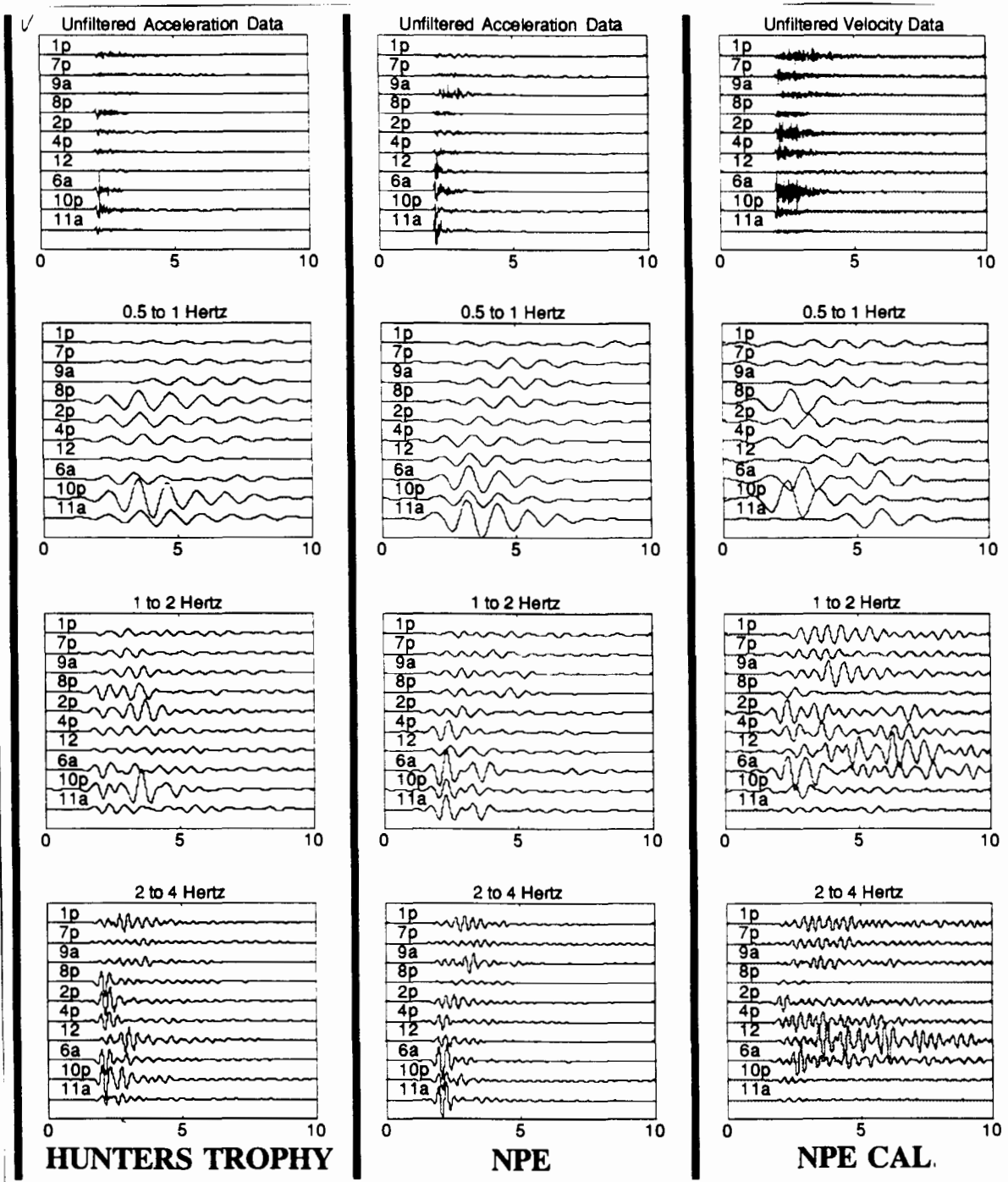
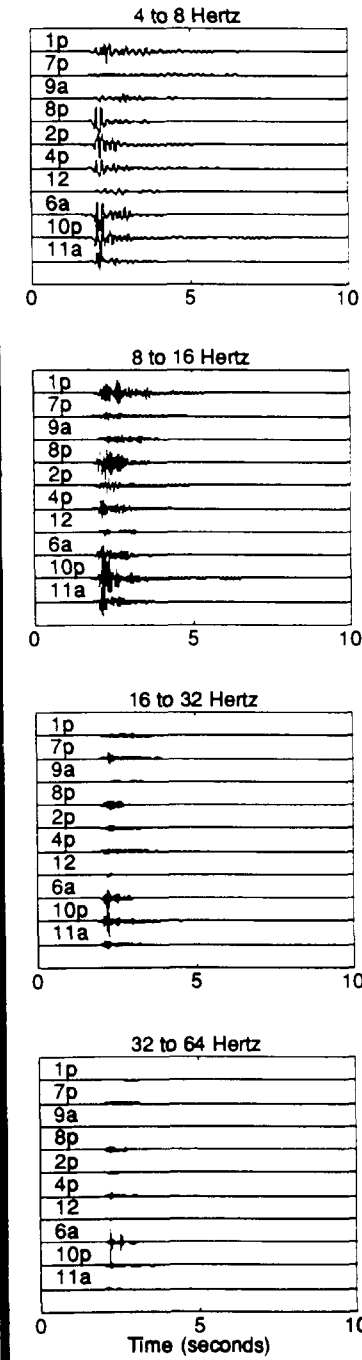
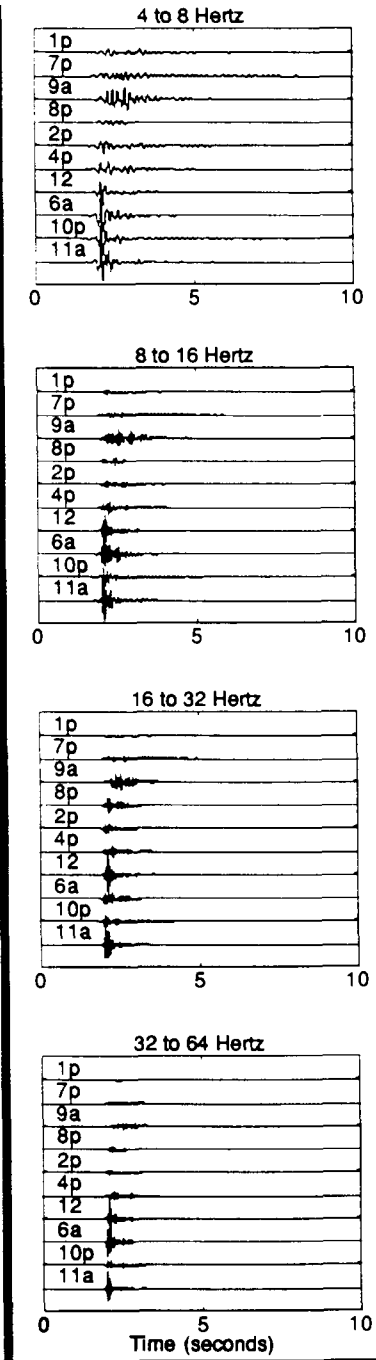


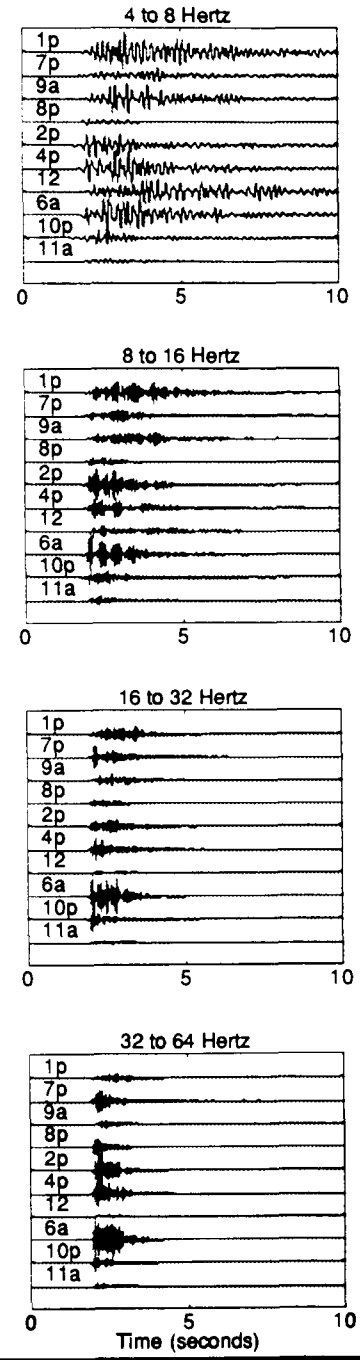
Figure 3a. Sample of unfiltered and filtered vertical waveforms from the Rainier Mesa Seismic Network.



HUNTERS TROPHY



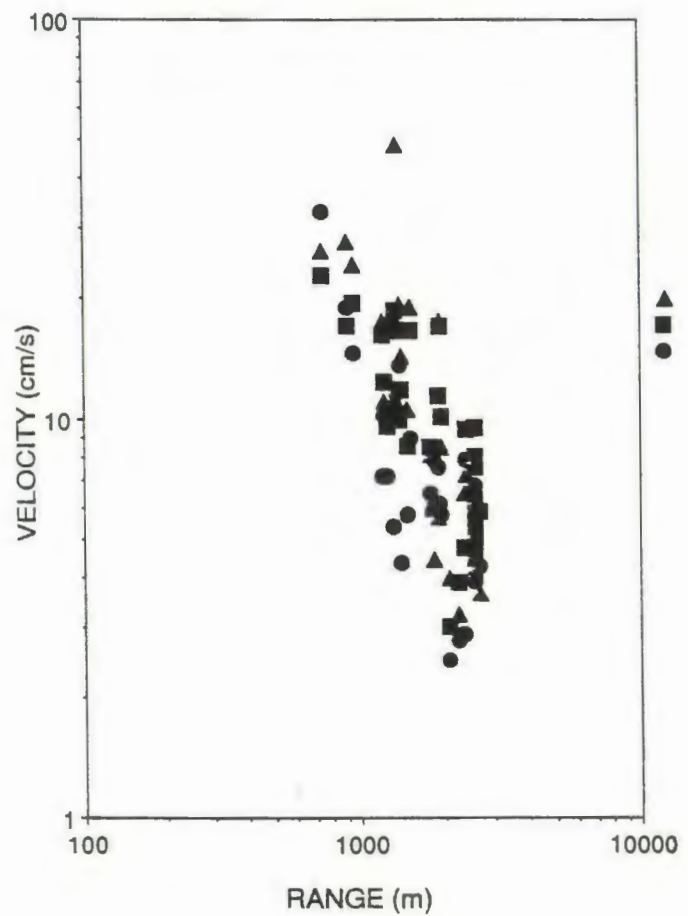
NPE



NPE CAL

Figure 3b. Sample of filtered vertical waveforms from the Rainier Mesa Seismic Network.

HUNTERS TROPHY DATA



NPE CAL PREDICTIONS AND DATA

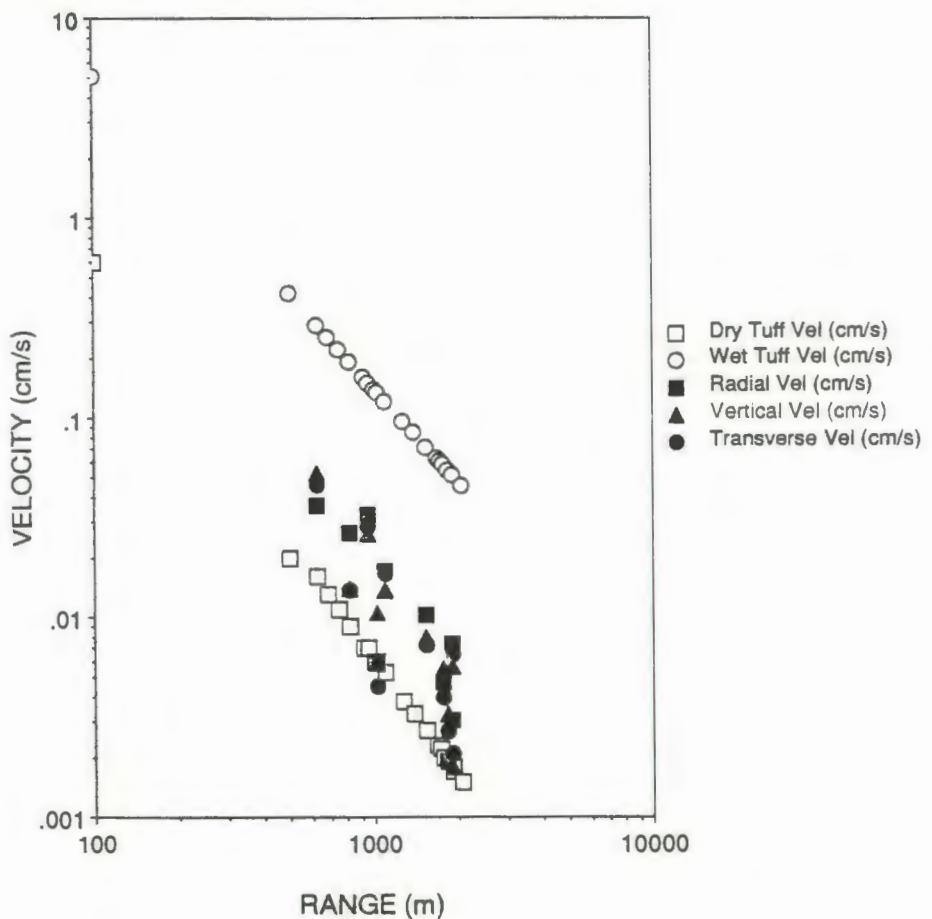


Figure 4. Peak network velocity amplitudes for HUNTERS TROPHY.

Figure 5. Peak network velocity amplitudes for the NPE CAL compared with Perret and Bass predictions for wet and dry tuff.

THE SMALL APERTURE ARRAY

The small aperture array (Figures 1 and 2) was fielded in order to quantify small scale variations in site response. The array consisted of 9 elements placed in a nested equilateral triangle configuration. The smallest triangle was 8 meters on a side, the intermediate triangle, 20 meters on a side, and the large triangle, 80 meters on a side. Each element was composed of a 3-component Terra Technology accelerometer for MINERAL QUARRY, HUNTERS TROPHY and the NPE. Sprengnether S-6000, 3-component seismometers were used for the NPE CAL. The sensors were recorded by Terra Technology 12-bit digital event recorders. The data were sampled at 200 samples/second. The array was controlled by a master recorder which triggered all other recorders in the array. This recorder also provided common WWVB corrected timing to each of the other array recorders.

Large variations in waveform character and response were observed across the array on all events. Figures 6, 7, and 8 compare the vertical component array waveforms from the HUNTERS TROPHY, NPE CAL, and the NPE events. The NPE CALIBRATION is the extreme example with an order of magnitude variation in peak response observed across the extent of the 80 meter array. This variability is also seen in the amplitude vs range plots in Figures 4 and 5. The array values in these plots - the vertical grouping of points at the same range - exhibit the same magnitude of scatter as do measurements across the full mesa network.

STOCHASTIC CHARACTERIZATION

The degree of observed spatial variability in site response across even the relatively small extent of the small aperture array suggests that stochastic characterization of the data set is required before analysis of source effects can begin. We chose to perform this characterization in the frequency domain utilizing only the amplitude information and discarding the phase information. For the small aperture array, amplitude spectra were computed for each element. A 1024 point sample window, 5.12 seconds in length, was used with a rectangular window. After amplitude spectra were computed a 7-point smoothing window was applied. Mean and the mean \pm 1 standard deviation were then computed in the log domain for each component of the array spectra. Examples of the mean and mean \pm 1 standard deviation spectra are shown in Figures 9, 10, and 11 for the vertical component of the NPE recorded at the small aperture array. To further quantify the degree of variability the coefficient of variation (CV) was used. The CV is defined as the ratio of the standard deviation to the mean and thus represents a normalized measure of the variability associated with a set of measurements. The array CVs for the NPE are shown to the right of each spectral plot in Figures 9, 10, and 11. The CVs are low for the long periods but begin to rise at 3 to 4 Hz., and approach 0.5 in the 10 to 100 Hz. band reflecting the increase in scattering effects across the 80 meter array for the shorter wavelengths.

6-129

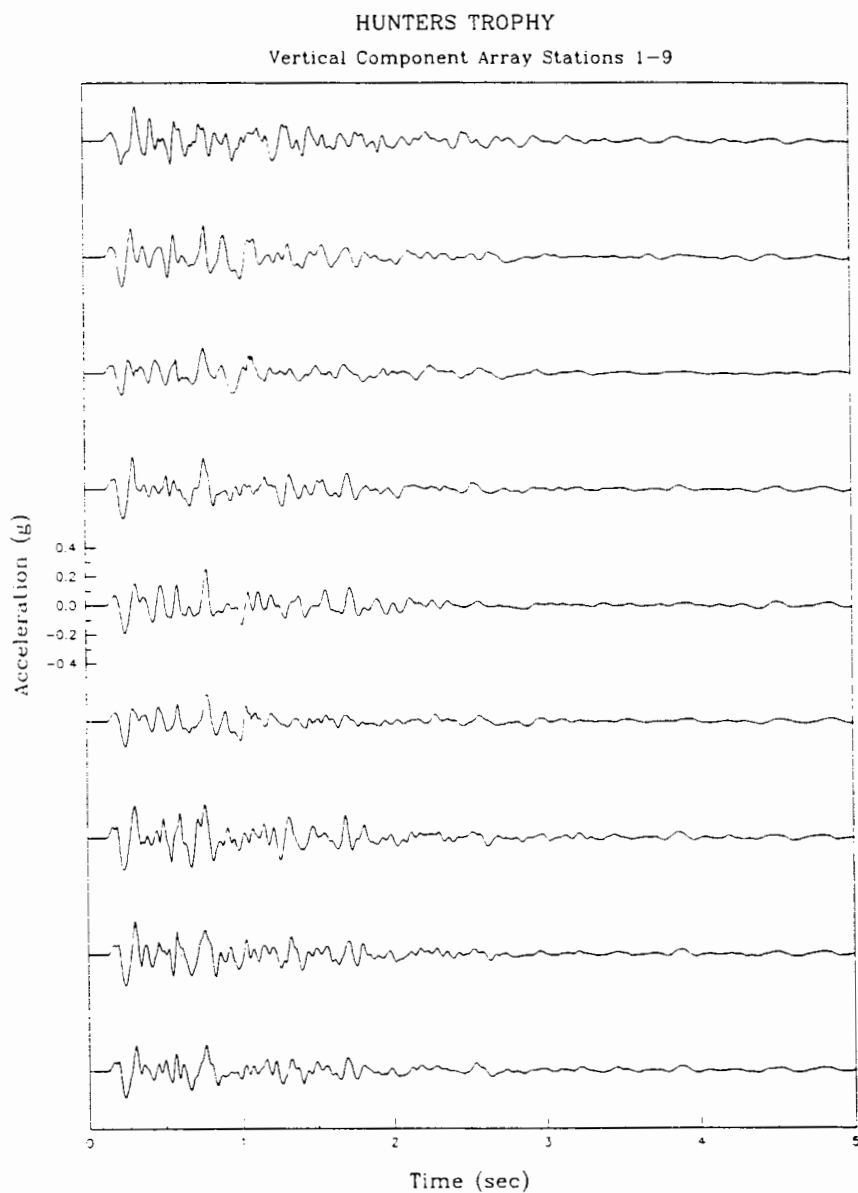


Figure 6. Vertical small aperture array records for HUNTERS TROPHY.

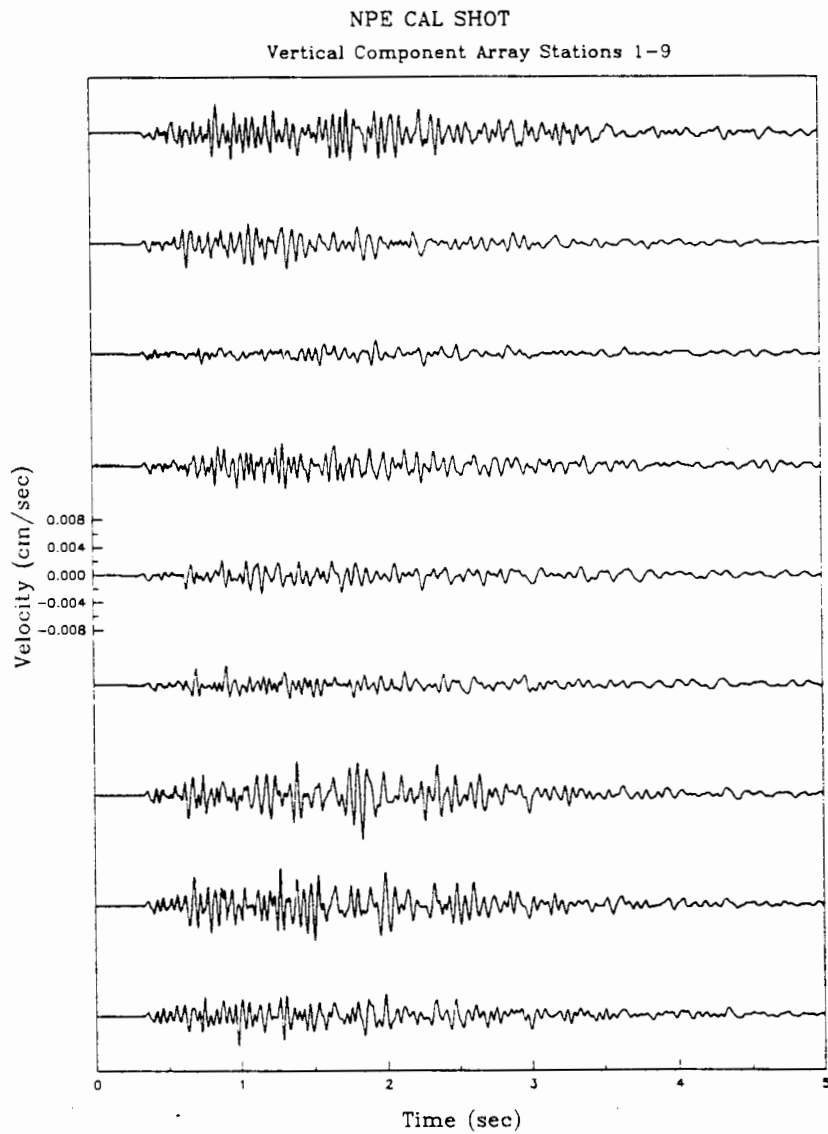


Figure 7. Vertical small aperture array records for the NPE CAL.

0E1-9

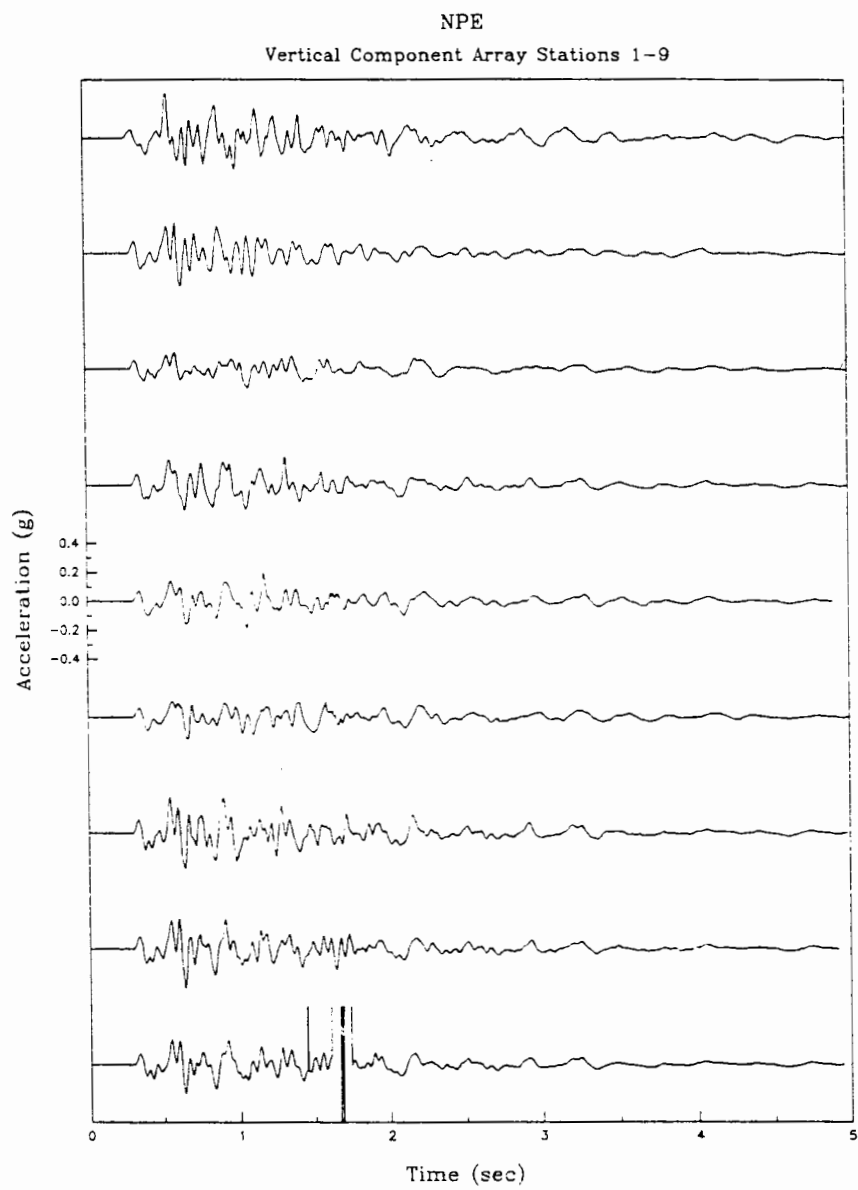


Figure 8. Vertical small aperture array records for the NPE.

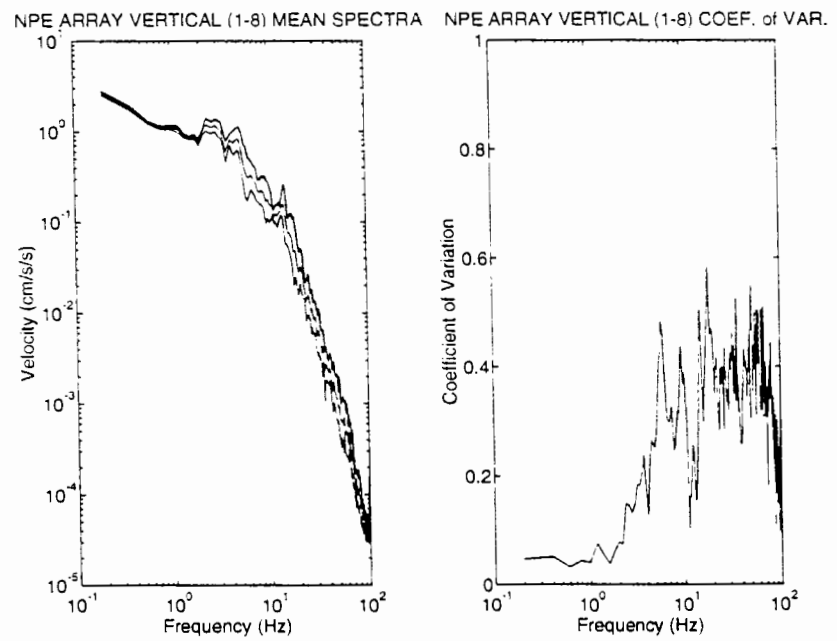


Figure 9. Mean and mean ± 1 standard deviation spectra with the coefficient of variation for the vertical component NPE records recorded at the small aperture array.

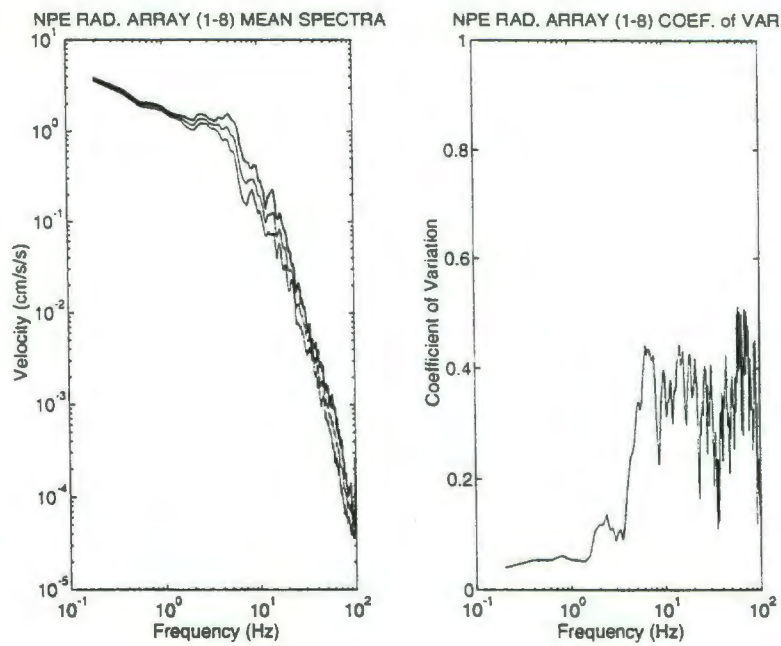


Figure 10. Mean and mean ± 1 standard deviation spectra with the coefficient of variation for the radial component of the NPE recorded at the small aperture array.

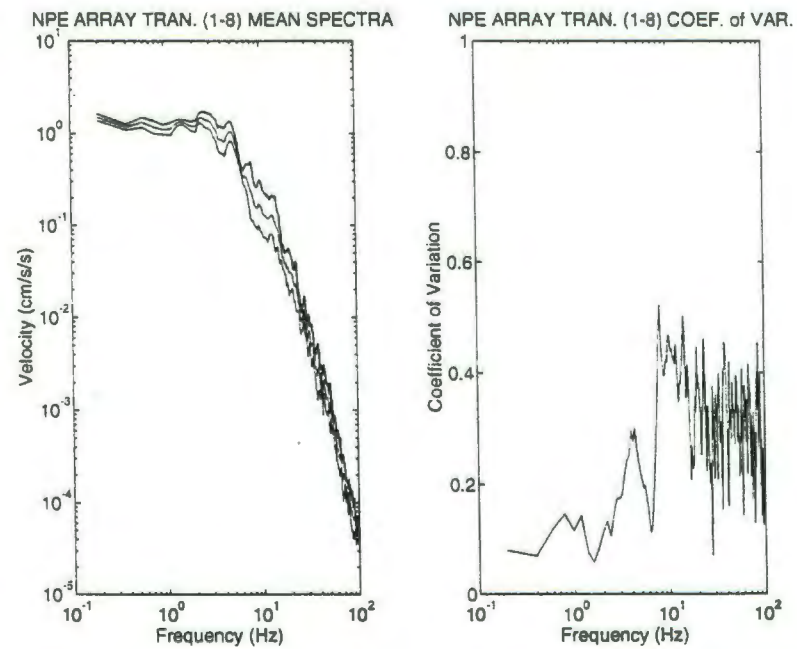


Figure 11. Mean and mean ± 1 standard deviation spectra with the coefficient of variation for the transverse component of the NPE recorded at the small aperture array.

Similar computations were performed for the NPE CAL, HUNTERS TROPHY and MINERAL QUARRY as observed at the small aperture array. Comparisons of the CVs for the 3 components are shown in Figures 12, 13, and 14. With the exception of the frequencies below 2 Hz. for the NPE CAL event, the CVs compare well from event to event. The high CVs below 2 Hz. on the NPE CAL are thought to be due to loss of signal because of the limited dynamic range of the 12-bit recorders. The similarity between array CVs from event to event indicates that the observed variability is indeed caused by local site effects.

The degree of variability observed in the small aperture array records of these explosive events demonstrates the need to separate stochastic and deterministic wave propagation effects before seismic source characteristics can be inferred from the data. Similar degrees of spatial variability in ground motion have been found at other sites. McLaughlin et al. (1983) discuss the station-to-station waveform coherence for near-source explosion accelerograms recorded on a nine-element array at Pahute Mesa. For this array (100-m interelement spacing), at a range of 6 km from an underground nuclear test, strong incoherent signals were found above 5 Hz on all components.

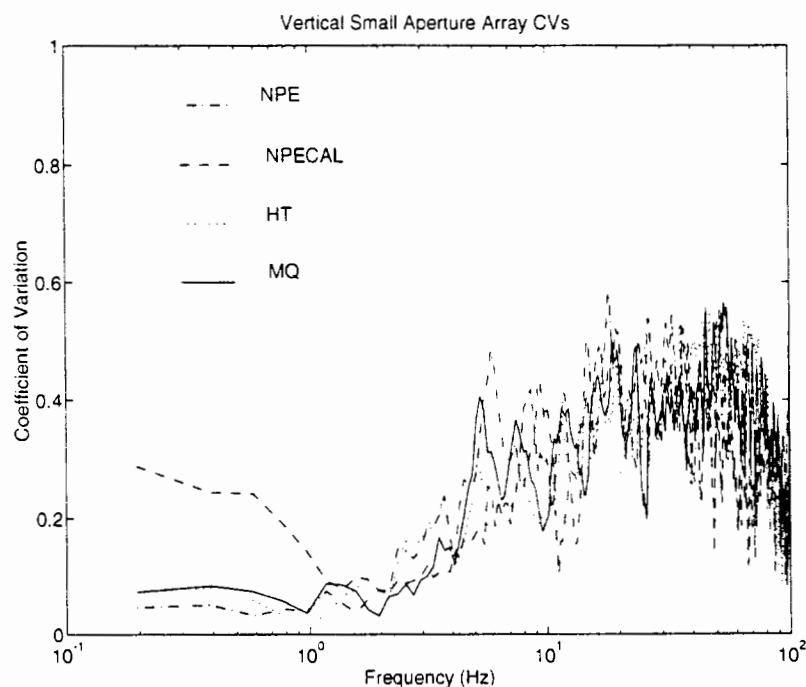


Figure 12. Comparison of vertical small aperture array CVs for MQ, HT, NPE, and the NPE CAL.

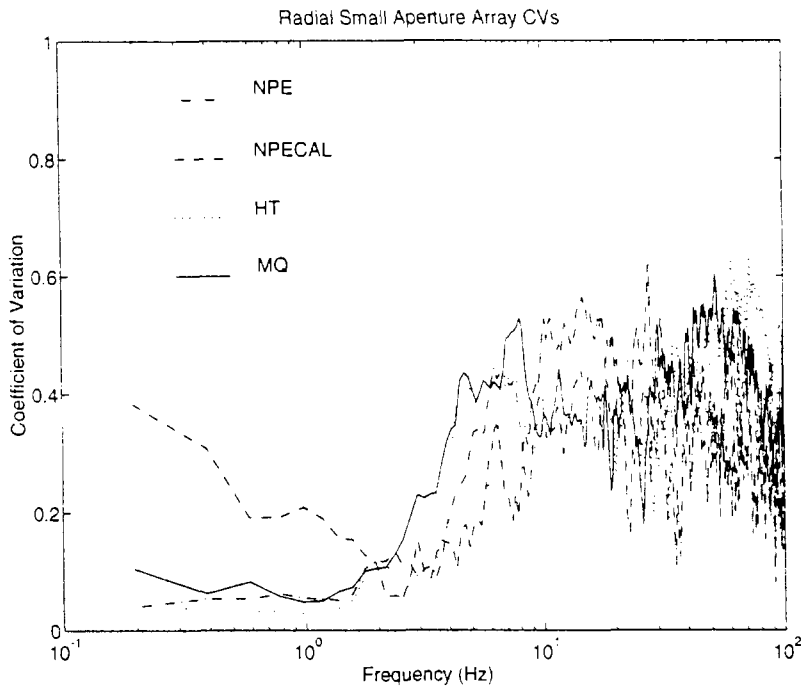


Figure 13. Comparison of radial small aperture array CVs for MQ, HT, NPE, and the NPE CAL.

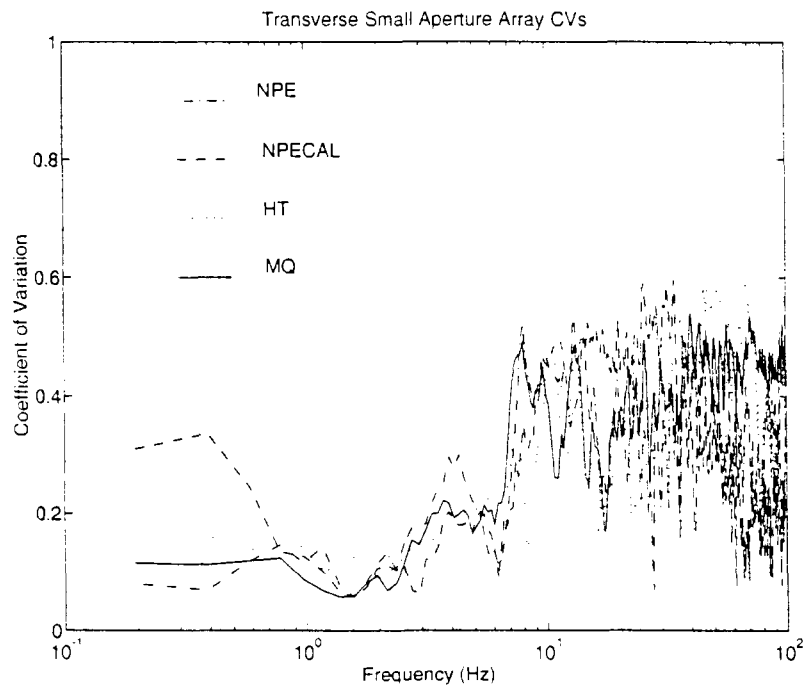


Figure 14. Comparison of transverse small aperture array CVs for MQ, HT, NPE, and the NPE CAL.

Vernon et al. (1985) discuss earthquake seismogram coherence for a nine-station array with an interstation spacing of 50 m located near the Pinyon Flat observatory in California. For observations at this array, P waves were found to be coherent to 25 to 35 Hz, with S waves coherent to 15 Hz. Menke et al. (1990) discuss the coherence of regional signals recorded at small (96-200 m spacing) scale arrays on hard rock sites in New England. They found that the spatial coherence at these array sites was on the order of one-sixth to one-half of a wavelength even though the arrays were placed in sites which appeared to be quite homogeneous. Vidale et al. (1990) found a lack of azimuthal symmetry and a large degree of incoherence in small-scale array observations of aftershocks of the Loma Prieta earthquake. Reinke and Stump (1991) discuss the spatial variability of near-source signals from small-scale explosions in alluvium. They found a loss of coherence above 15-30 Hz for array elements separated by a few tens of meters.

The results from the Rainier Mesa small aperture array together with the limited examples of similar studies found in the literature demonstrate the danger of making inferences of seismic source characteristics from single point measurements. With only one or two measurements it is not possible, above a given frequency, to distinguish between true source influences on the recorded waveforms and local site effects. The large number of measurements obtained by the Rainier Mesa seismic network enables local site effects to be smoothed out of the data set so that true source comparisons can be made for the various nuclear and chemical events. This is discussed in detail in the companion paper (Stump et al., These proceedings).

CONCLUSIONS

The seismograms recorded by the Rainier Mesa seismic network for the NPE, NPE CAL, MINERAL QUARRY, HUNTERS TROPHY, and MISTY ECHO events represent a unique data set for the study and comparison of source processes for underground nuclear and chemical explosions. The data set allows for the study and quantification of spatial variability in ground motion due to local geologic site effects. The degree of variability observed across the small scale of the small aperture array is perhaps initially discouraging. The consistency of the array CVs from event to event, however, gives encouragement that the data can be successfully analyzed for source effects in a stochastic fashion. The results from the small aperture array coupled with similar studies found in the literature point out the danger of inferring seismic source characteristics from single point measurements. The relatively large number of measurements obtained by the Rainier Mesa seismic network for the nuclear and chemical events allows the influences of small-scale variability in geology to be smoothed out so that true source characteristics can be determined. This is discussed in detail in the companion paper, (Stump et al., These proceedings).

ACKNOWLEDGEMENTS

This work was performed under the auspices of the Defense Nuclear Agency, the Air Force Phillips Laboratory, the Advanced Research Projects Agency by Southern Methodist University under contract F29601-91-D-DB20, and the U.S. Department of Energy by Los Alamos National Laboratory under contract W-7405-ENG-36.

REFERENCES

- McLaughlin, K., L. Johnson, and T. McEvily, Two-dimensional array measurements of near-source ground accelerations, **Bull. Seismol. Soc. Am.**, 73, 349-376, 1983.
- Menke, W., A. Lerner-Lam, B. Dubendorff, and J. Pacheco, Polarization and coherence of 5-30 Hz wavefields at a hard rock site and their relevance to velocity heterogeneities in the crust, **Bull. Seismol. Soc. Am.**, 80, 430-449, 1990.
- Perret, W.R. and R.C. Bass, Free-field ground motion induced by underground explosions, SAND74-0252, Sandia National Laboratories, Albuquerque, New Mexico, 1974.
- Reinke, R. and B. Stump, Experimental studies of stochastic geologic influences on near-source ground motions, in **Explosion Source Phenomenology**, S. Taylor, H. Patton, and Paul Richards, editors, Geophysical Monograph 65, American Geophysical Union, 1991.
- Vernon, F., J. Fletcher, L. Haar, T. Bolswick, E. Semenza, and J. Brune, Spatial coherence of bodywaves from local earthquakes recorded on a small aperture array, **EOS Trans. Am. Geophys. Union**, 66, 954, 1985.
- Vidale, J., O. Bonamassa, and S. Schwartz, Array studies of ground motions using aftershocks from the Loma Prieta Earthquake, **Seismol. Res. Letters**, 61, 24, 1990.

Stochastic Source Comparisons Between Nuclear and Chemical Explosions Detonated at Rainier Mesa, Nevada Test Site

**Brian W. Stump
D. Craig Pearson
Geophysics Group, EES-3, MS-C335
Los Alamos National Laboratory
Los Alamos, NM 87545**

**Robert E. Reinke
Field Command Defense Nuclear Agency
1680 Texas St. SE
Kirtland AFB, NM 87117**

I. INTRODUCTION/MOTIVATION

Seismic source functions are used to quantify the generation of body and surface waves from a wide variety of physical phenomena. Careful quantification of the relative excitation of the different seismic phases can be used to identify the source type. The geometry of the source has a strong influence on the types of waves a particular source generates. The different source types include earthquakes which are considered deviatoric in nature and explosions which are represented in their simplest form as isotropic or spherically symmetric. The deviatoric characteristic of earthquakes leads to efficient generation of shear waves while the symmetry of the contained spherical explosion results in primarily P wave excitation. Cylindrical explosive sources, typically found in the mining industry, result in reduced symmetry and somewhat enhanced shear wave generation although not as efficiently as that found from earthquakes. Identification of a source as a spherical explosion, cylindrical explosion or earthquake is partially dependent on these geometrical properties of the different source types.

Theory predicts that these different source types will have characteristically different time functions as well. A number of empirical discriminants for earthquakes and explosions are dependent upon the relative excitation of different frequency components of regional seismic phases. By combining these time or frequency domain effects with the geometrical excitation the most robust discriminants can be developed.

The focus of this study is the understanding of the time function effects for chemical and nuclear explosion sources detonated in a spherical geometry. Information developed here in combination with similar studies for earthquakes and mining explosions will be used to improve current discriminants, address the transportability of the discriminants to new regions and suggest new discriminants utilizing current data sources. The quantification of the seismic source time function for nuclear and chemical explosions provides the basis for identifying source differences that may develop as a function of yield as well as explosive type (chemical or nuclear). The yield effects are useful in yield determination as well as assessing detection and identification capabilities if seismic monitoring of such sources is important. Source effects attributable to yield can be used to establish new or verify existing scaling relations.

The characterization of the seismic source function can be completed in the time or frequency domain. Time domain characterization not only quantifies the total source strength but also how it is distributed in time. Frequency domain representations provide the ability to identify static offsets of the source, characteristic frequency associated with the physical size of the source and the smoothness of the energy deposition or high frequency decay. In the case of frequency domain representations the phase of the signal can either be included or discarded in the analysis. Ignoring the phase information in the source precludes the ability to track the distribution of source information as a function of time and as such is more restrictive.

The data that is utilized in this chemical/nuclear explosion source function study has been recovered from the free surface in the near-source region. As in all seismological studies, the observed data is linearly dependent upon both the propagation and source contributions. This study focuses on near-source data to maximize the bandwidth over

which the source comparison can be made and to make any propagation path corrections as simple as possible. It is well known that local receiver effects on observed waveforms can be quite strong. In order to mitigate these effects in a comparative way all the explosions sources were observed with a consistent set of receivers.

II. PROBLEM DEFINITION

An experimental program was begun five years ago to define the equivalent elastic source function for nuclear explosions. The NPE provided the opportunity to extend this investigation to chemical sources as well. As part of these integrated investigations, free-field (Olsen and Perrat, These Proceedings) and free surface (Reinke *et al.*, These Proceedings) observations were made on the nuclear explosions MISTY ECHO (ME, 10 DEC 88), MINERAL QUARRY (MQ, 25 July 90), HUNTERS TROPHY (HT, 18 Sept 92) and the chemical explosions NON-PROLIFERATION EXPERIMENT (NPE, 22 Sept 93) and NON-PROLIFERATION EXPERIMENT CALIBRATION (NPE CAL, 30 Oct 92) (Figure 1). The combination of free-field, free surface near-source network and free-surface tight array (8-80m) provides a unique opportunity for separation of propagation path effects from source processes. The range of different types of sources (chemical and nuclear) and different yields ($\sim 10^2$ to 10^6 lb. equivalent TNT) provides data for characterizing source dominated processes that may be important in monitoring and identifying explosions in other environments.

The characterization of the free surface data and quantification of propagation path effects is given in the paper by Reinke *et al.*, these proceedings. The results of the free surface near-source network and free surface tight array analysis indicate that at relatively low frequencies (<10 Hz) that *stochastic* propagation effects are important contributors to the observed waveforms (0.5-3.0 km range). The large scatter in the peak, near-source velocity data (Figure 2) is the simplest expression of this characteristic. Based upon this analysis and interpretation, a *stochastic* approach to source comparisons was designed and implemented.

This study makes no use of the signal phase but instead makes frequency domain comparisons of power spectral estimates. Implicit in this analysis is the importance of smoothing to reduce variances in the estimates. The variance reduction takes the form of averaging over neighboring frequency points for a single estimate and over multiple observations for the same source.

The focus is the identification of relative source differences as evidenced by the experimental data. The range of different source types and sizes allows constraint of the following aspects of the explosion source model:

- A. CHEMICAL/NUCLEAR SOURCE SIMILARITIES AND DIFFERENCES (NPE TO HT COMPARISON, Section III of this paper).
- B. UTILITY OF SMALL SCALE CALIBRATION EXPLOSIONS FOR SOURCE QUANTIFICATION (NPE CAL TO NPE COMPARISON, Section IV).
- C. EXPLOSION SOURCE SCALING OF SMALL YIELD NUCLEAR EXPLOSIONS (HT TO MQ COMPARISON, Section V).

The observations from this study were made in and on Rainier Mesa above the N-tunnel complex (Figure 1). The surface instrumentation consisted of force-balance accelerometers ($f_c > 100$ Hz) and Sprengnether S-6000, 2 Hz velocity sensors recorded by Refraction Technology 16 bit and Terra Technology 12 bit digital acquisition systems. Timing and location were provided by a combination of WWVB, GOES and GPS receivers. It is important to emphasize that for the MQ, HT, NPE CAL and NPE sources an identical set of receiver sites were used thus eliminating apparent source differences that are actually attributable to local receiver structure. Since the sources themselves are at different spatial locations (except NPE CAL and NPE), there are differences in propagation path effects that must be taken into account in the comparative studies. In many cases these propagation path differences are negligible. Smoothing over several different observations will be used to reduce these effects.

III. CHEMICAL/NUCLEAR SOURCE SIMILARITIES AND DIFFERENCES (NPE TO HT COMPARISON).

The primary purpose of the NPE was to address questions concerning similarities and differences between chemical and nuclear explosions as observed in the seismic wavefield. The experiment was designed to identify seismic source

differences between chemical and nuclear sources that could be used to discriminate between the two source types. Such a tool would be invaluable in monitoring a Comprehensive Test Ban Treaty (CTBT).

Figure 1 illustrates the close proximity of the NPE (chemical, 390 m depth) and HT (nuclear, 385 m depth) sources on Rainier Mesa. Each source was observed by the same near-source receiver array thus eliminating local receiver effects in such a comparison. The relative difference of the two source locations (273 m) results in small differences in total propagation distance (30%) for stations 1P, 1A, 2P, 4A, 4P, 7A, 7P, 9A, and 12 while other stations have

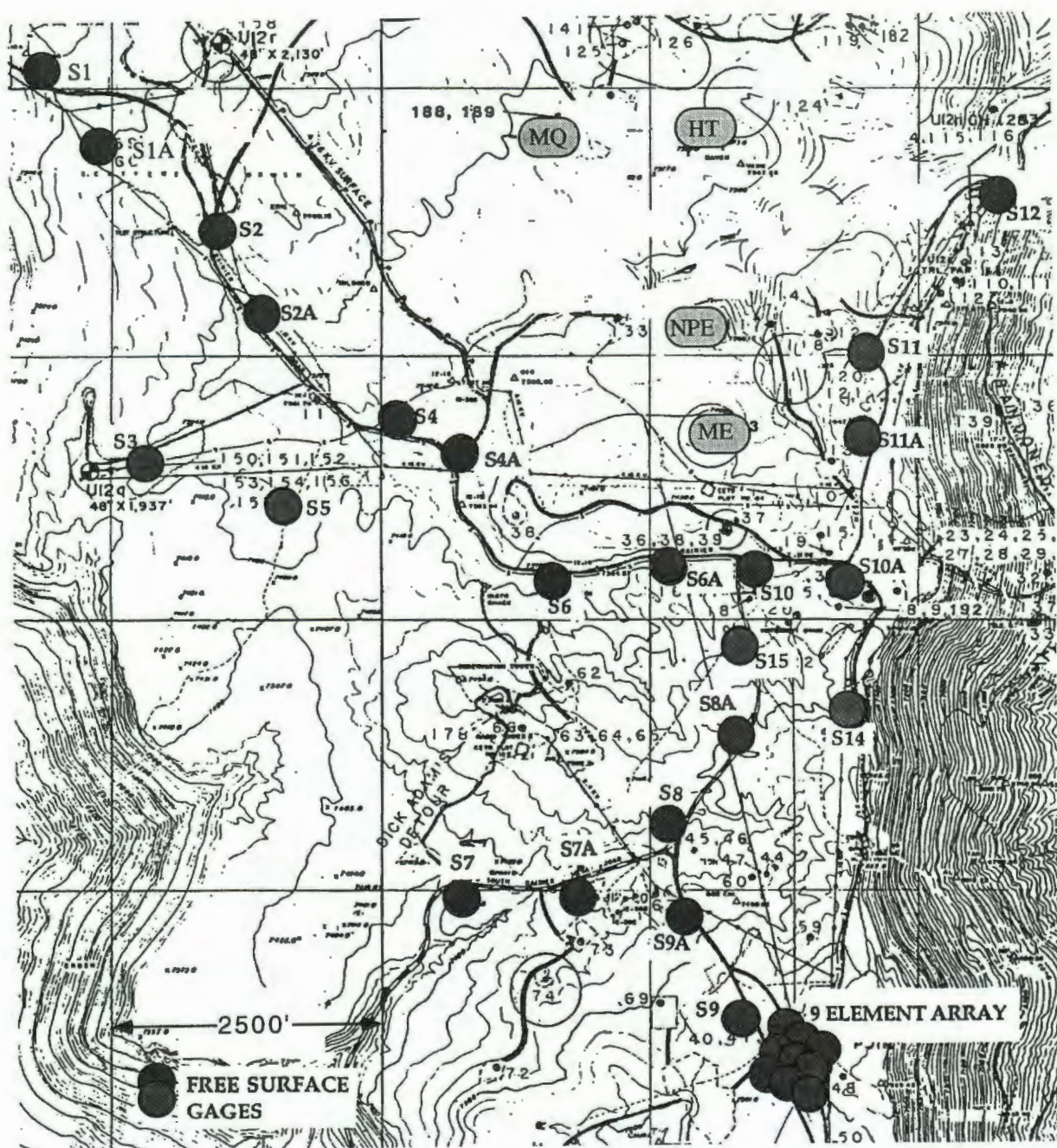
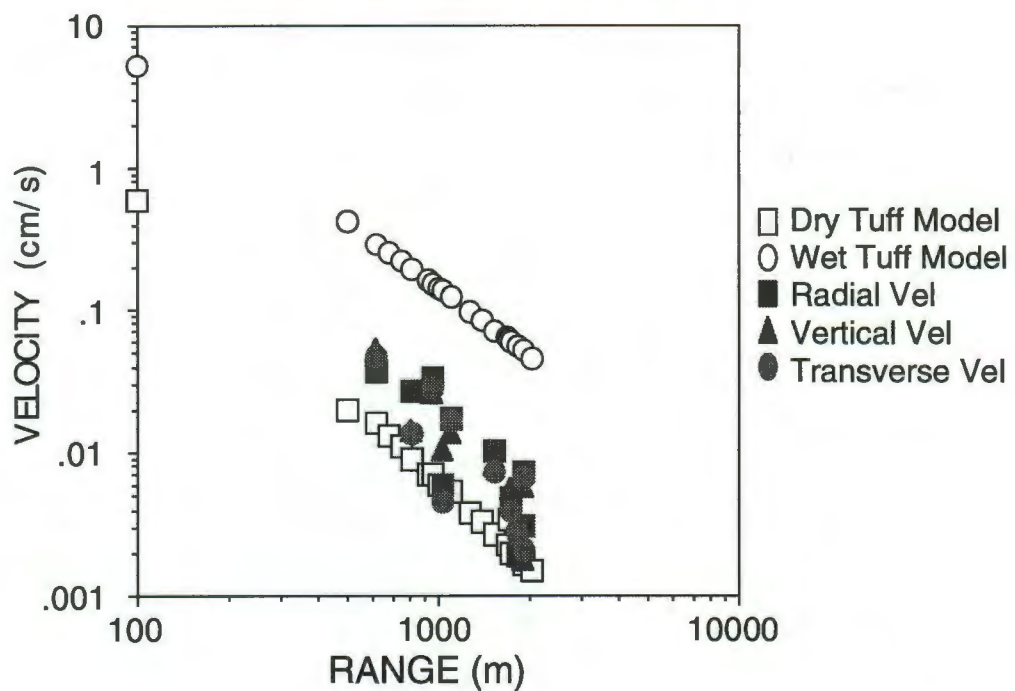


Figure 1: Rainier Mesa near-source free surface array for the experiments Misty Echo (ME), Mineral Quarry (MO), Hunters Trophy (HT), Non-Proliferation Experiment (NPE) and NPE CAL (same location as NPE).

NPE CAL PREDICTIONS AND DATA



HT DATA

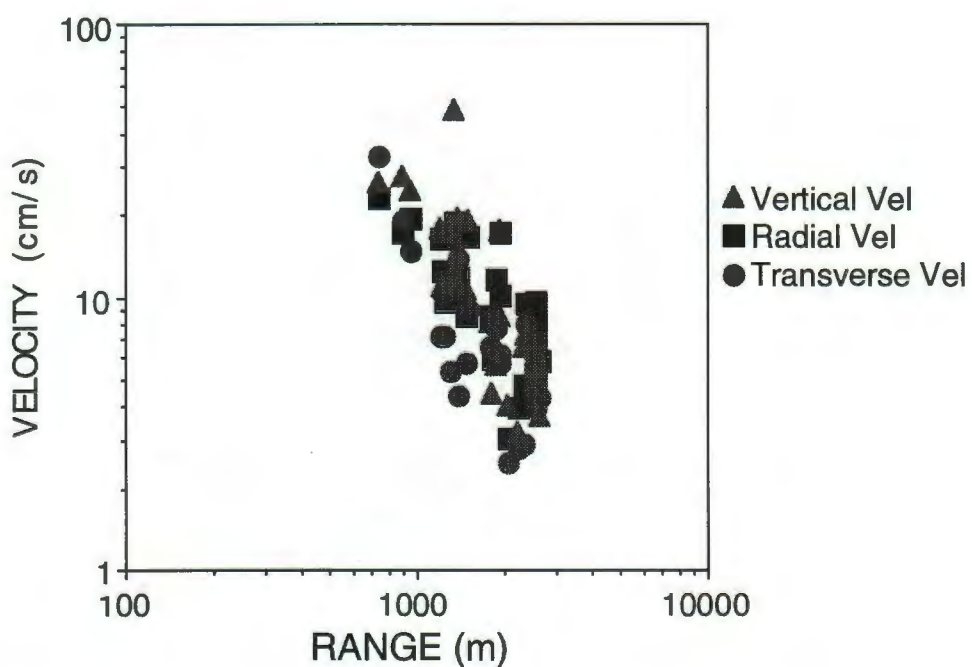


Figure 2: Peak velocity data for the radial (R), vertical (Z) and transverse (T) components of motion observed at the stations diagrammed in Figure 1 from the explosions NPE CAL (top) and HT (bottom). Predictions plotted for the NPE CAL (open symbols) are from the models of Perret and Bass (1974).

more significant differences in propagation distance. Figure 3 displays typical Z (vertical), R (radial) and T (transverse) acceleration time series and velocity spectral comparison at station 1A. This figure illustrates the earlier conclusion that phase information is easily contaminated by near-receiver or near-source structure. Significant differences in the time series are observed. In contrast the spectral comparisons show almost identical shapes and amplitudes over the bandwidth of the signal (0.36 to 100 Hz). The presence of a strong transverse component of motion is not consistent with an isotropic model of the source unless the geological structure is represented by a complex three dimensional structure where scattering into the transverse motions is important.

Stochastic comparisons designed to quantify source spectral similarities and differences were completed. The first step in this process was the identification of the bandwidth with acceptable signal to noise ratio. Comparison of the signal spectra to pre-event noise estimates and careful examination of the spectral shape led to a conservatively determined bandwidth of 0.36 to 100 Hz. The second step was the determination of an appropriate frequency domain smoothing window in order to reduce variances in the individual spectral estimates. Various numerical tests of different smoothing windows were performed and a window criteria which minimized the variance and bias of the spectral estimate was selected. A single window was chosen with a width of 3.48 Hz. At low frequencies the

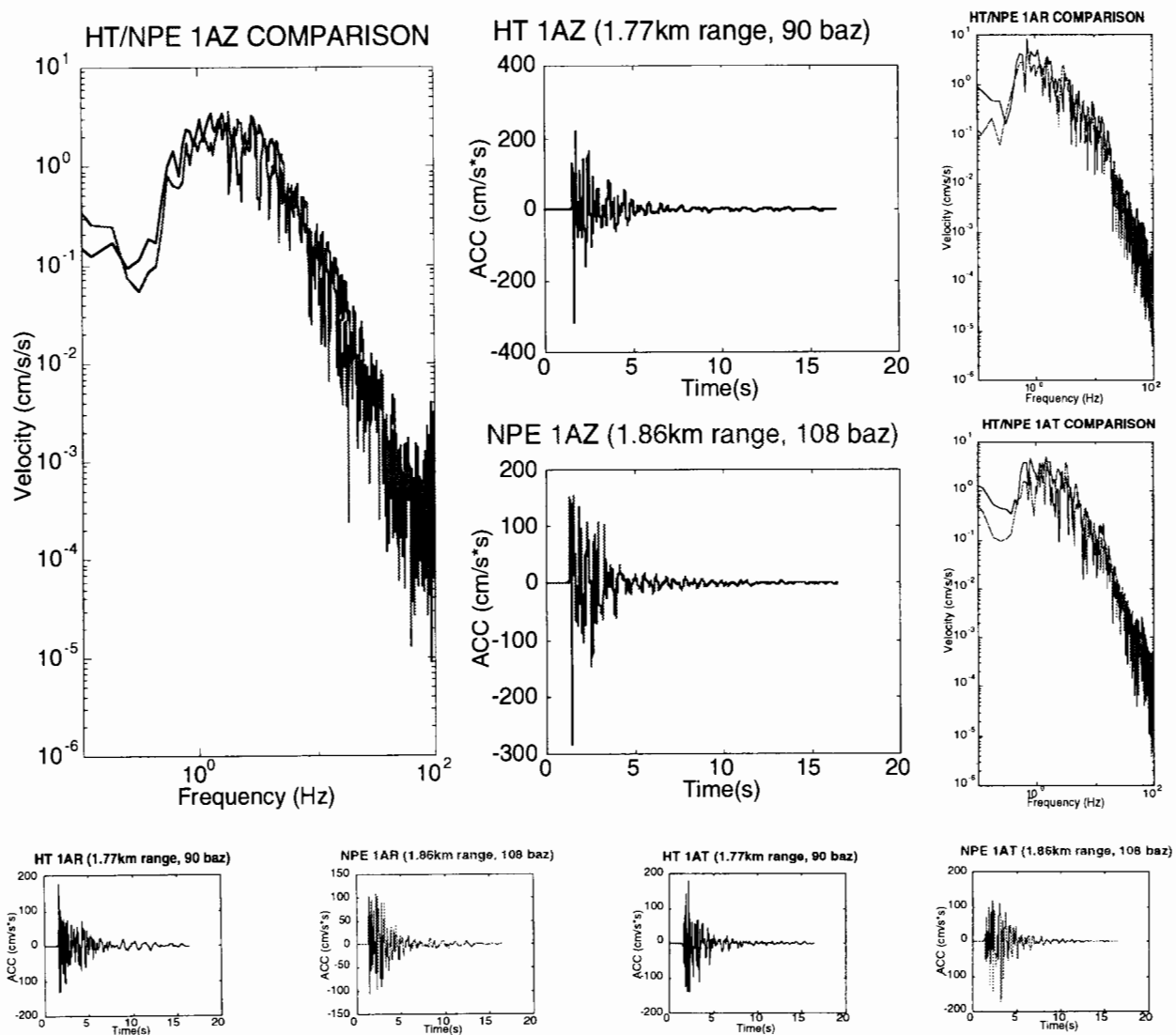


Figure 3: Comparison of the vertical accelerations from HT and NPE at Station 1A (Figure 1) in the time and frequency domain (left). Radial (R) and transverse (T) comparisons made in the smaller format to the right.

window which is centered on the frequency of the spectral estimate is allowed to grow to a width of 3.48 Hz as frequency increases. Figure 4 displays the smoothed spectra for station 1A and the resulting Z, R and T spectral ratios (HT/NPE). These three ratios have gross characteristics that are similar: (1) Flat from 0.36 to 8 to 10 Hz; (2) Low frequency ratio near 1; (3) High frequency ratio that increases with frequency; and (4) Significant high frequency variability.

In order to illustrate the parts of the spectral ratio characteristics that were source-station independent, the ZRT ratios from each station were combined into a single station dependent estimate, Figure 5. The mean (solid line) and log normal variance illustrates the small scatter in the low frequency estimates and the increased scatter with increasing frequency. The increase in variance occurs at 5 to 10 Hz. Taking a phase velocity of 2 km/s, the wavelength at which the scatter increases is 200 to 400 m, approximately the scale of the source separation. Arguing that the high frequency structure in the spectral ratio is a result of source location differences, the shape of the ratios for stations 1A and 2P (closest to one another) are similar, rising at high frequency, while the more distant station, 7P, decreases at high frequency (Figure 1).

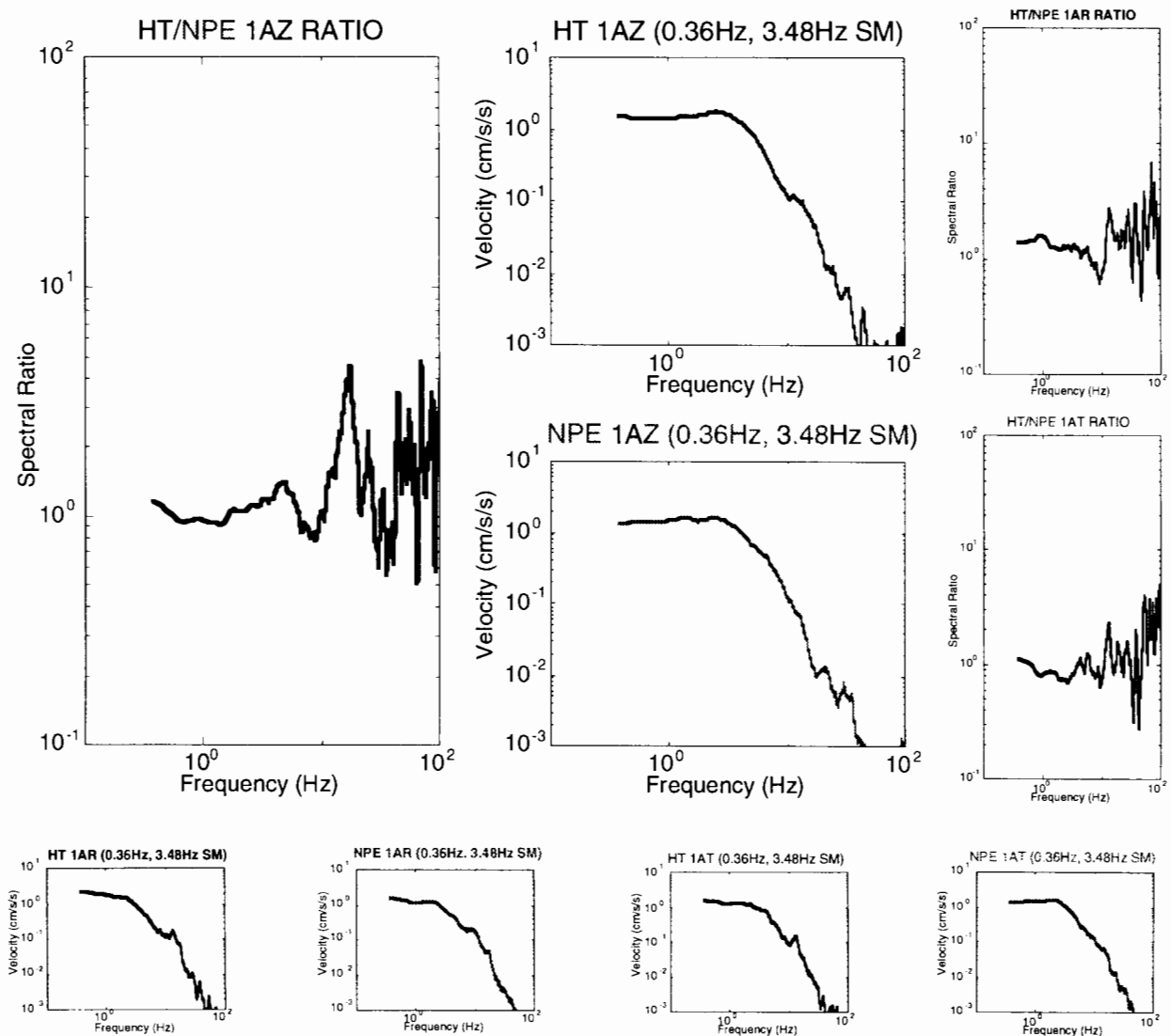


Figure 4: Smoothed spectra (Z to the left and R/T to the right) from HT and NPE at Station 1A (Figure 1) using a 3.48 Hz smoothing window. The spectral ratios (HT/NPE) of the smoothed spectra are also given.

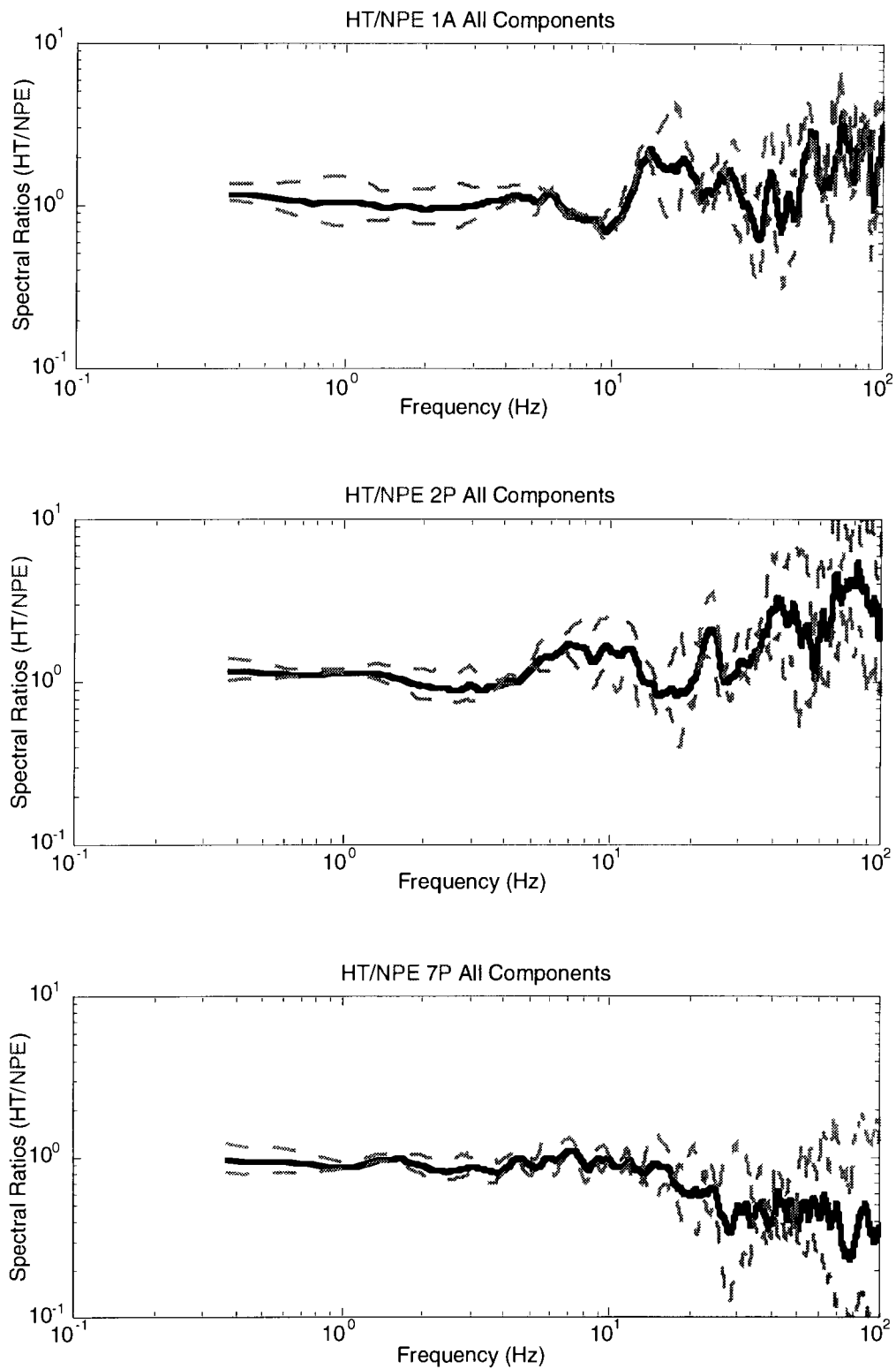


Figure 5: Mean spectral ratios (radial, vertical and transverse) at Stations 1A, 2P and 7P (Figure 1) for the explosions HT and NPE plotted as a solid line. The plus and minus one standard deviation (log normal) of the mean spectral ratio estimate is also plotted.

If the high frequency variation in spectral ratios is a reflection of the different locations of HT and NPE, as seen at each receiver then one might expect to average these differences by smoothing over a number of observations at different azimuths. Figure 6 displays the smoothed all component spectral ratio using all station pairs with propagation path differences of no more than 30%. The high frequency variations observed in the single components and single stations are eliminated although the variances in the spectral ratios increase with frequency as expected from the stochastic model.

This analysis defines significant source location related propagation path differences for the HT to NPE comparison in the near-source data. These variations can be smoothed to emphasize source processes. The resulting spectral comparison between NPE and HT is flat from 0.36 to 100 Hz with the ratio of the source strengths equal to 1. *There appear to be no significant spectral differences between this chemical and nuclear source in the near-source region from 0.36 to 100 Hz after stochastic propagation path effects are taken into account.*

IV. UTILITY OF SMALL SCALE CALIBRATION EXPLOSIONS FOR SOURCE QUANTIFICATION (NPE CAL TO NPE COMPARISON).

In order to quantify propagation path effects expected from the NPE and exercise the data acquisition systems, a small, 300 lb. (C-4), charge was emplaced and detonated at the center of the planned NPE source cavity prior to its excavation. This small source provided the opportunity to test the empirical Green's function approach to source scaling in the near-source region. Since the source was nearly four orders of magnitude smaller than the NPE and the dynamic range of the accelerometers (used for recording the NPE, HT, MQ) were limited, a set of Sprengnether S-6000, 2 Hz seismometers were used to record the NPE CAL at the same locations where the accelerometers were fielded for the other explosions. The instrument corner of the seismometer is in the band of interest for source comparisons, therefore this well known instrument response was taken into account prior to any spectral comparisons.

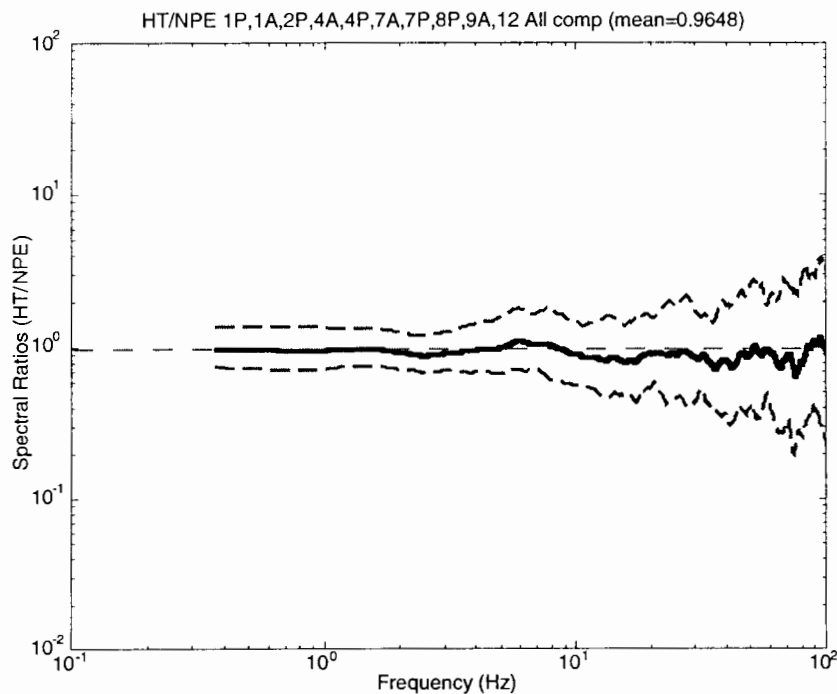


Figure 6: Mean spectral ratio (HT/NPE) determined averaging all station pairs (propagation path differences < 30%) and all components. Again the solid line is the mean with the plus or minus one standard deviation (log normal) characterizing the scatter in the individual estimates.

The smaller NPE CAL waveforms have a higher corner frequency, longer temporal duration, and more complexity than those observed from the NPE. Spectral comparisons in velocity illustrate the four orders of magnitude difference in spectral level at low frequencies, the order of magnitude difference in source corner frequency and the 0.48 to 100 Hz bandwidth of the data. Since the centroids of the NPE and NPE CAL sources are identical there should be no differences in propagation path effects for the two sources as long as the point source representation is appropriate. If secondary source processes such as spall are important contributors to the NPE waveforms, this assumption may not be valid. In order to improve the statistical significance of the source comparisons, the observed spectral ratios for all the Z, R, T and combined single station estimates were averaged as done in the previous analysis. The averaged ratio for NPE/NPE CAL is displayed in Figure 7. Unlike the HT/NPE comparison there are only small increases in variance of the ratios with frequency. This increase in variance with frequency in the previous case was explained in terms of the difference in propagation path between the two sources to be compared. In the NPE/NPE CAL comparison there is little difference in the propagation paths thus resulting in the reduced high frequency variances. Differences in the spatial extent of the two sources and secondary source contributions may be responsible for the slight increase in variance with frequency observed in this case.

As found for the HT/NPE comparisons, all the averaged results (Z, R, T and combined) produce a common source comparison. This result indicates that the generation of the transverse energy scales linearly with source size. One might conclude that this observation is consistent with a linear scattering mechanism for the generation of transverse energy.

These NPE/NPE CAL comparisons (Figure 7) support a 10^4 source difference between the two sources at long periods, a source corner for NPE near 2 Hz, f^{-2} spectral decay between corners and a corner frequency of 50-60 Hz for the NPE CAL. Comparison of these smoothed results with those from theory will be given in Section VI.

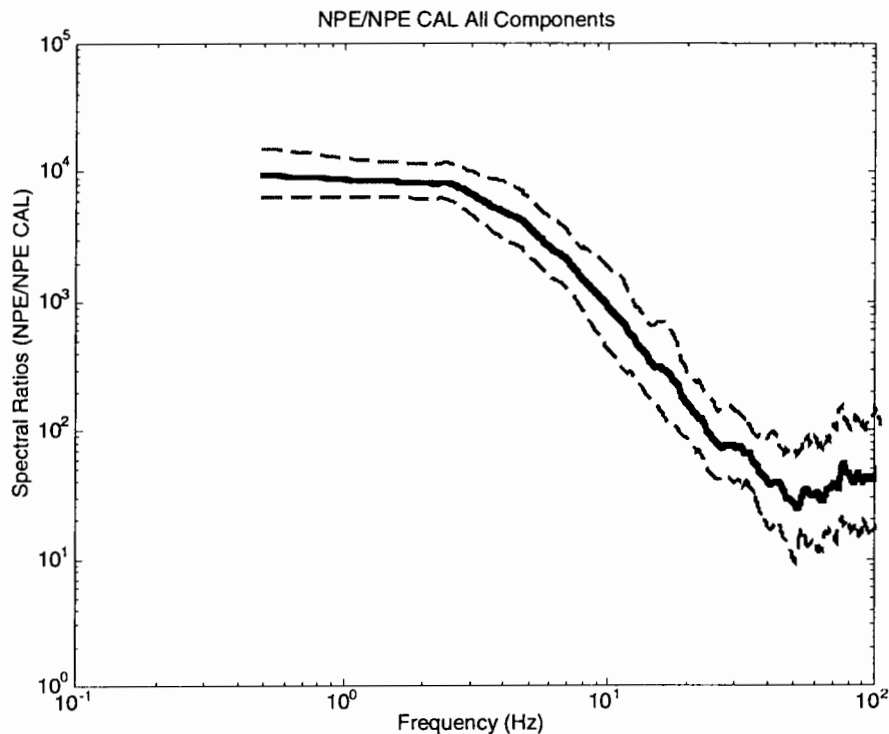


Figure 7: Mean spectral ratio (NPE/NPE CAL) determined averaging all station pairs (propagation path differences < 30%) and all components. Again the solid line is the mean with the plus or minus one standard deviation (log normal) characterizing the scatter in the individual estimates.

V. EXPLOSION SOURCE SCALING OF SMALL YIELD NUCLEAR EXPLOSIONS (HT TO MQ COMPARISON).

The last set of empirical comparisons allows the investigation of source differences between the two nuclear explosions MQ and HT. As Figure 1 indicates, the two sources are to the north of the testing area. Propagation path distance differences from the two sources to the stations to the south are small. This data provides the opportunity for quantifying differences in propagation path as well as differences in absolute source location. As was done in the case of the HT/NPE comparisons, all source-receiver distances that were no more than 30% different for the two sources were used to produce a combined smoothed spectrum (Figure 8). This ratio begins at low frequency with a value near 0.4 and rise to a plateau of 1 at 5 to 6 Hz. The variances in the ratio estimates increase as a function of frequency above 5 Hz just as observed in the HT/NPE comparisons.

A number of stations in the free surface array (6P, 6A, 7P, 7A, 8P, 9A, 10P) have propagation path differences between the two sources of less than 10%. These more limited data were used to estimate a second spectral ratio along with variances (Figure 9). The spectral variance estimates in this second set are dramatically reduced from those of the more inclusive data set. The resulting spectral ratio mean is nearly identical to the previous estimate. This result argues that much of the low frequency variation in the spectra (<5 to 10 Hz) is attributable to propagation path differences observed in the near-source region from these explosion sources. The higher frequency variations may be a result of near-source differences like the near receiver variations observed in the array measurements from a single source and reported by Reinke *et al.*, these proceedings.

The HT/MQ spectral ratios is consistent with an interpretation that the MQ explosion was larger than the HT explosion. This source size difference is reflected in the long period spectral ratio HT/MQ of 0.4. The source spectra for the two explosions merge at frequencies greater than 5 Hz above the corner frequency for each explosion.

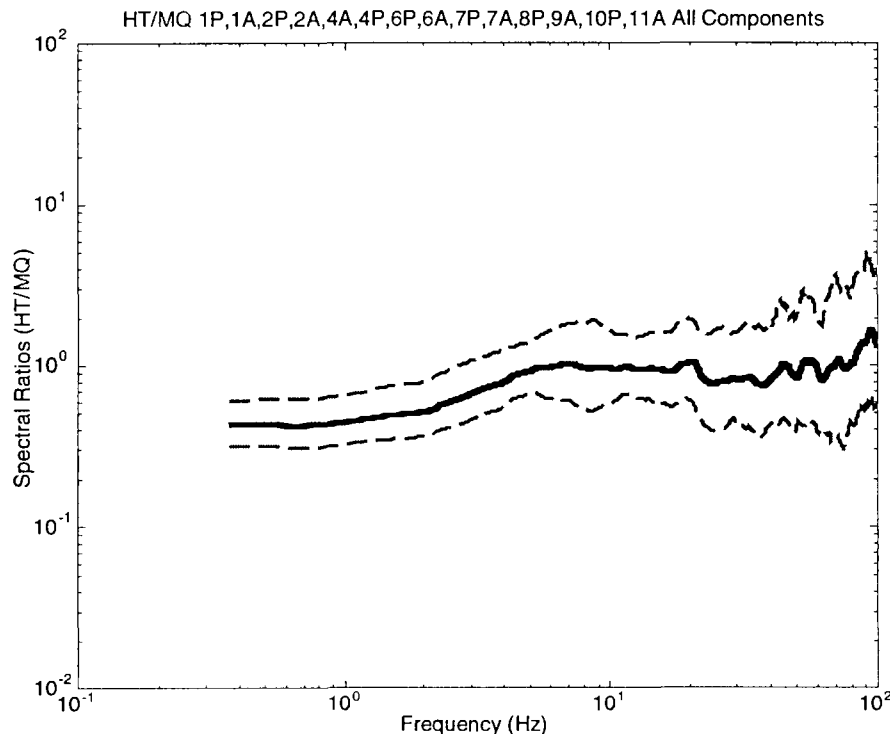


Figure 8: Mean spectral ratio (HT/MQ) determined averaging all station pairs (propagation path differences < 30%) and all components. Again the solid line is the mean with the plus or minus one standard deviation (log normal) characterizing the scatter in the individual estimates.

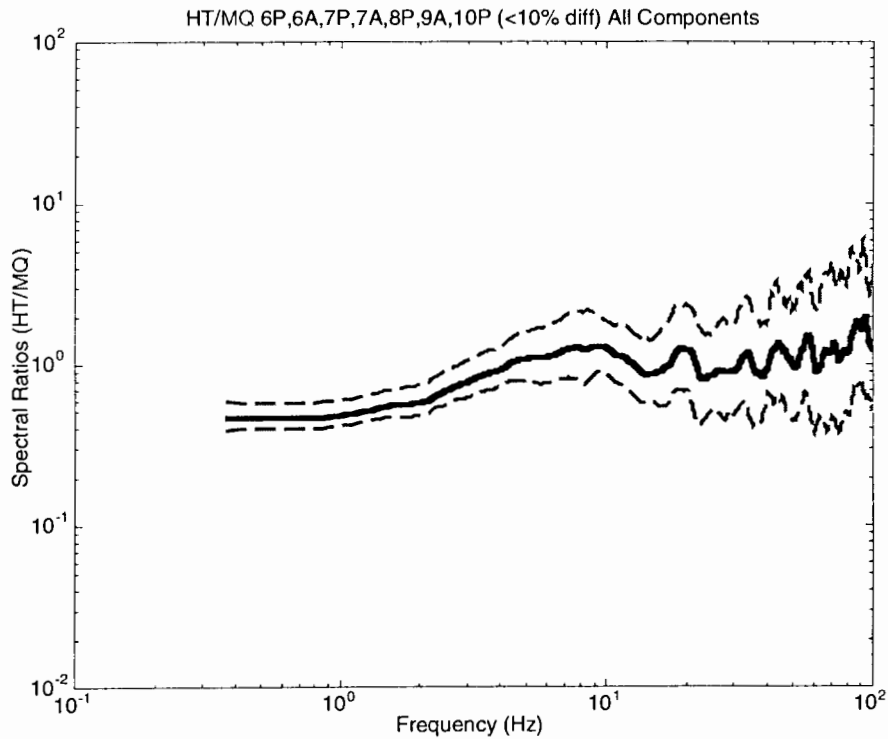


Figure 9: Mean spectral ratio (HT/MQ) determined averaging all station pairs (propagation path differences < 10%) and all components. Again the solid line is the mean with the plus or minus one standard deviation (log normal) characterizing the scatter in the individual estimates.

VI. SOURCE MODELS

The comparison of *NPE to NPE CAL* documents the strong yield effect between the 300 lb. C-4 calibration explosion (390 lb. equivalent TNT) and the 1 kiloton (kt) (equivalent TNT) NPE. In order to interpret these yield effects a set of Mueller Murphy source functions for wet tuff were calculated using the following material properties for the source region:

P Velocity	2.20 km/s
S Velocity	1.27 km/s
Density	1.85 gm/cc
Depth	400 m

RDP's for sources of 2, 1, and 0.00022 kt were calculated. These source functions which are calculated in the frequency domain provide the opportunity for comparison to the experimental source differences determined in the analysis of the data. Figure 10 compares spectral ratios of the 2/0.00022 kt and of the 1/0.00022 kt with the observed NPE/NPE CAL spectral ratios. The comparisons between the models and the data validate the Mueller-Murphy source model for wet tuff and suggest that source models with yields between 1 and 3 kt best describes the NPE/NPE CAL data. The long period spectral level difference, NPE corner frequency and NPE CAL corner frequency are all well replicated by the Mueller-Murphy source model.

The empirical data is consistent with the scaling relations incorporated into the Mueller-Murphy source model. It appears that this model is appropriate for wet tuff over the four orders of magnitude of yield represented by the NPE CAL and NPE explosions. The Mueller-Murphy model was developed for nuclear sources. The mean of the range of acceptable source models suggests that there is an approximate factor of two difference between nuclear and chemical coupling at large yields. This conclusion does not call upon a factor of two coupling enhancement for the smaller NPE CAL explosion.

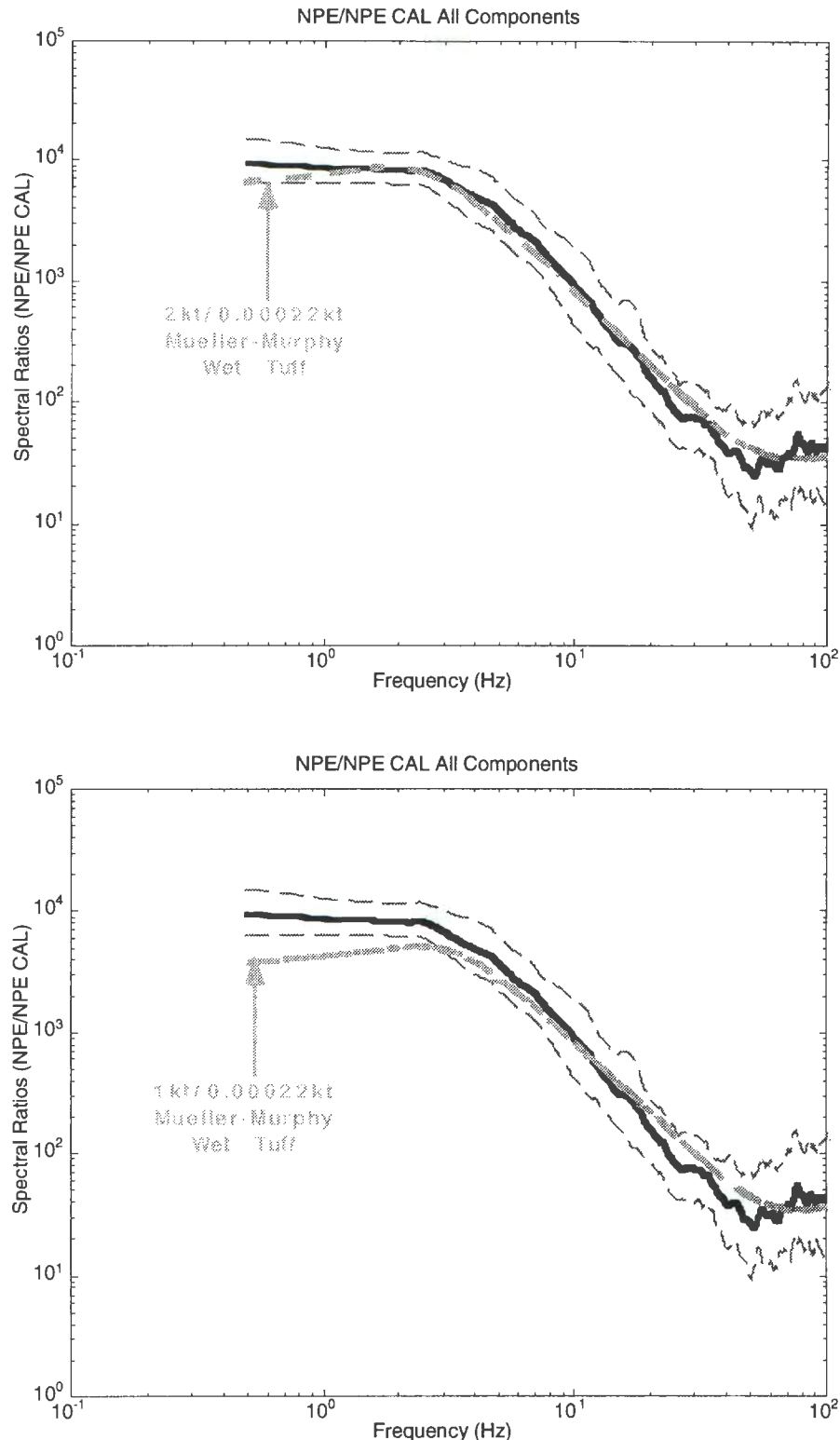


Figure 10: Comparison of the predicted spectral ratios from the Mueller-Murphy wet tuff model (thick/light dashed lines) and the NPE/NPE CAL empirical data (thick dark line).

Two alternate explanations for the apparent factor of two enhanced coupling for the NPE can be introduced. It is difficult to separate overshoot from long period spectral level with limited bandwidth data. If the NPE had significant overshoot associated with the source time function, then the limited bandwidth analyzed in this study would be unable to separate overshoot from the enhanced coupling postulated for the chemical explosion.

The NPE CAL explosion, since it was detonated at the same depth as the NPE, was highly overburied. This small explosion resulted in no surface spallation. The NPE although also overburied did spall at surface ground zero and so the possibility exists for secondary source contributions from spall to the NPE seismic source function. If these contributions boost spectral levels below the source corner frequency then this effect could also be interpreted as enhanced coupling for the chemical explosion. The fact that the NPE itself was overburied and that observed dwell times at surface ground zero were much less than 1 sec in duration argues that this secondary source effect was probably minimal.

VII. CONCLUSIONS

In the near-source region there are no apparent spectral differences between *HUNTERS TROPHY* and *THE NON-PROLIFERATION EXPERIMENT* in the bandwidth of 0.36 to 100 Hz. Figure 6 demonstrates the flat spectral ratio for these two events with a mean value of 0.96. Although the variance of the spectral ratio estimate increases as frequency increases the mean value shows little departure from the value of 1 across the entire bandwidth of the data. These results indicate that there is little information in the near-source wavefield that can be used to distinguish chemical from nuclear explosions. Although this result suggests that seismic waves cannot be used to discriminate nuclear explosions from chemical explosions, it also supports the use of large chemical explosions to replicate nuclear explosion effects. One could imagine a series of chemical explosion experiments to quantify source phenomenology, near-source material property effects, and regional explosion effects in areas where only earthquakes have been observed in the past.

Comparison of the empirical spectral ratios for the NPE and the NPE CAL suggest that the NPE is best replicated by a Mueller-Murphy model with a yield of about 2 kt. This conclusion is made in light of alternate interpretations in terms of source overshoot or spall contributions. The empirical data supports a Mueller-Murphy source time function for wet tuff. These comparisons also suggest that this model for wet tuff is extendible to quite small yield explosions. The yield of the NPE CAL is comparable in size to individual detonations in ripple fired mining explosions. This result suggests that a good starting point for such source models might be the Mueller-Murphy source time function, recognizing that the geometry for the NPE CAL is not the same as the cylindrical geometry of typical mining explosions. The source time function predicted by the Mueller-Murphy model may be appropriate but the geometrical effects of the mining explosions may be quite different. One would expect enhanced shear wave generation by the mining explosions.

The raw data display strong first order propagation path effects which must be taken into account prior to making any source comparisons. It was only because all these different types and sizes of sources were recorded by the same receiver array that this source comparison study could be undertaken. Even with the suite of constant receiver sites for the different sources significant spectral smoothing was necessary across neighboring frequency points and across different receiver sites in order to appropriately reduce the variances in the spectral estimates resulting from slightly different propagation paths from the different sources and variances introduced by the spectral estimation procedure.

In the case of Figure 6, thirty individual waveforms from each of the two explosions went into the spectral ratio estimate. It is not often in comparative source studies that redundancy in near-source observations of this magnitude are available. The spectral ratios calculated for the HT/MQ comparisons indicate that the number of observations in the averaging process can be reduced if the propagation path differences between the two sources are reduced. Comparison of Figures 8 and 9 indicates that if propagation path differences can be reduced to less than 10% (assuming the same receiver site) that statistical stable spectral ratios can be made to frequencies below 1 Hz with significantly fewer components. Variances at frequencies above 10 Hz are still large in this case as the wavelengths of this energy become equal to or shorter than the difference in propagation path.

In all comparisons (HT/NPE, NPE/NPE CAL, and HT/MQ) the analysis of transverse components of motion produced results that were identical to those from the radial and vertical components of motion. The mechanism for SH generation must be linked to the source function in the same way that the P and SV waves(radial and vertical motions) are linked. A linear scattering mechanism for the generation of transverse motions is consistent with these observations. These results suggest that the transverse component of motion receives a strong source imprint very close to the explosion.

ACKNOWLEDGMENTS

This work was performed under the auspices of the U.S. Department of Energy by Los Alamos National Laboratory under contract W-7405-ENG-36, Defense Nuclear Agency, Air Force Phillips Laboratory and the Advanced Research Projects Agency by Southern Methodist University under contract F29601-91-D-DB20. Special thanks go to Al Leverette for data acquisition. Karl Koch helped with the source modeling. The paper was improved by discussions with Steve Taylor, G.-S. Min and Tom Weaver.

REFERENCES

- Mueller, R. A. and Murphy, J. R., 1971. Seismic characteristics of underground nuclear detonations. Part I. Seismic scaling law of underground detonations, *Bull. seism. Soc. Am.*, **61**, 1675-1692.
- Perret, W. R. and Bass, R. C., 1974. Free-field ground motion induced by underground explosions, SAND74-0252, Sandia National Laboratories, Albuquerque, New Mexico.

Relative Source Comparison of the NPE to Underground Nuclear Explosions at Local Distances

Albert T. Smith
Lawrence Livermore National Laboratory

Abstract

The Non-Proliferation Experiment (NPE) provides an opportunity to compare broadband characteristics of chemical to nuclear explosions at a group of local stations (4 to 40 km distant). The locations for these stations were established on bedrock to record a small partially decoupled nuclear explosion and two nearby nuclear experiments, all shots within "N" Tunnel on Rainier Mesa, Area 12. These sites were also occupied to record aftershocks from the Little Skull Mountain earthquake and chemical explosions from the USGS Sierra Experiment. To minimize calibration errors during this period, redundant instrumentation were used for each event.

The analysis emphasizes the source characteristics of the different explosions. The 300-lb chemical calibration explosion allows removal of path effects from each explosion. The NPE and nearby experiments produce very similar waveforms. The decoupled nuclear explosion and the 300-lb chemical calibration explosion show higher frequency content consistent with a higher corner frequency for the sources.

Introduction

Monitoring a Comprehensive Test Ban Treaty in a region of surface and underground mining with numerous industrial explosions may entail local or near regional seismic stations. Discrimination of a clandestine nuclear explosion may rely on separating single, large explosions from the more numerous ripple-fired mining explosions. These single explosions could be large mine detonations, but they could also be decoupled nuclear detonations. The Non-Proliferation Experiment allowed us to compare both small and large, single detonations of chemical explosives to tamped and partially decoupled nuclear detonations at local distances using a constant suite of stations.

Experiment

The NPE offered an opportunity both to compare the source properties of chemical explosions to nuclear explosions and to remove the effects of path propagation from the source. Figure 1 shows the location of three seismic stations at local distances (4 to 50 km) from the site of the explosions below Rainier Mesa at the Nevada Test Site. Each station recorded earlier nuclear explosions and the NPE.

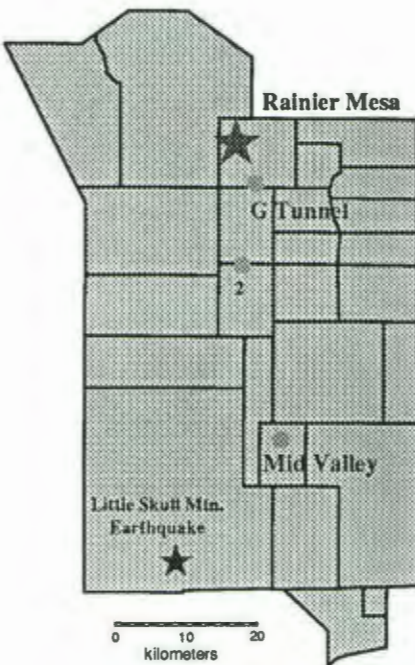


Figure 1: Map view of the Nevada Test Site showing the location of local seismic stations, G-Tunnel and Mid-Valley.

All the stations were located on competent bedrock so as to minimize station site effects on the incoming seismic waves. The figure also shows the location of the Little Skull Mountain earthquake; a limited number of its aftershocks were recorded at the Mid Valley site.

Each site was recorded on multiple vertical seismometers, the type depending on the expected amplitude of the arriving seismic waves. Both Geotech S-13 and S-750 seismometers were used at Mid Valley for most of the events. The close G-tunnel Road site recorded on a strong-motion accelerometers and S-13 seismometers. These duplications verified the calibration corrections and allowed a wide dynamic range.

The calibration explosion was a 300-lb shot fired at the location of the NPE prior to the excavation of the cavity; thus, it represents an ideal empirical Green's function to remove path propagation effects from the NPE and nearby explosions and to isolate the source properties. Near-source measurements confirm that the corner frequency of the calibration shot exceeds 50 Hz (Goldstein et al., 1994). The calibration shot was well recorded at the closest station, G-tunnel, but background noise limited the usable bandwidth at Mid Valley. Both tamped and partially decoupled nuclear explosions were recorded by the station sites. The partially decoupled explosion was detonated in a hemispherical cavity with an 11-m radius above approximately 2 m of alluvium.

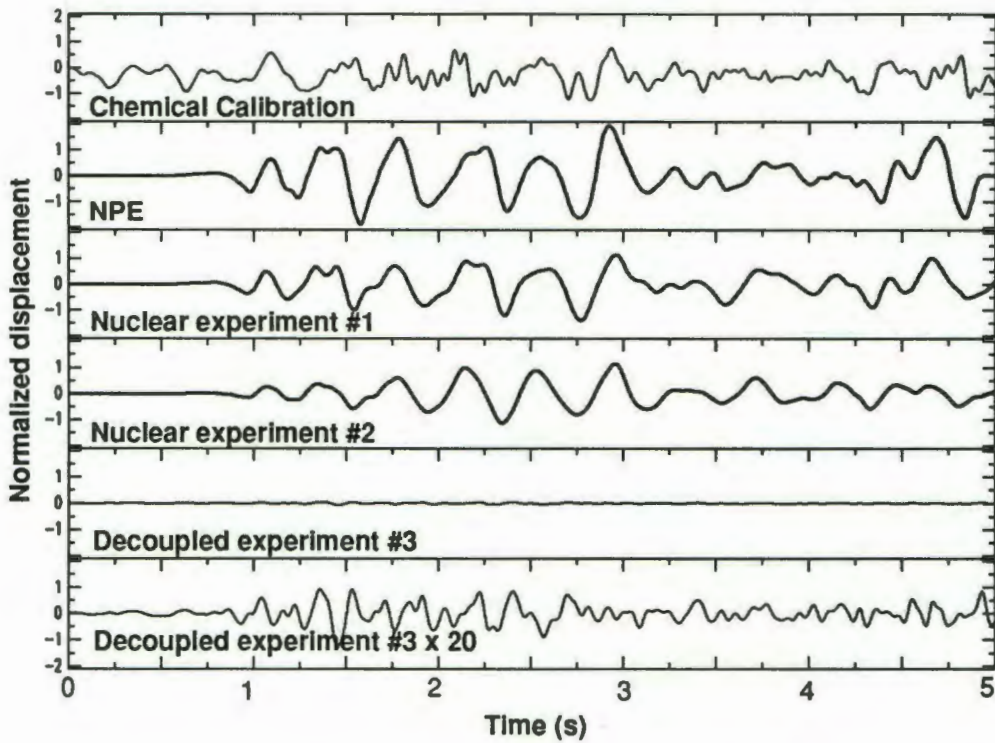


Figure 2. Seismograms from the Mid Valley station bandpassed from 2 to 20 Hz for five events: two tamped tunnel shots, a partially decoupled nuclear explosion, and two chemical explosions, the 300-lb chemical calibration explosion and the 1-kiloton NPE. The relative displacements are normalized by the yield of each event. The final trace for the partially decoupled explosion is multiplied by a factor of 20 to compare amplitudes at approximately the same scale.

Results

The waveforms for all the explosions are very similar at local distances. Figure 2 compares the first 4 seconds of each explosion recorded 40 km away at Mid Valley. The amplitudes are normalized by the explosive yield of each event; thus, amplitude differences should reflect coupling of the explosive into seismic waves. The two tamped nuclear explosives have very similar waveforms and normalized amplitudes.

The NPE also closely matches the tamped nuclear explosions, except its relative scaled amplitude is approximately a factor of 2 larger than these nuclear explosions. The calibration explosion is partially obscured by background noise; however, it also roughly scales with explosive energy.

To compare the waveforms to the partially decoupled experiment #3, the second trace for experiment #3 is multiplied by a factor of 20. This suggests a decoupling factor of approximately 20 for seismic waves propagating down and refracting to our distant sites. Surface observations above the detonation suggested a decoupling factor of approximately 70. The asymmetry in the cavity and the placement of the detonation introduces, then, a corresponding asymmetry in the coupling and the resulting seismic waves (e.g., Glenn, et al, 1985).

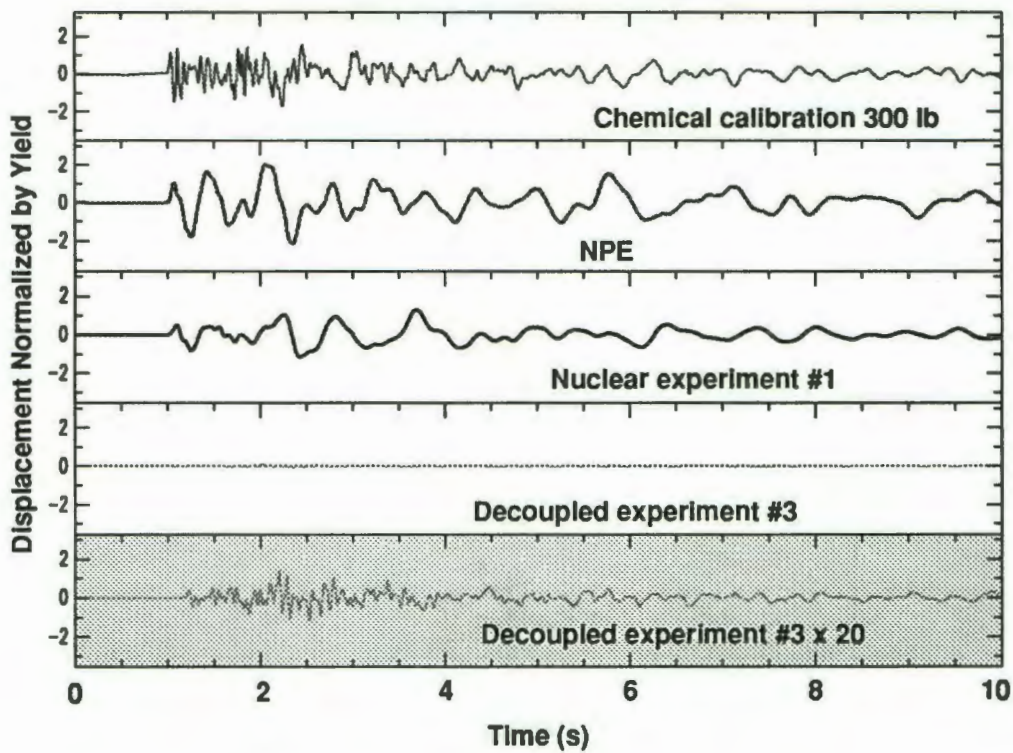


Figure 3. Seismograms from the G-tunnel station for four of the events from the previous figure. The same type of display is used as for Figure 2.

The same pattern between the NPE chemical explosions and the nuclear detonations appears at the closer station, G-tunnel Rd., at 4 km distance in Figure 3. However, the short propagation path and resulting lower attenuation emphasizes the higher frequencies contained in the small chemical calibration explosion and the decoupled nuclear explosion. Again the decoupling factor is approximately 20 relative to the "normal" tunnel shots in Rainier Mesa.

Even close-in to the explosions at the G-tunnel site, significant attenuation occurs at frequencies greater than 15 Hz. The NPE calibration explosions can act as an empirical Green's function and allow removal of the common path propagation effects for the events. Figure 4 illustrates the deconvolved displacement spectra for the NPE, a nuclear explosion, and the partially decoupled nuclear explosion. Both the relative displacement amplitude and frequency are normalized by the explosive energy of the devices.

At low frequencies the spectral amplitude for the NPE is approximately a factor of 2 larger than the nuclear explosions. This corresponds to the predictions of Glenn (this report) for the expected difference between a chemical explosion and a tamped nuclear explosion. The corner frequency for the sources are approximately 4 to 5 Hz; however, an accurate estimate was difficult without contamination from shear arrivals.

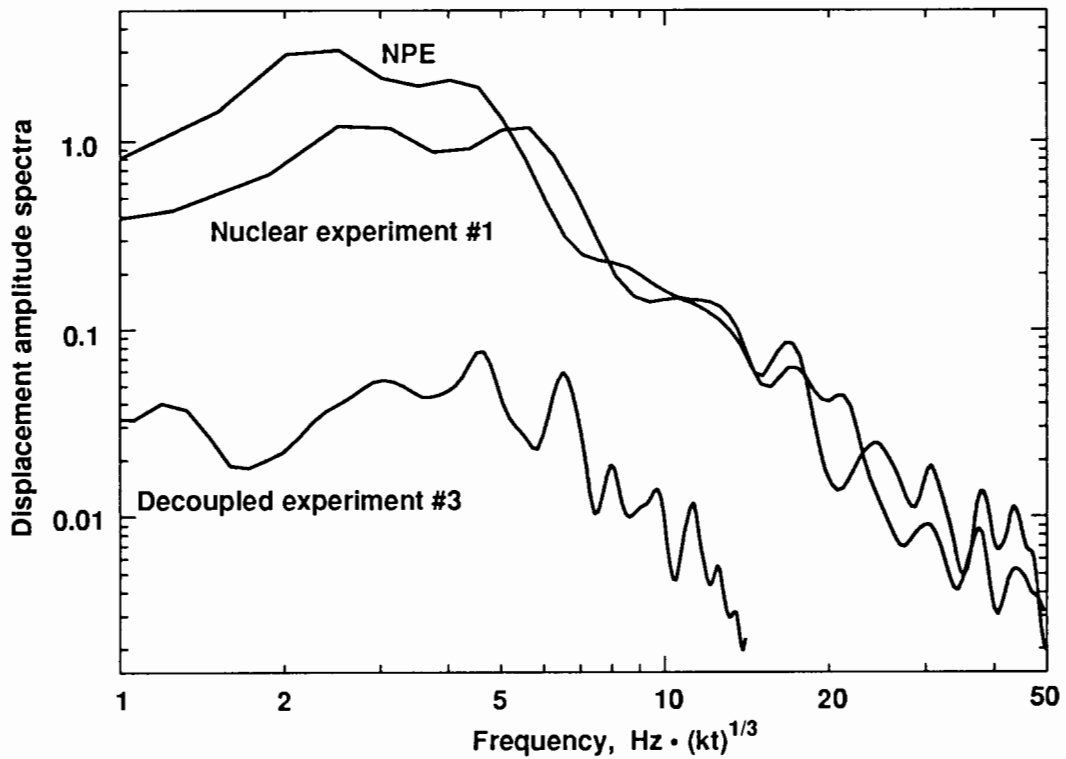


Figure 4. Spectra of three events using yield scaling for both the displacement amplitude and the frequency. Nuclear explosions with a consistent medium but different media should then scale to the same curve. The NPE shows large, low-frequency amplitude relative to the scaled nuclear explosions, verifying the qualitative observations in the scaled seismograms. The partially decoupled explosion shows a factor of 20 decrease in the expected amplitudes at all scaled frequencies.

The partially decoupled explosion shows a uniform decoupling of 20 for both low and high frequencies. Using an empirical Green's function to deconvolve the path has the advantage of restricting the spectrum to the actual source component. Decoupling ratios can then be based on the actual source yield, instead of comparing to ratios of larger tamped shots. The results can then be scaled to normalized frequency. Decoupling as great as 70 was observed for surface measurements above the shot point. The location of the shot point near the bottom of a hemispherical cavity is probably responsible for the much greater decoupling observed for upgoing seismic waves and the relatively low scaled frequency observed for the downgoing seismic waves.

Conclusions

Using seismic observations at local distances, the NPE shows no significant differences from tamped nuclear explosions detonated in the same area of Rainier Mesa. The earlier, small chemical calibration explosion also scaled like the larger explosions and provided a crucial Green's function for removing the propagation path of the partially decoupled nuclear explosion. After frequency and amplitude-yield scaling, the decoupling factor is approximately 20 at all frequencies. Comparing to previous results suggests strong directional effects introduced by the hemispherical cavity and the shot's location within the cavity.

References

Glenn, L. A., and P. Goldstein (1994), "The Influence of Material Models on Chemical or Nuclear-Explosion Source Functions," *Proceedings of the Symposium on the Non-Proliferation Experiment and Implications for Test Ban Treaties*, April 19-21, 1994, Rockville, MD, Lawrence Livermore National Laboratory, CA, CONF-9404100

Glenn, L. A., B. Moran, J. C. Ladd, and K. A. Wilson (1985), "Elastic Radiation from Explosively-loaded Ellipsoidal Cavities in an Unbounded Medium," *Geophys. J.R. Astr. Soc.*, **81**, 1, 231-242.

Goldstein, P. and S. P. Jarpe (1994), "Comparison of Chemical and Nuclear Explosion Source Spectra from Close-in, Local, and Regional Seismic Data," *Proceedings of the Symposium on the Non-Proliferation Experiment and Implications for Test Ban Treaties*, April 19-21, 1994, Rockville, MD, Lawrence Livermore National Laboratory, CA, CONF-9404100.

Modeling the NPE with Finite Sources and Empirical Green's Functions

Lawrence Hutchings, Paul Kasameyer, Peter Goldstein, and Steve Jarpe; Lawrence Livermore National Laboratory, P.O. Box 808, Livermore, California 94551.

Abstract

In order to better understand the source characteristics of both nuclear and chemical explosions for purposes of discrimination, we have modeled the NPE chemical explosion as a finite source and with empirical Green's functions. Seismograms are synthesized at four sites to test the validity of source models. We use a smaller chemical explosion detonated in the vicinity of the working point to obtain empirical Green's functions. Empirical Green's functions contain all the linear information of the geology along the propagation path and recording site, which are identical for chemical or nuclear explosions, and therefore reduce the variability in modeling the source of the larger event. We further constrain the solution to have the overall source duration obtained from point-source deconvolution results. In modeling the source, we consider both an elastic source on a spherical surface and an inelastic expanding spherical volume source. We found that the spherical volume solution provides better fits to observed seismograms. The potential to identify secondary sources was examined, but the resolution is too poor to be definitive.

Introduction

The Department of Energy, in cooperation with the Defense Nuclear Agency, conducted a 1-kiloton conventional explosion, the Non-Proliferation Experiment (NPE) at the Nevada Test Site on September 22, 1993. The purpose was to gather experimental information in a major problem area for stability and verification of a Comprehensive Test Ban Treaty. The purpose of this paper is to examine how the empirical Green's function method for synthesizing seismograms may provide useful information for characterizing nuclear explosions. The approach is to use a small explosion, detonated at the shot point of the larger explosion, to provide recordings of an impulsive point source, i.e. empirical Green's function. This approach has been explored with earthquakes (Hutchings and Wu, 1990; Hutchings, 1994; and Jarpe and Kasameyer, 1994) and has proven to work well. Whereas for earthquakes the mathematical solution of the representation relation can be solved explicitly by using small earthquakes to obtain empirical Green's functions (Hutchings and Wu, 1990), this is not true for explosions. This results in additional approximations when using empirical Green's functions to model explosions, and the significance of these approximations needs to be explored further.

The basic assumption of this work is that spatial distribution of the explosion source dimension can be resolved by fitting observed seismograms. A major constraint provided is the total duration of the explosion as provided by deconvolution from of the empirical Green's function with the large explosion. Such a deconvolution assumes that all the energy of both the large and small events occurs at a point, so that spatial and time delays are lumped together. It is shown that the spatial distribution results in phase delays of empirical Green's functions. In the frequency domain these delays have little effect on the shape of spectra, but in the time domain they have a significant effect on the waveforms of seismograms. The sensitivity of waveforms enables one to resolve differences in geometric size of near 50 m. Thus, the expectation is to differentiate between nuclear and conventional explosions by the difference in source size and rise time as a function of source yield.

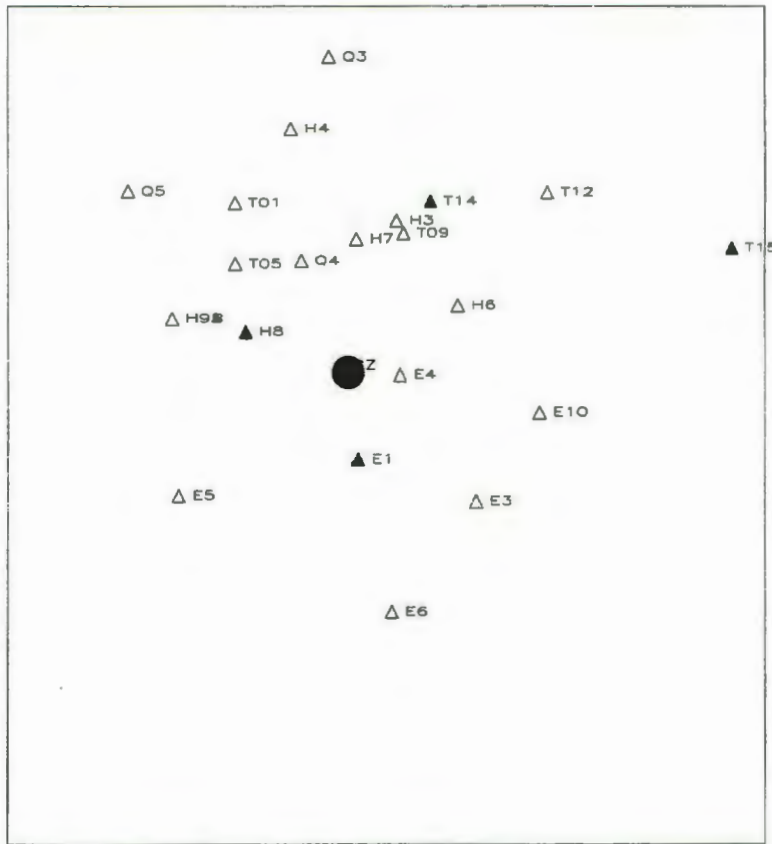


Figure 1. The location of the NPE (solid circle) and station used in this study (solid triangle).

Data

The NPE detonated 2.9 million pounds of blasting agent that resulted in approximately 1 kiloton of energy release. It was detonated at depth of 396 m, in the volcanic tuff of N-Tunnel in Area 12 of the Nevada Test Site in Rainier Mesa. A pre-shot explosion was recorded from the shot point of the NPE. Recordings of this event are used as empirical Greens functions in this study. Figure 1 shows the locations of recording stations and the NPE shot point, and Table 1 list their locations.

Table 1: Station Locations

Site id.	Latitude	Longitude	Elev* (relative)
E1	37.19910 N	116.20930 W	410m
H8	37.20220	116.21270	390
T14	37.20530	116.20710	0
T15	37.20140	116.20990	0

* elevation is relative to 0 at shot point.

Theory

Representation Relation

A solution of the elastodynamic representation relation in the absence of body forces can be expressed as (Aki and Richards, 1980, sec 3.1):

$$u_n = \int_A u_i(x', t') \Big|_{-a}^a C_{ijpq} v_j \bullet G_{np,q}(x, t; x', 0) dA \quad (1)$$

where the surface is chosen such that it includes, but does not coincide with a displacement discontinuity, as shown in Figure 2. The displacement u_i across the smaller surface A' is discontinuous $u_i \Big|_{-a}^a$, but the traction is continuous across the surface A' . v_j is the normal to the surface A' , j 's are directions in the coordinates of the larger surface A . C_{ijpq} are the elastic constants, and \bullet indicates convolution.

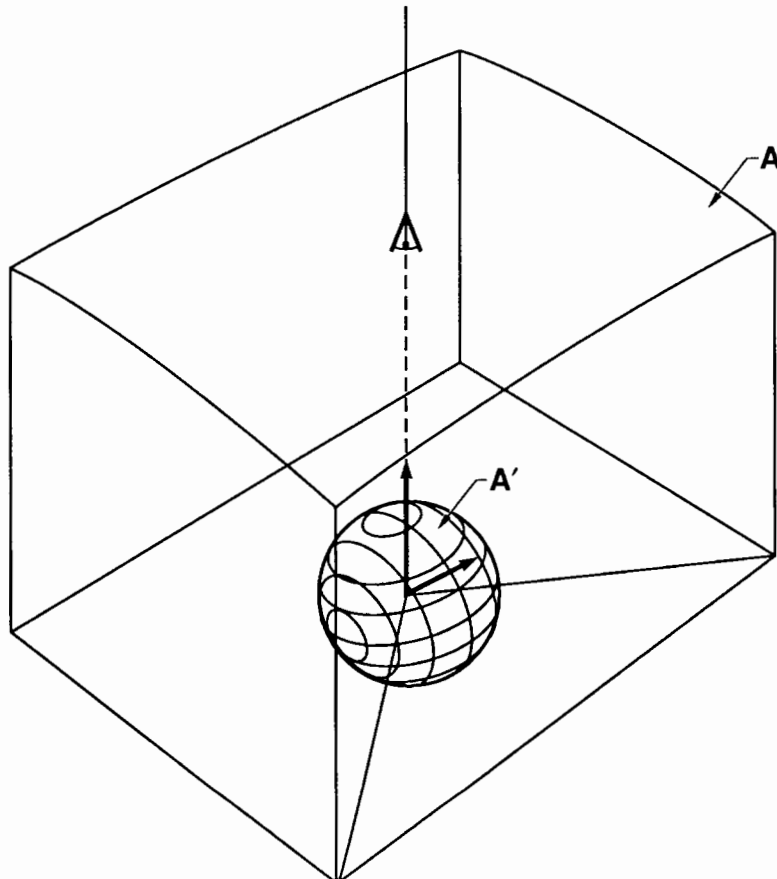


Figure 2. The sphere represents the elastic limit of the explosion, across which there is a displacement discontinuity. The surface A is the surface of a large volume that includes the sphere, and which there are no body forces.

Now, $u_i \Big|_{-a}^a \bullet G_{np, q}$ is the field of force couples, then define the integrand to the left of the convolution symbol as:

$$m_{pq} = \mu S(t') \{ [\hat{s}_q] \hat{n}_p + [\hat{s}_p] \hat{n}_q \} \quad (2)$$

where the bracketed terms with $[\hat{s}_q]$ are displacement cosines in the component direction across the surface with unit normal vector \hat{n}_q , and the time dependence is the same for all components.

The isotropic solution to the representation relation then is:

$$u_n = \int_A S(t') m_{ii} \bullet G_{ni, i} dA \quad (3)$$

since the displacement and unit normal are in the same direction.

Empirical Green's function

Now, an explosion small enough that it effectively occurs at a point and has an impulsive source can be expressed as:

$$e_n = \int_{\delta a} H(t') m_{ii} \bullet G_{ni, i} da \quad (4)$$

where $\delta a \rightarrow 0$, but the integral results in a contribution from all radial directions at the point. However, for Green's functions for a surface integral, we only want the Green's function in the radial direction of the larger surface. The solution for the Green's function normal to the larger surface is:

$$e'_n = M_{ii} H(t') \bullet G_{ni, i} \quad (5)$$

where M is the scalar seismic moment. The difference between these two solutions is shown in Figure 3. The problem is to use recordings of small explosions, solutions to Equation 4 [Figure 3(a)], to provide unidirectional, radial Green's functions, solutions to Equation 5 [Figure 3(b)]. A method to achieve this is discussed and tested below.

There are several observations that support using the approximation a single explosion to represent all Green's functions is that the scattering effects of geology are so large, that a unidirectional motion at some point at depth gets averaged out over the space to be essentially the same as three component motion. This has been shown to be true for small earthquakes, where the observed motions are very weakly dependent upon the focal mechanism solution (Hutchings and Wu, 1990; Jarpe and Kasameyer, 1993). Also, the symmetry of the point spherical solution will result

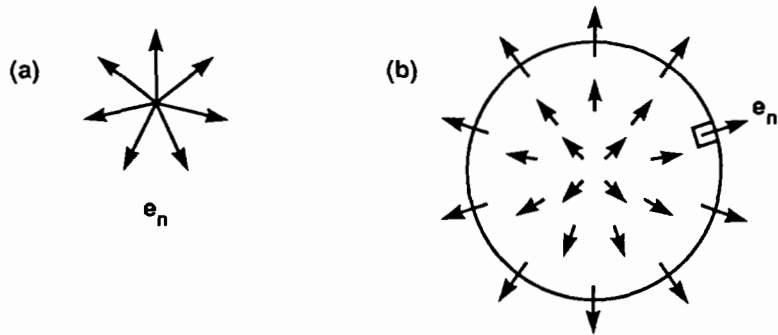


Figure 3a. A schematic drawing showing the radial rays of a point source. 3b: A schematic drawing showing the radial rays for a finite source; the Green's functions needed are only one 'ray' of those shown in 3a.

in non-radial components of motion cancelling out as the integral moves around the surface, leaving a positive and negative normal dipole solution along the surface.

Spherical Volume and Surface Solutions

A solution to Equation 3 using empirical Green's functions is expressed as:

$$u_n = \int_{\lambda} \frac{S'(t')}{M_o^e} \bullet e'_n(x, t) dA \quad (6)$$

where S' is the desired source function deconvolved with the step function of the empirical Green's function, and M_o^e is the scalar seismic moment of the small explosion source of the empirical Green's function.

A means to achieve the solution to Equation 6 by using actual recordings of small explosions (Equation 4) is schematically shown in Figure 4. By integrating over the surface of a sphere with the green's functions from Equation 4 one obtains a dipole, radial dislocation solution [Figure 4(a)]. This is because the non-radial components cancel. However, we want an outward normal dislocation solution. If one added an inner surface with the same solution to Equation 6, then you obtain a donut volume with outward and inward normal dislocation solutions [Figure 4(b)]. If one continues with smaller inner surfaces until all inner displacements have cancelled except the outer surface, an outer normal dislocation solution (Equation 6) remains. This is shown in Figure 4(c). This is expressed as:

$$u_n = \int_0^R \int_{\lambda} \frac{S'(t')}{M_o^e} \bullet e_n(x, t) dA dV \quad (7)$$

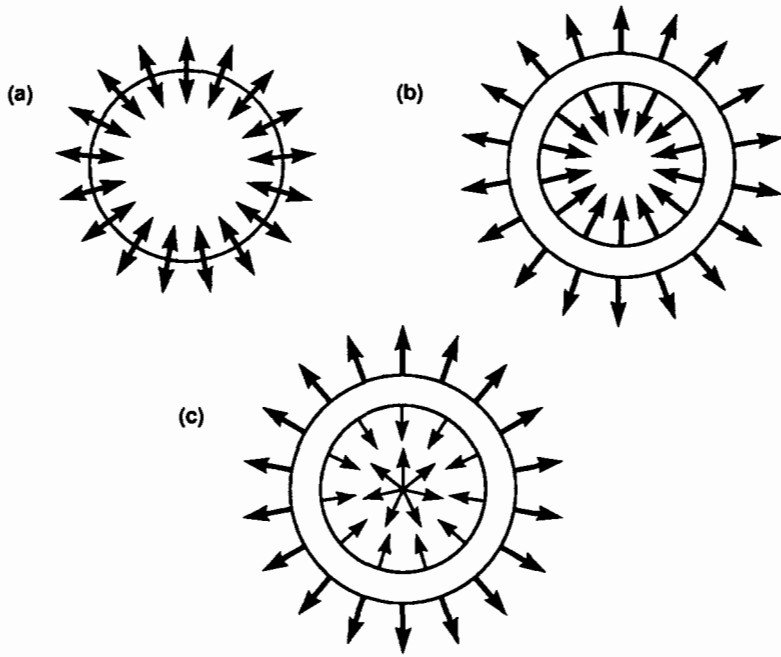


Figure 4. (a) A two dimensional view of rays resulting from integrating Green's function shown in Figure 3a over the surface of a sphere. (b) a view of rays that result when the integration is continued for progressively large surfaces. (c) the result when the integration is carried out from a point to an elastic radius. All inward rays are canceled, leaving the desired outward rays along the exastic surface. If this is repeated for progressively larger surfaces, then a volume integral solution can be obtained.

where R is the radius of the solution desired, and note that e_n is used instead of e'_n . There is some error due to the fact that not all outward and inward normal components cancel because of the slightly smaller surface areas of the inner circles. Now, if one wanted to obtain a volume solution, you would integrate out to progressively larger radii:

$$u_n = \int_0^R \int_A \frac{S'(t')}{M_o^e} \bullet e_n(x, t) dA dV dV \quad (8)$$

Discretized Solution

If the source function of the explosion is represented as a summation of step functions and the integral is solved by discretizing the dislocation surface, the discretized solution to equation 6 can be expressed as (Hutchings (1994)):

$$u_n(X, t) = \sum_{i=1}^N \sum_{k=1}^{L_i} \frac{\mu_i A_i s_{ik}}{M_{oi}^e} e_n(X, t_i' - \tau_i^r - \tau_k^s) \quad (9)$$

where u_n is displacement at position X , and t is time relative to origin time. Indices over i are for individual elemental areas of the surface, indices over k are over incremental changes for an element, N is the number of elements, L_i is the rise time at an element divided by the time step of the slip function $\Delta t'$, $\tau_k^s = k\Delta t'$, and t_i' is relative to origin time of the source event located at the i^{th} element. τ_i^r is the travel time of the explosion front from the shot point to the element. s_{ik} is the displacement increase at an element over the time step of the slip function. $e_n(X, t')$ is the seismogram from a small explosion used as an empirical Green's function for the i^{th} element with origin time and P - and S -wave arrival times corrected for location of the element. M_{oi}^e is the scalar seismic moment of the empirical Green's function used for the i^{th} element. A_i is an elemental area such that $\sum A_i$ equals the total area, and μ_i is rigidity. A_i is small enough that it does not exceed the area associated with the moment threshold for empirical Green's functions, and is also small enough that the time duration of discontinuous steps of the rupture front are shorter than the shortest period of interest; the latter is usually the strongest constraint (Hutchings and Wu, 1990).

The linear scaling factor for the empirical Green's function does not compromise the linear scaling relation between small and large explosions if the source event is small enough that it is effectively an impulsive point source explosion over the frequency range of interest. The discretized solution to equation 7 is:

$$u_n(X, t) = \sum_{j=1}^K \sum_{i=1}^N \sum_{k=1}^{L_i} \frac{\mu_i A_i s_{ik}}{M_{oi}^e} e_n(X, t_i' - \tau_i^r - \tau_k^s)_i \quad (10)$$

where j are indices over incremental volumes. A solution to equation 8 is:

$$u_n(X, t) = \sum_p \sum_j \sum_i \sum_k \frac{\mu_i A_i s_{ik}}{M_{oi}^e} e_n(X, t_i' - \tau_i^r - \tau_k^s)_i \quad (11)$$

where indices over p are for concentric spheres.

If empirical Green's functions were available for all portions of the elastic surface, Equations 10 and 11 would be exact solutions to the representation relation. The spatial dimension of the source volume are so small compared to the wavelengths of recorded arrivals that it is assumed the spatial dependence due to geology contributes an insignificant error to calculations, and that one recording of a small explosion as a Green's function is sufficient. All calculations in this study were made with the computer program EXPSYN developed for this report; which is a modification of EMPSYN (Hutchings, 1988). EXPSYN follows Equation 10 for elastic surface solutions, and Equation 11 for solid sphere solutions.

Elastic Surface

To resolve the elastic surface and the source rise time of the explosion, first consider time duration of the explosion dislocation:

$$\tau_o = \sum_{j=1}^n \delta(t_i' - \tau_j) \quad (12)$$

where τ_j includes all time delays. τ_o is obtained by deconvolution of recorded point source and the NPE (Goldstein and Jarpe, 1994). The total duration is a result of the spatial distribution of the source surface and the time distribution of the source function; but one cannot distinguish these contribution as they both add in τ_j 's. There is a trade-off between these contributions to the total duration. For a step rise time at the surface, the largest surface possible is that which gives the total source duration. For a point source, there is no spatial distribution and all the source duration is put into the rise time. In this paper, we put limits on the source size by putting limits on the source rise time; and we find that fitting observed seismograms put a very strong constraint on the choices of source size.

Observations

Empirical Green's Functions

Figures 5-8 show seismograms at stations E1, H8, T14, and T15 of the NPE and the pre-shot explosions. The shot point were the same. Stations E1 and H9 are located on the surface, and stations T14 and T15 are in tunnels. The propagation path effects for a particular station are essentially the same for both shots, except that the NPE had a non-linear volume around the shot point. The assumption here is that the NPE crushed rock for a volume, had non-linear wave propagation for a larger area, and linear wave propagation from the elastic radius on outward. We also assume below that the energy continues to radiate from the elastic radius for a period of time referred to below at the rise time.

The difference in character in the Green's functions (recordings of the pre-shot) in figures 5-8 show the variation is path effects between stations. Note that the surface recordings have much less higher frequency arrivals than the tunnel recordings. This is a typical effect, and is due to the attenuating properties of near surface material.

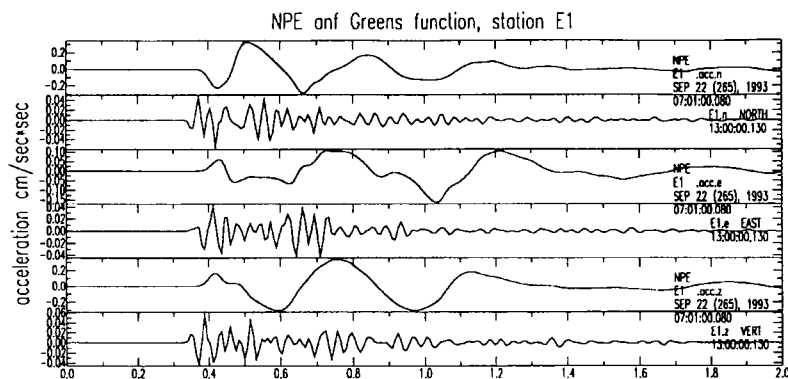


Figure 5. Acceleration recordings of the NPE and the pre-shot explosion at station E1. The recording of the pre-shot is an empirical Green's function.

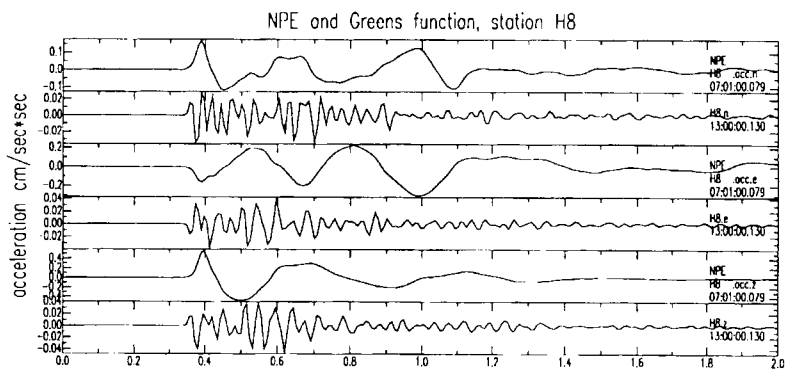


Figure 6. The same as for Figure 5, but at station H8.

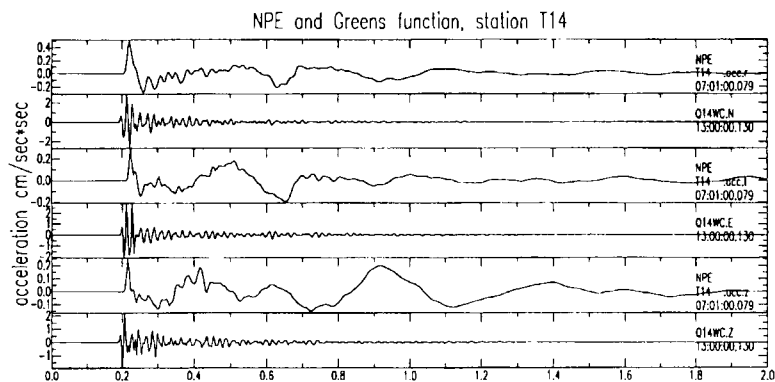


Figure 7. The same as for Figure 5, but at station T14.

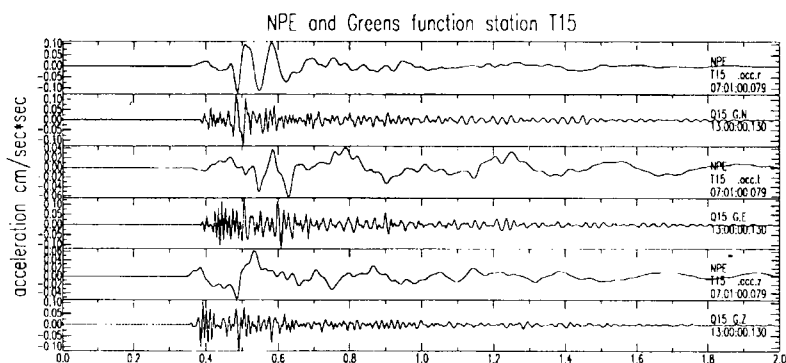


Figure 8. The same as for Figure 5, but at station T15.

Sensitivity Tests

Here we examine how sensitive synthesized seismograms are to variations in elastic radius and rise time. This is examined by synthesizing the main NPE explosion recordings. At this point we are not trying to match observed records, but just examining how synthesized records vary with changes in parameters.

Figures 9 and 10 show the effect at station T15 and T14 of modeling the source as a point source; spherical, elastic radius, surface, source; and a source volume. The sources all have the same total station duration of 0.25 s. The volume rupture has a rise time of 0.0 at the shot point, and linearly increases to 0.20 s at the elastic radius. The spherical, elastic radius solution has a rise time of 0.20 s at the elastic radius. It is apparent that the source cannot be modeled as a point source since it has too much high frequency, and that the spatial distribution of either an elastic radius solution or a volume solution significantly effects the synthesized seismograms. The volume solution approaches modeling the observed lower frequency content of the observed record, but it is not clear that a solid solution can be identified as the better source model.

Figures 11 and 12 show the effect of varying the rise time for a spherical elastic radius solution of 0.25 s at stations T15 and H8. There is a marked difference between rise time that differ by 0.2 s, but not those that differ by 0.1 s. The resolution of rise time is fairly poor for purposes of defining source rise times.

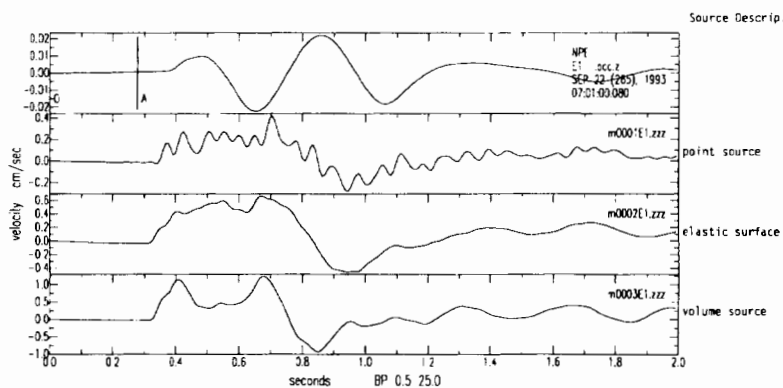


Figure 9. The effect of different source shapes on synthesized seismograms. Each synthesis has the same source duration of 0.25 seconds, but this is distributed differently for each source shape.

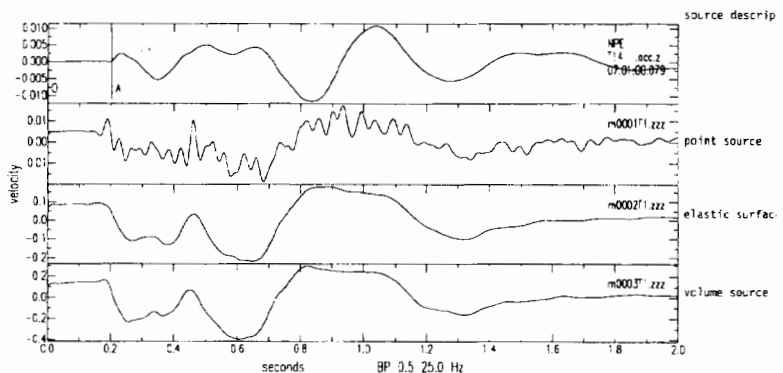


Figure 10. Same as for Figure 9.

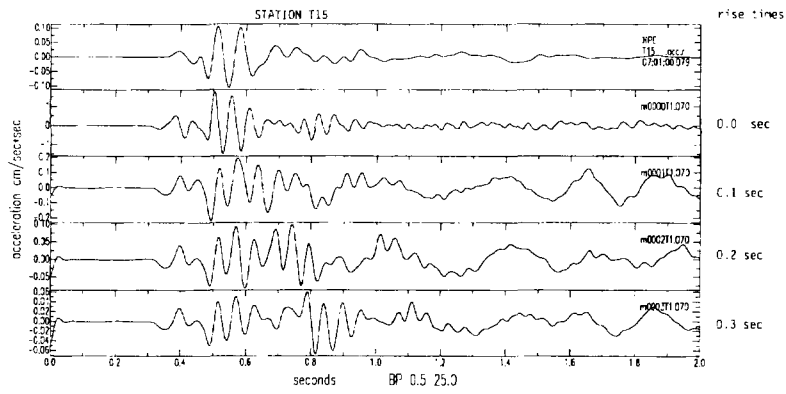


Figure 11. The effect of rise time on synthesized seismograms. Each synthesis is with an elastic surface source with 0.25 km radius, and rise time are varied from 0.0 to 0.3 seconds.

Synthesis

The best synthesized seismograms of the NPE with constraints previously discussed is shown in Figure 13. This is from an expanding spherical volume with diminishing rise time to simulate inelastic dissipation of energy. The volume has a radius of 0.25 km and an initial rise time of 0.25 s that diminishes to 0.0 at the elastic radius. The fit is fairly good at stations T14 and E1, but lacks the high frequency at stations H14 and T13. The lack of an excellent fit is considered due to the uncertainty in modeling parameters, and identification of secondary sources is probably not achievable with this resolution.

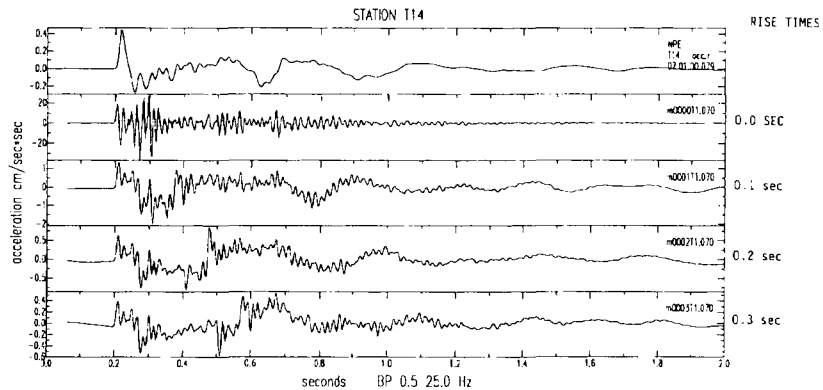


Figure 12. The same as for Figure 11.

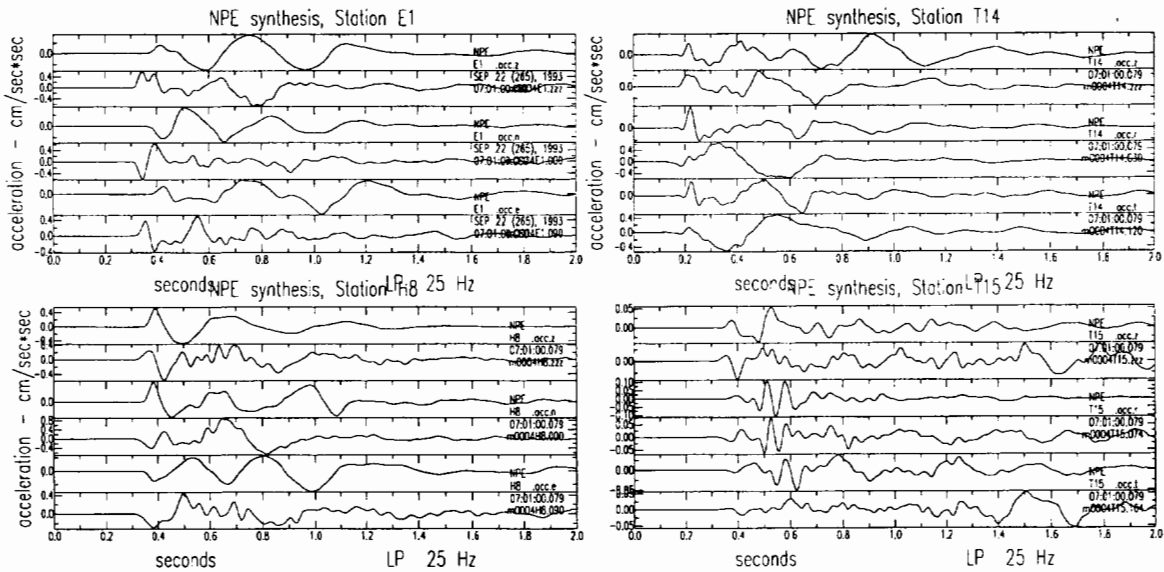


Figure 13. Solution for an expanding spherical volume solution utilizing equation 11.

Conclusions

In modeling the source, we consider both an elastic source on a spherical surface and an inelastic expanding spherical volume source. We constrained the solution to have the overall source duration obtained from point-source deconvolution results. We found that the spherical volume solution provides better fits to observed seismograms. The potential to identify secondary sources was examined, but the resolution is too poor to be definitive.

Bibliography

Blake, F.G. (1952) Spherical Wave Propagation in Solid Media. *Jour Acoust Soc Am*, **24**, pp 211-215.

Denny, Marvin D. and Lane R. Johnson (1991) The Explosion Seismic Source Function: Models and Scaling Laws Reviewed. *Explosion Source Phenomenology, Geophysical Monograph* 65.

Goldstein and Jarpe (1994) Deconvolution Results for the NPE Using Empirical Green's Functions. Proceedings of the Non-Proliferation Experimental Results and Implications for Test Ban Treaties, M. D. Denny, editor, L.L.N.L., Livermore, CA, Conf-9404100.

Hutchings, L. (1994) Kinematic Earthquake Models and Synthesized Ground Motion using Empirical Green's Functions. *Bul Seis Soc Am* **84**

Hutchings, L. (1991) ``Prediction'' of Strong Ground Motion for the 1989 Loma Prieta Earthquake using Empirical Green's Functions. *Bul Seis Soc Am* **81**, 1813-1837

Hutchings, L. (1988) Modeling Earthquake Ground Motion with an Earthquake Simulation Program (EMPSYN) that Utilizes Empirical Green's Functions. UCRL-ID-105890, Lawrence Livermore National Laboratory.

Hutchings, L. and Wu, F. (1990) Empirical Green's Functions from Small Earthquakes: A Waveform study of Locally Recorded Aftershocks of the 1971 San Fernando Earthquake. *J. Geophys. Res.* **95**, 1187-1214.

Jarpe, S.P., L.J. Hutchings, T.F. Hauk, and A.F. Shakes (1989) Selected Strong- and Weak-Motion Data from the Loma Prieta Earthquake Sequence. *Seis Res Letters*, **60**, 167-176.

Yield of the Non-Proliferation Experiment From the Leo Brady Seismic Net

**H. Douglas Garbin
Sandia National Laboratories
Department 9311**

Abstract

The Leo Brady Seismic Net (LBSN) has been used to estimate seismic yields on US nuclear explosion tests for over 30 years. One of the concerns that Non-Proliferation Experiment (NPE) addresses is the yield equivalence between a large conventional explosion and a nuclear explosion. The LBSN consists of five stations that surround the Nevada Test Site (NTS). Because of our previous experience in measuring nuclear explosion yields, we operated this net to record NPE signals. Comparisons were made with 9 nuclear tests in the same volcanic tuff medium and within an 800 m range of the NPE source. The resulting seismic yield determined by each nuclear test ranged from 1.3 to 2.2 kT. Using the same techniques in determining nuclear explosion yields, the 1 kT NPE was measured at 1.7 kT nuclear equivalent yield with a standard deviation of 16%. The individual stations show a non-symmetric radiation pattern with more energy transmitted to the north and south. Comparisons with a nuclear event does not show any obvious differences between the two tests.

Introduction

For over thirty years Sandia National Laboratories has operated a seismic net around the Nevada Test Site (NTS) in an ongoing effort to measure seismic yields of nuclear tests. The Leo Brady Seismic Net (LBSN) has evolved over the years to its present state with several upgrades to replace obsolete equipment and improve system response. The primary purpose of the net is to obtain a prompt seismic yield within a few hours of a nuclear event and report it to interested agencies. As a measure of how well this goal has been accomplished, studies show that comparisons of our seismic yields to the laboratories published final official yields had a one standard deviation of 16%¹. Although seismic yield estimation is our primary purpose, we have also recorded earthquakes and researchers have requested and used our data for additional studies dealing with verification and general geophysical research.

Figure 1 is a map with an outline of the state of Nevada and the LBSN sites marked. It consists of five stations arranged somewhat azimuthally symmetric around NTS at ranges between 110-400 km. They include Nelson NV, Leeds UT, Battle Mountain NV, Tonopah NV and Darwin CA. The configuration of the net has been stable in its present locations since 1967. The stations are situated in underground alcoves and the data is continuously transmitted from the site via dedicated leased lines to a central recording location in Las Vegas, NV. The data is digitized at each station with a 24 bit A/D converter and transmitted over phone lines with 9600 baud modems for storage on optical juke boxes. Natural seismic activity is only recorded when it is event detected by a long term short/term average algorithm. For scheduled events, the system is operated manually and turned on 60 sec prior to zero time and data is recorded for a total of 360 sec. There is a secondary dial up connection that is used to monitor state of health of each station. It can also be used to upload and download software to the station. Each station has two short period seismometers (GS-13) which are oriented so the components are aligned in a vertical and radial configuration with respect to a reference point at NTS. There are also three long period SL210/220 gauges oriented in a manner similar to the short period instruments. The additional long period component is arranged transversely with respect to NTS. All the signals are recorded at 50

samples/sec. Recently we have been recording the GS-13 signals on two additional channels at 250 samples/sec so each station has a total of 7 channels being recorded for each event.

LBSN Station Locations

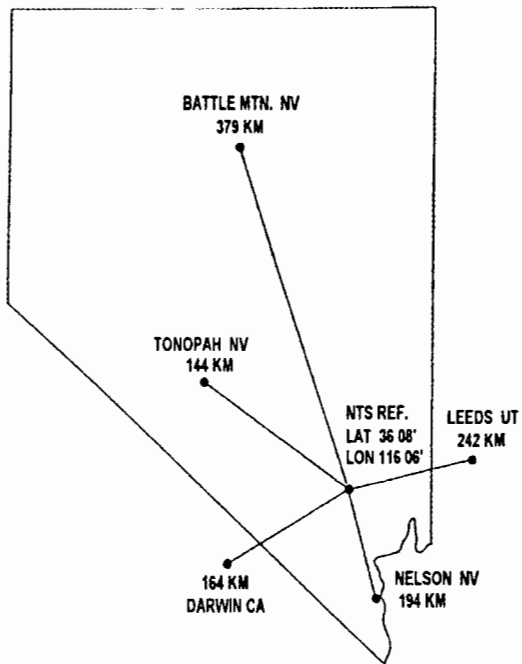


Figure 1

Method:

Historically, we have made yield estimates using only the short period data. This was the normal mode used by Leo Brady, the former Sandian who ran the net's daily operations and did the yield estimates. I also followed his general procedures. This procedure consists of measuring a number of easily identifiable peaks in the initial arrival of the wave. For the vertical component, these are denoted as V_a , V_b , V_c , and V_d . Similar measurements are also made on the radial components. The initial arrivals are used since these peaks are relatively free from later arriving phases or multipathed signals. Also an explosion is a pressure source and since the first arrivals are compressional waves, they are more representative of an explosion. Of course not all the chosen peaks are free of interference, so if a peak is contaminated by late arrivals, the amplitude may not be used in the estimate. Figure 2 is an example of measurable peaks from the NPE event. V_a is the amplitude measured from the signal arrival to the first peak and V_b , V_c and V_d are the next three peak to peak amplitudes. These four amplitudes are the major contributors to the yield estimates, but we have also used other reproducible amplitudes in the coda such as the largest peak to peak signal within 10 seconds of the time of arrival. This additional amplitude is added because it is possible for the first arrivals to be too small to detect for low magnitude events. Also the ranges may be such that P_n (head wave traveling along the mantle/crust boundary) and P_g (crustal p-wave) interfere with each other and produce unreliable results.

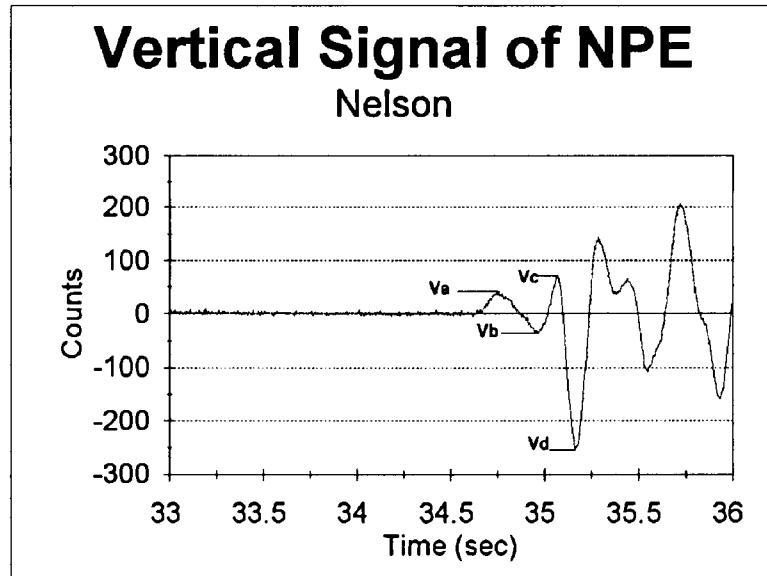


Figure 2

Two methods have been used in calculating seismic yields. Both methods require amplitude comparisons of reference events of known yields with the target event. One method divides the test site into a number of geophysical distinct regions in which each region would have similar geology and layering. This is possible because there have been hundreds of nuclear tests conducted at NTS so we can get a good statistical population for comparisons. For each of these regions, a calibration curve is determined relating the yield to each amplitude. This empirical calibration curve is of the form:

$$\log(Y) = a + b * \log(A) \quad (1)$$

where Y is the yield in kT.

A is one of the amplitudes described above.

a and b are constants determined by linear regression analyses.

The other method is similar, but makes a direct comparison of the target event to a known event. This again assumes a power relation such as equation (1) connecting the ratio of amplitudes to the yield. However in this case, we assume b-value to be 0.9 and by taking the ratio of the amplitudes, the a-value need not be known. I choose to use the former method, but I will show an example of the latter. There could be two reasons for not using a calibration equation. First, there may not be enough events to determine an equation for sufficient statistical accuracy. The second reason is there may not be enough of a yield range to estimate the slope b.

Before a yield estimate can be made, the procedure first requires finding a suitable suite of nuclear events as references to compare with NPE. Over the years, we have built a database that includes many physical properties of the source region at the location of the reference events. Prior to the test, this database is searched for events that have matching or similar medium properties to NPE, such as being within a certain distance of the target event, whether it is above or below the water table and within a certain range of gas filled porosity, etc. The idea behind these restrictions is to equalize the source area and the propagation path so any difference in the signals are due mainly to the source strength. Comparing NPE with nearby previous events allows us to minimize these non-source differences.

In this case, it was sufficient to search the database for all events within 800 m of NPE. The search listed nine suitable events that are located in N-tunnel and ranged as far back in time as 1970 and as recent as 1992. This spans a time when the net had two different short period instruments on line. The GS-13 seismometers were introduced in 1990 and prior to this year, the short period gauges were Benioff seismometers. Since the two instruments have different responses, before the Benioffs were completely removed, they were run in parallel with the GS-13 to record common seismic events and a transfer function was obtained between the two instruments. This transfer function allows us to convert the GS-13 signals into Benioff look alike signals. This is important because the database of amplitudes used in the yield estimates prior to 1990 only have Benioff amplitudes entered in it. Also, little digital data presently exists before 1981; most of the data is still on analog tape. Thus we must make the conversion from GS-13 to Benioff signals to compare with the database amplitudes.

Analysis

Much of the work can be done prior to the actual event. This includes identifying the reference events and extracting their amplitudes from a database. After the target event (NPE) has been recorded, it is converted from voltage to engineering units and plotted on a screen. A utility allows the amplitudes to be picked off a screen and automatically read into a database. A spreadsheet is setup for the yield analysis that consists of only those peaks that are common with the target event. The spreadsheet is built by extracting amplitudes of all the events from a database and writing them to ASCII files. A utility combines and sorts these files such that the rows contain the same wave phase. This file is imported into the spreadsheet for the analysis using the built in statistical functions of the program. The NPE yield resulting from of averaging ratios for each event is shown in Table I, where the units are kT.

TABLE I

NPE Yields Calculated from 9 Events

Event 1	Event 2	Event 3	Event 4	Event 5	Event 6	Event 7	Event 8	Event 9
1.26	1.46	1.52	1.55	1.50	1.83	2.22	2.07	1.60

The yields calculated for each event range from 1.3 to 2.2 kT with an average of 1.7 kT. All of the calculations give a yield larger than 1 kT for NPE. Events 6, 7, and 8 are the tests with the highest yields. They also produce the largest NPE calculated seismic yields and if they are excluded from the analysis, the average drops to 1.5 kT. In the evaluation of this empirical relation, the higher yield events bias the NPE calculations to higher seismic yield. The standard deviation of the total estimate is about 16%. The yields in TABLE I are obtained from a simple averaging of amplitude ratios of an event using equation (1) with b equal to 0.9. The standard deviations of NPE yield associated with each nuclear test vary considerably from about 15% to 40% of the mean. The higher standard deviations are associated with the larger events. This calculation implies that the NPE event has a seismic nuclear yield equivalence of about 1.5 to 1.7 kT. This is consistent with the near field in that calculations also show a seismic yield equivalence greater than 1 kT.

The above analysis compares individual events to NPE in making a yield determination. I did derive one calibration curve for comparison. Figure 3 is a plot of a calibration curve for R_b at Darwin with 9 reference events. I have used the same nomenclature as in figure 2, where R refers to the radial amplitude. A scale factor has been inserted in the yield values to normalize the smallest yield to 1 kT. The slope of this curve (b-value) is 0.85 which is close to 0.90 used in the above analysis. This results in a yield of 1.6 kT for NPE. The standard deviation of the regression analysis in the plot of figure 3 plot is 17%.

Plot of Amplitude vs Yield

Line is a regression plot of the data

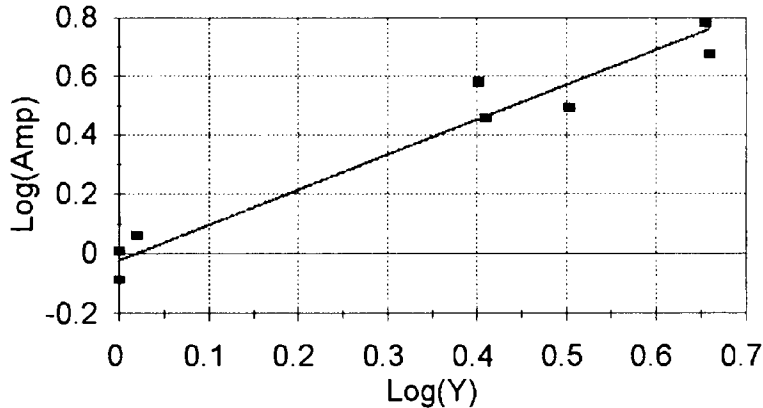


Figure 3
Calibration curve for the R_b phase

If instead of averaging over the whole net, we can look at individual stations and their yields. Table II is a list showing the NPE yields determined at each station. The number of amplitudes used in calculating these estimates at each site is much smaller than the entire net and thus the statistical basis is somewhat eroded. However, note the radiation pattern. Tonopah and Nelson which lie to the north and south respectively register larger yields than Leeds and Darwin which are to the east and west respectively. The total average is still about 1.7 kT, but there is directionality associated with the source.

TABLE II
Yields Calculated from Each Station

Darwin	1.53 kT
Leeds	1.54 kT
Nelson	1.91 kT
Tonopah	1.87 kT

This directionality is of concern because it effects yield estimates. The non-symmetric nature can be due to several factors such as stress relaxation and anisotropic medium in propagation paths. If we assume the cause of the observed asymmetry in the station yields is due to stress release during the NPE explosion, than an estimate can be made of the contribution of energy in stress release to the signal. Although there is a fair amount of vertical offsets in the local faults, assume the stress release is equivalent to a normal strike slip event. Since the yields are almost proportional to the various amplitudes in the regression analysis, let the yields be expressed by:

$$Y = a + b * \sin(2 * (\theta - \lambda)) \quad (2)$$

where Y is the yield in kT

θ is counter-clockwise angle off north in degrees

λ is counter-clockwise strike angle off north in degrees

a and b are constants.

This formula is based on the response of a horizontal double couple which models a vertical strike slip earthquake. Range need not be considered since yield is independent of station location. Although there are only four stations, a regression analysis is done to determine a, b, and λ . The results of the calculation give $a = 1.71$ kT, $b=0.23$ kT and $\lambda=24^\circ$ NNE. The parameter a is about the value of the average kT measured in the usual way which is not unexpected because the angular term should average to zero for a well distributed net. The factor b is the quadrupole amplitude energy in kT.. Figure 4 is a plot of the total yield radiation pattern with the estimates of the four stations superimposed on it. The plot also has the quadrupole radiation pattern inserted. The standard deviation of a and b are both quite small, 0.003 kT for both. A similar calculation was done on a nuclear event which results in a different radiation pattern. This is shown in figure 5 where the nuclear yield is normalized to NPE. The quadrupole contribution in this analysis is not constrained very well and has a standard deviation slightly larger than b itself. Perhaps another source type would fit the data better. i.e. dip slip. The strike angle for this event is about 90° different than NPE, $\lambda \approx 113^\circ$.

Radiation Pattern from NPE

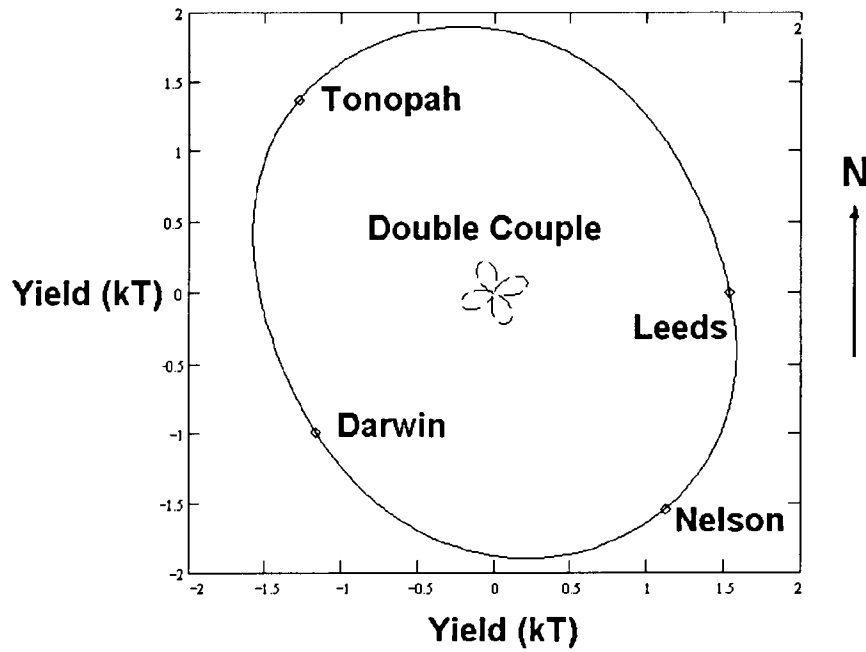


Figure 4

Radiation Pattern from Nuclear Event

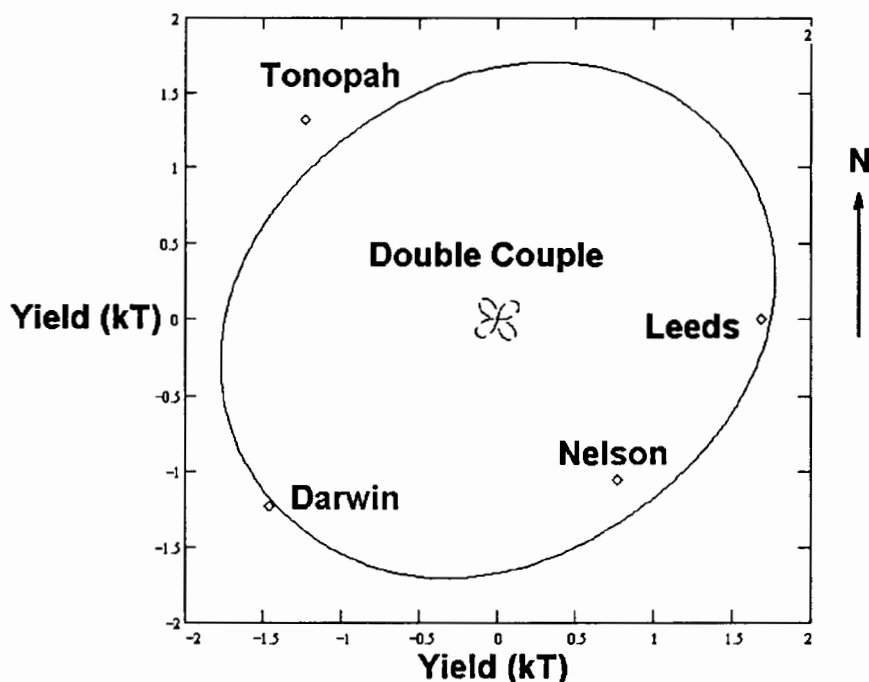


Figure 5

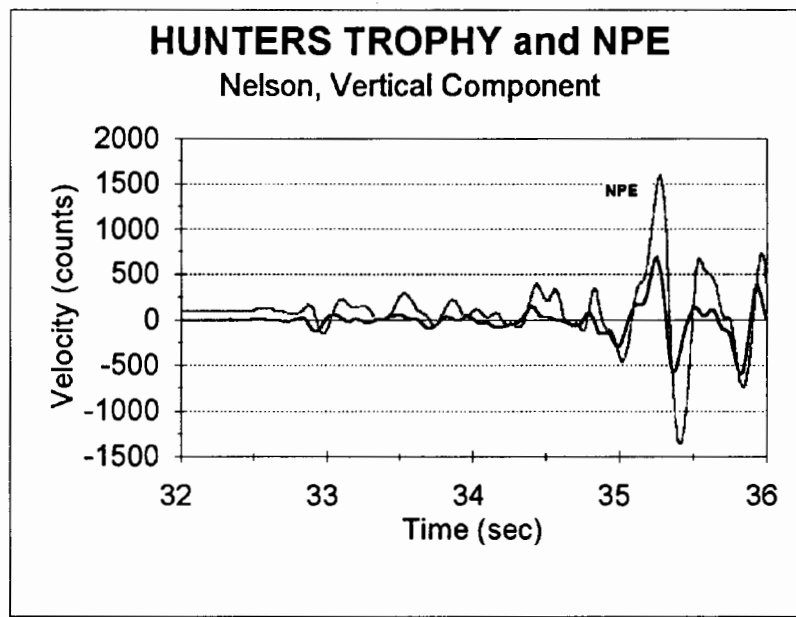


Figure 6

The close in free-field data showed some major differences between the NPE and nuclear explosions in both the time series and spectral plots². These differences were very noticeable at high frequencies above 30 Hz. To see if the signals reveal similar behavior at regional ranges, I compared LBSN seismograms of

NPE with a nearby nuclear event. Figure 6 is a plot of the high frequency vertical channels of HUNTERS TROPHY and NPE as recorded from the Nelson station. Only Nelson is compared because the high frequency channels were not operational on the other stations for HUNTERS TROPHY. The time series in the figure do not show any obvious differences in the initial arrivals. The amplitude differences are due to the gain settings. The high frequency channels sample at 250 Hz, however noise reduced the usable signal to frequencies less than 25 Hz. Figures 7 and 8 are spectral plots of HUNTERS TROPHY and NPE over the window which includes the first 60 seconds of the signal. The noise window is 15 seconds prior to signal arrival. In both cases, the signal and noise merge after 20 Hz. This is unfortunate since the free-field showed differences in signals at frequencies above 30 Hz. Figure 9 includes the spectral data of HUNTERS TROPHY and NPE superimposed on the same plot and very little difference can be detected between the two explosions. In fact figure 9 looks like just a single event because the two spectra merge so well. However other test sites may not be so unforgiving and have less regional attenuation. If this is the case, high frequency analysis may give differences between nuclear and conventional explosions.

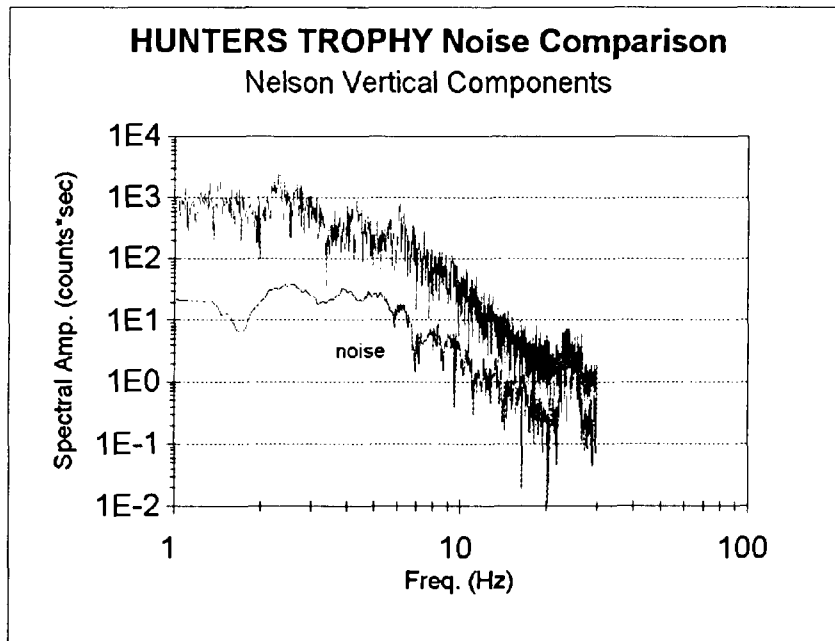


Figure 7

HUNTERS TROPHY signal and noise of vertical component at Nelson

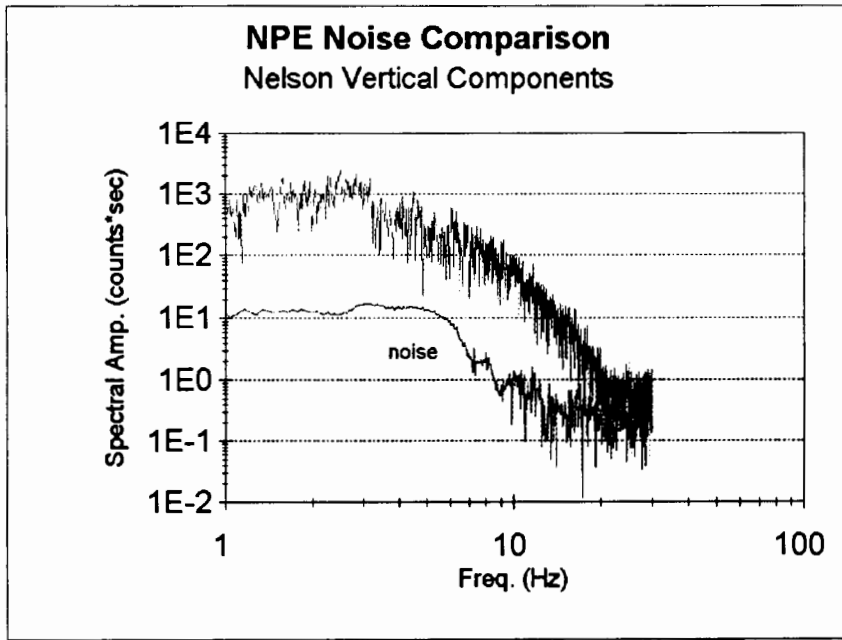


Figure 8

NPE signal and noise of vertical component at Nelson

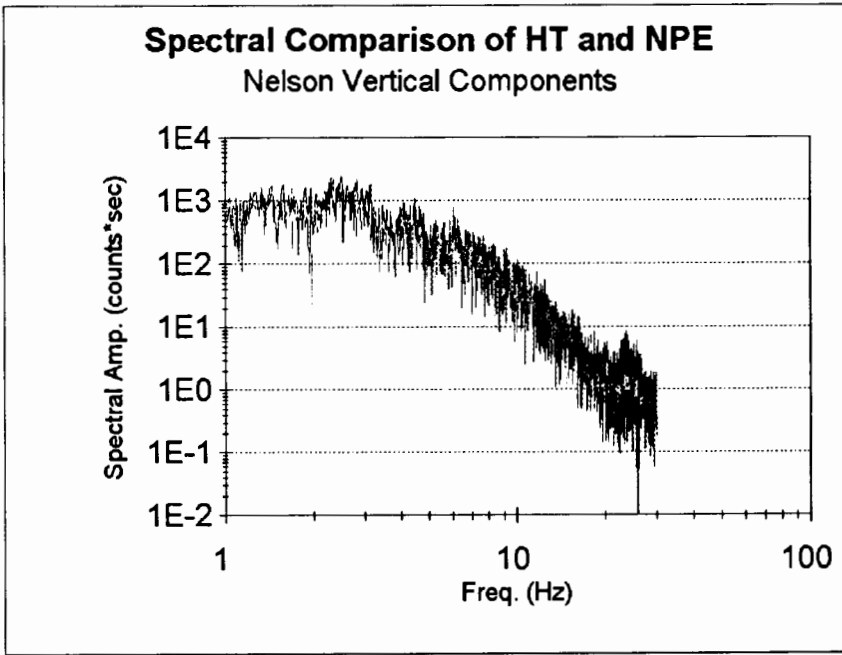


Figure 9

NPE and HUNTERS TROPHY Spectra Overlaid

Conclusions

Data from the LBSN was analyzed to obtain a yield equivalence of 1.7 kT for the 1 kT NPE conventional ANFO explosion. The analysis used 9 nuclear tests in N-tunnel within 800 m of the NPE source to make the estimate with a standard deviation of 16%. The larger events in the population biased the estimate to higher yields. There appears to be a skewed radiation pattern with the source and stronger signals transmitted to stations lying to the north and south. This radiation pattern is not the same for a nearby nuclear explosion and the standard deviation of the nuclear event analysis is quite high. In both cases, the non-symmetric contribution is an order of magnitude less than the explosion source. A first cursory look at NPE and HUNTERS TROPHY show no obvious differences in the signals or spectra to distinguish between the two sources. Near-field data indicated differences between NPE and nuclear events, but this property is masked at regional ranges by attenuation of the high frequencies.

Acknowledgments:

The successful operation of the Leo Brady Seismic Net is the consequence of the efforts of a DOE team consisting of EG&G, NV and Sandia National Laboratories. I would also like to acknowledge Preston Herrington and Larry Walker without whose support this project would not have proceeded.

References:

1. L. F. Brady and H.D. Garbin, "The Sandia National Lab Off-site Seismic Net", Conference on DOE Ground Motion and Seismic Programs On, Around, and Beyond the NTS", Albuquerque, NM, 4-5 November 1981.
2. H. D Garbin, "Free-Field Seismic Ground Motion on Non-Proliferation Experiment", Proceedings of the DOE Symposium on the NON-PROLIFERATION EXPERIMENT Results and Implications for test Ban Treaties, Rockville, MD, 19-21 April 1994.

This work was performed by Sandia National Laboratories under contract DE-AC04-76DP00789 with the US Department of Energy.

Lawrence Livermore National Laboratory Seismic Yield Determination for the NPE

Robert Rohrer
Lawrence Livermore National Laboratory

Abstract

The Lawrence Livermore National Laboratory recorded seismic signals from the Non-Proliferation experiment at the Nevada Test Site on September 22, 1993, at seismic stations near Mina, Nevada; Kanab Utah; Landers, California; and Elko, Nevada.

Yields were calculated from these recorded seismic amplitudes at the stations using statistical amplitude- yield regression curves from earlier nuclear experiments performed near the Non-Proliferation experiment. The weighted seismic yield average using these amplitudes is 1.9 kt with a standard deviation of 19%. The calibrating experiments were nuclear, so this yield is equivalent to a 1.9-kt nuclear experiment.

Results

The Non- Proliferation Experiment was performed in U 12 tunnel in Rainier Mesa at the Nevada Test Site September 22, 1993 at 0701 GMT at a depth of 400 m below the surface. The geodetic location was N $37^{\circ} 12' 4.8''$ W $116^{\circ} 12' 35.7''$. Seismic signals from this experiment were recorded at seismic stations near Mina, Nevada; Kanab, Utah; Landers, California; and Elko, Nevada operated by the Lawrence Livermore National Laboratory. The location of these stations is shown in Figure 1.

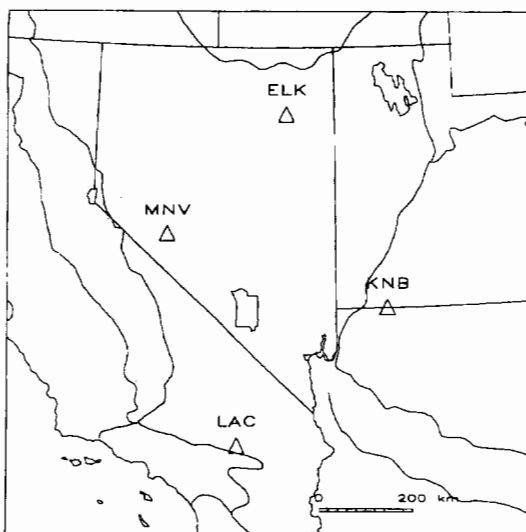


Figure 1. Location of the Mina, Kanab, Landers, and Elko LLNL seismic stations recording signals of the NPE.

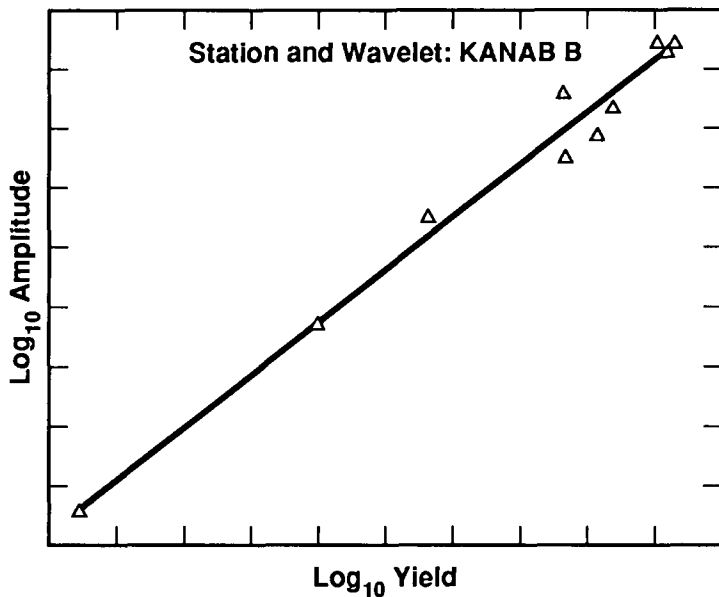


Figure 2. Amplitude vs yield regression line.

Yields were calculated from vertical component seismic amplitudes at the stations using statistical amplitude-yield regression curves from earlier nuclear experiments performed near the Non-Proliferation experiment. Data from eleven previous experiments were used in this calculation.

Nine of these experiments were less than 1 km from the Non-Proliferation experiment. Pn, Pg, or Lg waves can be used in the yield calculated.

A computer regression analysis code was used to plot the yield-amplitude data and to determine best straight line fit to the data in log-log space; i.e., $Y=E(1)+E(2)X$, where Y is the Log₁₀ of the seismic amplitude and X is the Log₁₀ of the yield and E(1) and E(2) are constants to be determined. The energy yield of a new experiment is then found from this log-linear relationship. Figure 2 shows the amplitude-yield regression curve for the Kanab Pn b wavelet for the previous experiments.

The waveforms from this chemical explosion were quite similar to that of a nearby nuclear explosion. Figures 3 and 4 show the waveforms from the Mina Station for the Non-Proliferation experiment and a nearby experiment, respectively. These waveforms resulted from passing the Mina vertical component signals through a filter designed to simulate the world-wide standard station short-period response. The similarity of the two waveforms is apparent. The Pn a,b,c amplitudes that were measured at the Mina station are shown in Figure 3.

The yields determined from the seismic signals recorded at the LLNL stations are listed in Table 1. All data were used except the Landers Pn a,b, and c amplitudes because the previous data gave an extremely poor fit to the yield-amplitude regression line. The VP amplitudes (Pg or Lg) in Table I are the maximum peak to peak amplitudes measured in the vertical component seismic

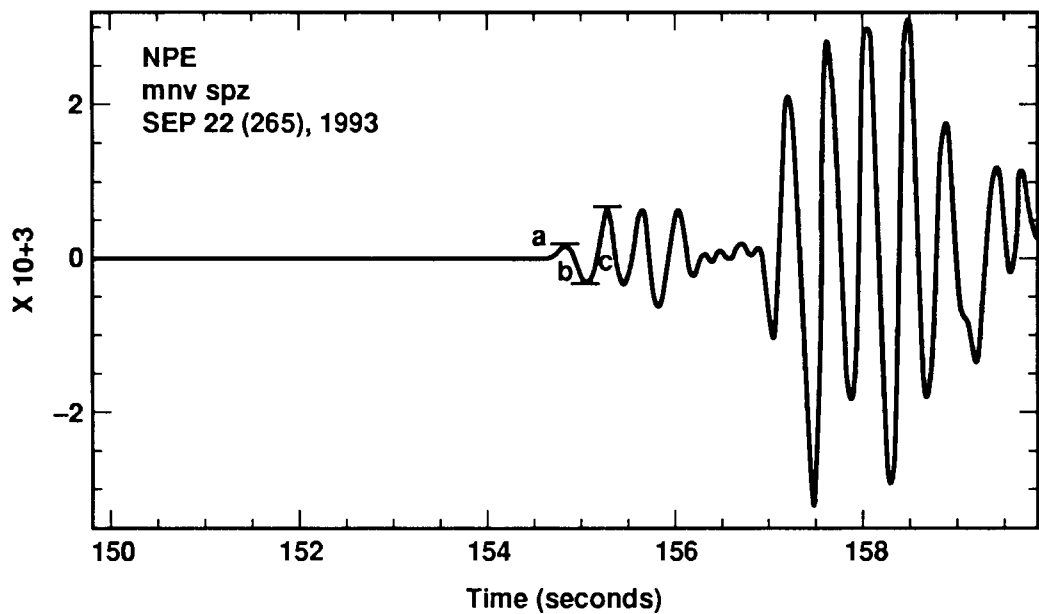


Figure 3. The short-period Pn and Pg portions of the signal recorded at the Mina station.

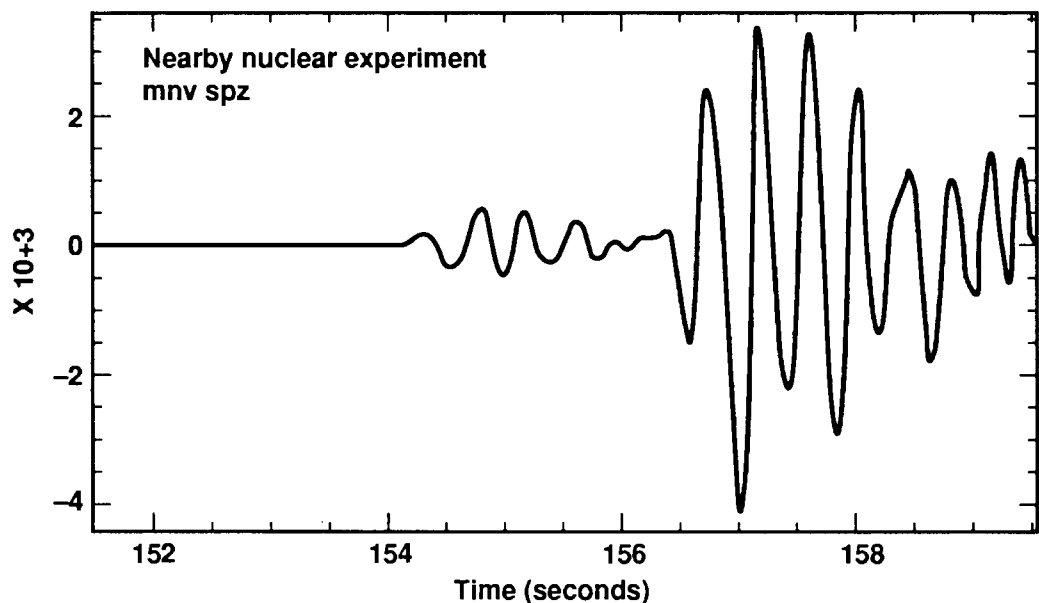


Figure 4. A nearby nuclear experiment remarkably similar to the NPE, also recorded at the Mina station.

signal. The yields range from 1.49 kt to 2.70 kt. however, the high yields had little weight in the final weighted yield calculation. The weight is determined by how well the data from the previous experiments fit the regression line. The weighted seismic yield of the Non-Proliferation experiment is 1.9 kt. The calibrating experiments were nuclear so this yield is equivalent to a 1.9 kt nuclear experiment. The standard deviation (std dev) of the estimates is 19%.

A second estimate of the yield was done by a direct comparison of seismic waveforms of the NPE to the waveforms of a nearby nuclear experiment. This also gave a yield of 1.9 kt.

Table 1. Results from the weighted regression analysis.

Summary of estimations for new event		Amplitude (nm)	Weight	Yield (kt)
Station			w	
MINA	A	111	126	2.13
MINA	B	422	101	2.11
MINA	C	827	49	2.18
KANAB	A	76	125	1.49
KANAB	B	379	104	1.83
KANAB	C	690	66	2.21
ELKO	A	15	25	2.70
ELKO	B	62	38	2.42
ELKO	C	99	31	2.44
MINA	VP	30848	57	2.36
KANAB	VP	9392	213	1.64
LANDERS	VP	4015	5	1.99
ELKO	VP	9174	38	2.15
<u>Weighted estimate for new event</u>				
log w		yield w (kt)		
0.2874		1.938		

Acknowledgments

Thanks are due to Larry Wetherom and Janet Ricca of the Lawrence Livermore National Laboratory for their fine work in recording the seismic signals from the NPE. This work was performed under the auspices of the U.S. Department of Energy by Lawrence Livermore National Laboratory under contract W-7405-Eng-48.

Investigations of the Low Frequency Seismic Waves Recorded at Near-Regional Distances from the Non-Proliferation Experiment

Howard J. Patton
Lawrence Livermore National Laboratory

Abstract

Seismic waves recorded at near-regional distances are used to characterize the source of the Non-Proliferation Experiment (NPE) and three selected nuclear explosions detonated in N-tunnel on Rainier Mesa. For periods longer than 5 sec, the signal-to-noise ratio is poor on most recordings of the NPE. A seismogram-stacking method is used in order to reduce background noise in coherent arrivals of Rayleigh waves. This method requires equalization of path dispersion and attenuation, which is accomplished in this study with empirical Green's functions. The stacked, equalized Rayleigh-wave spectra are inverted, along with spectral amplitudes of Lg waves with periods of 2 - 5 sec, for estimates of the seismic moment tensor. The NPE isotropic moment is 1.6×10^{14} Nt-m. The inferred static level of the reduced displacement potential is 825 m^3 , which is about two times smaller than the estimate from free-field data recorded within 1 km of the NPE. Moment tensors of the NPE and nuclear explosions are asymmetric, describing prolate ellipsoids of rotation with the long axis in the vertical direction. The asymmetries are among the largest for explosions on Pahute and Rainier Mesa. The non-isotropic component is a compensated linear vector dipole (CLVD), which may represent driven block motions occurring within a conical volume of material extending from the shot point (apex) to the free surface. The CLVD source can help explain some observations of scalloping in the spectra of Lg waves and Lg spectral ratios. Seismic radiation from the NPE is virtually indistinguishable from that of nearby nuclear explosions for frequencies below 1 Hz.

Introduction

The objective of this paper is to characterize the seismic radiation from the NPE at frequencies below 1 Hz. For this purpose, I examine Rayleigh waves in the long-period (LP) band from 5 to 25 sec period. The mid-period (MP) band, from 1 to 5 sec, is characterized using Lg waves. I will present the results of inverting the LP and MP observations for moment tensors of the NPE and nearby nuclear explosions. These results will be compared with results from studies of near-field seismic recordings. I will also interpret the moment tensor results for further insight into the generation of regional phases.

This study addresses several important issues for test ban treaty monitoring. The first issue is the usefulness of large single-charge chemical explosions to calibrate a source region, which may be a concern from a monitoring point of view at some future time. We would like to know if a chemical explosion looks like a nuclear explosion in terms of the radiated seismic signals and measurements that we make off them. Also important is the efficiency of the chemical source versus that of a nuclear explosion (i.e. energy coupling). The second issue concerns regional discriminants, and a physical understanding of these discriminants in terms of the source and the generation/propagation of regional phases. To the extent that chemical explosions look like nuclear explosions on plots of discriminants, we must understand what physical mechanisms are responsible for this. Indeed, a physical basis for discriminants is absolutely necessary for assessments of the reliability and transportability from one region to the next.

Methodology

LP Analysis. The NPE explosion occurred at 07:01 GMT , 22Sep93, on the Nevada Test Site (NTS) in N-tunnel on Rainier Mesa at a depth of 390 m. This explosion had an energy release equivalent to 1 kt and produced a regional body-wave magnitude, $m_b(Pn)$, of about 4.15. The LP signals for the NPE are weak compared to background noise levels. A small Rayleigh-wave signal with period near 10 sec is generally observable on near-regional recordings (ranges < 500 km). This signal is quickly swamped by microseismic noise at shorter periods on

almost every trace. Sources of noise with periods greater than about 16 sec are also a problem because of weak signal levels. Consequently, the Rayleigh-wave signals are narrow-band and generally have poor signal-to-noise ratio (S/N).

While it is true that regional signals in the LP band are weak, there are many recordings available because of the extensive instrumentation fielded on the NPE. Figure 1 is a map showing locations of field installations that were available for the NPE and utilized sensors with sufficient bandwidth to be of use in this study. Interested readers are referred to the paper by Denny and Zucca (1994) for further information about the field experiments and the data collected. The large number of recordings can be exploited to improve signal quality by using the coherency of LP signals from one station to the next. This is accomplished using a path equalization and stacking method described briefly in the following paragraphs.

Consider the complex spectrum, $O_j(\omega)$, of a regional seismogram recorded at the j th station. In the absence of noise, this spectrum is related to the source spectrum, $S_j(\omega)$, and to the transmission spectrum, $T_j(\omega)$, through the convolution theorem applied in the Fourier domain,

$$O_j(\omega) = S_j(\omega) T_j(\omega) \quad , \quad (1)$$

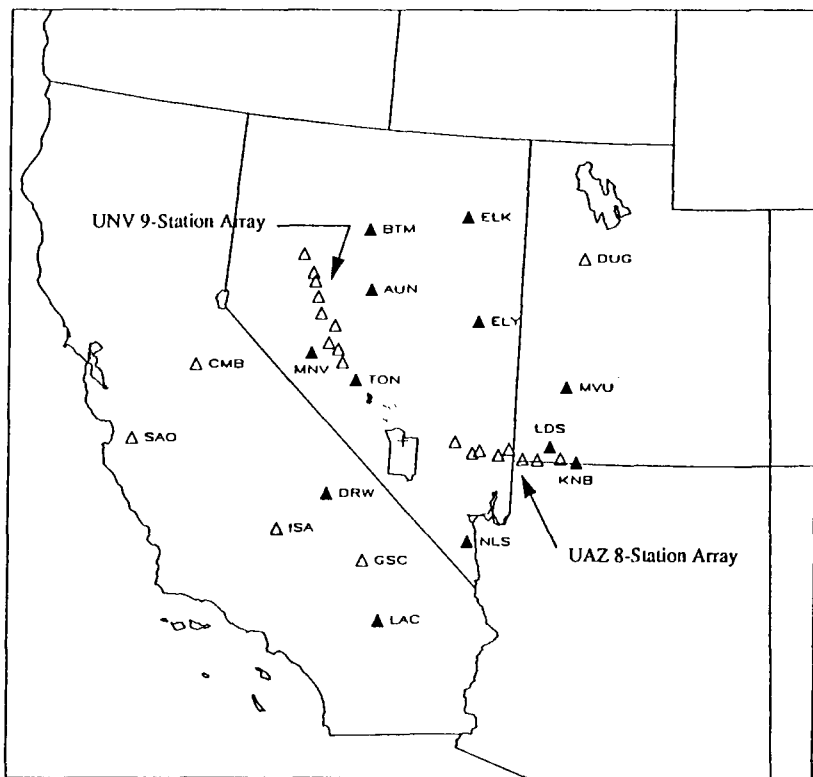


Figure 1. Map of western United States showing stations at regional distances from the NPE (cross) that recorded broadband digital seismograms considered for this study. Solid triangles are stations used in the present study; open triangles are stations for future studies. UNV - University of Nevada; UAZ - University of Arizona (see Denny and Zucca, 1994).

where ω is angular frequency. We define the path-equalized spectrum, $\mathcal{E}_j(\omega)$, for the j th station to be a spectrum which preserves information about the source, but normalizes propagation with a standard transmission spectrum, $T_o(\omega)$. Thus, we write the following equation,

$$\mathcal{E}_j(\omega) = S_j(\omega)T_o(\omega) , \quad (2)$$

which preserves the source information in (1). The object of this exercise is to obtain an estimate of the path-equalized seismogram (or spectrum) for each of the observed traces. Then, assuming that noise on the trace is additive with zero mean and variance, σ^2 , a superposition of path-equalized traces will constructively build up the coherent signal and suppress the random noise contribution. The sum or stack spectrum is

$$\sum_j \mathcal{E}_j(\omega) = T_o(\omega) \sum_j S_j(\omega) + \sum_j \mathcal{N}_j(\omega) , \quad (3)$$

where the second term on the right side of (3) is contributed by the noise and approaches zero as j increases, i.e.,

$$\bar{\mathcal{E}}(\omega) \rightarrow T_o(\omega) \bar{S}(\omega) , \text{ as } j \rightarrow \infty \quad (4)$$

where the bar refers to the average spectrum. The source spectrum, $S_j(\omega)$, is assumed to have the same phase for all stations, which is a reasonable assumption for explosions with relatively little tectonic release. If stations provide good azimuthal coverage, the modulus of the stack spectrum, $|\bar{\mathcal{E}}(\omega)|$, gives an estimate of the average source amplitude spectrum $|\bar{S}(\omega)|$, which is related to the isotropic part of the moment tensor.

For surface waves, the transmission spectrum model, $T_j(\omega)$, for the j th station may be written as follows,

$$T_j(\omega) = \frac{1}{\sqrt{r_j}} e^{-\eta_j(\omega)r_j} e^{\frac{i\omega r_j}{C_j(\omega)}} \quad (5)$$

where r_j is range, η_j is anelastic attenuation coefficient, C_j is phase velocity, and i is $\sqrt{-1}$. In this study, I used records from a nearby explosion as empirical Green's functions in order to remove the path effects for a particular station. Then, an estimate of the equalized spectrum can be made using the following expressions:

$$\mathcal{E}_j(\omega) \equiv \frac{O_j(\omega)}{O_j^{ref}(\omega)} S_j^{ref}(\omega) T_{oj}(\omega) \quad (6)$$

and

$$T_{oj}(\omega) = \frac{1}{\sqrt{r_o - \delta r_j}} e^{-\eta_o(r_o - \delta r_j)} e^{\frac{i\omega(r_o - \delta r_j)}{C_o}} , \quad (7)$$

where δr_j is the difference in range between the NPE and the reference explosion. In (7), the subscript o refers to the standard transmission model. An estimate of the path-equalized spectrum in (6) requires deconvolution of the observed complex spectra followed by convolution with the source spectrum model of the reference event, $S_j^{ref}(\omega)$, and a range-adjusted standard transmission spectrum, $T_{oj}(\omega)$. For this study, I used the NTS-TUC crustal model of Bache *et al.* (1978) with a modified surface layer (Patton, 1988) to compute η_o and C_o . r_o was arbitrarily set to 300 km.

MP Analysis. In the MP frequency band, the S/N quality of the data is much better. Only at the lowest frequencies (< 0.3 Hz) were the data for the NPE showing appearances of noise contamination. The procedures for processing Lg waves closely follow those applied by Patton (1988). Briefly, the vertical-component seismograms, corrected to ground velocity, are windowed around the arrivals of Lg using group velocities of 4.0 and 3.0 km/s. The cosine-tapered window is Fourier transformed, and the displacement spectrum is obtained by dividing by $i\omega$. The amplitude

spectrum is then smoothed with a five-point running mean, and corrections are applied for geometrical spreading and attenuation. The attenuation correction came from the study of Chavez and Priestley (1986). Finally, an average Lg amplitude spectrum is obtained by taking a log-average of the station spectra. Stations within 200 km of the source were left out of the average, because the time separation between Lg waves and Rayleigh waves is too small.

Data and Empirical Results

The wave form data used in this study come from the Livermore NTS Network (LNN), from Sandia's Leo Brady Regional Network, and from three portable stations installed by the University of South Carolina for the NPE (see Figure 1). In addition to the NPE, three nuclear explosions in N-tunnel on Rainier Mesa were also processed: MISTY ECHO (ME), MINERAL QUARRY (MQ), and HUNTERS TROPHY (HT). Only LNN and Sandia data were available for the nuclear events. Pertinent source information about these explosions are given in Table 1.

Table 1.

EXPLOSION SOURCE DATA

Name	Date	Origin Time (GMT)	Latitude (N)	Longitude (W)	DOB (m)	$m_b(P_n)$
MISTY ECHO	10DEC88	20:30	37.20	116.21	384	4.79
MINERAL QUARRY	25JUL90	15:00	37.21	116.21	389	4.51
HUNTERS TROPHY	18SEP92	17:00	37.21	116.21	400	4.18
NPE	22SEP93	07:01	37.20	116.21	390	4.16
HARZER	06JUN81	18:00	37.30	116.33	637	5.62
KEARSARGE	17AUG88	17:00	37.30	116.31	616	5.64

For the LP analysis, two explosions, HARZER and KEARSARGE, were selected to be reference events. They occurred on Pahute Mesa about 15 km from the NPE and the nuclear events (i.e. $\delta r_j < 15$ km). These events were chosen because of their excellent S/N characteristics and because they have seismic moment tensors already worked up (Patton, 1988) and hence $S_j^{ref}(\omega)$ are readily computed. Also, the portable sites used in this study were occupied on the HARZER test, and their seismograms served as empirical Green's functions. Source information for the reference events are also given in Table 1.

The path-equalization and stacking method is demonstrated on MQ for which the S/N ratio is fairly good. The time-domain results are shown in Figure 2a. The traces have been low-passed filtered at 0.2 Hz, so that the coherency of the surface-wave phases can be examined at the shortest periods. It can be seen that the coherency is quite good and that the stack seismogram has reduced noise. It should be kept in mind that the method preserves information about the amplitude radiation, and this is apparent in Figure 2a. Stations to the northwest and southeast have larger amplitudes compared to stations southwest and northeast of the source. The amplitude of the stack seismogram is about midway between the extremes seen on the records for Darwin and Nelson.

Results for the NPE are shown in Figure 2b. Here the seismograms have been filtered at 0.12 Hz, so that signals with periods near 10 sec can be seen on each trace. As expected the coherence of the 10 sec period waves is quite good. The stack seismogram shows much improved S/N quality.

The stack Rayleigh-wave spectra for the NPE and the three N-tunnel nuclear explosions are shown in Figure 3a. For the NPE and HT, the spectra show significant variability in the microseismic frequency band ($0.12 < f < 0.2$ Hz). Apparently, there are not enough seismograms in the stack to reduce the noise well below the signal level. The spectra for the larger shots are very smooth, and only at the lowest frequencies for MQ are there signs of some noise contamination. Despite the variability, the stack spectrum for the NPE clearly shows smaller amplitudes than the spectrum of HT. In Figure 3b, the spectra have been scaled using the $m_b(P_n)$'s in Table 1. The point here is to

MINERAL QUARRY

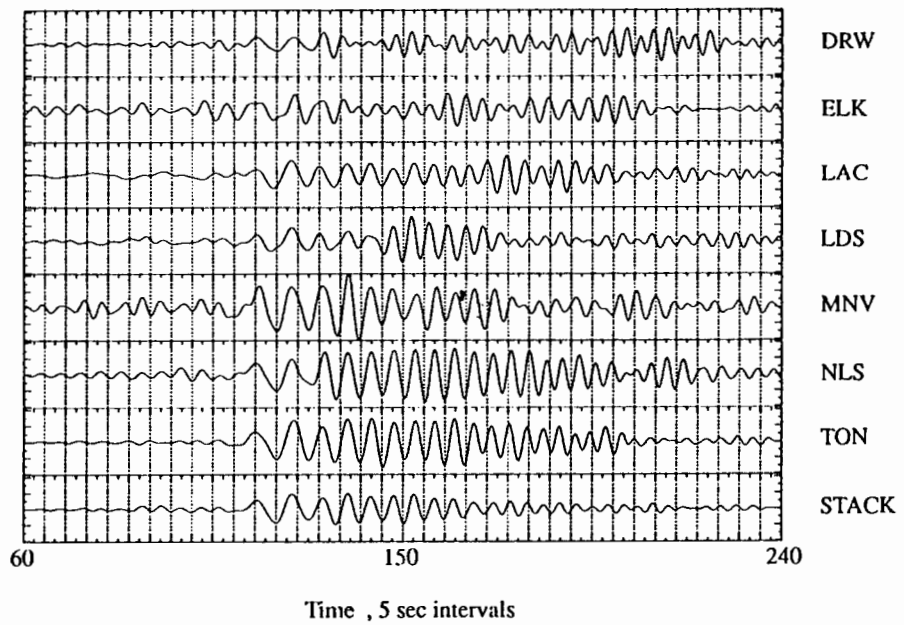


Figure 2a

NPE

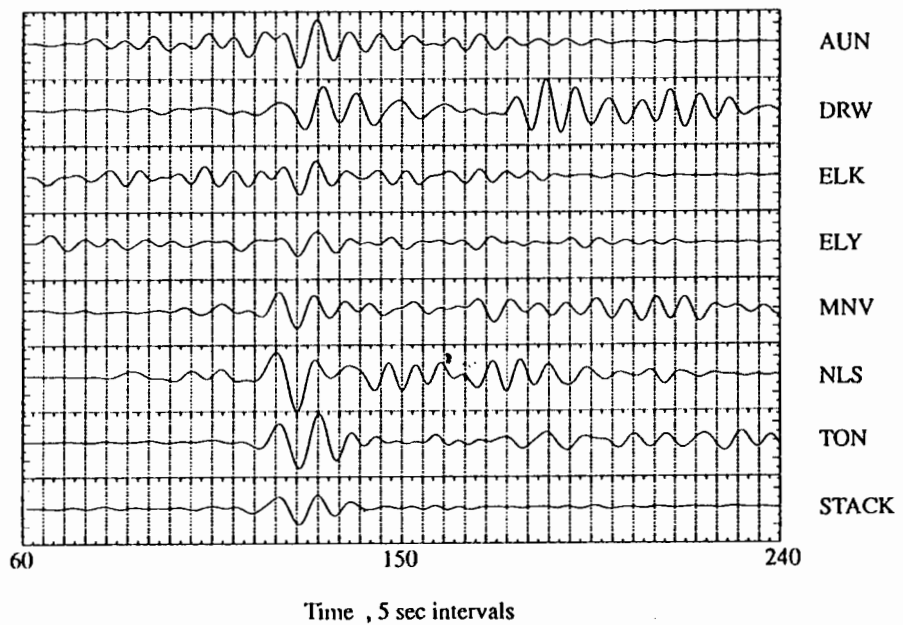


Figure 2b

Figure 2. Path-equalized waveforms. (a) A subset of waveforms analyzed for MQ and low-passed filtered at 0.2 Hz; (b) a subset of waveforms analyzed for the NPE and low-passed filtered at 0.12 Hz. The traces in each subset are plotted on a common scale.

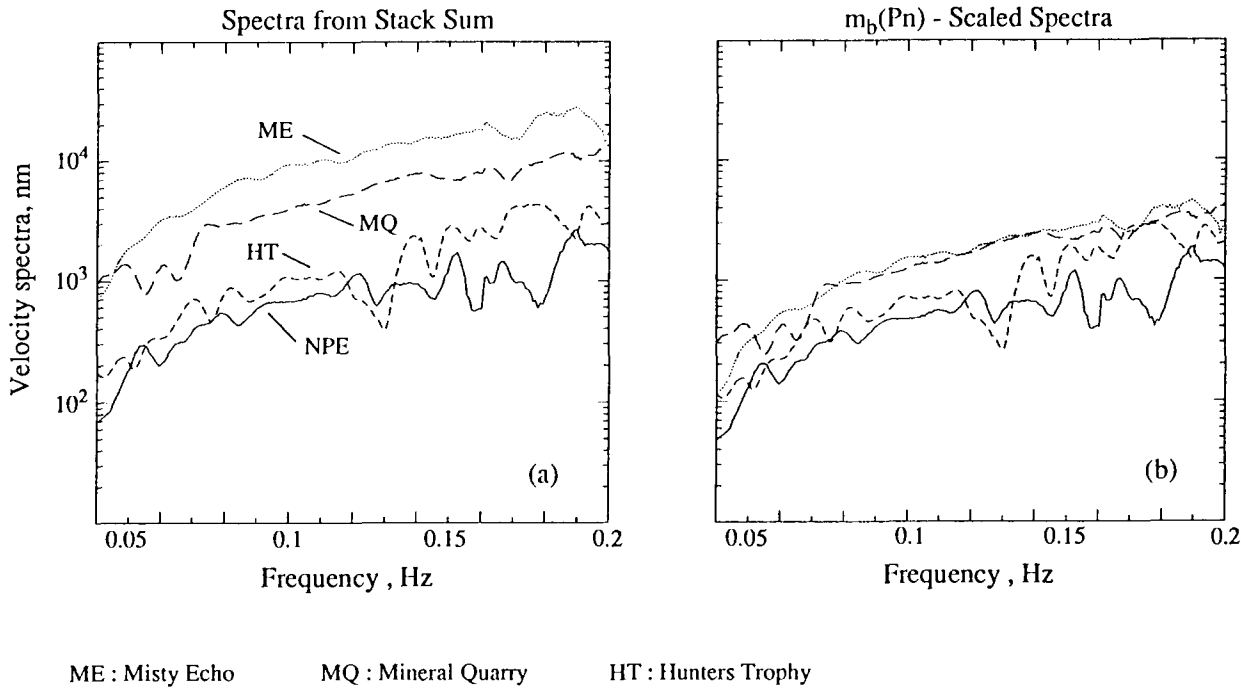


Figure 3. Rayleigh-wave spectra computed for the stacked sum.(a) Unscaled; (b) scaled.

show apparent coupling differences between these four explosions relative to that for Pn waves at 1 Hz. It is important to keep in mind that source mechanism can affect the average level of the Rayleigh-wave source spectrum. In the next section, the moment tensors are found to be quite similar except for their sizes; so mechanism cannot be the cause of the differences in Figure 3b.

The results for Lg waves in the MP band are shown in Figure 4. The average spectra are plotted in Figure 4a, where the NPE and HT spectra were cut at 0.3 Hz because of noise contamination. The spectra are scaled, again using the $m_b(Pn)$, and the results are plotted in Figure 4b. The scaled spectra overlay for frequencies greater than 0.7 Hz (i.e. the amplitude of 1-Hz Lg waves scale with the amplitude of 1-Hz Pn waves for these events). Less than 0.7 Hz, there are significant differences in the apparent coupling. It is interesting to note that these differences are similar to the differences seen in the scaled Rayleigh-wave spectra in Figure 3b.

Moment Tensor Results

An approach to inverting regional data for the complete seismic moment tensor is given in Patton (1988). For the sake of brevity, it will not be discussed here. However, there are some important modifications that must be made to this approach because of limitations in the present data set. In particular, the only LP spectrum available to us is the stack spectrum, which is an estimate of the average source spectrum for Rayleigh waves. Therefore, we cannot invert for the complete moment tensor because there is no information about deviatoric moments in this spectrum. In this study, all deviatoric moments are constrained to zero, and the inversion returns estimates of M_{xx} , M_{yy} , and M_{zz} , subject to the condition that $M_{xx} = M_{yy}$. Therefore, the solution has just two degrees of freedom, and I examine both of them below.

The inversions were done assuming a centroid depth of 400 m. Green's functions were computed for the modified crustal model of Bache *et al.* (1978) used in the LP stacking discussed above. Corrections for spall were not made in these inversions, because all of the explosions are overburied to some degree. The moment time dependence was assumed to be identical for all three moment-tensor elements. The time function (risetime and overshoot parameters, respectively: $k=15$, $B=4$; von Seggern and Blandford, 1972) has some overshoot. The moment tensor results are summarized in Table 2.

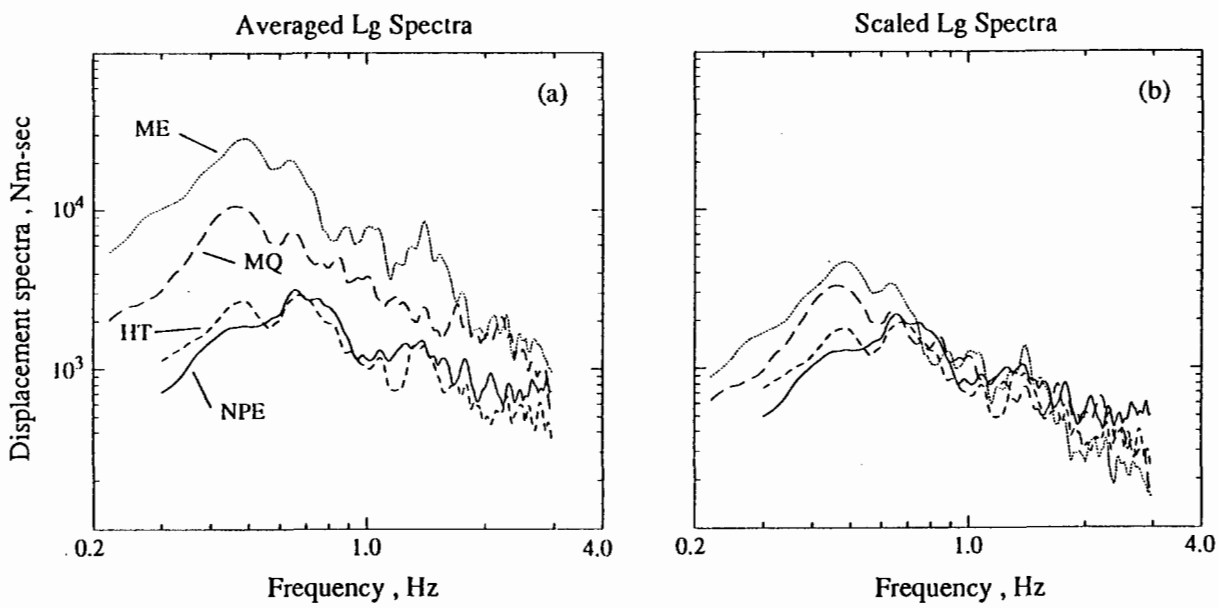


Figure 4. Network-averaged spectra for Lg waves. (a) Unscaled; (b) scaled.

Table 2.

MOMENT TENSOR RESULTS

Name	M_{zz}/M_{xx}	M_o $10^{14} \text{ Nt}\cdot\text{m}$	$\log M_o \cdot$ $1.1 m_b(P_n)^*$	Ψ_m^+ m^3
MISTY ECHO	2.9	24.8	10.13	10000
MINERAL QUARRY	2.9	9.4	10.01	3900
HUNTERS TROPHY	2.5	2.3	9.76	950
NPE	2.6	1.6	10.00	660

* Proportional to logarithm yield-scaled moment where yield is estimated from m_b/P_n for all events except the NPE. For the NPE, the yield is 1 kt.

+ Estimated using the equation, $\Psi_m = M_o / 4\pi \rho \alpha^2$ where ρ and α are the density and p-wave velocity, respectively. I used the values of 2000 kg/m³ and 3000 m/sec to compute the results in Table 2.

All of the moment tensor solutions can be described geometrically as prolate ellipsoids of rotation with the long axis oriented vertically. The vertical dipole moments are 2.5 - 3 times larger than the horizontal dipoles. These solutions are the most extreme realizations of prolate ellipsoids that I have encountered for explosions at NTS. Many Pahute Mesa explosions have similarly oriented ellipsoids but the vertical axis is only 1.5 - 2 times larger than the horizontal. The larger explosions, ME and MQ, are somewhat more elongated than HT and NPE (see Table 2). Removing the volumetric component from the solutions, the resulting tensor is a compensated linear vector dipole (CLVD). The strength of the CLVD is approximately 40-45% that of the isotropic source (monopole). I'll return to discuss implications of this result later in the paper.

The isotropic moment of the NPE is 1.6×10^{14} Nt-m. Using the formula relating the isotropic moment with the static level of the reduced displacement potential (Ψ_∞ ; Aki *et al.*, 1974), the estimate of Ψ_∞ is 660 m³. For this estimate, I used a density and p-wave speed of 2000 kg/m³ and 3000 m/s, respectively. The p-wave speed, in particular, may be too high in light of geologic characterizations of Rainier Mesa near N-tunnel (Baldwin *et al.*, 1994). A velocity of 2700 m/s would result in an estimate of Ψ_∞ about 25% larger (825 m³). These farfield estimates are 2 - 3 times smaller than the estimate of 2000 m³ from near-field data at a frequency of 1 Hz (Goldstein and Jarpe, 1994). There is suggestion in the near-field data (Goldstein, pers. comm.) and local data (Johnson, 1994) that the reduced displacement potential (RDP) decreases for frequencies below 1.0 Hz, but the data scatter is significant. At face value, the regional estimates, which are based on amplitudes in the 0.1 - 0.2 Hz range, and the near-field estimates, based on amplitudes near 1 Hz, appear to support overshoot in the RDP for the NPE.

To address energy coupling, I utilized estimates of the seismic moment in Table 2 scaled by total energy of the source. Estimates of the total energy of the source are obtained from the $m_b(Pn)$'s in Table 1 and a m_b -yield (W) relationship of the form, $m_b(Pn) = 0.9 \log W + \text{constant}$ (except for the NPE, where $W = 1 \text{ kt}$). In Table 2, $\log M_o - 1.1m_b(Pn)$ is proportional to the logarithm of yield-scaled moment. If I choose HT as a baseline, the following estimates of energy coupling factors are obtained: 2.3 for ME, 1.8 for MQ, and 1.7 for the NPE. The estimates for ME and the NPE are consistent with predictions based on initial energy densities (Glenn, 1993), while the estimate for MQ is not. It is important to keep in mind that these coupling factors were estimated from inferred source energies, and the actual source energies may give somewhat different results.

Discussion and Summary

In this paper, I have presented a characterization of the seismic radiation for frequencies below 1 Hz for the NPE and for three selected nuclear explosions detonated in N-tunnel on Rainier Mesa. Because the S/N ratio was poor in the LP band for the NPE, I implemented a method to stack seismograms in an attempt to reduce the background noise relative to coherent phase arrivals of Rayleigh waves recorded at near-regional stations. This involved path equalization using empirical Green's functions for several good S/N explosions located on Pahute Mesa. The method worked well on the signals, which show coherence for periods as short as 5 sec. The final stacked spectrum for the NPE and HT showed significant variability because noise levels were not reduced low enough compared to signal levels. Better S/N can be achieved by analyzing more records from other regional stations not used in this study.

The results from moment tensor inversions were used to investigate questions of energy coupling and source mechanism. Yield-scaled moments gave a coupling factor of 1.7 for the NPE relative to HT. ME and MQ also showed enhanced coupling. Comparing the regional estimates to nearfield estimates on the NPE, the Ψ_∞ inferred from the isotropic moment is 2 - 3 times smaller than the estimate from free-field data taken within 1 km of the source. This can be explained if there is over-shoot in the RDP spectrum, since the frequency at which the nearfield determinations were made is about 1 Hz, while the regional estimates are for 0.1 Hz.

Of some interest is the fact that all of the explosions gave moment tensors which showed relatively large asymmetries compared to explosions on Pahute Mesa. The moment tensors can be described geometrically as prolate ellipsoids of revolution with the long axis oriented vertically. After removing the volumetric component, the moment tensor is a CLVD source with about 40 - 45% strength of the explosion alone. I interpret this component to be representative of shear failure related to driven block motions. This failure probably occurs most intensively within a conical volume of material extending from the shot point (apex) to the free surface (Masse, 1981).

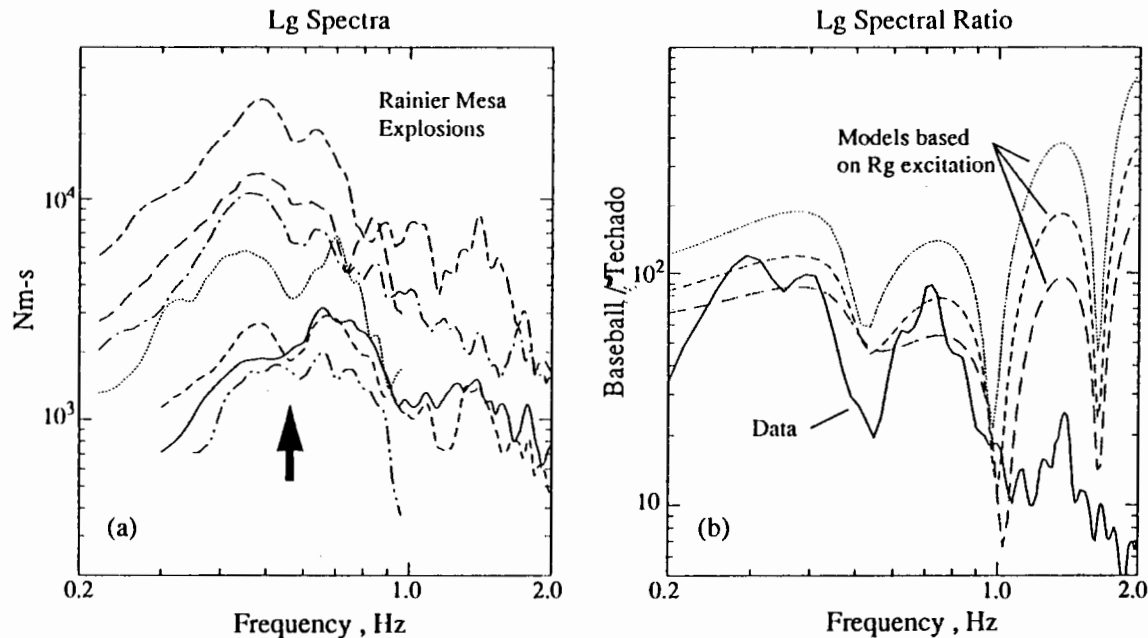


Figure 5. (a) Network-averaged spectra for Lg waves. These spectra are the same spectra in Figure 4a plus examples from several other nuclear explosions on Rainier Mesa. Arrow is placed at the frequency where all spectra exhibit scalloping. (b) Spectral ratios of Lg waves between BASEBALL and TECHADO, both on Yucca Flats. The observations are network averages. Three different models are shown with the observations, where the models were obtained by utilizing the Rg excitation spectrum and varying the strength of the CLVD source (see Patton and Taylor, 1994).

The explosion source model, monopole + CLVD, can explain other observations. Network-averaged Lg spectra are shown in Figure 5a. These are the same spectra that were shown in Figure 4a plus averaged spectra for several other Rainier Mesa explosions. All of these spectra are scalloped to some extent at 0.5 - 0.6 Hz. This scalloped feature is also present in Lg spectral ratio results shown in Figure 5b (Patton and Taylor, 1994). The spectral ratios are for two explosions on Yucca Flats, where an over-buried explosion, TECHADO, is used as an empirical Green's function to study the spectral characteristics of a nearby normal-depth explosion, BASEBALL. The scalloped appearance in the Lg spectral ratios is quite pronounced, and it occurs at roughly the same frequency as it does for the Rainier Mesa explosions.

The models in Figure 5b are based on Rg excitation for the monopole + CLVD source, varying the strength of the CLVD source. Patton and Taylor found that the only model which explains the scalloping in Lg spectral ratios was one with a sizable CLVD component. This source excites large Rg waves which scatter off topography (Jih, 1993) and near-surface velocity heterogeneity (Xie and Lay, 1994) into P and S waves. Some of these scattered body waves become trapped in the crust and go on to make up Lg waves. Scattering must take place close to the source for two reasons: (1) Rg attenuates rapidly by anelastic mechanisms and (2) the energy flux must travel at Lg velocity over a large percentage of the path to appear in the velocity window used in the Fourier analysis. This mode of Lg genesis is similar to the Rg \rightarrow S scattering model of Gupta *et al.* (1992), but with an important exception: the source of Rg waves must be a monopole + CLVD. (The CLVD is responsible for the scalloping; see Patton and Taylor, 1994.) Gupta *et al.* proposed a model where Rg is excited by just a monopole source. A monopole (or spherical) source alone cannot explain the scalloping of the Lg spectra in Figure 5 nor the absolute amplitude levels of Lg. The absolute amplitude levels are fit satisfactorily by the asymmetric moment tensors in Table 2.

Acknowledgments

This research was carried out while the author was on remote assignment at Phillips Laboratory Geophysics Directorate, Hanscom Air Force Base, Massachusetts. The author gratefully acknowledges support of the U. S. Air Force Office of Scientific Research under Intergovernmental Personnel Agreement and the support of the U.S. Department of Energy to the Lawrence Livermore National Laboratory under contract W-7405-Eng-48.

References

- Aki, K., M. Bouchon, and P. Reasenberg (1974). Seismic source function for an underground nuclear explosion, *Bull. Seism. Soc. Am.*, **64**, 131-148.
- Bache, T. C., W. L. Rodi, and D. G. Harkrider (1978). Crustal structures inferred from Rayleigh-wave signatures of NTS explosions, *Bull. Seism. Soc. Am.*, **68**, 1399-1413.
- Baldwin, M. J., R. P. Bradford, S. P. Hopkins, and D. R. Townsend (1994). Geologic characteristics of the NPE site in the U12n.25 drift of N-tunnel, Nevada Test Site, Abstr. in Arms Control and Nonproliferation Technologies, DOE/AN/ACNT-94A, p. 37.
- Chavez, D. E. and K. F. Priestley (1986). Measurement of frequency dependent Lg attenuation in the Great Basin, *Geophys. Res. Lett.*, **13**, 551-554.
- Denny, M. D. and J. J. Zucca (1994). Introduction: DOE Non-Proliferation Experiment, in Arms Control and Nonproliferation Technologies, DOE/AN/ACNT-94A, 8-21.
- Glenn, L. A. (1993). Energy density effects on seismic decoupling, *J. Geophys. Res.*, **93**, 1933-1942.
- Goldstein, P. and S. P. Jarpe (1994). Comparison of chemical and nuclear explosion source-time functions from close-in, local, and regional seismic data, Abstr. in Arms Control and Nonproliferation Technologies, DOE/AN/ACNT-94A, p. 40.
- Gupta, I. N., W. W. Chan, and R. A. Wagner (1992). A comparison of regional phases from underground nuclear explosions at East Kazakh and Nevada Test Sites, *Bull. Seism. Soc. Am.*, **82**, 352-382.
- Jih, R.-S. (1993). Directional excitation of Rg due to ripple-fired explosions: two-dimensional finite-difference simulations, in Proceedings of the Numerical Modeling for Underground Nuclear Test Monitoring Symposium, S. R. Taylor and J. R. Kamm, eds., Los Alamos National Laboratory Report No. LA-UR-93-3839.
- Johnson, L. R. (1994). Recording experiment on Rainier Mesa in conjunction with a reflection survey, Abstr. in Arms Control and Nonproliferation Technologies, DOE/AN/ACNT-94A, p. 46.
- Masse, R. P. (1981). Review of seismic source models for underground nuclear explosions, *Bull. Seism. Soc. Am.*, **71**, 1249-1268.
- Patton, H. J. (1988). Source models of the HARZER explosion from regional observations of fundamental-mode and higher mode surface waves, *Bull. Seism. Soc. Am.*, **78**, 1133-1157.
- Patton, H. J. and S. R. Taylor (1994). Analysis of Lg spectral ratios from NTS explosions: Implications for the source mechanisms of spall and the generation of Lg waves, *Bull. Seism. Soc. Am.*, **84**, preprint in press.
- von Seggern, D. and R. Blandford (1972). Source-time functions and spectra for underground nuclear explosions, *Geophys. J. R. astr. Soc.*, **31**, 83-97.
- Xie, X.-B. and T. Lay (1994). The excitation of Lg waves by explosions: A finite-difference investigation, *Bull. Seism. Soc. Am.*, **84**, 324-342.

Regional Seismic Observations of the Non-Proliferation Experiment at the Livermore NTS Network

William R. Walter, Kevin Mayeda, and Howard J. Patton,
Lawrence Livermore National Laboratory, Earth Sciences Division

Abstract

The Non-Proliferation Experiment (NPE), a 1-kiloton chemical explosion in N-tunnel at Rainier Mesa on the Nevada Test Site (NTS), was recorded by the four station, regional seismic Livermore NTS Network, (LNN). In this study we compare the NPE's seismic yield, frequency content, and discrimination performance with other NTS events recorded at LNN. Preliminary findings include:

- The NPE LNN average magnitudes are 4.16 for $m_b(P_n)$ and 4.59 for $m_b(L_g)$. Using published magnitude-yield relations gives nuclear equivalent yields of 2.3 and 2.2 kiltons respectively, implying enhanced coupling of chemical relative to nuclear explosions.
- A comparison of the NPE seismograms with those from similar magnitude N-tunnel nuclear explosions shows remarkable similarity over the frequency band 0.5 to 5.0 Hz. Outside this band the explosions show more variability, with the NPE having the least relative energy below 0.5 Hz and the most energy above 5 Hz when scaled by magnitude. Considering the variability within the N-tunnel nuclear explosions, these low- and high-frequency NPE-nuclear differences may not reflect chemical-nuclear source differences.
- The NPE was compared to a large number of NTS nuclear explosions and earthquakes as part of an ongoing short-period discrimination study of P_n/L_g , P_g/L_g , and spectral ratios in the P_n , P_g , L_g , and coda phases (Walter et al., 1994). For these discriminants, the NPE looks very similar to N-tunnel nuclear explosions and other NTS nuclear explosions, implying seismic identification of contained, non-ripple-fired, chemical explosions as non-nuclear may not be possible. However, such blasts might serve as surrogate nuclear explosions when calibrating seismic discriminants in regions where nuclear testing has not occurred.
- L_g transfer functions for the NPE and other NTS explosions show significant peaking in the 0.5 to 1.5 Hz frequency range which is not observed for normal depth NTS earthquakes. The transfer function is formed from the attenuation corrected L_g/P_n spectral ratio, and P_n is assumed to match the source spectra, as shown for the NPE by Goldstein et al. (this issue). The peaking in the explosion L_g transfer functions is consistent with a hypothesis that R_g to L_g scattering (e.g., Gupta, this issue) dominates the generation of L_g in explosions at frequencies below a few Hertz. This hypothesis helps explain the frequency dependence of P_n/L_g discriminants and the difference between L_g and P_n 1-2/6-8 Hz spectral amplitude ratios.

Introduction

The NPE was a fully contained 1-kiloton (kt) chemical explosion conducted within N-tunnel in Rainier Mesa at the Nevada Test Site (NTS). This event was recorded by the four broadband seismic stations of the Livermore NTS Network (LNN). The location and operation of these station is discussed in Rohrer (this issue). The purpose of this paper is to briefly summarize the regional seismic observations of the NPE at the LNN stations and compare them with the NTS nuclear explosions and earthquakes also recorded at these same stations. We also give a summary of some of our recent work (Walter et al., 1994) on the empirical observations and physical basis of short-period discrimination of NTS earthquakes and explosions.

Coupling and Waveform Comparison

Digital broadband records of NTS events are available from late 1979 to the present at the LNN stations,, and here we compare the NPE waveforms with nearby N-tunnel nuclear tests from the time period. Two short-period measures of event size, $m_b(P_n)$ (Denny et al., 1987) and the third peak $m_b(L_g)$ (Patton, 1988) were calculated for the NPE and some of the N-tunnel nuclear tests. These magnitudes are averaged over the four stations and are given in Table 1. Using the magnitude-yield relations of Vergino and Mensing (1990) for $m_b(P_n)$ and Patton (1988) for $m_b(L_g)$ gives nuclear equivalent yields of 2.2 and 2.3 kt, respectively, for the NPE. While the two standard-deviation uncertainty factors for these magnitude-yield relations are large, about 1.7, they suggest that within the uncertainty the NPE chemical explosion coupled more energy into seismic waves than an equivalent-yield nuclear explosion. These results are similar to other regional seismic yield estimates (see Rohrer, this issue; Garbin, this issue).

Table 1. N-Tunnel Explosions.

Event	$m_b(P_n)$	$m_b(L_g)$	6-8 Hz P_n/L_g	1-2/6-8 Hz L_g	1-2/6-8 Hz P_n	Depth (m)	Log r_a^2	% Gas Porosity
Tomme/Midnight	3.97	4.34	1.86	27.3	2.42	405	10.16	2.2
Diamond Beech	4.01	4.43	1.88	40.1	2.81	405	10.05	1.7
NPE	4.16	4.59	1.57	10.9	1.14	390	9.99	1.5
Hunters Trophy	4.18*	4.57*	1.97	14.9	1.15	385	10.10	1.6
Mineral Quarry	4.53	4.94	1.19	25.2	3.43	389	10.21	1.5
Miners Iron	4.65	4.91	1.14	48.9	9.64	390	10.22	1.5
Huron Landing	4.81	5.02	1.53	61.0	8.69	409	10.16	1.6
Misty Rain	4.70	5.23	1.31	37.9	4.97	389	10.13	1.2
Misty Echo	4.81	5.16	0.93	25.8	4.87	400	10.19	1.4

* magnitude from KNB, LAC and MNV only

The chemical NPE seismic waveforms recorded at the LNN stations show a remarkable similarity to the waveforms generated by the nearby N-tunnel nuclear explosions with similar magnitude in the passband from 0.5-5 Hz. For example Figure 1 compares the velocity seismogram of the NPE at station KNB with four similar sized N-tunnel shots whose amplitudes have been scaled by ten raised to $1.1 \text{ mb}(P_n)$, which is proportional to yield (Vergino and Mensing, 1990). At lower frequencies ($< 0.5 \text{ Hz}$), the NPE appears to have less relative energy than the N-tunnel shots when scaled by magnitude (see for example Figure 4b in Patton, this issue). At higher frequencies ($> 5 \text{ Hz}$), the NPE appears to have relatively more energy when scaled by magnitude, as shown by the relatively low 1-2/6-8 Hz spectral ratio values in Table 1. The N-tunnel nuclear explosions themselves show strong variability in relative energy content outside the 0.5-5 Hz band and it is not possible to conclude from one chemical explosion if these differences between the NPE and the N-tunnel nuclear shots represent any chemical-nuclear source difference. Given the variability within the nuclear explosions, any slight differences in chemical and nuclear seismic source functions is probably not useful as a practical chemical-nuclear discriminant.

The NPE and four nearby nuclear tests recorded at KNB

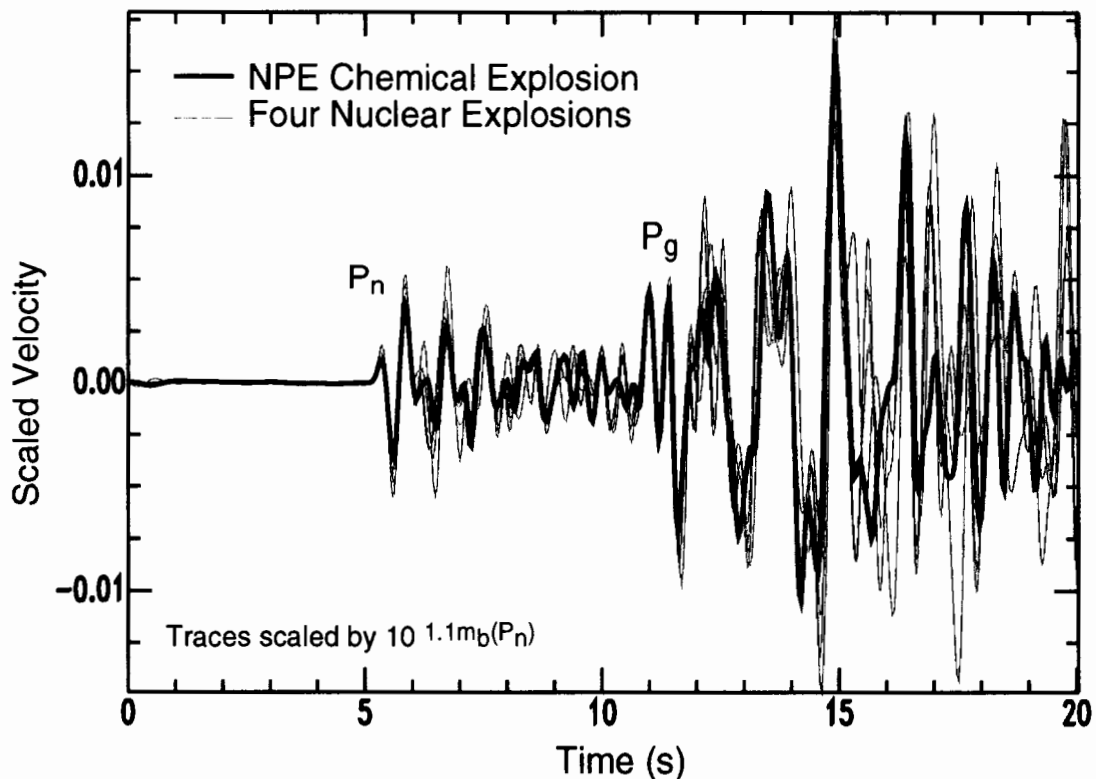


Fig 1. A comparison of the initial velocity records from the NPE and four similar magnitude N-tunnel nuclear explosions at the LNN station KNB. These vertical component traces have been scaled by $1.1 \text{ mb}(P_n)$, which is proportional to yield (Vergino and Mensing, 1990) and aligned in time. This station is about 310 km distant from the events and the start of the regional P phases have been labeled. The instrument responses are flat in displacement from about 0.1 to 5 Hz.

Short-Period Discriminants

Taking advantage of the recent earthquake activity at NTS, we are in the process of studying both the empirical and physical basis of best short-period earthquake and explosion discriminants (Walter et al, 1994). As part of this study we applied these discriminants to the NPE. These short-period discriminants fall into two classes, ratios of P to S energy in a particular frequency band (phase ratios), and ratios of low to high frequency energy within a seismic phase (spectral ratios).

Phase ratios for the NTS data are plotted as a function of frequency in Figure 2. Note the earthquake-explosion separation appears to increase as frequency increases for P_n/L_g . Focusing on the highest frequency with the most data, the NPE 6-8 Hz phase ratios are compared to those of NTS earthquakes and nuclear explosions in Figure 3. The P_n/L_g discriminant (Figure 3a) separates the earthquake and explosion populations means, but some events overlap. Note the NPE falls within the nuclear explosion population. The P_g/L_g discriminant, in Figure 3b shows a dependence on the explosion medium property with the low-gas-porosity explosions separating from the earthquakes better than the high-gas porosity explosions. The NPE was conducted in low gas porosity material and has P_g/L_g values close to those of nuclear explosions in similar material (see Figure 3b and Table 1).

The NPE P_n and L_g 1-2/6-8 Hz spectral ratios are compared to the NTS data in Figure 4a and 4b. The spectral ratios show a dependence on magnitude and explosion material properties with

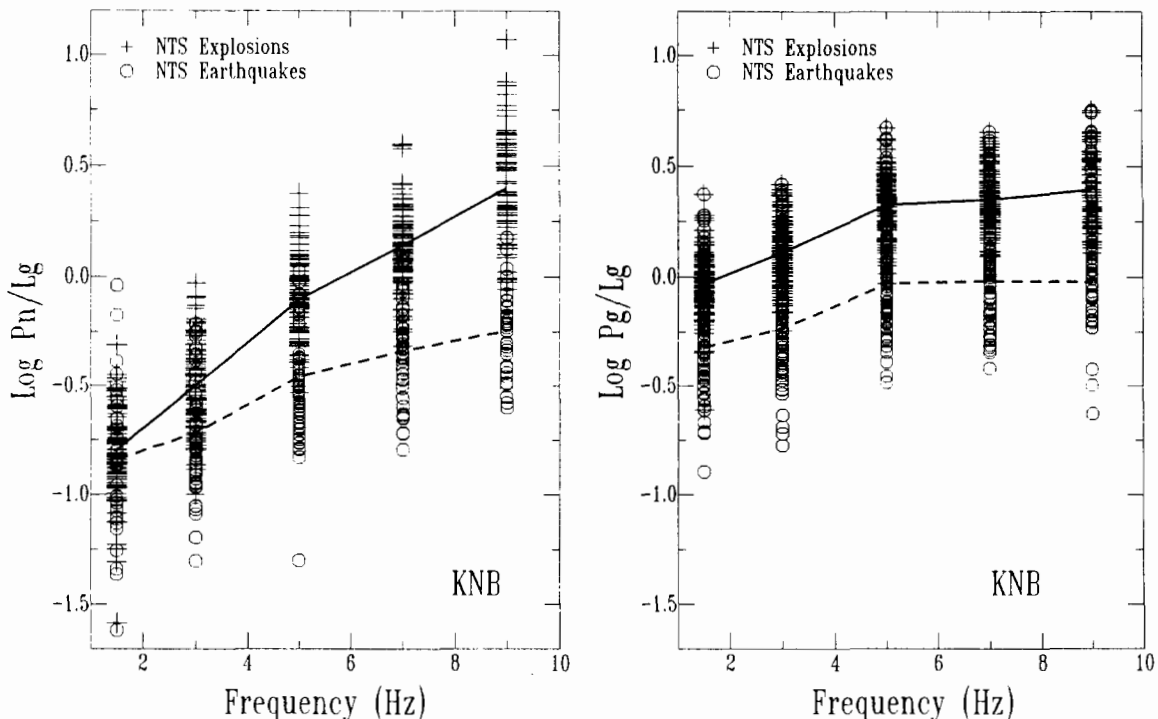


Fig 2. Phase ratios for NTS explosions and earthquakes in five frequency bands, 1-2, 2-4, 4-6, 6-8 and 8-10 Hz at KNB. The solid and dashed lines connect the average explosion and earthquake values respectively. (a) P_n/L_g shows increasing separation between event types with increasing frequency. (b) P_g/L_g show little change in separation as a function of frequency.

the larger magnitude ($M > 3.5$) high-gas porosity explosions separating from the earthquakes. Note that the explosion spectral ratio material property dependence is opposite that observed for P_g/L_g in Figure 3b, suggesting that a combined P_g/L_g -spectral ratio discriminant may perform better than either one alone (see Mayeda and Walter, this issue). Comparing Figures 4a and 4b, note the average separation between the earthquake and explosion populations appears larger for the L_g spectral ratio than for the P_n . The NPE has spectral ratios among the lowest of the low gas porosity explosions near magnitude 4, similar to the nearby nuclear explosion Hunter's Trophy (see Table 1).

The NPE chemical explosion plots with or very close to the nuclear explosions in the discrimination Figures 3 and 4. The discriminants presented here were designed to distinguish explosions from earthquakes and it is perhaps not surprising that they fail to distinguish the NPE from nearby nuclear explosions. Though we have only one chemical explosion point for comparison, other data also indicates that concentrated chemical and nuclear explosions scale similarly and cannot easily be seismically distinguished (e.g. Denny and Johnson, 1991). Fortunately many, if not most, large chemical explosions are ripple-fired (charges spread out in time and space) and may be discriminated by means other than those discussed here (see Richards, this issue). While large non-ripple-fired explosions may pose problems for discrimination, they may also provide opportunities, for example, serving as surrogate nuclear tests to calibrate discriminants in regions where nuclear testing has not occurred.

L_g Transfer Functions

As part of the short-period discrimination study using NTS data (Walter et al, 1994), we are examining the physical basis of these discriminants. The availability of empirical Green functions for two recent NTS events (NPE and Bristol) allows us to identify the source effects on the discriminants. Goldstein et al. (this issue) have shown the NPE's attenuation-corrected P_n spectrum matches the source spectrum obtained by deconvolving an empirical Green's function. We made a very similar observation for the nuclear explosion Bristol using the published source function, which was also obtained by deconvolving an empirical Greens function (Goldstein et al., 1994). Figure 5a shows the attenuation-corrected P_n spectra at KNB for Bristol compared to the scaled source spectral ratio. Note the good match between the frequency dependence of the source spectrum and the P_n spectrum. Figure 5b compares the attenuation-corrected L_g spectrum with the scaled source spectrum, but in this case the frequency dependence is quite different. The important conclusion to make from Figure 5 is that the Bristol P_n spectrum matches the source spectrum, but the L_g spectrum does not.

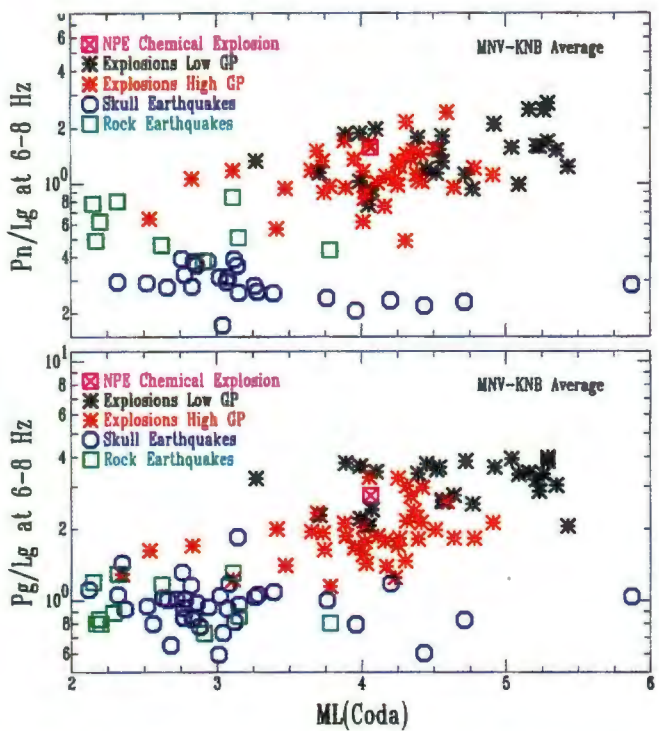


Fig. 3. The 6-8 Hz phase ratios for NTS earthquakes and explosions averaged over the station MNV and KNB. The Skull mountain earthquakes are normal depth events, the Rock Valley events are unusually shallow (< 3 km). The explosions are separated into high and low gas porosity events based on this source material property. (a) P_n/L_g separates the averages of each event type by there is some overlap. (b) P_g/L_g shows a dependence on the explosion source material property.

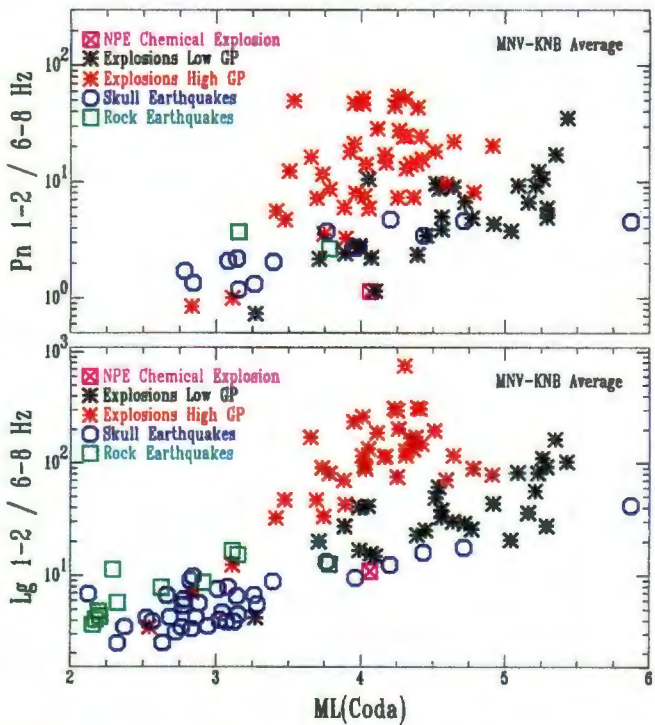


Fig. 4. 1-2 / 6-8 Hz spectral ratios for the same data as in Figure 3. (a) P_n spectral ratios show an increase with increasing magnitude and a material property dependence for the explosions with the high gas porosity events having larger P_n spectral ratios for a given magnitude. (b) L_g spectral ratio is similar to P_n except the explosions appear to have systematically higher ratios with respect to the earthquakes than seen for P_n .

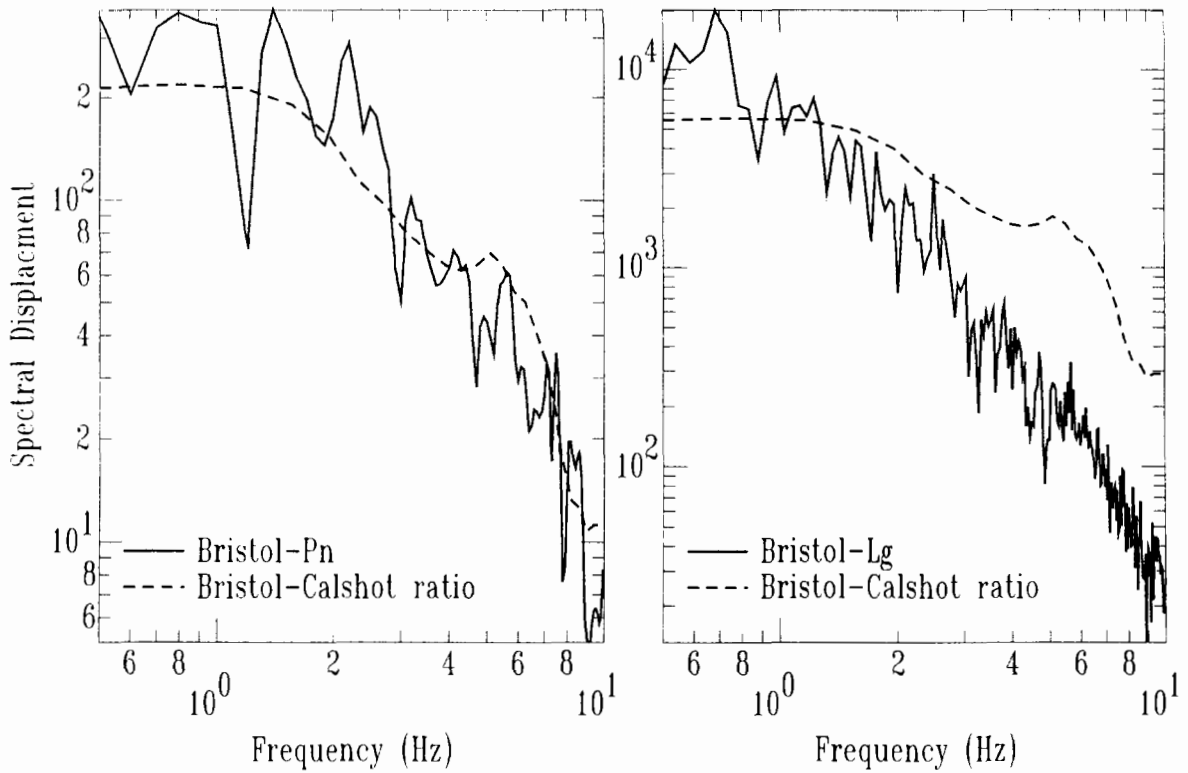


Fig. 5. Comparison of BRISTOL(a) Pn and (b) Lg spectra with source spectral ratio derived from a calibration shot used as an empirical Greens function (Goldstein et al 1994). The source spectra was scaled to match the 1 Hz level in each of the plots. Note the Pn spectra matches the frequency dependence of the source spectra but the Lg does not.

Generalizing from the NPE and BRISTOL observations that the attenuation corrected P_n spectrum matches the source spectrum, we can attempt to remove the source spectrum from L_g by forming attenuation corrected L_g/P_n spectral ratios as shown in Figure 6. Conceptually, explosions are pure P sources, so the L_g/P_n spectral ratios in Figure 6a can be thought of as "transfer functions," a frequency-dependent measure of how P source energy is converted to L_g . Since earthquakes have direct S sources and, in fact, radiate the majority of their energy as S waves, the earthquake L_g/P_n spectral ratios in Figure 6b represent this transfer function plus a constant value representing the relative S/P source strength.

The explosion transfer functions in Figure 6a show strong peaks in the 0.5–1.5 Hz range and then decrease with increasing frequency. In contrast, two comparable earthquakes shown in Figure 6b differ greatly from each other and are, on average, approximately constant with increasing frequency. Very similar differences in explosion and earthquake spectra have been observed in the path and receiver-site corrected L_g coda (see Mayeda and Walter, this issue). Freefield transverse component observations of the empirical Green's function and the NPE indicate that there is no identifiable secondary source, such as spall, generating the near-field S waves (Goldstein and Jarpe, this issue). Taken together, these observations are consistent with the idea that scattering and conversion near the source generate significant explosion L_g energy

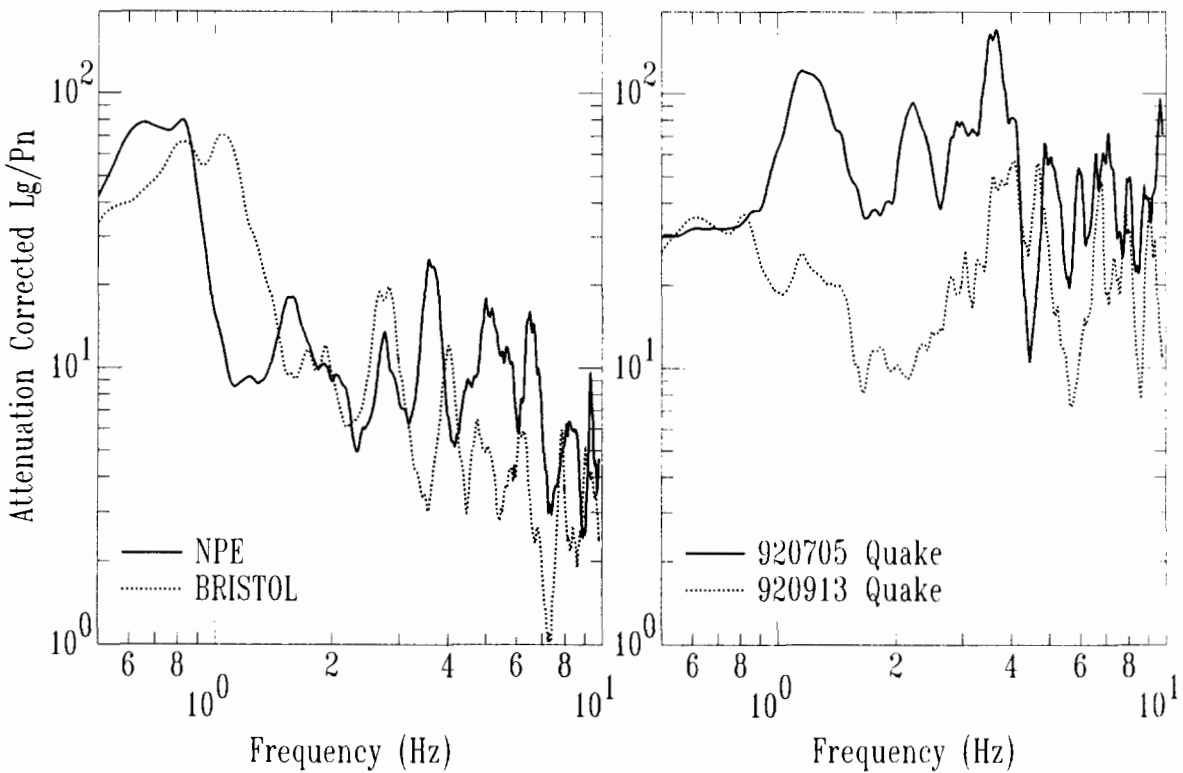


Fig. 6. Transfer functions formed from the attenuation corrected Lg/Pn spectral ratio for (a) two NTS explosions and (b) two similar sized Little Skull mountain earthquakes that occurred at NTS. Note the explosions both show peaks in the 0.5–1.5 Hz range and then decrease with increasing frequency. The earthquakes differ significantly from each other but are on average constant as frequency increases.

in the 0.5–1.5 Hz range, but contribute relatively little additional energy to the earthquake S source as observed in the Lg spectra.

One scattering and conversion mechanism that could explain the strong frequency dependence in explosions but not in normal depth earthquakes is Rg to Lg scattering (see Gupta, this issue). The short-period fundamental mode Rayleigh wave Rg amplitude is very sensitive to depth and is locally observed to be a large phase for very shallow events with a large spectral peak in the neighborhood of 0.5–1.5 Hz depending on the velocity structure. Rg is typically not strongly observed at regional distances and its energy is assumed to scatter into Pg , Lg , and the coda. If Rg to Lg scattering affects shallow events, one might expect very shallow earthquakes to not separate well from the shallow explosions when using Lg based discriminants. This is exactly what we observed in the NTS discrimination study for the unusually shallow (<3 km) Rock Valley earthquake sequence (Walter et al., 1994).

The strong frequency dependence of the explosion Lg transfer functions contrasted with the relative lack of frequency dependence in the earthquake transfer functions causes several short-period discriminant observations noted above. In particular, it causes the frequency-dependent

behavior of the P_n/L_g discriminant and improves the L_g spectral ratios discriminant when compared to the P_n . The observation that the P_n spectra represent the source spectra implies the material property dependence observed in Figure 4a is a source spectrum property. The similar source medium dependence observed for the L_g spectral ratios in Figure 4b imply this is also a source spectrum effect and not a path effect, such as velocity model dependent crustal trapping of pS (see Gupta, this issue). Finally, we note the material property dependence observed in Figures 3b, 4a and 4b seem to imply that it is lack of high gas porosity explosions in the rest of the world, rather than tectonic path differences. That explains why western U.S. short-period discriminant studies are different from similar studies in other regions of the world (Walter et al, 1994). These ideas will be explored further in future work.

Acknowledgments

This research was performed under the auspices of the U.S. Department of Energy by Lawrence Livermore National Laboratory under contract number W-7405-ENG-48.

References

- Denny, M. D., S. R. Taylor, and E. S. Vergino (1987), Investigation of m_b and M_S formulas for the western United States and their impact on the m_b/M_S discriminant, *Bull Seism. Soc. Am.*, 77, 987-995.
- Denny, M. D. and L. R. Johnson (1991), The explosion seismic source function: model and scaling laws revisited, in *Explosion Source Phenomenology*, American Geophysical Union Monograph, 65, 1-24.
- Denny, M. D., Ed. (1994), *Proceedings of the Non-Proliferation Experiment and Implications for Test Ban Treaties*, Lawrence Livermore National Laboratory, Livermore, CA, CONF-9404100.
- Goldstein, P., M. D. Denny, T. Hauk, and S. P. Jarpe, (1994), On-site seismic yield estimates for BRISTOL based on nuclear to chemical explosion spectral ratios and yield scaling, *Bull. Seism. Soc. Am.*, 84, 343-349.
- Patton, H. J., (1988), Application of Nuttli's method to estimate the yield of the Nevada Test Site explosions recorded on Lawrence Livermore National Laboratory's seismic system, *Bull. Seism. Soc. Am.*, 78, 1759-1772.
- Vergino, E. S., and R. W. Mensing, (1990), Yield estimation using regional $m_b(P_n)$, *Bull Seism. Soc. Am.*, 80, 656-674.
- Walter, W. R., K. Mayeda, and H. J. Patton (1994), Phase and spectral ratios discrimination between NTS earthquakes and explosions Part I: empirical observations, Lawrence Livermore National Laboratory, Livermore, CA, UCRL-JC-118551.

L_g Coda Moment Rate Spectra and Discrimination Using L_g Coda Envelopes

Kevin M. Mayeda and William R. Walter

*Treaty Verification Program, Earth Sciences Division,
Lawrence Livermore National Laboratory, L-205, Livermore, CA, 94550*

Abstract

Low magnitude seismic monitoring will depend largely on high frequency near-regional discriminants such as ratios of P to S energy (see Walter et al., this issue) and spectral amplitude ratios within P or S phases. Due to high frequency attenuation and sparse distribution of recording stations, small magnitude events will have to be identified with only a few stations, in some instances perhaps only one. Recently, stable single station magnitudes for explosions at NTS (Mayeda, 1993) and moment rate spectra for earthquakes throughout the western U.S. (Mayeda and Walter, 1994) have been estimated using L_g coda envelopes. The averaging nature of coda waves virtually eliminates the amplitude variability due to source radiation anisotropy and lateral variations in path geology between the source and receiver. In this study, we find that L_g coda spectral ratios are 3 to 4 times less variable than direct phase spectral ratio measurements. Events fired in low strength-high gas porosity material have higher spectral ratios than events in high strength-low gas porosity material, and thus discriminate well from earthquakes which have the lowest spectral ratios. In contrast, P_g/L_g phase ratios for events in low strength-high gas porosity material lie closest to the

earthquake population (see Walter et al., this issue). A combination of both discriminants performs better than either one does alone. Moment rate spectra for explosions show strong depth-dependent spectral peaking that is not observed in normal depth western U.S. earthquakes and is consistent with strong R_g to S scattering near the explosion source. This explosion spectral peaking will be explored in future work as part of a possible broadband discriminant.

Introduction

Spectral amplitude ratios between 1-2 and 6-8 Hz were studied by Taylor et al. (1988) for explosions at the Nevada Test Site (NTS) and western U.S. earthquakes. Among the three prominent regional phases used in their study (e.g., P_n, P_g, and L_g), the L_g spectral ratio showed the best separation between earthquakes and explosions. Mayeda (1993) showed that stable single-station estimates of magnitude could be made using narrowband L_g coda envelopes for NTS explosions. In this study, we investigate whether L_g coda spectral ratios can improve upon prior results which depend on the direct L_g. Unlike direct wave amplitude measurements which are highly dependent upon source anisotropy and geologic variation connecting source and receiver, the averaging nature of coda waves virtually eliminates these azimuthal dependencies.

Method

Narrowband coda envelopes from western U.S. earthquakes recorded by two Lawrence Livermore National Laboratory stations, MNV and KNB,

were source and site normalized using the coda method (e.g., Aki and Chouet, 1975, Phillips and Aki, 1987, Mayeda et al., 1991). To obtain frequency-dependent path corrections, we used the 3-D multiple scattering model of Zeng et al., (1991) and simultaneously fit to the data which ranged in distance from 40 to 700 km. For each frequency band, the best fitting scattering and intrinsic Q were found by use of a grid search which compared observed and synthetic source-normalized coda envelopes (Figure 1). Path-corrected source amplitude measurements were made (Figure 2) by fitting the observed unnormalized narrowband envelopes with synthetics. Multiple frequency bands were necessary due to the strong frequency-dependent nature of the

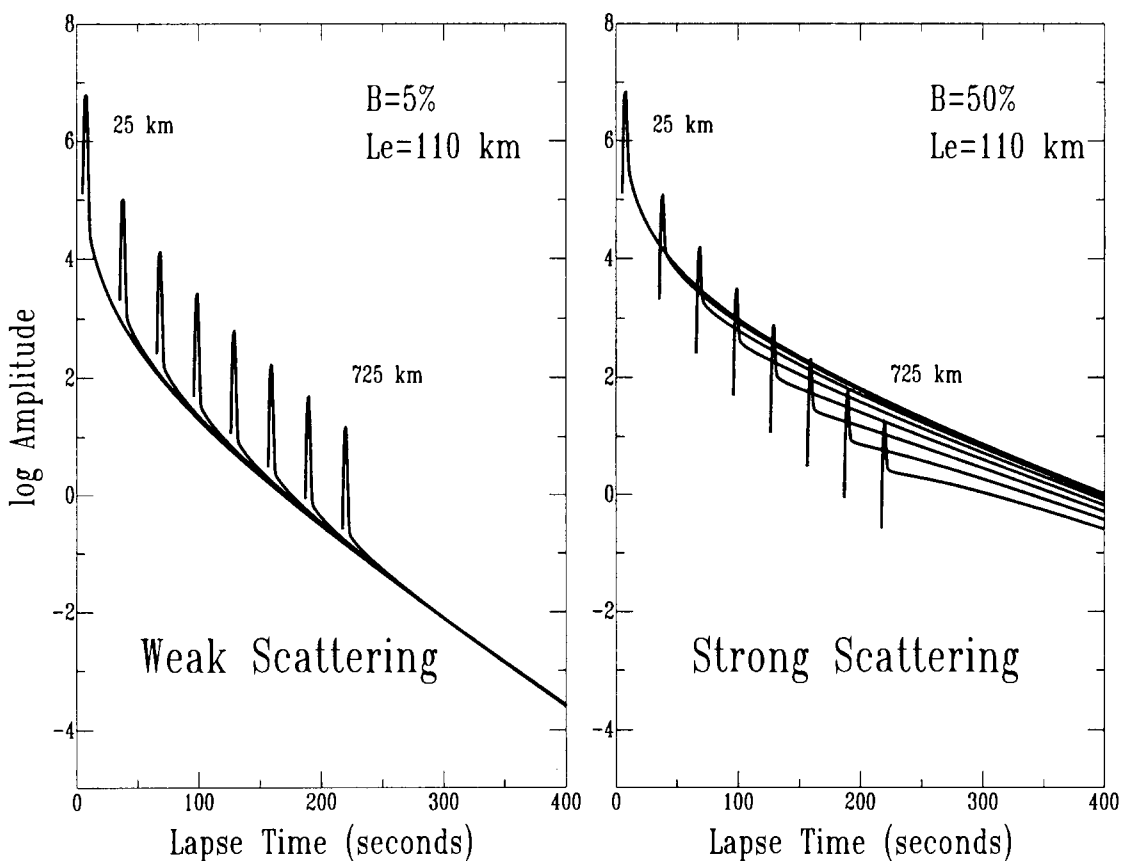


Figure 1 Synthetic envelopes for weak ($B=5\%$) and strong scattering ($B=50\%$) media with identical total mean free path, Le . B represents the contribution of scattering attenuation to the total attenuation. Notice that the direct wave decays the same amount over 700 km distance, but the coda envelopes are very different.

Coda Envelope Model Fitting for 1.5 and 7.0 Hz

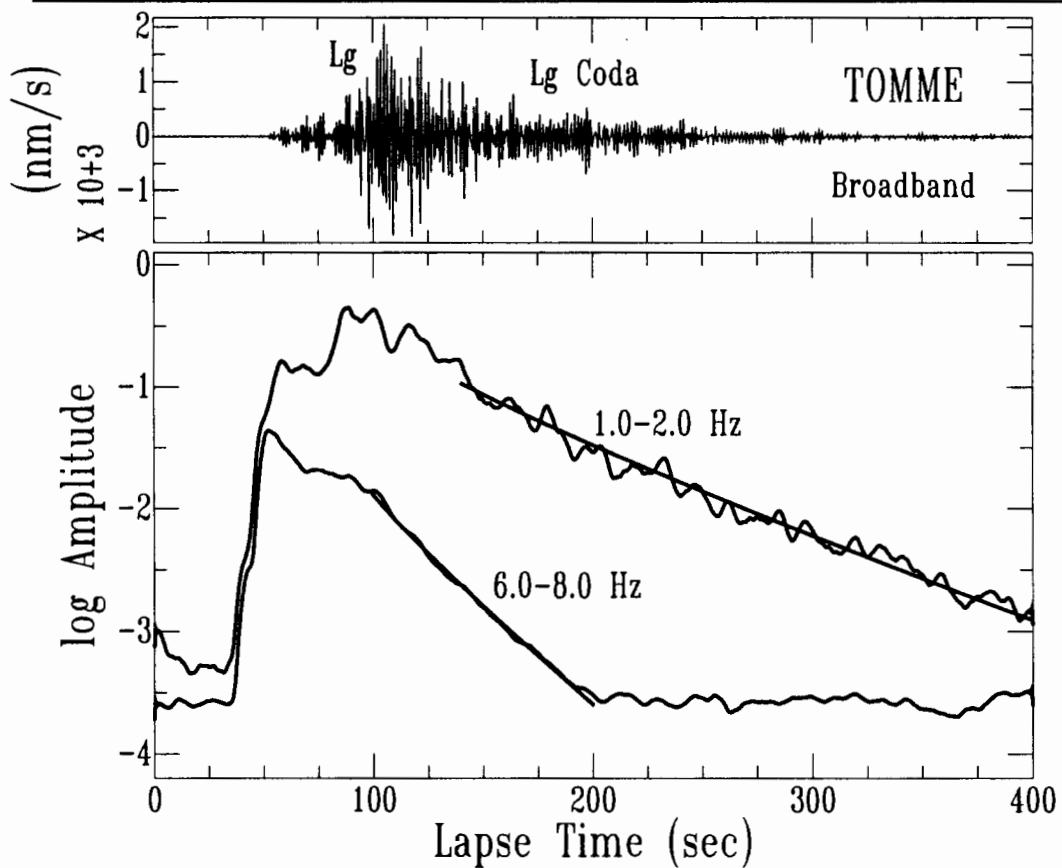


Figure 2 A typical broadband recording (top) and two corresponding narrowband envelopes (bottom). Amplitude measurements are made by matching the synthetic curves with the observed envelopes.

envelopes. In our case, we used 10 non-overlapping frequency bands ranging between 0.05 and 10 Hz. We observed small variability in each pair of narrowband measurements, further demonstrating the stability of the coda as well as the appropriateness of the path corrections (Figure 3). Any systematic offset in log amplitude between the two stations is the result of relative site effect between MNV and KNB. After correcting for any relative site effect between the two stations, we empirically corrected the amplitude for the actual site effect as follows. We assumed that the smallest events ($M_L < 2.5$) have corner frequencies above 10 Hz (e.g., event Skull 2 in Figure 4a), and therefore the path and site-corrected far-field displacement spectra should be

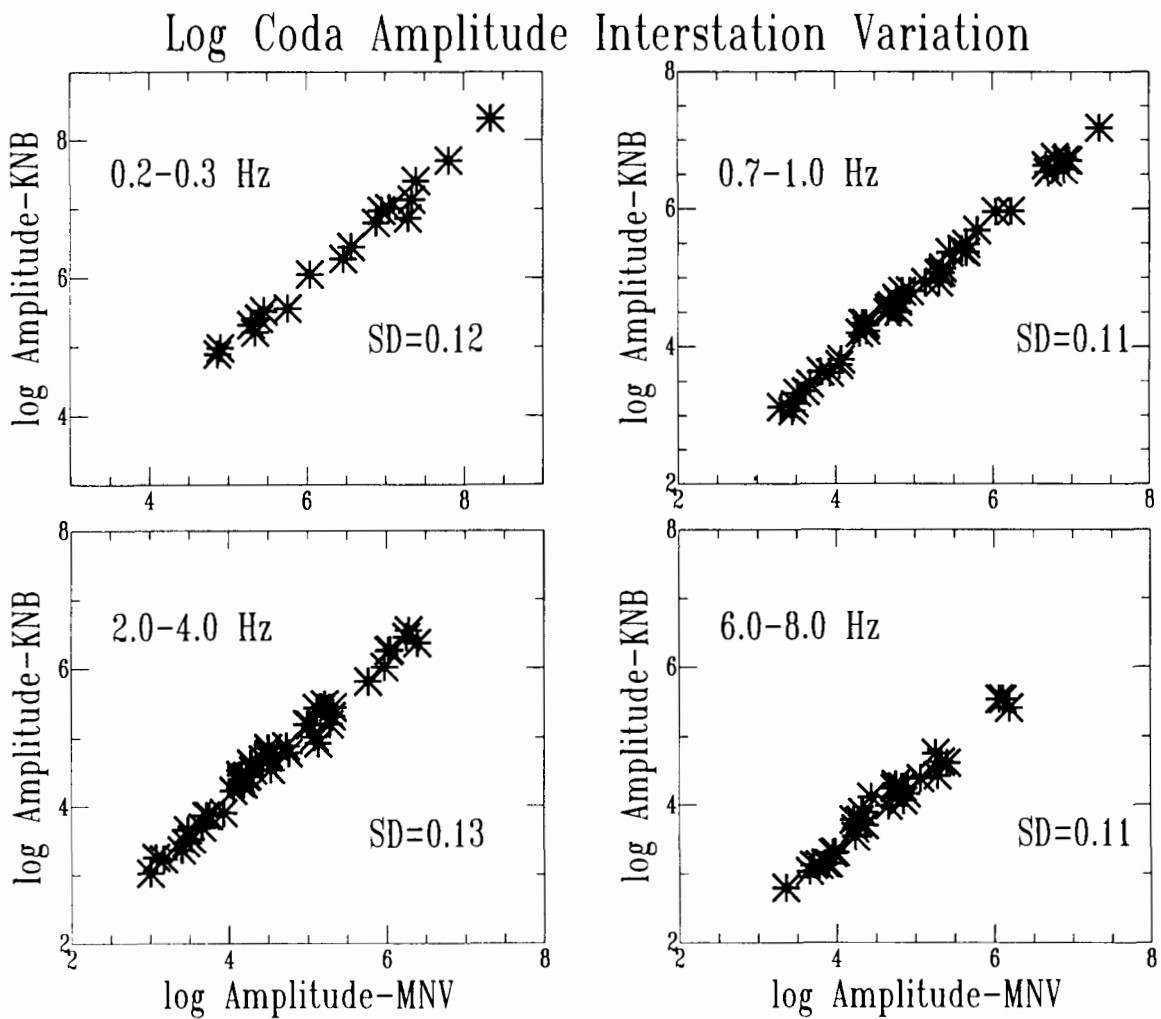


Figure 3 Path-corrected coda amplitude measurements are shown for a range of narrow bands. For each frequency, the interstation Lg coda amplitude variation is very small.

flat. The frequency-dependent site corrections obtained from the smaller events (e.g., Skull 2) are used to estimate moment rate spectra of the larger events.

Spectra for NTS explosions in Figure 4b show a size/depth-dependent peaking in the Lg spectra between 0.3 and 1 Hz, in sharp contrast to normal depth earthquakes in Figure 4a (see also Walter et al., this issue). This is may be the result of depth-dependent R_g to S scattering near the explosion source

Path and Site Corrected Earthquake Spectra

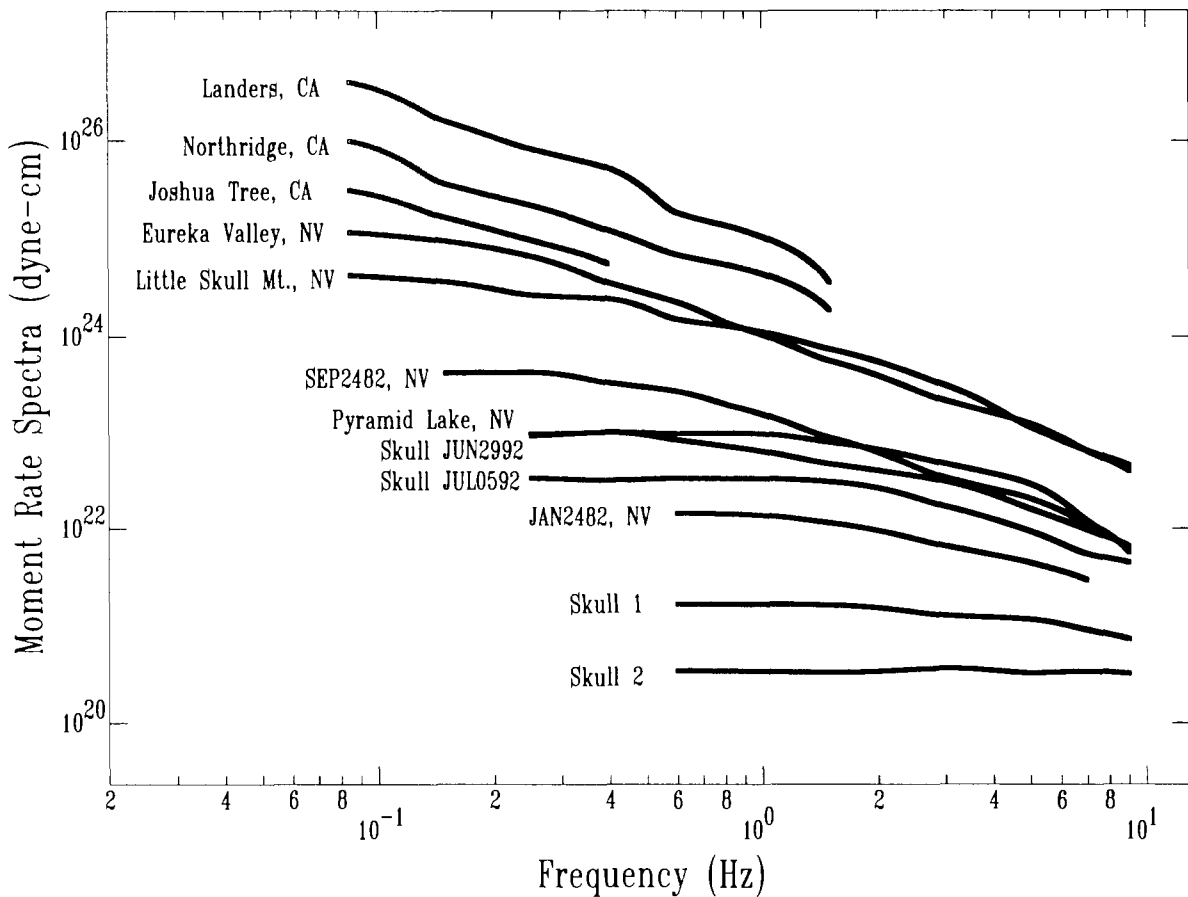


Figure 4a Moment rate spectra for western U.S. earthquakes were derived from site-corrected narrowband L_g coda amplitude measurements.

(e.g., Gupta, this issue). Broadband spectral shape differences between earthquakes and explosions are the subject of an ongoing discrimination study. The DOE Non-Proliferation Experiment (NPE), a 1 kiloton chemical explosion, and a nearby nuclear explosion are very similar in the 1.0 to 5.0 Hz band, whereas at frequencies below 1.0 Hz the NPE is deficient in energy.

To test the stability of single station discriminants we compared spectral ratios between MNV and KNB. As shown in Figure 5, L_g coda spectral ratios between the 1-2 and 6-8 Hz band exhibit significantly less variability than direct wave spectral ratios, ranging between 3 to 4 times smaller data standard deviation. The L_g coda spectral ratio discriminant

NTS Explosion Spectra

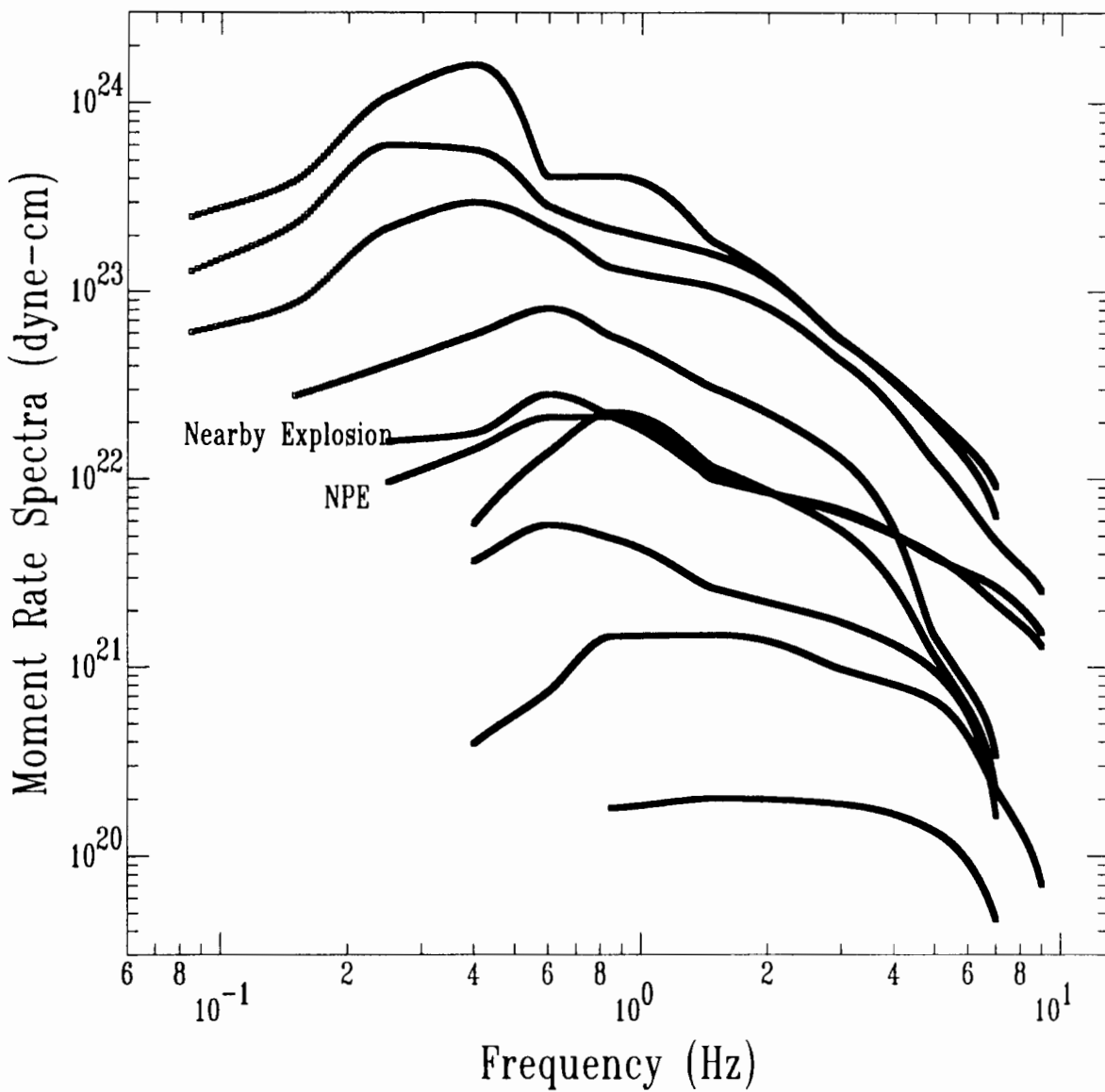


Figure 4b In contrast to normal depth earthquakes in Figure 4a, NTS explosions exhibit strong spectral peaking between 0.3 and 1.0 Hz. The NPE is similar to a nearby nuclear explosion between 1.0 and 5.0 Hz, but has smaller amplitude below 1.0 Hz.

shown in Figure 6 displays good separation for explosions in high gas porosity - low strength material, in contrast to P_g/L_g phase ratios (see Walter et al., this issue). We have combined P_g/L_g and P_n/L_g discriminants from Walter et al. and L_g coda spectral ratios to take advantage of the differences in material

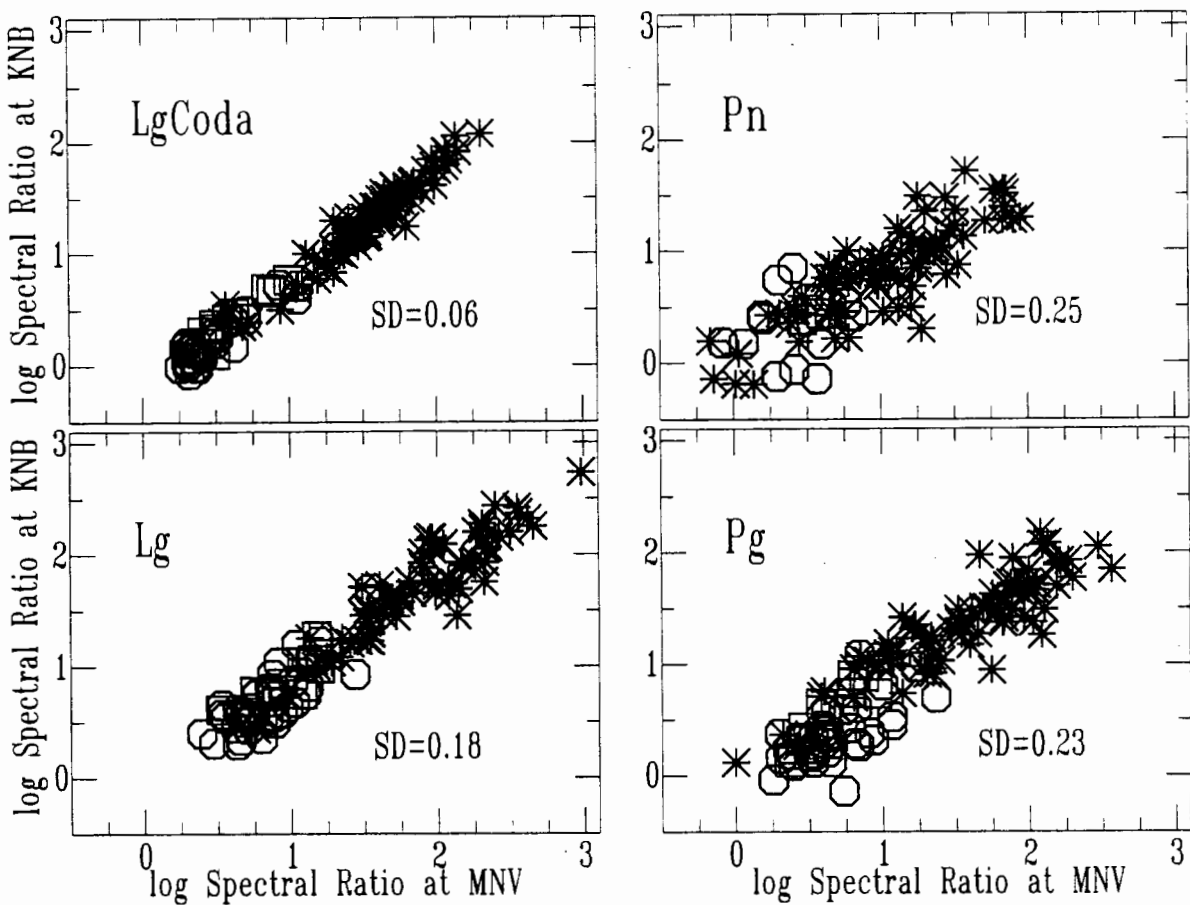


Figure 5 The interstation variation of the spectral ratio 1-2/6-8 Hz clearly shows that the L_g coda spectral ratio is 3 to 4 times less variable than L_g , P_g or P_n phases. The blue circles correspond to Little Skull Mt. earthquakes, red asterisks correspond to NTS explosions and green squares correspond to the unusually shallow Rock Valley earthquake sequence at NTS.

property dependence. As shown in Figure 7, the combined discriminant provides much better separation than either one does alone.

The present study included a number of events from Rainier Mesa, an area not included in the study of Taylor et al (1988). These Rainier Mesa events include most of the low gas porosity - high strength explosions for $M_L(\text{Coda}) < 5.0$, which explains why the L_g coda spectral ratio discriminant performance looks worse in Figures 6 than in the corresponding Figure 4d in Taylor et al. (1988). Finally, the unusually shallow sequence of earthquakes from Rock Valley ($z < 3$ km) indicate that earthquakes such as these may result in increased false alarms.

LgCoda (1-2/6-8) Hz Spectral Ratio at KNB

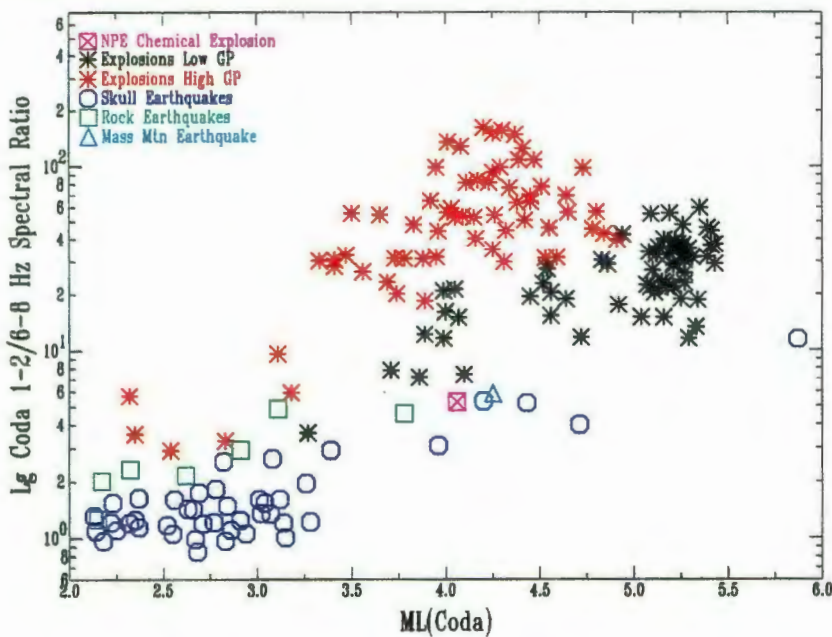


Figure 6 L_g coda spectral ratios are shown for events recorded at station KNB, roughly 300 km away. Notice that the explosions in high gas porosity-low strength material (red asterisks) discriminate well from earthquakes, whereas the events in low gas porosity-high strength material (black asterisks) fall closer to the earthquake population. The shallow Rock Valley sequence (green squares) appear intermediate between explosions and the normal depth Little Skull Mt. earthquake sequence (blue circles). Curiously, the NPE, a high strength-low gas porosity event, has the lowest spectral ratio for explosions with similar magnitudes and lies within the earthquake population.

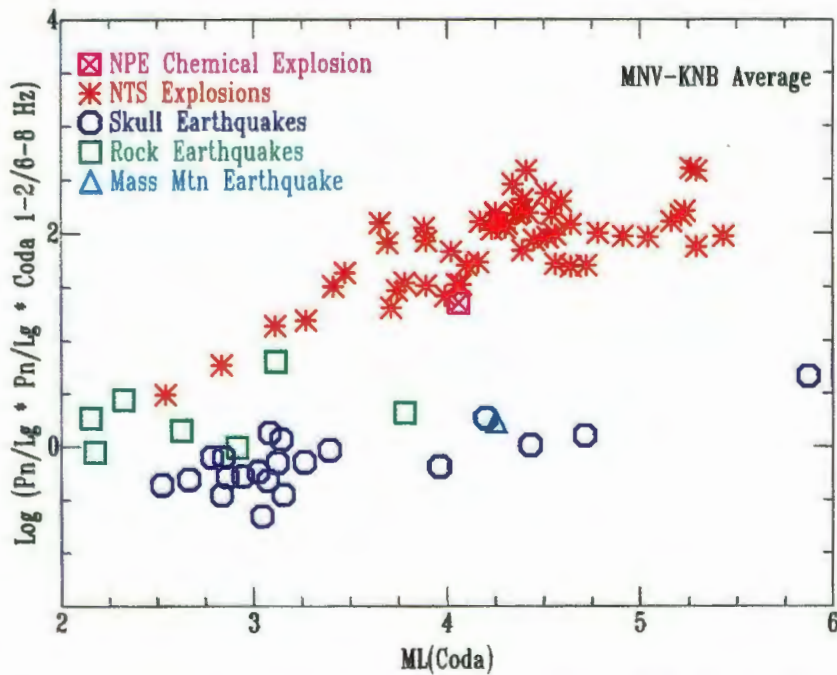


Figure 7 For events in common we have combined P_g/L_g and P_n/L_g phase ratios from Walter et al. (this issue) with L_g coda spectral ratios. Notice that the separation is considerably better than the L_g coda spectral ratio in Figure 6.

Summary

The L_g coda is shown to provide very stable single station estimates of path-corrected earthquakes source spectra. First, we found that moment rate spectra for normal depth earthquakes in the western U.S. do not exhibit the strong spectral peaking observed for NTS explosions. The strong depth-dependent peaking may be the result of near source R_g to S scattering (Gupta, this issue) and thus the coda derived explosion spectra still contain the R_g to S transfer function (see Walter et al., this issue). Explosion spectral shape differences will be explored in future work as a possible broadband discriminant.

Our spectral ratio study represents an extension of the earlier study by Taylor et al., (1988). We covered the same 1-2 / 6-8 Hz frequency bands as Taylor et al., however, the L_g coda spectral ratio appears to perform slightly better than the direct L_g , a consequence we believe of its extremely small interstation variability. Spectral ratios using the L_g coda are 3 to 4 times less variable than P_n , P_g and L_g spectral ratios. The stability of coda wave estimates make them ideal for low magnitude monitoring at a single station. The L_g coda spectral ratio dependence on material property is opposite that of P_g/L_g ratios (Walter et al., this issue) and thus a combination of the discriminants will improve upon the discrimination performance for normal depth earthquakes, especially at low magnitudes. As shown in Figure 7, a combined discriminant does perform better. However, these preliminary results also show that very shallow earthquakes may pose problems for short period discrimination at low magnitudes.

References

- Aki, K and B. Chouet (1975), Origin of coda waves: source, attenuation, and scattering effects, *J. Geophys. Res.* **80**, 3322-3342.
- Mayeda, K, S. Koyanagi, M. Hoshiba, K. Aki and Y. Zeng (1992), A comparative study of scattering, intrinsic and coda Q-1 for Hawaii, Long Valley, and Central California between 1.5 and 15.0 Hz,
- Mayeda, K. (1993), mb(LgCoda): a stable single station estimator of magnitude, *Bull. Seism. Soc. Am.*, **83**, 851-861.
- Mayeda, K. and W. R. Walter (1994), A new broadband magnitude based on coda envelopes (abstract), *Seism. Res. Lett.* **65**, 49.
- Phillips, W. S. and K. Aki (1986), Site amplification of coa waves from local earthquakes in central California, *Bull. Seism. Soc. Am.*, **76**, 627-648.
- Taylor, S. R., N. W. Sherman and M. D. Denny (1988), Spectral discrimination between NTS explosions and western United States earthquakes at regional distances, *Bull. Seism. Soc. Am.*, **78**, 1563-1579.
- Zeng, Y, F. Su, and K. Aki (1991), Scattering wave energy propagation in a medium with randomly distributed isotropic scatterers, 1, Theory, *J. Geophys. Res.* **96**, 607-619.

Dynamic Bayesian Filtering for Real-Time Seismic Analyses

David K. Blough

Alan C. Rohay

Kevin K. Anderson

Wesley L. Nicholson

**Pacific Northwest Laboratory
Richland, Washington**

Abstract

State space modeling, which includes techniques such as the Kalman filter, has been used to analyze many non-stationary time series. The ability of these dynamic models to adapt and track changes in the underlying process makes them attractive for application to the real-time analysis of three-component seismic waveforms. We are investigating the application of state space models formulated as Bayesian time series models to phase detection, polarization, and spectrogram estimation of seismograms. This approach removes the need to specify data windows in the time series for time averaging estimation (e.g., spectrum estimation). We are using this model to isolate particular seismic phases based on polarization parameters that are determined at a spectrum of frequencies. We plan to use polarization parameters, frequency spectra, and magnitudes to discriminate between different types of seismic sources. We present the application of this technique to artificial time series and to several real seismic events including the Non-Proliferation Experiment (NPE) two nuclear tests and three earthquakes from the Nevada Test Site, as recorded on several regional broadband seismic stations. A preliminary result of this analysis indicates that earthquakes and explosions can potentially be discriminated on the basis of the polarization characteristics of scattered seismic phases. However, the chemical (NPE) and nuclear explosions appear to have very similar polarization characteristics.

1 Introduction

The purpose of this paper is to introduce a statistical approach to characterizing seismic waveforms that combines and extends several existing procedures. The approach utilizes a methodology which can be applied in real-time and which simultaneously extracts frequency, magnitude, polarization, and arrival time information from three-component seismograms. In this paper, the focus is on near real-time estimation of polarization and a graphical display of the results. A complete description of the entire methodology with applications is in progress.

The statistical model underlying the methodology is a state space formulation of a time series model. It is dynamic in the sense that the parameters of the model are not fixed, but are allowed to adapt and change over time. This alleviates the need for the often untenable stationarity assumption and for data windows, since model parameters are updated as each new observation is obtained. The updating algorithm is a generalization of the Kalman filter. While the model could be developed from that point of view, we will adopt a more statistical exposition using a Bayesian approach to modeling.

These statistical models have had a wide area of application. They can be found in forecasting economic time series, real-time data quality control, target tracking, and remote sensing applications. In a sense, we seek to track the seismic signal in real time and extract relevant information; thus, these models are well suited to the task.

In order to test the plausibility of the methodology, several tests were run on artificial time series that were generated to have similar spectral and polarization characteristics to real data. We first apply the methodology to data recorded at Mina, Nevada, for the recent Non-Proliferation Experiment (NPE). We then apply the methodology to data recorded at Goldstone, California for three Nevada Test Site (NTS) explosions (including the NPE) and three aftershocks of the Little Skull Mountain earthquake that occurred at the NTS. Figure 1 provides a map showing the locations of events and stations.

Polarization estimates result from analysis of the eigenvalues and eigenvectors of the model-estimated 3x3 cross-covariance matrix of the three orthogonal components at each time increment. This method differs from previous approaches that use a covariance matrix calculated from three-component data within moving time windows. Once the cross-covariance matrix is estimated, we characterize the dimensionality of particle motion of the three-component seismogram in a manner similar to that of Jurkevics (1988) and Suteau-Henson (1991). Then by scaling the eigenvalues appropriately, we construct ternary diagrams which depict graphically the evolution of the dimensionality of particle motion over time. Waveform phase characterization proceeds from the resulting diagrams.

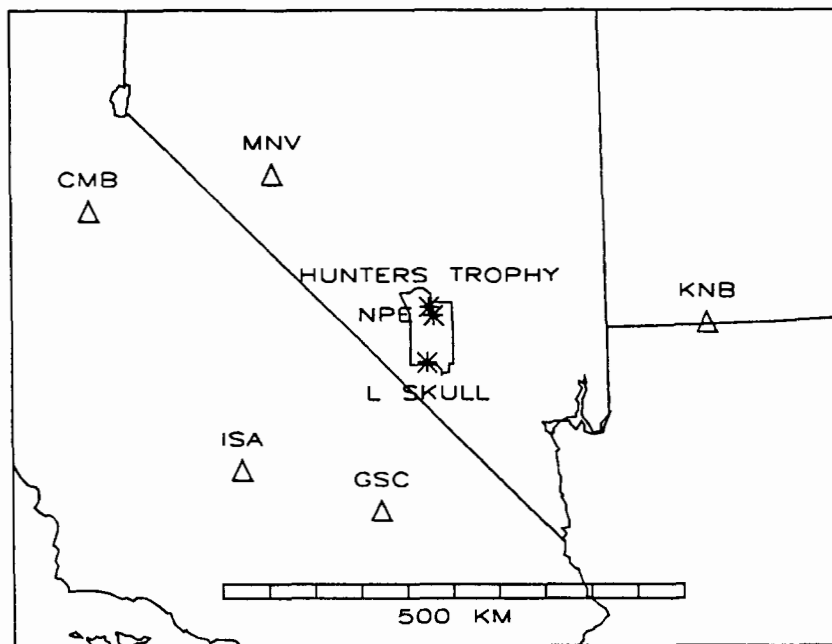


Figure 1. Location map showing the locations of NTS explosions Hunter's Trophy and the NPE, the locations of the Little Skull Mt. aftershocks, and the locations of several broad-band seismic stations that recorded the data used in this study.

2 Bayesian Statistical Approach: The Dynamic Linear Model

A brief overview of the dynamic linear model will now be given. Details of the estimation algorithm can be found in the literature. Particularly relevant discussions of the model can be found in West and Harrison (1989) and Gordon and Smith (1988).

The state space formulation of the model is described by two equations, the first is the observation equation and the second is the state equation:

$$Y'_t = F'_t \Theta_t + \nu'_t$$

$$\Theta_t = G_t \Theta_{t-1} + \Omega_t$$

The components of the model are defined as follows:

$Y'_t = (Y_{t1}, Y_{t2}, \dots, Y_{tq})$ is a q -vector of observations taken at time t .

$\nu'_t = (\nu_{t1}, \nu_{t2}, \dots, \nu_{tq})$ is a q -vector of observation errors at time t .

$\Theta_t = (\theta_{t1}, \theta_{t2}, \dots, \theta_{tq})$ is an $n \times q$ state matrix at time t , also referred to as the system matrix.

The columns are the state vectors of each of the q component time series.

$\Omega_t = (\omega_{t1}, \omega_{t2}, \dots, \omega_{tq})$ is an $n \times q$ matrix whose columns are the state or system evolution errors of the q component time series.

At each time t , F_t is a known $n \times 1$ matrix, often referred to as the regression matrix. Also at each time t , G_t is a known $n \times n$ matrix referred to as the state or system evolution transfer matrix.

The vector ν_t is assumed to be normally distributed with mean vector 0 and covariance matrix $V_t \Sigma_t$. V_t is a known scalar at time t . It can be used to allow for common measurement scales, common sampling variation, common occurrence of missing values and outliers. In lieu of these considerations it is often taken to be identically 1. Σ_t is an unknown $q \times q$ matrix representing the covariance information across the q component time series. The vectors ν_t are assumed to be distributed independently over time. The matrix Ω_t is assumed to have a matrix normal distribution with mean matrix 0, a time-dependent left covariance matrix, and right covariance matrix Σ_t . The Ω_t are assumed to be distributed independently over time and they are assumed to be independent of the vectors ν_t .

Parameters of the model are estimated within a Bayesian context. That is, a prior distribution for the state matrix is assumed. Given an observation Y_t , the prior distribution is updated by applying Bayes' Theorem. The resulting posterior distribution is then used as the prior distribution for time $t + 1$. The recursive nature of this algorithm makes it amenable to real-time processing of the data.

3 The Dynamic Linear Model for Three-Component Seismograms

In order to implement the dynamic linear model for three-component seismograms, specification of certain matrices in the above formulation is necessary. First of all, $q = 3$, and the observed vector of observations $Y'_t = (Y_{t1}, Y_{t2}, Y_{t3})$ corresponds to the north, east and vertical components of the observed seismogram. If the data is measured k times per second, we can incorporate frequency information in the model by defining the state matrix to be the Fourier coefficients of each component at *specified* frequencies. The choice of which frequencies to include in the model is up to the investigator; in order to cover the relevant spectrum in the data sets we analyzed, we chose the frequencies at 0.5, 1.0, 2.0, 4.0 and 8.0 Hz. This means then that Ω_t is a 10×3 matrix. The matrix G_t is then a 10×10 block diagonal matrix, where each block is a 2×2 matrix of the form

$$\begin{pmatrix} \cos \omega t & \sin \omega t \\ -\sin \omega t & \cos \omega t \end{pmatrix}$$

with ω corresponding to $(2\pi/2k)l$, for $l = 1, 2, 4, 8, 16$. The corresponding regression matrix is

$$F'_t = (1, 0, 1, 0, 1, 0, 1, 0, 1, 0).$$

Other approaches to modeling seismograms by way of statistical time series specify these matrices differently (Kitagawa and Gersch 1985). For example, it is well-known that any integrated autoregressive moving average (ARIMA) model can be phrased in state space form by specifying the component matrices of the model appropriately. (See for example, Chapter 9 of West and Harrison, (1989)). Thus, in fitting a model from the class of ARIMA models, a similar state space approach could be adopted, but the constituent matrices of the model would need to be modified accordingly.

3.1 Frequency Analysis

By tracking the estimated state matrix of Fourier coefficients, it is possible to monitor the frequency content of the waveform in real time. The elements of the state matrix can change and adapt to increases and decreases in the amplitude of the wave at each of the chosen frequencies. This aspect of the analysis will not be discussed in this paper. However, in conjunction with the phase analysis below, it should be possible to extract useful information from the waveform for real-time and *a posteriori* analyses. This is an area of ongoing research.

3.2 Polarization Analysis

The 3x3 matrix Σ_t represents the cross-component covariance matrix at time t . As such, its eigenvalues and eigenvectors at each time t provide information on the nature of the polarity of the waveform at that time.

We investigated the structure of Σ_t by constructing plots of functions of the eigenvalues and eigenvectors of S_t , the estimate of Σ_t produced by the model. We used the eigenvector corresponding to the largest eigenvalue to obtain time series plots of azimuth and incidence angle. We used the eigenvalues to obtain a ternary time series plots for phase characterization.

Specifically, let λ_{1t} , λ_{2t} , and λ_{3t} be the eigenvalues of S_t . Let $\lambda_{(1)t} \geq \lambda_{(2)t} \geq \lambda_{(3)t}$ denote the ordered eigenvalues of S_t . Define the quantities

$$l_t = \frac{\lambda_{(1)t}}{\lambda_{1t} + \lambda_{2t} + \lambda_{3t}}$$

$$c_t = \frac{\lambda_{(2)t}}{\lambda_{1t} + \lambda_{2t} + \lambda_{3t}}$$

$$s_t = \frac{\lambda_{(3)t}}{\lambda_{1t} + \lambda_{2t} + \lambda_{3t}}$$

The values l_t , c_t , and s_t measure the locus of particle motion represented by the seismogram at time t in terms of its linear, circular, and spherical polarization characteristics, respectively. Since the relative size of the three eigenvalues determines the dimensionality of the particle motion, displaying l_t , c_t , and s_t in a ternary coordinate system provides a simple mechanism for tracking dimensionality through time. Figure 2 illustrates the use of the equilateral triangle ternary diagram for this purpose. The three vertices $(1, 0, 0)$, $(0, 1, 0)$, and $(0, 0, 1)$ are the limiting mixture points where only a single eigenvalue is non-zero. When we

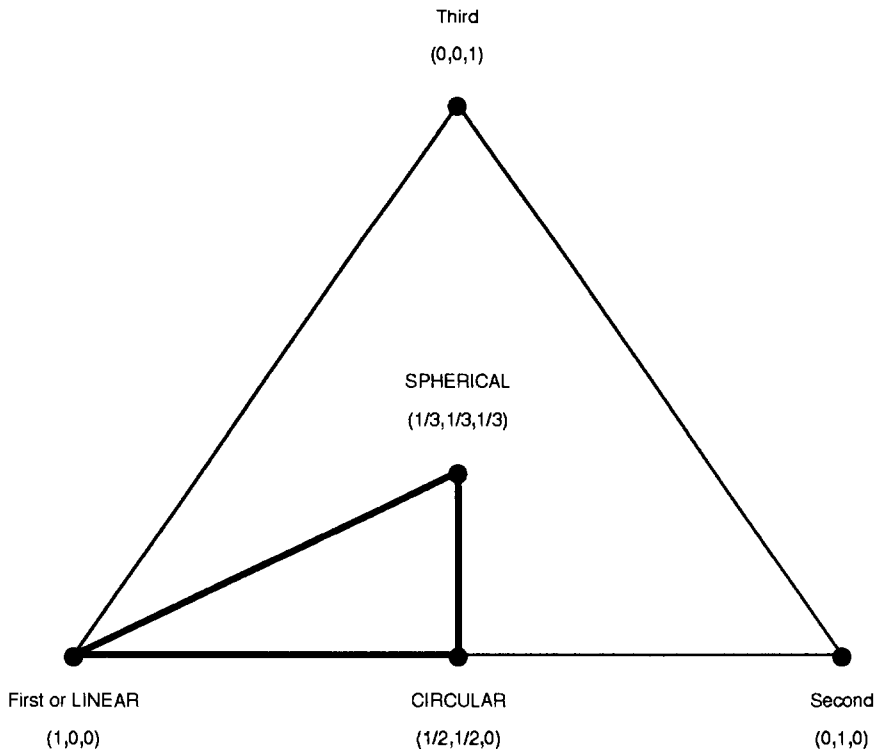


Figure 2. Ternary plot for display of particle motion eigenvalues. First, Second, and Third eigenvalues, as unordered, plot unconstrained in the equilateral triangle. As ordered with First largest, they plot in the bold triangle. Here, LINEAR, CIRCULAR, and SPHERICAL vertices define symmetric 1-, 2-, and 3-d motion, respectively.

order the eigenvalues, this constrains the coordinates to a subset of the triangle. For $l_t \geq c_t \geq s_t$, we are constrained to the region defined by the bold triangle. The vertices of this triangle define the three limiting polarization characteristics, linear, circular, and spherical. For linear polarization, one eigenvalue is non-zero and the corresponding eigenvector defines the direction of the one-dimensional rectilinear motion. Examples of such polarization include initial P-waves with near vertical incidence and the S-wave with near-horizontal incidence. For circular polarization, the two non-zero eigenvalues are equal and the particle motion is in the plane determined by the corresponding eigenvectors. Elliptical polarization is represented along the edge of the triangle between the linear and circular vertices. Examples of elliptical polarization include the Rayleigh wave and other surface waves. For spherical polarization, the eigenvalues are equal with unconstrained spatial motion. Examples include diffuse P-coda, crustal Lg wave, and some instances of noise.

In practice, few real particle motions are any of these classical polarization extremes. There is always at least a small amount of noise and there will be competing phases arriving close together. Thus, real P-wave, Rayleigh wave and scattered wave phases will be in the neighborhood of linear, circular (elliptical), and spherical polarizations, respectively.

4 Model Test Examples

We applied these modeling techniques to a variety of waveforms; several simulated seismic signals, the NPE recorded at Mina, Nevada, and NTS earthquakes and explosions recorded at Goldstone, California.

4.1 Simulated Seismic Signals

To test the model, we generated a time series of pulses embedded in noise. The pulses were chosen to have approximately the same amplitude spectrum as the Hunter's Trophy and Non-Proliferation Experiment waveforms at the Livermore network station KNB (Kanab, Utah). The pulses were approximately one second long and placed at time intervals of approximately 2 seconds. The placement was varied randomly within ± 0.5 seconds to eliminate spectral scalloping in the whole-signal spectrum. The noise was generated using a random sequence filtered to approximate the noise in the target recordings. The pulses were separated by intervals of background noise 0.5 to 1.5 seconds in duration. Figure 3 shows the resulting three-component waveform.

The sequence of seven three-component pulses as generated had slightly different azimuths and angles of incidence: the azimuths of the seven pulses were 290, 280, 290, 300, 290, 290, and 290 degrees; and the angle of incidence was 20 degrees, except for the next to last pulse where it was changed to 30 degrees.

The ternary diagram for this series showed a random scatter of points in the center of the plot reflecting the noise prior to the event. This was followed by a concentration of points at the linear vertex. Thus it captured the marked linearity during the onset of each of the impulsive spikes. Figure 4 illustrates the ability of the model to track changing incidence angle and azimuth. The solid line in each plot represents the true underlying structure. It is clear that the model can detect and track changes in incidence angle and azimuth, although its performance is better for azimuth tracking. Note that the plot in Figure 4 fails to show that the polarization returns to a random direction between the pulses. Experiments were made in the tuning of the

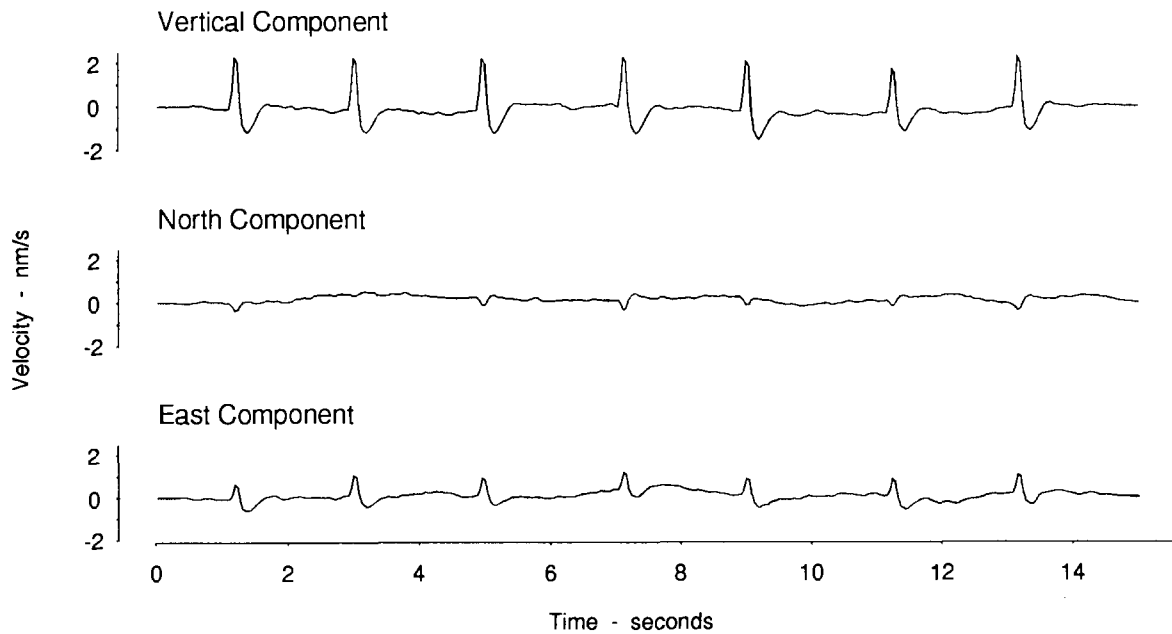


Figure 3. Artificial three-component seismogram for the seven pulse signal.

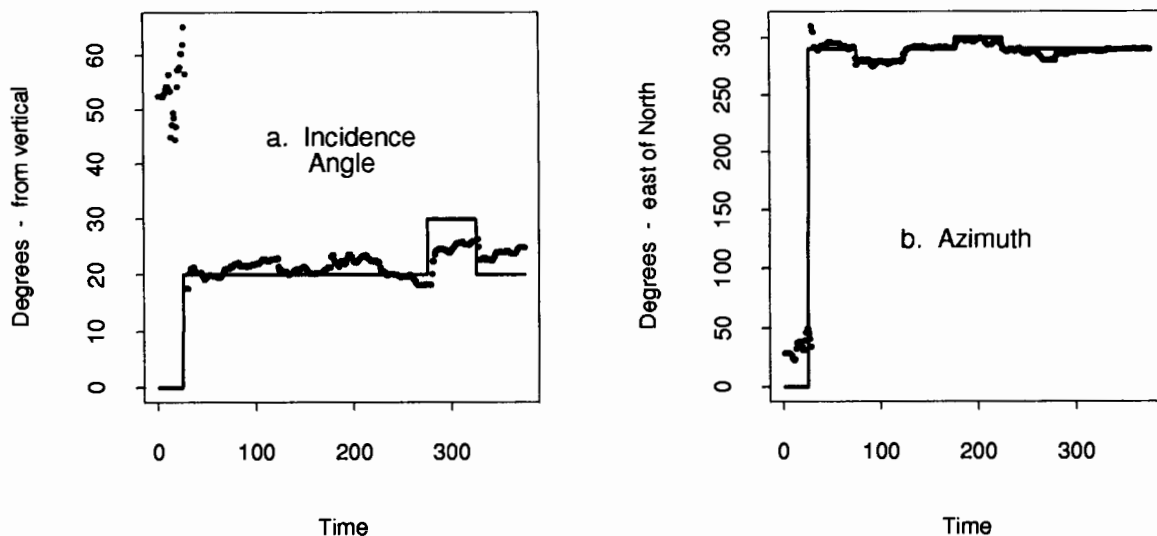


Figure 4. Theoretical (solid curves) and predicted (dots) incidence angle and azimuth estimates for the seven pulse artificial seismogram.

response time of the model to allow for a more rapid adjustment, but this tended to degrade the stability of the azimuth during the periods of strong polarization.

4.2 NPE at Mina, Nevada

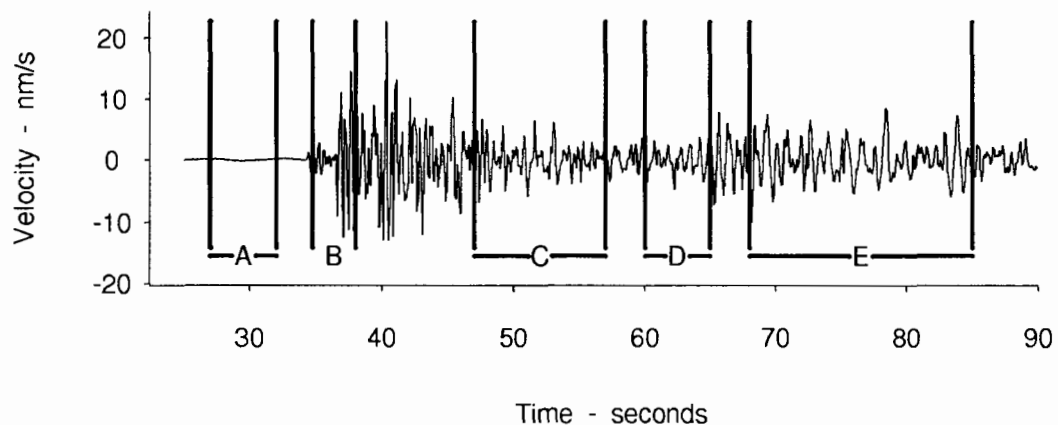
The NPE vertical-component waveform recorded at the Livermore network station MNV is shown at the top of Figure 5, where windows are selected to represent various types of seismic waves. The ternary plot in the lower portion of Figure 5 shows the relative amount of linear, circular, and spherical polarization for these windows. This example shows clear separation of different seismic phases: noise is three-dimensional, initial P-waves are nearly linear, and later-arriving scattered P-waves (the P-coda) are progressively more spherical with elapsed time. (This polarization can be visualized as “cigar-shaped.”) At the onset of shear and surface waves, the mix of polarizations shifts to a combination of circular and spherical, that remains stable throughout the later parts of the waveform. (This last polarization can be visualized as “disc-shaped.”)

On the basis of these observations, it appears that the polarization mixtures typify different combinations of waves: purely linear P-waves approaching the station on a direct line, followed by progressively scattered P-waves approaching from increasingly variable angles. As the amplitude of the scattered P-waves decreases, the onset of S-waves (generated near the explosion or as a result of other P- to S- conversions) and surface waves increases gradually. These wave types may tend to have a more two-dimensional (circular) polarization and therefore the mixture of scattered, two-dimensional polarizations lies very near the edge of the ternary diagram between circular and spherical.

4.3 Earthquakes and Explosions at Goldstone, California

Figures 6a, 6b, and 6c show the seismograms recorded at Goldstone, California (GSC), from three aftershocks of the June 28, 1992, Little Skull Mountain Earthquake. Figures 6d, 6e, and 6f show the seismograms from this station for three NTS explosions. Time windows labeled A, B, and C correspond to our selection of sections of Pg, P-coda, and S-coda that exhibited relatively stable polarization.

a. Vertical Component of Waveform



b. Ternary Plot of Particle Motion Eigenvalues

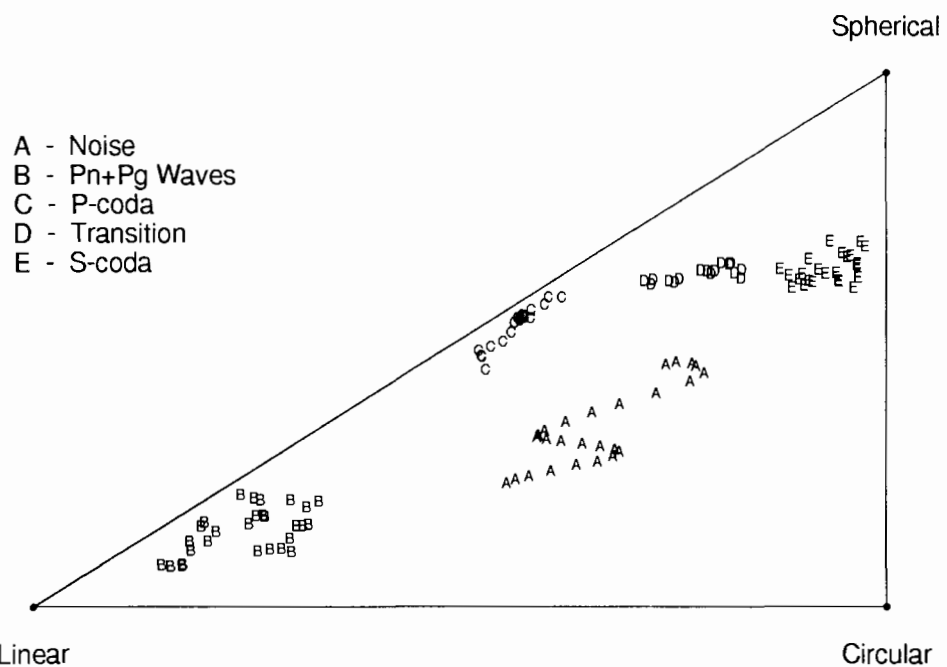
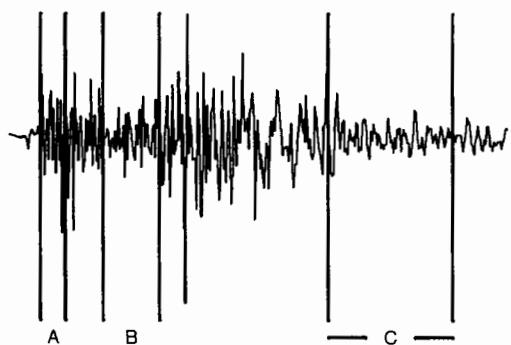
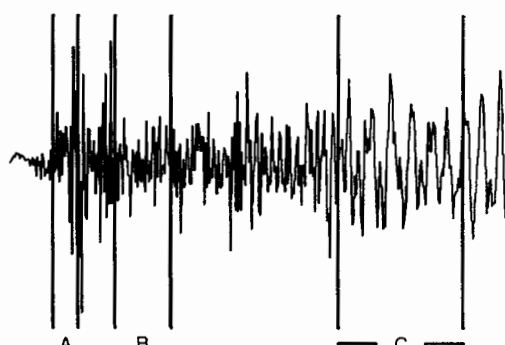


Figure 5. Dimensionality of particle motion of several NPE seismic phases as recorded at Mina, Nevada.

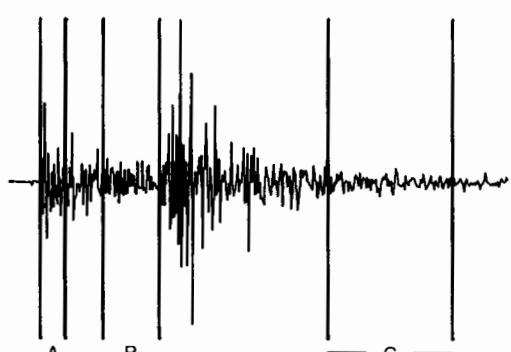
a. June 29, 1992, Aftershock



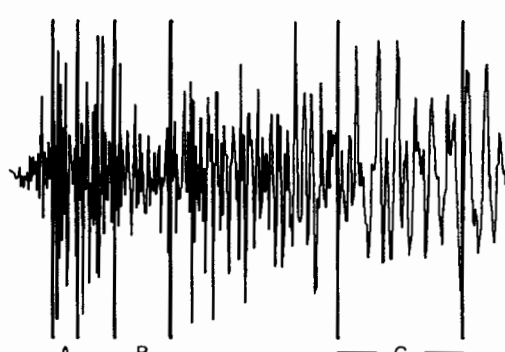
d. Hunter's Trophy



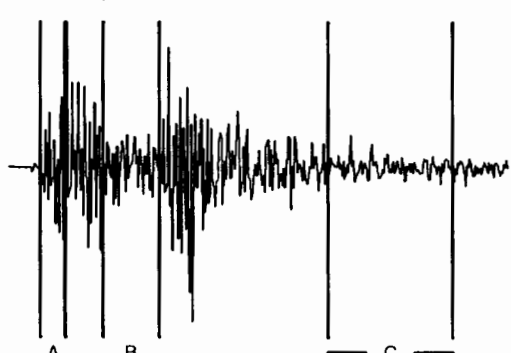
b. July 5, 1992, Aftershock



e. NPE



c. September 13, 1992, Aftershock



f. Bristol

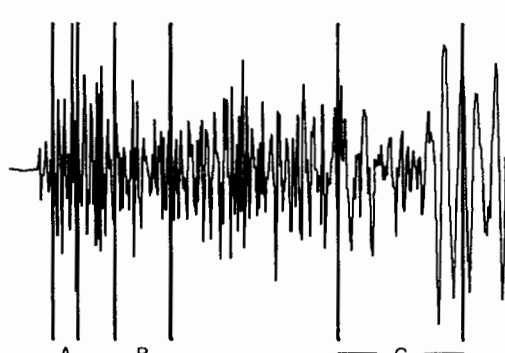
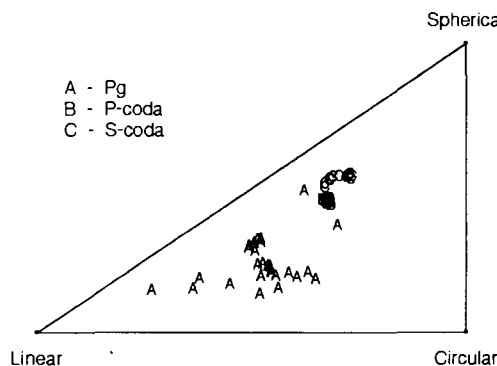


Figure 6. Seismograms of three Little Skull Mt. aftershocks and three NTS explosions as recorded at Goldstone, California. Windows A, B, and C sample Pg, P-coda, and S-coda phases, respectively.

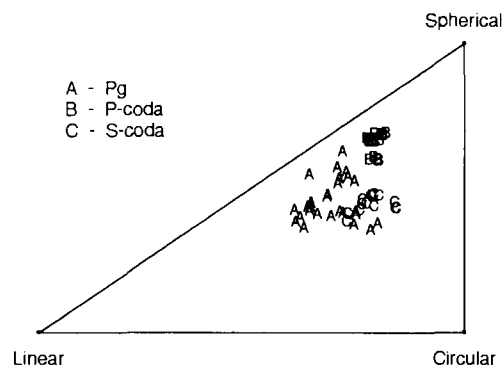
Figures 7a, 7b, and 7c show polarization diagrams for the three earthquakes. These three earthquakes all have magnitudes of approximately 4.4. The initial P-waves all exhibit a brief period of highly linear polarization, but the polarization appears to be much more chaotic than shown previously in Figure 5. Each of the three earthquakes has later P-wave coda and S-wave coda that are also very stable, but it is apparent that the P-coda and S-coda do not separate into different mixture types as shown previously.

Figures 7d, 7e, and 7f show polarization diagrams for three NTS explosions: Hunter's Trophy (magnitude 4.4), the NPE (4.1), and Bristol (4.6), respectively. These data do not show an initially linear polarization

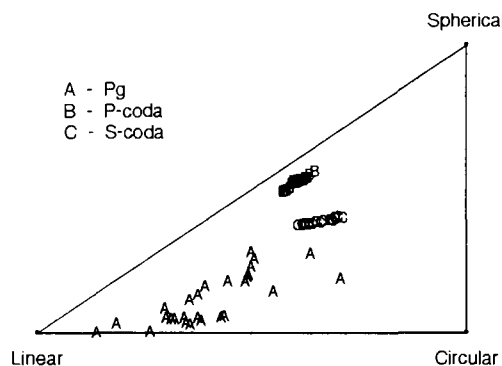
a. June 29, 1992, Aftershock



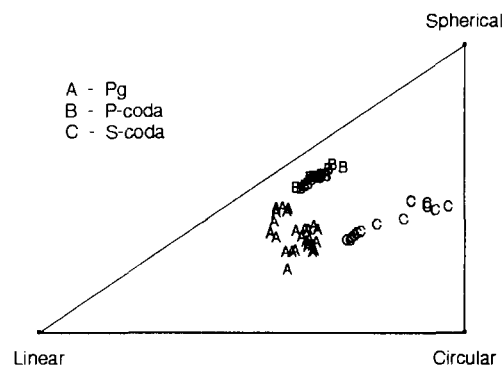
d. Hunter's Trophy



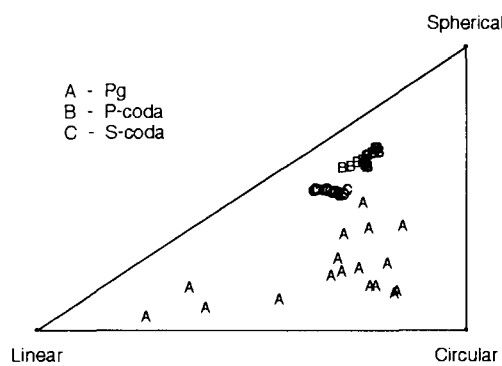
b. July 5, 1992, Aftershock



e. NPE



c. September 13, 1992, Aftershock



f. Bristol

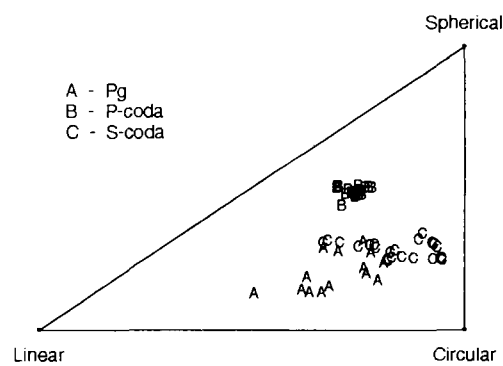


Figure 7. Dimensionality of particle motion of several phases of three Little Skull Mt. aftershocks and three NTS explosions as recorded at Goldstone, California.

for the P-waves. This is very different from the previous examples that exhibited at least brief periods of linearity in the P-wave. However, specific frequency polarization plots of the data indicate that the linear polarization is only evident at higher frequencies (above 5 Hz), while these diagrams are based upon an average of the polarization over frequencies between 0.5 and 8 Hz.

Although the P-wave polarization of these explosions appears to be limited to high frequencies, the P-coda and S-coda polarizations appear to be qualitatively similar to the example from MNV (Figure 5). The P-coda is mostly a mixture of linear and spherical polarization, while the S-coda is mostly a mixture of circular and spherical polarizations. A comparison of the NPE at MNV (Figure 5) and at GSC (Figure 7e) with Figures 7d and 7f shows that the NPE had the clearest separation between P-coda and S-coda of any of the three explosions. In fact, it appears that each of the three explosions maintains the relative mixture of P, P-coda, and S-coda polarizations, but that the event's entire pattern can shift position on the polarization diagram. Conversely, it is observed for the earthquakes (Figures 7a, 7b, and 7c) that P-coda and S-coda polarizations cannot be separated and can even reverse their relative positions on the polarization diagrams.

In summary, there appear to be several wave generation and wave propagation phenomena that can affect the mixture of polarization of seismic phases. These phenomena are probably different for explosions, where shear waves are generated by scattering in a near-surface, low velocity medium; and for earthquakes, which occur at greater depth and which directly radiate dominantly shear energy. Some of these differences appear to be exhibited in the relative mixture of polarization of different portions of the seismic waveforms presented above. However, data from additional stations and events are needed to fully understand these effects. Also, a refinement of the approach is needed to separate different frequency components.

5 Conclusions

We introduced a statistical approach to characterizing seismic waveforms that can be applied in real-time and which simultaneously extracts frequency, magnitude, polarization, and arrival time information from three-component seismograms.

We feel the application of dynamic Bayesian filtering to seismic analysis shows great promise. The models do need to be expanded to extract information relevant for phase characterization. We plan to use the model to detect and track compressional, shear, and scattered (coda) phases.

We have found that in specifying the tuning parameters of the model, there is a trade-off between precision in determining the azimuth and incidence angles and the capability of the model to adapt to rapid changes, a result common to other researcher's efforts.

We plan to improve the current spectral power model by incorporating elements of the physics of the local and regional wave propagation (Vidale 1986; Jepsen and Kennett 1990) to detect frequency-dependent polarization effects.

There is obvious potential for application of these techniques to a variety of seismic problems, such as seismic array azimuth and velocity determination, including three-component arrays. In addition, it appears to be possible to devise various outputs of the model to discriminate between earthquakes, chemical explosions, and underground nuclear explosions.

Acknowledgement. The research and data analysis reported here were supported by the U. S. Department of Energy, Office of Nonproliferation and National Security, under Contract DE-AC06-76RLO 1830.

References

- [1] Gordon, K. and Smith, A. F. M. (1988), *Modeling and Monitoring Discontinuous Changes in Time Series*, in *Bayesian Analysis of Time Series and Dynamic Models*, J.C. Spall, ed., New York: Marcel Dekker, Inc.
- [2] Jepsen, D. C., and Kennett, B. L. N. (1990), *Three-Component Analysis of Regional Seismograms*, Bulletin of the Seismological Society of America, Vol. 80, 2032-2052.
- [3] Jurkevics, A., (1988), *Polarization Analysis of Three-Component Array Data*, Bulletin of the Seismological Society of America, Vol. 78, 1725-1743.
- [4] Kitagawa, G., and Gersch, W. (1985), *A Smoothness Priors Time-Varying AR Coefficient Modeling of Nonstationary Covariance Time Series*, IEEE Transactions on Automatic Control, Vol. AC-30, 48-56.
- [5] Suteau-Henson, A., (1991), *Three-Component Analysis of Regional Phases at NORESS and ARCESS: Polarization and Phase Identification*, Bulletin of the Seismological Society of America, Vol. 81, 2419-2440.
- [6] Vidale, J. E., (1986), *Complex Polarization Analysis of Particle Motion*, Bulletin of the Seismological Society of America, Vol. 76, 1393-1405.
- [7] West, M. and Harrison, J., (1989), *Bayesian Forecasting and Dynamic Models*, New York: Springer-Verlag.

The Non-Proliferation Experiment recorded at the Pinedale Seismic Research Facility

Dorthe B. Carr
Sandia National Laboratories
Seismic Verification Technologies Department
Albuquerque, New Mexico 87185-0655

Abstract

The Non-Proliferation Experiment was recorded by five different seismic stations operated by Sandia National Laboratories at the Pinedale Seismic Research Facility, approximately 7.6° from the Nevada Test Site. Two stations are different versions of the Deployable Seismic Verification System developed by the Department of Energy to provide seismic data to verify compliance with a Comprehensive Test Ban Treaty. Vault and borehole versions of the Designated Seismic Stations also recorded the event. The final station is test instrumentation located at depths of 10, 40 and 1200 feet. Although the event is seen clearly at all the stations, there are variations in the raw data due to the different bandwidths and depths of deployment.

One Deployable Seismic Verification System has been operating at Pinedale for over three years and in that time recorded 14 nuclear explosions and 4 earthquakes from the Nevada Test Site, along with numerous other western U. S. earthquakes. Several discriminants based on the work by Taylor et al. (1989) have been applied to this data. First the discriminants were tested by comparing the explosions only to the 4 earthquakes located on the Test Site. Only one discriminant, $\log(L_g/P_g)$, did not show clear separation between the earthquakes and nuclear explosions. When other western U. S. events are included, only the m_b vs. M_s discriminant separated the events. In all cases where discrimination was possible, the Non-Proliferation Experiment was indistinguishable from a nuclear explosion.

Text of Presentation

The Pinedale Seismic Research Facility (PSRF) operated by the Air Force Technical Applications Center (AFTAC) is located in western Wyoming on the western front of the Wind River Mountains. PSRF is approximately 7.5-7.6° (830-850 km) from the northern end of the Nevada Test Site (NTS) (Figure 1). At the time of the Non-Proliferation Experiment (NPE) on September 22, 1993, Sandia National Laboratories was operating five stations at PSRF (Table 1). Two of the stations were different configurations of the Deployable Seismic Verification System (DSVS), developed for use with a Comprehensive Test Ban Treaty. A DSVS using the RSS3 configuration was installed in the spring of 1990. This configuration uses two Teledyne-Geotech seismometers, a S3 and a 54000, in two boreholes to record three component data between 0.01 and 50 Hz. The second DSVS with the RSS1 configuration, records three component data with a Guralp CMG-3 seismometer from 0.05 to 30 Hz. Both systems have

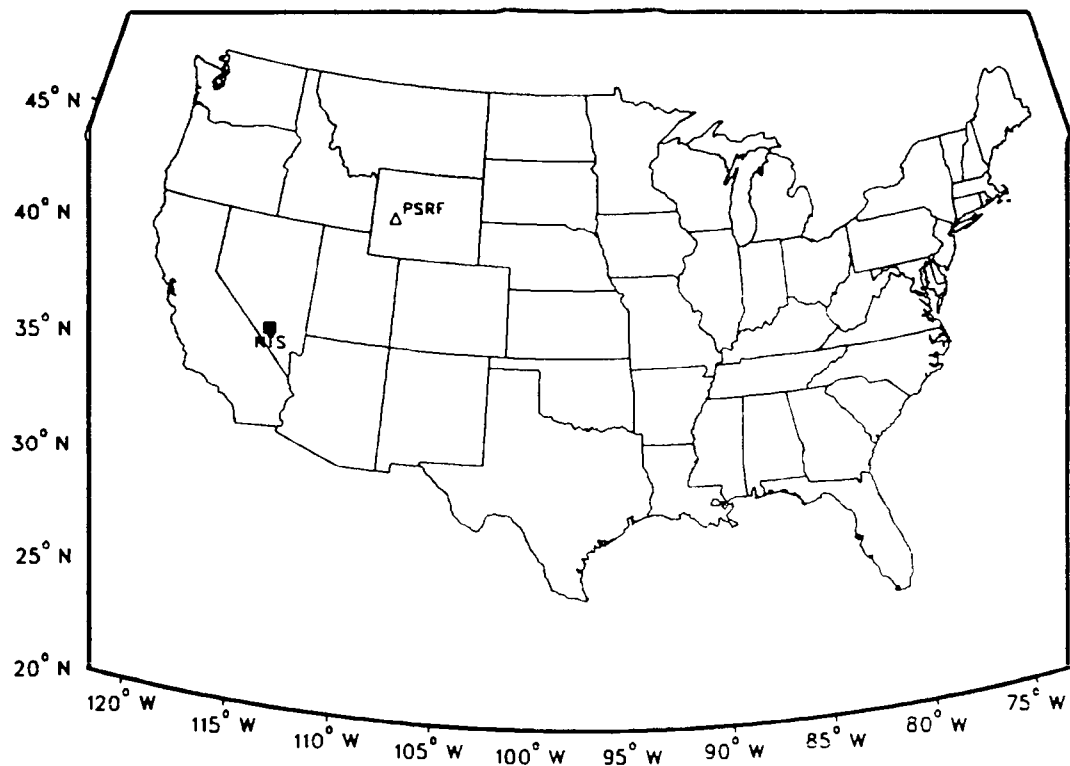


Figure 1. Map showing the location of the Pinedale Seismic Research Facility (PSRF) and the Nevada Test Site (NTS).

Table 1: Specifics of seismic systems operating at PSRF

SYSTEM	SEISMOMETER(s)	DEPTH	FREQUENCY BAND
DSVS/RSS3	Teledyne Geotech S3 Teledyne Geotech 54000	40 feet	0.01-50.0 Hz
DSVS/RSS1	Guralp CMG-3	40 feet	0.05-30.0 Hz
DSS (borehole)	Teledyne Geotech S3	100 meters	0.1-10.0 Hz
DSS (vault)	Teledyne Geotech GS13		0.1-10.0 Hz
experimental	Teledyne Geotech GS13	10 feet	1.0-50.0 Hz
	Teledyne Geotech GS13	40 feet	1.0-50.0 Hz
	Teledyne Geotech GS28	1200 feet	1.0-50.0 Hz

the seismometers at a depth of 40 feet. Two Designated Seismic Stations (DSS) were deployed at PSRF for four days around the NPE. DSS was developed for use with the Threshold Test Ban Treaty signed with the former Soviet Union. One DSS was in a borehole at approximately 100 meters and the other was in a vault around 8-10 feet deep. Both systems use Teledyne-Geotech seismometers and record three component data from 0.1 to 10 Hz. The last system operating at PSRF during the NPE is being used in an experiment to look at how noise varies with depth at PSRF. Three vertical seismometers, two Teledyne-Geotech GS13 and one Teledyne Geotech GS28, were deployed at different depths. One GS13 was in a shallow vault at 10 feet, and the other was in a deep vault at 40 feet. The GS28 was in a borehole at a depth of 1200 feet. All three seismometers recorded data from 1 to 50 Hz.

All of the stations recorded good data from the NPE (Figures 2-5). Figure 2 shows the vertical traces from the two DSVS stations (HF band, 0.5-50.0/30.0 Hz), the deep borehole at 1200 feet and the vault and borehole systems of DSS. All the traces are independently scaled so that the signals can be seen. The DSS instruments amplitudes are larger than the other three instruments by roughly a factor of 10^6 . The amplitude of the signal from deep borehole instrument is about a factor of 5 higher than the DSVS stations. The P_n arrival comes in clearly, with the first motion being down. All five traces have very similar signals when plotted out to see the first thirty seconds (Figure 3). The DSS stations were located approximately 1.5 miles from the other three systems, so the slight differences in the signals from DSS are most probably due to a combination of bandwidth and local geology. The P_g arrival should come in near 27 seconds, and although there is an increase in amplitude at this time (Figure 2), there is no clear onset of the P_g wave. There is no S_n arrival, which is not unusual in the western United States (WUS). The L_g arrival comes in clearly, especially on the deep borehole, DSS (Figure 5) and the IP band (0.01-2.5 Hz) of DSVS when high pass filtered. There are no clear surface waves on the LP band (0.02-0.05 Hz) of DSVS/RSS3 (Figure 4).

The signal to noise ration (SNR) of the P_n wave was greater than 12 dB for frequencies between 0.6 and 3.2 Hz. Out to 7.5 Hz, the SNR was still more than 2 dB. The signal went into the background noise at 9.5 Hz. A backazimuth for the NPE was calculated on DSVS/RSS3 using the three component method by Magotra et al. (1987). The backazimuth calculated was 206.4° , which is off by almost 19° . Two other NTS nuclear explosions, Mineral Quarry and Hunter's Trophy, were located close to the NPE. Calculated backazimuths for these two events were off by 5° and 13.5° respectively. An "array" backazimuth calculation using the five stations operating at PSRF for the NPE is not possible because of the timing on the DSS stations.

Sandia National Laboratories installed the first DSVS station (RSS3 configuration) in the spring of 1990. In the two and one half years the data was transmitted by satellite to Albuquerque, a good database of events occurring in the WUS was collected. Some of these events have been used to look at discrimination between earthquakes, nuclear explosions and the NPE at PSRF (Table 2, 3; Figure 6). Fourteen NTS nuclear explosions were recorded at PSRF, plus four earthquakes that occurred on or close

Pinedale stations

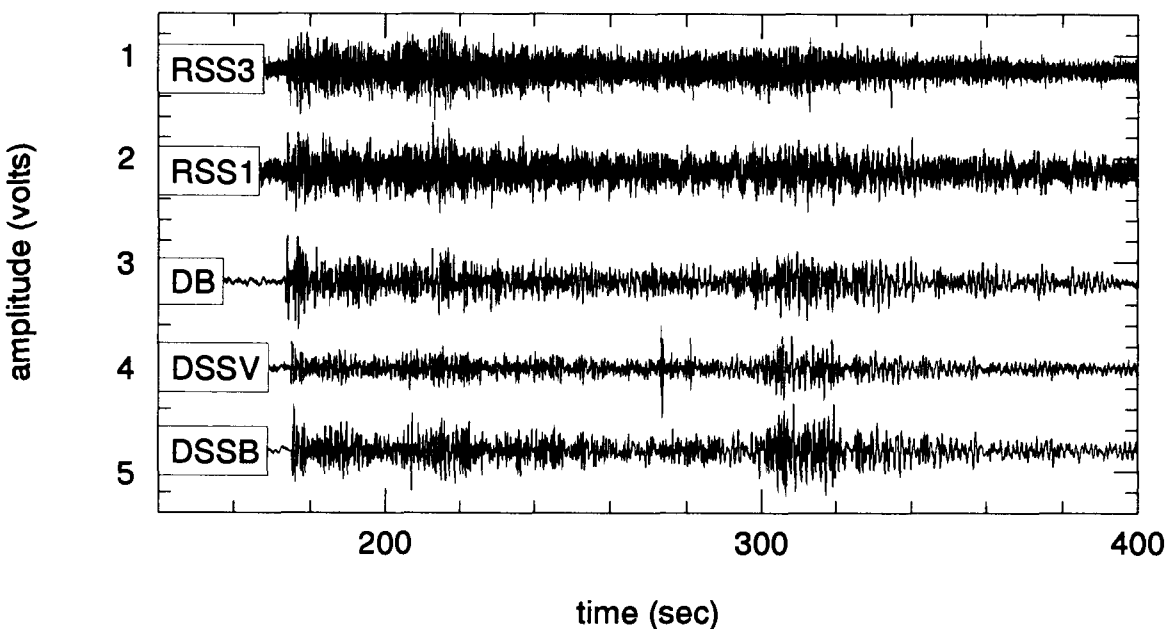


Figure 2. Vertical traces of the NPE from the stations operating at PSRF. The traces are independently scaled.

Pinedale stations

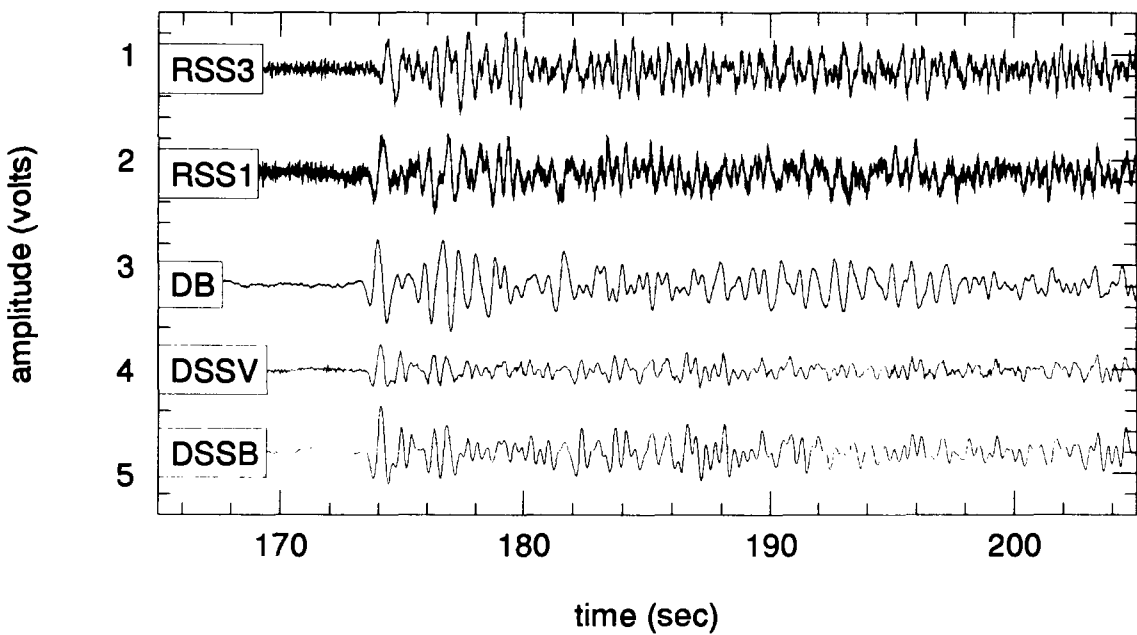


Figure 3. The first 30 seconds of the NPE as recorded at PSRF.

DSVS-RSS3 (vertical)

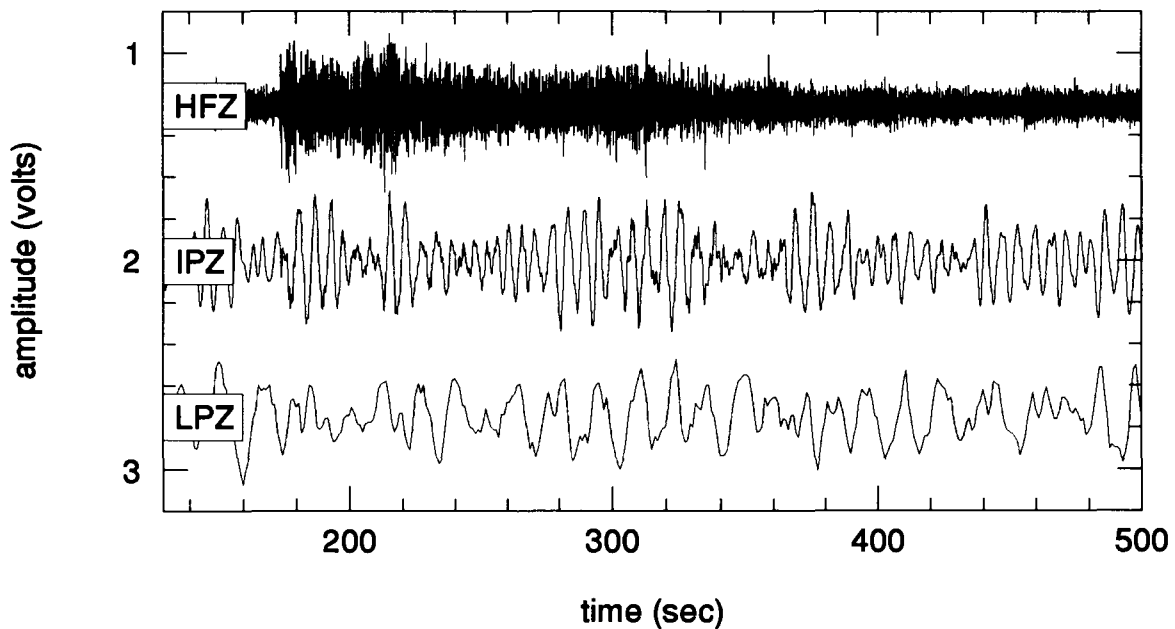


Figure 4. The vertical traces of the NPE on the three bands of DSVS/RSS3. The event is seen clearly on the IP band when high pass filtered at 0.5 Hz. There are no clear surface waves on the LP band.

DSS borehole

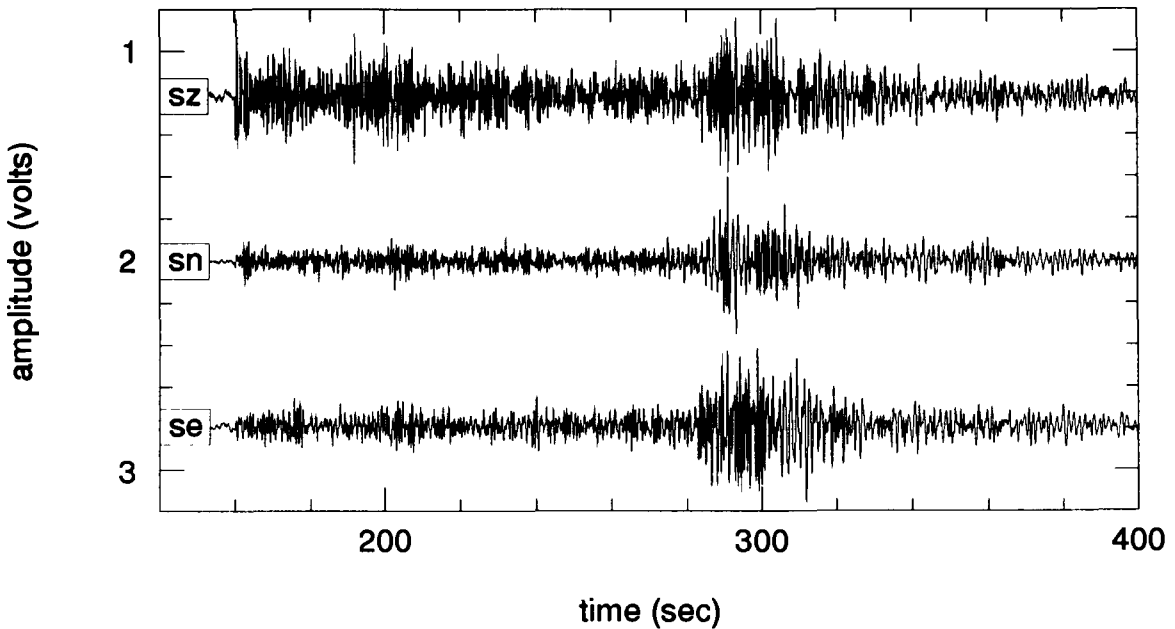


Figure 5. The NPE on all three components of the DSS in the borehole. Note the good L_g arrival.

DSVS-RSS3

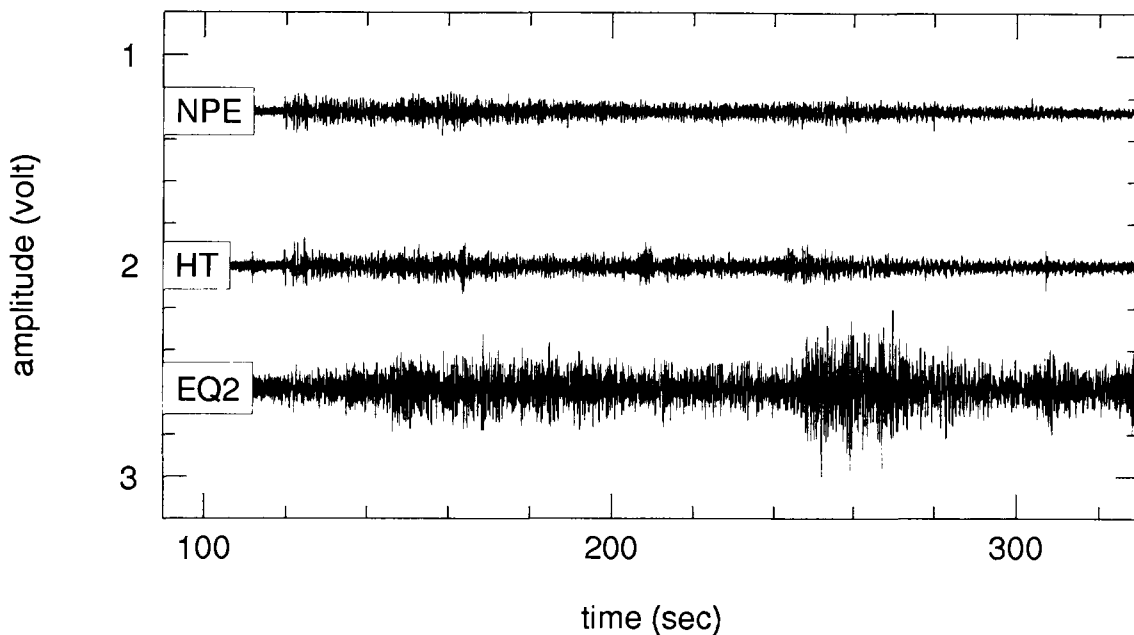


Figure 6. Map of the events used in the discrimination study at PSRF.

Table 2: NTS explosions and earthquakes

NAME	DATE	LOCATION	DISTANCE	NEIS m_b
BULLION #	13-JUN-1991	37.262N 116.420W	846.7 km	5.7
MINERAL QUARRY #	25-JUL-1990	37.207N 116.214W	839.3 km	4.7
HOUSTON #	14-NOV-1990	37.227N 116.371W	846.7 km	5.4
BEXAR	04-APR-1991	37.296N 116.313W	837.6 km	5.6
MONTELLO	16-APR-1991	37.245N 116.442W	849.4 km	5.4
FLOYDATA	15-AUG-1991	37.087N 116.002W	837.6 km	4.2
HOYA	14-SEP-1991	37.226N 116.428W	850.1 km	5.5
DISTANT ZENITH	19-SEP-1991	37.236N 116.166W	834.1 km	4.0
LUBBOCK	18-OCT-1991	37.063N 116.045W	842.1 km	5.2
BRISTOL	26-NOV-1991	37.096N 116.070W	840.6 km	4.6
JUNCTION	26-MAR-1992	37.272N 116.360W	842.3 km	5.5
GALENA	23-JUN-1992	37.124N 116.031W	836.0 km	3.9*
HUNTER'S TROPHY	18-SEP-1992	37.207N 116.210W	839.1 km	4.4
DIVIDER	23-SEP-1992	37.021N 115.998W	843.1 km	4.4
NPE	22-SEP-1993	37.126N 116.159W	839.6 km	4.1
EQ #1	29-JUN-1992	36.705N 116.293W	886.9 km	5.6
EQ #2	29-JUN-1992	36.686N 116.238W	885.6 km	4.3
EQ #3	29-JUN-1992	36.756N 116.236W	885.2 km	3.8
EQ #4	28-JUN-1992	36.419N 116.780W	939.0 km	4.4

no IP or LP data for this event

* local magnitude

Table 3: Western United States events

STATE	DATE	LOCATION	DISTANCE	NEIS m_b
Utah	22-MAR-1991	37.816N 112.995W	623.9 km	3.2
California	24-MAR-1991	37.645N 118.945W	979.5 km	3.3
Wyoming	13-APR-1991	42.031N 106.857W	236.6 km	3.2
California	04-MAY-1991	37.552N 118.432W	951.2 km	4.1*
Colorado	10-MAY-1991	37.466N 106.594W	641.9 km	3.4*
Nevada	17-MAY-1991	39.194N 114.960W	603.6 km	3.2*
New Mexico %	20-JUN-1991	33.619N 106.475W	1053.2 km	3.5*
Montana	18-JUL-1991	47.753N 113.841W	646.7 km	3.5
California/Nevada	12-AUG-1991	38.220N 118.750W	927.2 km	4.4
Utah	21-AUG-1991	39.364N 111.878W	426.6 km	3.3*
South Dakota ^	05-NOV-1991	44.350N 103.750W	499.2 km	2.5*
Utah	21-DEC-1991	37.567N 112.322W	625.2 km	3.6
New Mexico	02-JAN-1992	32.347N 103.124W	1290.0 km	4.7
Idaho	24-JAN-1992	43.999N 113.893W	373.6 km	2.7
Idaho	07-MAR-1992	44.530N 114.125W	416.0 km	3.8*
Montana	21-MAR-1992	47.267N 113.295W	579.1 km	3.7
Idaho	22-MAR-1992	44.582N 114.185W	422.8 km	4.3*
Nevada	24-MAR-1992	39.425N 119.924W	944.5 km	3.4*
Utah	24-JUN-1992	38.783N 111.554W	474.9 km	4.4*
California	09-JUL-1992	34.239N 116.837W	1140.4 km	5.6
Utah	11-JUL-1992	39.322N 111.123W	406.1 km	3.9
California	11-JUL-1992	35.210N 118.066W	1116.4 km	5.3
Nevada	16-JUL-1992	38.323N 116.159W	745.6 km	3.1*
Nevada	17-JUL-1992	38.387N 116.120W	738.3 km	3.1*
Idaho	28-AUG-1992	44.583N 113.323W	363.4 km	3.4
Utah	02-SEP-1992	37.090N 113.472W	715.0 km	5.8
California	19-SEP-1992	38.863N 122.793W	1194.3 km	4.6
Wyoming	02-NOV-1992	42.740N 104.389W	421.7 km	3.0*
Nevada	10-DEC-1992	39.682N 115.956W	636.1 km	3.2*
Utah	18-DEC-1992	39.729N 110.838W	355.5 km	3.1

% DOD explosion

^ rockburst

* local magnitude

to the test site with NEIS body-wave magnitudes between 3.8 and 5.6. Twenty-nine other WUS earthquakes at distances between 236 and 1290 km from PSRF were also collected for the study (Table 3). The event from South Dakota (5-Nov-1991) was classified as a rockburst in the PDE bulletin. Finally, a DOD explosion at White Sands, NM on 20-Jun-1991 was also included in the data base. Traces from the NPE, Hunter's Trophy and EQ #2 are in Figure 7. All these events had similar magnitudes in the PDE bulletin. There is much more L_g energy in the EQ #2 trace than for either explosion. Figure 8 shows the first 30 seconds of the NPE and Hunter's Trophy. The signals, especially in the first three to five seconds, look very similar at PSRF. Both of these explosions come from similar locations at the Test Site (Table 2). The discriminants used in the study are based on work done by Taylor et al. (1989) at the LLNL seismic network around NTS. Only discriminants that worked fairly well in that study were tried at PSRF: m_b vs. M_s , m_b vs. M_s^h , $\log(L_g/P_g)$, corner frequency and spectral ratios. Table 4 documents the methods used to calculate the discriminants.

The results of the discrimination studies can be seen in Figures 9 through 18. Figure 9 shows m_b vs. M_s for eleven NTS explosions, the four earthquakes on NTS and the NPE. There is good separation using this discriminant between nuclear explosions and earthquakes located on the Test Site. At this regional distance and test site, the NPE is indistinguishable from a nuclear explosion. Figure 10 is the same data as in Figure 9, plus the 29 WUS earthquakes and DOD explosion at White Sands. There is still fairly good separation between the explosions and earthquakes. Two earthquakes with m_b between 3.3 and 3.5 fall on the explosion side. They are the Wyoming earthquakes of 13-Apr-1991 and 02-Nov-1992 (Table 3).

The Forsyth (1976) M_s^h measures higher-mode surface waves earlier in the trace (Table 4). Figures 11 and 12 show m_b vs. M_s^h for only the NTS events and for all WUS events, respectively. There is good separation using this discriminant between nuclear explosions and earthquakes located at the Test Site. Again, the NPE is indistinguishable from a nuclear explosion. When WUS events are added (Figure 12), there is still fairly good separation between explosions and earthquakes for higher magnitude events. At $m_b < 3.6$, the discriminant breaks down, partly because there are no nuclear explosions at these magnitudes to compare to the WUS earthquakes.

Figure 13 shows the $\log(L_g/P_g)$ discriminant for all fourteen nuclear explosions, the four NTS earthquakes and the NPE. There is not a clear separation between earthquakes and explosions for this discriminant. The attenuation of higher frequency (> 8 Hz) energy and the recording site geology probably contribute to the "failure" of this discriminant. The data using all WUS events is in Figure 14.

Corner frequencies were calculated for eleven of the NTS nuclear explosions, the four earthquakes on NTS, the NPE and eleven WUS earthquakes with body-wave magnitudes in the PDE bulletin. Figure 15 shows the corner frequencies for all the events from NTS. There is good separation between the earthquakes and explosions, and the NPE is again indistinguishable from a nuclear explosion.

DSVS-RSS3

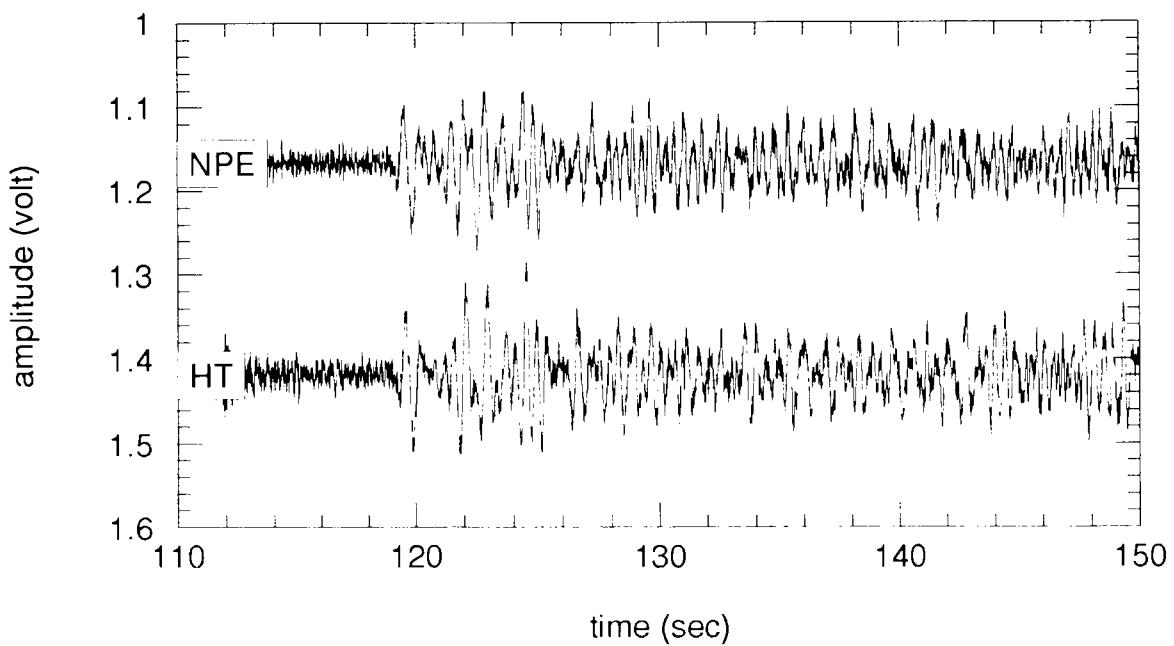


Figure 7. Vertical traces of the NPE, NTS explosion Hunter's Trophy and an earthquake at the southern end of NTS. The events have similar magnitudes. The traces are scaled relative to one another.

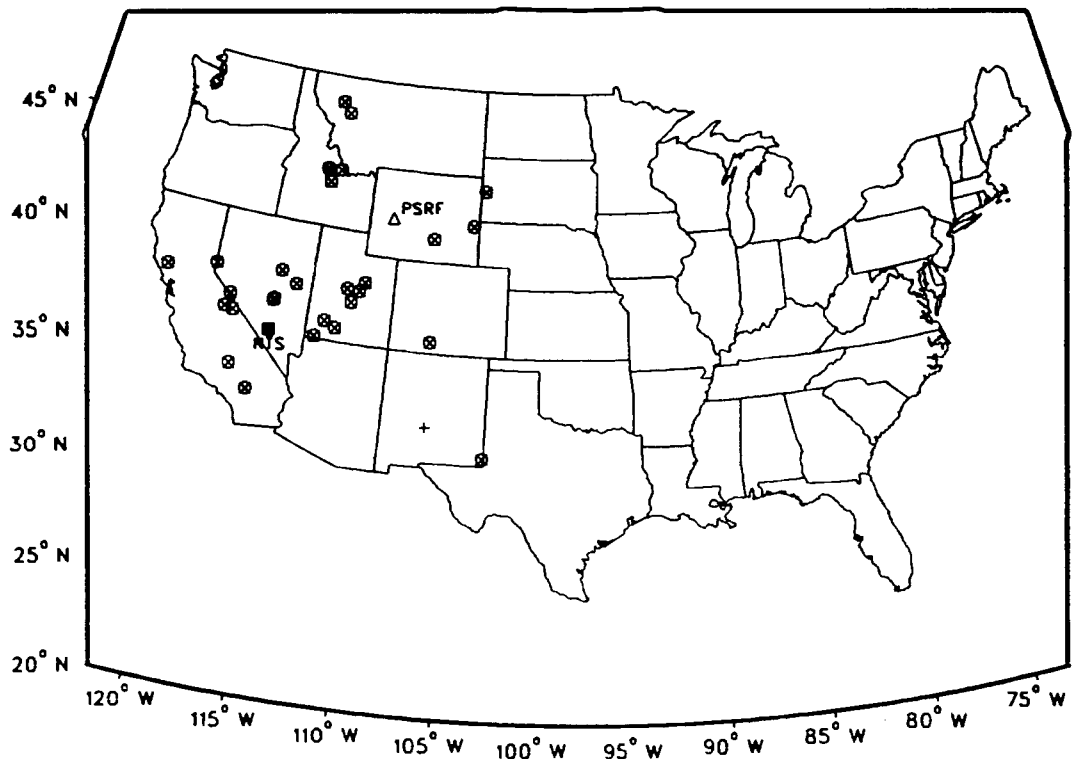


Figure 8. The first 30 seconds of the NPE and Hunter's Trophy for comparison.

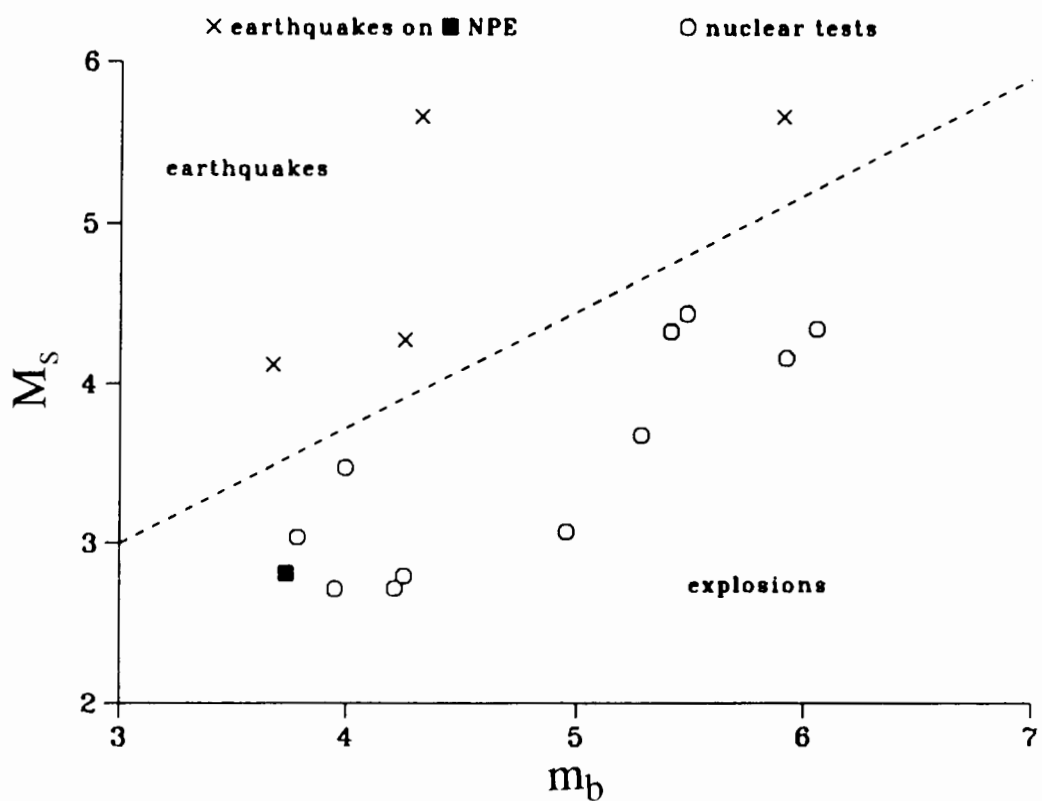


Figure 9. The discriminant m_b vs. M_s for events located on NTS.

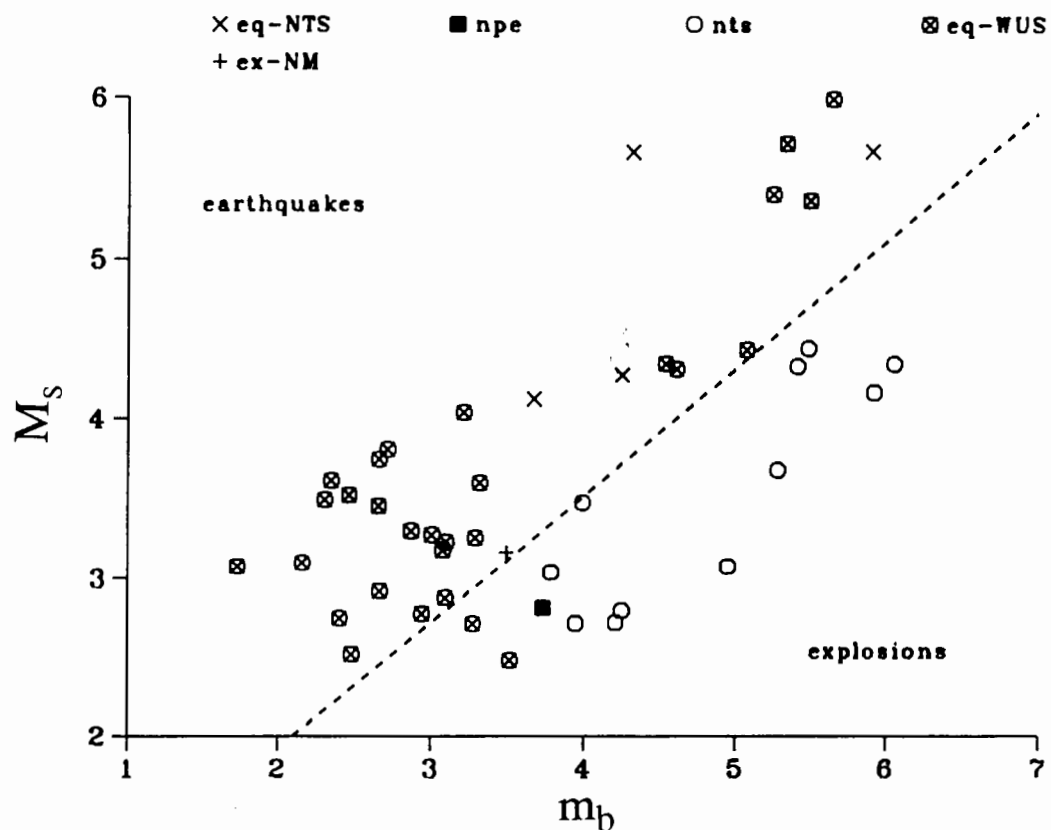


Figure 10. The discriminant m_b vs. M_s for events shown in Figure 9, plus other WUS earthquakes.

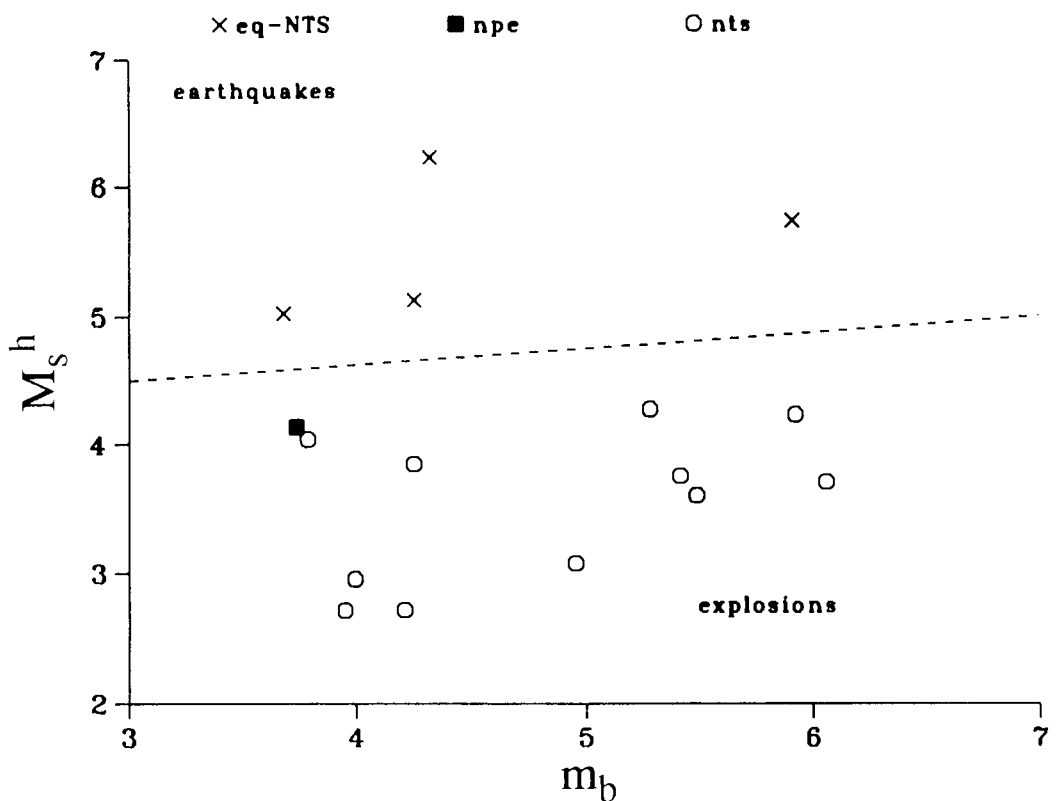


Figure 11. The discriminant m_b vs. M_s^h for events located on NTS.

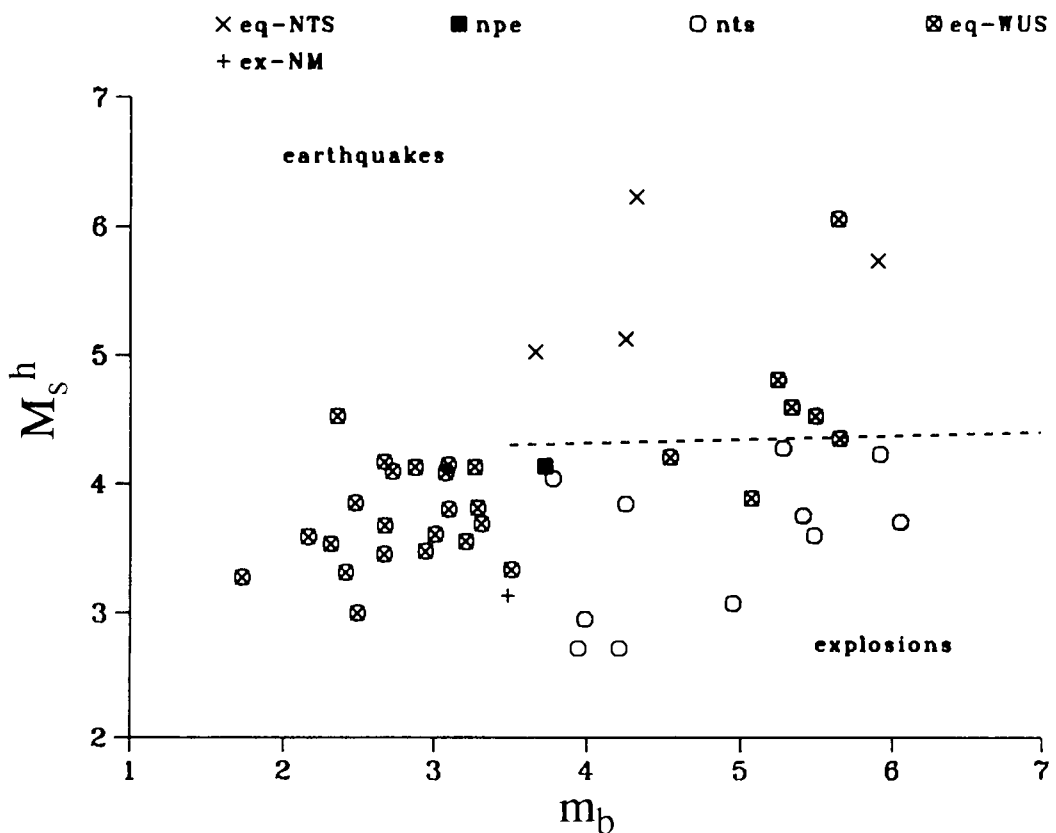


Figure 12. The discriminant m_b vs. M_s^h for events shown in Figure 11, plus other WUS earthquakes.

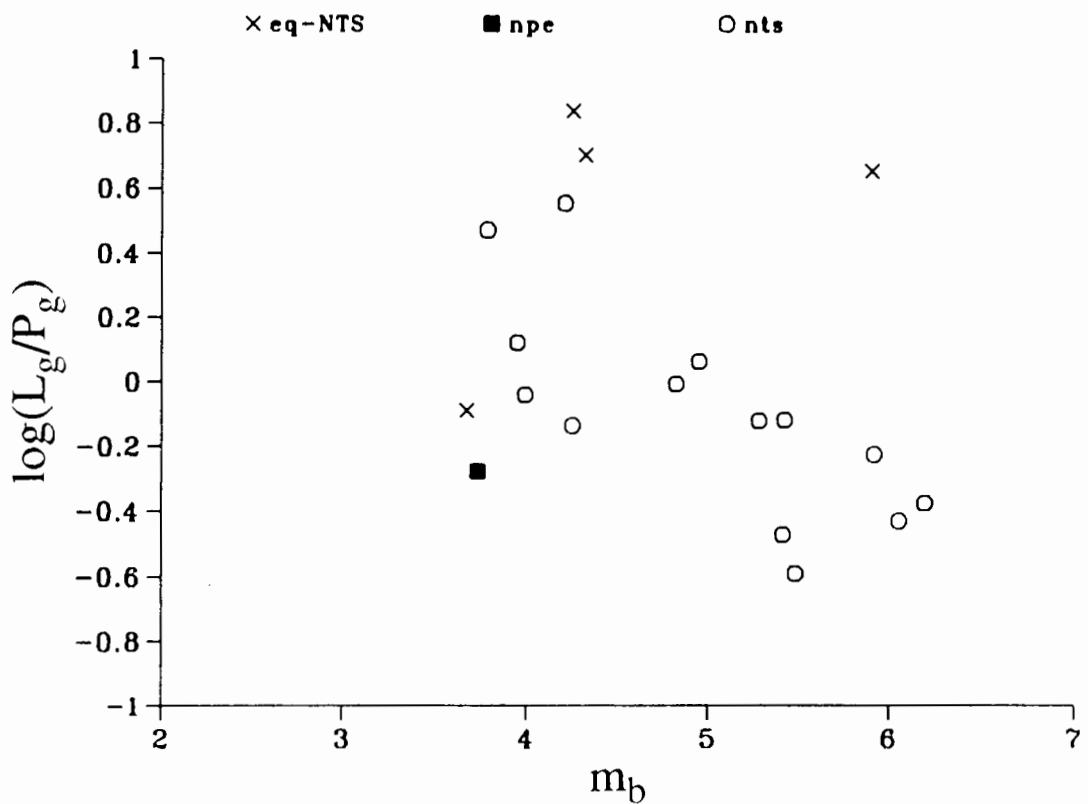


Figure 13. The discriminant m_b vs. $\log(L_g/P_g)$ for events located on NTS.

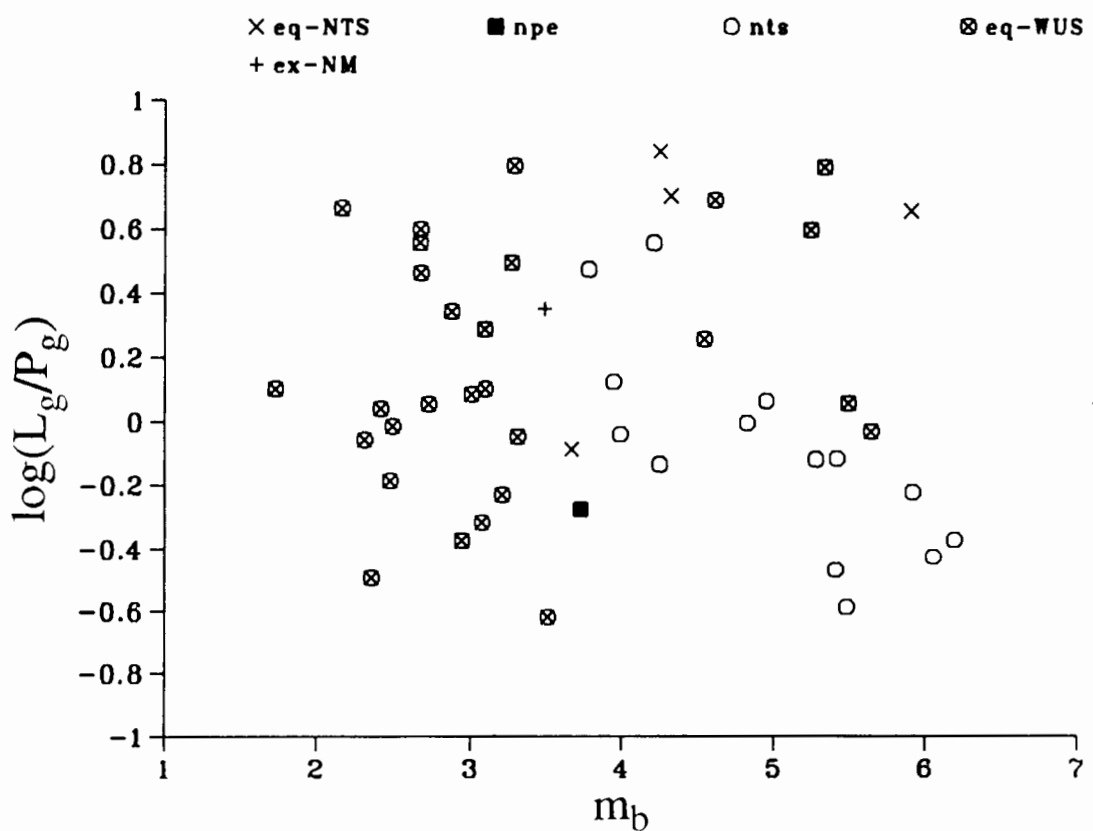


Figure 14. The discriminant m_b vs. $\log(L_g/P_g)$ for events shown in Figure 13, plus other WUS earthquakes.

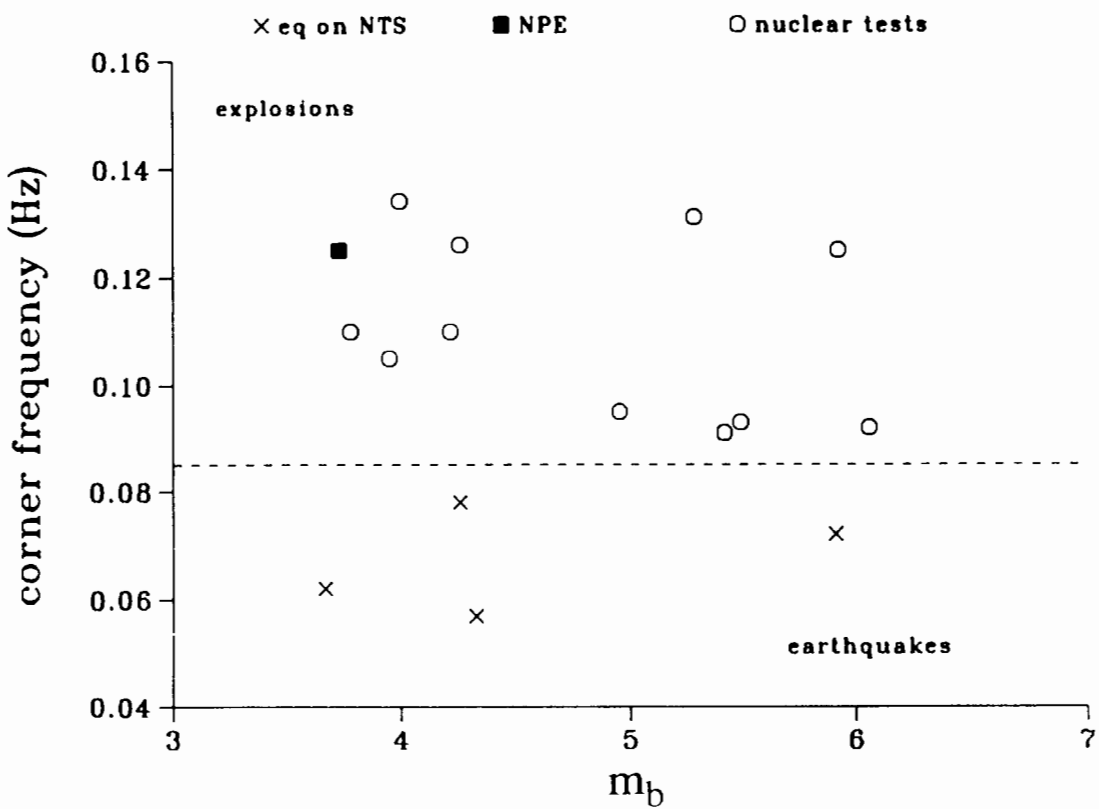


Figure 15. The discriminant m_b vs. corner frequency for events located on NTS.

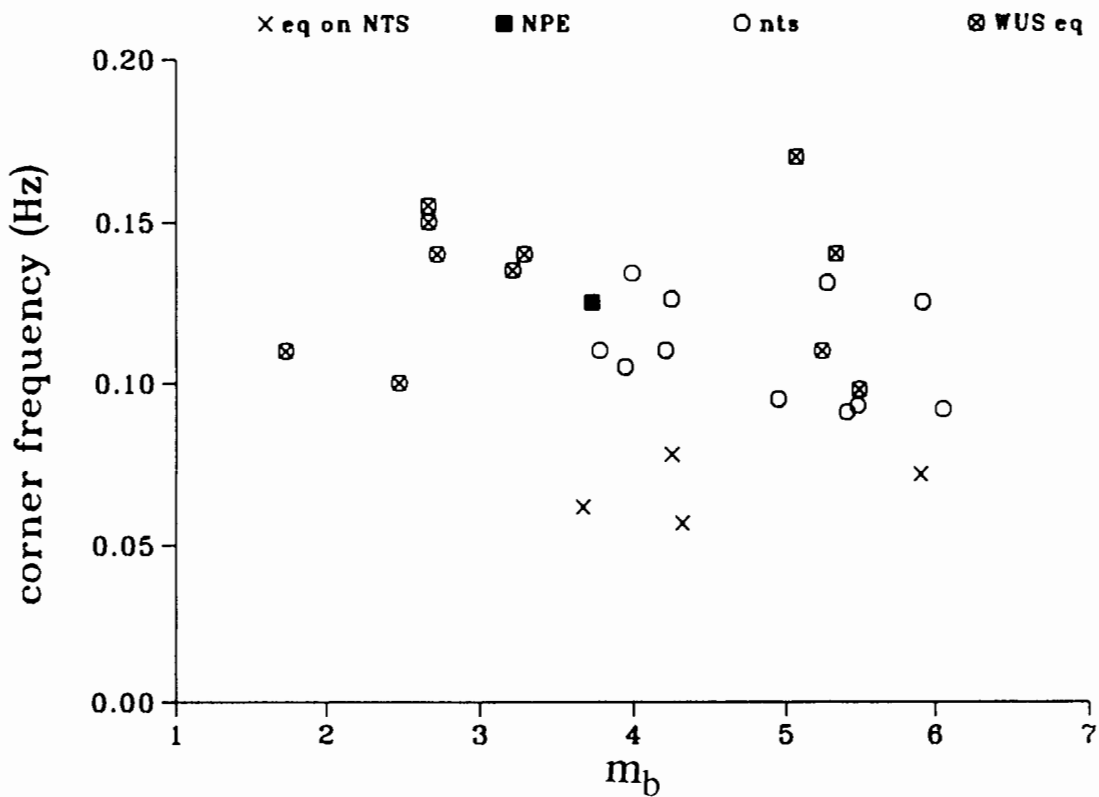


Figure 16. The discriminant m_b vs. corner frequency for events shown in Figure 15, plus other WUS earthquakes.

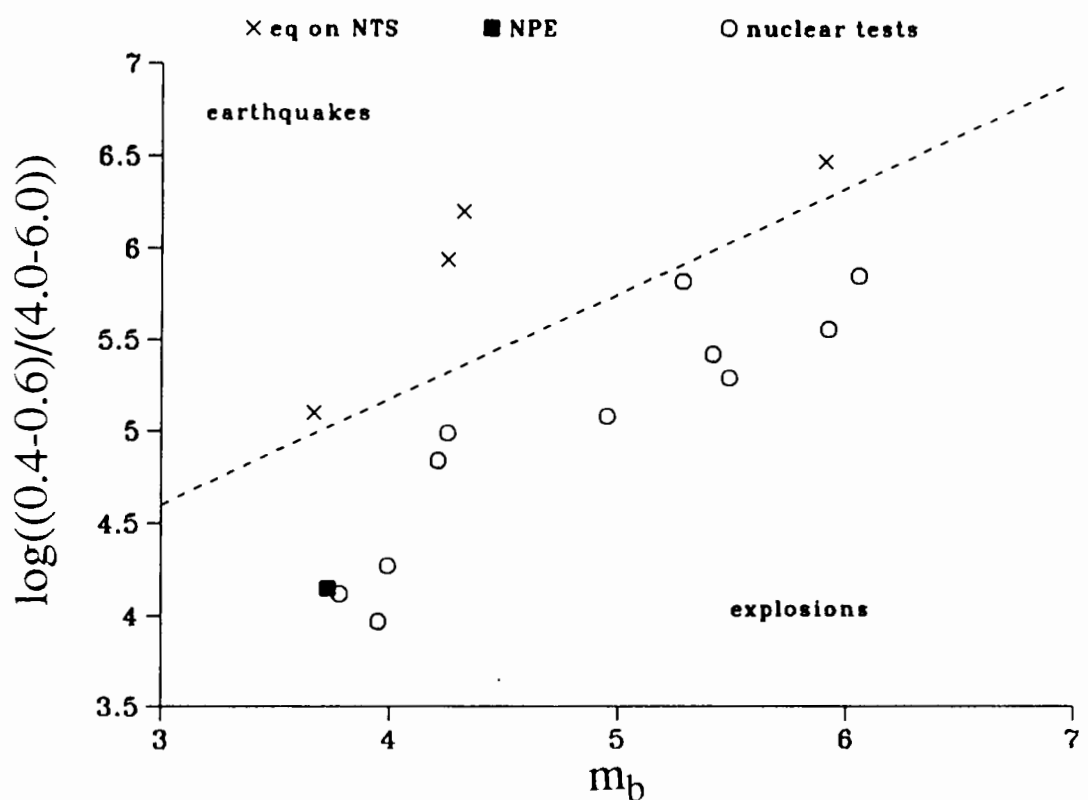


Figure 17. The discriminant m_b vs. spectral ratios for events located on NTS.

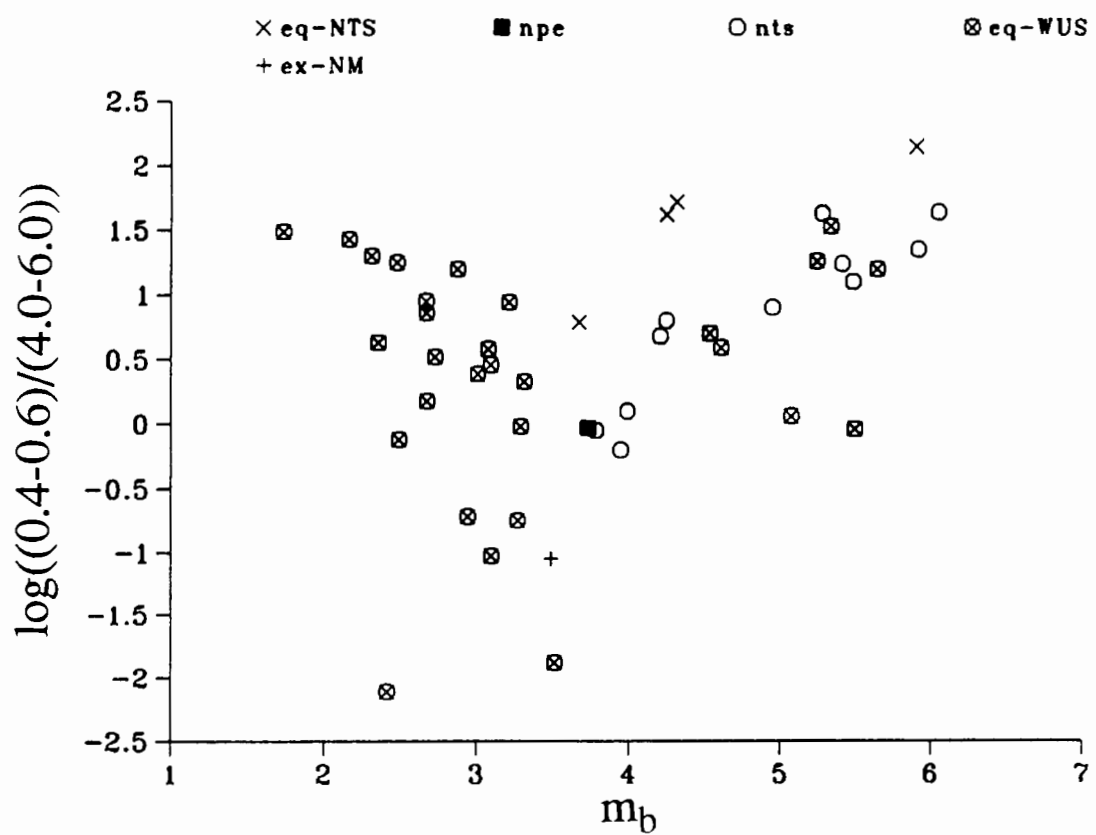


Figure 18. The discriminant m_b vs. spectral ratios for events shown in Figure 17, plus other WUS earthquakes.

Table 4: Methods used to determine the discriminants used in the study

1. m_b was calculated using the WUS magnitude formula by Evernden (1967):

$$m_b = -7.55 + 1.21 \log(A/T) + 3.06 \log(\Delta)$$

A = 0 to peak amplitude (nm) measured in the time window from the initial onset to $\Delta/6.0$ sec on HFZ

T = period (sec)

Δ = distance (km)

All the data was low-pass filtered at 4 Hz

2. M_s was calculated using the formula of Marshall and Basham (1972):

$$M_s = \log(A) + B'(\Delta) + P(T)$$

A = 0 to peak amplitude (nm) measured in the time window $\Delta/3.1$ to $\Delta/2.8 + 29.0$ sec on LPZ

B'(Δ) = distance correction

P(T) = period-dependent path correction

For approximately all events with $m_b < 4.0$, Rayleigh waves were not seen clearly on LPZ, so M_s is an upper bound of the noise.

3. M_s^h was calculated using the formula by Forsyth (1976):

$$M_s^h = \log(A) + B'(\Delta) + \log(T/T_0) + \log(7.5)$$

A = maximum amplitude (nm) measured in the time window of $\Delta/4.0$ to $\Delta/3.5$ sec on IPZ

B'(Δ) = distance correction from Marshall and Basham (1972)

T = period (sec)

$T_0 = 10$ seconds

4. The maximum peak-to-peak amplitudes of L_g and P_g were measured on HFZ after low-pass filtering at 10 Hz. The amplitude of L_g was measured in the time window $\Delta/3.8$ to $\Delta/3.0$ seconds and the amplitude of P_g was measured in the time window $\Delta/6.0$ to $\Delta/5.2$ seconds.
5. Corner frequencies were found by calculating the displacement spectrum on the IPZ band and measuring the corner frequency by eye.
6. Spectral ratios were calculated by comparing the average value of displacement using two spectral windows: 0.4-0.6 Hz on IPZ and 4.0-6.0 Hz on HFZ. Ratios were made for P_n (initial onset to $\Delta/6.0$ sec) and corrected for distance using a first-order correction.

The other WUS earthquakes have corner frequencies similar to the nuclear explosion (Figure 16). It appears that the NTS earthquakes have unusually low corner frequencies at PSRF.

Spectral ratio discriminants work best if the two frequency bands are not close together. At PSRF we are limited by the fact that the majority of events have signal going into the background noise between 7 and 10 Hz. In Figure 17 are the spectral ratios using 0.4-0.6 Hz over 4.0-6.0 Hz for all the events from NTS. There is no distance correction on this plot, since all the events are from the same area. The earthquakes and explosions separate using this discriminant and again, at this distance and test site the NPE is indistinguishable from a nuclear explosion. The WUS events are added in Figure 18 and a first order distance correction applied to the data. After adding in these earthquakes, there is no clear separation between earthquakes and explosions using spectral ratios.

Conclusion

The Non-Proliferation Experiment was recorded well at PSRF by all five systems Sandia National Laboratories was operating. The character of the seismic trace was similar to Hunter's Trophy, a nuclear explosion of similar size and location. All the regional discriminants tested with data from the DSVS/RSS3 located at PSRF worked for nuclear explosions and earthquakes located on or near NTS, except for $\log(L_g/P_g)$. In all cases, the NPE was indistinguishable from the nuclear explosions. When other WUS earthquakes are added, all the discriminants except m_b vs. M_s break down. Apparently for the other discriminants the path effects are very important.

Acknowledgments

This work was supported by the United States Department of Energy under Contract DE-ACO4-94AL85000.

References

- Evernden, J. F., (1967). Magnitude determination of regional and near-regional distances in the United States, *Bull. Seis. Soc. Am.*, **57**, 591-639.
- Forsyth, D. W., (1976). Higher mode Rayleigh waves as an aid to seismic discrimination, *Bull. Seis. Soc. Am.*, **66**, 827-841.
- Magotra, N., N. Ahmed and E. Chael, (1987). Seismic event detection and source location using single station (three-component) data, *Bull. Seis. Soc. Am.*, **77**, 958-971.
- Marshall, P. D. and P. W. Basham, (1972). Discrimination between earthquakes and underground explosions employing an improved M_s scale, *Geophys. J. R. astr. Soc.*, **28**, 431-458.
- Taylor, S. R., M. D. Denny, E. S. Vergino and R. E. Glaser, (1989). Regional discrimination between NTS explosions and western U. S. earthquakes, *Bull. Seis. Soc. Am.*, **79**, 1142-1176.

PRELIMINARY RESULTS ON THE NPE EXPERIMENT

Y. CANSI, R. CRUSEM, J.P. MASSOT, JL. PLANET AND B. MASSINON

CEA\LDG - BP12 - 91680 Bruyères-le-Châtel - FRANCE

INTRODUCTION

Answering to an invitation of the DOD, the Laboratoire de Détection et de Géophysique du Commissariat à l'Energie Atomique (CEA/LDG) participated to the seismic measurements associated with the NPE Experiment organized by the DOE at the Nevada Test Site.

Our main motivations were :

- to evaluate and compare the capabilities of detection and location of the two types of the so-called alpha stations which composed the Experimental International Seismic System (i.e. : the composite stations and the miniarrays) and this in a regional environnement,
- to calibrate these stations with a chemical blast of known energy within a given propagation structure.

STATIONS

Two composite stations and one miniarray have been set up at regional distances from the source in the Nevada state (*Figure 1*) :

- one composite station at 98 km in the NE azimuth from the source point in the vicinity of Pharanagat ; the site is on granite and the code name is HIK,
- one composite station at 104 km in the SE azimuth, in the Indian Springs region, on marble with the code name : MEE,
- a miniarray composed of 8 elements with an aperture of 1000 m, a minimum inter-element distance of 240 m, set up at a distance of 209 km from the source in the same azimuth as the MEE station, close to the LLNC station of Nelson ; the site is on sand. This miniarray has a central element, surrounded by one equilateral triangle of 400 m for each side, itself surrounded by a 4 elements square of 700 m for each side. Its coded name is NEL.

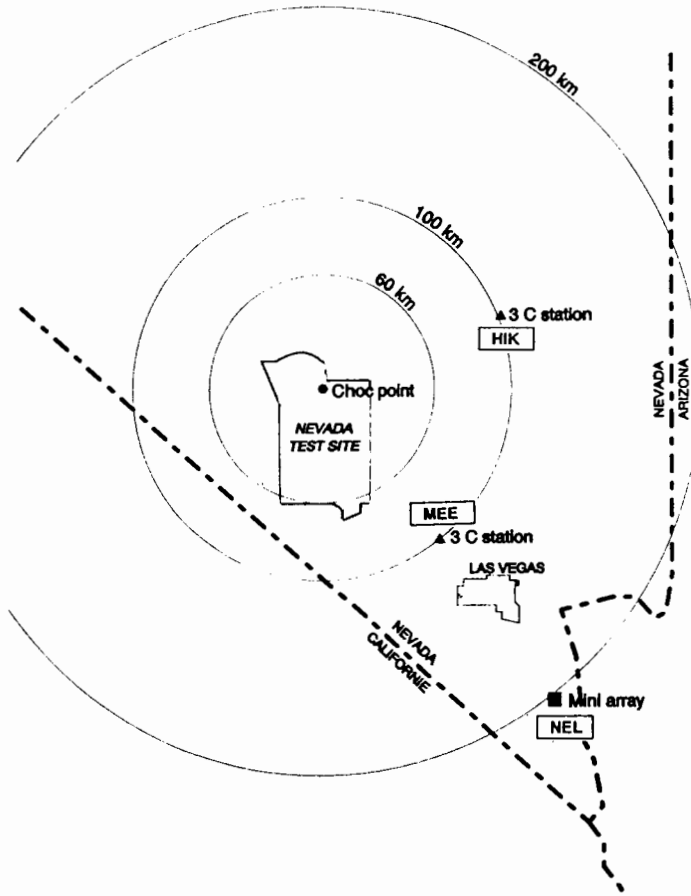


Figure 1 : Situation of the 2 composite stations and the miniarray for the NPE experiment.

Each composite station of HIK and MEE is composed of three SP seismometers measuring the ground velocity in the vertical, east-west, and north-south directions (LDG/ZM500 and LDG/HM500 seismometers).

The 8 elements of the miniarray are composed of SP seismometers measuring the vertical component of the ground velocity (LDG/ZM500 seismometers).

The data are recorded within the frequency band 0.5-60 hz at a sampling rate of 200 samples per sec and a dynamic range of 90 dB.

THE DATA

The seismic records of the NPE are clearly defined for the three sites precedently described. The data recorded by the miniarray are slightly saturated for some of the elements set up on the sand. This saturation has been corrected within an incertitude of the order of a few percents.

The seismograms of both the composite stations and the 2, 3, 4 miniarrray show up three main phases successively (*Figure 2, 3 and 4*) :

- a first arrival of weak amplitude associated with the direct compression phase or refracted phase depending on the distance,
- a reflected compression wave which gives the maximum amplitude on the vertical component,
- a shear wave with a maximum amplitude on the horizontal components.

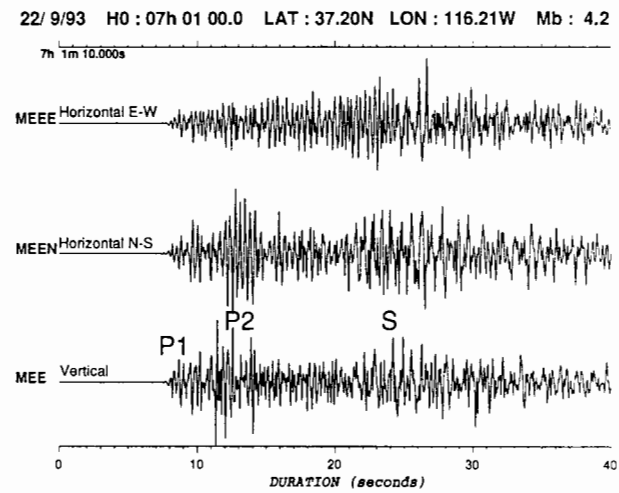
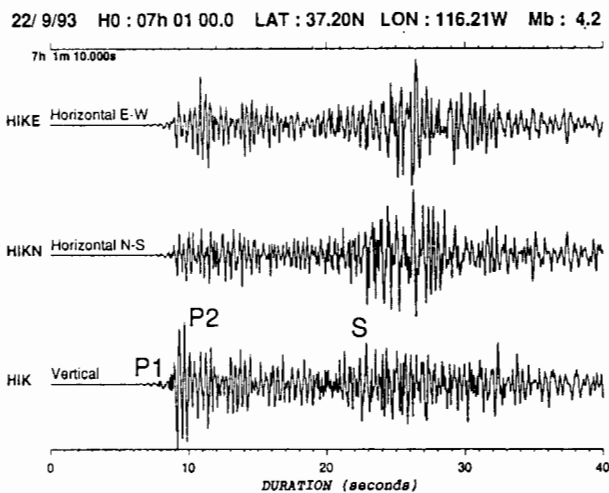


Figure 2 : Three component signals recorded at HIK.

Figure 3 : Three component signals recorded at MEE.

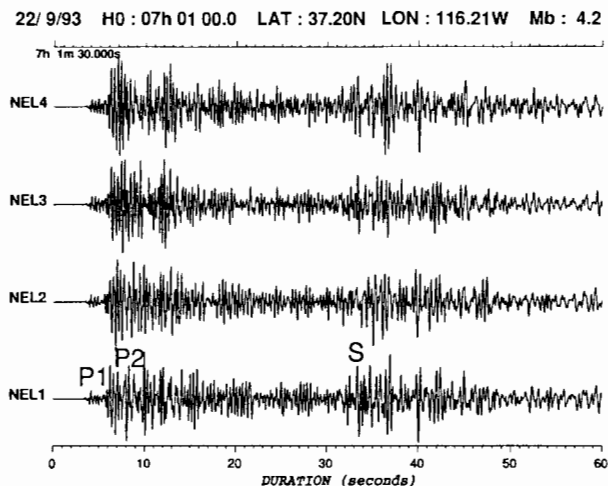


Figure 4 : Seismic signal (vertical component) recorded at 4 stations of the miniarrray.

There is no significant energy at frequencies larger than 25-30 hz for these distances (100 and 209 km) and the maxima occur between 3 and 7 hz (*Figure 5*).

The amplitudes of the vertical ground velocity are respectively for the three phases :

- HIK : 0.75 μs , 93 μs , 60 μs
- MEE : 0.78 μs , 61 μs , 39 μs
- NEL : 1.3 μs , 33 μs , 30 μs

DETECTABILITY

The detectability is a function of 2 main parameters :

- the amplitudes of the seismic waves depending on the blast energy, the distance and the propagation structure for the given wave,
- the permanent seismic noise level which depends on the site conditions.

For the NTS, the regional amplitude of the seismic waves varies with $W^{0.75}$ (Patton 1988). Considering the seismic noise figures for each station and a reasonable signal/noise ratio for an automatic detection system, it is possible to evaluate the detectability of the three stations.

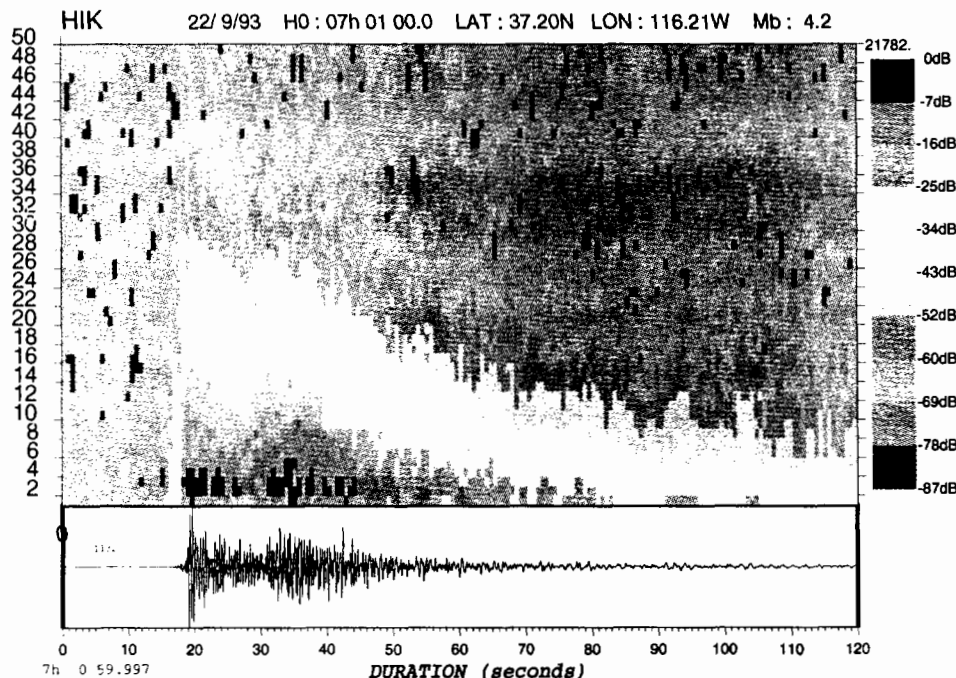


Figure 5 : Seismic signal (vertical component) recorded at NELSON with a SONOGRAM computation.

With a signal/noise ratio of 5 for the 2 composite stations and 2 for the miniarray (more sensitive by definition) we find out a detectability level respectively around 1 ton for the two stations and 5 tons in the conditions of coupling, propagation and sites of the NPE. For that estimation the equivalent nuclear energy of 2 kt has been taken for the NPE.

LOCATION

The locations obtained independently either by a composite station, or by a miniarray are evaluated here.

1. Composite stations : (*Figure 6 and 7*)

- this location is obtained manually in two steps,
- the onset times evaluation which gives the epicentral distance,
- the particle motion of the first P waves which leads to the azimuth determination.

Due to an incertitude of +/- 1 s on the S wave onset time determination, the distance incertitude is +/- 10 km at 100 km of distance.

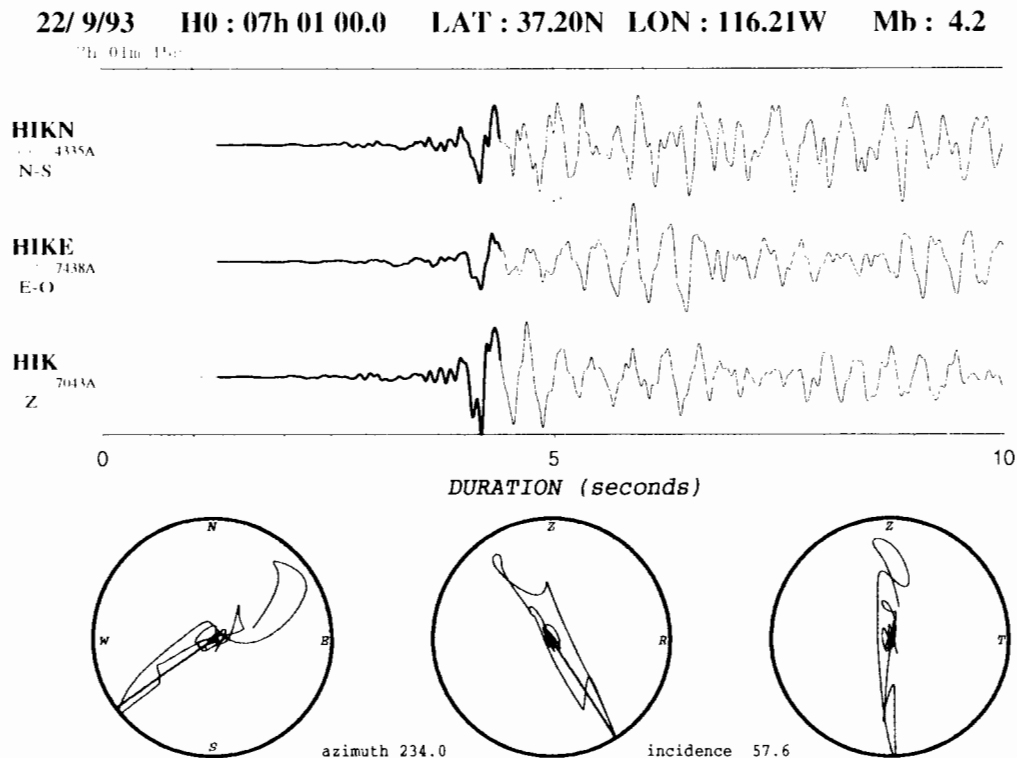


Figure 6 : On the first two seconds of signal, the particle motion gives a source azimuth of around 234° to be compared with the true azimuth of 237° .

22/9/93 H0 : 07h 01 00.0 LAT : 37.20N LON : 116.21W Mb : 4.2

T_h 0.11m 16.2

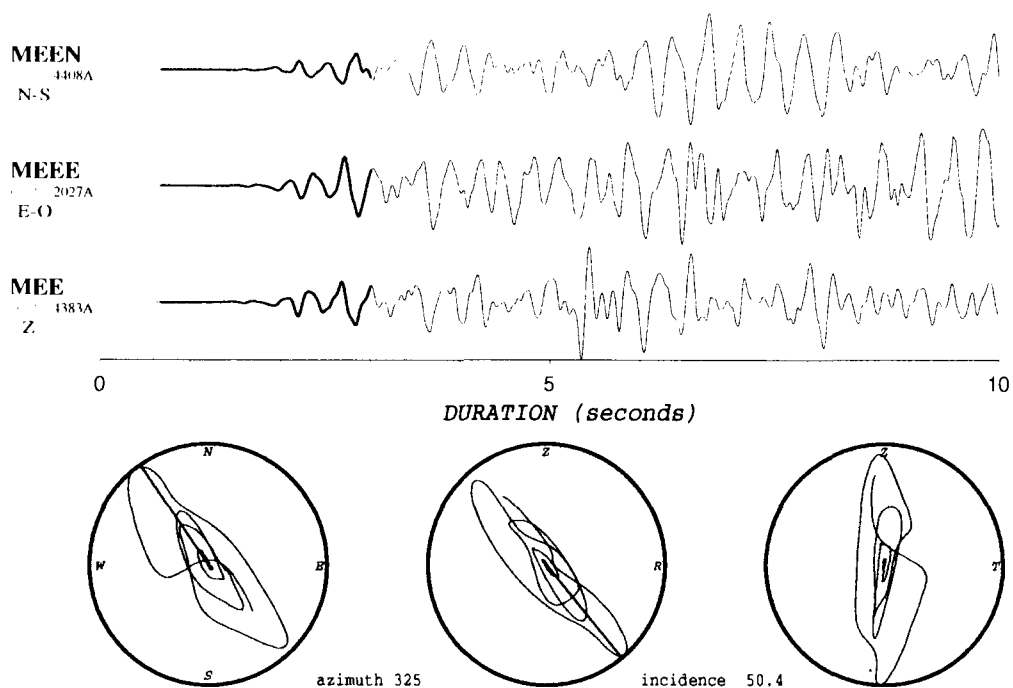


Figure 7 : Same as Figure 5. The source azimuth is found : 325° to be compared with the true one of 323° .

The source azimuth obtained on the first two seconds of the P wave signal leads to an underestimation of respectively 3 degrees (HIK) and 2 degrees (MEE).

2. Miniarrray :

The Nelson miniarrray located at 209 km from the NPE is composed of 8 SP seismographs recording the vertical component (*Figure 8*). Its theoretical response is obtained by computing the energy of each beam of an incident plane wave reaching the miniarrray vertically versus the corresponding wave number $k = f/v$, with f as the frequency, and v as the apparent velocity (*Figure 9*).

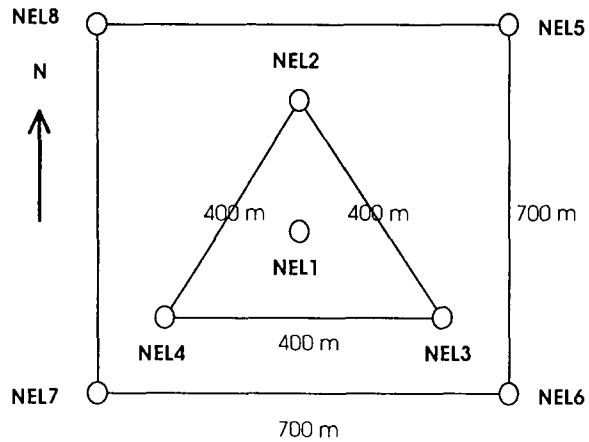
Miniarrays are able to increase the detectability of local and regional events by improving the signal/noise ratio of a single station. In addition to that, they are able to automatically locate these events by identification and association of the seismic phases which apparent velocities and azimuths are computed.

These computations are done after signal detection either by :

- the f-k method : (Capon 1969) :

in the $(0, K_x, K_y)$ plane, a plane wave is defined by a point M. The OM vector gives the azimuth, and its modulus is inversely proportional to the velocity of the plane wave.

NELSON MINI-ARRAY



NEL1: Latitude : $35^{\circ} 39' 16.0''$ N
 Longitude : $114^{\circ} 52' 37.5''$ W
 Altitude : 1140m

Figure 8 : Nelson miniarray.

- the correlation method : developed at LDG (Cansi 1993)

the time delays between onset times of the detected seismic wave reaching the elements of the miniarray are first computed by crosscorrelation , second the consistency of the results is checked and finally leads to the determination by least squares method of the apparent velocity and azimuth of the appropriate plane wave (Husebye 1969).

Two parameters characterize the miniarray in term of phase identification and association :

- the Nyquist wavenumber which is the half of the inverse of the smallest inter-elements distance ; it determines the largest wavenumber properly seen by the miniarray without any aliasing and is equal hereto 2.16 km^{-1} ,
- the radius of the - 1 dB contour of the miniarray response which is inversely proportional to the maximum aperture ; it defines the accuracy with which both the azimuth and the apparent velocity of the incident wave are evaluated. The corresponding f/V is here of the order of 0.4 km^{-1} (*Figure 9*).

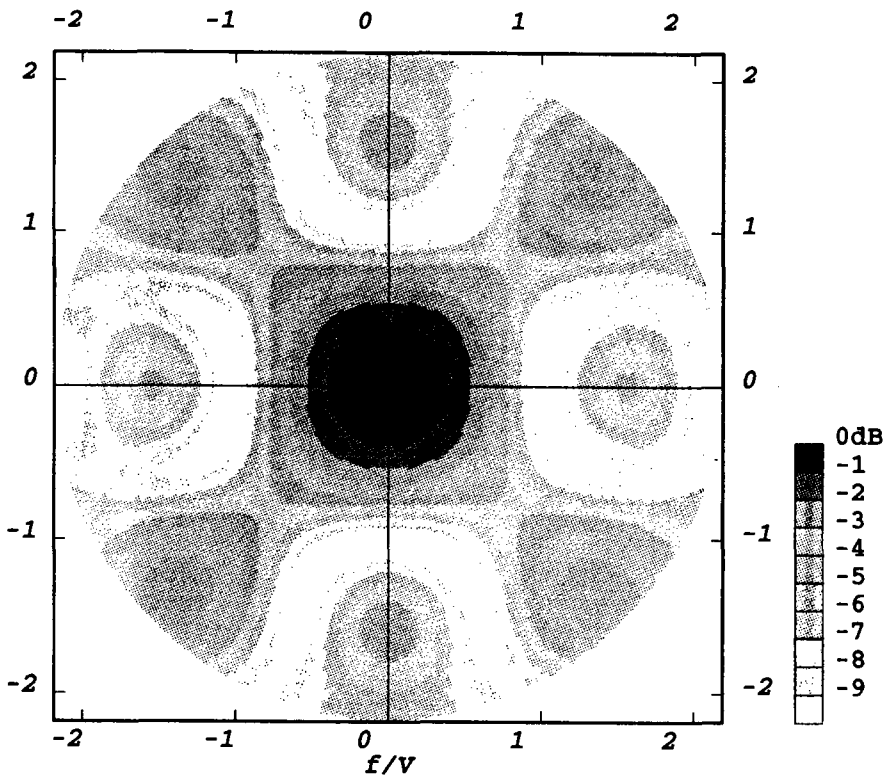


Figure 9 : Beam Forming Pattern for the Nelson miniarray.

The Nelson miniarray was in fact designed to have an optimum response for a wavenumber value of about 1 to 1.5 km^{-1} which corresponds to velocity of 6 to 8 km/s and a frequency of 8 Hz in the case of a regional P wave.

Despite a slight signal saturation already mentionned, two wave trains, one P wave train followed by an S wave train are clearly identified with dominant frequencies of 3 to 5 Hz and 2 to 3 Hz respectively. These frequencies are about 50 % smaller than the forecasted frequencies. Then the aperture of the miniarray happens to be too small for the real signals. Consequently azimuths and velocities evaluations are not optimized.

Furthermore the crustal model (*Figure 10*) for this particular epicentral distance (209 km) clearly shows an interference phenomena of several direct and refracted waves at the head of both P and S waves.

3. Results :

The whole seismic wave train has been analysed by using the two methods previously described with different time windows and frequency bands. The best results obtained by the two methods are very similar.

CRUSTAL MODEL

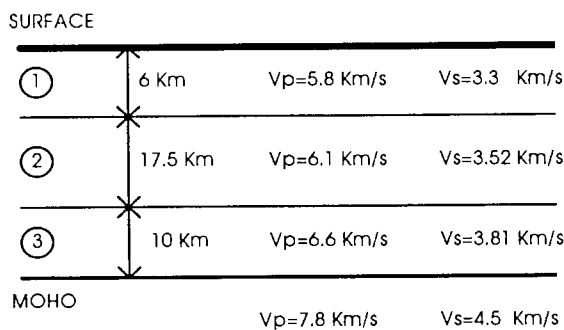


Figure 10 : Crustal model.

We have represented the f-k results on *Figure 11 and 12*:

- P phase :

Within the wave train, three arrivals P1, P2, P3 could be identified. P1 is composed of refracted waves and direct waves. P2 consists in subcritical refracted waves. Velocities are decreasing from 8.5 (P1) to 6.5 km/s (P2) approximately with a source azimuth decreasing from 360° (P1) to 315° (P2) to be compared to 326° (true azimuth). The P coda (P3) has much more instable features with no consistent velocities determinations and a correct mean azimuth but associated with large deviations.

- S waves :

S waves are hardly coherent at the scale of the miniarray as shown by the correlation method (*Figure 13*) and the computed velocities are always too weak (between 1.5 and 3 km/s) to be compatible with real S waves velocities. The azimuths are underestimated by more than 10 degrees.

As a result the automated location determination of the NPE would not have been possible by the Nelson miniarray only. Nevertheless a location by the identification of P1, P2 and S arrivals by the analyst lead to the following results :

Theoretical azimuth	Estimated azimuth	theoretical distance	estimated distance	error
326°	335°	209 km	209 km	33 km

The complexity of the seismic waveforms recorded at the Nelson miniarray has probably several origins : critical epicentral distance, propagation effects and site effects. The necessity of a preliminary calibration of both the region and site is clearly demonstrated here.

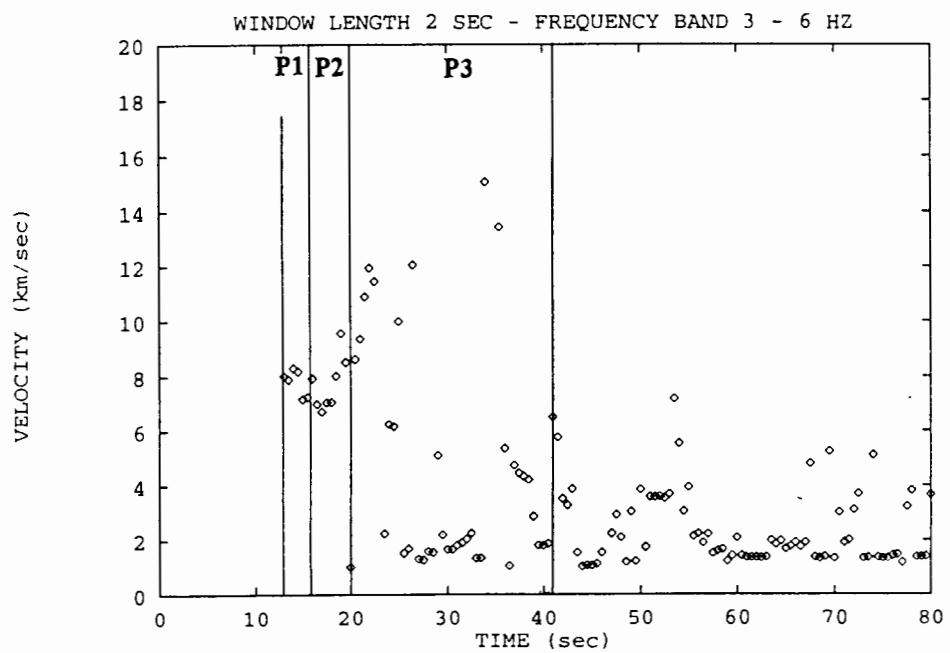
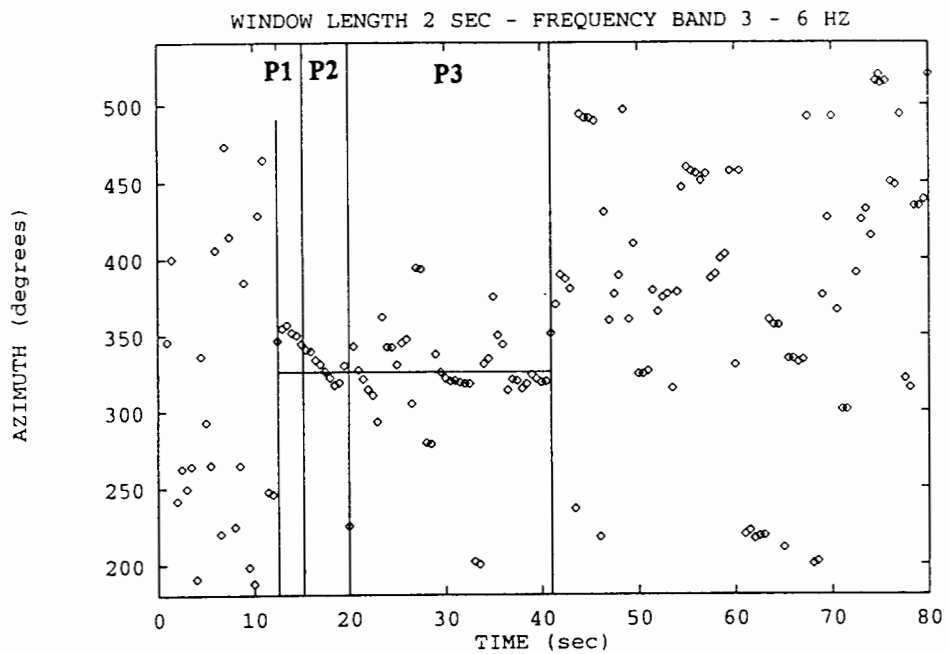


Figure 11 : f-k results for P-phase.

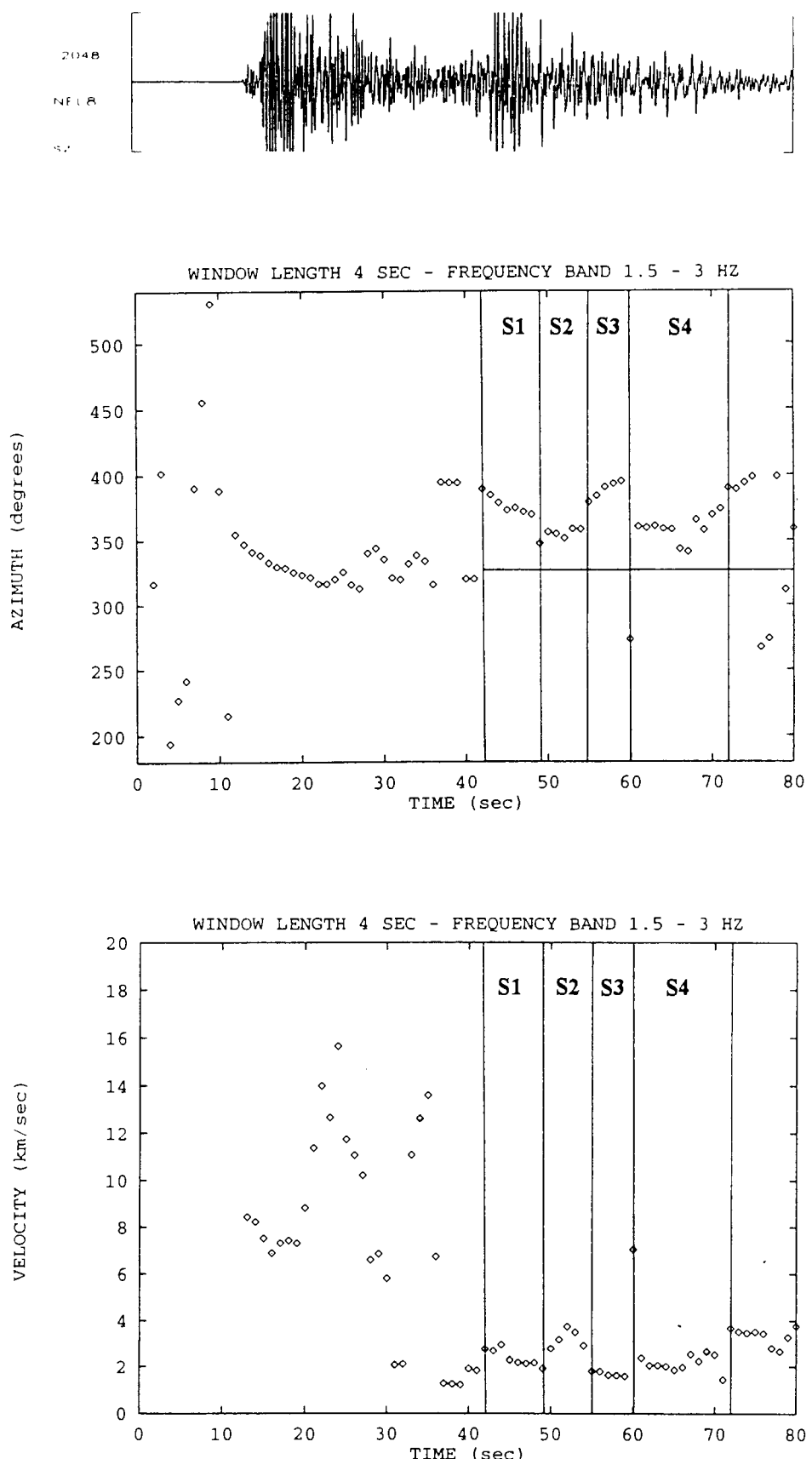


Figure 12 : f-k results for S-phase.

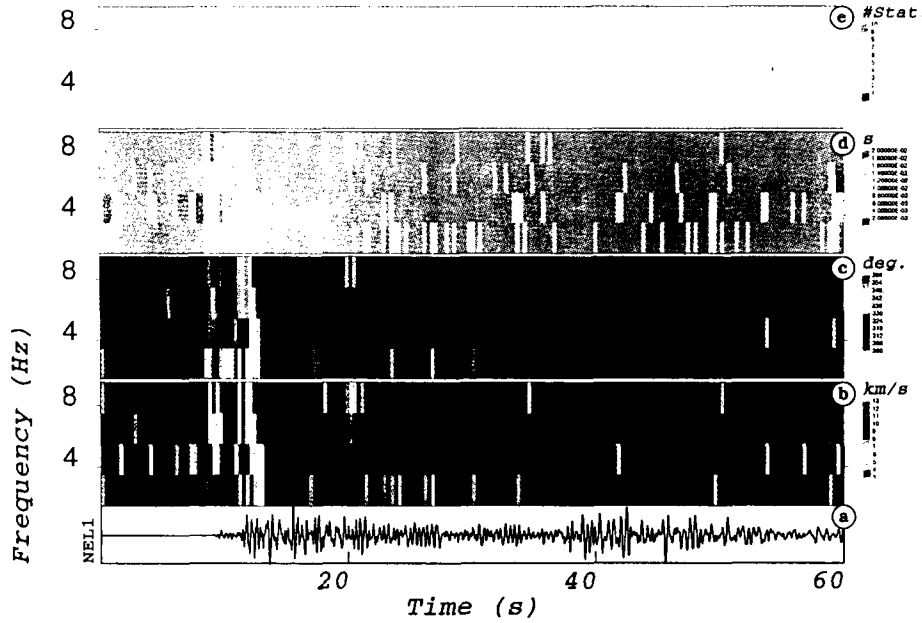


Figure 13 : Results obtained by the correlation method. Velocity, azimuth, consistency and number of stations used are displayed on the b, c, d and e plots as a function of frequency and time. Velocity and azimuth are plotted only for consistency lower than 0.01s.

CONCLUSION

Implemented in less than ten days by a four technician team in the Nevada state at regional distances from the Rainier Mesa, the three LDG seismic stations have recorded high quality signals generated by the NPE.

Their processing has pointed out several conclusions to take into account in the evaluation of a global seismic monitoring network.

The two composite stations give an estimate of the blast azimuth with less than 4 degrees of error and the miniarray overestimates the azimuth by 11 degrees. This last value is probably associated with the heterogeneity of the crust within the NTS region. Consequently, it seems important to calibrate the propagation paths before any estimation.

Concerning the miniarray, it appeared that the frequency content of the recorded waves was lower than the expected one and so that the aperture could have been increased for the benefit of a better location result.

REFERENCES :

Patton, H.J., Application of Nuttli's Method to Estimate Yield of Nevada Test Site Explosions Recorded on Lawrence Livermore National Laboratory's Digital Seismic System, Bull. Seis. Soc. Am., 5, 1759-1772, 1988.

Capon, J., High-resolution frequency-wave number spectrum analysis., Proc. IEEE, 57, 8, 1969.

Husebye, E.S., Direct measurement of dT/dD, Bull. Seis. Soc. Am., 59, 717-727, 1969.

Cansi, Y., Plantet, J.L. and Massinon, B., Earthquake location applied to a miniarray : K-Spectrum versus Correlation Method, Geophysical Research Letters, Vol.20, n° 17, 1819-1822, September 3, 1993.

Acknowledgments

The authors are grateful to Dr R. Alewine who kindly invited the LDG to participate to the seismic measurements associated with the NPE. They are also thankful to the University of Texas, the E.G and G, and the LLNL for providing their help during the experiment.

DISTANCE EFFECTS ON REGIONAL DISCRIMINANTS ALONG A SEISMIC PROFILE IN NORTHWEST NEVADA; NPE AND NUCLEAR RESULTS

David A. McCormack, AWE Blacknest, Brimpton, Berkshire RG7 4RS, UK

Keith F. Priestley, University of Cambridge, Cambridge, UK

Howard J. Patton, Lawrence Livermore National Laboratory, Livermore, CA

ABSTRACT

To address questions of discriminant transportability, it is important to understand how discriminants based on regional seismic phases are affected by regional variations in velocity structure. To examine this issue, we have recorded two explosions, the nuclear explosion Kinibito and the Non-Proliferation Experiment along a 300 km-long profile through western Nevada. We use these data to investigate the stability with distance of several proposed seismic discriminants. In this study we first estimate the apparent attenuation of the regional phases. The frequency dependent attenuation for P_g and L_g is found to be described by the relations $Q_{P_g} = (181 \pm 6)f^{0.59 \pm 0.02}$, $Q_{L_g}(\text{vertical}) = (217 \pm 6)f^{0.71 \pm 0.01}$, and $Q_{L_g}(\text{tangential}) = (180 \pm 10)f^{0.65 \pm 0.02}$. The amplitude decay for P_n is proportional to $\Delta^{-[1.84(\pm 0.20) + 0.48(\pm 0.04)f]}$ between 2 and 8 Hz. Since the geometrical spreading factor for a head wave is -2.2, this last relationship implies that the mantle lid is either high Q, has a positive velocity gradient with increasing depth, or both. We compare attenuation corrected amplitude ratios for P_n/L_g and P_g/L_g , and spectral ratios for P_n , P_g , and L_g , as a function of distance along the profile. We make these comparisons for the vertical component and for the total vector resultant using all three components of motion. The results show that the vector resultant reduces inter-station variability, especially in the P_n measurements. Also, the P_n spectral ratios (1-2 Hz)/(6-8 Hz) are brought into better agreement with the ratios for other phases when the vector resultant is used. The spectral ratios for L_g and P_g are reasonably stable along the profile, as are the amplitude ratios for P_g / L_g . The P_n / L_g ratios are similar to the P_g / L_g ratios for the 6-8 Hz band, but they are smaller in the 1-2 Hz band. These differences at low frequencies are made greater by attenuation corrections to the P_n amplitude. While these results may suggest that the source function is larger in the low frequency band for P_g and L_g waves than it is for P_n , more work is needed to understand the geometrical spreading and anelastic decay of P_n waves over this profile.

Introduction

Seismic measurements for monitoring compliance with nuclear testing treaties have traditionally relied upon a comparison of the short period (SP) teleseismic body wave magnitude m_b and the long period (LP) surface wave magnitude M_s . This discriminant has proven viable for events greater than

about m_b 4.5, and the physical basis for this discriminant is reasonably well understood (Douglas et al., 1971; Hudson and Douglas, 1975; Stevens and Day, 1985). To discriminate smaller earthquakes from explosions, which will be important for a Comprehensive Test Ban Treaty (CTBT), regional-distance observations must be used. There are many challenges posed by the use of regional seismograms for seismic discrimination. Among these are that (1) suitable measures of SP and LP energy must be found for regional observations since conventional m_b and M_s are defined for teleseismic data, and (2) once these measures are chosen, the regional dependences of these measures must be understood in order to assess the transportability of the discriminant from one geological region to another. Transportability is a problem because seismograms recorded at regional distances are complex, and it is not clear *a priori* how much of the observed complexity results from source differences and how much results from the effects of variation in the regional velocity structure. As a result, the utility of a discriminant in one region does not guarantee applicability in another region.

Various regional seismic discriminants have been proposed (Pomeroy et al., 1982), most of which involve amplitude comparison between phases. Regional phases are strongly affected by the propagation waveguide, and as pointed out by Kennett (1993) regional phases each have a different interaction with the crust and upper mantle velocity structure and these differences can impose their own amplitude pattern on the source amplitude pattern. Even for discriminants based on the spectral ratio of a single phase, the velocity and attenuation structure can influence the spectral fall-off. Therefore, before a proposed regional discriminant can truly be considered applicable, it is crucial to understand the influence of the propagation effects.

In this study we analyze two sets of seismograms which were recorded along a profile through western Nevada for two explosions at the Nevada Test Site (NTS): the nuclear explosion Kinibito which occurred on December 5, 1985, and the Nonproliferation Experiment (NPE), a chemical explosion which occurred on September 21, 1993. The objectives of these recordings are (1) to investigate the development of the regional phases P_n , P_g , and L_g , (2) to measure the frequency dependent attenuation of the regional phases, and (3) to investigate the stability of various proposed regional discriminants with distance. We feel that this is possible with these data because the crust and upper mantle velocity structure in the vicinity of this profile has been intensively studied; hence, propagation effects are reasonably well understood. In this report we discuss the data and make some preliminary comments on our progress towards these objectives. We first use these data to measure the apparent attenuation of the regional phases P_g and L_g . Measuring P_n attenuation is more problematic because it is not clear yet how the amplitude decay of this phase is affected by geometrical spreading. Using the preliminary attenuation measurements, we examine the stability of two proposed regional discriminants as a function of distance: (1) amplitude ratios between the P phases and the L_g phase, and (2) spectral ratios for the P_n , P_g , and L_g phases.

Field Recordings and Data

The 1985 Kinibito recordings were previously discussed by Chavez and Priestley (1986). Recordings for the Kinibito explosion were made at ten temporary sites along a profile extending northwest from NTS and covering the distance range 200 to 500 km (Fig. 1). All sites were located on or very near bedrock and consisted of concrete pads located either in mine tunnels or in 1 meter deep, buried vaults. In this manner we were assured of good coupling, stable temperatures, and minimal ground noise compared to shallow surface sites. The average station spacing is 22 km. All but one of the sites were instrumented with Kinemetrics PDR-2 digital event recorders and SV-1/SV-1 intermediate period vertical and horizontal seismometers. One site had a Geotech S-13 SP vertical component seismometer. In the data logger the data were passed through a low-pass, 2-pole Butterworth filter with a corner at 6.25 Hz and then digitized at a rate of 25 samples/second.

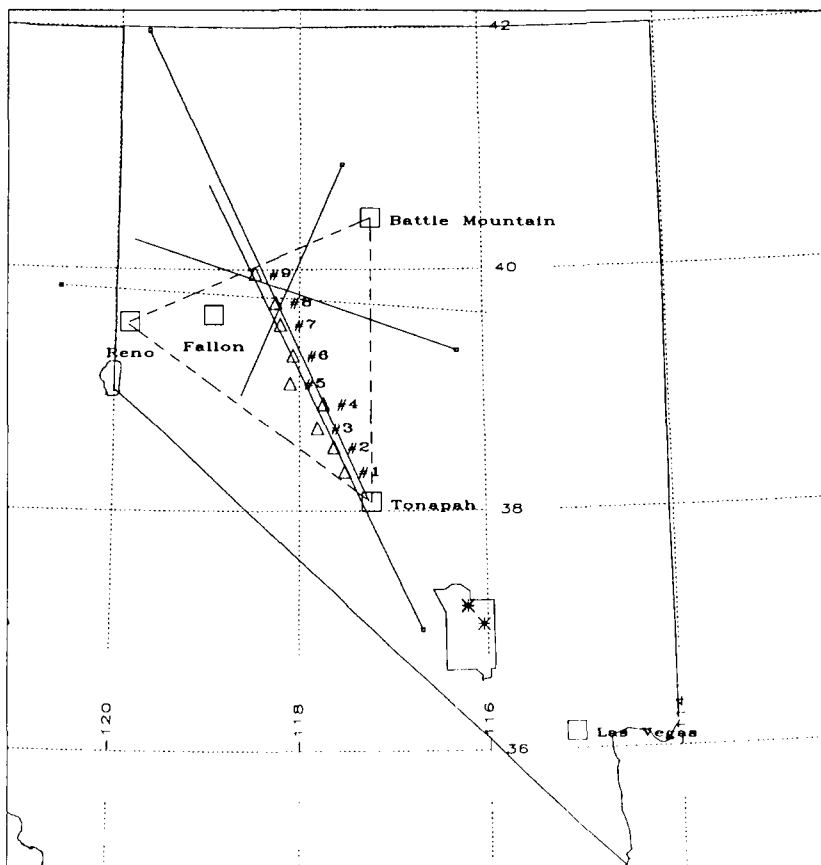


Figure 1. Map showing the locations of the seismograph sites which recorded the Kinibito and NPE explosions. Instruments were installed at all sites for the Kinibito explosion and sites 1 - 9 for the NPE explosion. The solid lines denote locations of other seismic data recorded in the region of the profile: refraction data (solid lines), reflection data (dotted lines), and surface wave data (dashed lines).

The 1993 NPE was recorded at nine sites along the same profile as the Kinibito recordings. The southern six instruments were located at the same mine tunnel sites (seismometer on the same concrete pier) as the Kinibito instruments; the northern three instruments were at vault sites within approximately 100 m of the surface sites used to record the Kinibito explosion. The instrumentation used to record the NPE explosion consisted of either Kinematic SV1/SH1 intermediate period seismometers or Guralp CMG-3ESP seismometers, and Geotech PDAS-1 digital data loggers. The data were digitized at 100 samples/second.

The crust and upper mantle structure in the vicinity of this profile has been the subject of a number of studies. Priestley and Brune (1978) and Priestley et al. (1980) examined fundamental and higher mode surface wave propagation between LP seismograph stations located at Reno and Tonopah. Priestley et al. (1982) examined P_n delays from NTS explosions along a profile coincident with the Kinibito/NPE profile. Hauge et al. (1987), Benz et al. (1990), Hawman et al. (1990), Holbrook (1990), Catchings and Mooney (1991), and Zelt and Smith (1992) interpreted the crust and uppermost mantle structure along the northern end of the profile using forward modeling and inversion of seismic refraction, wide angle reflection, near vertical reflection and gravity data. Priestley (unpublished results) has analyzed seismic data along a nearly coincident refraction profile. The locations of these profiles are shown in Figure 1. All these data suggest that the crustal thickness along the Kinibito/NPE profile is of near uniform thickness (31 ± 2 km). The crustal velocity profile can be summarized as varying between 3.5 to 5.2 km/s in the upper 2.5 km, between 6.0 and 6.3 km/s between 2.5 and 20 km depth, and between 6.5 and 7.0 km/s between 20 and 31 km depth. The P_n velocity along the profile is 7.85 ± 0.05 km/s. The surface wave results for this region suggest that there is a mantle lid approximately 30 km thick overlying a substantial upper mantle low velocity zone. The velocity gradient in the mantle lid is not well resolved.

Figure 2 is a record section of the vertical component profile recordings of the NPE explosion, and Figure 3 and 4 are the corresponding radial and tangential component record sections. Figure 5 is a record section composed of the vertical component seismograms from both the Kinibito and NPE explosions. Figure 6 is an enlargement of the first few seconds of the first arrival from Figure 5. All record sections are trace normalized. The times in Figures 2 – 5 are reduced by 7.8 km/sec; the time in Figure 6 has been adjusted so as to line up the first arrival. These plots will be discussed together.

Three phases are prominent in the record sections: P_n , P_g , and L_g . All of the recording ranges are greater than the P_g/P_n crossover range so P_n is the first arrival at all distances along the profile. The largest amplitude phase at all distances on the vertical component is P_g ; L_g is the largest amplitude phase at all distances on the tangential component. The P_n and P_g phase shows a general decay in amplitude with distance, however there are anomalous sites such as site 5 where the P wave amplitude is enhanced compared to nearby sites. This is most pronounced for P_n . This

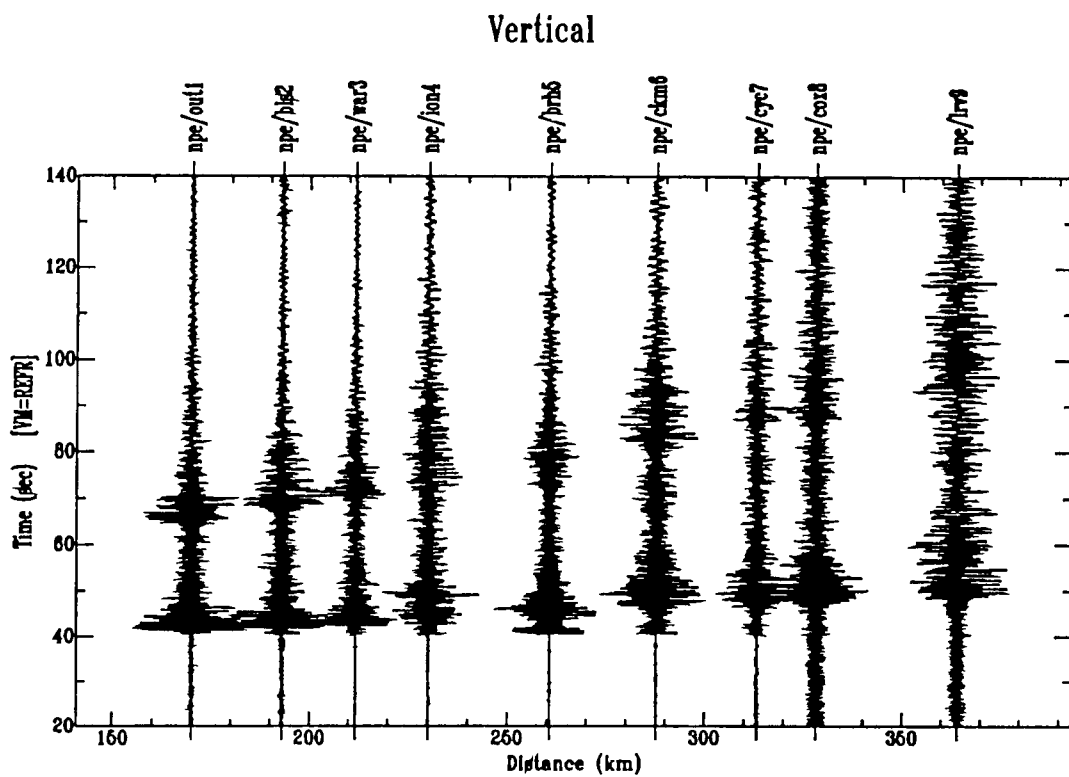


Figure 2. Vertical component seismograms for the NPE explosion recorded along the profile through northwest Nevada. All seismograms are trace normalized and time is reduced by $\Delta/7.8$ seconds.

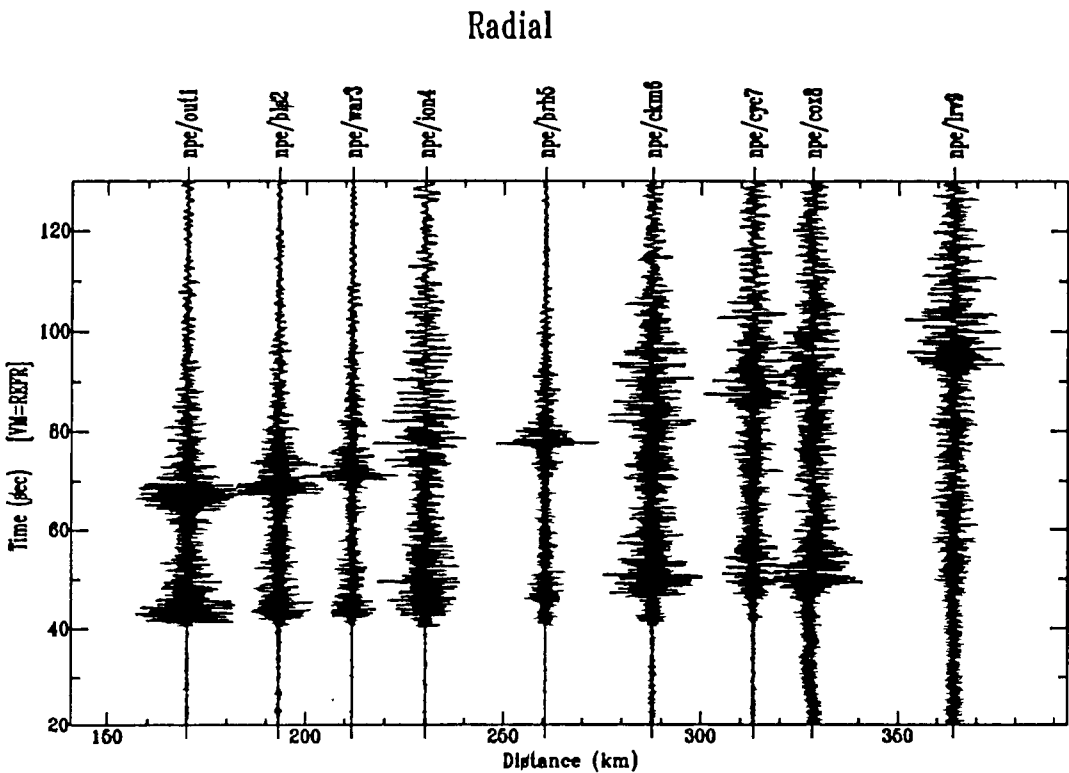


Figure 3. Radial component seismograms for the NPE experiment. Same format as Figure 2.

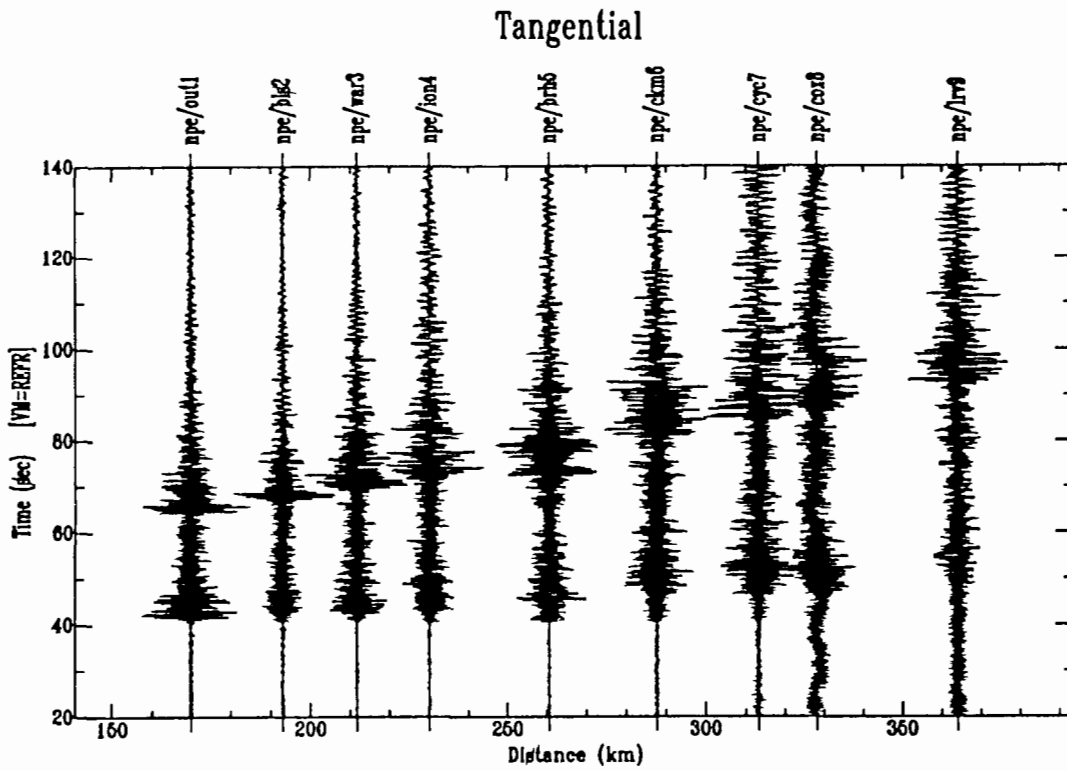


Figure 4. Tangential component seismograms for the NPE experiment. Same format as Figure 2.

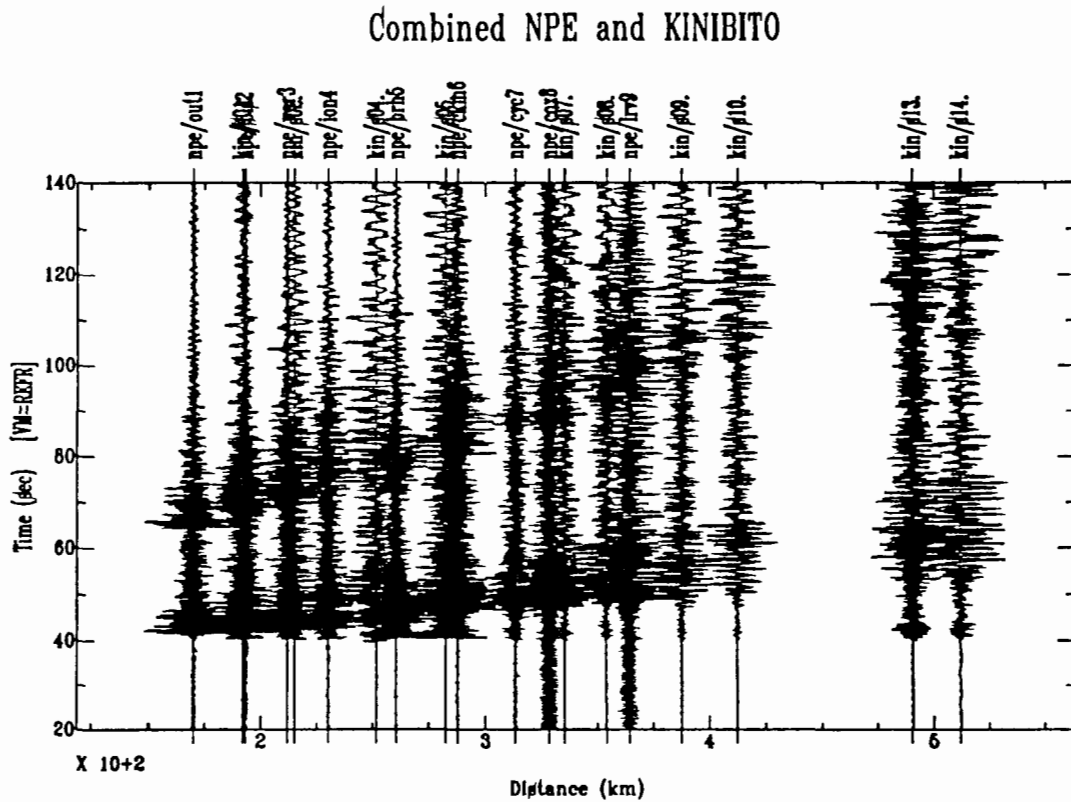


Figure 5. Vertical component seismograms for the Kinibito nuclear explosion and for the NPE experiment. Same format as Figure 2.

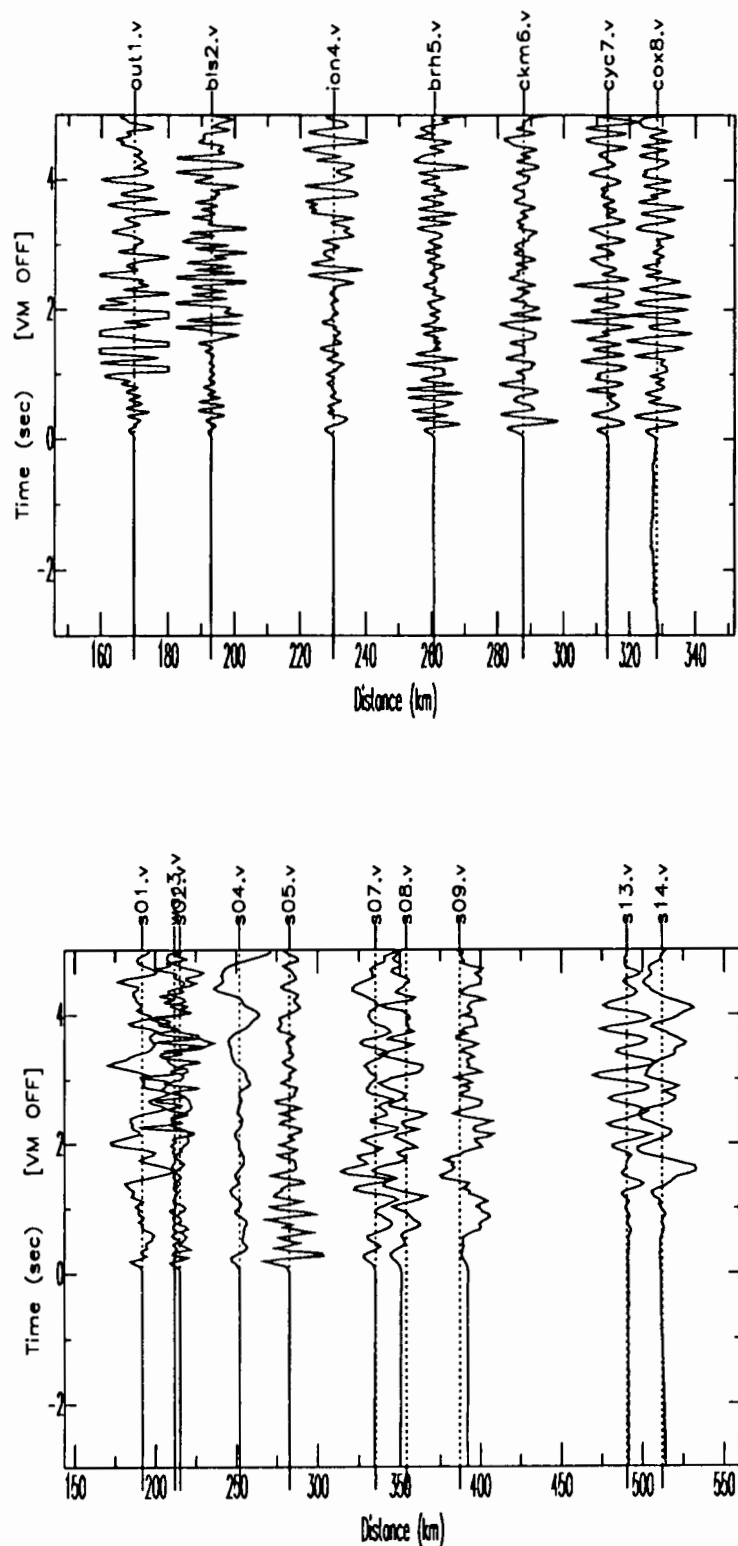


Figure 6. Enlargement of the first arrivals from Figure 5. Times have been shifted to align the first arrival: (a) Kinibito, (b) NPE.

enhancement is a recording site effect and not an instrumental effect since it was observed for both the Kinibito and NPE explosions.

The characteristics of the first arrival are more clearly seen in Figure 6. P_n is a high frequency phase to about 300 – 350 km distance. Over a short range (≈ 25 km) the high frequencies are lost and the first arrival becomes a low frequency, low amplitude arrival. This characteristic for P_n was previously noted by Priestley et al. (1982). At distances greater than about 350 km the first arrival is closely followed by a larger amplitude, dilatational arrival. Priestley et al (1982) suggested that this arrival may correspond to energy reflected from the base of the mantle lid.

P_g is a second arrival at all distance ranges; at the nearest ranges P_g is a more distinct phase. With increasing distance P_g becomes more protracted and is composed of several arrivals. At the largest ranges “ P_g ” consists of arrivals extending over 20 seconds. This change in character probably results from a change in the mode of propagation for P_g . At near distance ranges the observed P_g probably corresponds to a compressional wave refracted in the basement whereas at large distance ranges it corresponds to a compressional wave multiply reflected in the crustal wave guide.

Tangential component L_g is a prominent phase at all distances whereas the vertical component L_g amplitude is only slightly greater than the amplitude of the P_g coda at the largest range for the NPE recordings. The vertical component L_g amplitude for the Kinibito is still above the P_g coda at the largest distance ranges. This observed difference between the vertical and tangential components of L_g results from the higher level of vertical component P_g coda and not from any fundamental difference in the vertical and tangential component of L_g . The vertical component L_g observed at site 5 does not show the pronounced site effect seen for the P-wave at this site.

Attenuation

Chavez and Priestley (1986) measured the spatial decay of spectral amplitudes of the L_g wave train using profile recordings of the Kinibito explosion and Lawrence Livermore National Laboratory seismic network recordings of earthquakes. Analysis of the explosion data yielded the function $Q(f) = 206 f^{0.68}$ over the band $0.3 \text{ Hz} \leq f \leq 10 \text{ Hz}$. Similar analysis of earthquake data along paths over a broad region of the Great Basin yielded the function $Q(f) = (214 \pm 15) f^{(0.54 \pm 0.09)}$ over the band $0.3 \text{ Hz} \leq f \leq 10 \text{ Hz}$. Chavez and Priestley (1986) concluded that if the crustal sampling by L_g energy from nuclear explosions (near surface sources) is primarily in the shallow crust as has been suggested by Campillo et al. (1984), then their L_g attenuation results indicate a greater frequency dependence of apparent Q in the shallow crust than in the deeper crust.

We have measured the frequency dependent P_g and L_g attenuation from the NPE data, and P_g attenuation from the Kinibito data recorded along the profile. We inverted the spectra for the $Q(f)$ function in the following manner. The observed spectrum is modeled as

$$A(f, R) = \frac{S(f)}{R^{\eta}} \exp \left[\frac{-\pi f t}{Q(f)} \right]$$

where A is the spectral amplitude observed at a distance R , f is frequency, t is the travel time, S is the source term, and Q is the quality factor. We emphasize that since this model does not consider scattering it provides a measure of the apparent rather than the intrinsic Q . L_g has been successfully modeled as a surface wave (Knopoff et al. 1973; Panza and Calcagnille, 1975), so we have assumed that the frequency domain geometrical spreading scales with the square root of distance. Chavez and Priestley (unpublished work) found that the geometrical spreading factor for P_g was similar to the geometrical spreading factor for L_g . Taking the logarithm (base 10) of both sides the above equation gives

$$\log_{10} A(f, R) + \log_{10} R^{0.5} = \log_{10} S(f) - \left| \frac{1.364f}{Q(f)} \right| t$$

which is the equation for a straight line, with the source term as the intercept and the Q term controlling the slope. Fixing f , we know A , R , and t for each station and we solve for S and Q using least-squares. By looping over all frequencies we obtain the source and Q spectra. We computed the travel time using speeds of 6.0 and 3.5 km/s for P_g and L_g , respectively. Since L_g is an Airy phase, we feel justified in using a frequency independent travel time. The frequency dependent attenuation for P_g and L_g is found to be described by the relations $Q_{P_g} = (181 \pm 6)f^{0.59 \pm 0.02}$, $Q_{L_g}(\text{vertical}) = (217 \pm 6)f^{0.71 \pm 0.01}$, and $Q_{L_g}(\text{tangential}) = (180 \pm 10)f^{0.65 \pm 0.02}$ (Fig. 7).

The assumptions used to calculate P_g and L_g attenuation are not valid for P_n . The measurement of Q_{P_n} is complicated by the strong dependence of the inferred Q on the geometric spreading function. For a pure elastic headwave, the amplitude decays as $\Delta^{-0.5} L^{-1.5}$ where L is the distance of travel in the refracting medium. This ‘distance-squared’ fall-off is much faster than that observed in practice (Sereno, 1989). To account for this discrepancy P_n has been modeled as turning rays in the upper mantle lid. In this case the amplitude of P_n is very sensitive to the upper mantle velocity gradient (Hill, 1971). Since the effect of the upper mantle gradient is frequency dependent, two different frequency dependent processes – the attenuation and the geometrical spreading – are operating on the P_n waveform. Satisfactory separation of these processes is an unsolved problem, so some assumption must be made about the behavior of one or both of the processes so that analysis can proceed. In this study only the joint frequency dependence of the two phenomena is studied. A more complete analysis will be discussed elsewhere.

Following Chun et al. (1989), we parameterize the displacement power spectrum $P(f, \Delta)$ as

$$P(f, \Delta) = \frac{|S(f)SR(f)R(f, \Delta)|^2}{T}$$

where f is frequency, Δ is epicentral distance, T is time window duration, $S(f)$ is scaled source function, $SR(f)$ is receiver response (instrument and site response) and $R(f, \Delta)$ is the earth transfer

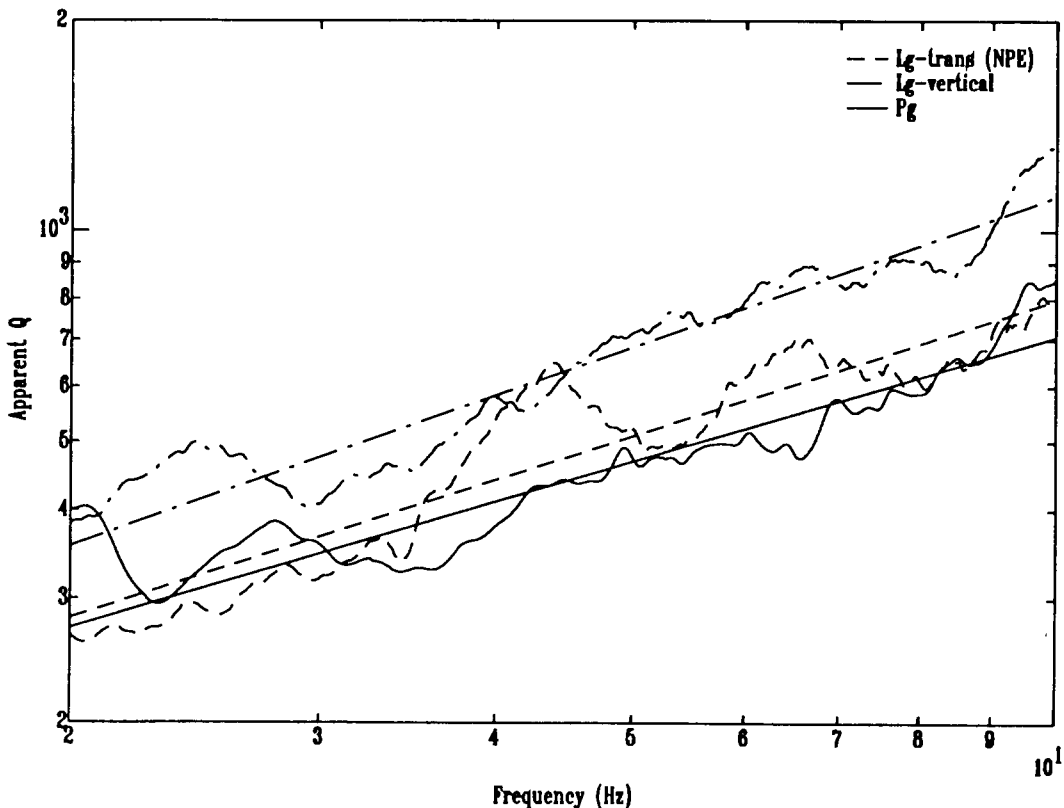


Figure 7. Apparent Q as a function of frequency for L_g and P_g . The P_g and the vertical component L_g results are from analysis of both the Kinibito and NPE data. The Kinibito results are given three times the weight of the NPE results because of the higher signal-to-noise for the Kinibito data.

function. Since $R(f, \Delta)$ is the only term of the parameterization which is distance dependent, we assume a transfer function of the form $\Delta^{-n(f)}$ (Chael, 1989). Taking logs we have:

$$\log P(f, \Delta) = D(f) - 2n(f) \log \Delta$$

where $D(f)$ contains all of the source and receiver function information and is distance independent.

A plot of $\log P$ versus $\log \Delta$ for a given frequency should be a straight line with gradient $-2n$ for that frequency. Repeated calculation for different frequencies enables the frequency dependence of n to be examined. We windowed the P_n phase, which is the first arrival at all ranges along the profile. The close proximity of the P_g arrival at close ranges results in short windows (< 1 sec) for some stations. This sets a lower limit to the usable frequency range. At large distances the signal-to-noise for P_n is poor. Smoothed displacement power spectra for P_n were calculated, and the variation of signal power with range was used to calculate n . The results are plotted in Figure 8. Because the signal-to-noise for Kinibito was higher than that for the NPE we gave the Kinibito

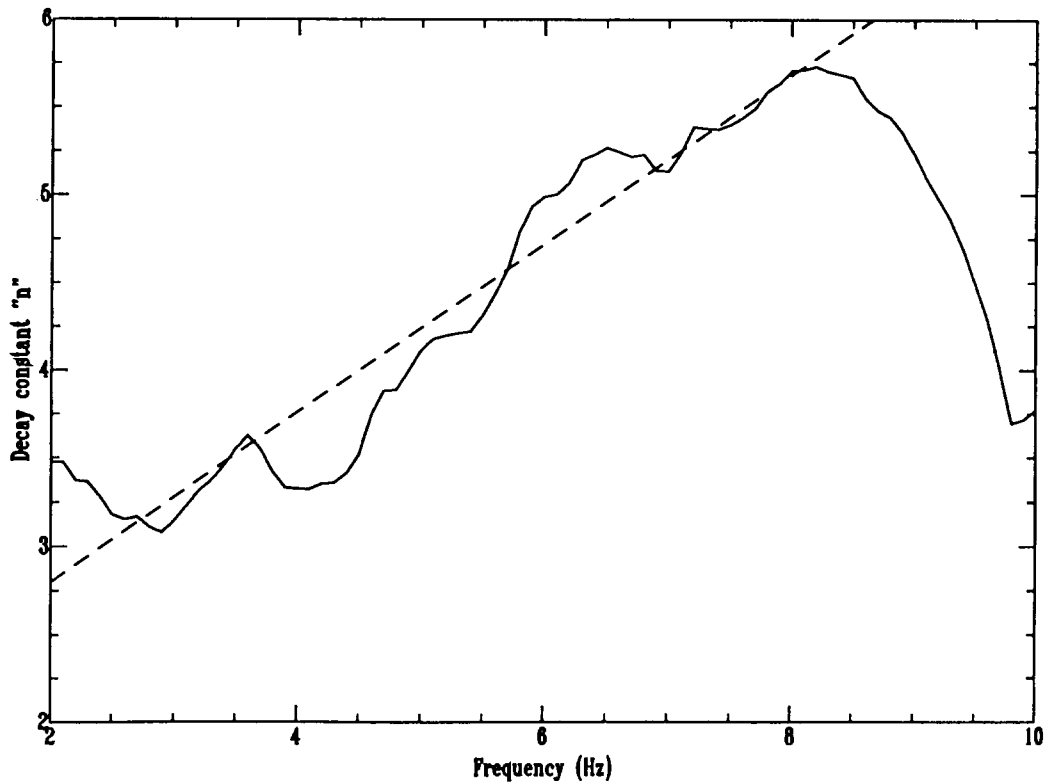


Figure 8. Decay constant n versus frequency for P_n : $\text{Amp}(P_n) \propto \Delta^{-n}$. The Kinibito results are given three times the weight of the NPE results because of the higher signal-to-noise for the Kinibito data.

measurements three times the weight of the NPE measurements. The results are unstable below 2 Hz, due to the short window lengths, and are unstable above about 8 Hz due to the poor signal-to-noise ratio, particularly at more distant stations. In the 2 to 8 Hz band there is a clear trend of decay constant n increasing with frequency. The least-squares best-fit yields a decay constant of the form $\Delta^{-[1.84(\pm 0.20) + 0.48(\pm 0.04)f]}$. The amplitude fall-off of a true headwave is approximately proportional to $\Delta^{-2.2}$ and is frequency independent. The low frequency limit of the expression obtained here is near this limit. The increase of fall-off with frequency reflects either frequency dependent attenuation in the mantle lid, or the effect of the mantle lid velocity gradient on the geometrical spreading.

Distance Effects on Proposed Regional Discriminants

In this section we examine the stability of two proposed regional seismic discriminants with range. First, we compare spectral ratios for P_n , P_g and L_g phases for raw, and for spreading and Q-corrected displacement spectral amplitudes averaged over the 1-2 Hz and 6-8 Hz frequency

bands. Secondly, we compare the P_n/L_g and P_g/L_g raw amplitude ratios, and the spreading and Q-corrected amplitude ratios for these two frequency bands. Following a suggestion by Kennett (1993) we investigate the utility of measuring amplitude and spectral ratios from the total vector resultant signal of the motion as a means of measuring the amplitude of the total wavefield. The vector sum $V(t_i)$ at each sample time t_i is computed from the three component time series data,

$$V(t_i) = [Z(t_i)^2 + R(t_i)^2 + T(t_i)^2]^{1/2}.$$

Kennett argues that the effect of 2-D and 3-D structures is to rotate the polarization planes of various observed phases away from those directions expected for a simple 1-D structure (Bostock and Kennett, 1990). The vector resultant is insensitive to such a rotation, and hence may be expected to be more stable in the presence of velocity heterogeneity. Four pairs of plots are shown (Fig. 9-12), representing spectral and amplitude ratios both without and with amplitude corrections due to decay from geometric spreading and attenuation, for both vertical component and vector resultant seismograms.

Figure 9 shows uncorrected and decay corrected spectral ratios for L_g , P_g , and P_n . The decay corrections applied for L_g and P_g are the corrections for Q derived in the previous section, plus

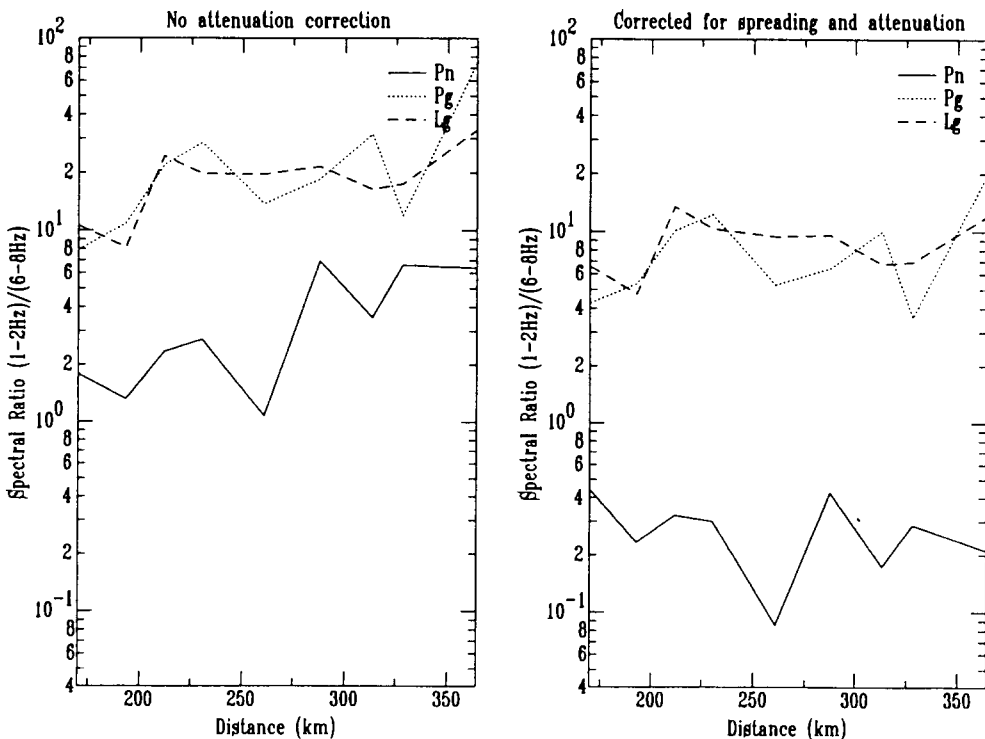


Figure 9. Vertical component displacement spectral amplitude ratios for P_n , P_g , and L_g , measured for the 1-2 and 6-8 Hz frequency bands, plotted as a function of range; (a) raw data, (b) attenuation corrected data.

an additional correction of $\Delta^{0.5}$ to correct for geometric spreading. For P_n , the composite decay relation established above is used. The corrected spectral ratios show no systematic change with distance, as they must be since we have used the trend of amplitude with range in each case to estimate the decay corrections. The remaining variation in spectral ratio with range may be principally attributable to variations in receiver effects along the profile, which have been ignored in this analysis. The spectral ratios for L_g and P_g are very similar, although P_g is more variable with range, due to variation in the high-frequency signal amplitude. The ratio for P_n is much lower and less than one, implying that there is less P_n signal at 1–2 Hz than at 6–8 Hz. While this is physically possible if the 1–2 Hz band of measurement happens to coincide with a hole in the P_n displacement spectrum, a more probable explanation for the observation is that it results from an over-correction for decay of P_n . Since the window over which the P_n decay relation was calculated runs only from 2 to 8 Hz, it would seem that extrapolation of this relationship to lower frequencies may not be valid.

Figure 10 shows plots of the ratios of relative phase amplitudes in the same frequency bands as used in the previous figure. The P_g/L_g amplitude ratios in both frequency bands are stable, and the corrected ratios are close to 1.0. The P_n/L_g amplitude ratio shows more variability. The high frequency amplitude ratio has similar behavior to that of the P_g/L_g ratios. The raw low frequency

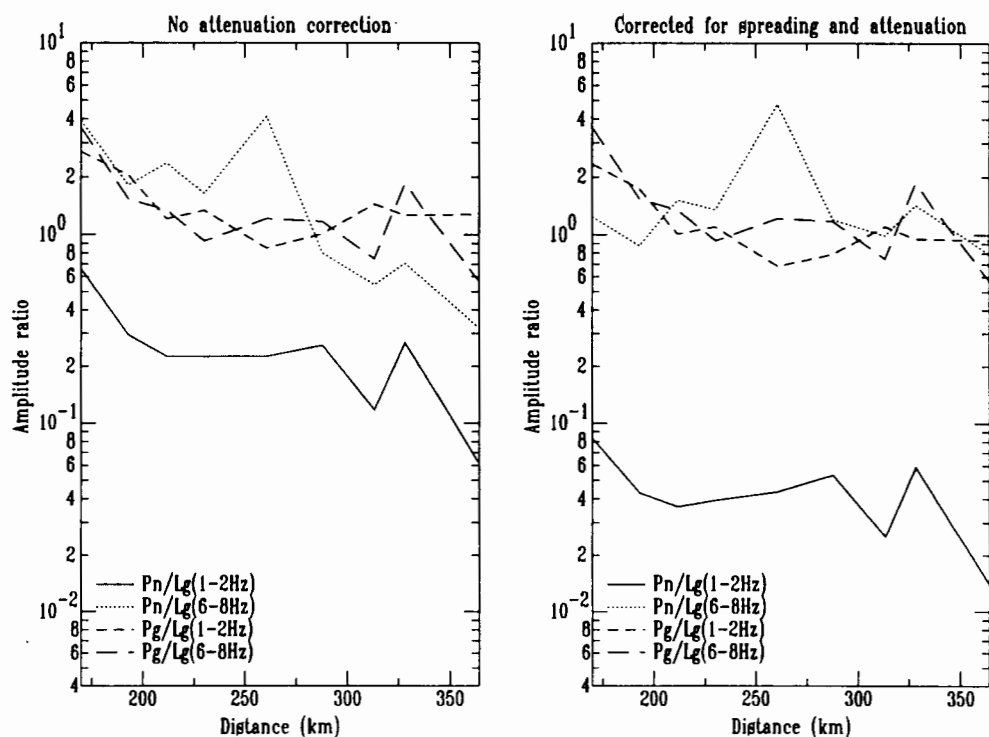


Figure 10. Low frequency (1–2 Hz) and high frequency (6–8 Hz) P_n/L_g and P_g/L_g vertical component displacement amplitude ratios plotted as a function of range; (a) raw data, (b) attenuation corrected data.

ratio is a factor of 4 smaller than P_g/L_g ratios, and the corrected ratio almost 20 times smaller, while the high frequency measurements are similar to the P_g/L_g ratios. Since P_g and L_g are both interpreted as trapped waves in the crust, and consequently have similar propagation paths, it is not surprising that they should scale so similarly with range. The propagation path of P_n through the upper mantle differs from the L_g propagation mode, and hence again there is no obvious reason why its propagation effect should behave similarly to L_g . The results indicate that reasonable corrections for geometric spreading and attenuation can be obtained for P_g and L_g , and for high frequency P_n . However, the results indicate that the decay behavior for P_n at low frequencies may be poorly represented by the model chosen, and this topic requires further investigation.

Figure 11 shows the same ratios as in Figure 9 but recalculated for the vector resultant signals. The inter-station variation is reduced, especially for P_n . Also, the spectral ratio for P_n based on the vector resultant measurement is in much better agreement with the spectral ratios for P_g and L_g for the case without attenuation correction (Figure 11a). A similar effect is observed in Figure 12 for the P_n/L_g amplitude ratios, comparing these results with the vertical component results in Figure 10. Again, however, there are systematic differences between the P_n results and the decay corrected discriminants involving just P_g and L_g . As the results in Figure 10b and 12b show, these differences are most significant for the low frequency band (1-2 Hz).

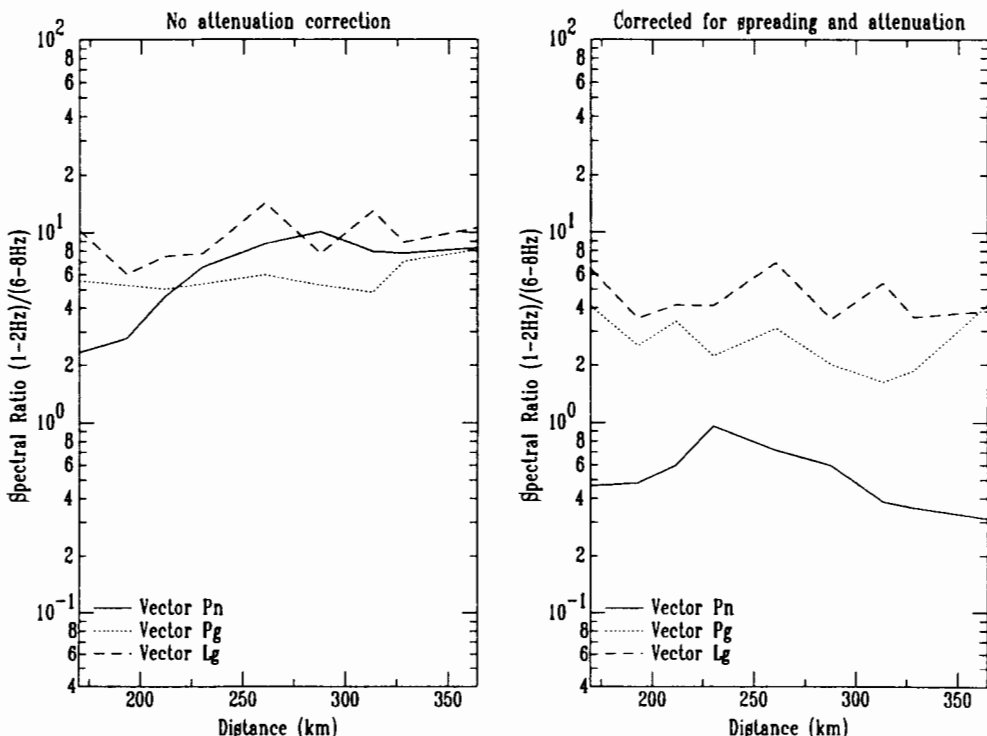


Figure 11. Full vector resultant displacement spectral amplitude ratios for P_n , P_g , and L_g , measured for the 1-2 and 6-8 Hz frequency bands, plotted as a function of range; (a) raw data, (b) attenuation corrected data.

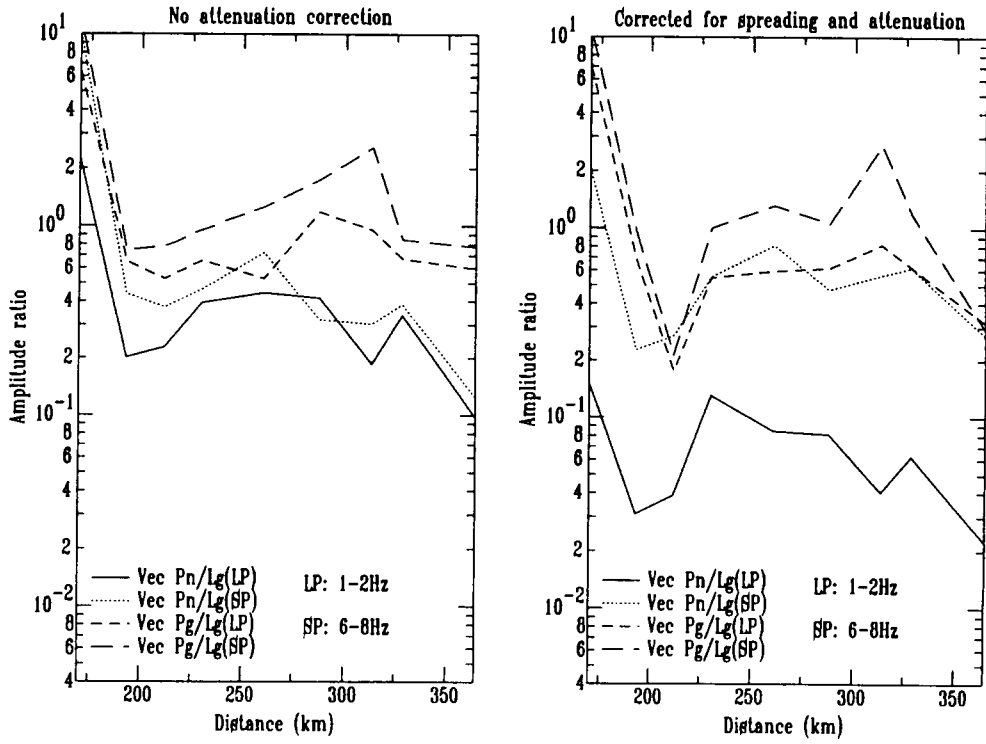


Figure 12. Low frequency (1-2 Hz) and high frequency (6-8 Hz) P_n/L_g and P_g/L_g full vector resultant displacement amplitude ratios plotted as a function of range; (a) raw data, (b) attenuation corrected data.

Summary

We have made seismic recordings of the NPE chemical explosion at nine sites along a profile through northwestern Nevada. The nuclear explosion Kinibito was previously recorded at the same sites along this profile. We have used recordings of both explosions to measure the attenuation for P_g and L_g . The frequency dependent attenuation for P_g and L_g is found to be described by the relations $Q_{P_g} = (181 \pm 6)f^{0.59 \pm 0.02}$, $Q_{L_g}(\text{vertical}) = (217 \pm 6)f^{0.71 \pm 0.01}$, and $Q_{L_g}(\text{tangential}) = (180 \pm 10)f^{0.65 \pm 0.02}$. The amplitude decay for P_n is proportional to $\Delta^{-[1.84(\pm 0.20) + 0.48(\pm 0.04)f]}$. Since the geometrical spreading factor for a head wave is 2.2, this last relationship implies that the mantle lid is either high Q, has a positive velocity gradient with depth, or both. Turning to the discriminants, the measurements of P_g and L_g spectral ratios (1-2 Hz/6-8 Hz) show weak distance dependence and relatively small inter-station variability. For P_n , the distance dependence is stronger and the inter-station scatter is larger. Similarly, the P_n/L_g amplitude ratios show stronger distance dependence than do P_g/L_g for both the low frequency (1-2 Hz) and the high frequency (6-8 Hz) bands. With the exception of one station along the profile, the inter-station scatter is not significantly different for P_n/L_g and P_g/L_g ratios. The vector resultant measurements appear to reduce the inter-station scatter for the measurements involving P_n ,

and to reduce the differences between P_n spectral ratios and the spectral ratios for other phases. Nevertheless, the differences in the spectral ratios for P_n waves and the differences in the amplitude ratios, especially for P_n/L_g at low frequencies, suggest that there may be real differences in the source functions for P_g and L_g compared to P_n . Still, it would be premature to make such conclusions without a more complete understanding of the propagation of P_n along this profile in northwestern Nevada. We intend to pursue this and several avenues suggested by the observations discussed here. These include the similarity in the propagation mode for P_g and L_g , and in the apparent increased stability of the full vector measurements of P_n .

Acknowledgements: We thank Alan Douglas for critically reading the manuscript. We also thank those who helped field the instruments in Nevada, specifically Bill Walter, Kevin Mayeda, Steve Hunter, and Phil Harbin, all from the Lawrence Livermore National Laboratory. Bill Walter and Steve Jarpe assisted in reading the field data, running quality control checks, and analyzing calibration pulses. Their assistance is gratefully acknowledged. This research was carried out while one of the authors (H.J.P.) was on remote assignment at Phillips Laboratory, Geophysics Directorate, Hanscom Air Force Base, Massachusetts. H.J.P. gratefully acknowledges the support of the U. S. Air Force Office of Scientific Research under an Intergovernmental Personnel Agreement and the support of the U. S. Department of Energy to the Lawrence Livermore National Laboratory under contract W-7405-Eng-48.

References

- Benz, H., R.B. Smith, and W.D. Mooney (1990). Crustal structure of the northwestern Basin and Range province from the 1986 Program for Array Seismic Studies of the Continental Lithosphere Seismic Experiment, *J. Geophys. Res.*, *95*, 21823 – 21842.
- Burdick, L.J., C.K. Saikia, and N.F. Smith, (1991). P_n for the Nevada Test Site, AGU Geophysical Monograph 65, 197 – 210.
- Bostock, M.G., and B.L.N. Kennett, (1990). The effect of 3-D structure on L_g propagation patterns, *Geophys. J. Int.*, *101*, 355 – 365.
- Campillo, M., J. Plantet, and M. Bouchon. (1984). Frequency – dependent attenuation in the crust beneath central France from L_g waves: data analysis and numerical modeling, *Bull. Seismo. Soc. Am.*, *75*, 1395 – 1411.
- Catchings, R.D., and W.D. Mooney (1991). Basin and Range crustal and upper mantle structure, northwest to central Nevada. *J. Geophys. Res.*, *96*, 6247 – 6267.
- Chael, E.P., (1989). The frequency dependence of P wave decay in eastern North America, *Seism. Res. Lett.*, *58*, 17 – 18.

Chavez, D. and K.F. Priestley (1986). Measurement of frequency dependent L_g attenuation in the Great Basin, *Geophys. Res. Lett.*, *13*, 551 – 554.

Chun, K.Y., R.J. Kokoski, and G.F. West, (1989). High-frequency P_n attenuation in the Canadian Shield, *Bull. Seismo. Soc. Am.*, *79*, 1039 – 1053.

Douglas, A., J.A. Hudson, and V.K. Kembhavi, (1971). The relative excitation of seismic surface and body waves by point sources, *Geophys. J. R. astr. Soc.*, *23*, 451-460.

Hauge, T.A., R.W. Allmendinger, C. Caruso, E.C. Hauser, S.L. Klemperer, S. Opdyke, C.J. Potter, W. Sanford, L. Brown, S. Kaufman, and J. Oliver, (1987). Crustal structure of western Nevada from COCORP deep seismic – reflection data, *Geol. Soc. Am. Bull.*, *98*, 320 – 329.

Hawman, R.B., R.H. Colburn, D.A. Walker, and S.B. Smithson, (1990). Processing and inversion of refraction and wide – angle reflection data from the 1986 Nevada PASSCAL experiment, *J. Geophys. Res.*, *95*, 4657 – 4691.

Hill, D.P., (1971). Velocity gradients and anelasticity from crustal body wave amplitudes, *J. Geophys. Res.*, *76*, 3309 – 3325.

Holbrook, W.S., (1990). The crustal structure of the northwestern Basin and Range Province, Nevada, from wide – angle seismic data, *J. Geophys. Res.*, *95*, 21843 – 21869.

Hudson, J.A., and A. Douglas, (1975). On the amplitudes of seismic waves, *Geophys. J. R. astr. Soc.*, *42*, 1039-1044.

Kennett, B.L.N. (1993). The distance dependence of regional phase discriminants, *Bull. Seismo. Soc. Am.*, *83*, 1155 – 1166.

Knopoff, L., F. Schwab, and E. Kausel, (1973). Interpretation of L_g , *Geophys J. R. Astron. Soc.*, *33*, 389 – 404.

Panza, G.F., and G. Calcagnille, (1975). L_g , L_i , and R_r from Rayleigh modes, *Geophys. J. R. Astron. Soc.*, *40*, 475 – 487.

Pomeroy, P.W., W.J. Best, and T.V. McEvilly, (1982). Test ban treaty verification with regional data – A review, *Bull. Seismo. Soc. Am.*, *72B*, 89 – 130.

Priestley, K.F., and J.N. Brune (1978). Surface waves and the structure of the Great Basin of Nevada and western Utah, *J. Geophys. Res.*, *83*, 2265 – 2272.

Priestley, K.F., J.A. Orcutt, and J.N. Brune (1980). Higher – mode surface waves and the structure of the Great Basin of Nevada and western Utah, *J. Geophys. Res.*, *85*, 7166 – 7174.

Priestley, K.F., A.S. Ryall, and G.F. Fezie (1982). Crust and upper mantle structure in the north-west Basin and Range Province, *Bull. Seismo. Soc. Am.*, *72*, 911 – 923.

Stevens, J.L., and S.M. Day (1985). The physical bases of $m_b : M_s$ and variable frequency magnitude methods for earthquake/explosion discrimination, *J. Geophys. Res.*, *90*, 3009 – 3030.

Sereno, T.J. (1989). Numerical modeling of P_n geometric spreading and empirically determined attenuation of P_n and L_g phases recorded in eastern Kazakhstan. SAIC 89/1555.

Zelt, C., and R.B. Smith (1992). Seismic traveltimes inversion for 2-D crustal velocity structure, *Geophys. J. Int.*, *108*, 16 – 34.

Separation of Source and Propagation Effects at Regional Distances

Peter Goldstein, Steve Jarpe, Kevin Mayeda, and William Walter
Lawrence Livermore National Laboratory

Abstract

Improved estimates of the contributions of source and propagation effects to regional seismic signals are needed to explain the performance of existing discriminants and to help develop more robust methods for identifying underground explosions. In this paper, we use close-in, local, and regional estimates of explosion source time functions to remove source effects from regional recordings of the Non-Proliferation Experiment (NPE), a one kiloton chemical explosion in N-tunnel at Rainier Mesa on the Nevada Test Site, and nearby nuclear explosions and earthquakes. Using source corrected regional waveforms, we find that regional Pg and Lg spectra of shallow explosions have significant low frequency (~1Hz) enhancements when compared to normal depth earthquakes. Data and simulations suggest that such enhancements are most sensitive to source depth, but may also be a function of mechanism, source receiver distance, and regional structure.

Introduction

The primary motivation for this study is to improve our understanding of regional propagation effects and their sensitivity to parameters such as source depth, source receiver distance, and regional structure. An improved understanding of regional propagation effects and their sensitivity to such parameters can help us understand the performance of existing discriminants and may allow us to develop more robust discriminants that can be used in other regions. Numerous studies have investigated the influence of source parameters and Earth structure on regional seismic signals (e.g., Campillo et al., 1984). In this study, we remove source effects from regional data using source spectra estimated from freefield data and empirical Green's function deconvolved local and regional data (Goldstein and Jarpe, 1994). We compare source corrected regional spectra of Nevada Test Site (NTS) earthquakes and explosions and identify significant spectral differences that we attribute to differences in depth. Reflectivity synthetic seismograms support our conjecture that the observed spectral differences are most sensitive to depth. These synthetics also suggest that regional spectra are sensitive to mechanism, source receiver distance, and Earth structure.

Source Corrected Regional Phase Spectra

A fundamental difficulty in assessing the influence of source parameters such as depth on regional seismograms has been the inability to separate source and propagation effects. We have overcome this

difficulty by deconvolving source contributions from the regional data using source spectra estimated from freefield, close-in, and local data. This approach is justified by the observation of consistent source spectral estimates at all these distances (Goldstein and Jarpe, 1994). For example, freefield, surface, local, and regional estimates of the source spectrum of the NPE are in excellent agreement (Figure 1). Details regarding the estimation of these source spectra are presented in Goldstein and Jarpe (1994).

Source corrected regional spectra were obtained by deconvolving source spectra, such as those shown in Figure 1, from Livermore Nevada Network (LNN) recordings of NTS explosions and earthquakes. For example, source corrected Pg spectra of NTS explosions and a normal depth (~8 km) earthquake are shown in Figure 2.

Note the consistent peak in the explosion Pg spectra between 0.5 and 1.0 Hz that is not present in the earthquake spectrum. We found similar differences between explosion and normal depth earthquake Lg spectra. Mayeda and Walter (1994) also noted these differences in source corrected coda spectra. Pn spectra do not show evidence of spectral peaking. In fact, attenuation corrected Pn spectra are very similar to source spectra estimated from freefield data (Figure 3).

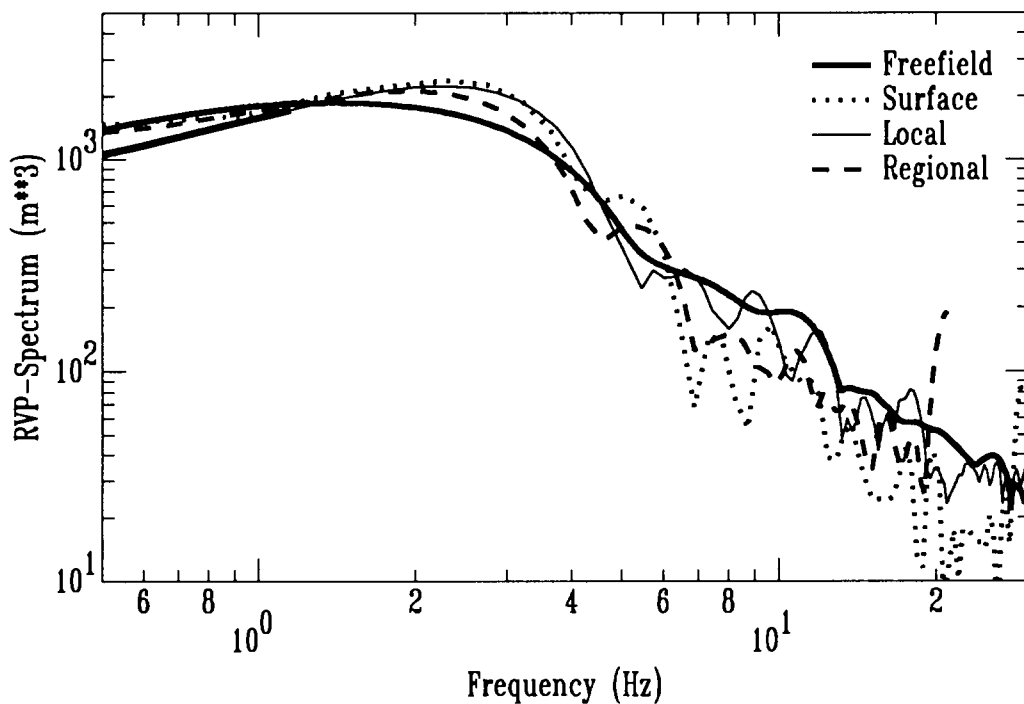


Figure 1. Comparison of freefield, surface, local, and regional estimates of the NPE source function. The NPE source function shows no dependence on distance or evidence of secondary sources.

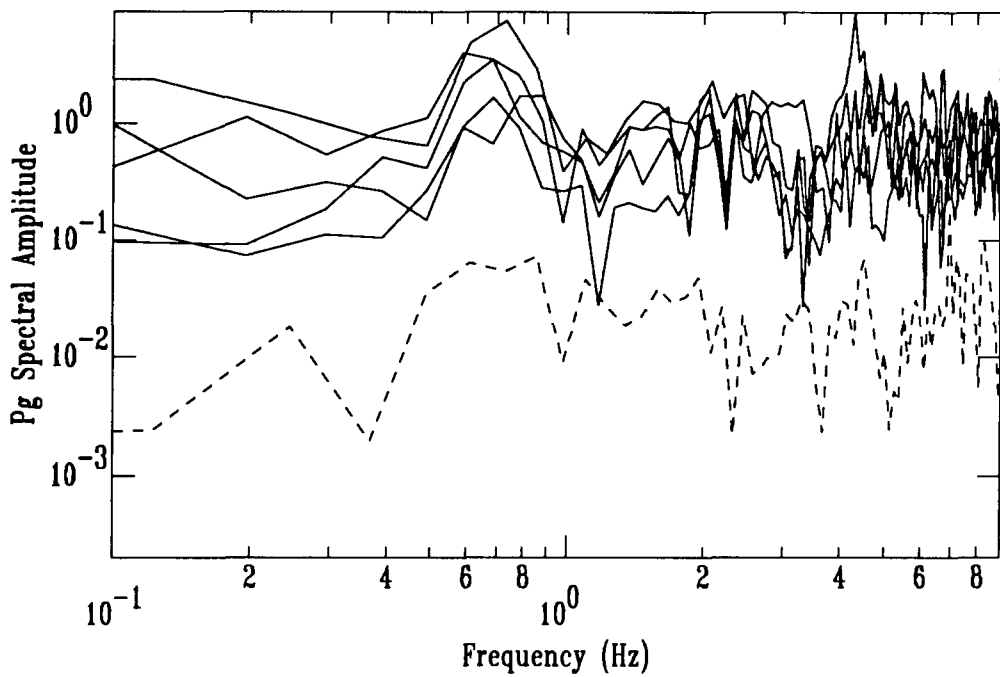


Figure 2. Comparison of source deconvolved, NTS earthquake and explosion Pg spectra. Spectra of source deconvolved NTS explosions at Rainier Mesa and Yucca Flats are indicated by the solid lines. A source deconvolved earthquake spectrum is indicated by the dashed line. The earthquake spectrum has been multiplied by a constant for ease of comparison with the explosions. The NTS explosion are peaked between 0.5 and 1.0 Hz.

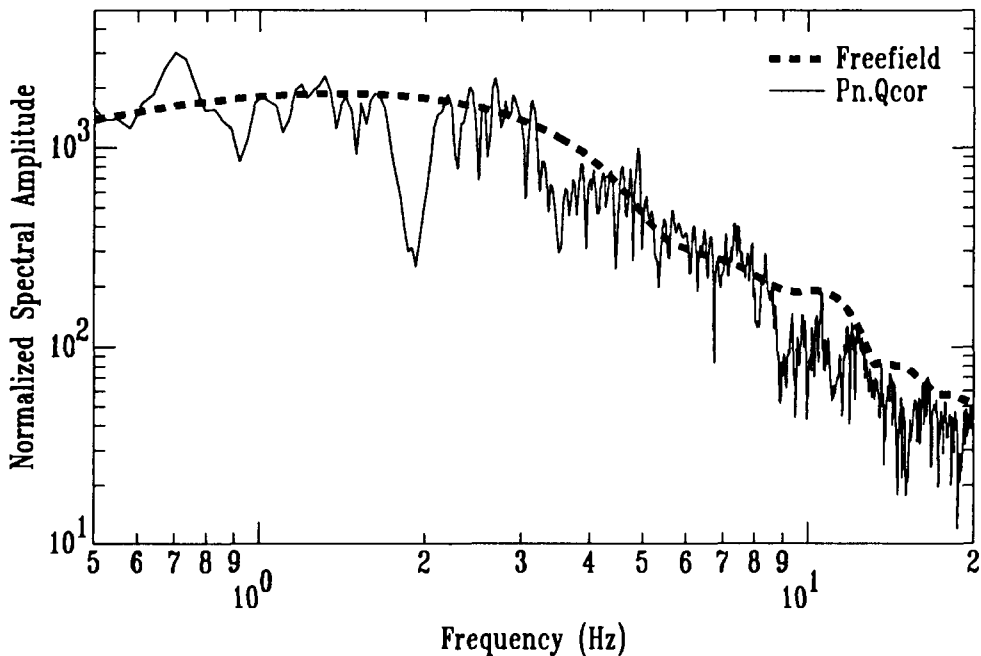


Figure 3. Comparison of the NPE's freefield source spectrum (thick dashed line) with its attenuation corrected, regional Pn spectrum (thin solid line). The spectra are in good agreement up to about 10 Hz.

We suggest that the differences between the spectra of the NTS explosions and the normal depth NTS earthquake are due mainly to differences in source depth. The normal depth earthquake was an aftershock of the Little Skull Mountain earthquake (Walter, 1993) and had a source depth in the 6 to 8 km range. Our conjecture that these spectral differences are related to depth is supported by our observation of small peaks in spectra of the very shallow Rock Valley, NTS earthquake which occurred between 1 and 3 km depth (Smith and Brune, 1993). Reflectivity synthetic seismograms also suggest that the observed spectral peaking is a depth effect. For example, using a model similar to that of Patton and Taylor (1984), we find that synthetic Pg spectra of a 500 m depth explosion is peaked near 1 Hz when compared to the synthetic Pg spectra of an 8 km deep earthquake (Figure 4).

Other factors that probably contribute to the observed spectral differences, include site effects, mechanism, and details of the regional structure. However, differences due to site effects are probably small because the observed spectral differences between shallow explosions and normal depth earthquakes occur at the same station. Based on reflectivity synthetic seismograms, mechanism can effect the amplitude of peaks in the spectra of shallow events and the absolute amplitudes of various phases but is of secondary importance when compared to the effects of depth. The significance of mechanism and details of the structure warrant additional investigation.

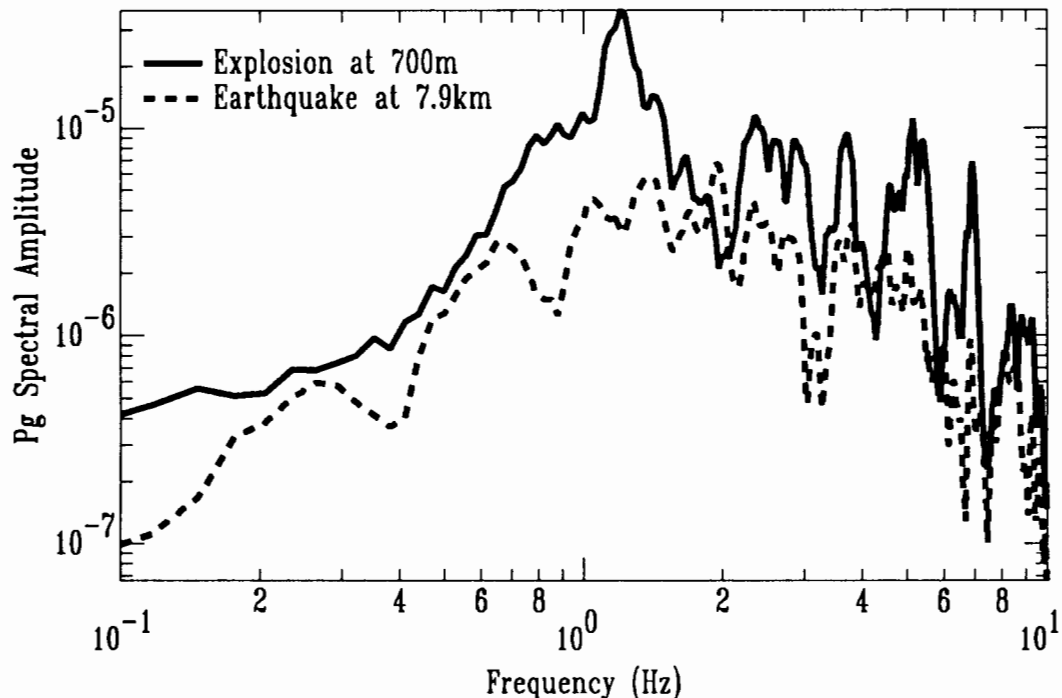


Figure 4. Synthetic spectra of an explosion at 500 m depth and an earthquake at 8 km depth. The shallow explosion spectra are enhanced at low frequencies relative to that of the normal depth earthquake. The exact location of the spectral peak depends on the details of the structure.

Conclusions

We have used close-in, local, and regional estimates of seismic source functions to deconvolve source effects from spectra of regional seismic waveforms. We find that source corrected, regional Pg and Lg spectra of NTS explosions are enhanced between 0.5 and 1.0 Hz when compared to spectra of a normal depth NTS earthquake. Based on preliminary analyses, shallow NTS earthquakes also show enhancements in their Pg and Lg spectra. Pn spectra of these events are relatively flat and, after correcting for attenuation, may provide a reasonable approximation to the source spectrum. We conclude that the observed spectral peaking of explosions and shallow earthquakes is a depth dependent path effect. Our goal is to improve our ability to predict such enhancements and their dependence on regional structure so that their effects on the performance of regional discriminants can be assessed and more robust discriminants can be developed.

Acknowledgments

This work has been performed under the auspices of the U.S. Department of Energy by Lawrence Livermore National Laboratory under Contract No. W-7405-Eng-48.

References

- Campillo, M., M. Bouchon, and B. Massinon (1984), "Theoretical study of the excitation, spectral characteristics, and geometrical attenuation of regional seismic phases", *Bull. Seis. Soc. Am.*, 74, 79-90.
- Goldstein, P., and S. P. Jarpe (1994), "Comparison of chemical and nuclear-explosion source spectra from close-in, local, and regional seismic data," *Proceedings of the Symposium on the Non-Proliferation Experiment Results and Implications*, M. D. Denny et al., editors, Lawrence Livermore National Laboratory, Livermore, CA, CONF-9404100, .
- Mayeda, K. M., and W. R. Walter (1994), "A new broadband magnitude based on coda envelopes," *Seis. Res. Lett.*, 65, 49.
- Patton, H. J., and S. R. Taylor (1984), "Q structure of the Basin and Range from surface waves," *J. Geophys. Res.*, 89, 6929-6940.
- Smith, K. D., and J. N. Brune (1993), "A sequence of very shallow earthquakes in the Rock Valley fault zone; southern Nevada test site," (abstract), *EOS suppl.*, 74, 417.
- Walter, W. R., "Source parameters of the June 29, 1992 Little Skull Mountain earthquake from complete regional waveforms at a single station, *Geophys. Res. Lett.*, 20, 403-406, 1993.

Southern Sierra Nevada Continental Dynamics Project: 1993 Field Observations of the NPE

G. Randy Keller
Department of Geological Sciences
The University of Texas at El Paso
El Paso, Texas 79968

Peter E. Malin
Department of Geology
Duke University
Durham, NC 27708-0235

Stanley D. Ruppert
LLNL, IGPP
Center for Geosciences
Livermore, CA 94550

and

***The Southern Sierra Nevada
Continental Dynamics Project Working Group**

Abstract

The Southern Sierra Nevada Continental Dynamics Project is a multidisciplinary, multi-institutional investigation of the cause of the uplift of the Sierra Nevada and its relationship to extension in the adjacent Basin and Range. A broad range of geologic and geophysical data have been collected as part of this project. These data include both passive and active seismic measurements, as well as gravity and magnetotelluric observations. Three seismic refraction/wide-angle reflection profiles were recorded: (1) a 325-km-long, north-south profile extending from just east of Mono Lake south across the Garlock fault, (2) a 400-km-long, east-west profile extending from Death Valley west across the Sierra Nevada to near the San Andreas fault, and (3) a 480-km-long, east-west profile deployed for the NPE. This profile extended from Beatty, Nevada, west across the Sierra Nevada along the previously recorded east-west profile and continued nearly to the Pacific Ocean. Up to 675 seismic recorders were deployed for each profile. These data are allowing us to develop refined models of the crustal and upper mantle structure of the southern Sierra Nevada and to evaluate alternative hypotheses for its uplift and for Basin and

Range extension. They also provide insight into the propagation of regional phases across complex structures.

**(The Working Group includes representatives from Duke Univ., Caltech, Univ. Nevada-Reno, Princeton, U.C. Riverside, Univ. of Texas at El Paso, San Diego State Univ., Stanford Univ., China Lake Naval Weapons Center, and the U.S. Geological Survey.)*

General Background

Several government agencies funded the Southern Sierra Nevada Continental Dynamics Project (SSCD) which allowed a consortium of research universities to spearhead a coordinated program of seismic and electrical studies of the Death Valley, southern Sierra Nevada, and San Joaquin Valley regions of California. The aim of this project was to establish, for a variety of basic scientific and practical purposes, the nature of the crust and upper mantle of these regions. A special effort was made to record the Non-Proliferation Experiment (NPE) at the Nevada Test site during the final phase of the field effort. The government agencies funding the SSCD project are the National Science Foundation, United States Geological Survey, the Air Force Office of Scientific Research, the Department of Energy, the Naval Air Weapons Station China Lake, and the Lawrence Livermore National Laboratory.

To investigate the lithospheric structure of this area and the propagation of regional seismic phases through it, two seismic experiments were designed: (1) a major, crustal and upper-mantle scale, refraction survey using shots in drill holes and the NPE as sources, recorded along NS and EW profiles covered with IRIS-PASSCAL, U.S. Geological Survey, and Geological Survey of Canada seismograph systems, and (2) a teleseismic converted wave survey using IRIS-PASSCAL, and French supplied seismographs.

Geophysical Background

Seismic observations of the lithospheric structure of the Sierra Nevada have produced conflicting interpretation (See Jones et al., 1994 and Savage et al., 1994 for recent summaries). Refraction profiles along the axis of the range have been interpreted to show a crust more than 50 km thick (Eaton, 1966; Pakiser and Brune, 1980). Disagreements over the identifications of phases and their interpretation has led to an alternative interpretation of a crust only about 40 km thick (Prodehl, 1979). Seismic profiles

transverse to the range were initially interpreted to require a thin (30 km thick) crust with very low mantle velocities (7.65 to 7.88 km/s) beneath the range (Carder et al., 1970; Carder, 1973). Again, alternative interpretations suggest that a thick crust might also be consistent with the observations (Pakiser and Brune, 1980). Ray-tracing models through both structures appear to indicate that the thinner crust better fits the observations (Bolt and Gutdeutsch, 1982). Abnormally low heat flow is consistent with the presence of a thick root (Roy et al., 1972). However, Crough and Thompson (1977) argue that the surface heat flow reflects the heat flux into the crust over 10 m.y. ago and does not reflect the modern tectonic configuration. Accordingly, the asthenosphere could have risen to near the base of the crust within the last 10 m.y. or so, presumably at the time extension began in Death Valley. Consistent with this idea, Mooney and Weaver (1989) show that the maximum depth of regionally recorded seismicity decreases from over 25 km beneath the San Joaquin Valley to about 15 km beneath the Sierra Nevada. This latter depth is comparable to the depth of seismicity beneath the Basin and Range to the east. This decrease could be due to elevation of the brittle-ductile transition as a result of asthenospheric heating from below.

Several seismic reflection and refraction profiles have been shot in the San Joaquin Valley area by the U.S. Geological Survey (e.g., Wentworth et al., 1987), giving both velocity and structural information north and south of our seismic profile. As recently summarized by Miller and Mooney (1994), the crustal structure of this area is very complex because it involves a number of accreted terranes.

Somewhat surprisingly, relatively little geophysical research has been done in the Death Valley area. The only seismic refraction line indicates a roughly 30 km thick crust to the east of Death Valley with a mean crustal P-wave velocity of about 6.1 km/s (Prodehl, 1979). The eastern end of the COCORP line across the Mojave Desert crosses the southern part of Death Valley, where a zone of reflections considered to represent Moho are about 30 km deep (Serpa et al., 1988). A large gravity high and topographic low that trends along the valley have been attributed to either outcrops of dense metamorphic rocks at the valley margins or thinner crust under Death Valley than under regions to the east and west. To our knowledge, no real quantitative attempt has been made to separate crustal thinning from lateral density contrast as the cause of these features. In May of 1994, the University of Texas at El Paso (UTEP) group reshot the easternmost of the SSCD shotpoints along with three other

shots to the southeast. The result is a series of interlocking profiles which will greatly enhance our knowledge of structure and wave propagation in the southern Basin and Range.

Equipment, Logistics, and Cooperation.

The bulk of the seismic recording equipment for the SSCD refraction and teleseismic surveys was provided by the national IRIS-PASSCAL instrument center at Stanford University, the U.S. Geological Survey in collaboration with UTEP, and the Geological Survey of Canada. The total number of recorders deployed numbered between 600 to 700 instruments.

For the refraction profiling field effort, the instruments were laid out on 2 profiles, each being greater than 300 km in length. We recorded both in-line and fan profiles simultaneously. A total of 24 explosions were recorded. Every effort was made to maximize the data collection, including recording of the NPE explosion at the Nevada Test Site, thereby answering major crustal and nuclear monitoring questions. The NPE effort is discussed in more detail below, but it provided an unique opportunity to record detailed data on upper mantle structure across California. Since the P_n phase plays a major role in Comprehensive Test Ban Treaty verification efforts, long range recordings of this phase are very important in order to provide data on waveform variations as it propagates through complex structures.

Over 50 individuals from more than a dozen institutions cooperated in the SSCD experiment. The bulk of leg work for permitting of shot points, roadways, trails, and ways-to-go along the teleseismic and refraction surveys was done by the university participants working with a Post Doctoral Research Fellow from Lawrence Livermore National Laboratories. The permits for the shot points and refraction survey points were signed by the U.S. Geological Survey. Some amount of helicopter reconnaissance was needed for both the permitting and survey of the refraction lines in the Sierra Nevada and Death Valley areas. It was necessary that all groups worked closely together to successfully deploy the large number of instruments along the seismic profiles.

The SSCD project fielded some 350 portable seismic recorders for the NPE explosion. The stations were equipped with a mixture of 3-component and vertical geophones, with both short period and broad-band responses. The various sensors were interleaved to give: (a) a 450 km profile across the

Sierra Nevada at 2 km station spacings and (b) local arrays placed both in a circle around Owens Lake and in 3 smaller apertures, at Darwin Plateau, Horse Shoe Meadow, and Mineral King (Figure 1). The arrays and 25 of the profile stations were also used to record earthquakes for several weeks. These events include a magnitude 3+ Death Valley event and the 5+ event in Oregon.

The data were distributed to the SSCD members in March, 1994 and await complete interpretation of the crustal structure information which is a very complex process. A record section for the profile NPE is shown in Figure 2. These data present an outstanding picture of the P_n phase as it propagates across the Sierra Nevada, San Joaquin Valley, and San Andreas fault regions. This phase is clear all across the record section to the westernmost stations which were deployed just east of Carmel, California. We have not had the time to conduct a detailed interpretation, but there is no evidence for a major crustal root

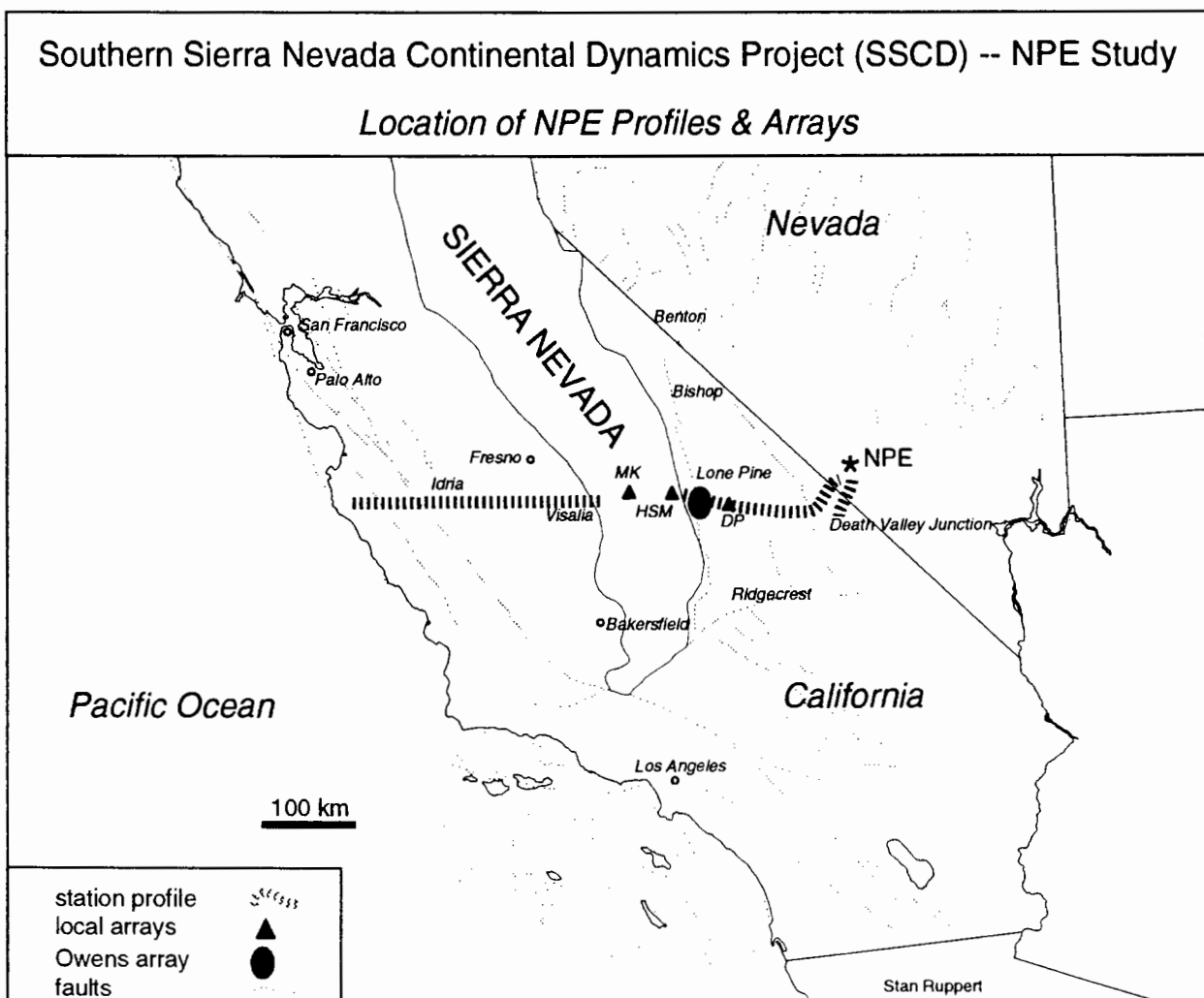


Figure 1. Index map showing the profile of seismic recordings obtained for the NPE.

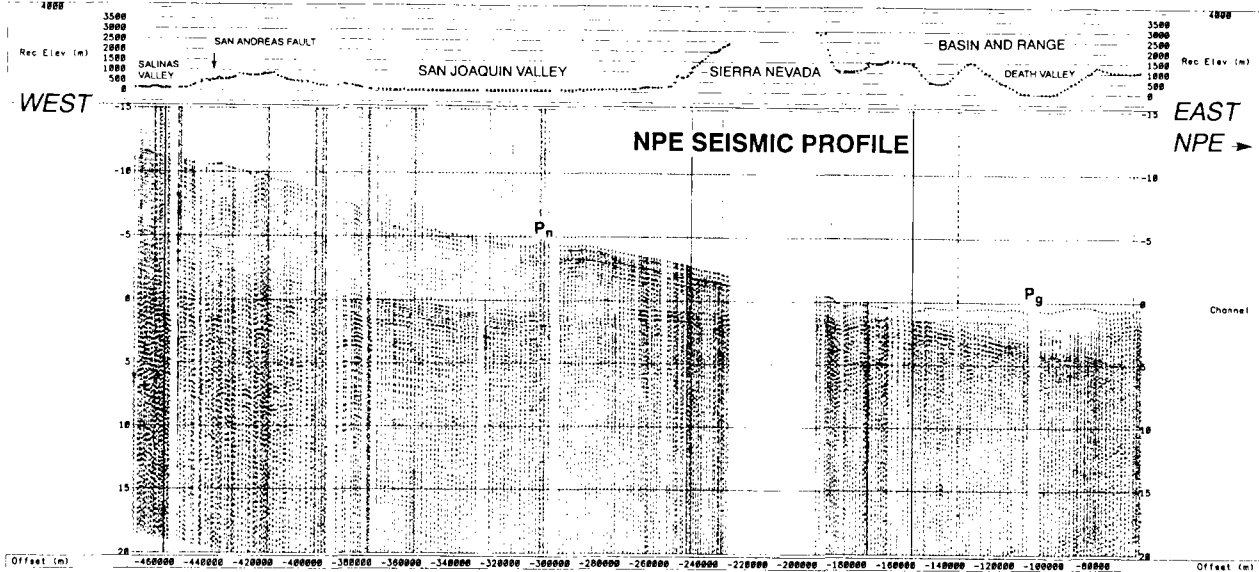


Figure 2. Record section for the NPE seismic profile. A reducing velocity of 8.0 km/sec was employed for display purposes. Reduced travel times in seconds are shown on the vertical axis. Small +'s denote first arrivals which are very clear on enlarged displays of the data.

beneath the Sierra Nevada. However, there are many indications of complexity in upper mantle structure. There are large variations in the amplitude relations between P_n and later arriving phases such as PmP . An understanding of such variations is important to treaty verification efforts. The broad band recording do show that longer period Lg type waves are clearly affected by the Sierra Nevada. We are combining these observations into model of seismic wave propagation across the region for both scientific and nuclear discrimination purposes. This project is an excellent example of what can be accomplished when universities and government agencies cooperate and pool resources.

REFERENCES

- Bolt, B.A., and R. Gutdeutsch, 1982. Reinterpretation by ray tracing of the transverse refraction seismic profile through the California Sierra Nevada, Part 1, Bull. Seis. Soc. Am. 72:889-900.
- Carder, D.S., 1973. Trans-California seismic profile, Death Valley to Monterey Bay, Bull. Seis. Soc. Am. 63:571-586.
- Carder, D.S., A. Qamar, and T.V. McEvilly, 1970. Trans-California seismic profile, Pahute Mesa to San Francisco Bay, Bull. Seis. Soc. Am. 60:1829-1846.
- Crough, S.T., and G.A. Thompson, 1977. Upper mantle origin of the Sierra Nevada uplift, Geology 5:396-399.

- Eaton, J.P., 1966. Crustal structure in northern and central California from seismic evidence, in Bailey, E.H., ed., Geology of Northern California, Calif. Div. Mines Geol. Bull. 190:419-426.
- Jones, C.H., H. Kanamori, and S.W. Roecker, 1994. Missing roots and mantle drips: Regional P_n and teleseismic arrival times in the Southern Sierra Nevada and vicinity, California, J. Geophys. Res., 99:4567-4601.
- Jones, C.H., 1987. Is extension in Death Valley accommodated by thinning of the mantle lithosphere beneath the Sierra Nevada, California? Tectonics 6:449-473.
- Miller, K.C. and W.D. Mooney, 1994. Crustal structure and composition of the southern Foothills Metamorphic Belt, Sierra Nevada, California, from seismic data, J. Geophys. Res., v. 99, p. 6865-6880.
- Mooney, W.D., and C.S. Weaver, 1989. Regional crustal structure and tectonics of the Pacific coastal states: California, Oregon, and Washington: in Pakiser, L.C., and W.D. Mooney (eds.), The Geophysical Framework of the United States, Geol. Soc. Am. Monograph 172.
- Moores, E.M., and H.W. Day, 1984. Overthrust model for the Sierra Nevada, Geology 12:416-419.
- Oliver, H.W., J.G. Moore, and R.F. Sikora, 1993. Internal structure of the Sierra Nevada batholith based on specific gravity and gravity measurements, Geophys. Res. Letters, 20:2179-2182.
- Pakiser, L.C., and J.N. Brune, 1980. Seismic models of the root of the Sierra Nevada, Science 210:1088-1094.
- Prodehl, C., 1979. Crustal structure of the western United States, USGS Prof. Paper, 1034, 74 pp.
- Roy, R.F., D.D. Blackwell, and E.R. Decker, 1972. Continental heat flow, in Robertson, E.C. (ed.), The Nature of the Solid Earth, 506-543 (McGraw-Hill).
- Saleeby, J.B., M.C. Blake, and R.C. Speed, 1991. Tectonic evolution of the southwest U.S. Cordillera - a synthesis of the C1 and C2 continent-ocean transects, Geol. Soc. Am. DNAG Transects Synthesis volume.
- Savage, M.K., L. Li, J.P. Eaton, C.H. Jones, and J.N. Brune, 1994. Earthquake refraction profiles of the root of the Sierra Nevada, Tectonics: in press.

Serpa, L., B. deVoogd, L. Wright, J. Willemin, J. Oliver, E. Hauser, and B. Troxel, 1988. Structure of the central Death Valley pull-apart basin and vicinity from COCORP profiles in the southern Great Basin, Geol. Soc. Am. Bull. 100:1437-1450.

Wentworth, C.M., M.D. Zoback, A. Griscom, R.C. Jachens, and W.D. Mooney, 1987. A transect across the Mesozoic accretionary margin of central California. Geophys. J.R. Astr. Soc. 89:105-110.

Zoback, M.D., C.M. Wentworth, and J.G. Moore, 1985. Central California seismic reflection transect: II - The eastern Great Valley and western Sierra Nevada, EOS 65(45):1073.

The NTS Ground Motion Data Base

Frederick N. App

Earth and Environmental Sciences Division
Los Alamos National Laboratory

I. Introduction

The NTS (Nevada Test Site) Ground Motion Data Base is composed of strong motion data recorded during the normal execution of the U. S. underground test program. It contains surface, subsurface, and structure motion data as digitized waveforms. Currently the data base contains information from 148 underground explosions. This represents about 4200 measurements and nearly 12,000 individual digitized waveforms. Most of the data was acquired by Los Alamos National Laboratory (LANL) in connection with LANL sponsored underground tests. Some was acquired by Los Alamos on tests conducted by the Defense Nuclear Agency (DNA) and Lawrence Livermore National Laboratory (LLNL), and there are some measurements which were acquired by the other test sponsors on their events and provided to us for inclusion in this data base. Included in the data set is the Los Alamos motion data from the Non-Proliferation Experiment (NPE).

II. Background

Ground motion measurements were originally fielded by Los Alamos in the early 1970s as a failure diagnostic for containment of underground nuclear explosions. Later, such measurements were used for "ground truthing" stress wave propagation codes used in analyzing the containment of the explosions. As more data became available, the Underground Test (UGT) community began using ground motion as a "figure of merit" in containment analysis.

In the early 1980s, we decided to build a formal data base of ground motion measurements, using the existing GEODES (Geologic Data Evaluation System) data base management system as the repository. This is a VAX-VMS based system for handling vector data in the *closed* computing environment. Data were retrieved from old analog tape recordings and all new measurements were put into the data base as soon as they were acquired.

In late 1993, Secretary O'Leary announced her openness policy. Many previously unannounced tests (classified CFRD) became unclassified. This, more than anything else, prompted us to consider moving the NTS ground motion data base into the open (unclassified) environment.

The effort to bring the data base into the open was begun January 2, 1994. We were motivated by the desires a) to provide convenient access to close-in strong motion data for all interested researchers involved in Arms Control and Non-Proliferation, b) to promote data exchanges between the labs, and c) to archive the ground motion data obtained over the years in support of the UGT Program.

Our objectives for the user interface were a) to provide maximum flexibility, b) to make the interface as user-friendly as possible, and c) to make the data base as machine/device independent as possible. Also, we placed strong emphasis on economy in maintenance and support, thus making the data base relatively insensitive to vagaries in funding and support.

With the above considerations in mind, we decided to incorporate the data base into the Los Alamos Integrated Computing Network (ICN) on the open CRAY-UNICOS computers. We developed a new data base management system (user interface) that would work efficiently in that environment.

III. Relevance to Arms Control and Non-proliferation

Underground nuclear explosions at the NTS have been conducted in all manner of geologic environments. Questions regarding how local geology influences the close-in source function (and then the seismic source function) can be addressed to a large degree with data available from the NTS. As examples, some events were conducted in extremely weak, friable materials (e.g., alluvium, bedded tuff) and others were conducted in dense, high strength materials (e.g., lava, welded tuff). Some events were conducted in water saturated environments while other sites were "dry". There are examples of events conducted in similar environments but at various yields and depths-of-burial (DOB). A strong factor in the siting choice for the NPE was the presence of nearby nuclear events, of various sizes, with which to compare NPE results. There are events conducted in both complicated and uncomplicated structural settings. There are events conducted near faults that experienced differential movement as a result of the explosions.

The above are cause and effect issues that have not yet been fully investigated by researchers in the area of Arms Control and Non-proliferation. The NTS data base provides an additional tool for such investigations.

IV. User Interface

The user interface is menu driven and requires a minimum of prior instruction in its use. It allows selection of events by name, geographic location, depth-of-burial, WP medium, distances from layer interfaces, and nature of the overburden material, or any combination of these. It allows selection of recording stations by name, by type (surface, subsurface, structure, etc.), by distance, and by emplacement medium, or any combination of these. It allows measurement selection by type (acceleration, velocity, or displacement) and direction component (radial, tangential, or vertical), or any combination of these.

The user can choose any of a number of actions to be applied to the event-station-measurement selections:

- 1) Can create a "miniature" data base which can in turn be used as a personalized data base for subsequent runs, and saved into the user's own storage area with minimal space requirements.

- 2) Can write a file containing only text (header) information for the selected events-stations-measurements. Headers include such information as Nevada coordinates, elevations, gauge types and ranges, emplacement mediums, general comments, etc.
- 3) Can write special "SAC" file(s) for input to the Lawrence Livermore National Laboratory (LLNL) developed Seismic Analysis Code.
- 4) Can write simple time vs. value ASCII file(s).
- 5) Can examine "raw" or "repaired" data, where repaired means that the data has had the effects of "glitches" such as noise spikes, clipping, gauge tilt and misorientation removed.
- 6) Can divert error and other informational messages away from the user console to a special text file if the user suspects that the session could result in an inordinately large number of messages.
- 7) Can plot the data.

There are extensive "help" packages available that are user accessible during a data base retrieval session.

V. Current Status

The Data Base is now accessible to all users who have, or can obtain, open access to the CRAY computers in the Los Alamos Integrated Computer Network (ICN). The user manual is available both on disk and as a separate Los Alamos Report (LA-UR-94-1538).

The goal is to make the data available to as much of the research community as possible—there are no restrictions on its use. Users can incorporate any or all of the data into their own local data bases if they so desire. We invite other researchers to make their strong motion data accessible to us for incorporation into this data base, and encourage the use of all of these data by the Arms Control and Non-Proliferation Community.

VI. Future

By common agreement, all data collected on the NPE is generally available to all researchers. We intend to incorporate all close-in motion data collected on the NPE into the data base so that it can be part of the much larger collection of data. We believe this would enhance the value of the NPE data. As time and funding permit, we will continue to put old data into the data base, including digitized records from paper plots, old reports, etc. Also, as more data becomes available from Los Alamos conventional underground explosions in support of the Subsurface Nudet Analysis Research (SNARE) Program, it will be entered into the data base—for access by the entire SNARE research community. We would like to incorporate data acquired by other test sponsors into this data base, just as we are providing the Los Alamos acquired data to the community at large.

Finally, we intend to integrate geologic and properties data (the complete geologic section at each event site along with the salient material properties) into the ground motion data base. This will provide

a very powerful capability for investigating the dependence of close-in motion on source region material properties.

VII. Summary

The NTS Ground Motion Data Base is the culmination of a mammoth effort in data acquisition, processing, and storage that has spanned a period of over 20 years and consumed countless man-hours. The data base provides our research community convenient access, *in the open environment*, to approximately 12,000 digitized waveforms of strong motion data from 148 underground explosions.

The data base is a valuable resource to the Arms Control and Non-Proliferation Programs, especially since Secretary O'Leary's declassification of previously unannounced tests. However, we believe that the value and usefulness of the data base would be at least doubled with a single stroke—the declassification of event yields. For almost any study involving underground explosions, the source energy term is vitally important. The current classification of yields makes use of such source terms cumbersome and expensive, and limits participation to certain researchers.

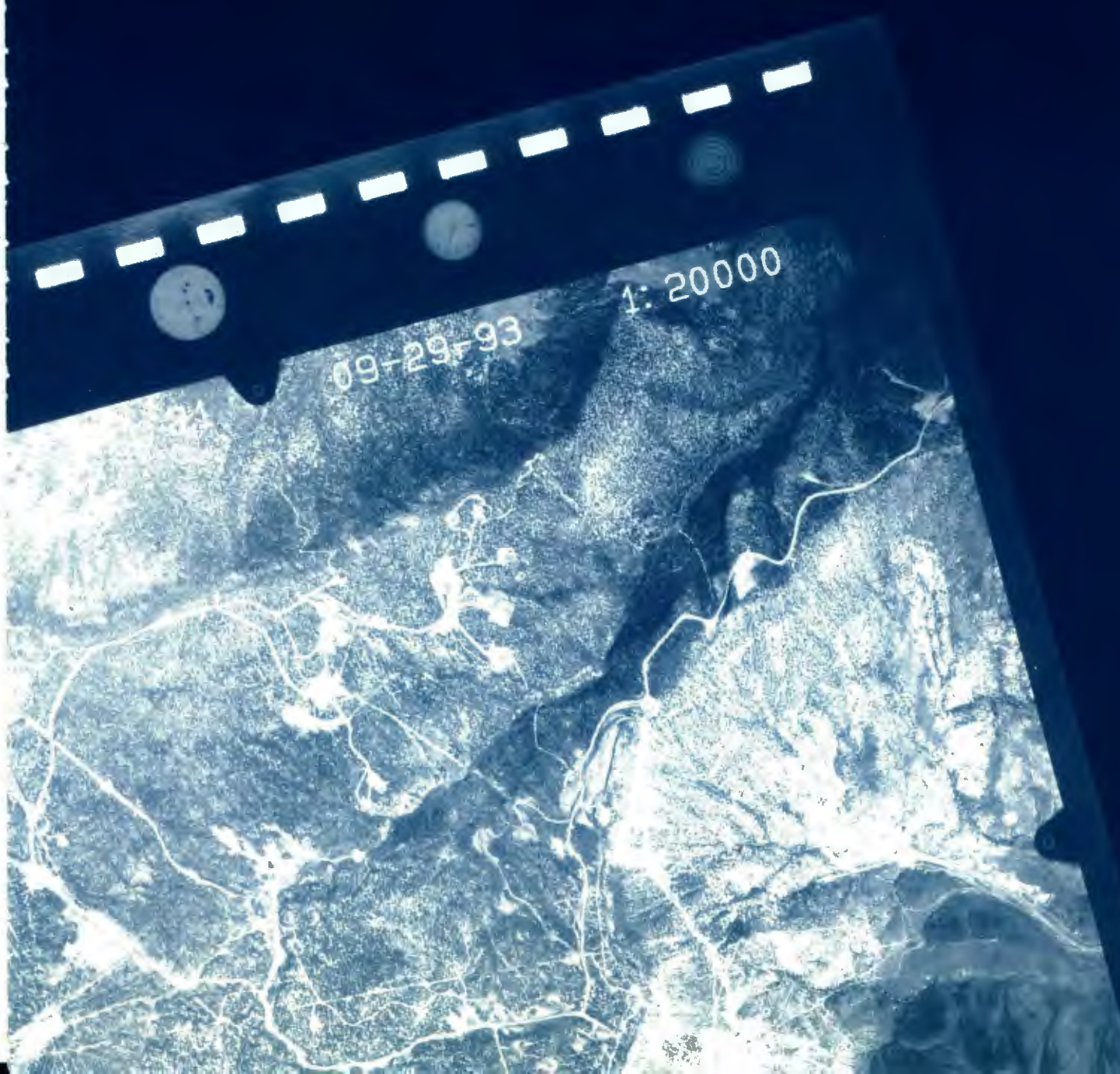
Finally, we encourage all interested parties to join in our efforts to make these strong motion data available to the entire Arms Control and Non-Proliferation community.

VIII. Acknowledgments

Many individuals contributed over the years to the effort of putting together this collection of data. Early participants were Judy Winterkamp, Jim Neergaard, and Nancy Marusak of the GEODES Project, who coordinated with Fred App and made the necessary changes to GEODES to accommodate ground motion data. Roy Saunders, Lorraine Medina, Carol LaDelfe, Bob Deupree, Fred App, and Roy Boyd all were active at one time or another in updating and adding data to the data base. Tom Tunnell and Albert Martinez of EG&G developed and applied data repair techniques to much of the data. LANL Group J-8 (now DX-12) had the very large task of actually acquiring and processing most of the data. Bob Fitzhugh of J-8 deserves special credit for tirelessly reviewing the data and assuring that it was of the highest possible quality. Bob Deupree was instrumental in getting data from other sources and for a time was key in keeping the data base effort going. George Jordan (EG&G) and Fred App collaborated on the development of the ntsgm retrieval program that allowed the move away from GEODES and the closed computing environment.

None of the Data Base work could have proceeded without the cooperation and long term support of Jack House, in his capacity as Nuclear Test Containment Program Manager, and Tom Weaver, as Deputy Group Leader of the EES-3 Geophysics Group. More recently, Wendee Brunish, in her capacity as Containment Leader, has lent her support to the effort. Finally, none of this would have happened without the concurrence of J-Division (now part of DX-Division) field test office for making the ground motion measurements in the first place.

NONSEISMIC TECHNOLOGIES



Atmospheric Methods for Nuclear Test Monitoring

David J. Simons
Los Alamos National Laboratory

History of Infrasound/Acoustic Monitoring

In 1979 the Department of Energy undertook a Research and Development program to examine the utility of so called "atmospheric methods" for the detection and monitoring of underground nuclear explosions. "atmospheric methods" are detection technologies which sense the disturbances in the air which result from ground motion above a nuclear explosion buried in the ground. This work was motivated by the understanding in 1979 that for a comprehensive test ban there would be several problems that seismic monitoring alone would not be able to address (in particular discrimination for shallow events). There was also the desire to seek out other detection phenomenology to fulfill the generally accepted idea that dual phenomenology should yield more information than any single phenomenology.

The DOE followed two line of research each developing a somewhat different detection scheme with sensitivity to different aspects of essentially the same phenomenon, that is the atmospheric pressure perturbations arising from the motion of the ground surface above a contained explosion. The *Near Infrasound Technique* concentrated on the detection of signals in the frequency range of 10 to 0.1 hertz at distances of several hundred kilometers away from ground zero, while the *Ionospheric Monitoring Technique* utilized radio wave sounding methods to detect disturbances in the ionosphere 100 to 150 kilometers in the atmosphere above an underground nuclear explosion. Over a ten-year period the DOE demonstrated a clear and unambiguous capability to utilize these methods to detect and discriminate underground nuclear explosions.

The Near Infrasound Technique for detecting underground nuclear explosions grew out of the U.S. experience with infrasound detection of atmospheric explosions utilized during the 1960s and 1970s. This method was very successful at detecting large (megaton class) explosions at great distances. Over the twenty year period several infrasound networks were in operation. At one time the DOD operated 20 infrasound stations worldwide. As a result of this experience there is a significant data base of detections. Theoretical relations for determining yield as a function of amplitude, distance and period have also been developed and backgrounds and noise have been quite thoroughly studied.

The Ionospheric Monitoring Technique for detecting underground nuclear explosions was first suggested by Louis Wouters who performed some initial first look calculations in 1977. He was motivated by some very poorly understood but very dramatic measurements of ionospheric disturbances resulting from atmospheric nuclear explosions in the late 1950s and early 1960s. A DOE-sponsored joint Los Alamos, Livermore, and Sandia research program investigating ionospheric disturbances from

underground nuclear explosions was undertaken as a result of Wouters investigation. This program investigated the various methods of detecting and measuring ionospheric disturbances resulting from earthquakes, atmospheric explosions and underground nuclear explosions and extracting information from the measurements. Data was gathered from more than 50 underground explosions, several atmospheric kiloton class conventional explosive tests and a number of earthquakes over a period of 10 years from 1979 to 1989.

Basic Phenomenology

Atmospheric signals from underground nuclear explosions result from the movement of the ground surface immediately above a buried explosion when the initial shockwave arrives at the surface. The most coherent part of this surface ground motion occurs within a few seconds of the underground blast when the compressional shockwave generated in the ground arrives at the ground air interface. The ground surface is moved upwards violently as the shockwave attempts to carry energy into the air across this ground-air interface. The extreme difference in density between the two media presents a very large effective impedance mismatch to this wave motion. The wave is therefore primarily reflected back into the ground giving rise to the reflected seismic wave (the Pp wave so often observed in seismic signals from underground nuclear explosions.) The interaction of the reflected wave and the incident wave causes a rupturing of the ground freeing a significant piece of earth to fly freely upward accelerated by the trapped wave energy within this so called spalled region. This spalled earth can travel upwards on the order of a meter (at accelerations in excess of 1 G) or so before falling backward under the force of gravity to come crashing down upon the earth. The ground motion and the induced air pressure perturbations have a relatively complex time behavior. The phasing of the initial spall surface motion results in a well focused weak air shock wave directed straight up into the atmosphere. The half power points of this focused beam are about 27 degrees apart (each side 13.5 degrees away from the vertical). There are weaker sidelobes which permit energy to be directed at much shallower angles away from the vertical direction. The slap-down of the spalled region also causes significant reverberations in the ground surface leading to less coherent rumblings in the air which are radiated more or less isotropically.

The two detection methodologies utilizing these low frequencies disturbance in the atmosphere as stated above have come to be known as *Near Infrasound* and *Ionospheric Monitoring*.

The Ionospheric Monitoring technique has concentrated on detecting the very strong air pressure pulse which is launched straight up above the underground explosion. This disturbance travels upwards into an increasingly more rarefied atmosphere. Simple conservation of energy leads to an ever increasing wave amplitude as less and less material is moved by the same amount of energy. This amplification is more than sufficient to compensate for the minor frictional dissipation. By the time this disturbance arrives at the ionosphere, some eight minutes after slapdown, it has become a 10%

pressure perturbation and spreads some 100 kilometers across the sky. The detection scheme for this physically large disturbance involves sending radio waves through the disturbed ionosphere with transmitters and receivers on the ground. Standard radar analysis yields easily interpretable signals. The pressure perturbation in the air coupling to the ionospheric electrons results in phase changes in the radiowaves (doppler in radar parlance) which are directly interpretable in terms of the original source at the ground.

The Near Infrasound technique detects the signal which is projected into the side-lobes of the seismic signal discussed above. Early experiences from utilizing very large atmospheric nuclear explosions as a source for infrasound demonstrated that near tidal acoustic gravity modes were excited by such explosions (Figure 1). These ultra low frequency waves traveled all the way around the world. The explosion also generated a nearly isotropic shockwave which was detectable at many hundreds to many thousands of kilometers from the explosion. Figure 2 shows the sound paths followed by these waves as they propagated up into the high atmosphere and were returned to the ground only to be reflected back upwards and continue around the world. These waves are effectively ducted between the earth's surface and the high altitude thermocline where the atmospheric temperature rises very rapidly yielding a corresponding increase in the sound speed. Since waves left the explosion at all possible inclination angles the entire space in the duct was in fact filled with the signal as it bounced between the ground and the thermocline. The ground motion signal unlike the atmospheric explosion generated wave is not isotropically generated. These air pressure perturbations travel out at lower elevation angles eventually moving up into the atmosphere as shown in Figure 2 and return to the ground in a like manner. As they are weaker than the atmospheric explosion case they will not be as easily detected at many bounces from the source region. The refraction occurs in any region in which the effective sound speed exceeds the sound speed on the ground. This can be caused by winds aloft in the 50 to 60 kilometer altitude region of the atmosphere or if there are no such winds when the waves arrive at the thermocline 100 kilometers in altitude. The perturbation travels back to the ground and fills the duct in a similar manner to that described above for the case of an atmospheric explosion.

The DOE Research Program on Detection of Underground Tests and the NPE

The Department of Energy developed very sensitive detection schemes for both Near Infrasound and Ionospheric Monitoring over several years of research using underground tests at the Nevada Test as the source of the disturbances. In the case of Ionospheric Monitoring the research effort demonstrated conclusively that kiloton class and larger underground nuclear explosions could be routinely detected by ionospheric techniques at distances up to 3000 kilometers. The phenomenology is very well documented and could be quite easily utilized for monitoring if the appropriate circumstances would arise. Routine monitoring for underground nuclear explosions by this inherently active technique proved to be too capital and labor intensive to justify operational deployment. While we do not believe that it is

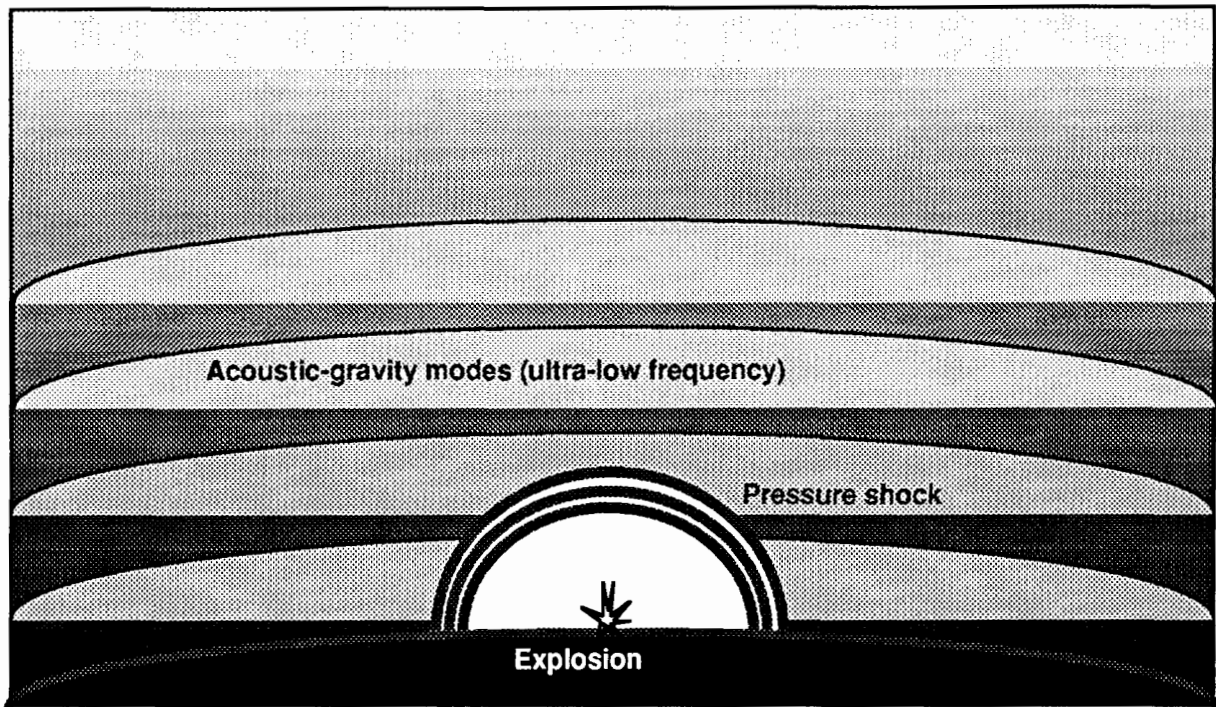


Figure 1. Atmospheric disturbance from large (MT) explosions.

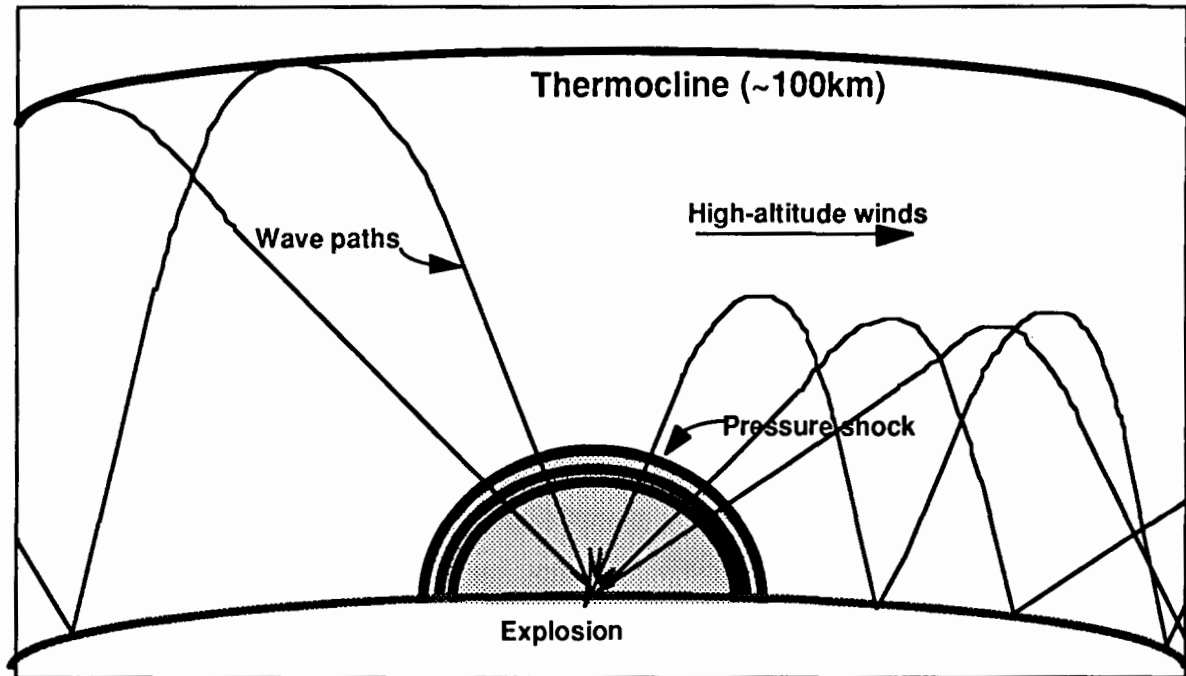


Figure 2. Atmospheric disturbance from explosions.

economically justifiable to utilize this technique in a worldwide monitoring regime there are circumstances in which important and unique data may be obtained utilizing the method. The DOE has supported a small research program, EDIT (Explosion Discrimination with Ionospheric Techniques) over the last two years to determine if the vast experience gained from this ionospheric research program might be applied to the special problem of discriminating quarry activities from underground explosions in particularly troublesome areas. Figure 3 shows the various ionospheric radar sounding methods that were utilized for the research program. These included verticle ionosondes, verticle and bistatics phase sounding and Over-the-Horizon radars. Table 1 summarizes the results of the research program.

Table 1. Results of the DOE Ionospheric Disturbance Program.

- Demonstrated detection of Underground tests at regional and continental distances.
- Developed discrimination between earthquakes, surface explosions and UGTs.
- Developed effective discrimination between signals and noise.
- Proved too expensive for general utilization at regional distances.

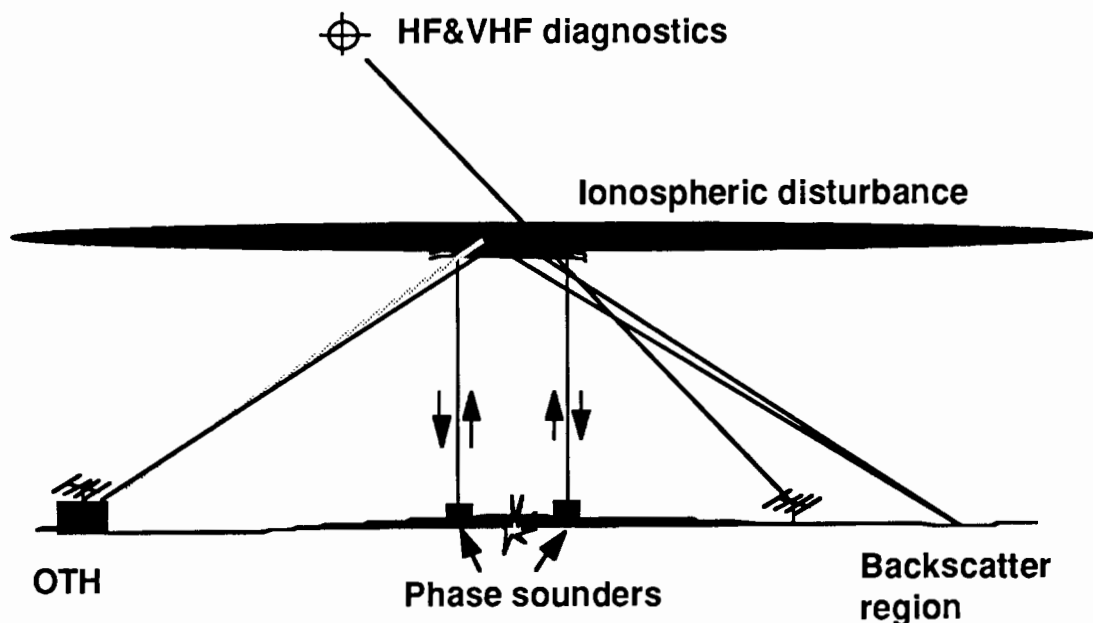


Figure 3. Ionospheric detection methods.

In a like manner the DOE Near Infrasound research program demonstrated detection of underground nuclear explosions at regional distances by examining the signals from more than 60 underground test at the Nevada Test Site. It also gathered data of near infrasound signals at regional distances from large earthquakes. The program pursued background and noise reduction studies as well as examining the impact of high altitude winds on signal strength. It was discovered that the signal amplitude could be corrected or normalized from standard high altitude wind models to achieve a reproducible signal amplitude which then made it possible to not only detect signals from underground nuclear explosions but to extract a measure of explosive yield from this data. The complex ducting of the signals between the thermocline and the earth required the use of signal propagation models to properly deduce the origin of the signals. These propagation models were developed and their utility was demonstrated for the case of Nevada Test Site explosions. The results of the research effort are summarized in table 2. If an infrasound system should be deployed by an international monitoring regime for purposes of detecting atmospheric nuclear explosions we feel that there will be some dual phenomenology gain from monitoring underground tests as well.

Table 2. Results of the DOE Near Infrasound Program.

- Demonstrated detection of underground explosions at regional distances on more than 60 tests.
 - Carried out background and noise reduction studies.
 - Derived wind normalization for amplitude correction.
 - Demonstrated appropriate propagation models.
 - Collected data set of signals from large Earthquakes.
-

The NPE was carried out to test all of the various detection methodologies that might have applicability to a Comprehensive Test Ban regime. Given the vast experience that DOE had with these atmospheric methods it seemed quite appropriate to test their synergism with the rest of the measurements to carried out for the NPE. There was one infrasound station located in St. George, Utah operated during the NPE. This station has been operated by Los Alamos as part of the underground test detection program for many years. Los Alamos also maintains a bistatic ionospheric sounding array which routinely monitored for underground test at the NTS. This array was also operated as part of the EDIT program for the NPE. The results of the atmospheric measurements experiments are presented later in this document.

Implications for a Comprehensive Test Ban regime

Far Infrasound (0.1 Hz to 0.001 Hz) in contrast to Near Infrasound (10 Hz to 0.1 Hz) has demonstrated applicability for monitoring for atmospheric nuclear explosions at distances in excessive a 1000 kilometers. The Near Infrasound is more effective within 1000 kilometers. The dependence of

frequency upon distance from the source results from the nonlinear stretching of strong acoustic signals. Combining both Near and Far infrasound detection within a single system provides better spatial coverage and extends infrasound utility to underground tests as well as atmospheric tests giving such a system broader monitoring scope. There are very strong arguments for inclusion of infrasound in a total monitoring regime. Figure 4 compares the optical signal of a free air nuclear explosion with one surrounded with 100 Megagrams of water. This is the amount of water contained in an approximately 3-meter radius sphere. It is fairly easy to detonate an explosion under three meters of water or dirt. The figure makes the same comparison for the air shockwave which is the source of the infrasound signal. While the optical signal becomes marginally recognizable the air shockwave is essentially unchanged. A similar result is obtained with very shallow burial in dirt. While both of these cases will result in a well contained debris cloud a distant signal is necessary to target collection resources. In this example the infrasound signal could serve as the alarm to enable the debris collection. This emphasizes the utility of infrasound measurements within the context of a CTBT. The cost and simplicity of such a detection system make it even more appropriate for countries other than the U.S. to build, field and operate as distributed parts of a worldwide regime.

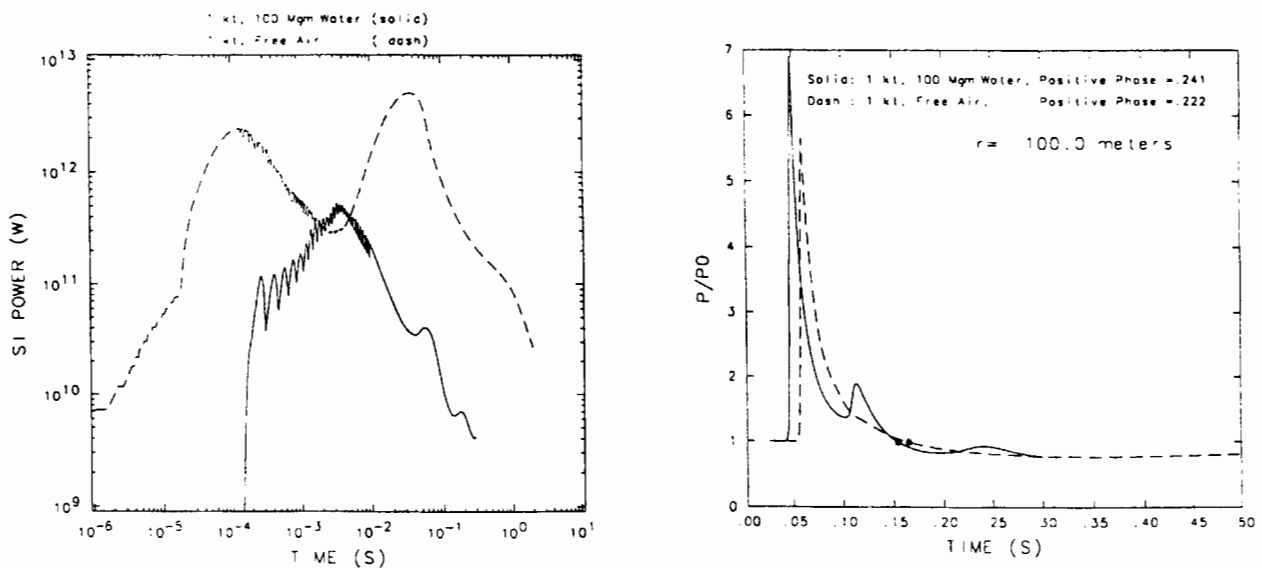


Figure 4. The atmospheric signal is very difficult to mask.

Ionospheric Measurements for the Non-Proliferation Experiment

T. Joseph Fitzgerald

Los Alamos National Laboratory, Los Alamos, New Mexico 87545

Abstract

The detection of explosions using ionospheric techniques relies on measuring perturbations induced in radio propagation by acoustic waves which disturb the electron density of the ionosphere. Such techniques have been applied to the detection of atmospheric explosions, underground nuclear tests, earthquakes, and surface mining explosions. The nighttime ionosphere presents a difficulty for the detection of explosions because in the absence of solar ionizing radiation the electron density in the altitude range of 90 to 200 km decays after sunset and perturbation effects are correspondingly reduced. On the other hand, acoustic waves produced by weak sources reach a maximum amplitude in the altitude range of 100 to 150 km and are highly attenuated at altitudes above 200 km. For safety reasons, most planned explosions are conducted during daylight which has limited our experimental measurements during nighttime. However a recent opportunity for a nighttime measurement occurred in connection with the Non-Proliferation Experiment which consisted of the detonation of a large chemical charge underground at the Nevada Test Site near midnight local time. Our results, based on a new technique of using medium frequency radio transmissions provided by commercial broadcasts to detect explosion effects, were negative. The most likely explanation for the negative result is that the radio transmissions did not reflect at a low enough altitude to sense the perturbations produced by the acoustic waves

1 Introduction

Los Alamos National Laboratory has made ionospheric measurements in conjunction with approximately eighty underground explosions at the Nevada Test Site; the original suggestion of the possibility of ionospheric disturbance following an underground explosion was made by *Wouters* [1971]. The surface ground motion above the explosion produces a low-frequency acoustic wave the energy of which is mostly directed vertically; air pressure perturbations in the lower atmosphere associated with the acoustic wave were measured by *Banister and Hereford* [1991]. The amplitude of the acoustic waves as they propagate vertically is controlled by four factors: a decrease due to geometric spreading, an increase due to propagating into lower air density, a decrease due to losses at shocks, and a decrease due to viscosity effects [*Banister*, 1982]. Viscosity increases greatly in the altitude regime for which the neutral mean free path reaches values of the order of the acoustic wavelength which usually occurs above 100 km. The amplitude of acoustic waves from weak sources near ground level reaches a maximum in the altitude range from 100 to 150 km.

Our detection technique measures perturbations imposed on radio waves propagating through the ionosphere by changes in electron density which alter the index of refraction of the radio waves. The electron density changes result from changes in neutral density accompanying acoustic waves which propagate to the ionosphere from the explosion. Thus the detection process demands that the ambient electron density be sufficient that the changes produce a noticeable variation of the index of refraction. The nighttime ionosphere presents a difficulty because the electron density in the lower ionosphere where the acoustic waves reach maximum amplitude decays after sunset. During the daytime the electron density of the lower ionosphere is maintained by two competing processes: production via solar ionizing radiation and recombination via a number of chemical reactions. During the nighttime, the electron density of the lower ionosphere decays by as much as an order of magnitude. On the other hand, diurnal changes in the electron density of the upper ionosphere are less severe because at the lower neutral density the production and recombination mechanisms differ and serve to sustain ionization through the night.

In this report we present our measurements of two explosions conducted at the Nevada Test Site (NTS). The first was made in conjunction with the Hunters Trophy nuclear test which was conducted during daylight. We employed the technique of reflection of high frequency radio waves to remotely detect acoustic waves produced by ground motion. The second measurement was made in conjunction with the Non-Proliferation Experiment (NPE), the detonation of a 1.4 kt charge of chemical explosive in almost the same location as the Hunters Trophy test. For the NPE measurement, we monitored the ionospheric reflection of transmissions of medium frequency broadcast stations.

2. Ionospheric Detection of Explosions

We have detected the air blast from unconfined explosions with yields of less than one ton using the sensitive technique of observing perturbations induced by acoustic waves on radio signals reflected from the lower ionosphere [Fitzgerald and Carlos, 1992]. This technique, which has been applied by many researchers to detect acoustic waves produced by surface explosions, earthquakes, and underground explosions, relies on the sensitivity of the reflection process to small perturbations in the ionosphere near the reversal point. By placing transmitters and receivers at ground sites so that the reflection region is over the explosion, we can remotely sense perturbations from distances of hundreds of kilometers. During daylight we have employed radio transmissions in the high frequency (hf) band (3-30 MHz) to monitor explosions. Medium frequencies (mf, .3-3 MHz) are highly absorbed during daylight while very high frequencies (vhf, 30-300 MHz) do not reflect. At night hf transmissions reflect at such high altitudes that detection of weak explosions becomes difficult. Medium frequencies suffer much less attenuation at night and reflect from altitudes that are sensitive to weak explosions.

2.1 Nighttime Ionosphere

The electron density distribution in the ionosphere is commonly described in terms of layers although the transition between them is not always distinct. The highest, the *F* layer, usually contains the maximum electron density in the ionosphere attained at altitudes of 200 to 300 km and equal to about 10^{12} m^{-3} . The *F* layer persists during the night with only a slightly decreased density although the altitude of the maximum rises. During daylight, the electron density in the lower ionosphere is strongly controlled by solar radiation. At the lowest altitudes, the *D* layer (60-90 km) causes absorption of radio waves propagating to the upper ionosphere; the *D* layer disappears at night. The electron density in the *E* layer (90-120 km) reaches a local maximum of about 10^{11} m^{-3} during daylight. Between the *E* and *F* layers there is often a transition layer designated *F1* which disappears at night. In the absence of solar ionizing radiation the phenomenology of the lower ionosphere during nighttime differs markedly from the typical daytime distribution and has been investigated using a variety of techniques: sounding rockets [Smith, 1970], incoherent scatter radar [Shen et al., 1976], and ionograms [Watts, 1957]. On average, there is a maximum in electron density between 100 and 110 km altitude; the value of the maximum depends upon the solar cycle. Wakai [1971] fitted the following line to measurements of peak electron density, N_m , obtained over a period of three years: $N_m = 2.21 \times 10^9 (1 + 0.0062 R) \text{ m}^{-3}$ where R is the sunspot number. The source of this peak, which defines what is called the nighttime *E* layer, has been attributed to hydrogen Lyman α and Lyman β scattered from the geocorona [Ogawa and Tohmatsu, 1966]. Imbedded in this layer, there often are additional layers with much higher density and narrower altitude distributions which are labeled sporadic *E* or *Es* because of their intermittent existence [Smith, 1970]. The cause of *Es*

layers is generally attributed to concentration of metallic ions of meteoritic origin by gravity waves in the neutral atmosphere [Hermann *et al.*, 1978]. The electron density at altitudes between the top of the nighttime *E* layer at 120 km and the bottom of the *F* layer at 180 km are about 10% of the peak density in the *E* layer under quiet conditions of the geomagnetic field [Wakai, 1971]. However, this valley often displays enhanced electron densities in a form labeled 'intermediate layers.' These layers appear at altitudes of 160 km with a peak concentration that increases with the disturbance level of the magnetic field; their height gradually decreases over a period of hours so that they merge with the nighttime *E* layer. Their origin appears to result from concentration of ionization produced by energetic particles of solar origin [Shen *et al.*, 1976]; the concentration mechanism is attributed to long period waves in the neutral atmosphere (solar tides) inducing ion motion along the magnetic field [Fujitaka and Tohmatsu, 1973]. The peak density can reach levels of one order of magnitude greater than that in the nighttime *E* layer [Wakai, 1971].

2.2 Measurement Technique

If one ignores the effect of the geomagnetic field, the index of refraction of the ionosphere for a radio wave of frequency, f , is $\sqrt{1 - f^2 / f_N^2}$ where f_N is called the plasma frequency [Davies, 1990]. The plasma frequency is proportional to the square root of the electron density: $f_N^2 = Nc^2 r_e / \pi$ where N is the electron density, c is the speed of light, and r_e is a constant (the classical electron radius). Using mks units, $f_N^2 \approx 81N$. A vertically propagating radio wave will be reflected at the altitude for which its index of refraction is zero; that is, the altitude for which $f = f_N$. Typical critical frequencies for reflection for the vertical reflection from the *E* layer range from 500 to 800 kHz while they range from 4 to 6.5 MHz for reflection from the *F* layer. For a sunspot number of 100, the critical frequency of the *E* layer is about 540 kHz; thus at night, for distances greater than 600 km, broadcasts in the medium-frequency am band (< 1500 kHz) will reflect from this *E* layer [Davies, 1990].

In our technique of remote monitoring of the ionosphere we use oblique propagation rather than vertical; that is, we locate a radio transmitter and receiver at spatially separated sites such that the explosion is close to the mid-path. This geometry makes the reflection process sensitive to acoustic waves propagating directly from the explosion to the ionosphere. It can be shown that oblique propagation at a frequency, f , is equivalent with some restrictions to vertical propagation at a frequency of $f \cos \phi_0$ where ϕ_0 is the angle of incidence of the ray upon the ionosphere [Davies, 1990]. That is, we can reflect at the same altitude in the ionosphere by increasing the frequency of our obliquely propagating radio transmission as we increase the separation our transmitter and receiver.

We broadcast multiple frequencies from each transmitter location; the frequencies are chosen so that they reflect from sufficiently separated altitudes to allow time delay discrimination of vertically propagating acoustic waves. The use of multiple frequencies also allows some redundancy in the measurements. We

detect the high frequency radio signals with Racal 6790GM receivers operated in continuous wave mode which produce a low-passed audio signal at a frequency between 20 to 50 Hz which is digitized and stored. Moreover, we employ a spatial array of antennas at the receive locations so that we could conduct interferometry and array processing of the disturbances.

2.3 *Hunters Trophy*

For the Hunters Trophy experiment we employed two transmitter locations, one at Tonopah Test Range (TTR) and the other at the EPA Farm in Area 15 of the NTS; we also employed two receiver locations, one near Well 5e (WLS) in Area 5 of the NTS and the other at Indian Springs AFB (ISP). The map in Figure 1 shows that these locations give sensitive regions over Area 19, Area 12, and Area 3. The primary path for the experiment was TTR—ISP which reflected almost directly over the site of the explosion. The frequencies of the transmissions, 2.83 and 2.93 MHz, were chosen to reflect in the *E* layer near 100 km altitude; the frequencies of the two transmit sites were offset by 30 Hz so that they could record simultaneously at each receive site. Figure 1 also shows the disposition of the receive arrays. The explosion was conducted at 1700 UT on Sept. 18, 1992.

The transmissions that we use for monitoring explosions have high phase and amplitude stability; therefore, variations in phase and amplitude of the received signal arise from propagation effects among which the reflection process is the most important. A convenient way of displaying the time variations of the received signal is to plot the power spectrum of the complex amplitude versus time. That is, our received signal can be written as $a(t) \cos 2\pi ft$ where $a(t)$ is a complex time series. Our radio receiver and data analysis removes the $\cos 2\pi ft$ variation which contains no information. Variations in the phase of $a(t)$ can arise from changes in the length of the propagation path; variations in the magnitude can arise from interference between multiple reflections, from focusing, and from variations in absorption. The time rate of change $a(t)$ is relatively slow so that power spectrum will usually show a peak near a frequency of 0 Hz. Figure 2 shows such a plot of the power spectrum versus time between 100 and 600 s after the Hunters Trophy test for the 2.83 MHz transmission between TTR and ISP, that is, the path reflecting almost directly over the explosion. There is a distinct broadening of the spectrum at about 320 s which corresponds to the acoustic travel time to the reflection altitude near 100 km. Such a broadening is also observed on the 2.93 MHz data but with a delay of about 2 s which corresponds to the differential delay to the slightly greater reflection altitude ($\sim .5$ km) of the higher frequency transmission. The perturbation for paths not reflecting directly above SGZ takes a different form than that shown in Figure 2; the perturbation is spread out in time between 330 and 350 s and appears as peak in frequency that moves from positive to negative Doppler shift. Our interpretation of this effect is that the perturbation produces a scattering from a point at the intersection of the spherically expanding acoustic wave and the horizontal plane of the reflection altitude [Fitzgerald and Carlos, 1992]. The phase path initially decreases as the intersection point

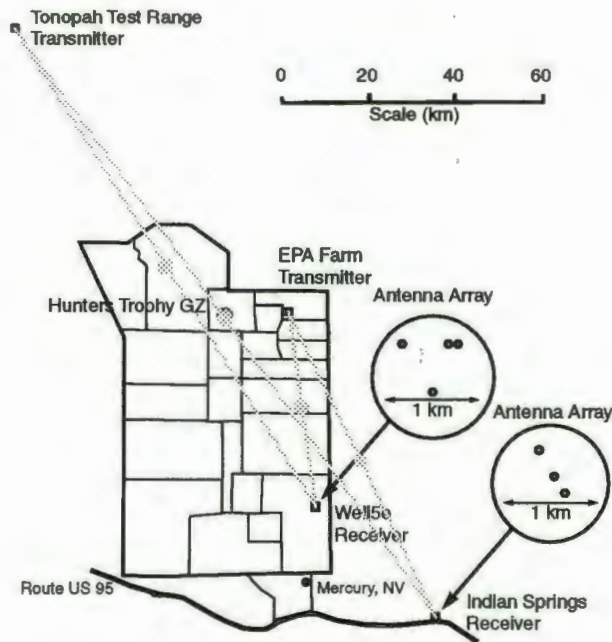
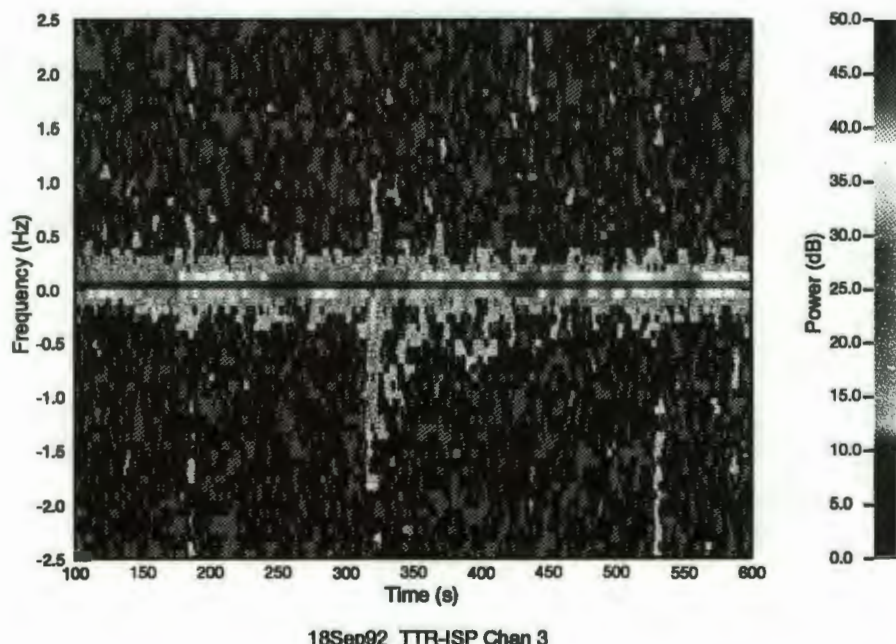


Figure 1: Map of transmit and receive locations for the Hunters Trophy experiment. The path from the Tonopah Test Range to the Indian Springs AFB reflected almost directly over the explosion.



18Sep92_TTR-ISP Chan 3

Figure 2: Power spectra versus time for the 2.83 MHz transmission from the Tonopah Test Range received at Indian Springs during the period from 100 to 600 s after the Hunters Trophy test. There is a broadening of the spectrum at about 320 s corresponding to the passage of the acoustic wave through the reflection altitude.

approaches midpath producing a positive Doppler shift; after passing through midpath the phase path increases producing a negative Doppler shift.

3. Non-Proliferation Experiment

The Non-Proliferation Experiment (NPE) was designed to compare measurements that have been obtained with various diagnostics that have been used to characterize nuclear explosions with the same measurements using a large chemical explosion as a source. A charge of 1.29 kt of a mixture of ammonium nitrate and fuel oil (ANFO) was detonated in a cavity in Area 12 of NTS near the site of the Hunters Trophy experiment at 7:01 UT on Sept. 22, 1993 [Zucca, 1993].

3.1 *Experiment*

Because the NPE was scheduled for the middle of the night, the network that we deployed for the Hunters Trophy event (Figure 1) would have had to use frequencies of less than 1 MHz to reflect in the *E* layer. We are uncertain of how well our transmitters would perform at such a low frequency; moreover, we did not have frequency authorization to operate in the am broadcast band. Therefore we chose instead to monitor the carrier of am broadcast stations near Las Vegas from a site near Tonopah, NV; the midpath for this geometry is over Area 12 of NTS. The frequencies of the monitored broadcasts were 720 (KDWN), 840 (KVEG), 920 (KORK), and 1140 kHz (KLUC); the signals at 720 and 840 kHz could be identified and were primarily from Las Vegas. At the two higher frequencies many stations were transmitting and the interference prevented any identification of the Las Vegas broadcasts. The stations at 720 and 840 kHz use powerful transmissions of 50 and 25 kW respectively and have only a limited competition from other broadcasts; the stations at 920 and 1140 kHz are limited to low power operation [Sennitt, 1993]. Figure 3 shows the locations of the transmit and receive sites in relation to the NPE explosion. The receiver site was located at 38.07° N, 117.12° W; the KDWN transmitter is located in Henderson, NV (36.04° N, 114.98° W) while the KVEG transmitter is located outside of Las Vegas at 36.43° N, 115.28° W. The location of the NPE event was 37.20° N, 116.21° W so that the mid-path of the KDWN transmission was 23 km from surface ground zero (SGZ) while the mid-path of the KVEG transmissions was 5 km from SGZ [Zucca, 1993]. We deployed two receive antennas separated by 460 m in the North-South direction; we monitored the four transmissions with each of the receive antennas using Racal 6790GM receivers operated in continuous wave mode with a narrow bandwidth filter that eliminated the sidebands caused by the amplitude modulation. Data storage and reduction were the same as described above for the Hunters Trophy experiment. As a check on the stability of the broadcast transmissions we monitored the 720 and 840 kHz frequencies using receivers at Los Alamos; we did not expect to see any effects of the NPE explosion in this data because the reflection point would be too far away.

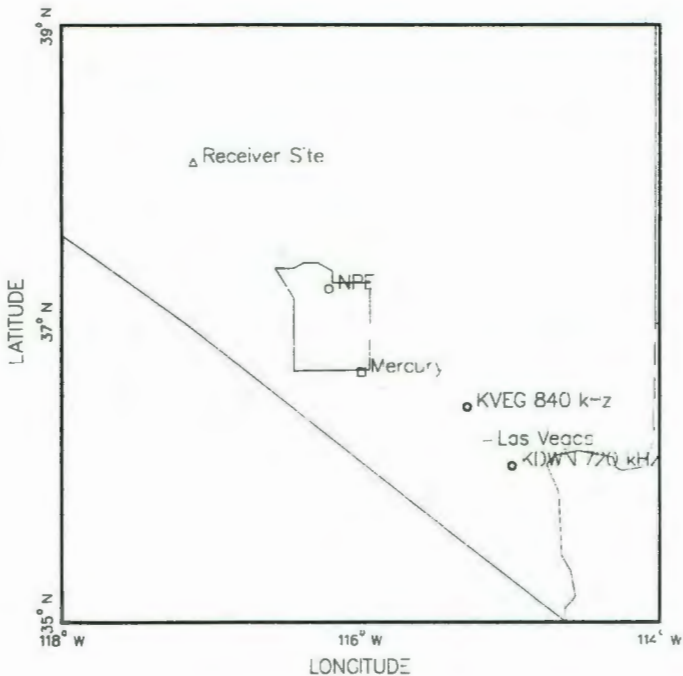
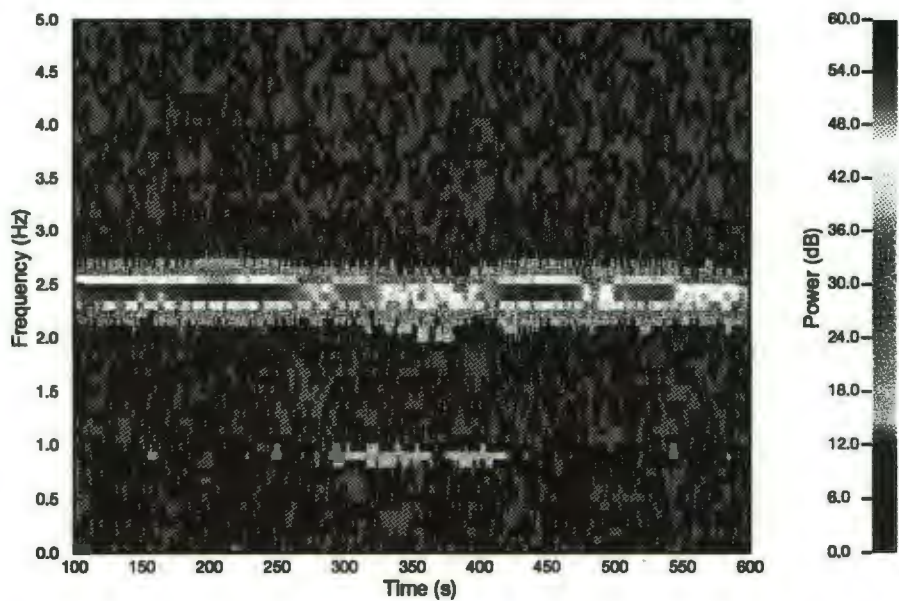


Figure 3: Map of transmit and receive locations for the Non-Proliferation Experiment (NPE). A receiver site near Tonopah, NV, was used to monitor broadcast stations near Las Vegas.

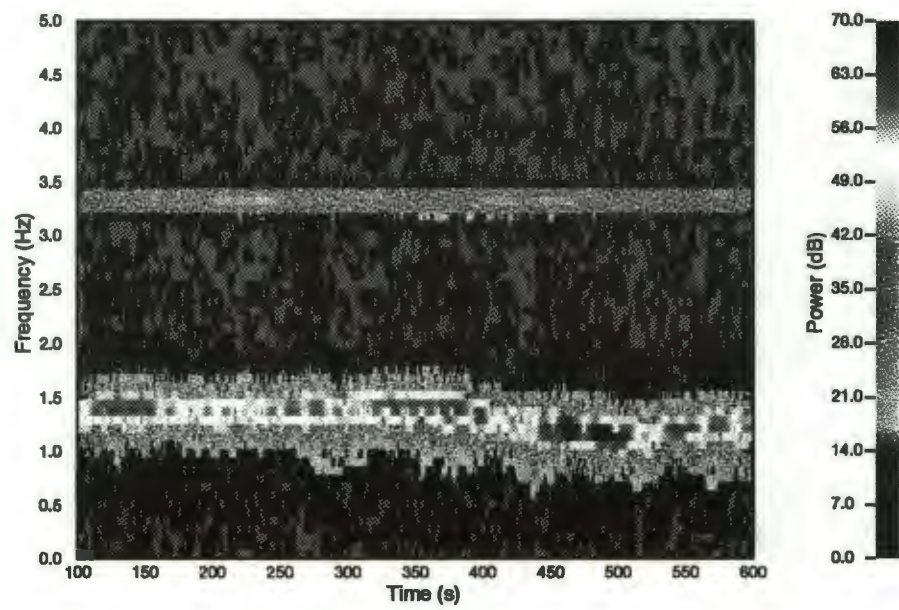
3.2 Results

Figure 4 shows the power spectra versus time for the 720 kHz frequency received at Tonopah for the period of 100 to 600 s after the NPE explosion; we identify the peak near 2.5 Hz as the carrier of the Las Vegas broadcast because it was the major peak in this data. The offset of 2.5 Hz is mostly a result of the difference in the reference oscillator at the transmitter compared to the Rubidium oscillator reference of our receivers and does not represent an ionospheric reflection effect. There is a weaker carrier at about 1 Hz which has not been identified. The 2.5 Hz peak displays long and short term fading indicative of ionospheric propagation effects. This power spectral display indicates that there were no short duration perturbations in this time interval of likely effects which could be attributed to the explosion at the 60 dB signal-to-noise level. Figure 5 is a similar display of power spectra versus time for the 840 kHz frequency received at Tonopah. The peak near 1 Hz is attributed to the Las Vegas broadcast; there is a weaker peak near 3 Hz that has not been identified. Again the offset of the 1 Hz peak is caused by a difference in the reference oscillator; there is also a long period drift of the centroid of the peak which is caused by an unstable reference at the transmitter. The peak does show short period fading indicative of interference of two or more propagation modes. There is no short duration perturbations during this time period which could be attributed to effects of the NPE explosion at the 70 dB signal-to-noise ratio.



22Sep93_Tonopah Chan 4

Figure 4: Power spectra versus time for the 720 kHz transmission received at Tonopah during the period from 100 to 600 s after the NPE explosion. The peak near 2.5 Hz is the carrier of the Las Vegas broadcast; no perturbations attributable to explosion effects are evident.



22Sep93_Tonopah Chan 5

Figure 5: Power spectra versus time for the 840 kHz transmission received at Tonopah during the period from 100 to 600 s after the NPE explosion. The peak near 1 Hz is the carrier of the Las Vegas broadcast; no perturbations attributable to explosion effects are evident.

4. Discussion

Preliminary results indicate that the ground motion near SGZ for the NPE was similar to that for Hunter's Trophy [Taylor, 1993]. It is likely that an acoustic pulse of similar amplitude and duration was produced for the two events; indeed, infrasound from the NPE was detected at St. George, Utah [Whitaker, 1993]. The absence of a definite signature in our data following the NPE is therefore puzzling.

4.1. Propagation

One possible explanation for our negative results is that we did not achieve reflection from the *E* Layer that we desired because the electron density was low. Solar activity as measured by the sunspot number, *R*, had decreased to a very low level of 40 during the week preceding the NPE. As indicated above, the peak electron density in the nighttime *E* Layer decreases with decreasing values of *R* and could have reached a level that would not have supported *E* Layer propagation between the 720 kHz broadcast transmitter and our receiver station. To test this hypothesis, we have computed a numerical raytrace for the 720 kHz frequency using a model ionosphere. The electron density distribution versus altitude was obtained from the International Reference Ionosphere (IRI) computer model using a sunspot number, *R* = 40, and a local time of 2300 [Rawer and Bradley, 1987]. A plot of the model density is shown in Figure 6; the maximum density in the *E* Layer is $2.14 \times 10^9 \text{ m}^{-3}$. Figure 7 shows the results of the raytrace for a frequency of 720 kHz (ordinary magneto-ionic mode); *T* represents the location of the transmitter and *R* the location of the receiver. The different lines show raypaths with different elevation angles; the highest elevation angle path represents a homed ray connecting the transmitter and receiver. This ray reflects in the *F* layer at an altitude of about 180 km. The low angle rays which reflect in the *E* layer approach to within about 40 km of the receiver but then penetrate the *E* layer and return to the ground at much greater distances. The other frequencies monitored were higher than 720 kHz and would penetrate the *E* layer at even lower elevation angles and thus would not approach as close to the receiver location. The extraordinary magneto-ionic mode has lower critical frequency than the ordinary mode and would also penetrate the *E* layer at lower elevation angles. These results indicate that the likely propagation for the frequencies monitored during the NPE experiment was via reflection in the *F* layer at altitudes above 150 km. Because the monitoring technique that we employed detects only the continuous wave carrier we do not have any information on the reflection altitude of the transmissions to confirm these raytraces. There should have been at least two propagation paths via the two magneto-ionic modes in either case which is the likely cause of the observed multi-path. Since the acoustic wave from the explosion would be greatly dissipated at the predicted reflection altitudes, we would expect that the ionospheric signature to be below the level of natural propagation fluctuations and not detectable.

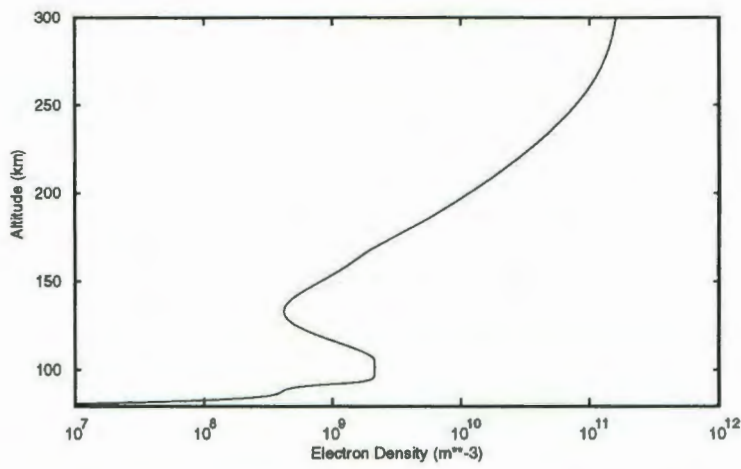


Figure 6: Model electron density versus altitude obtained from the International Reference Ionosphere for a sunspot number, $R = 40$, and a local time of 2300 [Rawer and Bradley, 1987].

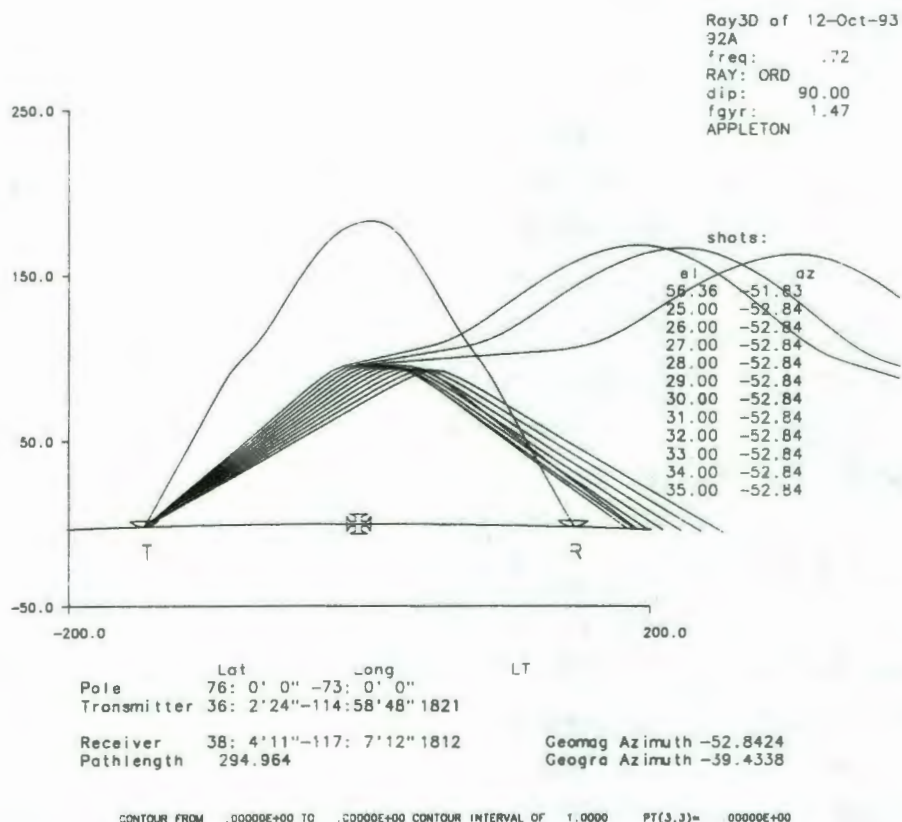


Figure 7: Numerical raytraces for the 720 kHz transmission using the model nighttime ionosphere. The predicted propagation model is via reflection in the F layer as shown by the path connecting the transmitter, T , and receiver, R .

4.2 Prediction of Effects

We may predict the level of effects that would have been observed if the 720 kHz transmission had reflected in the *E* layer for comparison to the data obtained during the NPE experiment. The first step is to obtain a description of the expected acoustic wave; we do this by assuming that the wave was comparable to that produced by the Hunters Trophy test. A description of the latter may be derived by matching numerical simulations to the measurements of the frequency shift of the received signal versus time (Doppler). We assume that the waveform has a simple symmetric profile consisting of a leading overdensity followed by an underdensity; the leading and trailing edges of the waveform are steep while there is a linear change in density in between. This waveform is called an N-wave because its profile has an N shape; the perturbation, $d(z)$, may be written

$$d(z) = \frac{az}{l} \left[\tanh \frac{z+l/2}{w} - \tanh \frac{z-l/2}{w} \right] \quad (1)$$

where z is distance relative to the center of the perturbation, a is the amplitude, l is the size of the perturbation, and w is the size of the leading and trailing edges. We assume that the acoustic perturbation radiates outward from SGZ at the sound speed, c , of 300 m/s without deformation; the local electron density, $n_e(\mathbf{r})$, at point $\mathbf{r} = (x,y,z)$ is altered by the factor $d(r - ct)$. We use a model ionosphere for n_e derived from IRI for the conditions holding during the Hunters Trophy test. We then raytrace numerically to an accuracy of <1 m every 0.1 s as the perturbation advances through the reflection altitude which for the 2.83 MHz transmission was at 94 km altitude. The raytrace calculates the phase path at each time from which we can derive a synthetic complex time series similar to the actual data. We then can analyze the synthetic time series to find the centroid of the peak frequency in the same manner as for the data. The results of such a simulation using inputs of $a = .0035$ km, $l = 0.85$ km and $w = .1$ km (Figure 8) produce a good match to the measured perturbation for Hunters Trophy which is also plotted.

With the parameters derived from the Hunters Trophy simulation we can simulate effects that would be observed at nighttime using a 720 kHz frequency. We take the path used during the NPE experiment but place the explosion at the midpoint rather than 20 km distant; we also use an ionosphere computed for a sunspot number of 100 rather than 40. Then the 720 km frequency reflects in the *E* layer at an altitude of about 94 km. We then raytrace every 0.1 s to obtain a complex time series in the same manner as for the Hunters Trophy simulation; the results are shown in Figure 9. The predicted frequency perturbation is smaller than that for the 2.83 MHz, daytime simulation; part of the difference is due to the difference in frequencies since, for the same phase path change in meters, the change in cycles, which is inversely proportional to the wavelength, would be smaller at the lower frequency. Comparison to the measured frequency shifts indicate that the predicted perturbation is less than the fluctuations in the data

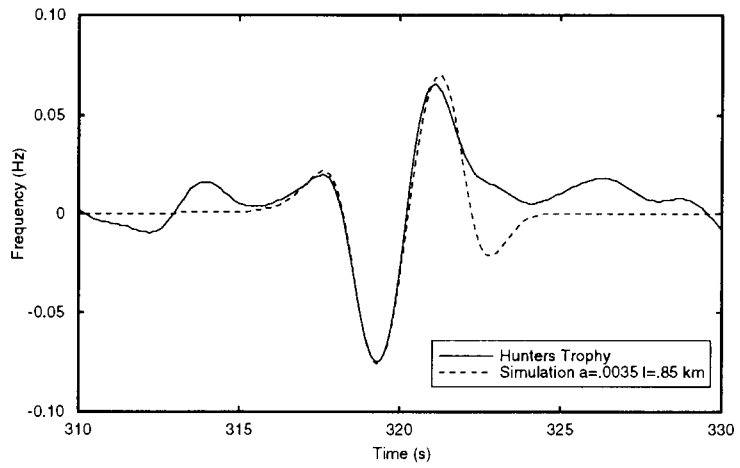


Figure 8: Comparison of the measured Doppler shift for Hunters Trophy and that predicted for acoustic wave with an amplitude of 0.35% and a length of 0.85 km.

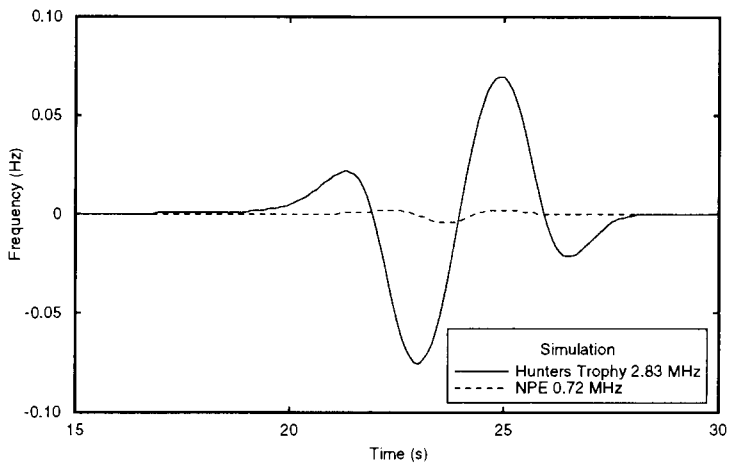


Figure 9: Comparison of the measured Doppler shift for Hunters Trophy and that predicted for acoustic wave with an amplitude of 0.35% for the Hunters Trophy conditions and the predicted Doppler shift for the same acoustic wave for the NPE conditions altered to achieve *E* layer reflection

while the Hunters Trophy perturbation is greater than the fluctuations. We would expect that the natural fluctuations would also be roughly proportional to frequency and so their level would be lower at 720 kHz than at 2.83 MHz. This discrepancy is consistent with a reflection of the 720 kHz at a higher altitude than the *E* layer because the amplitude of the acoustic-gravity waves causing the natural propagation fluctuations increases with altitude so that the *F* layer is usually more disturbed than the *E*. Another contribution to the discrepancy is the definite presence of multiple modes with slightly different Doppler shifts during the nighttime; because they fade at different times they can produce increased noise in the frequency estimate. It is likely that these multiple reflections are ordinary (*o*) and extraordinary (*x*) modes; during the daytime the *x* mode is more highly absorbed than the *o* mode so that essentially the *E* layer produces only one reflection path. From our simulation we can also predict the behavior of the power spectrum of the received signal versus time for comparison to the experimental results shown in Figures 4 and 5. Figure 10 shows the expected perturbation as a broadening of the power spectrum at the -30 dB level relative to the peak; although weak, this perturbation would be detectable under the conditions of the NPE experiment.

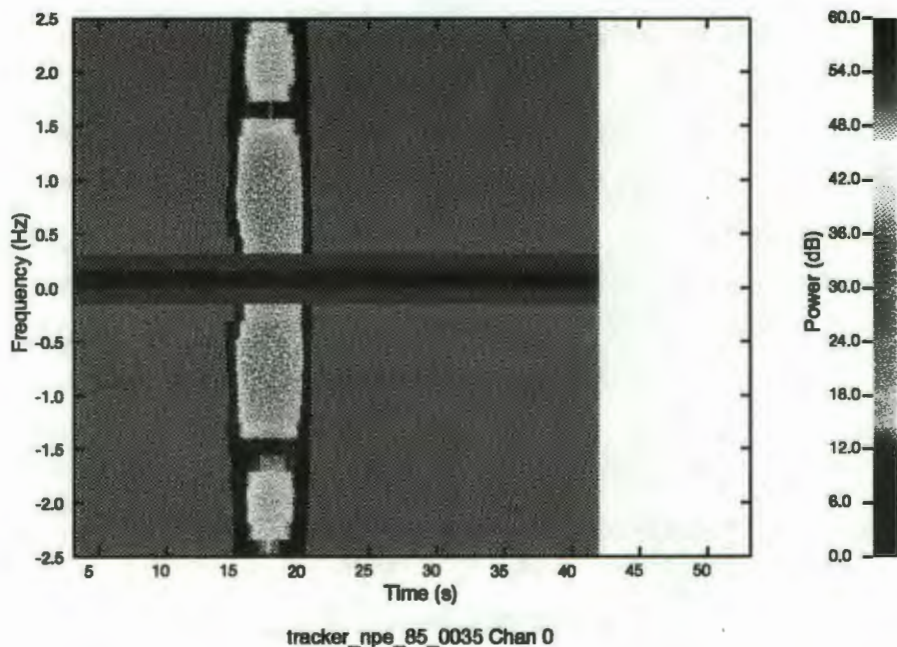


Figure 10: Predicted behavior of the power spectrum for the NPE simulation altered to achieve *E* layer reflection. The broadening of the spectrum would have been detectable under the NPE experimental conditions.

5 Conclusion

The detection of explosions during nighttime using ionospheric techniques remains problematical. Previous measurements of underground explosions indicate that using radio reflection of transmissions in the high frequency band is not effective because the sensitive altitude is so high that the acoustic waves from the explosion have dissipated. Our recent measurements in conjunction with the Non-Proliferation Experiment show that it is possible to use broadcast stations in the medium-frequency band as radio beacons to monitor the ionosphere above an explosion during the nighttime. Our results indicate that there were no effects that we could attribute to acoustic waves from the explosion although our model calculations indicate that an observable perturbation should have occurred if the desired propagation had been achieved. It is likely that because of an exceptionally low electron density the monitored transmissions reflected at altitudes too high to be useful. Although discouraging, this is only the first attempt using a new technique and deserves to be repeated with another source.

6 Acknowledgment

This work was performed under the auspices of the U. S. Department of Energy by Los Alamos National Laboratory under contract W-7405-ENG-36. Alfred Fernandez, Anthony Rose, and William Spurgeon of Los Alamos participated in the fielding and data collection for the Non-Proliferation experiment. Robert Carlos and Harold DeHaven of Los Alamos participated in the fielding and data collection for the Hunters Trophy experiment. Ray traces and the Doppler shift calculation presented in this report were obtained using the TRACKER computer code developed by Paul Argo of Los Alamos.

7 References

Banister, J. R., Radiation and propagation of short acoustical pulses from underground explosions, *Rept. SAND82-9754*, Sandia National Laboratory, Albuquerque, NM, 1982.

Banister, J. R. and W. V. Hereford, Observed high-altitude pressure waves from an underground and a surface explosion, *J. Geophys. Res.*, 31 , 5185-5193, 1991.

Davies, Kenneth, *Ionospheric Radio*, Peter Peregrinus, 1990.

Fitzgerald, T. J., Detection of mining explosions using ionospheric techniques, *Rept. LA-UR-93-3557*, Los Alamos National Laboratory, Los Alamos, NM, October, 1993.

Fitzgerald, T. J., and R. C. Carlos, The effects of 450 kg surface explosions at the E layer of the ionosphere, *Rept. LA-UR-92-3393*, Los Alamos National Laboratory, Los Alamos, NM, October, 1992.

Fujitaka, K., and T. Tohmatsu, A tidal theory of the ionospheric intermediate level, *J. Atmos. Terr. Phys.*, 35, 425-438, 1973.

Hermann, U., P. Eberhardt, M. A. Hidalgo, E. Kopp, and L. G. Smith, Metal ions and isotopes in sporadic E-layers during the Perseid meteor shower, *Space Res.*, 18, 249, 1978.

Ogawa, T. and T. Tohmatsu, Photoelectronic processes in the upper atmosphere, 2, The hydrogen and helium ultraviolet glow as an origin of the nighttime ionosphere, *Rep. Ionos. Space. Res. Japan*, 20, 1966.

Rawer, K. and P. A. Bradley, eds., International Reference Ionosphere—Status 1986/87, *Advances in Space Research*, 7, (6)1--129, 1987.

Sennitt, A. G., ed., *World Radio TV Handbook*, Billboard Books, 1993.

Shen, J. S., W. E. Swartz, D. T. Farley, and R. M. Harper, Ionization layers in the nighttime E region valley above Arecibo, *J. Geophys. Res.*, 31 , 5517-5526, 1976.

Smith, L. G., A sequence of rocket observations of night-time sporadic-E, *J. Atmos. Terr. Phys.*, 32 , 1247—1257, 1970.

Taylor, S., Los Alamos National Laboratory, Personal communication, 1993.

Watts, J. M., Complete night of vertical-incidence ionosphere soundings covering frequency range from 50 kc/s to 25 Mc/s, *J. Geophys. Res.*, 62 , 484-485, 1957.

Wakai, N., Study on the nighttime E region and its effects on the radio wave propagation, *J. Radio Research Laboratories*, 18 , 245—348, 1971.

Whitaker, R., Los Alamos National Laboratory, Personal communication, 1993.

Wouters, L. F., Ionospheric disturbances due to underground explosions and other sources—An elementary discussion, *Rept. UCID—16784*, Lawrence Livermore National Laboratory, Livermore, CA, 1971.

Zucca, J., DOE Non-Proliferation Experiment includes seismic data, *EOS, Trans. AGU*, 74, 587, 1993.

Infrasonic Measurements of the Non-Proliferation Experiment

Rodney W. Whitaker, Susan Noel, and Wayne Meadows

EES-5

Los Alamos National Laboratory

Group EES-5 operated two infrasonic arrays for the Non-Proliferation Experiment (NPE) executed on September 22, 1993, at 0701 UT. The arrays were located at the Nevada Test Site, 59 km from the event, and at St. George, UT, 231 km from the event. Before discussing the results, a few comments will help the reader understand certain aspects of these measurements. The NPE working point was close to 400 m below the surface in Area 12 of the NTS. For the event size and depth, surface ground motion may be rather small, and the surface ground motion is the source of the atmospheric signal. In a normal atmosphere, most of the acoustic energy would pass over the array at NTS, due to the negative sound speed gradient bending wave energy upward. At a 59-km distance, local meteorology can influence propagation through temperature inversions and low level winds. Thus, in the absence of local low-level ducts, essentially no signal would be expected at NTS. For St. George, the upper atmospheric winds (up to 50–60 km) can be a factor in the propagation. We do not have specific wind data for the time of the event and must appeal to the statistical value derived from the Stratospheric Circulation Index, which is 5 m/s to the east. This means we would expect a signal at St. George in about 12.5 to 13.5 minutes, with an average travel velocity of 0.29 km/s.

Time-delay beamforming is applied to the array outputs to search for the presence of correlated energy incident on the array. Data windows of 20-s duration are processed, and the azimuth of highest correlation is recorded. The data series is shifted by 10 s and the process is repeated. The results are displayed as standard beamform output plots of correlation coefficient, velocity of propagation, and azimuth as functions of time. Identifiable signals show as times of high correlation with fixed azimuths, for stationary sources. The results for St. George are given in Figure 1. The NPE acoustic signal is present at 071540 UT, with a peak correlation of 0.92. (Due to a clock offset, 3 minutes should be subtracted from the times shown in the figure.) The NPE signal is short, and the arrows help indicate the location. Figure 2 shows the raw channel data (volts vs time) for a 60-s window at the time of the signal. The signal is evident at 071540 UT, and the change in character of the data is clear. The derived azimuth is 270° compared to the calculated value of 276°. Although short, the signal has a high correlation. The average travel time is 0.30 km/s, in good agreement with expectations. Finally, the measured wind corrected amplitude is 0.21 mbars (dynes/cm²).

The beamforming analysis for the NTS array does not show the NPE signal. Given the distance to the source, most, if not all, the energy passed over the array. No signal was observed at the times which

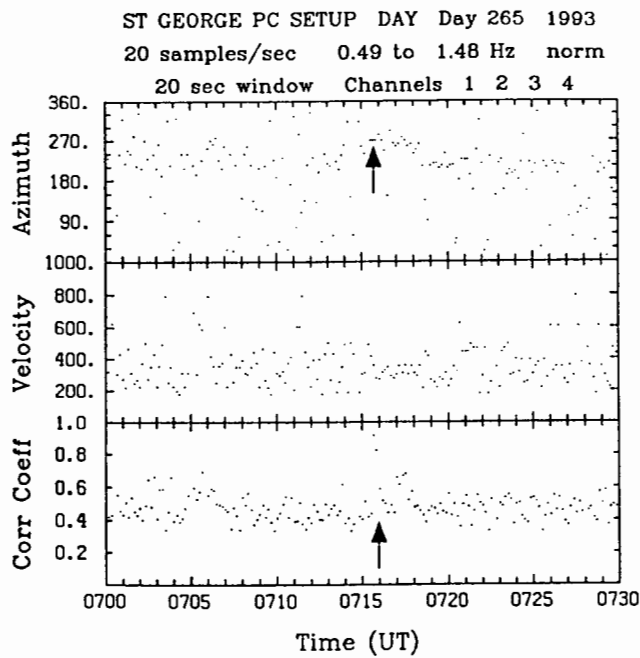


Figure 1. NPE array output at St. George. The signal is identified by the high correlation coefficient (>0.9) and constant propagation velocity and azimuth.

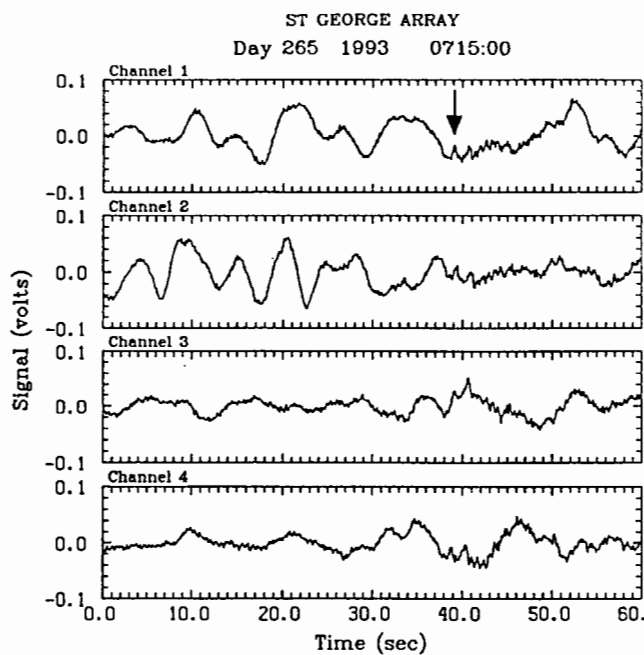


Figure 2. NPE signal at St. George. The wind-corrected amplitude is 0.21 mbars (dyne/cm^2) compared to other underground nuclear tests of the same energy.

would indicate the presence of low-level ducts. This result is not unexpected and is consistent with the experience on underground tests.

Based on the "quick look" analysis, we can state that in terms of wind-corrected amplitude, the NPE is close to underground nuclear tests of similar size. Future analysis will compare other characteristics.

Hydroacoustic Observations of the NPE

D. Harris*

T. Hauk*

E. Breitfeller*

G. D'Spain***

***Lawrence Livermore National Laboratory**

****Marine Physical Laboratory
University of California, San Diego**

Abstract

The NPE was observed by three hydrophone arrays located off of the coast of California: (1) a special sonobuoy pattern deployed for the Lawrence Livermore National Laboratory by COMPATWINGSPAC, U. S. Navy, (2) the SwellEx vertical line array deployed by the Marine Physical Laboratory, Scripps Institution of Oceanography, and (3) an array of the U.S. Navy SOSUS system. The P phase from the event was just visible in the sonobuoy data, very clear on the vertical line array (after beamforming), and moderately well recorded on the SOSUS array. Calibration of the SwellEx array hydrophones and electronics allows us to estimate the pressure level of the NPE P phase at 75-80 dB re 1 uPascal^{**2} / Hz between 2 and 9 Hz. We use observations of the HUNTERS TROPHY nuclear test to demonstrate several beamforming methods that use vertical line arrays to suppress the predominantly horizontally propagating ambient acoustic noise. Such arrays could be used to supplement seismic systems for monitoring inaccessible continental regions from adjacent oceans.

Introduction

The principal issue addressed in this paper is whether hydrophone arrays can supplement land-based seismic networks to monitor continental regions from adjacent oceans. Observations of the NPE and of HUNTERS TROPHY demonstrate detectable P phase waveforms for magnitude 4.4 events at a range of 620 kilometers. The sound pressure level of these observations indicates that arrays of hydrophones operating on continental shelves can detect small events at distances which are useful for monitoring purposes.

This paper also addresses the issue of hydrophone array configuration and signal processing for extracting seismic body phases from ambient acoustic noise. Our initial observations indicate that individual hydrophones are unlikely to perform well in a monitoring role, but that properly configured continental shelf arrays may do so. In particular, vertical arrays permit the separation of the predominantly horizontally-travelling ambient acoustic noise from vertically-travelling pressure waves converted from seismic body phases at the sea floor. We illustrate several simple beamforming schemes that provide significant processing gain with vertical line arrays using observations of HUNTERS TROPHY made with the Scripps Institution DIFAR array.

First we present the results of our sonobuoy deployment which demonstrates the low signal-to-noise ratios (SNR) to be expected from individual surface-suspended hydrophones.

Sonobuoy Deployment

DOE acquired low-frequency sonobuoys (VLF-IIA type) from the Naval Air Warfare Center, which were deployed to attempt observations of the NPE from two sites along the great circle path from NTS to the DIFAR site indicated in Figure 1. There were two experimental objectives: (1) to reoccupy the vertical DIFAR site where HUNTERS TROPHY was previously observed to make a direct comparison between large chemical and nuclear explosions, and (2) to study propagation off of the continent with two sonobuoy refraction lines separated by 51 nautical miles along that path. The VLF-IIA was chosen because its suspension is specially modified to decouple surface buoy motion from the hydrophone. Wave-induced hydrophone motion raises the noise floor well above the ambient acoustic noise, especially at frequencies below 10 Hz. The VLF-IIA is one of the quietest available air-deployable buoy systems in this (the seismic) frequency band.

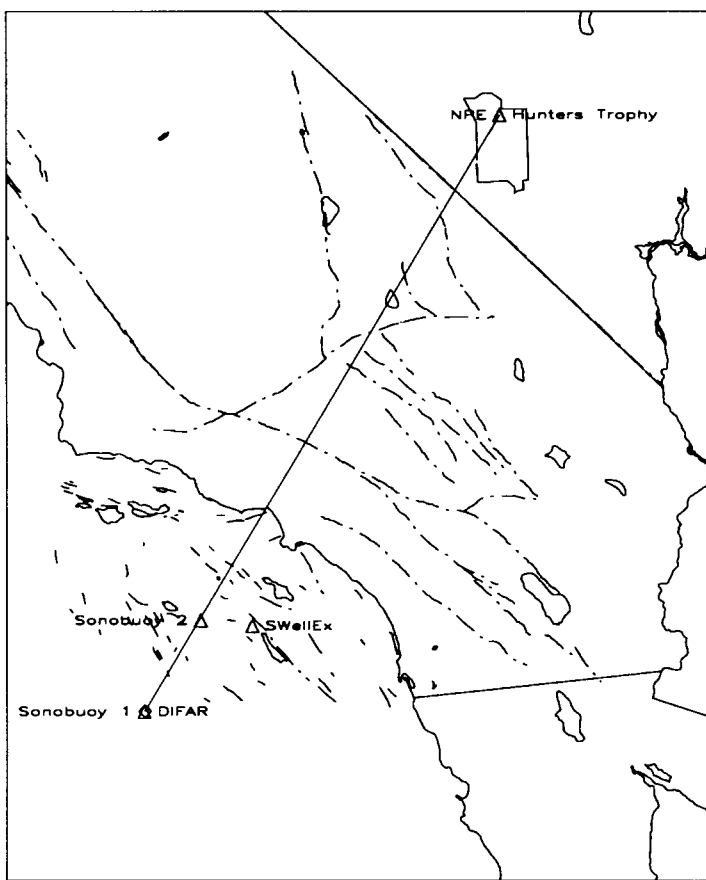


Figure 1 Map showing location in the Nuclear Test Site where HUNTERS TROPHY and the NPE were detonated and the locations of the three hydroacoustic systems described in this paper which observed these events. The vertical DIFAR array was approximately 620 km from HUNTERS TROPHY and the SwellEx array was approximately 500 km from the NPE. One of the two sonobuoy arrays was at the DIFAR site. The other was 94 km closer to NTS.

Each sonobuoy pattern was planned as a refraction line with 12 buoys spaced at 50 meter intervals and oriented along the great circle path to the test site as shown in Figure 2. This pattern was chosen to allow measurement of the horizontal velocity of converted seismic arrivals sweeping across the array (to allow phase identification). One of the issues we planned to address was which (and whether) seismic phases convert at the seafloor to produce observable acoustic arrivals. Because buoys drift, we planned to drop 4 SUS (Sound Undersea Source) charges in the calibration pattern indicated in Figure 2, to recover the relative hydrophone positions from measured arrival times of the (presumably) known sources.

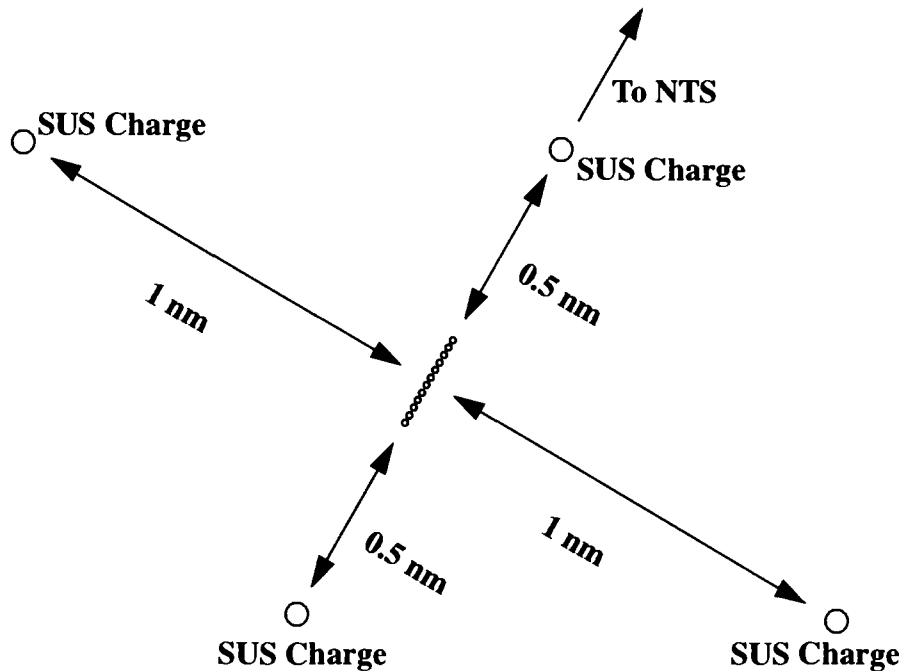


Figure 2 Planned configuration of the sonobuoy patterns dropped at the DIFAR and one other location, and the positions of the calibrating SUS charges. The spacing between the buoys was planned to be 50 meters. The SUS charges were planned to provide timing signals to estimate the relative locations of the buoys.

We were successful in deploying 12 sonobuoys at the DIFAR location (Figure 3), but only 9 sonobuoys at the second location 51 nautical miles closer to the NTS. The P3 aircraft used to drop and record from the buoys was positioned midway between the two patterns at an altitude of about 5000 feet. At this range and altitude, the heavy radio frequency interference (RFI) due to radio traffic in the LA basin and heavy commercial shipping communications caused us to lose reception for most of the buoys. Figure 4 displays the data recorded from the four best buoys of the pattern at the DIFAR location in the time window encompassing the expected NPE P arrival and filtered into the 3-8 Hz band. An arrival is discernable on the individual hydrophone traces, but not with an SNR sufficient for reliable automatic detection.

Scripps Institution of Oceanography Vertical DIFAR Array As Deployed During HUNTERS TROPHY

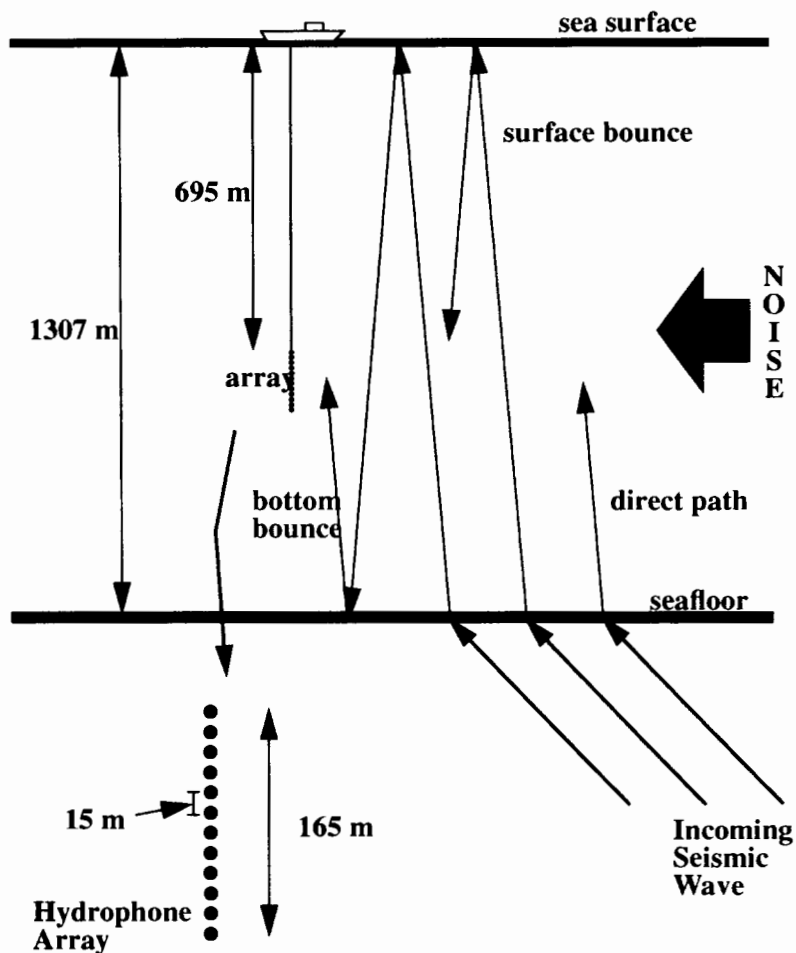


Figure 3 Typical configuration of a vertical line array suspended from a ship. This is the configuration of the vertical DIFAR array deployed by the Scripps Institution at the time of the HUNTERS TROPHY detonation. It shows 12 hydrophones at 15 meter spacing; 16 hydrophones were deployed, but not all were used in the processing of the data. The SwellEx deployment during the NPE was in shallower water (461 meters), and had 64 sensors spaced at 1.875 meter intervals. Our processing thinned the array, using just 9 of the sensors at approximately 15 meter intervals.

Beamforming (coherent summing) could improve the signal-to-noise ratio of the arrival, and would be best implemented using the relative locations of the hydrophones. We attempted to invert the arrival times of the observed impulsive shock signals from the four calibration SUS charges for relative hydrophone locations. The charges were dropped within 20 minutes of the NPE detonation, to minimize drift. However, the arrival times were inconsistent among the four buoys for which the data are shown in Figure 4, and attempts to estimate relative location failed. However, beamforming can be attempted assuming the converted P wave travels in a near-vertical direction. At vertical incidence, the relative hydrophone positions are unimportant, and the relevant beamforming operation is a straight sum of the individual hydrophone waveforms (no delays). The top trace in Figure 4 is a vertical beam, and does show an improvement in the SNR of the arrival. This observation is consistent with the observation being the NPE P phase.

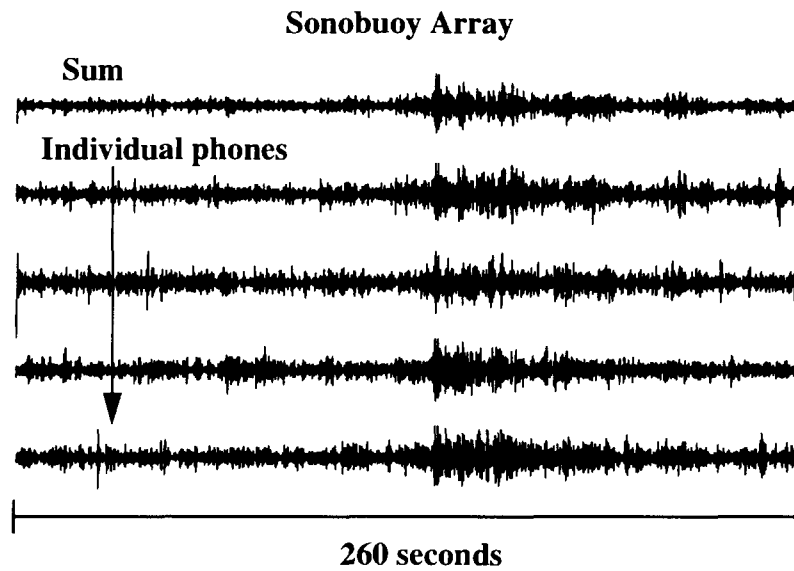


Figure 4 The sonobuoy pattern at the DIFAR location shows a signal at the correct time for the initial P arrival from the NPE. The top trace shows the sum of the four best sonobuoy waveforms; the remaining traces show the individual waveforms from the four buoys. The SNR is enhanced by a straight sum of the four waveforms indicating that the signal is propagating vertically. The data were filtered to reject noise outside of the 3-8 Hz band.

Based on our experience with this sonobuoy deployment, we cannot advocate the use of air-deployed sonobuoys as a nuclear test monitoring system. However, several procedural changes would improve the quality of observations. First, the buoys should not be so widely dispersed, particularly in a region of high RFI. The buoys should be within 5 nautical miles of the recording aircraft. Second, the SUS charges should be deployed much further from the pattern being calibrated, to minimize the effects of variations in SUS charge placement. At close ranges, even small variations can account for inconsistent shot arrival times. Third, the scientific group using the data should install its own portable digital recorder on the aircraft.

SwellEx NPE Observation

The NPE P phase was observed best by the SwellEx array deployed by Scripps Institution of Oceanography off of the northern tip of San Clemente Island. The SwellEx experiment was conducted for the Navy to study shallow water (continental shelf) propagation, and happened to be in place at the NPE shot time. The SwellEx is a vertical line array similar to that depicted in Figure 3, with the exception that it has 64 hydrophones spaced at 1.875 meter intervals. In addition, it was deployed in shallower water, 461 meters, than the DIFAR deployment illustrated in Figure 3. For the processing that we conducted, we subsampled the array, using every eighth hydrophone to employ an intersensor spacing of 15 meters. We used 9 hydrophones.

The NPE P arrival is especially clear after adaptive beamforming. Figure 5 shows the waveform from an individual hydrophone and the adaptive beam output, which combines all 9 waveforms in a manner designed to eliminate noise using an estimate of the local noise structure. Both waveforms have been filtered into the 2-10 Hz band. Not only is the initial P phase apparent, but a secondary (S?) phase is evident twenty to thirty seconds behind the P arrival.

SwellEx Array Signals Raw and Processed

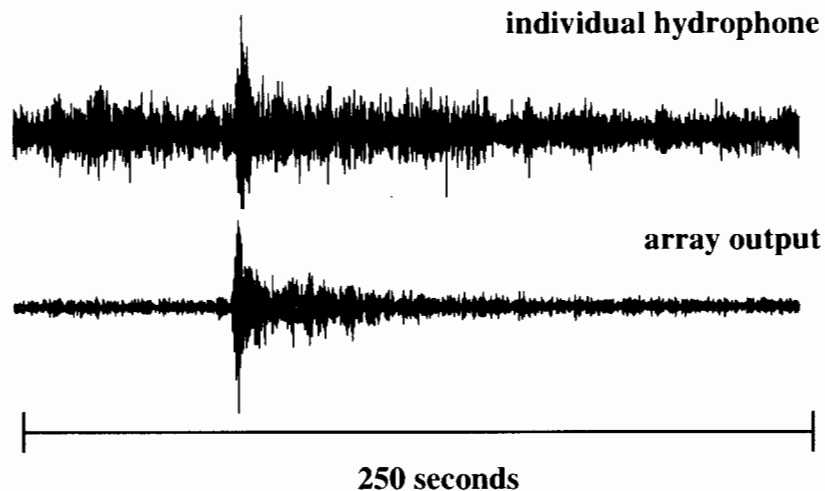


Figure 5 High resolution beamforming using the 9-element thinned subarray of the SwellEx array significantly enhances the SNR of the P and Lg (?) phases from the NPE. This plot shows the waveform from an individual hydrophone filtered into the 2-10 Hz band, and the beam resulting from an adaptive beamformer designed to reject noise of the type observed just prior to the signal. The noise in this example is probably non-acoustic, and is not well rejected by the simpler beamformers described in Figures 7 and 8.

The hydrophones and signal conditioning electronics are calibrated well in this system; consequently it was possible to make an estimate of the sound pressure level of the P arrival. Figure 6 displays a spectrum estimated from the most energetic 10 seconds of a P phase beam. For comparison, the spectrum of a post-beamforming noise sample is superimposed. The signal attains a sound pressure level of 85 dB re 1 uPascal^{**2} / Hz at its peak near 3 Hz, and is generally in the 75-80 dB range in the 2-9 Hz band. This spectral level is comparable to ambient noise in a high-noise coastal environment characterized by dense commercial shipping. For this reason, it is clear that single hydrophones will not detect small events on the order of 1 kiloton at this range. Hydrophone arrays are required. Because the adaptive beamforming method that performed so well in this example is somewhat complicated and computationally expensive, we look for simpler beamforming methods that could be implemented in low-power microprocessors.

Estimate of the NPE Signal Spectrum at the SwellEx Array

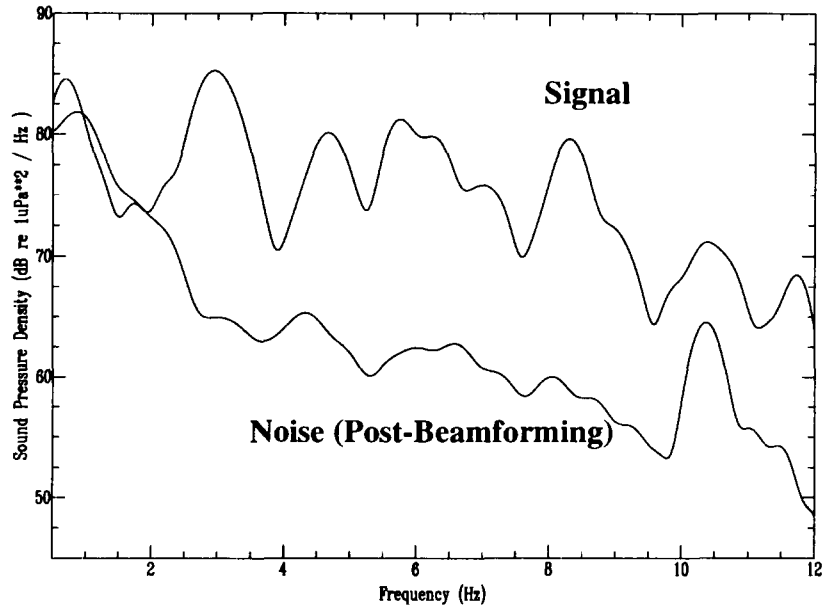


Figure 6 An estimate of the acoustic P spectrum (single hydrophone equivalent) made from a 9-element beam. The signal level averages 75-80 dB re 1 microPascal^{**2} / Hz over the 2-9 Hz band. In a coastal high noise environment, beamforming will be necessary to detect signals at this pressure level reliably.

SNR Improvement with Simple Beamformers

Incoming seismic waves refract into the water column, propagating nearly vertically there as pressure waves. In an environment with a perfectly flat sea floor, the signal will reverberate in a predictable fashion reflecting alternately from the free surface and from the bottom (Figure 3). Such high-angle reverberation imparts a spatial and temporal structure to the signal that is very unlike the dominant ambient acoustic noise. Ambient noise is predominantly horizontally-propagating acoustic energy from distant ships and storms.

Two signal processing approaches exploit the structural differences between signal and noise in order to suppress the noise: (1) beamforming to suppress horizontally-propagating noise, and (2) matched-field processing to compress the reverberant signal to a single higher-amplitude pulse.

Beamforming is the process of combining (shifting and summing) waveforms recorded across an array to enhance signals propagating from specified directions (by constructive interference). It is possible simultaneously to suppress noise propagating from other directions by placing appropriate nulls in the array response pattern (by destructive interference). The array response pattern is the directional response of the array beamforming operation to incoming plane waves. The responses of several downlooking beamformers designed to enhance signals propagating up from the bottom are shown in Figure 7. Generally the responses are maximum in the desired downward "look" direction. Ideally, to reject noise, they would be as close to zero as possible in all other directions. It is possible to force a zero response (null) in specific directions, the number of which may not exceed the number of hydrophones. The beamformers of Figure 7 employ different combinations of predetermined nulls in the horizontal and upward-looking vertical directions. The best among these options is a downlooking beam with both an uplooking and a horizontal null. Note that the beams with single nulls have significantly non-zero responses in either the horizontal or upward looking directions.

Matrix of Downlooking Beam Responses with Combinations of Directed Nulls For the DIFAR Array Geometry at 5 Hz

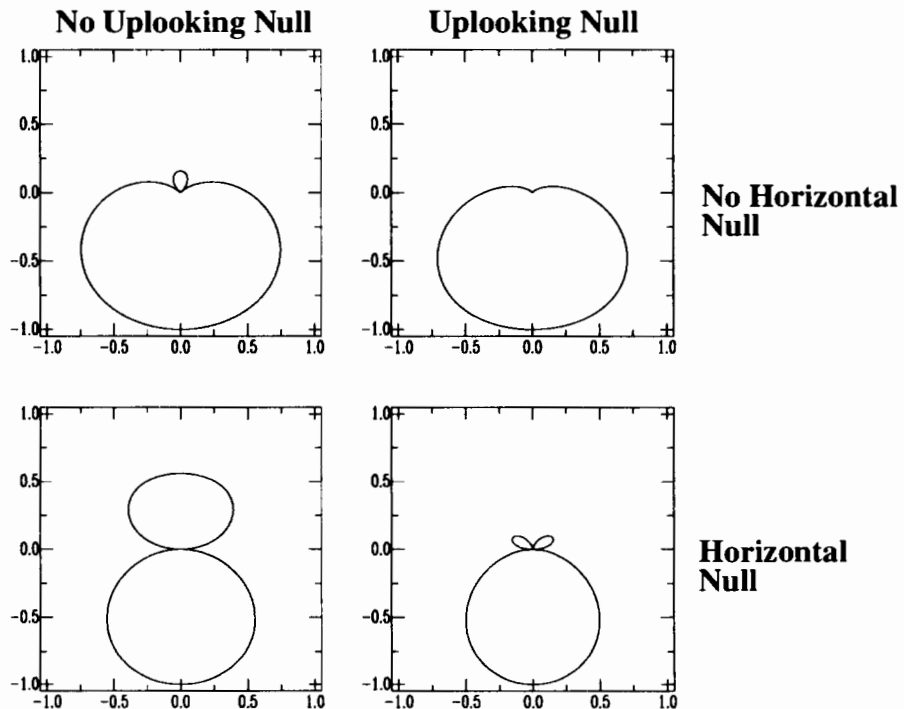


Figure 7 A matrix of 4 response patterns for the DIFAR array at 5 Hz corresponding to 4 different beamformers shows that significant processing gains should be possible against horizontal noise with the incorporation of null constraints in the horizontal and uplooking directions. The matrix shows a simple downlooking (endfire) beam in the upper left corner, and a beam incorporating a vertical uplooking and a horizontal null in the lower right corner. The remaining two response patterns have single nulls.

Data collected by the Scripps Institution of Oceanography vertical DIFAR array during the HUNTERS TROPHY nuclear test demonstrate the processing gains attainable by beamformers that make increasing use of the differences in signal and noise structure. Figure 8 shows the HUNTERS TROPHY P wave recorded by a single hydrophone filtered into the 3-7 Hz band. It is compared with three similarly filtered beams. The first beam is the simple downlooking beam (no nulls), and the second is the beam with nulls directed both horizontally and upward. Improved noise rejection in the horizontal direction results in a significant increase in signal-to-noise ratio. The third beam is the output of a simple matched field processor.

HUNTERS TROPHY Signal Processing Results: More Sophisticated Beamformers Suppress Noise More Effectively

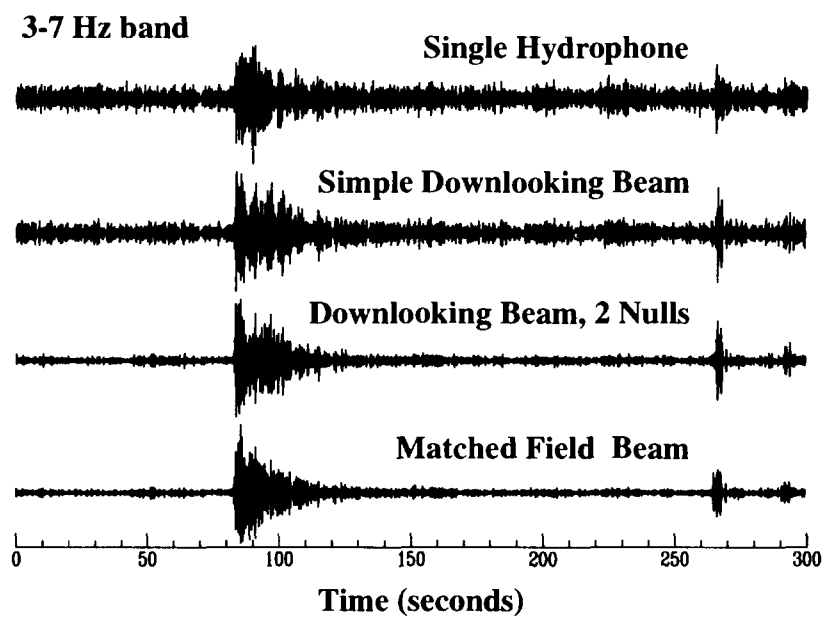


Figure 8 Significant processing gains are attained with processing that is non-adaptive, but more sophisticated than a simple beam. The plot shows a single hydrophone waveform filtered into the 3-7 Hz band (top), a simple downlooking beam, a downlooking beam with two nulls (refer to Figure 7), and a matched field beam. The term matched field refers to the practice of separating the upgoing and downgoing (reflected from the water surface) wavefields and then superimposing these two constructively to achieve a further factor of 2 processing gain.

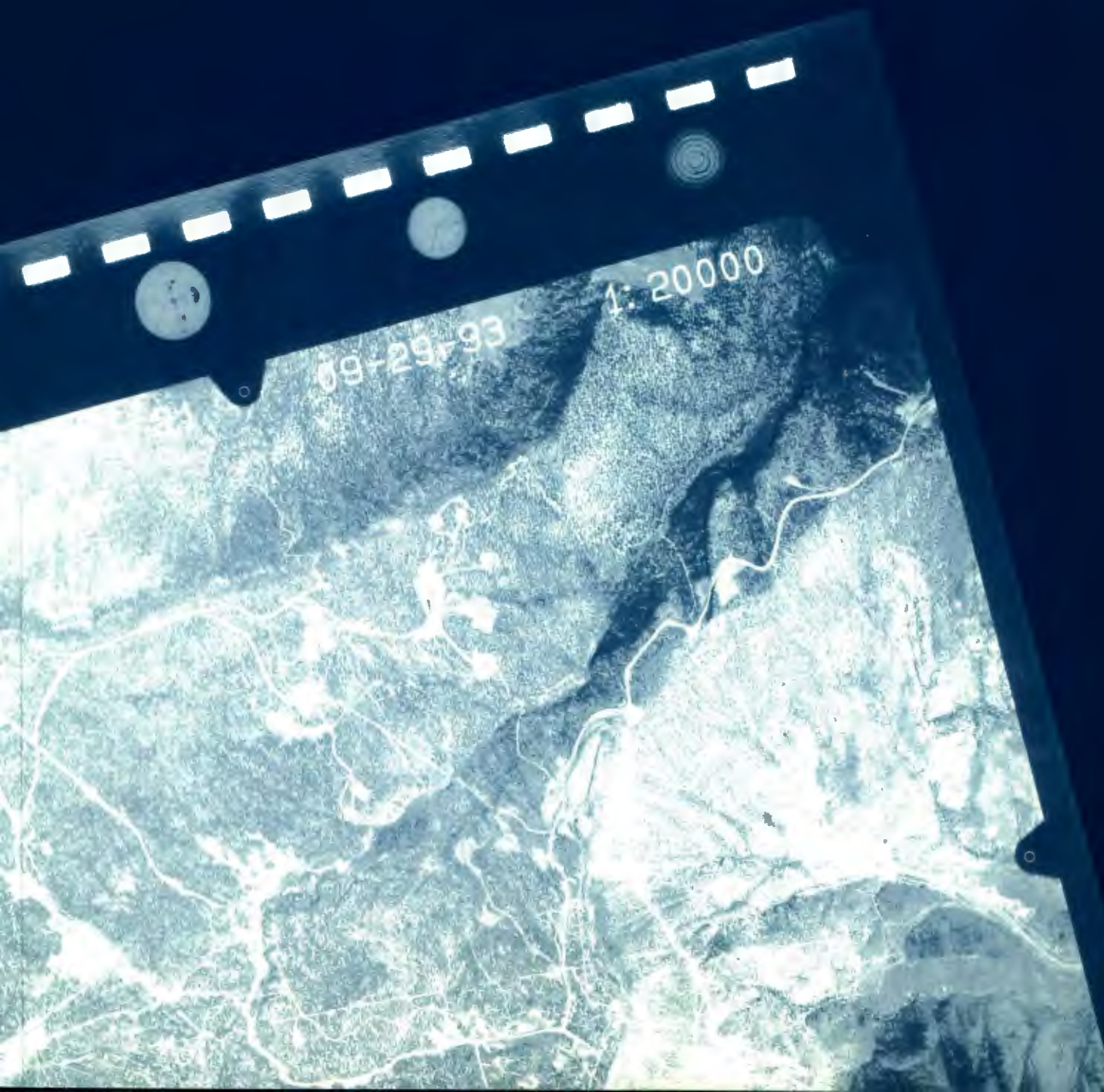
The matched field processor takes advantage of the known reverberant structure of the signal to enhance the signal-to-noise ratio. The simple version illustrated here combines the direct upcoming arrival of the P phase converted at the sea floor with its (predictable) downward travelling reflection off of the water surface. The processor works by directing symmetric beams (of the two-null variety) in uplooking and downlooking directions, then delaying the downlooking beam by the two-way travel time to the surface from the array, scaling it by minus one (to account for the reflection coefficient at the surface), and finally adding it to the uplooking beam. The result is often an additional 3 dB factor in noise rejection.

Conclusion

The NPE and HUNTERS TROPHY observations demonstrate the feasibility of using hydroacoustic stations located in continental shelf waters to detect continental nuclear tests. The value of vertical line arrays is especially apparent; these systems permit the separation of horizontally propagating noise from vertically-travelling converted seismic waves, and the separation of upgoing waves from downgoing waves. The latter wavefield decomposition offers the possibility of an essentially free factor of two gain in signal-to-noise ratio, using a simple form of matched field processing. The gain is free, because the two symmetric beams of the processor can be combined as one operation at no additional computational cost over a beamformer with null constraints. Because of cost issues, vertical line hydrophone arrays might not be deployed solely to augment land-based seismic systems for CTB monitoring. However, where they are deployed for other purposes, their potential for continental and oceanic seismic monitoring can be developed as a dual use.

Inexpensive vertical line arrays suspended beneath free-drifting buoys are being developed for global warming monitoring. Proposals to adapt such systems for oceanic nuclear test detection have appeared. If the hydrophones are properly spaced for long-range detection in the 25 Hz band, such arrays should function moderately well as free-drifting seismic stations in regions where it is expensive to deploy ocean bottom seismometers.

ON-SITE INSPECTION TECHNOLOGIES



An Overview of the On-Site Inspection Measurements from the Non-Proliferation Experiment

John J. Zucca
Lawrence Livermore National Laboratory

Abstract

An on-site inspection (OSI) is an in-person visit to a site to collect data and examine evidence in order to determine the source of an ambiguous event detected via remote monitoring systems or other measures. Its purpose is to determine whether the treaty has been violated, to deter violations, and to build confidence. At the time of this writing, it is anticipated that the Comprehensive Test Ban Treaty (CTBT) being developed in the Conference on Disarmament will contain OSI provisions. In an era of testing moratoria, the Non-Proliferation Experiment (NPE) provided a unique opportunity to investigate candidate OSI techniques.

On-site inspections could occur in three different contexts:

- After-the-fact inspections based on information from remote monitoring systems.
- Inspections prior to, during, and after large declared chemical explosions (e.g., a large mining explosion).
- Continuous monitoring inspections with unattended sensors at certain agreed-upon sites (e.g., previous test sites).

OSI monitoring techniques need to be designed to detect the phenomena and residual effects of nuclear explosions. In the underground case, the primary effects of interest for OSI are the electromagnetic pulse, shock waves, aftershocks, radioactive gas, rubble zone, and apical void. These effects are well known and the basic techniques for their detection well established. We designed our measurement program for the NPE to answer specific issues about these detection technologies. Our measurement program includes the following:

- Zerotime electromagnetic measurements
- Seismic aftershock survey
- Before and after electrical soundings
- Gas tracers introduced into the explosive
- Before and after multispectral overhead imagery from low-flying aircraft
- Before and after geologic surveys.

Introduction

Traditionally, OSIs are perceived as responses to underground events, although an evader may choose to carry out a test in the lower atmosphere over land or at sea. In this paper, underground events are the focus.

There are potentially several hundred events per year that could be candidates for on-site inspection. Figure 1 shows annual, global, cumulative, shallow (less than or equal to 60 km depth) events detected teleseismically (Ringdal, 1986). Since teleseismic networks typically cut off at magnitude $m_b = 4.5$, the data at the lower magnitudes are extrapolations. The plot shows approximately 100,000 shallow events per year between magnitude 2.5 and 3.5. Any event that is accurately located below 10 km is clearly not a nuclear explosion; therefore, some large fraction of these events will be "deep" compared to nuclear events when regional and local data are factored in. For the sake of argument, say that 1/6 of these events would be considered "shallow" after the inclusion of regional and local data. This would leave a total of about 16,000 shallow events per year. Then, if the seismic identification process is assumed to be 99% effective, 150 events per year between magnitude 2.5 and 3.5 could be considered ambiguous. Clearly, these are more events than can be inspected in a year. The procedures for triggering an OSI need to be designed such that there is a manageable number of events.

A nuclear detonation creates residual effects which would be objects of an OSI (Figure 2). The most important of these effects in the underground case are the release of radioactive gases, the generation of

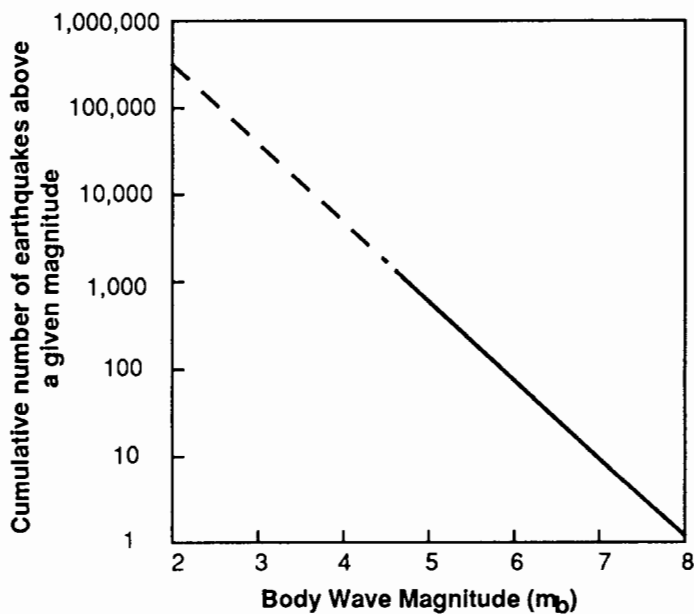


Figure 1. Cumulative global seismicity for events of less than 60 km depth (Ringdal, 1986). The dashed line below magnitude 4.5 indicates that the data are extrapolated to the lower magnitudes.

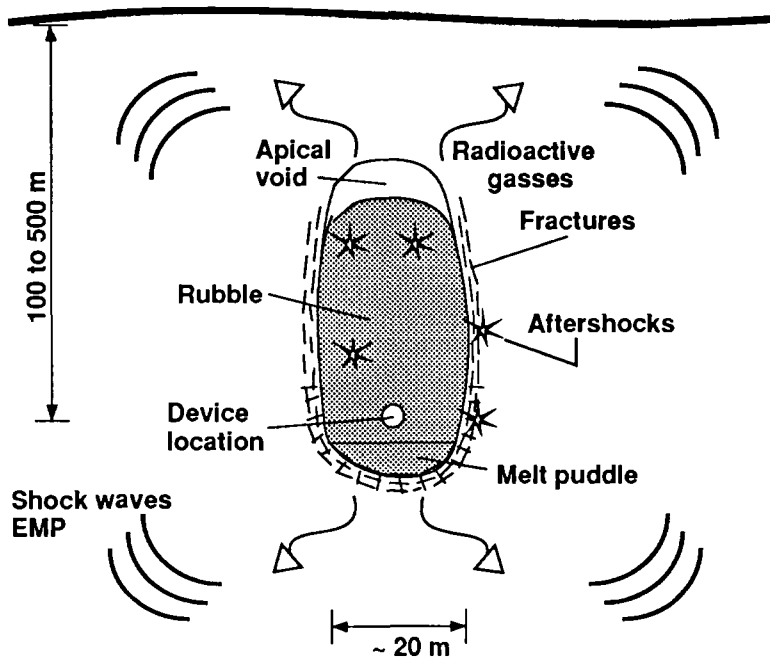


Figure 2. Cross section showing nuclear explosion phenomenology important for on-site inspection of underground seismic events.

aftershocks, and the formation of the cavity and rubble zone. The shock waves and electromagnetic pulse could be used during transparency measures to discriminate between nuclear and chemical explosions.

An evader would not conduct a clandestine test in the manner associated with normal testing practices. Such a test would be easily identified on overhead imagery from collapse craters or evidence of surface workings such as new roads and drill pads. An evader would probably take advantage of some other operation. For example, the legitimate workings of a mine could be used to cover clandestine operations. If the explosion were buried deep enough, it would not form a collapse crater and the activity associated with emplacement would be conducted underground, out of sight.

Based on remote monitoring systems currently envisioned for the treaty, the initial inspection area could be 1000 square kilometers (Figure 3). This area would have to be reduced during the course of the inspection. In the first step, a wide-area search would be conducted using available overhead imagery or imagery taken on-site from an aircraft. Next, a local-area search would be carried out on one or two smaller areas selected on the basis of the results of the wide-area search. This step would consist of detailed aerial surveys, surface geophysical surveys, and surveys looking for aftershocks, surface geologic evidence, and radioactive gases. Finally, a detailed investigation could be carried out on a small area to geophysically sound for the explosion cavity.

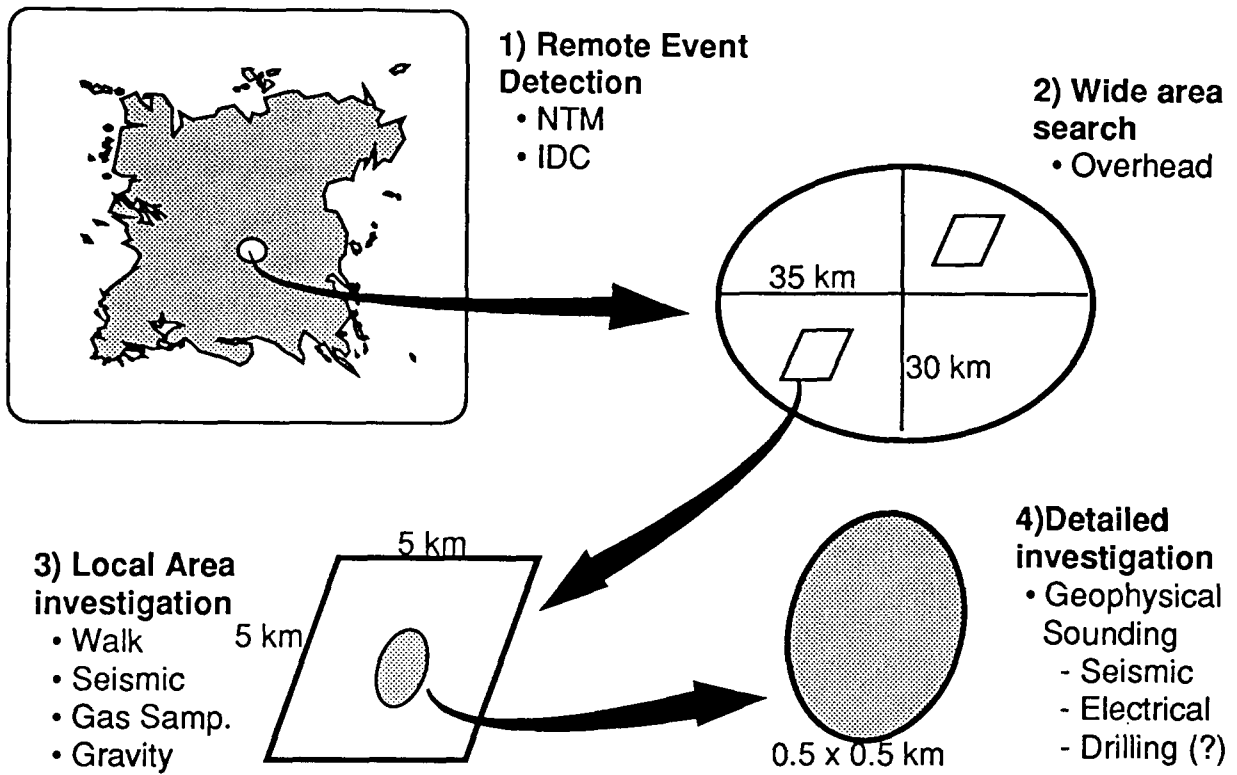


Figure 3. Successive reduction of the search area during an on-site inspection for an underground seismic event.

OSI measurements made on the NPE

The NPE measurement program was designed to study the phenomenological basis for several key technologies that could be used during an on-site inspection. The following measurements were carried out:

- Low-altitude overhead imagery.
- Aftershock monitoring.
- Monitoring for gas tracers introduced into the explosive.
- Geophysical sounding.
- Surface geologic studies.
- Electromagnetic pulse monitoring.

Each of these measurements is described in detail elsewhere in this volume. Following is a short discussion of each technology and a summary of the results from the NPE.

Low-altitude imagery

During the wide-area search, an aerial survey could show evidence of surface workings such as roads, mine tailings, cables, and shock-induced fractures. Multispectral images could be used to search for patches of ground that have been disturbed by violent shaking. The NPE offered an interesting

Aftershock monitoring

Virtually all large seismic events have subsequent aftershock sequences. Aftershock detection and location will help focus the local-area search. Aftershocks can continue for up to several months after an event. However, one to two weeks after an underground nuclear test there should be only a few aftershocks per day to one every several days. Tests detonated in cavities will have even fewer. A 16-station network was deployed on Rainier Mesa and operated for several months after zero time. The purpose of the experiment was to determine the length of time after the event that aftershocks could be detected and to determine whether there is a possibility to discriminate between earthquake and explosion aftershocks. Preliminary results suggest that explosion induced aftershock sequences contain a number of low-frequency events that are not observed in earthquake aftershock sequences. The presence of these aftershocks may be diagnostic of an underground explosion. (See Jarpe et al., this volume.)

Monitoring for gas tracers

Gas sampling and a radiation survey would be major activities of an inspection. Depending on the local geologic conditions, the radioactive gases could reach the surface in a matter of hours or only after several months. The most likely radionuclides to reach the surface are the noble gases and tritium. While diagnostic of a nuclear test, the isotopes of xenon have short half-lives and are probably not useful for OSI. Argon-37 is a reaction product of the device's radiation and the surrounding geologic material. It has a half-life of 35 days, which makes it a good indicator of a recent test. Krypton-85 with a half-life of 11 years is also produced from nuclear explosions, but there is already a world-wide background from fuel reprocessing. It is only indicative of a test if it is detected well above local background levels. Soil gas samples should be collected during low atmospheric pressure when soil gasses are flowing out of the ground. Two gas tracers (sulfur hexaflouride and helium-3) were introduced into the NPE explosion cavity. The purpose of the experiment was to determine the timing and aerial extent over which gasses reach the surface on an event that was unlikely to crater. No tracer gasses were detected during the first six months following this experiment. It appears that good containment and certain types of geologic conditions may delay the flow of gasses to the surface for many months. (See Carrigan et al., this volume)

Geophysical sounding

Geophysical sounding could be used to search for the rubble zone and the void above it during the inspection. Sounding techniques include direct-current resistivity, seismic reflection imaging, and others. Such surveys need to pass within a depth of burial on the surface to detect the target. Seismic reflection and electrical measurements were carried out for the NPE. The seismic reflection survey did not detect the cavity since it was not carried out at ground zero. However, these measurements did reveal useful information on the geologic structure of Rainier Mesa. (See Majer et al., this volume.) Magneto-telluric and electrical self-potential surveys were carried out before the explosion, and a self-

potential survey was repeated after the explosion. No significant features in the survey data could be attributed to the cavity. (See Sweeney, this volume)

Surface geologic studies

A visual and geological survey would be used to search for locations for the aftershock detection stations and to determine possible targets for detailed investigation. An intensive examination of the area would look for artifacts of the testing activity, such as surface workings and ground fractures. For the NPE, "before" and "after" searches for fractures were conducted on the surface of Rainier Mesa. No fractures were found. (See Townsend et al., this volume)

Electromagnetic pulse monitoring

For monitoring of large chemical explosions during transparency measures, electromagnetic pulse (EMP) monitoring offers a possible discriminant between nuclear and chemical explosions. The NPE offered a unique opportunity to monitor EMP from a large chemical explosion and to compare it to previous EMP measurements of nuclear explosions.

Three EMP experiments were fielded on the NPE. The first experiment, which consisted of two ELF (extremely low-frequency) stations, was deployed on top of Rainier Mesa. The results from these stations suggest that EMP from chemical explosions is at a lower frequency than comparable nuclear explosions. (See Sweeney, this volume.) The other two EMP experiments were set up near the mouth of the tunnel and were tuned to a much higher frequency band. (See Kelley et al. and Bell et al., this volume.)

Conclusion

At the time of this writing, it appears likely that OSIs for underground events will be an important part of the CTBT. The NPE played a significant role in the development of OSI techniques and provided a nuclear analog during a time of no nuclear testing. Consequently, we could test proposed OSI technology and develop a further understanding of the phenomenological basis for discriminating between nuclear and non-nuclear events on-site. Results from preliminary analyses of data collected during the NPE are presented in several papers in this volume. More detailed analyses are in progress regarding overhead imagery data, aftershock data, and the gas tracers that still have not been detected on the surface of Rainier Mesa.

Reference

Ringdal, F. (1986), "Study of Magnitudes, Seismicity, and Earthquake Detectability Using a Global Network," *Bull. Seis. Soc. Amer.*, 76 1641–1659.

**POST-TEST GEOLOGIC OBSERVATIONS MADE AT THE
NON-PROLIFERATION EXPERIMENT SITE, N-TUNNEL,
NEVADA TEST SITE**

by

**D. R. Townsend, R. P. Bradford, S. P. Hopkins, M. J. Baldwin
Raytheon Services Nevada
P.O. Box 328, Mercury, NV 89023**

and

**B. L. Ristvet
Defense Nuclear Agency
1680 Texas Street, SE
Kirtland Air Force Base, NM 87117-5669**

ABSTRACT

Qualitative evaluations of damage resulting from an underground explosion can provide valuable information concerning the size of the charge, as well as the location of a clandestine detonation. However, caution must be exercised during the appraisal because the effects of an explosion are a function of many factors in addition to yield. Construction techniques, the physical properties of the surrounding rock, and the depth of burial are all important considerations when evaluating the effects of an underground detonation.

Raytheon Services Nevada geologists documented underground and surface effects of the Non-Proliferation Experiment, as they have for all recent underground weapons-effects tests conducted by the Defense Nuclear Agency. Underground, the extent of visible damage decreased rapidly from severe at the closest inspection point 100 m from the Working Point, to insignificant 300 m from the Working Point. The severity of damage correlates in some instances with the orientation of the drift with respect to the shock-wave propagation direction.

No evidence of the Non-Proliferation explosion was visible on the mesa surface 389 m above the Working Point the day after the explosion.

INTRODUCTION

The Non-Proliferation Experiment (NPE) was detonated at 0001 hours on 22 September 1993. The NPE was conducted in a cylindrical cavity located 389.0 m below the surface of Rainier Mesa in south-central N-Tunnel. This report summarizes the post-event geologic observations conducted on the mesa surface and in the accessible drifts in the vicinity of the NPE.

UNDERGROUND EFFECTS

Introduction

The 78.3 meter-long U12n.25 NPE Access drift was mined from the Fast alcove of the U12n.23 MISTY ECHO drift complex. The NPE cavity was mined from the end of the Access drift as a cylinder 15.2 m in diameter and 5.2 m in height (Figure 1). The entire Access drift was stemmed with grout, but no other containment measures were employed.

The drifts in western N-Tunnel have been shock-conditioned by earlier nuclear tests detonated in the N-Tunnel complex. Figure 1 shows a map of N-Tunnel with locations of the nearby U12n.02 MIDI MIST, U12n.17 MISTY RAIN, and U12n.23 MISTY ECHO nuclear tests. The U12n.22 MINERAL QUARRY and U12n.24 HUNTERS TROPHY working points are located 718 m and 613 m, respectively, north of the NPE site. Construction Stations (CS) are given in feet and Range Stations (RS) are given in meters.

Effects

Raytheon Services Nevada (RSN) geologists made observations in the accessible areas of the N-Tunnel complex on 7 October 1993. Figure 2 shows the U12n.25 cavity, the surrounding drifts, and areas of damage discussed in this report. The following discussion begins with features located closest to the cavity.

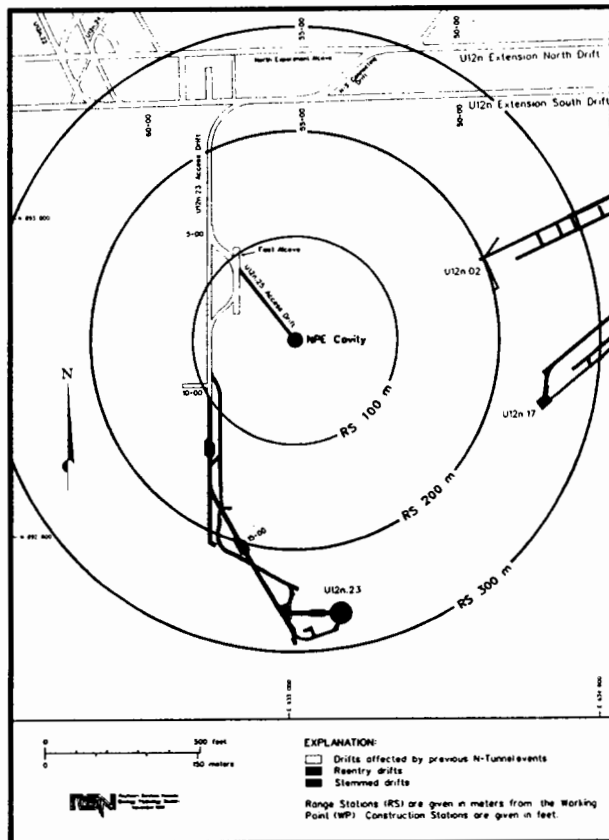


Figure 1 Map of south-central N-Tunnel showing location of the NPE site.

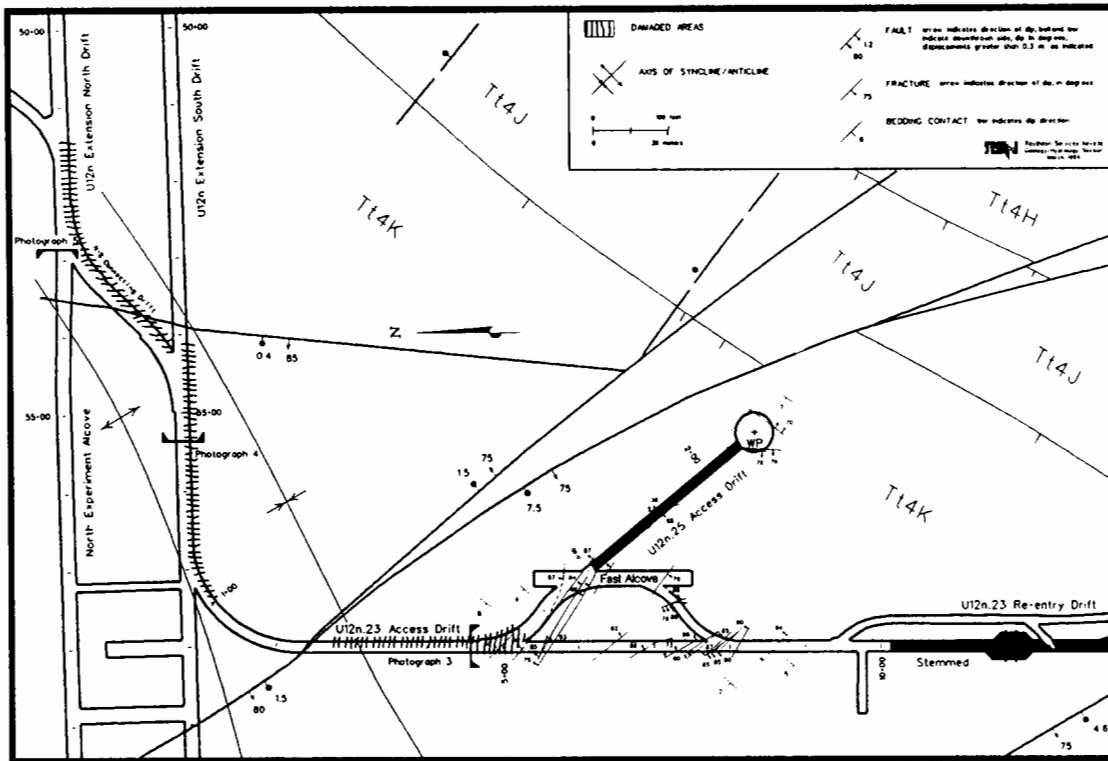


Figure 2 Geologic map of the NPE site showing damaged areas and locations of photographs 3, 4, and 5 (Figures 3, 4, and 5).

The most severe damage seen in the accessible parts of the complex occurred near the Fast alcove, east of the U12n.23 Access drift. This area was cordoned off after the test by tunnel safety personnel at CS 4+60 near the north entrance to the alcove. The northern access drift into the alcove was caved at its intersection with the U12n.23 Access drift, preventing closer investigation of the Fast alcove (Figure 3). In the U12n.23 Access drift, the invert had been heaved up as much as 0.3 m from CS 4+60 to 2+75, with the greatest displacement occurring closer to the Working Point (WP). The pillar point on the WP side of the U12n.23 Access drift/South Extension drift intersection had cracked, loosening slabs up to 0.3 m thick. Other damage to the U12n.23 Access drift consisted of minor cracking and flaking of the fibercrete on the left rib and back.

Damage in the N-Extension drift complex consisted of cracking and slabbing along ribs that were closest to the WP (the left ribs of the North and South Extension drifts and the N-S Connecting drift) and cracking and heaving of invert. Cracking and slabbing of the left rib extended from CS 1+00 of the U12n.23 Access drift into the South Extension drift, around the N-S Connecting drift, and to approximately CS 51+50 of the North Extension drift. Slabs of fibercrete and rock up to 0.3 m thick and 1.2 m in height were broken off of the left rib in this area, pulling rockbolts loose and stretching the wire mesh. In the Extension drifts, this damage occurred up to approximately 1.2 m above the invert, which is where the



Figure 3 Photo showing damage at the intersection of the North Access drift to the Fast alcove and the U12n.23 Access drift. Caving in the North Access drift (left background) and floor heave are evident. View is to the WP from CS 4+60 of the U12n.23 Access drift (see Figure 2). Photo by Johnson Controls.

original circular shape of the drift had been modified to a "keyhole" shape to produce a flat invert. Through this area, gravel along the left rib was thrown out into the drift, covering the rails and leaving a ditch along the rib up to 0.5 m deep. The invert was also heaved up to 0.6 m along the right rib, causing the rails to bend and tilt as much as 15° toward the left rib (Figure 4). A pressure ridge approximately 1 m wide and subparallel to the drift, extends from CS 55+50 to 54+70 in the South drift, and may branch into the N-S Connecting drift, which was partially repaired prior to our inspection. The area of greatest invert heave and tilt is centered at approximately CS 55+00, but does not correspond to any previously mapped geologic features in the N-Extension drift complex. The pattern of damage in this area suggests that the invert was lifted and rotated slightly counterclockwise by the NPE explosion. Other damage in the South Extension drift consisted of cracking of poured invert, minor invert heave, and minor spalling along the left rib of the drift.

In the North Experiment alcove, 1.2 m thick slabs of rock and fibercrete were broken from the left rib between the N-S Connecting drift and approximately CS 53+60. This area of damage is also located approximately 1.2 m above the invert at the height where the drift shape was modified to create a flat invert (Figure 5). Other damage in the Experiment alcove consisted of reactivation and enlargement of previously existing cracks in the poured invert caused by earlier nuclear events and minor flaking of fibercrete.



Figure 4 Photo showing area of maximum floor heave and tilt in the N-Extension South drift. Possible pressure ridge extends from left foreground to rail spur in the background. View is toward the portal from approximately CS 55+60 (see Figure 2). Photo by Johnson Controls.

Comparison with Previous Events

A direct comparison of underground effects caused by the NPE with those from previous nuclear tests in N-Tunnel is difficult due to less strenuous containment requirements associated with this experiment. Unstemmed drifts in which the NPE damage was observed were at a much closer range than is generally allowed for nuclear tests; the end-of-stemming in the most recent test in N-Tunnel was at RS 154, while stemming for the NPE extended only 78.3 m from the cavity. Most of the damaged areas noted after the NPE would have been located well within the stemmed region of a comparable nuclear test. At greater ranges, the visible effects of the NPE were similar to those observed following recent N-Tunnel nuclear events.

SURFACE EFFECTS

No mappable surface effects were found on the surface of Rainier Mesa following the NPE explosion (Figure 6).



Figure 5 Photo showing slabbing along the left rib of the North Experiment alcove 1.2 m above the invert. View is from intersection of the N-Extension North drift and the N-S Connecting drift (see Figure 2). Photo by Johnson Controls.

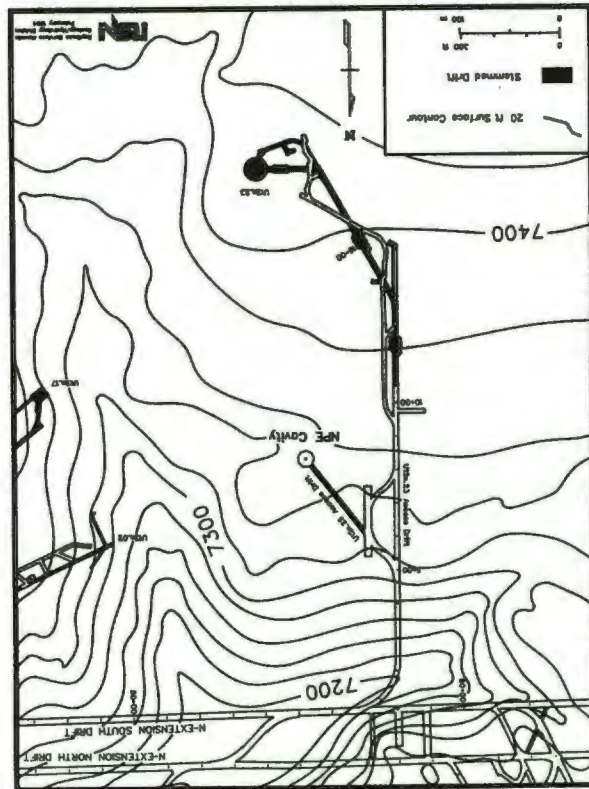


Figure 6 Map of surface of Rainier Mesa above the NPE site showing elevation contours.

SUMMARY

The U12n.25 Non-Proliferation Experiment was detonated on 22 September 1993. No mappable surface effects were observed by RSN geologists. Underground effects were documented on 7 October 1993. The most severe damage, seen in the accessible portions of the tunnel, occurred in the North Access drift to the Fast Alcove in the U12n.23 Drift complex and consisted of caving of the back and floor heave. In the remainder of the U12n.23 Drift complex, and in other areas of west-central N-Tunnel, damage included minor cracking and spalling of fibercrete, cracking of poured invert, and floor heave.

EMP from a Chemical Explosion Originating in a Tunnel

Bob Kelly

P-14, MS D410

Los Alamos National Laboratory

Los Alamos, NM 87545

March, 1994

Electromagnetic pulses generated by a chemical explosion deep in a tunnel have been detected by sensors placed on both sides of the portal. These detectors consisted of antennas, current transformers, B-dots, and D-dots. The main objective was to collect data for nonproliferation studies complementary to and in cooperation with seismic methods. The electric field strength at the portal was computed from the data to be on the order of 50 millivolts per meter, with a Fourier transform indicating that most of the energy occurs below about 3 MHz. Several of the sensors displayed periodic sharp spikes probably not related to the device. Surface guided waves were detected along power and ground cables plus the railroad track. Time dependent surface current and charge were measured on the portal door, which serves as a secondary source for external radiation.

Introduction

An electromagnetic pulse, caused by a chemical explosion, was detected in the portal area of N-tunnel at the Nevada Test Site. The main purpose was to collect data for nonproliferation studies complimentary to and in cooperation with seismic measurements. Whereas emplacement of the device in a cavity tends to mitigate seismic signals, it tends to enhance EMP production and vice versa.

The experimental objectives were: (1) Characterize the EMP secondary source at the portal, (2) Observe surface guided waves along the interior cables, (3) Determine time dependent current and charge on the portal door, (4) Investigate possible guidance of a pulse by the railroad tracks, (5) Measure any device generated signal on the phone and ground lines, (6) Detect radio frequency emission near the portal, (7) Attempt a comparison of the EMP generated from chemical and nuclear explosions.

Typical electric field strengths were several tens of millivolts per meter just outside the portal, with Fourier transforms indicating that the energy density resided mainly below about 3 MHz. Surface guided waves were detected in the vicinity of detector cables, power and ground cables, and the railroad track. The portal door (a wire mesh) serves as a secondary radiation source as shown by nonzero time dependent surface charge and current. Many of the sensors displayed sharp, periodic

spikes most likely not shot related; their origin is unknown at this writing except for those at 60 Hz and those on the phone line.

Condensed Abridgment of a Brief Summary of Basic Theory

Chemical explosions are caused by a rapid exothermic chemical reaction, which produces a gas and results in heat transfer. The normal chemical reaction that occurs in an explosion is combustion. Fuel elements, such as carbon or hydrogen react with oxidizing elements such as oxygen or a halogen. The system is capable of producing large quantities of carbon dioxide, carbon monoxide, water, and nitrogen, along with considerable heat.

Subsequent to detonation, an explosion produces an electromagnetic pulse (EMP). The spectrum and intensity are functions of such parameters as explosive type and particle size. There appears to be a time delay between detonation and emission, which may depend upon the mass of the explosive and the ignition method. The polarization, field strength, and radial dependence depend partly upon the receiving sensor location. The proximity of the explosive to the earth's surface affects the signal. Often, two distinct pulses are recorded. The first is directly associated with the explosion, whereas the second is probably dependent upon the height of the charge above ground. Keep in mind that the combustion products include heavy ionized atoms. The ignition method also influences the signal. For example, flame ignition of spherical charges lead to signals that differ from those initiated by an electric detonator.

There are several qualitative explanations of the EMP emission. For example, one possibility mentioned in the literature is generation produced by electric sparks between detonation products and case fragments. Probably the major contribution originates in an asymmetric separation of the positive and negative ions from the high explosive products as a result of high temperature. The asymmetry may originate in a number of ways such as the geometry of the immediate surroundings, current leads in electric detonation, and single point flame ignition. Recall that the generation of a dipole isn't sufficient for radiation; the dipole moment must have a nonzero second time derivative, which is equivalent to a nonzero first time derivative of the current.

There is some inconclusive evidence that the time delay between detonation and the appearance of EMP is proportional to the cube root of the explosive mass. There is further evidence of a functional dependence of the electric field strength on the mass. A statistical analysis of an excess of 100 experiments at various distances from several different charge masses shows that the magnitude of the electric field is directly proportional to the explosive mass.

In order for the electromagnetic pulse to propagate through a tunnel, it first must be coupled from the device to the tunnel. This problem partly depends upon the nature of the emplacement. For example, suppose the explosive is placed in an excavated cavity with one or more connecting tunnels. During, and for some time following the explosion, a time-dependent electromagnetic field is

established in the cavity. The cavity size and shape, plus the device location play a role in determining the EMP frequency spectrum.

The coupling problem consists of extracting a portion of the energy from the cavity via a tunnel. Clearly the tunnel has its own natural modes, and these are excited to an extent depending upon the electric and magnetic field orientations at the tunnel-cavity interface at any instant of time. It's clear that any arbitrary opening to the cavity will allow an electromagnetic pulse to enter. If there are conductors, such as cables or railroad tracks in the tunnel, the mode distribution is modified to include the possible existence of the extremely important transverse electromagnetic mode (TEM), which isn't possible in the absence of a conductor isolated from the tunnel walls.

A waveguide mode (non-TEM) may be propagated through a tunnel for all wavelengths less than approximately twice the largest transverse dimension. Wavelengths larger than this cutoff value are not propagated and therefore do not transport energy by this mode. All of the propagated modes are lossy ones because at the tunnel boundary, part of the energy is reflected and part is refracted into the surrounding medium. The refracted portion constitutes energy extracted from the wave and hence corresponds to a loss. Furthermore, the medium has a nonzero conductivity that enhances the loss.

The waveguide mode assumes tunnel propagation in the absence of conductors threading parallel to the walls. In practice, there are normally power lines, telephone lines, coax cables, pipes, railroad tracks, etc., which render the analysis to be more complicated. Yet, the very presence of a longitudinal conductor makes possible the existence of a TEM mode with no cutoff frequency. In addition, a conductor parallel to the walls can support a surface wave. One may define a surface wave as a wave propagating along an interface between two different media without radiation. A surface wave is bound to a surface, and radiation occurs only at curvatures, nonuniformities, and discontinuities.

The main characteristics of a surface wave are that its phase velocity is typically less than that in the surrounding medium and that the field strength decreases over a wavefront as one recedes from the surface; this is characteristic of an inhomogeneous wave such as is experienced in total internal reflection. Thus, the energy density decreases away from the surface.

The attenuation of the surface wave is complex because it depends upon the conductor location and frequency in addition to both conductor and tunnel wall electrical properties. At low frequencies (perhaps less than 10 MHz), the attenuation increases approximately at a rate proportional to frequency and goes through a maximum, corresponding to maximum tunnel wall absorption. As frequency increases, the attenuation begins to decrease because the energy density is becoming more concentrated around the wire with wall effects being less important. The attenuation goes through a minimum and begins to increase with increasing frequency. This enhancement is caused by the finite conductivity of the conductor as it affects the surface wave. The placement of the conductor in the tunnel has an important effect on attenuation. Minimum attenuation occurs when it's located at the geometric center, and it increases as the conductor approaches the tunnel wall.

The phase velocity is also affected by conductor placement. If the conductor is located at the tunnel center, v is less than the speed of light in vacuum, c . As it moves towards the wall, v increases and becomes greater than c . Note that this doesn't violate relativity, because the energy travels at the signal velocity (usually the same as group velocity).

The following is a theoretical speculation regarding the radiation pattern from the portal. Assume that a TEM wave is emitted from the portal. Recall that most likely this is the dominant mode because of the presence of conductors parallel to the tunnel (such as cables and railroad tracks). This wave will be an approximate inhomogeneous plane wave at the source (portal). It's inhomogeneous because the field strength varies over a surface of constant phase (wave front). This variation is unknown, so it will be ignored in the rough analysis. Temporarily, assume the wave to be monochromatic, then the angular distribution of radiated energy would approximate a Fraunhofer diffraction pattern. In practice, the wave isn't monochromatic, but may be thought of as a superposition of many monochromatic waves, each producing similar diffraction patterns but with different angular locations of nulls and secondary maxima and with different amplitudes. Thus, it's very likely that the superposition will wipe out the individual field variations and produce a relatively smooth radiation pattern, most likely peaked in the forward direction. This pattern would be further modified due to ground reflection and possible reflection from hills.

The portal serves as a secondary source of radiation. This is especially true for the NPE experiment because of the wire grid door. There are three important propagation modes for radiation from the portal to receiving sensors: (1) propagation along the earth's surface, (2) as a direct wave plus possibly the superposition with a ground reflected wave, (3) a sky wave by ionospheric refraction.

The ground wave follows the earth's contour. It's attenuated rather well for frequencies above 3 MHz. The electric field is mainly perpendicular to the earth's surface, but it always has a forward tilt. The phase velocity is less than the speed of light in vacuum, and the energy density drops off with altitude.

In the far field free space, both E and H have a $1/r$ dependence. If the direct wave has a ground reflected wave superimposed upon it, then E and H drop off as $1/r^2$. The field strength varies approximately as the product of both source and receiving antenna height. These characteristics result in a weak EMP signal much beyond the horizon. On the other hand, a temperature inversion enhances over-the-horizon propagation via atmospheric refraction.

Skyway propagation is by means of ionospheric refraction. As applied to EMP, this mode is useful only over a long distance, typically measured in hundreds or thousands of kilometers. Due to the fact that the ionosphere is an absorbing, anisotropic, dispersive, birefringent medium, sensitive information may be lost.

Experimental Set-Up

Four types of sensors were used: antennas, current transformers, B-dot and D-dot detectors. All were placed in the immediate vicinity of the portal.

(1) Antennas. Five antennas were employed: Horizontal and vertical dipoles, resonant at 50 MHz, a vertical monopole at the same resonant frequency, a horizontal 10 MHz dipole, and a helix. Note that these antennas are viewing fundamentally time domain phenomena, so that the frequency listings mainly tell the antenna length. The helix was designed to check for possible high frequency components in the 300 MHz range.

(2) Current transformers. Current transformers were placed around a main power line, a main ground line, a diagnostic cable, and a phone line. These measure the theta component of the surface guided magnetic field (not its time derivative) which can be translated into a sheath current. Unfortunately, access to the device location was denied at every request, so that there's no guarantee that any of the three cables actually led to the device vicinity.

(3) B-dots and D-dots. B-dots measure the time derivative of the tangential component of the magnetic field (equivalent to a surface current) and the time derivative of the normal component of the electric field (equivalent to a surface charge), respectively. These were placed on the wire mesh portal door and the railroad track.

Electric Field Strength

Electric field strength (magnitude of the E vector) is important for at least two reasons. First, the field strength is a major factor in the possibility of detection of the EMP at a given location for a given detector sensitivity and noise background, and this includes propagation through the ionosphere. Second, field strength is a function of yield or source strength, so that in principle, the latter may be estimated from E.

There were several spikes in the voltage vs time plot for both vertical and horizontal dipoles. In the block chart shown below, time is in milliseconds measured from detonation initiation, and electric field strength is in millivolts per meter. A blank in some of the horizontal dipole slots simply means that the signal wasn't clear enough to be certain of its validity.

	16	19	33	48	50	65	81	t in ms
vertical dipole		43	52	90			43	E in mV/m
horizontal dipole				34	34		27	E in mV/m

The average field strength for vertical polarization is on the order of 50 mV/m, whereas it's about 30 mV/m for horizontal polarization.

Fourier Transforms

The Fourier transform is important because sensors, amplifiers, and any other associated circuit elements are bandwidth limited. Thus a knowledge of the EMP frequency spectrum expected from a typical explosion aids in its detection. The reader should keep in mind that EMP is a time domain problem - not frequency domain. Most electromagnetic theory texts assume an imaginary exponential time dependence throughout, which is equivalent to a Fourier transform.

The transforms derived from the time plots are system transforms, namely, a convolution of the actual field at the antenna location with the antenna response, cable response, amplifier characteristics and any property of the digitizer.

The spectrum of nearly all of the sensors may be summarized by saying that most of the electromagnetically propagated energy was contained in the range of frequencies below about 3 MHz. There was a sharp drop in energy density for any frequency above 3 MHz. Four of the sensors had short time duration amplitude variations: monopole at 0.4 MHz, ground coil at 0.2 MHz, coax coil at 0.7 MHz, and the power coil at 1 MHz. The reason for these narrow variations is unknown as of this writing.

Spike Frequencies

Most of the sensors displayed sharp, periodic spikes on voltage vs time plots. Even though the origin of those spikes is unknown, it seems reasonable to assume that they're not caused by the device. A box displaying those frequencies is shown below.

vert. dipole	horiz. dipole	10 MHz horiz. dipole	helix	mono- pole	gnd coil	coax coil	pwr coil	door B-dots	phone coil
2.5 kHz 16 kHz	16 kHz	430 Hz	6.9 kHz	160 Hz	60 Hz	60 Hz	55 kHz	60 Hz	79 Hz 300 Hz

The 60 Hz spikes on the ground coil, coax coil, and door B-dots surely must originate in the line current frequency. The reason it doesn't show on the power coil is most likely because a high pass filter was used in anticipation of a 60 Hz signal. The phone coil spikes may possibly be explained by the four phase ringing voltage with a fundamental of 20 Hz ($4 \times 20 = 80$) and a 300 Hz base frequency of the dial tone. No device information was recorded on the phone coil.

Cable Currents

Current transformers were placed around three cables in the tunnel (ground line, power line, a diagnostic cable). Hopefully, all three led from the portal to near the device, but permission to check this was always denied. The surface waves guided by these cables induce sheath currents by virtue of the near discontinuity of the transverse tangential component of the magnetic field at the outer

conductor. By knowing the voltage to current transfer function of the coils, the following peak sheath currents were indirectly measured: ground coil – 0.05 amps; coax coil – 0.07 amps; power coil – 0.014 amps. It should be noted that the measured power coil current should be too low because a high pass filter eliminated the low frequency components.

Portal Door and Railroad Track Current and Charge Densities

B-dot and D-dot detectors were placed on the portal door and on one of the train track rails. Recall that a B-dot placed on a conducting plane measures the time derivative of the tangential magnetic field which may then be converted to surface current per unit length (the length being perpendicular to the field vector). A D-dot measures the time derivative of the normal component of the electric field (actually displacement vector) which may then be converted to surface charge density.

The peak current density on the track was about 6 amp/m which translates to about a half amp total at its peak on one of the rails for a very short pulse. The peak charge density was calculated to be about two nanocoulombs per square meter. Although several requests were made to assure a continuous rail from the portal to near the working point, all attempts to verify this by walking the tunnel were denied - we'll never know.

The portal door is actually a wire grid which should have surface currents and charge induced on it by the propagating waves. The D-dot on the door failed, but the two B-dots (one vertical and the other horizontal) measured a peak vertical current density of 6.4 amps/m and a horizontal current density of about 1.6 amps/m. Notice that this is in qualitative agreement with the results from the vertical and horizontal dipoles in that vertical polarization was stronger than horizontal.

Low-Frequency Electromagnetic Measurements at the NPE and Hunter's Trophy: A Comparison

**Dr. Jerry J. Sweeney, Earth Sciences Division,
Lawrence Livermore National Laboratory, Livermore, CA**

Abstract

Sensors and recorders were deployed for both the Non-Proliferation Experiment (NPE) and Hunter's Trophy to measure low-frequency (1-30 Hz) electric and magnetic fields accompanying the detonation. Two stations were used for each event, located at a slant range of about 500 m, with measurements of orthogonal horizontal electric field and orthogonal horizontal and vertical magnetic field. Signals were recorded digitally with at 200 Hz sampling rate. Separate magnetic and electric signals were recorded which can be related both to the detonation and the arrival of the shock wave. The detonation time signal from the nuclear explosion is a relatively short pulse occurring with no detectable delay (within 0.5 ms) after the detonation time. The signal from the chemical explosion is a broader waveform with delays ranging from 11-19 ms after the detonation time. The cause of the initial electromagnetic signal for both chemical and nuclear explosions is unknown; the differences between the NPE and Hunter's Trophy results may be related to the different mechanisms involved with plasma generation between nuclear and chemical explosions.

Introduction

The association of strong electromagnetic (EM) signals with atmospheric nuclear explosions is a well-known and extensively-studied phenomenon. EM signals have also been observed from surface chemical explosions by workers in the U.S. (*e.g.* Walker, 1970; Wouters, 1970; Kelly, 1993) as well as in the Former Soviet Union (FSU).

There is a strong broad-band prompt-time signal from an atmospheric nuclear explosion that has been observed with equipment designed to study Extremely Low Frequency — 0.1 Hz - 3000 Hz (ELF) signals (Balser and Wagner, 1963). The ELF signal is of interest because, at these low frequencies, attenuation is very low and the signal can be detected thousands of kilometers away. Balser and Wagner (1963) observed perturbation of greater than 10% in the fundamental earth-ionosphere cavity resonance frequency (Balser and Wagner, 1960), caused by an atmospheric nuclear explosion over Johnston Island, that persisted for about 5 hr. To our knowledge, similar effects have not been observed from chemical explosions.

Underground nuclear explosions also create EM signals that have been observed at distances close (5-10 km or less) to the source (Zablocki, 1966; Malik *et al.*, 1986; Sweeney, 1989). Wouters (1989) outlined four different mechanisms responsible for observed EM signals, each having a different EM spectrum.

Mechanisms at low frequencies, because of lower attenuation, are of special interest. Two low-frequency mechanisms were discussed by Wouters (1989): diamagnetic cavity plasma effect (magnetic bubble) and the magneto-acoustic effect (large-scale ground motion). Because of the relatively small magnitude of the source term for the magneto-acoustic effect, the magnetic bubble effect is probably the most important at ELF frequencies. Bevensee (1990) examined the ELF data from underground nuclear explosions reported by Zablocki (1966), Malik *et al.* (1986), and Sweeney (1989) to see how well it conformed to fields expected from a magnetic bubble. In general, near-field (the static field, at distances less than thousands of km from the source at ELF) field strength drops off as r^{-3} , where r is distance between the sensor and the working point. Bevensee (1990) concluded that the study was "...inconclusive, but does not rule out the magnetic bubble as the primary field source...".

The EM signal from atmospheric chemical explosions is caused by the separation of charges due to the high temperatures and mechanical energy of the explosion. The magnitude of the signal is proportional to the mass and efficiency of the explosive, while the EM spectrum depends on ignition time (Kelly, 1993). Because there is no EM data from chemical explosions approaching the size of historic atmospheric nuclear explosions, it is impossible to compare the relative effects at ELF frequencies. Furthermore, there is no data that we are aware of for EM signals detected from underground chemical explosions.

The significant factor with respect to underground nuclear explosions is that, while EM fields cannot be detected at ELF frequencies at regional or teleseismic distances, they can be detected at distances less than 5 km from the working point. While EM signals have been detected from surface chemical explosions, it is not known whether similar signals will be produced underground. Thus there exists the possibility that EM monitoring can be used as a discriminant between nuclear and chemical explosions in an On-Site Inspection (OSI) verification environment. The purpose of this program of field measurements (Hunter's Trophy and the Non-Proliferation Experiment) is to examine differences in the ELF EM environment between a nuclear test and a similar yield chemical test in the same geologic environment.

Hunter's Trophy data and analysis

Introduction

Previous work (Sweeney, 1989) has shown that electromagnetic (EM) signals in the ELF range of 1 to 40 Hz can be detected up to 5 km from ground zero of an underground nuclear explosion. The purpose of the ELF EM deployment for Hunter's Trophy was to see if a similar ELF signal could be detected at detonation time and to compare the results with possible similar signals that may be produced by the planned chemical explosive test (NPE) in similar geology.

Magnetometers and horizontal electrical detectors used for the Hunter's Trophy test were similar to those used by Sweeney (1989). Because of the short preparation time available for the deployment, we

were unable to field a vertical electric sensor. The PDR-2 data acquisition system used by Sweeney (1989) was no longer available, so we used newer Reftek seismic data acquisition systems, with an attached external hard disk storage unit, to perform initial data sampling and storage at each field station.

Field Set-up and Data Acquisition

Two ELF stations were fielded for the Hunter's Trophy event. Station H5 was located at Nevada Coordinates (feet) 894638N, 632302E and station E6 was located at 890543N, 633355E. Figure 1 shows these locations and the location of ground zero for Hunter's Trophy. Depth of burial for Hunter's Trophy was about 400 m. The horizontal distance to H5 and E6, respectively, is 290 m and 1180 m; this makes the slant range to H5 and E6 490 m and 1246 m, respectively.

A 6-channel and a 3-channel Reftek data acquisition unit were available for the Hunter's Trophy ELF deployment. We chose to use the 3-channel unit at the more distant E6 site and recorded three magnetic field components: vertical, radial, and tangential. At the H5 site we recorded vertical, radial, and tangential magnetic field components as well as the radial and tangential electric field components.

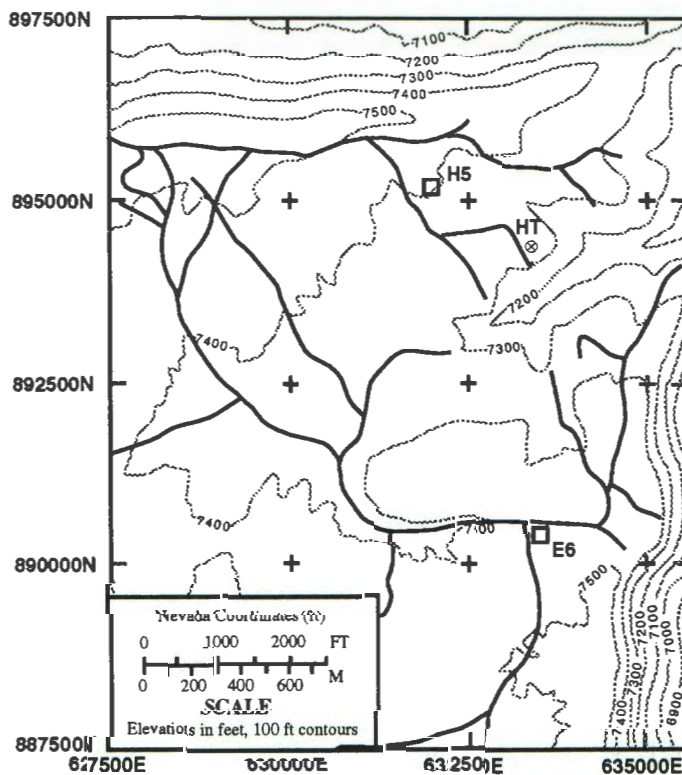


Figure 1. Location map for ELF stations used to monitor the Hunter's Trophy event. HT—ground zero for Hunter's Trophy, H5, E6—locations of ELF stations. Dark lines are roads.

Vertical electric was not recorded at the H5 site for the reasons given above. At each site the magnetic field was detected using the same magnetometer coils used by Sweeney (1989). These coils, which have internal noise much lower than the natural ambient levels, have a relatively flat frequency response between 0.1 and 100 Hz. At site H5 the horizontal electric field was detected with 40 m long telluric lines* at the ground surface. Steel stakes, about 25 cm long, were used as ground electrodes for the telluric lines.

The Reftek data acquisition units were set to sample each signal channel at 200 Hz (200 samples/s). Output of the magnetometers, which have built-in pre-amplifiers, was 100 mV/nT (millivolts/nanoTesla). This signal was further enhanced with amplifiers internal to the Reftek unit. The telluric signals were input to a separate high input impedance pre-amplifier with a gain of 197 before being routed through the internal amplifier of the Reftek unit.

Standard operating procedure at the NTS prevents any personnel from being in the forward areas during an underground nuclear test, so the data acquisition systems had to be triggered automatically. Because we did not know for sure whether or not we would detect a signal from Hunter's Trophy at these two stations, we could not depend on an event trigger, as is often used in remote seismic systems. Our only remaining choice was to turn on the system at the last allowable time before we evacuated the forward area and record to the hard disk continuously. We then had to rely on being able to return to the system after the forward areas were again open after the test to shut down the recorded before the event data on the disk were overwritten. This strategy was successful and ELF data were successfully recorded at both stations.

ELF Results for Hunter's Trophy

As outlined above, three magnetic field components were recorded at stations H5, 490 m from the working point, and at station E6, 1246 m from the working point. In addition, two horizontal components of the electric field were recorded at station H5. One problem we had not anticipated was that direct current (D.C.) offset would affect the recordings. The pre-amplifiers and recording system used by Sweeney (1989) contained built-in high-pass filters that precluded d.c. offset. In normal operations with seismic instruments, d.c. offset is not a problem with the Reftek units. However, at station E6, the magnetic signals recorded had a strong negative D.C. offset, causing negative portions of the signals, especially on the horizontal channels, to be clipped. As a result, only the vertical magnetic signal component at E6 is reliable. Another, less serious, problem arises from 60 Hz cultural noise which was especially strong at station E6, which was located about 250 m south of a 4.5 Kv transmission line.

Signals recorded at station H5 (radial and tangential electric— E_r , E_t ; and vertical, radial, and tangential magnetic— B_z , B_r , B_t) are shown in Fig. 2. Detonation occurred at 1700:00:078 UT on

* A telluric line consists of two separated grounded electrodes. One electrode serves as a reference for measuring the potential to the other electrode via a wire lying on the ground. Typical background noise levels in the ELF range are on the order of a few microvolts/m.

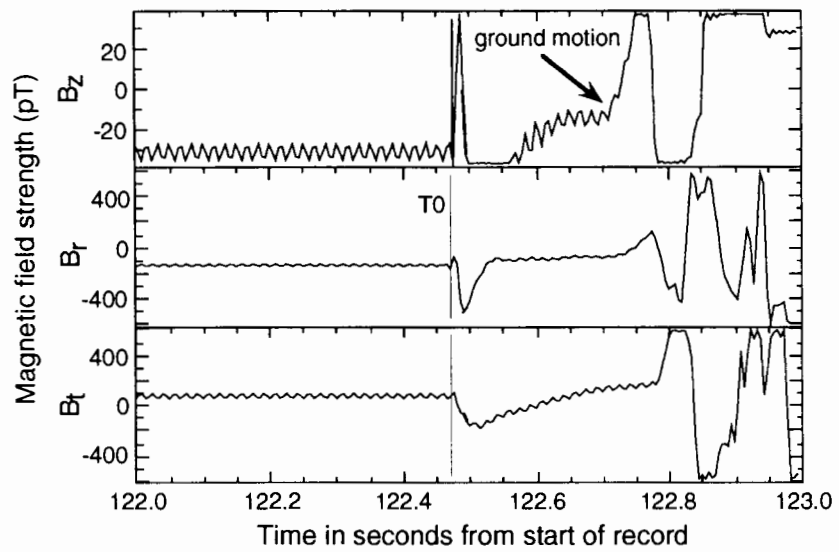


Figure 2a. Magnetic field signals from the Hunter's Trophy event at station H5. Detonation time (1700:00:078 UT) is indicated by the line "T0". The amplifier in the data acquisition system is saturated by the signal due to the ground motion, which arrives 0.2 to 0.3 seconds after T0. There is no detectable delay in the prompt ELF signal, which coincides with T0.

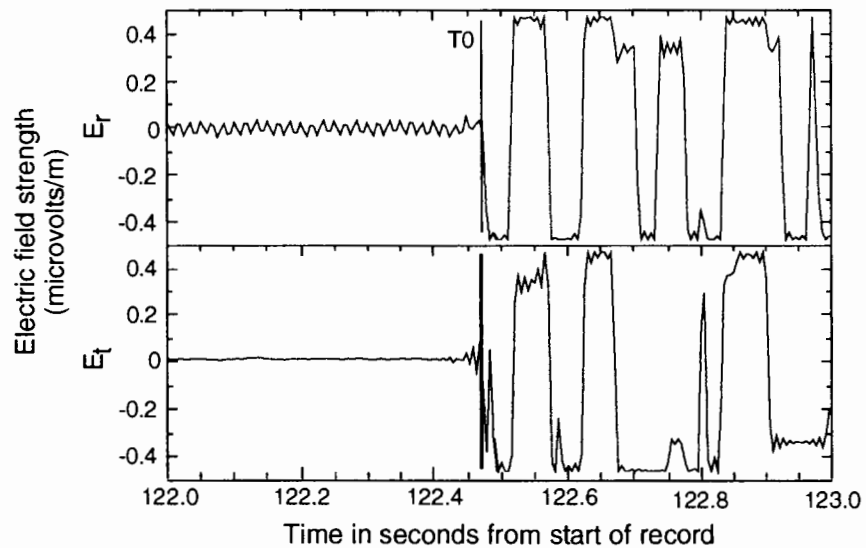


Figure 2b. Electric field signals from the Hunter's Trophy event at station H5. T0 marks detonation time, as for Fig. 2a. In this case, the arrival of the ground motion is obscured because of oscillations triggered by the initial ELF signal.

18 September, 1992. The sampling rate of 200 Hz, or 0.5 ms, limits the resolution of the signals associated with the detonation time (marked T0 on the plots). At station H5 there are very clearly defined prompt time magnetic signals and clear arrival of the ground motion, which creates a strong magnetic signal due to movement of the magnetometer within the earth's magnetic field. In Fig. 2a, the ground motion signal arrives about .24-.31 s after detonation. This represents an apparent seismic transmission velocity of the resolved components of 1860 m/s—a compressional wave velocity typical of shallow depths in this area of Ranier Mesa. The secondary rise in the B_z signal at 0.1 s after T0 in Fig. 2 is consistent with a wave velocity of about 5700 m/s. This may be an electrical signal, but more likely it is just the signal re-emerging from being clipped by the strong negative excursion of the initial pulse. The prompt time signals, which have an arrival time of 0.5 ms or less, are probably associated with the development of Compton electrons (and associated magnetic bubble?) in the underground fireball. It appears that the prompt time signals on the electric channels (E_r , E_t) at H5 saturated either the preamplifier or the Reftek amplifier and possibly induced oscillations in the system; as a consequence the ground motion arrivals are obscured on these channels.

Signals recorded at station E6 (B_z , B_r , B_t) are shown in Fig. 3. As discussed above, there was a strong negative D.C. offset in the signals at this station, causing the negative portion of most of the signals to be clipped. There is also a fairly large component of 60 Hz noise visible on the vertical channel. The arrival of the ground motion is readily apparent on all three traces at this more distant station, and there appears to be a prompt time signal only on the vertical trace. The arrival of the apparent ground motion on the

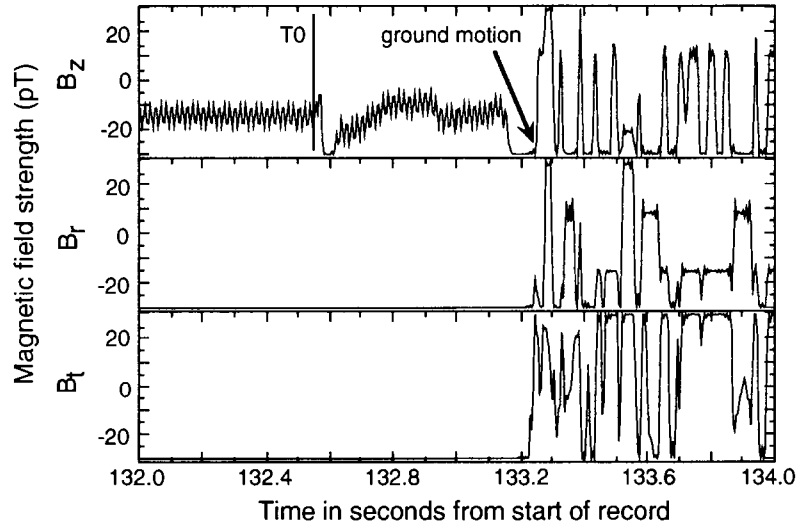


Figure 3. Magnetic field signals from the Hunter's Trophy event at station E6. T0 marks detonation time. Any possible signals from the horizontal components (B_r , B_t) have been lost because of a d.c. offset.

vertical trace occurs about 0.7 s after detonation, this corresponds to a seismic velocity of about 1800 m/s. There is no obvious signature for the arrival of a secondary electrical signal at this station, as was seen at H5. Because of the D.C. offset and clipping at this station, the absolute magnitude of the signals are suspect and it is not possible to compare signal strengths between stations H5 and E6.

In summary, magnetic and electric ELF EM signals were detected within a few milliseconds of detonation at station H5, located within 500 m of the working point of Hunters Trophy. A more distant station, E6, recording only the magnetic component, detected a similar ELF signal in the vertical component. Arrival of ground motion at the detectors is consistent with seismic wave propagation velocities. Equipment problems preclude quantitative comparison of signal amplitudes between the two stations.

300 lb calibration test — data and analysis

Introduction

The purpose of the ELF EM deployment for the 300 lb. calibration test was to see if a signal could be detected at distances less than a kilometer from the working point of an underground high explosive (HE) detonation. The working points for the calibration test and the later NPE test (results discussed below) are the same. Magnetometers, horizontal electrical detectors, and data acquisition systems used for the calibration test were the same as those used for Hunter's Trophy.

Field Set-up and Data Acquisition

Two ELF stations were fielded for the calibration test at different locations than those used for Hunter's Trophy. We expected that if an ELF EM signal were to be detected for a relatively small HE detonation, it would be much smaller than that recorded for Hunter's Trophy, so we picked station locations as close as possible to the working point. Station Q4 was located at Nevada Coordinates (feet) 893733N, 632582E and station E4 was located at 892829N, 633601E. Figure 4 shows these locations and the location of ground zero of the calibration test (and for the chemical kiloton test). Depth of burial in the tunnel was about 400 m. The horizontal distance to Q4 and E4, respectively, is 400 m and 300 m, this makes the slant range to Q4 and E4 566 m and 500 m, respectively.

A 6-channel Reftek data acquisition unit was used at site Q4, recording B_z , B_r , B_t and E_r and E_t . A 3-channel Reftek data acquisition unit was used at site E4, recording B_z , B_r , and B_t only. The Reftek data acquisition units were again set to sample each signal channel at 200 Hz. In order to eliminate possible

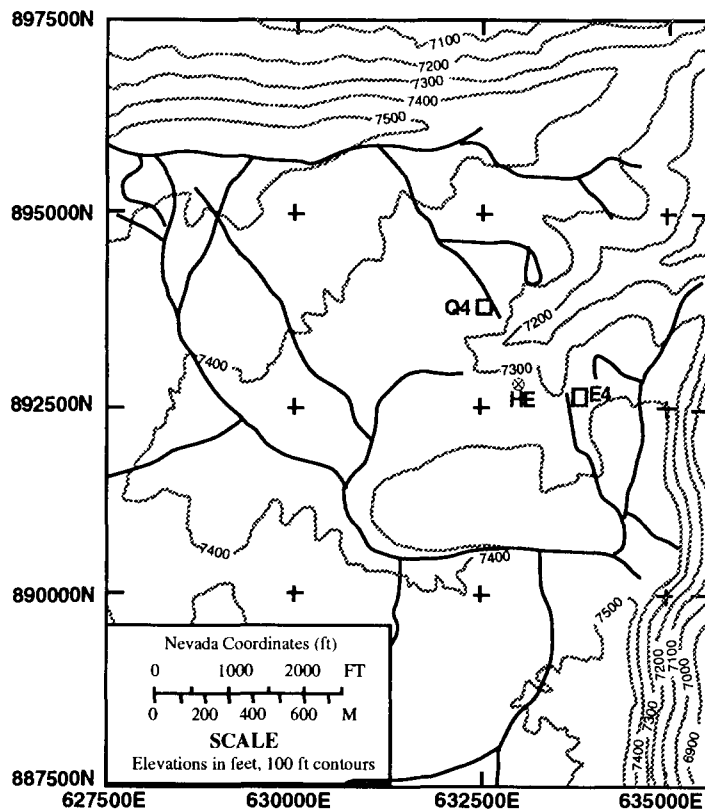


Figure 4. Location map for ELF stations used to monitor the calibration test and the NPE. HE—ground zero for 300 lb. test and the NPE, Q4, E4—locations of ELF stations. Dark lines are roads.

d.c. offset problems that occurred for the Hunter's Trophy test at site E6, we installed low frequency (about 0.1 Hz cutoff) high pass filters at the signal output from the magnetometers. (d.c. bias is eliminated by the pre-amplifier on the telluric channels.) In addition, 60 Hz notch filters (to eliminate 60 Hz) were used on the horizontal magnetic signal channels at station E4, which was very close the 4.5 Kv transmission line.

Results for the 300 lb. calibration test

Detonation of the HE took place at 13:00:130 UT on 30 October 1992. It was raining on Rainier Mesa at the time of the detonation. The disk drive failed some time before detonation at site Q4, probably because of water getting into a cable connection. Because of the disk drive failure, no data was obtained from Q4. Data from site E4 is shown in Fig. 5. The figure shows that the notch filters do help in elimination of 60 Hz noise, since the 60 Hz noise levels are much lower on the horizontal channels where the filters were used. In spite of the rather large background noise (which may have been enhanced by the wet

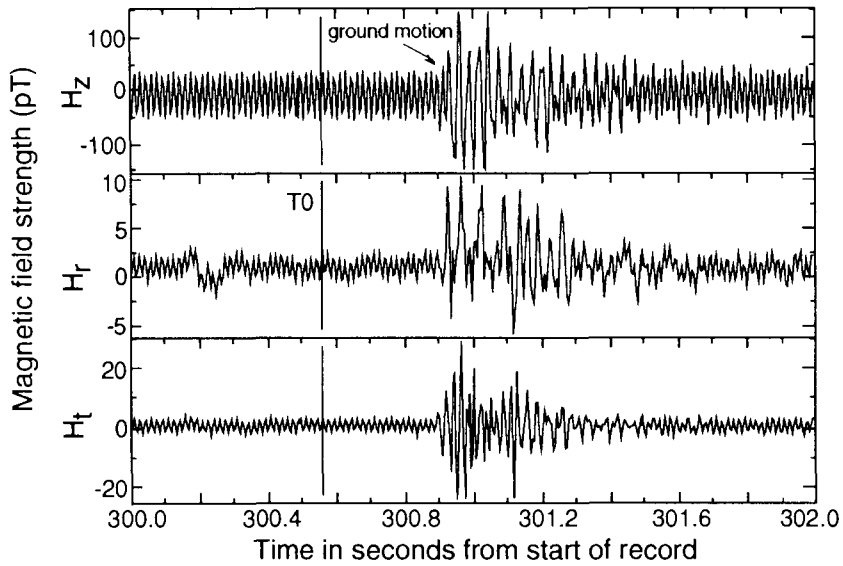


Figure 5. Magnetic signals recorded at station E4 during the calibration test of 30 October 1992. T0 marks the detonation time (1300:00:130 UT). The arrival of the ground motion implies a travel time of about 330 ms, for a signal velocity of about 1715 m/s.

conditions) the arrival of the compressional wave ground motion is easily seen. There is no indication of a prompt time signal at detonation time at this station. The travel time for the seismic wave, which arrives in about 0.33 s, is about 1715 m/s. This compares well to that seen for Hunter's Trophy.

Non-Proliferation Experiment (NPE)

Introduction

The purpose of the ELF EM deployment for the 1 Kt chemical explosion NPE was to see if an EM signal could be detected from a large underground explosion. In this case, the NPE was designed expressly to make comparisons between effects of nuclear (re: Hunter's Trophy) and chemical explosions of similar yield in similar geology. The working point for the NPE is the same as the calibration test explosion discussed above and at a similar depth to the working point as that for Hunter's Trophy. Magnetometers, telluric lines, and data acquisitions systems used for the NPE are essentially the same as those used for Hunter's Trophy and the calibration test, with minor changes as noted below.

Field Set-up and Data Acquisition

Two ELF stations were fielded for the NPE at the same locations used for the calibration test. See the discussion above for station location details. As was the case for the calibration test, vertical, radial, and tangential magnetic field components were measured at stations E4 and Q4. Radial and tangential electric field components were measured at station Q4. We did not field a vertical electric field sensor at Q4

because proximity of bedrock at the surface made it difficult to dig a hole deep enough to provide a stable base for the vertical electric antenna. As was the case for the calibration test, the slant range to stations Q4 and E4 is 566 m and 500 m, respectively.

A 6-channel Reftek data acquisition unit was used at site Q4, recording B_Z , B_r , B_t and E_r and E_t . A 3-channel Reftek data acquisition unit was used at site E4, recording B_Z , B_r , and B_t . As before, the Reftek sampling rate was 200 Hz. In order to reduce 60 Hz cultural noise, a 40 Hz low-pass filter, followed by a 60 Hz notch filter, were used on the magnetic channels at the output of the magnetometer and before input into the Reftek. A 0.1 Hz low-pass filter was also used on the magnetic channels to eliminate the d.c. offset, which caused problems during Hunter's Trophy. Low- and high-pass filters are built into the pre-amplifier used for the electrical measurements. With this arrangement, 60 Hz interference was adequately eliminated in the electrical signals and thus we did not need notch filters. For the NPE experiment, the telluric lines were resurveyed and the electrodes were further separated, to 100 m, to give more signal. In this experiment, the steel electrodes were replaced with porous copper sulfate electrodes of the kind used in spontaneous potential (SP) surveys. The ground was watered around the electrodes, keeping the contact resistance to values less than 2000 ohm.

ELF Results for the NPE

Signals recorded at station E4 and Q4 are shown in Figs. 6 and 7, respectively. At station E4, magnetic signals emerge from background about 19 ms after detonation time. The velocity represented by this

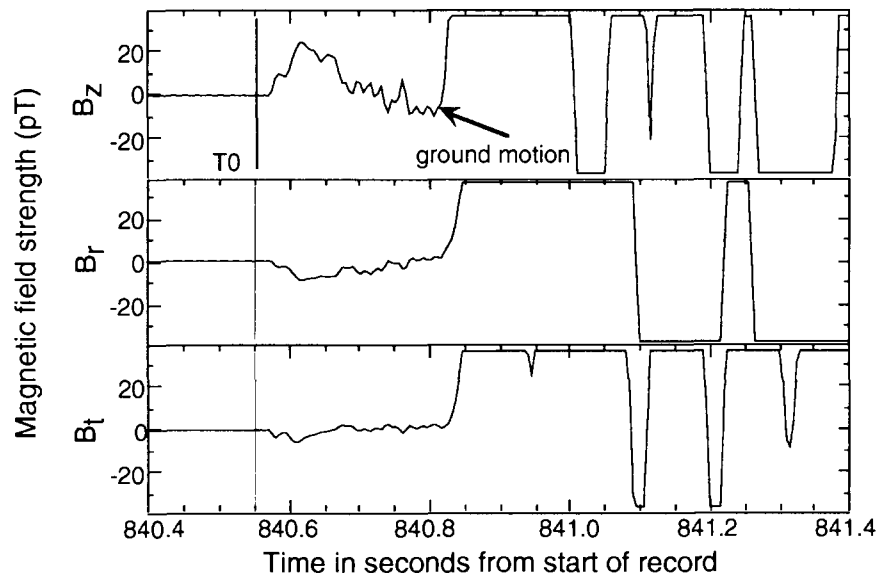


Figure 6. Magnetic field signals from the NPE experiment at station E4. T0 marks the detonation time (00:01:080 UT). Arrival of the ground motion saturates the amplifier in the data acquisition system.

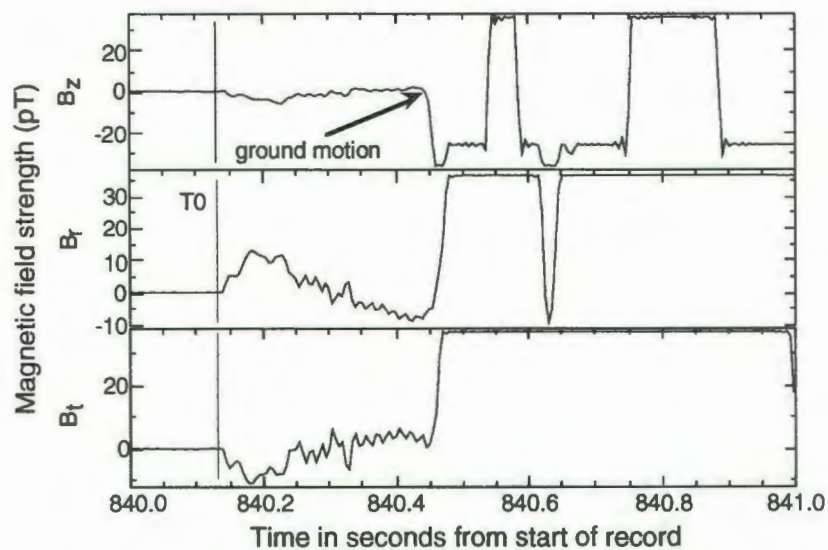


Figure 7a. Magnetic field signals from the NPE experiment at station Q4. T0 marks detonation time (00:01:080 UT). Arrival of ground motion saturates the amplifier of the data acquisition system.

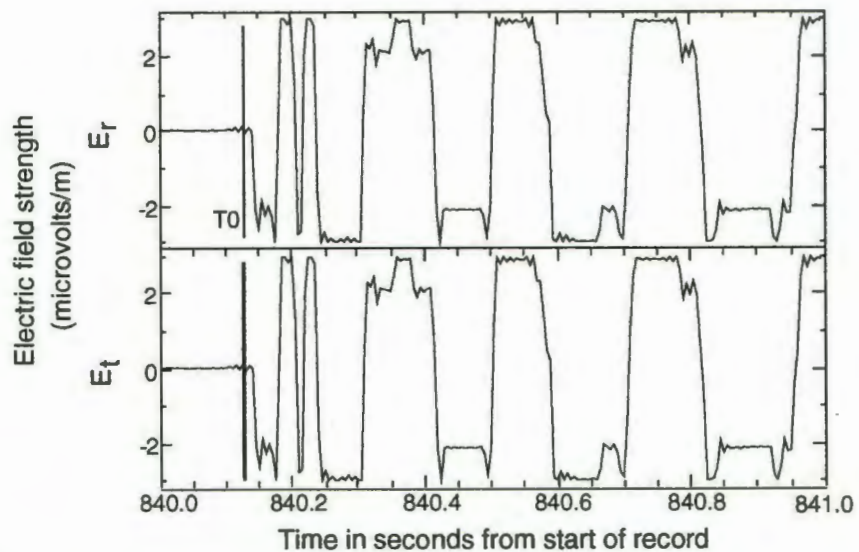


Figure 7b. Electric field signals from the NPE experiment at station Q4. T0 marks detonation time (00:01:080 UT). The initial electric signal saturates the amplifier of the data acquisition system.

early waveform (about 26,000 m/s) is much too fast to be due to local ground motion. The arrival of the seismic wave, about 260 ms after detonation, is quite clear and consistent with a velocity of about 1870 m/s. Note that the early pulse in this case has a much different character from the prompt time pulse associated with the nuclear explosion (Fig. 2); the chemical explosion pulse is broader (lower frequency) and lower in amplitude.

Signals similar to those at station E4 were also recorded from the magnetic and electrical sensors at station Q4 (Fig. 7). At this station the initial signal arrives somewhat earlier (11 ms) after detonation time and is seen on all components of the magnetic and electric fields measured. The arrival of the ground motion is clearly seen on the magnetic signals about 320 ms after detonation, with a velocity of about 1770 m/s. Arrival of the ground motion in the electrical signals is obscured by oscillations—presumably due to saturation of the amplifier by the initial input pulse. The initial magnetic signal at this station is similar in form to the signal recorded at E4, but the vertical component is much smaller.

The resolution of magnitudes of the initial broad pulse at station E4 are a magnitude vector pointing 75° downward (positive z for the vertical sensor) and radially outward (the negative r component is about four times greater than the negative t component). At station Q4 the resolved magnitude is a vector pointing about 30° upward and toward the SE (38° from the radial [east] direction).

Comparison of the NPE results with Hunter's Trophy

Low frequency EM pulse (EMP) signals were recorded from both Hunter's Trophy and the NPE chemical explosion. Two fundamental differences are apparent in the EMP signals from these two underground explosions (see Figs. 2, 3, 6, and 7). One difference is that the EMP from the nuclear test occurs immediately at detonation time, whereas there is a time delay for the initiation of the EMP from the chemical explosion. Similar time delays have been noted from surface chemical explosions and are related to the energy of the explosive (Kelly, 1993). The second difference is in the shape of the EMP. The EMP from the nuclear test is about 50 ms in duration (10 Hz) while that from the chemical explosion is about three times longer, on the order of 150 ms (3.3 Hz). These differences in pulse shape are most likely caused by the different mechanisms which cause the EMP. The observed EMP shape for the NPE is consistent with similar waveforms observed for surface explosions and is probably caused by the movement of ions within the explosion. The EMP from Hunter's Trophy is very similar to EMP signals observed at ELF frequencies for other nuclear explosions (Sweeney, 1989).

These observations have important consequences for discrimination of chemical and nuclear explosions in an OSI scenario. However, these results represent experience from only one underground chemical explosion. It is premature to suggest that these observations are typical, and much work needs to be done to determine scaling effects and how the EMP is attenuated with distance from the working point.

References

- Balser, M. and C.A. Wagner, 1960, Observation of earth-ionosphere cavity resonances, *Nature*, **188**, pp. 638-641.
- Balser, M. and C.A. Wagner, 1963, Effect of a high-altitude nuclear detonation on the earth-ionosphere cavity, *Jour. Geophys. Res.*, **68**, no. 13, pp. 4115-4118.
- Bevensee, R.M., 1990, *Examination of Yield Determination by the Magnetic Bubble Effect*, Lawrence Livermore National Laboratory Report UCRL-ID-106036, 35 pp.
- Kelly, R., 1993, *EMP from Chemical Explosions*, Los Alamos National Laboratory Report LA-UR-93-983, 35 pp.
- Malik, J., R. Fitzhugh, and F. Hormuth, 1985, *Electromagnetic Signals from Underground Nuclear Explosions*, Los Alamos National Laboratory Report LA-10545 MS UC-34.
- Sweeney, J.J., 1989, *An Investigation of the Usefulness of Extremely Low-Frequency Electromagnetic Measurements for Treaty Verification*, Lawrence Livermore National Laboratory Report UCRL-53899.
- Walker, C.W., 1970, *Observation of the Electromagnetic Signals from a High Explosive Detonation*, Lawrence Livermore National Laboratory Report UCRL-72150, 16 pp.
- Wouters, L.F., 1970, *Implications of EMP from High Explosive Detonation*, Lawrence Livermore National Laboratory Report UCRL-72149, 26 pp.
- Wouters, L.F., 1989, *The Underground Electromagnetic Pulse: Four Representative Models*, Lawrence Livermore National Laboratory Report UCID-21720, 49 pp.
- Zablocki, C.J., 1966, Electrical transients observed during underground nuclear explosions, *Jour. Geophys. Res.*, **71**, pp. 3523-3542

Comparison of the Non-Proliferation Experiment Aftershocks with Other Nevada Test Site Events

Steve Jarpe, Peter Goldstein, and J. J. Zucca

Lawrence Livermore National Laboratory

Abstract

As part of a larger effort to develop a system for on-site inspection of suspected nuclear testing sites, we have been working to identify phenomenology of aftershock seismicity which would be useful for discriminating between nuclear explosions, chemical explosions, earthquakes or other seismic events. The phenomenology we investigated includes the spatial distribution of aftershocks, the number of aftershocks as a function of time after the main event, the size of the aftershocks, and the frequency content of the aftershock signals. Our major conclusions are:

- An OSI must be conducted within 2 weeks of the occurrence of the suspect event in order to observe a sufficient number of aftershocks.
- Aftershocks of concentrated chemical explosions (such as the NPE) are indistinguishable from aftershocks of nuclear explosions.
- Earthquake and explosion aftershock sequences can be differentiated on the basis of depth, magnitude, and in some cases, frequency content of seismic signals.

Introduction

If a Comprehensive Test Ban Treaty (CTBT) is negotiated in the future, worldwide monitoring to detect nuclear explosions will be conducted using a variety of sensors. On-Site Inspections (OSIs) may be used to investigate suspicious events detected by the worldwide monitoring systems. These OSIs would use of a variety of methods to determine more accurately the location and identity of suspicious events (Zucca, this symposium). Aftershock monitoring is one of the methods that will be used in an OSI. Seismic monitoring for aftershocks of suspected nuclear explosions has two main goals: (1) more accurately determine the location of the suspect event by locating the aftershocks, and (2) to help determine the source type of the suspect event (e.g., explosion or earthquake).

Early studies addressed the concern that explosions could stimulate significant seismic activity (e.g., Boucher et al., 1969; Ryall and Savage, 1969; Hamilton and Healy, 1969). Results from these studies indicate that post-shot seismicity is constrained to the vicinity of the explosion in both space and time. Observations of post-shot seismic phenomena may also be useful for addressing questions related to containment of explosions. For example, Edwards et al., (1983) investigated the spatial and temporal distribution of aftershocks occurring within a few scaled depths of burial of several explosions at the Nevada Test Site (NTS) and noted that the distribution of activity was related to various features including nearby faults, structural and stratigraphic boundaries, and perhaps, in some cases, the water table level. In the late 1970s and early 1980s, when a CTBT was being considered, studies to determine the use-

fulness of aftershock monitoring for OSIs were conducted by the Lawrence Livermore, Los Alamos, and Sandia National Laboratories using nuclear explosions conducted at the Nevada Test Site (NTS). These studies primarily concentrated on the detection and location of aftershocks of nuclear explosions (Smith and Geil, 1982).

The major findings of these studies relevant to the OSI problem are

- All nuclear explosions with yields greater than approximately 1 kt produce aftershocks that are detectable at the ground surface.
- The number of aftershocks at a given time following the explosion varies greatly depending on local geologic conditions.
- The aftershock locations were usually centered around the working point and extended to a distance of less than approximately 5 cavity radii.
- Explosions sometimes produce aftershocks with anomalously low frequency content.

In this paper, we use published and unpublished results from some of these previous studies and new results from the NPE, other NTS explosions, and earthquakes to address the following issues:

- How many aftershocks occur after the main event, how big are they, and what is their distribution in time?
- Can chemical and nuclear explosions be discriminated based on their aftershocks?
- Can earthquakes and explosions be discriminated based on their aftershocks?

Aftershock Production Rate

We summarized results from previous studies and combined them with results from the NPE and the Hunter's Trophy nuclear test to determine the maximum time after the main event that an OSI aftershock deployment would detect a significant number of aftershocks. For purposes of discussion, we chose a lower limit of one event per day as sufficient activity to locate and characterize an aftershock sequence. Figure 1 shows the frequency of aftershock occurrence in events per day as a function of the number of days after the explosion for several explosions at NTS. The explosions are located on Rainier Mesa (Hunter's Trophy and the NPE), Yucca Valley (Redmud, Iceberg, and Baseball) and Pahute Mesa (Colwick and Emmenthal). The aftershock decay rates for these explosions fall into two populations that are correlated with location. The Pahute Mesa events have a higher rate of aftershock activity than the Rainier and Yucca events.

We attribute this higher rate of aftershock activity to two reasons: (1) The material in the vicinity of the working point was different for the two groups; the Pahute Mesa events were detonated in hard rock, *i.e.*, a densely welded tuff. The other events were detonated in softer, non-welded tuff. Explosions detonated in the stronger, harder material should produce more aftershocks because the stronger material can store and subsequently release more of the strain energy produced by the explosion. (2) The material above the working point and extending to the surface is much more competent at Pahute Mesa than at Rainier Mesa and Yucca Valley (average velocity 3 km/s at Pahute compared

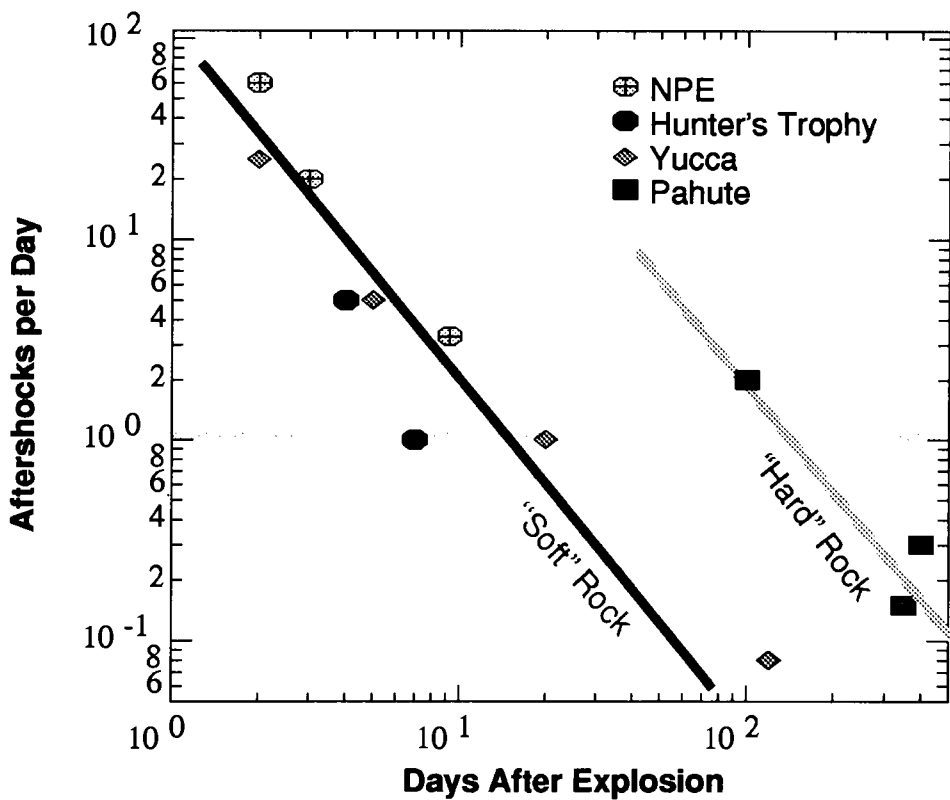


Figure 1. Number of nuclear explosion aftershocks per day detected by seismic sensors placed on the ground surface directly above the working point as a function of time after detonation. The “Yucca” explosions are Redmud, Baseball, and Iceberg. The “Pahute” explosions are Colwick and Emmenthal. The NPE and Hunter’s Trophy were in Rainier Mesa. A horizontal line is drawn at one event per day. “Soft” rock indicates explosions in non-welded tuff, and “hard” rock indicates explosions in welded tuff.

to 1.6 km/s at Rainier and Yucca), resulting in lower attenuation and correspondingly higher signal amplitudes at the surface of Pahute Mesa.

Based on the aftershock rates for the explosions studied, we find that the one-aftershock per day limit can range from approximately 10 days for explosions conducted in low-strength, high attenuation regions to 3 months or more for explosions conducted in areas with more competent geology.

Discrimination of concentrated chemical and nuclear explosions

We compare the number of aftershocks as a function of time and magnitude, and the waveform characteristics of the NPE aftershocks with those of other nuclear explosions, including Hunter’s Trophy, which was located 600 meters from the NPE. We found no differences that could be used to identify an event as a nuclear explosion or concentrated chemical explosion.

Figure 1 shows that the number of NPE aftershocks as a function of time is similar to other explosions on Rainier.

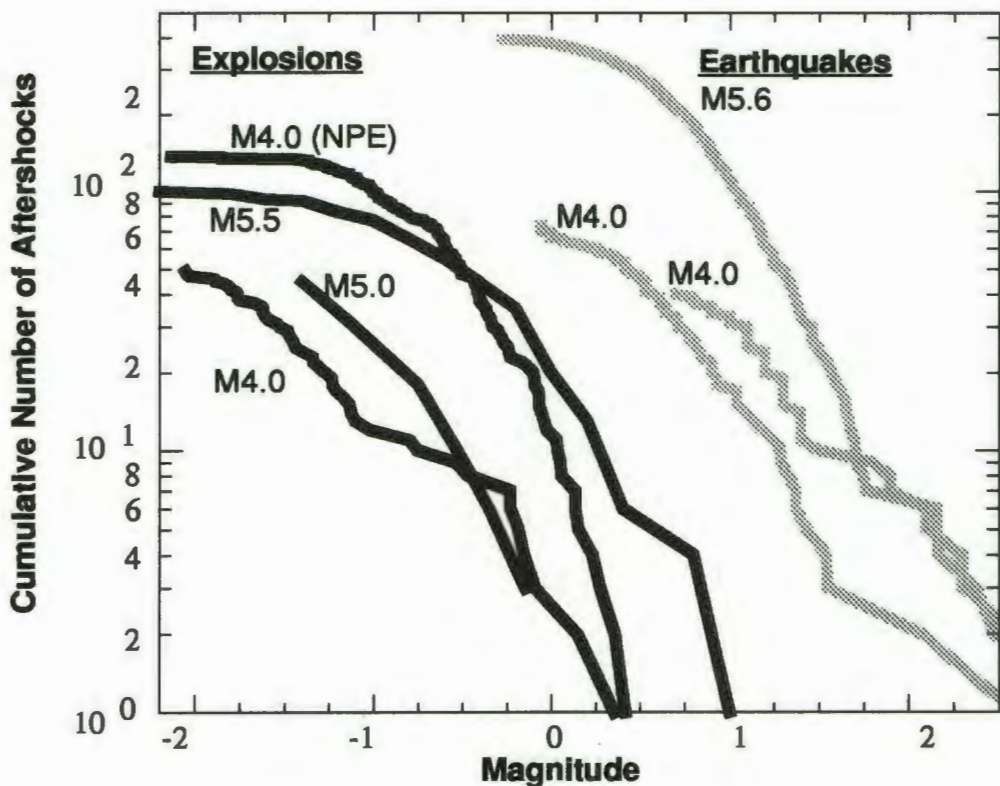


Figure 2. Magnitude-Frequency (B-value) plots for the aftershocks of the NPE and three nuclear explosions (one each from Pahute Mesa, Rainier Mesa, and Yucca Flat, solid black lines) and three earthquakes with magnitudes 5.6, 4.0, and 4.0 (gray lines). The vertical axis is the cumulative number of aftershocks with magnitude greater than the corresponding value on the horizontal axis. Explosions less than 150 kt did not produce aftershocks larger than magnitude 1.0, which is distinctly different from earthquake aftershock sequences.

ier Mesa (Hunter's Trophy) and Yucca Valley. The NPE produced 2 to 5 times more aftershocks than did Hunter's Trophy in a similar time period, but this difference is within the scatter of other explosions in similar geologic settings.

Figure 2 is a magnitude-frequency (or b-value) plot, which shows how the aftershocks are distributed by magnitude. Although the shape of the NPE distribution looks somewhat different from the nuclear explosion, the variation among the nuclear events is too large to consider the difference significant.

We compared the waveforms of NPE and Hunter's Trophy aftershocks recorded at the same station location approximately equidistant from the two explosions. We found no significant differences between aftershocks of the two explosions; Figure 3 shows a pair of aftershocks of similar size from the two explosions. All aftershocks located near the cavities of the two explosions were similar in character to the two shown in Figure 3. We will show later that these aftershocks have a much lower frequency content than comparable earthquake aftershocks.

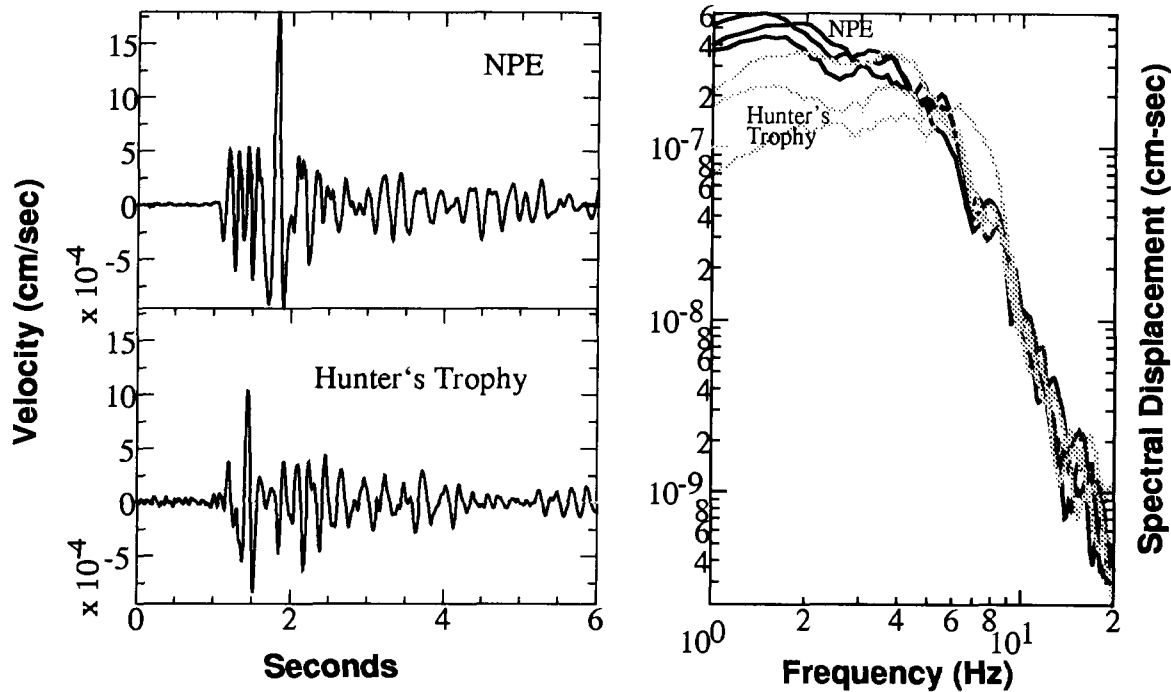


Figure 3. Magnitude 0.35 aftershocks of the NPE and Hunter's Trophy, recorded at the same station on the surface of Rainier Mesa, approximately 0.5 km from surface ground zero of both explosions. The waveforms and spectra of NPE and Hunter's Trophy aftershocks are very similar.

Discrimination of explosions and earthquakes

The depth of aftershocks is usually an excellent discriminant between explosions and earthquakes because most earthquakes occur at greater depths than explosions can easily be emplaced. The deepest nuclear explosions were approximately 2 km deep. Most earthquake aftershocks occur deeper than 5 km, except in intraplate areas such as New York State and central Australia (Marone and Sholz, 1988). Aftershocks of these intraplate earthquakes can occur within 1 km of the surface.

Earthquakes generally produce aftershocks nearly as large as the main event. The magnitudes of explosion aftershocks show much less correlation with the magnitude of the main event. For explosions with yields less than 150 kt, aftershocks have Richter magnitudes less than about 1.0 regardless of the explosion size. This is illustrated in Figure 2, where we compare magnitude-frequency distributions of explosion and earthquake aftershock sequences. This discriminant may not work as well for smaller main events ($M < 3$) because the largest earthquake aftershocks will be less than magnitude 3, and/or the explosions may not produce any detectable aftershocks.

A potential discriminant between explosion and earthquake aftershocks is based on the observation of anomalous "low-frequency" explosion aftershocks (Ryall and Savage, 1969; Smith and Geil, 1982). These low-frequency aftershocks have been observed following explosions conducted at Yucca Valley, Pahute Mesa, and Rainier Mesa; however, the fraction of the total number of aftershocks that are of this type varies greatly. Some explosions produce

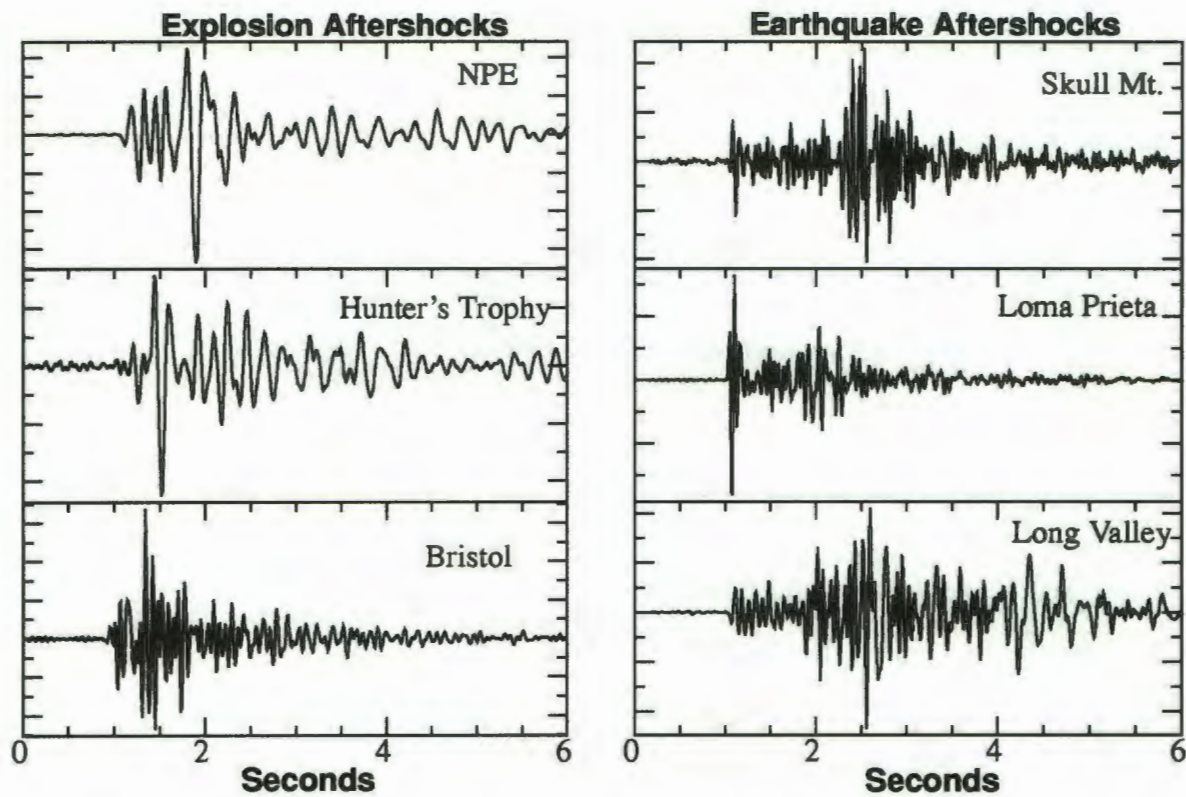


Figure 4. Explosion aftershocks recorded at the surface above the working point of three nuclear explosions. Shallow (< 3 km depth) earthquake aftershocks recorded at the surface at an epicentral distance of less than 3 km. Explosions produce low-frequency and high-frequency aftershocks, and earthquakes produce only high-frequency aftershocks.

only a few low-frequency events, and some, such as Hunter's Trophy and the NPE, produce almost exclusively low-frequency aftershocks.

Figure 4 compares example waveforms of “low-frequency” and “normal” explosion aftershocks and shallow earthquake aftershocks. Differences in frequency content between typical crustal earthquake aftershocks and low-frequency explosion aftershocks can be quantified by comparing their corner frequencies as a function of moment or magnitude. For example, a magnitude 1.0 earthquake aftershock with a stress drop of 30 bars (typical for crustal earthquake aftershocks) would have a corner frequency of approximately 100 Hz (Scholz, 1990, Brune, 1970). In contrast, magnitude 1.0 low-frequency explosion aftershocks have corner frequencies of 3 Hz, more than an order of magnitude less than that of their earthquake counterparts. This could be a very useful tool for identifying explosions from their aftershocks. The anomalous low frequency character of the explosion aftershocks suggest a relatively long source duration in comparison to most earthquakes. An alternative explanation is extremely high near-source attenuation. To explain our observations, the Q would have to be less than 1 within a 50-meter radius around the source. Such a low Q is physically unreasonable especially given that low Q rocks generally have low strength and would not be able to support the stresses needed to generate aftershocks.

Conclusions

Detection and characterization of post-event seismic activity can help identify ambiguous events in most environments, provided local seismic data acquisition begins soon enough: using the one event per day cutoff, a small (~1 kt) event in alluvium or tuff would require data from within a few weeks of the event. If the main event is in hard rock, a few months may be adequate. If five to ten (or more) events can be recorded, it should be possible to differentiate earthquake and explosion aftershocks based on a combination of observations of their locations, magnitudes, and waveforms. Discrimination of nuclear and chemical explosions based on their aftershocks could be a very difficult problem.

Acknowledgments

We would like to thank Don Rock, Pat Lewis, and Dan Ewert for assistance acquiring the NPE and Hunter's Trophy seismic recordings on Rainier Mesa. This work was performed under the auspices of the Department of Energy by the Lawrence Livermore National Laboratory under contract number W-7405-ENG-48.

References

- Boucher, Gary, Allan Ryall, and Austin E. Jones, "Earthquakes Associated with Underground Nuclear Explosions." *Journal of Geophysical Research* 74, 2271, 1969.
- Brune, James N., "Tectonic Stress and the Spectra of Seismic Shear Waves from Earthquakes." *Journal of Geophysical Research* 75, 4997, 1970.
- Edwards, C. L., M. D. Harper, T. A. Weaver, D. J. Cash, J. M. Ray, E. F. Homuth, "Microquake Activity Associated with Underground Nuclear Testing at the Nevada Test Site," Los Alamos National Laboratory, LA-8553-MS, 1983.
- Hamilton, R. M. and J. H. Healy, "Aftershocks of the Benham Nuclear Explosion," *Bulletin of the Seismological Society of America* 59, 2271, 1969.
- Marone, Chris, and C. H. Scholz, "The Depth of Seismic Faulting and the Upper Transition from Stable to Unstable Slip Regimes." *Geophysical Research Letters* 15, 621-624, 1988.
- Ryall, Alan and William U. Savage, "A Comparison of Seismological Effects for the Nevada Underground Test Boxcar with Natural Earthquakes in the Nevada Region," *Journal of Geophysical Research* 74, 4281, 1969.
- Scholz, Christopher H., *The Mechanics of Earthquakes and Faulting*, Cambridge University Press, Cambridge, 1990, Chapter 4.
- Smith, A. T., and R. G. Geil, "Microseismicity Following an Explosion," SSA abstract 1982.

Spontaneous Potential and Telluric Measurements on Rainier Mesa Related to the NPE

**Dr. Jerry J. Sweeney, Earth Sciences Division
Lawrence Livermore National Laboratory, Livermore, CA**

Abstract

We made measurements of spontaneous potential (SP) on Rainier Mesa to see if changes in subsurface electrical properties of rock related to the Non-Proliferation Experiment (NPE) explosion can be detected at the surface. A north-south line, repeated 3 times and running within 50 m of surface ground zero (SGZ) of Hunter's Trophy and within 20 m of SGZ of the NPE, was measured before and after the NPE. An east-west line, with one end within 20 m of SGZ of the NPE was also run before and after the NPE. High values of surface potential along the north-south line in the vicinity of the NPE apparently moved northward after the detonation. A similar change was not noted on the east-west line. A telluric line (0.025-0.1 Hz and 8.0 Hz) was also run prior to the NPE along the same north-south line as the SP measurement, but farther to the west of SGZ for Hunter's Trophy. There is a prominent high in the 8.0 Hz data in the northern part that may be related to a former nuclear test, but it could also be related to local geology. Results from these geophysical methods, while showing some promise for use in an on-site monitoring regime, also emphasize the need for repeatable background reference data.

Introduction

The requirements of the On-Site Inspection (OSI) environment—to locate the site of a clandestine underground nuclear explosion after it has been detonated—are truly challenging. Underground nuclear explosions may be detonated several hundred meters below the surface in order to contain the nuclear products as well as to conceal evidence of their occurrence. An important OSI need is for methods which can rapidly "home in" on a target site in a reconnaissance mode, with later detailed surveys to confirm the detonation location. In this paper we report on two reconnaissance geophysical methods that were evaluated for relevance to OSI in conjunction with the Non-Proliferation Experiment (NPE) on Rainier Mesa at the Nevada Test Site.

Spontaneous potential (SP) and E-field ratio telluric methods are two electrical survey methods which have shown promise for detecting subsurface changes in electrical properties related to underground nuclear explosions. Both of these methods are relatively easy to implement over moderately rugged terrain by two field personnel. Lines 1-2 km long can be surveyed in 1-2 days using these methods.

Spontaneous potential measurements simply involve the measurement of the d.c. potential between two points on the ground surface (they are also commonly done in boreholes and are a standard

measurement in oil exploration). The electric field at the surface of the earth varies both spatially and temporally. At very low frequencies (effectively d.c.) voltages are relatively constant and often repeatable over large areas. The source of the electrical potential causing an SP anomaly is electrochemical reactions or flow of either heat or fluid. The depth and strength of the source and conductivity of the overlying rock determine the amplitude and width of the anomaly. Thus the distance between survey measurement points will depend on the depth of the presumed source. When a surface survey is run, a centrally-located point is selected for a reference electrode and all measurements are then referenced to that point. Thus, for example, if the survey line is to be 2 km long, a single 2 km long wire will have to be pulled between the reference electrode to the end of the survey line. In order to reduce random variations in the measurements due to surface conditions, non-polarizing electrodes are used.

SP anomalies related to underground nuclear explosions were investigated by Corwin (1989) and McKague *et al.* (1991) in Yucca Flat at the Nevada Test Site. Strong anomalies (amplitude 20–80 mV compared to a measurement variability of ≈10 mV) were measured from nuclear explosions with working points both above and below the water table. A typical anomaly pattern was that of an inverted sombrero—a large central negative anomaly surrounded by a positive ring anomaly. McKague *et al.* found that the anomalies may take months to develop, they continue to evolve over months to years, and they are complex in character for a variety of reasons, including the interaction of closely-spaced explosions. McKague *et al.* (1991) found that the anomalies could be modeled with a time-dependent thermo-electric model which took into account regional geology, the broken alluvium developed in the collapse chimney above the working point, and realistic thermal and fluid flow conditions in the vicinity of the explosion. The conclusion of the study was that, on Yucca Flat, SP anomalies related to underground nuclear explosions are easily detected, but not easily interpreted.

The E-field telluric method was investigated for application in an OSI context at Yucca Flat by Didwall and Wilt (1983). This method utilizes time-varying electric fields associated with earth currents naturally induced by ionospheric and tropospheric electromagnetic activity to measure relative changes in subsurface conductivity. The depth of investigation depends on the "skin depth", or depth of penetration of the external fields, which in turn depends on the earth conductivity profile and the frequency monitored. Low frequencies will represent conductivities averaged over a greater depth than high frequencies; thus a variety of frequency bands are usually monitored during a survey to compare changes between deep and shallow levels of the ground. The equipment is relatively portable and lines 1–2 km long can easily be surveyed by two people in a day. Didwall and Wilt (1983) measured strong anomalies associated with underground chimneys associated with underground nuclear tests at Yucca Flat. The anomalies were best seen in data taken at the highest frequencies: 53–60 Hz and 100–125 Hz. This is consistent with a resistivity anomaly located at depths of about 300 m surrounded by rock with a conductivity of about 0.02 S/m.

The lengthy delay between the originally-planned (January-February 1993) and actual (September 1993) scheduling of the NPE gave us the opportunity to field both an SP survey and an E-field ratio survey on Rainier Mesa to test the applicability of these techniques in an area with geology different from Yucca Flat. SP measurements or electrical soundings, to our knowledge, have never before been conducted on Rainier Mesa, so we were not sure what the background would look like. Details of the surveys and the data collected are discussed below.

SP Surveys

A site central to the Rainier Mesa testing area and about 300 m from surface ground zero (SGZ) of the NPE was chosen as the reference point for the SP survey. Three survey lines were surveyed (using a 100 m fiberglass tape measure and a compass) to the north, south and east of this central reference point, as shown in Fig. 1. We ran the lines along existing roads as much as possible for ease of access, but it is not necessary to do so. The circuitous nature of the survey lines in some places comes about because of the need avoid some of the steeper terrain and (on the northern segment) because we wanted the line to pass close by the SGZ of the Hunter's Trophy underground nuclear event.

The SP survey equipment is quite simple, it consists of a set of electrodes, fine gauge wire on a spool, and a high impedance d.c. digital voltmeter. The electrodes we used are copper-copper sulfate porous pot electrodes (non-polarizing) manufactured by Tinker and Rasor, San Gabriel, California. The fine gauge wire we used is lacquer-coated copper wire of the type used for transformer windings. A 5 km long spool of this wire is about 12 cm in diameter and weighs less than 3 kg. The wire impedance is about 1 ohm per m. For safety reasons at NTS in remote areas, we used a two-person crew; but one person could easily complete the measurements. A two person team can easily measure about 2 km of line (40 stations) in one day.

In making SP measurements, random noise is minimized by having a good electrical connection with the ground. This is best accomplished by digging a shallow hole to where moist soil is found, if possible, and then placing the electrode in the hole so that the porous ceramic end of the electrode makes a good connection with the moist soil. The electrode is then covered with dirt to ensure a good connection and to minimize thermal effects. At the base reference station location (see Fig. 1) we implanted two electrodes in the ground and shaded them from the sun to minimize drift due to thermal fluctuations. One end of the wire is connected to the electrodes at the reference station and the wire spool is then pulled out to the next measurement station. At the measurement station, another shallow hole is dug, an electrode is emplaced, and the measurement is taken by measuring the d.c. voltage between the buried electrode at the station and the wire connected to the reference. Voltages measured are generally are in the tens of mV range. The electrode at the station is then pulled up and the wire is pulled to the next station. To complete an entire survey of a line, a continuous length of up to 1.5 km of wire had to be pulled.

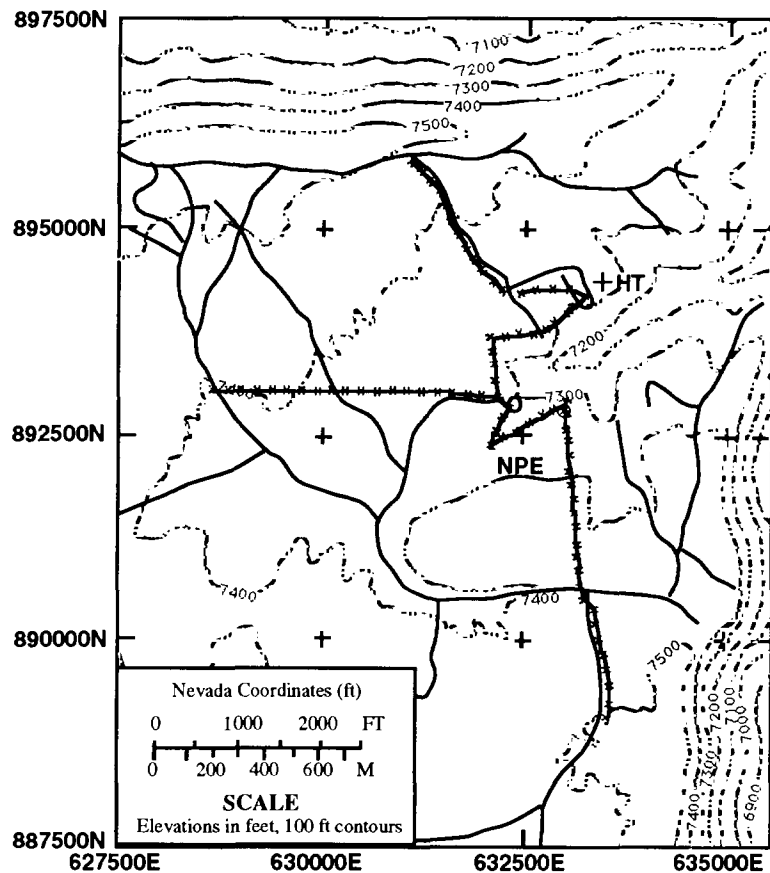


Figure 1. Location map of spontaneous potential measurements on Ranier Mesa. Each X marks the location of an SP measurement. The large circle in the middle of the figure is the location of the reference electrode station. Solid lines are roads. HT—surface ground zero of Hunters Trophy (nuclear), NPE—surface ground zero of the NPE detonation.

The north-south line of Fig. 1 was surveyed twice before the NPE detonation, in July and September, and again in November after the NPE test. The east-west line of Fig. 1 was measured once before the NPE detonation, in September, and once after the detonation, in November. All the data from the north-south line are shown in Fig. 2. The data are referenced to a straight north-south cross-section, so that when the survey line jogs to the east or west the data have been projected onto the reference line. Places where data points are closely spaced thus represent sections where the measured line jogs east or west. The data in Fig. 2 show a typical "bounce" of about ± 10 mV, and there is, with a few exceptions, about a ± 10 mV repeatability between the measurements at a given station. The average of the two sets of pre-NPE data can be seen to generally follow topography, as is shown in Fig. 3, with the exception of a high between about 800 m south and 1000 m south. The reference electrode is located at about 1100 m south, so the high corresponds to an area just to north of the head of the gully in Fig. 1 that runs to the northeast of the reference station (refer to the 7200 ft contour northeast of the reference station in Fig. 1).

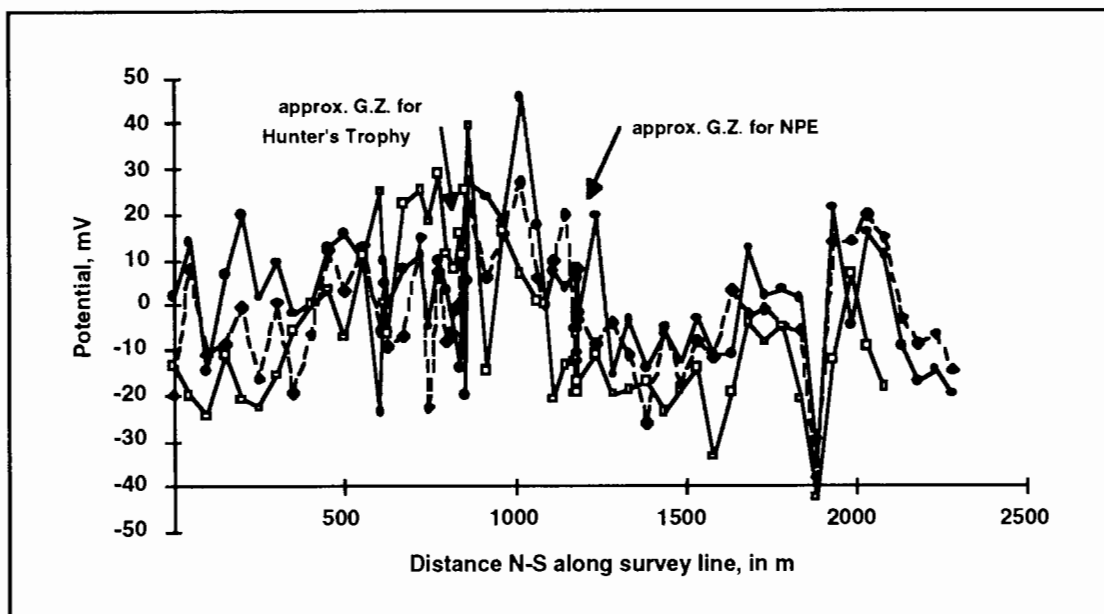


Figure 2. All SP data for the N-S line. Data from the survey lines have been projected onto a straight line. Dark circles—data taken in July; dark diamonds—data taken in September; open squares—data taken in November. Note locations of GZ for Hunders Trophy and the NPE. See Fig. 1 for location of line.

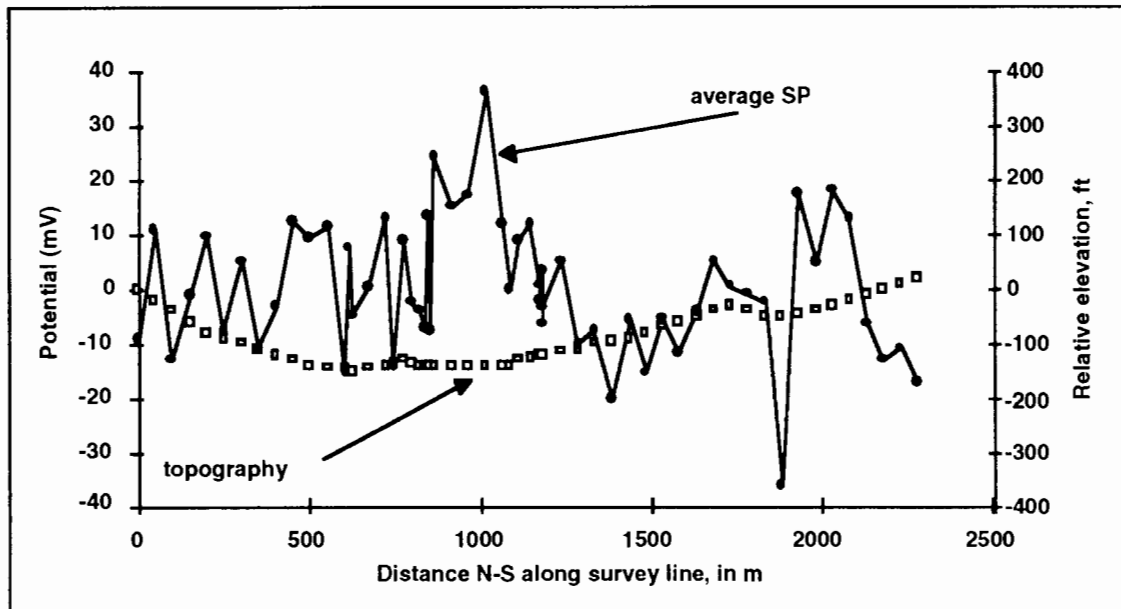


Figure 3. Average of the July and September SP data (before the NPE) compared to topography projected along a N-S line.

When the average of the SP measurements along the north-south line taken before the NPE are compared with the measurements after, as shown in Fig. 4, we see that the high SP zone (located between 600 m and 800 m south) has shifted to the north. The rest of the difference data along the line varies by ± 10 mV about a value of about -20 mV and does not represent a significant change. The post-NPE "anomaly" is about +30 mV, and 200 - 300 m wide. It is difficult to associate this anomaly with the detonation of the NPE because it is displaced about 400 m from SGZ and it has a form very different from the inverted sombrero pattern observed by McKague et al. (1991).

Data taken before and after the NPE detonation along the east-west line are shown in Fig. 5. The November data has a constant negative offset from the July data. When the difference between the two sets of data are plotted (Fig. 6), we see that, except for one odd data point, the differences are insignificant, showing a typical ± 10 mV station-to-station variation.

Electric Field Ratio Telluric Survey

During September, 1993, and before the NPE detonation, an E-field ratio telluric survey was run along a north-south profile, roughly parallel to that of the SP surveys, as shown in Fig. 7. Telluric surveys take advantage of natural sources (generally world-wide lightning discharges and ionospheric sources) to measure changes in subsurface conductivity. Alternating voltages are measured between two electrodes separated by a distance L. We used the same electrodes as for the SP measurements, with heavier gauge wire. The electrodes were buried the same way as for the SP measurements, but in this case we poured

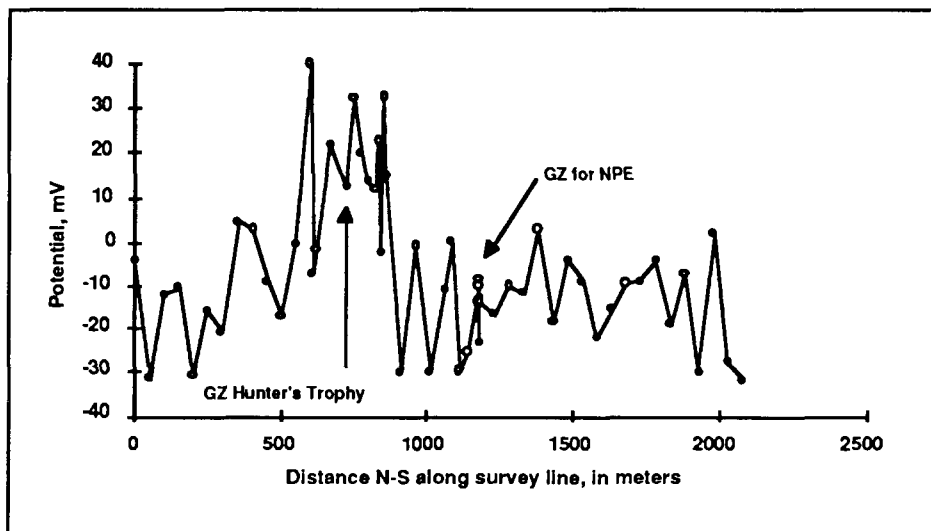


Figure 4. Difference between the average of the July and September SP data, taken before the NPE, and SP data taken in November, after the NPE. See Fig. 1 for location of line.

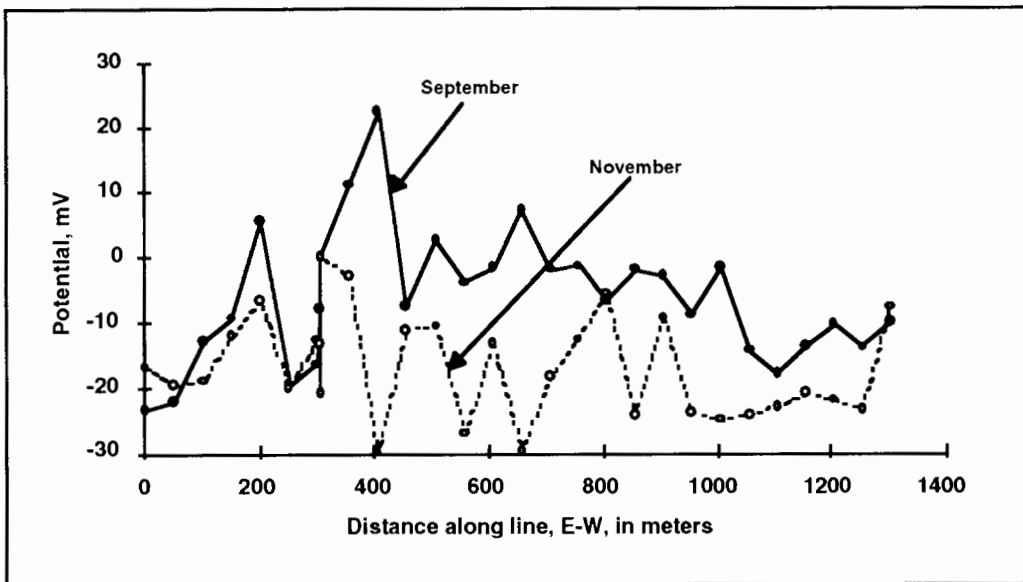


Figure 5. SP data from the E-W line. Measurements taken in September, before the NPE, and in November, after the NPE, are shown. See Fig. 1 for location of line.

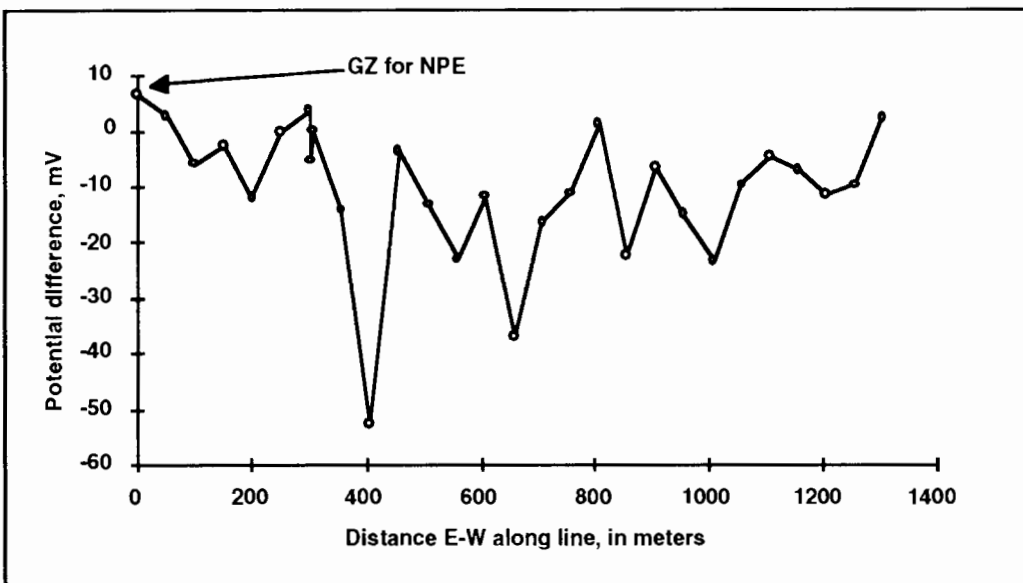


Figure 6. Difference between the November and September SP measurements along the E-W line. See Fig. 1 for location of line.

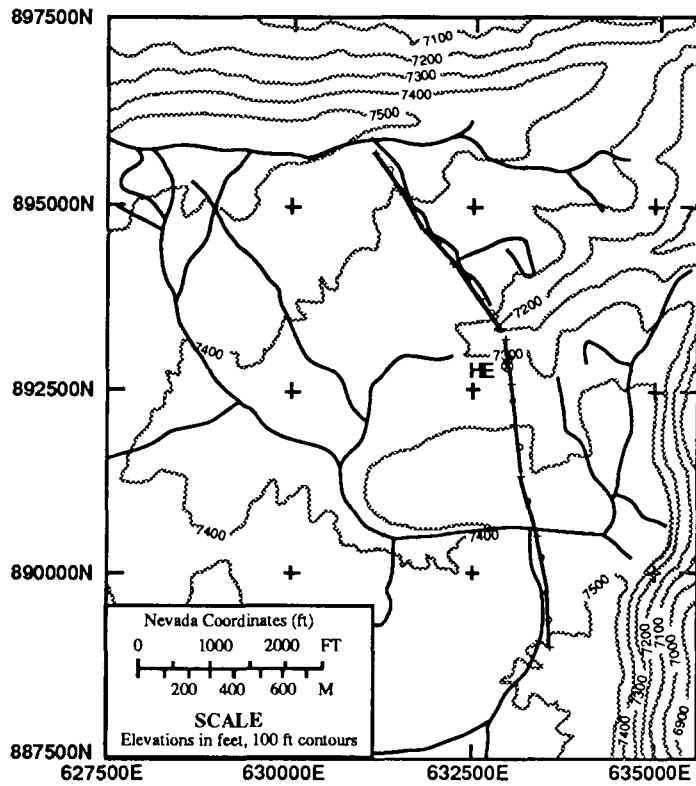


Figure 7. Location map for E-field ratio telluric lines.
HE—location of surface ground zero of the NPE. Dark lines are roads. Circles along the telluric line designate the center point of the forward and reversed sections. Crosses designate the end-points of the forward and reversed sections.

water into the holes to make the contact resistance at the electrodes as low as possible. We attempted to keep the resistance between the two electrodes below 5000 ohm. For the measurements on Rainier Mesa, we used an electrode spacing of 200 m. Thus a measurement station consisted of 1) a set of two reference electrodes, 2) an electrode 200 m to the south, and 3) an electrode 200 m to the north. The circles in Fig. 7 designate the center point of each measurement. Because of the nature of the terrain, we could not run a continuous north-south line; one line was run from the south end into the bottom of the ravine just north of SGZ for the NPE test. The other line was run from the north end of the ravine north to the end of the line; thus there is a short gap, located at the middle of the ravine, in the survey line. It took a two person team two full days to obtain all of the data for this line.

Leads from the "reference" dipole (between south and reference) and "forward" dipole (between north and reference) were run to a receiver which amplifies and narrow bandpass filters the signals in two separate but identical channels. The time domain signals are sent to an analog strip-chart recorder. We recorded signals in two pass bands; a low frequency band of 0.25 - 0.1 Hz (4-10 s) and a high frequency

band narrow passed at 8 Hz (the fundamental Schumann resonance mode). The electric field between two of the electrodes is $E = V/L$, where V is the voltage. When the lengths of the forward and reference dipoles are the same, the ratio of the two electric fields is: $E_2/E_1 = (V_2/L_2)/(V_1/L_1) = V_2/V_1$. The ratio of the electrical fields is proportional to the ratio of the resistivity averaged over the subsurface between the electrodes, thus variation in the field strength at a given frequency band indicates variation in subsurface resistivity. In practice, the analog waveforms recorded are visually scanned to pick out events that are correlated between the forward and reverse electrode pairs. The ratio of the two signals is then computed from the respective waveform amplitudes.

The depth over which the resistivity is averaged (usually referred to as the skin depth, or depth of penetration of the external signal) depends on the frequency and average subsurface resistivity, i.e. $d = 0.5 + (r/f)$, where d is the skin depth in km, r is resistivity in ohm-m, and f is the frequency in Hz. At Rainier Mesa, r is about 80 ohm-m, so the 8 Hz band represents averaging down to about 1.6 km and the 0.25-0.1 Hz band represents averaging 9 to 14 km deep. Thus the low frequency measurements give an indication of very deep changes in resistivity and the higher frequency measurements will reflect changes at shallower depths. We would have liked to take data at even higher frequencies to look at shallower levels, but above 8 Hz the natural signal sources are not as reliable and signals have to be recorded much longer to get good data.

The survey data along a line are generally referenced to the first station measured. For our data from Rainier Mesa, we used the most southerly station as a reference. Results of the survey are shown in Fig. 8. The top line shows the data from the 8 Hz (shallow) band and the bottom line is data from the lower frequencies (deeper). The deep levels show very little variation along the line, but the shallow data show an increase in the E-field ratio of about 50% along the line north of the ravine, about 1200 m north of the first station. This location corresponds to a roped off area west of the line which is above a possible collapse chimney from an old underground nuclear test. Thus this increase in the E-field ratio, which represents an increase average resistivity in the upper 1.6 km or so of the crust, may be related to fracturing and rubblization in the vicinity of a underground nuclear explosion.

Summary and Conclusions

The two types of electrical surveys described above were carried out in order to evaluate their possible value as a reconnaissance survey tool in the context of OSI operations and to compare geophysical effects caused by an underground nuclear and an underground chemical explosion of similar yield. SP surveys before and after the NPE detonation showed no obvious signatures related to the detonations, although a small positive anomaly along the north-south line was seen to shift away from SGZ. No SP anomalies were seen that could be clearly related to the Hunter's Trophy underground nuclear test. The E-field telluric ratio survey, which was run only once before the NPE, revealed no

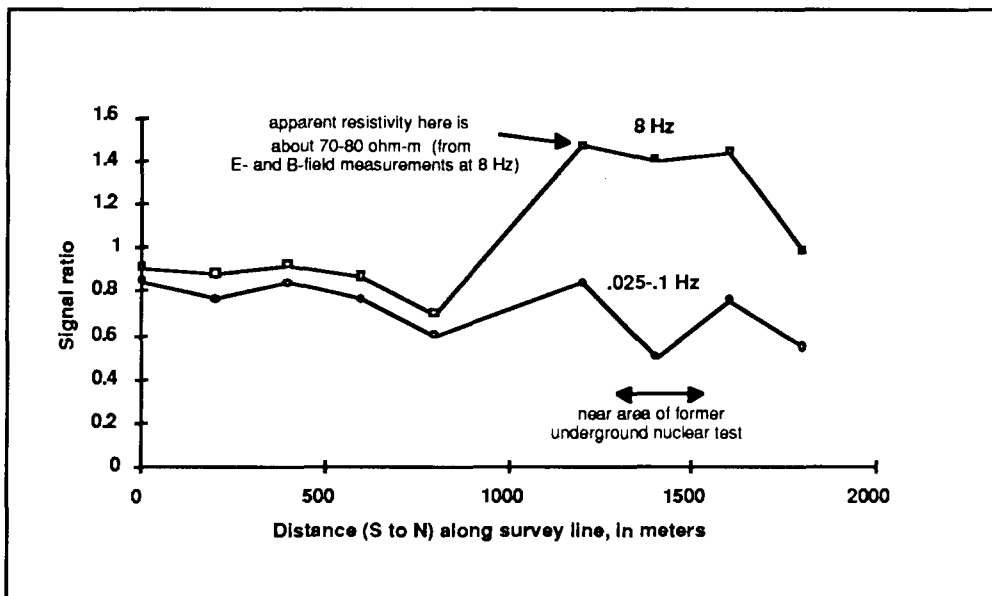


Figure 8. Telluric data, measured along a S-N survey line. See Fig. 7 for survey line location. Measurements made at 200 m intervals. Data at each point plotted are averages of ten or more amplitude ratios of forward and reversed telluric signals. Data at each station are referenced to the 0 m station location. A separate measurement of orthogonal electric (E) and magnetic (B) fields at the 1100 m north station indicated a resistivity at 8 Hz of 70-80 ohm-m. This point can serve as a reference for actual resistivities at each location.

anomalies in the vicinity of SGZ of the NPE, but showed a positive anomaly in the vicinity of a former underground nuclear test. In an area like Rainier Mesa, where there are extensive underground workings and there have been many past underground nuclear tests with a large range in yield, it is very difficult to sort out effects caused by any given single event, especially when the event occurs 400 m beneath the surface.

References

- Corwin, R.F., 1989, Self-potential investigation, Nevada Test Site, Mercury, Nevada, Lawrence Livermore National Laboratory Report UCRL-21187, P.O. 719-003, 70 p.
- Didwall, E.M., and M.J. Wilt, 1983, E-field ratio telluric techniques applied to cavity detection for OSI operations, Lawrence Livermore National Laboratory Report UCID-19780, 26 p.
- McKague, H.L., E. Kansa, P.W. Kasameyer, and R.F. Corwin, 1991, Detecting and modeling persistent self-potential anomalies from underground nuclear explosions at the Nevada Test Site, Proceedings of the 6th Symposium on Containment of Underground Nuclear Explosions, Lawrence Livermore National Laboratory Report CONF-9109114-Vol. 2, p. 159-174.

The Non-Proliferation Experiment and Gas Sampling as an On-site Inspection Activity: A Progress Report

Charles R. Carrigan

**Lawrence Livermore National Laboratory, Earth Sciences Division
Livermore, CA 94550**

Abstract

The Non-Proliferation Experiment (NPE) is contributing to the development of gas sampling methods and models that may be incorporated into future on-site inspection (OSI) activities. Surface gas sampling and analysis, motivated by nuclear test containment studies, have already demonstrated the tendency for the gaseous products of an underground nuclear test to flow hundreds of meters to the surface over periods ranging from days to months. Interaction between flow in fractures and diffusion in the porous matrix produces a "ratcheting" effect on the transport of gas in response to barometric pressure variations at the surface. Even in the presence of a uniform sinusoidal pressure variation, there will be a net flow of cavity gas toward the surface. To test this barometric pumping effect at Rainier Mesa, gas bottles containing sulfur hexafluoride (SF_6) and 3He were added to the pre-detonation cavity for the 1 kt chemical explosives test. Predetonation measurements of the background levels of both gases were obtained at selected sites on top of the mesa. The background levels of both tracers were found to be at or below mass spectrographic/gas chromatographic sensitivity thresholds in the parts-per-trillion (ppt) range. Post-detonation, gas chromatographic analyses of samples taken during barometric pressure lows from the sampling sites on the mesa indicate the presence of significant levels (300-600 ppt) of sulfur hexafluoride. However, mass spectrographic analyses of gas samples taken to date do not show the presence of 3He . To explain these observations, several possibilities are being explored through additional sampling/analysis and numerical modeling. Virtually all of the preceding, successful gas detection experiments have involved sites characterized by substantial fracturing, e.g., ring fractures, around surface collapse features. For the NPE, the detonation point was approximately 400 m beneath the surface of Rainier Mesa, and the event did not produce significant fracturing or subsidence on the surface of the mesa. Thus, the NPE may ultimately represent an extreme but useful example for the application and tuning of cavity gas detection techniques.

Introduction

The purpose of on-site inspection (OSI) is to verify the actual nature of an event that has been determined, by other means, to have at least some characteristics of a nuclear detonation. Thus, the primary goal is to verify the source of a high energy release event, e.g., nuclear explosion, chemical explosion, or natural energy release such as an earthquake or rock burst. An on-site inspection would usually involve fielding a group of experts and equipment at the site of the event. Surface analyses would include attempts to isolate radioactive particulate or gaseous

byproducts of the explosion. In the case of underground events, gas sampling at the surface potentially offers a much less expensive alternative to drilling and sampling cores for explosion debris.

Nuclear detonations produce gases that are uniquely characteristic of events involving fission or fusion. Argon-37 (^{37}Ar) is a result of irradiating the calcium in the soil at the site of an underground nuclear explosion with neutrons produced by fission and/or fusion [$\text{n} + ^{40}\text{Ca} \rightarrow ^{41}\text{Ca} \rightarrow ^{37}\text{Ar} + \alpha$]. The short (35-day) half-life of ^{37}Ar and its chemically inert nature make it an excellent indicator of recent detonations. One radioactive isotope of Xenon (^{133}Xe) is produced in even greater quantities than ^{37}Ar , but its half-life of only five days makes it unsuitable for sampling carried out weeks to months after a nuclear event. (A radioactive isomer of ^{131}Xe has an approximately ten-day half-life, but is produced in very much smaller quantities than ^{133}Xe .) Krypton-85 (^{85}Kr , half-life = 10.6 yr) is another inert, gaseous product of fission processes involving either uranium (^{233}U or ^{235}U) or plutonium (^{239}Pu) that is detectable at trace levels following nuclear tests. Tritium gas (T, half-life = 12 yr) with deuterium is often used as a component to produce thermonuclear reactions and may be a product of high energy release fusion reactions involving lithium deuteride (LiD). Even though it is not inert, combining with oxygen like the stable isotope of hydrogen to form tritiated water, it can be carried into the atmosphere with any water vapor that is neither adsorbed nor lost in the formation of hydrous phases.

In most locales, the background concentrations of radioactive Ar, Kr, and T are at trace levels. Analytical methods involving counting radioactive decays permit detection sensitivities that are below background levels. Thus, very low background values and high detection sensitivities for these gases make them ideal candidates for characterizing ambiguous, underground, high-energy release events.

Nonproliferation Experiment at Nevada Test Site

The Nonproliferation Experiment (NPE) involved the underground detonation of an ammonium nitrate and fuel oil explosive that released slightly more than one kiloton of explosive energy. The primary purpose of this experiment was to ascertain the current capability of treaty verification technology to seismically discriminate between instantaneously detonated chemical and nuclear explosions. This experiment also provided the opportunity to carry out a gas sampling study of the ability of Rainier Mesa to contain cavity gases produced by the chemical detonation. The chemical explosive was emplaced in a cavity that was connected to N Tunnel by a drift which was stemmed with grout prior to the detonation. At 400 m below the surface of the mesa, the detonation point was overburied. In fact, virtually no surface evidence, e.g., cracks and settling, for the explosion has been observed to date. Overburial is one possible means by which a treaty signator might attempt to evade detection during an on-site inspection.



Fig 1. The helium-3 bottle was placed on cavity floor prior to loading of explosive



Fig 2. The sulfur hexaflouride bottle was separated from explosion cavity by bulkhead to minimize the possibility for thermal decomposition of tracer gas.

The Gas Sampling Experiment

Since the NPE involved the detonation of chemical explosives, no radioactive gases were produced. To simulate the production of detectable gases, two different tracer gases were released at the time of detonation. Helium-3 is a stable isotope that has an exceedingly low natural abundance in the atmosphere. Because of its low background abundance, its inert nature and its chemical stability, i.e., it will not decompose, ${}^3\text{He}$ is a nearly ideal tracer gas and a bottle of this gas containing about 1000 liters (stp) was placed on the floor of the detonation cavity prior to its filling (Fig. 1). Laboratory mass spectrographic techniques permit detection of ${}^3\text{He}$ down to 0.1 ppt. Another gas bottle containing 115 lb of sulfur hexaflouride (SF_6) was also released by the detonation. This tracer is relatively inert and has a high decomposition temperature exceeding 500 °C (P. Lagus, personal communication, 1993). It is also detectable in the ppt range using much less costly gas chromatograph analyses. To minimize the chance of thermal decomposition, the bottle of sulfur hexaflouride was placed immediately outside the detonation cavity against the bulkhead cover (Fig. 2). Both sulfur hexaflouride and ${}^3\text{He}$ analyses have been carried out on gas samples obtained from different locations near the tunnel and on the surface near ground zero. Since both tracers were released in this experiment, surface samples that contain both tracers can more confidently be related to the NPE cavity gas source than can samples that contain only one or the other tracer gas. Soil gas samples suitable for mass-spectrographic and gas-chromatographic analyses are presently being obtained by REECO at NTS. Presently, the sampling techniques and sample containers are different for the ${}^3\text{He}$ and for the SF_6 collection efforts. Evacuated metal cylinders are used to obtain samples for ${}^3\text{He}$ analysis while Tedlar sample bags with special fittings are used to acquire samples for SF_6 gas chromatography. In sampling, bag and cylinder samples are taken contemporaneously. The sample locations are usually in the vicinity of existing fractures (no new ones have been located) although gas has been extracted directly from the soil at some sites on Rainier Mesa.

Theory of Soil-Gas Transport

Following a poorly contained, underground detonation, such as occurred in the Baneberry nuclear test of 1970, gas-propagated fracturing can allow pressure driven explosion byproducts to reach the surface immediately. In the range of underground explosion scenarios, such blowouts are at the opposite extreme from the well-contained NPE event that produced no new fracturing of the surface. Blowouts may dump copious amounts of explosion debris on the surface and are, therefore, more readily detectable than are scenarios like the NPE. Intermediate scenarios might involve post-detonation collapse of the cavity or chimney to produce subsidence at the surface with ring fracturing. By the time of collapse, the cavity pressure may have returned to a near atmospheric value. Both in this case and in the NPE scenario, only barometric pressure changes will be available to bring gaseous byproducts to the surface. These cases motivate the discussion that follows.

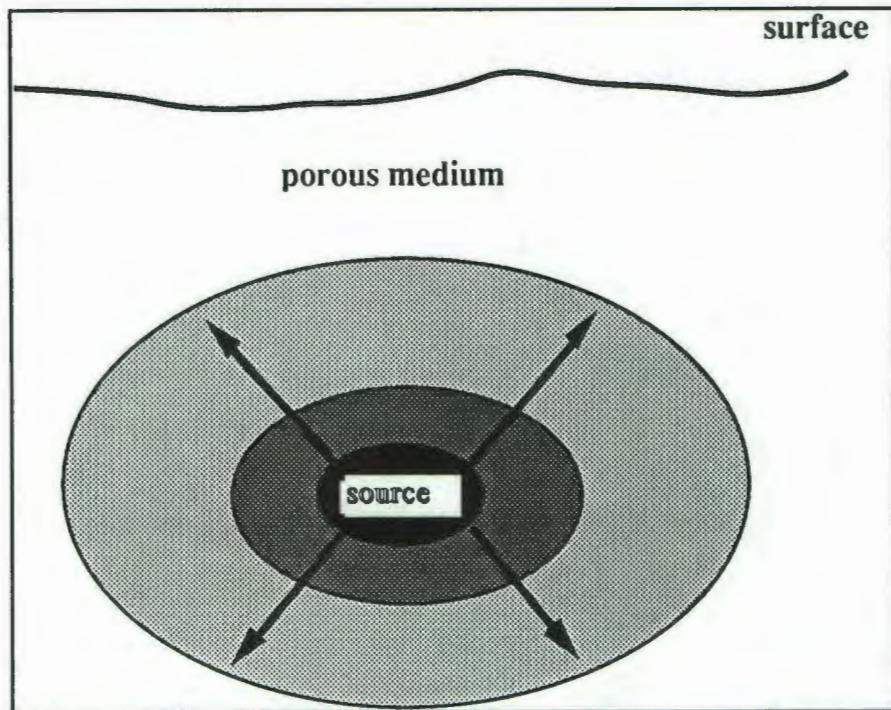


Fig 3. Gaseous diffusion is one mode of transport for contaminants. However, the diffusion rates are so low as to make this mechanism alone irrelevant for on-site inspection purposes.

Gaseous Diffusion Alone

Even when a blowout does not occur, the porous nature of the overburden would eventually allow detonation-produced gas from the cavity and surrounding halo (layer of gaseous byproducts surrounding the cavity injected by pressurized cavity) to get to the surface (Fig. 3). A typical value of the gas diffusivity D is $3 \times 10^{-6} \text{ m}^2/\text{s}$. The characteristic timescale t for a tracer gas to reach the surface by gaseous diffusion alone is given roughly by the relationship

$$t = d_b^2/D,$$

where d_b is the source depth of the gas which is approximately the depth of burial of the device. This equation predicts that the characteristic time required for a trace contaminant to diffuse to the surface from a device detonated at a depth of 400 m is $5 \times 10^{10} \text{ s}$, or about 1600 years. Gaseous diffusion alone is, thus, far too slow to be a useful nuclear gas transport mechanism for OSI purposes.

Gas Flow in Matrix Alone

In the absence of fractures, only connected pore space remains for the transport of cavity or halo gas. Pressure oscillations at the surface have the effect of alternately compressing and expanding gas in the pore space as illustrated in Figure 4 (Nilson et al., 1991). Thus, the displacement δ of a concentration front in the porous medium, as a result of a barometric variation, is simply given by

$$\delta/d = \Delta p/p_a,$$

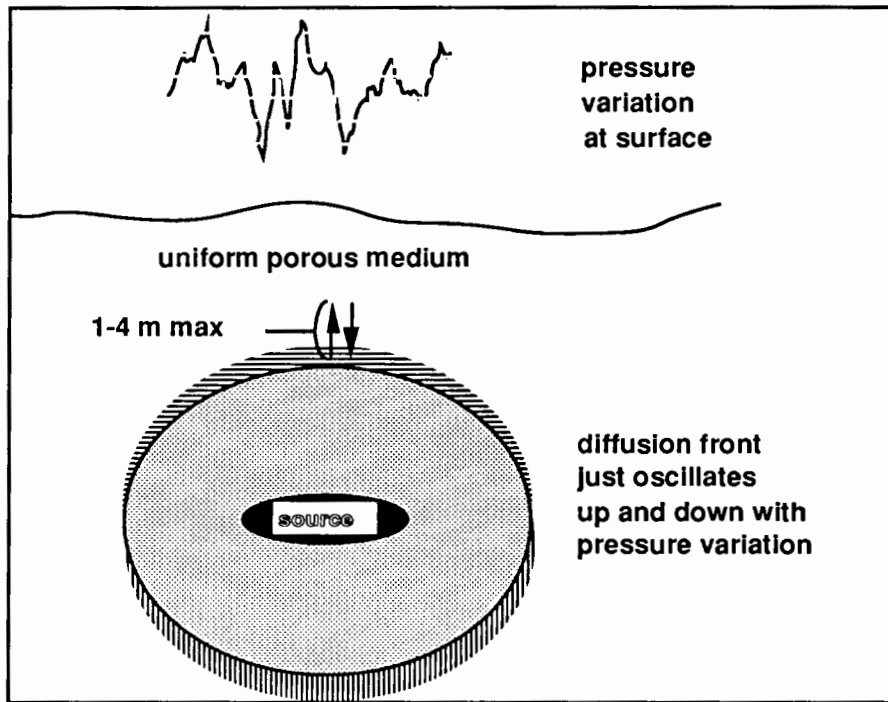


Fig 4. In uniform porous medium, pressure oscillations at the surface will only move a concentration distribution up and down by only a few meters about its original location.

where p_a is the ambient atmospheric pressure, Δp is the amplitude of the atmospheric pressure variation, and d is the vertical distance between the initial concentration front and the horizontal boundary beyond which atmospheric penetration is negligible (a good estimate is the water table since the compressibility of water is small compared to the atmosphere). The typical variations in weather at NTS include pressure variations that are in the range of 5–20 mb. If the initial concentration of gas is 200 m above the water table, we get a vertical fluctuation δ of $5 \times 200 / 1000$ to $20 \times 200 / 1000$ or 1 to 4 m, which is negligible.

Flow in a Narrow Fracture Only

On the other hand, if the pore space air is channeled into a fracture during the decompression phase, gas carrying a finite concentration of contaminant can rise from the halo zone to a much higher level along a narrow fracture. For fractures of length l and width w set in a matrix with a spacing of s and a porosity ϕ , a gas contained in the pore space of the halo of thickness h will rise a distance in the fracture of

$$d = h(\phi/w)(s\Delta p/p_a).$$

Taking $h=200$ m, $\phi = 0.10$, $w=0.001$ m, $s=6$ m, $\Delta p = 10$ mb and $p_a=1000$ mb, we find that the contaminant gas will rise 1200 m, which far exceeds the distance required to reach the surface (200 m) *if given enough time*. An estimate of the time required to reach the surface is just the average fracture flow velocity v_a divided by the depth to the halo zone $l = 200$ m. For plane parallel channel flow, this can be expressed in terms of the pressure difference and crack thickness as

$$t = l/v_a = 12\mu l^2/w^2\Delta p.$$

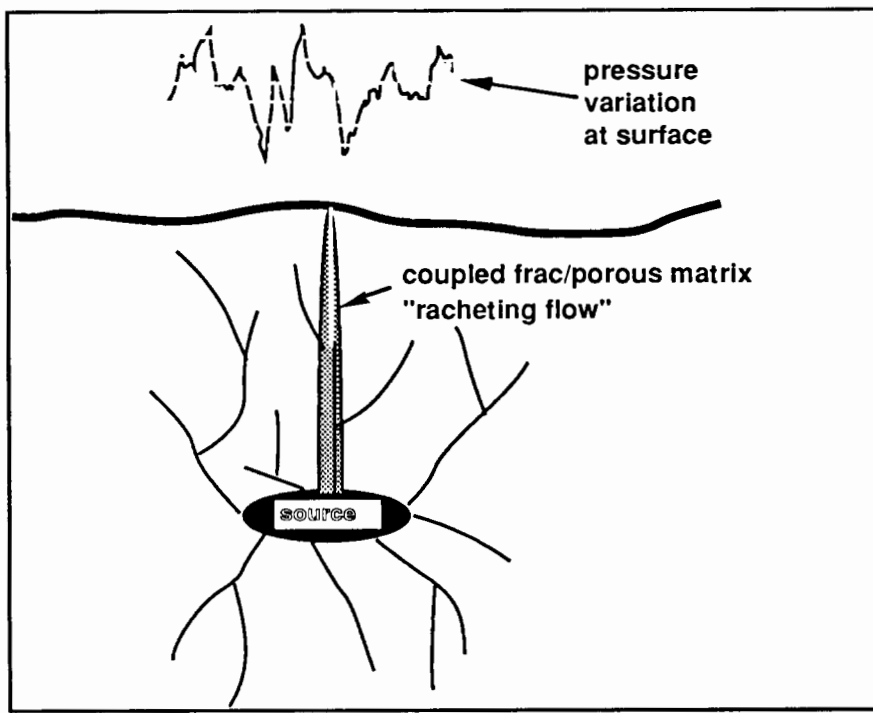


Fig 5. Gas flow along a fracture concurrent with diffusion in the porous matrix of the walls of the fracture results in a net transport of tracer or contaminant gas to the surface even if the surface pressure oscillations are weak, short term and purely sinusoidal.

Writing the 10-mb pressure drop as 10^3 nt/m^2 (1 bar = 10^5 nt/m^2) and assuming the gas viscosity μ to be $1.8 \times 10^{-5} \text{ kg/m s}$ (Bejan, 1984), we find the time for gas to rise to the surface to be less than 8640 s (0.1 day) implying a gas velocity in the fracture of about 0.023 m/s. This simplistic model, however, assumes no interaction between air in the fracture and air in the pore space of the fracture walls. In reality, as air rises in the fracture, the contaminant will be diffused into air in the matrix. Thus, the concentration of contaminant in the fracture flow will progressively decrease as it approaches the surface, and the contaminant concentration may be much too weak to be detected at the surface after only 0.1 days.

Barometric Pumping of Fracture-Matrix Flow with Gaseous Diffusion

While gaseous diffusion alone does not represent an adequate transport mechanism, if it is combined with surface barometric variations and the presence of fractures in the porous matrix, a much more rapid transport process may be identified. Referred to as barometric pumping, gaseous diffusion permits a "racheting" effect to exist during oscillatory flow in vertical fractures resulting from surface pressure fluctuations (Fig. 5). The upward flow of a given concentration of contaminant during subsequent periods of low pressure occurs from progressively higher levels, i.e., levels nearer the surface, in the fracture-matrix system. Thus, contaminated atmospheric gas in a fracture need not flow all the way to the surface in detectable quantities during a single oscillation period for trace values to reach the surface over times of days to weeks covering several or more atmospheric pressure oscillations.

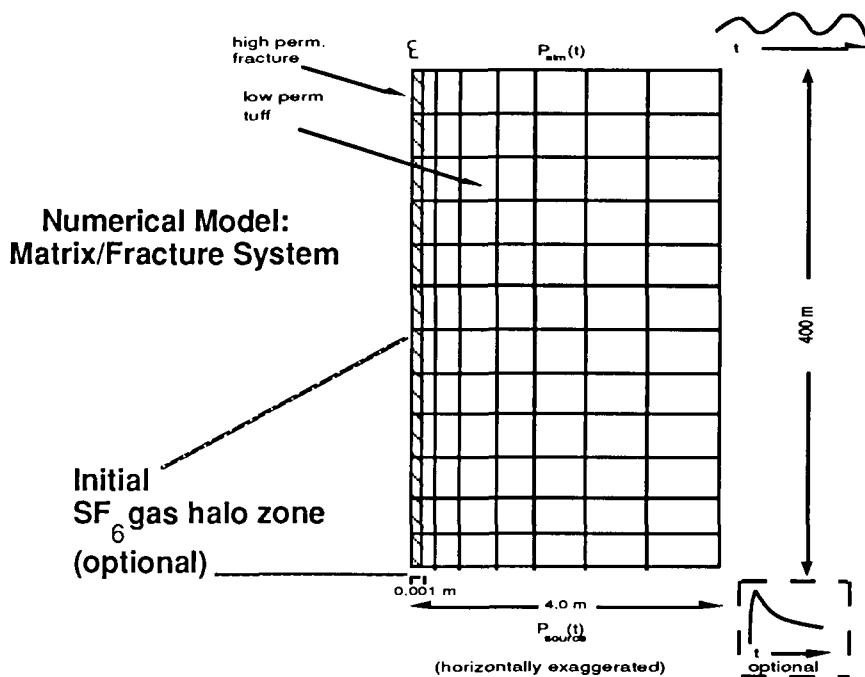


Fig 6. An integrated, finite-difference numerical model was used to simulate fracture-matrix flow of a tracer or contaminant gas. An oscillatory pressure condition was applied at the top to simulate variations in atmospheric pressure. Contaminant distribution was in 200-m-thick layer or in simulated cavity (not shown) at bottom of calculation domain.

Numerical Models of Barometric Pumping

Several numerical models have been developed to evaluate the mechanism of atmospheric or barometric pumping. The models are based upon NUFT (Nitao, 1993), a solver for multiphase, multicomponent, nonisothermal flow in a porous medium. NUFT is used to look at different aspects of the barotropic pumping problem including the concentration levels of cavity gases anticipated to reach the surface through a geometrically idealized coupled fracture-matrix system over the likely periods of time during which OSI monitoring occurs.

Description of Models

Two main models are developed for this analysis. They are likely to represent extremes of the possible distributions of trace gases following an underground nuclear detonation. The first model is similar to one developed by Nilson et al. (1991) for a nuclear test containment study. The geometry and essential details of the model are illustrated in Figure 6. This "halo" model assumes that trace nuclear gases are initially, uniformly distributed within the pore space of the material surrounding the point of detonation, i.e., trace gases are distributed in a halo about the detonation point. This halo is penetrated by uniformly spaced fractures extending to the surface.

In this study, typical values of the matrix porosity and permeability are 0.1 and 1 mD ($1 \times 10^{-15} \text{ m}^2$), respectively. For the penetrating fractures, the values of their thickness and spacing are taken to be 0.001 m and 6.4 m. The values characterizing the matrix are appropriate for volcanic tuff formations at NTS, and the fracture

characteristics fall within the range considered in the study of Nilson et al. (1991). The halo or contaminated layer is taken to be about 200 m thick and is overlain by another 200-m layer that is initially uncontaminated by radioisotopic products. The "halo" model is intended to represent the situation produced by gases being injected into the porous matrix during the period between detonation and the subsequent collapse of the cavity or chimney resulting from the detonation. Cavities or chimneys may collapse months to years following an event.

The alternative model also illustrated in Figure 6 assumes that the cavity at ambient pressure is the initial source of the radioisotopic gas. The gas can flow into the matrix of the bounding material, but the main volume of gas flows into fractures permeating the matrix and extending to the cavity. Both fracture and matrix properties for this case are taken to be identical to the values used in the "halo" model. Thus, for the same properties and barometric fluctuations, we can compare how the initial distribution of the gas at comparable pressures and the dynamical influence of a cavity affects the concentrations at the surface.

Barometric Pumping with Either Halo or Cavity Sources of Contaminated Gas

A model with sinusoidal pressure variations having an amplitude of 20 mbar and a period of 200 hours was used to determine the effect of barometric pumping on near surface (down to 30 m) gas concentrations. With time, the gas concentration in the matrix increases. It also gradually spreads out around the fracture owing to diffusion. This near-surface concentration increases in spite of the fact that there is no net flow of gas through the fracture. An example of how gas concentration varies with time is shown in Figure 7. A more quantitative plot illustrating how the calculated concentration of contaminant or tracer gas varies at the surface is given in Figure 8. Recalling that the initial concentration of tracer gas in the halo zone is 1×10^{-5} , the plot then indicates that concentrations of tracer sampled in the fracture at the surface would be reduced by 3–5 orders of magnitude during the likely period of measurement. The horizontal dashed line in Figure 8 represents the gas chromatograph sensitivity for these experiments. For a fracture-matrix system with the geologic and transport properties of this model, it would be expected that gas would be detected within the first few days following the onset of barometric pumping.

Decreasing either the period or amplitude of the pressure oscillations will increase the number of pressure oscillations required before measurable amounts of tracer gas get to the surface. A model assuming a ± 5 mbar amplitude pressure variation over a period of 20 hours resulted in a 100-m rise of tracer in the fracture during a 20-day span of time. This is a much slower rate of rise than in the 20 mbar-200 hr model, but it is, nonetheless, a very significant result. This is because most of the fluctuations of the diurnal kind are at the 5 mbar-20 hr level and an extrapolation of the computer model suggests that contamination would reach the surface within a few months and without the benefit of long, deep pressure lows.

The effect of a tracer contaminated cavity rather than a halo zone has been briefly considered to date, and more modeling needs to be done to fully understand how the cavity affects the pressure drop along the fracture. It was found that the large and long amplitude pressure lows did not produce tracer at the surface even over a 33-day span. In this model, the tracer would have to flow farther through uncontaminated matrix-fracture system because there was

no halo of tracer gas initially. In the weeks and months following a detonation with tracer released only in a cavity, chemical diffusion would cause a significant toll on concentration levels in the fracture.

Rainier Mesa Model

A model was developed to simulate the effects of a layer of alluvium on the surface of Rainier Mesa. In this model, fractures did not extend all the way to the surface but were truncated by a uniform layer of thickness 23 m with a 1-darcy ($1 \times 10^{-12} \text{ m}^2$) permeability. Even with this value of permeability, which is

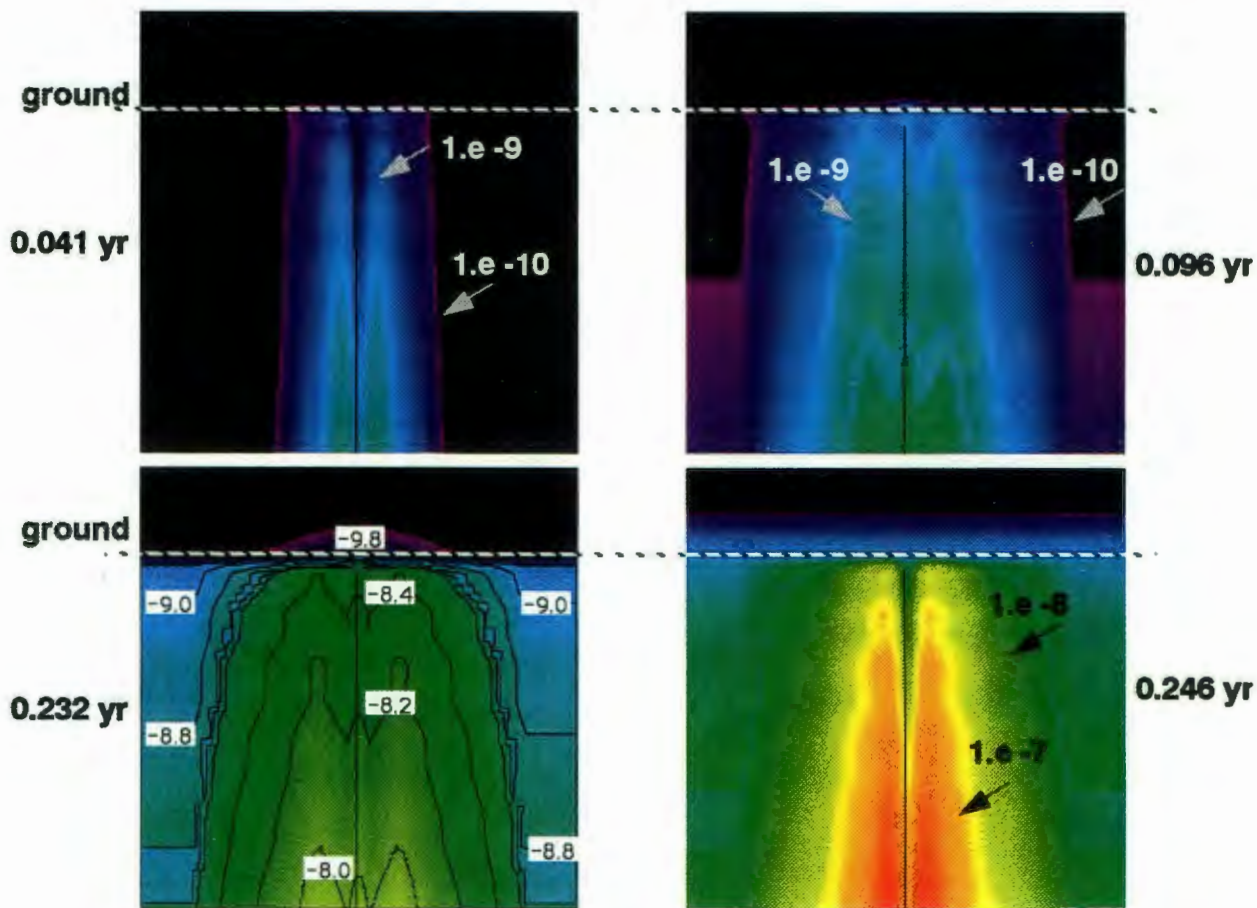


Fig 7. An integrated finite difference model of contaminant distribution as a function of time resulting from fracture-matrix flow: Gas flowing downward in a fracture is also pushed into the matrix pore space. Diffusion causes gas to migrate even further from fracture. This matrix gas is pushed out into fracture during upflow and eventually reaches surface. Gas concentration in pore space grows with time during the barometric pumping process. The tracer distribution is shown at four different times. The 0.001 m fracture is indicated in each figure by the narrow vertical black line near the center. Concentration values are indicated by color differences and by the numbers ($1.e-10 = 100 \text{ ppt}$) with log values of the concentration being displayed on contour overlays in the bottom left hand figure.

Concentration in Fracture Versus Time

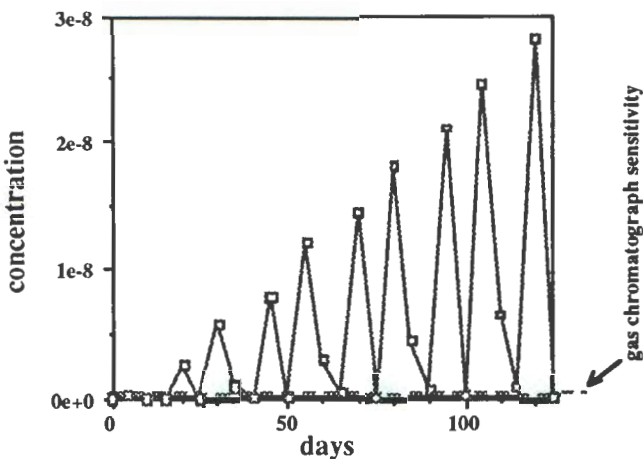


Fig 8. Concentration as a function of time is measured in the fracture at the surface. In this model, contaminant gas would be detectable after only a few days. Gas chromatograph sensitivity is indicated by the dashed horizontal line.

probably extremely high compared to that of the surface formation on Rainier Mesa, only a very slight rise was computed after almost one year of continuous 20 mbar-200 hr oscillations. Interestingly, immediately above the truncated fracture in the alluvium, the pressure variations had a full 20-mbar amplitude. However, pressure variations in the subadjacent fracture had a maximum amplitude of only about 1 mbar. This very low amplitude in the fracture is evidently a result of the difference in capacitance between the fracture and pore space.

Current Gas Sampling Results on Rainier Mesa

As stated above, no significant changes in the surface geology were noted following the detonation. A survey before the experiment showed evidence for pre-existing, soil-filled fractures in the alluvium and also several very small collapse features associated with previous, nearby underground nuclear tests. Pre-test gas sampling was carried out to establish a baseline concentration for both ^3He and SF₆. Maximum background levels were found to be a few parts per trillion for the tracers. Following the detonation, samples taken at the entrance to N tunnel showed no evidence for tracer leakage into the tunnel. Post-detonation sampling has also been carried out during periods of low barometric pressure on the top of Rainier Mesa at several tarped sites that cover old cracks and localized collapse features. Significant levels of SF₆ (300–600 ppt) were detected in air samples obtained less than one month following the detonation. All but one of the sampling sites fall within a surface radius about the NPE equal to the burial depth (400 m). However, levels of the ^3He tracer above background values have not been detected to date. Possible explanations for observing only one of the tracers are a potential diffusive effect delaying the arrival of the ^3He relative to the arrival of SF₆ at the surface or an underestimate of the SF₆ background levels during periods of falling barometric pressure. Additional surface samples will be taken at both existing, close-in and new, outlying

sites. One of the new sampling sites is on a fault that extends from the vicinity of the pre-detonation cavity to the surface (M. Baldwin, 1994, personal communication). Some of the new sample points will be set at selected locations in the soil at depths up to

10 m using a truck-mounted, hydraulic ram. These new observations interpreted in conjunction with further modeling should significantly improve our understanding of gas transport within Rainier Mesa.

Summary

Barometric pumping of trace gases from nuclear detonations may occur over periods ranging from days to years depending upon weather and soil properties. According to the models presented, detectable concentrations (< 100 ppt) of a radioactive gas would be produced by long and deep lows in a matter of just a few days assuming a 400 m overburden with minute fractures (0.001 m) extending to the surface and with a 200-m-thick halo or layer of contaminant emplaced around the detonation cavity by the pressurized flow of gas. Smaller diurnal fluctuations alone might require several years for detectable quantities of contaminant gas to reach the surface assuming the same fracture-matrix model. Fractures that are truncated before they reach the surface have much smaller associated pressure variations with the result that the barometric pumping mechanism will be less efficient in them. Gas sampling following detonation of the NPE suggests that Rainier Mesa may be an example of such a truncated fracture system. Because significant levels of SF₆ have been detected in the absence of ³He from sampling sites near the NPE, several new questions about gas transport need to be addressed before the role of barometric pumping at Rainier Mesa can be assessed. New gas sampling strategies and simulations are being designed to address these questions.

Acknowledgment

This work was performed under the auspices of the U.S. Department of Energy by the Lawrence Livermore National Laboratory under contract number W-7405-ENG-48 and in support of the Treaty Verification Program.

References

- Bejan, A. (1984), *Convection Heat Transfer*, 477 pages, John Wiley & Sons.
- Nitao, J. J. (1993), *Reference Manual for the NUFT Flow and Transport Code, Version 1.0*, Lawrence Livermore National Laboratory, Livermore CA., UCRL-ID-113520.
- Nilson, R. H., Peterson, E. W., Lie, K. H., Burkhard, N. R., and others (1991), "Atmospheric Pumping: A Mechanism Causing Vertical Transport of Contaminated Gases Through Fractured Permeable Media," *J. Geophys. Res.* **96**, 21933–21948.

Low-Altitude Overhead Imagery Acquisition Pre- and Post-NPE

William L. Pickles
Lawrence Livermore National Laboratory

Janet E. Shines, David L. Hawley, Michael D. Pelan, and Stanley B. Brewster, Jr.
EGG RSL

Abstract

We have successfully acquired all the planned overhead imagery (OHI) of the Non-Proliferation Experiment (NPE). The data set is very large and complete. Image mosaics of the area around the NPE Ground Zero (GZ) were taken at 37 12 6.948N by 116 12 35.496W on top of Rainier Mesa in Area 12 at NTS. The data were taken from a total of eight overflights on six different days. Preliminary analysis of the thermal infrared, 8–12.5-micron scanner band, taken before and after the NPE, shows some low-emission effects in virgin soil after the NPE. These effects could be due to the acceleration of the surface caused by NPE. Preliminary analysis of the visible high-resolution color RC-30 photography shows the senescence of oak leaves in an area of 2 km around GZ. Several other groups also independently observed this phenomenon when they returned to the mesa on Friday morning, 48 hours after the NPE. Detailed study of the photography and the scanner data will be necessary to map the actual aerial extent of the senescence. If the effect is proven to be limited to the area around GZ, then we will have supporting evidence that we have actually observed shock-induced premature senescence of oak leaves. Such overhead imagery could be used to help reduce the search area during an on-site inspection as part of the Comprehensive Test Ban Treaty verification activities.

Introduction

The purpose for acquiring this OHI data was to study changes that might be detected in the plants and soil on the top of Rainier Mesa as a result of the violent shaking of the ground caused by the explosion. This overhead imagery is seen as complementary to seismic data in the process of discrimination. We have learned that even for very small explosions such as NPE, which are deeply buried, the low-altitude, overhead imagery can serve to narrow the location of ground zero (GZ) within the seismic error ellipse. Careful study of the NPE's OHI data will be necessary because we have not observed any easily detectable changes in any of the imagery.

NPE OHI Acquisition

The flights for data acquisition were on September 20, 21, 22, 24, 29, and 30. "Predawn" flights took place on September 21, 22, 24, and 29, while "Solar-noon" flights took place on September 20, 22, 24 and 30. The weather conditions were ideal—dry and clear on all eight overflights. The NPE exploded on September 22 at 12:01 PDT, so the images taken at predawn on September 21 and at solar noon on September 20 are the "pre-explosion" reference images. The predawn images taken on September 22 were acquired just 5 hours after the explosion and were followed in another 5 hours by the solar noon images. Predawn and solar noon images were then acquired on Friday, September 24, and on September 29 and 30 to record longer term changes or possible erasure of changes in the days or weeks following the explosion.

EG&G Remote Sensing Laboratory (RSL) at Nellis Air Force Base in Las Vegas acquired the images in a Citation CE-550 twin-engine jet. Each overflight acquired visible-light, color photographs using the RC-30 large-format, forward-motion compensated camera and 11 wavelength bands of light from the blue to the thermal emission infrared using the Daedlus AADS1268 multispectral 11-channel imaging scanner. Eight of the Daedlus bands have wavelengths in visible light starting at 0.42 microns and ending at 1.05 microns. The remaining three bands are in the infrared. They are the 8.5–12.5 micron infrared thermal-emission band and the 2.08–2.35 micron and the 1.55–1.75 micron infrared reflection bands. Sets of images were acquired from altitudes of 1000 and 5000 feet above the surface of the top of Rainier Mesa at predawn and at solar noon on each day.

Two areas were imaged each day. The first was a square area, 4 km on a side, centered on GZ and imaged from the 1000-foot altitude. This required 13 separate overflights by the airplane. The ground speed for these 1000 foot overflights was 130 knots, which was low and slow enough so that the Daedlus multispectral imager had a spatial resolution of better than 1 m at the surface. This was a difficult set of conditions for RSL and pushed the limit of their capabilities. RSL, however, did successfully acquire all 13 flight lines at each time on all days. The second image area was a rectangle that extended 5 km north and south of GZ. These images were taken from an altitude of 5000 feet above the surface, which was high enough to acquire data in one 10-by-4-km strip.

Ground Truth and Geo-registration

Seventeen "space" or "thermal" blankets were placed on the top of Rainier Mesa to providing geo-registration to 1 m of all the images. The blankets are commercially available as rescue emergency blankets made from 1-by-2-m aluminized mylar. They appear as very bright, shiny squares in the solar noon optical images and as perfectly black, or cold, squares in the predawn thermal images. The latitude and longitude of each of these blankets were measured with commercial single-frequency, CA code only, surveying-quality GPS systems. The initial accuracy of the measured location of each blanket was about 80 m using a single GPS with CA code only. Later with two GPS receivers, having P code and dual and

single frequencies, the locations of each blanket were remeasured. The condition of each blanket was clean and undisturbed. All blankets were removed from the Mesa on November 11, 1993.

The blanket position measurements made with the two GPS receivers in differential mode are more accurate. Precision of 5–8 m is typical for this type of dual GPS "static survey" method using CA code only. The latitude, longitude, and altitude of one of the blankets, shown as number 1 on the map in Figure 1, is known to a few centimeters because of a nearby benchmark.

If this type of experiment is conducted again, a true "real-time differential GPS system" should be used. These commercially available systems can produce 1-m accuracy with a 2-hr measurement at each position of interest if the same four or five satellites are visible throughout the 2-hr measurement period.

Figure 1 is a digitized and geo-registered USGS topography map of Rainier Mesa on which the GZ is marked for the NPE and Hunters Trophy experiments. The map shows both the square image area, 4 km on each side, which was imaged from the 1000-ft-altitude overflights, and the larger area that extends 5 km north and south of GZ, imaged from 5000 ft. The location of the space blankets are also shown on the map. The latitude, longitude, and altitude of each blanket are shown.

Weather Data

The weather data, measured by RSL on top of the Mesa each day during the image-acquisition period, have been processed and are available as proof books. Included are soil surface temperature, air temperature, soil temperature 2 in. deep, wind speed, and wind direction every 5 min for 2 weeks.

Visible Color Photography

The high-resolution visible color film negatives taken by the RC-30 large-format camera were developed by RSL along with proof books. The RS-30 pictures are very high quality and the coverage of the area is extensive. The proof book photos can be used for stereoscopic viewing.

A Wild RC-30 large-format camera with a 153-mm lens and Aerocolor 9-by-9-in. film were used for all the visible photography. The sensitivity of the film was from 0.4 to 0.7 microns in three colors: yellow, magenta, and cyan. The photolab group at RSL also produced a map-like image that shows all 13 flight lines over GZ. This map helps locate particular proof photos among hundreds of photos in the books. The organization of the proof books and the documentation of the flight-line conditions is truly outstanding and easy for anyone to use.

Daedlus Scanner Data

The Daedlus scanner data were prepared by RSL. They removed the instrumental distortions known to be part of the way the scanner operates; used a calibration program for the thermal infrared band at 8–12 microns, which referenced the temperature of the internal blackbody standards inside the camera; and adjusted the image so that the one unit in the image is 0.1°C for the thermal band number 11 and 0.2°C for

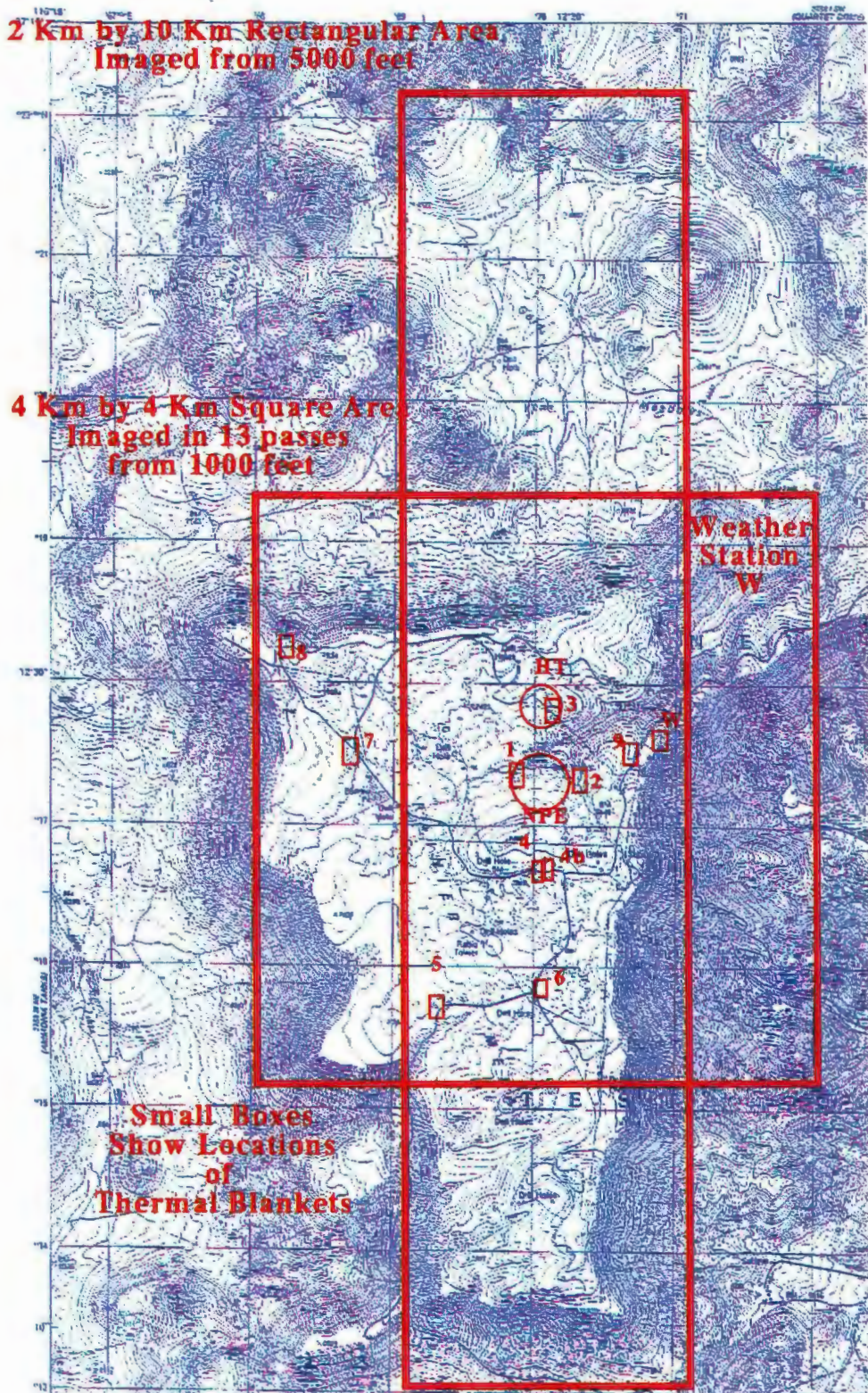


Figure 1. USGS map of Rainier Mesa showing the two areas that were imaged. The small numbers are the locations of the space blankets. GZ for NPE and Hunters Trophy are marked, and the latitudes and longitudes are printed at the top. The locations of the RSL weather station and ground truth panels are shown at the eastern edge of the top of the mesa.

the thermal band number 12. Unfortunately, this process introduces displacement up or down of all the pixels in the entire image RSL has not, however, calibrated the brightness of the reflectance bands using the images of the large calibration panels that were on top of the mesa at the weather station during each over flight. The Daedlus images are available on 8-mm magnetic tape in "raw" BSQ or Binary Band Sequential format.

Thermal Infrared Emission Images

Figure 2 shows a small part of the thermal infrared emission images (thermal band number 12 of the Daedlus scanner) that were taken before and after NPE. The area shown in the figure is a dirt crossroads just south of GZ. The area was chosen because it shows many features observed in the thermal infrared emission images, but all in close proximity to each other.

The September 21 image was taken at 05:15, predawn the day before NPE. The September 22 image was taken at 05:20 predawn, just 5 hours after NPE. The apparent low emission of virgin soil is shown as white pixels. Both low-emission space blankets are also shown as white pixels on both days. The images are pseudo-color, which means that different colors are chosen to represent different infrared emission levels. Each pixel in the image is assigned a numerical emission level. The legend in the lower left corner shows emission values between 1 and 180. A difference of 1 unit is equal to a change in temperature of 0.1°C. However, the values in the pixels are not temperatures because the offsets are not included in a way that calibrates the image.

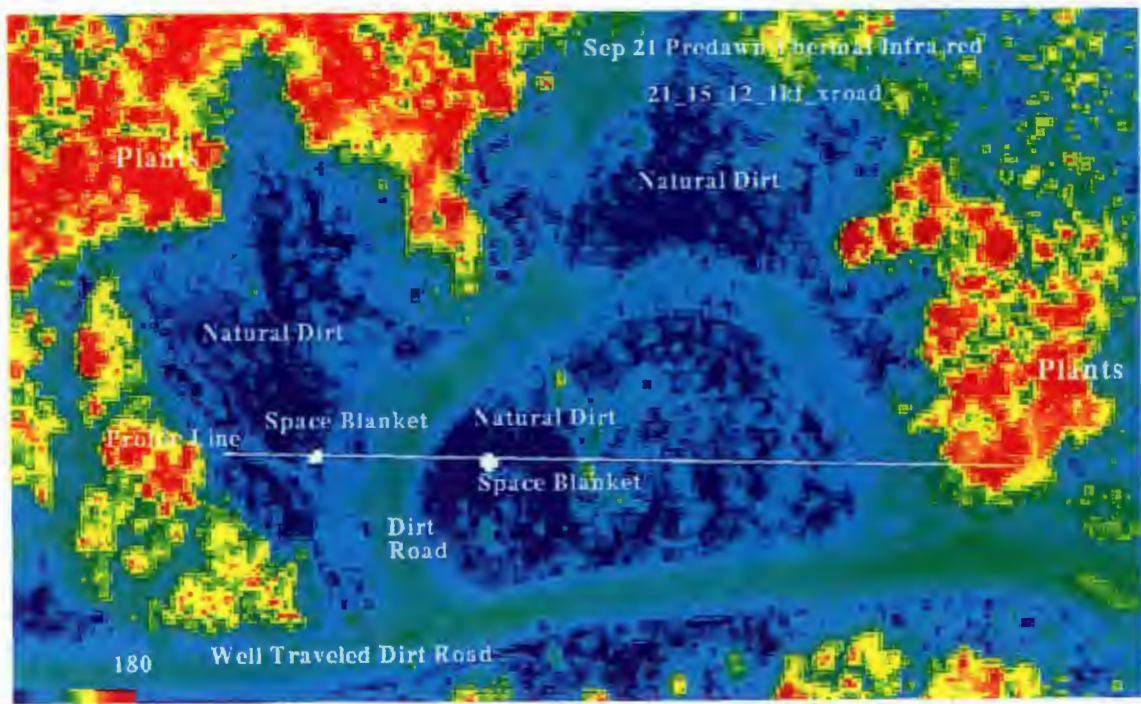
Figure 3 shows the actual numerical values of thermal infrared emissions found in each pixel along the line marked "Profile Line" in the two images in Figure 2. The similarity of the two profiles suggests that the only differences observed are due to a constant offset of about 30 in the data. It is not clear at this time what the source of this offset is. We are re-investigating the raw unprocessed scanner data to try to understand this phenomena.

Plant Stress Remote Sensing

The spatial resolution on the ground for all 12 Daedlus bands, was about 0.75 m. This excellent spatial resolution is particularly significant because the plants in the area are about 1 in size. The 0.75-m spatial resolution should help in the unfolding of "wavelength pixel-mixing" in the algorithms used for "supervised classification" to locate plant species that exhibit stress. Spatial resolution of 0.25 m would have been better so that more pixels would view only one plant, but this is beyond the capability of the existing DOE/RSL systems.

Dr. Gregory A. Carter, of the Science and Technology Laboratory, National Aeronautics and Space Administration, Stennis Space Center, Mississippi, has agreed to collaborate in our attempt to understand the effects on plants from the shock wave reaching the surface. Dr. Carter has commented that if the spall zone disturbs the micro-fine root-hairs, it is possible the flow of nutrients could be interrupted, and this

(a)



(b)

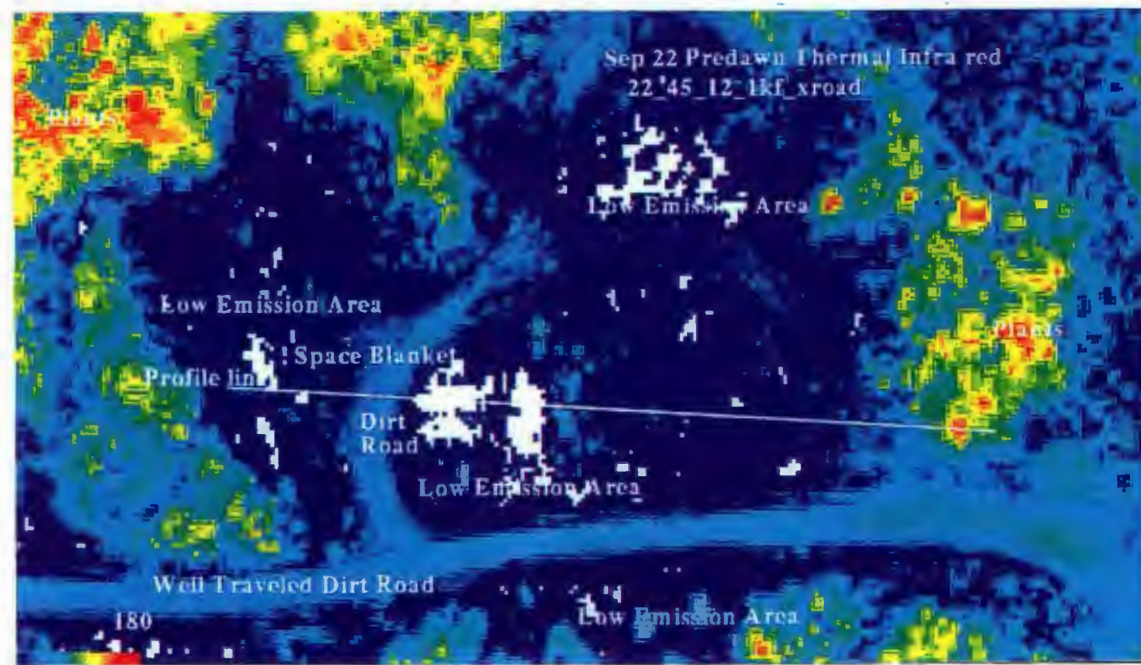


Figure 2. Thermal Infrared emission, 8 to 12 micron band, images that were taken before and after NPE. The area shown is a dirt crossroads just south of GZ. The area was chosen because it shows many of the features observed in the Thermal emission images all in close proximity to each other.

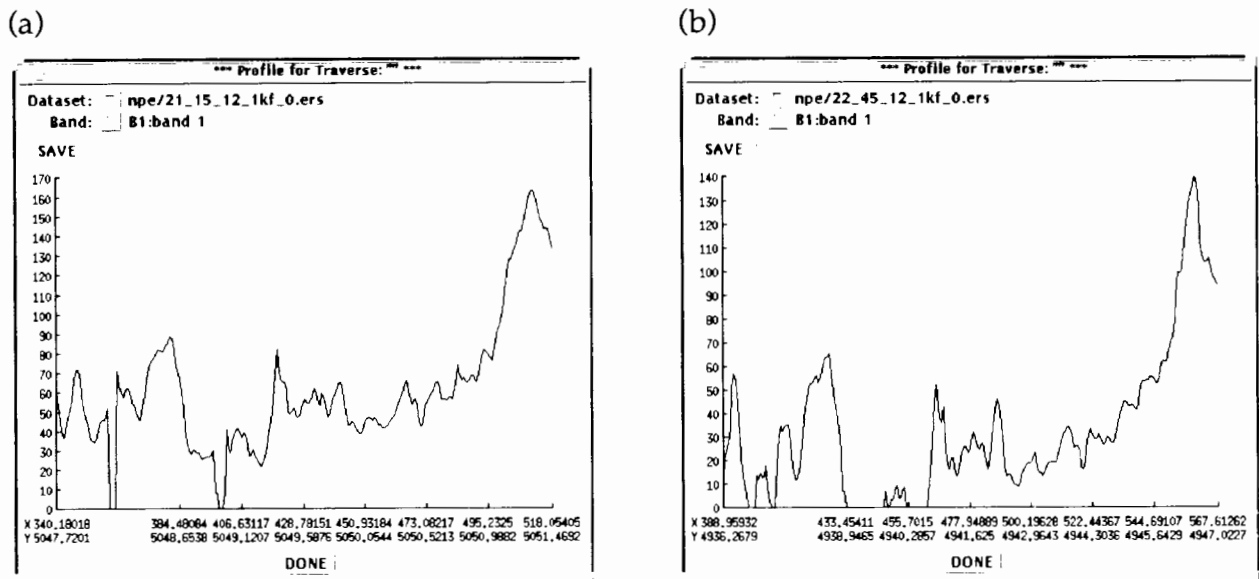


Figure 3. The actual numerical values of thermal infrared emissions found in each pixel along the line marked "Profile line" in the two images in Figure 2.

could then increase the rate of onset of senescence. Fortunately, Dr. Carter's work involves the same species (i.e., oaks) we observed undergoing shock-induced premature senescence after NPE. Premature senescence is only a small part of the large body of research on detecting plant stress by remote sensing. Dr. Carter's two excellent papers (1993 and 1994) show the detailed changes in the spectral reflectance and transmission of the plant leaves that occurs when plants are subjected to several kinds of stress. We are beginning to analyze the data to thoroughly investigate the plant stress effects.

Future Work

These plant stress detection techniques, if successful, could apply to other areas of nonproliferation and environmental monitoring. The analysis of the NPE scanner data should also provide guidelines for the design of advanced sensors specifically optimized for remote sensing measurements of plant stress. In the future we will need much finer spectral wavelength resolution and sub-meter spatial resolution to accurately distinguish plants that are stressed. I have begun to consider possible advanced sensor designs to accomplish this.

Summary of Distinguishing Features of the NPE OHI Dataset

1. "Space Blankets" were placed all around NPE GZ to provide accurate geo-registration of images.
2. Each Space Blanket is 1 by 2 m long and appears as 4 to 6 pixels in the scanner data.

3. Space Blanket geo-locations were measured using differential GPS.
4. Space Blankets appear cold or black during predawn and bright at solar noon.
5. Pixel size is 0.7 m in the scanner bands taken from 1000 ft.
6. Spatial resolution in the RC-30 film is excellent even from 5000 ft.
7. Some RC-30 pictures show all the space blankets in one negative.
8. Some visual photos have been digitized successfully and are being used for plant stress studies.
9. The excellent spatial resolution of the scanner data in the 600-micron bands will be helpful in plant stress studies that we are just beginning.

Preliminary evaluation of the NPE OHI data

1. Thermal infrared emission images in the 8–12-micron band show some intriguing low-emission effects in virgin soil after the NPE. These effects are being studied carefully to determine whether they are due to the acceleration of the surface caused by NPE. (Figures 2 and 3).
2. Plants show little change in the thermal infrared at predawn after the NPE.
3. Premature senescence (change to fall leaf colors) was observed 48 hours after NPE in oaks within 2 km of GZ.
4. Similar oak plants outside the 2-km radius were observed to have much less color change.

References

Gregory A. Carter (1993), "Responses of Leaf Spectral Reflectance to Plant Stress," *American Journal of Botany* 80(3), 239–234.

Gregory A. Carter (1994), "Ratio of Reflectance in Plant Stress," *International Journal of Remote Sensing* 15(3), 697–703.

EMP at the Non-Proliferation Experiment

John Bell

Systems Engineering Division, AWE, Aldermaston, UK

Abstract

This experiment presented an opportunity to field customized equipment designed to detect and record electromagnetic pulse (EMP) emanations from an explosion over a wide frequency range. Any data recorded could be used in conjunction with seismic methods to further non-proliferation studies.

No EMP emanations were detectable from the four sensors deployed outside the tunnel confines.

Introduction

The Non-Proliferation Experiment (NPE) was fielded by the Lawrence Livermore National Laboratory (LLNL), and designed to simulate a one kiloton nuclear explosion with chemical explosives. The modus operandi of generating the one kiloton energy release was by means of a blasting agent composed of a 50% ammonium nitrate water mixture and 50% ammonium nitrate fuel oil mixture, detonated by five Pentolite booster charges. This explosive mixture was detonated in the "N" Tunnel complex, located in area 12 at the Nevada Site (NTS), at 0001 hr on the 22 September 1993. The prime purpose of the experiment was to generate a seismic signature for comparison with an underground nuclear explosion of similar yield in the same geological area.

Thus, a unique window of opportunity arose with the cooperation of Los Alamos National Laboratory (LANL) to deploy at short notice customized AWE equipment designed to detect and record Electromagnetic Pulse (EMP) emanations. This was the first opportunity the UK has had for monitoring a large underground chemical explosion for EMP signatures propagated outside the tunnel confines.

Sensor Deployment and Location

Location of NPE experiment within the "N" tunnel complex, bearings N892,611.68 and E633,021.49. Four vertical Electric (E) field measurements were made using wideband capacitive probes, as indicated in Figure 1, plus one background cable terminated in 50 ohms (50R).

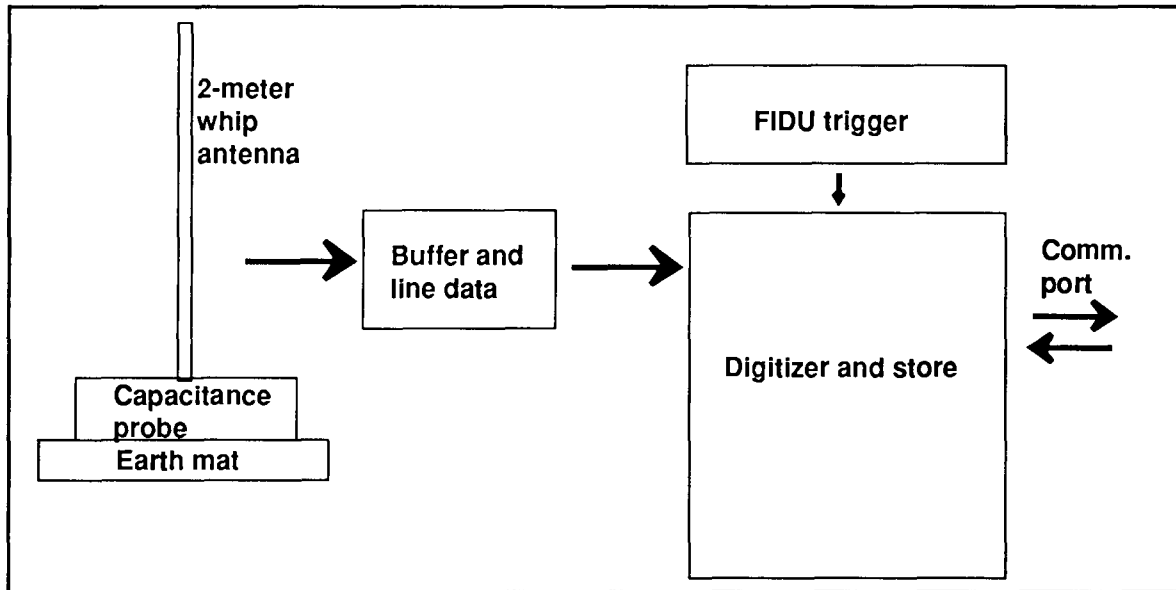


Figure 1. EMP detection system.

Details and location of the four systems and background deployment are tabulated below.

(i)	Location:	Hill	Probe:	100:1 Attenuation
	Probe:	25:1 Attenuation	Digitiser 3:	LeCroy 9424
	Digitiser 1:	LeCroy 7200	Trace 1:	0.50 volts/division
	Trace 1:	0.50 volts/division	Trace 2:	0.20 volts/division
	Trace 2:	0.10 volts/division	Trace 3:	0.10 volts/division
	Trace 3:	0.05 volts/division	Trace 4:	0.05 volts/division
	Trace 4:	0.01 volts/division, AC coupled.	Timebase:	50 ms/division. All traces locked.
	Timebase:	50 ms/division. All traces locked.	Trigger:	FIDUcial
	Trigger:	FIDUcial signal	Trig Level:	0.1V; External; +ve; DC
	Trig Level:	0.5V; External; +ve; DC	Trig Delay:	1 division into trace. (50 ms)
	Trig Delay:	1 division into trace. (50 ms)		
			(iv)	Location:
				Staging Area; Powered by petrol generator
(ii)	Location:	Tunnel Portal	Probe:	25:1 Attenuation
	Probe:	100:1 Attenuation	Digitiser 4:	LeCroy 9424
	Digitiser 2:	LeCroy 7200	Trace 1:	0.50 volts/division
	Trace 1:	0.50 volts/division	Trace 2:	0.20 volts/division
	Trace 2:	0.20 volts/division	Trace 3:	0.10 volts/division
	Trace 3:	0.10 volts/division	Trace 4:	0.05 volts/division
	Trace 4:	0.02 volts/division	Timebase:	50 ms/division. All traces locked.
	Timebase:	50 ms/division. All traces locked.	Trigger:	Internal Ch2; +ve;
	Trigger:	FIDUcial	Trig Level:	Normal
	Trig Level:	0.5V; External; +ve; DC	Trig Delay:	Level set to eliminate noise
	Trig Delay:	1 division into trace. (50 ms)		Centre of trace. (250 ms)
(iii)	Location:	Staging Area		

(v)	Location:	Tunnel Portal	Timebase:	FIDUcial
	Probe:	50R terminated cable	Trigger:	FIDUcial
	Digitiser 5:	Yokogawa 1200A	Trig Level:	0.1V; Internal Ch2; +ve;
	Trace 1:	0.005 volts/division		
	Trace 2:	0.20 ms/division		

Recording

With the exception of digitiser 4, all recording was accomplished in trailer 9103, as indicated on the sign schematic Figure 2. The FIDU pulse used for triggering , was generated by LANL in their mobile EMP diagnostic recording P-14 BUS, parked adjacent to trailer 9103 and was derived from the device firing signal. The Trigger Schematic, Figure 3, indicates the method of trigger signal distribution for the four systems.

Station 4 was a free standing recording system, housed in a pick-up truck for ease and speed of deployment. Power at 240 V, 50 Hz was supplied by a small 600VA petrol generating set via an on line uninterruptible power supply. (UPS). This provided an unattended operating time in excess of 7 hours. Triggering of this station was achieved by internal means from Ch2.

Results

Figure 4 gives the recorded data traces from the most sensitive ranges. With the exception of the Isolated Staging Area system, all digitisers triggered correctly at 00:01 hours, on 22 September 1993. The trigger level on the isolated system had to be adjusted to eliminate false triggers due to high background noise, which would have filled the limited available memory prior to the event.

With the sensitivities set, no EMP signals were detectable.

Acknowledgments

I wish to acknowledge M. J. M. Firth, M. G. H. Grundy, and S. Eatwell for fielding assistance and George Allred, Los Alamos National Laboratory, for photography.

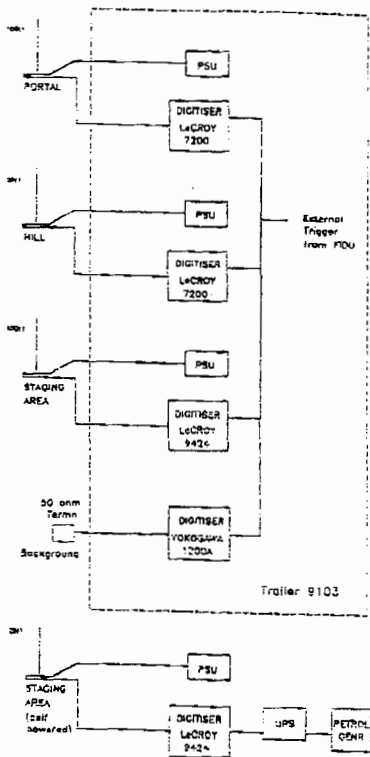


Figure 2. Signal schematic.

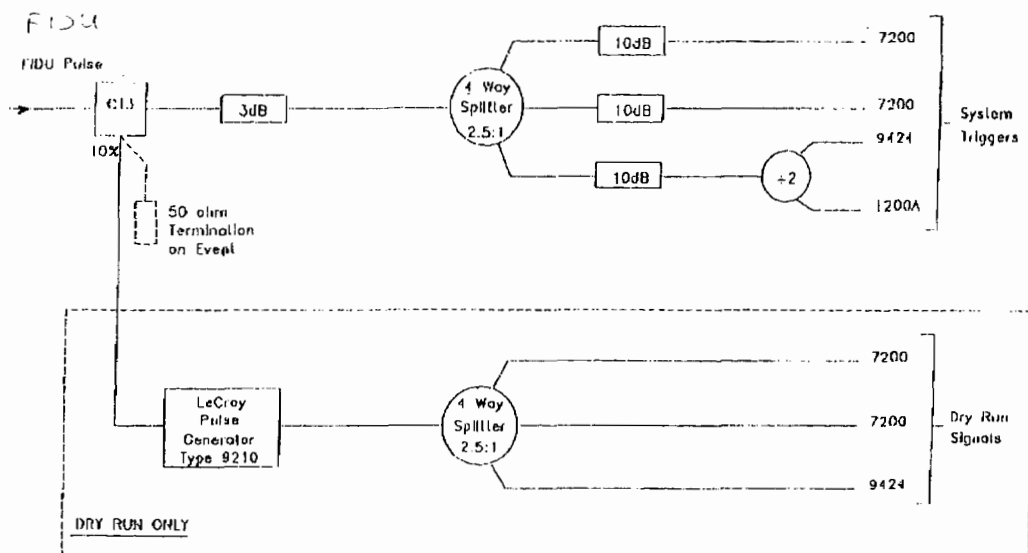


Figure 3. Trigger schematic.

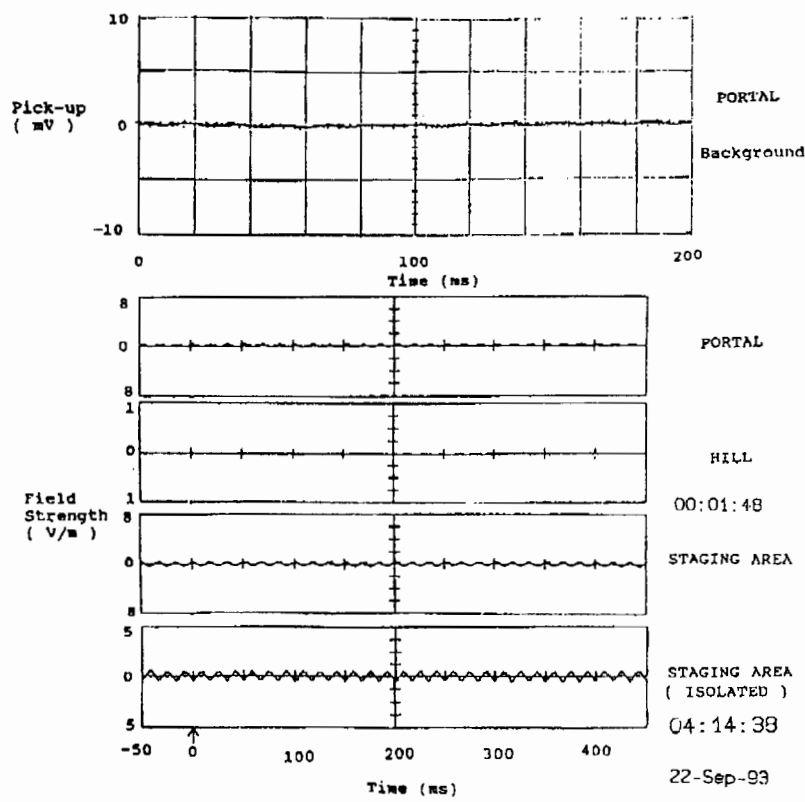
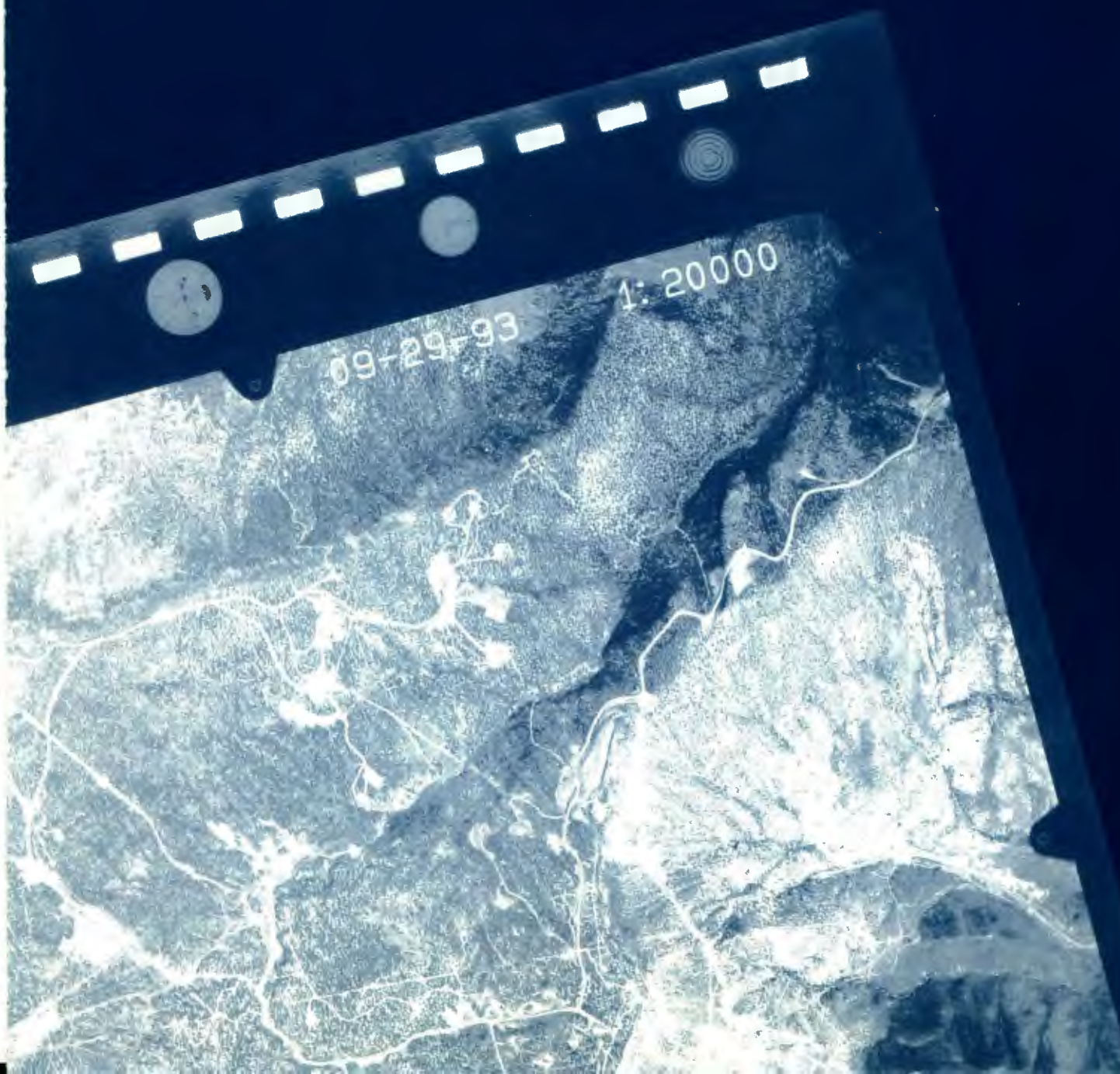


Figure 4. Vertical E-field measurement.

9

PANEL DISCUSSION



Panel Discussion

Compiled by Marvin D. Denny, Editor

The final session of the meeting was a panel discussion led by Dr. W. J. Hannon, Lawrence Livermore National Laboratory, Livermore, California. Panel members were Drs. Peter W. Basham, Dept. of Energy, Mines, and Resources, Canada; Lane Johnson, University of California, Berkeley, California; William Leith, USGS, Reston, Virginia; Arthur McGarr, United States Geological Survey, Menlo Park, California; Paul G. Richards, University of Columbia, Lamont-Doherty Geological Observatory, Palisades, New York; David J. Simons, Los Alamos National Laboratory, Los Alamos, New Mexico; Terry C. Wallace, University of Arizona, Tucson, Arizona; and John J. Zucca, Lawrence Livermore National Laboratory, Livermore, California. The Panel addressed four questions before time ran out. The following responses have been reconstructed from written input received from panel members.

Question 1. Identify four results, concepts, or issues related the material presented at the symposium that you think people should remember. Why are they worth remembering?

Johnson: The first result is rather general, but I was impressed by the fact that there are numerous advantages of performing controlled experiments which are designed to address specific verification issues. In the past, most research on verification problems has been accomplished by collecting data from explosions that were detonated for completely different reasons, and thus there was little control over the experiment. With the NPE this was not the case, as specific problems could be identified and studied by a variety of different approaches. Although much of this analysis and comparison is yet to be done, the papers of the past two days suggest that a focused approach will produce some useful results. A second issue of considerable importance is to understand why the methods appear to have consistently overestimated the yield of the NPE. Does this mean that the NPE was unusual in some way, or does it mean that different scaling relationships are required for nuclear and chemical explosions? A third result which I found interesting was the fact that electromagnetic pulses appear to successfully discriminate between nuclear and chemical explosions. The fourth aspect of the symposium that was quite useful was the fact that both seismic and atmospheric results were present at the same meeting. The comparison and coordination of these two methods appear to be a fruitful area for further research.

Leith: It is worth remembering that the NPE, as a chemical explosion, is not like most chemical explosions, and therefore not typical of "problem events" for CTB monitoring. It might best be viewed as the "control experiment" for what could be a series of explosion experiments that are more typical of what we expect to be problem events under a CTB.

McGarr: (1) Producing buried, compact, tamped chemical explosions of 1 kt or greater presents substantial technical challenges. (2) At the same energy release chemical explosions have a greater seismically measured yield than do nuclear explosions. This difference, however, evidently is not useful for discrimination. Whatever differences there are that can be used to differentiate chemical and nuclear explosions do not seem to persist out to the elastic radius. (3) m_b/M_S still seems to be one of the best means to discriminate between earthquakes and explosions, although there are regional complications. Mining induced events present a problem for this discriminant in that many of them plot in the explosion field. (4) As yields get smaller the possibility for confusing signals (e.g., industrial explosions, earthquakes) increases dramatically.

Richards: Numerous papers on discrimination at this symposium may be summarized as follows: If you are able to get seismic data containing frequencies higher than about 100 Hz, then it might be possible to tell some differences between the NPE and a nuclear explosion of similar yield. If you cannot get access to such data (which requires being very close), then you would not be able to tell the difference between the two types of sources. The differences are due to the different spatial scale of the two types of sources, and the source duration (the time they are putting out energy). This result was not unexpected. However, the result is not representative of typical problems in discriminating between chemical and nuclear explosions, because almost all chemical explosions of any size are ripple-fired and intended to break rock, so they have different signals from a deep, well-contained shot like the NPE.

Zucca: As the presentations during the symposium showed, from the OSI point of view the NPE was an example of clever evasive testing. It was carried out in an area of active mining, so that movement of tailings and equipment could be legitimately explained, there was no obvious surface expression of the explosion such as fractures or craters, and the tracer gasses have not reached the surface after 6 months. A significant result was Sweeney's paper on extremely low-frequency electromagnetic measurements, in which he suggested that the prompt pulse could be used as an on-site, zero-time, discriminant between chemical and nuclear explosions.

Question 2. What experiments should be carried out in the future to improve chemical explosion, nuclear explosion, discrimination?

Johnson: For a contained explosion, this is a difficult question. It would be interesting to know if the differences are related primarily to energy density, or if there are some other factors operating. I would suggest that it might be best to start with some numerical experiments with the hydrodynamic codes and determine if there is general agreement concerning such results. Actually, some of these questions may be answered before the final analyses of the NPE are completed.

Leith: It could be informative to conduct a "typical" large, surface mining explosion to test the ability of

seismic sensors, in both the near- and far-field, to separate the two signals and identify the buried event. In another experiment, it would be desirable to test the feasibility of decoupling a large explosion in a nonspherical cavity, preferably one excavated in hard rock. Such a test could also be used to study the containment of explosions in decoupling cavities.

McGarr: (1) For noninvasive discrimination, 1 kt seems to be currently impossible. At 5 kt, however, it may be possible to discriminate on the basis of difference in the source rise time, which are greater for chemical explosions. (2) Because buried, compact chemical explosions appear to be excellent surrogates for nuclear explosions of comparable yield, an interesting test of any global monitoring system might be set up by contracting with a "red team" to detonate a kiloton chemical explosion anywhere in the world, with a sizable bonus if it is not properly identified.

Richards: The best would be to find a mine that is carrying out both single and ripple-fired explosions and to compare the signals from these types of sources as recorded at various distances. Once good recordings are available from each type of shot, then experiments can be conducted in which linear combinations of the two types of signals are processed to see how well the single fired shot can be recognized even in the presence of a strong ripple-fired shot. Another very important point is that nuclear explosions are going out of style; and indeed if various moratoria and then the CTBT hold up, we won't have any more of them, perhaps for many years, until trouble comes. For purposes of designing the monitoring system, it is therefore imperative that we document as best we can the phenomena of nuclear explosions themselves and specifically their seismic signal for sources and receivers in various environments. I suspect that the national weapons labs have numerous databases that are familiar to certain individuals, but that are very difficult to use or are even not known to many potentially interested users. One of the most important papers at this meeting, in the long term, may have been the one describing an effort to make strong ground motion data from underground nuclear explosions available to researchers via the internet. Similarly for Russian data, we should help them to make their databases available. We can always carry out more chemical experiments, but these nuclear explosion databases will disappear unless a conscious effort is made to save them.

Zucca: I identify two areas in OSI that show promise for chemical and nuclear discrimination: gas sampling and electromagnetic pulse monitoring. Detecting and identifying soil gasses coming from nuclear or chemical explosions require a knowledge of their transport through porous, fractured media so that the time required and the aerial extent of seepage can be determined. We need more tracer experiments in mines and other situations where OSIs could be carried out to establish a wide experience base. When we go to do an actual OSI, this knowledge will enable us to effectively design a gas sampling scheme. The electromagnetic pulse may be the only direct nuclear, chemical discriminant available. Unfortunately, our theoretical understanding of the generation of the pulse is poor. Therefore, we need

to build up our empirical understanding by making more measurements of the types taken at the NPE on chemical explosions.

Question 6. How many chemical explosions per year are likely to have characteristics sufficiently like nuclear explosions to preclude high confidence discrimination? Consider various levels such as 10, 100, and 1000 tons.

Basham: When considering how many chemical explosions per year to worry about, it is important to keep in mind what will be the detection threshold of the global seismic monitoring system. Estimates for the alpha network range from about a body wave magnitude of 3.0 in North America and northern Europe to 3.8 in parts of the southern hemisphere. If we add about a half of a magnitude unit to have any chance of at discrimination, we get into the magnitude range where we will want to know how many explosions to expect. The number is not exceeding large, and most will be ripple-fired with signatures generally visible in the spectra. If there are worries below these implied magnitude thresholds, then they will have to be handled by bilateral arrangements that are not necessarily part of the international verification system.

Leith: Most chemical explosions are small (<100 tons), shallow (on the surface), ripple-fired, and occur in known mining regions. Thus, they emit seismic signals that are seismologically unlike nuclear explosions. Nevertheless, there will be real seismic discrimination problems from large mining explosions. First, data from many existing seismic stations may be inadequate to identify the ripple-fired character of most chemical explosions; processing techniques require high-frequency data that are not generally available (for example, most seismic data collected at 20 samples per second will not be adequate to resolve typical blast delays). Second, the limited data we have on blasting in foreign countries suggests that ripple firing is less common in some countries of nuclear monitoring concern (e.g., India). More research is needed in this area, both to estimate the scope of the problem and to establish the viability of the discrimination techniques.

McGarr: I cannot offer any numbers, but from what was presented by Paul Richards and Bill Leith, it seems that for yields of 100 tons or less, there are far too many chemical explosions to permit confident discrimination. The threshold of discrimination may be about 1 kt, although, from what was presented, I think 5 kt may be closer the point of confident identification. A distinction must be made between compact and delayed detonation, of which the latter is fairly easy to discriminate.

Richards: At the level of 1 kt and above, well coupled, there have been no chemical explosions that would present a problem until the NPE. Of course the NPE was done for very special, noncommercial reasons, and so is not likely to be repeated, at least in a context that would present CTBT verification problems. At the level of 100 tons and above, well coupled, I think there could be a few per week in the

U. S. alone, until special efforts are taken to instrument specific mining areas. We do not know about other countries at present, although we are making inquiries.

Question 7. Are there combinations of seismic and non-seismic methods that should be explored for identification of chemical and nuclear explosions or combinations of each?

Basham: Obviously, radioactive debris monitoring is the way to discriminate nuclear explosions from chemical ones, if sensors can get on-site. Sensors will get on-site if the events are (with remote monitoring) sufficiently suspicious to warrant OSI, or if the chemical explosion is of sufficient size to require prior notification, as is being suggested in some draft treaties.

Johnson: I believe that the combined analysis of three different types of waves—electromagnetic, acoustic in the atmosphere, and elastic in the solid earth—is worth pursuing. In particular, the combination of the acoustic and the elastic might help in sorting out such matters as depth of source, spall, and tectonic release.

McGarr: Seismic networks can assess yields within a factor of 2 for chemical and nuclear explosions of 1 kt or greater. For discrimination between chemical and nuclear explosions with yield less than 5 kt, local observations, possibly underground, are probably necessary. Moreover, compact, buried chemical explosions greater than 5 kt seem improbable.

Richards: In the early 1960s, when seismology really got started on the identification problem, the need was to discriminate between explosions and earthquakes, and to make progress we had to carry out much basic research about earthquakes. Now, in the mid 1990s, to learn to discriminate between chemical and nuclear explosions, we have to learn basic properties of chemical explosions as used in practice for various purposes such as mining and quarrying. Mining is a very big industry, on the scale of billions of dollars per year, and it is common to hear that “every mine is different.” However, the characteristics of ripple firing (the practice that dominates use of chemical explosives) are more or less the same from region to region, and seismic methods alone can discriminate these types of blasts without use of nonseismic methods.

Zucca: If transparency provisions for zero-time, on-site measurements of large chemical explosions are included in the CTBT, we will need to define a measurement suite. At this time, I would recommend a combination of gas sampling for radioactive noble gases, strong-motion seismic sensors for shock-wave recording, a local seismic network for determining aftershock locations, and low-frequency electromagnetic sensors for pulse detection. This sensor suite should be tested on large chemical explosions so that the interactions can be understood before it is needed on a treaty-sanctioned deployment.

09-29-93

1: 20000

